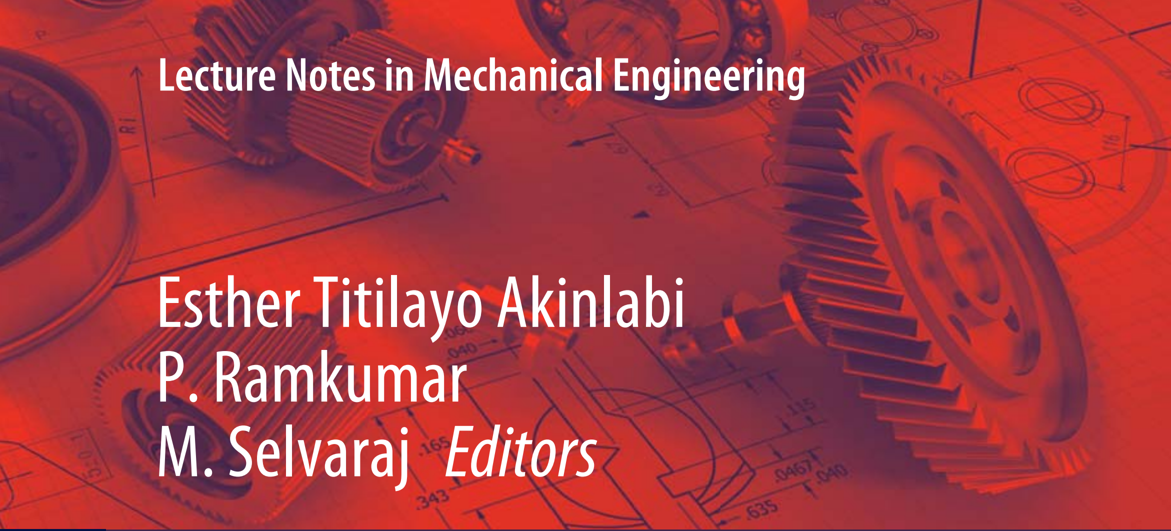

Lecture Notes in Mechanical Engineering

Esther Titilayo Akinlabi
P. Ramkumar
M. Selvaraj *Editors*

Trends in Mechanical and Biomedical Design

Select Proceedings of ICMechD 2019

Springer

Lecture Notes in Mechanical Engineering

Lecture Notes in Mechanical Engineering (LNME) publishes the latest developments in Mechanical Engineering—quickly, informally and with high quality. Original research reported in proceedings and post-proceedings represents the core of LNME. Volumes published in LNME embrace all aspects, subfields and new challenges of mechanical engineering. Topics in the series include:

- Engineering Design
- Machinery and Machine Elements
- Mechanical Structures and Stress Analysis
- Automotive Engineering
- Engine Technology
- Aerospace Technology and Astronautics
- Nanotechnology and Microengineering
- Control, Robotics, Mechatronics
- MEMS
- Theoretical and Applied Mechanics
- Dynamical Systems, Control
- Fluid Mechanics
- Engineering Thermodynamics, Heat and Mass Transfer
- Manufacturing
- Precision Engineering, Instrumentation, Measurement
- Materials Engineering
- Tribology and Surface Technology

To submit a proposal or request further information, please contact the Springer Editor of your location:

China: Dr. Mengchu Huang at mengchu.huang@springer.com
India: Priya Vyas at priya.vyas@springer.com
Rest of Asia, Australia, New Zealand: Swati Meherishi at swati.meherishi@springer.com
All other countries: Dr. Leontina Di Cecco at Leontina.dicecco@springer.com

To submit a proposal for a monograph, please check our Springer Tracts in Mechanical Engineering at http://www.springer.com/series/11693 or contact Leontina.dicecco@springer.com

Indexed by SCOPUS. The books of the series are submitted for indexing to Web of Science.

More information about this series at http://www.springer.com/series/11236

Esther Titilayo Akinlabi · P. Ramkumar ·
M. Selvaraj
Editors

Trends in Mechanical and Biomedical Design

Select Proceedings of ICMechD 2019

Springer

Editors
Esther Titilayo Akinlabi
University of Johannesburg
Johannesburg, South Africa

P. Ramkumar
Indian Institute of Technology Madras
Chennai, Tamil Nadu, India

M. Selvaraj
Sri Sivasubramania Nadar (SSN) College
of Engineering
Chennai, Tamil Nadu, India

ISSN 2195-4356 ISSN 2195-4364 (electronic)
Lecture Notes in Mechanical Engineering
ISBN 978-981-15-4487-3 ISBN 978-981-15-4488-0 (eBook)
https://doi.org/10.1007/978-981-15-4488-0

This Springer imprint is published by the registered company Springer Nature Singapore Pte Ltd.
The registered company address is: 152 Beach Road, #21-01/04 Gateway East, Singapore 189721, Singapore

Preface

We are delighted to publish the selected papers presented in the second international conference on Mechanical Engineering Design 2019 (ICMechD 2019) held at Sri Sivasubramania Nadar (SSN) College of Engineering, Chennai, India during 25–26 April 2019.

In this book, around 100 quality papers in the areas of design of machines and mechanisms, fatigue and fracture mechanics, finite element analysis, fluid mechanics and heat transfer, robotics, biomedical and control engineering, thermal and engine engineering, tribology, wear and surface engineering and vibration engineering were selected for publication.

We are happy to put together this collection of thoughtful papers on the theme of "Mechanical Engineering and Biomedical Design". We are sure that this book will help to nurture knowledge among the research society.

We are grateful to the reviewers for their valuable suggestions for improving the quality of the papers. Also, we thank the session chairs and organizing committee members for their steadfast support and suggestions.

Johannesburg, South Africa — Esther Titilayo Akinlabi
Chennai, India — P. Ramkumar
Chennai, India — M. Selvaraj

Contents

About the Editors

Professor Esther Titilayo Akinlabi is a Full Professor at the Department of Mechanical Engineering Science, Faculty of Engineering and the Built Environment, University of Johannesburg, South Africa. She has had the privilege to serve as a Head of Department of the Department of Mechanical Engineering Science and as the Vice Dean for Teaching and Learning at the University of Johannesburg. Her research interest is in the field of modern and advanced manufacturing processes – Friction stir welding and additive manufacturing. Her research in the field of laser based additive manufacturing includes laser material processing and surface engineering. She also conducts research in the field of renewable energy, and biogas production from waste. She is a rated National Research Foundation (NRF) researcher and has demonstrated excellence in all fields of endeavors. Her leadership, mentorship and research experience is enviable as she guides her team of postgraduate students through the research journey. She is a recipient of several research grants and has received many awards of recognition to her credit. She is a member of the prestigious South African Young Academy of Science and registered with the Engineering Council of South Africa. Prof Akinlabi has filed two patents, edited two books, published five books and authored/co-authored over 400 peer-reviewed publications.

Dr. P. Ramkumar is currently working as an Associate Professor in the Department of Mechanical Engineering in IIT Madras. Prior to coming to IIT Madras, he was an Associate Professor at SSN College of Engineering, Chennai. Dr. Ramkumar received his B.E in Mechanical Engineering from College of Engineering, Guindy, Anna University and his M.Tech (Industrial Tribology) from IIT Madras. He obtained his Ph.D. (2003-07) from University of Southampton with specialisation of Engine Tribology, UK and did his post-doctoral fellowship in University of Leicester (2009-10), UK for developing high speed Cam-Tappet tribometer Rig. He has 14 years research experience in the field of tribology and engine tribology. He won the best presentation award for his PhD from IMechE, London, UK in 2005. His primary research interests are in the field of tribology, engine tribology, gearbox design, wind turbine gearbox bearing failures, biotribology, multilayer coatings, ionic fluids, wear modelling and developing new composite materials for brake applications. He has published more than 20 papers in peer-reviewed journals and 40 international conference proceedings including 1 patent as well. As sole PI, he has received two research grants with total worth of US $1.4M, while as Co-PI US $ 14M from DST. Currently, he is handling a lot of consultancy projects from GE, Caterpillar, Rane, Ford, Kone Elevator and L&T. In his supervision 3 MS scholars and 14 M. Tech. students were graduated and currently he is supervising 8 Ph.D., 5 MS research scholars, 2 project associates, 1 JRF and 2 M.Tech. degrees students. He is a member in IMechE, IoP, STLE, and life time member in TSI. He is reviewer to various top journals including Applied Surface Science, Mechanism and Machine Theory, Part J : Journal of Engineering Tribology, Surface Coatings and Technology, Tribology International, Tribology Letters, Wear, etc.

Dr. M. Selvaraj, Associate Professor in the Department of Mechanical Engineering at Sri Sivasubramania Nadar (SSN) College of Engineering has over 20 years of teaching experience. He did his B.E. in Mechanical Engineering from Madurai Kamaraj University, M.E. in Engineering Design from Government College Technology, Coimbatore and Ph.D. from Anna University, Chennai. His research areas are mechanical vibrations, composites and modeling of friction stir welding. He has authored 14 papers in journals of national and international repute and presented over 20 papers in various conferences. He is a member of Indian Society of Technical Education (ISTE) and American Society of Mechanical Engineers (ASME).

Design of Machines and Mechanism

Rigid Logged Coupling: An Improved Coupling with Less Material and Low-Stress Concentration

Aniket Modak

Abstract The paper is about a new coupling design that can be used to connect two shafts in the same line without any axial or angular misalignment. The goals of the new design are to reduce the amount of material required to produce other couplings and reduce the chances of failure due to different stress distribution patterns. Rigid flanged coupling is used as a reference for comparison. The design consists of mainly three parts body, pins and logs (strips of metal used to connect the body). The holes are done on outer surfaces of the hexagonal or a square prism of each body while one surface of each body faces each other. The logs are used to join the two bodies with the help of pins in the holes. The coupling is designed using Autodesk Fusion 360. Proper mathematical analysis of the couplings is done to get the difference in the material used. This design can be used to connect both, shafts with the same diameter or shafts with different diameters. The design has less stress concentration around holes and in whole design in general and is similar in the manufacturing process as the presently available couplings. For the safety of the operator or user, the coupling is covered with a protective case to avoid the failed parts (if any) to hit the operator or the user. The dimensions are found using stress analysis and considering the modes of failure for each section of the part. Shear and tensile failure have been considered at the parts of the assembly. The bending effect has also been considered for parts wherever adequate. The stress analysis results have also been found out using Autodesk Fusion 360. To observe the effects and results of stress analysis, similar working conditions have been simulated with the coupling designed in Autodesk Fusion 360.

Keywords Coupling · Rigid · Logged · Design

A. Modak (✉)
Jalpaiguri Government Engineering College, Jalpaiguri, West Bengal, India
e-mail: am2019@me.jgec.ac.in

E. T. Akinlabi et al. (eds.), *Trends in Mechanical and Biomedical Design*,
Lecture Notes in Mechanical Engineering,
https://doi.org/10.1007/978-981-15-4488-0_1

1 Introduction

Most of the rigid couplings popularly in use today comprise two flanges attached to each other and transmitting motion, power and torque. This particular method of coupling is required to join two shafts that are one from the power receiving end and the other power generation end. The flanges, for manufacturing, require a lot of metal and due to the various methods by which they are joined, stress is also concentrated to certain parts which lead to failure of the flanges or a high factor of safety needs to be considered.

The use of the designed coupling is to use less material considering the same factor of safety and even more reduction of material when less factor of safety is considered due to the reduction in stress concentration in power transmission areas.

2 Design Process

2.1 Logged Coupling

See Figs. 1 and 2.

2.2 Empirical Relations [1]

Empirical relations are mostly the pre derived, assumed and universally accepted relations. In this derivation, the empirical relations are kept the same as rigid flanged coupling.

Fig. 1 Full assembly

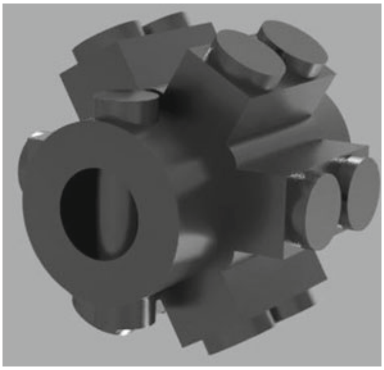

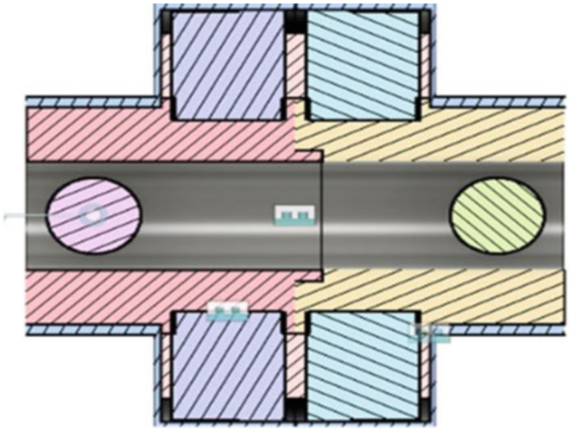

Fig. 2 Section of full assembly

$$d = \sqrt[3]{\frac{16M}{\pi\tau}} \tag{1}$$

$$d_h = 2d \tag{2}$$

$$l_l = d \tag{3}$$

$$l_h = 1.5d \tag{4}$$

$$t = d \tag{5}$$

$$D_{\text{in}} = 2.5d \tag{6}$$

$$b_1 = 1.25d = \frac{D_{\text{in}}}{2} \tag{7}$$

$$d_1 = \frac{0.5d}{\sqrt{N}} \tag{8}$$

In the above relations, the terms used have the following meanings (Table 1):

d Diameter of the shaft
M Moment
τ Torque to be transmitted
d_h Diameter of the hub of flange
l_l Length of the flange
l_h Length of the hub
t Thickness of the flanges
D_{in} Inner diameter of the flange (Flanged coupling)

Table 1 Values for no. of side of polygon with respect to diameter in mm

Value of N	d start	d end
3, 4	0	20
6	20	80
8	80	120
10	120	–

All the calculations for rigid logged coupling have been done for diameter size 20–80, that is, $N = 6$

b_1 Size of outer edge
d_1 Diameter of pins.

2.3 *Shear Failure of Log*

See Fig. 3.

$$\textbf{Shear area} = \frac{\boldsymbol{b}}{\mathbf{2}} * \boldsymbol{h}$$

$$\tau = \frac{P}{\frac{b}{2} * h} \tag{9}$$

$$P = \mathrm{M}/\left(\frac{D_{\mathrm{in}}}{2} * \frac{\sqrt{3}}{2}\right) \tag{10}$$

$$b \leq b_1 \tag{11}$$

Fig. 3 Maximum shear area of log

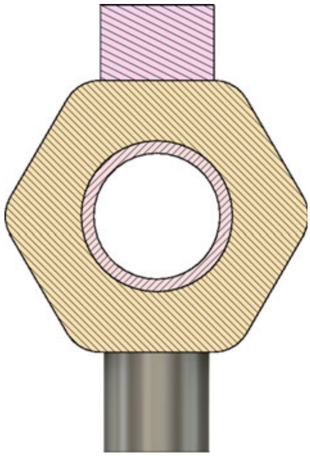

$$\tau = \mathrm{M}/\left\{\left(\frac{D_{\mathrm{in}}}{2} * \frac{\sqrt[2]{3}}{2}\right) * \left(\frac{b}{2} * h\right)\right\} \tag{12}$$

$$b * h = 8\mathrm{M}/\left\{2.5 * d * \sqrt{3} * \tau\right\} \tag{13}$$

$$\tau * \frac{\pi}{4} * d_1^2 = P \tag{14}$$

$$d_1^2 = \mathrm{M}/\tau * \left(\frac{D_{\mathrm{in}}}{2} * \frac{\sqrt[2]{3}}{2}\right) * \frac{\pi}{4} \tag{15}$$

$$d_1 = 4 * \sqrt{\mathrm{M}/\left\{\tau * \left(2.5 * d * \sqrt{3}\right) * \pi\right\}} \tag{16}$$

In the above relations the new terms used has following meanings:
b: Breadth of the log.

2.4 If Pins Are Loosely Kept [Bending Consideration]

See Fig. 4.

$$M = P * \frac{l_b}{2} \tag{17}$$

$$P = \frac{M}{\frac{D_{\mathrm{in}}}{2} * \frac{\sqrt{3}}{2}} = \frac{4M}{2.5 * d * 2 * \sqrt{3}} \tag{18}$$

$$M_b = \frac{4Ml_b}{2.5 * d * 2 * \sqrt{3}} \tag{19}$$

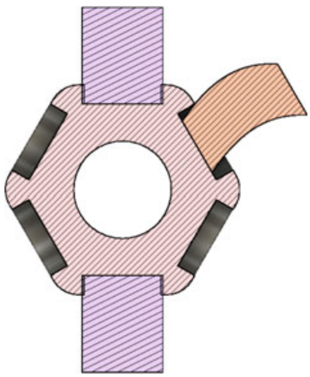

Fig. 4 Bending of pin

$$\sigma_b = \frac{32M_b}{\pi d_1^3} \tag{20}$$

$$\sigma_b = \frac{32}{\pi d_1^3} * \frac{4M}{2.5 * d * 2 * \sqrt{3}} \tag{21}$$

$$d_1 = \sqrt[3]{\frac{64 * M * l_b}{2.5 * \sqrt{3} * d * \pi * \sigma_b}} \tag{22}$$

2.5 Shear Stress in Connecting Pin

See Fig. 5.

$$\tau = \mathrm{P}/\left\{\frac{\pi}{4} * d_2^2\right\} \tag{23}$$

$$\tau = \mathrm{M}/\left\{\frac{d_h}{2} * \frac{\pi}{4} * d_2^2\right\} \tag{24}$$

$$\therefore d_2 = \sqrt{4\mathrm{M}/\{\pi * d * \tau\}} \tag{25}$$

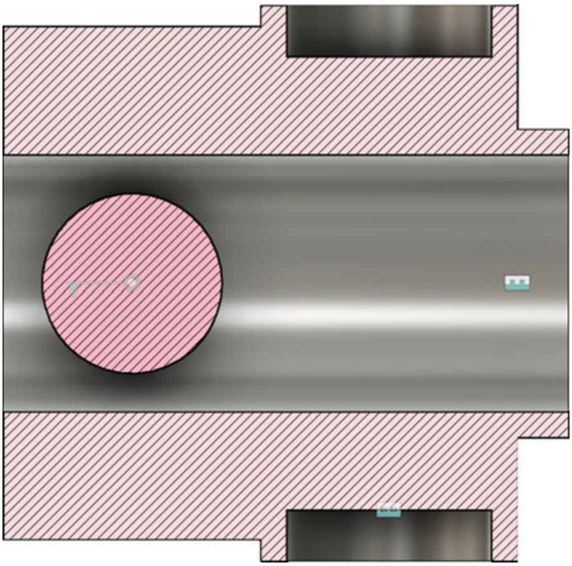

Fig. 5 Shear area of connecting pin

3 Simulation Data and Results

The rigid logged coupling and the rigid flanged coupling were simulated in Autodesk Fusion 360 under different conditions; the conditions of rigid logged coupling having more tough testing conditions.

The conditions and results are listed below for both rigid flanged and rigid logged coupling.

3.1 General Settings

See Tables 2, 3, 4 and 5.

Table 2 General

Contact tolerance	0.1 mm
Remove rigid body modes	No

Table 3 Mesh

Average element size (% of model size)	
Solids	10
Scale mesh size per part	No
Average element size (absolute value)	–
Element order	Parabolic
Create curved mesh elements	Yes
Max. turn angle on curves (deg.)	60
Max. adjacent mesh size ratio	1.5
Max. aspect ratio	10
Minimum element size (% of average size)	20

Table 4 Adaptive mesh refinement

Number of refinement steps	0
Results convergence tolerance (%)	20
Portion of elements to refine (%)	10
Results for baseline accuracy	Von Mises stress

Table 5 Materials

Component	Material	Safety factor
Component 1:1	Steel	Yield strength

Table 6 Mesh

Type	Nodes	Elements
Solids	4800	2682

Table 7 Pressure1

Type	Pressure
Magnitude	4.8 MPa

Table 8 Pressure2

Type	Pressure
Magnitude	1.896 MPa

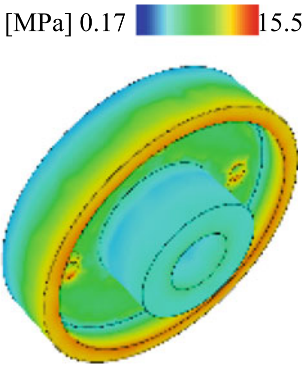

Fig. 6 Von Mises

3.2 *Rigid Flanged Coupling*

See Tables 6, 7, and 8.

3.2.1 Results

See Fig. 6.

3.3 *Rigid Logged Coupling*

Loads (Tables 9, 10, and 11).

Results (Fig. 7).

Table 9 Mesh

Type	Nodes	Elements
Solids	5948	3383

Table 10 Pressure1

Type	Pressure
Magnitude	4.8 MPa

Table 11 Pressure2

Type	Pressure
Magnitude	7.8 MPa

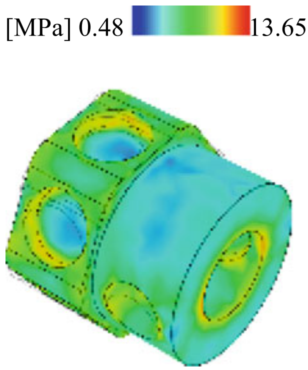

Fig. 7 Von Mises

4 Dimensions for Construction

4.1 Shaft

$$d = \sqrt[3]{\frac{16M}{\pi \tau}}$$

4.2 Flange

$$\begin{aligned} d_h &= 2d \\ l_h &= 1.5d \\ t &= d \end{aligned}$$

$$D_{\text{in}} = 2.5d$$
$$b_1 = 1.25d = \frac{D_{\text{in}}}{2}$$

4.3 Log

$$b * h = \frac{8M}{2.5 * d * \sqrt{3} * \tau}$$
$$l_l = 2d$$
$$b < b_1$$

h is the height of the log.

4.4 Pin

$$d_1 = \sqrt[3]{\frac{64 * M * l_b}{2.5 * \sqrt{3} * d * \pi * \sigma_b}}$$
$$d_1 = 4 * \sqrt{\frac{M}{\tau * \left(2.5 * d * \sqrt{3}\right) * \pi}}$$

4.5 Nut

$$d_{\text{inner}} = d_1$$
$$l_n = 0.8 * d_1$$

4.6 Connector Pin

$$\therefore d_2 = \sqrt{\frac{4M}{\pi * d * \tau}}$$

4.7 Protective Case

$$d_{p_c} = D_{\text{in}} * \frac{\sqrt[2]{3}}{2} + 2h + 10$$

4.8 Material Saved as Compared to Rigid Flanged Coupling

$$5.14488467d^3 - 6bhd - \frac{\pi}{8}Ndd_1 + 15\pi d_1^2$$

5 Conclusions

The following comparisons can be drawn by the analysis of the two couplings namely the rigid flanged and the rigid logged one (Table 12).

With respect to the results of simulations and derived equations, it can be stated that logged coupling gives a better performance with less material and stress concentration.

Table 12 Comparison

Serial No.	Rigid flange coupling	Basis	Rigid logged coupling
1.	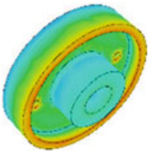 Maximum: 15.5 MPa	Stress	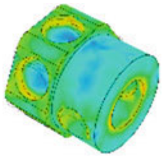 Maximum: 13.65 MPa
2.	Excess material required to be built	Material	$5.14488467d^3 - 6bhd - \frac{\pi}{8}Ndd_1 + 15\pi d_1^2$ Volume material saved

Reference

1. Design of Machine elements by Bhandari

An Efficient Grey Water Stagnancy Handler

K. Banumalar, M. Aiswarya, M. Asvanthini Eswari, and M. Karthika

Abstract This work proposes the idea of "Human hair boom skimmer" in addition to the conventional flow grey water treatment. The conventional method of treating grey water doesn't pose a promising solution in reducing the amount of oil content from it. Rather than discarding the human hair, it can be used to absorb the oil from the grey water. The oil adsorption capability of wasted hair fibers could produce valuable solutions for our prevalent and modern society. Our concept "An Efficient Grey Water Stagnancy Handler" concentrates on three major phases: Phase-1, deals with the drastic problem being faced by the surrounding environment with slip and falls due to the improper collection of grey water from the bathroom floors, Phase-2 address the eco-friendly and cost-efficient methodology to treat the grey water, Phase-3 tackles the dwindling water resources for crops cultivation by the diversion of processed water to the required place wherein immediate need of it. Thereby, the grey water from the bathroom sink is no doubt a valuable resource that can be used to alleviate the water shortage problems and increase water conservation in individual households. Therefore, an alternative eco-friendly method rather than the conventional method as mentioned above could pose a firm solution.

Keywords Grey water · Skimmer · Irrigation control

1 Introduction

This work on "An efficient grey water stagnancy handler" highlights the solutions for the slip and falls in the bathroom, water scarcity for crops cultivation, dwindling of ground water resources. Every year about 235,000 people over age 15–65 visit emergency rooms because of injuries suffered in the bathroom, and almost 14% are being hospitalized. In this case, about one-third of the injury happens while bathing or showering. Injuries increase with the age and get peaking after 85, according to

K. Banumalar (✉) · M. Aiswarya · M. Asvanthini Eswari · M. Karthika
Department of Electrical and Electronics Engineering, Mepco Schlenk Engineering College, Sivakasi, Tamil Nadu, India
e-mail: kbanumalar@mepcoeng.ac.in

E. T. Akinlabi et al. (eds.), *Trends in Mechanical and Biomedical Design*,
Lecture Notes in Mechanical Engineering,
https://doi.org/10.1007/978-981-15-4488-0_2

the research results. But injuries around the tub or shower are proportionately most common among those ages 15–24 and least common among those over 85. Injuries in or near the bathtub or shower account for more than two-thirds of emergency room visits. In addition to this, about 85% of water resources are deployed in the agriculture sector in India. Every year, hundreds of farmers committing suicides and unable to deal with the devastating effects of water shortages on their crop production. Small farmers being poor and can't afford more advanced agriculture tools to extract water and to conserve it. The adversity for small farmers is poverty and illiteracy. As the population increases, the utilization of groundwater and surface water for the domestic, industrial sectors and agriculture exaggerate, leading to tensions and extreme pressure on the environment. Groundwater is a critical resource for farmers. Over half the irrigated agricultural areas is dependent on groundwater. According to 2016 World Bank report made it clear that our groundwater levels are sharply falling and showing a downward trend. Over 50% of the country is already facing extremely high-water stress. This document explains the ways and means to avoid the stagnation of water in the bathroom and also poses the solution to reduce the oil content in the grey water than by the conventional treatment method [1, 3] and to meet the dwindling water resources for the crop cultivation. The objective of our work:

1. To reduce the oil content in the grey water with an idea of human hair boom and coconut husk skimmer.
2. To improve the oil content reduction than the conventional grey water treatment method.
3. To clear the blockage for plants to produce food through photosynthesis with no effect of oil content in recycled grey water.

2 Proposed System

The overall system has been divided into three major parts, which include stagnancy prevention, grey water treatment, and garden irrigation as shown in Fig. 1.

2.1 Phase-1: Stagnancy Handler—Effective Collection

Figure 2 shows the implementation of stagnancy handler with the help of pervious concrete. The main objective of this part is to collect the water that falls on the bathroom floors with the implementation of pervious concrete tiles over the floors [2]. As of now, the grey water has been diverted through small opening from the bathrooms. It is clear that not fully the entire water that falls on the floor gets diverted. Little or some water may stagnant in the floors which makes the floor prone to slip. Therefore, it's very important to make the floor free from water so that contact

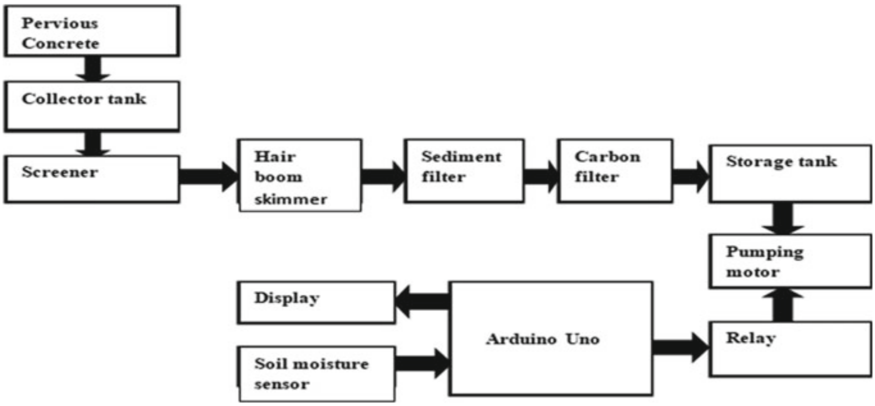

Fig. 1 Overall flow of an efficient grey water stagnancy handler

Fig. 2 Implementation of pervious concrete

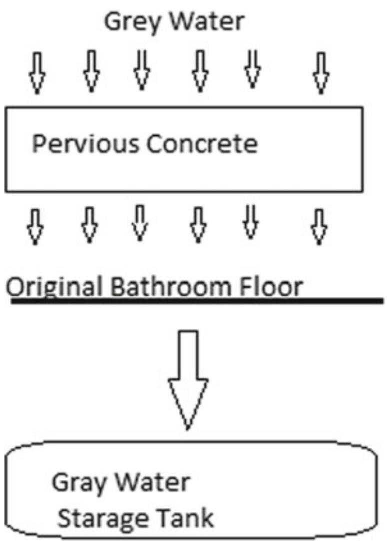

between the feet and ground is never lost, thereby the possibility of loss balance can be reduced. Pervious concrete can be inserted as tiles, over the bathroom ground area so that water that falls on it would get percolate through them and made to get collected in a storage tank.

2.2 Phase-2: Water Retreatment

Grey water denotes the waste water coming from the bathroom floors. This grey water collected in a storage tank can be reused for non-potable purposes, with mild filtration. According to the study about the characteristic of this grey water, it is clear that grey water can be reused in gardens with little or no treatment.

Besides, the untreated grey water can't be stored for more than one day. The organic matter present in it gets multiplied over time results in bad odour and makes the water unhealthy. It may also pose serious issues when this water (with pathogens from sick people) comes into contact with humans. However, if the water left untreated, this water can't be extended for our future use. After taken into consideration, its effect and nature it is necessary to treat the water to remove the bacteria and viruses. Figure 3 depicts the proposed grey water treatment.

This treatment includes three stages:

Stage 1: Screening: water collected in the storage tank is made to pass through lint filter, thereby small suspended particles in grey water would be eliminated.

Stage 2: Human Hair boom skimmer [3], the grey water contains oils in it which may remove efficiently by using hair boom. As these hair booms are made of nylon cloth filled with human hair, thereby making it cost-efficient when compared to other skimming polymer materials. The manual operation of this hair boom skimming process has been undertaken in an environmental laboratory and positive testing results are obtained from the final skimmed water sample.

Stage 3: Filtration

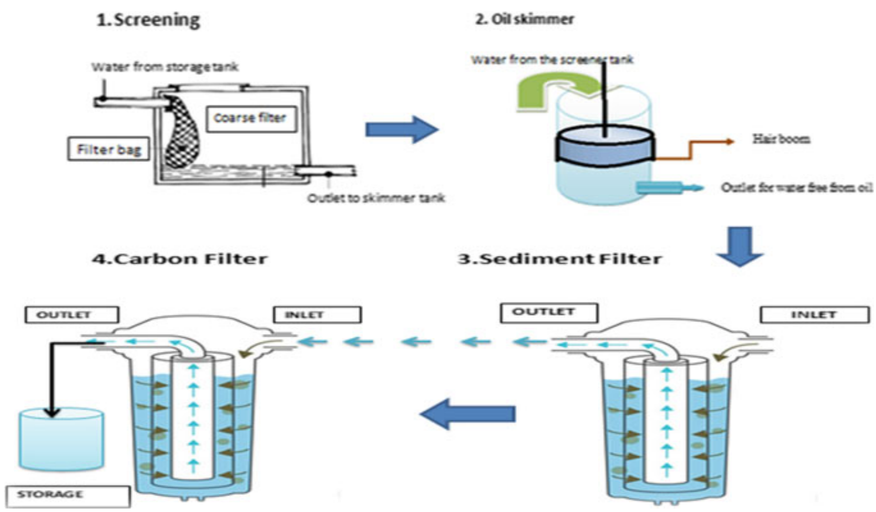

Fig. 3 Proposed water treatment method

- Sediment filter: Sediment filter acts as a sieve to remove any particulate matter that can be transported by fluid flow and which eventually is deposited as a layer of solid particles on the bed or bottom of the grey water.
- Carbon filter: Carbon filtering is a method of filtering that uses a bed of activated carbon to remove contaminants and impurities using chemical adsorption.

After the completion of the entire treatment, the water should be suitably stored in a storage tank.

2.3 Phase-3: Auto Irrigation Control

The treated water is now suitable for watering gardens. In order to make the irrigation to plants automatic and efficient, by sensing the moisture content of the soil the water is diverted to the plant's usage. As a result, plants would get sufficient supply of water depending upon its requirement without overflow and prevents the spoilage of root system [4].

Figure 4 depicts the auto irrigation control, which is achieved with the help of interfacing soil moisture sensor, pumping motor, and display with Arduino Uno. With the sensing of soil moisture content, the motor turns on and off to pump the water.

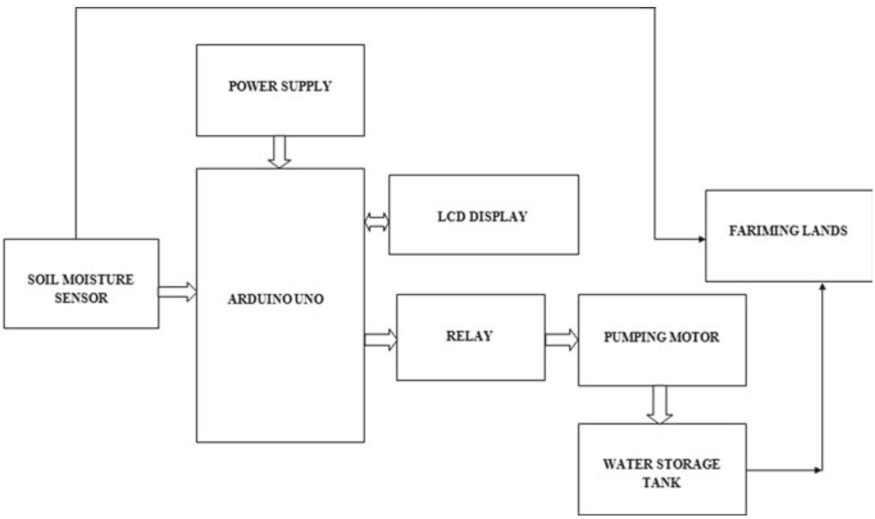

Fig. 4 Auto irrigation control

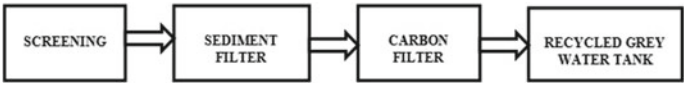

Fig. 5 Conventional treatment method

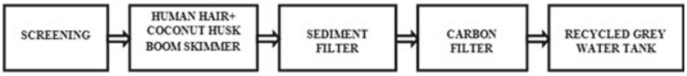

Fig. 6 Grey water treatment employed with human hair and coconut husk

3 Results and Analysis

3.1 Conventional Grey Water Treatment

Figure 5 shows conventional treatment method. Initially the grey water is screened to remove the small and medium particles present in it. After the screening process, the treatment of grey water is followed by passing the outcome of screened grey water into the sediment filter. In this sediment filtration, very small particulates get removed and it is sent to the carbon filter to reduce the hardness content in the grey water. Finally, the water is being collected into a recycled storage tank for future usage. The treated grey water sample is found with oil content left in it. When this water is being used for plantation purposes, the plant growth is diminishing day by day.

3.2 Novel Idea of Grey Water Treatment

In order to reduce the amount of oil content in the resultant treated sample, a novel idea is proposed to introduce the human hair and coconut husk skimmer between the screening and sediment filtration process as shown in Fig. 6. The resultant grey water after the skimming with human hair and coconut husk and with the conventional flow, the amount of oil content is greatly reduced [5–10].

3.3 Hardware Arrangement

Figure 7 depicts the complete flow of the project from left to right. The process starts with the effective collection of grey water from the bathroom floors with an arrangement of pervious concrete over the floors. The collected water from the floors is collected in a pink storage tank. The water from the pink tank is pumped into the

Fig. 7 Hardware setup

orange storage tank with the help of mini submersible water pump(motorpump1). The water pumping is controlled with the help of two float switch(waterlevelsensor1and waterlevelsensor2) inside the skimming tank. The grey water once reached the top float switch the motor 1 in the storage tank turns off. The wheel and clamp arrangement with hair and coconut husk enters into the up and down motion for a period of 10 s. After this, the wheel setup moves forward by giving pulse to 2 dc motor in the wheel to reach the compressing tank with sieve arrangement to dispose of the adsorbed oil content in the boom through to and fro motion into the sieve. After compression, the wheel is given with the pulse to move backward and to reach the skimmer tank for further filtration. This process continues and the entire flow is being controlled by the Arduino Mega kit. The water from the skimming tank is pumped into another storage tank with the help of motorpump2 after the skimming process. The treated grey water is now allowed to pass through two filters sediment and carbon filter to remove the hardness content in the grey water. The treated water from the filters is now stored in a tank for the auto irrigation purpose. This control is achieved with the sensing of soil moisture content and Arduino control. Depending upon the moisture content the water pumping turns on and off.

3.4 Experimental Result

Our experimental results are shown in Table 1.

Our experimental results are shown in Table 1. The quantity of input grey water sample is about 3.5 L and the quantity of output grey water sample is about 2.5 L. In conventional grey water treatment the amount of oil content reduction is about 11.27% whereas, with human hair and coconut husk, it is found that the reduction of

Table 1 Comparative analysis of grey water samples

S. No	Method of treatment	Amount of oil content (mg/L)	Percentage of decrease (%)
1	Conventional method [5]	282.3	11.27
2	Coconut husk skimming method	300.18	5.6
3	Oil skimming method (human hair boom + coconut husk)	250.48	21.25
4	Combination of three methods (human hair boom skimming + coconut skimming + conventional method) [6]	166.9	47.51

Quantity of input water sample = 3.5 L
Quantity of output water sample = 2.5 L
Amount of oil content in untreated grey water sample = 318.08 mg/L

oil content is 21.25%. The entire treatment process of our project results in 47.51% reduction of oil content in the grey water sample.

4 Conclusion

This project thereby highlights the socio-economic importance of the grey water handling technique to meet the following situations, with the reuse of discarded human hair, the additional stress on the environment by human hair waste disposal can be drastically reduced. The effective collection of grey water from bathroom floors with the use of pervious concrete can reduce the slip and fall accidents faced by the seniors inside the bathrooms. Water scarce problems for the farming lands can be met out for this proposed method.

References

1. Jadhav AS, Naniwadeka MY, ShindeN HS, Anekar V (2011) Study of adsorbtion of oil from oily water using human hair. Int J Adv Eng Technol II:37–51
2. Obla KH (2010) Pervious concrete—an overview. Indian Concr J 84(8)
3. Gupta A (2014) Human hair waste and its utilization: gaps and possibilities, Hindawi Publishing Corporation. J Waste Manage
4. Capral A (2001) Scicolone: wastewater reuse by drip irrigation. Trans Biomed Health 5
5. Parameshwara Murthy PM, Sadashiva Murthy BM, Kavya S (2016) Greywater treatment and reuse: a technological review. Crit Rev Environ Sci Technol 41(7):657–698
6. Singh S, Pradhan N, Ojha n, Roy b, Bose S (2016) Grey water treatment and its application in cultivation of plants. Asian J Asian J Microbiol Biotechnol Environ Sci 18(4)

7. Ingole NW (2013) Adsorption of oil from waste water by using human hair. J Environ Sci Comput Sci Eng Technol 3
8. Capra A (2011) Wastewater reuse by drip irrigation. Trans Biomed Health 5
9. Libutti A, Gatta G, Gagliardi A, Vergine P, Pollice A, Beneduce L, Disciglio G, Tarantino E (2018) Agro-industrial wastewater reuse for irrigation of a vegetable crop succession under Mediterranean conditions. Agric Water Manage 196:1–14
10. Valipour M, Singh VP (2016) Global experiences on wastewater irrigation: challenges and prospects. In: Balanced urban development: options and strategies for liveable cities

Experimental Design and Testing of Scale Development Reduction System in Domestic Water Geysers

Kabilan Sankar, Karthick Selvam, and K. Joy Ashwin

Abstract The aim of this project is to reduce the extent of scale formation in domestic water geysers with minimal investment that is efficient in cleaning and can be commercialized for consumer use. Modern water geysers have the disadvantage of a life of maximum of one year due to formation of scales on the heating coil and the walls of the geyser thereby reducing the efficiency of boiler and decreasing the life of geyser. The geyser is to be fitted with a 3D printed polymer float bounded by a soft brush. The variation in level of water inside the geyser will cause up and down movement of the float, brushing the internal wall of the geyser removing any salt presence. A nozzle system will be activated during the manual cleaning phase to provide a more efficient cleaning for the internal parts of the geyser and to wash away the salts from the brushes while drain them through a separate pipe. A valve system controls the direction of flow of fluid during the cleaning. The testing was done for a period of 240 days. The results showed a significant improvement in the performance of the geyser and reduced the extent of scale formation.

Keywords Domestic water geyser · Scale formation · 3D printed polymer float · Nozzle system · Valve system

1 Introduction

Scale formation occurs due to the presence of salts in water. Generally, water is classified into two types based on presence of salt. One type is hard water, and the other type is soft water. The main reason for scale formation in the water geyser is hard salts that present in the water. The presence of hard salt in water leads to clogging of the geyser outlet pipe and malfunction of electrical units due to leakage

K. Sankar (✉) · K. Selvam · K. J. Ashwin
Department of Mechanical Engineering, KCG College of Technology, Chennai, India
e-mail: sankar.kabilan@gmail.com

K. Selvam
e-mail: karthicksks473@gmail.com

E. T. Akinlabi et al. (eds.), *Trends in Mechanical and Biomedical Design*, Lecture Notes in Mechanical Engineering,
https://doi.org/10.1007/978-981-15-4488-0_3

of water leading to formation of scale formation of salt deposition and rust formation which in turns to corrosion. Scale formation also leads to gradual occurrence of pitting on the inner metal surface forming minute cracks or craters. McAdam and Parsons [1] performed experiments on calcium carbonate scale formation and control. Muryanto et al. [2] demonstrated the effects of calcium carbonate and salt deposits in clogging of pipes and major pipelines. Gal et al. [3] have performed experiments on calcium carbonate salt solubility in pipe clogging and their formation on the circumference of pipes. Kourtidou et al. [4] have worked on the impact of scale deposition in geysers and their connection to corrosion of metal. Tyler et al. [5] worked on experiments that studied the growth of scale deposition with increase in temperature. The scale formation in water geyser will reduce the life expectancy of the geyser and damages the electrical wiring in the form of leaks [6]. There are two types of hardness in water, temporary hardness and permanent hardness. Temporary hardness is a type of water hardness caused by the presence of dissolved bicarbonate minerals (calcium bicarbonate and magnesium bicarbonate). When dissolved, these minerals yield calcium and magnesium cations and carbonate and bicarbonate anions (CO_3^{2-}, HCO_3^{-}) [7]. Permanent hardness is hardness that cannot be removed by boiling. When this is the case, it is usually caused by the presence of calcium sulfate/calcium chloride and/or magnesium sulfate/magnesium chloride in the water, which do not precipitate out as the temperature increases. The presence of the metal cations makes the water hard [8] and increases the rate of salt deposition on the surface of the vessel in use [9, 10]. Hence, it will increase the maintenance cost and decrease the life expectancy of the geysers.

2 Methodology

Initially, two identical one-liter water geysers were selected for performing this experiment. Water geyser 1 did not have the scale reduction system installed inside, whereas water geyser 2 had the scale reduction system installed inside it. Water geyser 1 was used at a frequency of twice a day for a 240-day period. Water geyser 2 had its tank drilled at two locations, nozzles were installed on the walls of the geyser and the float is fitted inside the geyser. The float has some clearance between the geyser wall and itself which is filled by the brush. This brush bounds the float. The buoyancy force by the inlet water pushes the float up, brushing against the wall scrapping any salt presence. The cleaning phase was done once every month, thus totaling for eight times during this experiment. The properties of water such as hardness and salt deposits in it were periodically tested every month. The growth of scale development inside the geyser was also noted. Results were tabulated and plotted in the form of graphs.

3 Experiment Details

3.1 Construction

The water geyser tank was made up of stainless steel. The two side of the cylindrical tank was drilled for attaching nozzles. The nozzles were attached to the cylindrical wall, with the help of adhesives, to spray the water to the internal surface of tank to reduce the initial scale formation. The two valves are connected to the geyser system to control water flow as shown in Fig. 1. The one pair of valves was connected in the inlet to control inlet flow and another pair was connected in the outlet to control outlet flow. The ABS polymer float was placed inside the water geyser. The brush bounds the ABS polymer float to wipe out the scale formation vertically inside the geyser. The connecting pipes were used to connect the nozzle and valves to allow the fluid to the inlet flow. The gray water that is present inside the geyser after the

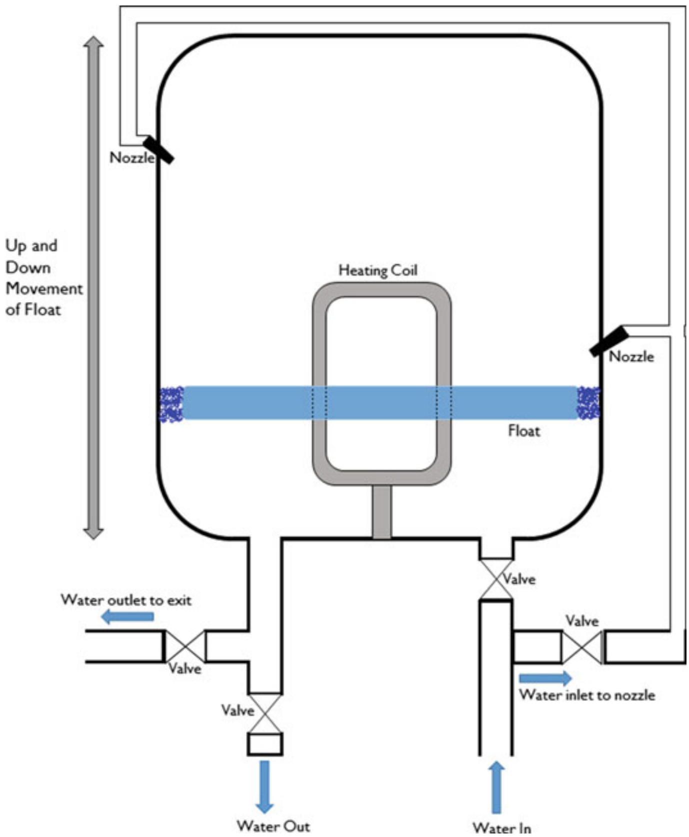

Fig. 1 Construction design of water geyser

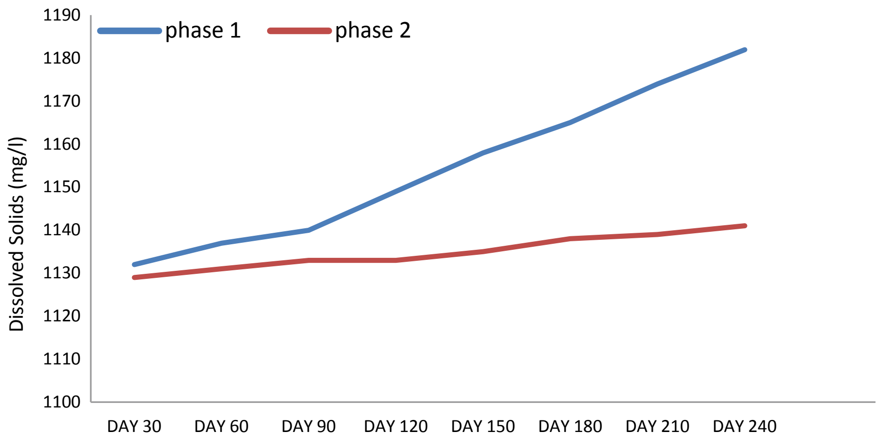

Fig. 2 Comparison of total dissolved solids in mg/l

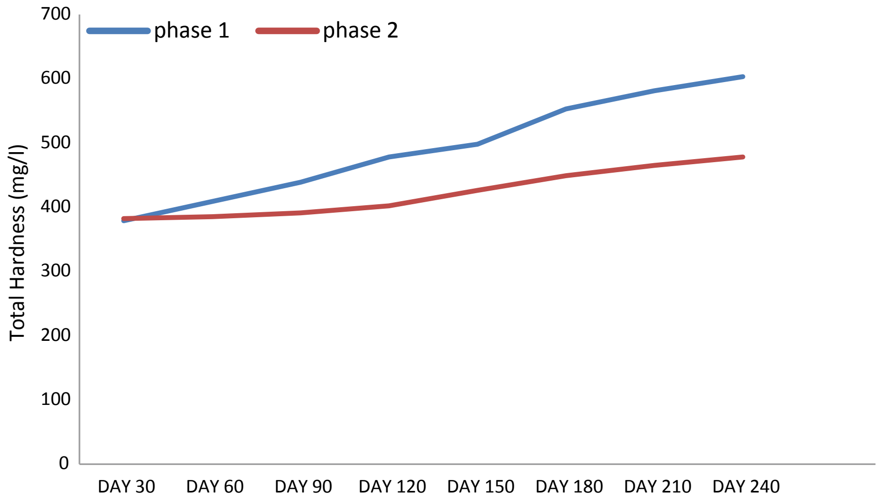

Fig. 3 Comparison of total hardness in mg/l

cleaning phase is exited through a separate outlet drain where the water is diverted using the valve system.

3.2 *Working*

The primary aim of the project is to study the formation of scales in the geyser and its effects on the efficiency of boiler, water output, and clogging of pipes. Testing of water was initiated to get the result for the two phases. Water from both the geysers were provided for testing at an external water testing laboratory in Chennai, India. The results of water hardness and dissolved solids were obtained directly from the laboratory upon submission of water samples. From the results of these two phases, we performed an analysis to compare both the set of results to find the conclusion.

Phase 1
The geyser was setup without our cleaning system to test the scale deposition rate and water quality for 34 weeks. The geyser was operated at a frequency of two times per day for 240 days where the water was heated to a temperature of 85 °C. The input water sample was tested initially. After a period of 240 days, we opened up the geyser to find out the thickness of scale deposited in the geyser. The rate of scale development was studied every month. The hardness and salt deposits value of the water were also noted. The results were tabulated.

Phase 2
Now, the geyser was setup with our cleaning system, and the same frequency of operation was continued for a period of 34 weeks. The cleaning was done once per month. The geyser operated well for 240 days heating water to a maximum temperature of 85 °C. The rate of scale development was studied every month. The hardness and salt deposits value of the water were also noted. The results were tabulated.

4 Results

4.1 Sample Collection and Testing

The output of the experiment is based on three parameters, total dissolved salts, total hardness content, and scale formation layer. Our aim is to reduce the value of these parameters by implementing our cleaning system. At the end of every 30-day period, we collected water sample from the output of the geyser. As phase 1 does not have any cleaning system, we could directly collect the water from the outlet of the geyser. However, in phase 2, the cleaning system is activated and only after that the water sample is collected from the geyser. The water samples are collected and submitted for testing at an external water testing laboratory in Chennai, India. The laboratory tests the water for total dissolved salts and total hardness, and we got the results directly from them. The results of each period are tabulated and plotted in the form of a graph.

Phase 1: without scale reduction system
Phase 2: with scale reduction system.

Table 1 Total dissolved solids in mg/l relative to the number of days

	Day 30	Day 60	Day 90	Day 120	Day 150	Day 180	Day 210	Day 240
Phase 1	1132	1137	1140	1149	1158	1165	1174	1182
Phase 2	1129	1131	1133	1133	1135	1138	1139	1141

4.2 Total Dissolved Solids

The water sample is collected from the geyser at the end of every 30-day period to test for content of dissolved solids present in the water. Both the phases are started on the same day. At the end of the 30-day period, water sample is collected from the outlet of the geyser and sent for testing to an external water testing laboratory. It can be seen from the results table that the value of total dissolved solids increases rapidly in phase 1 geyser compared to phase 2 geyser. In phase 1, the scale development is more, and hence, there is a possibility of those salts on the walls of the geyser to be dissolved into the new water that has entered the geyser. In phase 2 geyser, the cleaning system removes the salt clearing the internal walls of the geyser of any salt. Thus, the rise in value is minimal for phase 2 (Table 1).

4.3 Total Hardness Content

The water sample is collected from the geyser at the end of every 30-day period to test for total hardness content present in the water. Both the phases are started on the same day. At the end of the 30-day period, water sample is collected from the outlet of the geyser and sent for testing to an external water testing laboratory. Hardness of water generally depends on the area of source of water and increases with frequency of usage of geyser since more salts get deposited over a period of time as evident in the results of phase 1. However, in phase 2, the geyser with the cleaning system is able to reduce the rate of increase of hardness content because the cleaning system removes the salts deposited from the internal wall of the geyser. Thus, we are able to control the rate of increase of hardness to a considerable extent (Table 2).

Table 2 Total hardness content in mg/l relative to the number of days

	Day 30	Day 60	Day 90	Day 120	Day 150	Day 180	Day 210	Day 240
Phase 1	379	409	439	478	498	553	581	603
Phase 2	382	385	391	402	462	449	465	478

Table 3 Scale formation in mm relative to the number of days

	Day 30	Day 60	Day 90	Day 120	Day 150	Day 180	Day 210	Day 240
Phase 1	0	0.16	0.39	0.53	0.67	0.89	1.0	1.15
Phase 2	0	0	0.1	0.12	0.15	0.18	0.22	0.24

4.4 Scale Formation

Scale formation is the layer of salt deposited on the internal wall of the geyser due to the salts present in the water and frequent heating and cooling of the water present inside the geyser. This layer of scale's thickness varies at different points on the geyser. Thus, we take the average of five readings. The task of measuring the scale thickness is a tedious task as the thickness value is in millimeters. Thus, in order to obtain accurate result, we peeled a small layer of the scale from the geyser wall and measured using a digital gauge. A small layer of scale can be peeled or scraped off the wall. This layer is highly delicate and fragile, and so the utmost care was taken to take the reading as soon as it is peeled within the geyser. Initial readings were tough as the scale layer was of negligible thickness. However, with increase in time, it was possible to obtain the readings by repeated trial and errors (Table 3).

5 Conclusion

It is clear from Fig. 4 that the growth of scale inside the geyser has been brought down to a considerable extent in phase 2 compared to phase 1. The reduced scale film also helped with maintaining the hardness value of the water as shown in Fig. 3, since the

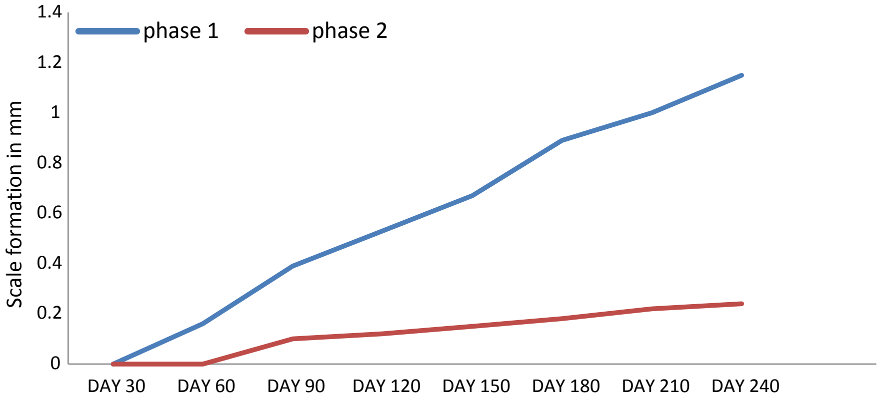

Fig. 4 Comparison of scale formation in mm

presence of salts is lesser inside the geyser. The total dissolved solids in the water are also maintained as shown in Fig. 2 as there is very limited amount of scale film for it to dissolve into. From the overall experiments and analysis performed, we can conclude that the cleaning system proved successful in its task by efficiently removing the scale deposition on geyser with minimal labor. This has had a significant effect on the life of the geyser and improves the durability as such. The installation of this setup is also simplified and easier, thus reducing the maintenance cost of the geyser. Servicing a geyser is a tedious task. It either requires an expert or had to be taken to a service center for servicing. The geyser has to be opened every time, and scales have to be scrapped using an abrasive sheet or any other scale removal method every time. The float system substitutes this process, making the task easier and reducing the scale formation to a considerable extent. Furthermore, the efficiency of the geyser is also increased by consuming less energy when compared to energy consumption during presence of scales in geyser. This can be justified the presence of less salts in the water. Overall, the experiment was successful, and the results are in favor.

References

1. McAdam J, Parsons SA (2004) Calcium carbonate scale formation and control. Published Views Environ Sci Technol 3(2)
2. Muryanto S, Bayuseno AP, Usamah M, Mamun H (2014) Calcium carbonate scale formation in pipes: effect of flow rates, temperature, and malic acid as additives on the mass and morphology of the scale. Procedia Chem 9:69–76
3. Gal JY, Bollinger JC, Tolosa H, Gache N (1996) Calcium carbonate solubility: a reappraisal of scale formation and inhibition. Published Talanta 43(9):1497–1509
4. Kourtidou D, Chaliampalias D, Tarani E, Pavlidou E (2019) Deposition of Ni-Al coatings by pack cementation and corrosion resistance in high temperature and marine environments. Elsevier Corros Sci 148:12–23
5. Tyler J, Taler D (2007) Tubular type heat flux meter for monitoring internal scale deposits in large steam boilers. J Heat Transf Eng 28(3):230–239
6. Jamialahmadi M, Muller-Steinhagen H (2011) Scale formation during nucleate boiling—a review. Corros Rev 11(2)
7. The National Board of Boiler and Water Pressure Vessel Inspectors. https://www.nationalboard.org/index.aspx?pageID=164&ID=224. Last accessed on 23 Jan 2019
8. Shen HJ, Xie ZB (2010) The causes and solutions of boiler scale in steam appliances. Published Appl Mech Mater 37–38:1421–1424
9. Suez Water Technologies Webpage. https://www.suezwatertechnologies.com/handbook/chapter-12-boiler-deposits-occurence-and-control. Last accessed 02 Oct 2018
10. Aries Chemicals Webpage. https://www.arieschem.com/boiler-deposit-scale-control/. Last accessed 10 Sept 2018

Transient Analysis of Rotor System

D. S. Megharaj and Amit Malgol

Abstract This paper introduces a transient vibration investigation of horizontal rotor system with three distinctive disk positions mounted on a shaft, for the simply supported case. The material properties of the shaft and disk are the same. A transient analysis is performed to obtain the amplitudes for three distinctive disk positions. A force is applied on the disk for a small time frame. Design a dynamic rotor structure; it is essential to decide the vibration parameter, i.e., natural frequency, critical speeds, and amplitudes. The transient analysis was performed by "ANSYS" parametric design tool. The results obtained from the analysis are helpful for the design of the rotor system.

Keywords Rotor dynamics · Transient · ANSYS · Amplitudes

1 Introduction

Transient vibration is non-occasional motion occurs in a rotating system. Transient vibration is non-periodic motion in actual circumstances. When a vehicle experiences a pot opening, the amplitudes diminish gradually because of the stiffness, damping, and force acting on the system. The amplitude of the system decreases depending on the system parameters and time. In the transient system, a load is applied for a small period, and hence, due to this time-dependent loading, the vibration decay gradually. The vibration energy must be less than the rotational energy of a system. The parameters of rotating systems play a vital role in maintaining the stability of a system. The systems are classified as a linear system and nonlinear system. All systems, in reality, are a nonlinear system, but a system with small oscillations or amplitudes

D. S. Megharaj
Department of Mechanical Engineering, Islamiah Institute of Technology, Bangalore, Karnataka, India
e-mail: megharajds1@gmail.com

A. Malgol (✉)
Department of Mechanical Engineering, National Institute of Technology, Calicut, Kerala, India
e-mail: amitmalgol123@gmail.com

E. T. Akinlabi et al. (eds.), *Trends in Mechanical and Biomedical Design*,
Lecture Notes in Mechanical Engineering,
https://doi.org/10.1007/978-981-15-4488-0_4

are considered as a linear system. It is essential to decide the dynamic parameters of a rotor, i.e., natural frequency, whirling speeds, and amplitudes. In a system, there can be nonlinearity due to geometry, misalignments, loose supports, unbalance mass, etc. In the design of a rotating system, the disk mass, bearing stiffness, and damping are important parameters. For a dynamic system, the oscillation gradually reduces and ultimately vanishes, and such a phenomenon of a dynamic system is known as transient vibration. Transient vibration may involve free or forced vibrations or both. The time-dependent transient solution briefs about a variety of sufficiency regarding time under an action a force for a small period.

The investigation of the transient system is progressively imperative in spinning machinery generally for high-speed rotors—the two important elements of study in a dynamic rotor system. The first component is the time-based analysis. The physical components are crucial, but that cannot be particularly legitimated as an element of recurrence precedents that are conducted of bearings, seals, and dampers. The second component characterizes the time-subordinate reaction instances of transient reaction framework comprise of synchronous engines and blowers and motors. Generally, a disk, coupling or a disk with blades attached to a shaft such a rotating system is called as a rotor. Applications of a rotating system are pumps, generators, auto engines, blowers, steam turbines, etc. Instability in a rotating system is the primary cause of failure. In a rotating system, changing some parameters, i.e., disk mass, stiffness, disk position, and different parameter of the rotor system, the amplitudes of the rotating system can be diminished, and such design modification helps us to operate in suitable and safe conditions.

The modal analysis and harmonic analysis of the rotor for three distinct positions of the rotor disk system are performed. In the analysis, natural frequency and critical speeds of the rotating system increase as the disk position moves toward the support, as well the amplitudes decrease presented by Malgol and Potdar [1]. Sharama [2] considered the random form of vibration due to loss of blade and the vibration frequency and demonstrated that nearly at all the working velocities, three-component control law gives more negative eigenvalues signifying better transient properties.

The stationary and transient motions in rotor systems with higher critical speeds exceed by the operating speeds. The rotor of a turbo-driven pump assembly is used in rocket engines where the rated speed of which exceeds the second basic speed and in which rings serve as sealing. Babukanth and Vimal [3] constructed an FE model of a rotor in which the shaft segments are considered as beam and considering the shear deformation. The blade wheels and the seal rings are considered as rigid disks and elastically attached on a solid bodies. Malcolm [4] described the traditional analysis approach which sights the dynamic performance of a rotor framework as an element of recurrence and investigates rotor elements in the time area and drawing nearer into the non-direct routine. Volokhovskaya and Barmina [6] delineated the underlying redirection in twisting and leftover unbalances of rotor framework to the size of the amplitudes of its transient vibrations at normal frequencies underneath its working turn recurrence on the summary. Szolc et al. [5] study shows a difference between various dynamic and static characteristics of dynamic, asynchronous motor and properties of rotor-shaft system. Balakh and Nikiforov [7] considered the effects

Table 1 Material properties of the rotor

Sl. No	Parameters	Value	Units
1	Shaft and disk material	Mild steel	–
2	Young's modulus (E)	2×10^{11}	N/m^2
3	Density (ρ)	7800	kg/m^3
4	Poisson's ration (μ)	0.33	–

Table 2 Data of the disk and shaft

Sl. No	Parameters	Value	Units
1	Diameter of shaft (d)	0.01	m
2	Diameter of disk (D)	0.15	m
3	Thickness of disk (t)	0.01	m
4	Length of shaft (L)	0.4	m
5	Mass of disk (M)	1.3783	kg

of hydrodynamic force due to interaction of rotor and seal lead to disappearance of critical speed with increasing stiffness. Jangde et al. [8] described the dynamics of the single rotor system. Fleming et al. [9] investigated the transient response of rotor system supported with rolling element bearing with internal clearance. The dead band clearance shows a significant effect on the synchronous rotor response. Annentrout and Gunter [10] described the characteristics of rotor system with consideration of squeeze film damper and hydrodynamic effects.

2 Methodology

2.1 ANSYS Modeling

The rotor model consists of a shaft and disk. To develop a model of rotor, Table 1 shows the properties of the rotor, and Table 2 shows the data of disk and rotor which are considered in ANSYS. Figure 1 shows the model of the rotor.

2.2 Transient Analysis in ANSYS

The transient response of the rotor system is performed, and a 100 N time-dependent load is applied on the disk for 1 s. Three different load step files are written, i.e., when there is no load on the rotor system, a load applied for 1 s, and load removed from the rotor system, performed for cases of different disk position. The time history post-processor in ANSYS is utilized to draw amplitude versus time plot for rotor

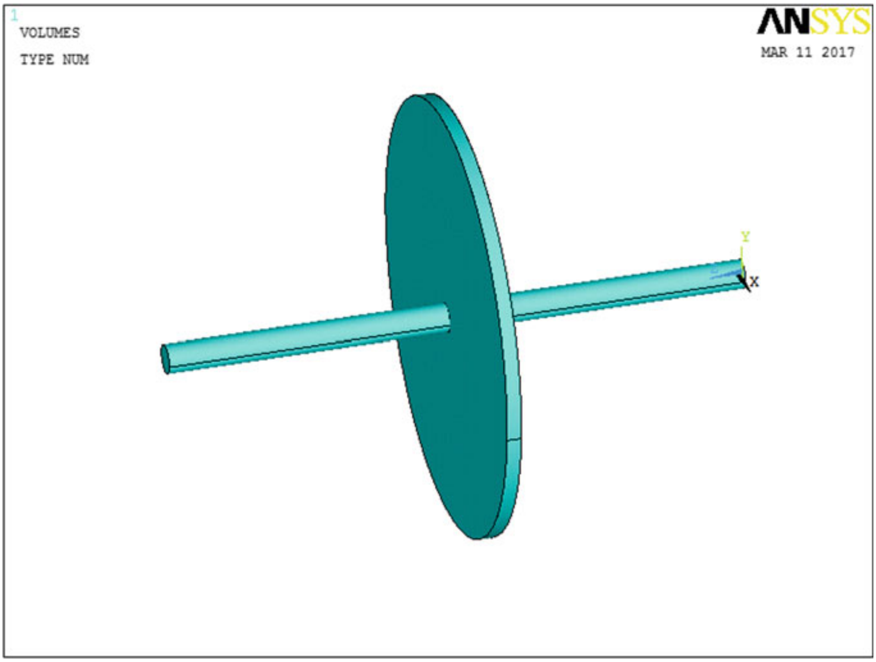

Fig. 1 Rotor model in ANSYS

system by selecting a node on mid of disk, and maximum and minimum amplitudes are obtained at the maximum time (20 s) and minimum time (0.01 s) for the selected node. Figures 2a, 3a, and, 4a show the deviation of amplitude concerning the time of the rotor system for three different positions of a disk mounted on a horizontal shaft for a simply supported case. Figures 2b, 3b, and, 4b show that the amplitudes of vibration increase with the natural frequency, and after the first critical speed, again amplitudes of vibration decrease for three different disk positions for damping ratio = 0.2.

2.2.1 For the Position of Disk $a = 0.2$ m and $b = 0.2$ m

See Fig. 2.

2.2.2 For the Position of Disk $a = 0.133$ m and $b = 0.267$ m

See Fig. 3.

a

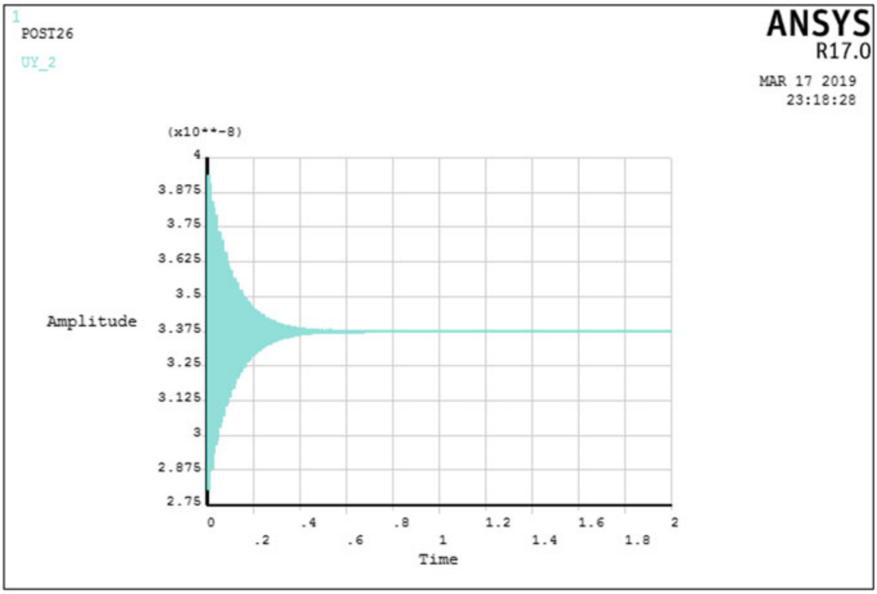

b

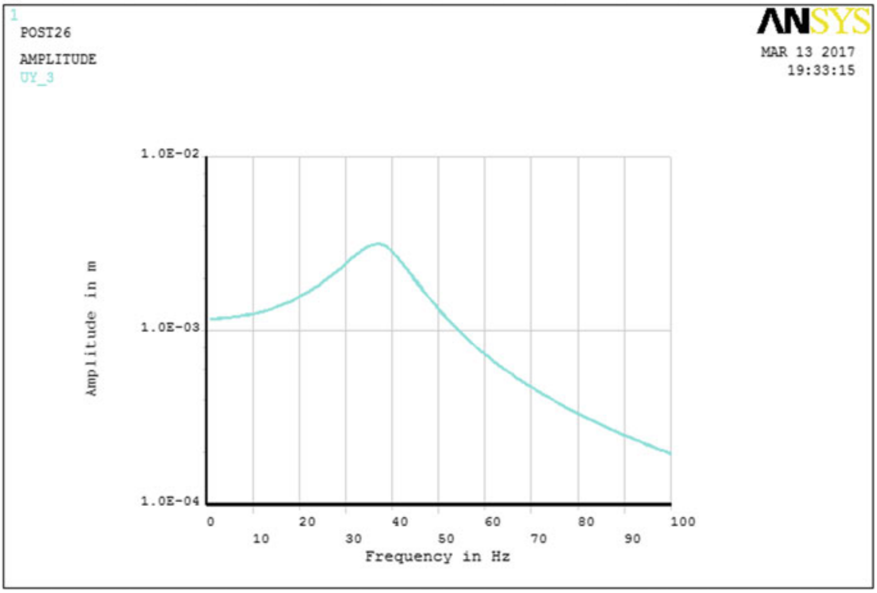

Fig. 2 **a** Amplitude versus time plot for $a = 0.2$ m and $b = 0.2$ m. **b** Variation of amplitudes of vibration with operating frequency of rotor system at damping ratio = 0.2

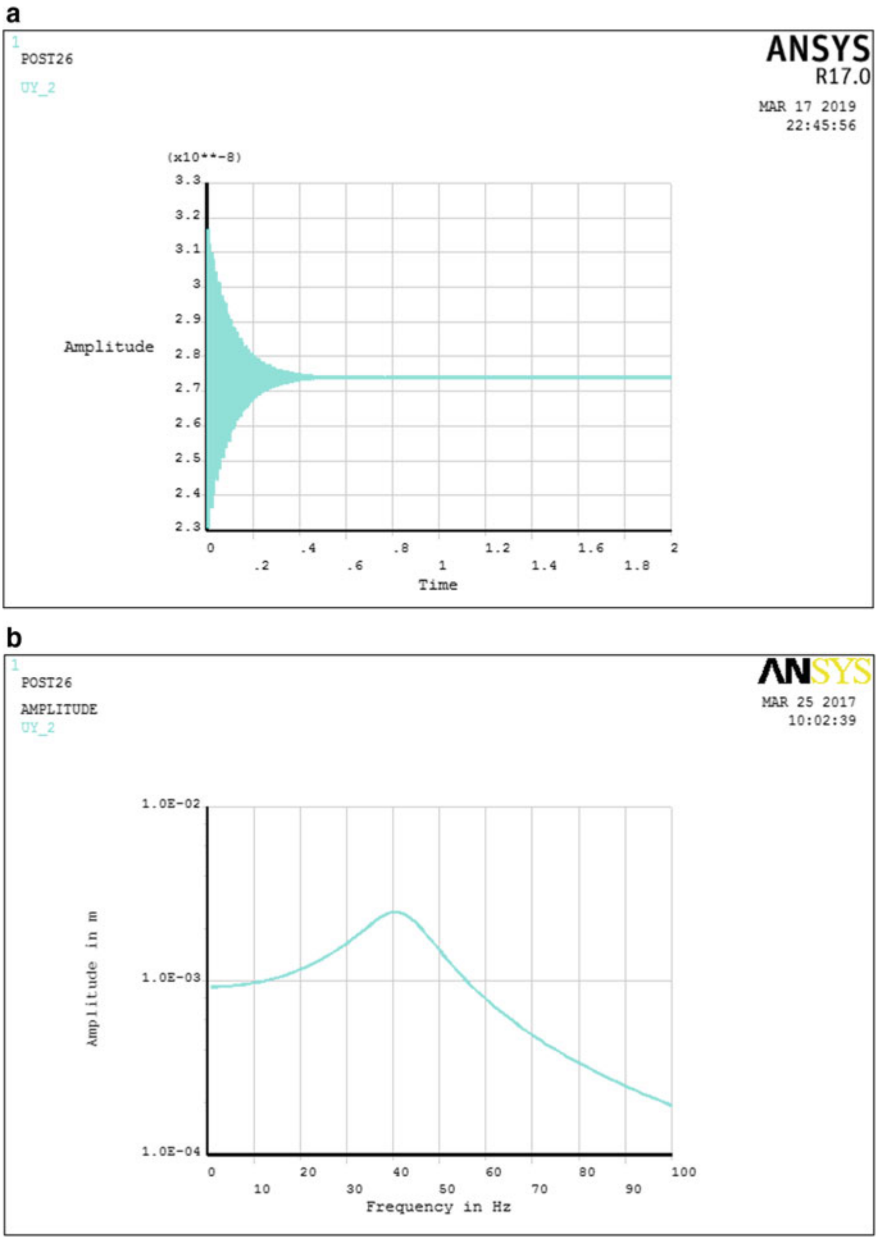

Fig. 3 **a** Amplitude versus time plot for $a = 0.133$ m and $b = 0.267$ m. **b** Variation of amplitudes of vibration with operating frequency of rotor system at damping ratio = 0.2

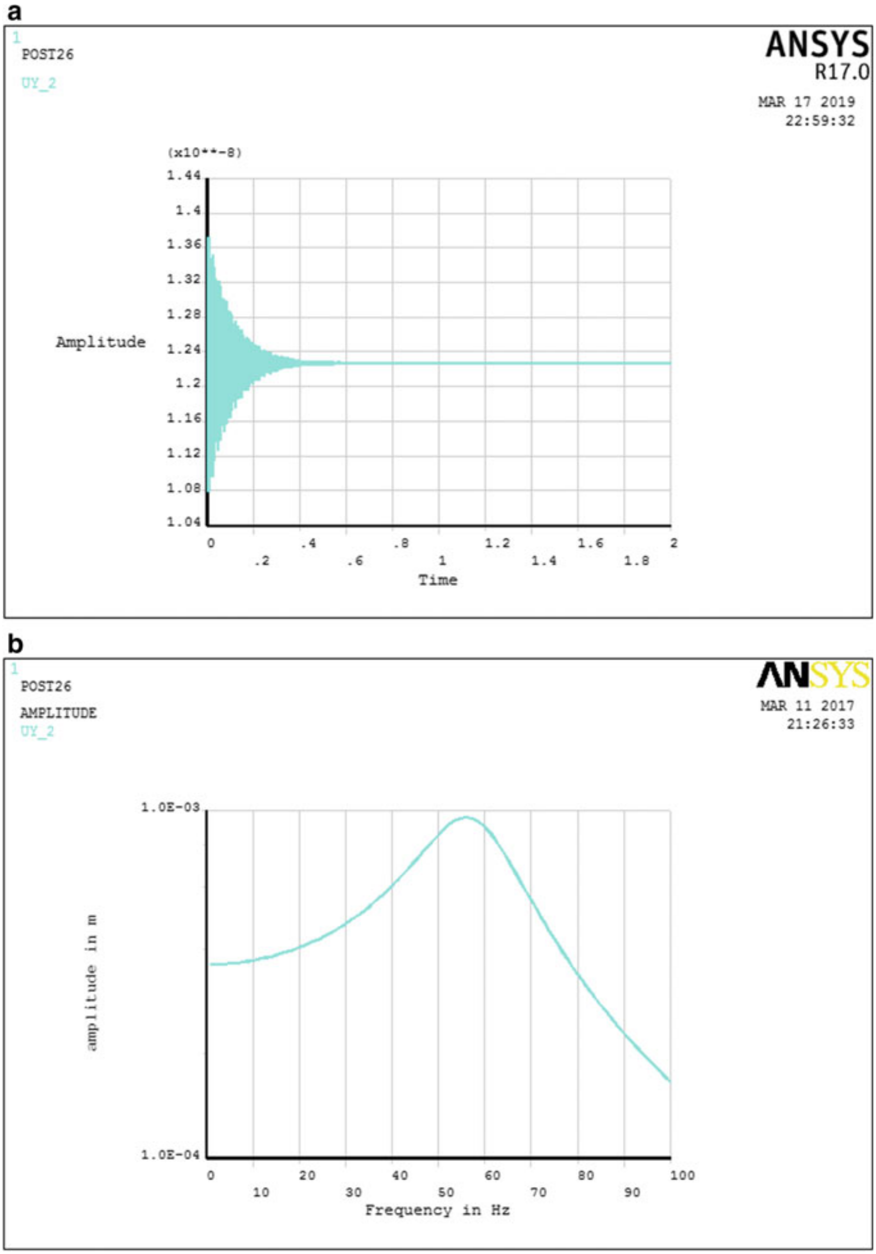

Fig. 4 **a** Amplitude versus time plot for $a = 0.066$ m and $b = 0.334$ m. **b** Variation of amplitudes of vibration with operating frequency of rotor system at damping ratio = 0.2

2.2.3 For the Position of Disk $a = 0.066$ m and $b = 0.334$ m

See Fig. 4.

3 Analytical Method

The equation of motion for free undamped vibration is given

$$mx'' + kx = 0 \tag{1}$$

where,

k Stiffness of shaft
m Mass of the disk.

The natural frequency of undamped free vibration

$$f_n = \frac{1}{2\pi}\sqrt{\frac{k}{m}} \tag{2}$$

The equivalent stiffness for a rotor with the disk at middle position simply supported case

$$K_{\text{eq}} = \frac{48EI}{L^3} \tag{3}$$

where,

E Young's modulus (MPa)
I Area moment of inertia (m^4)
L Shaft length (m).

The stiffness for a disk with offset or different position is given by

$$K = \frac{3EIL}{a^2b^2} \tag{4}$$

The equation of motion for damped forced vibration

$$mx'' + cx' + kx = F_o \sin(wt) \tag{5}$$

The amplitudes of vibration (X) are obtained on solving Eq. (5) as

$$X = \frac{\frac{F_o}{K}}{\sqrt{\left(1 - r^2\right)^2 + (2\xi r)^2}}$$

where,

$r = \frac{\omega}{\omega_n}$	Frequency ratio,
f_n	Natural frequency of the system (Hz),
F_o	Applied force on the disk (N),
ω	Excitation frequency (Hz),
ξ	Damping ratio, and
X	Amplitude of forced vibration (m).

Deflection for a rotor with disk offset position for the simply supported case is given by

$$\delta = \frac{Wa^2b^2}{3EIL} \tag{6}$$

where,

W Weight of the disk (kg).

Natural frequency for a rotor with disk offset position for the simply supported case is given by

$$f_n = \frac{1}{2\pi}\sqrt{\frac{g}{\delta}} \tag{7}$$

$$f_n = \frac{0.4987}{\sqrt{\delta}} \tag{8}$$

4 Results

See Table 3.

5 Conclusion

The academic finite element ANSYS tool is good to know the dynamic behavior of the rotor. Transient investigation of rotor system for three distinct disk positions is achieved. A load of 100 N is applied on the disk for 1 s. In all the different cases, we can observe that amplitudes are gradually reduced due to the application of a load dependent on time, and plots are obtained for variation amplitudes concerning time, for simply supported rotor system under the action of time-dependent load. For mid disk position, the stiffness of rotor is less compared to disk location near to the support, and hence, comparing mid disk position and disk close to the support,

Table 3 Analytical and ANSYS results

Sl. No.	Position of disk		Node	Result	Results		
					ANSYS results		Analytical results
	a (m)	b (m)			Minimum value	Maximum value	Maximum value
1	0.2	0.2	Mid disk	Time	0.001	2	2
				Y component of displacement	2.080325×10^{-8}	3.98376×10^{-8}	3.9582×10^{-8}
2	0.133	0.267	Mid disk	Time	0.001	2	2
				Y component of displacement	2.30689×10^{-8}	3.1676×10^{-8}	3.1196×10^{-8}
3	0.066	0.332	Mid disk	Time	0.001	2	2
				Y component of displacement	1.07849×10^{-8}	1.37206×10^{-8}	1.2022×10^{-8}

the amplitude of forced vibration is lower for disk closer to the support. Therefore, the higher the stiffness value lowers the vibration amplitudes. As the disk, location closer to the support increases stiffness with decreasing amplitudes of vibration. Further, we can conclude that using a suitable damping ratio, the vibration amplitude of system reduces, and changing disk position the amplitude further reduces to a minimum value. These parameters are useful in the design of the rotor system and finally conclude that the vibration amplitudes depend on the effect of position of the disk, properties, and geometry of the rotor system. This investigation helps us in a steady-state and safe operation of the rotating system. Further, these investigations can be carried out for different materials, multi-disk rotor system, and experimental verification.

The transient analysis with different disk positions can be utilized for design modification of a real rotor system such as textile rotor. The textile rotor is used to wind the band. The gyroscopic effect is considered in the system. The analysis shows that the amplitude of vibration decreases as the disk position nearer to the support compared to the mid position of the disk on the shaft.

References

1. Malgol A, Potdar Y (2017) Modelling and simulation of single rotor system. Int J Latest Technol Eng Manage Appl Sci 6(4):163–169

2. Sharma N, Shekhar S, Dutt JK (2018) Transient excitation suppression capabilities of electromagnetic actuators in rotor-shaft systems. Struct Health Monit Photogrammetry DIC 6:185–194
3. Babukanth G, Vimal Teja M (2012) Transient analysis of disk brake by using ANSYS software. Int J Mech Ind Eng 2(1):21–25
4. Malcolm E Time transient analysis and non-linear Rotordynamics, Applied Machinery Dynamics Co.
5. Szolc T, Konowrocki R, Pisarski D, Pochanke A (2018) Influence of various control strategies on transient torsional vibrations of rotor-machines driven by asynchronous motors. In: Proceedings of the 10th international conference on rotor dynamics, IFToMM 2018, 205–220
6. Volokhovskaya OA, Barmina OV (2016) Effect of initial bending and residual eccentricity of a turbine rotor on its transient vibration amplitudes. J Mach Manuf Reliab 45(2):113–121
7. Balakh LY, Nikiforov AN (2013) The reduction of the vibration level in high-speed rotor systems by means of floating seal rings. J Mach Manuf Reliab 42(4):276–280
8. Jangde V, Chouksey M, Patil J, Jain V (2015) Modal and Transient analysis of single disc rotor system. Int J Res Mech Eng Technol 5(2):30–33
9. Fleming DP, Murphy BT, Sawicki JT, Poplawski JV (2006) Transient response of rotor on rolling element bearing with clearance. In: Seventh international conference on rotor dynamics sponsored by the international federation for the promotion of mechanism and machine science (IFTOMM), Vienna, Austria, 25–28 Sept 2006
10. Annentrout RW, Gunter EJ (1999) Transient modal analysis of nonlinear rotor-bearing systems, RODYN Vibration Analysis, Inc. 1932 Arlington Boulevard Charlottesville, VA 22903-1560

Investigating the Contact Load Capacity of Asymmetric Helical Gears

P. Dinesh Babu, Swathi Balaji, and P. Marimuthu

Abstract Gears are one of the machine elements used to transmit a torque from one point of application to another point of application of a mechanical system through the shaft. In many applications, the power flow is unidirectional. In this case, asymmetric gears preferred over the symmetric gears. The present work focuses on evaluating the contact stress through finite element analysis for the symmetric and asymmetric helical gears. To calculate the stress between the contact points of the gears the Lagrange multiplier algorithm is applied. Probable increase in the percentage of contact load capacity of asymmetric helical gear is measured and is duly compared with values obtained for symmetric helical gear.

Keywords Asymmetric helical gear · Contact stress · Finite element analysis · Symmetric helical gear

1 Introduction

Gear is a machine element that transmits movement and power from in between connecting shafts through progressive engagement teeth and finds its applications in automobile gearbox and places where the power transmitting distance is shorter. Gears are also used to vary speed, magnitude and direction and are normally preferred because of its high transmission efficiency. Originally, symmetric tooth profiles are proposed and designated for involute gears [1]. But the condition on drive side is different from that of the coast side during meshing is a well-agreed fact while designing. The use of asymmetric gears in unidirectional power transmission reduces contact stress and increases load-carrying capacity per gear size [2, 3] and durability to the tooth profile. Increasing the contact ratio along with the operating pressure angles is possible with asymmetric tooth profiles and is beyond the scope of limits offered by conventional gears. When torque is transmitted along any particular

P. Dinesh Babu · S. Balaji · P. Marimuthu (✉)
School of Mechanical Engineering, SASTRA Deemed to be University, Thanjavur, India
e-mail: marimuthu@mech.sastra.edu

E. T. Akinlabi et al. (eds.), *Trends in Mechanical and Biomedical Design*,
Lecture Notes in Mechanical Engineering,
https://doi.org/10.1007/978-981-15-4488-0_5

direction, asymmetric gears are more appropriate for those applications. Asymmetric tooth profiled gears also impart tooth stiffness and higher load sharing by also simultaneously maintaining the preferred pressure angle and contact ratio.

When load is applied on two mating gears the contact stresses arising at the point of contact of coupling gears change. This leads to failure of gear tooth such as pitting, surface wear and scuffing on the surface of the tooth [4]. Pitting occurs due to continuous application load on contact surfaces which happens at the time of meshing. Stress occurring at the contact point is considered as a limiting factor for engineers. Francesco and Marini [5] considered the drive side assigned with a low-pressure angle tooth profile and a high-pressure angle was given for coast side tooth profile called buttress teeth profile. For symmetric gears with equal pressure angles, there is decreased bending stress but, no changes in the contact stresses. Yi-Cheng along with Chung-Biau [6] studied stresses at the contact point for helical gears with localized bearing contact. Their results give information about the influence of gear parameters on the distribution of stress. Hwang [4] investigated the contact stresses developed on mating gear pairs. Their results were calculated at different points of contact and they showed the variation in contact stress.

The gears design presented in this is different from the ones presented in [5]. Here large pressure angle is provided to drive side profile and low-pressure angle for coast side involute profile. The load-carrying capacity largely depends on the pressure angle. Increase in pressure angle increases radii curvature and decreases Hertzian contact stress [7, 8]. In this paper, contact stresses for asymmetric helical gear, pair is identified and measured using finite element analysis (FEA) to study the effect of different pressure angles on drive side and coast side and these values are compared with symmetric helical gears for same gear parameters. SolidWorks 13 is used to design 3D models gear pairs and FEA software Ansys 14.0 is for the analysis.

2 Materials and Methods

2.1 Modelling of Gears

With respect to the Cartesian coordinates along x and y directions, the involute of a circle is defined by the parametric equation

$$x = r(\cos t + t \sin t) \tag{1}$$

$$y = r(\sin t - t \cos t) \tag{2}$$

In symmetric gears, tooth profiles are generated form single base circles whereas in asymmetric gear two base circles are present. One is for coast side involute and another one is for drive side involute. SolidWorks is utilized for designing 3D gear models. Equation driven curves are used for accurate modelling. Coast side involute curve is drawn from first base circle with pressure angle 20° and drive side involute from second base circle with pressure angle 35° (Figs. 1 and 2).

Parametric equation for coast side involute is

$$x = b_{d1} \times 0.5 \times (\cos(t + \pi/2 + 2.9 \times \pi/180) + t \times \sin(t + \pi/2 + 2.9 \times \pi/180)) \tag{3}$$

Parametric equation for drive side involute is

$$y = d_{b2} \times 0.5 \times (\sin(t + \pi/2 - 1.37 \times \pi/180) - t \times \cos(t + \pi/2 + 1.37 \times \pi/180)) \tag{4}$$

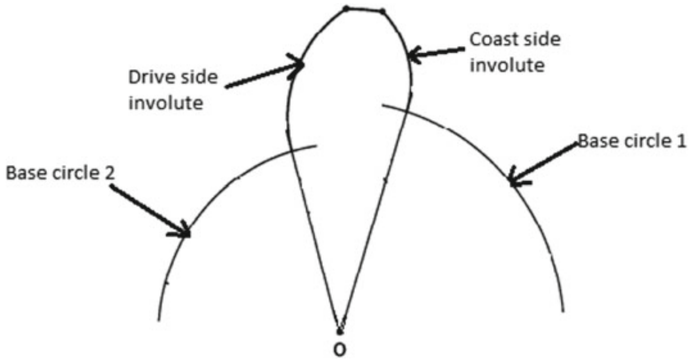

Fig. 1 Asymmetric involute

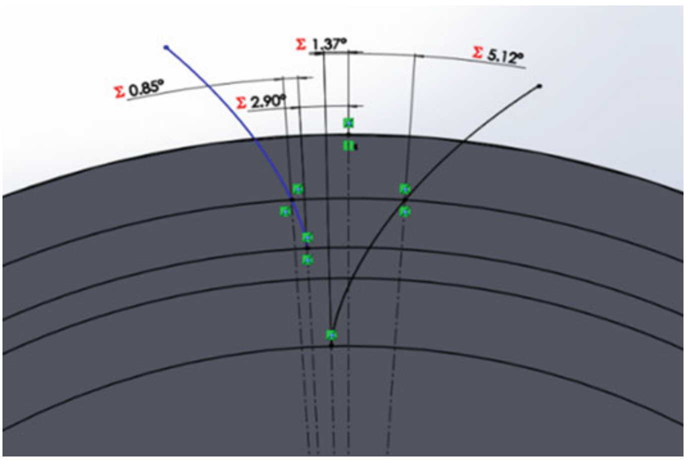

Fig. 2 Involutes of pressure angle 20○ and 35○

Table 1 Asymmetric pinion and helical gear pair parameters

Symbol	Pinion	Gear
m_{n}	2.5 mm	2.5 mm
z_1, z_2	24	32
α_c	20°	20°
α_d	35°	35°
B	20°	20°
gw	20 mm	20 mm
m_t	2.66044 mm	2.66044 mm
d_{a1}	68.8507 mm	90.1342 mm
d_{p1}	63.8507 mm	85.1342 mm
d_{b11}	60 mm	80 mm
d_{b22}	52.3034 mm	69.7379 mm
dr_1	57.6007 mm	78.8842 mm
pa_1	15°	11.25°

2.2 *Finite Element Analysis*

The models have been developed through SolidWorks modelling software and imported in finite element solver Ansys 14.0 for the static structural analysis. To compare the results, same finite element mesh tetrahedral has been used for each pair of gears. Torque of 59,000 N-mm is applied at the hub of pinion. The material properties of the pinion and gear material are listed in Tables 1 and 2.

To reduce the computational time and save computer memory, fine mesh is not recommended for the entire gear model. Only teeth in contact have been meshed with lesser element sizes to favour obtaining a reasonable accuracy of results (Fig. 3). Face refinement is done to teeth that are in contact by splitting the faces in Design Modeller. Mechanical contact between pinion and gear pair is modelled as flexible–flexible and interference treatment is set to adjust to touch. Friction is neglected at the contact surfaces and Augmented Lagrange formulation has been chosen for the calculation (Fig. 4).

The following assumptions have been accepted:

Table 2 Data on properties of steel

Properties	Values
Density	7850 kg/m^3
Modulus of elasticity	210 GPa
Poisson's ratio	0.3
Fatigue	275 MPa
Ultimate tensile strength	690 MPa
Yield strength	410 MPa

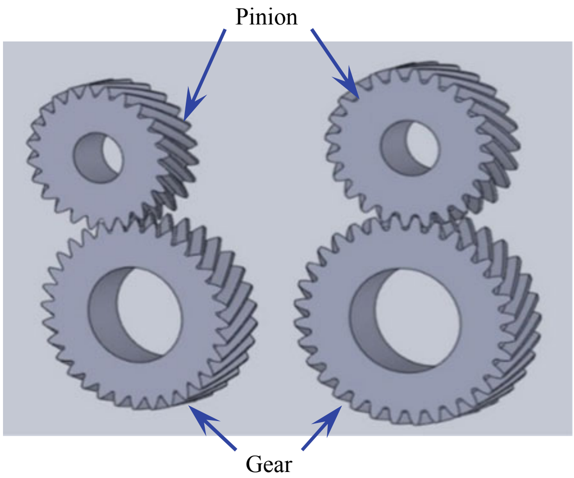

Fig. 3 Asymmetric helical gear pair and symmetric helical gear pair

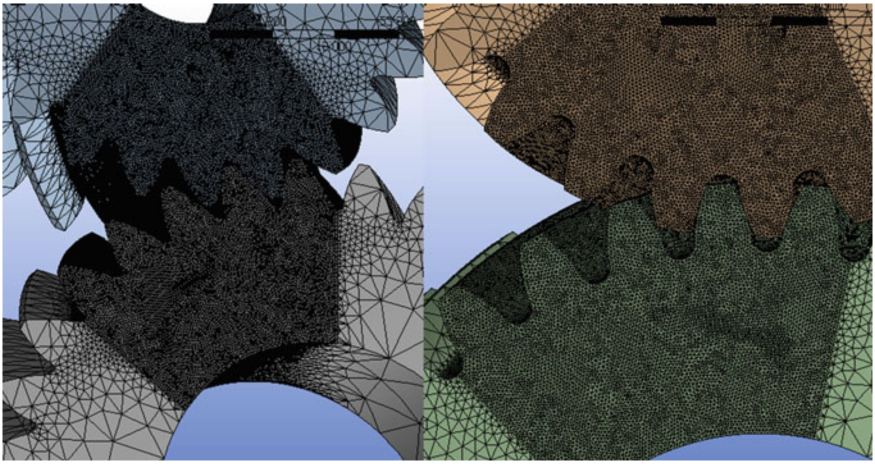

Fig. 4 Finite element model of asymmetric and symmetric helical gear

1. Frictional is neglected in the contact region.
2. Both pinion and gear are made of isotropic and homogeneous material.

The gear assembly is operated under the boundary conditions of the following:

- Gear hub is fixed.
- Remote boundary condition is applied to pinion.
- 59,000 N-mm torque is applied at the hub of pinion.

According to Lewis beam strength equation gear is like a simple cantilever beam where the root is considered as fixed support and tooth is considered as base. The load acting at pitch point along the pressure line can be resolved into radial component and tangential component using a drive side pressure angle. The effect of radial force is neglected and only the tangential component of force is taken into account.

Solution is done for von Mises stresses at the contact surfaces and fillets.

3 Results and Discussion

The von Mises stress for the asymmetric and symmetric helical gear pair is determined through finite element analysis. The von Mises stress plot at the contact region of asymmetric and symmetric helical pair is shown in Figs. 5 and 6. It is observed that the von Mises stress of the asymmetric helical gear is significantly lower than that of the symmetric helical gear.

Figures 7 and 8 shows the von Mises plot at the root region of the asymmetric and symmetric helical pinion. It is noticed that the von Mises of the asymmetric helical pinion is higher than that of the symmetric helical pinion.

The von Mises stress of asymmetric and symmetric helical gear at the contact region is compared and it is shown in Fig. 9. It is inferred that the von Mises stress at the contact region of asymmetric helical gear is 34.92% lower than that of the symmetric helical gear. An increase in the pressure angle and the load sharing results to a significant reduction of von Mises stresses at the contact region. For the through-hardened gears, module is determined based on the contact stresses at the contact region. Since the von Mises is maximum at the contact region, it is considered for design criteria to calculate the module. Hence, the contact load capacity can be improved using asymmetric helical gear drives.

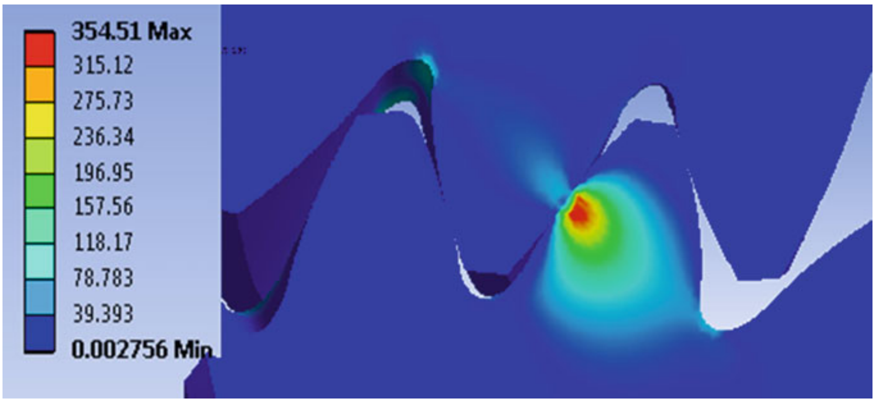

Fig. 5 von Misses stress of asymmetric helical gear at the contact region

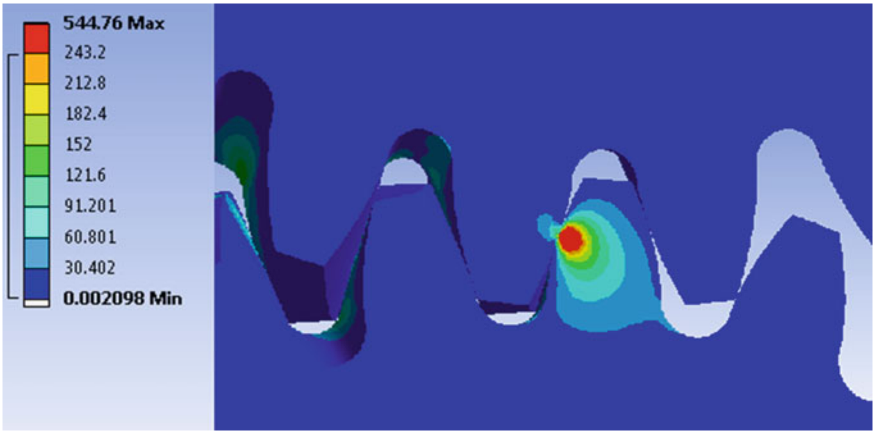

Fig. 6 von Misses stress of symmetric helical gear at the contact region

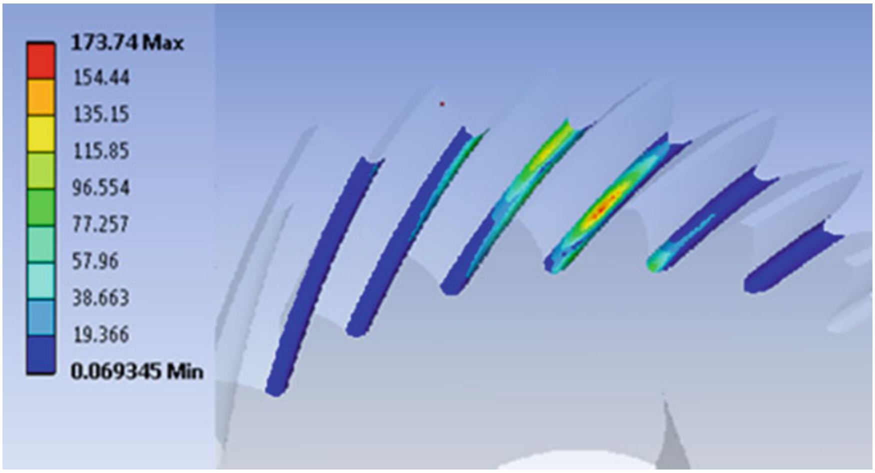

Fig. 7 von Mises stress of asymmetric helical pinion at the root region

Similarly, the von Mises at the root region of the asymmetric and symmetric helical pinion is compared and it is shown in Fig. 10. It is noticed that the von Mises stress at the root of asymmetric helical pinion is 33.83% is higher than the symmetric helical gear pair due to increase in the moment arm. For the case hardened gears the module is determined based on the stress at the root region.

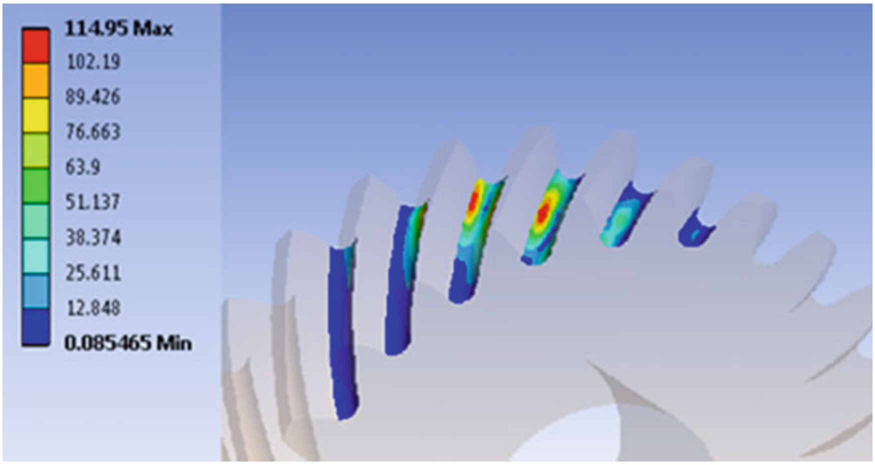

Fig. 8 von Mises stress of symmetric helical pinion at the root region

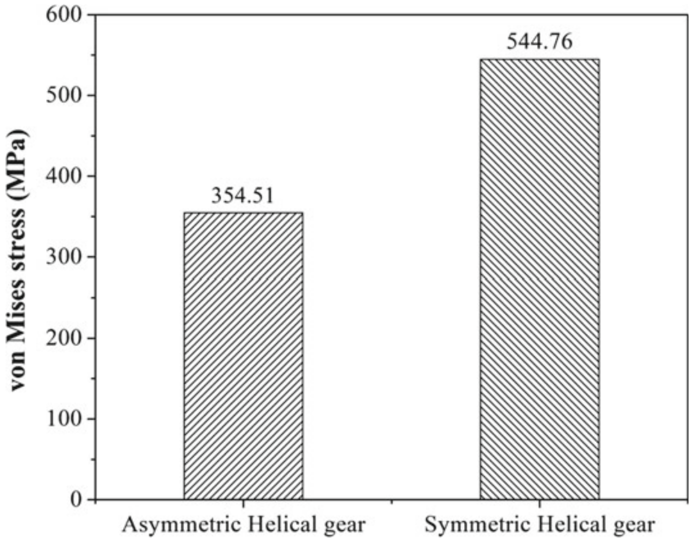

Fig. 9 Comparison of von Mises stress of asymmetric and symmetric helical gear pair at the contact region

4 Conclusion

The following inferences are made based on the quasi-static structural analysis:

1. Asymmetric involute helical gear has been developed using parametric equations.

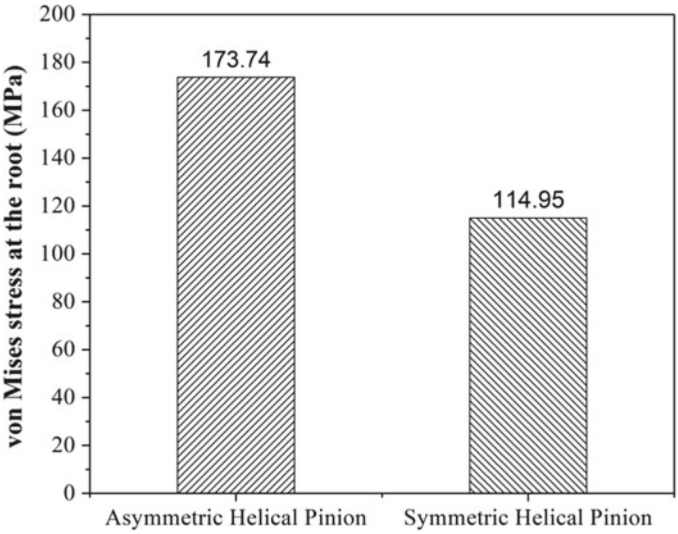

Fig. 10 Comparison of von Mises stress of asymmetric and symmetric helical pinion at the root region

2. Larger pressure angle should be considered as a drive side to reduce the contact stresses.
3. von Mises Stresses are determined through finite element analysis for the asymmetric and symmetric helical pinion and gear pairs.
4. The maximum von Mises for symmetric and asymmetric helical gear is 544.76 MPa and 354.51 MPa respectively. There is a 34.92% reduction in the von Misses stress for an asymmetric helical gear compared to symmetric helical gear. Hence, the contact load capacity can be improved the through hardened gears. At the same time, the bending load capacity decreases for the asymmetric helical pinion.

Acknowledgements The authors are grateful to Science and Engineering Research Board (SERB), Department of Science and Technology, India for providing financial grant (File No. ECR/2017/000425) to do this work.

References

1. Buckingham E (1963) Analytical mechanics of gears. Dover, New York
2. Kapelevich A (September, 2011) Designing asymmetric gears 37–51
3. Kapelevich A (2000) Geometry and design of involute spur gears with asymmetric teeth. Mech Mach Theory 35:117–130
4. Hwang S-C, Lee J-H, Lee D-H, Han S-H, Lee K-H (2013) Contact stress analysis for a pair of mating gears. Math and Comp Modelling 57:40–49

5. Di Francesco G, Marini S (1997) Structural analysis of asymmetrical teeth: reduction of size and weight. Gear Technol 14(5):47–51
6. Yi-Cheng CB (2012) Stress analysis of a helical gear set with localized bearing contact. Finite Elem Anal Des 38:707–723
7. Marimuthu P, Muthuveerappan G (2016) Design of asymmetric normal contact ratio spur gear drive through direct design to enhance the load carrying capacity. Mech Mach Theory 95:22–34
8. Marimuthu P, Muthuveerappan G (2016) Investigation of load carrying capacity of asymmetric high contact ratio spur gear based on load sharing using direct gear design approach. Mech Mach Theory 96:52–74

Close-Proximity Dynamic Operations of Spacecraft with Angles-Only Rendezvous in a Circular Phasing Orbit

Thangavel Sanjeeviraja, R. Santhanakrishnan, S. Lakshmi, and R. Asokan

Abstract Through this paper, it is to assess a closed-loop guidance algorithm for the range of observability of angles-only by rendezvous position and proximity operation. The prominence and influence of Clohessy–Wiltshire dynamics (CWD) is an emerging area which deals with angles-only guidance coupling algorithm and relative position. Observability analysis of the of rendezvous at a low earth circular orbit, as opposed to one spacecraft remaining fixed in its orbit, and the implications for total times are expended. A closed-loop guidance design scheme is generally based on unscented Kalman filter (UKF) and coupling relationship. The proposed method is used in the analysis and the following results are obtained for an initial separation, initial state uncertainties, line-of-sight angles correctness and ΔV (change in velocity) from the navigation and guidance accuracy. The novelty of the approach is to minimize the delta-V for close-proximity operation in phasing spacecraft to the other.

Keywords Rendezvous docking · Proximity operation · Circular phasing · Guidance control and Clohessy–Wiltshire dynamics

1 Introduction

Autonomous spacecraft rendezvous plays an important role in many space missions to enabling technology. In 1967, a successful autonomous spacecraft rendezvous [1] was tested; since then, bounteous mission proposals have been lunched and attempted

T. Sanjeeviraja (✉) · R. Santhanakrishnan · R. Asokan
Department of Aeronautical Engineering, Hindustan University, OMR Padur, Chennai 603103, India
e-mail: stvaero@gmail.com

S. Lakshmi
Department of Electronics and Communication Engineering, Tagore Engineering College, Chennai 600048, India

E. T. Akinlabi et al. (eds.), *Trends in Mechanical and Biomedical Design*,
Lecture Notes in Mechanical Engineering,
https://doi.org/10.1007/978-981-15-4488-0_6

by NASA, Soviet Russia, European Space Agency (ESA), Japan Aerospace Exploration Agency (JAXA) and China National Space Association (CNSA), and methods were assorted for exploring an autonomous rendezvous and docking operation. In addition, Demonstration of Autonomous Rendezvous Technology (DART) [2], Orbital Express (OE), [3] and Experimental Small System (XSS) [4] have been developed by USA to demonstrate the possibility of autonomous rendezvous and docking technologies. Due to space race, Russian Federal Space Agency's Soyuz progress a spacecraft, ESA has designed an Automated Transfer Vehicle (ATV) and JAXA's H-II Transfer Vehicle (HTV) [5] and were considered to rendezvous with the International Space Station (ISS). Recently, CNSA also has conducted several rendezvous and docking tests with Tiangong-1 (TG-1) target spacecraft since 2011 [6].

Many researchers have shown a keen interest in flight safety during the process of spacecraft rendezvous and docking, on-orbit tasks, exclusively in the close-proximity operation to avoid the collision into the target [7]. In the aforementioned research [8], the authors are strenuous to safety in the rendezvous trajectory planning. Another practical approach is proposed in Ref. [8], the strategy for initial separation and considering the measurement uncertainties in a planned trajectory, for optimized collision avoidance. This case aimed to send separate spacecraft to rendezvous with the ISS. It allows the station to remain fixed in orbit, incessantly conducting experiments, while fresh crews and supplies are brought to it, from the ground.

2 Problem of Interest

This investigation will focus on close-range rendezvous in the Hill frame using the Clohessy–Wiltshire equations and phasing orbits for rendezvous of spacecraft on the same orbit. Rendezvous is important to crucial objectives such as resupply, in-orbit spacecraft servicing and repair, contingency planning (e.g. proposed Space Shuttle "rescue" missions) and in-orbit construction. One of the main literature gaps to which this research will attempt to contribute is the topic of planning of spacecraft guidance and control over multiple stages in the presence of uncertainties.

2.1 Solution Method: Relative Motion

This section describes the solution method of relative motion. Figure 1 shows the RSW (Radial, Along Track and Cross Track) coordinate frame, where R is in line with the position vector, S is in the direction of the velocity vector but aligned with the horizontal (perpendicular to the position vector), and W is normal to R and W (forming a right-handed system); Hill's equations are a convenient way to express relative spacecraft dynamics in the RSW frame (see Fig. 1) when two spacecraft are close together. They are derived, assuming that the satellites are only a few km apart,

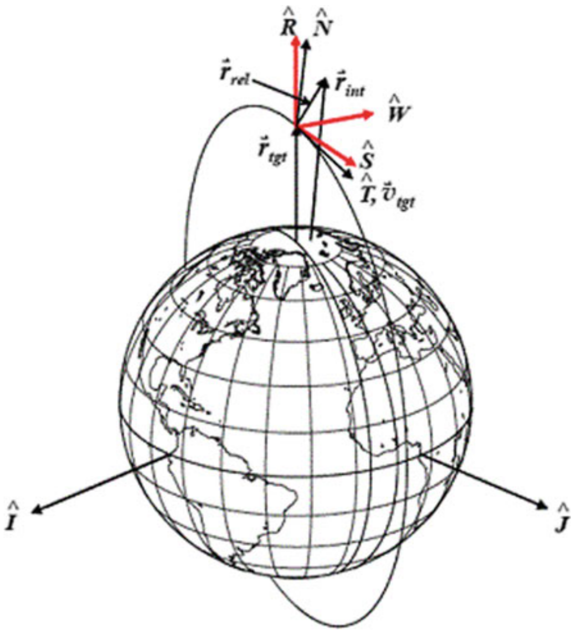

Fig. 1 RSW coordinate frame

the frame (origin of the RSW frame) is in a circular orbit and there are no external forces, such as solar radiation pressure or drag. Figure 1 shows RSW coordinate frame where *x*, *y* and *z* correspond to *r*, *s* and *w,* respectively, and the equation is as follows:

$$
\begin{aligned}
x(t) &= \frac{x_0}{\omega}\sin\omega t - \left(3x_0 + \frac{2y_0}{\omega}\right)\cos\omega t - \left(4x_0 + \frac{2y_0}{\omega}\right) \\
y(t) &= \left(6x_0 + \frac{4y_0}{\omega}\right)\sin\omega t + \frac{4x_0}{\omega}\cos\omega t - (6x_0 + 3y_0)t + \left(y_0 + \frac{2x_0}{\omega}\right) \\
z(t) &= z_0\cos\omega t + \frac{z_0}{\omega}\sin\omega t
\end{aligned} \tag{1}
$$

$$
\begin{aligned}
y(t) &= (6\omega x_0 + 4y_0)\cos\omega t - 2x_0\sin\omega t - (6x_0 + 3y_0) \\
z(t) &= -z_0\omega\sin\omega t + z_0\cos\omega t
\end{aligned} \tag{2}
$$

Setting the first three equations equal to zero ($x = y{=}z = 0$) and solving the velocities give the necessary velocities to set the spacecraft, on a trajectory to reach the origin of the RSW frame (usually centred on a target spacecraft) for a given time to rendezvous. Those equations are shown below, where $\omega = \sqrt{\frac{\mu}{a2_{\text{tgt}}}}$ with a_{tgt} being the radius of the circular orbit of the target/origin of the RSW frame. Collectively this will be called v_0 because it is the initial velocity in the RSW frame of the intercept trajectory. Figure 2 shows that relative motion coordinates for better understanding.

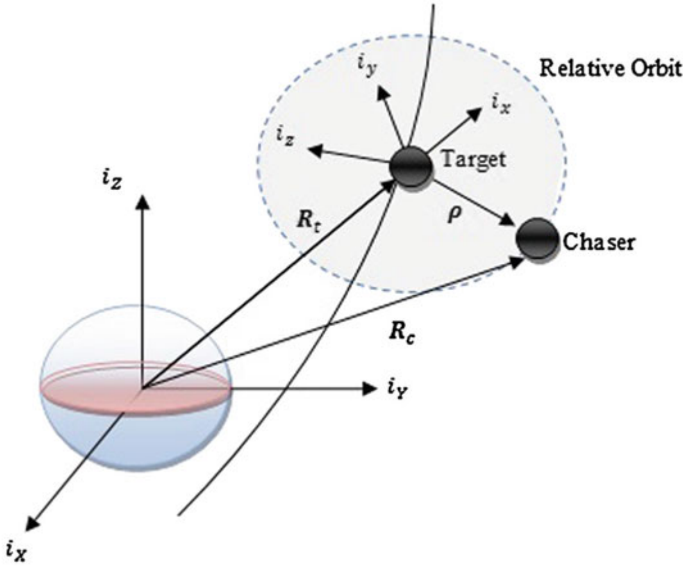

Fig. 2 Represent the coordinates of relative motion

Note that initial velocity in the y-direction must be solved first because initial velocity in the x-direction is a function of $\frac{dy_0}{dt}$.

$$
\begin{aligned}
x_0 &= \frac{-\omega x_0(4 - 3\cos\omega t) + 2(1 - \cos\omega t)y_0}{\sin\omega t} \\
y_0 &= \frac{(6x_0(\omega t - \sin\omega t) - y_0)\omega\sin\omega t - 2\omega x_0(4 - 3\cos\omega t)(1 - \cos\omega t)}{(4\sin\omega t - 3\omega t)\sin\omega t + 4(1 - \cos\omega t)^2} \\
z(t) &= -z_0\omega\cot\omega t
\end{aligned} \tag{3}
$$

2.2 Clohessy–Wiltshire Dynamics

The well-known method of Clohessy–Wiltshire equation, for the relative motion dynamics, is to the near-circular orbit. The two-body problem assumption made a space between the target and the chaser. The distance, compared from the target to the centre of Earth, is very small. The following equations are appropriate in the relative position of chaser.

$$
\begin{aligned}
f_x &= \ddot{x} - 2\omega z \\
f_y &= \ddot{y} + \omega^2 y
\end{aligned}
$$

$$f_z = \ddot{z} + 2\omega x - 3\omega^2 z \tag{4}$$

where ω represents the angular rate of RSW frame. The axis of x, y and z describes the elements of $\boldsymbol{r}(t), f_x, f_y$ and the outward forces on the chaser element is f_z. The discrete propagating equation for the system state is $\boldsymbol{X} = [\boldsymbol{r}; \boldsymbol{v}]$. Equation 4 is utilized for ignoring the disturbing forces and the pulse manoeuvre scheme, the expression of propagating equation, for $\boldsymbol{X}$ can be described below

$$\varphi(k,0)\begin{bmatrix} 1 & 0 & 6\{\omega(t_k - t_0)\} & 4\sin[\omega(t_k - t_0)] & 0 & 2\{1 - \cos[\omega(t_k - t_0)]\} \\ 0 & \cos[\omega(t_k - t_0)] & 0 & 0 & \frac{\sin[\omega(t_k - t_0)]}{\omega} & 0 \\ 0 & 0 & 4 & -3\cos\left[\omega(t_k - t_0)\left\{\frac{2\cos[\omega(t_k - t_0)] - 1}{\omega}\right\}\right] & 0 & \frac{\sin[\omega(t_k - t_0)]}{\omega} \\ 0 & 0 & 6\{\omega(t_k - t_0)\} & \cos[\omega(t_k - t_0) - 3] & 0 & 2\sin[\omega(t_k - t_0)] \\ 0 & -\omega\sin[\omega(t_k - t_0)] & 0 & 0 & \cos[\omega(t_k - t_0)] & 0 \\ 0 & 0 & 3\omega\sin[\omega(t_k - t_0)] & -2\sin[\omega(t_k - t_0)] & 0 & \cos[\omega(t_k - t_0)] \end{bmatrix} \tag{5}$$

And, Eq. 2 is re-expressed as,

$$X_k = \Phi(k,0)X_0 + G\Delta v \tag{6}$$

where G represents the control-driven matrix:

$$G = \Phi(k,0)\left[0_{6\times 3}, I_{3\times 3}\right] \tag{7}$$

3 Observation Equations

In the observation equation, two reasonable assumptions are to be made to establish the equation. It will make the analysis, easier in the following section. Initially, the RSW reference frame, of the chaser and target, can be observed, as being parallel in the setting up of the proximity operation.

In this case, an orbital height 400 km is considered (Altitude of International Space Station) and the primary distance mark, between the chaser and target, is 10 km, and the accuracy of orbital phase angle in a deviation will be about 1.472×10^{-3} rad. Even the poor camera setup. In addition, make the angle deviation will be smaller, even when the equivalent, when, the chaser should not be far away from the target. The obtained measurement transformation equation is from chaser to target RSW frame. Figure 3 shows the relative measurement geometry.

$$\begin{bmatrix} \varepsilon \\ \theta \end{bmatrix} = \begin{bmatrix} -10 \\ 0 - 1 \end{bmatrix} \begin{bmatrix} \dot{\varepsilon} \\ \dot{\theta} \end{bmatrix} + \begin{bmatrix} 0 \\ \pi \end{bmatrix} \tag{8}$$

The second assumption can be realized by attitude control, when the camera measuring frame is coinciding with the chaser's RSW frame which has been demonstrated

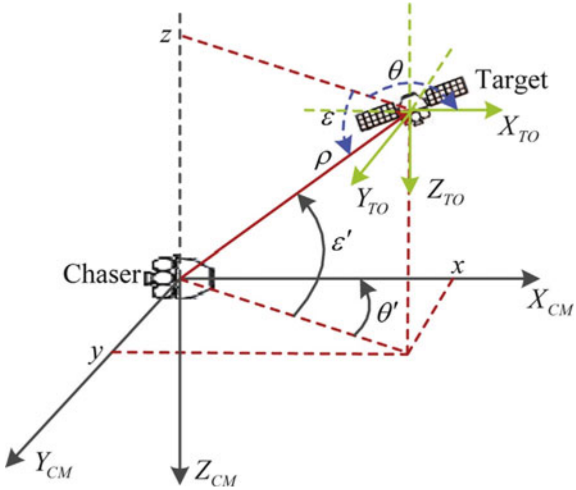

Fig. 3 Relative measurement geometry

in PRISMA mission. Then, an observation equation in the target's RSW frame is to be obtained.

$$z_1 = e + v_e = \arctan \frac{z}{\sqrt{x^2 + y^2}} + v_e;$$
$$z_2 = \theta + v_e = \arctan \frac{z}{\sqrt{x^2 + y^2}} + v_e \quad (9)$$

The phase of mid-range proximity for a cooperative and non-cooperative target can be used in both Eq. 7 (observation equation) and Eq. 8 (measurements transformation equation), where x, y and z unit vectors are representing the element of the line of sight, as well as θ and ε are the azimuth angle and the elevation, respectively, $v\theta$ and $v\varepsilon$ are the measurement noises. It is commonly modelled as zero-mean Gaussian noise, i.e. $v \sim N(0, \sigma^2)$ and $v \sim N(0, \sigma^2)$.

3.1 Observability Analysis

For the circular phasing rendezvous case, we have two spacecraft initially on the same circular orbit, as shown in Fig. 4. Conceptually, this method transfers the intercepting spacecraft onto a phasing orbit, with a differing period, than the initial orbit. The period, of this phasing orbit, is chosen, as such, that alerts the desired number of full orbits, when the intercepting spacecraft returns to the initial orbit, at the same time, as the target spacecraft [5], when the target leads the interceptor, the phase angle, is negative.

Fig. 4 Phasing orbit

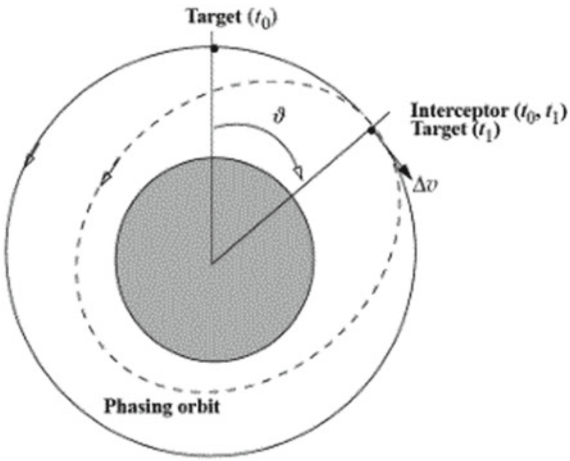

When the target spacecraft leads the intercepting spacecraft, the intercepting spacecraft must "speed up", and thus must enter an orbit, with the smaller semi-major axis (faster orbital period) to "catch up" to the target spacecraft. Similarly, if the target spacecraft is trailing, the intercepting spacecraft must "slow down" and enter a phasing orbit with the larger semi-major axis (slower orbital period) to allow the target spacecraft to "catch up". Mathematically, this is performed using the equations given below [5]. Note that, this assumes two-impulse transfers, with instantaneous application of delta-V.

Figure 2 shows the phase angle θ is negative in this case where the target leads the interceptor, θ is positive, when the interceptor leads the target.

First, we must find the angular velocity of the target spacecraft $\omega_{\text{tgt}} = \sqrt{\frac{\mu}{a2_{\text{tgt}}}}$. Then, the time of the phasing orbit is given by

$$\tau_{\text{phase}} = \frac{k_{\text{tgt}}(2\pi) + \theta}{\omega_{\text{tgt}}} \tag{10}$$

where k_{tgt} is the desired number of orbits, the target spacecraft completes before rendezvous? Using that, the semi-major axis, of the phasing orbit, can be found with the expression

$$a_{\text{phase}} = \left(\mu\left(\frac{\tau_{\text{phase}}}{2\pi k_{\text{int}}}\right)^2\right)^{\frac{1}{3}} \tag{11}$$

where k_{int} is the desired number of orbits, the intercepting spacecraft completes before rendezvous? For the analyses in this project, $k_{\text{int}} = k_{\text{tgt}}$ for simplicity, though, this certainly needs not to be true. Another important consideration is the radius of perigee of the phasing orbit when the phasing orbit is smaller than the initial orbit (θ is

Fig. 5 Spacecraft orbits for circular phasing rendezvous in the PQ frame

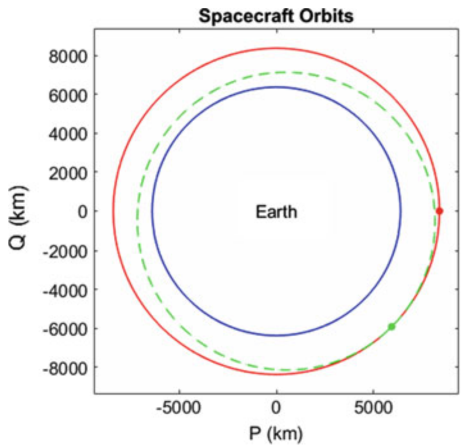

negative). The phasing orbit must not intersect the central body (Earth for this project) or go too far into the atmosphere. $r_p = 2a_{\text{phase}} - r_a$ with $r_a = a_{\text{tgt}}(a_{\text{tgt}} = a_{\text{initial}})$ for the intercepting spacecraft. For this project, r_p is not allowed to drop lower than 160 km perigee altitude above Earth. Finally, the ΔV required, for the intercepting satellite, is found by taking the difference of the velocity on the initial orbit and the velocity on the transfer orbit where it intersects the initial orbit. There will be two burns of equal magnitude and opposite direction, so the total

$$\Delta v = 2\left|\sqrt{\frac{2\mu}{a_{\text{tgt}}} - \frac{\mu}{a_{\text{phase}}}} - \sqrt{\frac{\mu}{a_{\text{tgt}}}}\right| \tag{12}$$

An example solution using this method is illustrated in Fig. 5. Here, the initial orbit has a radius of 8.378 * 103 and the target spacecraft is the red spacecraft (solid orbit line). The target spacecraft has initial true anomaly of 0°, while the intercepting spacecraft (green point, dotted line) has true anomaly of 315°, giving a phase angle of −45°. Working through the process above with $k = 1$ gives the result below, with total delta-$V = 0.6579$ km/s and a time to rendezvous of 1.86 h. The designed closed-loop guidance system is represented in Fig. 6.

4 Rendezvous in Circular Phasing Orbit

Given the orbital radius of the target spacecraft and the coordinates of the intercepting spacecraft in the RSW frame of the target, the ΔV, required to rendezvous in a desired amount of time, can be calculated.

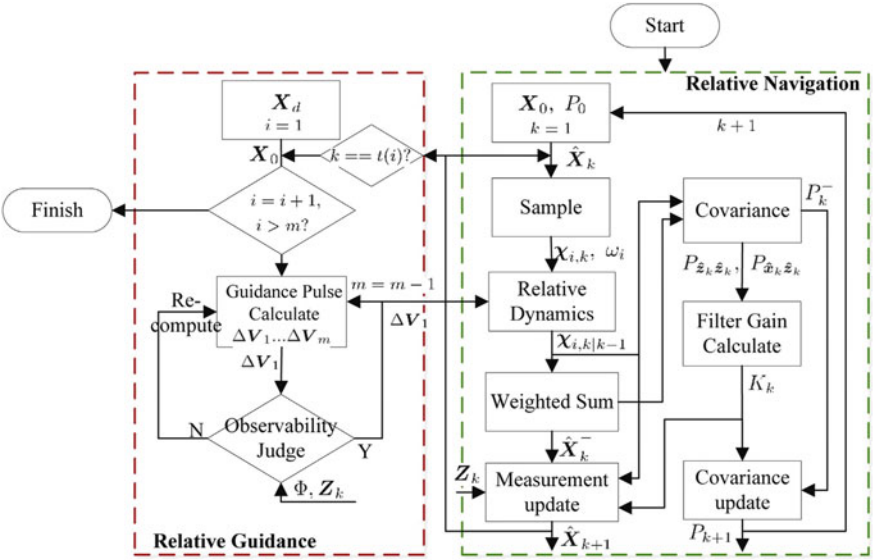

Fig. 6 Designed closed-loop guidance model

4.1 *Extension*

The rendezvous problem in this context is typically posed, as having one spacecraft rendezvous, with a second passive spacecraft, that does not manoeuvre. In this extension, the idea, of rendezvous at an intermediate point, will be explored. This also includes investigating rendezvous locations for more than two spacecraft as well. These types of investigations are becoming more important, as mission designers increasingly utilize multi-spacecraft systems, to accomplish mission goals. For example, NASA's Asteroid Redirect Mission requires a manned spacecraft to rendezvous, with an asteroid sample, that will be placed in lunar orbit [9].

A possible Mars sample return mission would, likely, require some type of Mars ascent vehicle to rendezvous, with a spacecraft in Mars orbit, before returning to Earth [10]. Finally, future manned Mars missions may require the coordination/rendezvous of multiple supply spacecraft, which has been sent to the planet, ahead of time [11]. There is a growing interest in future space mission concepts which involve the interaction of multiple spacecraft/satellites [12–16]. In each of these cases, the multiple spacecraft involved would have the ability to manoeuvre and the finding of an intermediate rendezvous point may help reduce the demand on a single spacecraft, that may not have the required ΔV or time available. It may even reduce the total ΔV or time to rendezvous.

4.2 Circular Phasing Extension

To explore intermediate rendezvous points for circular phasing rendezvous, the same process, as above, is followed with only minor modification. Here, the "target satellite" is, instead, a point in the initial orbit that, the other spacecraft's aim to rendezvous with. This point defined, by its initial true anomaly, is at the start of the simulation thus evolves with time. The circular phasing method, as described above, is performed for each satellite in the system, across the full range of possible rendezvous locations, to examine the trends. For the two-satellite case, the minimum time case (initial true anomaly of target orbit = 240° for $k = 4$) is animated below, to illustrate the method.

Setting up the initial true anomaly, of the target orbit equal to the initial true anomaly of satellite 1, is equivalent to the setting up of the rendezvous point at satellite 1. Satellite 2 is leading the target orbit (θ is positive), and thus satellite 2 must enter a phasing orbit with greater semi-major axis to rendezvous with satellite 1. Recall that

$$\Delta v = 2\left|\sqrt{\frac{2\mu}{a_{\mathrm{tgt}}} - \frac{\mu}{a_{\mathrm{phase}}}} - \sqrt{\frac{\mu}{a_{\mathrm{tgt}}}}\right| \tag{13}$$

This expression shows, that transfer orbits with smaller required, because, all the other parameters in the equation are constant. Thus, the leading satellite should rendezvous with the trailing satellite when using phasing orbits to achieve rendezvous with two spacecraft at a minimum ΔV cost. Another interesting relation, to note, is the drop off in ΔV part way, through the plot (at around 200 degree) (Fig. 7).

This occurs because the phase angle switches from negative (trailing the target) to positive (leading the target). This switch is a result of the phase angle, being the

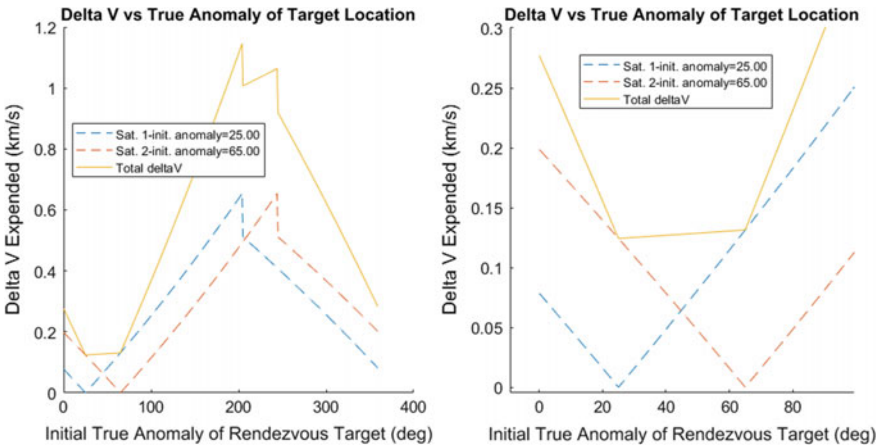

Fig. 7 Delta versus true anomaly of target location

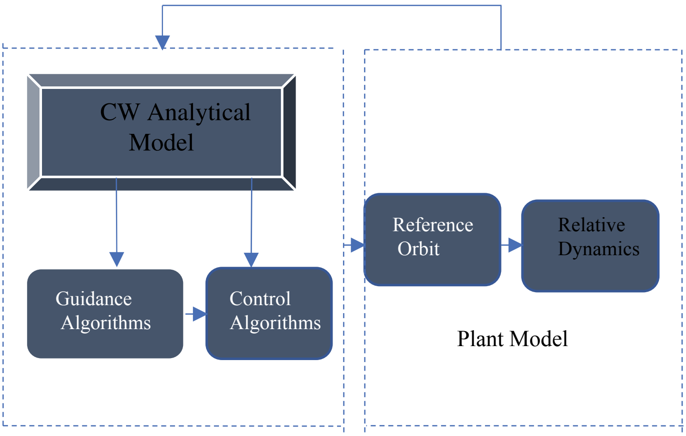

Fig. 8 Schematic approach of control system

smaller of the two angles between the two position vectors, and changes the phasing orbit from being smaller than the initial orbit to being larger than the initial orbit. This larger orbit, however, is not as extreme, a change, as was required for the previous orbit, so ΔV is required drops (Fig. 8).

Effect of varying target location identifies ΔV which is required for a continuous rendezvous. There are also trends observed in rendezvous time, plotted below. Note that, while using one of the satellites as a rendezvous point can minimize ΔV; this does not save total time, because the second satellite must still complete its phasing orbits. Figures 9, 10, 11, 12, 13 and 14 represent that, an intermediate rendezvous orbit is better if minimizing this time is more important than minimizing ΔV. This time minimizing point occurs, where both satellites are still trailing the target initially and thus enter phasing orbits with periods, faster than the phasing orbits needed, when leading the target. Once, one of the satellite transitions leads the target, its rendezvous time jumps up and leaves behind a minimum.

Note that, this minimum is highly expensive in terms of ΔV, because it is the scenario with the greatest changes in orbit needed, to achieve rendezvous (the smaller the phasing orbit, the more ΔV needed to transfer to it).

4.3 Relative Motion Extension

The relative motion rendezvous problem was extended in a similar manner, with the target, being a selected arbitrary orbit rather than on a specific spacecraft. However, for this problem, the initial orbits, of the spacecraft, were defined by using the classical orbital elements and then transformed into the RSW frame [4].

$$x = \delta r$$

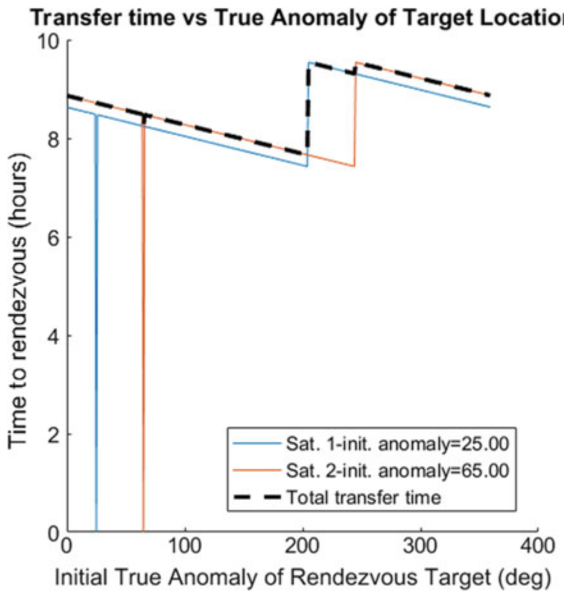

Fig. 9 Rendezvous versus true anomaly

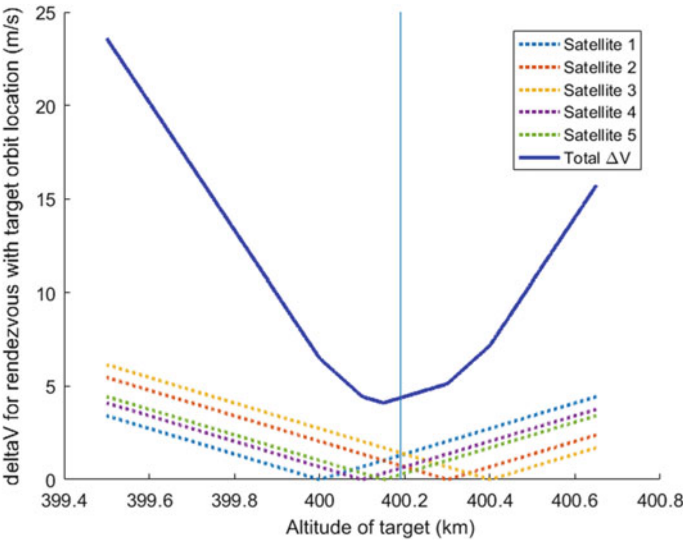

Fig. 10 Delta-V versus altitude

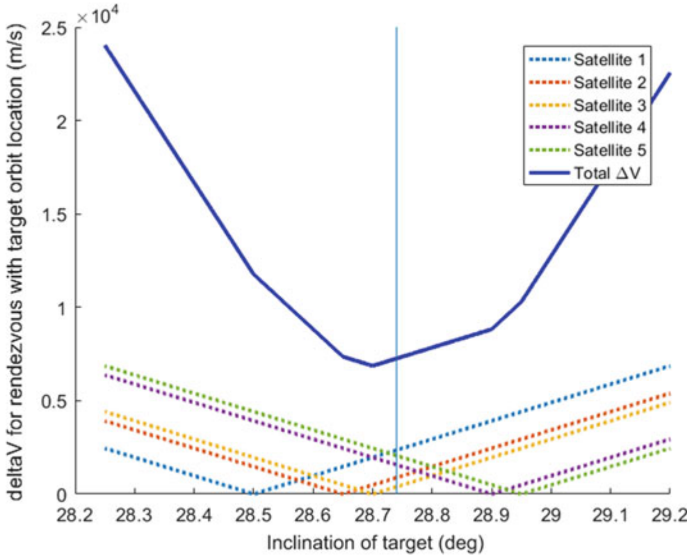

Fig. 11 Delta-V versus inclination

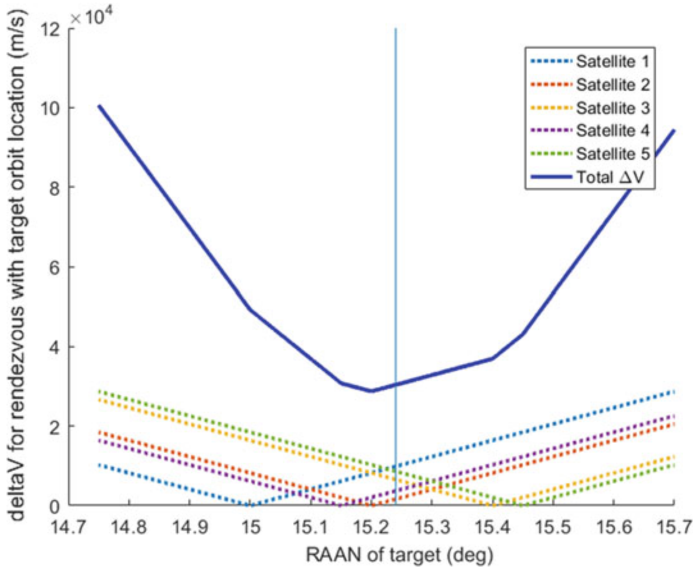

Fig. 12 Delta-V versus RAAN

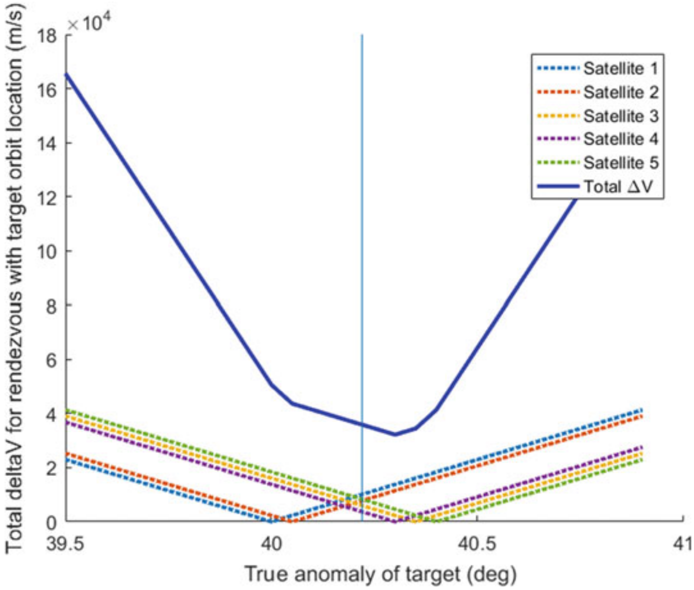

Fig. 13 Delta-V versus true anomaly

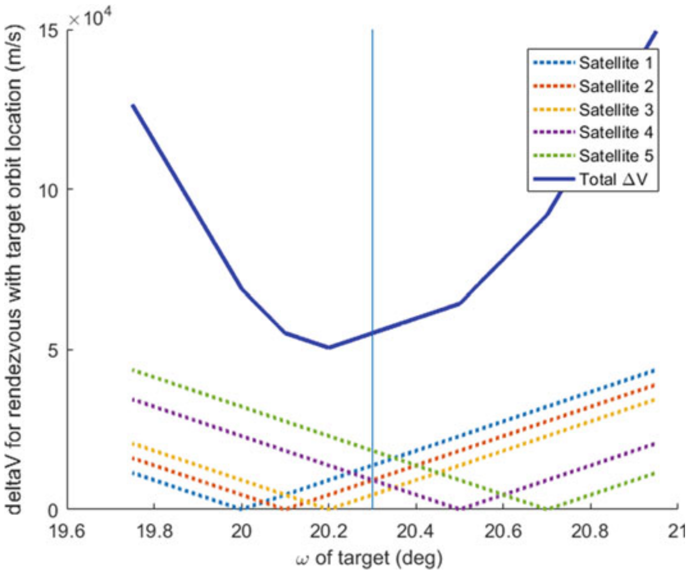

Fig. 14 Delta-V versus argument of perigee

$$
\begin{aligned}
y &= r(\delta\theta + \cos i\delta\Omega) \\
z &= r(\sin\theta i - \cos\theta \sin i\delta\Omega
\end{aligned}
\tag{14}
$$

$$
\begin{aligned}
x &= -\frac{v_r}{2a}\delta a + \left(\frac{1}{r} - \frac{1}{p}\right)h\delta\Omega \ldots \\
&\quad + (v_r a q_1 + h\sin\theta)\frac{\delta q_1}{p} + (v_r a q_2 - h\cos\theta)\frac{\delta q_2}{p} \\
y &= -\frac{3v_t}{2a}\delta a - v_r\delta\theta + (3v_t a q_1 + 2h\cos\theta)\frac{\delta q_1}{p} \ldots \\
&\quad + (3v_t a q_2 + 2h\sin\theta)\frac{\delta q_2}{p} + v_r\cos i\delta\Omega \\
z &= (v_t\cos\theta + v_r\sin\theta)\delta i + (v_t\sin\theta - v_r\cos\theta)\sin i\delta\Omega
\end{aligned}
\tag{15}
$$

Equations from [5] have been used to convert from orbital elements to RSW frame. This gives the ability to see the ideal target location in terms of different orbital elements. In cases with an odd number of satellites, the optimal location, instead, appears to be on the same orbit, as the middle satellite (middle meaning the satellite in between the other satellites with respect to whichever orbit element is being varied). Thus, with an even number of satellites, it may be beneficial to look at intermediate orbits; depending on the distribution of satellites, there may not be one on an orbit that would be optimal to target for rendezvous. Of course, this analysis is only confined to these specific parameters. A more generalized investigation would give more concrete recommendations. Further, investigation, of the coupling between varying different parameters, may also be of interest.

5 Conclusion

In this project, some more conventional rendezvous problems, with goals of reaching a non-manoeuvring spacecraft, have been described. These methods used two-body dynamics for the circular phasing orbits and dynamics transformed into a relative motion frame to calculate delta-*V*, required for rendezvous. We then extended these same methods to look at rendezvous in intermediate orbits. We showed that for circular phasing orbits, to minimize delta-*V*, the leading satellite should rendezvous with the trailing satellite, if ΔV minimization is a priority and the leading satellite has sufficient ΔV. However, when minimizing time while still using circular phasing orbits, there may be a more desirable intermediate rendezvous orbit, depending on the mission and how important time versus ΔV is. In this case, for $t_f = 5$ min, $\Delta V_1 = 1.2918$ m/s, $\Delta V_2 = 1.2054$ m/s and $\Delta V_{\text{total}} = \Delta V_1 + \Delta V_2 = 2.4972$ m/s.

The extension in the relative frame also gave insight into intermediate rendezvous locations and indicates that rendezvous orbits that do not coincide with a spacecraft should be considered in some cases (even number of spacecraft with certain initial conditions). Analyses, such as these, can be useful for the understanding of how to balance resource usage across multiple spacecraft, considering the different needs for each, as opposed to globally optimizing a solution, that may not be optimal for a single spacecraft. Further research would ideally extend the relative motion analysis to investigate more general conditions and to ensure that, the initial conditions of the spacecraft do not exceed the distances allowable by Hill's equations. An even a better investigation would be the research optimal control solutions for two or more spacecraft attempting to rendezvous where the different parameters could be varied, based on needs of the mission.

References

1. Fehse W (2003) Automated rendezvous and docking of spacecraft. Cambridge University Press (2003)
2. Rumford TE (2003) Demonstration of autonomous rendezvous technology (DART) project summary. In: Proceedings of SPIE—The international society for optical engineering, Orlando, Florida (2003)
3. Stamm S, Motaghedi P (2004) Orbital express capture system: concept to reality. In: Proceedings of SPIE—The international society for optical engineering 54(19):78–91
4. Davis TM, Melanson D (2004) XSS-10 microsatellite flight demonstration program results. In: Proceedings of SPIE—The international society for optical engineering, vol 54, no 19, pp 16–25
5. Chullen C, Blome E, Tetsuya S (2011) H-II transfer vehicle (HTV) and the operations concept for extravehicular activity (EVA) hardware
6. Stone R (2012) A new dawn for China's space scientists. Science 36(60):1630–1635
7. Luo YZ, Sun ZJ (2017) Safe rendezvous scenario design for geostationary satellites with collocation constraints. Astronautics 1(1):71–83 (2017)
8. Chu X, Zhang J, Lu S, Zhang Y, Sun Y (2016) Optimised collision avoidance for an ultra-close rendezvous with a failed satellite based on the Gauss pseudo spectral method. Acta Astronaut 128(1):363–376
9. Shi S, Yang1 L, Lin J, Ren Y, Guo S, Jigui (2018) Measur Sci Technol 29(4)
10. Li JR, Li HY, Tang GJ (2011) Research on the strategy of angles-only relative navigation for autonomous rendezvous. Sci China Technol Sci 54(7):1865–1872
11. Grzymisch J, Ficher W (2014) Observability criteria and unobservable manoeuvres for in-orbit bearings-only navigation. J Guidance Control Dyn 37(4):1250–1259
12. Klein I, Geller D (2012) Zero delta-v solution to the angles-only range observability problem during orbital proximity operations. In: Itzhack Y (ed) Bar-Itzhack memorial symposium, Haifa, Israel
13. Zhang Y, Huang P, Song K, Meng Z (2019) An angles-only navigation and control scheme for non-cooperative rendezvous operations. IEEE Trans Ind Electron
14. Geller D, Klein I (2014) Angles-only navigation state observability during orbital proximity operations. J Guidance Control Dyn 37(6):1976–1983
15. Gasbarri P, Sabatini M, Palmerini G (2014) Ground tests for vision based determination and control of formation flying spacecraft trajectories. Acta Astronaut 102(1):378–391
16. Gong B, Geller D, Luo J (2015) Initial relative orbit determination analytical error covariance and performance analysis for proximity operations. In: AAS 15-723, 2015 AAS/AIAA astrodynamics specialist conference, Vail, Colorado USA

Optimal Dimensional Synthesis of Rhombus Path Generating Adjustable Four-Bar Mechanism

Ganesan Govindasamy, Rajakumar S. Rai, and Gadudasu Babu Rao

Abstract Precise and continuous generation of rhombus path by adjustable four-bar mechanism is investigated and confirmed using Reconstructed Adjustable Parameter Curve (RAPC) technique. RAPC method is able to extract adjustable parameter value of intermediary path points along the path generation profile corresponding to uniformly incremented crank angle values. Harmonic Spacing (HS) algorithm is used to improve the precision points spacing along the perimeter of intended rhombus path. Optimal dimensional synthesis of adjustable four-bar mechanism makes use of these precision points. Simulation of motion of adjustable four-bar mechanism to generate profile path of rhombus is carried out to verify the dimensional synthesis of the linkage. Optimization combining Genetic Algorithm (GA) and Pattern Search (PS) is implemented to synthesize rhombus path generating mechanism. Results show the achievement of precise and continuous path generation with high accuracy for the selected rhombus path profile.

Keywords Rhombus path · Adjustable Four-bar linkage · Reconstructed adjustable parameter curve

1 Introduction

Path generation is the motion of coupler point to trace a path profile. Point-to-point path generation is to follow the computed precision points while the trajectory between the computed points is approximated. The other type of path generation is of continuous type which specifies whole path with many points which approximately pass through the specified curve. Adjustable mechanism is neither equal to sophisticated flexible robot nor equal to non-adjustable mechanism. It takes the mid-position between non-adjustable mechanism and robot [1] in terms of speed, precision and

G. Govindasamy (✉) · R. S. Rai · G. B. Rao
Department of Mechanical Engineering, Karunya Institute of Technology and Sciences, Karunya Nagar, Coimbatore, Tamil Nadu 641114, India
e-mail: vivajijaya67@gmail.com

E. T. Akinlabi et al. (eds.), *Trends in Mechanical and Biomedical Design*, Lecture Notes in Mechanical Engineering,
https://doi.org/10.1007/978-981-15-4488-0_7

simplicity. In contrast to analytical methods that satisfy fewer precision points precisely, optimization methods such as Genetic Algorithm, Pattern Search, and Neural Networks etc. satisfy many precision points. Haws and Kay [2] used an adjustable mechanism employing a cam-link to generate one-fourth of a square and a cardioid path. Kohli and Singh [3] made use of cam-link linkages to generate exact path. Ogawa et al. [4] synthesized adjustable multi-link linkages to produce L-shaped and straight lines paths connecting several precision points. Mundo and Gatti [5] employing non-circular gears synthesized five-bar linkages for accurate path generation. Mundo et al. [6] synthesized adjustable cam linkage mechanism to adjust the position of the fixed pivot of link using a cam for exact path generation. Ghoshal and Chanekar [7] synthesized adjustable linkages in two stages in order to reduce the variables required to design a linkage.

Synthesis of continuously adjustable crank-rocker linkage to produce rectangular path was tried by Zhou [8]. Attempt has also been made by Hrishikesh et al. [9] synthesized adjustable four-bar linkage to generate a rectangle path by improving the slope continuity of the adjustable link length curve. Ganesan and Sekar [10] used graphical method to obtain adjustable parameter curve (APC) from the dimensions of the mechanism synthesized by Zhou [8] to produce rectangular path. Ganesan and Sekar [11] optimally synthesized continuously adjustable linkages to generate rectangle with filleted corners. Ajith Kumar et al. [12] synthesized continuously adjustable linkages to generate rectangle with chamfered corners, rectangle with full chamfering and one DOF cam-link adjustable mechanism to generate oblong-hole path.

It has been found from the above literature that the rhombus path generation mechanism is not attempted. Section 2 presents adjustable linkage model, precision points on rhombus path, dimensional synthesis using hybrid optimization. Section 3 presents RAPC method to extract path points on the rhombus path for one degree incremental value of crank for one revolution. Section 4 presents the results of precise rhombus path generation for various path points. Conclusions and scope for future work are presented in Sect. 5.

2 Adjustable Linkage Model to Generate Rhombus Path

Zhou's [8] four-bar adjustable mechanism model is used in the synthesize to generate precise and continuous rhombus path, as shown in Fig. 1, in which a rocker (L_3) is carried by a slider (D) which forms the adjustable link. This adjustable link length (S) from the fixed point (A) in the direction of x'-axis of a local co-ordinate frame to the pin joint between the rocker and slider is called 'adjustable link length or parameter' of the mechanism. Link AB is crank (L_1). In triad link BCM, side BC forms coupler link (L_2), side BM (L_6) carries coupler point (M). In this mechanism, the required adjustable parameter values (S) are determined so that the coupler point can trace closed rhombus path precisely when the crank makes one revolution.

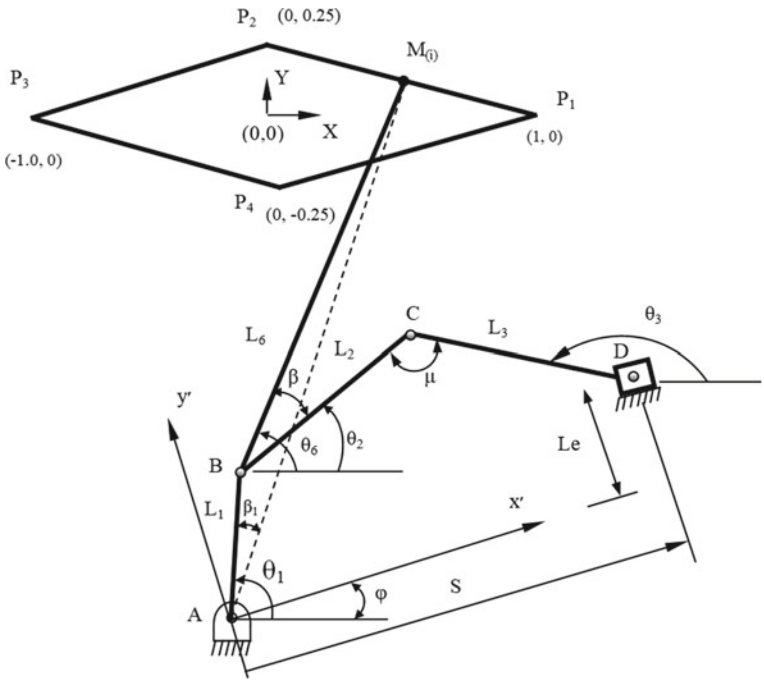

Fig. 1 Adjustable linkage model

2.1 Precision Points of Rhombus Path

Coupler point has to travel along the four sides of the rhombus path which comprises two obtuse angles and two acute angles between the sides. Difficulty arises when the coupler point negotiating the vertices where it changes direction. This demands closer precision points near the vertices. The following harmonic spacing algorithm satisfies the closer precision points at the ends of a straight line or an arc.

$$x_j = \frac{(x_i + x_f)}{2} + \frac{(x_i - x_f)}{2}\left[\cos\left(\frac{(j-1)}{N-1}\right)\right] \tag{1}$$

where x is variable with an interval $[x_i, x_f]$ and $j = 1, 2, \ldots N$, x_j-intermediary point coordinate value, x_i-initial point coordinate value, x_f-end point coordinate value. N (number of precision points inclusive of initial point and end point) (Fig. 2).

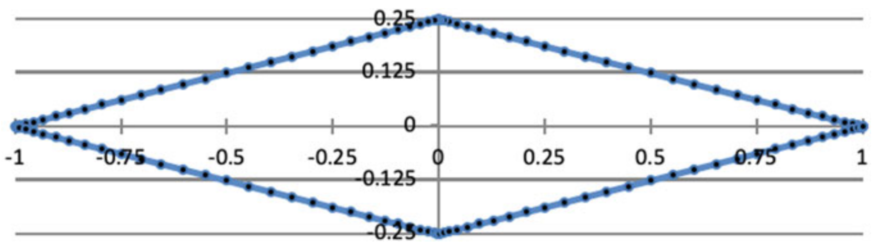

Fig. 2 Precision points of rhombus path

2.2 Synthesis of Mechanism to Generate Rhombus Path

The coordinates of the precision points are extracted from Eq. (1) and used in the synthesis as the known values of the coupler points. The mechanism is synthesized using Eqs. (10)–(21) which govern the geometry of the intended mechanism to satisfy all the 360 precision points. Synthesized mechanism's unknown independent parameters (ϕ, x_A, y_A, β, L_e, L_2, L_3) and dependent parameters (L_6 and L_1) are given in Table 1.

The objective is to minimize link length value (S) for a set of independent variables (ϕ, x_A, y_A, β, L_e, L_2, and L_3) of the linkage whose lower bound (LB) values are −3, −2, 2.5, 2.5, 1, 50, −90 and upper bound (UB) values are −2, −1, 4, 4, 2, 80, −60 respectively for these variables. The difference between the maximum adjustable link length and minimum adjustable link length is the error function i.e. minimization

Table 1 Parameters of the synthesized adjustable mechanism

Optimized rhombus path generation parameters and other variables	Values of the variables and other parameters
Fixed pivot x-coordinate value (x_A)	−2.3554
Fixed pivot y-coordinate value (y_A)	−1.4542
Coupler length (L_2)	3.5747
Rocker length (L_3)	3.8811
Slider offset length (L_e)	1.4641
Coupler point arm angle (β)	62.9637°
Frame orientation angle (θ)	−78.6008°
Crank length (L_1)	0.8345
Coupler pointer length (L_6)	2.8225
Starting crank angle value when pointer is at P_1 (θ_1)	23.4315
Maximum value of adjustable link length (S_m)	6.1869
Minimum value of adjustable link length (S_n)	5.7168
Error function (E_a)	0.4701

of this error is the objective of the synthesis of the mechanism.

$$E_{\mathrm{a}} = S_{\mathrm{m}} - S_{\mathrm{n}} \tag{2}$$

Initial value of L_1 and L_6 are 1.0 and 2.5 unit respectively. Penalty factor and population size are given 400 and 20 respectively and tournament selection method is used. Objective function must satisfy the following constraint functions (3)–(8) to satisfy link length criterion of Grashof and also to avoid linkage dead points.

$$|L_{\mathrm{ce}}|_{\max} - L_3 \leq 0. \quad \text{Where} \quad L_{\mathrm{ce}} = y'_C - L_e \tag{3}$$

$$L_1 + \sqrt{S_m^2 + L_e^2} - L_2 - L_3 \leq 0 \tag{4}$$

$$L_2 - L_3 + L_1 - \sqrt{S_{\mathrm{n}}^2 + L_e^2} \leq 0 \tag{5}$$

$$L_1 - L_2 + L_3 - \sqrt{s_{\mathrm{n}}^2 + L_e^2} \leq 0 \tag{6}$$

$$L_2^2 + L_3^2 - \left(\sqrt{S_{\mathrm{n}}^2 + L_e^2} - L_1\right)^2 - 2L_2L_3\cos\mu_1 \leq 0 \tag{7}$$

where $\mu_1 = 20°$ and S_{n}, minimum value.

$$L_2^2 - L_3^2 + \left(\sqrt{S_{\mathrm{m}}^2 + L_e^2} + L_1\right)^2 + 2L_2L_3\cos\mu_2 \leq 0 \tag{8}$$

where $\mu_2 = 160°$ and S_{m}, maximum value.

In order to trace the path points on the path profile by the pointer in the right order and overcome 'order defect' during full rotation of the crank in the anti-clockwise direction at uniform angular velocity a constraint Eq. (9) is forced.

$$(\theta_1)_i < (\theta_1)_{i+1} \tag{9}$$

2.3 Optimization Using Genetic Algorithm Followed by Pattern Search

In Genetic Algorithm (GA) optimum value of the objective function may not be always reached due to the stopping criteria imposed on GA. This requires further exploration of search space. By changing the stopping criteria, it is possible to find the optimum solution. However, it may require many more function evaluations to reach the optimum value. A local search can be a more efficient in such a scenario.

Pattern search is used for local search that starts from the point where GA reached [12]. Table 1 shows the parameters of the synthesized adjustable mechanism after the optimization process.

3 Rhombus Path Generation Using RAPC Method

RAPC method is used to generate rhombus path. The sides of the rhombus path are inclined to the global x-axis and angles between the sides are acute and obtuse. The equations required to find the path points for uniform incremental values of the crank rotation along the four sides of the rhombus are explained in the following paragraphs. The coordinates of the four vertices of the rhombus P_1, P_2, P_3 and P_4 are shown in Fig. 1. The closed rhombus path is represented by $P_1P_2P_3P_4P_1$.

It is anticipated that the coupler point (M) of coupler link in the mechanism travel through the complete profile path, shown in Fig. 1, through endless path points for uninterrupted generation of intended path. Path point refers to any point on the boundary of the rhombus. RAPC method [11] verifies whether the intended rhombus path generation is achieved for N number of points. Path points on the boundary of rhombus are obtained from synthesized values (x_A, y_A, ϕ, β, L_2, L_1, L_3, L_e and L_6) of the mechanism. Number of precision points N is taken as 360 for better result. Precision points used and their corresponding crank angles obtained in the synthesis do not match to uniform crank arm angular displacements.

However, the dependent and independent variables satisfying the precision points along the designated profile must also satisfy infinite number of path points for precise and continuous generation of desired path. The coordinate values of the first precision point M_1 at P_1 is (1, 0) and corresponding angular position $(\theta_1)_1$ is obtained from Table 1. Precision point at P_1 and initial path point are one and the same. The length between first path point M_1 and fixed point A is given by Eq. (10). Equation (11) gives the angle between link L_1 and line AM_1.

$$L_{AM(1)} = \sqrt{\left(x_{M(1)} - x_A\right)^2 + \left(y_{M(1)} - y_A\right)^2} \quad (10)$$

$$\beta_{1(1)} = \cos^{-1}\left(\frac{L_1^2 + L_{AM(1)}^2 - L_6^2}{2L_1 L_{AM(1)}}\right) \quad (11)$$

Equation (12) also can be used to get $(\theta_1)_1$. In Eq. (12) the $\pm$ sign specifies the two alignments of dyad ABM as presented in Fig. 1 as continuous and dashed lines.

$$(\theta_1)_1 = \tan^{-1}\left[\left(y_{M(1)} - y_A\right), \left(x_{M(1)} - x_A\right)\right] \pm \beta_{1(1)} \quad (12)$$

The Eqs. (13) and (15) give values of coordinates of joint B for first path point. Equation (14) gives angle $(\theta_6)_1$.

$$x_{B(1)} = x_A + L_1 \cos\theta_{1(1)} \tag{13}$$

$$\theta_{6(1)} = \tan^{-1}\left[\left(y_{M(1)} - y_{B(1)}\right), \left(x_{M(1)} - x_{B(1)}\right)\right] \tag{14}$$

$$y_{B(1)} = L_1 \sin\theta_{1(1)} + y_A \tag{15}$$

The value of β is got from synthesized values (Table 1). The coordinates of joint C_1 are attained from Eqs. (16)–(18)

$$\theta_{2(1)} = \theta_{6(1)} - \beta \tag{16}$$

$$x_{C(1)} = L_2 \cos\theta_{2(1)} + x_{B(1)} \tag{17}$$

$$y_{C(1)} = L_2 \sin\theta_{2(1)} + y_{B(1)} \tag{18}$$

For ease of analysis of slider dyad a local coordinate frame is used. Joint A is taken as the local coordinate origin. Coordinates of joint C in local coordinate are obtained from Eqs. (19) and (20) from the global coordinates.

$$x'_{C(1)} = \left(x_{C(1)} - x_A\right)\cos\varphi + \left(y_{C(1)} - y_A\right)\sin\varphi \tag{19}$$

$$y'_{C(1)} = -\left(x_{C(1)} - x_A\right)\sin\varphi + \left(y_{C(1)} - y_A\right)\cos\varphi \tag{20}$$

Location of the slider from fixed the pivot A is given by, adjustable link length, $S_{(1)}$ when the coupler is indicating the first path point, is found from Eq. (21).

$$S_{(1)} = x'_{C(1)} \pm \sqrt{L_3^2 - \left(y_{C(1)} - L_e\right)^2} \tag{21}$$

For the first path point, using Eqs. (10)–(21), adjustable parameter value $S_{(1)}$ is obtained. The second path point is obtained by intersection of line P_1P_2 at $M_{(2)}$ and an arc of length L_6 from joint B. This gives the coordinates $X_{M(2)}$ and $Y_{M(2)}$ of the path point $M_{(2)}$ from Eqs. (22)–(24) after incrementing the crank by 1°.

$$\left(y_{M(2)} - y_{B(2)}\right)^2 + \left(x_{M(2)} - x_{B(2)}\right)^2 = L_6^2 \tag{22}$$

$$y_{M(2)} = m x_{M(2)} + d, \tag{23}$$

where 'm' is slope, and 'd' is intercept.

Substituting $y_{M(2)}$ in Eq. (22) and simplifying gives a quadratic Eq. (24) in $x_{M(2)}$.

$$a x_{M(2)}^2 + b x_{M(2)} + C = 0 \tag{24}$$

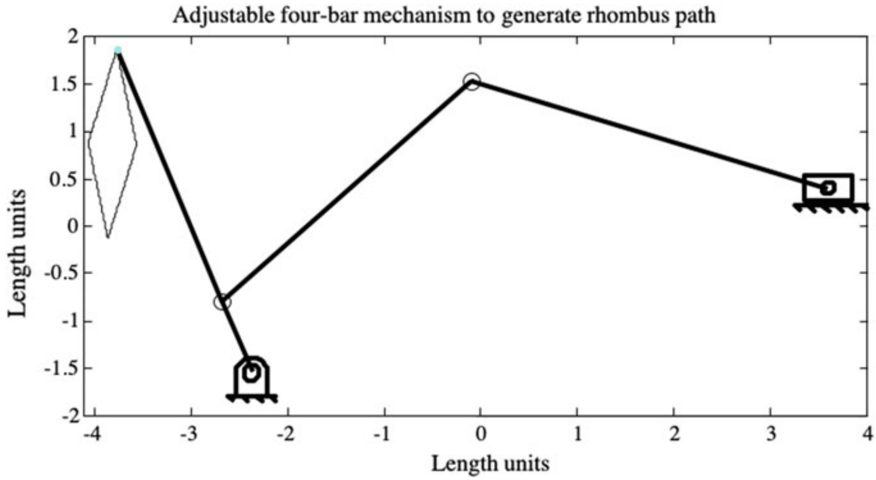

Fig. 3 Synthesized mechanism to generate rhombus path

where $a = (1+m)^2$, $b = \left(2dm - 2my_{B(2)} - 2x_{B(2)}\right)$, and $C = y_{B(2)}^2 + x_{B(2)}^2 + d^2 - 2dy_{B(2)} - L_6^2)$

Solving Eq. (24) for $x_{M(2)}$ and substituting in Eq. (22) gives $y_{M(2)}$ in Eq. (25).

$$y_{M(2)} = y_{B(2)} \pm \sqrt{L_6^2 - (x_{M(2)} - x_{B(2)})^2} \tag{25}$$

Incrementing crank angle by $\Delta\theta_1$ and substituting $x_{M(2)}$, $y_{M(2)}$ through Eqs. (10)–(21) in the place of x_{M1}, $y_{M(1)}$ to get the adjustable parameter value $S_{(2)}$.

Same procedure is followed till all the path points along P_1P_2 until the value of $x_{M(1)}$ value is less than or equal to 0 and $y_{M(1)}$ value is less than or equal to 0.25. Similarly path points for the other sides of the rhombus are obtained using the required slope and intercept values in the Eqs. (23). Thus the adjustable parameter values $S_{(1)}$ and corresponding θ_1 values of all the path points constitute the RAPC method. These path points are used to generate the required rhombus path. Figure 3 shows synthesized adjustable mechanism to generate rhombus path.

4 Results and Discussions of Rhombus Path Generation

Figure 4 shows the desired and generated rhombus path for different number of path points. As mentioned in the previous section, the rhombus path generation displays deviation from the desired path only at the corner points. Figures 5, and 6 show closer view of corner point at P_2 and P_3 respectively.

The deviation from the desired path at P_2 is more for 360 path points which correspond to 1° crank angle increment compared to 720 and 1440 path points which

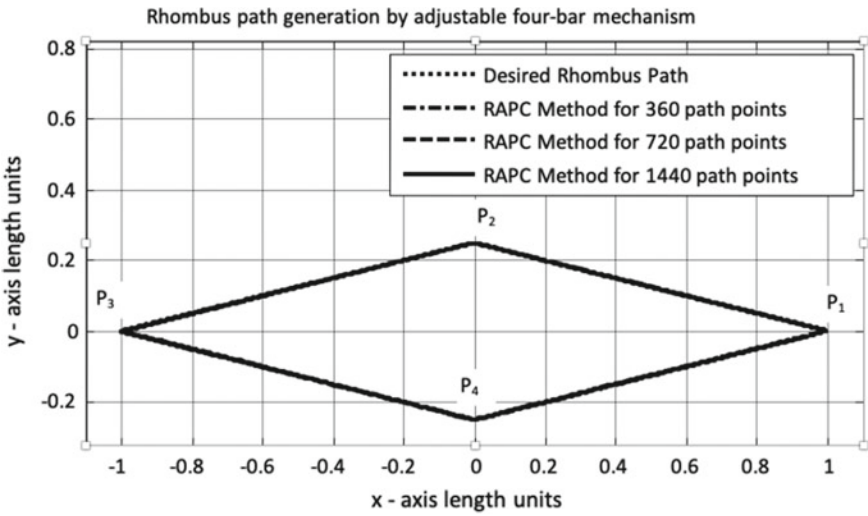

Fig. 4 Desired and generated rhombus paths

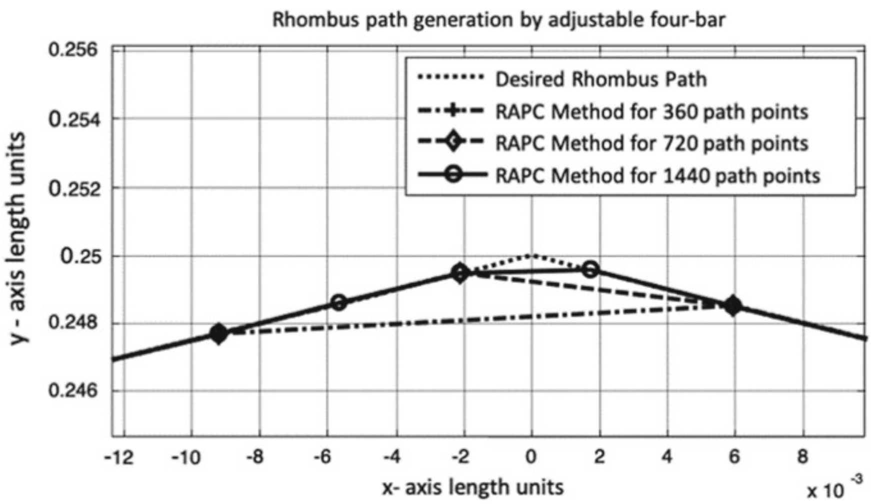

Fig. 5 Closer view of desired and generated rhombus paths at P_2

correspond to half and quarter degree crank rotation respectively. The deviation at P_3 is the lowest. The decimal values of Fig. 6 validates the accuracy of the RAPC method proposed in the case of rhombus path generation. Validity of this path generation is compared and verified with the path generation of corners-chamfered-rectangle [12] and found correct for precise and continuous rhombus path generation as shown in Fig. 6. Deviation error from the desired path in terms of area is the lowest at P_3 corner compare to P_2 and P_4 corners of rhombus path.

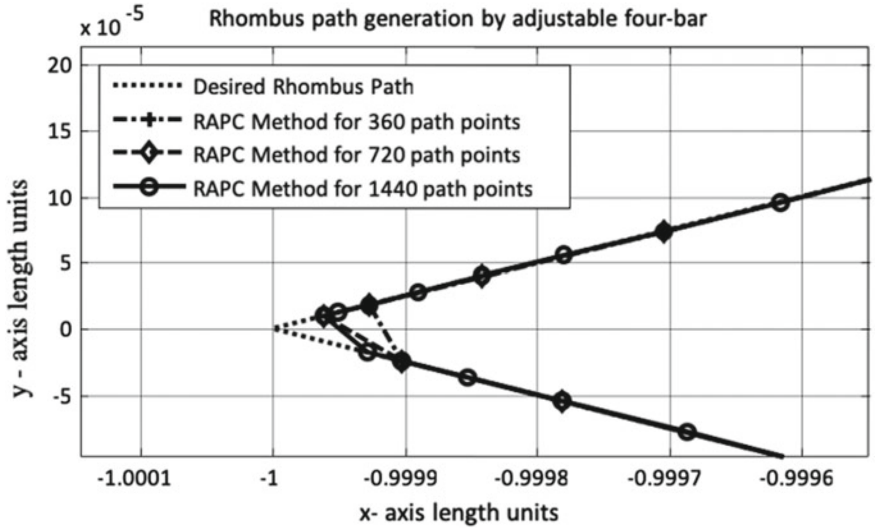

Fig. 6 Closer view of desired and generated rhombus paths at P_3

It is to be noted that the RAPC method comfortably handles both obtuse and acute angle of the rhombus path at P_2 and P_3 corners and predicts the deviation with high accuracy as shown in Figs. 5 and 6 respectively. Figure 7 shows synthesized and RAP curves for different path points.

5 Conclusions

Precise rhombus-path generation mechanism is synthesized and its precision is verified using reconstructed adjustable parameter curve method using 360,720 and 1440 path points. Increasing path points further, the desired curve can be attained. RAPC method is used to verify the results. The results show that the adjustable parameter curve required to generate rhombus path has sharp turning points which can further be studied by filleting the two obtuse vertices.

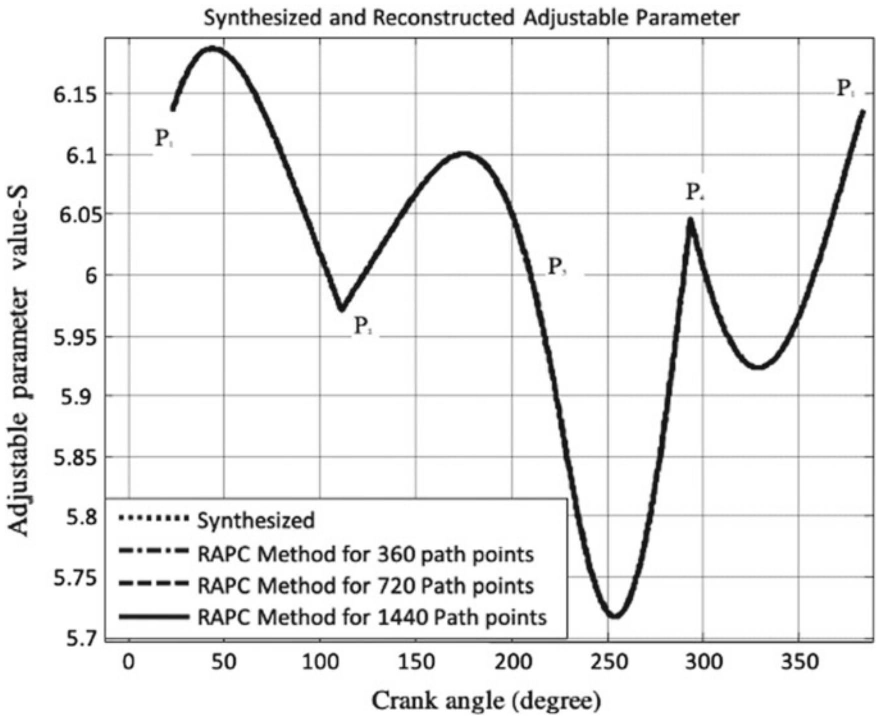

Fig. 7 Synthesized and RAP curves of rhombus path generation

References

1. Chong P, Sodhi RS (2010) Optimal synthesis of adjustable mechanisms generating multiphase approximate paths. Mech Mach Theory 45:989–996
2. Kay F, Haws R (1975) Adjustable mechanisms for exact path generation. ASME J Eng Ind 97(2):702–707
3. Singh Y, Kohli D (1981) Synthesis of cam-link mechanism for exact path generation. Mech Mach Theory 16(4):447–457
4. Shimojima H, Ogawa K, Fujiwara A, Sato O (1983) Kinematic synthesis of adjustable mechanisms. Bull JSME 14:621–632
5. Mundo D, Gatti G (2008) A graphical-analytical technique for the synthesis of noncircular gears in path-generating geared five-bar mechanisms. Trans CSME 32(3–4):488–497
6. Mundo D, Liu JY, Yan H (2006) Optimal Synthesis of cam-linkage mechanisms for precise path generations. J Mach Des 128:1253–1260
7. Chanekar PV, Ghoshal A (2013) Optimal synthesis of adjustable planar four-bar crank-rocker type mechanisms for approximate multi-path generations. Mech Mach Theory 69:263–277
8. Zhou H (2009) Dimensional synthesis of adjustable path generation linkages using the optimal slider adjustment. Mech Mach Theory 44:1866–1876
9. Hrishikesh Y, Ameya P, Gunesh R (2013) Optimum synthesis of path generating adjustable mechanisms with improved slope continuity. Trans Can Soc Mech Eng 37(2):197–214
10. Ganesan G, Sekar M (2014) Kinematic analysis of rectangular path generating adjustable four-bar linkage. Appl Mech Mater Trans Tech Publ 592–594:1094–1098

11. Ganesan G, Sekar M (2017) Optimial synthesis and kinematic analysis of adjustable four-bar linkages to generate filleted rectangular paths. Mech Based Des Struct Mach 45(3):363–379
12. Ajith Kumar G, Ganesan G, Sekar M (2018) Near perfect path generation of corners-chamfered-rectangle and single synthesis cam-link mechanism to generate special-slot path. Mech Based Des Struct Mach 46(4):483–498

Sensor Fusion for Automotive Dead Reckoning Using GPS and IMU for Accurate Position and Velocity Estimation

Lalith Prabu Nalla Perumal and Arockia Selvakumar Arockia Doss

Abstract In recent years, detecting the position of the vehicle is an important task. The goal of detecting the position of the vehicle can be achieved using Global Positioning System (GPS) technology by getting approximate position data of the ego-vehicle. For better and accurate positioning, automotive dead-reckoning can be used. Automotive dead-reckoning (ADR) technology is a high-end navigation system. In this paper, an ADR is used to calculate the position based on the distance and direction of the vehicle traveled from the last known location. This gives an accurate estimation of the 3-axis position and velocity components based on vehicle data retrieved from GPS and Inertial Measurement Unit (IMU) sensor. ADR not only allows full coverage in indoor car parking, tunnels, and underpasses but also effectively eliminates the impact of multipath effects in urban canyons. The vehicle is incorporated with sensors that record wheel rotation along with the steering direction and the sensors are allowed to take continuous measurements with the help of the last known location. The position and velocity shall be corrected even if quality GPS data is available. In case of partial GPS blockage, the estimation shall be done with different strategy/weightage factors. In case of complete GPS blockage, the prediction shall continue for some approximation time, with the help of vehicle and IMU sensor data. Finally, various experiments are conducted using Kalman filter and extended Kalman filter, and the prediction results are found to be satisfactory.

Keywords Navigation system · Kalman filter · ADR · PS · IMU · Prediction

1 Introduction

Across the globe, advanced driver assistance system (ADAS) technology is one of the most and fastest growing technologies. The main purpose for ADAS technology is used to make comfort to the driver and reduce the accidents. Corresponding

L. P. Nalla Perumal · A. S. Arockia Doss (✉)
School of Mechanical Engineering, Vellore Institute of Technology, Chennai, Tamil Nadu 600127, India
e-mail: arockia.selvakumar@vit.ac.in

E. T. Akinlabi et al. (eds.), *Trends in Mechanical and Biomedical Design*, Lecture Notes in Mechanical Engineering,
https://doi.org/10.1007/978-981-15-4488-0_8

to ADAS technology, a high integrity navigation system for vehicle is developed. Mainly, two types of sensors are required to compute the navigation system. One is dead-reckoning sensor and another is external sensor. Dead-reckoning sensors (IMU Sensor) will accumulate more error with respect to time. External sensor will give an accurate position of ego-vehicle with the help Global Positioning System (GPS) [1, 2]. In actual time, GPS technology is mostly used for locating and pointing out the position and assists for the vehicle. The signals from GPS are so wobbly because of huge buildings and constructions which will give inaccuracy to indicate the position. To get the better of these conditions, the GPS system and dead-reckoning system are integrated [3]. This trustworthy system is used to reduce GPS errors and guide to evaluate the dead-reckoning system [4]. Integrating with GPS is two different types of approaches: one is tightly coupled and another one is loosely coupled. Loosely coupled integration method is mainly used when any one of the sensors get failed with lower processing time, and it will get results from another sensor by using less state vector. The main drawback in tightly couple is that the state vector size and will increase with large processing time. Similarly, the disadvantage in loose couple is that it is unworkable to give measurement update from GPS filter where GPS gives inaccurate signal [5]. Usually, dead-reckoning sensors are not easy to compute, and it generates errors with respect to time [5]. Basically, IMU sensors are the combination of accelerometer, gyroscope, and magnetometer and are implemented as the sensor fusion [6] with Kalman filter (KF) and extended Kalman filter(EKF) of GPS and IMU [7].

1.1 Kalman Filter

Kalman Filter is an optimal state estimation algorithm and iterative mathematical process that uses a set of equation and consecutive data input. The KF can estimate the ego-vehicle position. GPS unit can be equipped with an ego-vehicle. For minimum distance, Kalman will estimate and give high accuracy position, and it follows the law of physics, by integrating its ego-vehicle velocity by continuously following the steering wheel angle and wheel revolutions. This type of smart approach is called dead reckoning, but sometimes it will accumulate small errors due to drift over time. Basically, KF has two major steps to predict and update. This is the famous technique for filtering and prediction in linear Gaussian systems. By physics' law of motion, it will change the ego-vehicle position with respect to time in prediction step. Similarly, new covariance and new estimated position will be calculated. As it may be the velocity of ego-vehicle which is proportional to the covariance, it is found to be doubted about the precise value of the dead-reckoning estimating position with high velocity of the ego-vehicle but undoubted about the estimating position of the ego-vehicle when moving with low velocity. The state transition probability and measurement probability must be linear and with added Gaussian noise. This probability therefore assumes linear dynamics and in this form is called linear Gaussian. In update steps, the measurement of ego-vehicle is observed from GPS unit. The relative covariance from prediction step will tell that the new measurement is doubtful or un-doubtful for updated prediction. Discrete KF is proposed in this work; generally, it is used for stochastic system.

1.2 Kalman Filter Algorithm with Equations

Figure 1 shows the workflow of each step of the KF algorithm with equations. Figure 2 shows the effects of Kalman gain between measurements and estimation, where X—State matrix, P—State covariance matrix (represents errors in the estimate), U—Input matrix, W—Process noise matrix, Q—Process noise covariance matrix, R—Sensor noise covariance matrix (measurement error), H—Conversion matrix ($C = H$), K—Kalman gain.

Prediction Process

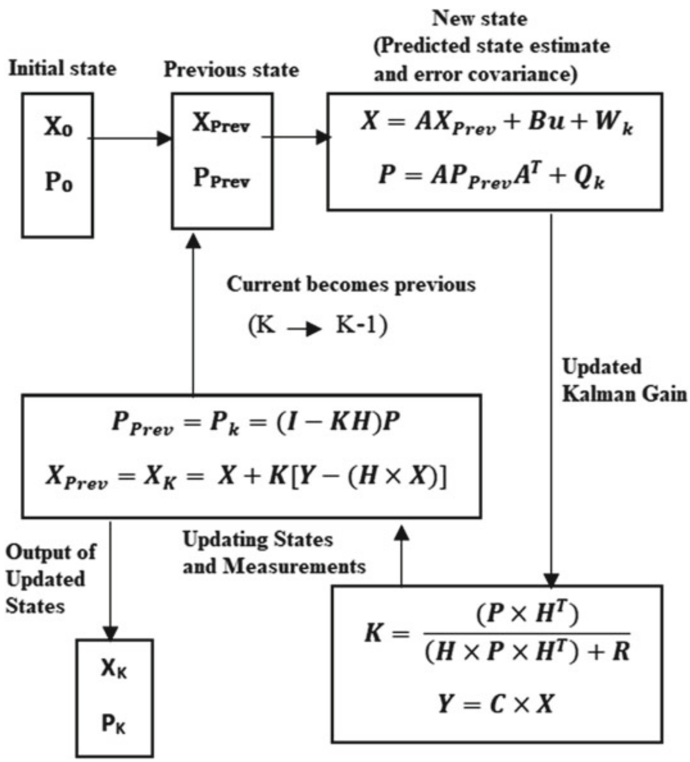

Fig. 1 Algorithm flowchart of KF

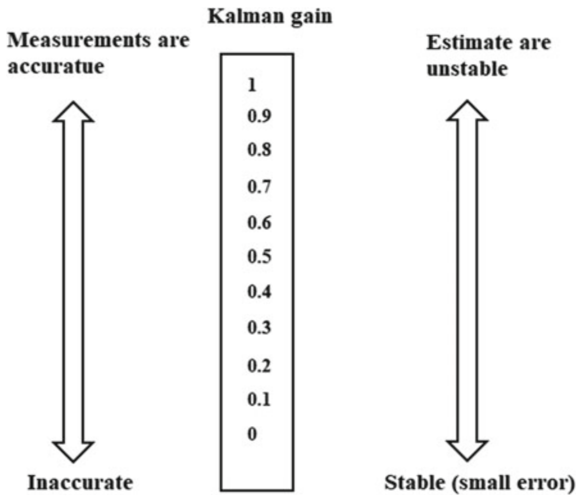

Fig. 2 Effects of Kalman gain

$$X = AX_{\text{Prev}} + Bu + W_k \tag{1}$$

It predicts the estimate of the next state based on the previous state $\boldsymbol{X}_{\boldsymbol{k}-1}$ and control input $\boldsymbol{u}_{\boldsymbol{k}}$. A and B matrices map $\boldsymbol{X}_{\boldsymbol{k}-1}$ and $\boldsymbol{u}_{\boldsymbol{k}}$, respectively. It predicts the covariance matrix of the next estimate. Prediction process of any system is never perfect. For this reason, some noise is added into the prediction of covariance matrix. This equation is derived from Riccati equation.

$$P = AP_{\text{Prev}}A^T + Q_k \tag{2}$$

Update Process

$$K = \frac{\left(P \times H^T\right)}{\left(H \times P \times H^T\right) + R} \tag{3}$$

It calculates Kalman gain, a factor which weights the measurement against prediction. A higher Kalman gain will bring the final estimate closer to the measurements while a lower Kalman gain will make a good estimate for the prediction.

$$X_{\text{Prev}} = X_K = X + K[Y - (H \times X)] \tag{4}$$

It updates the state vector. This is the final state estimate that forms the filter. Using the weightage factor K, the equation modifies the prediction by some portion of the innovation Y. If Y and HX are equaling system state, and the measurements are perfectly accurate.

$$P_{\text{Prev}} = P_k = (I - KH)P \tag{5}$$

It updates the covariance matrix. The update step can give only result in a reduction of covariance because the update step adds sensor information to the estimate. This is the reason to subtract the covariance and product of Kalman gain and covariance.

1.3 Extended Kalman Filter Algorithm with Equations

Usually, linear system cannot give accurate prediction results in practically. Hence using EKF can able to reach the accurate prediction. Figure 3 explains the workflow of each step about EKF algorithm with equations.

The EKF tranquilizes the linearity assumption by assuming that the state transition and measurement probabilities are controlled nonlinear functions.

$$X_k = f(X_{k-1}, u_k, w_k)$$

$$y_k = h(X_k, v_k)$$

where $f \rightarrow$ predicted state from the previous estimate, $h \rightarrow$ predicted measurement from the predicted state. The functions of f and h cannot be applied to the covariance directly. Instead a matrix of partial derivatives (the Jacobian) is computed. At each timestamp, the Jacobian is evaluated with current predicted states. This process

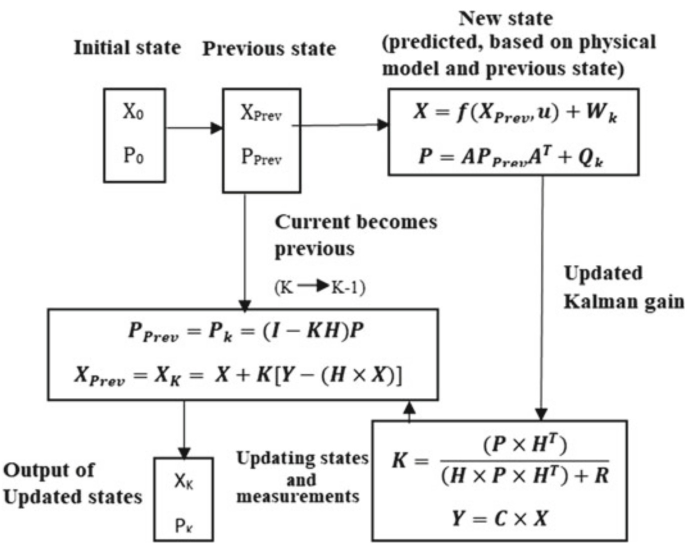

Fig. 3 Mathematical equations of algorithm flowchart of EKF

essentially linearizes the nonlinear function around the current estimate. This is the major differences between Kalman and EKF. The EKF is additionally using Jacobian in the predicted states but not in KF, where X—State matrix, $F(X, U)$—Nonlinear state transition matrix, P—State covariance matrix (represents errors in the estimate), U—Input matrix, W—Process noise matrix, Q—Process noise covariance matrix, R—Sensor noise covariance matrix (measurement error), F, H—Jacobian matrix, K—Kalman gain, Y—Measurement state, Z—Measurement noise low quality of IMU devices are highly decrease estimating the position when bad GPS signal occurs.

In autonomous vehicle, unnecessary noises are filtering out for effective positioning method [8]. By Kalman and EKF algorithm, performance shows that the comparison of unfiltered (measurement) and filtered (Kalman output) data [9]. Using CarMaker software will create the environment. EKF is used in the filtering process with vehicle dynamics models. By different scenarios, the simulation environment will give the different data collected and used to estimate the position of the ego-vehicle [10]. There are few techniques to find the position of the ego-vehicle when GPS is not available. Basically, GPS will give in the form of latitude and longitude. There are few techniques to convert lateral and longitude into position of X and Y like flat earth and Gauss–Kruger, and it will give good accuracy. Experimental results explained that the KF and EKF estimation-based algorithm was observed for signal measurement and correlated with raw data [8] to check whether accuracy is improved or its again robust to retain positioning output during short term of GPS signal dropout [11]. From the literature survey, KF and EKF are one of the best methods for estimating the prediction values for linear system and nonlinear system, respectively. This algorithm is mainly used for GPS available and unavailable. The proposed system software implementation is made clear in Sects. 3 and 4, respectively.

2 Proposed System

In this work, KF and EKF algorithms are proposed to estimate and predicting the positions (P_x and P_y), velocity (V), yaw (ψ). Figure 4 shows the visionary of the proposed work. Receiving the data from IMU and vehicle sensors with the combination of static and dynamic data, and it will be accumulated to the KF and EKF which gives static data. Usually, KF can able to predict for linear system, and especially, EKF can able to predict for nonlinear system. These filters are mainly used to eliminate noise and predict the states.

3 Implementation

In this research work, the data is developed from CarMaker software and collected data consign to the model. Figure 5 shows the kinematic model to evaluate the process

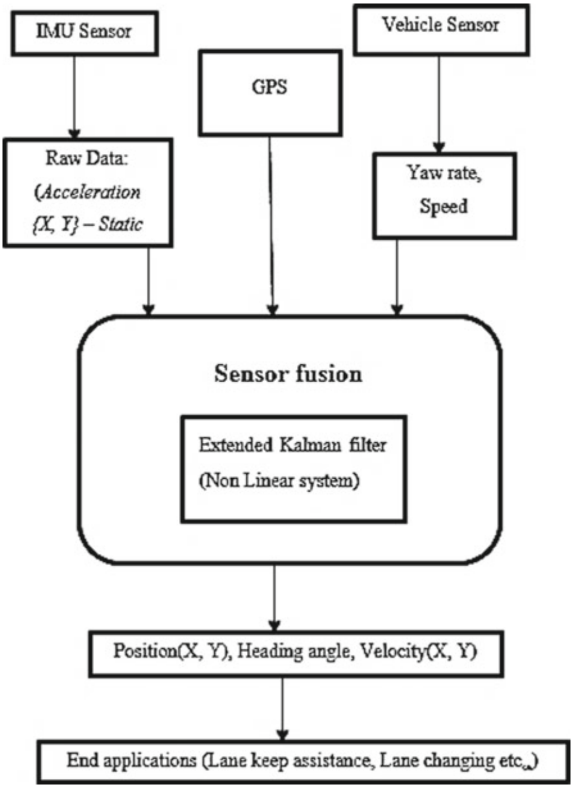

Fig. 4 Overview of methodology of the project

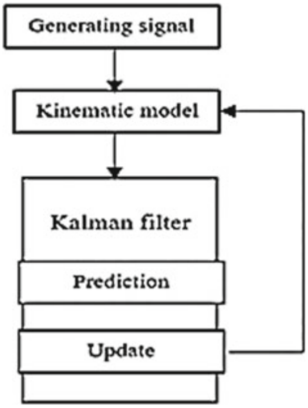

Fig. 5 Process of KFs

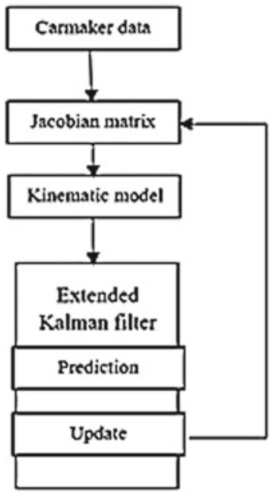

Fig. 6 Calculation of discrete KF

in KF. Figure 6 shows the process flow of EKF, and both the processes are similar; but in EKF before kinematic model, Jacobian matrix is used to nonlinear to linearize system.

3.1 Discrete Kalman Filter (DKF) Without Using CarMaker Data

Figure 7 shows the conversion mathematical equation flowchart of DKF. It has several steps to follows initially to generate the raw acceleration signal.

3.2 Extended Kalman Filter (EKF) Using CarMaker Data

In EKF, there are two steps: prediction and update. The flowchart of EKF when GPS available and unavailable is shown in Fig. 8. When GPS is not available, EKF should take past data values to estimate the position for few seconds. There are some few techniques available for prediction. One technique is disable the updating part and estimate the position, and another technique is without disable the updating part and take the GPS available past data of P_x, P_y, yaw and measurement velocity. In this case, it is not require to update velocity because velocity will get vary continuously. Velocity will entirely depend upon the ego-vehicle drive. Velocity details will be received from vehicle sensor. Basically, GPS will give lateral and longitude data of P_x, P_y, and yaw, not velocity. Hence, when GPS is unavailable, it is possible

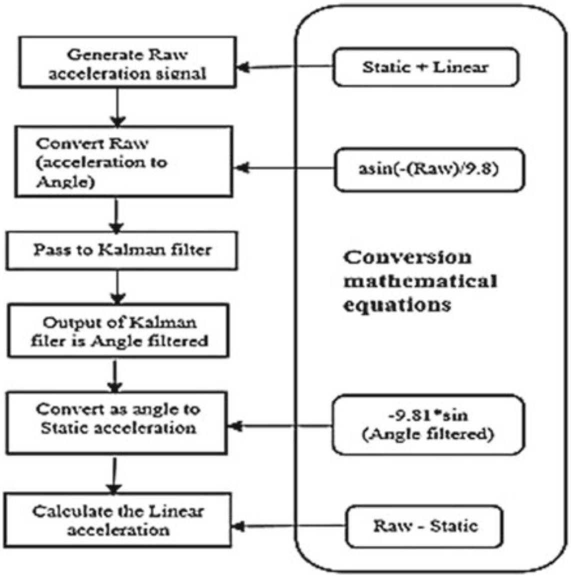

Fig. 7 Conversion mathematical equations flowchart of DKF

to estimate the position by this technique. This technique will give more accuracy results than disable update technique.

4 Experimental Results and Discussion

Figures 9 and 10 show the discrete KF output of linear acceleration and static angle in OCTAVE.

Figures 11, 12 and 13 show the output of EKF in OCTAVE, and here there are four states and two measurements. The states are position (x, y), velocity, yaw angle, and the input as acceleration and yaw rate. Hence the Jacobian matrix should be (4×4). In the plots, it has clearly shown that all the three states are predicted properly when GPS is unavailable. From the experimental results, it is found that the EKF prediction works satisfactory. X-axis is time for the above graphs. Y-axis for position (x, y) is in meters, and yaw is in degrees. Here velocity is measurement hence there is no point to predict the velocity because from the ego-vehicle will get data continuously from the vehicle sensor. GPS data does not give velocity of the vehicle, and it will give only position and yaw rate.

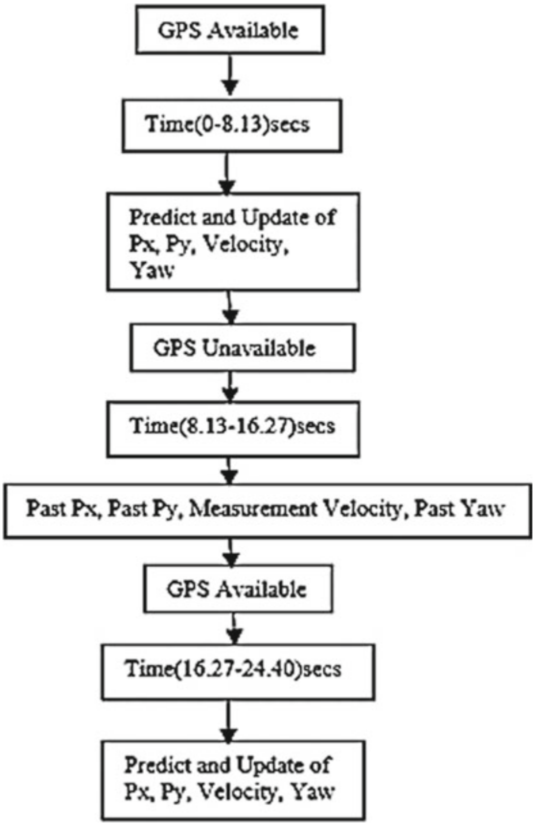

Fig. 8 Flowchart of EKF when GPS available and unavailable

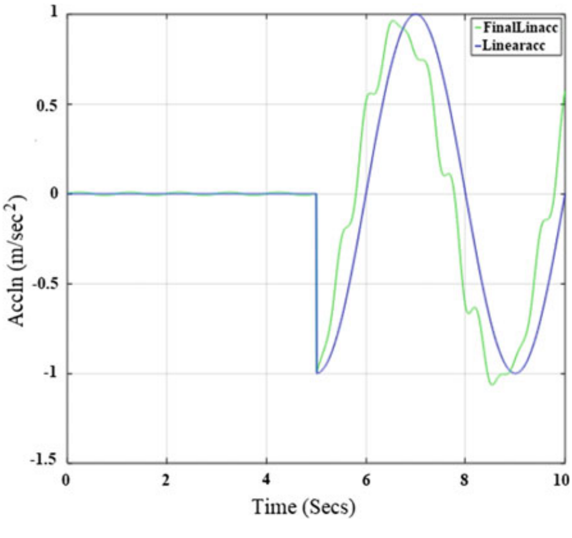

Fig. 9 Linear acceleration

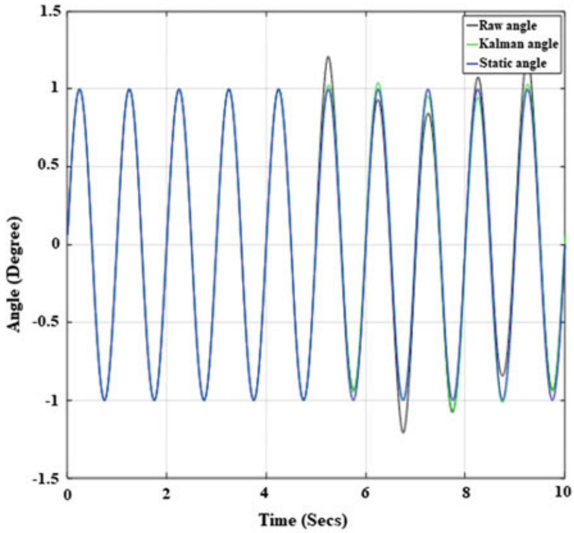

Fig. 10 Static angle

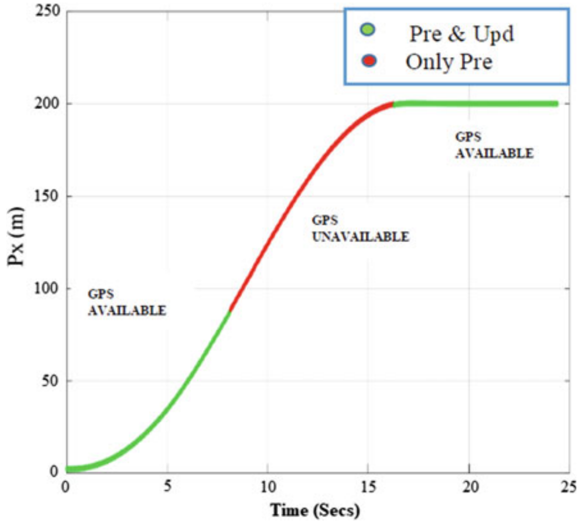

Fig. 11 P_x (Original and prediction)

5 Conclusion

Based on the study of Automotive dead-reckoning fusion sensor system, the prediction of ego-vehicle position and velocity are obtained irrespective of the availability of the GPS signal using KF and EKF. Kalman Filter is found to be producing accurate results for linear system, but the system is considered to be as nonlinear system; due to this nonlinearity issue, an Extended Kalman Filter is incorporated to predict the

Fig. 12 P_y (Original and prediction)

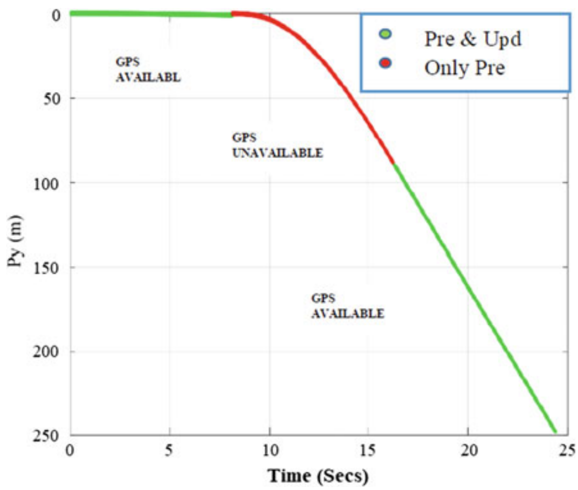

Fig. 13 P_y (Original and prediction)

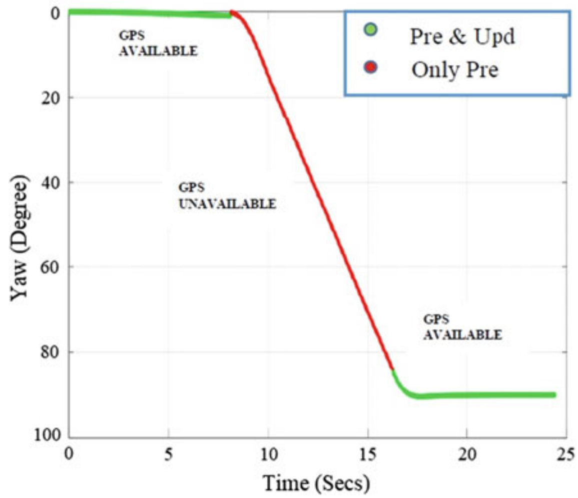

position and velocity for nonlinear system. EKF is found to be suitable for nonlinear system. The experimental results are taken based on three sets of time varying with 8.13 seconds; in the first set of time (0–8.13) seconds, the GPS is available. But in the second set of time (8.13–16.27) seconds, have unavailability of GPS, and finally in the third set of time (16.27 to 24.40) seconds, the GPS is available. Based on the experimental results, it is found that in the first and third sets of time the GPS data received accurately; but in the second set of time, the EKF will start to predict current state with the help of past state. In this condition, the EKF is found to be predicted up to the accuracy level of 95–98% when the GPS is in unavailable time, i.e., when the sensor data are not received accurately. In the future, the researcher can focus with the fusion of EKF with flat earth/Gauss–Kruger technique. This technique is used for conversion process which is used to convert the three-dimensional points to two-dimensional planes. It is used to calculate the position with the help of latitude and longitude.

References

1. Li Q, Fang Z, Li H (2004) The application of integrated GPS and dead reckoning positioning in automotive intelligent navigation system. Positioning 1.08(2004):0
2. Tarfe VS, Arockia Selvakumar A (2016) Path tracing for ground wheeled robot in partially known environment. Int J Inf Commun Technol 9(3):356–365
3. Dicu N, Andreescu G-D, Gurban EH (2018) Automotive dead-reckoning navigation system based on vehicle speed and YAW rate. In: 2018 IEEE 12th international symposium on applied computational intelligence and informatics (SACI). IEEE
4. Zhao L, Ochieng WY, Quddus MA, Noland RB (2003) An extended Kalman filter algorithm for integrating GPS and low cost dead reckoning system data for vehicle performance and emissions monitoring. J Navig 56(2):257–275
5. Fakharian A Gustafsson T, Mehrfam M (2011) Adaptive Kalman filtering based navigation: An IMU/GPS integration approach. In: 2011 International conference on networking, sensing and control. IEEE
6. Groves PD (2013) Principles of GNSS, inertial, and multisensor integrated navigation systems. Artech House
7. Kasargod S et al (2014) Vehicle navigation system with dead reckoning. U.S. Patent No. 8,825,397, 2 Sept 2014
8. Jang S et al (2015) A study on integration of particle filter and dead reckoning for efficient localization of automated guided vehicles. In: 2015 IEEE international symposium on robotics and intelligent sensors (IRIS)
9. Romaniuk S, Gosiewski Z (2014) Kalman filter realization for orientation and position estimation on dedicated processor. Acta Mechanica et Automatica 8.2(2014):88–94
10. Lanfelt C, Rogenfelt A. Dead Reckoning during safe stop of autonomous vehicles.
11. Zhang M, Liu K, Li C (2016) Unmanned ground vehicle positioning system by GPS/dead-reckoning/IMU sensor fusion. In: 2nd Annual international conference on electronics, electrical engineering and information science (EEEIS 2016). Atlantis Press

Optimal Dimensional Synthesis of Double-Semi-circle and Double-Semi-ellipse Path Generating Adjustable Four-Bar Mechanisms

Ganesan Govindasamy, Gadudasu Babu Rao, and Rajakumar S. Rai

Abstract Synthesis of adjustable four-bar mechanisms to generate continuous and precise path of double-semi-circle-straight-line (DSCSL) and double-semi-ellipse-straight-line (DSESL) path generation is investigated and verified. Harmonic spacing (HS) algorithm is used to improve precision points spacing along the intended profile paths. Bi-cubic interpolation is used to extract adjustable parameter value of intermediary path points along the profile of path generation conforming to uniformly incremented crank rotation value. Precision points are used in the synthesis to get dimensional values of link lengths and other parameters of adjustable mechanisms. Motion simulation of adjustable mechanism to generate intended coupler path profiles is carried out to verify the dimensional synthesis of the mechanisms. Pattern search (PS) is implemented in the synthesis of mechanism from the results of genetic algorithm (GA) as a hybrid method. Results demonstrate continuous and precise path generation of selected path profiles.

Keywords Double-semi-circle-straight-line path generation · Double-semi-ellipse-straight-line path generation · Adjustable path generation mechanism

1 Introduction

Path generation is the motion of coupler point to trace a path profile. Point-to-point path generation is to follow the computed precision points while the trajectory between the computed points is approximated. The other type of path generation is of continuous type which specifies whole path with many points which approximately pass through the specified curve. Adjustable mechanism is neither equal to sophisticated flexible robot nor equal to non-adjustable mechanism. Adjustable mechanism takes the middle ground between robot and non-adjustable mechanism

G. Govindasamy (✉) · G. B. Rao · R. S. Rai
Department of Mechanical Engineering, Karunya Institute of Technology and Sciences, Karunya Nagar, Coimbatore 641114, India
e-mail: vivajijaya67@gmail.com

E. T. Akinlabi et al. (eds.), *Trends in Mechanical and Biomedical Design*, Lecture Notes in Mechanical Engineering,
https://doi.org/10.1007/978-981-15-4488-0_9

[1]. The characteristics of non-adjustable mechanism such as precision, high speed, and simplicity and some of the abilities of flexible multi-axis robots are similarly attained in adjustable mechanisms. In contrast to analytical methods that satisfy fewer precision points precisely, optimization methods like genetic algorithm, pattern search, neural networks, etc., satisfy many precision points. Haws and Kay [2] used an adjustable mechanism employing a cam-link to generate one-fourth of a square and a cardioid path. Kohli and Singh [3] made use of cam-link linkages to generate exact path. Ogawa et al. [4] synthesized adjustable four-bar multi-link linkages to generate L-shaped and straight lines paths passing through several precision points. Mundo and Gatti [5] employing non-circular gears in between two input links synthesized optimally five-bar linkages for precise path generation. Mundo et al. [6] synthesized adjustable mechanism with a cam-link to adjust the location of fixed pivot of the driven side link for exact path generation. Ghoshal and Chanekar [7] synthesized adjustable four-bar linkages in two stages in order to reduce number of variables in the linkage design.

Synthesis of continuously adjustable four-bar crank-rocker linkage to generate rectangle path was attempted by Zhou [8]. Attempt has also been made by Hrishikesh et al. [9] synthesized adjustable four-bar linkage to generate a rectangle path by improving the slope continuity of the adjustable link length curve. Ganesan and Sekar [10] used graphical method to obtain adjustable parameter curve (APC) from the dimensions of the mechanism synthesized by Zhou [8] to produce rectangular path. Ganesan and Sekar [11] optimally synthesized adjustable four-bar linkages to generate rectangular path with filleted corners. Ajith Kumar et al. [12] synthesized continuously adjustable four-bar mechanisms to generate corners-chamfered-rectangle, fully-chamfered-rectangle, and rectangle employing RAPC method to design an adjustable four-bar cam-linkage mechanism with one DOF to generate oblong-hole path.

It has been found from the literature that the DSCSL and DSESL path generation mechanisms are not investigated. Section 2 presents adjustable linkage model, precision points on DSCSL and DSESL path, and dimensional synthesis using hybrid optimization. Section 3 presents bi-cubic interpolation of adjustable parameter values of precision points and their corresponding crank angles to extract path points along the DSCSL and DSESL paths for one degree increment of crank rotation for one revolution. Section 4 presents the results of precise DSCSL and DSESL path generation for various path points. Conclusions and scope for future work are presented in Sect. 5.

2 Adjustable Mechanism Model to Generate DSCSL and DSESL Paths

Zhou's [8] four-bar adjustable mechanism model is used in the synthesis to generate precise and continuous DSCSL and DSESL paths, as shown in Fig. 1 for DSCSL

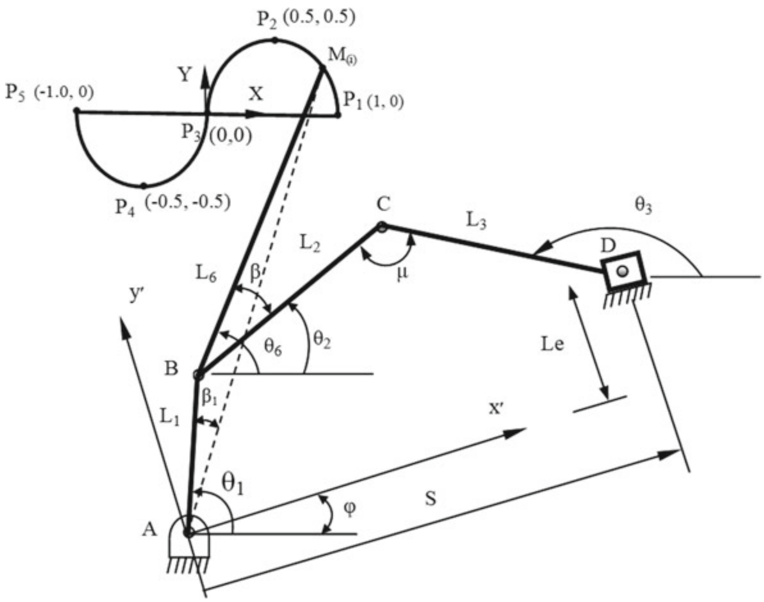

Fig. 1 Adjustable linkage model

path, in which a rocker (L_3) is carried by a slider (D) which forms the adjustable link. This adjustable link length (S) from the fixed point (A) in the direction of x'-axis of a local co-ordinate frame to the pin joint between the rocker and slider is called 'adjustable link length or parameter' of the mechanism. Link AB is crank (L_1). In triad link BCM, side BC forms coupler link (L_2), and side BM (L_6) carries coupler point (M). In this adjustable four-bar mechanism, the required adjustable parameter values (S) are determined so that the coupler point can trace DSESL and DSCSL paths precisely when the crank makes one revolution.

2.1 Precision Points Algorithm for DSCSL and DSESL Paths

Coupler point has to travel along the $P_1P_2P_3P_4P_5P_1$ path which comprises two inverted semi-circles joined by a straight line as shown in Fig. 1 and DSESL path, which comprises two inverted semi-ellipses, with semi-major axis is twice the semi-minor axis, joined by a straight line.

Difficulty arises when the coupler point negotiating P_1, $P_{3,}$ and P_5 positions where it changes direction drastically. This demands closer precision points near these points. The following harmonic spacing algorithm (1) satisfies the closer precision points at the ends of a straight line or an arc [11] as shown in Fig. 2.

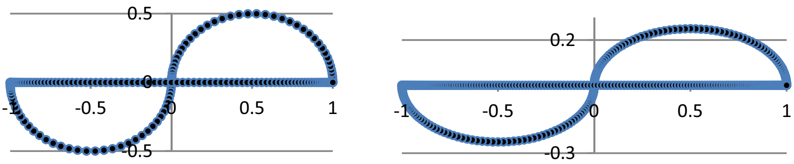

Fig. 2 Precision points of DSCST and DSEST paths

$$x_j = \frac{(x_i + x_f)}{2} + \frac{(x_i - x_f)}{2}\left[\cos\left(\frac{(j - 1F)}{N - 1}\right)\right] \tag{1}$$

where x is variable with an interval $[x_i, x_f]$ and $j = 1, 2, \ldots N$, x_j—intermediary point coordinate value, x_i—initial point coordinate value, and x_f—end point coordinate value. N—number of precision points inclusive of initial point and end point.

2.2 *Mechanism Synthesis of to Generate DSCSL and DSESL Path*

The coordinates of the precision points are extracted from Eq. (1) and used in the synthesis as known values of the coupler points. The mechanism is synthesized using Eqs. (10)–(21) which govern the geometry of the intended mechanism to satisfy all the 360 precision points. The unknown parameters (x_A, y_A, ϕ, β, L_2, L_3, L_e) and dependent parameters (L_1 and L_6) of the synthesized mechanisms are given in Table 1.

The objective is to minimize adjustable link length value ‘S’ for a set of independent variables (x_A, y_A, L_2, L_3, L_e, β and ϕ) of the adjustable linkage whose lower bound (LB) values are −2.5, −2, 2.2, 3, 1.1, 50, −90 and upper bound (UB) values are −1.5, −1.2, 3.5, 4, 70, −70, respectively, for these variables for DSCSL path. The adjustable link length range forms the error function, i.e., minimization of this error is the objective of the synthesis of the mechanism.

$$E = S_{\mathrm{m}} - S_{\mathrm{n}} \tag{2}$$

Initial values of L_1 and L_6 are 1.0 and 2.5 units, respectively. Penalty factor, population size, and selection method used are 400, 20, and tournament, respectively. Objective function must satisfy the following constraint functions (3)–(8) to satisfy link length criterion of Grashof and to evade dead points of the linkage.

$$|L_{\mathrm{ce}}|_{\max} - L_3 \le 0 \quad \text{Where} \quad L_{\mathrm{ce}} = y'_C - L_e \tag{3}$$

$$L_1 + \sqrt{S_{\mathrm{m}}^2 + L_e^2} - L_2 - L_3 \le 0 \tag{4}$$

Table 1 Parameters of the synthesized adjustable mechanism

Optimized parameters and other variables of the mechanisms	Values of the variables	
	DSCSL path	DSESL path
Fixed pivot x-coordinate value (x_A)	−2.4989	−2.3567
Fixed pivot y-coordinate value (y_A)	−1.6616	−1.1997
Coupler length (L_2)	3.4999	3.9949
Rocker length (L_3)	3.7406	4.9681
Slider offset length (L_e)	1.7253	1.3351
Coupler point arm angle (β)	65.1044°	54.6772°
Frame orientation angle (θ)	−70.6490°	−64.5652°
Crank length (L_1)	0.9145	0.8968
Coupler pointer length (L_6)	3.0139	2.6756
Starting crank angle value when pointer is at P_1 (θ_1)	7.8913	13.1390
Maximum value of adjustable link length ($S_{\rm m}$)	6.5365	8.2772
Minimum value of adjustable link length ($S_{\rm n}$)	5.9345	7.3500
Error function ($E_{\rm a}$)	0.6020	0.9272

$$L_1 + L_2 - L_3 - \sqrt{S_{\rm n}^2 + L_e^2} \leq 0 \tag{5}$$

$$L_1 + L_3 - L_2 - \sqrt{s_{\rm n}^2 + L_e^2} \leq 0 \tag{6}$$

$$L_2^2 + L_3^2 - \left(\sqrt{S_{\rm n}^2 + L_e^2} - L_1\right)^2 - 2L_2L_3\cos\mu_1 \leq 0 \tag{7}$$

where $\mu_1 = 20°$ and $S_{\rm n}$ (minimum value)

$$L_2^2 - L_3^2 + \left(\sqrt{S_{\rm m}^2 + L_e^2} + L_1\right)^2 + 2L_2L_3\cos\mu_2 \leq 0 \tag{8}$$

where $\mu_2 = 160°$ and $S_{\rm m}$ (maximum value).

In order to trace the path points on the path profile by the coupler point in the correct order and overcome ‘order defect’ when the crank is rotated in the anti-clockwise direction at uniform angular velocity, an additional constraint Eq. (9) is forced.

$$(\theta_1)_i < (\theta_1)_{i+1} \tag{9}$$

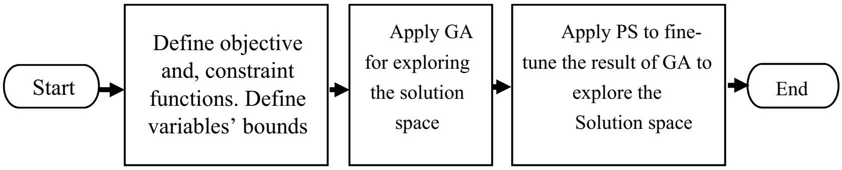

Fig. 3 Hybrid optimization process flowchart

2.3 Optimization Using Genetic Algorithm and Pattern Search

In genetic algorithm (GA), optimum value of the objective function may not be always reached due to the stopping criteria imposed on GA [13]. This requires further exploration of search space. By changing the stopping criteria, it is possible to find the optimum solution. However, it may require many more function evaluations to reach the optimum value. A local search can be a more efficient in such a scenario. Pattern search [14] is used for local search that starts from the point where GA reached thus making a hybrid optimization process (Fig. 3).

3 Bi-cubic Interpolation Method to Generate Path Points

Bi-cubic interpolation method is used to generate intermediate path points of DSCSL and DSESL paths. The coordinates of P_1, P_2, $P_3 P_4$ and P_5 of DSCSL geometry are shown in Fig. 1. Coupler path is represented by $P_1 P_2 P_3 P_4 P_5 P_1$.

It is anticipated that the coupler point (M) of a four-bar adjustable mechanism travels through the complete profile path, shown in Fig. 1, through endless number of path points for uninterrupted path generation. Here, precision point refers to the points obtained by harmonic spacing on the perimeter of the DSCSL. Precision points on the DSCSL path are obtained from the values of x_A, y_A, ϕ, β, L_2, L_3, L_e, L_1 and L_6 of the mechanism synthesized. The number of precision points (N) is taken as 360 for better results.

Precision points used and their corresponding crank angles obtained in the synthesis do not match to uniform crank arm angular intervals. Coordinate value of the first precision point M_1 at P_1 is (1, 0) and corresponding angular position $(\theta_1)_1$ is obtained from Table 1. The length between fixed point A and first path point M_1 is obtained from Eq. (10). From Eq. (11), the angle between line AM_1 and link length L_1 is obtained.

$$L_{AM(1)} = \sqrt{\left(x_{M(1)} - x_A\right)^2 + \left(y_{M(1)} - y_A\right)^2} \tag{10}$$

$$\beta_{1(1)} = \cos^{-1}\left(\frac{L_1^2 + L_{AM(1)}^2 - L_6^2}{2L_1 L_{AM(1)}}\right) \tag{11}$$

Equation (12) also can be used to get $(\theta_1)_1$. In Eq. (12), the $\pm$ sign specifies the two alignments of dyad ABM as presented in Fig. 1 as continuous and dashed lines.

$$(\theta_1)_1 = \tan^{-1}\left[\left(y_{M(1)} - y_A\right), \left(x_{M(1)} - x_A\right)\right] \pm \beta_{1(1)} \tag{12}$$

Equations (13) and (15) give values of coordinates of joint B for first path point. Angle $(\theta_6)_1$. is given by Eq. (14).

$$x_{B(1)} = x_A + L_1 \cos\theta_{1(1)} \tag{13}$$

$$\theta_{6(1)} = \tan^{-1}\left[\left(y_{M(1)} - y_{B(1)}\right), \left(x_{M(1)} - x_{B(1)}\right)\right] \tag{14}$$

$$y_{B(1)} = y_A + L_1 \sin\theta_{1(1)} \tag{15}$$

The value of β is obtained from synthesized values (Table 1). The coordinates of joint C_1 are attained from Eqs. (16)–(18)

$$\theta_{2(1)} = \theta_{6(1)} - \beta \tag{16}$$

$$x_{C(1)} = x_{B(1)} + L_2 \cos\theta_{2(1)} \tag{17}$$

$$y_{C(1)} = y_{B(1)} + L_2 \sin\theta_{2(1)} \tag{18}$$

For ease of analysis of slider dyad, a local coordinate frame is used. Joint A is taken as the origin of the local coordinate. Coordinates of joint C in local coordinate are obtained from Eqs. (19) and (20) from the global coordinates.

$$x_{C(1)} = \left(x_{C(1)} - x_A\right)\cos\varphi + \left(y_{C(1)} - y_A\right)\sin\varphi \tag{19}$$

$$y_{C(1)} = -\left(x_{C(1)} - x_A\right)\sin\varphi + \left(y_{C(1)} - y_A\right)\cos\varphi \tag{20}$$

Location of the slider from fixed the pivot A is given by, adjustable link length, $S_{(1)}$ when the coupler is indicating the first path point, is found from Eq. (21).

$$S_{(1)} = x_{C(1)} \pm \sqrt{L_3^2 - \left(y_{C(1)} - L_e\right)^2} \tag{21}$$

Equations (10)–(21) give adjustable parameter $S_{(1)}$ value. Similarly, APV for all the precision points and corresponding angles is obtained from optimal synthesis process. Thus, $S_{(i)}$ where $i = 1, 2, \ldots, 360$, adjustable parameter values of precision

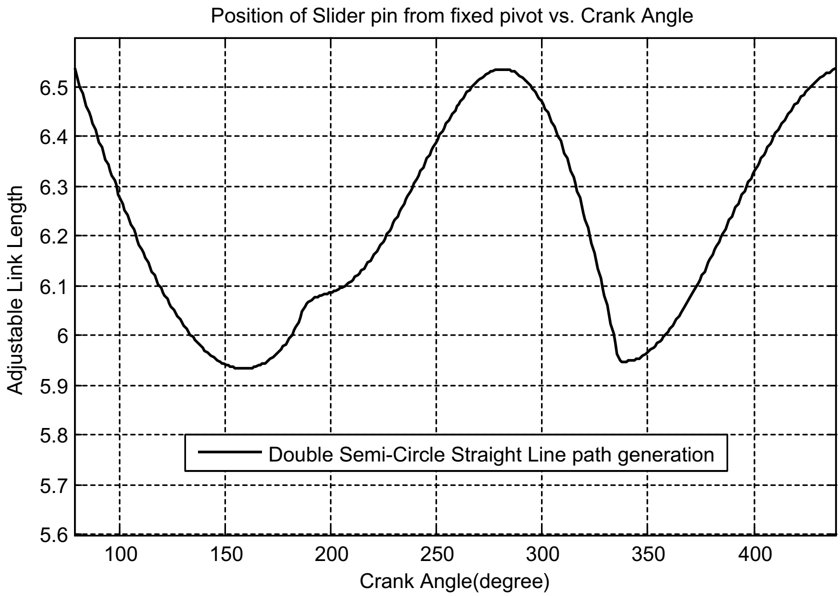

Fig. 4 Adjustable link length (S) versus crank angle for DSCSL path

points are obtained. But the difference between θ_2 values of successive precision points is not uniform. A bi-cubic interpolation method is used to get path point for incremental crank angle (1°) values from 360 precision points and corresponding crank arm positions (θ_2) using MATLAB bi-cubic interpolation. Figure 4 shows adjustable link length (S) versus crank angle incremented by 1° for DSCSL path generation.

Synthesized adjustable mechanism to generate DSCSL path, employing bi-cubic interpolated path points in the animation, is shown in Fig. 5. Similar approach is used to synthesize adjustable mechanism shown in Fig. 6 to generate DSESL path.

4 Results and Discussion of DSCSL and DSESL Path Generation

Figure 7 shows the desired and generated DSCSL path for different number of path points. In the previous section, it is mentioned, the DSCSL path generation also displays desired path deviation at the corner point of P_5. Figure 8 show the closer view at transition point from curve to straight line at P_5.

The deviation from the desired path at P_5 is more for 360 path points which correspond to 1° crank increment compared to 720 (half degree crank increment) path points. Similar deviation is also observed at curved portions of the generated

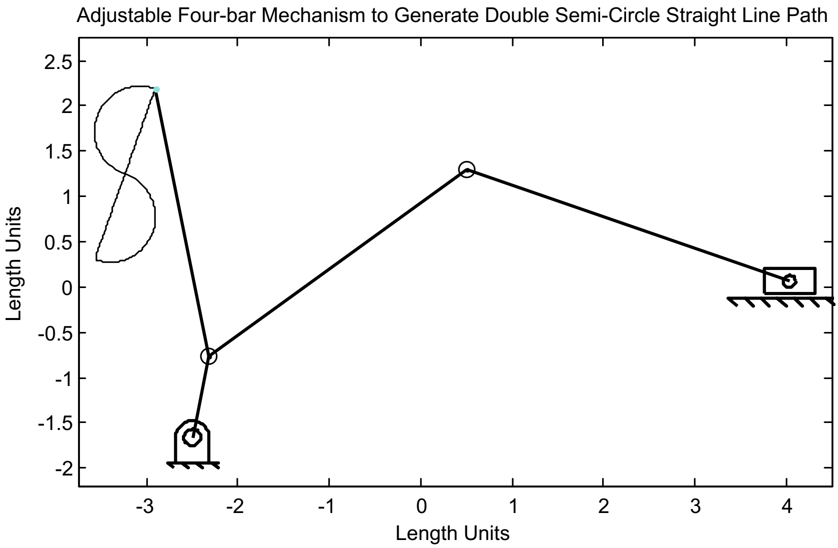

Fig. 5 Synthesized mechanism to generate DSCSL path

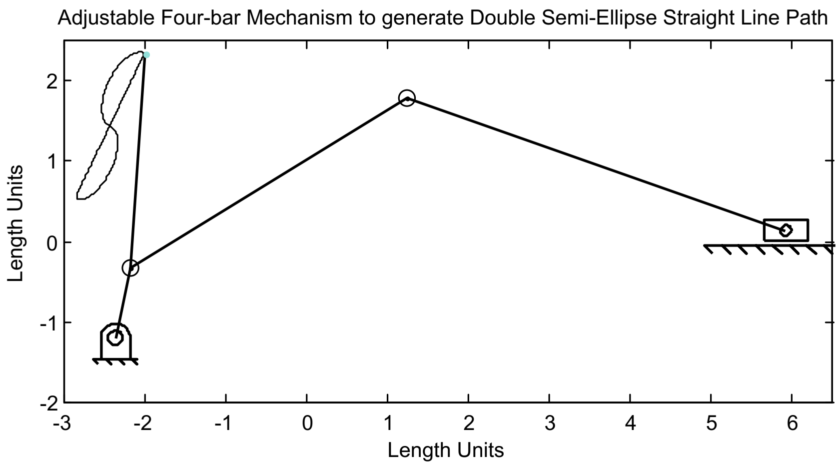

Fig. 6 Synthesized mechanism to generate DSESL path

path. It is clear from Fig. 8 that when the number of path point increases, generated path approaches desired DSCSL path. The decimal values of Fig. 8 validate the accuracy of the bi-cubic interpolation method proposed in the case of DSCSL path generation. Validity of this path generation is compared and verified with the path generation of filleted rectangular path [11] and corners-chamfered-rectangle [12] and found correct for continuous and precise path generation of DSCSL as depicted in

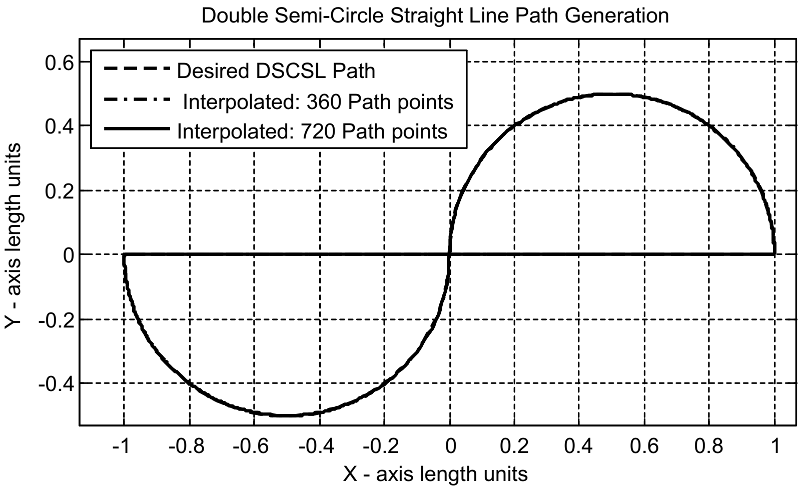

Fig. 7 Desired and generated DSCSL path

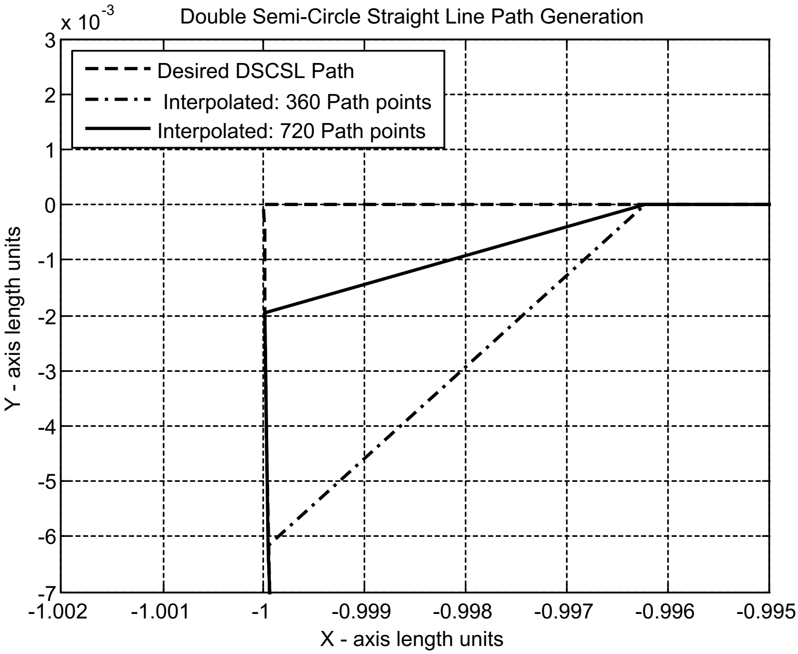

Fig. 8 Closer view of generated DSCSL path at P_5 point

Figs. 7 and 8. In Fig. 8, a closer view of P_5 point is given. Generated path approaches perfect DSCSL path when the number of path points is increased. Similarly DSESL path is verified but not presented for brevity of the paper.

5 Conclusions

Precise DSCSL and DSESL path generation mechanisms are synthesized and their precise path generation is verified using bi-cubic interpolation method using 360 and 720 path points. Increasing path points further, the desired curve can be approached. Bi-cubic interpolation method requires less computational time than RAPC method. However, RAPC method is superior to bi-cubic interpolation method since former uses synthesized trajectory on which path points are obtained. Verification of precise path generation for DSCSL and DSESL using RAPC method is suggested as future work.

References

1. Chong P, Sodhi RS (2010) Optimal synthesis of adjustable mechanisms generating multiphase approximate paths. Mech Mach Theory 45:989–996
2. Kay F, Haws R (1975) Adjustable mechansims for exact path generation. ASME J Eng Ind 97(2):702–707
3. Singh Y, Kohli D (1981) Synthesis of cam-link mechanism for exact path generation. Mech Mach Theory 16(4):447–457
4. Shimojima H, Ogawa K, Fujiwara A, Sato O (1983) Kinematic synthesis of adjustable mechanisms. Bull JSME 14:621–632
5. Mundo D, Gatti G (2008) A graphical-analytical technique for the synthesis of noncircular gears in path-generating geared five-bar mechanisms. Trans CSME 32(3–4):488–497
6. Mundo D, Liu JY, Yan H (2006) Optimal synthesis of cam-linkage mechanisms for precise path generations. J Mach Des 128:1253–1260
7. Chanekar PV, Ghoshal A (2013) Optimal synthesis of adjustable planar four-bar crank-rocker type mechanisms for approximate multi-path generations. Mech Mach Theory 69:263–277
8. Zhou H (2009) Dimensional synthesis of adjustable path generation linkages using the optimal slider adjustment. Mech Mach Theory 44:1866–1876
9. Hrishikesh Y, Ameya P, Gunesh R (2013) Optimum synthesis of path generating adjustable mechanisms with improved slope continuity. Trans Can Soc Mech Eng 37(2):197–214
10. Ganesan G, Sekar M (2014) Kinematic analysis of rectangular path generating adjustable four-bar linkage. Appl Mech Mater Trans Tech Publ 592–594:1094–1098
11. Ganesan G, Sekar M (2017) Optimial synthesis and kinematic analysis of adjustable four-bar linkages to generate filleted rectangular paths. Mech Based Des Struct Mach 45(3):363–379
12. Ajith Kumar G, Ganesan G, Sekar M (2018) Near perfect path generation of corners-chamfered-rectangle and single synthesis cam-link mechanism to generate special-slot path. Mech Based Des Struct Mach 46(4):483–498
13. Goldberg DE (2009) Genetic algorithms in search, optimization, and machine learning. 4th impression. Pearson Education, New Delhi
14. Conn AR, Goiuld NI, Toint PL (1997) A globally convergent augmented Lagrangian Barrier algorithm for optimization with general inequality constraints and simple bounds. Math Comput 66:261–288

Effect of Interference on a Floating Axis Epitrochoidal Hydrostatic Unit

Harish Ramachandran, Aditya Shriwastava, and Abhijit Nag

Abstract In the present work, the effect of inclusion of interference on the performance of an Epitrochoidal Hydrostatic Rotary Piston Machine, namely Orbit motor is studied by building its mathematical model and implementing the algorithm in MATLAB. In this approach, the rotor is rigid, rollers are elastic and interference between the rotor and the stator is provided by changing the roller radius, chordal thickness and the pitch circle radius. In an Orbit motor of interference-fit type, the contact points and the rotor center deviate from their original position as found in an Orbit motor of perfect-fit type. A corrective technique based on minimum potential energy of the system is used to obtain the rotor center of an interference-fit motor, starting from the geometrically obtained rotor center of a perfect-fit motor, correcting itself to its final position. For various positions of the output shaft, the forces and torque acting on the rotor are calculated. For positions other than those corresponding to that of maximum compression and maximum expansion of chambers, it is found that a net unbalanced torque acts on the rotor. This torque tends to bring the rotor back to the nearest position of maximum compression. Apart from the determination of the unbalanced torque, the variation of deformation and maximum contact pressure at the contact points between the rotor and the stator due to sole inclusion of interference, for the first two phases of the rotor rotation is also investigated.

Keywords Orbit motor · Interference-fit · Unbalanced torque · Contact deformation · Maximum contact pressure

Nomenclature

$[\boldsymbol{e}_i]_\Omega$	Position vector of the ith point on the periphery of the rotor in Ω frame
$[\boldsymbol{e}_i]_\Gamma$	Position vector of the ith point on the periphery of the rotor in Γ frame
$\boldsymbol{F}$	Resultant force acting on the rotor

H. Ramachandran (✉) · A. Shriwastava · A. Nag
Birla Institute of Technology, Mesra, Ranchi, Jharkhand 835215, India
e-mail: rharish6696@gmail.com

E. T. Akinlabi et al. (eds.), *Trends in Mechanical and Biomedical Design*,
Lecture Notes in Mechanical Engineering,
https://doi.org/10.1007/978-981-15-4488-0_10

Π	Potential energy of the system due to deformation at the contacts
δ_j	Magnitude of deformation of the jth roller
$\boldsymbol{f_j}$	Reaction force acting on the rotor due to deformation of the jth roller
ξ	Angular displacement of the output shaft in counter-clockwise direction
ξ_0	Phase angle, $\xi_0 = \frac{\pi}{Z(Z-1)}$
K_i	Center of the ith roller for $1 \le i \le Z$. Also known as the crunode
N'_i	Contact point of the rotor with the ith roller for $1 \le i \le Z$ for a perfect-fit motor
N_i	Contact point of the rotor with the ith roller for $1 \le i \le Z$, for an interference-fit motor
N''_i	Estimated point of contact of the rotor with the ith roller for $1 \le i \le Z$, for an interference-fit motor
S	Stator center
O	Rotor center of an interference-fit motor
O'	Rotor center of a perfect-fit motor
O''	Estimated rotor center of an interference-fit motor
r	Radius of the inner centrode
R	Radius of the outer centrode
A	Distance of epitrochoid generating point from the center of the outer centrode or radius of a circle passing through the roller centers
r_{m}	Amount of constant difference modification (i.e. the parallel shifting of the profile), also equal to the roller radius
k	Stiffness coefficient of the roller
c	Center to center distance between the rotor and the stator
C_i	ith Chamber
Z	Number of rollers
Δr_{m}	Amount of change in the roller radius
Δc_{t}	Amount of change in the chordal thickness
Δp_{cr}	Amount of change in the pitch circle radius
n	Number of points in which periphery of the rotor is divided
Δ	Amount of shift of O'' in each computational step
$\boldsymbol{T}$	Net torque acting on the rotor
Γ	Coordinate frame $\{X\ Y\ Z\}$ attached to the stator with center at point 'S'
Ω	Coordinate frame {x y z} attached to the rotor with center at point 'O'''
Π_i	Initial potential energy of the system
Π_{f}	Final potential energy of the system
ξ_{i}	Initial position of the output shaft
ξ_{f}	Final position of the output shaft
$\Delta\xi$	Increment in the output shaft rotation
w	Width of the rotor

1 Introduction

Orbit motor is a Low Speed High Torque (LSHT) hydraulic motor capable of providing high torque to inertia ratio. The heart of this motor comprises of a rotor and a stator, where the stator consists of 'Z' equispaced rollers. The difference between the number of rollers and the number of lobes on the rotor is always unity. The geometric design technique for the epitrochoid generated rotor and stator profile was first developed by Ansdale and Lockley [1] while working on the design of Wankel engine and similar Rotary Piston Machines (ROPIMAs). Investigations on epitrochoidal profile useful in ROPIMAs were carried out in more detail by Colbourne [2, 3] where he described a unique method for finding the envelope of the trochoids which perform the planetary motion. Robinson and Lyon [4] developed the actual useful profile in ROPIMAs, which is a constant difference shifted profile known as the constant difference modified epitrochoid.

In the geometrically form-closed rotor-stator set, all the rollers are in contact with the rotor creating closed volumes known as the chambers. These chambers vary in size as the rotor rotates about its orbiting center (i.e. the rotor is floating and performs epicyclic motion about the stator center). When pressurized fluid is supplied to certain predetermined chambers [5], some rollers experience deformation, while in others gaps are generated. If gaps are generated at the transition contacts (i.e. contacts separating the High-Pressure Zone (HPZ) from the Low-Pressure Zone (LPZ)), there is a reduction in pressure differential of fluid due to leakage from HPZ to LPZ [6, 7]. This leakage will reduce the efficiency of the motor. In an Orbit motor, profile of both the rotor and the stator are the working profile, thus external sealing is not possible at the contacts. A feasible solution to eliminate this inter-chamber leakage is by introducing interference between the rotor and the stator. Three popular methods of introducing interference [8] are by modifying the following:

1. Roller radius (Fig. 1a).
2. Chordal thickness (Fig. 1b).
3. Pitch circle radius (Fig. 1c).

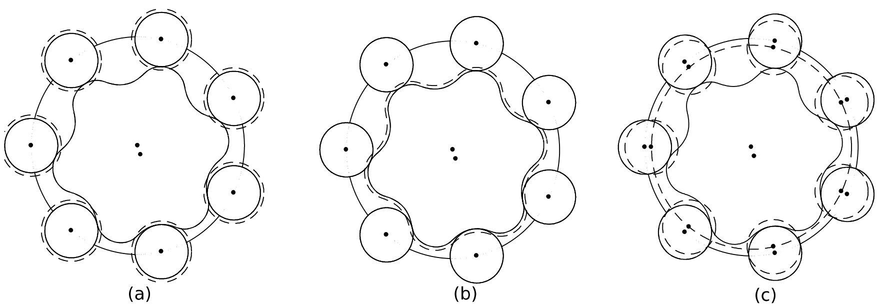

Fig. 1 **a** Interference provided by an increase in roller radius. **b** Interference provided by increase in chordal thickness. **c** Interference provided by decrease in pitch circle diameter

In this study, interference is provided between the rotor and the stator by a combination of all the three methods mentioned above and all the chambers of the motor are at zero gauge pressure to investigate the effect of sole inclusion of interference.

Experimentally, it has been observed that in an Orbit motor of interference-fit type, the rotor is stable only at certain discrete positions. When the rotor is disturbed from these positions, it returns to the nearest stable position. But, there is no mathematical justification available in open literature to explain this experimental observation.

This paper provides a mathematical model to determine the effect of interference on the performance of Orbit motor. The model justifies the above-mentioned experimental observation by calculating the unbalanced torque acting on the rotor for various positions of output shaft. Apart from the unbalanced torque variation, the variation of roller deformation and maximum contact pressure with output shaft rotation due to the sole presence of interference is also determined.

The remainder of the paper is subdivided as follows: The next section presents the underlying assumptions considered while formulating the model and a general overview of the algorithm. Section 3 delineates each key aspect of the algorithm. Section 4 presents the results on the effect of introducing interference and finally, the conclusions of the investigation are drawn in Sect. 5.

2 Perfect-Fit Versus Interference-Fit

For an Orbit motor of perfect-fit type, when all the chambers are at zero gauge pressure, there is neither deformation nor gap generated at the contacts. This type of motor is purely hypothetical as there will always be some amount of manufacturing or assembly error. But, in an Orbit motor of interference-fit type, even when all the chambers are at zero gauge pressure, there is some deformation at all the contacts. As a consequence, there will be a reaction force exerted by each roller on the rotor. Due to these reaction forces, in general, there also will be an unbalanced torque acting on the rotor. The present investigation aims at finding the nature of this unbalanced torque acting on the rotor, deformation of the rollers and the maximum contact pressure for various positions of the rotor.

The initial position and position of the rotor when the output shaft is rotated by ξ is shown in Fig. 2a and b respectively.

Let ξ be the angle by which the rotor rotates from its initial position in counter-clockwise direction. To calculate the unbalanced torque acting on the rotor, for a particular ξ, an external torque is applied on the rotor, such that rotor is in static equilibrium. This externally applied torque has the same magnitude as that of the unbalanced torque but acts in the opposite direction.

In this investigation, the following assumptions are taken into consideration while formulating the approach mentioned in the upcoming section:

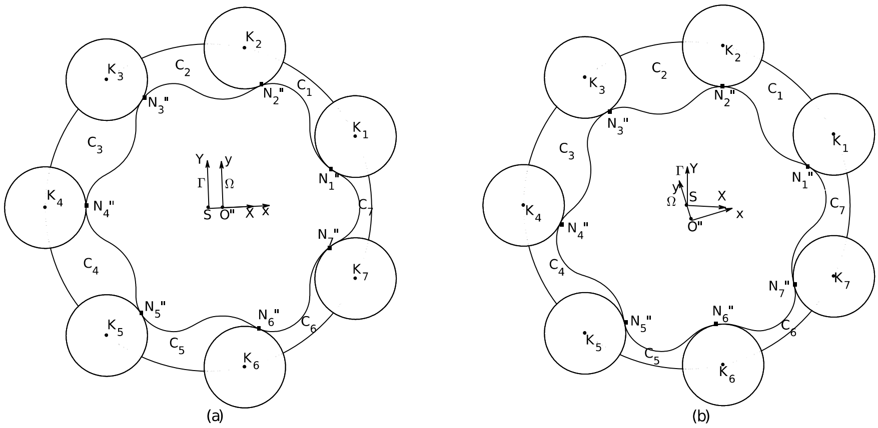

Fig. 2 **a** Initial position of the rotor. **b** Position of the rotor when output shaft is rotated by an angle ξ

1. Rotor is a rigid body.
2. Rollers are elastic and exert reaction force on the rotor which is linearly proportional to deformation at the contacts [14].
3. Coefficient of friction is zero at all the contacts.

3 Contact Analysis of an Interference-Fit Motor

3.1 Determining the Initial Rotor Center

When the rotor rotates about its own axis by an angle ξ, its orbiting center revolves around the stator center by an angle $\xi(Z-1)$ in the opposite direction. Thus, the position vector of the point O' (rotor center of a perfect-fit motor) in the stator frame, Γ is given by Eq. 1.

$$[\boldsymbol{O}']_\Gamma = c\begin{bmatrix}\cos(-\xi(Z-1))\\ \sin(-\xi(Z-1))\\ 0\end{bmatrix} \tag{1}$$

To determine the position vector of point O (rotor center of an interference-fit motor), a new point O'' representing estimated rotor center is introduced. If there is no error in estimation, $O'' \equiv O$. A corrective method based on minimization of the potential energy of the system is adopted to find O'' closest to O. In this study, the system comprises of the rigid rotor and the elastic rollers. Initially, let the estimated rotor center, O'' coincide with O' (rotor center of a perfect-fit motor).

3.2 Profile Generation of the Rotor

Let the periphery of the rotor be divided into 'n' points as shown in Fig. 3. Position vector of the ith point on the periphery of the rotor with respect to its own frame, Ω ($[\boldsymbol{e}_i]_{\boldsymbol{\Omega}}$) is given by Eq. 2.

$$[\boldsymbol{e}_i]_{\boldsymbol{\Omega}} = \begin{bmatrix} A\cos(\theta_i) + c\cos(Z\theta_i) - r_{\mathrm{m}}\cos(\theta_i + \phi_i) + \Delta c_{\mathrm{t}}\cos(\theta_i) \\ A\sin(\theta_i) + c\sin(Z\theta_i) - r_{\mathrm{m}}\sin(\theta_i + \phi_i) + \Delta c_{\mathrm{t}}\sin(\theta_i) \\ 0 \end{bmatrix} \tag{2}$$

where

$$\theta_i = \frac{2\pi}{n} \times i \tag{3}$$

and

$$\phi_i = \tan^{-1}\left(\frac{R\sin(\theta_i(Z-1))}{A + R\cos(\theta_i(Z-1))}\right) \tag{4}$$

Fig. 3 Division of periphery of the rotor into 'n' points

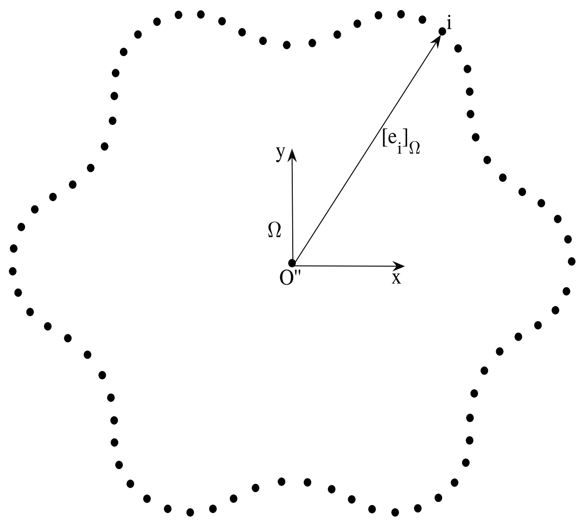

3.3 Transforming Profile of the Rotor from the Rotor's Frame to the Stator's Frame

Frame Ω (Rotor's frame) is related to frame Γ (Stator's frame) by a rotation tensor $\boldsymbol{Q}$ and the position vector of point O'' in frame Γ is given by $[\boldsymbol{O}'']_\Gamma$ then,

$$[\boldsymbol{e}_i]_\Gamma = [\boldsymbol{O}'']_\Gamma + [\boldsymbol{Q}]_\Gamma[\boldsymbol{e}_i]_\Omega \tag{5}$$

where

$$[\boldsymbol{Q}]_\Gamma = \begin{bmatrix} \cos(\xi) & -\sin(\xi) & 0 \\ \sin(\xi) & \cos(\xi) & 0 \\ 0 & 0 & 1 \end{bmatrix} \tag{6}$$

and initially, let the rotor center of an interference-fit motor coincide with the rotor center of a perfect-fit motor (Refer Eq. 7).

$$[\boldsymbol{O}'']_\Gamma = [\boldsymbol{O}']_\Gamma = c\begin{bmatrix} \cos(-\xi(Z-1)) \\ \sin(-\xi(Z-1)) \\ 0 \end{bmatrix} \tag{7}$$

3.4 Determining Center of the Rollers

The center of all the rollers lies on a circle of radius ($A + \Delta p_{\mathrm{cr}}$), centered at S and occurs at an angular interval of $2\pi/Z$. Thus, the position vector of point Kj (i.e. center of the jth roller), in frame Γ is given by Eq. 8.

$$[\boldsymbol{K}_j]_\Gamma = (A + \Delta p_{cr})\begin{bmatrix} \cos\left(\frac{\pi(2j-1)}{Z}\right) \\ \sin\left(\frac{\pi(2j-1)}{Z}\right) \\ 0 \end{bmatrix} \quad \forall 1 \le j \le Z \tag{8}$$

3.5 Contact Point Determination

The estimated contact point, N_j'', can be considered to be the point on the periphery of the rotor closest to the point K_j (Refer Appendix). Thus, the position vector of the point N_j'' ($\forall 1 \le j \le Z$) in Γ frame will be equal to $[\boldsymbol{e}_l]_\Gamma$, where l is a point on the periphery of the rotor which is closest to point K_j. It is mathematically shown in Eq. 9. A similar approach was adopted by Lin et al. [9] to determine the contact points in a cycloidal speed reducer.

$$[\boldsymbol{N}_j'']_{\boldsymbol{\Gamma}} = [\boldsymbol{e}_l]_{\boldsymbol{\Gamma}} \tag{9}$$

iff,

$$\|\boldsymbol{e}_l - \boldsymbol{K}_j\| \leq \|\boldsymbol{e}_i - \boldsymbol{K}_j\| \quad \forall 1 \leq i \leq n$$

3.6 Deformation and Reaction Force at the Contacts

The contacts in this analysis are modelled as linear springs with stiffness coefficient 'k' as shown in Fig. 4. Shung and Pennock [10] also used a similar model to estimate the contact forces.

The magnitude of deformation in jth roller and the reaction force exerted by the jth roller (due to its deformation) on the rotor, in Γ frame ($[\boldsymbol{f}_j]_{\boldsymbol{\Gamma}}$), is determined using Eq. 10 and Eq. 11.

$$\delta_j = (r_{\mathrm{m}} + \Delta r_{\mathrm{m}}) - \|[\boldsymbol{N}_j'']_{\boldsymbol{\Gamma}} - [\boldsymbol{K}_j]_{\boldsymbol{\Gamma}}\| \tag{10}$$

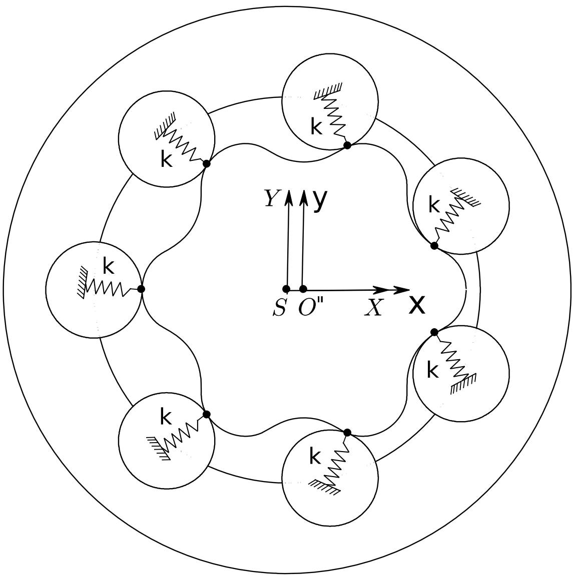

Fig. 4 Contact force model

$$[\boldsymbol{f}_j]_\Gamma = k\delta_j \frac{[\boldsymbol{N}''_j]_\Gamma - [\boldsymbol{K}_j]_\Gamma}{\|[\boldsymbol{N}''_j]_\Gamma - [\boldsymbol{K}_j]_\Gamma\|} \quad \forall 1 \leq j \leq Z \tag{11}$$

The stiffness coefficient (Refer [11]) of the roller is obtained using Eq. 12.

$$k = \frac{\pi w}{4\left(\frac{1-\nu^2}{E}\right)\left(1 + \frac{\pi}{4}\right)} \tag{12}$$

3.7 Unbalanced Torque Calculation

Potential energy of the system and the net reaction force acting on the rotor in Γ frame is obtained from Eqs. 13 and 14 respectively. Here, the potential energy of the system is simply equal to the elastic strain energy stored in the rollers as the rotor is rigid.

$$\Pi = \sum_{j=1}^{Z} \frac{1}{2} k\delta_j^2 \tag{13}$$

$$[\boldsymbol{F}_\Gamma] = \sum_{j=1}^{Z} [\boldsymbol{f}_j]_\Gamma \tag{14}$$

Now, point O'' is shifted along the direction of F by an amount Δ. The potential energy is calculated in this new state. If potential energy decreases, the above-mentioned procedure is repeated all over until it starts to increase, i.e. the procedure is iterated until the local minima of potential energy is obtained. At this state of local minima, point O'' will be within a circle of radius Δ centerd at O (Fig. 5). Smaller the value of Δ, closer is the point O'' to the point O and more accurate result is obtained. At this state of minimum potential energy, the torque acting on the rotor with respect to the stator frame 'Γ' is calculated using Eq. 15.

$$\boldsymbol{T} = [001] \sum_{j=1}^{Z} [\boldsymbol{N}''_j]_\Gamma - [\boldsymbol{O}'']_\Gamma \times [\boldsymbol{f}_j]_\Gamma \tag{15}$$

The whole process is repeated for different values of ξ and the results are presented in the next section. The algorithm of the proposed approach is presented in the form of a flowchart depicted in Fig. 6.

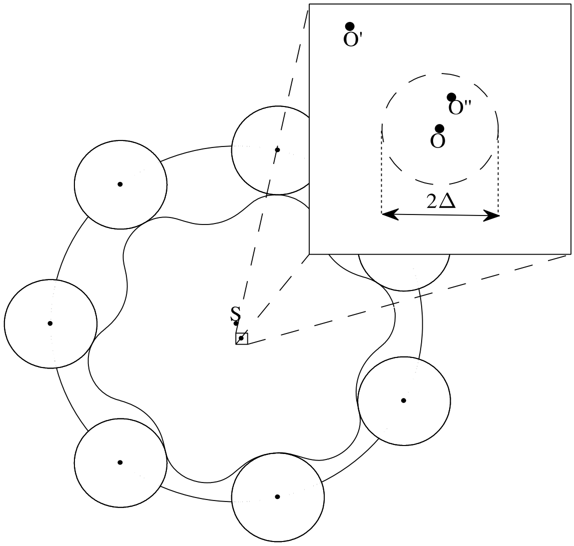

Fig. 5 Uncertainty in the estimated rotor center

3.8 Flowchart of the Proposed Approach

See Fig. 6.

4 Results and Discussion

The results are obtained for the numerical data of the design and computational parameters as shown in Table 1.

4.1 Variation of the Unbalanced Torque and Potential Energy of the System

The potential energy plot (Fig. 7b) has a local minimum in the positions corresponding to maximum compression of the chambers ($\xi = 2n\xi_0$ where, $n \in \mathbb{Z}$). The positions of local minima correspond to the state of stable equilibrium. There is no unbalanced torque (Fig. 6a) acting on the rotor in these positions. When the rotor is disturbed from these positions, an unbalanced torque acts on the rotor. This unbalanced torque brings the rotor to the nearest state of stable equilibrium.

Local maxima of the potential energy (Fig. 7b) is observed in the positions corresponding to the maximum expansion of the chambers ($\xi = (2n + 1)\xi_0$ where, $n \in \mathbb{Z}$). The unbalanced torque (Fig. 7a) is also zero at these positions. When the rotor

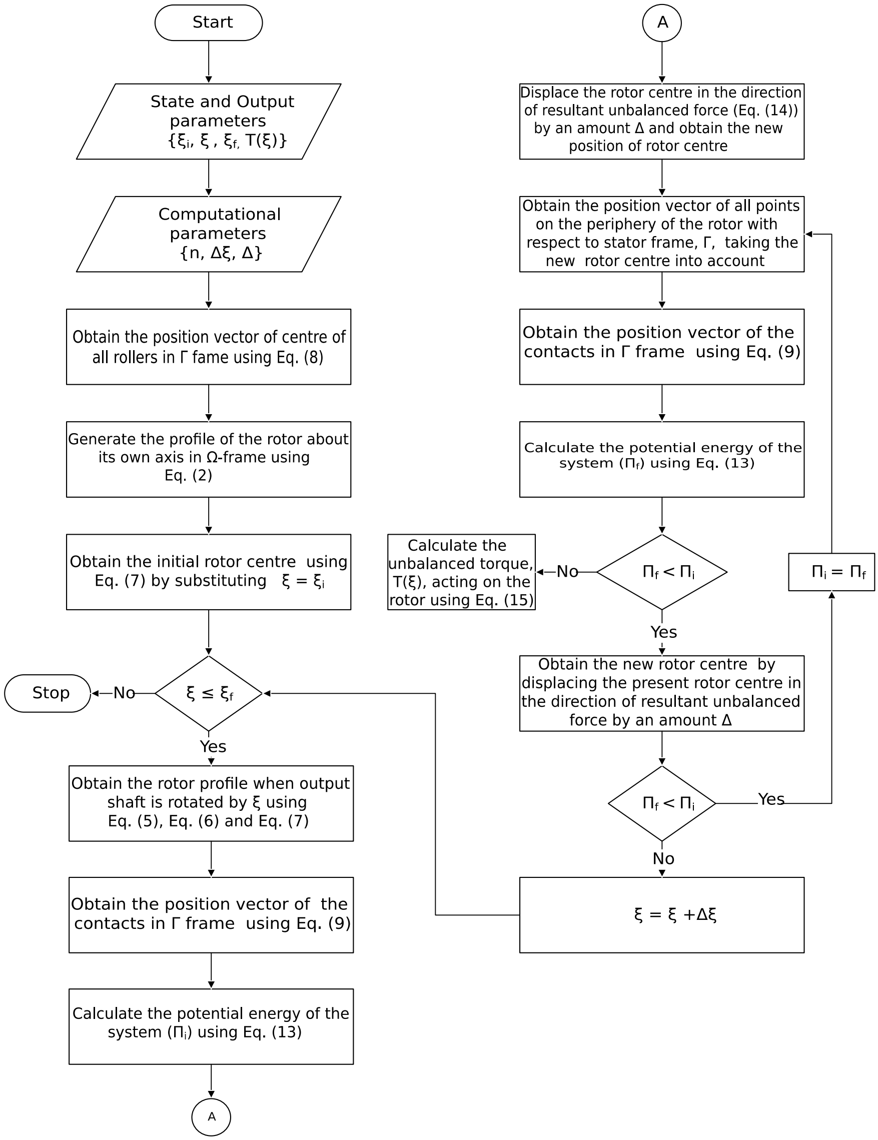

Fig. 6 Flowchart of the proposed approach

is disturbed from these positions, the unbalanced torque acts on the rotor in such a way that it brings the rotor to the nearest state of maximum compression. Thus, the positions of local maxima correspond to the state of unstable equilibrium.

For any other position of the rotor in between the states of local maxima and local minima, the unbalanced torque acts on the rotor in such a way that it brings the rotor to the nearest state of stable equilibrium.

Table 1 Numerical data of design and computational parameters

Parameter category	Parameter	Values
Geometry [12]	R	19.67 mm
	A	31.98 mm
	r_{m}	7.97 mm
	c	2.81 mm
	w	10 mm
	Z	7
Material	k	9.87×10^{8} N/m
Interference	Δr_{m}	71 µm
	Δc_{t}	−51 µm
	Δp_{cr}	−41 µm
Computational	n	10,000
	Δ	10^{-3} µm

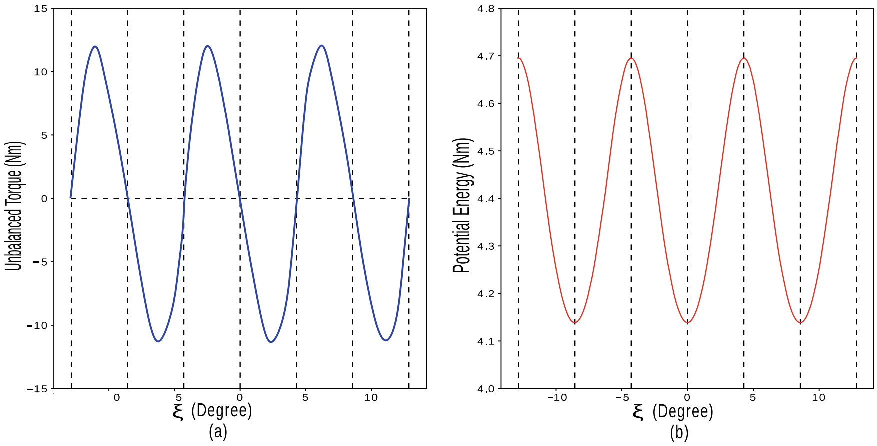

Fig. 7 Variation of **a** unbalanced torque and **b** potential energy of the system with output shaft rotation

4.2 Deformation at the Contacts

Figure 8 shows the variation of deformation (δ) of all the rollers with the output shaft rotation (ξ) for an Orbit motor of interference-fit type (Refer Table 1). It can be observed from the plot that all the rollers experience positive deformation. This plot has a similar nature compared to a plot obtained by Maiti and Nagao [13] for an interference-fit motor using trial and error method.

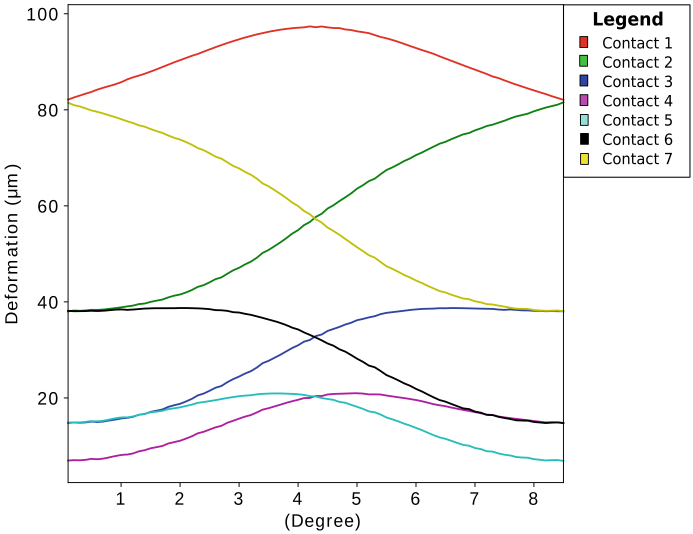

Fig. 8 Variation of deformation in the rollers, due to the presence of interference with output shaft rotation (ξ)

4.3 Estimation of Maximum Contact Pressure

Due to the inclusion of interference between the rotor and the stator, the contact points are prestressed. Contact force exerted by each roller on the rotor is determined using Eq. 11. The maximum contact pressure evaluated at each contact is obtained using the Hertzian contact theory [14], assuming a cylinder on cylinder contact (Refer Eq. 16) (Fig. 9).

The following assumptions are taken into consideration while implementing the Hertzian contact stress model: the surfaces in contact are smooth, the contact are non-conformal, no lubrication exists at the contacts, deformation at the contact is small compared to the radius of curvature of the contacting bodies and only radial loading exists at the contacts.

$$\sigma_i = \frac{2\|[\boldsymbol{f}_j]\|}{\pi b w} \tag{16}$$

'b' is known as the half-contact bandwidth, given by Eq. 17

$$b = \sqrt{\frac{8\|[\boldsymbol{f}_j]\|\left(\frac{1-\nu^2}{E}\right)}{\pi w\left(\frac{1}{R_{\text{roller}}} + \frac{1}{R_{\text{rotor}}}\right)}} \tag{17}$$

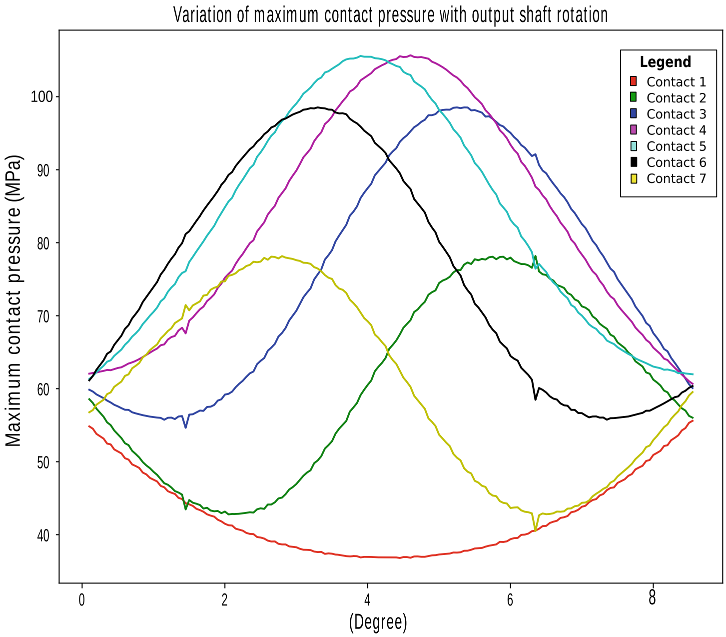

Fig. 9 Variation of contact pressure on the roller with output shaft rotation

R_{rotor} and R_{roller} are the radius of curvature of the rotor and the roller respectively.

$$
\begin{aligned}
R_{\text{rotor}} &= \frac{((x')^2 + (y')^2)^{\frac{3}{2}}}{|x'y'' - y'x''|} \\
x &= A\cos(\theta) + c\cos(Z\theta) - r_{\text{m}}\cos(\theta + \phi) + \Delta c_t \cos(\theta) \\
y &= A\sin(\theta) + c\sin(Z\theta) - r_{\text{m}}\sin(\theta + \phi) + \Delta c_{\text{t}} \sin(\theta) \\
x' &= \partial x / \partial \theta \quad y' = \partial y / \partial \theta \\
R_{\text{roller}} &= r_{\text{m}} + \Delta r_{\text{m}}
\end{aligned}
\tag{18}
$$

5 Conclusion

Leakage problem through the transition contacts can be mitigated or made zero by providing interference between rotor and stator. But, as a result of that, an unbalanced torque ripple is introduced. It is obvious that this unbalanced torque will increase the load holding and the braking torque capacity, but will decrease the overall torque efficiency. The aim of the study was to investigate the nature of this unbalanced torque generated due to the sole inclusion of interference. The unbalanced torque has a sinusoidal nature and at zero gauge pressure in all the chambers, it was observed that the unbalanced torque tends to bring the rotor to the nearest state of stable equilibrium, i.e. it orients the rotor in the nearest position corresponding to maximum compression of the chambers. Future researchers can use this model to optimize the design parameters of the motor by performing a trade-off between the magnitude of unbalanced torque and the amount of leakage at the contacts.

Appendix

Figure 10a–e shows the forces acting on the rotor for different positions of the output shaft. It can be clearly seen that for the positions of the rotor corresponding to maximum compression (Chamber C_7 in Fig. 10b) and maximum expansion (Chamber C_3 in Fig. 10d) of the chambers, the forces acting on the rotor are symmetrical. Thus, the net torque about the rotor center is zero in these positions as observed in Fig. 7a.

Figure 11 shows the enlarged view of Roller-1 in contact with the rotor. Let the periphery of the rotor be divided into five points. To determine which point out of these five is the contact point for roller 1, the algorithm calculates the distance of each point from the roller center $K1$ and selects the point which is closest to $K1$. From Fig. 11, it is clear, that $d3$ has the smallest value. Therefore, point 3 is the contact point.

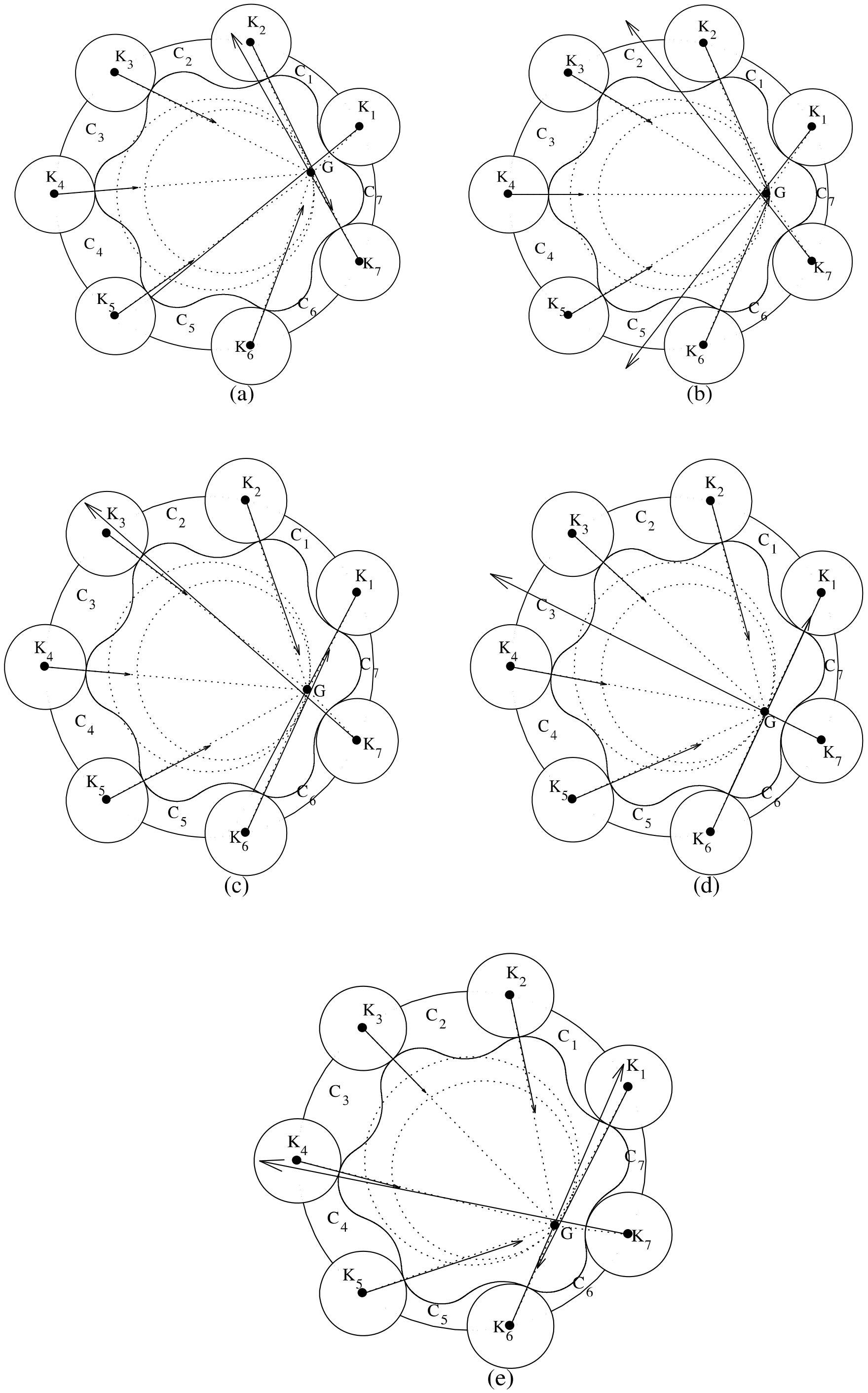

Fig. 10 Forces acting on the rotor for **a** $\xi = -0.5\xi_0$, **b** $\xi = 0$, **c** $\xi = 0.5\xi_0$, **d** $\xi = \xi_0$, **e** $\xi = 1.5\xi_0$

Fig. 11 Contact point estimation

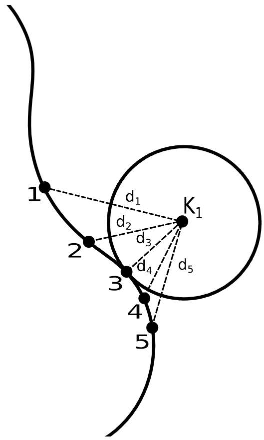

References

1. Ansdale R (1968) The Wankel RC engine, 1st edn. Iliffe, London
2. Colbourne J (1974) The geometry of trochoid envelopes and their application in rotary pumps. Mech Mach Theory 9(3–4):421–435
3. Colbourne J (1975) Gear shape and theoretical flow rate in internal gear pumps. Trans Can Soc Mech Eng 3(4):215–223
4. Robinson F, Lyon J (1976) An analysis of epitrochoidal profiles with constant difference modification suitable for rotary expanders and pumps. J Eng Ind 98(1):161–165
5. Maiti R (1992) Distributor valve port sequences in epitrochoid generated rotary piston machine 'ROPIMA' type hydrostatic units. Arch Appl Mech 62(4):223–229
6. Maiti R (1991) Active contact stresses at epitrochoid generated rotor-stator set of fixed axis or equivalent system type hydrostatic units. J Eng ind 113(4):465–473
7. Maiti R (1993) Active contact problems in epitrochoid generated floating axis orbital rotary piston machines. J Eng Ind 115(3):337–340
8. Nag A (2015) Analysis of active contacts in epitrochoid generated form closed rotor-stator set with specific reference to hydrostatic motor performance. Ph.D. thesis, IIT Kharagpur
9. Lin K-S, Chan KY, Lee J-J (2018) Kinematic error analysis and tolerance allocation of cycloidal gear reducers. Mech Mach Theory124:73–91
10. Shung J, Pennock G (1994) The direct contact problem in a trochoidal-type machine. Mech Mach Theory 29(5):673–689
11. Cornell R (1981) Compliance and stress sensitivity of spur gear teeth. J Mech Des 103(2):447–459
12. Nag A, Maiti R (2013) Unification of epitrochoid origin profile design approaches for external lobed star member used in hydrostatic and gear units. Proc Inst Mech Eng Part C: J Mech Eng Sci 227(2):299–310
13. Maiti R, Nagao M (1999) Prediction of starting torque charecterstics of epitrochoid generated orbital rotary piston hydraulic motors. JSME Int J Ser C 42(2):416–426
14. Jhonson K (1985) Contact mechanics, 1st edn. Cambridge University Press, Cambridge, UK

Design and Analysis of Rocker Arm Shaft in IC Engine Hino Series for Reduction of Assembling Dismantling Time

R. Iruthayaraj, S. Palani, R. Ajay Vishal, T. Living Rockson, and K. Anand

Abstract Nowadays, in automobile industries the major competition exists in the field of design and cost of any product. Automobile plays a vital role in our daily life. One of the important components of the automobile is the engine of the automobile. Assembling and dismantling of the engine are difficult and tedious process. It is considered as time-consuming process also. If it is in the case of any valve leak, valve bend or due to any abnormal combustion in the engine, then the total set-up of the engine is to be dismantled part by parts for reworking purpose. The engine involves the large number of parts, and it takes too much of time for removing them completely into individual part. For reducing the time consumption, "the replica of rocker arm shaft" is designed. By using this, whole cylinder head is dismantled from the engine without any major damage. The time consumption would be very less, comparing with the existing method. The ultimate aim of our project is to reduce the time consumption for dismantling and reassembling of engine, without any major damage to engine parts and other surrounding parts.

Keywords IC engine · Rocker arm · Assembling · Dismantling · Time-consuming

1 Introduction

Ashok Leyland is an Indian automobile company headquarters in Chennai, India. It is owned by the "Hindu group", it is the second-largest commercial vehicle manufacturer of buses in the world and the tenth-largest manufacturer of trucks globally. It is operating nine plants; Ashok Leyland also makes spare parts and the engines for industrial and marine applications. Engines are the heart of the automobiles. Engines are used to move up the whole automobile body. Value analysis and value engineering should be employed in the engine design. In most of the automobiles, different varieties of engines are used. Engine varies depending upon the size, variety, type,

R. Iruthayaraj · S. Palani · R. Ajay Vishal (✉) · T. Living Rockson · K. Anand
Department of Mechanical Engineering, Vel Tech Multitech, Avadi, Chennai, Tamilnadu 600062, India
e-mail: ajayvishalr07@gmail.com

E. T. Akinlabi et al. (eds.), *Trends in Mechanical and Biomedical Design*,
Lecture Notes in Mechanical Engineering,
https://doi.org/10.1007/978-981-15-4488-0_11

applications, specialized purposes. Engine's capacity also varies depending upon the application for light-duty vehicles; four cylinder engines are used; for heavy-duty vehicles, such as trucks and lorries, six cylinder engines are used such as H-series engines. H stands for "Hino". H-series engine is used for heavy-duty purpose; H-series engine is huge in construction. It comprises of many major and minor components. In H-series engine, many parts are available. Several important parts of the H-engines are intake and exhaust values, intake and exhaust manifold, rocker arm assembly, cylinder head, cylinder top, fuel injector pipe, fuel injector, bolts, nuts, studs, common rails, injector pipes, turbocharger, exhaust gas recirculation, poppet valves, tappet valves, pushrod, camshaft, flywheel, piston head, rocker arm shaft, fuel filter, fuel sump and thermostat.

Nassef and Elkhabit [1] investigated the failure of a rocker arm shaft of a passenger car. The shaft failed by brittle fracture across one of the four holes supporting the shaft into the cylinder head. Microscopic observation of the failed shaft revealed that the four dark etching areas are surface hardened zone of martens tic microstructure. Microscopic investigation of the failed shaft reveals the presence of microcracks close to the supporting holes. This premature failure has occurred by the rapid crack propagation because of the lower toughness of martensite that excluding design reasons, failures such as consequential failure, improper lubrication, faulty manufacturing. For all the above reasons and given the results of the above investigation, such failure is attributed to improper heat treatment of the shaft during manufacturing. It is recommended to conduct a proper heat treatment to the whole body of the arm in order to prevent recurrent failures in the future [1].

Chirag et al. [2] focused to reduce the bottleneck areas by applying necessary techniques for improving the productivity. It is found that the main areas where bottleneck happens are head assembly key up station, tappet line and hot testing of engines. It is notified that various non-value added (NVA) activities and with the help of pare to principle; they sorted out most probable causes, i.e. traffic problem of cart, unwanted movements and handling of equipments, etc. By applying all these techniques, then the productivity improvement in one assembly system causes improvement in other subsystem too, NVA reduction by proper sequences of arrangement in activities by the installation of new tool and trouble shooting for head sub assembly, tappet line sub assembly and hot test cells etc [2]. Mujahid and Sheikh [4] reviewed the various types of rocker arms based on the sources from the last 40 years, in order to understand the rocker arm, for its problem identification and further optimization. In their work, the various types of rocker arms and their materials are studied. Rocker arm is an important component of engine; failure of rocker arm makes an engine useless and also requires costly improvement. The most suitable material for the rocker arm is steel because it has better fatigue strength than the aluminium [3].

Bache and Swaminadhan [4] discussed the failure of rocker arm in valve actuating mechanism to study and analyse the stresses generated, and they are modelling the rocker arm using CATIA CAD software and various regions of stresses and deformation found out using OPTISTRUCT-RADIOSS structural analysis solver which gives solution for structural optimization using finite element analysis (FEA). The main purpose of their study is to determine the value of stresses in rocker arm at extreme conditions. The design can be optimized by reducing the amount of material used. Stresses within the rocker body are calculated by using finite element analysis and validated with type help of result obtained by using analytical mathematical formulae [4]. Sonwane and Debase [5] started the discussion as currently manufacturing industries are facing a greater competition in the market. Due to this, competition among industries is trying to improve and increase both quality productivity continuously. So the main focus was given on the review of recent research related to the continuous improvement of automobile engines assembly line and a case study of automotive industry. The present work gives an overview of previously done research work and for new research; it gives a direction for continuous improvement of automobile engine assembly line. Also with the help of case study, it is explained how to reduce major breakdown causing production loss at engine assembly line [5].

Gide et al. [6] proposed that the purpose of valve train is to operate the inlet and outlet valves of engine. The valve train mainly consists of rocker arm, pushrod, cam, poppet valve and spring for keep the valve in closed position. The valve spring parameters are optimized based on the space availability, buckling of pushrod and natural frequency of system. It is observed that the valve jump engine speed with respect to optimized valve spring is enhanced. In order to capture the dynamic behaviour of the valve train system closely, each coil of the nested valve springs is modelled as separate flexible body and the contacts between coils of these flexible bodies are established [6]. Vinay Kumar and Sudeendra Srinivas [7] used ANSYS Software to design and perform structural analysis of the rocker arm. The geometric model of the rocker arm is developed and created by using CAD Software CATIA. The present work deals with the three-dimensional solid modelling, design and analysis of rocker arm of an IC engine. The rocker arm is designed, and the forces on the same are calculated. The structural analysis is carried out using different materials in order to arrive at optimized design of rocker arm. The finite element method is the most popular approach and found commonly used for analysing fracture mechanics problem [7].

Jadhav et al. [8] found that the rocker arms oscillate about rocker arm shaft because of action of push rod on one side and spring action on other side which causes bending of rocker arm; as a result, the bending stresses have induced the failure of rockers which takes place due to these stresses. Their research work deals with the theoretical and finite element analysis of rocker arm. The bending stress developed by the theoretical and finite element analysis of rocker arm is under static condition. Among the above two methods, the most static condition is considered for better results of rocker arm [8]. Bansod and Neigh [9] stated that the internal combustion engine, the tappet noise, is a major function. The tappet noise is a noise made by the lash or clearance between rocker arm and valve stem in an engine tappet noise that is characterized by its characteristic "Take Take" sound which is clearly audible when the engine dynamometer runs at 1400 rpm. The noise of the tappet generally occurred by the improper setting of tappets at the subassembly of tappet section and at the main section of assembly stations. By various corrective actions are counter measures taken as per the requirements of the tappet sections, provides increased tension of the timing gear chain for better and noiseless performance [9]. Shyam and Thacker [10] shown the main objective of any organisation is to increasing the productivity and profitability in order to increase the productivity and profitability. They reduce the defects and rejection of the product by the seven quality control tools and techniques. In today's competitive market, the major concern is to satisfy the customers for their requirements [10].

In our research work for reducing the time consumption, "the replica of rocker arm shaft" is designed. By using this, whole cylinder head is dismantled from the engine without any major damage. The time consumption would be very less, comparing with existing method. Our ultimate aim of this project is to reduce the time consumption for dismantling and reassembling of engine, without any major damage to engine parts and other surrounding parts.

2 Designing the Replica of Rocker Arm Shaft Identification of the Problem

2.1 Identification of the Problem

In engine assembly shop, the major problem exists in the cylinder head, due to valve leak, valve bend, etc. If so, then it is subjected to rework cylinder head in the rectification area.

2.2 Selection of Suitable Solution

As the engine comprises of many components, and due to its complex structure, "the replica of rocker arm shaft" is designed to remove the cylinder head together with major parts, without causing any damage to other parts.

2.3 Design Calculation of the Shaft

Known details: Diameter of shaft = 19 mm; Length of the shaft = 723 mm; Maximum equivalent stress = 115.91 Mpa; Deformation (or) deflection = 0.6 mm 5. Load = 183 kg = 1765.8 N.

Finding the tensile stress,

Tensile stress, $\sigma_t = F/A = 1739.23/(\pi/4 \times d^2)$.

$$\sigma_t = F/A = 1739.23/(\pi/4 \times d^2)$$

Finding the torque (M_t):

$$M_t = \frac{\pi}{4}\left(\tau \times D^3\right)$$
$$M_t = \frac{\boldsymbol{\pi}}{4}\left(115.91 \times 18^3\right)$$
$$M_t = 1.33 \times 10^{16}\,\mathrm{N\,m}$$

To find the maximum shear stress (N/mm^2), Bending stress is:

$$\sigma_b = M_y/\mathrm{I} = \left(M_y\right)/\left(\frac{\pi}{32}\right) \times \left(d^4\right)$$
$$M_b = (W \times L)/4$$
$$= 1789.23 \times 723\,\mathrm{mm}$$
$$M_b = 323.40\,\mathrm{N\,m}.$$
$$\sigma_b = (323.40 \times 0.6\mathrm{e}^{-3})/\left(\frac{\pi}{32} \times 18^4\right)$$
$$= 1.508\,\mathrm{N/mm^2}$$
$$\tau_{max} = 16/(\pi \times d^3)\sqrt{(M_b \times K_b)^2 + (M_t \times K_t)^2}$$

K_b and K_t for suddenly applying load with minor shock $K_b = 1.5$ to 2 take $K_b = 1.5$.
$K_b = 1.0$ to 1.5 take $K_t = 1.0$ Symbols and Names.
Here, σ_b = Bending stress, M_t = Maximum torque, σ_t = Tensile stress.
K_b, K_t = Minor shocks applied.

To find maximum torque,

$$\tau_{max} = 16/(\pi \times d^3)\surd(M_b \times K_b)^2 + (M_t \times K_t)^2$$
$$\tau_{max} = (16)/(\pi \times d^3)\surd(323.40 \times 1.5)^2 + \left(1.56 \times \mathrm{e}^{16} \times 1\right)^2$$
$$= (16)/(\pi \times 18^3)\surd(323.40 \times 1.5)^2 \times 2.43 \times \left(10^3\right)$$
$$= (16)/(\pi \times 18^3) \times 1.55 \times 10^{16}$$
$$\tau_{max} = 1.15 \times 10^{13}\,\mathrm{N/mm^2}$$

After designing the replica of the rocker arm shaft, the drafting for the particular shaft is performed by using the SolidWorks software. This drafting action can accomplish by the use of SolidWorks. This drafting helps us to understand clear structure and dimensions of the rocker arm shaft. The design of the replica of rocker arm shaft is designed first with proper designation. After the designing process, drafting action has been performed for previewing the rocker arm shaft.

The drafting view of the replica of rocker arm shaft is shown in Fig. 1.

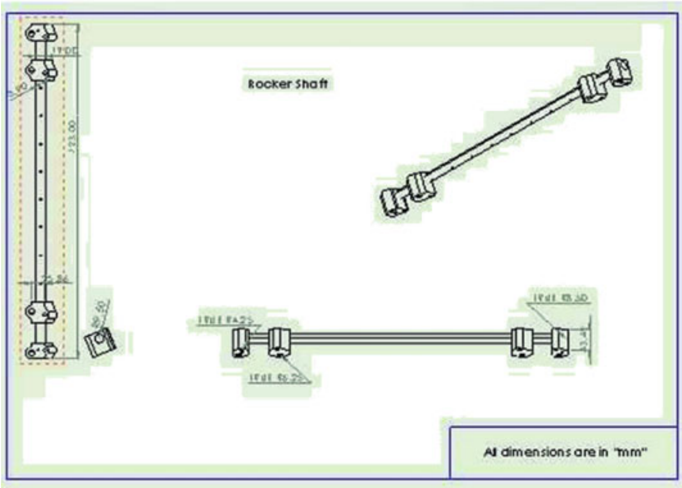

Fig. 1 Drafting view of the replica of rocker arm shaft

In the real rocker arm shaft, rocker arms are available in the rocker arm shaft. The purpose of existing rocker arm shaft is to transmit the radial motion of the cam lobe into the linear movement to operate the poppet valves for opening and closing the flow. In the replica of rocker arm shaft, there a long shaft, 2 movable (adjustable) support rocker valves and 2 both side fixed rockers. In this replica of rocker arm shaft, rocker arms are not involved. The main purpose of this shaft is to hold and withstand the weight of the cylinder head. Figure 2 shows the design of the shaft using CATIA software.

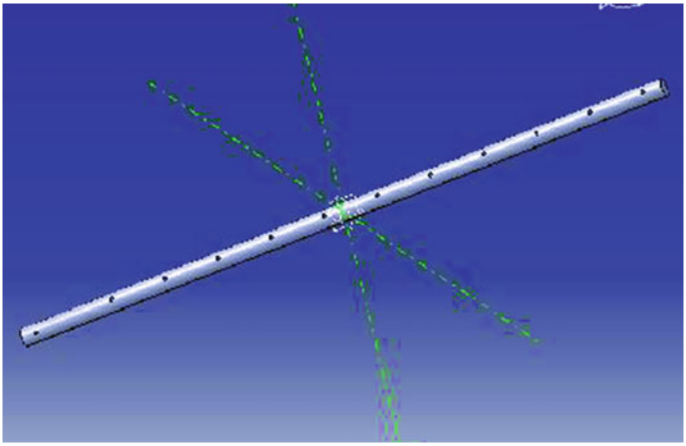

Fig. 2 Design of shaft using CATIA software

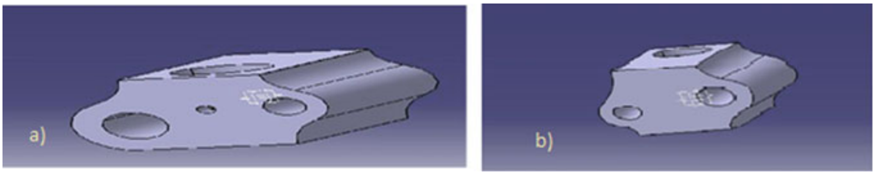

Fig. 3 Design of part. **a** Left side, **b** right side using CATIA software

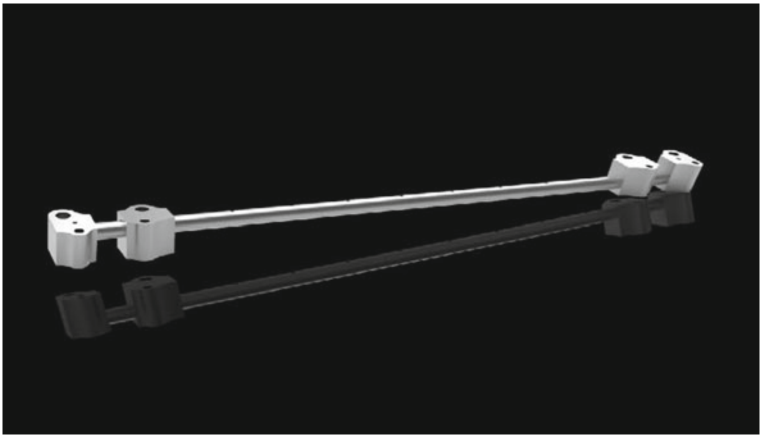

Fig. 4 3D view of rocker arm shaft assembly using SolidWorks

The designs of parts (a) left side (b) right side using CATIA software are shown in Fig. 3.

After designing the rocker arm shaft, the shaft is to be manufactured and fitted into the cylinder head. The rocker arm shaft is to be fitted into the holes of the cylinder head, bolted up and lifted by using the crane hook. The 3D view of rocker arm shaft assembly using SolidWorks is shown in Fig. 4.

2.4 Principles of Operation

Engine varies according to the size, variety, type, applications and other specialized purposes. Engine's capacity also varies depending upon the application such as light-duty vehicles and heavy-duty vehicles. For light-duty vehicles, 4 cylinder engines are used, and for heavy-duty vehicles, such as trucks, Lorries, 6 cylinder engines such as H-series engines are used (H stands for "Hino" which is used). In an internal combustion engine, the cylinder head (often informally abbreviated to just head) sits above the cylinders on top of the cylinder block. Due to these complex structure that involving many parts, in the engine, identification of error in the engine is difficult, if the engine is not functioning. After the identification of the error in particular part, i.e. fuel injectors in the cylinder head, and then only the rework or the rectification work of cylinder head is performed.

In general, same as the assembling process, disassembling process is very difficult and time-consuming one. Due to its complex structure, each and every part is to be removed carefully for the reworking purpose. Engine is absorbed abnormal combustion, and then we proceed to check out the fuel injector problems. In early process to remove the cylinder head, the following things are to done. The following parts to be removed are rocker arm shaft, exhaust manifold, fuel injector, remove the rocker arm shaft from the head, remove inlet and exhaust manifold, and then remove exhaust gas recirculation (EGR), turbocharger and TG Elbow, Thermostat, common rail injector, cylinder head bolts, valve cap, leak pipes and gaskets. Disassembling of parts is time-consuming sometimes disassembling causes damage to the parts. For this, we are designing the special shaft which looks similar to the rocker arm shaft, i.e. “replica of rocker arm shaft”. Electrically operating hook is used to hold and lift the whole cylinder head set-up with the replica of rocker arm shaft, from the top of the engine. Then, we can easily rework with the cylinder head, which was lifted and hung over the engine through crane hook.

3 Results and Discussion

Time Calculation by Existing Method
Dismantling:
Step 1:
Inlet and Exhaust manifold; Rocker Arm Shaft; EGR, Thermostat, Common Rail and injector = 35 min
Step 2:
Turbocharger and Elbow; Cylinder Head bolts, Manifold Gaskets; Valve cap pins, Lube oil Pipes = 30 min
Step 3:
Banjo Bolt, Tappet; Oil Supply Line and Liners; Other Exterior Parts = 15 min.

In this method for dismantling the cylinder head, time consumption is 1 h 20 min.
Assembling
After finished, they dismantle the parts to check and analyse the damages in piston. For reassemble, they consume the same time. In this method, we found the drawbacks, which they are more time consumption and material damaging for the removing process. So, we use the new technique in the removal of cylinder head to avoid unwanted things.

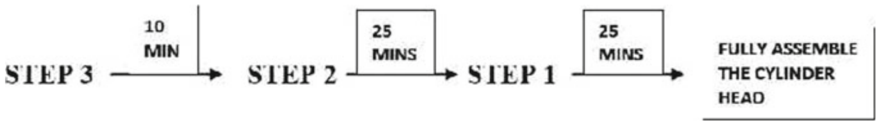

Total time taken for assembling = 10 + 25 + 25 = 60 min.

Time Calculation by proposed Method
Dismantling
Step 1:
Removing the Rocker Arm Shaft; Further, Bolts nuts of this component = 15 min
Step 2:
Exhaust and Inlet pipes Springs; Valve cap, Fuel Liner = 10 min
Step 3:
EOT is placed at in the Dummy Rocker Arm shaft = 5 min
It can be pulled upside to rigid condition.

Assembling
Due to its more complexity structure, the assembling of the single engine is considered as the time-consuming process. It requires more manpower for fixing it with proper proportions and alignments. As in case of any problem or any improper assembling, the whole set-up is to be removed or dismantled one by one. Same as the assembling process, disassembling process is very difficult and time-consuming one. Due to its complex structure, each and every part is to be removed carefully for the reworking purpose.

Total time taken for assembling = 5 + 10 + 10 = 25 min.

In this method, the time consumption for assembling is 25 min, which is very less compared to the existing method. Figure 5 shows the pie chart for time utilized (a) exiting and (b) proposed methods. Figure 5 shows the pie chart for time utilized (a) exiting and (b) proposed methods (Table 1).
Total Time Saved by Overcoming the Old Technique

$$\text{Total time saved} = (\text{Total time taken by normal method})$$

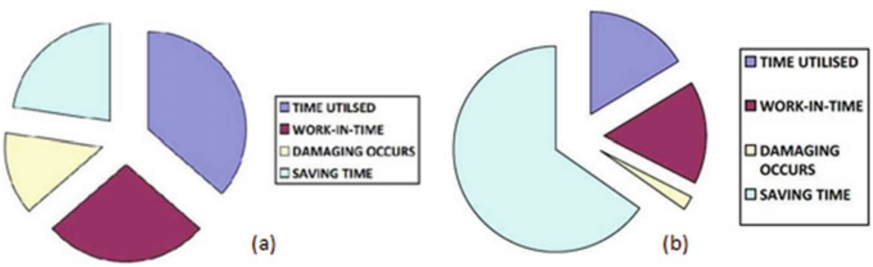

Fig. 5 Pie chart for time utilized. **a** Exiting, **b** proposed methods

Table 1 Comparison of total time taken by both existing method and new method

Sl. no.	Technique used	Dismantling time	Assembling time	Total time
1	Normal method	1 h: 20 min	1 h	2 h: 20 min
2	Proposed method	30 min	25 min	55 min

$$
\begin{aligned}
&-(\text{Total time taken by proposed method})\\
&= (2\,\text{h: }20\,\text{min}) - (55\,\text{min})
\end{aligned}
$$

Total time saved = 1 h: 25 min.
By comparing those two methods, proposed method is considered as the most promising method. In existing method, the total time used is **2 h: 20 min**. And in the proposed method, the total time used is **55 min.** The total time saved by proposed method is **1 h: 25 min.**

4 Conclusions

In the proposed technique, the dismantling time of cylinder head may be reduced in a greater extent compared to the traditional technique. By overcoming the time consumption of dismantling of cylinder head, rate of production may be increased. Here, also avoid the damages of the surrounding parts of the cylinder heads. The replication of rocker arm shaft may be used to remove the cylinder head in effective manner without removing the major parts such as inlet and exhaust manifold, and EGR. Also In this research work designed the rocker arm shaft and given for manufacturing, after receiving the product, able to calculate the time consumption by using this method. By using this replica of rocker arm shaft, easily remove the cylinder head for the reworking purposes. Furthermore, improve the production rate by reducing the time consumption for rectifying the defective engines.

References

1. Nassef GA, Elkhabit A (2016) Analysis of a failed rocker arm shaft of passenger car engines. Sci Direct 5(6):10–14
2. Deotare CK, Dabade UA (2015) Productivity improvement in engine assembly line at GM India Ltd. Pune, India. Int J Latest Trends Eng Technol 6(1):9–16
3. Mujahid S, Sheikh S (2013) Design and analysis of rocker arm. Int J Mech Eng Rob Res 2(3):191–197
4. Bache S, Swaminadhan P (2018) Design and static structural analysis of rocker arm in IC engine. Int J Eng Sci Res Technol 7(4):755–763(2018)
5. Sonwane AB, Debase DA (2017) Continuous improvement of automobile engine assembly line: A review and case study. J Adv Sci Technol 13(1):245–252

6. Gide S, Shrives J, Kharde RR. Review on critical speed improvement in single cylinder engine valve train. Int J Innov Eng Res Technol. ICITDCEME'15 conference proceedings ISSN No 2394-3696
7. Vinay Kumar D, Sudeendra Srinivas B (2017) Design and fabrication of rocker arm. Int J Core Eng Manage NCETME 193–200. ISSN 2348-9510
8. Jadhav S, Patil PJ, Mulik, PV (2018) Experimental and finite element analysis of rocker arm for bending failure. Int J Adv Eng Res Dev 5(7):1–9(2018)
9. Bansod N, Neigh HS (2015) Tappet noise reduction in motor cycle engine. Int J Eng Dev Res 3(2):461–474
10. Bambharoliya SH, Thacker HR (2015) Reducing reduction rate in small scale machining unit using seven quality control tools. Int J Eng Dev Res 3(4):582–586

Kinematic Analysis and Dimensional Synthesis of Filleted-Rhombus Path Generating Adjustable Four-Bar Mechanism

Ganesan Govindasamy, Clinton Wilson, and K. Neeraj

Abstract Dimensional synthesis and kinematic analysis of adjustable four-bar mechanism to generate accurate and uninterrupted path of Filleted-Rhombus are investigated. Harmonic Spacing (HS) algorithm is used to improve the positioning of precision points along the intended profile path. Reconstructed adjustable parameter curve (RAPC) is employed to extract adjustable link length value of intermediary path points along the intended path conforming to an equally incremented crank rotation value. Simulation of motion of adjustable mechanism to generate the intended coupler path is carried out to verify the dimensions of the links and other parameters of the mechanism. Optimization employing Genetic Algorithm (GA) followed by Pattern Search (PS) is implemented using MATLAB codes in the synthesis of mechanism. Results show precise and continuous coupler path to generate filleted-rhombus profile and variation of kinematic parameters versus crank angle.

Keywords Kinematic analysis of adjustable mechanism · RAPC · Adjustable four-bar linkage · Filleted-Rhombus path

1 Introduction

Kinematic synthesis is applied to obtain motion generation, function generation and path generation of mechanisms. Path generation is the motion of the coupler point to trace a path profile. Point-to-point path generation is to follow the computed precision points while the trajectory between the computed points is approximated. The other type of path generation is of the continuous type which specifies the whole path with many points that approximately pass through the specified curve. Adjustable mechanism is neither equal to sophisticated flexible robot nor equal to non-adjustable mechanism. It takes the mid-position between non-adjustable mechanism and robot [1] in terms of speed, precision and simplicity. In contrast to analytical methods

G. Govindasamy (✉) · C. Wilson · K. Neeraj
Department of Mechanical Engineering, Karunya Institute of Technology and Sciences, Karunya Nagar, Coimbatore, Tamil Nadu 641114, India
e-mail: vivajijaya67@gmail.com

E. T. Akinlabi et al. (eds.), *Trends in Mechanical and Biomedical Design*,
Lecture Notes in Mechanical Engineering,
https://doi.org/10.1007/978-981-15-4488-0_12

that satisfy fewer precision points precisely optimization methods such as Genetic Algorithm, Pattern Search, and Neural Networks, etc. satisfy many precision points. Haws and Kay [2] used an adjustable mechanism employing a cam-link to generate one-fourth of a square and a cardioid path. Kohli and Singh [3] made use of cam-link linkages to generate an exact path. Ogawa et al. [4] synthesized adjustable multi-link linkages to produce L-shaped and straight lines paths connecting several precision points. Mundo and Gatti [5] employing non-circular gears synthesized five-bar linkages for accurate path generation. Sodhi and Russel [6] applied a new design method for adjustable slider-crank mechanisms to realize two-phase path generation. Mundo et al. [7] synthesized adjustable cam linkage mechanism to adjust the position of the fixed pivot of the link using a cam for exact path generation. Ghoshal and Chanekar [8] synthesized adjustable linkages in two stages in order to reduce the variables required to design a linkage.

Synthesis of continuously adjustable crank-rocker linkage to produce rectangular path was tried by Zhou [9]. Ganesan and Sekar [10] used a graphical method to obtain an adjustable parameter curve (APC) from the dimensions of the mechanism synthesized by Zhou [9] to produce a rectangular path. Ganesan and Sekar [11] optimally synthesized adjustable linkages to generate a rectangle with filleted corners. Ajith Kumar et al. [12] synthesized continuously adjustable linkages to generate rectangle with chamfered corners, rectangle with full chamfering and one DOF cam-link adjustable mechanism to generate oblong-hole path.

It has been found from the above literature that the precise filleted-rhombus path generation mechanism and kinematic analysis of such a mechanism are not attempted. Section 2 presents an adjustable linkage model, precision points on filleted-rhombus path, dimensional synthesis using hybrid optimization. Section 3 presents RAPC method to extract path points on the filleted-rhombus path for one degree incremental value of crank for one revolution. Velocity and acceleration analysis of various links of mechanism to produce filleted-rhombus path is given in Sect. 4. Section 5 presents results and discussions. Conclusions and suggestions are presented in Sect. 6.

2 Filleted-Rhombus Path Generating Adjustable Mechanism

Four-bar adjustable mechanism model of Zhou's [9] is used in the synthesis to generate a precise and continuous filleted-rhombus path, as shown in Fig. 1, in which a rocker (L_3) is carried by a slider (D) which forms the adjustable link. This adjustable link length (S) from the pivot (A) along the x'-axis of a local coordinate system to the pin joint between the rocker and slider is called 'adjustable parameter' of the mechanism. Link AB is crank (L_1). In triad link BCM, side BC forms coupler link (L_2), side BM (L_6) carries coupler point (M). In this adjustable four-bar mechanism, the required adjustable parameter values (S) are determined so that the coupler point can trace filleted-rhombus path precisely when the crank makes one revolution.

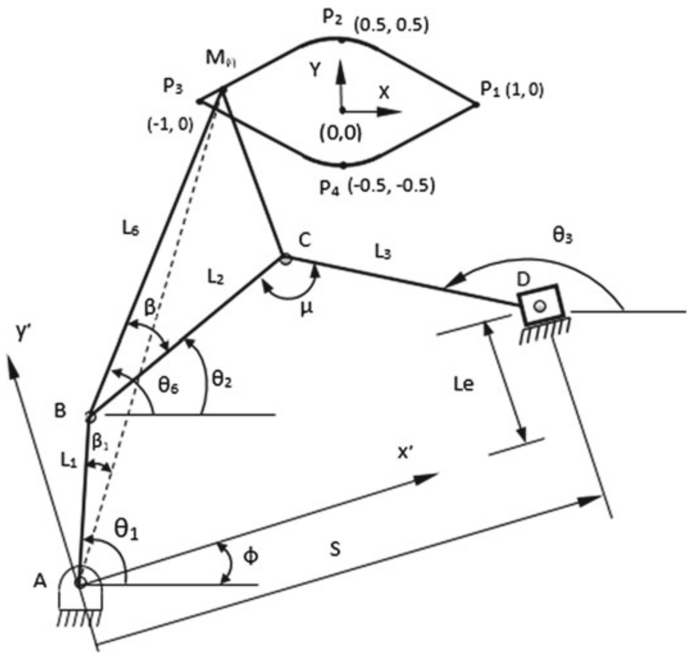

Fig. 1 Adjustable mechanism model

Coupler point has to travel along the $P_1P_2P_3P_4P_1$ path which comprises four straight lines and two arcs as shown in Fig. 1. The difficulty arises when the coupler point negotiates a change in direction. This demands closer precision points near the points where changes in direction take place. The following harmonic spacing algorithm satisfies the closer precision points at the ends of a straight line or an arc.

2.1 Precision Points Algorithm for Filleted-Rhombus Path

Difficulty arises when the coupler point negotiating positions where it changes direction drastically. This demands closer precision points near these points. The following harmonic spacing algorithm (1) satisfies the closer precision points at the ends of a straight line or an arc as shown in Fig. 2.

$$x_j = \frac{(x_i + x_f)}{2} + \frac{(x_i - x_f)}{2}\left[\cos\left(\frac{(j-1)}{N-1}\right)\right] \tag{1}$$

where x is variable with an interval $[x_i, x_f]$ and $j = 1, 2, \ldots, N$, x_j-intermediary point coordinate value, x_i-initial point coordinate value, x_f-endpoint coordinate value, N (number of precision points inclusive of initial point and end point).

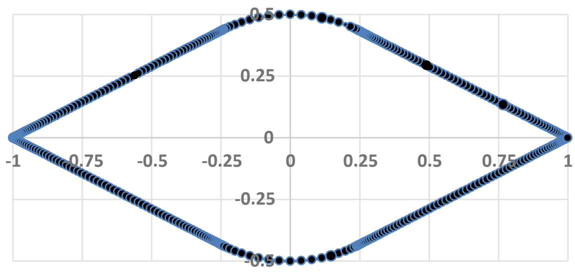

Fig. 2 Precision points of filleted-rhombus path

2.2 *Synthesis of Mechanism to Generate Filleted-Rhombus Path*

The coordinates of the precision points are extracted from Eq. (1) and used in the synthesis as the known values of the coupler points. The mechanism is synthesized using Eqs. (10)–(21) which govern the geometry of the intended mechanism to satisfy all the 360 precision points. Synthesized mechanism's unknown independent parameters (ϕ, x_A, y_A, β, L_e, L_2, L_3) and dependent parameters (L_6 and L_1) are given in Table 1.

The objective is to minimize link length value (S) for a set of independent variables (ϕ, x_A, y_A, β, L_e, L_2, and L_3) of the linkage whose lower bound (LB) values are −3, −2, 2.5, 2.5, 1, 50, −90 and upper bound (UB) values are −1.5, −1.0, 4, 4, 2, 80, −50, respectively, for these variables. The difference between the maximum

Table 1 Parameters of the synthesized mechanism

Optimized filleted-rhombus path generation parameters and other variables	Values of the variables and other parameters
Fixed pivot x-coordinate value (x_A)	−2.4952
Fixed pivot y-coordinate value (y_A)	−1.3322
Coupler length (L_2)	3.9999
Rocker length (L_3)	3.9713
Slider offset length (L_e)	1.9776
Coupler point arm angle (β)	53.8528°
Frame orientation angle (θ)	−78.2318°
Crank length (L_1)	0.8689
Coupler pointer length (L_6)	2.8715
Starting crank angle value when pointer is at P_1 (θ_1)	20.8642
Maximum value of adjustable link length (S_m)	6.5327
Minimum value of adjustable link length (S_n)	5.8469
Error function (E_a)	0.6858

adjustable link length and minimum adjustable link length is the error function, i.e. minimization of this error is the objective of the synthesis of the mechanism.

$$E_{\mathrm{a}} = S_{\mathrm{m}} - S_{\mathrm{n}} \tag{2}$$

Initial value of L_1 and L_6 are 1.0 and 2.5 units, respectively. Penalty factor and population size are given 500 and 20 respectively and tournament selection method is used. Objective function must satisfy the following constraint functions (3)–(8) to satisfy link length criterion of Grashof and also to avoid linkage dead points.

$$|L_{\mathrm{ce}}|_{\max} - L_3 \leq 0 \,\text{Where}\, L_{\mathrm{ce}} = y'_C - L_e \tag{3}$$

$$L_1 + \sqrt{S_{\mathrm{m}}^2 + L_e^2} - L_2 - L_3 \leq 0 \tag{4}$$

$$L_2 - L_3 + L_1 - \sqrt{S_{\mathrm{n}}^2 + L_e^2} \leq 0 \tag{5}$$

$$L_1 - L_2 + L_3 - \sqrt{s_{\mathrm{n}}^2 + L_e^2} \leq 0 \tag{6}$$

$$L_2^2 + L_3^2 - \left(\sqrt{S_n^2 + L_e^2} - L_1\right)^2 - 2L_2L_3\cos\mu_1 \leq 0 \tag{7}$$

where $\mu_1 = 20°$ and $S_{\mathrm{n}} =$ minimum value

$$-L_2^2 - L_3^2 + \left(\sqrt{S_{\mathrm{m}}^2 + L_{\mathrm{e}}^2} + L_1\right)^2 + 2L_2L_3\cos\mu_2 \leq 0 \tag{8}$$

where $\mu_2 = 160°$ and $S_{\mathrm{m}} =$ maximum value

In order to trace the path points on the path profile by the pointer in the right order and overcome 'order defect' during full rotation of the crank in the anti-clockwise direction at uniform angular velocity, a constraint Eq. (9) is forced.

$$(\theta_1)_i < (\theta_1)_{i+1}. \tag{9}$$

2.3 Optimization Employing Genetic Algorithm Followed by Pattern Search

In the Genetic Algorithm (GA) optimum value of the objective function may not be always reached due to the stopping criteria imposed on GA.

This requires further exploration of the search space. By changing the stopping criteria, it is possible to find the optimum solution. However, it may require many more function evaluations to reach the optimum value. A local search can be more efficient in such a scenario. Pattern search is used for local search that starts from the point where GA reached thus making a hybrid optimization process.

3 Filleted-Rhombus Path Generation Using RAPC Method

Reconstructed adjustable parameter curve method is employed to extract path point of filleted-rhombus path. The required equations to find path points for uniform incremental values of the crank rotation along the four straight lines and two circular-arcs of radius 0.5 units of filleted-rhombus are described in the remaining section. Closed filleted-rhombus path is given by $P_1P_2P_3P_4P_1$.

It is anticipated that the point (M) of coupler link in the mechanism travel through the complete profile path, shown in Fig. 1, through endless path points for uninterrupted generation of intended path. Path point refers to any point on the filleted-rhombus path. Path points on the filleted-rhombus path are obtained from synthesized values (x_A, y_A, ϕ, β, L_2, L_1, L_3, L_e and L_6) of the mechanism. Number of precision points N is taken as 360 for better results. Precision points used and their corresponding crank angles obtained in the synthesis do not match to uniform crank arm angular displacements.

The coordinate values of the first precision point M_1 at P_1 is (1, 0) and corresponding angular position $(\theta_1)_1$ is obtained from Table 1. The length between first path point M_1 and fixed point A is given by Eq. (10). Equation (11) gives the angle between link L_1 and line AM_1.

$$L_{AM(1)} = \sqrt{\left(x_{M(1)} - x_A\right)^2 + \left(y_{M(1)} - y_A\right)^2} \tag{10}$$

$$\beta_{1(1)} = \cos^{-1}\left(\frac{L_1^2 + L_{AM(1)}^2 - L_6^2}{2L_1L_{AM(1)}}\right) \tag{11}$$

Equation (12) also can be used to get $(\theta_1)_1$. In Eq. (12) the ±sign specifies the two alignments of dyad ABM as presented in Fig. 1 as continuous and dashed lines.

$$(\theta_1)_1 = \tan^{-1}\left[\left(y_{M(1)} - y_A\right), \left(x_{M(1)} - x_A\right)\right] \pm \beta_{1(1)} \tag{12}$$

The Eqs. (13) and (15) give values of coordinates of joint B for first path point. Equation (14) gives angle $(\theta_6)_1$.

$$x_{B(1)} = x_A + L_1 \cos\theta_{1(1)} \tag{13}$$

$$\theta_{6(1)} = \tan^{-1}\left[\left(y_{M(1)} - y_{B(1)}\right), \left(x_{M(1)} - x_{B(1)}\right)\right] \tag{14}$$

$$y_{B(1)} = L_1 \sin\theta_{1(1)} + y_A \tag{15}$$

The value of β is got from synthesized values (Table 1). The coordinates of joint C_1 are attained from Eqs. (16)–(18)

$$\theta_{2(1)} = \theta_{6(1)} - \beta \tag{16}$$

$$x_{C(1)} = L_2 \cos\theta_{2(1)} + x_{B(1)} \tag{17}$$

$$y_{C(1)} = L_2 \sin\theta_{2(1)} + y_{(1)} \tag{18}$$

For ease of analysis of slider dyada local coordinate frame is used. Joint A is taken as the local coordinate origin. Coordinates of joint C in local coordinates are obtained from Eqs. (19) and (20) from the global coordinates.

$$x'_{C(1)} = \left(x_{C(1)} - x_A\right)\cos\varphi + \left(y_{C(1)} - y_A\right)\sin\varphi \tag{19}$$

$$y'_{C(1)} = -\left(x_{C(1)} - x_A\right)\sin\varphi + \left(y_{C(1)} - y_A\right)\cos\varphi \tag{20}$$

Location of the slider from fixed the pivot A is given by, adjustable link length, $S_{(1)}$ when the coupler is indicating the first path point, is found from Eq. (21).

$$S_{(1)} = x'_{C(1)} \pm \sqrt{L_3^2 - \left(y_{C(1)} - L_e\right)^2} \tag{21}$$

For the first path point, using Eqs. (10)–(21), adjustable length $S_{(1)}$ is attained. The second path point is obtained by the intersection of line P_1P_2 at $M_{(2)}$ and an arc of length L_6 from joint B. This gives the coordinates $X_{M(2)}$ and $Y_{M(2)}$ of the path point $M_{(2)}$ from equations by solving an arc and straight line after incrementing the crank by 1°. Substituting $x_{M(2)}$, $y_{M(2)}$ through Eqs. (10)–(21) in the place of x_{M1}, $y_{M(1)}$ to get the adjustable parameter value $S_{(2)}$.

Intersection of two arcs along the filleted part of the profile is used to find path points. Using the known slope and intercept values of the straight lines path points along the straight line are obtained. Thus, $S_{(i)}$ where $i = 1, 2, \ldots, 360$, adjustable length values of path points are obtained. These path points are used to construct the required filleted-rhombus path. Figure 3 shows a synthesized mechanism to generate filleted-rhombus path. Figure 4 shows the adjustable link length (S) versus crank angle incremented by 1° for filleted-rhombus path generation. It is related to a non-adjustable mechanism by fixing the slider at a mean position.

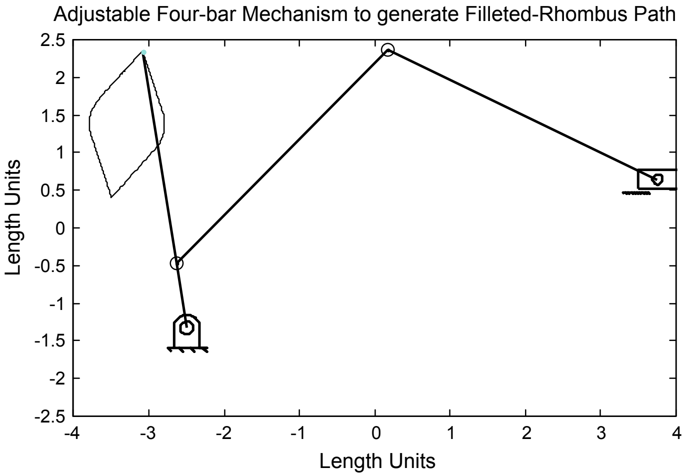

Fig. 3 Synthesized adjustable mechanism

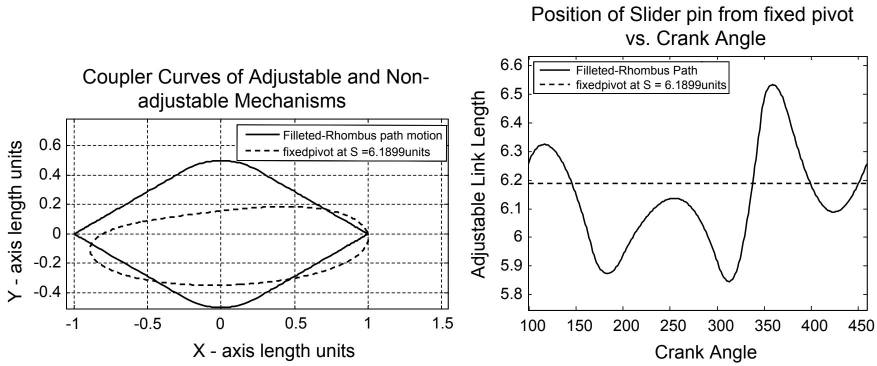

Fig. 4 Generated coupler path and adjustable parameter curve (APC) required

4 Kinematic Analysis of the Mechanism

For every incremental value of crank rotation, positions of the links in the mechanism are found from known dimensions of the links and alignment angles of coupler $(\theta_2)_i$ and rocker $(\theta_3)_i$. From known velocity of crank, coupler and rocker velocities are found from Eq. (22) and coupler and rocker angular accelerations are obtained from Eq. (23).

$$\begin{bmatrix} -L_2\sin\theta_2 & L_3\sin\theta_3 \\ -L_2\cos\theta_2 & L_3\cos\theta_3 \end{bmatrix} \begin{Bmatrix} \dot{\theta}_2 \\ \dot{\theta}_3 \end{Bmatrix} = \begin{Bmatrix} L_1\dot{\theta}_1\sin\theta_1 \\ L_1\dot{\theta}_1\cos\theta_1 \end{Bmatrix} \tag{22}$$

Kinematic analysis is of the mechanism is related to a non-adjustable mechanism by fixing the moving pivot at a mean value of S_{m} and S_{n}.

$$\begin{bmatrix} -L_2\sin\theta_2 & L_3\sin\theta_3 \\ -L_2\cos\theta_2 & L_3\cos\theta_3 \end{bmatrix} \begin{Bmatrix} \dot{\theta}_2 \\ \dot{\theta}_3 \end{Bmatrix} = \begin{Bmatrix} L_1\ddot{\theta}_1\sin\theta_1 + L_2\dot{\theta}_2^2\cos\theta_2 + L_1\dot{\theta}_1^2\cos\theta_1 - \cos\theta_3 L_3\dot{\theta}_3^2 \\ L_1\ddot{\theta}_1\cos\theta_1 - L_2\dot{\theta}_2^2\sin\theta_2 - L_1\dot{\theta}_1^2\sin\theta_1 - \sin\theta_3 L_3\dot{\theta}_3^2 \end{Bmatrix} \tag{23}$$

5 Results and Discussion

Figure 5a–d shows the variation coupler angle, velocity, acceleration and rocker acceleration, respectively versus crank angle. Figure 5a shows that the coupler angle varies non-uniformly with crank angle. Figure 5b shows coupler angular velocities

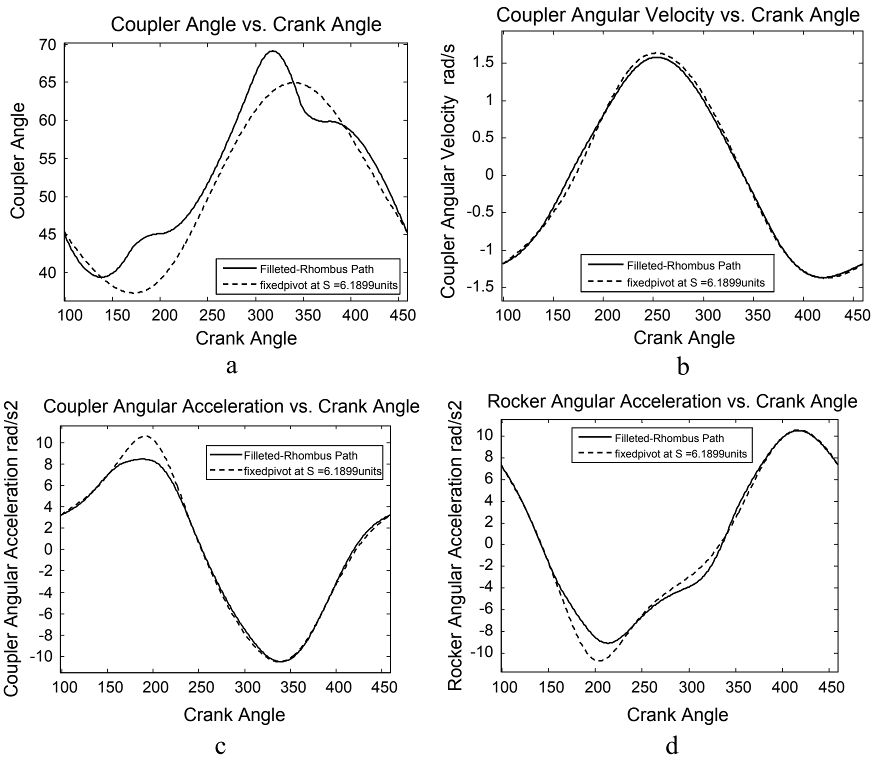

Fig. 5 Kinematic parameters versus crank angle

are almost the same. Figure 5c, d shows that the maximum magnitude of coupler acceleration and rocker acceleration are less than non-adjustable mechanism.

6 Conclusion

Precise filleted-rhombus path generation mechanism is synthesized. Its path points for one degree crank rotation are extracted. Kinematic analysis performed for the mechanism to generate filleted-rhombus path. Adjustable link length curve required to generate filleted-rhombus path does not show any sharp turning points. This observation motivates us to explore the possibility of converting this mechanism to achieve one degree of freedom with the help of a cam-link.

References

1. Chong P, Sodhi R (2010) Optimal synthesis of adjustable mechanisms generating multiphase approximate paths. Mech Mach Theory 45:989–996
2. Kay F, Haws R (1975) Adjustable mechanisms for exact path generation. ASME J Eng Ind 97(2):702–707
3. Singh Y, Kohli D (1981) Synthesis of cam-link mechanism for exact path generation. Mech Mach Theory 16(4):447–457
4. Shimojima H, Ogawa K, Fujiwara A, Sato O (1983) Kinematic synthesis of adjustable mechanisms. Bull JSME 14:621–632
5. Mundo D, Gatti G (2008) A graphical-analytical technique for the synthesis of noncircular gears in path-generating geared five-bar mechanisms. Trans CSME 32(3–4):488–497
6. Russell K, Sodhi RS (2005) On design of slider-crank mechanisms Part II: multi-phase path and function generation. Mech Mach Theory 40:301–317
7. Mundo D, Liu JY, Yan H (2006) Optimal synthesis of cam-linkage mechanisms for precise path generations. J Mach Des 128:1253–1260
8. Chanekar PV, Ghoshal A (2013) Optimal synthesis of adjustable planar four-bar crank-rocker type mechanisms for approximate multi-path generations. Mech Mach Theory 69:263–277
9. Zhou H (2009) Dimensional synthesis of adjustable path generation linkages using the optimal slider adjustment. Mech Mach Theory 44:1866–1876
10. Ganesan G, Sekar M (2014) Kinematic analysis of rectangular path generating adjustable four-bar linkage. Appl Mech Mater Trans Tech Publ 592–594:1094–1098
11. Ganesan G, Sekar M (2017) Optimial synthesis and kinematic analysis of adjustable four-bar linkages to generate filleted rectangular paths. Mech Based Des Struct Mach 45(3):363–379
12. Ajith Kumar G, Ganesan G, Sekar M (2018) Near perfect path generation of corners-chamfered-rectangle and single synthesis cam-link mechanism to generate special-slot path. Mech Based Des Struct Mach 46(4):483–498

Experimental Investigations of Initial Push Forces on an Industrial Trolley

Masepogu Wilson Kumar, Gadudasu Babu Rao, K. Balasubramanian, and I. Kantharaj

Abstract Manual material handling using push-pull trolleys in small- and medium-scale enterprises is an inevitable activity. A study carried out on a push-pull trolley using push-pull force gauge, surface electromyography, electro-goniometer, and heart rate monitor helped the researchers to find an appropriate handle height of a trolley for industrial use. Central composite design, a response surface methodology, was used for designing experiments. These experiments were carried out in a laboratory using five subjects with stature 1650, 1730, 1740, 1750 and 1820 mm, at 125 kg load under five different heights of handle, viz. 900, 950, 1000, 1050 and 1100 mm. A 35% of reduction was found in the initial forces after using 1100 mm handle height by the subjects during the pushing activity.

Keywords Manual material handling · Push-pull forces · Handle height · Trolley · Central composite design (CCD)

1 Introduction

The use of poorly designed manual material handling (MMH) equipments like push-pull trolleys may consume extreme energy from the industrial workers. The efforts of the industrial workers can be reduced in the tasks, especially in pushing and pulling the heavily loaded trolleys by providing ergonomically designed manual material handling assisting devices. Height adjustable handles for the MMH carts or trolleys can be of great use to all the industrial workers.

MMH tasks such as lifting or lowering, carrying and pushing or pulling are physical work activities that involve the exertion of considerable force because a particular load is heavy or the cumulative loads during working days are heavy [1]. Pushing and pulling tasks can be ergonomically evaluated at the workplace through the assessment of the magnitude of forces exerted by the subject/worker on the trolley. The push or pull forces are often distinguished as initial forces which are required to

M. Wilson Kumar (✉) · G. B. Rao · K. Balasubramanian · I. Kantharaj
Karunya Institute of Technology and Sciences, Coimbatore, Tamil Nadu 641114, India
e-mail: wilson@karunya.edu

E. T. Akinlabi et al. (eds.), *Trends in Mechanical and Biomedical Design*,
Lecture Notes in Mechanical Engineering,
https://doi.org/10.1007/978-981-15-4488-0_13

move the object from the initial position, whereas the sustained forces are required to keep the object in constant or varied speed or velocity. The ending forces may be equal or more like initial forces to stop or bring the trolley to halt [2]. The laboratory experiments investigated the maximum acceptable forces for a particular population using handle heights, distance and frequencies matching to different pushing tasks from a psychosocial point of view [3]. Laboratory experiments conducted on a cart with two different moving speeds 1.8 and 3.6 km/h and three different heights of exertion 660, 1090 and 1520 mm found that pulling a cart ended up in more back loading than pushing. Body weight of subject ranging from 50 to 80 kg affected the lower-back loadings more significantly in pulling for forces 98, 198 and 294 N (50% increase as body weight increase from 50 to 80 kg) than in pushing (25% increase) [4].

Pushing and pulling should be carried out on an ergonomically well-designed cart/trolley for transferring heavy loads. These redesign strategies including the various MMH tasks and equipment will positively reduce the costs involved in compensation claims [5]. The laboratory experiments conducted on the trolley with five female and five male university students, two trolley loads 73 and 181 kg revealed that the initial forces were upward for the shoulder height and downward for knuckle height, whereas the least vertical forces were found to be at elbow height during pushing and pulling on the carpet surface. Here, the most direct horizontal push occurred at the elbow height after using three different handle heights [6].

Maximum acceptable forces tables were developed after conducting investigations on various types and frequencies of repetitive wrist motion including wrist flexion with a power grip, wrist flexion with a pinch grip and wrist extension with a power grip [7]. Force exertions and muscle activities were analysed while operating a manual-guided vehicle using two 3D load cells for measuring push-pull forces and a wireless EMG system to measure the eight muscle groups involved in cart pushing and pulling activities. It was found that the force direction and handle height variations are significant in most cases except for ending force and for the EMG of the anterior deltoid [8].

Peak push forces reached 200 N for females and 500 N for male subjects when they pushed at different heights for the loads ranging from 45 to 450 kg using an adjustable handle height with a load cell attached to a typical industrial cart [9]. Modified EMG-assisted biomechanical model was designed for evaluating lifting tasks to evaluate push-pull tasks, and person-specific biologically assisted models were developed to understand the spine loading during various push-pull conditions [10].

From the information given above, it is required to find the suitable handle height of the trolley based on the anthropometry of the local population. The work reported in this paper is an experimental study using different handle heights. Five university students were selected as subjects for conducting the experiments in the laboratory on a four-wheeled trolley, and the best suitable handle height is reported here. This study used heart rate monitor, surface electromyography (sEMG) and electro-goniometer for validating the results.

2 Materials and Methodology

2.1 Subjects

The age, height and weight of five male subjects are given in Table 1. They have participated in the laboratory experiments on the push-pull trolley. These subjects were healthy and reported to have no history of musculoskeletal disorders.

2.2 Trolley

A four-wheeled push-pull trolley was used to conduct the experiments as shown in Fig. 1. It has an adjustable handle height ranging from 900 to 1100 mm. The trolley was fitted with four polyurethane caster wheels of 100 mm diameter and

Table 1 Age, height and weight of the subjects

Subject number	Age (yrs)	Stature (mm)	Weight (kg)
1	19	1650	68
2	19	1730	59
3	18	1740	61
4	19	1750	85
5	19	1820	58

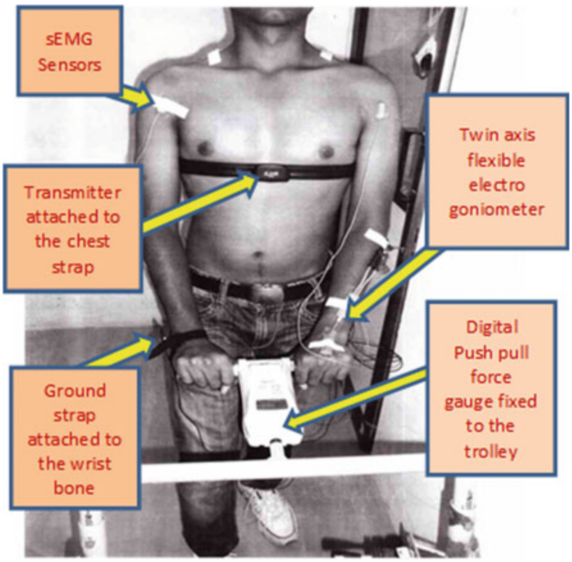

Fig. 1 sEMG and goniometer sensors attached to the subject; push-pull gauge attached to the trolley's horizontal handle bar

38 mm width. The front wheels were non-swivelling, but the two hind wheels near the handle side are 360° swivelling.

All the four wheels were oriented in the forward direction before the starting of each trial. The handle was firmly welded to the horizontal base structure at an angle of 110°. The push-pull force gauge was fixed to the trolley handle, whereas the EMG sensors, twin-axis flexible goniometer and polar heart monitor were fixed on the subject.

2.3 Force Measurement

A SHIMPO FGV-1000 HX push-pull gauge was used to measure the pushing force with an accuracy of ±0.2% full-scale measures up to 5000 N with a sample rate of 1000 times per second. It has a four-digit LCD display which is 180° reversible. The peak values can be viewed by selecting a peak button. An M10 hexagonal nut (internal threaded) was welded at the centre of the horizontal handle bar of the trolley to which the force gauge was fastened.

2.4 Heart Rate Measurement

Polar RS100 heart rate monitor which measures, displays and also records the heart rate was used for continuous recording during the trials. The elastic strap holds the transmitter (detects the heart rate) around the subject's chest. The wrist unit and chest strap were worn by every subject before the start of each trial. The wrist unit needs to be switched on just before the trial run and to be stopped when the subject reaches the finishing point of the 15,000 mm distance and the average heart rate for that trial to be recorded. This device works with an accuracy of ±0.5 s at 25 °C/77°F temperature and also an accuracy of ±1% or 1 bpm, during steady-state condition having a measurement range between 15 and 240 beats/minute (bpm).

2.5 Surface Electromyography (SEMG)

Precision bipolar EMG sensors SX230, Biometrics Ltd. London, UK, were used in this study. Due to the high quality of the SX230 electronics, with this little skin preparation, an ultra-high-quality signal was obtained without the use of conductive gels or creams. Highly flexible grade, 1.25-m-long ground reference R306 was used for grounding purpose. These sensors were placed over the bulk muscles, viz. flexor digitorum, deltoid and upper trapezius parallel to the longitudinal axis of the muscle fibres on each subject. The output was square-rooted for each average value. The

EMG signals were acquired real time and were saved in the micro SD of the DataLOG unit and were simultaneously transmitted via Bluetooth to the laptop.

2.6 Flexible Goniometer

The twin-axis flexible electro-goniometer SG65 was attached on the subject's dorsal surface. The telescopic block was fixed over the third metacarpal and the distal block over the midline of the forearm, with the wrist in the neutral position. This sensor can simultaneously measure the angles up to two planes of movement, viz. wrist flexion/extension and radial/ulnar deviation and works with an accuracy of $\pm 2^{\circ}$ measured over 90° from the neutral position and has better than $\pm 1^{\circ}$ repeatability.

2.7 DataLOG

The portable DataLOG MWX8 unit (small, light weighted and battery operated) was used to acquire experimental data. This device has a colour graphics LCD, joystick, micro-SD card interface, accommodates eight analogue lead wires and two digital wires simultaneously with a real-time wireless data transfer via Bluetooth linked to a laptop facilitating an automatic backup to the micro-SD card.

2.8 Biometrics Analysis Software v8.51

Biometrics software v8.51 was used to save and analyse the raw data that was acquired in real time through DataLOG. Prior to the starting of trials, the connectivity of the DataLOG and sensors were inspected for its readiness. The channels used were zeroed, and sensitivity was set for the goniometer and EMG. At the end of each trial, the acquired raw data was saved in the laptop computer for further analysis. The SX230 EMG pre-amplifier has the capacity in detecting low-level signals in a noisy environment. A high-pass filter was used to remove the DC offsets due to membrane potentials, and a low-pass filter was used to filter the unwanted frequencies above 450 Hz. The EMG raw data was filtered using an RMS filter for a better amplitude values, and using the vertical markers, the first four seconds of time was selected for measuring the muscle activity generated during the initial pushing in millivolts (mV).

2.9 Experimental Design

Design-Expert DX9 software was used to formulate the design of experiments. Central composite design (CCD) of RSM method was used to study the effect of several variables influencing the output responses by varying them simultaneously and carrying out a limited number of twenty experimental combinations as shown in Table 1. A three factorial with five-level CCD matrix was used to design the experiments to predict the effects of the handle height and load in the trolley on push force exerted by the subjects. Each trial was conducted thrice, and an average was taken for prediction.

2.10 Task and Procedure

Electrical activity generated within the muscles was measured using surface EMG electrodes placed on the left-arm flexor digitorum of the subjects. The experimental procedures were explained to the subjects, and written consent was also obtained. Three trials were performed for each set of the run (combination), and the average of the three trials was taken as the input data in the CCD matrix of the DOE software as given in Table 2.

Each subject has to push the trolley for three times at his own walking pace and at every handle height for fifteen metres. They were alerted by a human voice for each trial. The subject has to stop on his own when he reaches the finish line. All the initial pushing forces were recorded and saved in the system. An average of the three trials was calculated and analysed further in the DoE software.

3 Results and Discussions

3.1 Initial Pushing Force Analysis

Figure 2 shows the initial pushing force exerted by five male subjects at five different handle heights when the total weight of the trolley was 125 kg (weight of the empty trolley 50 kg and load in the trolley is 75 kg). The maximum force recorded by all the subjects was in the range from 110 to 125 N when the height of the handle was at 900 mm. The exerted pushing force gradually decreased as the height of the handle increased from 900 to 1100 mm. It was found that the pushing force exerted by all the subjects was ranging from 80 to 95 N at the handle height of 1100 mm resulting in a reduction of 25.5% of the effort required to push the trolley as the handle height has to be below the elbow height. It also shows that Subject 1 exerted a force of 118 N when compared to Subject 5 who exerted a force of 125 N at the handle height 900 mm. The force exertion gradually decreased as the handle height increase from 900 to 1100 mm.

Table 2 Design matrix coded factors with corresponding values

Run number	Design matrix coded factors			Subject height (mm)	Handle height (mm)	Trolley load (kg)
	Factor 1	Factor 2	Factor 3			
1	1	−1	1	1780	950	169
2	1	−1	−1	1780	950	106
3	−1	1	1	1690	1050	169
4	0	2	0	1740	1100	138
5	−1	1	−1	1690	1050	106
6	0	0	0	1740	1000	138
7	0	0	0	1740	1000	138
8	−1	−1	1	1690	950	169
9	0	0	0	1740	1000	138
10	1	1	−1	1780	1050	106
11	2	0	0	1820	1000	138
12	0	0	0	1740	1000	138
13	0	0	−2	1740	1000	75
14	−2	0	0	1650	1000	138
15	−1	−1	−1	1690	950	106
16	0	−2	0	1740	900	138
17	0	0	0	1740	1000	138
18	1	1	1	1780	1050	169
19	0	0	2	1740	1000	200
20	0	0	0	1740	1000	138

Fig. 2 Initial push force (*N*) on 100 mm wheel at load 125 kg

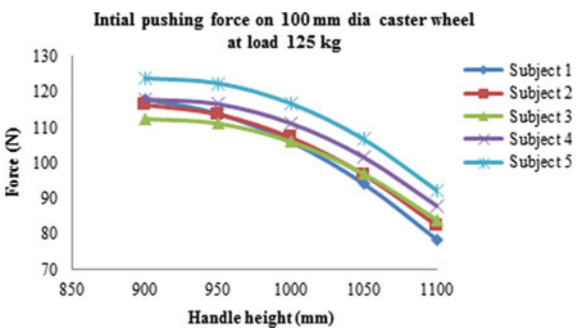

3.2 *Heart Rate Analysis*

Figure 3 shows the heart rate of all the five subjects experienced at five different handle heights when the total weight of the trolley was 125 kg. It can be observed that all the subjects experienced heart rate ranging between 70 and 83 beats per

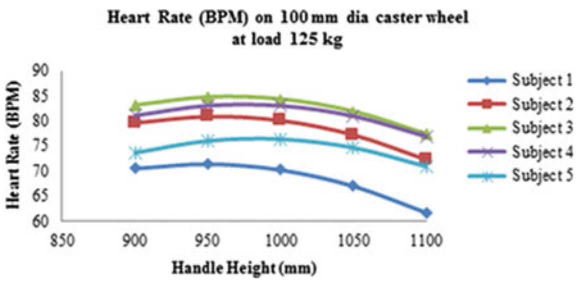

Fig. 3 Heart rate (BPM) during initial pushing of the trolley

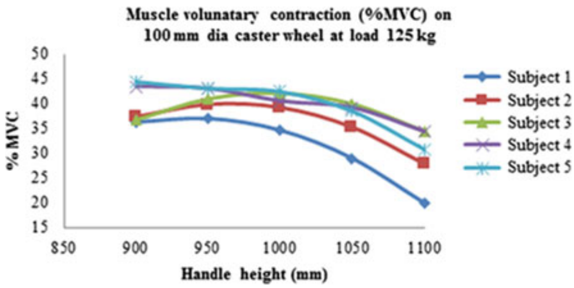

Fig. 4 %MVC for the left-arm flexor digitorum muscle during initial pushing of the trolley on the 100 mm wheel at load 125 kg

minute (bpm) when the handle height was set at 900 mm, and the heart rate ranges from 60 to 78 bpm when the handle height was set at 1100 mm. Subjects 1 and 5 (the shortest and the tallest) experience a lesser heart rate compared to Subjects 2, 3 and 4 (with medium heights).

3.3 EMG Analysis

Figure 4 shows the recorded muscle activity measured in microvolts during initial pushing for the five subjects at five different handle heights. It was found that the muscle force was higher for the Subjects 4 and 5 when the handle height is 900 mm. For Subjects 1 and 2, the maximum occurs at the handle height 950 mm, and for Subject 3, the maximum occurs at handle height 1000 mm. It was also found that the muscle activity for all the subjects decreased when the height of the handle is 1100 mm.

3.4 Goniometer Analysis

Figure 5 shows the wrist extension measured using the flexible goniometer for all the five subjects at five different handle heights. The wrist extensions for all the five

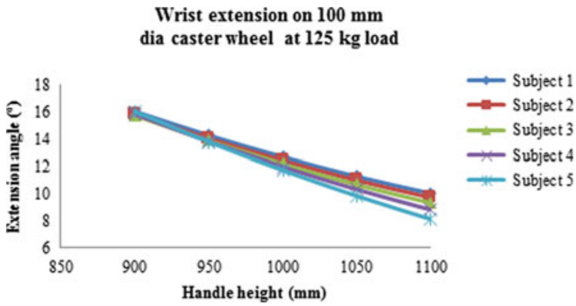

Fig. 5 Wrist extension (°) of left-arm wrist and forearm during initial pushing of the trolley on 100 mm wheel at load 125 kg

subjects were found to be about 16 degrees when the handle height was 900 mm. It was observed that the wrist extensions have gradually decreased (8–12) degrees with the increase of the handle height to 1100 mm. The optimal handle height should be in between 900 and 1150 mm. Generally, the handle height should be slightly below the elbow height. There should be at least 200 mm distance from the back edge of the trolley to the handle in order to provide a good room for normal walking [11, 12].

It can be observed that the results of push-pull gauge, heart rate analysis, sEMG analysis and goniometer analysis show that the handle height of 1100 mm tends to give reduced push forces, heart rate and muscle forces for the subjects while pushing a loaded trolley.

4 Conclusions

It was found that the usage of handle height of 1100 mm reduced 25–35% of the pushing efforts (including muscle force and heart rate) exerted by the subjects when compared to 900 mm handle height. It can be taken as the most comfortable height for the selected population whose anthropometric data provides the range of height from 1650 to 1820 mm. The forces exerted, the heart rate experienced, the muscle activity generated and the wrist extensions were considerably low at a handle height of 1100 mm when compared to the other handle heights.

References

1. Darcor and Ergoweb® (2001) The ergonomics of manual material handling-pushing and pulling tasks. Darcor Casters, 7 Staffordshire Place, Toronto, Ontario, Canada M8W 1T1, www.darcor.com Ergoweb, 93 West Main Street, P.O. Box 1089, Midway, Utah 84049 USA, www.ergoweb.com
2. Jansen Jorrit P, Marco JM, Hoozemans AJ, van der Beek MHW, Frings-Dresen MH (2002) Evaluation of ergonomic adjustments of catering carts to reduce external pushing forces. App Ergon 33:117–127

3. Snook SH, Ciriello VM (1991) The design of manual tasks: revised tables of maximum acceptable weights and forces. Ergonomics 34:1197–1213
4. Lee KS, Chaffin DB, Herrin GD, Waikar AM (1991) Effect of handle height on lower-backloading in cart pushing and pulling. Appl Ergon 22(2):117–123
5. Ciriello VM, Snook SH (1999) Survey of manual handling tasks. Int J Ind Ergon 23:149–156
6. Al-Eisawi KW, Kerk Congleton J, Amendola A, Jenkins OC, Gaines WG (1999) The effect of handle height and cart load in the initial forces in cart pushing and pulling. Ergonomics 42:1099–1113
7. Snook SH, Vaillancourt DR, Ciriello VM, Webster BS (1995) Psychophysical studies of repetitive wrist flexion and extension. Ergonomics 38(7):1488–1507
8. Lin C-L, Chen M-S, Wei Y-L, Wang M-JJ (2010) The evaluation of force exertions and muscle activities when operating a manual-guided vehicle. Appl Ergon 41:313–318
9. Resnick ML, Chaffin DB (1995) An ergonomic evaluation of handle height and load in maximal and submaximal cart pushing. Appl Ergon 26(3):173–178
10. Theado EW, Knapik GG, Marras WS (2007) Modification of an EMG-assisted biomechanical model for pushing and pulling. Int J Ind Ergon 37:825–831
11. Wilson Kumar M, Vijay SJ, Vasudev KL, Darius Gnanaraj S (2017) Reduction of discomfort in pushing an industrial trolley using ergonomics. IOP Conf Ser Mater Sci Eng 263:062042
12. Masepogu WK, Sahu M, Vijay SJ (2020) Experimental investigations on the effect of wheel size on an industrial trolley. In: Advances in materials and manufacturing engineering. Lecture notes in mechanical engineering, Springer, pp 557–564

Mathematical Analysis of Stiffness of Orthotropic Beam with Hollow Circular and Rectangular Cross-sections

Michael C. Agarana, Esther T. Akinlabi, and Anuoluwapo M. Olanrewaju

Abstract Stiffness and strength of mechanical materials have to be thoroughly investigated to avoid functional and physical failures. This study investigates, analytically, the stiffness of wood beam, which is an example of orthotropic material, with different cross-sectional areas. The moment of inertia for each type of wood, considered, was analysed. The axial stiffness and bending stiffness were also computed for different cross-sectional areas. Comparisons were made and results are consistent with the ones in the literature. Specifically, it was observed that the cross-sectional areas of wood have a lot of influence on its mechanical properties. The axial stiffness, bending stiffness, shear stresses and moment of inertia of the orthotropic solid materials, considered, depend on their cross-sectional areas, to a large extent.

Keywords Stiffness · Orthotropic beam · Mathematical analysis · Hollow cross-sections

1 Introduction

In material science and solid mechanics, orthotropic materials have material properties that differ along three mutually-orthogonal twofold axes of rotational symmetry. They are a subset of anisotropic materials because their properties change when

M. C. Agarana (✉) · A. M. Olanrewaju
Department of Mathematics, Covenant University, Ota, Ogun, Nigeria
e-mail: michael.agarana@covenantuniversity.edu.ng

A. M. Olanrewaju
e-mail: anu.olanrewaju@covenantuiversity.edu.ng

M. C. Agarana · E. T. Akinlabi
Department of Mechanical Engineering Science, University of Johannesburg, Auckland Park Kingsway Campus, P.O. Box 524, Johannesburg 2006, South Africa
e-mail: etakinlabi@gmail.com

E. T. Akinlabi
Department of Mechanical Engineering, Covenant University, Ota, Ogun, Nigeria

E. T. Akinlabi et al. (eds.), *Trends in Mechanical and Biomedical Design*,
Lecture Notes in Mechanical Engineering,
https://doi.org/10.1007/978-981-15-4488-0_14

measured from different directions. So every orthotropic material is anisotropic. A familiar example of an orthotropic material is wood [1, 2].

Stiffness is the ability of the material to resist deformation or deflection (functional failure). Understanding the roles that stiffness play is essential to the decision process when choosing foundational support to minimise risk [2, 3]. Stiffness is different from strength. Strength is a measure of the anxiety that can be connected to a material before it for all time disfigures (yield quality) or breaks (rigidity). In the event that the forced stress is not as much as the yield strength, the material comes back to its unique shape when the stress is expelled. On the off chance that the connected anxiety surpasses the yield quality, plastic or perpetual twisting happens, and the material can never again come back to its unique shape once the load is evacuated [3–5].

A polygon is a two-dimensional shape with no less than three sides that are straight and create interior angles where they meet. Polygons can be regular or irregular. A regular polygon is a polygon with all sides of equivalent length and every interior angle of equivalent measure. An irregular polygon, on the other hand, is a polygon that is not regular. That is, an irregular polygon is a polygon that does not have all sides of equivalent lengths and all interior angles equal. Polygons can have any number of sides insofar as there are at least three of them. A lot of n-sided polygons have special names [5–8]. A polygon with three sides is a triangle. A polygon with four sides is known as a quadrilateral and one with five sides is a pentagon. A polygon with six sides is a hexagon, one with seven sides is known as a heptagon, and a polygon with eight sides is an octagon, and so on [8, 9].

The difference between bending moment and moment of inertial is as follows: the reaction induced in a structural element when an external force or moment is applied to the element causing the element to bend is referred to as the bending moment, while moment of inertia is the capacity of a cross-section to resist bending [9–12].

Rigidity of an object, otherwise known as bending stiffness, is the measurement of the extent to which the member resists bending deformation in response to an applied load. This paper analyses, mathematically, the stiffness and strength of wood, an orthotropic material, with a regular diagonal cross-sectional area of different number of vertices.

2 Formulation of Problem

$$E \equiv \sigma(\varepsilon)\varepsilon = F/A\Delta L/L_0 = FL_0A\Delta LE \equiv \frac{\sigma(\varepsilon)}{\varepsilon} = \frac{F/A}{\Delta L/L_0} = \frac{FL_0}{A\Delta L}$$

Strain can be expressed as

$$\xi = \Delta L/L \tag{1}$$

where

ξ strain (m/m) (in/in)
ΔL elongation or compression (offset) of the object (m) (in)
L length of the object (m) (in).

Stress can be expressed as

$$\sigma(\xi) = F/A \tag{2}$$

where

$\sigma(\xi)$ stress (N/m^2, lb/in^2, psi)
F force (N, lb)
A area of object (m^2, in^2).

Young's modulus (E) can be expressed as

E stress/strain.

$$E = \frac{\sigma(\xi)}{\xi} = \frac{F}{A}.\frac{L_0}{\Delta L} = \frac{FL_0}{A\Delta L} \tag{3}$$

where

$\sigma(\xi)$ is the tensile stress;
ξ is the engineering extentional strain;
E is the Young's modulus (modulus of elasticity);
F is the force exerted on an object under tension;
A is the actual cross-sectional area, which equals the area of the cross-section perpendicular to the applied force;
ΔL is the amount by which the length of the object changes (ΔL is positive if the material is stretched and negative when the material is compressed);
L_0 is the original length of the object.

The Young's modulus of a material can be used to calculate the force it exerts under specific strain

$$F = EA\Delta LL_0 \quad F = \frac{EA\Delta L}{L_0}$$

F is the force exerted by the material when contracted or stretched by ΔL. The force F is given as

$$F = \frac{EA\Delta L}{L_0} \tag{4}$$

The axial stiffness is given as

$$k = \frac{AE}{L} \tag{5}$$

The bending stiffness is given as

$$K = \frac{F}{w} \tag{6}$$

where

F is the applied force
w is the deflection.

Substituting Eq. (6) into (8) gives

$$K = \frac{\frac{EA\Delta L}{L_0}}{w} = \frac{EA\Delta L}{wL_0} \tag{7}$$

The moment of inertia of the wood beam, along the x-axis, with different cross-sections are given as follows:

$$I_{xc} = \frac{\pi (d)^4}{64} \tag{8}$$

$$I_{xr} = \frac{1}{2}bh^3 \tag{9}$$

$$I_{xch} = \frac{\pi}{64}\left[(d_2)^4 - (d_1)^4\right] \tag{10}$$

$$I_{xrh} = \frac{1}{12}BH^3 - \frac{1}{12}bh^3 \tag{11}$$

where

d	is thediameter of the circular cross-section
b	is the horizontal distance of the cross-section
h	is the height of the cross-section
d_2	is the diameter of the outer circle of the cross-section
d_1	is the diameter of the inner circle of the cross-section
B and H	are the horizontal distance and height of the outer rectangle of the cross-section
B and h	are the horizontal distance and height of the inner rectangle of the cross-section
I_{xc}	is the moment of inertia of wood beam with a circular cross-section.
I_{xr}	is the moment of inertia of wood beam with a rectangular cross-section.
I_{xch}	is the moment of inertia of wood beam with a circular hollow cross-section.
I_{xrh}	moment of inertia of wood beam with a rectangular hollow cross-section

3 Numerical Example

Considering uniform blocks of wood beam with the following cross-sectional areas: circular, rectangular, hollow circular and hollow rectangular, stiffness of such structures of wood is calculated and compared. Different values length (L), cross-sectional area (A) and value of Young's modulus of wood, were used to carry out the numerical analysis of the stiffness of block of wood beam with different cross-sectional areas and lengths. For brevity, only the cases of Oak wood beam with four different cross-sections were considered in this paper.

The moment of inertia of the wood hollow circular beam is obtained using Eq. (10), converting inches to meters, as follows:

$$I_{xch} = \frac{\pi}{64}\left[(d_2)^4 - (d_1)^4\right] = \approx 0.0000008549\,\mathrm{kg\,m^2} \tag{12}$$

The axial stiffness of the wood hollow circular beam is obtained by adopting Eq. (5) and taken the Young's modulus of Oak wood beam as 12,300 MPa:

$$\begin{aligned} k &= \frac{A_2E - A_1E}{L} \\ &= \pi r_2^2\frac{E}{L} - \pi r_1^2\frac{E}{L} \\ &= \frac{22}{7}\frac{E}{L}\left[r_2^2 - r_1^2\right] \\ &= \frac{22}{7}\left(\frac{12{,}300}{40 \times 0.03}\right)\left[\left(\frac{5.0}{2} \times 0.03\right)^2 - \left(\frac{3.6}{2} \times 0.03\right)^2\right] \\ &\approx 87.27\,\mathrm{N/m} \end{aligned} \tag{13}$$

The bending stiffness of the wood hollow circular beam is obtained by adopting Eq. (6) and taken the Young's modulus of Oak wood beam as 12,300 MPa:

$$K = \frac{EA_2\Delta L}{wL_0} - \frac{EA_1\Delta L}{wL_0} = \frac{\Delta LE}{wL_0}(A_2 - A_1) \tag{14}$$

The deflection w is given as

$$w = \frac{L^3F}{3EI_x} \tag{15}$$

Substituting Eq. (4) into (15) gives

$$w = \frac{L^3\frac{EA\Delta L}{L_0}}{3EI_x} \tag{16}$$

Substituting Eq. (16) into Eq. (14) and simplifying gives

$$K = \frac{3EI_x}{L^3} \tag{17}$$

Substituting the value of the parameters gives

$$\begin{aligned} K &= \frac{3(12{,}300)(0.0000008549)}{(40 \times 0.03)^3} \\ &\approx 0.02\,\mathrm{Nm}^2 \end{aligned} \tag{18}$$

The moment of inertia of the wood hollow rectangular beam cross-section is obtained using Eq. (11):

$$\begin{aligned} I_{xrh} &= \frac{1}{12}BH^3 - \frac{1}{12}bh^3 \\ &= \frac{1}{12}\left[6(0.0254).\{12(0.0254)\}^3\right] - \frac{1}{12}\left[4(0.0254).\{10(0.0254)\}^3\right] \\ &\approx 0.0002222\,\mathrm{kg\,m}^2 \end{aligned} \tag{19}$$

The axial stiffness of the wood hollow rectangular beam, whose cross-section can be obtained by adopting Eq. (5) and taken the Young's modulus of Oak wood beam as 12,300 MPa:

The area of the outer rectangle A_2 is

$$\begin{aligned} &12(0.0254) \times 6(0.0254) \\ &= 1.83\,\mathrm{m}^2 \end{aligned} \tag{20}$$

The area of the inner rectangle A_1 is

$$\begin{aligned} &10(0.0254) \times 4(0.0254) \\ &= 1.02\,\mathrm{m}^2 \end{aligned} \tag{21}$$

Therefore,

$$\begin{aligned} k &= \frac{A_2E - A_1E}{L} \\ &= \frac{E(1.83 - 1.02)}{0.03(40)} \\ &= \frac{12{,}300(0.81)}{1.2} \\ &\approx 8.3\,\mathrm{N/m} \end{aligned} \tag{22}$$

The bending stiffness of the wood hollow rectangular beam with length 40 inches, whose cross-section can be obtained by adopting Eq. (17) and taken the Young's modulus of Oak wood beam as 12,300 MPa:

$$\begin{aligned} K &= \frac{3EI_x}{L^3} \\ &= \frac{3(12{,}300)(0.0002222)}{(40 \times 0.03)^3} \\ &\approx 4.74\,\mathrm{Nm}^2 \end{aligned} \tag{23}$$

Now, in order to compare with the hollow solid shapes, the moment of inertia, axial stiffness and bending stiffness of both wood beam with a circular cross-section and wood beam with rectangular cross-section are considered in this section. The moment of inertia of the wood circular beam, assuming the hollow is not there, is obtained using Eq. (8), and converting inches to meters, as follows:

$$\begin{aligned} I_{xc} &= \frac{\pi(d)^4}{64} \\ &= \frac{22}{7}\frac{(5.0 \times 0.03)^4}{64} \\ &\approx 0.00002486\,\mathrm{kg\,m}^2 \end{aligned} \tag{24}$$

The moment of inertia of the wood rectangular beam, assuming the hollow is not there, is obtained using Eq. (9), and converting inches to meters, as follows:

$$\begin{aligned} I_{xr} &= \frac{1}{2}bh^3 \\ &= \frac{1}{2}(6 \times 0.03)(12 \times 0.03)^3 \\ &\approx 0.004199\,\mathrm{kg\,m}^2 \end{aligned} \tag{25}$$

The axial stiffness of the wood circular and wood rectangular beam, assuming there is no hollow, are obtained by adopting Eq. (5) and taken the Young's modulus of Oak wood beam as 12,300 MPa:

For circular cross-section

$$\begin{aligned} k &= \frac{AE}{L} \\ &= \frac{\pi r^2(12{,}300)}{(40 \times 0.03)} \\ &= \frac{22}{7}\left(\frac{5}{2}\right)^2\left(\frac{12{,}300}{1.2}\right) \\ &\approx 201339.29\,\mathrm{N/m} \end{aligned} \tag{26}$$

For rectangular cross-section

$$
\begin{aligned}
k &= \frac{AE}{L} \\
&= \frac{(12 \times 6 \times 0.03)(12{,}300)}{(40 \times 0.03)} \\
&\approx 22.14\,\text{N/m}
\end{aligned}
\tag{27}
$$

The bending stiffness of the wood circular and rectangular beam with length 40 inches, whose cross-section, assuming the hollows are not there, can be obtained by adopting Eq. (20) and taken the Young's modulus of Oak wood beam as 12,300 MPa:

For Circular cross-section

$$
\begin{aligned}
K &= \frac{3EI_x}{L^3} \\
&= \frac{3(12{,}300)(0.00002486)}{(40 \times 0.03)^3} \\
&\approx 0.53\,\text{Nm}^2
\end{aligned}
\tag{28}
$$

For Rectangular cross-section

$$
\begin{aligned}
K &= \frac{3EI_x}{L^3} \\
&= \frac{3(12{,}300)(0.004199)}{(40 \times 0.03)^3} \\
&\approx 89.67\,\text{Nm}^2
\end{aligned}
\tag{29}
$$

4 Results and Discussion

From the analysis result values, depicted in Table 1, it can be seen that the value of the

Table 1 The stiffness and moment of inertia for Oak wood beam with different cross-sections

S/N	Cross-section	I_{xc} (kg m^2)	I_{xr} (kg m^2)	I_{xch} (kg m^2)	I_{xrh} (kg m^2)	k (N/m)	K (Nm^2)
1	Circular hollow	–	–	0.0000008549	–	87.27	0.02
2	Rectangular hollow	–	–	–	0.0002222	8.3	4.74
3	Circular	0.00002486	–	–	–	201,339.29	0.53
4	Rectangular	–	0.004199	–	–	22.14	89.67

moment of inertia for both the rectangular cross-section (I_{xr}) and rectangular hollow cross-section (I_{xrh}) are greater than that of the circular cross-section (I_{xc}) and circular hollow cross-section (I_{xch}). This implies that the wood beam with a rectangular cross-section can resist rotational force than the wood beam with a circular cross-section. This also suggests that the stress in the wood circular beam is less than that in the wood rectangular beam, going by the formula for stress of a beam: The axial stiffness (k) value for both circular and circular hollow cross-sections is higher than that of rectangular and rectangular hollow cross-sections. This implies that more force is required to produce unit axial deformation in the wood circular beam than in the wood rectangular beam. However, the value of the bending stiffness (K) for both rectangular cross-section and rectangular hollow cross-section is higher than that of circular and circular hollow cross-sections. This implies that the former is more rigid than the later. It shows that the resistance of a member against bending deformation is higher in the wood rectangular beam than in wood circular beam. It is also observed that the moment of inertia of all the cross-sections considered in this paper is less than one ($I_{xch} < I_{xrh} < I_{xc} < I_{xr} < 1$). The wood beams without hollow cross-section seem to resist rotation than the ones with hollow cross-section.

5 Conclusion

This study set out to analyse mathematically the stiffness of orthotropic beam of different cross-sections. Wood, an example of orthotropic material, was considered. Also, Oak, a type of wood, with Young's modulus of 12,300 MPa, was considered. The moment of inertia, axial stiffness and bending stiffness for an Oak wood beam with different cross-sections were analysed. The special cross-sections considered are circular cross-section, rectangular cross-section, hollow circular cross-section and hollow rectangular cross-section. This study revealed that the type of cross-section of an Oak wood beam affects its stiffness. It was noticed among the types of cross-sections considered, that an Oak wood beam with rectangular cross-section has the highest bending stiffness, and the one with hollow circular cross-section has the least bending moment. Also, the highest moment of inertia goes to the Oak wood beam with rectangular cross-section, and the lowest goes to the beam with the hollow circular cross-section. Therefore this would help a structural engineer to make an informed decision on the type of wood beam to use in construction, as regards the cross-section, in order to minimise the risk of bending due to eternal forces.

Acknowledgements The authors hereby acknowledge the support of Covenant University and the University of Johannesburg towards the successful completion of this study.

References

1. Agarana MC, Ede AN (2016) Free vibration analysis of elastic orthotropic rectangular inclined damped highway supported by Pasternak Foundation under moving aerodynamic automobile. In: Proceedings of the world congress on engineering 2016 June 29–July 1, London, UK, pp 9708–981
2. Agarana MC, Agboola OO (2015) Dynamic analysis of damped driven pendulum using laplace transform method. Int J Math 26(3). ISSN 0974-570X (online) 0974-5718(Print)
3. Burnett C (2016) Mental strength and stiffness: what's the difference? ThermoFisher Scientific. https://www.thermofisher.com/blog/metals/metal-strength-and-stiffness-whats-the-difference/
4. Agarana MC, Gbadeyan JA, Ajayi OO (2016) Dynamic response of inclined isotropic elastic damped rectangular Mindlin Plate resting on Pasternak Foundation under a moving load. In: Proceedings of the international multi conference of engineers and computer scientists, March 16–18, 2016, Hong Kong, pp 713–716
5. Agarana MC, Gbadeyan JA (2015) Finite difference dynamic analysis of railway bridges supported by Pasternak foundation under uniform partially distributed moving Railway vehicle. In: Proceedings of the world congress on engineering and computer science 2015, vol II WCECS 2015, October 21–23, 2015, San Francisco, USA
6. Agarana MC, Ede AN (2016) Free Vibration analysis of elastic orthotropic rectangular inclined damped highway supported by Pasternak Foundation under moving aerodynamic automobile. In: Proceedings of the world congress on engineering 2016 June 29–July 1, London, UK, pp 978–981
7. https://en.wikipedia.org/wiki/Young%27s_modulus
8. https://physics.stackexchange.com/questions/153008/what-is-difference-between-homogeneous-and-isotropic-material
9. http://www.engineeringtoolbox.com/young-modulus-d_417.html
10. https://en.wikipedia.org/wiki/Regular_polygon
11. https://www.mathsisfun.com/geometry/regular-polygons.html
12. Friswell MI, Adhikan S, Lei, Y (2007) Vibration analysis of Beams with non-local foundations using the finite element method. Int J Numer Methods Eng 71:1365–1386

Analytical Investigation of the Stiffness of Homogenous Isotropic Mechanical Materials with Different Cross-sections

Michael C. Agarana, Esther T. Akinlabi, and Okwudili S. Ogbonna

Abstract In order to achieve the required high level of mechanical material components as regards sustainability and safety, the stiffness of such materials has to be thoroughly investigated to avoid failure. This study investigates, analytically, the stiffness of some mechanical materials with different cross-sectional areas, whose mechanical properties are homogeneous and isotropic. The exerted force for steel material solids with different cross-sections was investigated. Comparisons were made and results are consistent with the ones in literature. A computer software, Maple, was used to plot the three-dimensional graphs of the relationship between the parameters. Specifically, it was observed that the steel hollow rectangular beam cross-section has a high axial stiffness compared to that of steel hollow circular beam cross-section. Also, the moment of inertia of the steel beams, considered, depend on their cross-sectional areas.

Keywords Stiffness · Homogeneous isotropic materials · Analytical investigation · Cross sections

M. C. Agarana (✉)
Department of Mathematics, Covenant University, Ota, Ogun, Nigeria
e-mail: michael.agarana@covenantuniversity.edu.ng

M. C. Agarana · E. T. Akinlabi · O. S. Ogbonna
Department of Mechanical Engineering Science, University of Johannesburg, Auckland Park Kingsway Campus, P.O. Box 524, Johannesburg 2006, South Africa
e-mail: etakinlabi@gmail.com

O. S. Ogbonna
e-mail: sokwudili@gmail.com

E. T. Akinlabi
Department of Mechanical Engineering, Covenant University, Ota, Ogun, Nigeria

E. T. Akinlabi et al. (eds.), *Trends in Mechanical and Biomedical Design*,
Lecture Notes in Mechanical Engineering,
https://doi.org/10.1007/978-981-15-4488-0_15

1 Introduction

Isotropic materials are materials with indistinguishable estimations of a property every direction. Glass and metals are good examples of isotropic materials [1]. A homogeneous material, on the other hand, is a material with similar properties at each point; it is uniform without inconsistencies. Materials can be both homogeneous and isotropic, in terms of properties; however, these two have diverse implications as regards their property of body and heading of the position [2]. The distinction between the two is that homogeneous material has a similar group of properties at each place, but an isotropic material has a similar-looking in the majority of the bearings at various purposes of the property. For example, steel demonstrates isotropic behaviour, although its microscopic structure is non-homogeneous [3–5].

Strain is "deformation of a solid due to stress"—change in dimension divided by the original value of the dimension. Stress is force per unit area. There are different types of stress [5–9]: T*ensile* stress, Compressive stress and Shearing stress. Stiffness is the rigidity of an object. Young's modulus, otherwise called the flexible modulus, is a measure of the solidness of strong material. It is a mechanical property of direct flexible strong materials. [10, 11]. The measure of the stiffness of solid material is known as elastic modulus or Young's modulus. A material with a very high Young's modulus can be approximated as rigid. Young's modulus is the ratio of stress to strain [12, 13]. In beams, the area moment of inertia can be used to predict deflection. In this study, the stiffness of such block of steel in the form of beam with circular hollow and rectangular hollow cross-sections was investigated. In particular, the axial stiffness, Bending stiffness and moment of inertial, for beam with circular hollow and rectangular hollow cross-sectional areas, were analyzed. Also, the second moment of area of these solids was investigated.

2 Formulation of Problem

The force F, exerted by the material when displaced by ΔL can be written as follows:

$$F = \frac{EA\Delta L}{L_0} \tag{1}$$

This is achieved by using Young's modulus.
The axial stiffness is given as

$$k = \frac{AE}{L} \tag{2}$$

where

A the cross-sectional area,

E Young's modulus,
L the length of the element.

The bending stiffness is given as:

$$K = \frac{F}{w} \tag{3}$$

where

F the applied force,
w the deflection.

Substituting Eqs. (1) into (3) gives

$$K = \frac{EA\Delta L}{\frac{L_0}{w}} = \frac{EA\Delta L}{wL_0} \tag{4}$$

3 Numerical Example

The moment of inertia of the steel hollow circular beam is obtained, converting inches to meters, as follows:

$$I_x = \frac{\pi}{64}\left[(d_2)^4 - (d_1)^4\right] \approx 0.0000008549\,\text{kgm}^2 \tag{5}$$

where

$d_2 = 0.20055$ (the longer diameter)
$d_1 = 0.20000$ (the shorter diameter).

The axial stiffness of the steel hollow circular beam is obtained by adopting Eq. (5) and taken the young's modulus of the beam as 209 Mpa:

$$k = \frac{A_2E - A_1E}{L} = 0.98\left[\frac{22}{7}\left(\frac{0.127}{2}\right)^2 E - \frac{22}{7}\left(\frac{0.091}{2}\right)^2 E\right] \approx 1.27\,\text{N/m} \tag{6}$$

The bending stiffness of the steel hollow circular beam is obtained by adopting Eq. (6) as follows:

$$K = \frac{EA_2\Delta L}{wL_0} - \frac{EA_1\Delta L}{wL_0} = \frac{\Delta LE}{wL_0}(A_2 - A_1) \tag{7}$$

Substituting the deflection, w, and some manipulation gives:

$$K = \frac{3EI_x}{L^3} \tag{8}$$

Substituting the value of the parameters gives:

$$K = \frac{3(209)(0.000001)}{1.016^3} \approx 0.0006\,\mathrm{Nm}^2 \tag{9}$$

The moment of inertia of the steel hollow rectanguar beam cross-section is obtained as follows:

$$I_x = \frac{1}{12}BH^3 - \frac{1}{12}bh^3 \approx 0.0002222\,\mathrm{kg\,m}^2 \tag{10}$$

where

B the breadth of the outer part of the hollow rectangle
B the breadth of the inner part of the hollow rectangle
H the height of the outer part of the hollow rectangle
h the height of the inner part of the hollow rectangle.

The axial stiffness of the steel hollow rectangle beam was calculated to obtain:

$$k = \frac{A_2E - A_1E}{L} = \frac{E(1.83 - 1.02)}{0.0254(40)} \approx 166.62\,\mathrm{N/m} \tag{11}$$

The bending stiffness of the steel hollow rectangular beam was obtained:

$$K = \frac{3EI_x}{L^3} = \frac{3(209)(0.0002222)}{1.016^3} \approx 0.13284\,\mathrm{Nm}^2 \tag{12}$$

4 Results and Discussion

From the analysis, it can be gathered that the value of the moment of inertia and the bending stiffness of both steel hollow circular beam and steel hollow rectangular beam, under consideration in this paper, is less than one. However, the moment of inertia of the steel hollow rectangular beam is greater than that of steel hollow circular beam. This suggests that the stress in the steel hollow circular beam is less than that in the steel hollow rectangular beam, going by the formula for stress of a beam:

$$\partial = \frac{M_Y}{I} \tag{13}$$

where σ is the stress, M is the internal moment, y is the distance from the neutral axis and I is the area moment of inertia. Both the axial stiffness and bending stiffness of the steel hollow rectangular beam are greater than that of steel hollow circular beam. This implies that the former is more rigid than the later. It shows that the resistance of a member against bending deformation in higher in the steel hollow rectangular beam than in steel hollow circular beam. Also, more force is required to produce unit axial deformation in of steel rectangular circular beam than in of steel hollow circular beam. From Fig. 3, the moment of inertia of the steel hollow circular beam increases as the inner diameter decreases and outer diameters increase. This implies the smaller the hollow in the beam the higher the moment of inertia which suggests less stress on the beam (Figs. 1, 2, 4, 5 and 6).

Fig. 1 Show 3D plotting of the relationship between *Ix*, *d*2 and *d*1 for the circular hollow beam

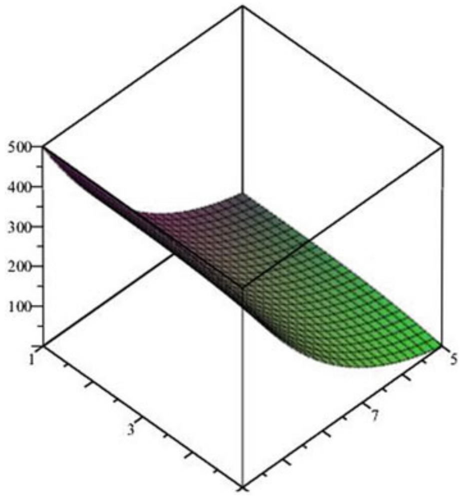

Fig. 2 Show 3D plotting of the relationship between *k*, *A* and *L* for the circular hollow beam

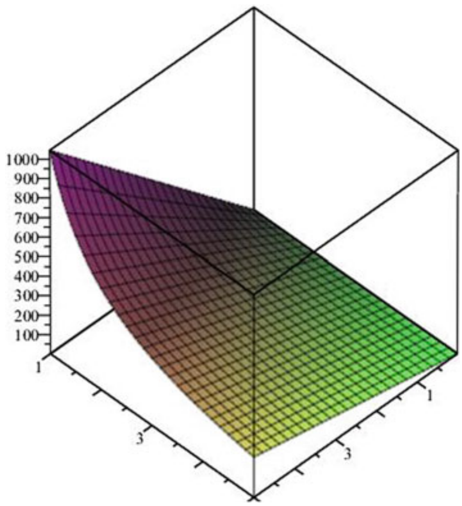

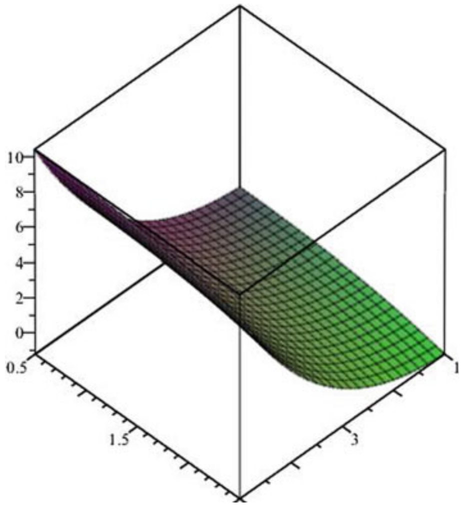

Fig. 3 Showing 3D plotting of the relationship between *K*, *Ix* and *L* for the circular hollow beam

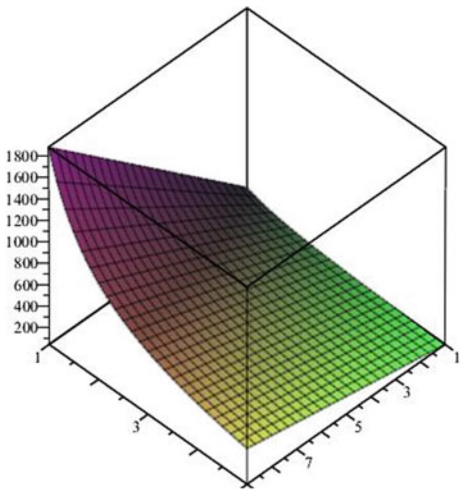

Fig. 4 Shoing 3D plotting of the relationship between I_x, *H*, and *h* for the rectanglar hollow beam

5 Conclusion

The study set out to investigate analytically the stiffness of homogenous isotropic mechanical materials with different cross-sections. Steel circular hollow beam and steel rectangular hollow beam were used as case studies. The moment of inertia, the strain, the stress, the stiffness, the deflection, the Young modulus and the relationship between these were investigated and analyzed mathematically. It was observed that the steel hollow rectangular beam is more rigid than the steel hollow circular beam,

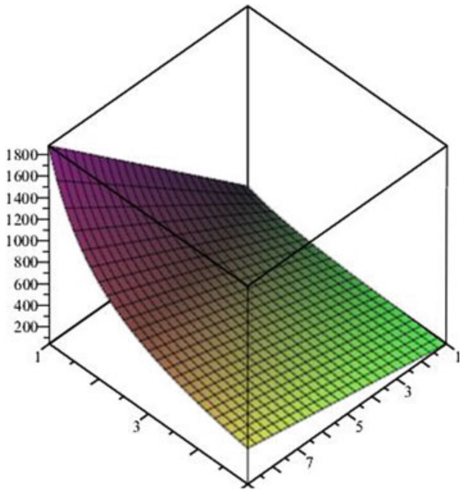

Fig. 5 Showing 3D plotting of the relationship between k, A, and I for the rectangular hollow beam

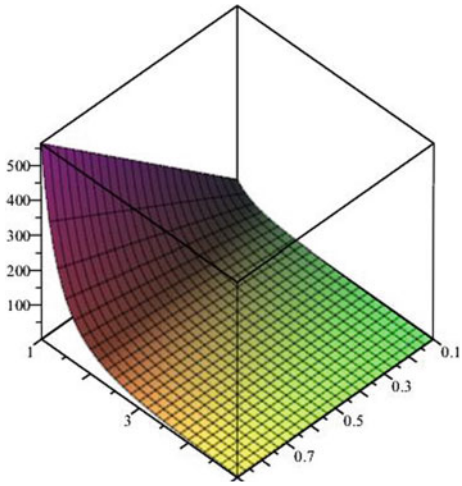

Fig. 6 Showing 3D plotting of the relationship between K, I_x, and L for the rectangular hollow beam

going by the numerical values used to calculate their axial stiffness and bending stiffness.

Acknowledgments The authors acknowledge the supports received from Covenant University and the University of Johannesburg, where the first author is presently a post-doctoral fellow.

References

1. Agarana MC, Gbadeyan JA, Ajayi OO (2016) Dynamic response of inclined isotropic elastic damped rectangular mindlin plate resting on Pasternak foundation under a moving load. In: Proceedings of the international multi conference of engineers and computer scientists 2016, Hong Kong, pp 713–716
2. Gbadeyan JA, Dada MS (2006) Dynamic response of a mindlin elastic rectangular plate under a distributed moving mass. Int J Mech Sci 48:323–340
3. Zhang T, Zheng G (2010). Vibration analysis of an elastic beam subjected to a moving beam with flexible connections. Am Assoc Civil Eng 136(1):120–130
4. Agarana MC, Gbadeyan JA (2015) Finite difference dynamic analysis of railway bridges supported by Pasternak foundation under uniform partially distributed moving Railway vehicle. In: Proceedings of the world congress on engineering and computer science, vol II, October 21–23, 2015, San Francisco, USA
5. Agarana MC, Ede AN (2016) Free vibration analysis of elastic orthotropic rectangular inclined damped highway supported by Pasternak Foundation under moving aerodynamic automobile. In: Proceedings of the world congress on engineering 2016 June 29–July 1, London, UK, pp 978–981
6. Agarana MC, Gbadeyan JA, Emetere M (2016) On response of elastic isotropic damped shear highway bridge supported by sub-grade to uniform partially distributed moving vehicle. Int J Appl Eng Res 11(1):244–258
7. Kumar Y (2013) Differential transform method to study free transverse vibration of monoclinic rectangular plates resting on Winkler foundation. Appl Comput Mech 7:145–154
8. Rasian KR, Zain F, Sheer A (2013) Differential transform method for solving non-linear systems of partial differential equations. Int J Phys Sci 8(38):1880–1884
9. Agarana MC (2010) Torsional rigidity of beams of given areas with different cross sections. J Math Assoc Nigeria (Abacus) 37(2):117–123
10. Li R, Zhang Y, Tian B, Liu Y (2009) On the finite integral transform method for exact bending solutions of fully clamped orthotropic rectangular thin plates. Appl Math Lett 22(12):1821–1827
11. Agarana MC, Agboola OO (2015) Analysis of torsional rigidity of circular beams with different engineering materials subjected to St. Venant Torsion. IMPACT: Int J Res Eng Technol 3(2):33–46
12. Agarana MC, Agboola OO (2015) Dynamic analysis of damped driven pendulum using laplace transform method. Int J Math Comput 26(3):99–109
13. Agarana MC, Iyase SA (2015) Analysis of Hermite's equation governing the motion of damped pendulum with small displacement. Int J Phys Sci 10(12):364–370

Fatigue and Fracture Analysis

Fatigue Analysis of Vocal-Folds Using Discretized Aeroelastic Model

Veda Samhitha Kanduri, James Emilian, and Venkatramani Jagadish

Abstract Voice disorders are common physiological challenges that arise largely due to vocal fatigue, i.e. fatigue of vocal folds and associated phonatory structures. Since the incurrence of fatigue in vocal folds directly depends on the qualitative and quantitative nature of the dynamical signature of vocal fold oscillations, the hitherto literature has resorted to estimating the time histories and stress histories of the vocal fold oscillations. Often, vocal fold dynamics are rid with different types of complexities. Therefore, the literature often resorts to the use of a mathematical model that closely resembles the human phonatory system. Modelling the mechanism of vocal folds as a two-mass model with 2DOF provides a reasonably accurate depiction of the same. In order to obtain the real-time histories of the vocal fold vibrations, a continuously changing parameter called phonation threshold pressure (PTP) is defined so as to describe the extent of accumulated fatigue. PTP can be determined numerically for a given set of physical and physiological parameters of the system. Since the vocal fold vibrations are of varying amplitude as time progresses, it is necessary to use a standard counting algorithm for fatigue analysis, like the Rainflow-Counting algorithm. Then, the incurred damage is computed with the help of a S-N curve and the Miner's rule. With the time span of phonation as the control parameter and PTP as a continuously changing parameter, the responses of the system are systematically obtained. Later, comparisons on the fatigue damage are made.

Keywords Vocal fatigue · PTP · Rainflow-counting algorithm (RFC)

1 Introduction

Voice production involves the self-sustained, flow-induced oscillations of the vocal folds. Vocal folds are a layered structure of three different tissues, namely, epithelium, lamina propria and thyroarytenoid muscles. Prolonged phonation can damage these layers due to mechanical fatigue induced. Vocal fatigue is the root cause of several

V. S. Kanduri · J. Emilian · V. Jagadish (✉)
Department of Mechanical Engineering, Shiv Nadar University, Greater Noida, India
e-mail: j.venkatramani@snu.edu.in

E. T. Akinlabi et al. (eds.), *Trends in Mechanical and Biomedical Design*,
Lecture Notes in Mechanical Engineering,
https://doi.org/10.1007/978-981-15-4488-0_16

conditions, from vocal fold lesions, up to sleep apnea. After the fatigue of vocal folds has taken place surrounding structures compensate for the reduced vocal-fold activity, in turn, fatiguing and damaging themselves with prolonged phonation. Hence, it is of prime importance, clinically, and economically, to study fatigue and identify precursors to irreversible damage so that the same can be avoided.

Existing literature in the field of vocal fatigue extensively covers objective and subjective parameters to detect fatigue, mechanisms of fatigue, etc. [1]. So far no attempt has been made to quantify fatigue and develop a framework to predict precursors to fatigue. Here, we use the simplified two-mass model, as formulated in [2] to extract the vibration characteristics of the vocal folds. Then, taking into consideration the material properties of the multilayered vocal fold, the stress time histories are computed. The RainFlow counting algorithm (RFC) along with the Miner's rule is used to compute the accumulated damage.

The organization of the paper is as follows. A brief overview of the mathematical model is provided in Sect. 2. Section 3 presents a brief overview of vocal fatigue and its quantification using the RainFlow-Counting algorithm and Miner's rule. In Sect. 4 the system response over different lengths of phonation, along with the corresponding stress histories and damage levels are presented.

2 Mathematical Model

The model used in our study is a two-mass model developed by Herzel et al. in [2], which is a simplification of the Ishizaka and Flanagan model [3]. Herzel's model takes into account the basic principle of the possibility of a phase difference between the lower and upper edge of the vocal fold which has been proven to be a necessary condition for phonation. For the sake of simplicity, we have ignored the cubic nonlinearities introduced in [3] to account for the non-linear nature of vocal fold tissue. We also have ignored the role of subglottal and supraglottal structures and their resonances in phonation. Despite this being a gross simplification of the actual dynamics of phonation, we still obtain the bifurcations that are observed to occur in excised larynges [4], and hence this approach of solving simplified equations for the purpose of analyzing fatigue is validated.

The motions of the masses are described by the following equations:

$$m_i \ddot{x}_i + r_i \dot{x}_i + k_i x_i + \Theta(-a_i) c_i (a_i/2l) + k_c \big(x_i - x_j\big) = F_i(x_1, x_2) \tag{1}$$

where

$$\Theta(x) = \begin{cases} 1, & x > 0 \\ 0, & x \leq 0 \end{cases} \tag{2}$$

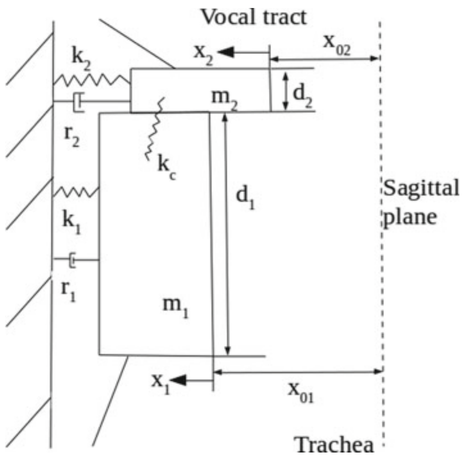

Fig. 1 Schematic representation of the two-mass model

where m_i, k_i, k_c, c_i, r_i, P_i are masses, spring constants, coupling constant, additional spring constants for collision, damping constants and pressure inside the glottis, respectively. Here $i = 1, 2$ represents the lower and upper masses, respectively.

The forces F_i acting on the masses m_i are given by

$$F_i = ld_i P_i \tag{3}$$

The following parameters correspond to our standard, symmetric vocal fold:

$m_1 = 0.125$, $m_2 = 0.025$, $r_1 = 0.02$, $r_2 = 0.02$, $k_1 = 0.08$, $k_2 = 0.008$, $c_1 = 3k_1$, $c_2 = 3k_2$, $k_c = 0.025$, $d_1 = 0.25$, $d_2 = 0.05$, $a_{01} = a_{02} = 0.05$ and $\rho = 0.0013$.

All the above values are in centimeters, grams, milliseconds and their combinations.

For further details on the mathematical model, refer [2].

2.1 Phonation Threshold Pressure (PTP)

PTP is defined as the minimum lung pressure to be exerted, all other conditions remaining constant, for phonation onset (defined as loss of stability of system via Hopf bifurcation and onset of oscillations).

Application of the Bernoulli's equation to our model, including the assumption of buildup of jet gives:

$$P_s = P_1 + \left(\frac{\rho}{2}\right)\left(\frac{U}{a_1}\right)^2 = P_0 + \left(\frac{\rho}{2}\right)\left(\frac{U}{a_{min}}\right)^2 \tag{4}$$

Here,

$$a_{\min} = \min(a_{1l}, a_{2l}) + \min(a_{1r}, a_{2r}) \tag{5}$$

where P_s is subglottal pressure, P_0 is supraglottal pressure, U is volume flow velocity and ρ is air density.

Accumulation of fatigue in vocal folds due to prolonged phonation changes several characteristics of the vocal folds, and all such changes have been observed to ultimately change PTP [5]. Since PTP has been proven to be a good indicator for fatigue as it closely correlates with perceived exertion of phonation (PPE) [6], it is used as the parameter that varies with time and accounts for the fatigue accumulated in the system. Data from [6] was used to find the variation of PTP as time progresses, during a continuous vocal loading task. Since the variation of PTP with time is not available in the literature, we have approximated as a linear function.

$$P_s = 0.2030\left(\frac{t}{1800}\right) + 2919 \tag{6}$$

where P_s is in cm of H_2O and t is in s.

The above relation is useful in our objective of setting benchmarks of PTP values for different levels of fatigue, as presented later in this paper.

3 Vocal Fatigue and Its Quantification

The hallmark of vocal fatigue is considered to be the self-report of an increased sense of effort with prolonged phonation. Vocal fatigue occurs due to several biomechanical and neuromuscular factors. These include fatigue of the respiratory and laryngeal muscles, fatigue of the non-muscular vocal-fold tissues, and changes in the viscous properties of the vocal folds.

The potential mechanisms that contribute to vocal fatigue are

1. Neuromuscular fatigue
2. Non-muscular tissue fatigue and viscosity.

Mechanical fatigue comes under non-muscular tissue fatigue. This sort of fatigue reflects the amount of cyclic stresses that a material can tolerate before breaking down. Fatigue is the progressive structural damage that results from stress imposed by strain on the material. Because of the deformation of the three layers of the vocal folds, they are subjected to mechanical stresses with every cycle of vocal-fold oscillation during phonation. These extended cyclic stresses result in fatigue damage of the vocal fold tissue. Many fatigue damage theories have been used over the past years and they indicate that fatigue damage is strongly associated with the cycle ratio, (n_i/N_i) where n_i and N_i are number of stress cycles of a specific stress amplitude exerted on the specimen and the number of cycles to failure for that stress amplitude, respectively.

In this model, the vocal folds are subjected to cyclic loads. Since the amplitude of the loading is changing with time, it is difficult to determine which cycles contribute to fatigue and their corresponding amplitudes. Hence, several cycle counting techniques have been introduced to reduce a complicated variable amplitude loading history into a number of discrete simple constant amplitude loading events, which are associated with fatigue damage. And out of all these methods, Rainflow-cycle (RFC) counting method is generally regarded as the method leading to the best estimators of 'fatigue life'. This is a method to determine the number of cycles present in a stress history and along with the SN-curve, the fatigue damage is evaluated using a Palmgren-Miner linear damage accumulation theory. Hence, RFC method breaks down any load-time history into its constituent fatigue cycles so as to estimate the fatigue life.

4 Results and Discussions

The governing equations of motion are written in state-space form and solved in MATLAB using an adaptive time-step Runge–Kutta ODE solver, to obtain time-responses of the system for different values of the control parameter.

The governing equations can be written as:

$$\dot{x}_1 = v_1 \tag{7}$$

$$\dot{v}_1 = \frac{1}{m_1}\Big(P_1 l d_1 - r_1 v_1 - k_1 x_1 - \Theta(-a_1) c_1 \frac{a_1}{2l} - k_c(x_1 - x_2)\Big) \tag{8}$$

$$\dot{x}_2 = v_2 \tag{9}$$

$$\dot{v}_2 = \frac{1}{m_2}\Big(-r_2 v_2 - k_2 x_2 - \Theta(-a_2) c_2 \frac{a_2}{2l} - k_c(x_1 - x_2)\Big) \tag{10}$$

$$P_1 = P_\mathrm{s}\left[1 - \Theta(a_{\min})\left(\frac{a_{\min}}{a_1}\right)^2\right]\Theta(a_1) \tag{11}$$

$$a_1 = a_{01} + 2l x_1 \tag{12}$$

$$a_2 = a_{02} + 2l x_2 \tag{13}$$

$$a_{\min} = \begin{cases} a_1, \text{ if } 0 < x_1 < x_2 \\ a_2, \text{ if } 0 < x_2 \leq x_1 \\ 0, \quad \text{if otherwise} \end{cases} \tag{14}$$

The function $\Theta(x)$ is approximated as:

$$\Theta(x) = \begin{cases} \tanh[50(x/x_0)], & x > 0 \\ 0, & x \le 0 \end{cases} \tag{15}$$

The differential equations mentioned above are solved using ODE solver over a time span of 1 h and the time responses are plotted. The amplitudes of the masses are observed to be within 0.15 mm (see Fig. 2). Similarly, the time responses are plotted for the 2nd and 3rd hour of phonation and they are observed to be within 0.2 mm and 0.3 mm respectively (see Figs. 3 and 4). As expected, a phase difference is observed between the motion of the two masses which, as mentioned earlier, is a necessary

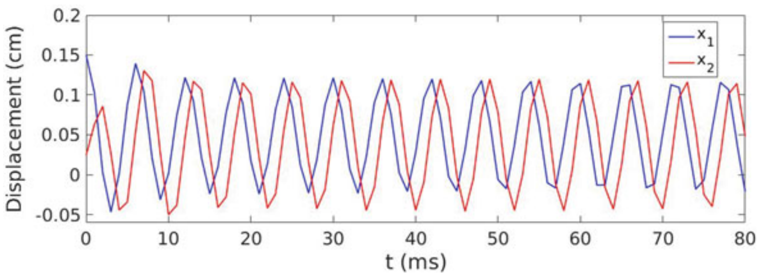

Fig. 2 A section of the time response obtained for 1 h of phonation

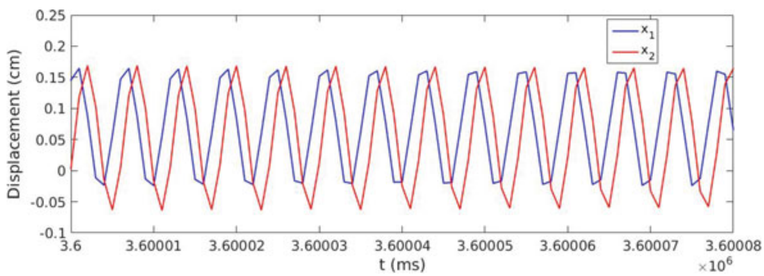

Fig. 3 A section of the time response obtained for 2 h of phonation

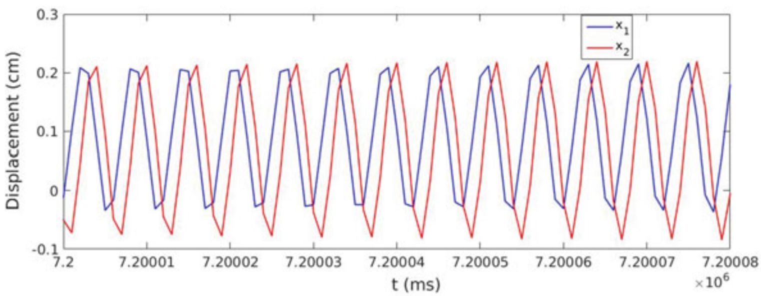

Fig. 4 A section of the time response obtained for 3 h of phonation

condition for phonation. In this way, the time responses can be obtained for different time durations of phonation so as to understand the dynamics of vocal folds.

From these time responses, the corresponding stress histories are obtained using tensile and compressive stress–strain equations. A linear relationship between stress and strain is assumed to obtain the stress–time history:

$$\sigma = E\varepsilon \tag{16}$$

where E is Young's modulus of vocal folds in the transverse direction, for low moduli of strains [7].

From the stress history plots above, we can see that, for 1 h of phonation, the maximum stress amplitude is observed to be 0.0086 g/(cm) (ms)^2 (see Fig. 5). In the same way, the maximum stress amplitudes for 2 and 3 h of phonation are observed to be 0.012 and 0.0139 g/(cm) (ms)^2 (Figs. 6 and 7). Hence, it can be inferred that, as time progresses and fatigue accumulates, the vocal folds experience a higher magnitude of stress.

Now, our objective is to find the amount of fatigue incurred for different lengths of continuous phonation using RFC algorithm. To apply Rainflow-Counting Algorithm, stress-time history and S-N curve of the vocal folds are required.

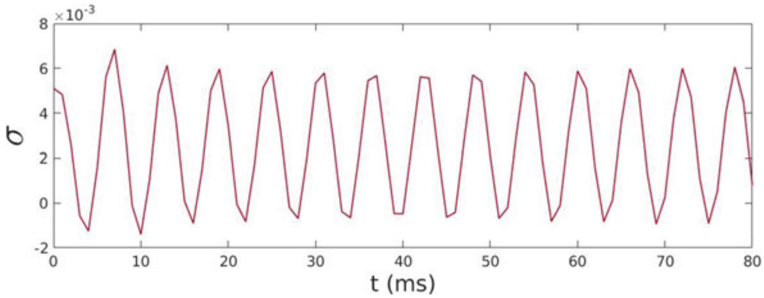

Fig. 5 A section of stress history obtained for 1 h of phonation

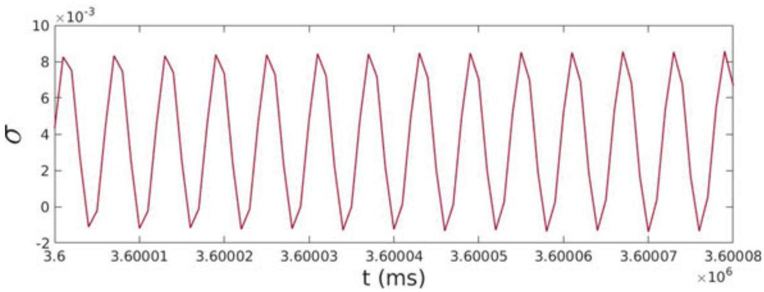

Fig. 6 A section of stress history obtained for 2 h of phonation

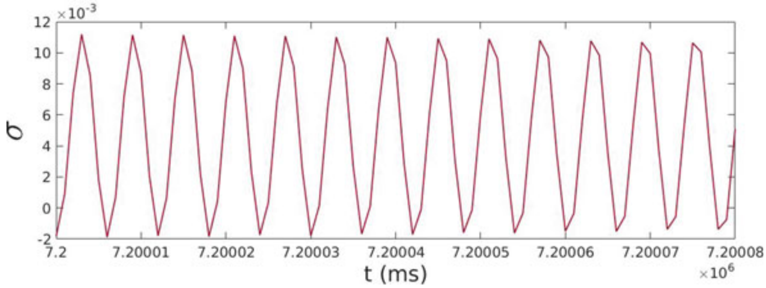

Fig. 7 A section of stress history obtained for 3 h of phonation

Since existing literature does not detail the S-N curve of this multilayered, anisotropic structure, and because calculating the same is beyond the scope of this paper, we have used the S-N curve of the Achilles tendon [1], since it is similar in characteristics to the vocal fold, and especially to the lamina propria, which is the most prone to fatigue damage of the three layers that compose the vocal fold (see Fig. 8).

Now, using the WAFO toolbox in MATLAB, the amount of damage (D) is calculated for different lengths of phonation and is tabulated in Table 1.

As seen from the data, the damage value is higher for a longer duration of phonation. The PTP value at the end of phonation is also found to be higher for a longer

Fig. 8 S-N curve of Achilles tendon

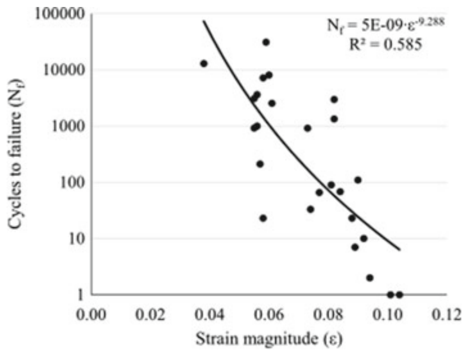

Table 1 Amount of damage for different lengths of phonation

S. No.	Duration of phonation (h)	Damage index	PTP (at end of phonation duration) (cm of H_2O)
1	1	2.8501×10^{-25}	3.325
2	2	4.4930×10^{-24}	3.731
3	3	4.0110×10^{-23}	4.137

phonatory duration. Hence, these PTP values can be linked to their respective damage indices.

5 Concluding Remarks

This study is thus a preliminary attempt at quantifying the amount of damage incurred in vocal folds and linking the same to a measurable, objective quantity (PTP). This has been done as a step towards recognizing precursors to permanent, serious damage to the vocal folds. This study hence provides a framework for quantifying fatigue for preventive applications. To make this study directly useful in reality, a few improvements are in order—a separate study is required to estimate the S-N curve of a realistic model of the vocal folds; tissue nonlinearities have to be taken into account; perturbations in the aerodynamic forcing have to be considered, and the role of subglottal and supraglottal structures in aiding phonation have to be addressed. Future work will focus on improving accuracy of the damage estimates by implementing the above improvements. Further, the results of this study will prove useful when corroborated with in vivo and ex vivo experimental studies on vocal fold fatigue, and the authors intend to take up the same in future projects.

References

1. Edwards WB (2018) Modeling overuse injuries in sport as a mechanical fatigue phenomenon. Exerc Sport Sci Rev 46(4):224–231
2. Steinecke I, Herzel H (1995) Bifurcations in an asymmetric vocal-fold model. J Acoust Soc Am 97(3):1874–1884
3. Ishizaka K, Flanagan JL (1972) Synthesis of voiced sounds from a two-mass model of the vocal cords. Bell Syst Tech J 51(6):1233–1268
4. Herzel H, Berry D, Titze I, Steinecke I (1995) Nonlinear dynamics of the voice: signal analysis and biomechanical modeling. Chaos 5(1):30–34
5. Solomon NP (2008) Vocal fatigue and its relation to vocal hyperfunction. Int J Speech-Lang Pathol 10(4):254–266
6. Chang A, Karnell MP (2004) Perceived phonatory effort and phonation threshold pressure across a prolonged voice loading task: a study of vocal fatigue. J Voice 18(4):454–466
7. Alipour F, Vigmostad S (2012) Measurement of vocal folds elastic properties for continuum modeling. J Voice 26(6):816–821

Response of a Layered Composite Beam Subjected to Static Loading Using Point Interpolation Meshless Technique

Kunal S. Shah, Appaso M. Gadade, and Sanjiv M. Sansgiri

Abstract The present work proposes a meshless model to analyze the response of laminated composite beam under different types of static loading. The point interpolation method based on polynomial basis function is used for solving 1D higher-order beam theory equations. The distribution of transverse shear strain and stresses along thickness are obtained using Reddy's shape function. A displacement response of a laminated beam is obtained for several lamination schemes, aspect ratio, and boundary conditions. The authenticity of the present algorithm is confirmed by comparing results with different cases from literature.

Keywords Laminated composite beam · Higher-order beam theory · Meshless method · Point interpolation method

1 Introduction

The requirement of composite materials is growing continuously in most of the industries. Composite materials can be formulated mathematically using different types of shear deformation theories. Computer-based analysis for solving problems in solid mechanics, fluid dynamics or thermodynamics, etc. has increased due to ease, accuracy, and time efficiency. In the last two decades, many authors have shown keen interest in the numerical approach based on the meshless method, which differs from finite element methods on the basis of approximate techniques. The domain representation in the finite element method depends on the mesh of elements. The

K. S. Shah · S. M. Sansgiri
Mechanical Engineering, Army Institute of Technology, Pune 411015, India
e-mail: kunalshah26194@gmail.com

S. M. Sansgiri
e-mail: drsanjivmsansgiri@gmail.com

A. M. Gadade (✉)
Mechanical Engineering Department, Thapar Institute of Engineering and Technology, Patiala 147004, India
e-mail: appagadade@gmail.com

E. T. Akinlabi et al. (eds.), *Trends in Mechanical and Biomedical Design*,
Lecture Notes in Mechanical Engineering,
https://doi.org/10.1007/978-981-15-4488-0_17

shape of the element also needs to be as regular as possible to have valid results, which is not possible in complex geometries, so the analyst has to spend a lot of time in creating an appropriate mesh. Also, remeshing at each step is required in case of an adaptive analysis. The accuracy of secondary or derivative variables such as strains and stresses in solid mechanics is not adequate. The meshless methods give an advantage over these issues. The various meshless methods with different types of approaches and approximation techniques were reviewed [1, 2]. The point interpolation method is one of the approximation techniques used for stress analysis of two-dimensional solids [3, 4]. The meshless methods based on global weak forms were described practically with MATLAB code [5].

A mathematical approach for analyzing laminated composite structures has been developed from classical laminate plate theories to higher-order shear deformation theory [6]. The higher-order shear deformation theory present displacement and stresses more accurately than classical or first-order theory. It accounts for the parabolic distribution of transverse shear strain through thickness [7]. The exact solutions of these different types of shear deformation theories were analyzed for the bending of symmetrical and asymmetrical laminated beams [8]. The meshless method based on multi-quadric radial basis function was used for higher-order beams and plates analysis [9]. The radial point interpolation method was used for the analysis of 2D laminated composite beam [10].

The present paper focuses on the behavior of static bending of the laminated beam with respect to change in lamination scheme, boundary condition, and aspect ratio subjected to uniformly distributed load as well as a point load.

2 General Formulation

The displacements (u, v, w) are considered along with Cartesian coordinates (x, y, z) respectively. The displacement v is assumed to be zero. Thus (u, v, w) are the function of x and z. In higher-order Beam Theory (HBT), the displacement field considers a quadratic variation of transverse strain vanishing at the free surface. Hence, shear correction factor is not required. Field variables can be represented as axial displacement (u_0), transverse displacement (w_0), rotation about normal to the mid-surface (θ_x) and slope ($\partial w_0 \big/ \partial x$). Thus, the displacement field can be written as [9],

$$u = u_0 + z\theta_x + \alpha z^3\left(\theta_x + \frac{\partial w_0}{\partial x}\right); \quad w = w_0 \tag{1}$$

where

$$\alpha = -4/3h^2$$

The linear strain vectors corresponding to displacement fields in (1) can be written as

$$\{\varepsilon\} = \left\{ \varepsilon_1 \ \varepsilon_5 \right\} \tag{2}$$

where

$$\begin{aligned}
\varepsilon_1 &= \left(\frac{\partial u}{\partial x}\right) = \varepsilon_1^0 + z\varepsilon_1^1 + z^3\varepsilon_1^3; \\
\varepsilon_5 &= \left(\frac{\partial u}{\partial z} + \frac{\partial w}{\partial x}\right) = \varepsilon_1^0 + z^2\varepsilon_5^2
\end{aligned} \tag{3}$$

The strain–displacement relations of the HBT are

$$\begin{aligned}
&\varepsilon_1^0 = \left(\frac{\partial u_0}{\partial x}\right);\ \varepsilon_5^0 = \left(\theta_x + \frac{\partial w_0}{\partial x}\right); \\
&\varepsilon_1^1 = \left(\frac{\partial \theta_x}{\partial x}\right);\ \varepsilon_1^3 = \alpha\left(\frac{\partial \theta_x}{\partial x} + \frac{\partial^2 w_0}{\partial x^2}\right); \\
&\varepsilon_5^2 = 3\alpha\left(\theta_x + \frac{\partial w_0}{\partial x}\right)
\end{aligned} \tag{4}$$

Thus, vector of strain components is

$$\{\bar{\varepsilon}\}^{\mathrm{T}} = \left\{ \varepsilon_1^0 \ \varepsilon_1^1 \ \varepsilon_1^3 \ \varepsilon_5^0 \ \varepsilon_5^2 \right\} \tag{5}$$

and vector of field variable can be represented as

$$\{U\} = \left\{ u_0 \ w_0 \ \tfrac{\partial w_0}{\partial x} \ \theta_x \right\} \tag{6}$$

The constitutive law gives a relation between stress and strain of laminated beam as

$$\begin{Bmatrix} \sigma_1 \\ \sigma_5 \end{Bmatrix} = \begin{bmatrix} \overline{Q}_{11} & 0 \\ 0 & \overline{Q}_{55} \end{bmatrix} \begin{Bmatrix} \varepsilon_1 \\ \varepsilon_5 \end{Bmatrix} \tag{7}$$

where $\overline{Q}_{ij}$ are transformed material stiffness components of kth lamina at angle of fiber orientation $\left(\alpha^k\right)$ as described by Reddy [11].

3 Point Interpolation Method

The $\hat{U}(x)$ is a continuous function in a domain Ω. It can be represented by a set of field nodes and approximated at point of interest using polynomial basis function

[12] as

$$\hat{U}^{\mathrm{T}}(x) = P^{\mathrm{T}}(x) P_m^{-1} U = \sum_{i=1}^{n} \phi_i u_i = \Phi^{\mathrm{T}}(x) U \tag{8}$$

where $\Phi(x)$ is a vector of shape functions defined by

$$\Phi^{\mathrm{T}}(x) = P^{\mathrm{T}}(x) P_m^{-1} = \left\{ \phi_1(x) \ \phi_2(x) \ \cdots \ \phi_n(x) \right\} \tag{9}$$

The variation of Eq. (8), can be written as,

$$\delta \hat{U}_{4\times 1} = \Phi_{4n\times 4n} \delta U_{4n\times 1} \tag{10}$$

Consider a one-dimensional laminated composite beam on a domain Ω bounded by Γ. The weak form of equilibrium equation can be obtained by using the Galerkin method.

$$\int_{\Omega} (L\delta U)^{\mathrm{T}} D (LU) \mathrm{d}\Omega - \int_{\Omega} \delta U^{\mathrm{T}} b \mathrm{d}\Omega - \int_{\Gamma_t} \delta U^{\mathrm{T}} \bar{t} \mathrm{d}\Gamma = 0 \tag{11}$$

where L is a differential operator, b is body force vector, $\bar{t}$ is traction force at the natural boundaries and $\bar{u}$ is displacement at the essential boundaries.

Replacing the trial functions, test functions into the weak from Eq. (11), which provides the final discretized equation,

$$[K]_{(4n\times 4n)} \{U\}_{(4n\times 1)} = \{F\}_{(4n\times 1)} \tag{12}$$

where 'n' is number of nodes in domain around point of interest,

$$[K]_{4n\times 4n} = \int_{\Omega} [B]_{4n\times 5}^{\mathrm{T}} [D]_{5\times 5} [B]_{5\times 4n} \mathrm{d}\Omega \tag{13}$$

$$\{F\}_{(4n\times 1)} = \int_{\Omega} \Phi_{(4n\times 1)} \bar{t} \mathrm{d}\Gamma + \int_{\Omega} \Phi_{(4n\times 1)} b \mathrm{d}\Omega \tag{14}$$

$$[B]_{5\times 4n} = [L]_{5\times 4} [\Phi]_{4\times 4n} \tag{15}$$

$[D]$ is material property matrix represented as,

$$[D] = \sum_{k=1}^{NL} \int_{z_{k-1}}^{z_k} [T]^{\mathrm{T}}\left[\overline{Q}\right][T]\mathrm{d}z = \begin{bmatrix} [A_1] & [B_1] & [E_1] & 0 & 0 \\ [B_1] & [C_1] & [F_1] & 0 & 0 \\ [E_1] & [F_1] & [H_1] & 0 & 0 \\ 0 & 0 & 0 & [A_5] & [C_5] \\ 0 & 0 & 0 & [C_5] & [F_5] \end{bmatrix} \tag{16}$$

where

$$(A_1, B_1, C_1, E_1, F_1, H_1) = \sum_{k=1}^{n} \int_{z_k - 1}^{z_k} \overline{Q}_{11}\left(1, z, z^2, z^3, z^4, z^6\right)$$

$$(A_5, C_5, F_5) = \sum_{k=1}^{n} \int_{z_k - 1}^{z_k} \overline{Q}_{55}\left(1, z^2, z^4\right)$$

and [T] is a matrix of coefficient of strain vector

$$[\mathrm{T}] = \begin{bmatrix} 1 & z & z^3 & 0 & 0 \\ 0 & 0 & 0 & 1 & z^2 \end{bmatrix} \tag{17}$$

The constraints are applied by a direct method, which modifies the global force vector,

$$\left\{F_{ij}\right\} \Rightarrow \begin{cases} \bar{u}_i & i = j \\ F_j - K_{ji}U_i & i \neq j \end{cases} \tag{18}$$

4 Results and Discussion

The present study is confirmed with the help of numerical results for different cases of the laminated beam. The relation of material properties considered in order to obtain nondimensional results is

$$E_{11} = 0.04E_{22},\ G_{12} = G_{13} = 0.5E_{22},\ G_{23} = 0.2E_{22},\ \nu_{12} = 0.25$$

where E_{11} and E_{22} are Young's modulus in longitudinal and transverse direction of lamina, respectively. G_{12}, G_{23}, and G_{13} are the rigidity modulus along longitudinal and transverse plane and ν_{12} is Poisson's ratio. All laminae are considered to be of equal length and thickness made up of the same orthotropic material. Thus, maximum nondimensional transverse displacement can be obtained by,

$$\bar{w} = \frac{100E_{22}h^3}{Pl^3} w_{\max} \tag{19}$$

where P is point load, l and h are length and total height of the laminated beam respectively. For uniformly distributed load $P = q_0 l$ with q_0 as load per unit length.

Constraints are applied as hinged-hinged (H-H), clamped-hinged (C-H), clamped-clamped (C-C), and clamped-free (C-F) by restricting the degree of freedom as explained in Table 1. The present work is validated by nondimensional transverse displacement obtained using MATLAB program with previously available literature. Tables 2, 3, and 4 represents a comparison of maximum nondimensional transverse displacement for different boundary conditions such as hinged-hinged, clamp-clamp, and clamp-free respectively. The results are obtained for three different aspect ratios 10, 20, 100, etc. The lamination schemes considered for results are [0], [90], and $[0/90]_s$ respectively. Two types of mechanical loads are applied on a laminated beam, which is point load and Uniformly Distributed Load (UDL). Results satisfy the requirement of validation. Table 5 shows results for laminated beam subjected to clamped-hinged condition continuing the pattern of lamination scheme and aspect ratio as explained before.

Figure 1 shows the effect of aspect ratio over the maximum nondimensional displacement of the beam with lamination scheme $[0/45/-45/90]_s$ for different boundary

Table 1 Restricted degree of freedom for restricted node

Boundary condition	Restricted degree of freedom
Clamped	$u_0, w_0, \theta_x, \partial w_0 / \partial x$
Hinged	u_0, w_0
Free	–

Table 2 Non-dimensional maximum transverse displacement ($\bar{w}$) of simply supported laminated beam

l/h	Author	Lamination scheme					
		0	90	$[0/90]_s$	0	90	$[0/90]_s$
		UDL			Point load		
10	Present	0.9220	16.3356	1.2609	1.5847	26.4259	2.2025
	Reddy [11]	0.9250	16.3750	1.1370	1.6000	26.5000	1.9910
	Sadek [10]	1.0130	16.5190	1.4243	1.7740	26.7760	2.5308
20	Present	0.6983	15.7734	0.8475	1.1458	25.3108	1.4063
	Reddy [11]	0.7000	15.8130	0.8160	1.1500	25.3750	1.3480
	Sadek [10]	0.7130	15.8330	0.8785	1.1750	25.4140	1.4665
100	Present	0.6264	15.5934	0.7140	1.0035	24.9524	1.1446
	Reddy [11]	0.6280	15.6330	0.7130	1.0010	25.0150	1.1430
	Sadek [10]	0.6270	15.5880	0.7445	1.0040	24.9440	1.1938

Table 3 Nondimensional maximum transverse displacement ($\bar{w}$) of clamped-clamped laminated beam

l/h	Author	Lamination scheme					
		0	90	$[0/90]_s$	0	90	$[0/90]_s$
		UDL			Point load		
10	Present	0.4127	3.8577	0.6545	0.8246	7.7133	1.3077
	Reddy [11]	0.4250	3.8750	0.5700	0.8500	7.7500	1.1410
	Sadek [10]	0.4160	3.8600	0.6820	0.9180	7.8520	1.4919
20	Present	0.1982	3.3035	0.2755	0.3962	6.6065	0.5506
	Reddy [11]	0.2000	3.3120	0.2490	0.4000	6.6250	0.4980
	Sadek [10]	0.1990	3.3070	0.2841	0.4080	6.6340	0.5842
100	Present	0.1277	3.1246	0.1472	0.2553	6.2493	0.2944
	Reddy [11]	0.1280	3.1320	0.1460	1.7930	6.2650	0.2920
	Sadek [10]	0.1280	3.1230	0.1536	0.2250	6.2460	0.3074

Table 4 Nondimensional maximum transverse displacement ($\bar{w}$) of clamped-free laminated beam

l/h	Author	Lamination scheme					
		0	90	$[0/90]_s$	0	90	$[0/90]_s$
		UDL			Point load		
10	Present	7.1625	152.6064	8.9464	18.3361	404.9809	22.5062
	Reddy [11]	7.2000	153.0000	8.5200	18.4000	406.0000	21.5800
	Sadek [10]	7.1580	152.7160	9.0838	18.4790	405.7620	23.0457
20	Present	6.2821	150.3726	7.3477	16.5570	400.4974	19.2400
	Reddy [11]	6.3000	150.7500	7.2300	16.6000	401.5000	19.0100
	Sadek [10]	6.3120	150.5300	7.6924	16.6620	401.0490	20.1650
100	Present	5.9970	149.6549	6.8233	15.9840	399.0597	18.1809
	Reddy [11]	6.0100	150.0000	6.8200	16.0200	400.0000	18.1800
	Sadek [10]	5.9970	149.2020	6.7287	16.0240	397.8760	17.9304

Table 5 Nondimensional maximum transverse displacement ($\bar{w}$) of clamped-hinged laminated beam

l/h	Lamination scheme					
	0	90	$[0/90]_s$	0	90	$[0/90]_s$
	UDL			Point load		
10	0.5927	7.3377	0.8925	1.0864	12.7107	1.6528
20	0.3443	6.6971	0.4504	0.6044	11.5385	0.8005
100	0.2628	6.4916	0.3010	0.4523	11.1672	0.5184

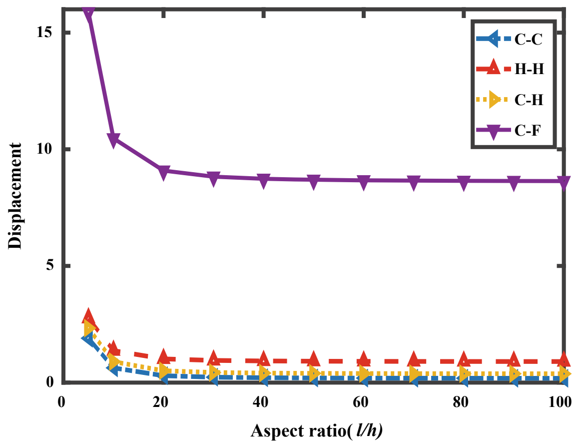

Fig. 1 Graph of displacement versus aspect ratio with lamination scheme $[0/45/-45/90]_s$ and different boundary conditions subjected to UDL

conditions obtained using the present approach. The results state that the clamped-free boundary condition shows more maximum nondimensional displacement for all aspect ratios. Maximum nondimensional displacement decreases with increasing aspect ratio initially and then remains constant for all boundary conditions. Figure 2 shows nondimensional displacement of layered composite beam for lamination scheme $[\theta_4/0_4/\theta_4]$ and different boundary conditions at aspect ratio 10. The results show that displacement increases with increasing lamination angle. Clamped-free boundary conditions show more response as compared to others for all lamination angles. Figures 3, 4, 5 and 6 shows the transverse displacement of laminated beam with lamination scheme $(0/45/-45/90)_s$ and aspect ratio 10. The beam is subjected to point load and UDL with boundary conditions hinged-hinged, clamped-hinged, clamped-free, and clamped-clamped respectively. Behavior of beam deflection due to boundary conditions is captured. The laminated beam shows maximum deflection

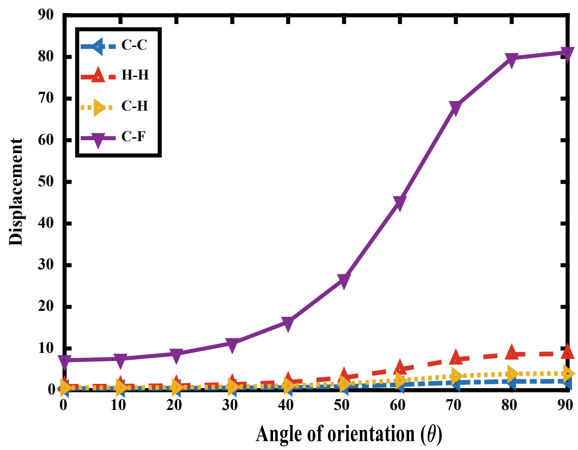

Fig. 2 Graph of displacement versus lamination scheme $[\theta_4/0_4/\theta_4]$ with aspect ratio 10 and different boundary conditions subjected to UDL

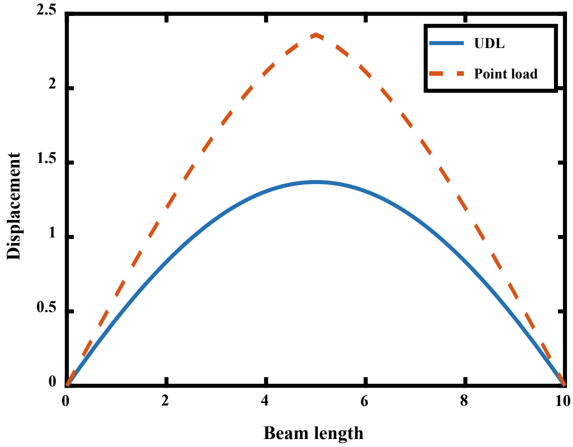

Fig. 3 Graph of displacement of midplane versus nodes with lamination scheme $[0/45/-45/90]_S$, aspect ratio 10 and hinged-hinged beam

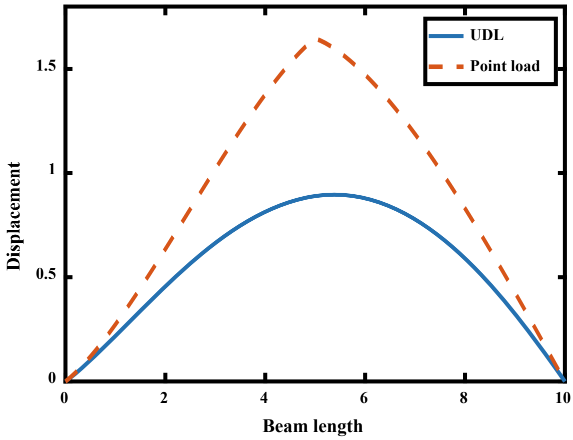

Fig. 4 Graph of displacement of midplane versus nodes with lamination scheme $[0/45/-45/90]_S$, aspect ratio 10 at clamped hinged beam

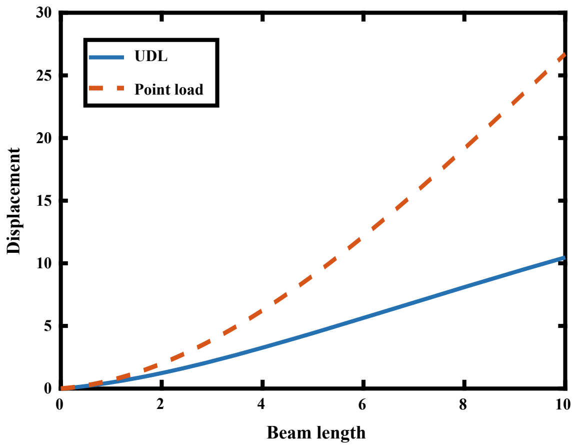

Fig. 5 Graph of displacement of midplane versus nodes with lamination scheme $[0/45/-45/90]_S$, aspect ratio 10 and clamped-free beam

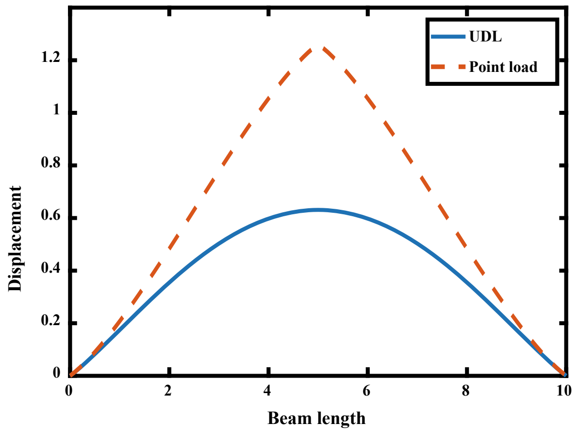

Fig. 6 Graph of displacement of midplane versus nodes with lamination scheme $[0/45/-45/90]_S$, aspect ratio 10 and clamped-clamped beam

at its midpoint for (*C-C*, *C-H*, and *H-H*) boundary conditions while *C-F* shows maximum deflection at its edge with no constraints. It can be predicted that the effect of point load on deflection is more as compared to UDL.

5 Conclusion

The present study infers that the higher-order beam theory using the meshless method shows accurate results as correlated to classical or first-order shear deformation theory. The application of constraints in point interpolation method is done by direct method similar to FEM, thus easier as compared to other meshless methods. The behavior of laminated beam is observed by plotting various graphs of displacement with respect to lamination scheme, aspect ratio, loading condition, and boundary conditions. As aspect ratio (l/h) increases the displacement reduces and becomes consistent after crossing 20. Minimum displacement is observed for the lamination scheme with angle [$\theta = 0°$] and it increases and approaches the maximum at an angle [$\theta = 90°$]. The nondimensional displacement obtained for concentrated point load is more as compared to a uniformly distributed load.

References

1. Belytschko T, Krongauz Y, Organ D, Fleming M, Krysl P (1996) Meshless methods: an overview and recent developments. Comput Methods Appl Mech Eng 139:3–47
2. Liu GR (2016) An overview on meshfree methods: for computational solid mechanics. Int J Comput Methods 13(5):1630001–1630042
3. Liu GR, Gu YG (2001) A point interpolation method for two-dimensional solids. Int J Numer Methods Eng 50:937–951

4. Liu GR, Zhang GY, Dai KY (2005) A linearly confirming point interpolation method (LC-PIM) for 2D solid mechanics problems. Int J Comput Methods 2(4):645–665
5. Nguyen VP, Rabczuk T, Bordas S, Duflot M (2008) Meshless methods: a review and computer implementation aspects. Math Comput Simul 79:763–813
6. Abrate S, Sciuva MD (2017) Equivalent single layer theories for composite and sandwich structures: a review. Compos Struct 179:482–494
7. Reddy JN (1984) A simple higher order theory for laminated composite plates. J Appl Mech 51:745–752
8. Khdeir AA, Reddy JN (1997) An exact solution for the bending of thin and thick cross-ply laminated beams. Compos Struct 37:195–203
9. Ferreira AJM, Roque CMC, Martins PALS (2004) Radial basis functions and higher-order shear deformation theories in the analysis of laminated composite beams and plates. Compos Struct 66:287–293
10. Sadek SHM, Belinha J, Parente MPL, Natal Jorge RM, César JMA, Ferreira AJM (2017) The analysis of composite laminated beams using a 2D interpolating meshless technique. Acta Mech Sin 1–18
11. Reddy JN (2004) Mechanics of laminated composite plates and shells, 2nd edn. CRC Press LLC
12. Liu GR (2003) Mesh free methods: moving beyond the finite element method, 1st edn. CRC Press LLC

Dynamic Behaviour of Laminated Composite Beam Undergoing Moving Loads

Lalit Babu Saxena, Appaso M. Gadade, and Sanjiv M. Sansgiri

Abstract This study is about dynamic response of laminated composite beam undergoing moving loads. Rotary inertia and shear deformation effects are considered by using Timoshenko Beam Theory (TBT). Finite Element Method (FEM) is applied to discretize the structural element into space and for time discretization Classical Midpoint Rule with Midpoint Acceleration (MPR-MPA) is employed which is a part of Generalized Single Step Single Solve (GSSSS) family of algorithms. A MATLAB code is developed to obtain dynamic responses such as dynamic magnification factor and maximum dynamic deflection at the mid-span of simply supported isotropic and laminated composite Timoshenko beam. Numerical results are obtained and validated with the literature available and it shows good agreement.

Keywords Timoshenko beam theory · Midpoint rule with midpoint acceleration · Moving loads · Laminated composite beam · Dynamic magnification factor · Finite element method

1 Introduction

Moving load problems is of great interest to engineers. Dynamic deflection, vibrations and stresses effects vary greatly in structures as compared to effects due to static deflection, vibration and stresses. Bridges subjected to moving vehicle loads, railway tracks subjected to moving train loads, landing aircraft on carrier are some of the common moving load cases. In 1905, Krylov [1] examined the simply supported

L. B. Saxena · S. M. Sansgiri
Mechanical Engineering, Army Institute of Technology, Pune 411015, India
e-mail: 2666466saxena@gmail.com

S. M. Sansgiri
e-mail: drsanjivmsansgiri@gmail.com

A. M. Gadade (✉)
Mechanical Engineering Department, Thapar Institute of Engineering and Technology, Patiala 147004, India
e-mail: appagadade@gmail.com

E. T. Akinlabi et al. (eds.), *Trends in Mechanical and Biomedical Design*,
Lecture Notes in Mechanical Engineering,
https://doi.org/10.1007/978-981-15-4488-0_18

beam case under a point load where the mass of beam was taken more as compared to the mass of the load. In 1908, Timoshenko [2] solved the same case using the eigenfunctions method. In 1972, Fryba [3] proposed many studies related to structures under moving loads. However, few studies have been done on the dynamic behaviour of layered composite beams undergoing moving loads. In 1998, Kadivar and Mohebpour [4] analyzed induced vibrations in asymmetric layered beam subjected to moving loads. In 2003, Zibdeh and Abu Hilal [5] studied stochastic response of layered composite beams under random moving loads. In 2005, Kavipurapu [6] studied dynamic behaviour of glass/epoxy simply supported beams undergoing moving loads in hygro-thermal environment. In 2008, Kiral and Kiral [7] presented dynamic behaviour of symmetric layered beams undergoing moving loads using a 3-D model based on classical lamination theory. In 2011, Mohebpour et al. [8] studied the dynamic behaviour of layered beams under moving oscillators. In 2012, Kahya [9] investigated dynamic response of layered beams undergoing moving loads using multi-layered beam element. In 2016, Tao et al. [10] studied nonlinear dynamic behaviours in thermal environment of fiber metal layered beams under moving loads. In 2017, Chen et al. [11] investigated nonlinear dynamic behaviours of fiber metal layered beam resting on elastic foundation undergoing moving harmonic load and thermal load. It is clear from the literature that no one has used MPR-MPA technique for solving moving load problems yet.

2 General Formulation

Consider a layered composite Timoshenko beam consisting of n orthotropic layers with principle material coordinates (x_1^k, x_2^k, x_3^k) of kth lamina oriented at an angle θ^k to laminate coordinate, x. The thickness, width and length of beam are h, b and l, respectively (see Fig. 1). Origin of the material coordinates at the middle of laminate.

Displacement field for Timoshenko Beam Theory is

$$u(x, z, t) = u_0(x, t) + z\phi(x, t) \text{ and } w(x, z, t) = w_0(x, t) \tag{1}$$

where (u, w) are displacements along (x, z) coordinates, respectively, u_0 and w_0 are the displacements of a point on the midplane $(x, 0)$ and ϕ is the rotation of the transverse normal.

Linear strain vectors corresponding to displacement fields are

$$\varepsilon_{xx} = \varepsilon_1 = \frac{\partial u}{\partial x} \text{ and } \varepsilon_{xz} = \varepsilon_5 = \frac{\partial w}{\partial x} + \frac{\partial u}{\partial z} \tag{2}$$

that can be written as

$$\{\varepsilon_l\} = \left\{ \varepsilon_1 \;\; \varepsilon_5 \right\}_l^T \tag{3}$$

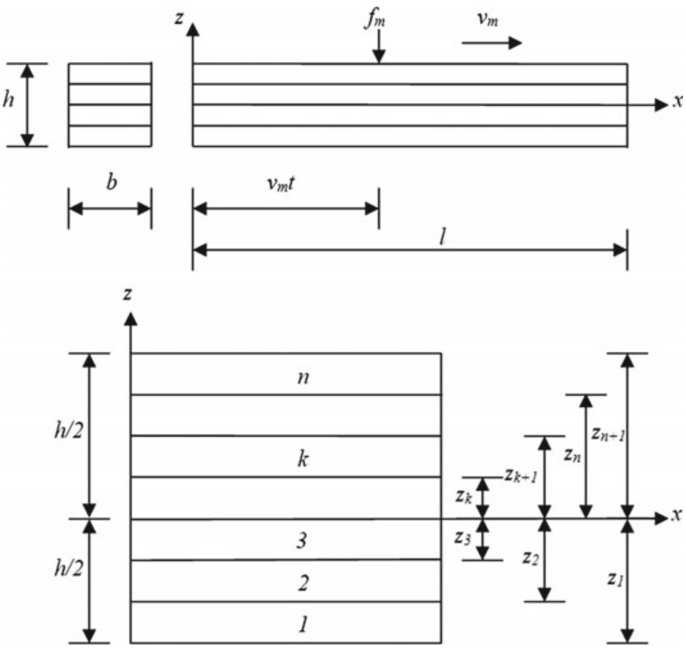

Fig. 1 Displacement field model and layers arrangement

The associated strains for the assumed displacement field can be written as

$$\left.\begin{aligned} \varepsilon_i &= \varepsilon_i^0 + z\psi_i^0 \quad (i = 1, 5) \\ \varepsilon_1 = \varepsilon_1^0 + z\psi_1^0 \text{ and } \varepsilon_5 &= \varepsilon_5^0 + z\psi_5^0 \end{aligned}\right\} \tag{4}$$

The strain–displacement relations are

$$\varepsilon_1^0 = \tfrac{\partial u_0}{\partial x},\ \psi_1^0 = \tfrac{\partial \phi}{\partial x},\ \varepsilon_5^0 = \phi + \tfrac{\partial w_0}{\partial x},\ \psi_5^0 = 0 \tag{5}$$

from Eqs. (3) and (4)

$$\{\varepsilon_l\} = [T]\{\bar{\varepsilon}_l\} \tag{6}$$

where $[T]$ is the thickness matrix expressed as

$$[T] = \begin{bmatrix} 1 & z & 0 \\ 0 & 0 & 1 \end{bmatrix} \text{ and } \{\bar{\varepsilon}_l\}^T = \left\{ \varepsilon_1^0 \ \psi_1^0 \ \varepsilon_5^0 \right\} \tag{7}$$

Using (5), Eq. (7) can be rewritten in matrix form as

$$\{\bar{\varepsilon}_l\} = [L]\{\Lambda\} \tag{8}$$

where $[L]$ is the differential operator and is given by

$$[L] = \begin{bmatrix} \partial/\partial x & 0 & 0 \\ 0 & 0 & \partial/\partial x \\ 0 & \partial/\partial x & 1 \end{bmatrix} \text{ and } \{\Lambda\} = \left\{ u_0 \ w_0 \ \phi \right\}^{\mathrm{T}} \tag{9}$$

where $\{\Lambda\}$ is the mid-plane displacement vector for the C^0 continuous model.

The Stress–Strain relation for a lamina with respect to the fiber-matrix coordinate axis can be given as

$$\left\{\sigma_p\right\} = \left[\overline{Q}^k\right]\left\{\varepsilon_p\right\} \text{ it can be written as, } \begin{Bmatrix} \sigma_{xx} \\ \tau_{xz} \end{Bmatrix} = \begin{bmatrix} \overline{Q}_{11} & 0 \\ 0 & \overline{Q}_{55} \end{bmatrix} \begin{Bmatrix} \varepsilon_{xx} \\ \gamma_{xz} \end{Bmatrix} \tag{10}$$

where

$$\left.\begin{aligned} \overline{Q}_{11} &= Q_{11}\cos^4\theta_k + Q_{22}\sin^4\theta_k + 2(Q_{12} + 2Q_{66})\sin^2\theta_k\cos^2\theta_k \\ \overline{Q}_{55} &= Q_{55}\cos^2\theta_k + Q_{44}\sin^2\theta_k \end{aligned}\right\} \tag{11}$$

and

$$\left.\begin{aligned} &Q_{11} = \tfrac{E_{11}}{(1-\mu_{12}\mu_{21})},\ Q_{22} = \tfrac{E_{22}}{(1-\mu_{12}\mu_{21})},\ Q_{12} = \tfrac{\mu_{21}E_{11}}{(1-\mu_{12}\mu_{21})}, \\ &Q_{44} = G_{23}, \qquad Q_{55} = G_{13}, \qquad Q_{66} = G_{12} \end{aligned}\right\} \tag{12}$$

where Q_{ij} are material constants, $\overline{Q}_{ij}$ are the transformed material constants. Material properties E_{11} and E_{22} are Young's modulus in longitudinal and transverse directions. G_{12} is Rigidity modulus in longitudinal plane whereas, G_{13} and G_{23} are Rigidity modulus in transverse plane. Poisson's ratios are μ_{12} and μ_{21}. θ_k is the angle of fiber orientation of lamina.

Material property matrix can be expressed as

$$[D]_{3\times3} = [T]^{\mathrm{T}}_{3\times2}\left[\overline{Q}^k\right]_{2\times2}[T]_{2\times3} \text{ it can be written as, } [D] = \begin{bmatrix} \overline{Q}_{11} & z\overline{Q}_{11} & 0 \\ z\overline{Q}_{11} & z^2\overline{Q}_{11} & 0 \\ 0 & 0 & \overline{Q}_{55} \end{bmatrix} \tag{13}$$

It can further be expressed as

$$[D] = b \times \sum_{k=1}^{\mathrm{NL}} \int_{z_{k-1}}^{z_k} [T]^{\mathrm{T}}\left[\overline{Q}^k\right][T]\mathrm{d}z = \begin{bmatrix} A_1 & B_1 & 0 \\ B_1 & E_1 & 0 \\ 0 & 0 & S_1 \end{bmatrix}_{3\times3} \tag{14}$$

where

$$(A_1, B_1, E_1) = b \times \sum_{k=1}^{\mathrm{NL}} \int_{z_{k-1}}^{z_k} \overline{Q}_{11}^k \left(1, z, z^2\right) \mathrm{d}z \text{ and } S_1 = b \times \mathrm{K} \sum_{k=1}^{\mathrm{NL}} \int_{z_{k-1}}^{z_k} \overline{Q}_{55}^k \mathrm{d}z \quad (15)$$

where (A_1, B_1, E_1, S_1) are stiffness coefficients, NL is number of layer. K is shear correction factor and its value is 0.833 for rectangular cross-section [12].

3 Finite Element Formulation

In this study, a C^0 higher-order cubic finite element is used. Every element has hence four nodes which are equally spaced with three DOF per node and are used to interpolate both, displacement field as well as geometric coordinates.

The trial function can be written as

$$\{\Delta\} = \sum_{i=1}^{Z} N_i \{\Delta_i\} \text{ and } \{\Delta\} = \left\{ u_0 \; w_0 \; \phi \right\}^{\mathrm{T}} \quad (16)$$

where Z = total number of nodes per element, N_i = shape functions for ith node.

The shape functions of higher-order cubic element can be written as

$$\left.\begin{array}{l} N_1 = -\frac{9}{16}(\xi - 1)\left(\xi - \frac{1}{3}\right)\left(\xi + \frac{1}{3}\right), \; N_2 = \frac{27}{16}(\xi - 1)(\xi + 1)\left(\xi - \frac{1}{3}\right), \\ N_3 = -\frac{27}{16}(\xi - 1)(\xi + 1)\left(\xi + \frac{1}{3}\right), \; N_4 = \frac{9}{16}(\xi + 1)\left(\xi - \frac{1}{3}\right)\left(\xi + \frac{1}{3}\right) \end{array}\right\} \quad (17)$$

The strains are related to displacement by strain–displacement matrix $[B]$ as,

$$[B] = [L][N] \quad (18)$$

where $[N]$ is given by,

$$[N] = \begin{bmatrix} N_{u_0} \\ N_{w_0} \\ N_{\phi} \end{bmatrix} = \begin{bmatrix} N_1 & 0 & 0 & N_2 & 0 & 0 & N_3 & 0 & 0 & N_4 & 0 & 0 \\ 0 & N_1 & 0 & 0 & N_2 & 0 & 0 & N_3 & 0 & 0 & N_4 & 0 \\ 0 & 0 & N_1 & 0 & 0 & N_2 & 0 & 0 & N_3 & 0 & 0 & N_4 \end{bmatrix} \quad (19)$$

Elemental stiffness matrix and mass matrix is computed by transforming the physical coordinate system $(x, 0)$ into natural coordinate system $(\xi, 0)$ and can be written as,

$$[K] = \int_{-1}^{1} [B]^{\mathrm{T}}[D][B] \det[J] \mathrm{d}\xi \text{ and } [M] = \int_{-1}^{1} [N]^{\mathrm{T}} \rho [I][N] \det[J] \mathrm{d}\xi \quad (20)$$

where $[J]$ is the Jacobian matrix. ρ is the density of the material and $[I]$ is mass coefficients matrix and can be expressed as,

$$[I] = \begin{bmatrix} I_0 & 0 & I_1 \\ 0 & I_0 & 0 \\ I_1 & 0 & I_2 \end{bmatrix} \text{ where } (I_0, I_1, I_2) = b \sum_{k=1}^{\mathrm{NL}} \int_{z_{k-1}}^{z_k} \left(1, z, z^2\right) \mathrm{d}z \tag{21}$$

The moving load is a concentrated mass acting at a point on layered composite Timoshenko beam and the load (f_m) is moving from left to right (see Fig. 1). The point load due to concentrated mass can be represented as,

$$f_\mathrm{m}(x, t) = W_\mathrm{m} \delta[x - x_\mathrm{m}(t)] \text{ and } W_\mathrm{m} = -mg \tag{22}$$

where δ is Dirac delta function and W_m is the weight of moving mass, m is mass and g is the gravitational acceleration and its value is 9.81 m/s^2. v_m is moving load velocity in m/s. x_m is mass location at time t and is given by

$$x_\mathrm{m}(t) = v_\mathrm{m} t \tag{23}$$

At any given time t mass is located at l_m on element e. Mass location relative to element length L_e can be represented as

$$\eta(t) = l_\mathrm{m}/L_\mathrm{e} \tag{24}$$

The discretized force vector can be written as

$$f_\mathrm{m}(t) = W_\mathrm{m} N_{w_0}(\eta(t)) \tag{25}$$

4 Solution Technique

MPR-MPA is an explicit second-order accurate Linear Multistep method (LMS). MPR-MPA is a time-stepping algorithm that defines the derivatives with respect to time. All LMS algorithms including MPR-MPA and Newmark method are found within GSSSS family of algorithms.

Equation of motion can be expressed as

$$M\ddot{u} + C\dot{u} + Ku = f_\mathrm{m}(t) \tag{26}$$

Initial conditions are

$$\dot{u}(0) = \dot{u}_0 \text{ and } u(0) = u_0 \tag{27}$$

MPR-MPA algorithm is defined by

$$\left.\begin{aligned}(M+\frac{1}{2}C\Delta t+\frac{1}{4}K\Delta t^2)\Delta\ddot{u} &= -M\ddot{u}_n - C(\dot{u}_n+\frac{1}{2}\ddot{u}_n\Delta t)\\ &- K(u_n+\frac{1}{2}\dot{u}_n\Delta t+\frac{1}{4}\ddot{u}_n\Delta t^2)+\frac{1}{2}(f_n+f_{n+1})\end{aligned}\right\} \tag{28}$$

$$\left.\begin{aligned}u_{n+1} &= u_n+\dot{u}_n\Delta t+\frac{1}{2}\ddot{u}_n\Delta t^2+\frac{1}{2}\Delta\ddot{u}\Delta t^2\\ \dot{u}_{n+1} &= \dot{u}_n+\ddot{u}_n\Delta t+\frac{1}{2}\Delta\ddot{u}\Delta t \text{ and } \ddot{u}_{n+1}=\ddot{u}_n+\Delta\ddot{u}\end{aligned}\right\} \tag{29}$$

5 Results and Discussion

Ratio of maximum dynamic deflection to maximum static deflection is known as Dynamic Magnification Factor (*DMF*). *SP* is the Speed Parameter, which is ratio of fundamental time period to actual time taken by the moving load to travel the entire beam length (T_f/T).

The present results using FEA and MPR-MPA algorithm shows good agreement with the published results. Data 1 of Table 1 is used in Table 2. At critical velocity v_{cr}, $T_f = T$ so *SP* will be 1. Maximum *DMF* of simply supported beam is at $SP = 1.25$. At low speeds, maximum dynamic displacement is nearly equal to maximum static displacement but at higher speeds, it is 170% of the maximum static displacement. In case of extremely higher speeds when $SP > 1.25$, the *DMF* starts decreasing so also the maximum dynamic displacement. The critical velocity and fundamental time period are calculated by

$$v_{cr} = (\omega_1 l)/(i\pi),\ \ i = 1, 2, 3\ldots \text{ and } T_f = l/v_{cr} \tag{30}$$

where ω_1 is the first fundamental frequency of the beam.

Data 2 of Table 1 is used in Table 3. The maximum *DMF* of simply supported layered composite beam occurs between $SP = 1.2$ and 1.3. The $v_{cr} = 311.2$ m/s

Table 1 Required input data

No.	Description	References
Data 1	$f_m = 4.45$ N, $l = 0.1016$ m, $b = h = 0.00635$ m, $E = 2.068 \times 10^{11}$ N/m^2, $\rho = 10{,}686.9$ kg/m^3, $\nu = 0.3$	[4]
Data 2	$f_m = 4.45$ N, $l = 0.1016$ m, $b = 0.00635$ m, $h = 0.00745$ m, $E_{11} = 1.448 \times 10^{11}$ Pa, $E_{22} = 9.65 \times 10^9$ Pa, $G_{12} = G_{13} = 4.136 \times 10^9$ Pa, $G_{23} = 3.447 \times 10^9$ Pa, $\rho = 1389.297$ kg/m^3, $\nu_{12} = 0.25$	[4]

Table 2 *DMF* at mid-span of simply supported isotropic beam (20 time steps are used)

SP	v_m (m/s)	Present	FEM [8]	FEM [4]	FEM [13][a]	SIM [14]	FEM [15]	Analytical [16]	Analytical [17]
0.125	15.6	1.054	1.053	1.063	1.049	1.042	1.055	–	1.025
0.250	31.2	1.141	1.139	1.151	1.121	1.082	1.112	1.110	1.121
0.500	62.4	1.270	1.267	1.281	1.266	1.266	1.252	1.240	1.258
0.750	93.6	1.571	1.569	1.586	–	–	–	–	1.572
1.000	124.8	1.687	1.687	1.704	1.703	1.662	1.700	1.680	1.701
1.250	156.0	1.710	1.711	1.727	–	–	–	–	1.719
1.500	187.2	1.679	1.681	–	–	–	–	–	–
2.000	250.0	1.524	1.528	1.542	1.540	1.518	1.540	1.540	1.548

SIM: Structural Impedence Method
[a]Using nonconforming plate element with 25 time steps

Table 3 *DMF* at mid-span of symmetric $[\theta/-\theta/-\theta/\theta]$ angle-ply simply supported AS/3501-6 graphite-epoxy beam (50 time steps are used for better convergence)

SP	0.13	0.26	0.52	0.78	1	1.3	1.56	1.82
v_{m}	40.9	81.8	163.6	245.4	311.2	409	490.8	572.6
0°	1.054	1.132	1.270	1.565	1.636	1.655	1.627	1.561
SP	0.125	0.25	0.50	0.75	1	1.25	1.50	2
v_{m}	15	30	60	90	120	150	180	240
30°	1.058	1.129	1.263	1.575	1.697	1.715	1.683	1.532
SP	0.12	0.24	0.48	0.72	1	1.2	1.44	1.68
v_{m}	10.2	20.4	40.8	61.2	87	102	122.4	142.8
60°	1.058	1.093	1.202	1.531	1.700	1.724	1.704	1.658
SP	0.12	0.24	0.48	0.72	1	1.2	1.44	1.68
v_{m}	10.2	20.4	40.8	61.2	86.8	102	122.4	142.8
90°	1.059	1.094	1.203	1.532	1.700	1.723	1.704	1.657

is maximum for 0° angle-ply beams while it is minimum, $v_{\mathrm{cr}} = 86.8$ m/s at 90° angle-ply beams. As the ply orientation increases, the critical velocity decreases. The maximum *DMF* is between 1.655 and 1.724 while 1.724 is for the 60° angle-ply beams. Stiffness response of 0° angle-ply beams is maximum in comparison to any other ply orientation.

Data 2 of Table 1 is used for the graphs (see Fig. 2). It can be seen from the graphs that maximum static displacement occurs at center of beam, but the maximum dynamic displacement occurs at nearly three quarters from the left end of the beam. This is due to the delay in time and this time delay increases as v_{m} increases. This time delay is more beyond the critical nonlinear region as compared to below the critical linear region. The pattern of graphs is same for all simply supported isotropic and layered composite beam at any velocity and ply scheme.

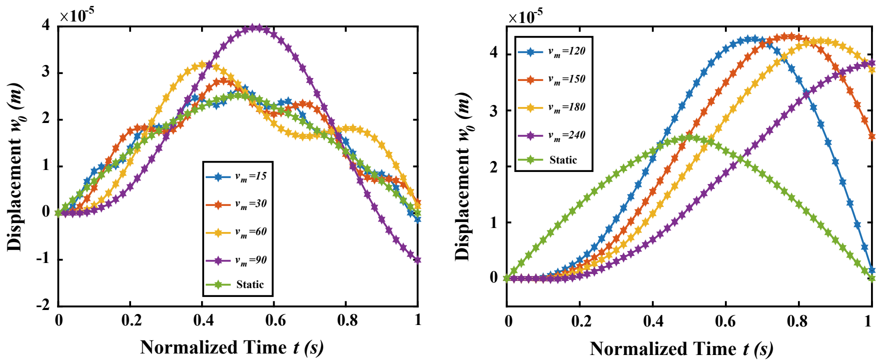

Fig. 2 Maximum transverse displacement w_0 (m) versus Normalized time t (s) at mid-span of symmetric [30/−30/−30/30] angle-ply simply supported beams

6 Conclusions

FEM along with MPR-MPA explicit numerical time discretization technique is robust enough to handle moving load structural dynamic problems. At very low speed, maximum dynamic deflection is almost equal to static deflection but at higher speeds, maximum dynamic deflection is greater than 170% of static deflection. Initially as speed increases, the dynamic magnification factor and maximum deflection increase but at very high speed, the dynamic magnification factor and the maximum deflection decrease. Layered composite beam with symmetric [0/−0/−0/0] angle-ply lamination scheme shows a much stiffer response as compared to any other angle-ply lamination scheme. It hence contributes to minimum transverse deflection. The maximum *DMF* of simply supported beams occurs in the range $SP = 1.2$–1.3. The maximum dynamic displacement occurs at nearly three-quarter of the beam due to delay in time and this time delay increases as the v_{m} increases. Due to high strength, low density, long term durability, greater corrosion and fatigue resistance, the laminated composite material specially graphite-epoxy beams can be used in bridge structures instead of conventional ones.

References

1. Krylov AN (1905) Mathematical collection of papers of the Academy of Sciences, vol 61. Saint Petersburg, Russia
2. Timoshenko SP (1908) Forced vibration of prismatic bars. Izvestiya Kievskogo Politekhnicheskogo Instituta, Russia
3. Fryba L (1972) Vibration of solids and structures under moving loads. Noordhoff International Publishing, Groningen, Netherland
4. Kadivar MH, Mohebpour SR (1998) Finite element dynamic analysis of unsymmetric composite laminated beams with shear effect and rotary inertia under the action of moving loads. Finite Elem Anal Des 29:259–273
5. Zibdeh HS, Abu Hilal M (2003) Stochastic vibration of laminated composite coated beam traversed by a random moving load. Eng Struct 25:397–404
6. Kavipurapu PK (2005) Forced vibration and hygrothermal analysis of composite laminated beams under the action of moving loads. West Virginia University, Morgantown, West Virginia
7. Kiral Z, Kiral BG (2008) Dynamic analysis of a symmetric laminated composite beam subjected to a moving load with constant velocity. J Reinf Plast Compos 27:19–32
8. Mohebpour SR, Fiouz AR, Ahmadzadeh AA (2011) Dynamic investigation of laminated composite beams with shear and rotary inertia effect subjected to the moving oscillators using finite element method. Compos Struct 93:1118–1126
9. Kahya V (2012) Dynamic analysis of laminated composite beams under moving loads using finite element method. Nucl Eng Des 243:41–48
10. Tao C, Fu Y, Dai HL (2016) Nonlinear dynamic analysis of fiber metal laminated beams subjected to moving loads in thermal environment. Compos Struct 140:410–416
11. Chen Y, Fu Y, Zhong J, Tao C (2017) Nonlinear dynamic responses of fiber metal laminated beam subjected to moving harmonic loads resting on tensionless elastic foundation. Compos B 131:253–259
12. Cowper GR (1966) The shear coefficient in Timoshenko's beam theory. ASME 335–340
13. Taheri MR, Ting EC (1990) Dynamic response of plates to moving loads finite element method. Comput Struct 34:509–521

14. Taheri MR, Ting EC (1989) Dynamic response of plate to moving loads structural impedence method. Comput Struct 33:1379–1393
15. Yoshida DM, Weaver W (1971) Finite element analysis of beams and plates with moving loads. IABSE 31:179–195
16. Filho FV (1966) Dynamic influence lines of beams and frames. J Struct Div 371–386
17. Meirovitch L (1967) Analytical methods in vibrations. The Macmillan Company, New York

Demystifying Fractal Analysis of Thin Films: A Reference for Thin Film Deposition Processes

F. M. Mwema, Esther T. Akinlabi, and O. P. Oladijo

Abstract In this article, a variety of synthetic (or simulated) surfaces of various morphologies of thin films and their fractal analyses are presented. Similar scaling factors have been used to generate the synthetic images in Gwydion™ software. The surfaces are based on the actual morphologies arising from various thin film deposition techniques. Using actual thin films of CdTe deposited by radio-frequency (RF) sputtering technique, we have successfully shown that the fractal analyses on the synthetic surfaces can be used to explain, theoretically, the development and self-affinity of various thin films. Based on this validation, the results of fractal analyses on different morphologies of thin films were generated using different fractal methods in Gwydion software. The methods used here include Minkowski functionals, height-to-height correlation, areal autocorrelation, and power spectral density functions. The article will be a good resource for explaining the fractal behavior and morphology of thin films arising from different deposition methods.

Keywords Correlation · Fractal · Minkowski · Surfaces · Thin films

1 Introduction

During the deposition process of thin films, there are different morphologies of structures formed depending on the deposition type, process parameters, films, and substrate types [1]. Scanning probe microscopy (SPM) techniques such as atomic force microscope (AFM) are used to study the surface morphology of various thin films and coatings [2–5]. The micrographs obtained from the SPM techniques are used to undertake roughness analyses such as statistical [6, 7] and fractal measurements [8–12]. Fractal methods offer a detailed description of lateral roughness [13] and the nature of the surface morphology can be captured [14]. Although fractal

F. M. Mwema (✉) · E. T. Akinlabi · O. P. Oladijo
University of Johannesburg, Johannesburg, South Africa
e-mail: fredrick.mwema@dkut.ac.ke

O. P. Oladijo
Botswana International University of Science and Technology, Palapye, Botswana

E. T. Akinlabi et al. (eds.), *Trends in Mechanical and Biomedical Design*, Lecture Notes in Mechanical Engineering,
https://doi.org/10.1007/978-981-15-4488-0_19

characterization is widely reported in the literature [6, 12, 15–17], very little is reported on the relationship between the fractal measurements and the structure type/morphologies of the films. Therefore, the purpose of this work is to generate fractal profiles (using Minkowski functionals, autocorrelation, height-height correlation, and power spectral density functions) based on theoretical/synthetic surfaces of different morphologies.

2 Methods

Various synthetic morphologies of thin films were produced using scanning probe microscopy (SPM) software Gwydion (Fig. 1). These films depict different structural types that are obtained through various deposition processes such as sputtering and thermal spray. These structures are columnar, ballistic, fibrous, and pile-up structures (Fig. 1) and represent some of the most common morphologies observed in thin films. The process of creating synthetic (simulated) surfaces in Gwydion software are described elsewhere [18, 19]. All the images were single-layer, with a maximum

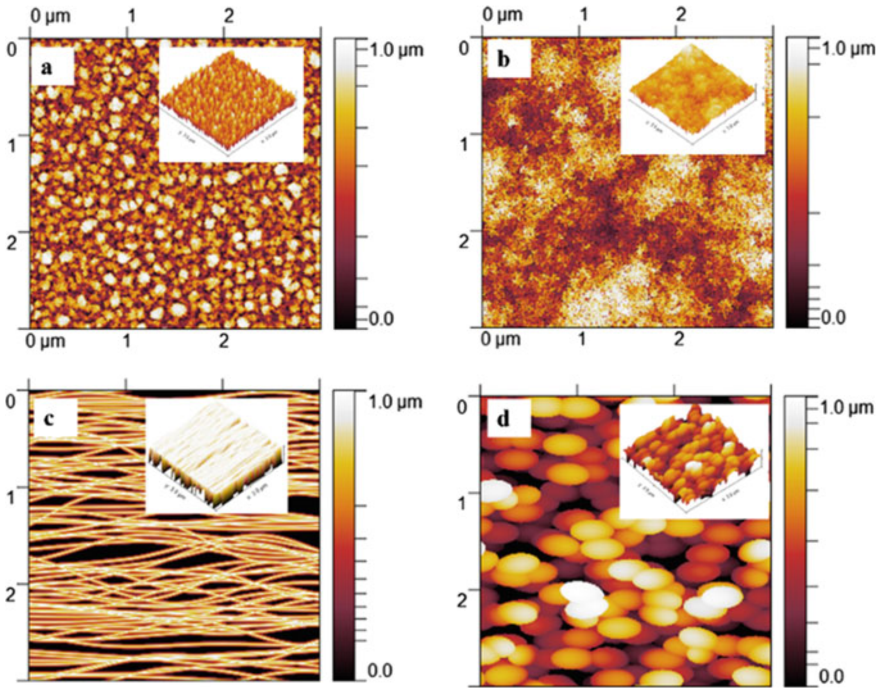

Fig. 1 Illustrating simulated surfaces of thin films consisting of various structural morphologies **a** columnar **b** ballistic **c** fibrous, and **d** pile-up particles. Corresponding 3D images are shown as insets on each image

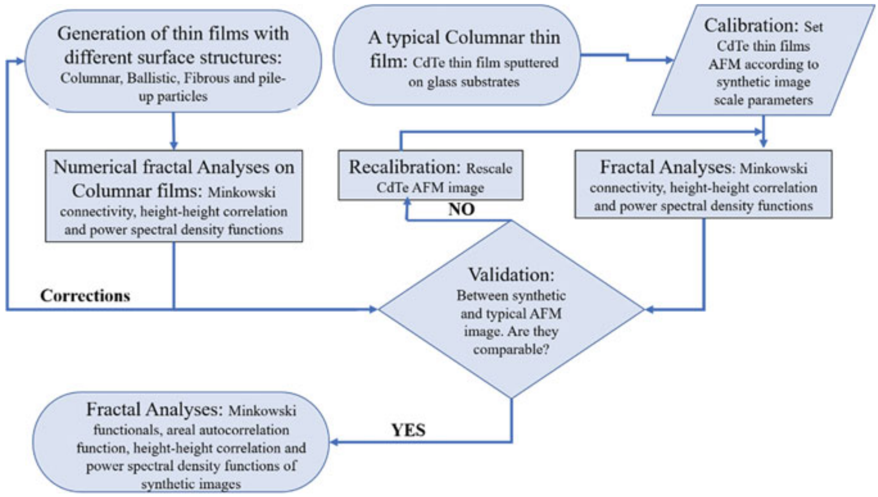

Fig. 2 Flowchart illustrating the image and fractal analyses procedures

height of 1000 nm and a scan area of 3 × 3 μm^2. The fractal analyses of the simulated AFM images were undertaken according to the flowchart in Fig. 2. To validate the simulated fractal analyses, fractal values of a typical columnar AFM of CdTe thin films sputtered on glass substrates (Fig. 3) were computed and compared to the simulations. This process was iterative until comparable results were obtained (e.g., Fig. 4). Subsequently, all computations were conducted for the other simulated structure and results presented in Table 1.

3 Results and Discussions

The results of the fractal analyses of the simulated AFM surfaces of thin films are presented in Table 1. A short description of the results in Table 1 is as follows:

- Minkowski connectivity (X): Negative values dominate the X for columnar, ballistic, and fibrous structures whereas positive dominates for pile-up particles. The profiles vary with the type of structures.
- Minkowski boundary: There are significant differences; while columnar and ballistic tend to nearly Gaussian profiles, the maximum values of boundary lengths for fibrous, and pile-up are skewed right and left, respectively.
- Minkowski volume: The profiles for columnar, ballistic and pile-up particles are symmetrical about $V = 0.5$, and exhibit S-shape [11, 20, 23]. The fibrous structures are asymmetrical and exhibit quarter-circle shaped Minkowski volume.
- Power spectral density: For columnar surface structures, the profile has a flat region at low frequencies and linearly decreasing PSD at high frequency with

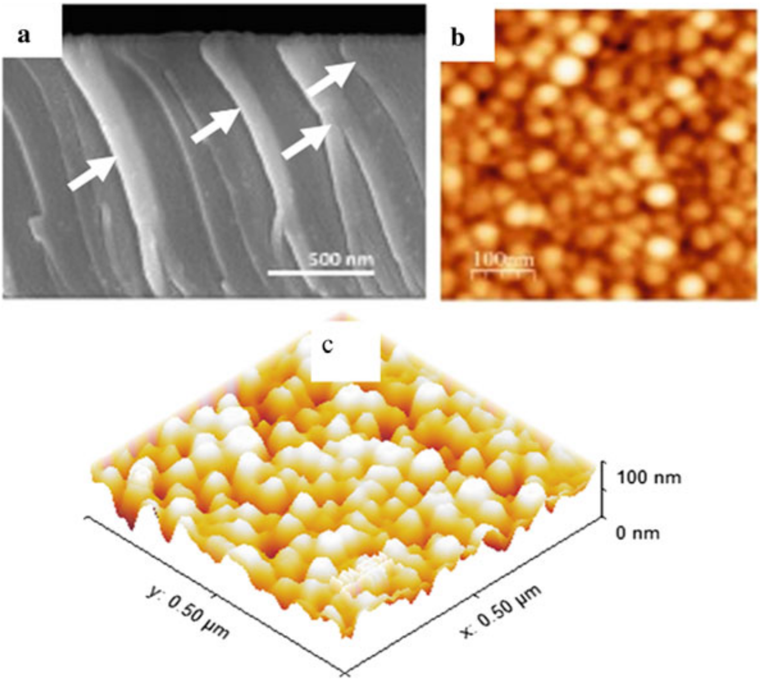

Fig. 3 **a** SEM micrograph along the cross-section of CdTe thin films deposited by RF magnetron sputtering. The white arrows show columnar structures of the films perpendicular to the substrate. **b** Showing the AFM image (scan area of $0.5 \times 0.5\ \mu m^2$) at the top surface of the films. Recalibrated 3D AFM image of the CdTe films. Obtained from Camacho-Espinosa et al. [22] under open access creative commons

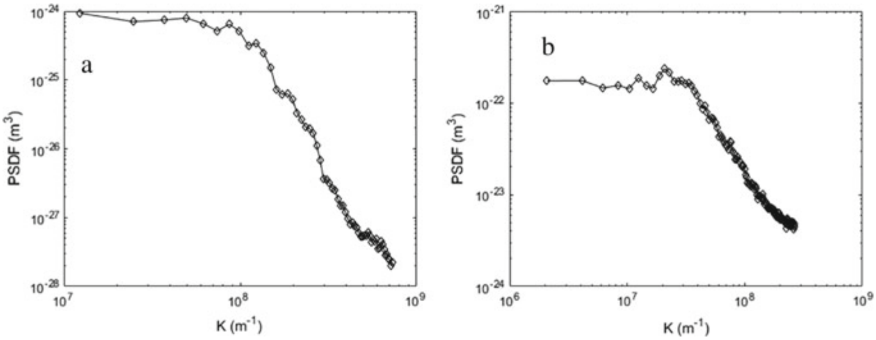

Fig. 4 Bi-logarithmic plots for power spectral density (PSDF) against the spatial frequency (k) of (**a**) typical columnar CdTe films deposited on glass substrates and **b** the corresponding simulated profile plot. The shapes of the profiles are comparable and are characterized by withers at the transition region between the flat and the linear areas of the PSDF profile

Table 1 Illustrating various fractal analyses results from different simulated (synthetic) structures of thin films

Analysis	Type of structure for thin films			
	Columnar	Ballistic	Fibrous	Pile-up particles
	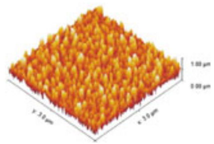	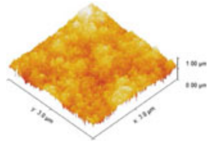	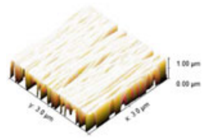	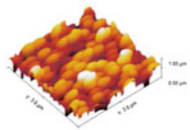
Minkowski connectivity	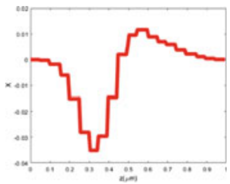	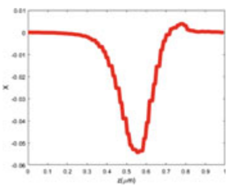	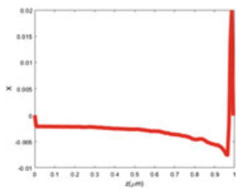	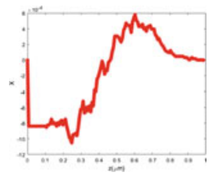
Minkowski boundary	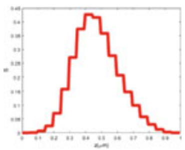	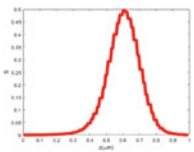	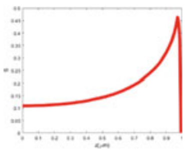	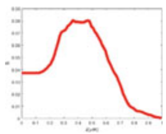

(continued)

Table 1 (continued)

Analysis	Type of structure for thin films			
	Columnar	Ballistic	Fibrous	Pile-up particles
Minkowski volume	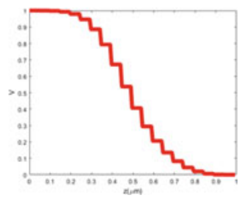	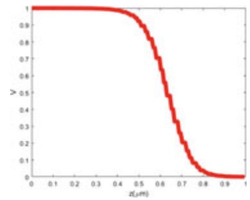	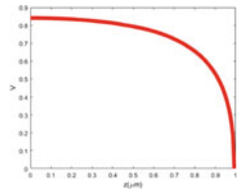	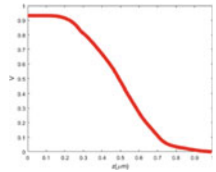
Power spectral density function	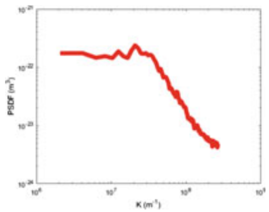	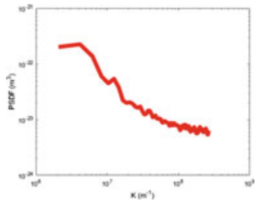	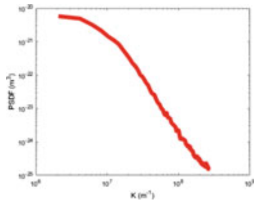	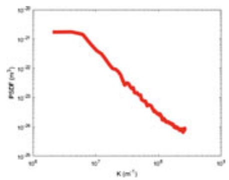

(continued)

Table 1 (continued)

Analysis	Type of structure for thin films			
	Columnar	Ballistic	Fibrous	Pile-up particles
Areal autocorrelation function	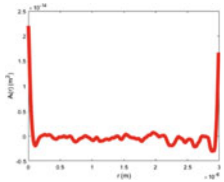	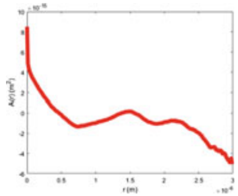	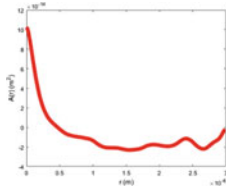	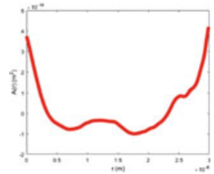
Height-height correlation/structure function	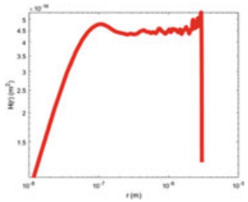	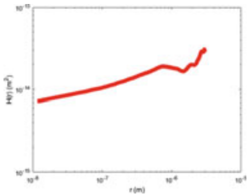	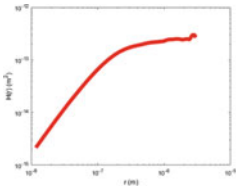	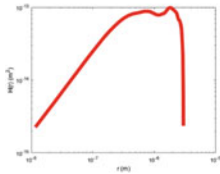

withers at the transition point [21, 24, 25]. For ballistic surfaces, the 1-d PSD profile consists of flat region and nonlinearly decreasing PSD. The flat region is not clear in fibrous surfaces whereas the pile-up surfaces have distinct flat and linear regions at low and high spatial frequencies respectively.

- Areal autocorrelation (ACF): For columnar surfaces, the profile exhibit oscillatory behavior with decreasing and increasing values at low and high shifts respectively. The ACF decreases sharply to nearly $r = 1.0$ and then nearly remains constant for ballistic and fibrous. For pile-up surfaces, the ACF profile exhibit *U*-shape.
- Height-height correlation (HCF): The HCF increases with r for all surfaces up to certain values. At very large *r* (mounded surface characteristics) oscillatory behavior of the profile was observed for columnar and ballistic surface structures [12, 23, 25]. The flat region (at large r) is not distinct for ballistic surfaces. The HCF decreases at nearly constant r at the end of the flat region for columnar and pile-up surfaces.

4 Conclusion

The profile plots of the most common fractal analyses of thin film surfaces of different synthetic morphologies have been presented. The surfaces were generated using Gwydion software and a typical validation of the columnar structure showed that the software provides a good approximation of deposited films. Profiles of Minkowski functionals, autocorrelation, height-height correlation and power spectral density functions of the synthetic morphologies (columnar, ballistic, fibrous and pile-up particles) presented in Table 1 will be a useful reference in relating the fractal results to the films' deposition techniques and conditions.

References

1. Mwema FM, Oladijo OP, Akinlabi SA, Akinlabi ET (2018) Properties of physically deposited thin aluminium film coatings: a review. J Alloy Compd 747:306–323. https://doi.org/10.1016/j.jallcom.2018.03.006
2. Eaton P, West P (2010) Atomic force microscopy. Oxford University Press Inc., New York
3. Mwema FM, Akinlabi ET, Oladijo OP (2019) Correction of artifacts and optimization of atomic force microscopy imaging: a case of thin aluminum films for prosthetic applications. In: Kumar K, Paulo Davim J (eds) Design, development, and optimization of bio-mechatronic engineering products, IGI Global, pp 158–179. https://doi.org/10.4018/978-1-5225-8235-9.ch007
4. Kwoka M, Ottaviano L, Szuber J (2007) AFM study of the surface morphology of L-CVD SnO_2 thin films. Thin solid films 515:8328–8331. https://doi.org/10.1016/j.tsf.2007.03.035
5. Sobola D, Ţălu S, Solaymani S, Grmela L (2017) Influence of scanning rate on quality of AFM image: study of surface statistical metrics. Microsc Res Tech 80(12):1328–1336. https://doi.org/10.1002/jemt.22945

6. Erinosho MF, Akinlabi ET, Johnson OT (2018) Characterization of surface roughness of laser deposited titanium alloy and copper using AFM. Appl Surf Sci 435:393–397. https://doi.org/10.1016/j.apsusc.2017.11.131
7. Mwema FM, Oladijo OP, Sathiaraj TS, Akinlabi ET (2018) Atomic force microscopy analysis of surface topography of pure thin aluminium films. Mater Res Express 5(4):1–15. https://doi.org/10.1088/2053-1591/aabe1b
8. Stach S, Sapota W, Ţălu S, Ahmadpourian A, Luna C, Ghobadi N, Arman A, Ganji A (2017) 3-D surface stereometry studies of sputtered TiN thin films obtained at different substrate temperatures. J Mater Sci Mater Electron 28(2):2113–2122. https://doi.org/10.1007/s10854-016-5774-9
9. Ţălu S, Stach S, Raoufi D, Hosseinpanahi F (2015) Film thickness effect on fractality of tin-doped In2O3 thin films. Electron Mater Lett 11(5):749–757. https://doi.org/10.1007/s13391-015-4280-1
10. Ţălu S, Bramowicz M, Kulesza S, Solaymani S (2018) Topographic characterization of thin film field-effect transistors of 2,6-diphenyl anthracene (DPA) by fractal and AFM analysis. Mater Sci Semicond Process 79:144–152. https://doi.org/10.1016/j.mssp.2018.02.008
11. Salerno M, Banzato M (2005) Minkowski measures for image analysis in scanning probe microscopy. Microsc Anal 19(4):13–15
12. Yadav RP, Kumar M, Mittal AK, Dwivedi S, Pandey AC (2014) On the scaling law analysis of nanodimensional LiF thin film surfaces. Mater Lett 126:123–125. https://doi.org/10.1016/j.matlet.2014.04.046
13. Yadav RP, Dwivedi S, Mittal AK, Kumar M, Pandey AC (2012) Fractal and multifractal analysis of LiF thin film surface. Appl Surf Sci 261:547–553. https://doi.org/10.1016/j.apsusc.2012.08.053
14. Senthilkumar M, Sahoo NK, Thakur S, Tokas RB (2005) Characterization of microroughness parameters in gadolinium oxide thin films: A study based on extended power spectral density analyses. Appl Surf Sci 252(5):1608–1619. https://doi.org/10.1016/j.apsusc.2005.02.122
15. Dallaeva D, Talu S, Stach S, Skarvada P, Tomanek P, Grmela L (2014) AFM imaging and fractal analysis of surface roughness of AlN epilayers on sapphire substrates. Appl Surf Sci 312:81–86. https://doi.org/10.1016/j.apsusc.2014.05.086
16. Starodubtseva MN, Starodubtsev IE, Starodubtsev EG (2017) Novel fractal characteristic of atomic force microscopy images. Micron 96:96–102. https://doi.org/10.1016/j.micron.2017.02.009
17. Raoufi D (2010) Fractal analyses of ITO thin films: a study based on power spectral density. Phys B Condens Matter 405(1):451–455. https://doi.org/10.1016/j.physb.2009.09.005
18. Nečas D, Klapetek P (2012) Gwyddion: an open-source software for SPM data analysis. Cent Eur J Phys 10(1):181–188. https://doi.org/10.2478/s11534-011-0096-2
19. Klapetek P, Necas D, Anderson C (2013) Gwyddion user guide 1–122. http://gwyddion.net/download/user-guide/gwyddion-user-guide-en.pdf
20. Mwema FM, Akinlabi ET, Oladijo OP, Majumdar JD (2019) Effect of varying low substrate temperature on sputtered aluminium films. Mater Res Express 6(5):056404. https://doi.org/10.1088/2053-1591/ab014a
21. Mwema FM, Oladijo OP, Akinlabi ET (2018) Effect of substrate temperature on aluminium thin films prepared by RF-magnetron sputtering. Mater Today Proc 5(9/3):20464–20473. https://doi.org/10.1016/j.matpr.2018.06.423
22. Camach-Espinosa E, Rosendo E, Díaz T, Oliva I, Rejon V, Peria J (2014) Effects of temperature and deposition time on the RF- sputtered CdTe films preparation. Superf. y vacío 27(1):15–19. http://smctsm.org.mx/ojs/index.php/SyV/article/view/148
23. Mwema FM, Akinlabi ET, Oladijo OP (2019) Fractal analysis of hillocks: a case of RF sputtered aluminum thin films. Appl Surf Sci 489:614–623. https://doi.org/10.1016/J.APSUSC.2019.05.340
24. Shakoury R, Rezaee S, Mwema FM, Luna C, Ghosh K, Jurečka S, Ţălu S, Arman A, Korpi AG (2020) Multifractal and optical bandgap characterization of Ta_2O_5 thin films deposited by electron gun method. Opt Quantum Electron 52(2). https://doi.org/10.1007/S11082-019-2173-5

25. Mwema FM, Akinlabi ET, Oladijo OP (2020) Fractal analysis of thin films surfaces: a brief overview. In: Awang M, Emamian S, Yusof F (eds) Advances in material sciences and engineering. Lecture notes in mechanical engineering. Springer, Singapore. https://doi.org/10.1007/978-981-13-8297-0_28

Dynamic Analysis of Rectangular Aluminum Plate Under Transverse Loading Using Finite Difference Algorithm

Michael C. Agarana, Esther T. Akinlabi, and Michael O. Ikumapayi

Abstract Aluminum is one of the most used mechanical elements in Manufacturing. This paper focuses on the analysis of its dynamic response of an Aluminum plate, under a moving load. The moving load, in this case, is assumed to be partially distributed. Rotatory inertia and damping effects were neglected, while the effect of shear deformation was put into consideration. Also, the rectangular Aluminum plate was supported by a simple form of foundation. A numerical algorithm–Finite difference was adopted in solving the mathematical model governing the deflection of plates under moving load under consideration. It was observed, among other results, that the maximum amplitude of the deflection of the Aluminum plate is a function of the contact area of the load and velocity of the moving load, which is in line with the results in the literature.

Keywords Stiffness · Homogeneous isotropic materials · Analytical investigation · Cross sections

1 Introduction

Loads moving on flat materials are a common occurrence in Mechanical Engineering, Civil Engineering and related disciplines. In building and geotechnical structures, also, plate analysis is often carried out, especially those resting on a subgrade [1].

M. C. Agarana (✉)
Department of Mathematics, Covenant University, Ota, Nigeria
e-mail: michael.agarana@covenantuniversity.edu.ng

E. T. Akinlabi · M. O. Ikumapayi
Department of Mechanical Engineering Science, University of Johannesburg, Johannesburg, South Africa
e-mail: etakinlabi@gmail.com

M. O. Ikumapayi
e-mail: oikumapayi@uj.ac.za

E. T. Akinlabi
Department of Mechanical Engineering, Covenant University, Ota, Nigeria

E. T. Akinlabi et al. (eds.), *Trends in Mechanical and Biomedical Design*,
Lecture Notes in Mechanical Engineering,
https://doi.org/10.1007/978-981-15-4488-0_20

In this study, the situation is modelled as dynamic response of a rectangular plate supported by an elastic foundation. The mechanical behaviour of the foundation and the form of interaction between it and the plate was analyzed. In Winkler model, unlike in Pasternak, it is assumed that the foundation consists of linear elastic springs that are closely spaced and independent of each other [2–4].

Aluminum is a decent conduit of power and heat. It is light and strong. It can be pounded into sheets (malleable) or maneuverer out into wires (ductile). It is an exceptionally receptive metal, in spite of the fact that it is not corrosive. Aluminum anticipates corrosion by framing a little, thin layer of aluminum oxide on its surface. This layer shields the metal by keeping oxygen from achieving it. Corrosion cannot happen without oxygen. In light of this thin layer, the reactivity of aluminum is not seen. Numerous things are made of aluminum. Quite a bit of it is utilized as a part of overhead electrical cables. It is additionally broadly utilized as a part of window casings and airplane and ship bodies. It is found at home as pans, soda pop jars and cooking foil. Aluminum is likewise used to coat auto headlamps and smaller plates [5].

Transverse loading or force is a force applied vertically to the plane of the longitudinal axis of a configuration, an example is a wind load. In an elastic material, it causes it to bend and rebound from its original position, with inner tensile and compressive straining associated with the change in curvature of the material. Transverse force increases the slanting deflection [6].

Finite difference methods (FDM) are numerical methods for solving differential equations by approximating them with difference equations, in which finite differences approximate the derivatives. FDMs are thus discretization methods [7, 8]. This study adopted the finite difference algorithm to analyze the effect of the moving load on an aluminum rectangular plate resting on a elastic subgrade.

2 Formulation of Problem

An Aluminum plate, with a moving load and different boundary conditions, was considered. The load is relatively small, so its inertia can be neglected, and is traversing along the mid-space on the surface of the rectangular aluminum plate, supported by a Winkler foundation. The following assumptions were made: The rectangular Aluminum plate is of constant cross-section, the moving load traverses with a constant speed, the moving load is guided in such a way that it keeps contact with the plate throughout the motion, the plate is continuously supported by a Winkler foundation, the moving load is a partially distributed moving load, and that the rectangular Aluminum plate is elastic [8–10].

The governing equation is as follows [10–12]:

$$\frac{B\rho h^3}{12}\frac{\partial^3 \psi_x}{\partial x \partial t^2} + \frac{\partial^2 m_x}{\partial x^2} + \frac{\partial^2 m_{xy}}{\partial x \partial y}$$

$$+\frac{B\rho h^3}{12}\frac{\partial^3\psi_y}{\partial y\partial t^2}+\frac{\partial^2 m_y}{\partial y^2}+\frac{\partial^2 m_{xy}}{\partial x\partial y}-\rho h\frac{\partial^2 w}{\partial y^2}+kw$$
$$+m_f\frac{\partial^2 w}{\partial t^2}=p(x,y,t) \tag{1}$$

where ψ_x and ψ_y are local rotations in the x and y directions respectively, m_x and m_y are bending moments in the x and y directions, respectively, m_{xy} is the twisting moments, h and h_1 are thickness of the plate and load, respectively, ρ and ρL are the densities of the plate and the load per unit volume, respectively. $w(x, y, t)$ is the traverse displacement of the plate at time t, g is acceleration due to gravity. K is the foundation stiffness. Also, $B = B_x B_y$, where B_x and B_y are well-defined in papers [1, 2, 4]. The right-hand side of Eq. (1) which represents the applied force can be expressed as follows [12–14]:

$$p(x,y,t)=\frac{1}{\mu\varepsilon}\left[-M_L g-M_L\frac{\partial^2 w}{\partial t^2}\right]B \tag{2}$$

Substituting Eq. (2) into Eq. (1) and rearranging gives:

$$\frac{B\rho}{12}\left[h^3\left\{\frac{\partial^3\psi_x}{\partial x\partial t^2}+\frac{\partial^3\psi_y}{\partial_y\partial t^2}\right\}+Lh_1^3\left\{\frac{\partial^3\psi_x}{\partial x\partial t^2}+\frac{\partial^3\psi_y}{\partial_y\partial t^2}\right\}\right]+\frac{\partial^2 m_x}{\partial x^2}+2s\frac{\partial^2 m_{xy}}{\partial x\partial y}+\frac{\partial^2 m_y}{\partial y^2}$$
$$-\rho h\frac{\partial^2 w}{\partial y^2}+Kw+m_f\frac{\partial^2 w}{\partial t^2}=\frac{-M_L}{\mu\xi}\left[g+\frac{\partial^2 w}{\partial t^2}\right]B \tag{3}$$

Application of the boundary conditions to the non-dimensional form of Eq. (3) yields the equations that were solved. A simply supported rectangular Aluminum plate has been taken as an illustrative example. If the edge $y = 0$ of the Aluminum plate, the deflection w along this edge must be zero. Also, there are no bending moments along this edge, this makes it rotate freely with respect to the x-axis [15–17].

3 Solution Method

Equation (3) was solved using a numerical method based on the finite difference algorithm. This third-order partial differential equation was converted to first-order partial differential equations, then transformed into its equivalent algebraic form using finite difference method.

The finite difference definition of first-order partial derivative of a function $F(x, y, t)$, say, with respect to x, y and t, respectively, can be written as follows [18–20]:

$$\frac{\partial F}{\partial t}=\frac{1}{4r^*}\left[F^{K+1}_{i+1,j+1}+F^{K+1}_{i+1,j}+F^{K+1}_{i,j+1}+F^{K+1}_{i,j}-F^{K}_{i+1,j+1}-F^{K}_{i+1,j}-F^{K}_{i,j+1}-F^{K}_{i,j}\right] \tag{4}$$

$$\frac{\partial F}{\partial x} = \frac{1}{4h^*}\left[F_{i+1,j+1}^{K+1} + F_{i+1,j}^{K+1} - F_{i,j+1}^{K+1} - F_{i,j}^{K+1} + F_{i+1,j+1}^{K} + F_{i+1,j}^{K} - F_{i,j+1}^{K} - F_{i,j}^{K}\right] \quad (5)$$

$$\frac{\partial F}{\partial y} = \frac{1}{4k^*}\left[F_{i+1,j+1}^{K+1} + F_{i+1,j}^{K+1} - F_{i,j+1}^{K+1} - F_{i,j}^{K+1} + F_{i+1,j+1}^{K} + F_{i+1,j}^{K} - F_{i,j+1}^{K} - F_{i,j}^{K}\right] \quad (6)$$

where, F is the function value of the centre of a grid, which is well approximated by the average of its values at the grid nodes [20].

$$F\left(x + \frac{h^*}{2}, y + \frac{k^*}{2}, t + \frac{r^*}{2}\right) = \frac{1}{8}\left[F_{i+1,j+1}^{K+1} + F_{i+1,j}^{K+1} + F_{i,j+1}^{K+1} + F_{i,j}^{K+1} + F_{i+1,j+1}^{K} + F_{i+1,j}^{K} + F_{i,j+1}^{K} + F_{i,j}^{K}\right] \quad (7)$$

The above finite difference definition was used on Eq. (3) and a set of algebraic equations to be solved for the dependent variables emerged. These sets of algebraic equations were written in matrix form and solved using computer programs in conjunction with computer software—Octave.

4 Results Discussion

The numerical calculations were carried out for a simply supported rectangular Aluminum plate supported by a simple subgrade subjected to a moving load. Both rotatory and damping effects were neglected. The dynamic response of the Aluminum plate at various times, for a specific value of foundation stiffness, K, and different values of velocity, was evaluated and represented in Fig. 1. It can be seen that the maximum amplitude is highest at the highest value of velocity considered. This implies the higher the velocity the higher the deflection of the aluminum plate. Figure 2, on the other hand, shows the Comparison of the effect of different values of foundation stiffness, K, on the deflection of Aluminum plate resting on a subgrade when velocity u takes a particular value. It was observed that the higher the foundation stiffness the less the deflection of the aluminum plate. The effect of the contact area of the load with the plate was also considered; Fig. 3 shows the plotting for different values of contact area, A, as a function of time. It was observed that the

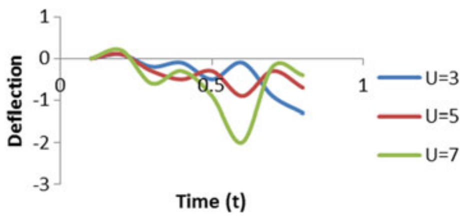

Fig. 1 Deflection of aluminum plate at $K = 200\ \text{Nm}^2$ and different values of velocity and time

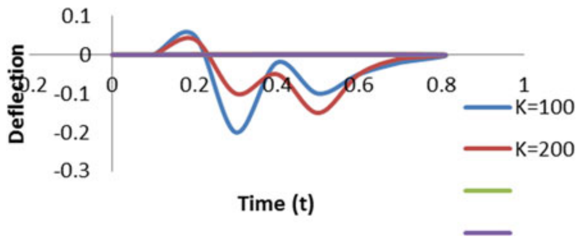

Fig. 2 Comparing the effect of $K = 100$ Nm^2 with $K = 200$ Nm^2 on the deflection of aluminum plate resting on Winkler foundation when velocity $u = 5.5$ (m/s)

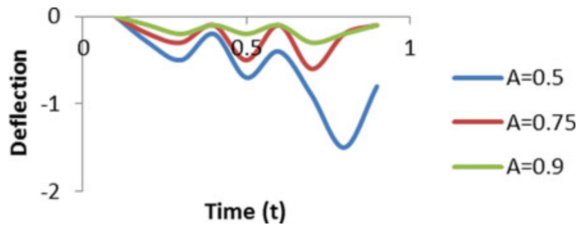

Fig. 3 Deflection of the plate at $K = 100$ Nm^2 and various value of contact area A (m^2) and time t (s)

response maximum amplitude of the rectangular Aluminum plate decreases with an increase in the contact area, A, for a fixed value of velocity U.

5 Conclusion

The structure of interest was Aluminum rectangular plate on an elastic subgrade, under the influence of a moving load. A numerical algorithm was adopted in solving the resulting first-order coupled partial differential equations obtained from the equations governing such simply supported Aluminum plate. The effect of rotating inertia and damping were neglected but the effect of shear deformation and gravitational force were considered. The elastic plate is the Aluminum rectangular plate. The study of such a problem is of practical importance because of its applications in Engineering. Numerical discussion of the deflection of the Aluminum plate on a subgrade was presented. Among other results, it was observed that the velocity, contact area of the load with the plate, foundation stiffness and the material properties of Aluminum, affect the deflection of the plate under consideration, as a partially distributed load moves on it. In Fig. 1, it can be seen that the maximum amplitude of the deflection occurred when the highest value of velocity; as the velocity increases the maximum amplitude also increases. Figure 2 shows that the maximum amplitude of the deflection increases as K decreases in value. In the figure, it can clearly be seen that the higher the value of the contact area the lower the maximum amplitude of the deflection. Some assumptions were taken for brevity sake, The study has contributed to scientific knowledge by showing that velocity, contact area of the load with the Aluminum plate, the material properties of Aluminum and the subgrade, on which the Aluminum plate rests, have significant effect on the deflection of the Aluminum plate to a uniform partially distributed moving load.

Acknowledgements The authors hereby acknowledge the supports of Covenant University and the University of Johannesburg towards the successful completion of this study.

References

1. Gbadeyan JA, Agarana MC (2014) Dynamic analysis of railway bridges supported by winkler foundation under uniform partially distributed moving railway vehicle. Int J sustain Develop plann 135(of WIT Transactions on built environment):873–883
2. Agarana MC, Gbadeyan JA (2015) Dynamic response of mindlin elastic plate resting on pasternak foundation under uniform partially distributed moving load. Aust J Appl Math 2(3):17–26
3. Agarana MC, Ede AN (2016) Application of differential transform method to vibration analysis of damped railway bridge on pasternak foundation under moving train. In: Proceedings of the world congress on engineering, June 29–July 1, London, UK, pp 978–981
4. Dowell EH (1974) Dynamic analysis of an elastic plate on a thin elastic foundation. J Sound Vib 35:343–360
5. https://simple.wikipedia.org/wiki/Aluminium
6. https://www.corrosionpedia.com/definition/1599/transverse-loading
7. https://en.wikipedia.org/wiki/Finite_difference_method
8. Agarana MC, Gbadeyan JA, Emetere M (2016) On response of elastic isotropic damped shear highway bridge supported by sub-grade to uniform partially distributed moving vehicle. Int J Appl Eng Res 11(1):pp 244–258, ISSN: 0973–4562
9. Law RTDCS (1982) 1982 for vibrating plates. Am J Phys 50(3)
10. Fryba L (1972) Vibration of solids and structures under moving loads. Noordloff International Publishing Groningen, The Netherlands
11. Civalek O (2005) Large deflection static and dynamic analysis of thin circular plates resting on two parameter elastic foundation HDQ/FO couple methodology approaches. Int J Comput Mech 2(2):271–29
12. Agarana MC, Gbadeyan JA, Agboola OO, Anake TA, Adeleke OJ (2015) Dynamic response of an inclined railway bridge supported by winkler foundation under a moving railway vehicle. Aust J Basic Appl Sci 9(11):355–361
13. Agarana MC, Ede AN (2016) Free vibration analysis of elastic orthotropic rectangular inclined damped highway supported by pasternak foundation under moving aerodynamic automobile. In: Proceedings of the world congress on engineering 2016 June 29–July 1, London, UK, pp 978–981
14. Agarana MC, Agboola OO (2015) Dynamic analysis of damped driven pendulum using laplace transform method. Int J Math 26(3):0974–5718
15. Gbadeyan JA, Dada MS (2006) Dynamic response of a Mindlin elastic rectangular plate under a distributed moving mass. Int J Mech Sci 48:323–340
16. Zhang T, Zheng G (2010) Vibration analysis of an elastic beam subjected to a moving beam with flexible connections. Am Assoc Civ Eng 136(1):120–130
17. Gbadeyan JA, Dada MS (2007) The effects of linearly varying distributed moving loads on beams. J Eng Appl Sci 2(6):1006–1011
18. Friswell MI, Adhikan S, Lei Y (2007) Vibration analysis of beams with non-local foundations using the finite element method. Int J Numer Methods Eng 71:1365–1386

19. Agarana MC, Gbadeyan JA, Ajayi OO (March, 2016) Dynamic response of inclined isotropic elastic damped rectangular Mindlin plate resting on Pasternak foundation under a moving load. In: Proceedings of the international multi conference of engineers and computer scientists 2016. Hong Kong, pp 713–716
20. Agarana MC, Gbadeyan JA (October, 2015) Finite difference dynamic analysis of railway bridges supported by Pasternak foundation under uniform partially distributed moving Railway vehicle. In: Proceedings of the world congress on engineering and computer science 2015, vol. II. WCECS 2015, San Francisco, USA, pp 21–23

Ballistic Performance of Light Weight Magnesium (AZ31B) and Aluminium (AL 6061) Plates Using Numerical Method

M. Selvaraj, S. Suresh Kumar, and Ankit Kumar

Abstract Ballistic performance of lightweight Aluminium (Al6061) and Magnesium (AZ31B) plates has been determined using numerical method. In recent days, Aluminium and Magnesium plates are widely used in various structures because of their light weight and low density. Magnesium is 33% lighter than Aluminium and 77% lighter than Steel whereas Aluminium is one-third the weight of Steel. In the present work, the numerical ballistic performance has been investigated for different projectile velocity using ABAQUS finite element code to understand the impact behaviour, energy-absorbing capability and failure modes. The conical-shaped projectile was used and the plate thickness for both alloys was kept constant. The investigation has been done with three different velocities such as 100, 400 and 800 m/s. For the constant volume of Magnesium and Aluminium targets considered, lower depth of penetration and higher ballistic performance was observed for Magnesium target. The simulation result was verified by conducting a low-velocity impact test on the Gas Gun Test Setup and a good correlation was observed.

Keywords Ballistic performance · AZ31B magnesium plate · Al6061 aluminium plate · Depth of penetration

1 Introduction to Light Weight Targets

Magnesium and Aluminium alloys are gaining popularity in almost all the field of engineering because of their novel feature of light weight to high strength characteristic. Recent research works indicate that the use of Aluminium and Magnesium alloys is increasing day to day especially in the field of ballistic protection and armour applications. Both these alloys are ductile, highly formable, light weight and possess good strength. But still, use of these alloys in ballistic protection is limited due to

M. Selvaraj (✉) · S. Suresh Kumar · A. Kumar
Department of Mechanical Engineering, Sri Sivasubramaniya Nadar (SSN) College of Engineering, Kalavakkam, Chennai 603110, India
e-mail: selvarajm71@gmail.com

E. T. Akinlabi et al. (eds.), *Trends in Mechanical and Biomedical Design*, Lecture Notes in Mechanical Engineering,
https://doi.org/10.1007/978-981-15-4488-0_21

the cost and time involved in developing material accordance with ballistic characteristics. The preparation of light weight alloys for possible ballistic protection is limited due to the lack of exposure in metallurgical behaviour of lightweight materials. A large number of experiments are done to improve the light weight material and rework it to increase its strength as well as stiffness for possible ballistic applications. Friction stir processing of alloys using nanoparticles (Carbon Nano Tubes, Zirconium Oxide and Graphene) to improve surface stiffness is also done. The experimental ballistic impact is a highly non-linear dynamic phenomenon exhibiting high strain rates, deformation and fracture with constantly varying boundary conditions enabling researchers to opt for numerical simulation. Numerous experimental investigations have been conducted so far for a normal or an oblique projectile impact on the homogeneous or sandwiched metallic or composite plate. But the cost and time involved in ballistic experiments restrict the researcher's dependency on experiments for all impact-related studies. The complexity of the ballistic impact and penetration events often limits the general use of closed-form analytical solutions. Thus, a numerical simulation analysis is often preferred and resorted as a supplement to ballistic experiments. Simulations help in developing new projectiles and armours in a shorter period and permit easy design modifications and improvements. They reduce the experimental needs to a minimum extent of limiting to acceptance or a qualification test. However, only a few numerical studies at ordnance velocities are available because it is largely dependent on numerical inputs (material and fracture models) and numerical formulations.

Recent developments in commercial finite element codes are capable of simulating the complex ballistic impact events. The numerical simulation using finite element (FE) codes requires a sophisticated constitutive model, equation of state and in-built failure criteria as numerical inputs either individually or in combination to appropriately capture the complete behaviour of ballistic events. A number of constitutive models are available in the literature with varying capabilities in characterizing the material behaviour during impact. Many of them are material dependent and developed empirically or semi-empirically based on plasticity approach. They offer different levels of difficulty in finding a number of material constants presented in material models from different physical tests that are mostly and completely not available in the public domain.

1.1 Concept of Ballistic Impact Mechanism

At low impact velocities (about few hundred meters per second), the penetration resistance of a material is governed by the dynamic deformation mechanisms within the projectile and target. However, as the impact velocity increases into the hypervelocity regime (several thousand meters per second), hydrodynamic effects dominate and the penetration behaviour becomes controlled by only the density of the impacted material and projectile. Since the resistance of a material against penetration by low-velocity projectiles is controlled by dynamic deformation and impact fracture mechanisms, many researchers have involved themselves in the study of ballistics. In general, the ballistic performance depends upon the thickness, strength, ductility, toughness, acoustic impedance and density of both the target material and projectile and the velocity of the projectile. Figure 1 shows the different failure mechanisms caused by ballistic impact.

For thin targets that are much softer than the projectile, the panel bends creating tensile hoop stress in the plate. This leads to a failure by the growth of several radial cracks which leads to a "petalling mode" of failure. Whereas thicker materials projectile/material combinations lead to crater formation on the impact face and a "plug" that is pushed out of the plate. The crater forms because of the plastic flow needed to accommodate the volume of the projectile. The "plug" results from high shear stresses and large (adiabatic) shear band formation in the material near the periphery and just ahead of the projectile. In this case, increasing the material's shear strength and strain and strain rate hardening are important. For shear plugging to occur in thicker targets, very high stress is required. Instead, the projectile penetrates

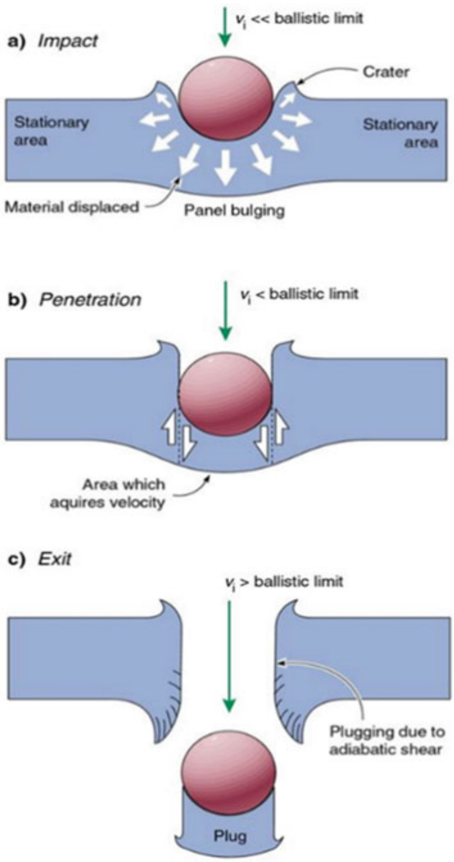

Fig. 1 Projectile penetration mechanism for a soft material impacted by a hard projectile [1]

by “ductile hole enlargement” which is governed by the dynamic flow stress of the target material. Efforts to increase the resistance to penetrate have focused upon the development and use of materials of very high yield strength. However, other failure modes can then begin to become important (for example, spallation and fracture). Visco-plasticity is a theory in continuum mechanics that describes the rate-dependent inelastic behaviour of solids. Rate-dependence indicates that the deformation of the material depends on the rate at which loads are applied. The inelastic behaviour causes the material to undergo unrecoverable deformations when a load level is reached. Rate-dependent plasticity is important for transient plasticity calculations.

2 Literature Review

Many researchers have studied the ballistic performance of aluminium-based targets. Gupta et al. [2] conducted experiments on aluminium plates of one mm thickness by using a gas gun and projectiles with blunt and hemispherical noses. Target plate was impacted with varying impact velocity. Impact and residual velocities of the projectile were measured. It was noticed that ballistic limit was higher for hemispherical projectiles than that for blunt projectiles. The effect of nose shape on the deformation of the plate was also studied. Numerical simulations of the impact were conducted by using an explicit finite element code. “Johnson–Cook elasto-viscoplastic model” was used to carry out the analysis. Results obtained from finite element simulations were compared with those of experiments. Good correlation was found between the two. Iqbal et al. [3] conducted an experimental and finite element investigation to explore the influence of target to projectile diameter ratio (*D*/*d*) on the ballistic performance and failure mechanism of thin aluminium plates. 1100-H12 aluminium target plates of 1 mm thickness were impacted by 19 mm diameter ogive and blunt-nosed projectiles. The *D*/*d* ratio was varied by varying the span diameter of the target keeping the projectile diameter constant, 19 mm. The finite element simulations were carried out at *D*/*d* ratios 3.6, 5, 7.9, 10, 15, 20, 25, 30, 35 and 40. The validation of the simulation results was carried out by performing experiments at *D*/*d* ratio 3.6, 5, 7.9, 10 and 15. The total work done in plastic deformation of the target was disintegrated into circumferential, radial, axial and tangential stretching. An initial increment in D/d ratio from 3.6 to 10 has been found to have a prominent effect on the ballistic limit, particularly against blunt-nosed projectile. It was observed that subsequent increase in the *D*/*d* ratio, however, could not influence the ballistic resistance significantly. The energy absorption in plastic deformation was found maximum for *D*/*d* ratio 10. The maximum energy dissipation occurred in circumferential stretching against bunt and in tangential stretching against ogive nosed projectile. The minimum energy dissipated in axial stretching against both the projectile. Madhu et al. [4] studied the phenomenon of ordnance velocity impact of a projectile on monolithic plates. In their work, an experimental study of normal and oblique impacts of all ogive shaped, hard steel projectile on single and layered plates of mild steel and aluminium were investigated. The projectiles were fired at an impact velocity of about 820 m/s. The plate thickness was varied in the range 10–40 mm and the ratio of plate thickness to the diameter of the projectile varied in the range 1.5–13.0. Observations on target damage and measurements of the incident and residual velocities for different angles of impact were presented. Plate thickness for which the incident velocity is the ballistic limit was determined. Computer simulations were carried out using a hydrodynamic code to simulate the normal impact of a projectile and they compared these with the experimental results. They performed the experiments to evaluate the response of these plates of intermediate thickness when layered, and the results were compared to the results of a single plate of the same total thickness. The aforementioned attempts are limited to a single steel target subjected to various projectile impact. Lack of work was observed to determine the ballistic performance of lightweight targets using numerical method. In the present work, effort has been made to determine the ballistic performance of light weight targets using numerical method.

3 Numerical Determination of Ballistic Performance

The numerical simulation was carried out using finite element code ABAQUS 6.14, which is well known for simulation of non-linear dynamic explicit impact testing problems which gives an accurate result. The software has good flexibility to manipulate the target material properties, testing procedure, controlling environment, taking most of the inputs into account for getting almost accurate result moreover it is very user friendly and flexible with varying requirements. The target used for Mg AZ31B was 115 mm × 115 mm × 4 mm and Al6061 was 115 mm × 115 mm × 3 mm and the conical steel projectile was used with 9 mm diameter. The projectile hits on the target at 0° angle at three different velocities such as, low (100 m/s), medium (400 m/s) and high (800 m/s). Both the Magnesium and Aluminium targets were meshed with 10,894 elements and 16,692 nodes whereas projectile was meshed with 169 elements and 168 nodes. The field outputs required for these simulations are Principle stress, Principle strain, Johnson–Cook damage initiation criteria at the integration point (JCCRT) and Kinetic energy absorbed by the target. Material properties of AZ31B and Al6061 with Johnson–Cook damage model is assigned to the target plate. Boundary conditions were applied and step time was given for solving the simulation. The edges of the plate were completely constrained for all degrees of freedom and the projectile was provided with only *Z*-axis displacement at different velocities as mentioned above according to the requirement. After had assigned the boundary conditions, the simulation was run to determine the output parameters. Mesh convergence study was conducted in order to determine the optimum number of elements. Figure 2a–c shows the meshed target and projectile. The tensile yield strength of the Aluminium and Magnesium targets are 276 MPa and 200 MPa respectively.

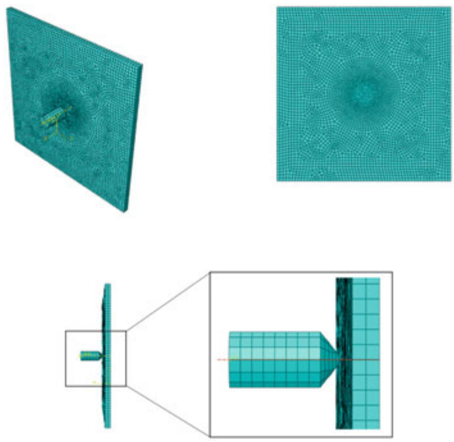

Fig. 2 **a** Target plate with projectile, **b** meshed target plate, **c** contact region of target and projectile

The numerical simulation was mainly focused to determine the maximum principle stress (S) at the integration point, equivalent plastic strain (PEEQ) at the integration point, Johnson–Cook damage initiation criteria at the integration point (JCCRT) and Kinetic energy absorbed by the plate. The simulation gives a closer observation of how the material is about to behave under different impact conditions. The test specimen was modelled in such a way that, the weight of both the alloys remains same for various target thickness. Since Magnesium alloy is lighter than aluminium alloy, the plate thickness of aluminium specimen will be less than the Magnesium specimen to keep their weight same. The dimensions of Mg AZ31B is 115 mm $\times$ 115 mm $\times$ 4 mm. The optimum thickness for aluminium is calculated as follows:

(Density $\times$ Volume) Al $=$ (Density $\times$ Volume) Mg

$2700 \times 0.115 \times 0.115 \times t = 1780 \times 0.115 \times 0.115 \times 0.004$

Thickness, $t = 0.00263$ m ≈ 0.003 m.

Standard thickness of 3 mm was considered to facilitate easy availability of Aluminium plate. The projectile used in the present work is of standard steel material which is hardened and is conical in shape. The dimensions are of 9 mm diameter and 15 mm length.

4 Result and Discussion

Ballistic performance of lightweight Aluminium and Magnesium targets subjected to different velocities of the projectile was carried out using ABAQUS numerical code. The following observations were made from the numerical simulation. It was noted that maximum induced impact stress in AZ31B is more than in Al6061 due to which a crack is formed on the rear portion of AZ31B plate. Both targets showed the formation of a dent and no crack was observed in Aluminium target. Thus one can expect Magnesium target can withstand more impact stress compared to Aluminium target. Figure 3 shows the impact stress distribution of light weight targets for a projectile velocity of 100 m/s.

It was also noticed that plastic Strain in AZ31B is less compared to Al6061. This is due to higher elongation of, Al6061 compared to AZ31B before failure, which also proves aluminium is more ductile than Magnesium. JC damage initiation in AZ31B is less than in Al6061 which signifies that aluminium is more ductile it starts to deform earlier when compared to Magnesium. Higher depth of penetration was observed for Al6061 than AZ31B plate due to higher plastic strain.

Figure 4 shows the impact stress distribution of light weight targets at higher velocity. At higher projectile velocity (800 m/s) higher impact stress was observed for Magnesium target compared to Aluminium. Thus one can expect higher impact

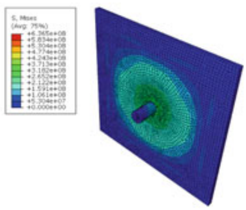

a Magnesium Target (AZ31B)

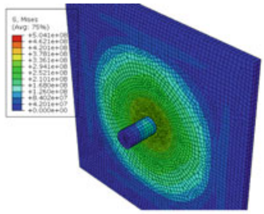

b Aluminium Target (Al6061)

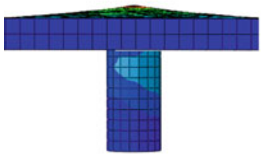

c Depth of Penetration - Magnesium Target (AZ31B)

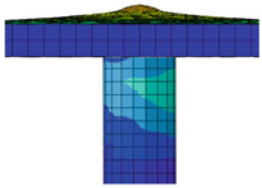

d Depth of Penetration - Aluminium Target (Al6061)

Fig. 3 Projectile velocity of 100 m/s

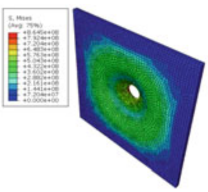

Magnesium Target (AZ31B)

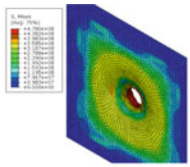

Aluminium Target (Al6061)

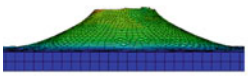

Depth of Penetration - Magnesium Target (AZ31B)

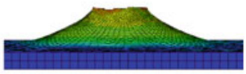

Depth of Penetration - Aluminium Target (Al6061)

Fig. 4 Projectile velocity of 800 m/s stress for Magnesium target irrespective of projectile velocity. This may be due to higher thickness of Magnesium target compared to Aluminium for the same volume considered. In this condition also lesser plastic strain and JC damage initiation was observed for Magnesium target compared to Aluminium due to higher ductility of Aluminium target compared to Magnesium.

5 Summary

Numerical and Experimental estimation of ballistic performance was performed on Magnesium AZ31B and Aluminium 6061 targets to compare their failure behaviour under various projectile impact velocity. The impact velocity ranging between 100 and 800 m/s was considered for numerical simulation and 100 m/s was considered for experimental work. Good correlation of depth of penetration was observed for the numerical and experimental results. One can expect better ballistic performance for Magnesium target compared to Aluminium target of the same weight. Hence, AZ31B can be recommended to replace Al6061 wherever the application is suitable, since it is lighter in weight and better in impact strength compared to Al6061.

References

1. Arias A, Rodríguez-Martínez JA, Rusinek A (2008) Numerical simulations of impact behaviour of thin steel plates subjected to cylindrical, conical and hemispherical non-deformable projectiles. Eng Fract Mech 1635–1656
2. Gupta NK, Iqbal MA, Sekhon GS (2006) Experimental and numerical studies on the behavior of thin aluminum plates subjected to impact by blunt-and hemispherical-nosed projectiles. Int J Impact Eng 32(12):921–1944
3. Iqbal MA, Tiwari G, Gupta PK, Bhargava P (2015) Ballistic performance and energy absorption characteristics of thin aluminium plates. Int J Impact Eng 77:1–15
4. MadhuV, Bhat TB, Gupta NK (2003) Normal and oblique impacts of hard projectile on single and layered plates—an experimental study. Defence Sci J 53(2):147–156

Comparison of Energy Absorption Characteristics of the Plain Fold and Spot-Welded Fold Tubes Under Three-Point Bending

M. Nalla Mohamed and R. Sivaprasad

Abstract Thin-walled square tubes are used as automotive vehicular crash structures since they can be easily constrained at the endpoints. These tubes are generally produced by costly extrusion process and special mold designs are required for making the same. This research work proposes a novel idea of making by folding thin metal sheets into square tubes that can be easily prepared, cost-effective and flexible in sectional shape. However, spot welding can be used to enhance the bending resistance and energy absorption. Bending collapse of tubes is one of the most important deformation mechanisms to be ascertained to ensure the safety of people or cargo under accidental crash events. Three-point bending tests are generally employed to investigate the bending characteristics and hence performed on plain folded and spot-welded fold tubes. Results revealed that spot-weld and number of turns have an important influence on the bending resistance of the folded tubes. The comparison between traditional tubes and welded tubes showed that the welded tubes outperform the traditional tubes in some aspects like minimizing the peak force and maximizing energy absorption. Adopting a number of turns further increased the bending resistance of the tubes compared with traditional square tubes.

Keywords Crush force · Fold tubes · Spot-weld

1 Introduction

In the past decades, thin-walled tubes are widely used as energy absorbers as they can absorb a large amount of energy during a vehicle crash event [1–5]. Among them, square tubes are mostly preferred since they can be easily constrained at end points [6]. Particularly, square tubes made of aluminium are preferred due to its lightness

M. Nalla Mohamed (✉) · R. Sivaprasad
Department of Mechanical Engineering, Sri Sivasubramaniya Nadar (SSN) College of Engineering, Kalavakkam, Kancheepuram District, Tamilnadu, India
e-mail: nallamohamedm@ssn.edu.in

R. Sivaprasad
e-mail: spsivaprasath50@gmail.com

E. T. Akinlabi et al. (eds.), *Trends in Mechanical and Biomedical Design*,
Lecture Notes in Mechanical Engineering,
https://doi.org/10.1007/978-981-15-4488-0_22

and progressive deformation behaviour during crash [7]. Hence, investigation of energy absorption and folding mechanisms of aluminium square tubes has been done in the last decade using analytical, experimental and numerical methods [8–10]. In recent years, multi-wall thickness square tubes have been used to improve the crashworthiness performance of tubes. A common obstacle for the manufacturing of such tubes is that (i) costly extrusion process and (ii) special mold is required to fabricate such structures. Of particular interest, this research work proposes a novel idea of making by folding thin metal sheets into square tubes that can be easily prepared, cost-effective and flexible in sectional shape. Multi-wall thickness and multi-cell sections can be easily obtained by the number of folding layers. This method of preparation is cost-effective as well as obtained with less effort when compared to extrusion method [11]. At the same time, the bending resistance of the folded tubes is not as good as heir axial crushing resistance. However, the loading directions have an important influence on the bending resistance of folded square tubes [12]. Folded tubes with weaker configurations in the compression region show less bending resistance and energy absorption. Hence upward closing is needed for folded tubes to improve bending resistance of the structure. Various methods are available to improve the crashworthiness performance and increase the energy absorption efficiency of them. Upward closing through welding is one of the options to change the deformation behaviour and increase the energy absorption capacity and efficiency of them [13]. Several investigations have been performed experimentally, theoretically and numerically to study the bending behaviour of the welded section. For instance, experimental studies have been performed to test the bending of the simple structure joined by spot-weld [14, 15]. Some researchers examined the static collapse and the bend behaviour of hybrid hat section stub columns [16, 17]. The above-mentioned literature review shows that more information is available on the bending behaviour of square tubes but that relating to folded tubes with welded section was scanty. This shortcoming motivated the authors to suggest a new design of folded tubes for enhancing the safety of the vehicles. In this paper, bending collapse responses of plain fold and weld fold tubes under three-point bending are investigated. The bending resistance and energy absorption characteristics of suggested tubes with various configurations are analyzed, and the outcomes are compared with that of traditional extruded tubes. The relative merits of tubes are analyzed, and some conclusions are drawn for such folded tubes subjected to bending loads.

2 Experimental Methodology

2.1 Material Properties

The structural material used for the folded tubes in this experiment is aluminium alloy AA6061-O with a chemical composition of 98.05% Al, 0.62% Fe, and 0.41% Mg. Mechanical properties of AA6061-O were determined using standard tensile

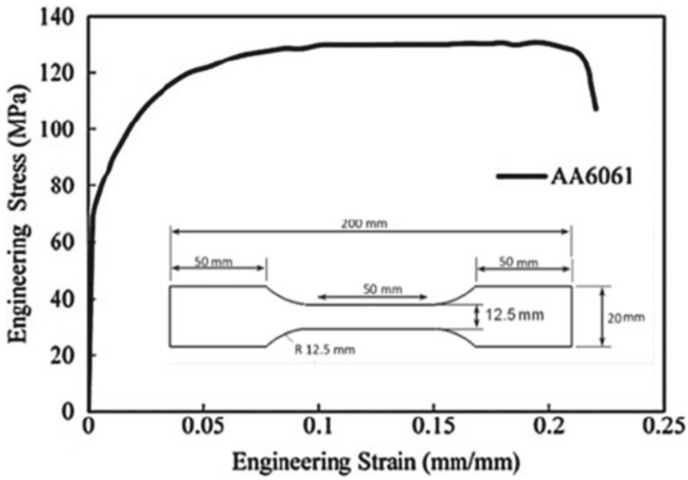

Fig. 1 Stress–strain curves of AA6061-O

specimens as defined in ASTM standard E8M. The aluminium alloy 6061-O was selected due to its common usage in automotive parts and aircraft structures, such as wings and fuselages for crash energy management. Figure 1 presents the engineering stress–strain curves for AA6061-O.

2.2 Fabrication of Plain Fold and Weld Fold Square Tubes

Aluminium alloy AA6061-O sheets of 1 mm thickness were folded into square tubes.

During the folding of sheets, fillets were created along the lateral edges which reduces the stress concentration during bending, unlike fillets are rare in commercially available extruded square tubes. The effective thickness of the fold tube was increased by increasing the number of turns as shown in Fig. 2.

Four types of both plain fold and weld fold tubes were fabricated with AA6061-O sheets with 1 mm thickness as shown in Figs. 3 and 4, respectively. The length of each specimen is 180 mm and average cross-sectional width is 30 mm and corner radius is measured to be 2 mm. During bending the sheet, it was ensured to give bending allowances to compensate spring back and distortion errors and ensured to achieve structural accuracy. In the case of weld folded tubes, spot welds of 6 mm diameter were provided longitudinally along the loose end of the folded tube at 30 mm of interval.

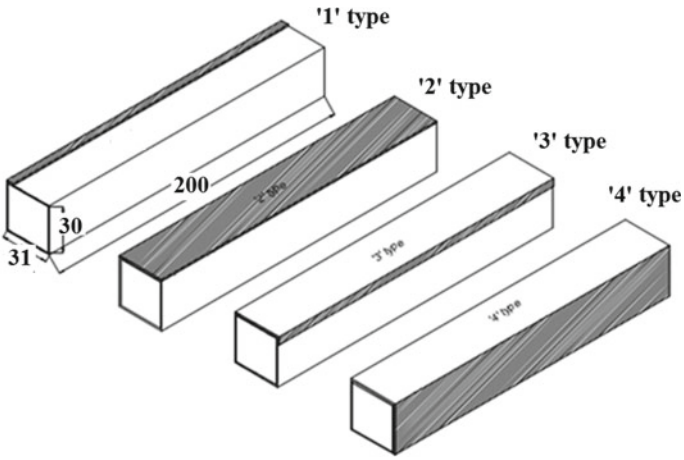

Fig. 2 Dimensions for the specimens

Fig. 3 Fabricated plain fold tubes

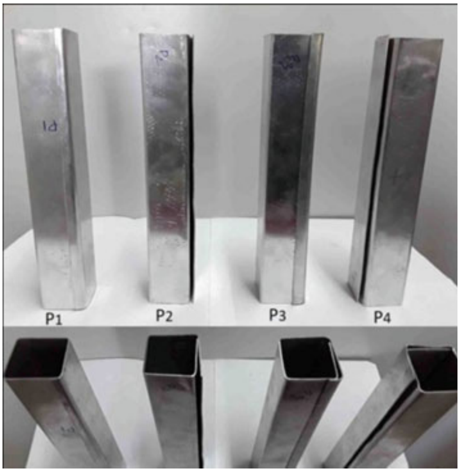

2.3 Experimental Setup

Quasi-static three-point bending tests were performed in a computerized UTM of 60 *t* capacity with computer control and data acquisition systems, which is shown in Figs. 5 and 6. The diameter of the cylindrical punch is 25.4 mm and the span between the supports 140 mm. The displacement of the punch head was moved at 2 mm/min during quasi-static loading. The punch force response versus punch displacement data was recorded by a digital data acquisition system for each specimen.

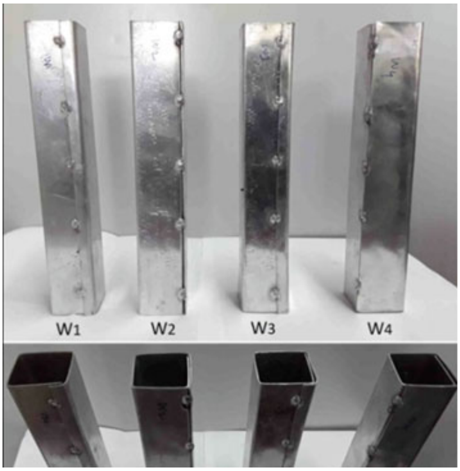

Fig. 4 Fabricated weld fold tubes

Fig. 5 Three-point bending setup

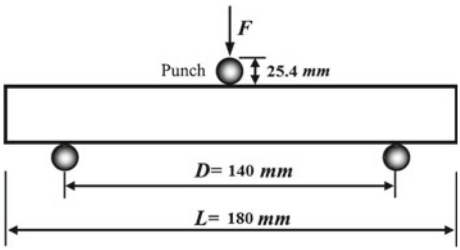

Fig. 6 Geometry for three-point bending test

3 Results and Discussions

The deformation patterns and punch force–displacement responses of the plain fold and welded fold tubes are analyzed here. The closing side of the tube is kept at the top and in contact with the punch. Figure 7 shows the bending deformation history of the "P_1" tube at the difference punch displacement level. It was observed that the deformation in the corner regions is the major energy dissipation mechanism for bending collapse. It was also observed that, in P_1 and P_2 types, the overlapping walls of the tubes separated during the loading which leads to the weakening of

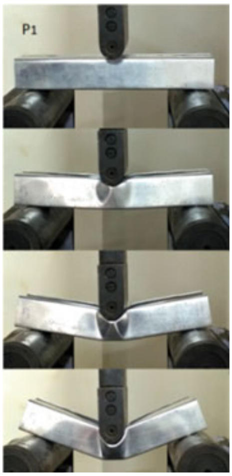

Fig. 7 Bending deformation history of P_1 type fold tube

corner regions. Hence, it leads to the drop of force response and consequently, the energy dissipation of P_1 and P_2 is less than that of other types. But P_3 and P_4 exhibit the highest bending resistance. This is due to the fact that there are three vertical sides to deform and dissipate energy when bending in this direction. The dissymmetry resistance of the three vertical sides also brings some extent of twist during the deformation of specimen, as shown in Fig. 8. Figure 9 shows the punch force versus displacement curves for all the plain folded tubes. Figure 10 shows energy versus displacement curves for all the plain folded tubes. When the number of turns increased, the bending resistance was also increased. Maximum peak force is obtained for P_4 type and minimum peak force is obtained for P_1 type. As the bending resistance increased consequently the energy absorption also increased.

It should be mentioned that the welding had some influence on the bending responses of the folded tubes. It is interesting to find that, highest energy absorption and mean bending resistance were observed for all the four types of welded fold tubes

Fig. 8 Deformation pattern of all the plain folded tubes

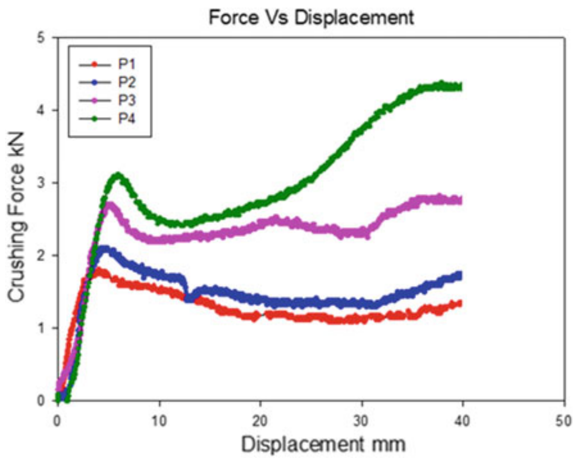

Fig. 9 Punch force versus displacement curves for all the plain folded tubes

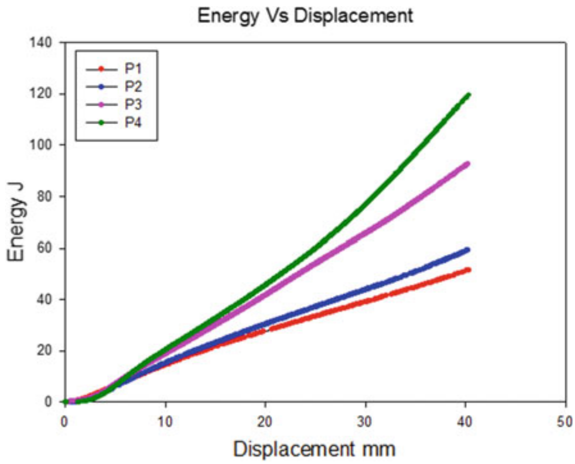

Fig. 10 Energy versus displacement curves

compared to their corresponding plain folded tubes. For type I, the difference is about 10%, while for all other types, the difference is 25% compared to their counterpart. The increase of energy absorption for a corresponding increase of turns is relatively regular and the increase in percentage is generally around 10–25% (Figs. 11 and 12). Figure 11 presents deformed shape of welded tubes (W_1) under 3-point loads with different span. Final deformed shape of all the welded tubes under 3-point bending test is presented in Fig. 12.

The performances of plain fold and weld fold tubes under three-point bending loading were discussed in the previous sections. However, it should be proved that whether they outperform traditional single tube. The force responses of the welded tubes are compared with traditional square tubes (SQ) having the same width of 30 mm and thickness 1 mm in Fig. 14. As shown in Fig. 13, the bending resistance

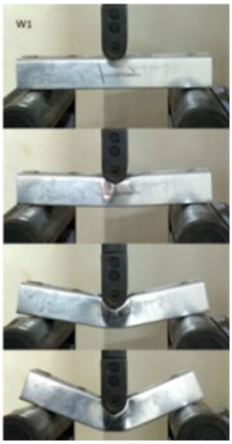

Fig. 11 Deformed shapes of welded tubes (W_1) under 3-point loads with different span

Fig. 12 Final deformed shape of welded tubes in 3-point bending test

of W_4 is superior to the traditional extruded square tubes. Similarly, the energy absorption capacity of W_4 tube is 2 times than that of traditional square tubes which is evidenced from Fig. 15.

4 Conclusion

Quasi-static three-point bending characteristic of plain fold and weld fold tubes is analyzed experimentally in the present work. The bending resistance and energy absorption characteristics are compared, and the conclusions are summarized as follows:

- The P_1 type plain folded tubes failed easily due to separation of fold side and hence the energy absorption is less. Hence use of single side fold tubes is not advisable for crashworthy applications.

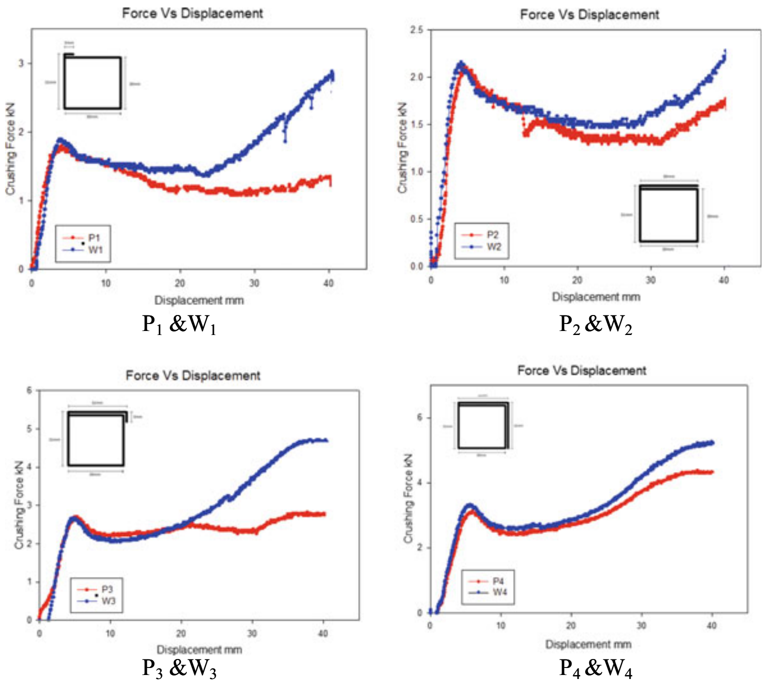

Fig. 13 Comparison of punch force versus displacement curves between plain fold and weld fold tubes

Fig. 14 Comparison of punch force versus displacement curves between extruded square tube and weld fold tube

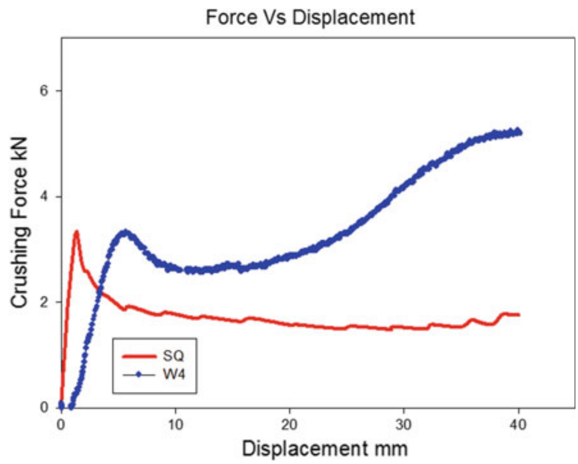

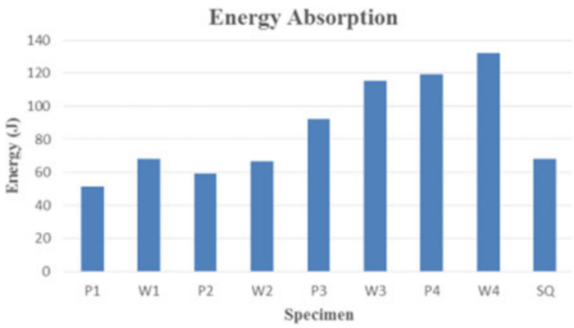

Fig. 15 Comparison of energy dissipation capacity of proposed tubes with extruded square tube

- The energy absorption and mean crushing force of folded tubes under three-point bending are found to be directly proportional to the number of vertical side panels. Hence P_3 and P_4 types exhibited more bending resistance compared to P_1 and P_2 types. The application of folded tubes with more vertical side panels is hence suggested for transverse loading.
- Experimental results proved that the weld folded tubes had more stable response due to the non-separation of the overlapping side compared with plain folded tubes. Hence weld tubes with more vertical sides had more bending resistance and energy absorption than the plain folded one.
- Bending resistance and energy absorption of the weld fold tube is superior to the extruded square tube. Hence the cost-effective and easily prepared approach of manufacturing tubes through metal sheet bending is suggested for safety protection in automotive applications.

References

1. Abramowicz W, Jones N (1986) Dynamic progressive buckling of circular and square tubes. Int J Impact Eng 4:243–270
2. Alghamdi AAA (2001) Collapsible impact energy absorbers, an overview. Thin-Wall Struct 39:189–213
3. Alavi NAJ, Hamedani H (2010) Comparative analysis of energy a sorption and deformations of thin walled tubes with various section geometries. Thin-Wall Struct 48:946–954
4. Nalla Mohamed M, Yuvarajan P, Umasankar M (2015) Energy enhancement of long cylindrical tubes with grooves subjected to axial impact. App Mech Mater 787:345–349
5. Nalla Mohamed M (2017) New insight to energy absorption characteristics of long circular tubes with stiffeners as controllable energy-dissipating devices. Procedia Eng 173:1300–1406
6. Chen S, Haiyan Y, Fang J (2018) A novel multi-cell tubal structure with circular corners for crashworthiness. Thin-Wall Struct 122:329–343
7. Zhang X, Zhang H, Ren W (2018) Axial crushing of tubes fabricated by metal sheet bending. Thin-Wall Struct 122:252–263
8. Jensen, Langseth M, Hopperstad OS (2004) Experimental investigations on the behaviour of short to long square aluminium tubes subjected to axial loading. Int J Impact Eng 30:973–1003
9. Galib DA, Limam A (2004) Experimental and numerical investigation of static and dynamic axial crushing of circular aluminum tubes. Thin-Wall Struct 42:1103–1137

10. El-Hage H, Mallick PK, Zamani N (2006) A numerical study on the quasi-static axial crush characteristics of square aluminum-composite hybrid tubes. Compos Struct 73:505–514
11. Zhang X, Zhang H, Ren W (2016) Bending collapse of folded tubes. Int J Mech Sci 117:67–78
12. Bai J, Meng G, Wu H, Zuo W (2019) Bending collapse of dual rectangle thin-walled tubes for conceptual design. Thin-Wall Struct 135:185–195
13. Zhang X, Zhang H, Leng K (2019) Experimental and numerical investigation on bending collapse of embedded multi-cell tubes. Thin-Wall Struct 127(2018):728–740
14. Zhang X, Zhang H, Wang Z (2016) Bending collapse of square tubes with variable thickness. Int J Mech Sci 106:107–116
15. Bilston D, Ruan D, Candido A, Durandet Y (2019) Parametric study of the cross-section shape of aluminum tubes in dynamic three-point bending. Thin-Wall Struct 136:315–322
16. Lee S, Hahn C, Rhee M, Oh JE (1999) Effect of triggering on the energy absorption capacity of axially compressed aluminum tubes. Mater Des 20:31–40
17. White MD, Jones N (1999) Experimental quasi-static axial crushing of top-hat and double-hat thin-walled sections. Int J Mech Sci 41:179–208

An Efficient Energy Absorber Based on Welded Fold Tubes for Automotive Applications

M. Nalla Mohamed and R. Sivaprasad

Abstract Thin-walled square tubes have proven their energy-absorbing capability in the automotive industries for safety applications. Unfortunately, special mold designs are required while making these tubes through extrusion process. This fabrication technique is in lack of flexibility or leads to low cost-effectiveness. In place of the existing extruded square tubes, this paper presents a novel energy absorber by folding thin metal sheets into tubes that are easily fabricated and cost-effective. However, it is unsafe to use these folded tubes directly due to its global buckling failure with low-energy absorption. Therefore, methods to improve the energy absorption characteristics of thin-walled structures have become essential. Spot and continuous welding are the effective joining techniques which can be used to enhance the energy absorption. In order to test the suitability of these tubes for crashworthiness, quasi-static tests were performed using a universal testing machine. The energy absorption capacity of these welded folded tubes was analyzed and compared with traditional square tubes with the same mass to quantify the relative merits. It was found that spot welding leads to a reduction in peak force and continuous welding leads to a reduction in performance due to its global bending. The results showed that the initial peak force of spot-welded tube is 10–15% lower than the continuous weld and 20–25% lower compared to the extruded square tube. Finally, it was found that spot-welded tubes had more crush length than that of continuous and plain folded one which leads to an increase in energy absorption. The outcomes of the present study would facilitate the design of welded tubes with better energy absorption.

Keywords Continuous weld · Folded weld tubes · Spot weld

M. Nalla Mohamed (✉) · R. Sivaprasad
Department of Mechanical Engineering, Sri Sivasubramaniya Nadar (SSN) College of Engineering, Kalavakkam, Kancheepuram District, Tamilnadu, India
e-mail: nallamohamedm@ssn.edu.in

R. Sivaprasad
e-mail: spsivaprasath50@gmail.com

E. T. Akinlabi et al. (eds.), *Trends in Mechanical and Biomedical Design*,
Lecture Notes in Mechanical Engineering,
https://doi.org/10.1007/978-981-15-4488-0_23

1 Introduction

Thin-walled square tubes are being used in the vehicle body for increasing the crashworthiness and consequently decreasing injuries [1]. Over the past few decades, a lot of effort has been focused on investigating the energy absorption capability of traditional square tubes using theoretical, numerical, and experimental methods [2–4]. Although the conventional square tubes demonstrated good performance for energy absorption, the high initial peak force is the crucial problem that has the potential to cause serious injury to the occupants [5]. Also, special mold designs are required while making these tubes through extrusion process. The present extrusion process is in lack of flexibility or leads to low cost-effectiveness [6]. As an alternative, folded tube by bending metal sheets is put forward in this situation. Moreover, their easy fabrication, cost-effective and flexible in both sectional shape and geometric parameters attracted the researcher. At the same time, these folded tubes cannot be used directly as energy absorber due to its irregular deformation or switch to global buckling failure mode which leads to the poor energy absorption [7]. If the folded tubes are in closed-form, the deformation may be progressive again and also much stable and regular. Hence, they may compete with traditional tubes [8]. The closed-form of the folded tubes can be achieved by joining techniques like welding. It is a very cheap and affordable technology to join metals sheets. Several investigations have been performed experimentally, theoretically and numerically to study the crushing behaviour of welded section. For instance, experimental studies have been performed to test the crashworthiness of quasi-static of the simple structure joined by spot weld [9, 10]. Some researchers examined the static collapse and the bend behaviour of hybrid hat section stub columns [11, 12].

The above-mentioned literature review shows that more information is available on the crushing behaviour of square tubes but that relating to folded tubes with welded section was scanty. This shortcoming motivated the authors to suggest a new design of folded tubes for enhancing the safety of the vehicles.

This paper aims at addressing the crushing characteristics of spot and continuous welded fold tubes under axial crushing experimentally. Folded tubes were tested for comparison purposes. The performance indices such as peak crush force (PCF) and the energy absorption capacity (EA) of the proposed tubes were compared with traditional square tubes for better understanding the merits.

2 Experimental Methodology

2.1 Material Properties

The material used for the folded tubes in this experiment is aluminium alloy AA6061-O with a chemical composition of 98.05% Al, 0.62% Fe, 0.41% Mg. Mechanical properties of AA6061-O were determined using standard tensile specimens as defined

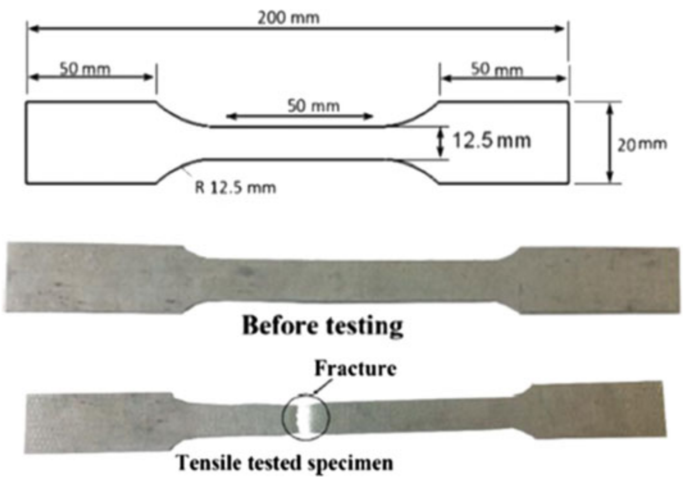

Fig. 1 Geometric details of tensile specimen

Fig. 2 Stress–strain curves of AA6061-O

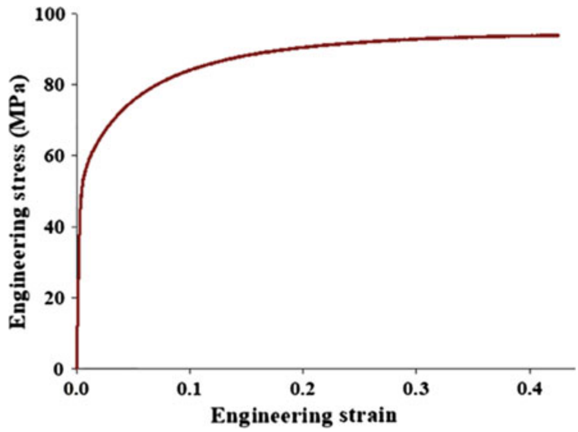

in ASTM standardE8M. The geometric details and the fractured specimen after the test are shown in Fig. 1. Figure 2 presents the tensile engineering stress–strain curves.

2.2 Fabrication of Spot and Continuous Folded Tubes

First, two sets of four different types of plain folded square sections were fabricated using Aluminium alloy AA6061-O sheets with 1 mm thickness as shown in Fig. 3. The length of the specimens is 180 mm and the width of the inside square is 30 mm. The aluminum sheets are bent by using a square steel rod and fillets are formed

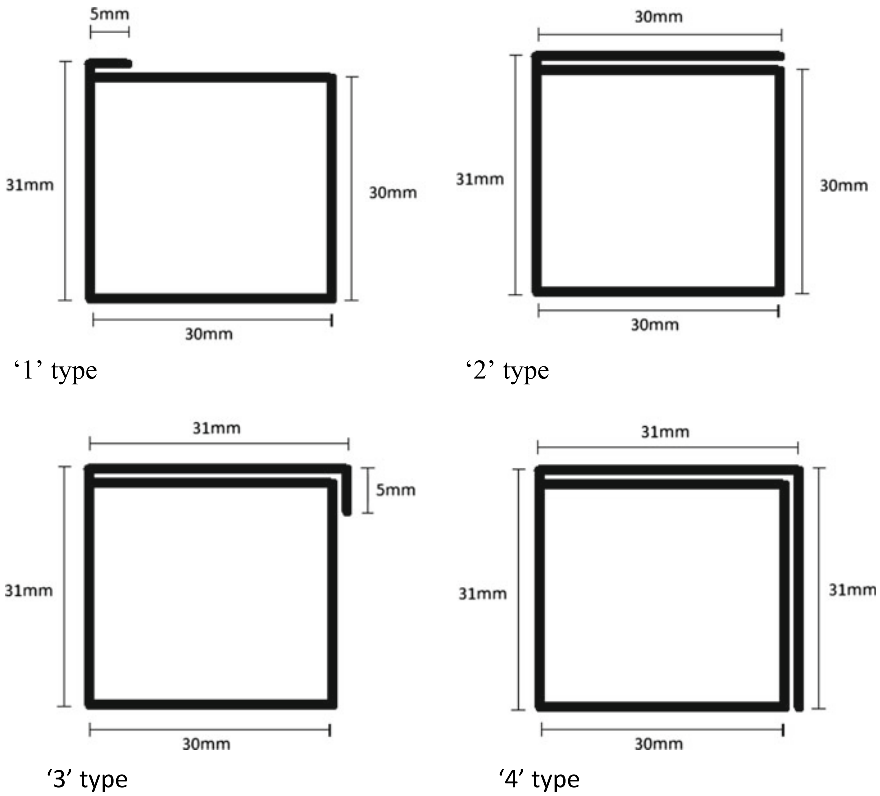

Fig. 3 Dimensions for the specimens

in the corners. The radius of the fillets in the specimens is measured to be 2 mm. Special care was taken to achieve a very high structural accuracy with reduced spring back and artificial errors. Then, spot welds were done with 6 mm diameter spots and 30 mm pitch in the first set of plain folded tubes [13]. Continuous welds were also done with the second set of plain folded tubes. Representative specimens are shown in Fig. 4.

2.3 Equipment and Procedure

In order to better understand the deformation characteristics of proposed tubes, the quasi-static axial compress tests were performed. Universal Testing Machine (UTM) of model number TUE CN-600 with 60 t capacity manufactured by Fine group's company shown in Fig. 5 is chosen to conduct the test. The test tubes are placed between two parallel rigid platens. The tests were conducted by a cross-head moving

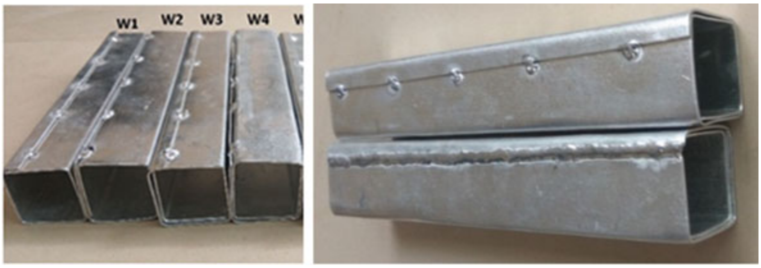

Fig. 4 Fabricated tubes specimen spot and continuous welded tubes

Fig. 5 UTM machine

at preselected speeds of 2 mm/min. The compressive load was gradually applied up to the deformation was 80% of the tube length. The variation of reacting force and axial displacement was recorded automatically by a digital data acquisition system. Typically, these data can be used to derive information on the energy-absorbing characteristics.

3 Results and Discussions

3.1 *Quasi-static Test on Plain Folded Welded Square Tubes*

To investigate the influence of the welding, we compare the crash behaviour of the folded tubes with spot and continuous welding in this section. The comparison of the deformation history of the spot-welded (SW1-type specimen) and continuous welded fold tubes (CW1 type) at different values of axial compression are shown in Fig. 6. It is observed that all types of spot-welded tubes deformed progressively which leads to more energy absorption. But, in con welded tubes, the fold started with progressive deformation followed by global buckling failure. Hence, during experiments, tests were stopped when the tubes lost structural resistance. This type of global buckling failure is recommended to be avoided in crashworthy applications due to their unpredictable results in energy absorption performance. The comparison of the final deformation mode of all the welded fold tubes is given in Fig. 7.

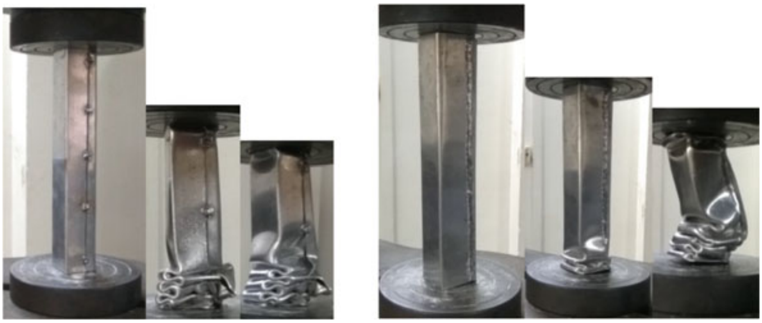

a) Spot weld specimen b) Continuous weld specimen

Fig. 6 Comparison of the deformation history of spot weld and continuous weld specimen

Fig. 7 Crushing pattern of all spot welded fold tubes

The comparative results of axial crush force versus deformation behaviour of the spot and continuous welded tubes tested under static loading conditions are depicted in Fig. 8. The results showed that the continuous welded tubes showed a fluctuating mean crush force, whereas the spot-welded tubes showed a gradual mean force due to its progressive deformation. Initial peak force increased when the number of fold increased. The total energy absorbed by the spot and continuous welded tubes obtained through experiments was compared and the comparison is depicted in Fig. 9. From the comparative plot, it was observed that the spot-welded tube absorbed more energy than the continuous one. Specimens having higher wall thickness gained comparatively higher crushing energy absorption capacity than the other specimens considered. The energy absorption capacity of the spot weld tubes was found in the range of 405–1144 J and the increase in energy absorption capacity was estimated as 30–40% compared with continuous weld tubes.

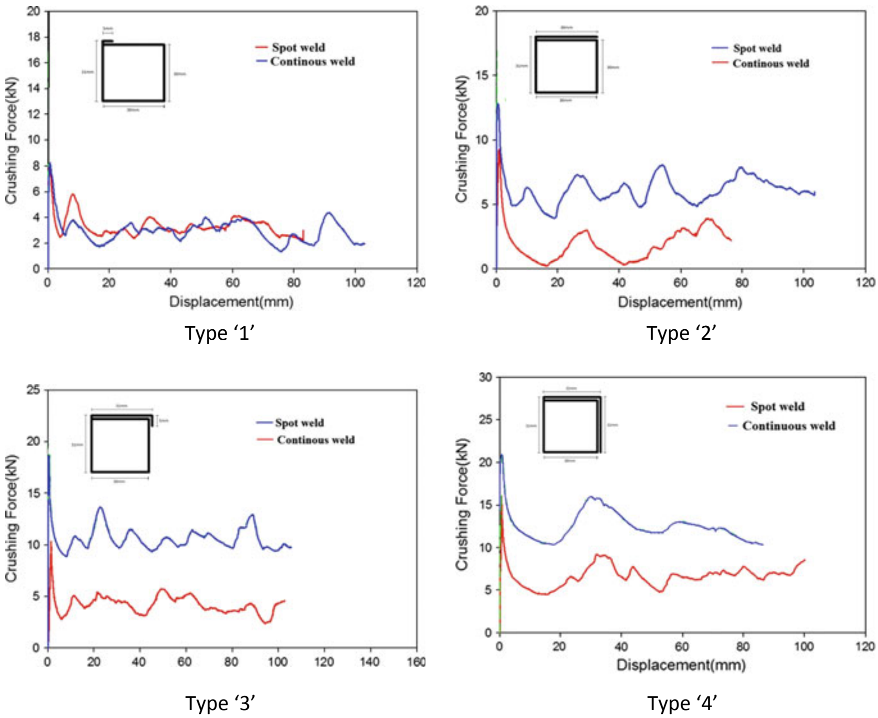

Fig. 8 Comparison of axial crush force versus deformation of spot and continuous welded tubes

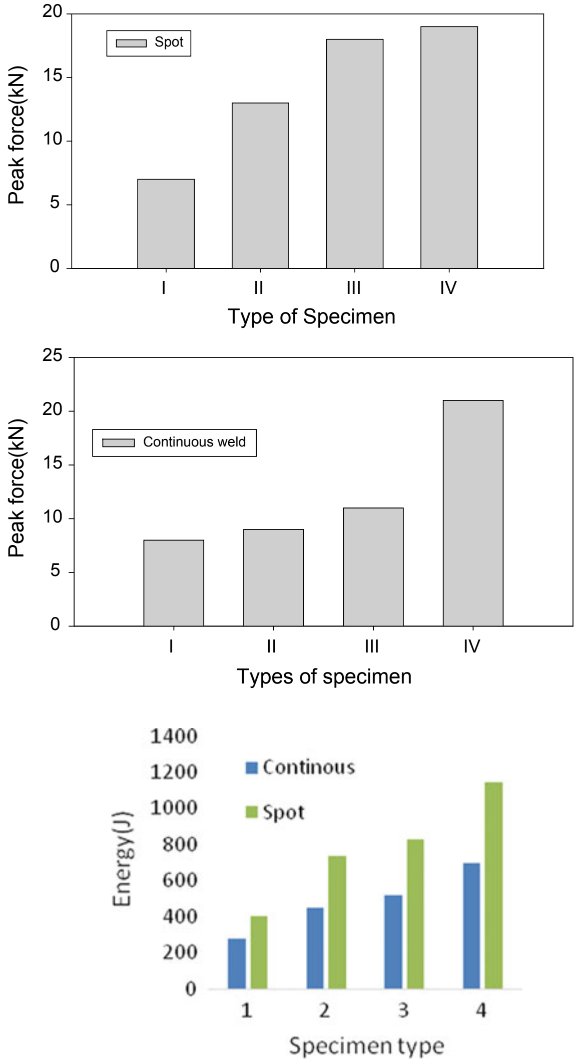

Fig. 9 Comparison of peak force and energy absorption of fold weld tubes

4 Conclusion

Axial crushing of spot and continuous weld folded tubes was experimentally investigated in this paper. The major results are summarized as follows:

- Continuous weld folded tubes failed in local buckling under axial crushing. In addition, the local buckling failure will greatly reduce the crush resistance of welded tubes and should be avoided by considering the stability of the structure in design. Instead, spot weld in the overlapped side helped to avoid this instability during deformation.

- The initial peak force of spot and continuous weld tube is 10–15% significantly lower than the extruded square tube and can be used as a good alternative to the conventional energy-absorbing structures that are sensitive to deceleration level.
- The energy absorption efficiency (SEA) of spot-welded tubes approaches that of the traditional square tube with the increase of the number of overlapped side.
- In summary, in order to meet the mass requirements of energy-absorbing components in automobile industries, the spot-welded fold tubes are most suitable as energy absorbing members due to their cost-effective for small-scale production, easily prepared, and flexible in both sectional shape and geometric parameters.

References

1. Langseth M, Hopperstad OS (1996) Static and dynamic axial crushing of square thin—walled aluminum extrusions. Int J Impact Eng 18:949–968
2. Jensen M, Langseth OS (2004) Hopperstad, Experimental investigations on the behaviour of short to long square aluminium tubes subjected to axial loading. Int J Impact Eng 30:973–1003
3. Galib DA, Limam A (2004) Experimental and numerical investigation of static and dynamic axial crushing of circular aluminum tubes. Thin-Wall Struct 42:1103–1137
4. El-Hage H, Mallick PK, Zamani N (2006) A numerical study on the quasi-static axial crush characteristics of square aluminum-composite hybrid tubes. Compos Struct 73:505–514
5. Bodlani SB, Yuen SCK, Nurick GN (2009) The energy absorption characteristics of square mild steel tubes with multiple induced circular hole discontinuities-part 1: experiments. J Appl Mech 76:041012
6. Zhang X, Zhang H, Ren W (2018) Axial crushing of tubes fabricated by metal sheet bending. Thin-Wall Struct 122:252–263
7. Zhang X, Zhang H, Ren W (2016) Bending collapse of folded tubes. Int J Mech Sci 117:67–78
8. Ohkubo Y, Akamatsu T, Shirasawa K (1974) Mean crushing strength of closed-hat section members. SAE Paper 740040
9. Yoon J, Cazacu O, Mishra RK (2013) Constitutive modeling of AZ31 sheet alloy with application to axial crushing. Mat Sci Eng A565:203–212
10. Song J, Zhou YF, Guo FL (2013) A relationship between progressive collapse and initial buckling for tubular structures under axial loading. Int J Mech Sci 75:200–211
11. Lee S, Hahn C, Rhee M, Oh JE (1999) Effect of triggering on the energy absorption capacity of axially compressed aluminum tubes. Mater Des 20:31–40
12. White MD, Jones N (1999) Experimental quasi-static axial crushing of top-hat and double-hat thin-walled sections. Int J Mech Sci 41:179–208
13. Song HW, Fan ZJ, Yu G, Wang QC, Tobota A (2005) Partition energy absorption of axially crushed aluminum foam-filled hat sections. Int J Solids Struct 42:2575–2600

Finite Element Analysis

Finite Element Modelling of a Compression Test on AISI 1016 Cylindrical Steel: A Review

V. Musonda and E. T. Akinlabi

Abstract Predicting the material flow behaviour of steel is always an important undertaking especially when there is a need to decide on a suitable material required for a particular application. Compression test is normally considered as a standard bulk workability test and a common quality control test, which can be applied to hot forging operations, or cold upset forging. The test is useful when the friction conditions, especially in hot working, require an evaluation. The flow stress data for metals at various temperatures and strain rates could also be predicted. The aim of this study was to conduct a hot compression test on AISI 1016 carbon steel using finite element modelling (FEM) in order to predict the flow stress behaviour of the material including the damage prediction due to shear cracking. Three lubricating conditions namely: Coulomb $\mu = 0.3$(lubricated), shear $\mu = 0.3$ lubricated and dry $\mu = 0.7$ were used in the modelling. The results indicate that the largest deformation appears as a shear cross in form of an hourglass in the plastic zone of the specimen at the centre of the cylinder and varies according to the lubricating condition, while the less deformed regions are stagnant as dead-metal zones (DMZ). The highest damaging parameter, though moderate appears at the bulge of the cylinder and this can be the source of shear cracking in the material. It was also observed that there is inhomogeneous deformation inside the workpiece, which could result in substantial damage to the forging process and forging quality respectively. Besides, inhomogeneous deformation could also worsen the finish-forging process.

Keywords Material flow behaviour · Compression test · Flow stress · FEM · DMZ · Shear cross · Damage prediction

V. Musonda (✉) · E. T. Akinlabi
Department of Mechanical Engineering Science, University of Johannesburg, Auckland Park Kingsway Campus, P.O. Box 524, Johannesburg 2006, South Africa
e-mail: musondachandi@gmail.com

V. Musonda
Department of Mechanical Engineering, School of Engineering, The University of Zambia, Great East Road Campus, P.O. Box 32379, Lusaka, Zambia

E. T. Akinlabi
Department of Mechanical Engineering, Covenant University, Ota, Ogun, Nigeria

E. T. Akinlabi et al. (eds.), *Trends in Mechanical and Biomedical Design*,
Lecture Notes in Mechanical Engineering,
https://doi.org/10.1007/978-981-15-4488-0_24

1 Introduction

The compression test is an extensively employed method for attaining the flow curve of metallic materials. Principally, the method is simple to use and that a cylindrical specimen is commonly used and placed between reasonably rigid platens or dies in order to provide a stress state of simple compression. This, however, is on condition that the movement is not constrained at the loaded interfaces [1]. From a metal forming perspective, the description of strain hardening during plastic deformation becomes realistic when flow curves are used. Moreover, the mechanical behaviour of metals can be modelled and the constitutive equations of plasticity, which may be nonlinear, can be set up. Flow curves obtained from a compression test are also key in the estimation of the forces and pressures applied on the workpiece and the dies. Furthermore, these curves can be used as a guide in controlling the process operating conditions, which apparently is fundamental to the realisation of practical engineering solutions. The biggest challenge in the cylindrical compression test, however, is how to minimise friction at the workpiece–die interface so that homogenous deformation can be achieved. Homogeneous deformations in a compression test are only possible under frictionless conditions against the compression platens. Such conditions guarantee a flawless cylindrical shape during the compression test. This, however, is on condition that the material of the cylinder is isotropic [2]. Numerous reasons, nevertheless, have been reported [3] for not attaining homogeneous plastic deformation conditions practically. First, the quality of lubricants used on the workpiece-die interface can affect the result upon which the experimental procedure depends. Moreover, the "barrelling" effect which is evident as a flaw will always be present and hence it is not possible to guarantee frictionless conditions, even if the most effective lubricants are used [3, 4]. This is also an indication that there is residue friction related with the compression test, which is always present regardless of the presence of the lubricant at the material-die interface.

Inhomogeneous deformation, nonetheless, is characterised by a bulging, or barrelling effect when friction is present at the interface [2]. During the sliding motion of the cylinder in the radial and outward direction, the frictional stresses appear to come against this motion over the die platens so that the friction shear stresses can reduce the radial outward flow of the top and bottom faces of the cylinder next to the die platens. There is, however, a need to compensate for this reduction of the radial flow, and this is achieved by a corresponding increase in the metal flow outwards in the middle of the cylinder. Therefore, the frictional effect between the die and the tooling instantaneously transforms into a flow pattern called barrelling. Barrelling appears on the outer circumferential surface at the midheight of the cylinder, and the material develops a shape similar to a barrel. The bulging effect also increases with an increased amount of friction and the shape becomes more pronounced throughout the compression stroke. Conical metal-dead zones then appear as stagnant regions inside and on both sides of the horizontal midplane of the cylinder, at each end of the specimen [5]. The plastic deformation of the material inside the DMZ, is not as much, compared with the rest of the material in the cylinder. This variation in the

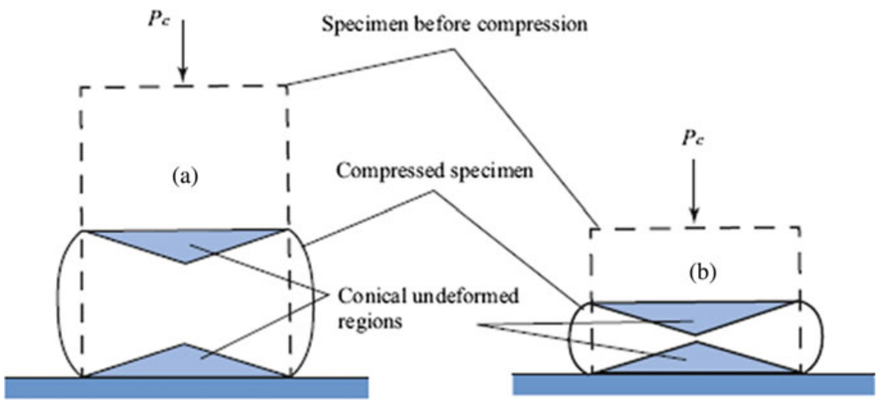

Fig. 1 Conical metal-dead zones owing to the friction at the interface during the compression test. **a** Has the larger length to diameter ratio, **b** smaller length to diameter ratio [5]

deformation patterns within the volume of the material is what creates the inhomogeneity in the cylinder compression with friction. Figure 1, shows conical metal-dead zones formed owing to the friction at the interface during the compression test.

Friction plays a key role in metal forming process due to its influence on the energy required for the compressive force. Over and above, friction affects the flow behaviour in the material inside the die including the quality of the product and tool life [6]. Theoretical and numerical investigations have been used in the barrel compression test analysis in order to evaluate the frictional effects on strain-hardening behaviour of the material [7]. According to the theoretical analysis, the strain-hardening exponent of the material affects the profiles of the barrel [5]. However, analytical evaluation of the cylinder compression test is a very difficult process to comprehend. This has been attributed to the complex nature of the stress–strain distribution and the tribological conditions within the contact zone. Therefore, researchers have been compelled to use Finite Element (FE) analysis as a pragmatic and effective tool to resolve the problem [7].

During compressive deformation of a specimen, there is a change in the area of its cross-section as the material spreads over the die. During this increase in the area, the frictional stresses between the specimen and the die act in the opposite direction to the flow of the material and hence providing a negative compressive force inwards. A negative sign to denote the direction of frictional stresses is usually indicated in the flow curves. Therefore, the regions of the specimen, which are in contact with the die including the regions just near the die, are subjected to triaxial compressive stresses [2, 5]. A cutting line is usually visible around these highly stressed regions at the edge of the cylindrical specimen. On the other hand, the compressive forces in the transverse direction, restrain the outer flow of the specimen material and these forces are at maximum on the surfaces at the ends, which are in contact with the dies. A gradual decrease by these forces is also noticed near the midlength of the specimen [5]. The flow curve during the reduction of the specimen in length at any given value is characterized by an upward shift. This is on condition that the ratio of initial diameter D_{0c} to initial length $\boldsymbol{L_{0c}}$, i.e. D_{0c}/L_{0c} of the specimen increases. Some of the factors that influence the forming load are die geometry and the forming speed especially in hot forming [2].

The Upper Bound Method (UBM) [8] has been reported to be useful in analysing the pressure applied against the die and the load required during the forming process. The method is based on the computation of the energy consumption in the process, obtained from the flow field in the actual forming process although the velocity field may be discontinuous on a finite number of imaginary internal surfaces [9]. The UBM is known for providing quick and precise solution to many 2D or 3D forming problems. Using UBM, the total power consumption for a particular metal forming process can be calculated according to [2, 10, 11] such that:

$$\dot{W}_{\mathrm{T}} = F \cdot v_{\mathrm{s}} = \dot{W}_{\mathrm{D}} + \dot{W}_{\mathrm{S}} + \dot{W}_{\mathrm{F}} = \int_V \overline{\sigma}\dot{\overline{\varepsilon}}\mathrm{d}V + \int_A k|\Delta v|\mathrm{d}A + \int_A \tau_i v_i \mathrm{d}A \tag{1}$$

In Eq. (1), $\dot{W}_{\mathrm{T}}$, is the total power, F, is the forming load and v_{s} the velocity of forming die or punch velocity, $\dot{W}_{\mathrm{D}}$ is the power required to deform the workpiece homogeneously, $\dot{W}_{\mathrm{S}}$ is the power required to shear-deform the workpiece. Shear deformation occurs if some or all of the workpiece material flows through a velocity discontinuity during the course of forming, $\dot{W}_{\mathrm{F}}$ is the power consumed due to frictional sliding of workpiece material over the interface between the die and the workpiece, $\overline{\sigma}$ and $\dot{\overline{\varepsilon}}$ are the equivalent stress and strain rate respectively, Δv is the magnitude of the velocity discontinuity surfaces S_{D}.

Applying the UBM to the axisymmetric cylinder, the compressive force during the forming process when the friction factor m is applied, can be calculated from a series of equations as articulated [2]:

$$\begin{gathered}\dot{W}_{\mathrm{D}} = \int_V \overline{\sigma}\dot{\overline{\varepsilon}}\mathrm{d}V = \pi R^2 h \cdot \overline{\sigma} \cdot \tfrac{v_{\mathrm{D}}}{h} = \pi R^2 \overline{\sigma} v_{\mathrm{D}} \\ W_s = 0 \text{ (shows that the velocity discontinuity is not there)}\end{gathered} \tag{2}$$

$$\begin{aligned}\dot{W}_{\mathrm{F}} &= 2\int_A \tau_i v_i \mathrm{d}A = 2\int_A \frac{m\overline{\sigma}}{\sqrt{3}} \cdot \frac{v_{\mathrm{s}} r}{2h} \cdot 2\pi r \mathrm{d}r = 2\frac{m\overline{\sigma} v_s 2\pi}{2\sqrt{3}\cdot h}\int_0^R r^2 \mathrm{d}r \\ &= \frac{2m\overline{\sigma} v_s \pi R^3}{3\sqrt{3}\cdot h}\end{aligned}$$

Summation of the three parts: $\dot{W}_{\mathrm{D}}$, $\dot{W}_{\mathrm{s}}$ and $\dot{W}_{\mathrm{F}}$ leads to Eq. (3)

$$\begin{aligned}\dot{W}_{\mathrm{T}} &= F \cdot v_{\mathrm{s}} = \dot{W}_{\mathrm{D}} + \dot{W}_{\mathrm{S}} + \dot{W}_{\mathrm{F}} \\ &= \int_V \overline{\sigma}\dot{\overline{\varepsilon}}\mathrm{d}V + 0 + \int_A \tau_i v_i \mathrm{d}A = \pi R^2 \overline{\sigma} v_{\mathrm{s}} + \frac{2\pi m}{3}\frac{\overline{\sigma}}{\sqrt{3}}\frac{v_{\mathrm{s}} R^3}{h}\end{aligned} \tag{3}$$

Hence, the compressive force is finally calculated as shown in Eq. (4)

$$F = \frac{\dot{W}_{\mathrm{T}}}{v_{\mathrm{s}}} = \pi R^2 \overline{\sigma}\left(1 + \frac{2\mu R}{3\sqrt{3} \cdot h}\right) \tag{4}$$

Evaluation of the material performance during the production process at an industrial level for components such as turbine discs and turbine shafts require an understanding of the microstructure evolution during their forming process [12]. Such components are considered as safety components; and therefore, recrystallization and grain growth during the hot forging process of these components becomes important. FEM is so far capable of analysing these events.

Aero-engine turbine discs, for example, are IN718 Nickel (Ni)-based superalloys, and obtaining a uniform and fine microstructure for these alloys is important to ensure that the required mechanical properties are obtained for these safety components. However, various microstructural defects such as coarse and duplex grain, respectively, can occur during the forging of IN718 turbine discs [13]. Therefore, obtaining the optimum parameters for designing the forging process becomes important [13]. Hence, a justification to conduct a quality control test such as compression can be made. Compression test studies have been reported [14–20] in which the characteristics of deformation as well as the evolution of the microstructure mechanism of superalloy IN718 have been described. These studies confirm some typical industrial applications of the test as applied to aero-engine turbine discs and shafts [13]. AISI 1016 steel was used in this study because it is one of the commonly used material in upsetting operations. The compression test results of AISI 1016 shows the deformation behaviour typical of an hourglass in “X” configuration at the centre of the cylinder and dead-metal zones at the top and bottom of the cylinder. This deformation pattern is similar to the one depicted in a 3D simulated model of a Forged final shape of a turbine rotor shown in [12]. Therefore this test provided an insight into what could be expected when other important components such as aero-engine turbine discs or turbine shafts or rotors are to be manufactured.

2 Material Specifications and FEM Modelling

In this study, a hot compression test simulation was conducted on AISI 1016 carbon steel and DEFORM-3D database was used to obtain the mechanical and thermophysical properties of this material. The 2D axisymmetric model was used in the simulation and the deformation patterns were obtained in 2D and 3D views after the post-processing. The ASTM medium length standards for the specimen as articulated [21] was adopted in this study. This standard considers a cylindrical specimen used for general purpose, to have the initial length L_{0c} to initial diameter D_{0c} ratio to be equal to 3, i.e. $L_{0c}/D_{0c} = 3$. Table 1 shows the medium length cylindrical specimen

Table 1 Medium length cylindrical specimen dimensions [21]

	Initial length (L_{0c}) (mm)	Initial diameter (D_{0c}) (mm)	L_{0c}/D_{0c}
1	38.1	12.7	3
2	60.325	20.2692	2.976
3	76.2	25.4	3
4	85.725	28.575	3

dimensions. The initial length (L_{0c}) and initial diameter (D_{0c}) used in the simulation were 76.2 mm and 25. 4 mm respectively which gives a ratio of 3 as per the standard.

A cylindrical specimen was used in the simulation and compressed isothermally between two flat polished dies (or platens). The initial dimensions of the specimen were $D_{0c} = 25.4$ mm and $L_{0c} = 76.2$ mm respectively. The compression platens can be either tool steel, tungsten carbide, or ceramic composite, depending on the temperature, and these should be flat and parallel according to ASTM E209 [22]. The maximum reduction in height was 75% at a constant speed of 2 mm/s and a maximum displacement of 57.2 mm. This speed was related to the crosshead at a constant temperature of 1200 °C. Tables 2 and 3 shows the type of lubricating

Table 2 Friction types and state variables during a hot compression test of AISI 1016 carbon steel

Friction type	Coefficient of friction (μ)	Strain-rate effective (s^{-1}) (step 450)	Stress-effective (MPa) (step 450)	Total displacement (mm) (step 450)	*XY* strain-effective (step 450)
Coulomb	0.3 (Lubricated)	0.786	62.9	57.2	2.36
Shear	0.3 (Lubricated)	0.718	61.9	57.2	1.92
Dry	0.7	0.928	64.6	57.2	2.48

Table 3 Friction types and state variables during a hot compression Test of AISI 1016 Carbon Steel

Friction type	Coefficient of friction (μ)	Damage factor (Max) (step 450)	Load (N) (step 450)	Force (N) (step 450)	Normal Pressure (Max.) (MPa) (step 450)
Coulomb	0.3 (Lubricated)	0.333	1e+05	768	223
Shear	0.3 (Lubricated)	0.250	9.52e+04	923	253
Dry	0.7	0.342	1.05e+05	721	194

conditions used and the results of the state variables obtained after a post-processing in DEFORM-3D. The final step 450 of the simulation results was used as the basis for comparing the deformation patterns in the compressed material given the variations in the three lubricating conditions at the interface.

3 Results and Discussion

3.1 Stress and Strain Rate Effective

The largest deformation patterns in all the friction types indicate that the highest stress appears inside the cylinder at the centre, and these patterns are characterised by a typical shear band. The degree of deformation, however, depends on the value of μ. Figure 2a, b shows the three-dimensional FEM-predicted distribution of the maximum stresses and deformation bands when the coulomb and shear conditions are used. Figure 2c, d shows the respective 2D stress and strain rate patterns for the shear condition. Figure 2e shows the highest stress at 64.6 MPa, which occurred when a dry interface ($\mu = 0.7$) was used. In all the lubricating conditions used in the study, the deformation pattern showed a shear cross or hourglass with less deformed stagnant regions appearing at the top and bottom cylinder as dead-metal zones. The bulging or "barreling" effect appeared in the middle of the cylinder with moderate deformation.

A visible cutting line (Fig. 2a) at the top and around the cylinder shows the effect of high tensile stresses acting in the direction around the circumference of the cylinder. Inhomogeneous deformation was largest in dry friction conditions and this was characterised by jerky or serrated yielding as shown on the *XY* stress graph in Fig. 2e. The *XY* stress was 30.1 MPa at maximum stress-effective of 64.6 MPa. Figure 3a, b shows the FEM-predicted distribution in 2D axisymmetric for stress-effective and strain rate-effective when $\mu = 0.3$ (coulomb lubricated).

3.2 Strain Rate–Effective and Strain Distribution

The distribution of strain rate and strain was homogenoues during the initial stages of compression in shear and dry conditions and this was characterised by an insignificant effect of barelling in the middle of the cylinder. The distribution, however, was inhomogenous towards the end of the compression test and the barelling effect was significant though moderate. During the last stage, the deformation pattern transformed into a shear band in a clearly visible "*X*" configuration and the corresponding *XY* graph was typical of a jerky or serrated yielding, indicating that, the deformation was not homogenous. Figure 4a shows the FEM-predicted distribution of effective strain rate with a jerky flow in shear ($\mu = 0.3$) beginning after 18 s of compression.

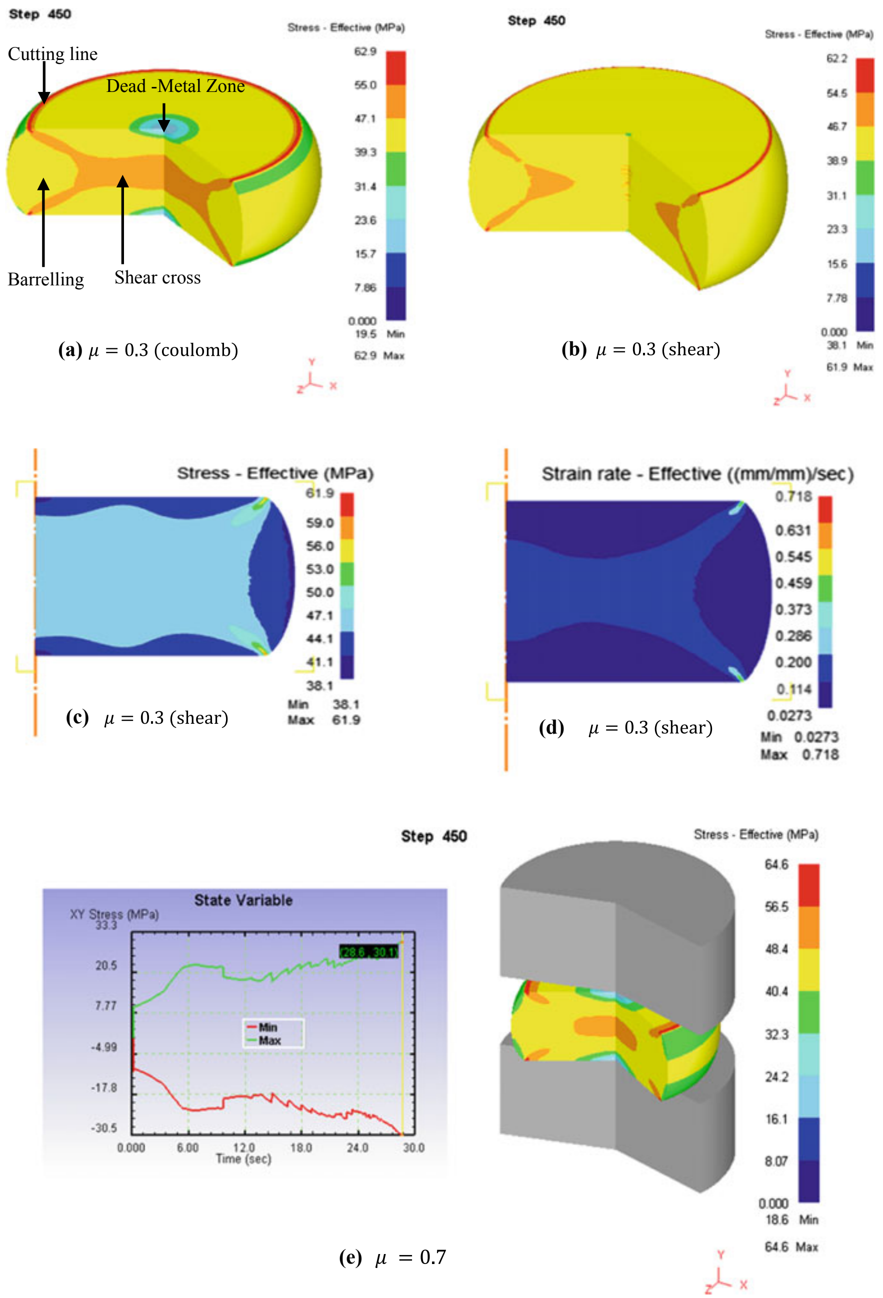

Fig. 2 FEM-predicted distribution of maximum stresses and deformation bands in hot compression of AISI 1016 cylinder **a** 62.9 MPa when Coulomb $\mu = 0.3$ lubricated, **b** 61.9 MPa when Shear $\mu = 0.3$ lubricated, **c**, **d** 2D axisymmetric patterns, **e** Jerky flow in XY stress ($\mu = 0.7$)

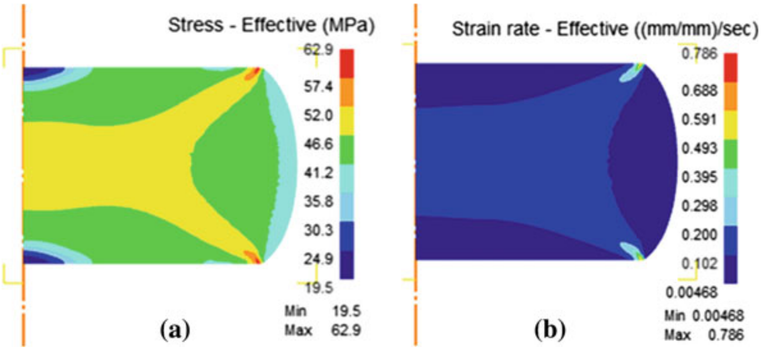

Fig. 3 FEM-predicted distribution in 2D axisymmetric. **a** Stress-effective (62.9 MPa), **b** strain rate-effective (0.786 s^{-1}) when $\mu = 0.3$ (coulomb lubricated)

This behaviour continued until the last stage of compression when strain rate-effective was 0.718 s^{-1}. Figure 4b shows FEM-predicted distribution of effective strain rate with an uneven flow curve at the beginning of compression followed by a pronounced jerky flow occurring between 18 and 24 s of the compression stage when $\mu = 0.7$. After 24 s of compression, a near steady flow curve was noticed until the last stage of compression at 0.928 s^{-1}. This behaviour is different from that depicted in a shear flow curve where the curve was steady during the initial stages of compression until after a jerky flow began after 18 s of compression.

The frictional resistance values (red curve on the graph) in the two graphs alluded to are very close to the true values (green curve on the graph) with the absolute error being 0.016 in shear and 0.014 for dry condition. This translates into 4 and 1.6% errors respectively. The frictional resistance values were assumed to be theoretical in all the cases and they were very close to the true values. The strain rate, however, was not uniform in a dry condition ($\mu = 0.7$) as can be seen from the irregular flow curve (Fig. 4b) during the initial 75% maximum reduction. This was followed by a jerky flow curve before a near steady flow was assumed until the final compression stage.

The FEM-predicted 2D axisymmetric distribution patterns for stress and strain rate for dry condition presented in Fig. 5a, b showed the highest stress and strain rate-effective values of 64.6 MPa and 0.928 s^{-1}, respectively. Figure 6, shows the FEM prediction for the largest deformation in "*X*" configuration at the center of the cylinder when strain-effective is 2.48 in dry condition. It should be noted that the frictional resistance values (in red) and the true values (in green) in the *XY* strain–effective graph (Fig. 6) are very close to each other despite some minor deviations in the flow curve. The flow curve also shows a slight deviation from the typical load-stroke compression curve. It can, therefore, be deduced that a dry workpiece-die interface promotes inhomogeneous deformation in a hot compressed workpiece.

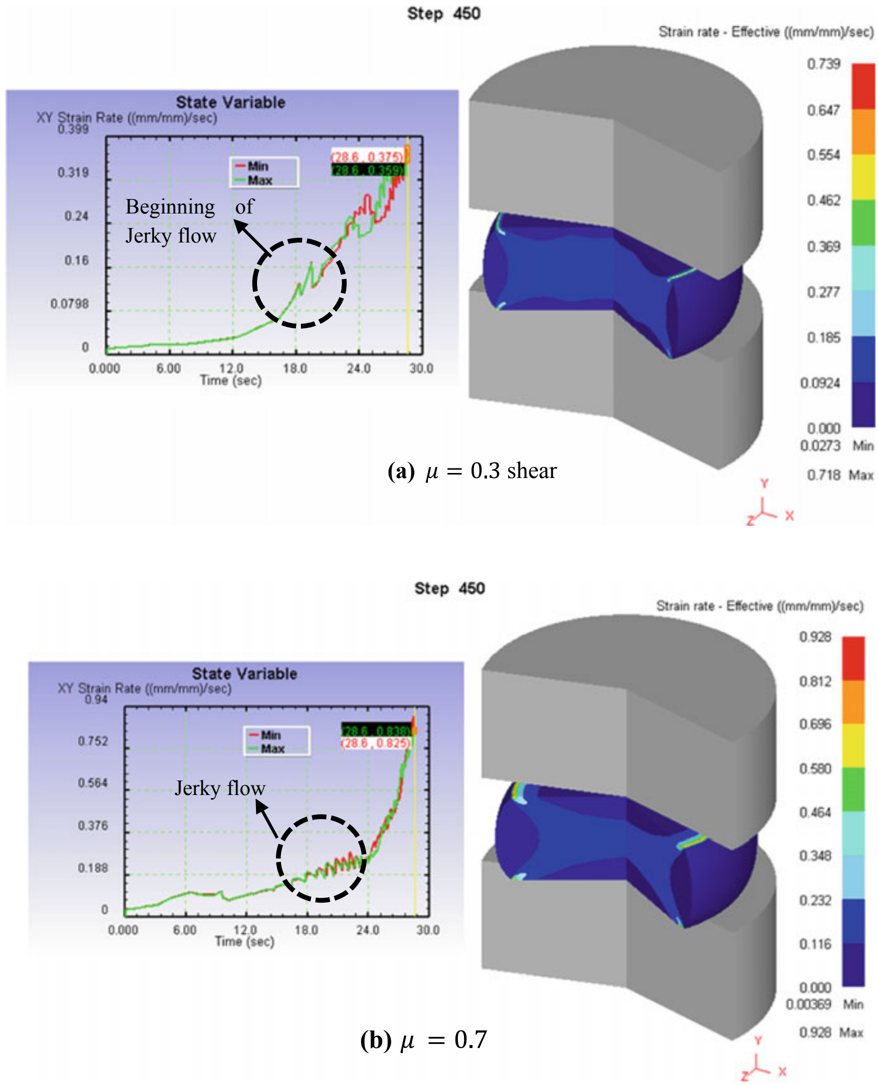

Fig. 4 FEM-predicted distribution of effective strain rate in the plastic zone of the specimen at the centre in hot compression of AISI 1016 cylinder. **a** *XY* strain rate at 0.718 s^{-1} in shear, **b** *XY* strain rate at 0.928 s^{-1}

3.3 Damage Parameter During Loading

The most probable site for the crack initiation and consequently fracture in a ductile material during a hot compression test could occur in the bulged portion of a cylinder. Figure 7 confirms that the highest damage parameter can be predicted to occur in the middle of the bulge. The high tensile stresses acting in the direction around

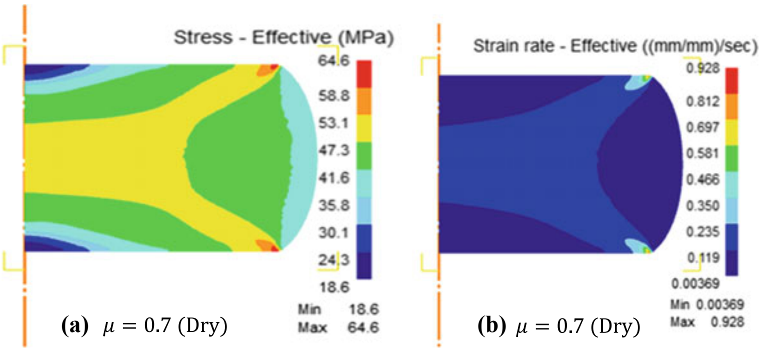

Fig. 5 FEM-predicted 2D axisymmetric distribution patterns for stress and strain rate. **a** Stress-effective(64.6 MPa), **b** strain rate-effective (0.928 s^{-1}) when $\mu = 0.7$ (dry)

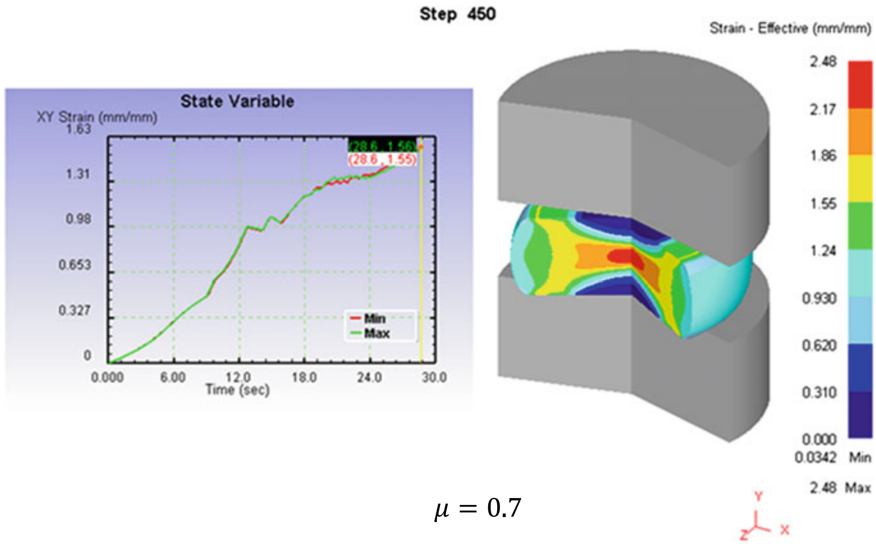

Fig. 6 FEM-predicted distribution of strain-effective in the plastic zone with the largest deformation appearing in "*X*" configuration at the center

the circumference of the cylinder are responsible for this damage. Strain softening can affect the rate of decrease in the strength of the material, and when this amount exceeds the permissible proportion of the increase in the area of the specimen, a "kink" develops in the specimen to indicate the unstable mode of deformation [23]. This mode of deformation was predicted by FEM in the damage parameter evaluation for the dry condition. However, the damage parameters in all the lubricating conditions in this study exhibited a steady exponential curve except for the dry condition, which showed a "kink" (in black dashed circle) in the early stages of compression. After this point, the curve was steady until the last stage. The highest damaging factor

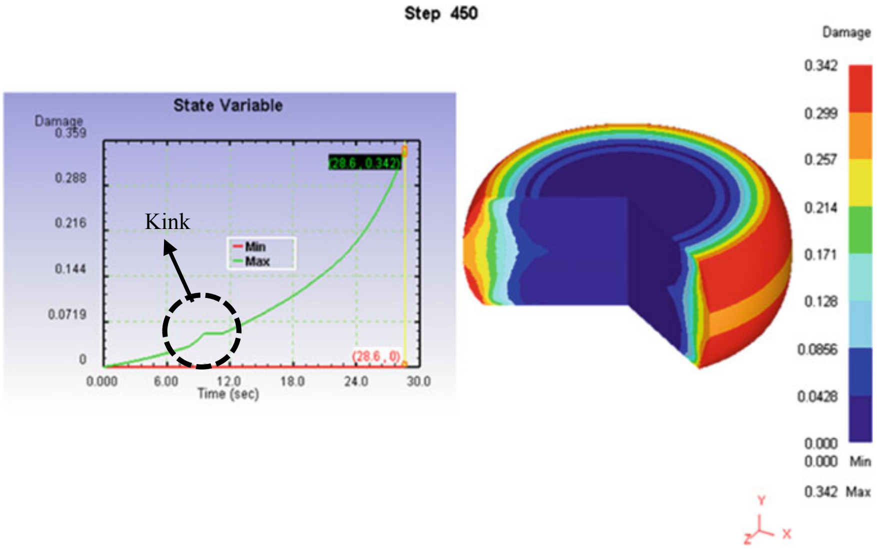

Fig. 7 FEM-predicted damage in a hot compression of AISI 1016 steel cylinder with maximum damage factor of 0.342 occurring in the middle of the bulge when $\mu = 0.7$, with a kink in the flow curve

occurred in dry condition with a maximum value of 0.342. Figure 8, also shows the load-stroke prediction curve with the maximum load of 1.05e+05 N at Strain-Total-Von misses of 2.48 maximum for dry condition ($\mu = 0.7$). This value corresponds to the highest deformation pattern inside the cylinder at the center.

4 Concluding Remarks

In this study, it has been shown that the deformation conditions in a hot cylindrical compression test can be characterized by FEM. The input to the FEM simulation was the workpiece material AISI 1016 carbon steel and the coefficient of friction (COF) data for coulomb $\mu = 0.3$(lubricated), shear $\mu = 0.3$(lubricated) and $\mu = 0.7$(dry) conditions were used. These conditions were used to compare the deformation patterns of homogenous and inhomogenous conditions. High stress values were noted in dry and coulomb conditions with dry having the highest at 64.6 MPa while coulomb had 62.9 MPa and shear 61.9 MPa. In all the conditions, the damage factor was characterised by an exponential curve except for the dry condition, which showed a “kink” during the initial stages of the compression. The least damage factor of 0.250 occurred under shear conditions. The 3D deformation patterns at the centre and inside of the cylinder in all the conditions were characterised by a typical hourglass or shear cross in the plastic zone of the specimen. Areas of less deformed material appeared as stagnant zones popularly known as dead-metal zones. The maximum

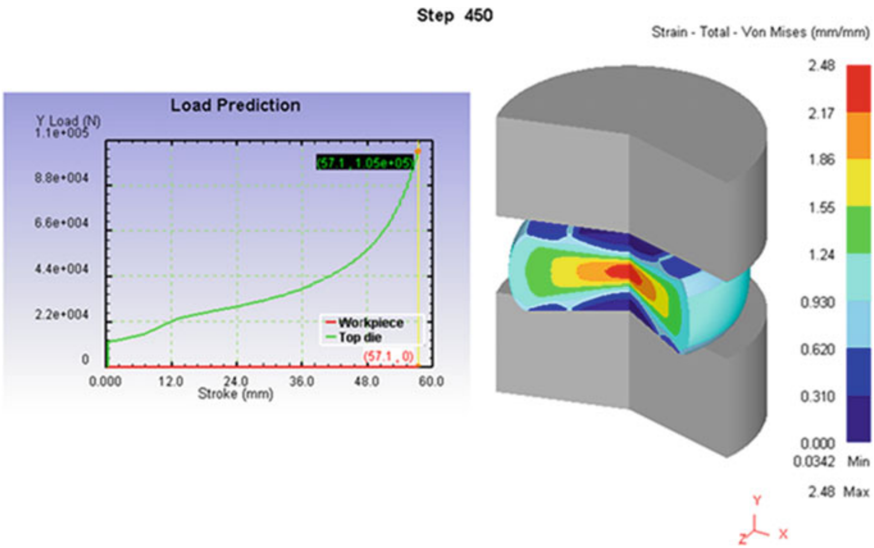

Fig. 8 FEM-load-stroke prediction and largest deformation in a hot compressed steel with strain-total Von Misses of 2.48 when $\mu = 0.7$ at maximum load of 1.05e+05 N

strain occurs at the center inside the cylinder and on the edge of the cylinder. It has also been demonstrated that homogenous deformation is not guaranteed with particular use of lubricant at the interface. However, there is confirmation in this study, that dry conditions lead to non-uniformity of strain rate which results in inhomogeneous deformation patterns. It can, therefore, be deduced that barrelling makes the determination of the true axial compression stress complicated when the compression test is used to measure the flow properties of the material. The remedy to the "barrelling" effect is to evaluate the properties of the material, die geometry and the kind of lubricant used in the compression test if homogenous deformation has to be achieved.

References

1. Williams JG, Chaiwut G (2008) Using the simple compression test to determine Young's modulus, Poisson's ratio and the Coulomb friction coefficient. Int J Solids Struct 45:4448–4459
2. Valberg HS (2010) Applied metal forming. Including FEM analysis. Cambridge University Press
3. Christiansen P, Martins PAF, Bay NO (2016) Friction compensation in the upsetting of cylindrical test specimens. Exp Mech 56(7):1271–1279. https://doi.org/10.1007/s11340-016-0164-z(2016)
4. Shahriari D, Sadeghi MH, Ebrahimi GR, Kim KT (2011) Effects of lubricant and temperature on friction coefficient during hot forging of Nimonic 115 superalloy. Kovove Mater 49:375–383. https://doi.org/10.4149/km_2011_5_375

5. Bhaduri A (2018) Mechanical properties and working of metals and alloys. Springer Series in Materials science, vol 264. https://doi.org/10.1007/978-981-10-7209-3_2
6. Erinosho MF, Akinlabi ET (2016) Study of friction during forging operation. Proceedings of the World Congress on Engineering, vol II, WCE, 29 June–1 July, London, UK
7. Yao Z, Mei D, Shen H, Chen Z (2013) A friction evaluation method based on barrel compression test. Tribol Lett 51:525–535. https://doi.org/10.1007/s11249-013-0164-4(2013)
8. Prager W, Hodge PG (1941) Theory of perfectly plastic solids. Wiley, New York
9. Wu WT, Jinn JT, Fischer CE (2003) Modeling techniques in forming processes (Chap. 15). In: Dieter GE, Kuhn HA, Semiatin SL (eds) Handbook of workability and process design, pp 220–231. https://doi.org/10.1361/hwpd2003p220
10. Altan T, Oh S-I, Gegel HL (1983) Metal forming: fundamentals and applications. ASM Int 131–142
11. Avitzur B (1968) Metal forming: processes and analysis. McGraw-Hill, New York
12. Li X, Kopp R, Wolske M (2005) Development of forgeable Ni-base alloys for USC steam turbine applications by use of microstructure simulation and formability testing. In: Loria EA (eds) Superalloys 718, 625, 706 and derivatives, TMS (The Minerals, Metals & Materials Society)
13. Zhang HY, Zhang SH, Li ZX, Cheng M (2009) Hot die forging process optimization of superalloyIN718 turbine disc using processing map and finite element method. In: Proceedings of IMechE, vol 224: Part B: J Eng Manuf. https://doi.org/10.1243/09544054jem1571 (2009)
14. Srinivasan N, Prasad YVRK (1994) Microstructural control in hot working of IN-718 superalloy using processing map. Metall Mater Trans A 25:2275–2284
15. Medeiros SC, Prasad YVRK, Frazier WG, Srinivasan R (2000) Microstructural modelling of metadynamic recrystallization in hot working of IN718 super-alloy. Mater Sci Eng A 293:198–207
16. Zhou LX, Baker TN (1994) Effects of strain rate and temperature on deformation behaviour of IN718 during high temperature deformation. Mater Sci Eng A 177:1–9
17. Zhou LX, Baker TN (1995) Effects of dynamic and metadynamic recrystallization on microstructures of wrought IN-718 due to hot deformation. Mater Sci Eng A 196:89–95
18. Thomas A, El-Wahabi M, Cabrera JM, Prado JM (2006) High temperature deformation of Inconel 718. J Mater Process Technol 177:469–472
19. Yuan H, Liu WC (2005) Effect of the delta phase on the hot deformation behaviour of Inconel 718. Mater Sci Eng A 408:281–289
20. Wang Y, Shao WZ, Zhen L, Yang L, Zhang XM (2008) Flow behaviour and microstructures of superalloy718 during high temperature deformation. Mater Sci Eng A 497:479–486
21. Davis HE, Troxell GE, Wiskocil CT (1964) The testing and inspection of engineering materials, 3rd edn. McGraw-Hill Book Company, New York
22. ASTM E 209-65 (1993) Standard practice for the compression tests of metallic materials at elevated temperature. ASTM International
23. Dieter GE (2003) Hot compression test (Chap. 6). In: Dieter GE, Kuhn HA, Semiatin SL (eds) Handbook of workability and process design, pp 61–67. https://doi.org/10.1361/hwpd2003p061, (2003)

Evaluation of Tie Wing Deformation in 0.022 Inch Stainless Steel Orthodontic Bracket—A Finite Element Analysis

Akhil Minu Ajayan, V. Magesh, P. Harikrishnan, and D. Kingsly Jeba Singh

Abstract Orthodontics is the field of dentistry, which deals with the misalignment (malocclusion) of teeth and its treatment for correcting the improper bite in the jaw. Orthodontic brackets are a component of fixed appliances that are used in orthodontics that aligns and rectifies the misalignment. Archwires are used to control the movement of teeth by giving load on the bracket, which transfers the force to the teeth. Since the nineteenth century, with the development of orthodontics, various models of brackets that varies in shape and size were invented. The response behaviour and the effect on the bracket for the load applied by the archwire varies for different shape and slot size. As a result, the deformation and stress evolved on the bracket varies. Thus, our study aims to find the tie wings deformation in a conventional orthodontic bracket. Archwire is made to rotate with different angles inside the slot of the bracket. In our methodology, the bracket and archwire assembly were modelled, meshed and finite element analysis (FEA) was done on the brackets to evaluate the tie wings deformation for the various angle of twist on the archwire as done in a clinical situation.

Keywords Tie wing deformation · Conventional bracket · Angle of twist · Finite element analysis

A. M. Ajayan (✉) · V. Magesh
Department of Mechanical Engineering, SRM Institute of Science and Technology, Kattankulathur, Kancheepuram, Tamil Nadu, India
e-mail: akhilminu_ajayan@srmuniv.edu.in

V. Magesh
e-mail: mageshv@srmist.edu.in

P. Harikrishnan
Teeth "N" Jaws Centre, Lake Area, Nungambakkam, Chennai, Tamil Nadu, India

D. Kingsly Jeba Singh
School of Mechanical Engineering, SRM Institute of Science and Technology, Kattankulathur, Kancheepuram, Tamil Nadu, India

E. T. Akinlabi et al. (eds.), *Trends in Mechanical and Biomedical Design*, Lecture Notes in Mechanical Engineering,
https://doi.org/10.1007/978-981-15-4488-0_25

1 Introduction

For correcting the malocclusion or improper alignment in teeth, orthodontic brackets are used. The improper alignments include under bite, overbite, crooked and crowded teeth. A force is transferred from the archwire to the teeth; through the brackets used in the fixed appliance therapy. When there is force transfer mechanics, possibilities of bracket and wire deformation are more. By applying a force in the bracket slot, force moments are received during the treatment of malocclusion [1]. The stability of a tooth root in a location is related to the rectangular archwire and bracket relationship. The variables like interincisal angle, overjet and optimal teeth positioning are rectified using incisor torque. Torque expression applied by the archwire is affected by torsion magnitude, wire dimension, play between wire and bracket, bracket deformation and length of the bracket and wire [2–4]. Though experimental studies used for finding bracket deformation is built upon complicated design principles, it fails to graphically display the deformation and stress distribution in both bracket and wire [5–7]. Clinically, the archwire is twisted in various angles called the angle of twist for the correction of malocclusion in teeth.

The Finite element analysis (FEA) is one of the appropriate tools for finding the stress distribution and deformation in orthodontic applications [8, 9]. Few FEA findings were done, showing the slot wall deformation of the orthodontic brackets [10, 11]. Studies on tie wing deformation using FEA in a bracket was carried out by applying a couple on the bracket slot [12]. Our hypothesis in this study includes rotating the archwire in the bracket with various angles of twist in the bracket. Thus, we evaluated the tie wing deformation by twisting the archwire in various angles in 0.022-inch stainless steel (SS) bracket.

2 Materials and Methods

Standard Edgewise maxillary right central incisor SS Bracket with 0.022 inch × 0.028 inch slot (Leone, Italy) and a rectangular SS archwire size of 0.019 inch × 0.025 inch (G&H Orthodontics, USA).

The bracket dimensions were measured using an Optive LITE OLM vision measuring system (Hexagon Manufacturing Intelligence, Great Britain). The 2D profile of the orthodontic bracket was exported as an output file from the machine. This 2D profile was converted into a 3D model using AutoCAD (Autodesk, USA), and was exported to Solidworks (Dassault Systemes, France) for assembling the archwire with the orthodontic bracket. Finite element (FE) model for the assembly was generated using Hypermesh (Altair Engineering, USA) as pre-processor. The assembly model was meshed using hexahedral and pentahedral elements for maintaining the mesh flow as shown in Fig. 1. The meshed model was analysed using Ansys Workbench (Ansys, Inc, USA) as the processor. Linear, elastic and isotropic materials were used (Table 1).

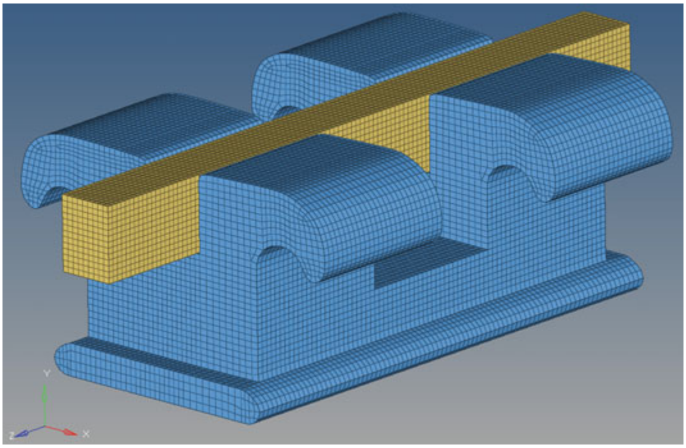

Fig. 1 Finite element model of bracket and wire assembly

Table 1 Material properties of stainless steel

Property	Value
Density	7.750 kg m^{-3}
Young's modulus	1.93×10^5 MPa
Poisson's ratio	0.3
Bulk modulus	1.693×10^5 MPa
Shear modulus	0.7355×10^5 MPa
Yield strength	207 MPa
Ultimate Strength	586 MPa

3 Finite Element Analysis of Bracket

The archwire which is placed inside the slot is twisted in different angles for simulating the palatal root torque condition. The angle of twist varied from 5° to 25° with an interval of 5°. The bracket base was fixed to arrest the translation in x, y and z axis. The deformed bracket and archwire are shown in Fig. 3 with an angle of twist of 25°. In the FEA, the nodal deformation on the top surface of the bracket for the four wings was measured for evaluating the tie wing deformation of the bracket wire assembly as shown in Fig. 2.

The archwire is made to rotate in the clockwise direction known to be as Labial crown torque by giving angle of twist on the wire. The wings on the right of the bracket are known to be Gingival Wings and the wings on the left to be occlusal wings.

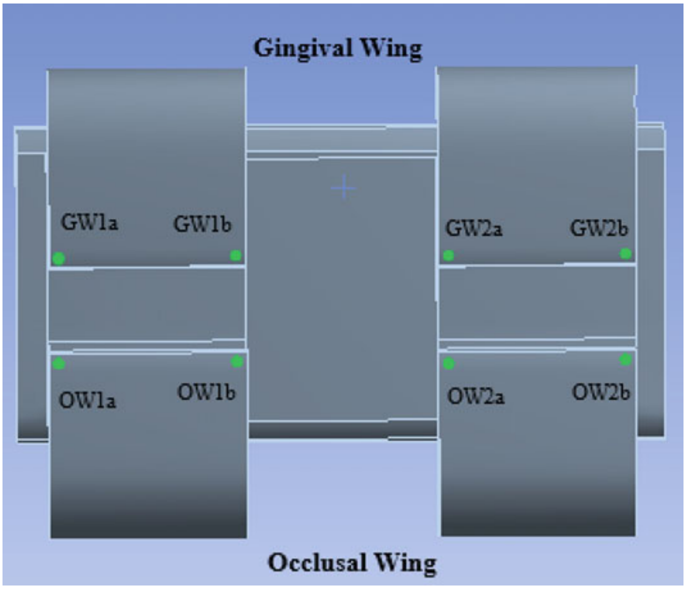

Fig. 2 Nodal points for tie wing deformation (OW—Occlusal Wing, GW—Ginigival Wing)

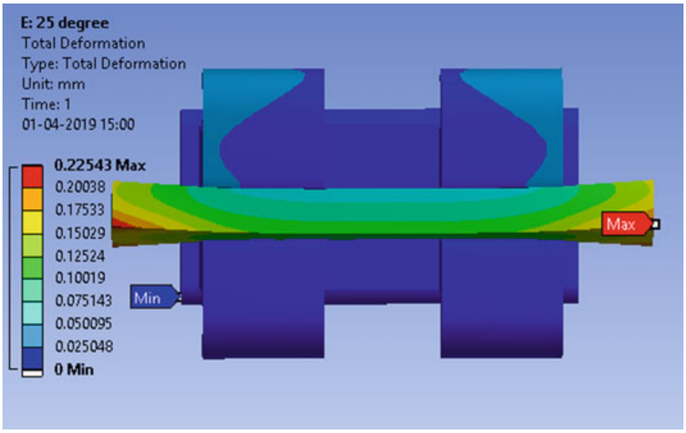

Fig. 3 Deformation of bracket and wire for an angle of twist with 25°

4 Results and Discussion

The FEA of orthodontic bracket with archwire was done for evaluating the tie wing deformation with an angle of twist varying from 5° to 25° on the archwire. The archwire was twisted at both ends with similar to the clinical conditions. The analysis results are shown below.

Figure 4a, b depict the orthodontic bracket tie wing deformation by applying an angle of twist on the archwire. For the applied angle of twist, bracket wire assembly showcased varying tie wing deformation for different angles of twist and which varied between the four wings.

From Tables 2 and 3 and Figs. 5 and 6, it is proved that, when palatal root torque is applied on the wire, Gingival wing undergoes more deformation than the occlusal wing in both *x*- and *y*-axis, and the outer edges of the wing undergoes more deformation than the inner edges as the wire is twisted at its ends. As the wire is twisted only at the ends, the load acting on wire throughout its length also varies. Therefore, the

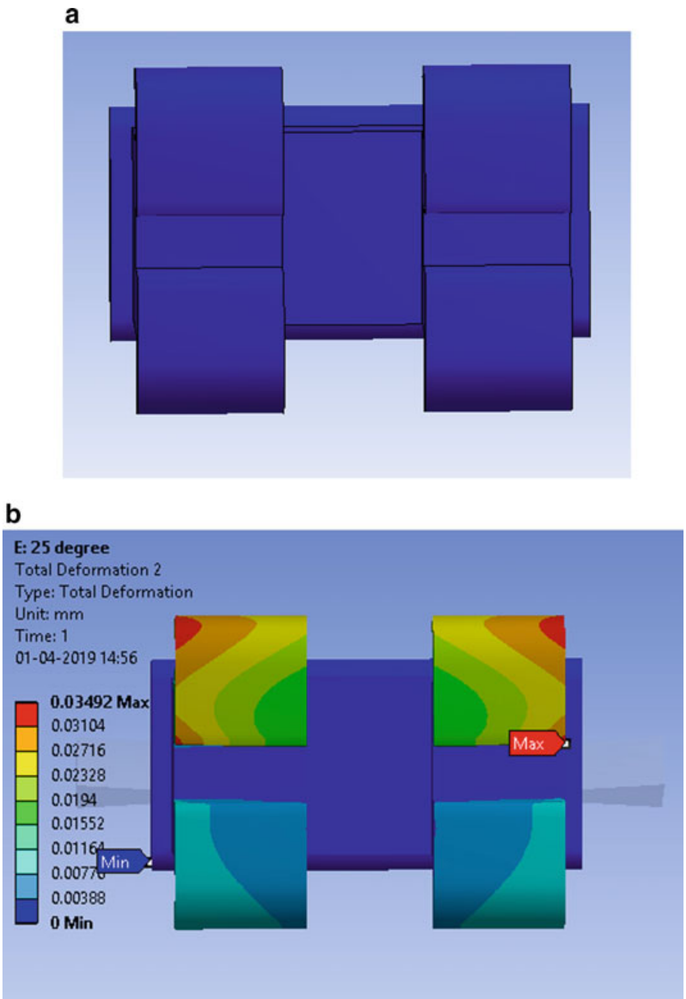

Fig. 4 **a** Bracket with 0° angle of twist on the archwire. **b** Bracket with 25° angle of twist on the archwire

Table 2 Nodal deformations in gingival and occlusal tie wings in *x*-axis

Angle of twist (degree)	Tie wing deformation in *x*-axis (μm)							
	GW1a	GW1b	GW2a	GW2b	OW1a	OW1b	OW2a	OW2b
5	0	0	0	0	0	0	0	0
10	4.412	2.268	2.271	4.406	1.043	0.432	0.432	1.042
15	13.191	6.854	6.855	13.206	3.346	1.396	1.396	3.345
20	22.09	11.493	11.502	22.095	5.973	2.508	2.508	5.981
25	31.272	16.105	16.157	31.115	9.003	3.688	3.739	9.054

Table 3 Nodal deformations in gingival and occlusal tie wings in *y*-axis

Angle of twist (degree)	Tie wing deformation in *y*-axis (μm)							
	GW1a	GW1b	GW2a	GW2b	OW1a	OW1b	OW2a	OW2b
5	0	0	0	0	0	0	0	0
10	0.995	0.685	0.686	0.994	0.129	0.156	0.157	0.129
15	2.989	2.104	2.097	3.007	0.431	0.507	0.508	0.428
20	4.965	3.482	3.512	4.907	0.774	0.883	0.893	0.778
25	7.009	5.031	4.992	7.024	1.178	1.333	1.343	1.175

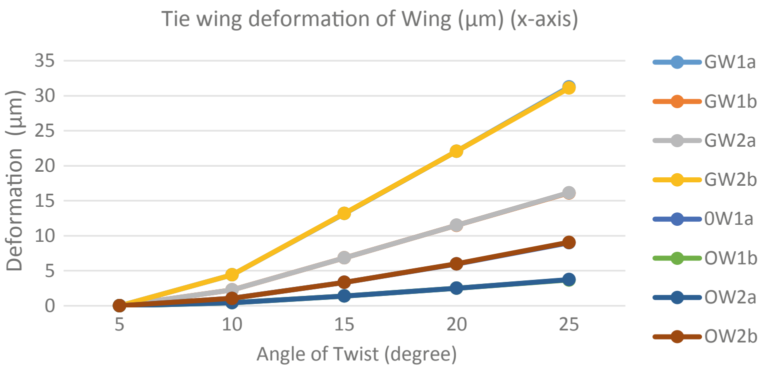

Fig. 5 Graphical representation for nodal deformations in gingival and occlusal tie wings in *x*-axis

deformation of the inner edges of wing is comparatively lower than the outer edges. The deformation in occlusal wing is found to be 25% of gingival wing deformation.

From the analysis, it is observed that the angular deformation also occurs on the tie wings when the archwire is twisted. Table 4 and Fig. 7 presents the tie wing angular deformation in gingival and occlusal wings. Thus, the angular deformation of tie wing is more in the location where bracket and wire are in contact.

Figure 8 shows the stress distribution in the bracket for the angle of twist of 25°. The point on which the bracket and the wire comes in contact with each other,

Fig. 6 Graphical representation for nodal deformations in gingival and occlusal tie wings in *y*-axis

Table 4 Tie wing angular deformation in gingival and occlusal wings

Angle of twist (degree)	Tie wing angular deformation (degree)							
	GW1a	GW1b	GW2a	GW2b	OW1a	OW1b	OW2a	OW2b
5	0	0	0	0	0	0	0	0
10	12.92	17.31	17.31	12.92	7.09	20.69	20.82	7.09
15	12.98	17.59	17.53	13.05	7.38	20.81	20.85	7.33
20	12.88	17.36	17.49	12.72	7.42	20.17	20.40	7.45
25	12.63	17.34	17.17	12.72	7.45	19.87	19.76	7.39

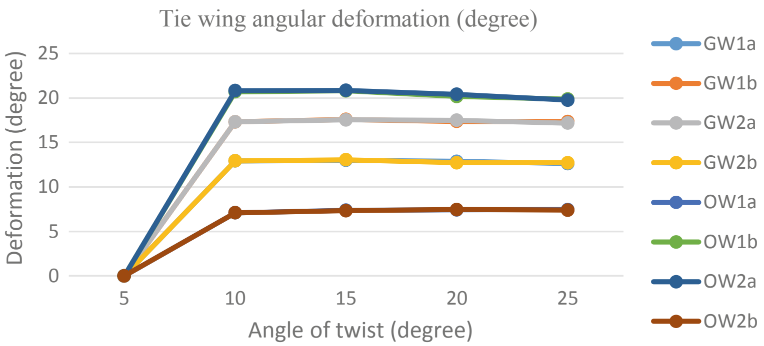

Fig. 7 Graphical representation for tie wing angular deformation

experiences maximum stress. Also, the point at which the stress concentration occurs is where the maximum load acts.

Figure 9 illustrates that the stress distribution in the wire throughout its length is not uniform. The point where bracket and wire are in contact undergoes maximum

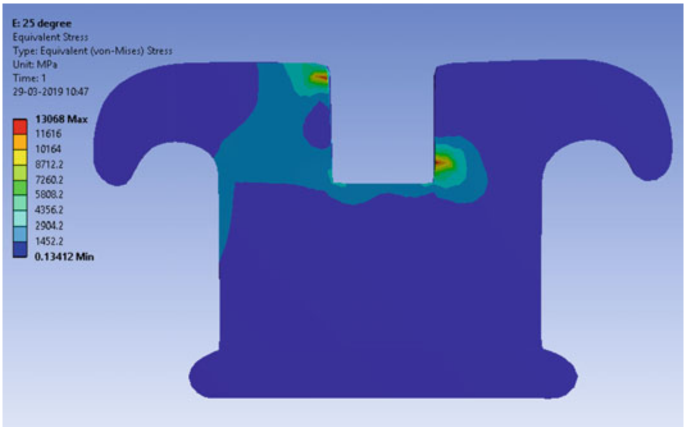

Fig. 8 Stress distribution in the bracket for 25°

Fig. 9 Stress distribution in the wire for 25°

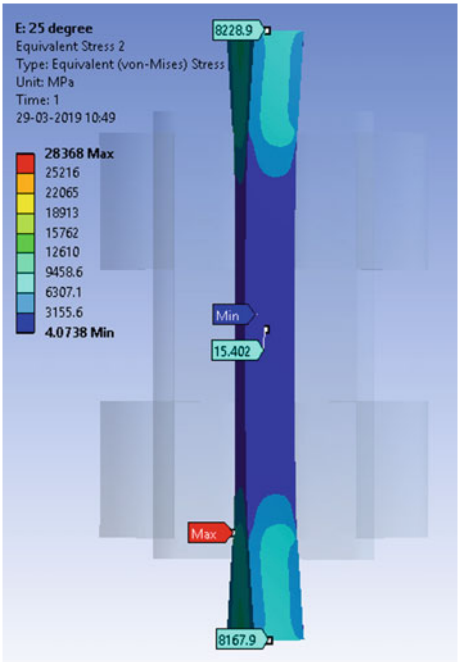

stress, while the middle portion of the wire undergoes minimum stress. As both the ends of the wire are twisted, they undergo an average stress.

5 Clinical Significance

Clinically, various angles of twist are applied for finer tooth movements. In this study, for the applied palatal root torque more deformation was recorded in the gingival tie wings than the occlusal tie wings. These deformations might indirectly indicate not only changes in the bracket tie wings but also in the bracket slot as well. Hence, clinicians should be aware of these bracket changes which will affect the final tooth positioning.

6 Conclusion

This *Insilico* study evaluated the tie wing deformation in 0.022-inch. SS orthodontic bracket by varying the angle of twist on the archwire. It is concluded that the tie wing deformation varies for the applied angle of twist by the archwire on the bracket. Thus, tie wing deformations on bracket have greater clinical significance with the angle of twist on the archwire.

Funding This work was funded by the SRM Institute of Science and Technology under selective excellence initiative program.

References

1. Wagner JA, Nikolai RJ (1985) Stiffness of incisor segments of edgewise arches in torsion and bending. Angle Orthod 55(1):37–50
2. Odegaard J, Meling E, Meling T.: An evaluation of the torsional moments developed in orthodontic applications, an in vitro study. Am J Orthod Dentofac Orthoped 105(4):392–400
3. Siatkowski RE (1999) Loss of anterior torque control due to variations in bracket slot and archwire dimensions. J Clin Orthod 33(9):508–510
4. Fischer H, Orthuber W, Es-Souni M, Meyer S (2000) Torque transmission between square wire and bracket as a function of measurement, form and hardness parameters. J Orofac Orthoped 61(4):258–265
5. Lacoursiere RA, Nobes DS, Homeniuk DL, Carey JP, Badawi HH, Major PW (2010) Measurement of orthodontic bracket tie wing elastic and plastic deformation by arch wire torque expression utilizing an optical image correlation technique. J Dent Biomech
6. Major TW, Carey JP, Nobes DS, Heo G, Major PW (2011) Measurement of plastic and elastic deformation due to third-order torque in self-ligated orthodontic brackets. Am J Orthod Dentofac Orthop 140(3):326–39
7. Melenka GW, Nobes DS, Major PW, Carey JP (2013) Three-dimensional deformation of orthodontic brackets. J Dent Biomech 4(1758736013492529)
8. Wakabayashi N, Ona M, Suzuki T, Igarashi Y (2008) Nonlinear finite element analyses: advances and challenges in dental applications. J Dent 36(7):463–471
9. Papageorgiou SN, Keilig L, Hasan I, Jäger A, Bourauel C (2016) Effect of material variation on the biomechanical behaviour of orthodontic fixed appliances: a finite element analysis. Eur J Orthod 38(3):300–7

10. Harikrishnan P, Magesh V, Kingsly J, Singh D (2017) Comparison of slot deformation in stainless steel and ceramic brackets during torque—a finite element analysis. South Eur J Orthod Dentofac Res. https://doi.org/10.5937/sejodr4-1284, May 2017
11. Magesh V, Harikrishnan P, Kingsly J, Singh D (2018) Finite element analysis of slot wall deformation in stainless steel and titanium orthodontic brackets during simulated palatal root torque. Am J Orthod Dentofac Orthoped 153(4)
12. Magesh V, Harikrishnan P, Sekhar TC (2018) Finite element analysis of orthodontic bracket tie wing deformation due to labial crown torque. IOP Conf Ser: Mater Sci Eng 402(012085)

A Finite Element Analysis to Study the Effect of Various Loading Conditions on the Intervertebral Disc in L4–L5 Section of Lumbar Spine

J. Daniel Glad Stephen, M. Prakash, V. K. Nevedha, and Manu Pandey

Abstract Lower back pain has been one among the difficulties faced in general, occurring in prevalent due to natural intervertebral disc failures in the lumbar spine region. Studies are required to examine natural disc failures due to day to day activities. A model of human lumbar spine section L4-L5 was generated to check for stability of natural disc under various loading conditions using finite element analysis. Computer tomography scan images were compiled together to generate a three-dimensional model of lumbar spine section L4-L5 by segmentation technique. Further, the model was prepared along with the generation of cortical bone, annulus pulposus, nucleus pulpous, vertebral endplates and corresponding ligaments. The material properties for each of the components were incorporated into the model from the literature available and meshed for analysis. The L4–L5 lumbar spine section model created, upon being checked for different motions of spine showed satisfying results yielding normal human motion preservation. Natural disc deformation parameters were observed under different loading conditions for daily activities.

Keywords Lumbar spine · Intervertebral disc failure · Finite element analysis

1 Introduction

There are basically four regions of the spinal column—cervical (C1–C7), thoracic (T1–T12), lumbar (L1–L5), sacral (S1–S5). Since the lumbar vertebrae are the strongest and largest among all, they are optimized for structural support rather than flexibility. There are intervertebral discs present in between the vertebral bodies that provide a cushion to distribute and transmit the forces.

These discs are responsible for linking the surfaces of the vertebrae and is sandwiched between upper and lower endplates. Intervertebral discs provide the required flexibility in the spine and are a medium to transmit and distribute loads.

J. Daniel Glad Stephen · M. Prakash (✉) · V. K. Nevedha · M. Pandey
Department of Mechanical Engineering, SRM Institute of Science and Technology, Kattankulathur 603203, India
e-mail: prakashmuniyandi@gmail.com

E. T. Akinlabi et al. (eds.), *Trends in Mechanical and Biomedical Design*, Lecture Notes in Mechanical Engineering,
https://doi.org/10.1007/978-981-15-4488-0_26

Natural discs consist of gelatinous nucleus pulposus center surrounded by annulus fibrosus structure (Fig. 2). The highly layered annulus is well oriented by fibrous collagen in the proteoglycan matrix. Nucleus comprises mainly of collagen, proteoglycan, and water [1].

There are various intervertebral disc diseases which include degenerative disc, bulging disc, herniated disc, thinning disc, and disc degeneration with osteophyte formation. Degeneration, basically the deterioration of the tissue, affects the material property of the tissues in the disc and thereby changing the behavior and function of the disc. The major cause of lower back pain and disability observed in the adults is due to the degenerative disc disease in the lumbar region of the spine.

With intervertebral disc failures, arises normal motion discomfort and difficulties in pursuing daily activities. Such cases can be cured by medication as well as surgical procedures consisting of either spinal fusion or total disc replacement using artificial implants. Pain relief occurs by stopping the motion of the painful disc by the direct bone connection between the vertebrae surrounding the painful disc in the spinal fusion procedure. Artificial disc replacement aims at removing the worn or damaged disc material and replacing it with a prosthetic implant [1].

The implant loads for different activities show a large inter- and intra-individual variation depending on the way the activities were performed [2]. To start with the study, the primary need is to understand the various activities performed by the body, the physiologic range and pattern of motion, and the method to be undertaken to perform the study.

In an earlier study, it is found out that most of the individuals do not use the full range of motion (ROM) and employ only a small part of their full active ROM when performing the daily activities [3]. Xia et al. [4] have observed that each of the vertebral levels reacts differently to external loads applied at different vertebral levels. A large variation in the pressure at the L4–L5 level was observed by Dreischarf et al. for different body positions [5]. The technique for the determination of the various loads acting on the lumbar spine is found to be well correlated with body weight [6]. The loading within the spine nearly shows a linear relationship with the body weight and height though the height does not have much influence [7].

The body posture and activities that necessitate flexion in the spine results in higher forces when compared to the spine in a neutral position or extension indicating that both influence the loads in lumbar spine [8]. Higher compressive load is experienced by the intervertebral disc in an upright position [9]. Miller et al. [10] have observed that the lumbar motion segments could resist considerably larger compression loads in bending without failure. Studies have indicated that the application of follower load can deliver realistic results for motion simulation [11].

There are generally two methods to conduct the biomechanical study: finite element analysis (FEA) and in vitro cadaveric test. Finite element analysis involves creating a computational model and is used for the simulation of biomechanical behavior of the spinal segment, whereas in vitro cadaveric tests are generally used to observe the normal motion responses with varying loading conditions in the cadaveric specimen. Finite element (FE) is a very efficient and powerful technology in the biomechanics of the spine segment in the lumbar region. A 3-D geometric model was created which includes the anatomical structure based on the Computer Tomography (CT) and Magnetic Resonance Imaging (MRI) data [12].

The present FEM method applies segment-wise compressive preload and the modifications can easily be made to apply the varying compression loads at different levels of the lumbar spine [13]. Once the finite element model (FEM) is validated, the further evaluation of range and pattern of motion of the L4–L5 spine segment under different loading conditions during daily activities can be done. The main focus lies under evaluating the condition of intervertebral disc subjected to various loading conditions under different daily task categories.

2 Materials and Methods

CT scan images of the vertebral section were obtained and compiled together to generate a three-dimensional model of lumbar spine section L4–L5 by segmentation technique. The surfaces were smoothened further by editing the three-dimensional data. A finite element L4–L5 lumbar spine section was modeled comprising of 95,457 solid elements and nine cable elements (Fig. 1a).

Structural eight-noded solid elements are used for cancellous bone, cortical bone, vertebral endplates, annulus pulposus and nucleus pulposus (Fig. 2), and the isotropic linear material properties such as Young's modulus and Poisson ratio values are chosen from literature [14]. During the application of compression load, annulus has been found to experience large tensile strains in a radial direction with time [15]. So

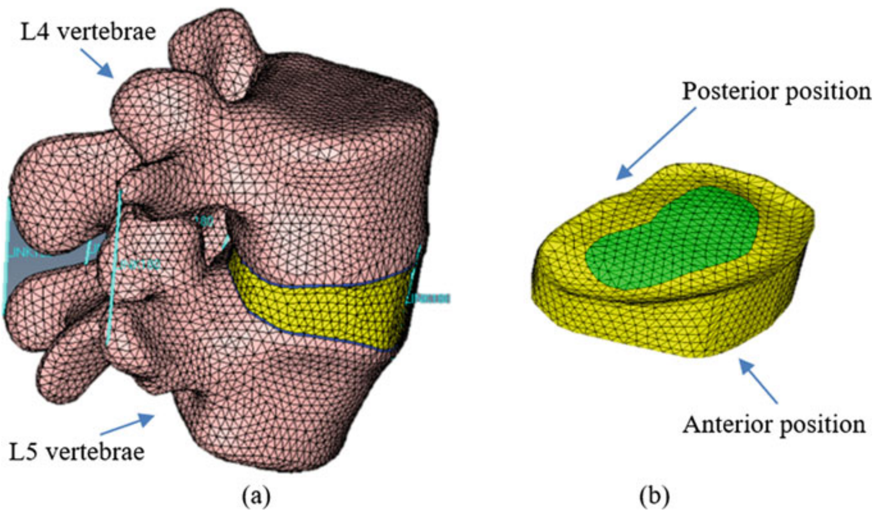

Fig. 1 **a** FE model of the L4–L5 lumbar spine section. **b** Enlarged view of L4–L5 intervertebral disc showing anterior and posterior positions

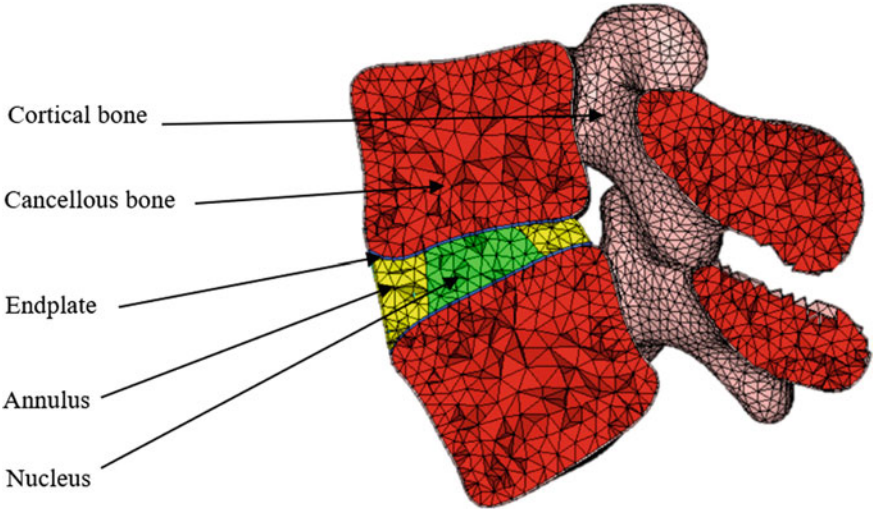

Fig. 2 Sectional cut view of L4–L5 finite element model created detailing various components

that annulus pulposus was thus assumed to have non-linear, hyperelastic behavior in this study by using the constant as per the Ref. [16].

Ligaments were integrated into the L4–L5 section created and represented by two-noded, three-dimensional spar elements having three degrees of freedom at each node. Linear isotropic behavior was incorporated into all seven ligaments of the lumbar spinal unit (anterior longitudinal ligament, posterior longitudinal ligament, ligament flavum, facet capsulary ligament, intertransverse ligament, interspinous ligament, and supraspinous ligament) created. Properties comprising of Young's modulus and cross-sectional area values were specified for all ligaments [14]. The L4–L5 curved facet joint was created as surface contact elements. The material characteristics of each of the components used in FE model have been mentioned in Tables 1 and 2.

Table 1 Material properties of different components present in the L4–L5 FE model

Components	Young's modulus (MPa)	Poisson's ratio	References
Cancellous bone	100	0.2	[14]
Cortical bone	12,000	0.3	[14]
Endplate	24	0.4	[14]
Nucleus	1	0.499	[14]
Annulus	(Hyperelastic, Mooney-Rivlin) $c_1 = 0.42$, $c_2 = 0.105$		[16]

Table 2 Material properties of various ligaments in the lumbar spine

Components	Young's modulus (MPa)	Cross-section (mm^2)	References
Anterior longitudinal ligament	7.8	63.7	[14]
Posterior longitudinal ligament	1	20	[14]
Ligamentumflavum	1.5	40	[14]
Facet capsulary ligament	7.5	30	[14]
Intertransverse ligament	10	1.8	[14]
Interspinous ligament	1	40	[14]
Supraspinous ligament	3	30	[14]

The inferior surface of L5 vertebra was rigidly constrained for all degrees of freedom. Moments of 10 Nm were applied on the superior surface of L4 vertebra to measure an angular range of motion for all spine motions (flexion, extension, left lateral bending, right lateral bending, left axial rotation and right axial rotation). Further, to examine the deformation pattern of intervertebral discs subject to various loading conditions during daily activities, compression load was applied on the superior surface of the L4 vertebra. The load administered for various daily activities was obtained from the literature.

3 Results and Discussion

For the L4–L5 lumbar section, loading condition of 10Nm was utilized as provided by the study of Yamamoto et al. [17] and angular range of motion for each of the spinal motions (flexion, extension, lateral bending) was observed as shown in Fig. 3. Each motion of spine has been examined and compared to the in vitro experimental

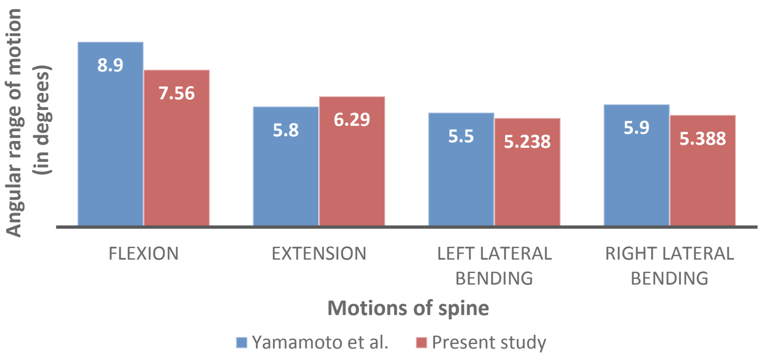

Fig. 3 Comparison of ROM data between in vitro experimental data [17] and the present study

Table 3 ROM data of the FE model compared to Yamamoto et al. [17]

Motions of spine	Yamamoto et al.	Present study
Flexion	8.9 ± 0.7	7.6
Extension	5.8 ± 0.4	6.3
Left lateral bending	5.5 ± 0.5	5.2
Right lateral bending	5.9 ± 0.5	5.4

data obtained by Yamamoto et al. [17]. The validation of axial rotation has been excluded since further focus lies distinctively on studying the natural disc deformation pattern under various loading conditions. The values of ROM under the same loading condition as acquired in this study are listed down as in Table 3.

In order to examine the condition of intervertebral disc during daily activities carried out, a further study was undertaken to make use of the validated finite element model generated. Activities such as standing, walking, twisting, jumping, coughing and laughing were chosen for analysis. Loading details for various activities have been acquired from the study [18]. A compression load was applied under each case on the superior surface of the L4 vertebra in a vertically downward direction distributed uniformly over its surface. Disc deformation and Von Mises stress values were procured to understand their correlation with varying loads. The acquired results have been mentioned in Fig. 5a–l.

In Fig. 4, an increase in the amount of compression load shows a consistent increase in the amount of disc deformation. The least value of displacement has been accounted for standing (Fig. 5a) whereas the highest value for laughing condition (Fig. 5f) in this study. The displacement values vary from the least value of 2.4 mm to the highest of nearly twice this amount. The deformation plot of the natural disc suggests that a greater part of displacement can be sighted by the anterior region of the disc under the compression load. Although the deformation values are higher in cases of coughing, laughing and jumping (Fig. 5c–f) only a less portion of anterior region experiences such change along with an expeditious decrease in deformation traveling towards the posterior area. Whereas standing and walking conditions with lesser compression load in comparison (Fig. 5a, b), still has a stronger influence over

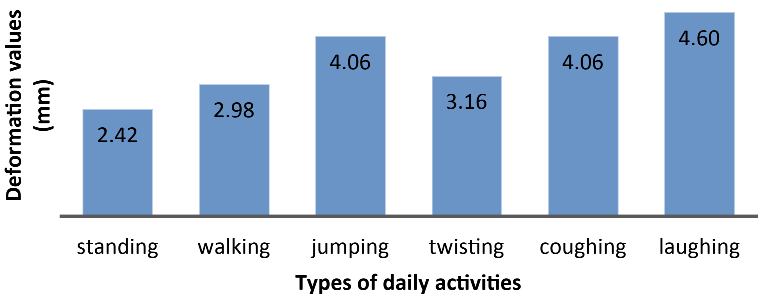

Fig. 4 Natural disc displacement variation for different activities

Loading condition	Displacement	Von mises stress
Standing Load applied 700 N	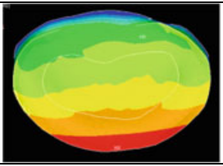	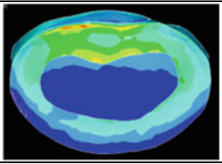
	(a) Maximum displacement - 2.42 mm	(g) Maximum stress – 1.24 N/ mm^2
Walking Load applied 850 N	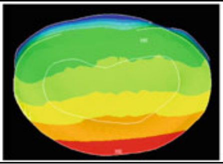	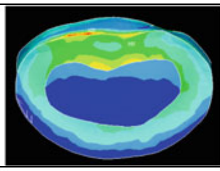
	(b) Maximum displacement - 2.98 mm	(h) Maximum stress – 1.39 N/ mm^2
Jumping Load applied 1100 N	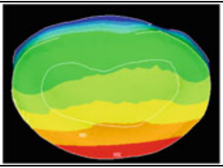	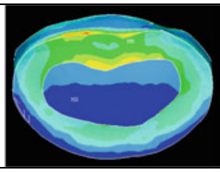
	(c) Maximum displacement - 4.06 mm	(i) Maximum stress – 1.71 N/ mm2
Twisting Load applied 900 N	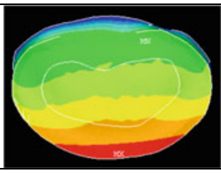	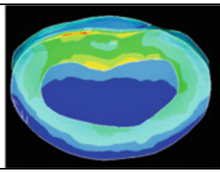
	(d) Maximum displacement - 3.16 mm	(j) Maximum stress – 1.44 N/ mm2
Cough ing Load applied 1100 N	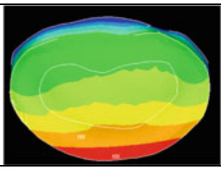	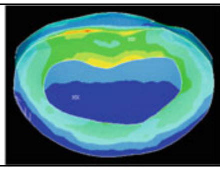
	(e) Maximum displacement - 4.06 mm	(k) Maximum stress – 1.71 N/ mm2
Laugh ing Load applied 1200 N	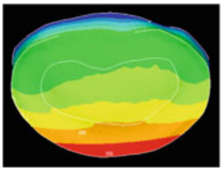	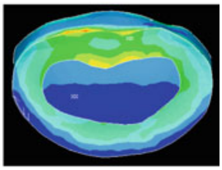
	(f) Maximum displacement - 4.60 mm	(l) Maximum stress – 1.93N/ mm2

Fig. 5 Contour plots of the natural disc under various loading conditions **a** deformation plot **b** stress plot (the anterior and posterior positions of the disc have been depicted in Fig. 1b)

a slightly larger portion of the anterior region of the intervertebral disc followed by a gradual decrease in its value bringing out the uniform distribution of deformation.

With the increasing value of load under varying daily activities, the maximum stress has been observed to considerably increase in magnitude. The range of maximum stress observed in the disc model varies from 1.24 to 1.93 N/mm^2. For all mentioned activities under the study, the stress induced in natural disc noticeably increases with depth as it reaches the L5 section. Stress concentration is more prevalent in the posterior area of disc consisting of annulus pulposus for all activities undertaken in our study.

In cases of walking, standing and twisting maximum stress is observed to be concentrated at the posterior disc rim (Fig. 5g, h, j). In contrast to this, rest activities show a lesser concentration of maximum stress in the same position. Incremental rise in the magnitude of stress in the lateral direction of the disc has been observed under jumping, coughing and laughing activities as shown in Fig. 5i, k, l. Furthermore, in activities of coughing, jumping and laughing maximum stress is found to have more concentration at depths closer to L5 surface compared to the rest.

4 Conclusion

In conclusion, the FE model generated was useful in carrying out a deformation analysis of intervertebral discs under varying loads that act on the lumbar spine region in accordance with the activity performed or posture attained. The loading value is influenced if a complex posture or activity is performed. It is seen that high forces on the spinal segment increase the amount of displacement and the stress induced in the natural disc and which eventually causes degeneration. Disc deformation and stress plots suggested activities like coughing, jumping and laughing have a greater impact on natural disc functioning chosen in this study. The results obtained can be used further in postoperative motion analysis of the lumbar spine region in performing a variety of daily tasks.

Acknowledgements This work was supported by the Biomechanics lab, Department of Mechanical Engineering, SRMIST, Kattankulathur–603203. We thank Mr. Raja. D, Asst Professor (S.G) and Research Head, Biomechanics lab, Department of Mechanical Engineering, SRMIST, Kattankulathur–603203. For assistance to improve the manuscript.

References

1. Kurtz SM, Edidin A (2006) Spine Technology handbook, 2nd edn
2. Rohlmann A, Pohl D, Bender A, Graichen F, Dymke J, Schmidt H, Bergmann G (2014) Activities of everyday life with high spinal loads. PLoS One 9(5):e98510
3. Bible JE, Biswas D, Miller CP, Whang PG, Grauer JN (2010) Normal functional range of motion of the lumbar spine during 15 activities of daily living. J Spinal Disord Tech 23(2):106–112

4. Li G, Wang S, Passias P, Xia Q, Li G, Wood K (2009) Segmental in vivo vertebral motion during functional human lumbar spine activities. Eur Spine J 18(7):1013–1021
5. Dreischarf M, Schmidt H, Shirazi-Adl A, Arjmand N, Rohlmann A (2015) Estimation of loads on human lumbar spine: a review of in vivo and computational model studies. J Biomech 49(6):833–845
6. Ledet EH, Sachs BL, Brunski JB, Gatto CE, Donzelli PS (2000) Real-time in vivo loading in the lumbar spine: part 1. Interbody implant: load cell design and preliminary results. Spine (Phila. Pa. 1976) 25(20):2595–2600
7. Han KS, Rohlmann A, Zander T, Taylor WR (2013) Lumbar spinal loads vary with body height and weight. Med Eng Phys 35(7):969–977
8. Ledet EH, Tymeson MP, DiRisio DJ, Cohen B, Uhl RL (2005) Direct real-time measurement of in vivo forces in the lumbar spine. Spine J 5(1):85–94
9. Wang S, Park WM, Kim YH, Cha T, Wood K, Li G (2014) In vivo loads in the lumbar L3-4 disc during a weight lifting extension. Clin Biomech 29(2):155–160
10. Miller JAA, Schultz AB, Warwick DN, Spencer DL (1986) Mechanical properties of lumbar spine motion segments under large loads. J Biomech 19(1):79–84
11. Rohlmann A, Zander T, Rao M, Bergmann G (2009) Applying a follower load delivers realistic results for simulating standing. J Biomech 42(10):1520–1526
12. Li H, Wang Z (2006) Intervertebral disc biomechanical analysis using the finite element modeling based on medical images. Comput Med Imaging Graph 30(6–7):363–370
13. Renner SM, Natarajan RN, Patwardhan AG, Havey RM, Voronov LI, Guo BY, Andersson GBJ, An HS (2006) Novel model to analyze the effect of a large compressive follower pre-load on range of motions in a lumbar spine. J Biomech 40(6):1326–1332
14. Shin DS, Lee K, Kim D (2007) Biomechanical study of lumbar spine with dynamic stabilization device using finite element method. CAD Comput Aided Des 39(7):559–567
15. Schmidt H, Shirazi-Adl A, Galbusera F, Wilke HJ (2010) Response analysis of the lumbar spine during regular daily activities-A finite element analysis. J Biomech 43(10):1849–1856
16. Dreischarf M, Zander T, Shirazi-Adl A, Puttlitz CM, Adam CJ, Chen CS, Goel VK, Kiapour A, Kim YH, Labus KM, Little JP, Park WM, Wang YH, Wilke HJ, Rohlmann A, Schmidt H (2014) Comparison of eight published static finite element models of the intact lumbar spine: predictive power of models improves when combined together. J Biomech 47(8):1757–1766
17. Yamamoto I, Panjabi MM, Crisco T, Oxland T (1989) Three-dimensional movements of the whole lumbar spine and lumbosacral joint. Spine J. 14(11):1256–1260
18. White III AA, Panjabi MM (1990) Clinical biomechanics of the spine, 2nd edn

Numerical Simulation of a Small-Scale Shock Tube Using OpenFOAM®

Satheesh Kumar Aravind, Anugya Singh, and B. T. Kannan

Abstract Shock waves are a phenomenon that can be produced under constrained conditions inside a shock tube. These waves have a wide scope of studies due to their multi-disciplinary applications. Therefore, in the present work, the main focus is to conduct transient numerical simulations of a small-scale shock tube which has been designed and fabricated. Comparison of 1D, 2D, and 3D cases, and grid independence studies have been carried out successfully along with parametric study by variation of driver section pressures. Simulations are conducted using the open-source Computational Continuum Mechanics toolbox, OpenFOAM®. Processing of the simulated data is carried out using Paraview via quantitative and qualitative methods.

Keywords Shock tube · Shock wave · Transient · OpenFOAM® · Visualization

1 Introduction

The shock waves can be created using various experimental setups for studying the behavior and physics of different gas dynamics phenomena. It is multi-disciplinary in nature and thus there are many ways to generate a shock wave, one such apparatus which produces shock wave is a shock tube. It can generate a shock wave with the sudden rupture of a diaphragm which separates the driver (high-pressure) and driven (low-pressure) sections.

The initial idea and the field of research in shock tube were developed a century ago and since then many experimental advancements have been achieved in this

S. K. Aravind (✉) · A. Singh · B. T. Kannan (✉)
Department of Aerospace Engineering, SRM Institute of Science and Technology, Kattankulathur 603203, India
e-mail: askerp001@gmail.com

B. T. Kannan
e-mail: skyinventorbt@gmail.com

A. Singh
e-mail: anu2riks@gmail.com

E. T. Akinlabi et al. (eds.), *Trends in Mechanical and Biomedical Design*,
Lecture Notes in Mechanical Engineering,
https://doi.org/10.1007/978-981-15-4488-0_27

field by different pioneering scientists and engineers throughout the last century. The introduction of Computational Fluid Dynamics (CFD) brought in a major change in the field of Fluid Mechanics. Numerical simulations of normal shock wave reflections were carried out by Weber et al. [1] in a two-dimensional channel for the investigation of the unsteady viscous interaction aspects of bifurcation of the shock. It indicated that the shear layer in the bifurcation being unsteady in nature and the vortices of large and small scales lead to the creation of complex flow patterns and heat transfer phenomena. Amir et al. [2] developed a two-dimensional Euler solver for shock tube applications which validated the performance of a short-duration hypersonic shock tube facility based on shock speed and pressure. An experimental and numerical study on shock was made by Moradi et al. [3] in which both driver and driven gas used was air. The CFD was conducted in a two-dimensional geometry with a transient form of laminar viscous flow regime and the results were in good compatibility with the experimental results. Further numerical simulations on the flow evolution mechanism inside the shock tube were done by Kiverin and Yakovenko [4] in which the flow patterns behind the shock waves and temperature non-uniformities in shock tube with ignition were investigated. Another detailed parametric CFD study on the characteristics of the shock train inside the shock tube was done by Kim et al. [5] which on the complex flow phenomena due to the interaction caused between the reflected shock wave and boundary layer leading to the generation of shock train. Since it has multi-disciplinary applications Luan et al. [7] conducted a shock tube simulation attached with a small exit nozzle to support the analysis of chemical mixtures and its reactions. The flow physics inside the tube and the nozzle were investigated and it was concluded that for most chemical kinetic applications, the influence of flow field inside the shock tube can be neglected.

Thus, the main focus of the present work is to conduct numerical simulations using the open-source Computational Continuum Mechanics toolbox, OpenFOAM® on a shock tube using two different solvers viz. sonicFoam and rhoCentralFoam, to conduct qualitative (visualization) and quantitative (pressure, density, and velocity) post-processing and compare the results obtained with the theoretical and the experimental results which have been carried out [6].

2 Computational Methodology

2.1 Geometry and Meshing

The geometry was created along x, y, and z-axes using OpenFOAM®. Geometries were created for one-dimensional (1D), two-dimensional (2D) and three-dimensional (3D) cases with a length of driver section of 1 m and driven section of 1.5 m, as can be seen in Figs. 1 and 2. The 1D and 2D geometry were created the same with unit thickness and the boundary conditions determine the solution of the equations in the

Fig. 1 Geometry for 1D and 2D case

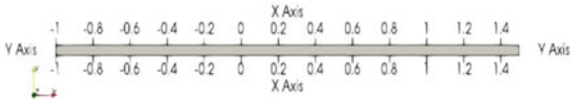

Fig. 2 Geometry for 3D case

required direction. The geometry was created with respect to the experimental setup which had been fabricated [6].

For 1D and 2D geometries, a single block and in the 3D case, a four-blocks were used with following edge/face names, i.e., Ends, Walls, Front, and Back, to obtain uniform structured grid and the ease of meshing. Many iterations of meshing were considered following from 1D to 3D for capturing of the shock wave. Figures 3, 4, and 5 are provided as an example of the meshes that were created, and Table 1 shows the number of cells included in each case.

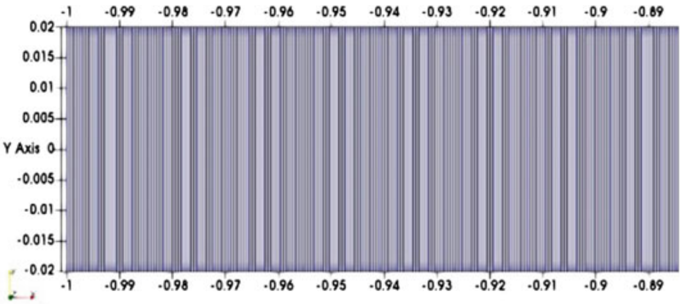

Fig. 3 1D mesh with 5000 cells

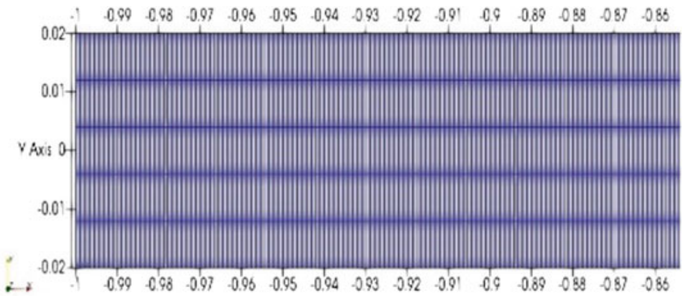

Fig. 4 2D mesh with 25,000 cells

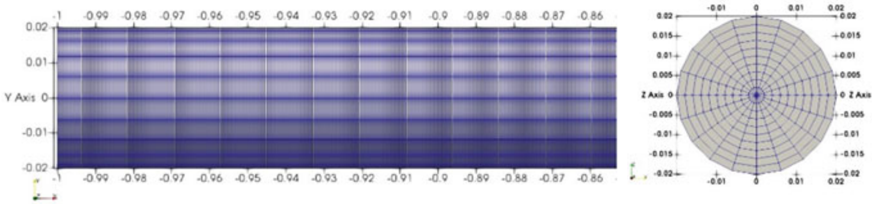

Fig. 5 3D mesh (front and side view) with 1,000,000 cells

Table 1 Number of cells and its distribution in each case of mesh

Case	Case number	Number of divisions in each direction			Total number of cells
		X	*Y*	*Z*	
1D	1	2000	–	–	2000
	2	2500	–	–	2500
	3	3000	–	–	3000
	4	5000	–	–	5000
	5	10,000	–	–	10,000
2D	6	5000	5	–	25,000
	7	5000	10	–	50,000
	8	5000	40	–	200,000
3D	9	5000	5	5	500,000
	10	5000	5	10	1,000,000

2.2 *Governing Equations*

The flow inside the shock tube in “sonicFoam” which is a transient pressure-based solver for trans-sonic/supersonic, laminar or turbulent flow of a compressible gas is governed by the Eqs. 1–6 [8]. The mass and momentum conservation equations are given as follows:

$$\frac{\partial \rho}{\partial t} + \nabla \cdot (\rho \vec{u}) = 0 \tag{1}$$

$$\frac{\partial \rho \vec{u}}{\partial t} + (\vec{u} \cdot \nabla)\rho \vec{u} - \nabla \cdot R_{\text{eff}} = -\nabla p \tag{2}$$

The energy equation is given as follows:

$$\frac{\partial \rho e}{\partial t} + \nabla \cdot (\rho \vec{u} e) + \frac{\partial \rho K}{\partial t} + \nabla \cdot (\rho \vec{u} K) + \nabla \cdot (\vec{u} p) - \nabla \cdot (\alpha_{\text{eff}} \nabla e) = 0 \tag{3}$$

where, ρ: Density, e: Internal Energy, K: Kinetic Energy, p: Pressure, $\vec{u}$: Velocity Vector, R_{eff}: Stress Tensor notation in OpenFOAM®, α_{eff} is the effective thermal diffusivity.

The governing equation of "rhoCentralFoam" which is a density-based compressible flow solver based on central-upwind schemes of Kurganov and Tadmorare [9]. The continuity equation is given as follows:

$$\frac{\partial p}{\partial t} + \frac{\partial}{\partial x_i}(u_i \rho) = 0 \tag{4}$$

The momentum equation is given by:

$$\left(\frac{\partial \widehat{u}_i}{\partial t}\right)_I + \frac{\partial}{\partial x_j}\left(u_i \widehat{u}_j\right) + \frac{\partial p}{\partial x_i} = 0 \tag{5}$$

The energy equation is given as follows:

$$\left(\frac{\partial \widehat{E}}{\partial t}\right)_I + \frac{\partial}{\partial x_k}\left[u_k\left(\widehat{E} + p\right)\right] - \frac{\partial}{\partial x_i}\mu u_j\left(\frac{\partial u_j}{\partial x_i} + \frac{\partial u_i}{\partial x_j} - \frac{2}{3}\frac{\partial u_k}{\partial x_k}\delta_{ij}\right) = 0 \tag{6}$$

From $\widehat{E}$, the temperature is calculated through,

$$T = \frac{1}{C_v}\left(\frac{\widehat{E}}{\rho} - \frac{u_k u_k}{2}\right) \tag{7}$$

where p: Pressure, T: Temperature, t: time, ρ: Density, μ: Dynamic Viscosity, δ: Kronecker delta, u_i: velocity vector, k: Turbulent Kinetic Energy, x: Space Variable, i, j, k: Tensor Indices, E: Energy.

The algorithm used by both the solvers is PIMPLE which is a combination of SIMPLE (Semi-Implicit Method for Pressure-Linked Equations) and PISO (Pressure Implicit with Splitting of Operators).

2.3 Boundary Conditions

For all the cases, "patch" was assigned to both the ends. In 1D case, all the rest of the faces were assigned "empty" whereas in 2D case, only the front and back faces were assigned "empty" while the top and bottom were assigned to 'wall (no slip)'. However, in the 3D case, all the faces except the ends were assigned to "wall (no slip)".

The pressure in the driver and driven sections were 199,948 Pa and 101,325 Pa respectively, and temperatures in the driver and driven sections were 300.15 K for the initial case validation with the experimental results. Four more cases were carried out with all other parameters as constant and increase in driver section pressures as follows: 225,000 Pa, 250,000 Pa, 275,000 Pa and 300,000 Pa.

A region was defined using coordinates from the position of the diaphragm to the end of the driven section of the tube and the gas in both the sections was given as air. The simulation was made to run from $t = 0$ s to $t = 0.0035$ s, to draw similarities from the experimental data [6].

3 Results and Discussion

Paraview was used to conduct post-processing of the data obtained from the numerical simulations. Initially, grid independence study was carried out in each direction, as can be seen from Fig. 6, curves of Case 1 to 3 and Case 4 to 5 overlap over each other completely. The change in curvature from Case 3 to 4 can be observed, due to the increment in the number of cells. Since Case 4 was most efficient and accurate, the number of cells in the X direction was fixed to 5000 for further analysis.

Similarly, grid independence study was carried out for 2D and 3D cases separately and it was found that all of them overlapped successfully. Hence, the number of cells in Y and Z direction was fixed at 5 and 10, respectively, in order to capture the properties of the shock wave with increasing time. Another comparison was drawn between the selected cases from 1D, 2D, and 3D as shown in Fig. 7. It can be seen that all the curves overlap over each other with a very slight difference. Therefore, for saving computational time and resources, Case 4 was selected for conducting parametric studies by varying the driving section pressures.

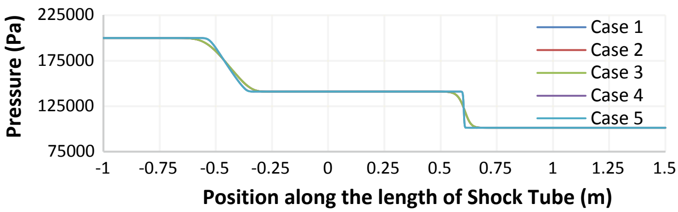

Fig. 6 1D grid independence study at time $t = 0.0015$ s

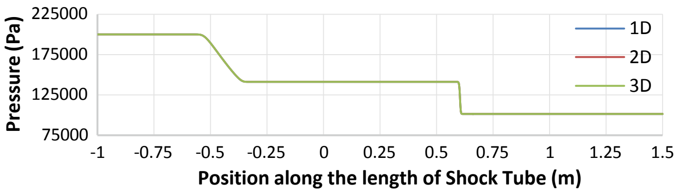

Fig. 7 1D, 2D, and 3D case comparison at time $t = 0.0015$ s

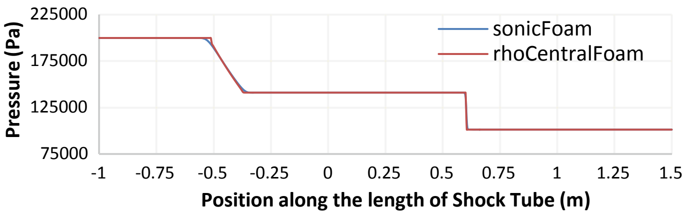

Fig. 8 Comparison of solvers at time $t = 0.0015$ s

Once the meshing was finalized, the comparison of both solvers was carried out. As shown in Fig. 8, only a slight difference is present between both the curves which can be observed at the pressure drop that occurs in the driver section region across the expansion fan. Thus, for obtaining data on the velocity of the particles in between the shock wave and the expansion fan and the density inside the shock tube sonicFoam and rhoCentralFoam were used, respectively.

The difference in pressure at different time steps can be seen in Figs. 9 and 10. At $t = 0$ s, the change of pressure is visible as a sudden single drop in the curve, after the rupture of the diaphragm as the time increases there are two pressure drops in the in curvature, due to the creation of expansion fan and shock wave. The constant

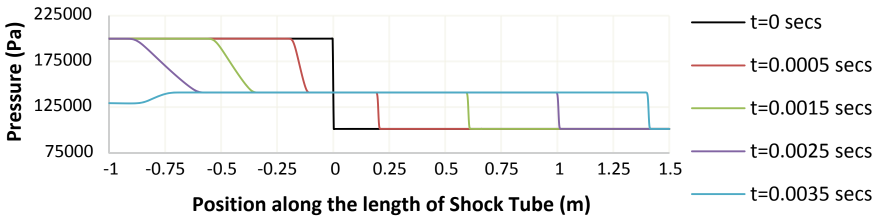

Fig. 9 Pressure variation inside the shock tube at different time steps using “sonicFoam”

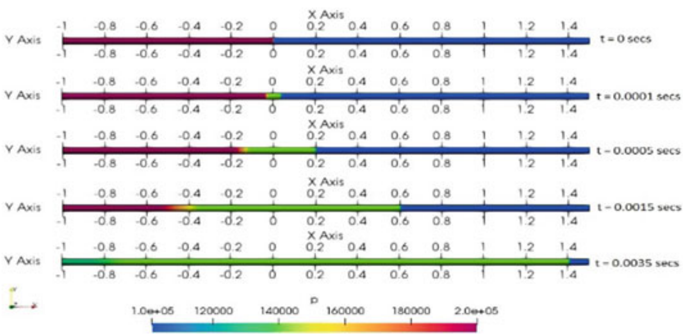

Fig. 10 Pressure contour plot inside the shock tube at different time steps using “sonicFoam”

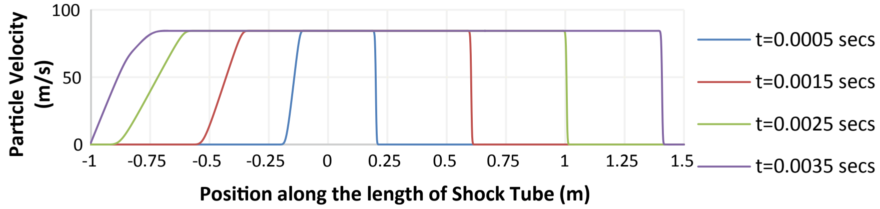

Fig. 11 Velocity of the particles in between the shock wave and the expansion fan inside the shock tube at different time steps using 'sonicFoam'

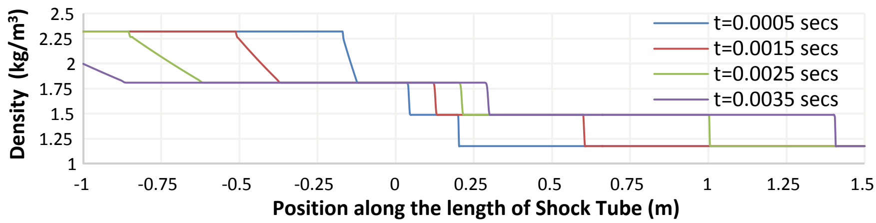

Fig. 12 Density variation inside the shock tube at different time steps using "rhoCentralFoam"

line after the first pressure drop depicts that the pressure does not change in between the expansion fan and shock wave.

Figure 11 shows the particle velocity in between the expansion fan and shock wave at different time steps. Since there is no pressure difference between the particles behind the shock tube and behind the shock wave, therefore, the Velocity of Particles remains constant in this region as can be seen from the figure.

The variation of density inside the shock tube at different time steps is shown in Figs. 12 and 13 shows the gradient contour plot of density. The presence of the contact surface which is an imaginary separation line between the gases in the driver and driven section can be seen. There are three drops in the curves in each time step, due to the sudden change in the density.

The temperature variation inside the shock tube at different time steps is captured in Figs. 14 and 15. The temperature is uniform throughout the tube at time $t = 0$ s as given in the input boundary condition. But, once the shock wave is produced, it can be seen that there is a sudden increase in temperature behind the shock tube till the contact surface where the temperature drops and remains constant till the expansion fan. This sudden increase in temperature is caused due to abrupt pressure differences created inside the shock tube.

Figure 16 shows the pressure variation inside the shock tube with different driver section pressures. The distances between the curves increase with the increase in pressure values, but due to the same driven section pressure given in all the cases, curves overlap towards the end which is the portion in front of the shock wave.

The Mach number and the velocity of the particles in between the expansion fan and shock wave were calculated using the following formulae [10, 11]:

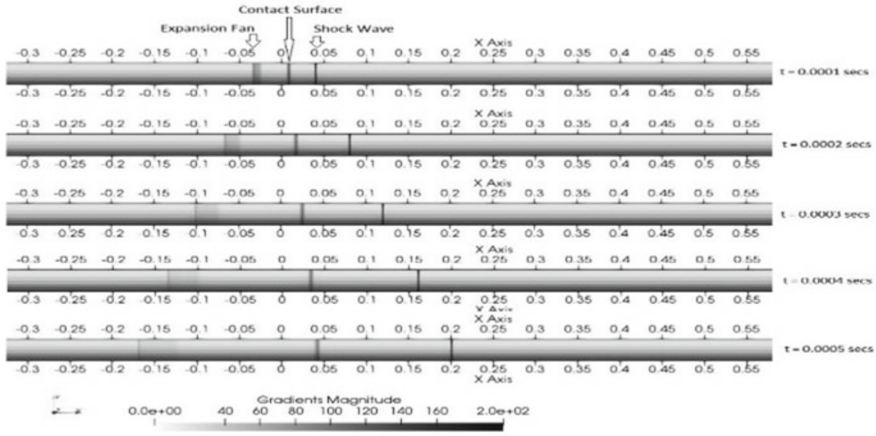

Fig. 13 Density gradient plot inside the shock tube at different time steps using 'rhoCentralFoam'

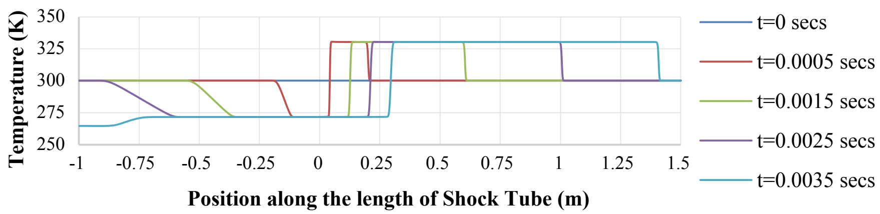

Fig. 14 Temperature contour plot inside the shock tube at different time steps using "sonicFoam"

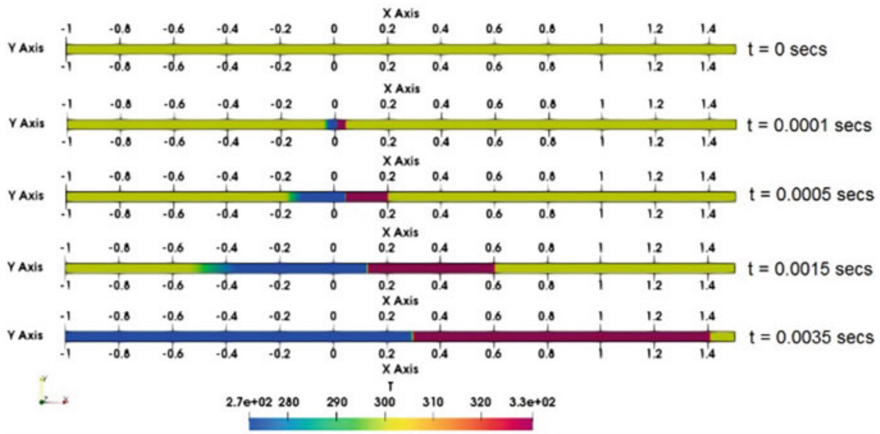

Fig. 15 Temperature contour plot inside the shock tube at different time steps using "sonicFoam"

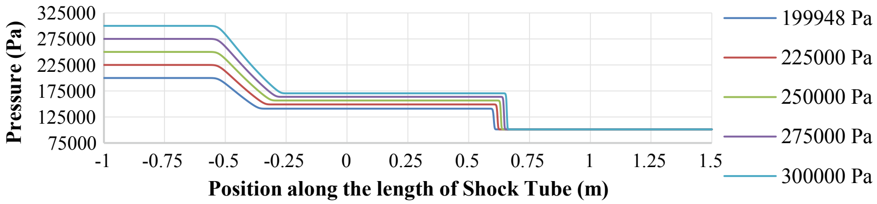

Fig. 16 Comparison of the pressure variation plots with different driver section pressures inside the shock tube at $t = 0.0015$ s

$$\frac{P_2}{P_1} = 1 + \frac{2\gamma_1}{\gamma_1 - 1}\left(M_1^2 - 1\right) \tag{8}$$

$$V_2 = \frac{2C_1}{\gamma_1 + 1}\left(M_1 - \frac{1}{M_1}\right) + V_1 \tag{9}$$

where P_1: Pressure in front of the Shock Wave (Pa), P_2: Pressure behind the Shock Wave (Pa), γ_1: Heat Capacity Ratio (for air = 1.4), M_1: Shock Mach Number, V_1: Velocity of particles in front of the Shock Wave (m/s) (i.e., 0), V_2: Velocity of particle behind the Shock Wave (m/s), C_1: Speed of Sound in the medium (346 m/s for air in 300.15 K).

Theoretical calculations were done using gas dynamic isentropic relations inside a shock tube and the comparison of values is shown in Table 2.

The difference between the theoretical, experimental (in the case of 199,948 Pa driver section pressure: Shock Mach Number = 1.155; Velocity of Particles = 83.39 m/s [6]) and computational Shock Mach Number is under 10.52% and for the Velocity of Particles, it is under 1.63% for all the cases. This is due to the lack of following boundary conditions: a The viscous effects of the fluid and friction effects added by the walls. b As the shock wave moves forward, a boundary layer is formed behind the shock wave which causes dissipation in the kinetic energy as heat which is conveyed to the walls via heat transfer. This causes deceleration of shock wave and acceleration of the contact surface as the time increases.

Table 2 Comparison of the values obtained with different driver section pressures

Driver section pressure (Pa)	Shock mach number		Velocity of particles (m/s)	
	Computational	Theoretical	Computational	Theoretical
199,948	1.282	1.16	84.5	85.9
225,000	1.296	1.19	99	100.82
250,000	1.309	1.21	112.08	112
275,000	1.321	1.24	123.91	125
300,000	1.333	1.26	134.7	134.5

4 Conclusion

Numerical simulation of a Shock Tube was conducted using the open-source Computational Continuum Mechanics toolbox, OpenFOAM®. The geometry used was inspired by the fabricated Shock Tube [6]. Grid independence study was carried out in 1D, 2D, and 3D to fix the number of divisions in each direction using ten different mesh cases. The pressure curves obtained were compared to finalize the mesh for further analyses. The selected mesh was used to compare two different solvers viz. sonicFoam and rhoCentralFoam. The sonicFoamsolver was used to study the differences in Pressure and Temperature and also the Velocity of Particles in between the Shock Wave and Expansion Fan, and rhoCentralFoam solver was used to study the density differences at various time steps. The driver section pressures were varied to conduct a parametric study keeping all other parameters as constant. The Shock Mach Number and Velocity of Particles were calculated using the data obtained and compared for the cases of driver section pressure values. The difference in the simulated and theoretical data was found to be due to the lack of comprehensive boundary conditions. Pressure and Temperature contour and Density gradient plots revealed the magnitude of the pressure, temperature, and density gradient, respectively, at different time steps along with the direction of the motion of Shock Wave, Expansion Fan, and the contact surface inside the shock tube.

Acknowledgements The authors acknowledge the usage of Advanced Computing Laboratory (ACL), Department of Aerospace Engineering at SRM Institute of Science and Technology (SRMIST) for the simulations performed towards the present research work.

References

1. Weber YS, Oran ES, Boris JP, Anderson JD Jr (1995) The numerical simulation of shock bifurcation near the end wall of a shock tube. Phys Fluids 7:2475–2488
2. Amir A-F, Yusoff M, Yusaf T (2008) Numerical simulation of inviscid transient flows in shock tube and its validations. Int J Math Phys Eng Sci 2
3. Moradi A, Fard FM, Mani M, Ranjbar M, Mottaghipour M (2012) Experimental and numerical investigation of AUT shock tube. Eur J Exp Biol 2(5):1820–1826
4. Kiverin A, Yakovenko I (2018) On the mechanism of flow evolution in shock-tube experiments. Phys Lett A 382(5):309–314. ISSN 0375-9601
5. Kim DW, Kim TH, Kim HD (2017) A study on characteristics of shock train inside a shock tube. Theor Appl Mech Lett 7(6):366–371. ISSN 2095-0349
6. Singh A, Aravind S, Kannan BT (2020) Studies on blasting effects of shock waves from a small – Scale shock tube. AIP Conference Proceedings, vol 2204, p 030003
7. Luan Y, Olzmann M, Magagnato F (2018) Simulation of a shock tube with a small exit nozzle. J Thermal Sci 27
8. Petrescu M (2015) Computational fluid dynamics in mesoscopic nozzles. M.S. thesis, McGill University
9. Winter M (2013) Benchmark and validation of Open Source CFD codes, with focus on compressible and rotating capabilities, for integration on the SimScale platform. M.S. thesis, Chalmers University of Technology

10. Bokil M (2010) Characterization of the pressure wave from a shock tube using numerical simulations. M.S. thesis, The University of Utah
11. Information on https://nptel.ac.in/courses/101106040/chapter%203.pdf. (Module 13, Experimental Aero (Gas) Dynamics, NPTEL Course by Dr. Job Kurian)

Contact Stress Analysis on a Functionally Graded Spur Gear Using Finite Element Analysis

V. Aravind, S. Adharsh, D. Prakash, S. Martin Vinoth, and P. Marimuthu

Abstract Gears are one of the most essential and most significantly used power transmitting parts. Spur gears are more commonly used in practice as it is easy to manufacture and it is simple in design. The failure of gear is mainly attributed to stresses developed in the gears. Contact and bending stresses developed in the gears significantly reduce the lifetime of the gears being used. Materials which are tailored for specific applications can be put under test to minimise the stresses developed and increase the lifetime. Functionally graded materials are advanced materials with spatial gradation in composition to achieve specifically tailored properties. This work attempts to implement functionally graded materials (aluminium-steel, steel-zirconium) in the gears drives. Further, finite element analysis is used to evaluate its contact stresses for various distributive laws (exponential, linear, and power). In addition to that, the contact stress of the functionally graded spur gear is compared to a conventional gear material (EN8 Steel) to evaluate its contact load capacity. The contact stresses were assessed for various torque values. It was found that the change in the distributive laws influenced the contact stresses induced in gear. Also, aluminium-steel showed comparatively less contact stress compared to steel-zirconium and homogeneous steel.

Keywords Functionally graded material · Finite element analysis · Spur gear · Contact analysis

1 Introduction

Gears are one of the most widely used power transmitting parts. This is because of its ability to change the magnitude, speed, and direction of the power source. Contact and bending stresses become an important parameter in determining the life of the spur gear. Contact stress in the dominant stress comparatively. Lewis equation and Hertz contact equations are analytically used to calculate the bending and contact stress

V. Aravind · S. Adharsh · D. Prakash · S. Martin Vinoth · P. Marimuthu (✉)
School of Mechanical Engineering, SASTRA Deemed to Be University, Thanjavur, India
e-mail: marimuthu@mech.sastra.ed

E. T. Akinlabi et al. (eds.), *Trends in Mechanical and Biomedical Design*,
Lecture Notes in Mechanical Engineering,
https://doi.org/10.1007/978-981-15-4488-0_28

of the spur gear widely [1]. Bending stresses do not influence the materials being considered [2]. Finite element analysis proves out to be a useful technique to solve the contact stress problem [3, 4]. Bharat Gupta et al. suggested that the change in module had changed the contact behaviour of the gear [5]. Seouk-chuk Hwang et al. carried out contact stress analysis on a 2D spur gear on the various changes in positions using AGMA standards and found that the design considered was stricter than the AGMA Standards [6]. Gaurav Mehta et al. conducted contact stress analysis on spur gear using two different materials and suggested that a wide range of materials could provide a variety of contact stresses [7]. This was also confirmed by the results of K. Sivakumar et al. who conducted contact stress analysis for different materials [8]. S. Rajesh Kumar et al. used a composite material in spur gear analysis using FEM with different rotational speed and found out that it influenced the behaviours like stress, strain, deflection, etc. [9]. The above literature shows the influence material has on the contact stress of a spur gear. Experimental procedures tend to be not only expensive, but any design error is very laborious to rectify, whereas finite element technique is relatively simple and is comparatively less arduous. Hence, finite element-based contact stress analysis is perceived as an alternative to experimental methods.

Functionally graded materials are advanced composite materials with spatial gradation in its structure and composition to achieve specifically tailored properties [10]. Functionally graded materials are characterised by changing the property gradient concerning its spatial position. Tohid Mahmoudi et al. conducted a thermomechanical analysis on a functionally graded wheel-mounted brake disc and concluded that the stresses and factor of safety considerably improved compared to the conventional cast iron [11]. Haidar F. Al-Qrimli et al. reviewed and suggested that FGM could solve the contact tooth surface problem of the gears [12]. M. M. Shahzamanianet et al. conducted thermal and mechanical analysis on a functionally graded brake disc and found mechanical and thermal properties could be influenced by the distribution of FGM with variable parametric constant distributed under power law [13]. Aravind et al. conducted the bending stress analysis for various distributive laws and found that the distributive laws had considerable influence on the deformation of the spur gear [14]. Soufi Mohammadi et al. concluded from his stress and strain analysis of a functionally graded annular plate and found that inhomogeneity of the material influenced the mechanical behaviour of the article [15].

From the above-reviewed literature, it was found that functionally graded materials can be employed in spur gears for enhancement of contact properties. This work tries to evaluate the contact stress behaviour of two pairs of the functionally graded spur gear. The materials are distributed radially along the involute profile of the gear. Various laws such as linear, exponential, and power laws were used. Power laws were varied with different parametric constant, and its behaviour was studied. Other behaviours such as equivalent strain and total deformations were also observed for different cases. The problem was using a commercially used FE software ANSYS. The problem was solved for two pairs of FGM using various distributive laws.

2 Spur Gear Design and Model

The 2D spur gear was designed and simulated in ANSYS 14.5. The design of the 2D spur gear is given in Table 1. The geometry of the spur gear is shown in Fig. 1. The spur gear design was divided into 20 equal segments radially, and material properties were distributed across its involute profile based on the governed law.

2.1 Numerical Simulation and Procedure

Finite element analysis of the given spur gear was performed in ANSYS 14.5. The simulation was 2D plane strain [16]. The driving end of the gear was given a torque and frictionless support, and the driven end was given fixed support on the inner rim. The contact was frictional with a frictional coefficient of 0.15 for the homogeneous case [4]. Since the coefficient of friction of functionally graded material is unknown, no separation contact pair was assumed. The contact formulation of augmented Lagrange was chosen. Quad mesh with an element size of 1 mm was used to solve the problem. A fine mesh was provided in the edges to get an accurate result. The element size was fixed with convergence study and is shown in Fig. 2.

Table 1 Spur gear parameter

Parameter	Value
Pitch circle diameter	65 mm
Internal diameter	31.75 mm
Outer diameter	68 mm
Pressure angle	20°
Face width	10 mm
No. of teeth	20

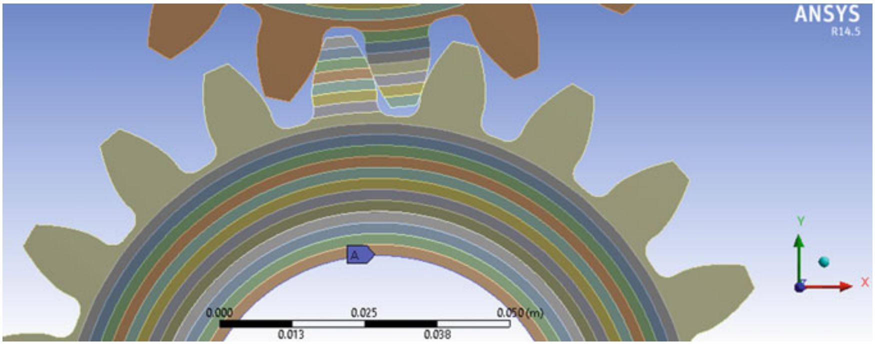

Fig. 1 Geometry of the spur gear

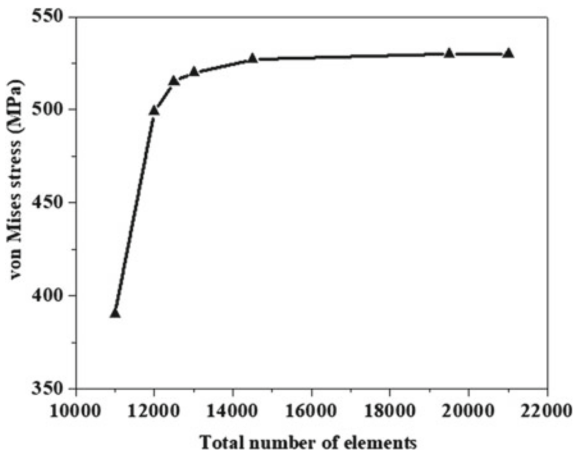

Fig. 2 Mesh convergence study

The boundary conditions and the meshed geometry are shown in Figs. 3 and 4.

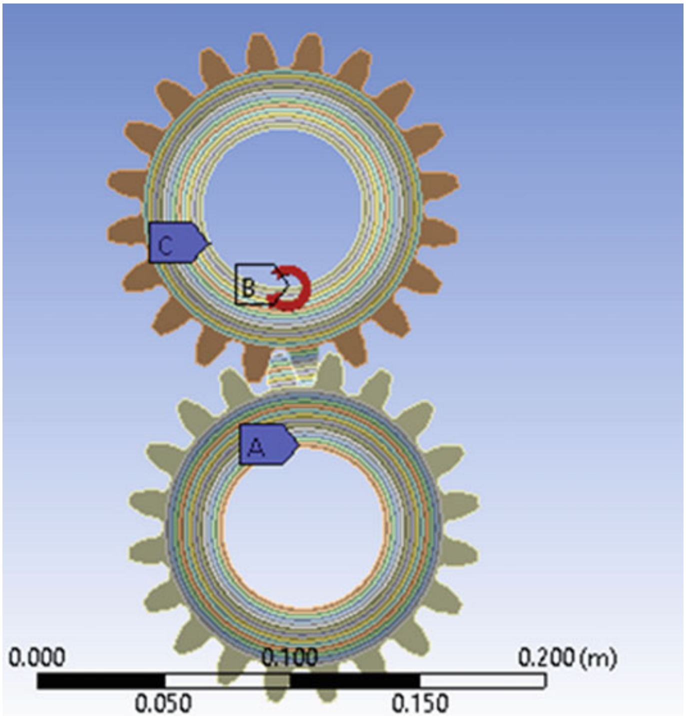

Fig. 3 Boundary condition

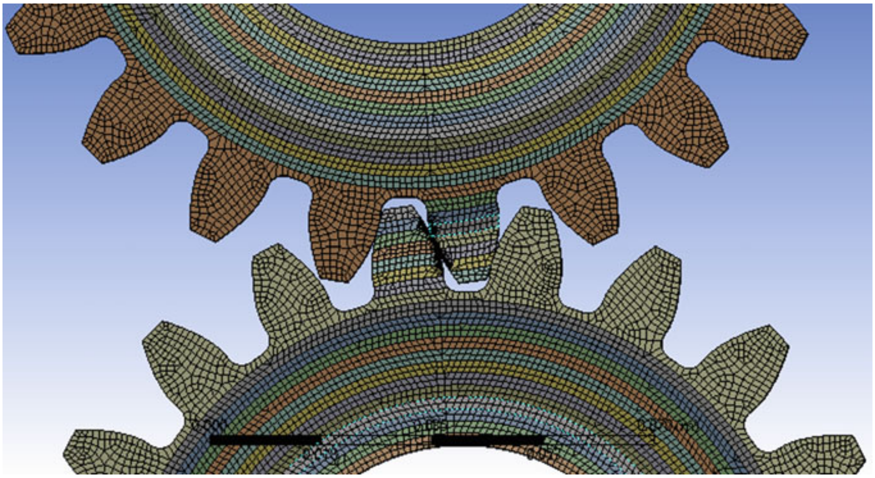

Fig. 4 Meshed geometry

2.2 Material Property and Distributive Law

The pairs of functionally graded materials chosen were Al-steel and steel-zirconium. Homogeneous pairs of steel and zirconium were selected for comparison [14]. The materials were distributed across the gear involute profile. The material was distributed from the inner radius to the outer radius. The inner radius of the gear had the former FGM material dominant (aluminium and steel). The outer radius of the gear had later FGM material dominant (steel and zirconium). Using the inner and outer radius as the boundary condition and the distributive laws as the equation, an equation for distribution was generated. The equation was used to generate discrete material property for the radially divided 20 segments of the gear. The material property was designated to the 20 equally divided segments based on the equation. The distributive laws used were linear, exponential, and power law with four parametric constants. The properties of the materials are shown in Table 2. The governing equations are shown in Table 3.
Where $P(r)$ is the property chosen across the radial profile, $\beta = (1/(a - b)) * \ln(P_A/P_B)$, a and b are the inner and outer radius of the gear, m is the slope, and c is the y-intercept. P_A is the property of the material in the inner region, and P_B is

Table 2 Material properties

S. No.	Material	Young's modulus (GPa)	Density (kg/m^3)	Poisson's ratio
1	Aluminium-steel	$E_A = 70$ $E_B = 200$	$\rho_A = 2700$ $\rho_B = 8166$	$\mu_A = 0.3$ $\mu_B = 0.33$
2	Steel-zirconium	$E_A = 200$ $E_B = 244$	$\rho_A = 8166$ $\rho_B = 5700$	$\mu_A = 0.33$ $\mu_B = 0.288$

Table 3 Distribution laws

Law	Representation	Equation
Exponential	EX	$P(r) = P_o e^{\beta r}$
Linear	LI	$P(r) = mr + c$
Power law	$P(k)$	$P(r) = P_A + (P_B - P_A) * (x - a/a - \mathrm{b})^k$

the property of the material in the outer region. k is the parametric constant. Hertz equation was used to calculate the maximum contact stress and for validation of the case.

$$\sigma_C = \sqrt{\frac{F\left(1 + \frac{R_1}{R_2}\right)}{R_1 B\pi\left[\frac{(1-\vartheta_1^2)}{E_1} + \frac{(1-\vartheta_2^2)}{E_2}\right]\sin\phi}} \tag{1}$$

where σ_c is the maximum contact stress, F is the force, R_1 and R_2 is the pitch circle radii, B is the face width of the spur gear, E_1 and E_2 are the Young's modulus of the gear, ϑ is the Poisson's ratio, and Φ is the pressure angle.

3 Results and Discussion

The test was conducted for two material pairs (Al-Steel and Steel-Zr). The torque was varied from 100 to 250 Nm with an increment of 50 Nm. The materials were distributed using linear, exponential, and power law. Four values of the parametric index were used in power law ($k = 1, 2, 3, 4$). As a sample case, the von Mises stress distribution of homogeneous steel is shown in the figure. The maximum stress developed is 529.98 MPa, under a torque of 100 Nm.

3.1 Influence of Torque

In all cases, the maximum von Mises stress increases with an increase in the torque value. The variation of contact stress with torque is shown in Fig. 5. Similar trends are observed in both materials. The maximum stress in case of Steel-Zr is 1021 MPa and for Al-Steel is 911 MPa. The value of contact stress increases by 82.6% for an increase of contact stress from 100 to 250 for Steel-Zr distributed exponentially. Similarly, an increase of 85.5% was seen in Al-Steel sample distributed exponentially. Al-Steel showed comparatively less stress for all the laws under the given torque value. The distribution of Young's modulus and Poisson's ratio could in the contact region account for the difference in the contact stresses of the material.

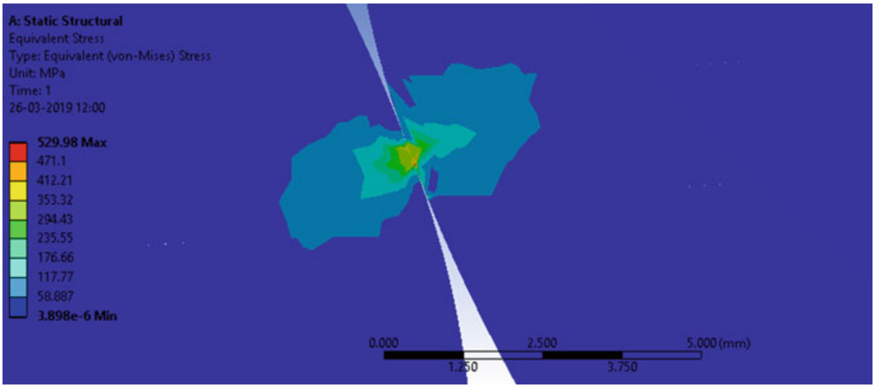

Fig. 5 von Mises stress plot for a sample case of homogeneous steel

The variation of equivalent strain with torque is shown in Fig. 5. As depicted in the figure, the equivalent strain is found out to be less in the case of Steel-Zr compared to Al-Steel. The highest value of strain is obtained for Al-Steel pair under a torque of 250 Nm as 0.0055. The equivalent strain increases with an increase in the torque value. The Steel-Zr shows a percentage increase of 80.8% increase in its strain value when the torque is varied from 100–250 Nm. Similarly, the Al-steel shows an increase of 90.5%.

Similar to stress and strain, the total deformation also varies linearly concerning torque. The variation of total deformation under torque is shown in Fig. 5. It can be seen from that equivalent strain, and total deformation is less in the case of Steel-Zr and is high for Al-Steel sample. This can be explained by the distribution of Young's modulus in the contact region. Increase in Young's modulus increases the stress, whereas it has an indirect influence on the strain and total deformation values. The highest deformation was found for the Al-Steel sample (7.28×10^{-5} m). The least was 1.72×10^{-5} m for the Steel-Zr under 100 Nm. The percentage increase when the torque varies between 100 and 250 Nm was 141% for Steel-Zr and 144% for Al-Steel.

3.2 Influence of Material Distribution

The materials were distributed along the radial profile of the spur gear in 6 different fashion [linear, exponential, power law ($k = 1, 2, 3, 4$)]. The influence of material distribution under a constant torque is shown in Fig. 6. The contact stress is found out to be highest for the Steel-Zr under linear distribution. It can also be seen that contact stresses developed are almost similar for power law $k = 1$ and linear. This is because of the similarity in distributional behaviour. The highest value of contact stress is 575 MPa for Steel-Zr under linear distribution; as the value of k increases,

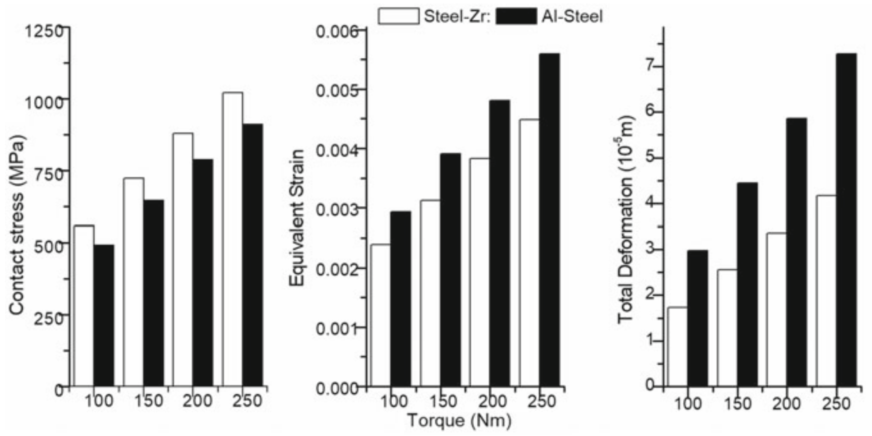

Fig. 6 Variation of contact stress, equivalent strain, total deformation varying torque

it can be seen that the values of contact stress decrease. The value of k can further be increased beyond 4 to increase the value of contact stress. In all the cases, Steel-Zr showed comparatively more stress than Al-Steel.

The variation of equivalent strain under varying material distribution is shown in Fig. 6. The equivalent strain is less in the case of Steel-Zr and more comparatively for Al-Steel. The value of equivalent strain is least for the linear distribution law. A power law with $k = 1$ and linear law show similar strain behaviour. As the k value increases, it can be seen that the value of strain increases. The highest value observed for Al-Steel under power law $k = 4$ as 0.00329.

Total deformation shows similar behaviour as strain under various material distributions. The variation of total deformation under different laws is shown in the figure. The total deformation increases with increase in the value of k. Total deformation is higher for Al-Steel comparatively. The highest value of total deformation is observed for Al-Steel as 4.06×10^{-5} m under power law $k = 4$ and the lowest for Steel-Zr as 1.5728×10^{-5} m under linear distribution (Fig. 7).

4 Conclusion

Functionally graded materials showed significantly fewer stresses when compared to conventional materials. The amount of stresses induced in Al-Steel pair is about 15% less than that of traditional steel material (power law $k = 4$). The distributive laws played a significant role in deciding the stresses, strains, and the total deformation induced in the materials. A power law with $k = 4$ showed least stresses in both the pairs of FGMs. The total deformation is less as in the case of linear law. This is because of the distribution of material with higher Young's modulus in the contact region. This also explains why the contact stresses are high compared to other distributive laws as

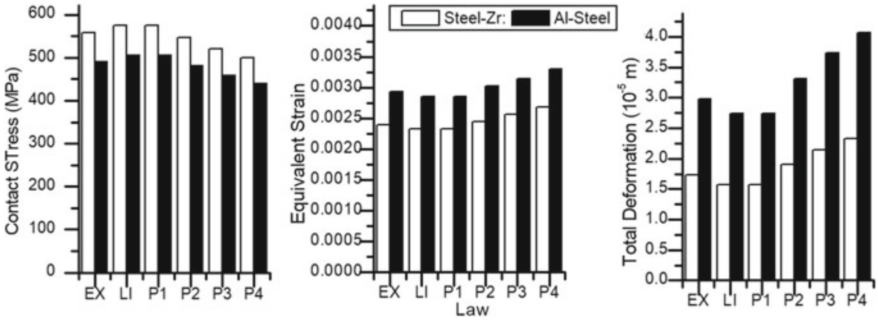

Fig. 7 Variation of contact stress, equivalent strain and total deformation under various law

contact stress is directly proportional to the square root of Young's modulus. Also, varying the material distribution can significantly help us in designing the properties of the materials in the contact region. Hence, functionally graded materials can be used as a substitute in place of conventional materials in gears as it helps us in tailoring the desired properties and can be used to increase the lifetime of the gears significantly.

Acknowledgements The authors are grateful towards Science & Engineering Research Board (SERB), Department of Science and Technology, India, for providing financial grant (File No. ECR/2017/000425) to do this work.

References

1. Pawar P, Utpat A (2015) Analysis of composite material spur gear under static loading condition. Mater Today Proc 2:2968–2974. https://doi.org/10.1016/j.matpr.2015.07.278
2. Prabhakaran S, Ramachandran S (2014) Bending stress and contact stress analysis of a spur gear for material steel C45. Inf (Jpn) 17:4599–4611
3. Hassan A (2009) Contact stress analysis of spur gear teeth pair. World Acad Sci Eng Techn 58:611–616
4. Farhan M, Karuppanan S, Patil S (2015) Frictional contact stress analysis of spur gear by using finite element method. Appl Mech Mater 772:159–163. https://doi.org/10.4028/www.scientific.net/AMM.772.159
5. Balaji D, Prabhakaran S, Harish Kumar J (2017) Analysis of surface contact stress for a spur gear of material steel 15Ni2Cr1Mo28. ARPN J Eng Appl Sci 12
6. Hwang S-C, Lee J-H, Lee D-H, Han S-H, Lee K-H (2013) Contact stress analysis for a pair of mating gears. Math Comput Model 57. 10.1016/j.mcm.2011.06.055
7. Mehta G, Somani M, Narendiranath Babu T, Watts T (2018) Contact stress analysis on composite spur gear using finite element method. Mater Today Proc 5:13585–13592. https://doi.org/10.1016/j.matpr.2018.02.354
8. Sivakumar K, Saravana Manikandan MT, Sethuraman B, Rajagopalan S, Hariharan R (2015) Contact stress analysis of a spur gear tooth pair for two different materials. Int J Appl Eng Res 10

9. Rajeshkumar S, Manoharan R (2017) Design and analysis of composite spur gears using the finite element method. IOP Conf Ser Mater Sci Eng 263:062048. https://doi.org/10.1088/1757-899X/263/6/062048
10. Shirvanimoghaddam K, Naebe M (2016) Functionally graded materials: A review of fabrication and properties. Appl Mater Today 5:223–246. https://doi.org/10.1016/j.apmt.2016.10.001
11. Mahmoudi Tohid, Parvizi Ali, Poursaeidi E, Rahi Abbas (2015) Thermo-mechanical analysis of functionally graded wheel-mounted brake disk. J Mech Sci Technol 29:4197–4204. https://doi.org/10.1007/s12206-015-0914-3
12. Al-Qrimli H, Ataollahi Oshkour A, Alnaimi F, Mahdi, FA (2015) Material design consideration for gear component using functionally graded materials. Int J Mater Eng Innov 6:243–256. 10.1504/IJMATEI.2015.072849
13. Shahzamanian M, Sahari B, Bayat M, Mustapha F, Ismarrubie ZN (2013) Elastic contact analysis of functionally graded brake disks subjected to thermal and mechanical loads. Int J Comput Methods Eng Sci Mech **14**:10–23. 10.1080/15502287.2012.698701
14. Aravind V, Adharsh S, Prakash D, Babu K (2019) Stress analysis on functionally graded spur gear: select proceedings of ICEMMM 2018. https://doi.org/10.1007/978-981-13-1724-8_39
15. Soufi Mohammadi A, Sabokroohieh P, Falakian A, Hadi A, Hosseini M, Ehsani F (2013) Stress and strain analysis of functionally graded annular plate subjected to transverse loading
16. Cornell RW (1983) Compliance and stress sensitivity of spur gear teeth. J Mech Des 103. 10.1115/1.3254939

Finite Element Analysis of Knee Joint with Special Emphasis on Patellar Implant

M. A. Kumbhalkar, D. T. Rangari, R. D. Pawar, R. A. Phadtare, K. R. Raut, and A. N. Nagre

Abstract Patella is supporting part of knee and also guide for quadriceps or patellar tendon. Patellar implant is used for proper functioning of patella after injury. For implant, it is required to cut injured portion of host patella and keep remaining part minimum up to 12–14 mm and overstuffing of 2 mm to prevent patellar fractures. The patellar implant makers provide only 8-mm-thick implant to maintain original patellar thickness which is difficult to achieve especially in patients with host bone thickness less than 20 mm. Hence, there is need to analyze for reduction in thickness of patellar implant from 8 to 6 mm for perfect engagement with adequate residual bone. The critical force analysis on host patella with tendon is carried out for quadriceps force, patellofemoral force, and patellar tendon force using analytical and finite element method. Two cases are considered for the force and stress analysis of patella, and the comparison of various implant thicknesses is discussed.

Keywords Patella · Knee joint · Finite element analysis · Patellar implant (button) · Patellofemoral force

M. A. Kumbhalkar
Assistant Professor, Department of Mechanical Engineering, JSPM Narhe Technical Campus, Pune, Maharashtra, India
e-mail: manoj.kumbhalkar@rediffmail.com

D. T. Rangari
Lecturer, Department of Pharmacy, Government Polytechnic, Amravati, Maharashtra, India

R. D. Pawar (✉) · R. A. Phadtare · K. R. Raut · A. N. Nagre
Student, Department of Mechanical Engineering, JSPM Narhe Technical Campus, Pune, Maharashtra, India
e-mail: pawarr062@gmail.com

E. T. Akinlabi et al. (eds.), *Trends in Mechanical and Biomedical Design*,
Lecture Notes in Mechanical Engineering,
https://doi.org/10.1007/978-981-15-4488-0_29

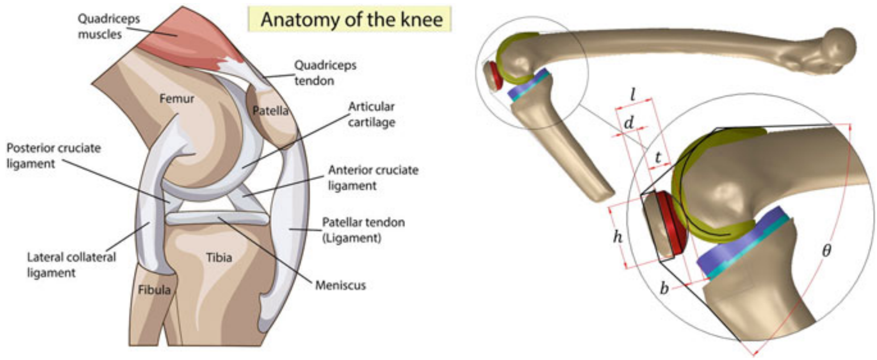

Fig. 1 Anatomy of knee and biomechanical model of knee joint with patellar implant [1]

1 Introduction

The rotary motion of knee joint is based on the successful movement between femur-tibia and patella. The tendons attached at femur and tibia cover and compress patella toward femur while rotary motion of knee joint. Due to compressive force or frictional force between femur and patella, the patella may damage and therefore it is required to provide implant over it. Figure 1 shows biomechanical model of knee joint with patella implant.

For the possible movement of knee joint, it is necessary to maintain patellar thickness after knee arthroplasty [1]. The host patella thickness is required to maintain up to 12–14 mm during knee arthroplasty for the patellar thickness less than 20 mm, and standard implant of 8 mm is used to recover original patellar thickness [1–3]. Sometimes intraoperative patellar thickness increases due to 8 mm standard patella implant for the person having original patellar thickness less than 20 mm. If the original thickness of patella is not maintained by applying patellar implant, then the knee cannot bend at that extent and pain will occur during walking, climbing, or running. Hence, for perfect meeting of original patella thickness after operation, it is required to use patella implant having thickness less than 8 mm. This research aim is to check effect on patellar implant by reducing its thickness from 8 mm to 6 mm at various flexion angles.

2 Mathematical Formulation and Force Analysis

As per the experimental study done in various literature papers, it is observed that the tendons attached with tibia and femur will stretch while motion due to which a compressive force is acted on patella. The magnitude of forces and direction acting on leg vary with the knee flexion angle and weight. Two lateral forces i.e., patellar tendon force and quadriceps force are acting on patella which acts patellofemoral reactive force toward contact point of patella and femur. Patellar tendon force acting between the patella and tibia, patella quadriceps force acting between patella and femur, and patella femoral force acting on patella as a compressive because of the forward moment are locked due to the quadriceps and ligament. A free body diagram for forces acting on patella is shown in Fig. 2.

The patellofemoral force is acting on patella at various knee flexion angles at different conditions of human movement. The full body weight of human is acting on knee joint at straight condition which is fixed at end of tibia, but while walking, climbing, or running, the moment acts at joint which distributes body weight into different forces. The free body diagram of patellofemoral joint with force distribution and joint flexion moment is shown in Fig. 3 [4, 5]. As patella changes its own position according to flexion angle, forces acting on patella change according to the flexion angle. The main three forces acting on patella, i.e., quadriceps force, patella tendon force, and patellofemoral forces are derived by considering various angular movements at joint.

Also other two elements are plotted as free body diagrams, i.e., for patellar tendon and for quadriceps tendon where the forces, angles, and the different lengths are shown. For force analysis on patella, specific geometric form is not considered but the specific thickness of patella is considered during finite element analysis. Fekete et al. [4] considered dimensionless parameters to simplify the results of relationship between patella and tendon and are given in Table 1.

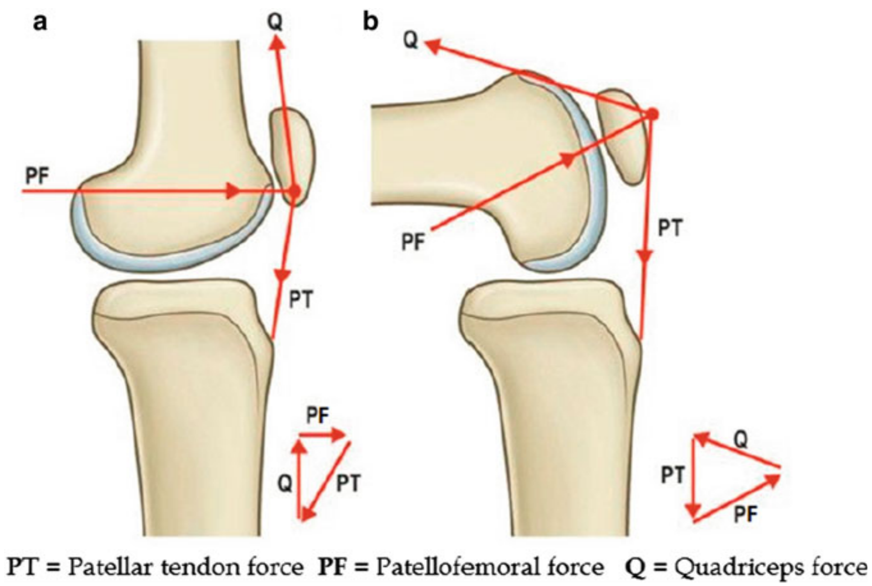

Fig. 2 Forces acting on patella [13]

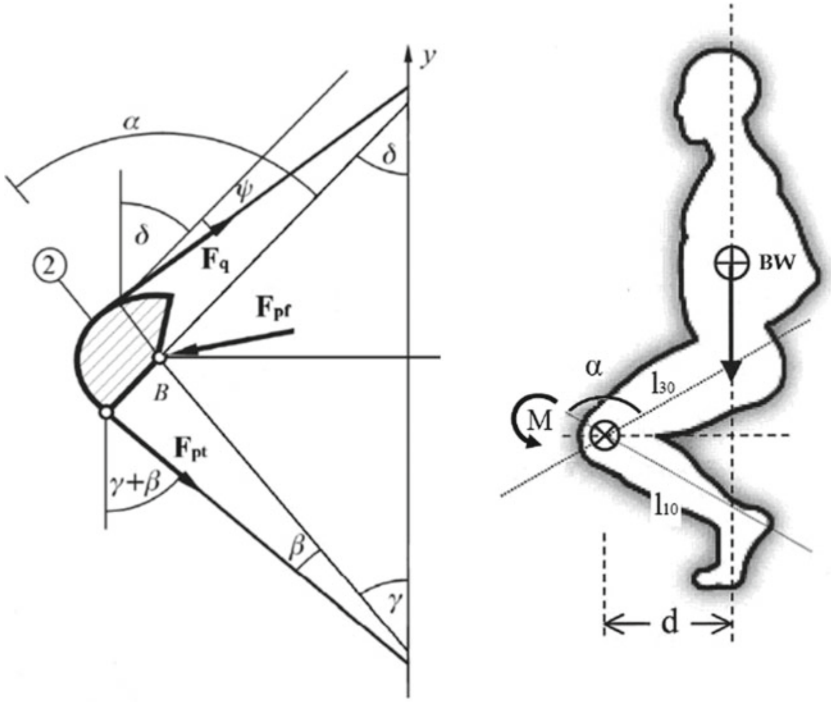

Fig. 3 Free body diagram of patellofemoral joint and joint flexion moment by Fekete et al. [4] and Mason et al. [5]

Table 1 Dimensionless parameter [4]

Description	Formulas
Dimensionless, intersected tibia length function	$\lambda_1 = {}^{l_1}/_{l_{10}}$
Dimensionless, intersected femur length function	$\lambda_3 = {}^{l_3}/_{l_{30}}$
Dimensionless length patella tendon	$\lambda_p = {}^{l_p}/_{l_{10}}$
Dimensionless thickness of shin	$\lambda_t = {}^{l_t}/_{l_{10}}$
Dimensionless thickness of thigh	$\lambda_f = {}^{l_f}/_{l_{30}}$

2.1 Patellar Tendon Force

From Fig. 3, free body diagram of tibia and femur gets separated to find its force distribution. Figure 4 illustrates the forces acting on tibia due to patellar tendon and body weight. The lengths denoted in free body diagram as length of tibia (l_{10}), length between line of action of tibia and body weight (l_1), length of patellar tendon (l_p), length from axis of tibia, and tibia tuberosity (l_t). Taking the moment at point *B*, by fixing the point *B*.

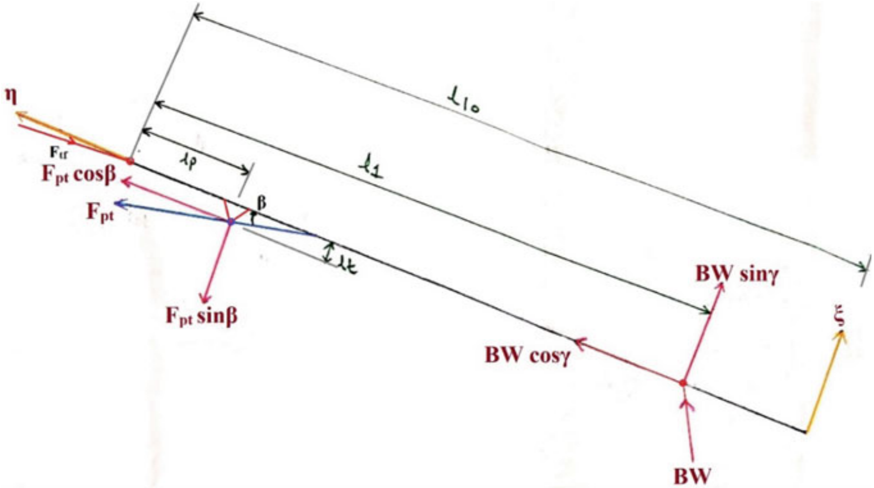

Fig. 4 Forces acting on tibia and patellar tendon

$$\sum \mathrm{MB} = 0$$
$$0 = -l_{\mathrm{p}} \cdot f_{\mathrm{pt}} \cdot \sin\beta - l_{\mathrm{t}} \cdot f_{\mathrm{pt}} \cdot \cos\beta + l_1 \mathrm{BW} \cdot \sin\gamma$$
$$l_1 \mathrm{BW} \cdot \sin\gamma = l_{\mathrm{p}} \cdot f_{\mathrm{pt}} \cdot \sin\beta + l_{\mathrm{t}} \cdot f_{\mathrm{pt}} \cdot \cos\beta$$
$$l_1 \mathrm{BW} \cdot \sin\gamma = f_{\mathrm{pt}}\left(l_{\mathrm{p}} \cdot \sin\beta + l_{\mathrm{t}} \cdot \cos\beta\right)$$
$$f_{\mathrm{pt}} = \mathrm{BW} \cdot \frac{l_{\mathrm{p}} \cdot \sin\gamma}{l_{\mathrm{p}} \cdot \sin\beta + l_{\mathrm{t}} \cdot \cos\beta} \tag{1}$$

Rearranging Eq. (1)

$$\frac{f_{\mathrm{pt}}}{\mathrm{BW}} = \frac{l_{\mathrm{p}} \cdot \sin\gamma}{l_{\mathrm{p}} \cdot \sin\beta + l_{\mathrm{t}} \cdot \cos\beta} \tag{2}$$

$$\frac{f_{\mathrm{pt}}}{\mathrm{BW}} = \frac{\lambda_1 \cdot \sin\gamma}{\lambda_{\mathrm{p}} \cdot \sin\beta + \lambda_t \cdot \cos\beta} \tag{3}$$

2.2 *Quadriceps Force*

Figure 5 illustrates the forces acting on femur due to quadriceps tendon and body weight. The parameters denoted in free body diagram are length of femur (l_{30}), length between line of action of tibia and body weight (l_3), angle between the axis of femur and quadriceps force (ψ), and angle between the axis of femur and line of action of body weight (δ). Taking moment at point B, by fixing the point B.

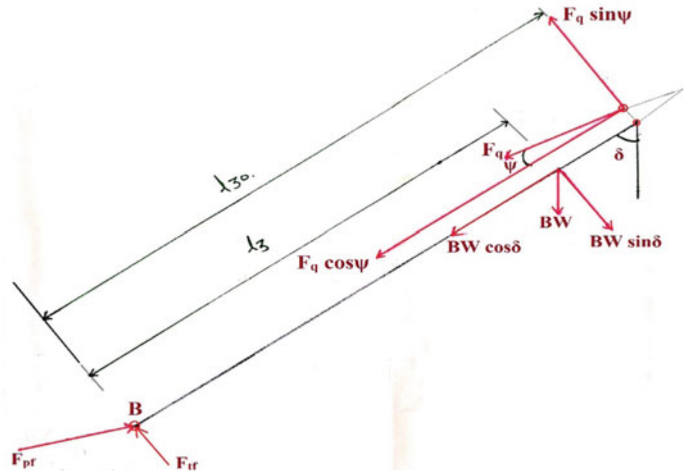

Fig. 5 Forces acting on femur

$$
\begin{aligned}
&\sum \mathrm{Mb} = 0 \\
&0 = l_{\mathrm{f}} \cdot f_{\mathrm{q}} \cdot \cos\psi + l_{30} f_{\mathrm{q}} \cdot \sin\psi - l_3 \mathrm{BW} \cdot \sin\delta \\
&\delta = \alpha - \gamma \\
&\psi = 0 \text{ Assumption} \\
&l_3 \mathrm{BW} \cdot \sin\delta = l_{\mathrm{f}} \cdot f_{\mathrm{q}} \cdot \cos\psi + l_{30} f_{\mathrm{q}} \cdot \sin\psi \\
&\mathrm{BW} = \frac{f_{\mathrm{q}}(l_{\mathrm{f}} \cdot \cos\psi + l_{30} \cdot \sin\psi)}{l_3 \cdot \sin\delta} \\
&\frac{f_{\mathrm{q}}}{\mathrm{BW}} = \frac{l_3 \cdot \sin\delta}{l_f \cdot \cos\psi + l_{30} \cdot \sin\psi} \\
&\frac{f_{\mathrm{q}}}{\mathrm{BW}} = \frac{\lambda_3 \sin(\alpha - \gamma)}{\lambda_{\mathrm{f}}}
\end{aligned} \tag{4}
$$

2.3 *Patellofemoral Force* ($\mathbf{F}_{pf}$)

It is reaction force acting on femur through patella and ligament forces that is quadriceps and tendon forces which is obtained from F_{q} and F_{pt} forces by parallelogram theorem of resultant forces.

By using equilibrium equation,

$$\sum fy = 0$$

$$
\begin{aligned}
&\sum fx = 0 \\
&0 = f_{\mathrm{q}} \sin\delta - f_{\mathrm{pt}} \sin(\gamma + \beta) + F_{\mathrm{pfx}} \\
&F_{\mathrm{pfx}} = -f_{\mathrm{q}} \sin\delta - f_{\mathrm{pt}} \sin(\gamma + \beta) \\
&0 = f_{\mathrm{q}} \cos\delta - f_{\mathrm{pt}} \cos(\gamma - \beta) + F_{\mathrm{pfy}} \\
&F_{\mathrm{pfy}} = -F_{\mathrm{q}} \cos\delta + F_{\mathrm{pt}} \cos(\gamma + \beta)
\end{aligned}
$$

Resultant of two concurrent forces (Law of Parallelogram)

$$
\begin{aligned}
&\frac{f_{\mathrm{pt}}}{\mathrm{BW}} = \frac{\sqrt{f_{\mathrm{pfx}}^2 + f_{\mathrm{pfy}}^2}}{\mathrm{BW}} = \frac{\sqrt{f_{\mathrm{q}}^2 + f_{\mathrm{pt}}^2 - 2 f_{\mathrm{q}} f_{\mathrm{pt}} \cos(\beta + \delta + \gamma)}}{\mathrm{BW}} \\
&\frac{f_{\mathrm{pt}}}{\mathrm{BW}} = \frac{\sqrt{f_{\mathrm{q}}^2 + f_{\mathrm{pt}}^2 - 2 f_{\mathrm{q}} \cdot f_{\mathrm{pt}} \cos(\beta + \delta + \gamma)}}{\mathrm{BW}}
\end{aligned} \tag{5}
$$

2.4 Case Study

Two cases having different body weight and height are considered to find patellar tendon force, quadriceps force, and patellofemoral force as per the formulae derived in Sects. 2.1, 2.2, and 2.3 for various flexion angles. The manual drawings of both cases having weight 74 kg and 61 kg and height 5.9 ft. and 5.5 ft., respectively, are drawn to plot various lengths and angle for calculation of forces. As the tibia and femur length vary with respect to height and weight, these two different cases are considered for force calculation. The manual drawings of two cases are shown in Fig. 6, and all parameters like length, angle, and dimensionless values are shown in Table 2.

The mathematical formulation represents forces acted on knee joint at quasi-static condition, and it is exposed to high magnitude of compression force during walking, climbing, and running condition [6, 7]. As per literature [8–10], the force acting on knee joint during walking is 1.3 times body weight, during climbing stair is 3.3 times body weight, and during knee bends is 7.8 times body weight. The compression force and area of articular contact increase with knee flexion and are max between 60° and 90° [11, 12].

3 Finite Element Analysis of Patella

In this paper, finite element analysis technique is used for stress analysis of knee joint with special emphasis on patellar implant with varying thickness from 6 to 8 mm. For finite element analysis of patella, a critical CAD model of knee joint

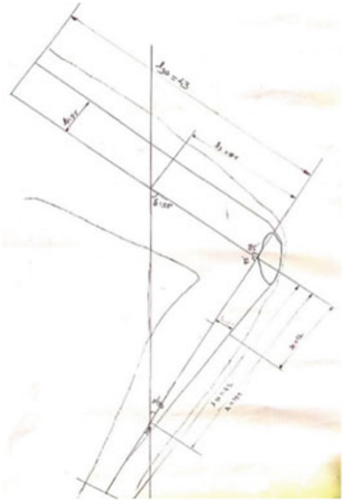

(a) CASE-I: Person having weight 73 kg and height 5.9 feet

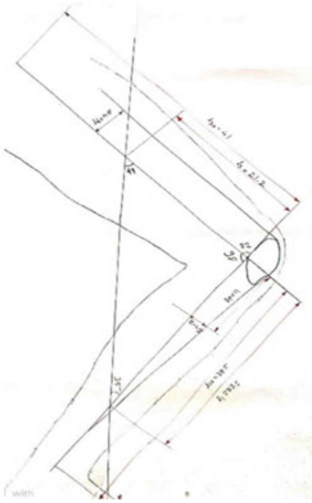

(b) CASE-I: Person having weight 61 kg and height 5.5 feet

Fig. 6 Manual drawing of two different case study for force calculation

Table 2 Parameters of two different cases

Sr. No.	Parameter	CASE-I	CASE-II
1.	BW	73 kg	61 kg
2.	L_1	29.5 cm	27.5 cm
3.	L_3	18.5 cm	21.2 cm
4.	L_f	5.5 cm	4.5 cm
5.	L_p	12 cm	11 cm
6.	L_t	2.7 cm	2.3 cm
7.	L_{10}	42 cm	38.5 cm
8.	L_{30}	43 cm	41 cm
9.	λ_3	0.4302	0.517
10.	λ_1	0.7023	0.714
11.	λ_p	0.2857	0.285
12.	λ_t	0.0642	0.059
13.	λ_f	0.1279	0.109
14.	γ	30 º	35º
15.	δ	55º	47º
16.	A	85º	82º
17.	B	10º	8º

with patella and tendon is prepared in solid modeling software CATIA and its stp file is imported in FEA tool, ANSYS. At first, the analytical patellofemoral force is verified with ANSYS result by applying boundary condition as patella tendon force and quadriceps force at the end of tendon and is fixed and at femur end. This reaction force is exactly matched by analytical and finite element method, and the results are shown in Table 3. All three forces are also calculated for different conditions such as walking, climbing, and running as per the ratio discussed in 2.4, and patellofemoral force is verified in ANSYS at different knee flexion angles.

The research aim is to replace standard available patellar implant of 8 mm thickness to minimum 6 mm thickness for the host patella size of less than 20 mm thickness. Hence, the stress analysis is carried out on host patella first and checks stresses induced at point of contact of patella and femur. Then, the stress analysis is carried out on patella with implant for different thicknesses. For stress analysis, direct patellofemoral force is applied on upper surface of patella and femur is fixed at end. The patellar implant with varying thickness is shown in Fig. 7, stress analysis result on contact point of patella and femur is shown in Fig. 8, and stresses on patella are

Table 3 Force acting on patella for two different cases and at different flexion angles using analytical and finite element method

Condition	Case	Case-I			Case-II		
	Flexion angle	65°	85°	110°	65°	85°	110°
Static	F_{pt}	2427.42	2289.7	4460.6	2894.90	2539.36	3976.63
	F_q	1714.39	2026.1	3022.5	2207.16	2109.85	3021.42
	F_{pf}	2390.31	3186.9	6358.2	3015.2	3301.48	5545.8
	F_{pf} (FEA)	2390.3	3186.9	6358.3	3015.2	3301.5	5545.8
Walking	F_{pt}	3186	2983.7	5850.5	3763.3	3301.1	5169.5
	F_q	2242.9	2652.8	3958.5	2869.3	2742.8	3927.8
	F_{pf}	3134.8	4161.6	8335.1	3919.5	4291.8	7209.5
	F_{pf} (FEA)	3134.9	4161.7	8335	3919.7	4291.9	7209.5
Climbing	F_{pt}	8087.6	7574.1	14851.3	9553.2	8379.9	13122.9
	F_q	5693.6	6733.9	10048.5	7283.6	6962.5	9970.60
	F_{pf}	7957.65	10564	21158.2	9950.3	10894.9	18301.1
	F_{pf} (FEA)	7957.8	10564	21158	9950.2	10895	18301
Running	F_{pt}	19116.2	17902.4	35103.2	22580.2	19807	31017.71
	F_q	13457.6	15916.8	23750.9	17215.8	16456.8	23567.12
	F_{pf}	18808.9	24970.2	50010.5	23518.7	25751.5	43257.32
	F_{pf} (FEA)	18,809	24,970	50,010	23,519	25,752	43,257

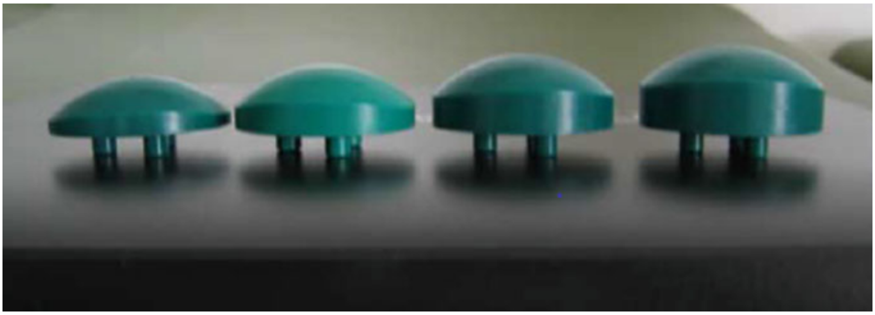

Fig. 7 Patellar implant (button) with varying thickness [3]

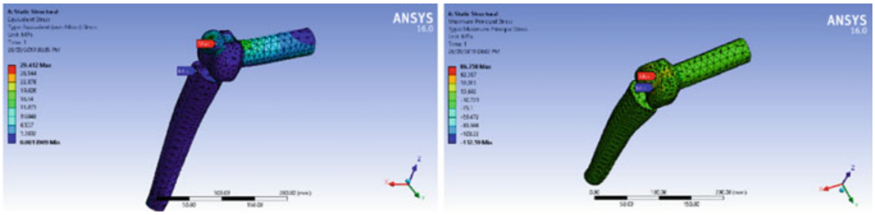

Fig. 8 Equivalent stress and maximum principal stress acting on contact of patella and femur at knee joint

shown in Fig. 9.

Stress analysis on host patella with patellar implant is also carried out using finite element analysis. The host patella is cut from interior side and keeps 12 mm thickness of posterior part of patella where 8 mm implant is fitted. The maximum principal stress and equivalent stress on patellar implant are shown in Fig. 10, and the results are given in Table 4 for flexion angle of 110° and 65°.

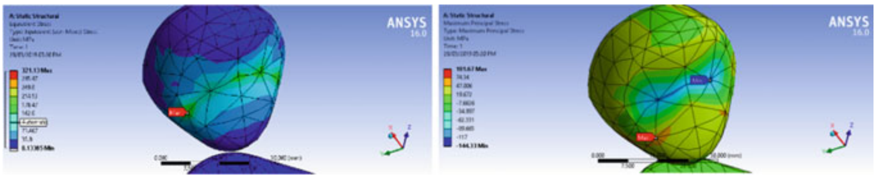

Fig. 9 Equivalent stress and maximum principal stress acting on patella

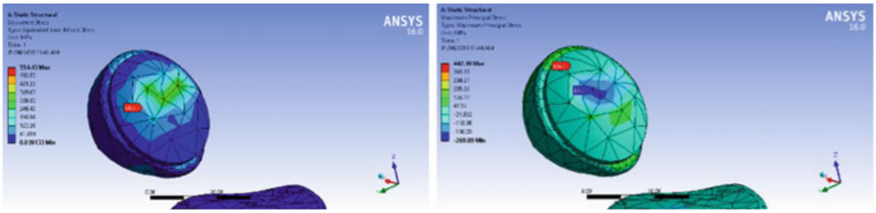

Fig. 10 Equivalent stress and maximum principal stress on patellar implant using finite element analysis

Table 4 Maximum principal stress and equivalent stress result for host patella and patellar implant for various condition at 110° and 65° flexion angle

Angles		65°			110°		
Condition	Stresses	Host patella	8 mm implant	6 mm implant	Host patella	8 mm implant	6 mm implant
Static	Max principle stress	4.146	14.115	8.109	12.926	56.241	53.608
	Equivalent stress (von misses)	8.8343	24.579	22.4	40.827	70.487	69.158
Walking	Max principle stress	5.438	18.515	10.637	16.946	73.729	70.277
	Equivalent stress (von misses)	11.58	32.24	29.38	53.522	92.405	90.662
Climbing	Max principle stress	13.804	46.998	27.001	43.016	187.16	178.39
	Equivalent stress (von misses)	29.412	81.84	74.58	135.86	234.56	230.14
Running	Max principle stress	32.629	111.08	63.817	101.67	442.38	421.66
	Equivalent stress (von misses)	69.521	193.43	176.29	321.13	554.43	543.97

4 Results Validation

Dr. Anoop Jhurani et al. [2] carried out an experimentation on 54 female patient knees to restore the native patellar thickness less than 20 mm. This experimentation has been observed for the period of two year which proved that the 6.2 mm thickness plastic patellar button can be used instead of 8 mm thickness to restore native patellar thickness less than 20 mm. A vernier caliper was used to measure and restore intraoperative patellar thickness during total knee arthroplasty as shown in Fig. 11.

Shelburne et al. [8] and van Eijden et al. [13] reported critical force analysis to estimate the quadriceps force, patello tendon force, and patellofemoral force at different gait cycle and flexion angles shown in Fig. 12. At maximum extension of patellofemoral joint quadriceps force is obtained as 2000 N, whereas the maximum force is obtained as 8000 N at 75° flexion angle. Patello tendon force becomes progressively smaller than quadriceps force at large flexion angles and reaches a maximum of 5000 N at 60° flexion angle. At all flexion angles, a patellofemoral force is smaller than quadriceps force [13].

Also, the forces acting on patella for two different cases during walking (Fig. 13) are revealed that the quadriceps force produced for maximal extension is 2243 N at 65° flexion angle and maximum patellofemoral force is 8335 N at 110° flexion angle. The forces acting in the literature paper nearly equal the forces acting on the patella for the cases considered in research.

A finite element analysis has been carried out to find stresses in patellofemoral cartilage due to internal and external rotations of the femur influencing contact areas, pressures, and cartilage stress distributions [14]. Besier et al. [14] analyzed a finite element mesh model of patellofemoral joint as shown in Fig. 14 which illustrated the element contact between quadriceps and patellar tendon and also within the femoral and patellar cartilage. The simple joint stresses due to contact area and stresses in patellar cartilage shown in Fig. 14 by finite element method revealed that the peak

Fig. 11 Intraoperative measurement of patellar thickness using vernier caliper [2]

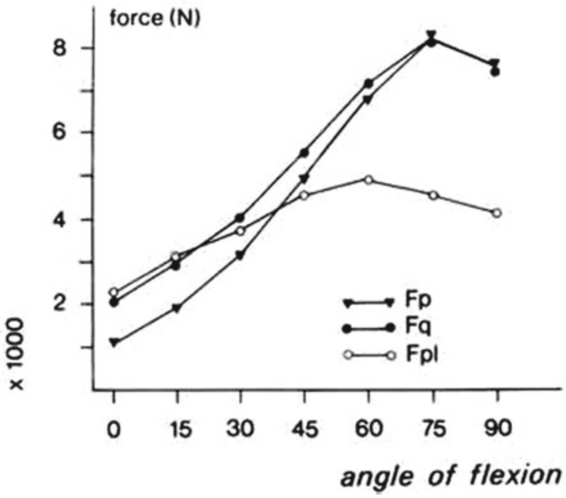

Fig. 12 Forces acting on patella versus flexion angle [8, 13]

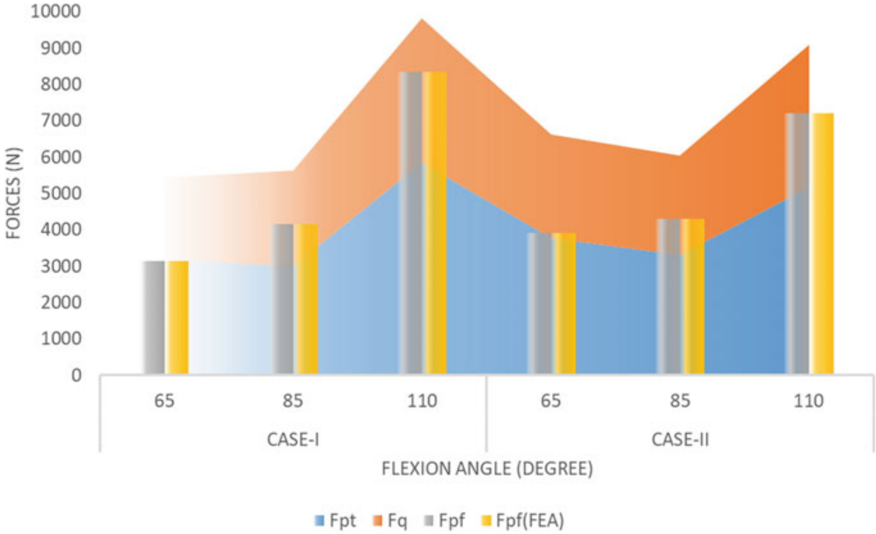

Fig. 13 Force acting on patella during walking for two different cases and at various flexion angles

stress values is obtained as 3.5 MPa at static or neutral condition for 15° internal and external femoral rotation which is lower than mean stress values.

A finite element analysis of patellar knee joint also revealed that the maximum principal stress is obtained as 4 MPa at static condition for host patella which is increased to 8 MPa for 6 mm patellar implant at 65° flexion angle. The stresses in patella are increased for different conditions, i.e., walking, climbing, and running.

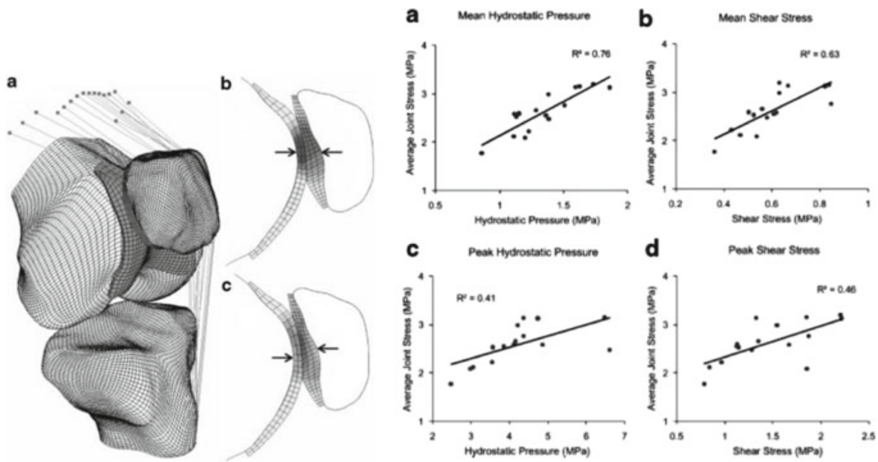

Fig. 14 Finite element mesh of the patellofemoral joint and correlations between simple measures of joint stress and stresses estimated in the patellar cartilage by the finite element method [14]

From finite element analysis, it is observed that the stress in 6.2 mm patellar implant is less than 8 mm patellar implant for every condition as shown in Fig. 15.

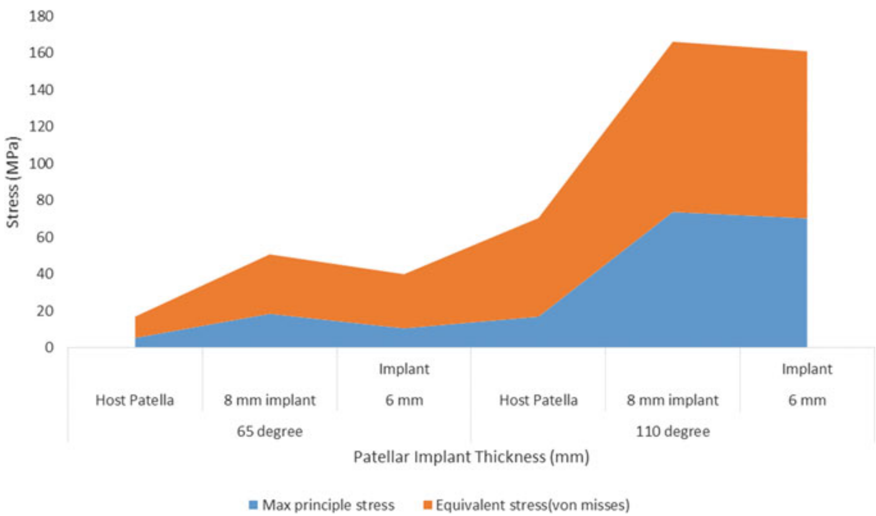

Fig. 15 Maximum principal stress and equivalent stress for host patella and patellar implant during walking

5 Conclusion

The mathematical formulation for biomechanical model of patellar knee joint is carried out to find forces acting on patella using free body diagram. The patellar tendon force, quadriceps force, and patellofemoral forces are calculated for two different cases of 61 and 73 kg person at various flexion angles, i.e., at 65°, 85°, and 110°. The analytical patellofemoral reaction forces are verified using finite element analysis which is obtained by applying patellar tendon force and quadriceps force at the end. The stress analysis on host patella and patellar implant with 8 mm and 6 mm thickness is carried out which reveals that the stress increases for 8 mm patellar implant than host patella and the stress reduces for 6 mm patellar implant than 8 mm. From the results, it can be concluded that the 6 mm patellar implant can be used instead of 8 mm implant during intraoperative arthroplasty for patella thickness less than 20 mm.

References

1. Abolghasemian M, Samiezadeh S, Sternheim A, Bougherara H, Lowry Barnes C, Backstein DJ (2014) Effect of patellar thickness on knee flexion in total knee arthroplasty. J Arthroplasty 2(1):80–84
2. Jhurani A, Agarwal P, Aswal M, Saxena P, Singh N (2018) Safety and efficacy of 6.2 mm patellar button in resurfacing less than 20 mm thin patella: a matched pair analysis. Knee Surg Rel Res 30(2):153–160
3. Bengs BC, Scott RD (2006) The effect of patellar thickness on intraoperative knee flexion and patellar tracking in total knee arthroplasty. J Arthroplasty 21(5):650–655
4. Fekete G, Csizmadia BM, Wahab MA, De Baets P, Vanegas-Useche LV, Bíró I (2014) Patellofemoral model of the knee joint under nonstandard squatting. Dyna 81(183):60–67
5. Mason JJ, Leszko F, Johnson T, Komistek RD (2008) Patellofemoral joint forces. J Biomech 41:2337–2348
6. Kainz H, Reng W, Augut P, Wurm Simone (2012) Influence of total knee arthroplasty on patellar kinematics and contact characteristics. Int Orthop 36(1):73–78
7. Nareliya R, Kumar V (2011) Biomechanical analysis of human femur bone. Int J Eng Sci Technol 3(4)
8. Shelburne KB, Torry MR, Pandy MG (2005) Muscle, ligament, and joint-contact forces at the knee during walking. Med Sci Sports Exerc 37(11)
9. Heegard J, Leyvraz PF, Curnier A, Rakotomanana L, Huiskes R (1995) The biomechanics of the human patella during passive knee flexion. J Biomech 28(11):1265–1279
10. Pokorny J, Kren J (2007) The patellofemoral joint and the total knee replacement. Appl Computat Mech 595–602
11. Magister S, Yarboro S (2018) Biomechanical evaluation of a novel suture augment in patella fixation. Am J Orthop 46(6):E468–E473
12. Hsu HC, Luo ZB, Rand JA, NauAn K (1996) Influence of patellar thickness on tracking and patellar femoral contact characteristics after total knee arthroplasty. J Arthroplasty 11(1):69–80
13. van Eijden TMGJ, Weijs WA, Kouwenhoven E, Verburg J (1987) Forces acting on the patella during maximum voluntary contraction of the quadriceps femoris muscle at different knee flexion/extension angles. Acta Anat 129:310–314
14. Besier TF, Gold GE, Delp SL, Fredericson M, Beaupre´ GS (2008) The influence of femoral internal and external rotation on cartilage stresses within the patellofemoral joint. J Orthopaedic Res

Simulation and Hardware Implementation of Interleaved SEPIC Converter with Valley-Fill Circuit for HBLED System

B. Lakshmi Praba and R. Seyezhai

Abstract LED lamps are nowadays preferred for lighting compared to the fluorescent lamps due to its longer lifetime and low power consumption. But the design of driver circuits designed for high brightness (HB) LED demands high power factor, more reliability, high efficiency and precise control. Therefore, to achieve this, a single-stage power factor correction model (PFC) and valley-fill is proposed in this paper. Valley-fill incorporated in SEPIC reduces the strain on output diode and middle capacitor, thus achieving great power factor and competence. Further to moderate the ripple at input and output stages, an interleaving concept is applied to SEPIC with valley-fill circuit. The combination of interleaving and valley-fill circuit leads to reduced voltage ripple, improved power factor and efficiency. A simulation study of the proposed SEPIC converter is carried out by MATLAB/SIMULINK. The performance factors such as source power factor, supply THD, supply distortion factor, supply displacement factor, power loss, output voltage ripple and efficiency are computed, and the results are compared with the classical SEPIC converter without valley-fill circuit. A prototype of an interleaved SEPIC converter is assembled to confirm the simulation results.

Keywords Light-emitting diode (LED) · Valley-fill · Power factor correction (PFC) · Source displacement factor · Total harmonic distortion (THD) · Interleaved · High brightness (HB)

B. Lakshmi Praba (✉)
Department of Electrical and Electronics Engineering, Sri Sivasubramaniya Nadar (SSN) College of Engineering, Kalavakkam, Chennai, India
e-mail: prabarv.93@gmail.com

R. Seyezhai
Department of Electrical and Electronics Engineering, REC Lab, Sri Sivasubramaniya Nadar (SSN) College of Engineering, Kalavakkam, Chennai, India

E. T. Akinlabi et al. (eds.), *Trends in Mechanical and Biomedical Design*,
Lecture Notes in Mechanical Engineering,
https://doi.org/10.1007/978-981-15-4488-0_30

1 Introduction

Electrical lighting sources are important in day-to-day life. The first incandescent lamp was invented in 1879, followed by the invention of fluorescent lamps in 1938, which achieved a milestone in the history of electrical engineering. Greatly new types of electrical lamps were devised, namely mercury lamps (HPM), sodium lamps (HPS), metal halide lamps (MH), and flash lamps filled with inert gas. Due to the disadvantages of electrical lamps, this paper deals with LED. On comparing with the electrical lamps, LEDs are more efficient, very small in size, light up very quickly, and it will achieve full brightness in under a microseconds. A LED lamp is a type of solid-state lighting that contains light-emitting diodes as the source of light.

For this LED lighting applications, we can choose any type of converters like boost, buck, Cuk and SEPIC. But, this paper fully deals with SEPIC converter because the SEPIC converter has improved supply power factor and reduced ripple related to other types of converters. A single-stage interleaved SEPIC converter has 50% reduced ripple compared to classic SEPIC converter.

A single-stage interleaved SEPIC converter for LED lighting is discussed in project where the model is functioned in intermittent conduction mode (DCM) with buck operation [1, 2]. The proposed topology is a modified SEPIC converter by combining the classical SEPIC and interleaved SEPIC with the middle capacitor substituted by a valley-fill circuit. This additional circuit is employed to reduce stress on the freewheeling diode and the middle capacitor, thus achieving high power factor and efficiency. Furthermore, interleaving concept is applied to the proposed SEPIC which reduces the ripple at input and output stage. The combination of interleaving and valley-fill circuit results in reduced output voltage ripple, improved power factor and efficiency.

Simulation studies of the SEPIC converter are done using MATLAB/SIMULINK. The performance factors such as input power factor, supply THD, supply distortion factor, supply displacement factor, power loss, output voltage ripple and efficiency are computed, and the results are compared with the classical SEPIC. To normalize the output and improvement in source power factor, closed-loop current control methods are implemented.

The broadsheet is arranged as follows: Division 2 discusses about different topologies of AC–DC SEPIC converter. Division 3 focuses on the design equation of proposed model. Division 4 grants the simulation results. Division 5 is pact with current control techniques, and finally Division 6 grants the conclusion and the results.

2 Proposed Topologies

A DC–DC single-ended primary inductor is an individual kind of converter. It may operate as buck, boost and also buck–boost. The SEPIC converter output has been

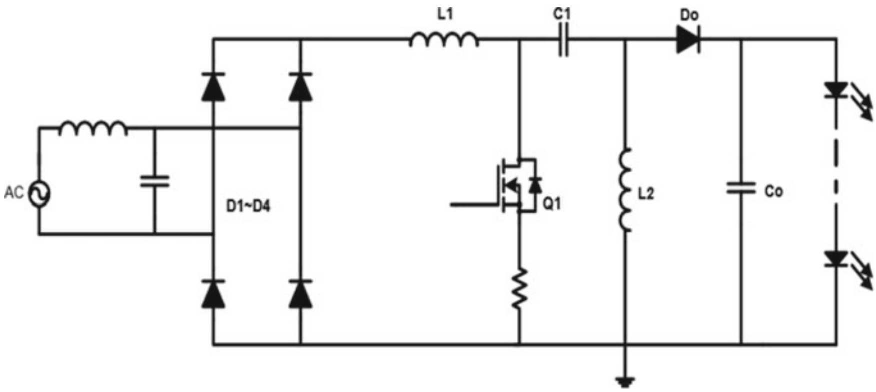

Fig. 1 Circuit diagram for AC–DC SEPIC converter

varied by changing the duty cycle of the devices. There is a mutual exchange between the capacitor and the inductor in the SEPIC converter.

The topologies of AC–DC power factor modification converter analysed in this project are as follows:

A. Conventional AC–DC SEPIC
B. Conventional AC–DC SEPIC with valley-fill circuit
C. Interleaved AC–DC SEPIC converter
D. Interleaved AC–DC SEPIC converter with valley-fill

A. **Conventional AC–DC SEPIC Converter**

From Fig. 1, when the main switch is conducting, current I_{L1} increases and the current I_{L2} goes negative. When the device brought to off, the capacitor current I_{C1} is equal to the current through the inductor I_{L1}, as inductor does not permit the instantaneous change in the current [3]. When current through the inductor L_2 falls to zero, the converter goes to DCM.

B. **Conventional AC–DC SEPIC Converter with Valley-Fill**

The circuit of SEPIC converter with valley-fill is exposed in Fig. 2. The valley-fill comprises of two capacitors and three diodes. The two capacitors are charged in series and parallel to feed the load. The converter operates in DCM. The switches and passive elements are assumed to be ideal. The significance of valley-fill circuit is that it leads to the output diode as well as the middle capacitor, maintaining the power factor, resulting in high efficiency [4].

C. **Interleaved AC–DC SEPIC Converter**

Interleaving topology has been used in electronics field, predominantly in great power applications. Since in great power applications, strain across the device can go outside the limit, the power device cannot handle. In this case, interconnecting the devices

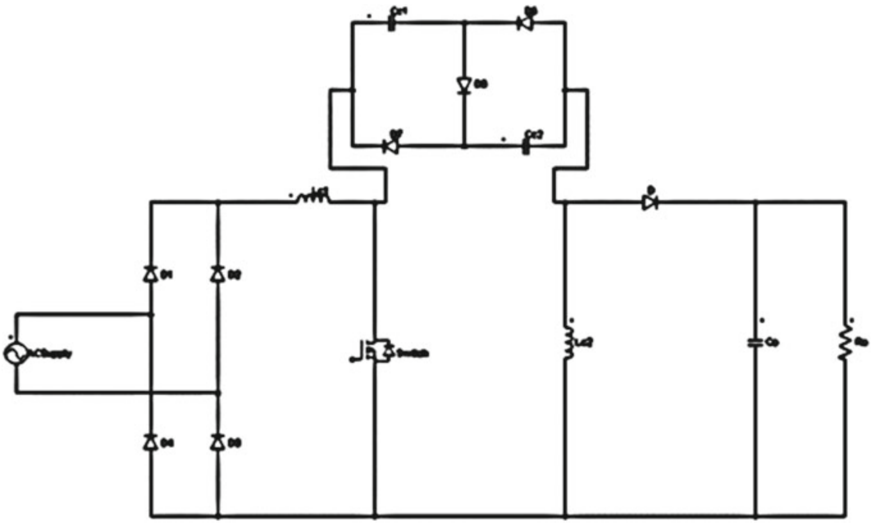

Fig. 2 Circuit diagram for AC–DC SEPIC with valley-fill

can provide the solution, but one major concern is the current sharing and voltage sharing [5]. There is another solution, that is paralleling the converters instead of the power devices. The concept of interleaving provides ripple cancellation and better thermal performance. Figure 3 illustrates the circuit of AC–DC interleaved SEPIC.

The process of an interleaved SEPIC is like conventional SEPIC, but this is operated in buck mode. In buck operation, there is no overlap between the device conductions. Therefore, at a time one switch will conduct.

D. **Interleaved AC–DC SEPIC with Valley-Fill**

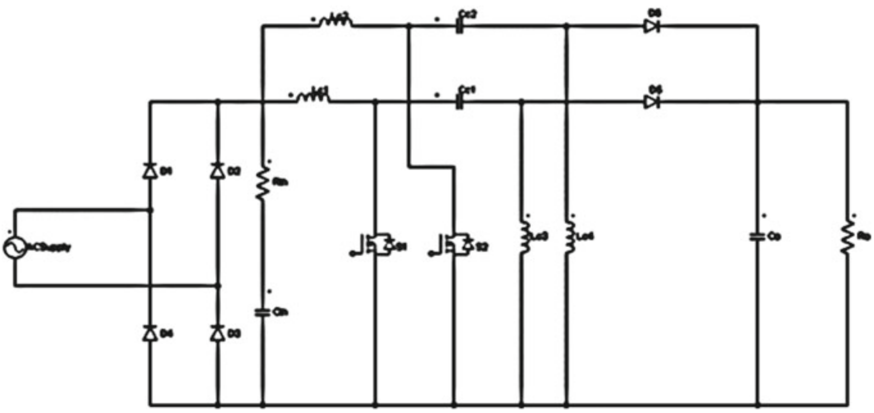

Fig. 3 Circuit of interleaved AC–DC SEPIC converter

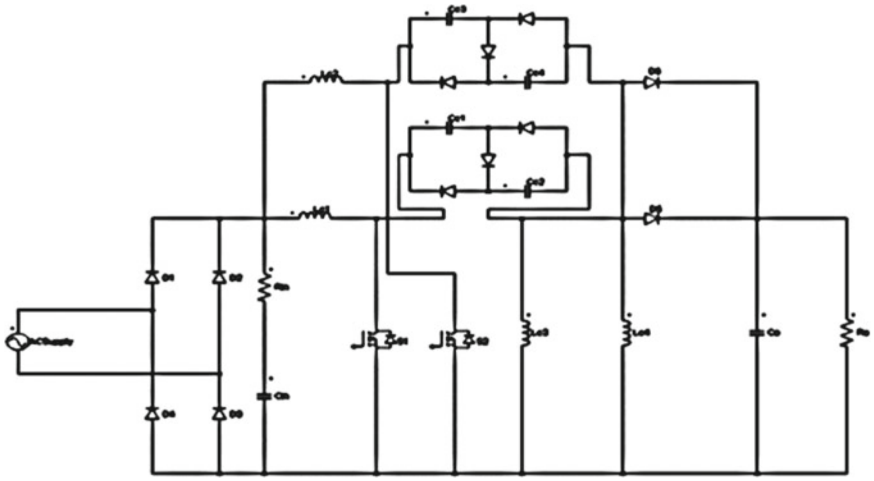

Fig. 4 Course diagram for interleaved AC–DC SEPIC with valley-fill

Interleaved AC–DC SEPIC is displayed in Fig. 4. The converter works in discontinuous current mode. This topology can result in extraordinary power factor also able to withstand great power using compact circuit.

When the device S_1 is turned on, S_2 is in off state. The capacitors C_1 and C_2 are charging towards input voltage with leftward positive plate. An inductor L_3 will remain charging, capacitor C_2 will be discharging via S_2, L_4. It creates the diode D_4 to be reversed bias. Subsequently, S_1 is turned off, D_1 will be forward biased, and an inductor L_1, L_2 will be discharged via the load.

3 Design Equations

The SEPIC is operated in DCM mode, and the design equations are as follows:

The conversion gain is given by

- Conversion gain $\dfrac{V_{\mathrm{o}}}{V_{\mathrm{in}}} = \dfrac{D}{1 - D}$ (1)

where V_0 is the output voltage, V_{in} is the input voltage, and D D is the duty cycle.

The inductor value is given by

- Inductor $L_{\mathrm{c}} = \dfrac{D V_{\mathrm{in}}}{\Delta I_0 2 f_{\mathrm{s}}}$ (2)

where f_{s} is the switching frequency, ΔI_0 is 30 to 50% of I_0.

The filter capacitor value is given by

- Capacitor $C_C = \dfrac{DI_0}{\Delta V_0 2 f_s}$ (3)

  where ΔV_0 is 1 to 5% of V_0.

4 Simulation and Results

All the topologies of SEPIC discussed in Sect. 4 are simulated in MATLAB/SIMULINK. Constructed based on design equations, and also model parameters are calculated and are exposed in Table 1.

The MATLAB simulation for conventional AC–DC SEPIC is exposed in Fig. 5.

The output of conventional AC–DC SEPIC is exposed Fig. 6, where the output voltage obtained is about 15.50 V.

The supply current THD of conventional AC–DC SEPIC exposed in Fig. 7, where the supply current THD obtained is about 18.38%.

The AC–DC conventional SEPIC with valley-fill MATLAB simulation diagram is exposed in Fig. 8.

The output waveform of conventional AC–DC SEPIC with valley-fill is depicted in Fig. 9, where an output voltage obtained is about 14.40 V.

The supply current THD of the conventional AC–DC SEPIC with valley-fill is exposed in Fig. 10, where the supply current THD obtained is about 12.96%.

The simulation circuit of an interleaved AC–DC SEPIC is exposed in Fig. 11.

Output waveform of an interleaved AC–DC SEPIC is exposed in Fig. 12, where the output voltage obtained is about 20.07 V.

Supply current THD of interleaved AC–DC SEPIC is exposed in Fig. 13, where supply current THD obtained is about 14.28%.

Simulation diagram of an interleaved AC–DC SEPIC with valley-fill is exposed in Fig. 14.

The output voltage of interleaved AC–DC buck SEPIC power factor circuit incorporating valley-fill is exposed in Fig. 15, where output voltage obtained is about

Table 1 Simulation parameters

Parameters	Values
Input voltage	22 V
Inductors	110 μH
Capacitors	225 nF
Switching frequency	50 kHz
Duty ratio	0.45
Filter capacitor	497 μF
Load resistor	40 Ω

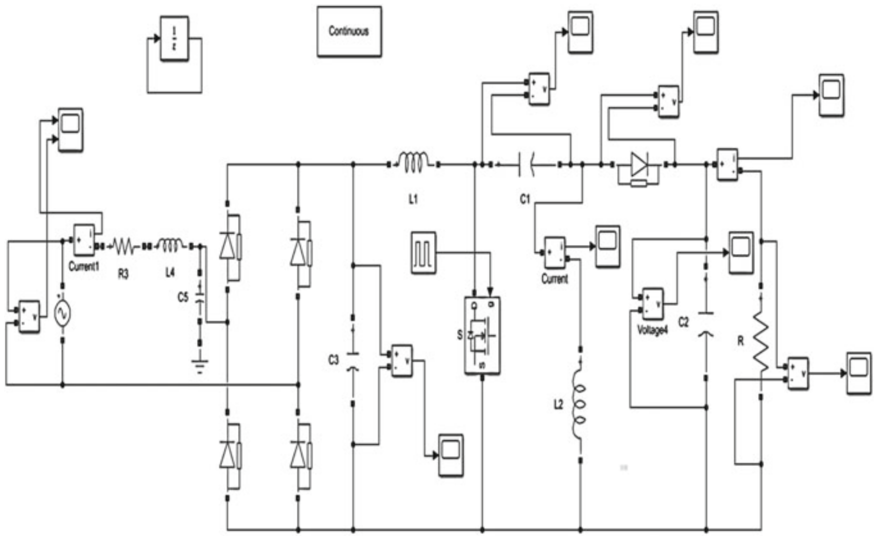

Fig. 5 MATLAB simulation diagram of conventional AC–DC SEPIC

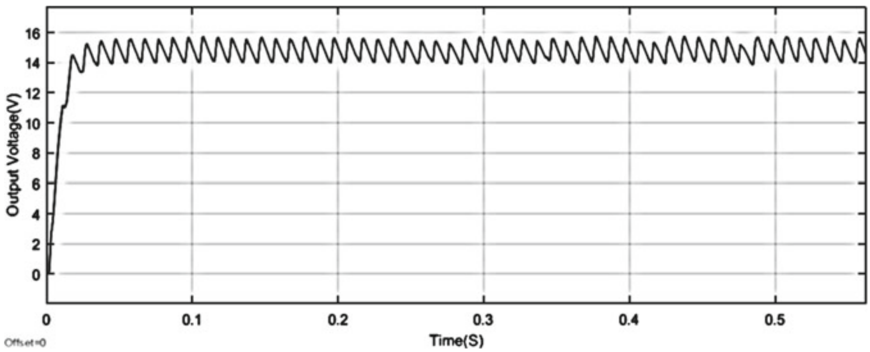

Fig. 6 Conventional AC–DC SEPIC output voltage

18.92 V.

The supply current THD of the interleaved AC–DC SEPIC with valley-fill is exposed in Fig. 16, where the supply current THD obtained is about 5.42%.

The performance parameters like output voltage ripple, supply THD, supply power factor, supply distortion factor, supply displacement factor, power losses, and efficiency are computed and that parameters are exposed in Table 2 [6].

From Table 2, the interleaved AC–DC SEPIC converter with valley-fill has the better performance compared to the other three topologies. This topology has improved power factor, supply current THD, displacement factor, reduced losses, and also improved efficiency.

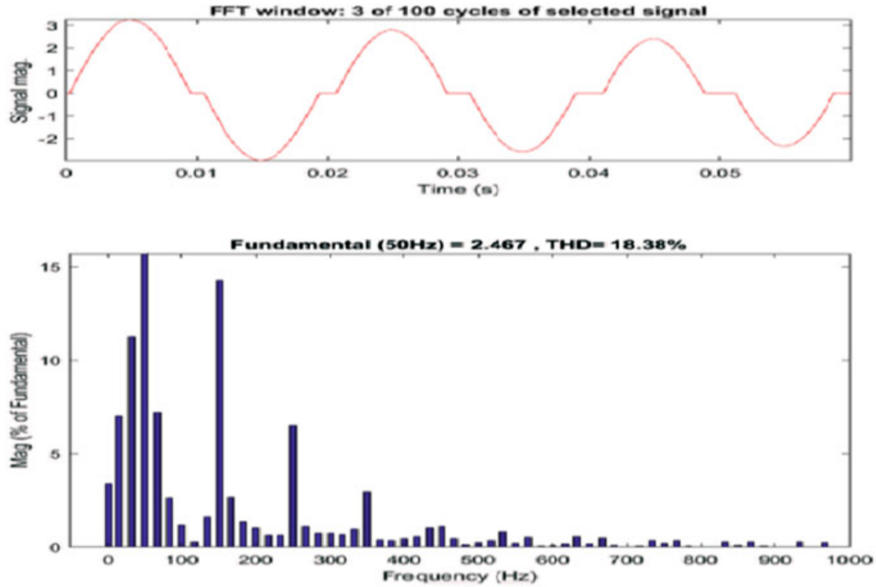

Fig. 7 Supply THD for conventional AC–DC SEPIC

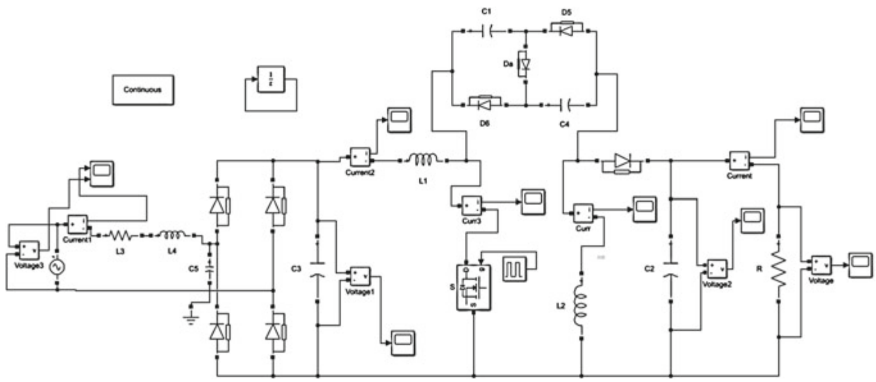

Fig. 8 MATLAB simulation circuit of conventional AC–DC SEPIC with valley-fill

5 Closed-Loop Current Control Techniques

To further reduce the supply current THD, current shaping techniques are employed. For this work, the methodologies such as peak current and average current control methods are executed in MATLAB/SIMULINK. By these techniques, the power factor is enhanced with lower harmonic profile of supply current [7].

- Peak current control technique

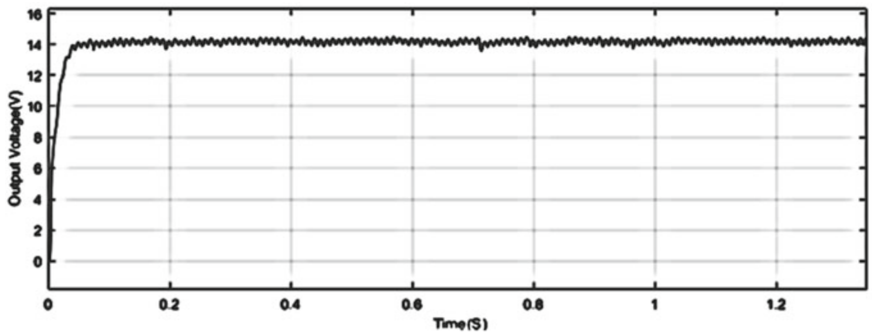

Fig. 9 Output voltage waveform of conventional AC–DC SEPIC with valley-fill

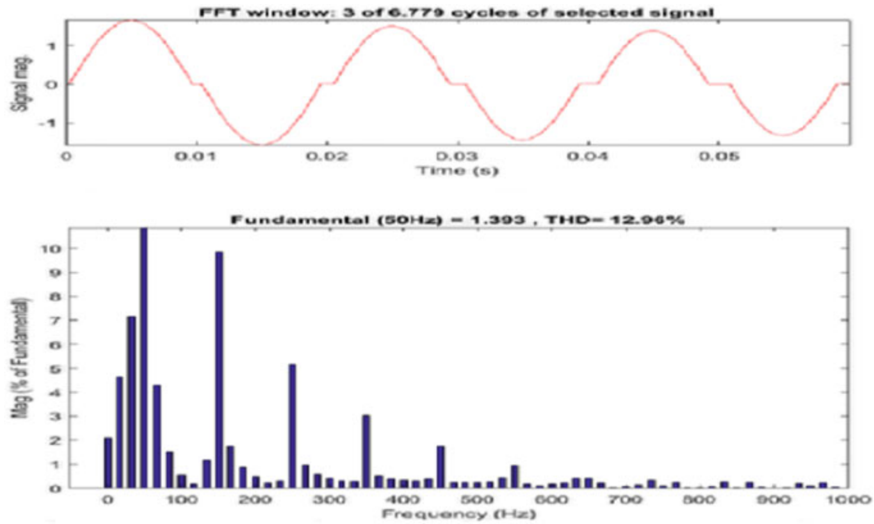

Fig. 10 Supply THD of conventional AC–DC SEPIC with valley-fill

In voltage loop, Verror is created and the output is matched with reference voltage. A fault voltage, the sinusoidal reference current is multiplied to produce the reference current. Whenever an inductor current reaches zero, switch is in on condition and it reaches the reference current, reset the flip-flop and the switch tends to off state.

- Average current control technique

Average current control scheme is a two-loop control technique that has inner current and the outer voltage control loop. The average inductor current is taken as the reference and the inductor current is mandatory to follow it. The switch becomes on; whenever the inductor current touches zero, the switch is turned off.

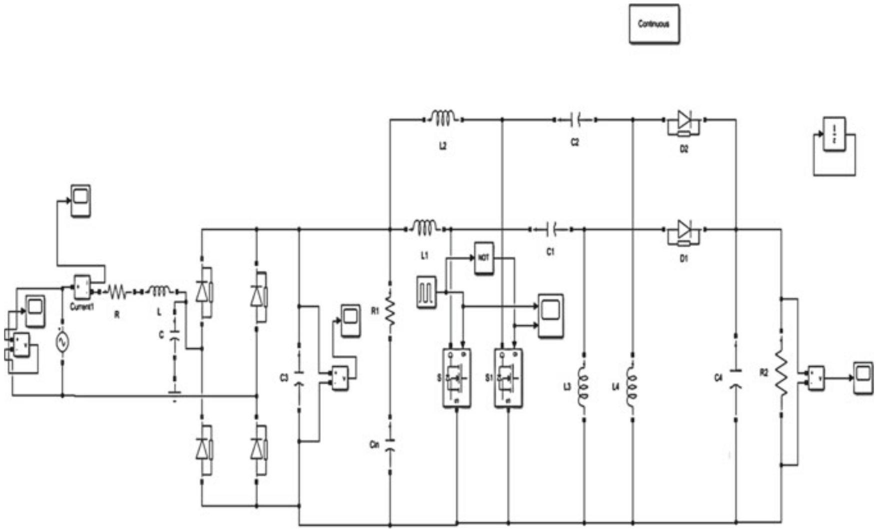

Fig. 11 MATLAB simulation circuit of interleaved AC–DC SEPIC

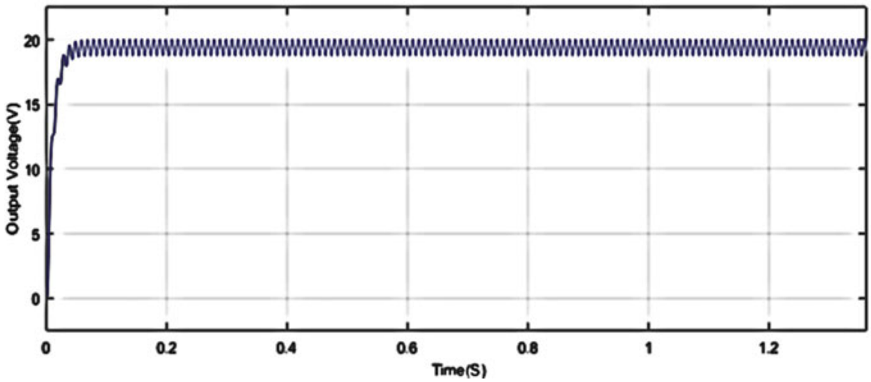

Fig. 12 Output voltage waveform of interleaved AC–DC SEPIC

The MATLAB simulation diagram for peak current control method of interleaved AC–DC SEPIC is exposed in Fig. 17.

The output voltage waveform for the interleaved AC–DC SEPIC with valley-fill in peak current control mode is exposed in Fig. 18, where output voltage obtained is about 18.65 V.

The supply current THD for an interleaved AC–DC SEPIC with valley-fill in peak current control is shown in Fig. 19, where the supply current THD obtained is about 4.66%.

The MATLAB simulation circuit for interleaved AC–DC SEPIC with valley-fill in average current control mode is shown Fig. 20,

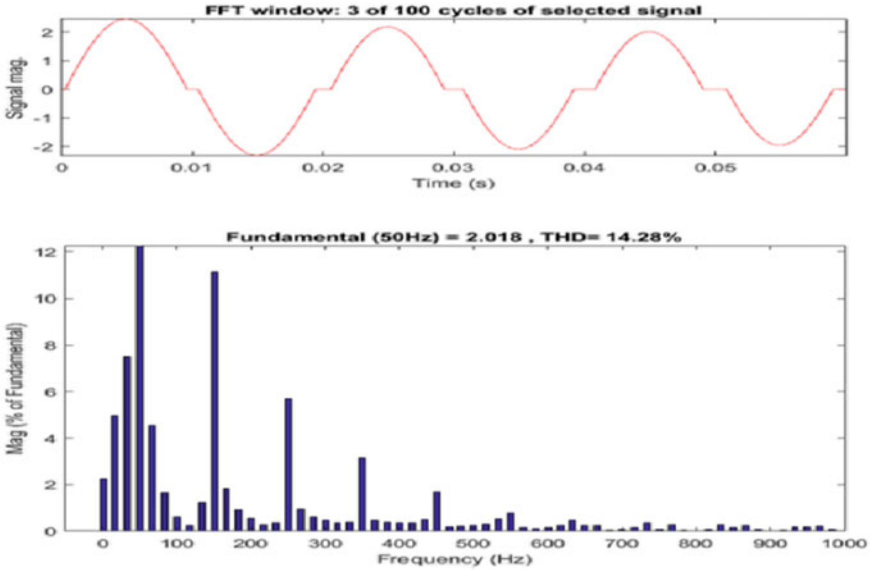

Fig. 13 Supply current THD of interleaved AC–DC SEPIC converter

An output voltage for interleaved AC–DC SEPIC with valley-fill in average current control is exposed in Fig. 21, where output voltage obtained is about 18.53 V.

The supply current THD of interleaved AC–DC SEPIC with valley-fill in average current control scheme is exposed in Fig. 22, where supply current THD obtained is about 3.78%.

From Table 3, the interleaved AC–DC SEPIC converter with average current control method has the better performance compared to other topologies. This has the better power factor, improved efficiency, reduced supply current THD, and reduced losses. Moreover an interleaved AC–DC SEPIC is most preferable for LED applications.

6 Hardware Implementation

Hardware prototype of interleaved AC–DC SEPIC with valley-fill is developed employing MOSFET switches, gate driver circuit, and power circuit. Pulses to the switches are generated using ARDUINO software. These pulses are then given to the ARDUINO board. The output of proposed converter and the performance parameters are calculated and verified. Experimental setup of an interleaved AC–DC SEPIC converter with valley-fill circuit is constructed based on the specifications that are shown in Table 4.

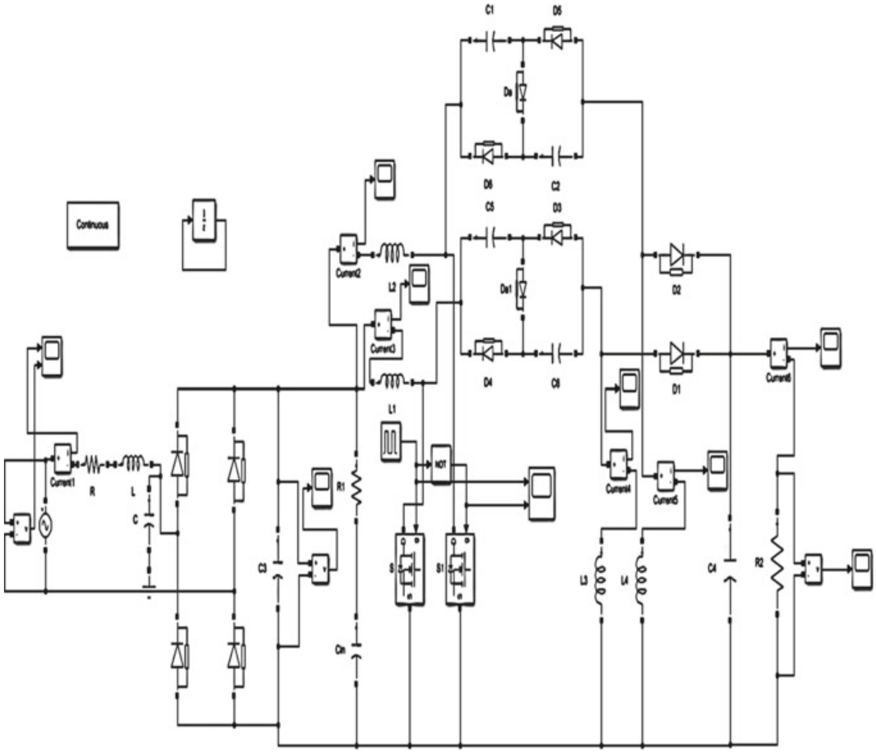

Fig. 14 MATLAB simulation circuit of interleaved AC–DC SEPIC converter with valley-fill

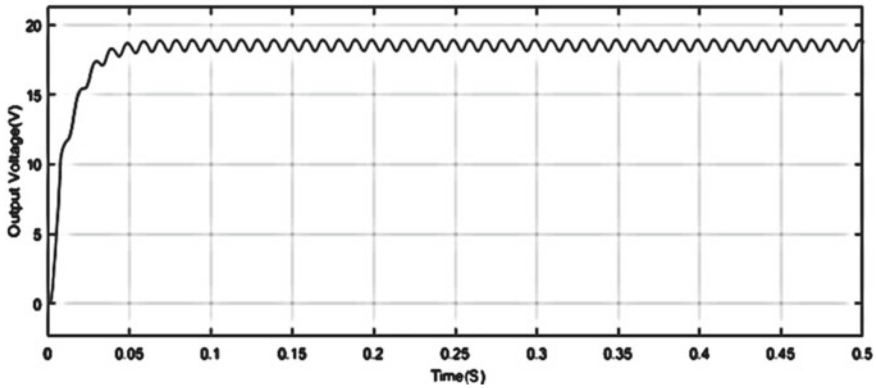

Fig. 15 Output voltage waveform of an interleaved AC–DC SEPIC with valley-fill

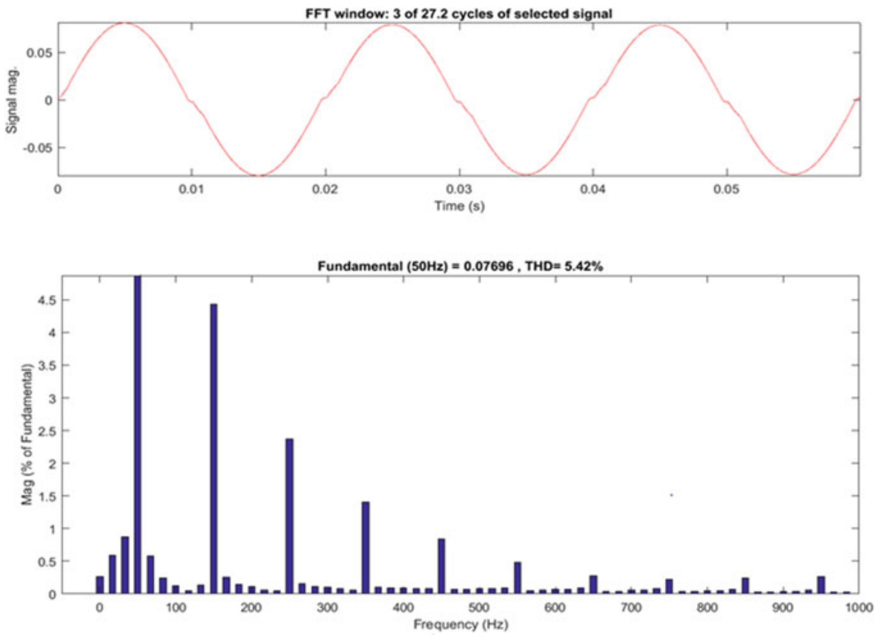

Fig. 16 Supply current THD of interleaved AC–DC SEPIC converter with valley-fill

Table 2 Evaluation of performance parameters

Topology	O/P (V)	O/P ripple (%)	Supply current THD (%)	Supply power factor	Supply distortion factor	Supply displacement factor	Total power losses (W)	Efficiency (η) (%)
Con-SEPIC	15.5	10.2	18.38	0.779	0.034	0.78	12.5	68.75
Con-SEPIC valley-Fill	14.4	2.8	12.96	0.845	0.054	0.841	10.5	73.75
Interleaved SEPIC	20.0	6.85	14.28	0.873	0.0698	0.871	8.52	78.75
Interleaved SEPIC valley-fill	18.9	3.4	5.42	0.891	0.184	0.902	7.54	80.75

Pulses generated for the switches present in interleaved AC–DC SEPIC converter using ARDUINO UNO board are shown in Fig. 23.

Experimental setup of the proposed converter contains a rectifier for AC–DC conversion, and this rectifier is integrated with an interleaved SEPIC with valley-fill is exposed in Fig. 24. An output voltage obtained is about 18.1 V.

Output voltage ripple is calculated using DSO and that is shown in Fig. 25. The output voltage ripple obtained is about 3.11%.

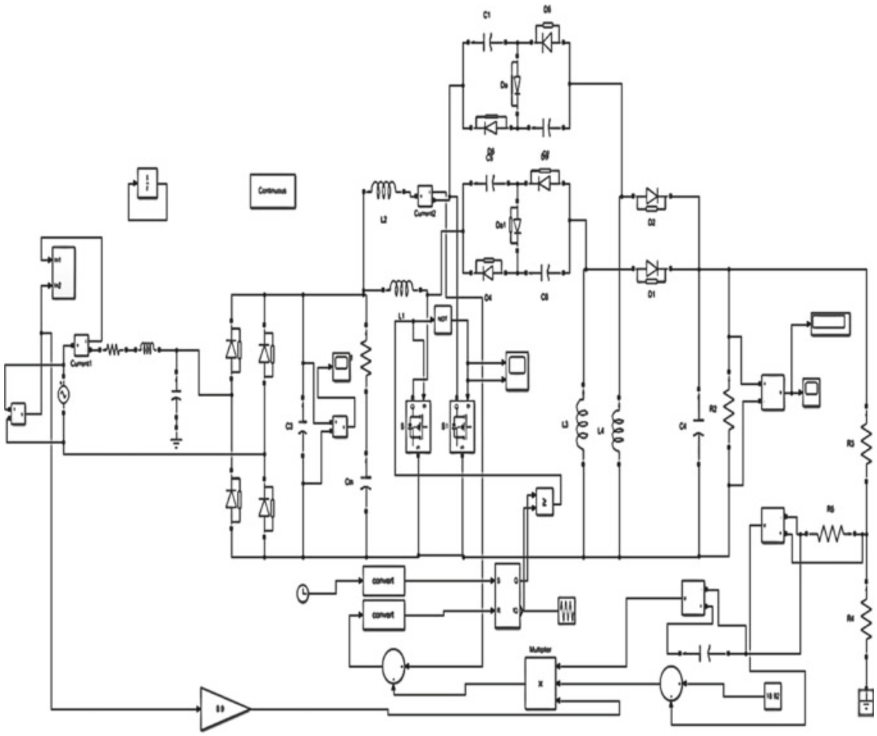

Fig. 17 Simulation circuit of interleaved AC–DC SEPIC with valley-fill in peak current control mode

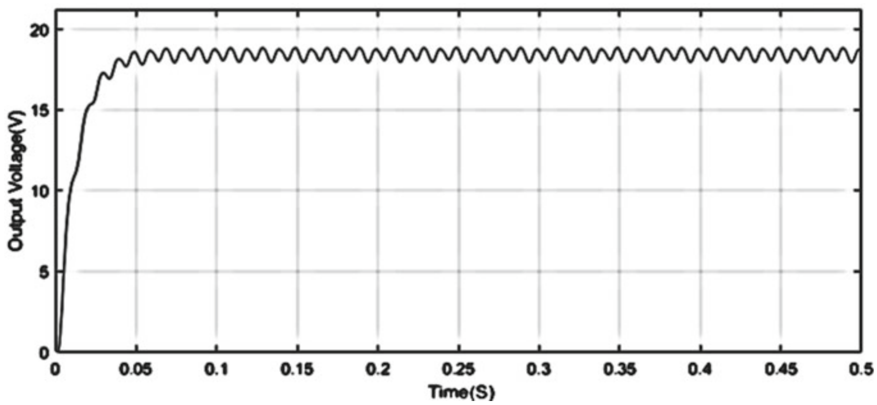

Fig. 18 Output voltage waveform of interleaved AC–DC SEPIC in peak current control mode

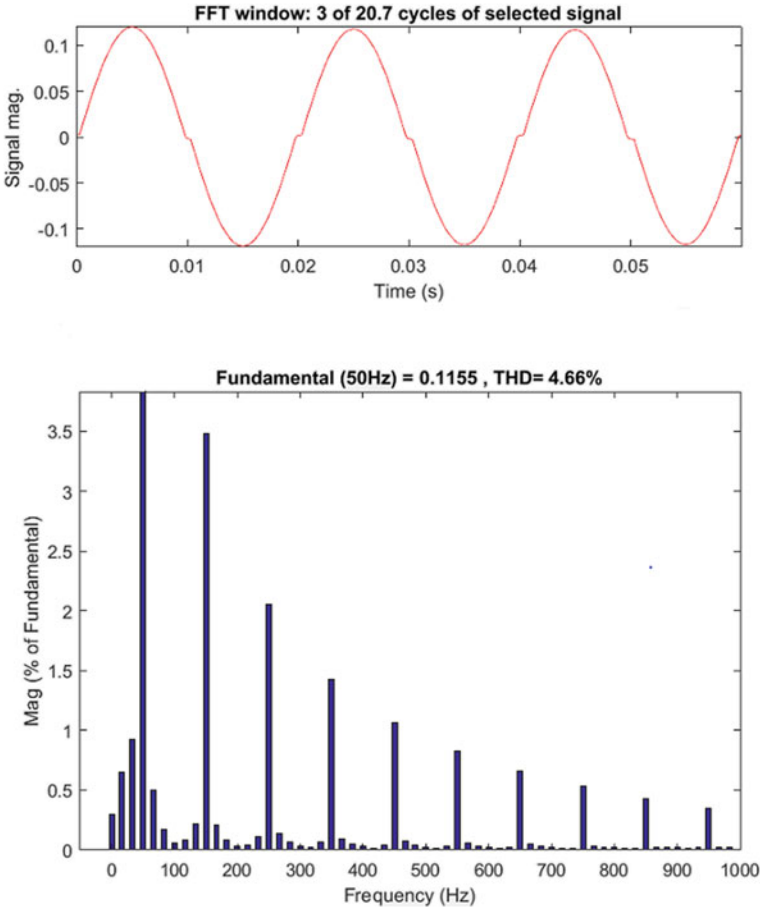

Fig. 19 Supply current THD of interleaved SEPIC peak current control technique

7 Conclusion

In this paper, conventional AC–DC SEPIC is used for power factor correction in supply side. Interleaved buck SEPIC power factor correction circuit incorporating valley-fill circuit is investigated. From the results, it is found that the valley-fill circuit results in reduced output voltage ripple, improved power factor, and better spectral quality of the supply current waveform compared to the conventional SEPIC converter. Moreover, the presented topology provides a high efficiency with reduced losses, and hence, this converter will be a suitable one for LED applications. The simulation has been carried out using MATLAB/SIMULINK. Hardware prototype has been developed, and the results are validated.

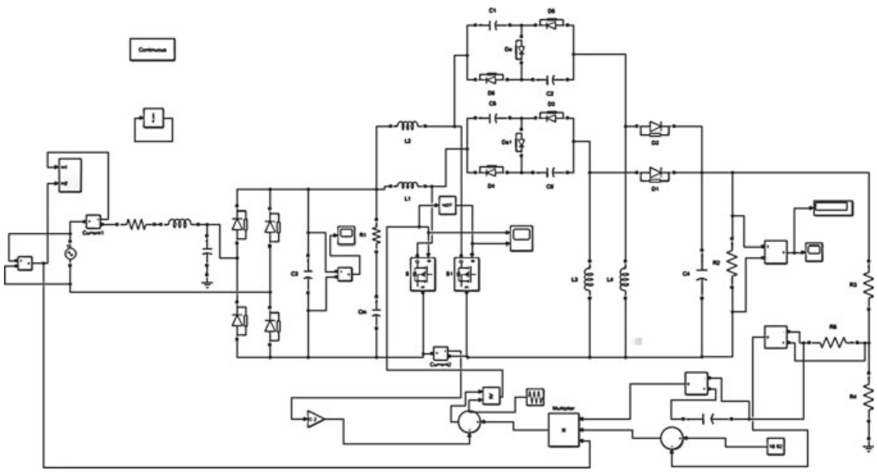

Fig. 20 Simulation circuit of interleaved AC–DC SEPIC with valley-fill in average current mechanism

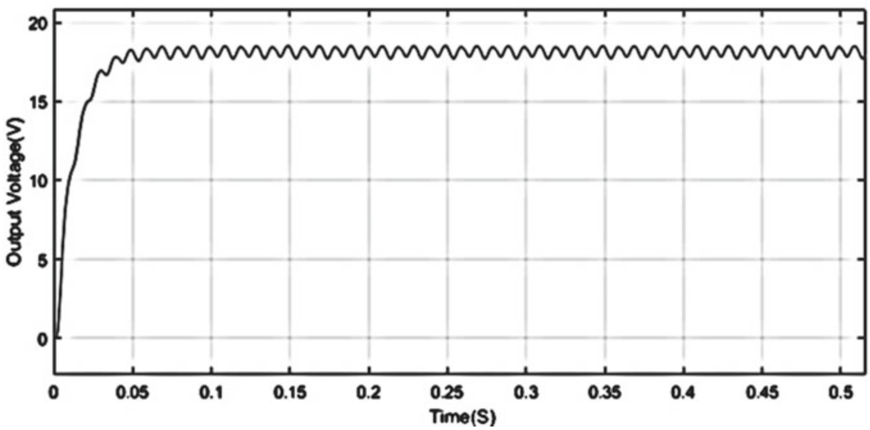

Fig. 21 Output voltage waveform for average current control

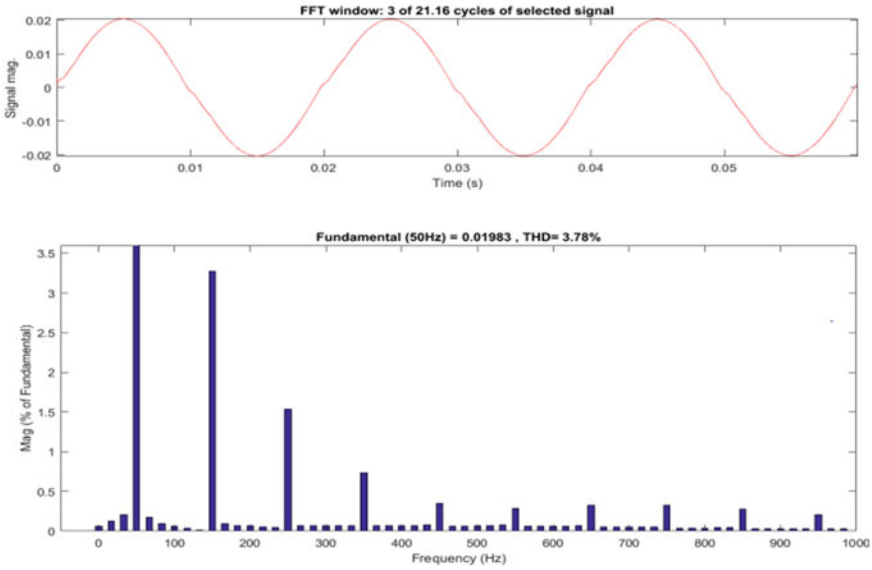

Fig. 22 Supply current THD of interleaved SEPIC in average current control method

Table 3 Comparison between current control techniques and open loop

Techniques	O/P voltage	O/P voltage ripple (%)	THD (%)	Power factor	Distortion factor	Displacement factor
Open loop	18.92	3.4	5.42	0.891	0.184	0.902
PCC	18.65	3.8	4.66	0.901	0.226	0.906
ACC	18.53	3.2	3.78	0.915	0.259	0.912

Table 4 Hardware specifications

Parameters	Values
Input voltage	22 V
Inductors	110 μH
Capacitors	225 nF
MOSFET switch	IRF 840
Switching frequency	50 kHz
Filter capacitor	497 μF
Load	40 Ω
Diode	MUR50
Transformer	(0–24) V

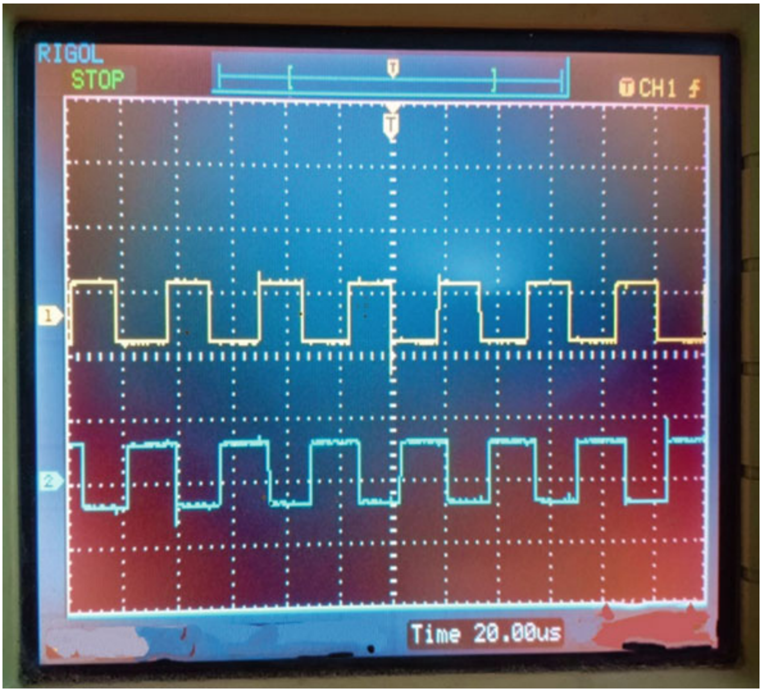

Fig. 23 Pulse pattern for the switches

Fig. 24 Experimental setup

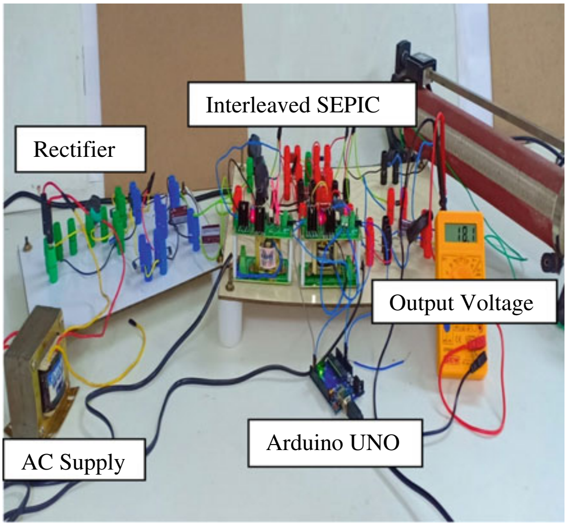

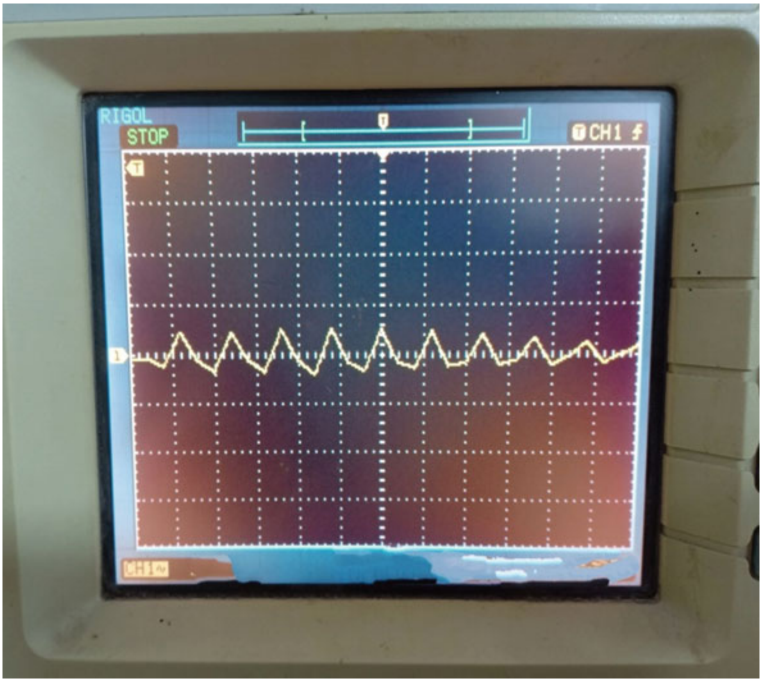

Fig. 25 Output voltage ripple. Maximum voltage is 18.1 V, minimum voltage is 17.7 V, output ripple voltage is 3.11%

References

1. Hu Q, Zane R (2010) LED driver circuit with series-input connected converter cells operating in continuous conduction mode. IEEE Trans Power Electron 25(3):574–582
2. Saravanan S, UshaRani P (2014) Review of bridgeless discontinuous conduction mode SEPIC power factor correction rectifier. IEEE international conference (ICGCE), pp 594–599, 02 June 2014
3. Lodh T, Majumder T (2016) High gain and efficient integrated flyback SEPIC converter DC-DC with leakage energy recovery mechanism. International conference on signal processing, communication, power and embedded system, SCO PES, 7955689, 2016-10, 1109
4. Costa MAD, do Proda RN, Campos A, Seidal AR (2003) An analysis about valley-fill filters applied to electronic ballasts. in Conference Record of IAS Annual Meeting, pp 779–784
5. Duran E, Galan J, Sidrach-de-Cardona M, Segura F (2008) An application of interleaved DC-DC converters to obtain I-V characteristic curves of photovoltaic modules. In: 34th annual conference of IEEE industrial electronics, April 2008, pp 2284–2289. http://dx.doi.org/10.1109/iecon.2008.4758313
6. Calleja AJ, Alonso JM, Ribas J, Lopez E, Cardesin J, Garcia J, Rico-Secades M (2002) Electronic ballast based on single stage high power factor topologies: a comparative study. In: Proceedings of IEEE IECON Conference, pp 1196–1201
7. Azcondo FJ, Branas C, Casanueva R, Bracho S (2005) Power-mode controlled power-factor corrector for electronic ballast. IEEE Trans Power Electron 52(1):56–65

Finite Element Analysis of a Two-Post Rollover Protective Structure of an off-Highway Motor Grader

V. Kumar, G. Mallesh, and K. R. Radhakrishna

Abstract Rollover protective structure (ROPS) is a critical safety system mounted on off-highway equipments, which serves as a safety structure for an operator survival during rollover accidents. ROPS is classified as single post, two post, four post, and multi-post; selection of this ROPS depends on the type of the application. Commonly used off-highway equipments are dump truck, articulated scrapers, dozers, water sprinklers, excavators, loaders, motor grader, etc.; among these equipments, motor graders were extensively used in off-highway and mining works. It is noticed from the accidents summary reported by the Directorate General of Mine and Safety, India, and Occupational Safety and Health Administration (OSHA), USA, that a significant failure was noticed by the motor grader ROPS structure. Hence, it is necessary to study the failure behavior and strength criteria of rollover protective structure. In the present research work, attempts are made to study the failure behavior and strength of a two-post motor grader (25 tons GVW) ROPS using finite element analysis (FEA) software ANSYS. Further, an interlock section was introduced in the ROPS column to minimize the overall size and to enhance the performance of the ROPS. Later, comparative analysis has been done on this ROPS in terms of maximum deformation, rate of energy absorption, and C.G height. It is evident from the results that proposed ROPS has 30% reduction in overall size, 5% reduction in weight, and enhanced C.G of height. Further, the proposed ROPS meets the performance requirement of existing standards.

V. Kumar (✉)
Department of Mechanical Engineering, Sri Jayachamarajendra College of Engineering, Mysore, India
e-mail: kumarvaradaraj1973@gmail.com

G. Mallesh
Department of Mechanical Engineering, Sri Jayachamarajendra College of Engineering, JSS Science and Technology University, Mysore, India
e-mail: mallesh@sjce.ac.in

K. R. Radhakrishna
BEML Limited, Bangalore, Karnataka, India
e-mail: cgmq@beml.co.in

E. T. Akinlabi et al. (eds.), *Trends in Mechanical and Biomedical Design*, Lecture Notes in Mechanical Engineering,
https://doi.org/10.1007/978-981-15-4488-0_31

Keywords Rollover Protective Structure · Deflection-Limiting Volume · Energy Absorption · Motor Grader · FEA

1 Introduction

Rollover protective structure (ROPS) is a critical safety system mounted on off-highway equipments, which serves as a safety structure for an operator survival during rollover accidents (Fig. 1).

A survey of rollover accidents was conducted for off-highway vehicle operators at the different parts of the country [1] and found that slope, uneven terrain, loose soil, and harsh environment are related to the working situations (Fig. 2). Similarly, break failure, over turn, high center of gravity, and visibility lead to the failure of ROPS. Further, it is observed that dump truck, dozer, excavator, scrapers, and motor graders were commonly used off-highway vehicles. It is evident from the Occupational Safety and Health Administration (OSHA), USA, that around 16% of failure is noticed only

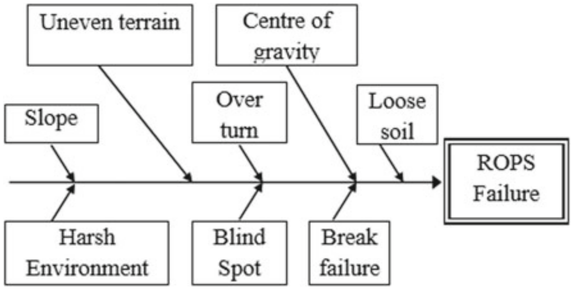

Fig. 1 Cause–effect diagram for ROPS failure

Fig. 2 Motor grader with ROP structure [BEML]

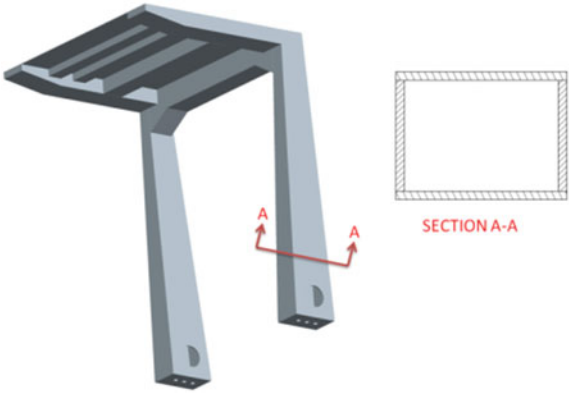

Fig. 3 ROPS with variable rectangular cross section

by the motor grader [2]. Hence, in this paper, attempts are made to design and develop new ROPS structure for motor grader by considering the safety of an operator.

Figure 2 shows the motor grader which is commonly used in off-highway for grading and is classified as light, medium, and heavy equipment based on gross vehicle weight (GVW) of the machine. Companies such as BEML, Mahindra & Mahindra, Komatsu, Volvo, Case, LeeBoy, Caterpillar, and Tata Hitachi are the major manufacturer of motor grader in India. Based on GVW, various types of cross sections were used to design and develop ROPS by various manufacturers. C-section, square, rectangular, and variable sections are widely used along with circular sections in ROPS to resist impact, bending, and torsion load during rollover. It is evident from the literature and manufacturer catalogue that variable rectangular cross sections shown in Fig. 3 were preferred in ROPS design due to its higher resistance to impact load and energy absorption capability [3].

As per ISO: 3164 standard [4], ROPS is required to satisfy the safety requirements; during rollover accident, any structural part should not enter deflection-limiting volume (DLV) shown in Fig. 4 [5–7].

Many researchers are attempted to study the performance of ROPS using expensive physical testing [5] and simulation modeling technique. Physical testing is a tedious and cumbersome procedure; the simplicity and power of analytical tools, like finite element method (FEM), have overshadowed intricate methods like physical testing. Henceforth, finite element analyses were carried out on existing two-post ROPS structure and proposed ROPS model to evaluate the performance as per ISO: 3471 standards [8].

The detailed dimensions of the ROPS were taken physically on the existing ROPS placed on the motor grader at manufacturer's site. Based on the dimensions, 3D models were developed using CAD modeling software.

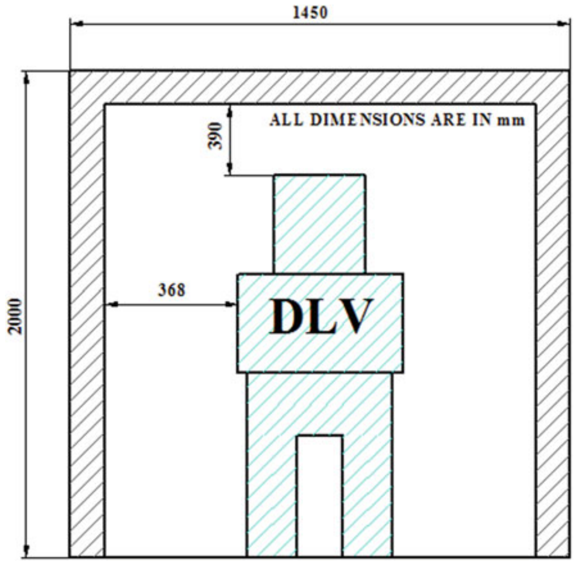

Fig. 4 Size and deflection-limiting volume for ROPS

2 Finite Element Analysis of ROPS

The finite element method has evolved as a specialized technique for the general numerical solution method applicable to a broad range of physical problems. In general, the finite element method is based on a theory, whereby an original object is viewed as an assembly of discrete building blocks called elements. The application of the method involves dividing the body into an optimum number of blocks. These blocks are connected to each other at specified points known as nodes, forming a network called mesh. The number of elements is determined by two factors—the capability of the computer being used and the accuracy of the results. The realistic use of finite element method for solving the problem involves preprocessing, analysis, and post-processing. The preprocessing involves the preparation of data such as nodal coordinates, element connectivity, boundary conditions, loading, and material properties. The analysis stage involves stiffness generation, stiffness modification, and solution of the equations resulting in the evaluation of nodal displacements and derived quantities such as stresses. The post-processing deals with the presentation of the results. In the present research, 3D models were developed using CAD software and are converted into *.iges file formats and are imported into the analyses environment to carryout static and dynamic analyses of existing and proposed ROPS (Figs. 5, 6 and 7).

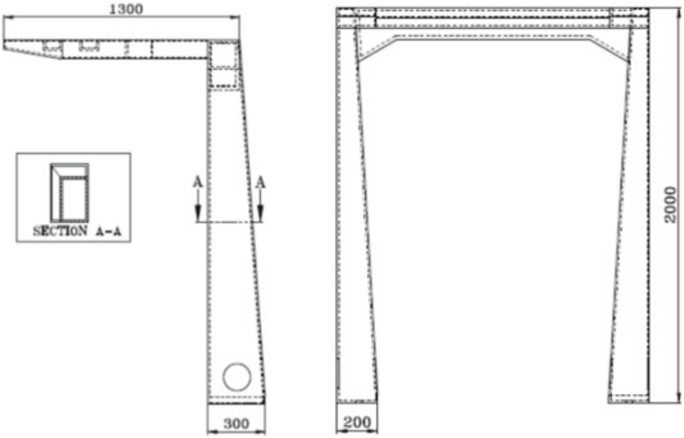

Fig. 5 Existing ROPS drawings

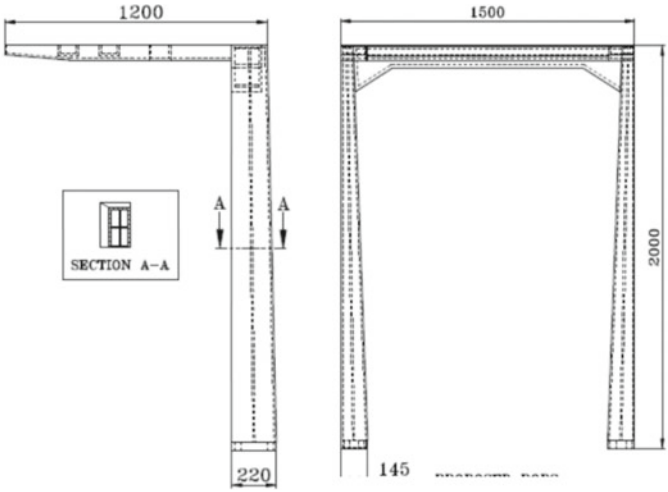

Fig. 6 Proposed ROPS drawings

2.1 Physical and Mechanical Properties of ROPS

ASTM A 500 Gr C is commonly used material to manufacture ROPS by various companies. Hence, in this research, ASTM A 500 Gr C material is used for existing and proposed ROPS. The properties of ASTM A 500 Gr C are yield strength 325 MPa, ultimate strength is 490 MPa, Young's modulus 200 GPa, Poisson's ratio 0.3, and density is 7850 kg/m^3; these properties and 10-node tetrahedral elements shown in Fig. 8 are used to discretize the domain into number of finite elements. Finite element model of the proposed ROPS structure is shown in Fig. 9.

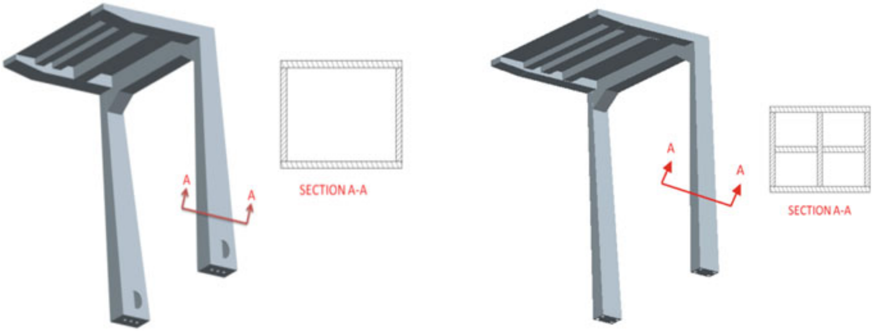

Fig. 7 3-D models of existing and proposed ROPS

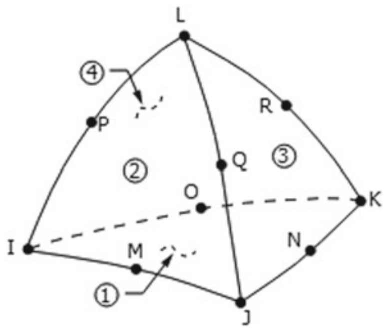

Fig. 8 3-D 10-node tetrahedral element

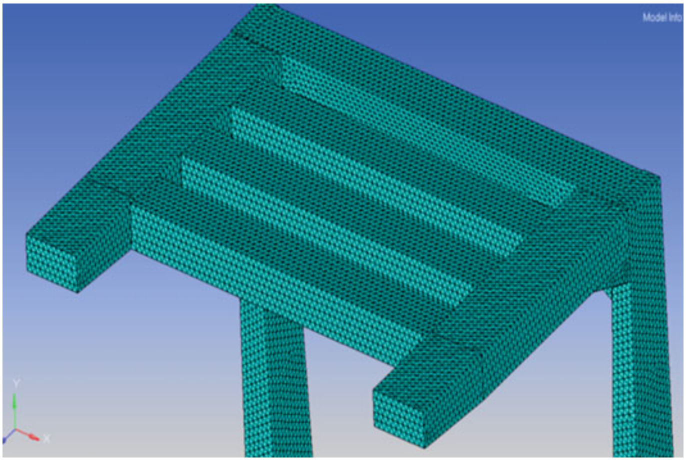

Fig. 9 Finite element model of a ROPS

2.2 Loads and Boundary Conditions for Static Analysis of ROPS

It is noticed that as per the failure summary during rollover the ROPS is subjected to various types of load such as lateral, vertical, and longitudinal loads. Magnitude of the loads is calculated based on gross vehicle weight (GVW) as per ISO 3471 standard. For a motor grader with the mass ranging from 2140 to 38,010 kg, the following formulas are used to determine lateral, vertical, and longitudinal loads. These loads are applied on two-post ROPS as shown in Fig. 10 to determine deformation and stresses induced in the ROPS (Table 1).

$$\text{Lateral Load} = 70{,}000 \times \left(\frac{m}{10{,}000}\right)^{1.1} \tag{1}$$

$$\text{Vertical Load} = 9.6\ \text{m} \tag{2}$$

$$\text{Longitudinal Load} = 56{,}000 \times \left(\frac{m}{10{,}000}\right)^{1.1} \tag{3}$$

As the ROPS is mounted on the main frame of the motor grader using fasteners, bottom of the posts is constrained in all the directions and different loading conditions.

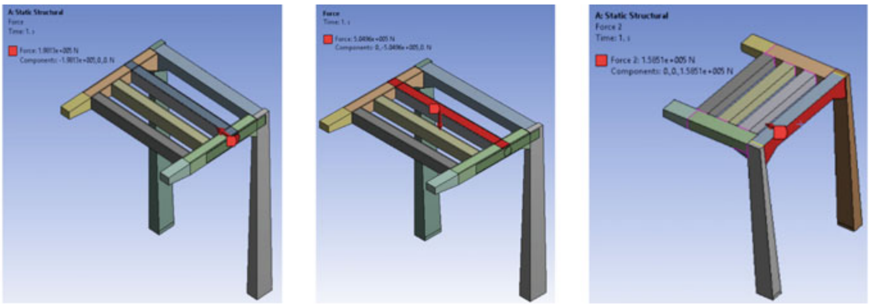

Lateral load Vertical load Longitudinal load

Fig. 10 Position of loads on ROPS [1]

Table 1 Loads on ROPS

Machine mass (kg)	Lateral load (N)	Vertical load (N)	Longitudinal load (N)
25,750	198,131	504,958	158,505

3 Dynamic Analysis of ROPS

Same load and boundary conditions are used to determine the dynamic behavior of the ROPS during rollover. During rollover as per the failure summary and literatures, it is found that ROPS is subjected to impact load, and many researchers are attempted to conduct experiments to know the dynamic behavior of the ROPS and noticed that conducting the experiments is costlier, time-consuming, tedious, and cumbersome procedures. Hence, attempts are made to analyze the dynamic characteristics of the ROPS using FEA. Further, it is noticed that during rollover, ROPS are subjected to impact load between the ground surface and the ROPS results in energy absorption by both ROPS and the ground. To simplify the model, the ground surface was idealized as a rigid body that is able to transfer kinetic energy to the ROPS (energy absorbed by the ROPS). During 1971, Klose and Chou et al. introduced the concept of FEA to estimate the energy absorption using MADYMO software. Therefore, it is essential to determine the energy absorption capacity of ROPS to estimate the failure criteria. Hence, in this research work, attempts are made to determine energy absorption capacity using theoretical Eq. (4) as per ISO: 3471 standard and results were compared with advanced finite element software.

$$U = \frac{\Delta 1 F1}{2} + (\Delta_2 - \Delta_1)\frac{F_1 + F_2}{2} + \cdots + (\Delta_N - \Delta_{N-1})\frac{F_{N-1} + F_N}{2} \quad (4)$$

where
F = Force,
Δ = Deflection
U = Energy absorption by ROPS.

4 Results and Discussions

4.1 Static Analyses

A critical analysis was carried out using finite element analyses software ANSYS 15.0 to estimate deformation due to lateral, vertical, and longitudinal load for the existing ROPS. It is noticed from the Fig. 11 that maximum deformation of 47.1, 18.59, and 16.97 mm is due to lateral, vertical, and longitudinal loads, respectively. Further, similar analyses were conducted for the proposed ROPS with same load and boundary conditions. Figure 12 shows the deformation due to different loads; it is evident from the results that deformation in the proposed ROPS may increase but the proposed model exhibits safe deformation limits. It is also observed from the Table 2 that existing model is robust and consumes lots of material; further, it is observed that center of gravity of the proposed ROPS is minimum compared to the existing and hence the stability of the vehicle can be improved with the new design.

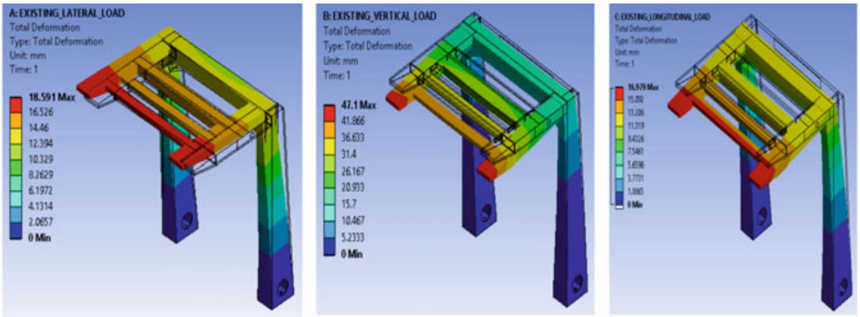

Lateral Load Vertical Load Longitudinal Load

Fig. 11 Deformation of existing ROPS

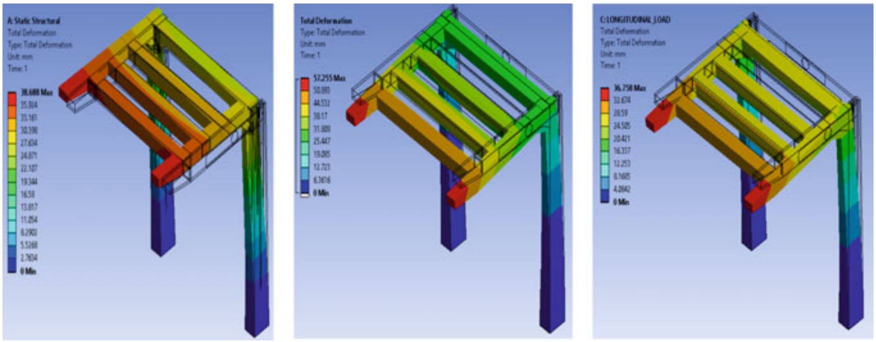

Lateral Load Vertical load Longitudinal Load

Fig. 12 Deformation of proposed ROPS

Table 2 Design characteristics of existing and proposed ROPS

Description		Existing ROPS	Proposed ROPS
Mass, kg		565	542
Center of gravity (CG) of height, mm		1489	1422
Deformation, mm	Lateral	18.5	38.6
	Vertical	47.1	57.2
	Longitudinal	16.9	36.7
Von Mises Stress, MPa	Lateral	514	526
	Vertical	578	520
	Longitudinal	195	324

The study revealed that results obtained from the FEA are in good correlation with physical testing and results of other researchers [5, 7, 9–11]. Hence, the proposed ROPS model achieved 30% reduction in size and 5% reduction in overall weight with respect to the existing ROPS.

4.2 Dynamic Analysis

It is observed from the failure summary that ROPS is subjected to impact loads which are dynamic in nature with time; therefore, it is necessary to study the dynamic behavior before finalizing the design. It is evident from the literature that most of the ROPS failure is due to lateral load. Hence, in this research work, dynamic behavior of the proposed ROPS was carried out for lateral load to understand the failure.

It is evident from the literature that energy absorption capacity of the ROPS plays a vital role in the dynamic response of a structure, and dynamic behavior of the proposed ROPS is given in Table 3. Further, it is noticed that as per ISO:3471 energy absorption capacity is dependent on the gross vehicle weight of the motor grader; for the present study, energy absorption for the ROPS is 48,973 J and time taken for the deformation of 38.68 mm is 28.89 ms. Similarly, for a load of 198 kN, the energy absorbed by the structure for a displacement of 204.5 mm was found to be 658,845.3 J and the time taken to deform is 90 ms. Hence, as per the results, the proposed ROPS is safe and meets standard performance requirements.

5 Conclusions

Finite element analyses of existing and proposed ROPS models for a motor grader were conducted to know the static and dynamic behavior during rollover accidents and found that the proposed ROPS enhances the safety of the operator; based on the results, the following conclusions were drawn;

- Proposed Interlock cross section ROPS achieves 30% reduction in overall size.
- Lower the center of gravity height by 67 mm and significant weight reduction
- Optimization of size ensures better operator visibility.
- Due to multiple impact loads during rollover accidents energy absorption capacity of proposed ROPS increases compared to the existing ROPS.
- Proposed ROPS structure meets the performance criteria as per ISO 3471 standard.

Table 3 Dynamic response of ROPS

Time, ms	Displacement, mm	Load, KN	Energy, J
0	0	0	−0.1825
5	10.0437	11	292.6258
10	22.90393	22	2782.431
15	37.00793	33	10155.37
20	39.43152	44	27282.38
25	57.86955	55	43847.95
28.8997	*65.5*	*65*	*48973.18*
30	67.03812	66	62680.51
35	80.79097	77	100824.5
40	89.95954	88	164361.1
45	103.7124	99	242545.6
50	112.881	110	330949.7
55	126.6338	121	429340.6
60	135.8024	132	537958
65	149.5553	143	446923.2
70	158.7238	154	489307.6
75	172.4767	165	531692
80	181.6452	176	574076.4
85	195.3981	187	616460.9
90	*204.5667*	*198*	*658845.3*
95	218.3195	209	701229.7
100	227.4881	220	743614.1
105	241.241	231	785998.5
110	250.4095	242	828382.9
115	264.1624	253	870767.3
120	287.0838	264	913151.7

References

1. International standard-3471 (2008) Earth-moving machinery—roll-over protective structures—laboratory tests and performance requirements
2. Hinze JW, Teizer J (2011) Visibility-related fatalities related to construction equipment. Saf Sci 49:709–718
3. Nagel GM, Thambiratnam DP (2004) A numerical study on the impact response and energy absorption of tapered thin-walled tubes. Int J Mech Sci 46(2004):201–216
4. International standard-3164 (2013) Earth-moving machinery–Specification for deflection limiting volume
5. Thambiratnam DP, Clark BJ, Perera NJ (2009) Performance of a rollover protective structure for a bulldozer. J Eng Mech 135:31–40
6. Stockton AD, O'Neill DH, Hampson CJ (2002) Methods for optimising the effectiveness of roll-over protective systems. Silsoe Research Institute for the Health and Safety Executive,

United Kingdom, 425/2002
7. Karlinski J, Dzialak P, Ptak M (2013) Simulation tests of roll-over protection structure. Arch Civil Mech Eng 13:57–63
8. Mandal A, Sengupta D (2000) The analysis of fatal accident in Indian coal mines. Indian statistical institute, 203 BT Road Kolkata -700035, AMS classification number, primary 6207, secondary 62P99, 62N05
9. Clark BJ, Thambiratnam DP, Perera NJ (2006) Analytical and experimental investigation of the behavior of a rollover protective structure. Struct Eng 84(1):29–34
10. Karlinski J, Rusinski E, Smolnicki T (2008) Protective structures for construction and mining machine operator. Automat Construct 17:232–24
11. Thambiratnam DP, Clark BJ, Perera NJ (2008) Dynamic response of a rollover protective structure. Comput Aided Civil Infrastruct Eng 23(6):448–464

Fluid Mechanics and Heat Transfer

Investigating the Route to Flutter in a Pitch–Plunge Airfoil Subjected to Combined Flow Fluctuations

Nivedhithaa Santhakumar, Divyangi Singh, and Venkatramani Jagadish

Abstract The dynamics and response a pitch–plunge airfoil with cubic hardening nonlinearity in the pitch degree of freedom are investigated numerically. The aerodynamics is assumed to be linear and modeled using the unsteady aero-dynamical formulation. The flow is fluctuating in both the longitudinal and vertical directions. The fluctuating flow is mathematically modeled as a long time-scale random process. The mean flow speed is used as the bifurcation parameter, and response analysis is carried out by systematically varying the bifurcation parameter. The route to flutter is presented, and the role of noisy flow fluctuations in the same is analyzed by examining the dependency on noise intensity.

Keywords Flutter · Intermittency · Vertical turbulence · P-bifurcation

1 Introduction

1.1 A Subsection Sample

Aeroelastic phenomena involve the dynamic interaction between the inertial, structural and aerodynamic forces of a fluid-structural system. In the case of a wing or any control surface subjected to an incoming airstream, under certain flow conditions, the structure experiences a dynamic instability known as flutter. Flutter is an unstable self-feeding behavior in which the aerodynamic forces couple with the elastic and inertial nature of the structure, resulting in sustained limit cycle oscillations ('LCOs') beyond a particular critical value of mean flow speed of wind. The appearance of LCOs in aeroelastic systems is considered undesirable, as it can induce fatigue damage in the structural components and affect the structural integrity, posing a threat to the structural safety. Consequently, investigating the onset and route to flutter attracts considerable research attention. Methods for prediction and characterization of flutter

N. Santhakumar · D. Singh · V. Jagadish (✉)
Department of Mechanical Engineering, Shiv Nadar University, Greater Noida, India
e-mail: j.venkatramani@snu.edu.in

E. T. Akinlabi et al. (eds.), *Trends in Mechanical and Biomedical Design*,
Lecture Notes in Mechanical Engineering,
https://doi.org/10.1007/978-981-15-4488-0_32

behavior have existed for decades; however, the nonlinear nature of both the airfoil structure and the aerodynamic environment continue to make this phenomenon difficult to model precisely. Worn hinges of surfaces and loose control linkages may be the sources structural nonlinearities—which can be approximated by cubic, hysteresis or a bilinear nonlinearity. This paper focusses on the cubic structural nonlinearity [1].

In case of uniform deterministic flow, onset of flutter is identified by birth of LCOs. At a certain critical velocity, the system will undergo a change from damped oscillations to LCOs, and the critical point becomes a supercritical Hopf bifurcation point. In reality, the input flow comprises many irregularities which have the capability to change the dynamical nature of the aeroelastic responses, and a Hopf bifurcation analysis proves to be insufficient in this case. In-field situations involve flow fluctuations both in the longitudinal and vertical direction. Further, vertical fluctuations being more ubiquitous [2] act as an external forcing and can bring about radical changes in the response dynamics [3].

The open problems this paper aims to tackle include: flutter prediction under turbulent flow conditions and resolution cum interpretation of the dynamical response signatures obtained, with emphasis on ascertaining the role of fluctuations in the vertical direction with respect to the airfoil. Vertical turbulence is a pervasive phenomenon [3] whose role in airfoil response dynamics and flutter prediction is unresolved, with studies [4, 5] on combined turbulence providing only transitional changes in the topology of the joint probability density function of the state variables.

2 Problem Description

2.1 Aeroelastic Model

A two-degree-of-freedom airfoil oscillating in pitch 'α' and heave 'y' is considered—which are modeled by rotational and translational springs that are attached to the elastic axis at a point. The choice of a bending–torsion model comes from experiments conducted on a cantilever wing that shows flutter oscillations primarily along the flexural and torsional modes of the structure. The structural equations are derived from Fung [1] (Fig. 1).

$$m x_\alpha b\ddot{\alpha} + m\ddot{y} + K_h y = -L(t) \tag{1}$$

$$I_{EA}\ddot{\alpha} + m x_\alpha b\ddot{y} + K_\alpha \alpha + K_3\alpha^3 = M_{EA}(t) \tag{2}$$

In the above equations, U is the speed of the oncoming wind; bx_α is the distance from the elastic axis to the airfoil center of mass; ba_h is the semi-chord of the airfoil; I_{EA} is the moment of inertia about the elastic axis; K_h and K_α are the linear plunge and pitch spring stiffnesses, respectively, and K_3 is the coefficient of nonlinear plunge

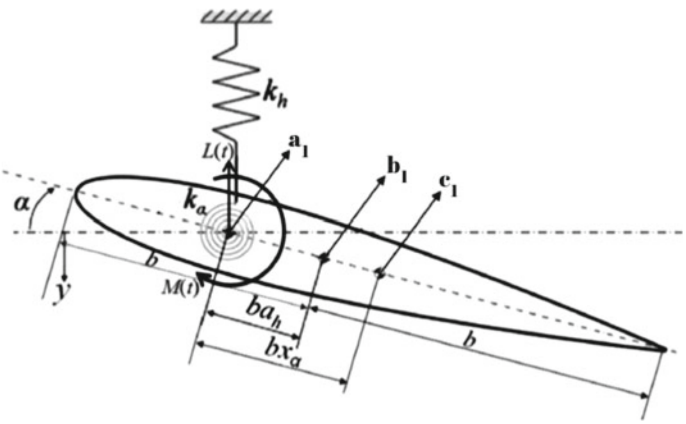

Fig. 1 Schematic of airfoil

stiffness. $L(t)$ and $M_{\mathrm{EA}}(t)$ are the unsteady lift and moment generated due to the aerodynamic effects, with τ representing non-dimensional time.

The unsteady aerodynamic load, owing to the longitudinal component, assuming incompressible, inviscid flow, is estimated via Duhamel's integral and the two-state representation of Wagner's function, which accounts for the wake structure developing behind the airfoil.

$$L_{\varphi}(t) = \pi\rho b^2[\ddot{y} + U\dot{\alpha} - ba_h\ddot{\alpha}] + 2\pi\rho bU\left[\omega_{\frac{3}{4}}\varphi(0) - \int_0^t \omega_{\frac{3}{4}}\varphi(s)\frac{\mathrm{d}\varphi(t-s)}{\mathrm{d}s}\mathrm{d}s\right] \tag{3}$$

$$M_{ea\varphi}(t) = \pi\rho b^2\left\{ba_h\ddot{y} - b[0.5 - a_h]U\dot{\alpha} - b^2\left[a_h^2 + \frac{1}{8}\right]\ddot{\alpha}\right\} + 2\pi\rho b^2[0.5 + a_h]U\left[\omega_{\frac{3}{4}}\varphi(0) - \int_0^t \omega_{\frac{3}{4}}\varphi(s)\frac{\mathrm{d}\varphi(t-s)}{\mathrm{d}s}\mathrm{d}s\right] \tag{4}$$

where

$$\omega_{\frac{3}{4}} = \dot{y} + U\alpha + b[0.5 - a_h]\dot{\alpha} \tag{5}$$

$$\varphi(\tau) = 1 - \Psi_1 e^{-\epsilon_1\tau} - \Psi_2 e^{-\epsilon_2\tau} \tag{6}$$

The constants $\Psi_1 = 0.165$, $\Psi_2 = 0.335$, $\varepsilon_1 = 0.0455$ and $\varepsilon_2 = 0.3$ are obtained from Jones [7].

Vertical turbulence also contributes to the aerodynamic force and moment. The unsteady effects are expressed in terms of Kussner's function which accounts for compounded circulation as a gust hails the leading edge of the airfoil.

$$L_{\psi}(t) = 2\pi\rho bU\left[\omega_t\psi(0) - \int_0^t \omega_t\psi(s)\frac{\mathrm{d}\psi(t-s)}{\mathrm{d}s}\mathrm{d}s\right] \tag{7}$$

$$M_{ea\psi}(t) = 2\pi\rho b^2[0.5 + a_h]U\left[\omega_t\psi(0) - \int_0^t \omega_t\psi(s)\frac{\mathrm{d}\psi(t-s)}{\mathrm{d}s}\mathrm{d}s\right] \tag{8}$$

$$\psi(\tau) = 1 - 0.5792e^{-0.1393\tau} - 0.4208e^{-1.802\tau} \tag{9}$$

The equations of motion are obtained upon the combination of Eqs. 7 and 8 with Eqs. 3 and 4, while the pitch angle and the angle of attack are taken to be the same. Four additional states, two lag terms in Wagner's function and two lag terms in Kussner's function, are introduced for the transformation of the above integro-differential equations into differential form. The transformation facilitates the solution procedure while allowing the delineation of the model into components of a traditional mechanical system consisting of inertia, damping, stiffness and external forcing terms. The non-dimensional aeroelastic equations of motion in the differential form can be obtained from [3].

2.2 Flow Model

The flow speed U is assumed to comprise of a mean flow U_m superimposed with a randomly longitudinally fluctuating flow component $f(\tau)$, where τ is the non-dimensional time. A simple model [6] for the input flow fluctuation is utilized:

$$U = U_m + f(\tau) \tag{10}$$

$$f(\tau) = U_m\sigma_1 \sin(\omega_r\tau) \tag{11}$$

$$\omega_r(\tau) = \omega_o + \kappa R(\tau) \tag{12}$$

The uniform flow is superimposed with a sinusoidal component whose frequency of oscillation varies with time about a dominant frequency. U_m is the mean wind speed, σ indicates the amplitude of the fluctuating component and $\omega_r(t)$ is the frequency of the sinusoid. Here, κ is a constant and R is a uniformly distributed random variable that takes values in [0, 1] at each instant of time.

The function $g(\tau)$ accounts for fluctuation in the vertical direction. The fluctuating flow is mathematically modeled as a long time-scale random process.

$$g(\tau) = U_m\sigma_2 \sin(\omega_r\tau) \tag{13}$$

3 Results and Discussion

The eighth-order aeroelastic system is then expressed in state-space form and solved numerically. A fourth-order Runge–Kutta scheme is used to obtain the time responses.

The cases presented are for an airfoil with the following non-dimensional airfoil parameters:

$$k_3 = 400; \quad \frac{\omega_y}{\omega_\alpha} = 0.6325; \quad x_\alpha = 0.25; \quad r_\alpha = 0.5; \quad a_h = -0.5; \quad \mu = 100$$

For the given set of parameters, the deterministic flutter speed U_m is 4.3 [3].

3.1 Vertical Turbulence

A three-stage analysis is carried out for analyzing the effect of vertical turbulence on the response of the airfoil.

Firstly, in addition to longitudinal turbulence, an impulse forcing in the vertical direction is introduced, to isolate the response corresponding to the impulse. Further, the airfoil response is interpreted by means of a stochastic bifurcation analysis in case of fluctuating flows. The P-bifurcation (J-PDF) is concerned with a qualitative topological change in the probability structure of the dynamic behavior as a control parameter is varied. Shown below are some of the pitch time histories and J-PDFs. The plunge response time histories are qualitatively similar to the pitch responses (Figs. 2 and 3).

Low-amplitude noisy response is observed to grow in amplitude (intermittency) and give rise to random LCOs. The shape of the J-PDF changes from a bell-shaped bi-dimensional one to a crater shape. These results are in accordance with those obtained for a longitudinal turbulence analysis [6].

For the next step, longitudinal noise intensity was varied for a fixed vertical noise intensity, to gauge the effect of variation in longitudinal turbulence in the presence of a constant vertical fluctuation (Figs. 4, 5 and 6).

As mean flow speed is increased, a response typical of LCOs is not observed. However, a high-frequency noisy response is noticed, with greater prominence of high amplitude oscillations alongside bursts of lower amplitude oscillations. The corresponding J-PDF shows a crater with two peaks, with turbulence distorting the structure of the LCOs. However, upon variation of intensity, demarcation of responses into separate regimes is not apparent through qualitative analysis involving PDFs.

Further, intensities of fluctuations in both directions are varied, to capture responses and simulate real-time in-field conditions (Figs. 7 and 8).

A decaying response with noisy intermittent bursts is observed in the response for $U_m = 3.5$ and magnitude of noise intensity in either direction being 0.1. The J-PDF for this case shows a collection of peaks. An LCO-like response is obtained for

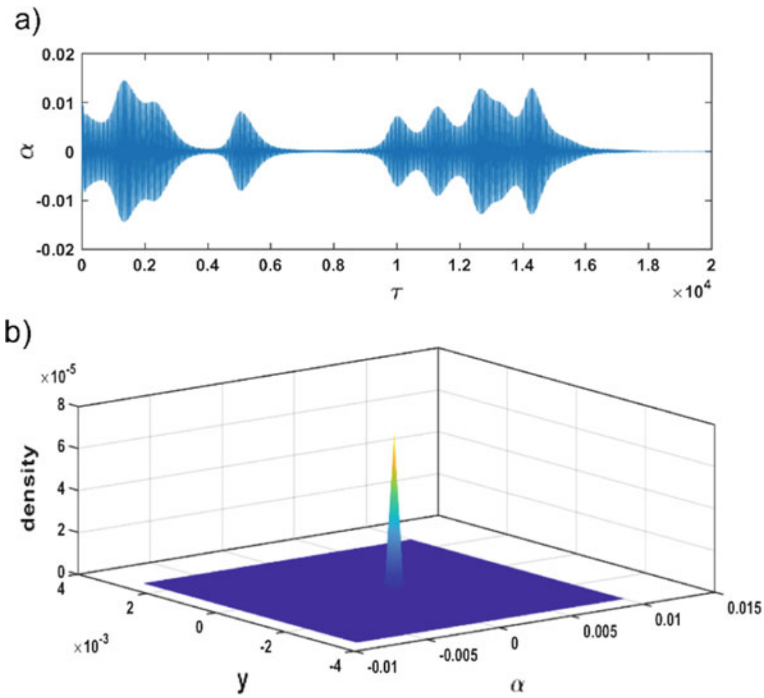

Fig. 2 **a** Pitch response and **b** J-PDF for $U_m = 4.5$ at $\sigma_1 = 0.5$

$U_m = 8.5$ with longitudinal and vertical noise intensities being 0.3 and 0.1, respectively. The corresponding J-PDF shows a crater with two peaks.

4 Conclusion

A study of airfoil response under combined fluctuations has been carried out for a two-degree-of-freedom pitch–plunge airfoil with respect to the mean speed of the flow and the noise intensities. The mean flow speed of the longitudinal and vertical components is used as the bifurcation parameter. A three-step analysis has been undertaken, consisting of time histories and J-PDFs. It is observed that the pre-flutter response displays a distinct noisy signature akin to an intermittent behavior. This observation is substantiated from the J-PDFs as well. Further, with increase in the noise intensity, the responses display an uncertain transition from one basin of attraction to another. However, the specific role of longitudinal or vertical component's contribution toward this behavior could not be identified. The authors will take up this interesting problem in a subsequent study.

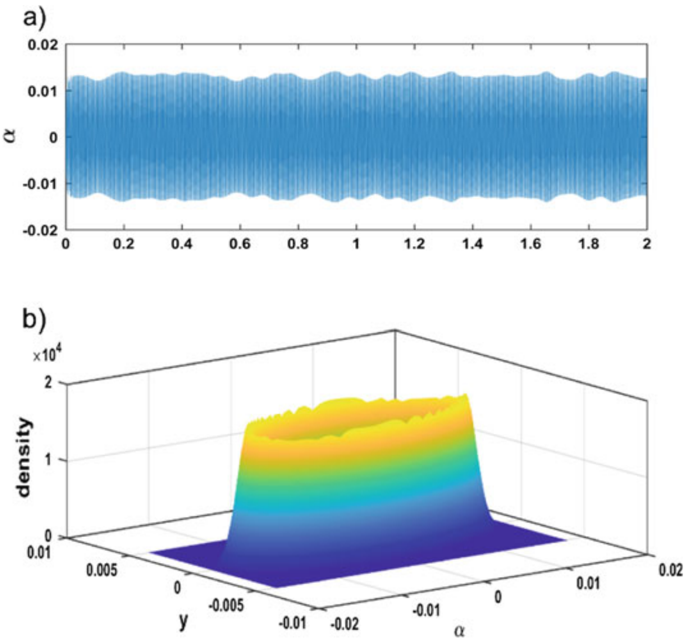

Fig. 3 **a** Pitch response and **b** J-PDF for $U_m = 6$ at $\sigma_1 = 0.1$

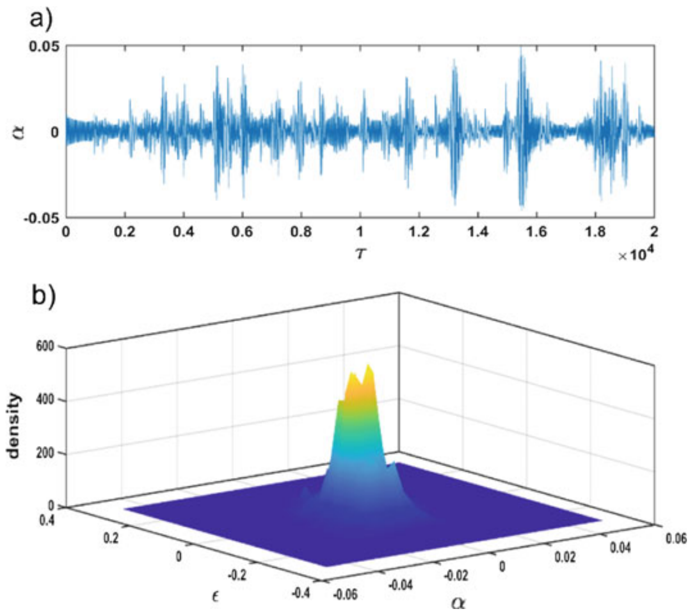

Fig. 4 **a** Pitch response and **b** J-PDF for $U_m = 4.5$ at $\sigma_1 = 0.6$ and $\sigma_2 = 0.2$

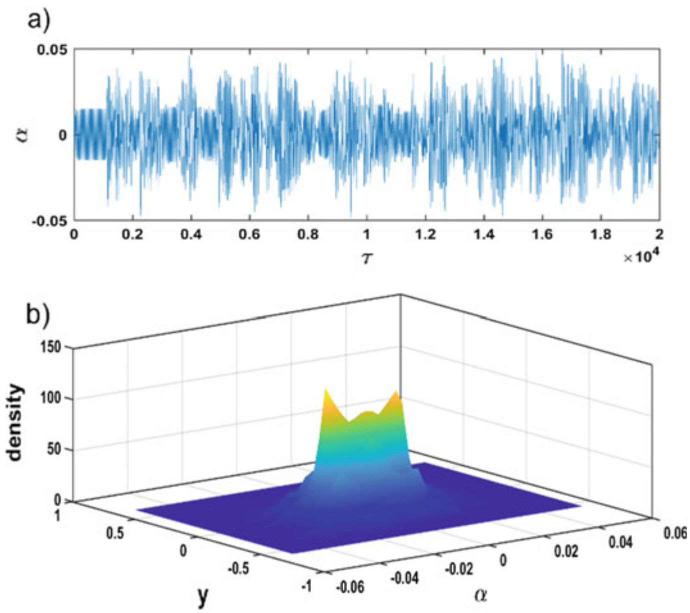

Fig. 5 **a** Pitch response and **b** J-PDF for $U_m = 6.5$ at $\sigma_1 = 0.1$ and $\sigma_2 = 0.2$

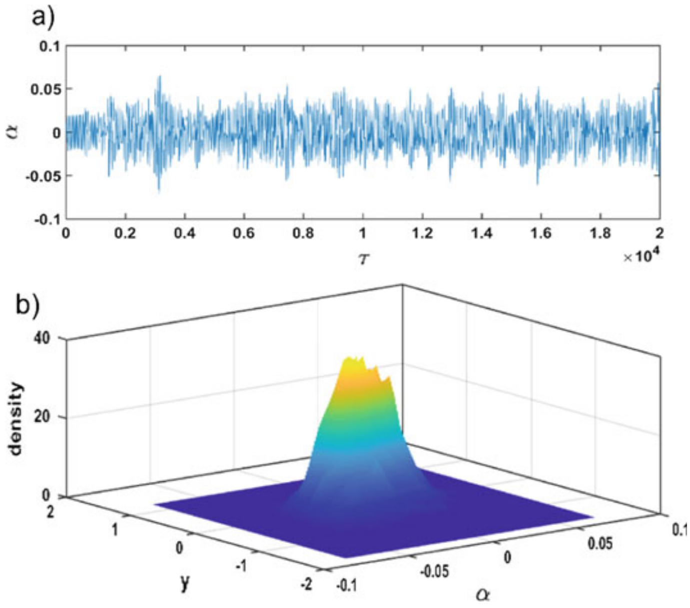

Fig. 6 **a** Pitch response and **b** J-PDF for $U_m = 8.5$ at $\sigma_1 = 0.6$ and $\sigma_2 = 0.2$

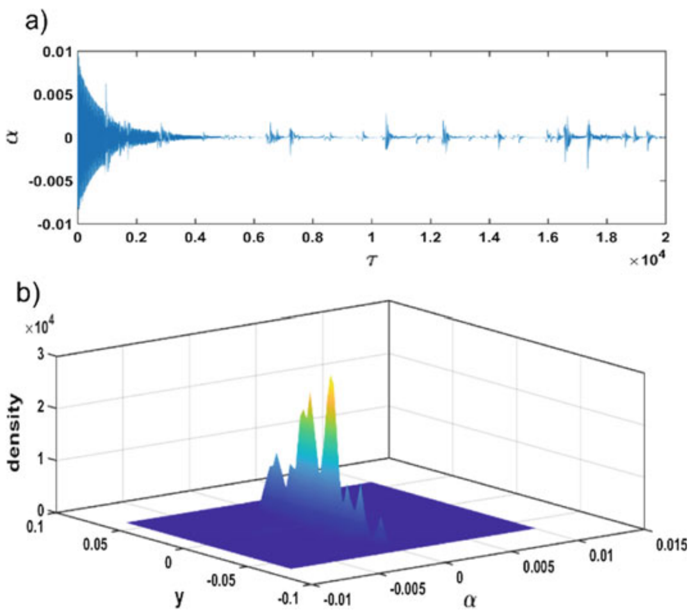

Fig. 7 **a** Pitch response and **b** J-PDF for $U_m = 3.5$ at $\sigma_1 = 0.1$ and $\sigma_2 = 0.1$

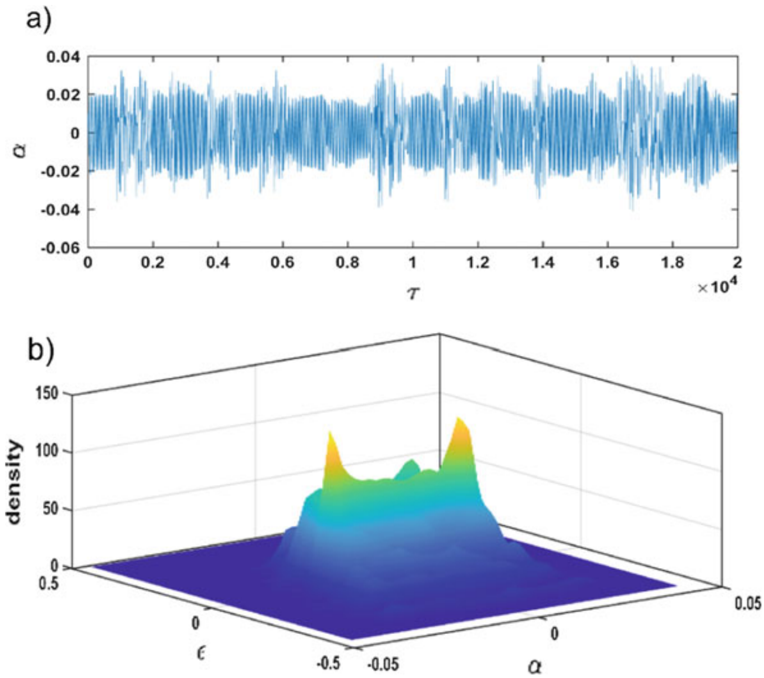

Fig. 8 **a** Pitch response and **b** J-PDF for $U_m = 8.5$ at $\sigma_1 = 0.3$ and $\sigma_2 = 0.1$

References

1. Lee B, Jiang L, Wong Y (1999) Flutter of an airfoil with a cubic restoring force. J Fluids Struct 13:75–101
2. Fung YC (1993) An introduction to the theory of aeroelasticity. Dover
3. Hoblit FM (1988) Gust loads on aircraft: concepts and applications. Am Inst Aeronaut Astronaut
4. Poirel D, Price SJ (2007) Bifurcation characteristics of a two-dimensional structurally non-linear airfoil in turbulent flow. Nonlin Dyn 48(4):423–435
5. Zhao D, Zhang Q, Tan Y (2009) Random flutter of a 2-DOF nonlinear airfoil in pitch and plunge with freeplay in pitch. Nonlin Dyn 58(4):643
6. Venkatramani J (2017) Intermittency in pitch-plunge aeroelastic system. Doctoral dissertation
7. Jones RT (1940) The unsteady lift of a wing of finite aspect ratio. NACA Reports 681

A Computational Study on the Effect of Supercritical CO_2 in a Combustor

Vishnumaya Nair and Selvaraj Prabhu

Abstract The ability of supercritical carbon dioxide (sCO_2) oxy-combustion power cycles like Allam cycle to capture 99% of the carbon produced in combustion started gaining attraction nowadays. The Allam cycle works at extreme pressure conditions (200–300 bar), and it substantially increases the efficiency. To promote and accelerate the growth and development of combustors for such cycles, a study on kinetic models using sCO_2 as diluent has to be conducted by exposing it to extreme operating conditions such as higher pressures (300 bar) and high inlet temperatures (1000 K) along with different levels of CO_2 dilution. The paper focuses on identifying the effect of supercritical CO_2 in a combustor where the fuel used is methane by analyzing its impact on parameters such as temperature and ignition delay time (IDT) for the CH_4–O_2–CO_2 mixture with variation in CO_2 dilution. The software ANSYS Chemkin-Pro is used for the initial simulations where two zero-dimensional models are analyzed with the above said conditions of pressure and temperature for various mixture ratios of CH_4–O_2–CO_2. Saudi Aramco 2.0 mechanism is used for Chemkin simulations. Finally, computational fluid dynamics (CFD) simulation of combustor is done in ANSYS Fluent by importing GRI-Mech 3.0 and the reduced Aramco 2.0 mechanisms and compared the results for different CO_2 dilutions.

Keywords Allam cycle · CFD · GRI-Mech 3.0 · Saudi Aramco 2.0

1 Introduction

Supercritical CO_2 (sCO_2) cycles make use of a combustor which burns fuel and pure oxidizer with the CO_2 acting as a diluent and temperature moderator. sCO_2 is used as the working fluid medium in supercritical carbon dioxide power cycle.

V. Nair · S. Prabhu (✉)
Department of Mechanical Engineering, Amrita School of Engineering, Amrita Vishwa Vidyapeetham, Coimbatore, India
e-mail: s_prabhu1@cb.amrita.edu

V. Nair
e-mail: vishnumayanair1995@gmail.com

E. T. Akinlabi et al. (eds.), *Trends in Mechanical and Biomedical Design*, Lecture Notes in Mechanical Engineering,
https://doi.org/10.1007/978-981-15-4488-0_33

Delimont et al. [1] have discussed the geometry and boundary conditions likely to be seen in an oxy-fuel combustor using sCO_2 which are specifically relevant to the upcoming 1 MWth combustor design and also the behavior of sCO_2 swirl-stabilized fuel injector is studied by analyzing the effect of various design variables such as geometry of the chamber, injection, cooling schemes and mainstream flow angle. As the growing demand for energy and the usage of fossil fuels alarm the world about the irreversible climatic change due to global warming, there must be an action taken in order to reduce and completely eliminate such critical situations, and one such initiative can be in the form of reducing emissions which can be accomplished with the support of supercritical CO_2 combustors as a result of which Manikantachari et al. [2] have performed detailed study on the reductions of mechanisms to be used for sCO_2 combustor simulations. Only very few data are available for combustors operating close to the Allam cycle conditions, which is currently the precursor for direct sCO_2 power cycles, and hence, Strakey [3] has attempted to study the turbulent length and time scales along with the turbulent flame speed with the help of CFD and simplified 0D and 1D flame calculations. Liu et al. [4] have done a comparison of auto-ignition delay measurement of CH_4–O_2–CO_2 from the shock tube with the numerical simulation. Full carbon capture together with the higher efficiencies is inevitable for the successful operation of the plant. Zhu [5] has described the innovative power generation systems using novel cycles like sCO_2 power cycles which have the potential for achieving the above said characteristics at lower costs and also help in providing alternative power generation systems. Zhu [5] has also discussed the turbomachinery, heat exchangers, combustors and materials to be used with the sCO_2 cycles.

The Allam cycle (high pressure, low pressure ratios, combustion of oxygen-fuel) is one such new sCO_2 cycle design including carbon capture and storage. It is a highly recuperated sCO_2 cycle with just a modest rise in the combustion engine temperature as described by Zhu [5]. In this process, two combustion products formed are, carbon dioxide and water, respectively, where an oxy-methane mixture is burned using carbon dioxide as a diluent, in a direct-fired combustion plant. A combustion operating pressure of 300 bar, an inlet temperature of 750 °C and an outlet temperature of 1150 °C are the nominal conditions as defined by the Allam cycle. Pryor et al. [6] have done the measurements of different ignition delay times and time histories of methane species for methane-O_2 mixtures at a high CO_2 diluted environment using shock tube and laser absorption spectroscopy at pressures between 6 and 31 atm. A supercritical fluid has some liquid as well as some gas properties. The validation of the chemical kinetic mechanism for supercritical CO_2 (sCO_2) oxy-methane combustion that can be used for computational fluid dynamic code (CFD) simulations in oxy-combustion development has been described by Vasuet al. [7]. Iwai et al. [8] have carried out a 3-D CFD simulation of the combustor internal flow field in order to obtain information on mixing of fuel oxidizer, position of the flame and heat transfer near the wall. Ratna Kishore et al. [9, 10] have done different studies on laminar burning velocities using different diluent concentrations. The CO_2 peculiarities are a relatively low critical pressure of 7.4 MPa and a critical temperature of 31 °C. As a result, CO_2 can be directly compressed to supercritical pressures and heated to supercritical conditions under moderate conditions. In its supercritical state, CO_2 is also approximately twice as dense as steam. The high density and volumetric heat capacity of sCO_2 make it more energy dense compared to other working fluids. A smaller plant footprint can therefore be achieved with the reduction in size of all components of the system such as the turbine and heat exchangers.

This research contributes to the growth and expansion of new technologies and methods that are cleaner and also more cost effective. The work is done with CO_2 as the primary diluent at higher pressures and temperatures which is not a much explored area. This research will validate the Aramco mechanism for supercritical conditions and extend the work for the combustor analysis.

1.1 Chemical Kinetic Mechanisms

The precise modeling of combustion processes requires a chemical kinetic mechanism that is valid for the range of conditions under study. The mechanism considered for this simulation is GRI-Mech Version 3.0 with 53 chemical species and 325 reactions [11], which is used for modeling the natural gas combustion. A more recently developed mechanism, referred to as Saudi Aramco 2.0, has also been considered for the methane–air combustion mechanism. Saudi Aramco 2.0 mechanism consists of 493 species and 2714 reactions that can be used for fuel up to six carbon components. The above mentioned mechanism can be used for natural gas combustion.

ANSYS Chemkin-Pro. Chemkin-Pro is used in modeling as well as simulating complex gas phase and surface chemistry reactions and has been used for doing the constant volume combustor and perfectly stirred reactor (PSR) simulations in order to understand the changes in ignition delay time and combustion temperature with CO_2 dilution in CH_4–O_2 mixture at elevated temperatures and pressures. The variations in IDTs and combustion temperatures are also noted with N_2 as the diluent. The Aramco 2.0 mechanism is one of the most accurate mechanisms, and the validation against a large array of experimental analysis has been performed for this mechanism, and hence, it is employed for simulating the combustor with CH_4–O_2–CO_2 mixture at different mixture ratios.

2 Constant Volume Reactor

The mixture of all gas particles are assumed to be uniform and homogeneously mixed inside the constant volume reactors. A closed 0-D constant volume batch reactor and perfectly stirred reactor are used for the analysis. The ignition delay times of a CH_4–O_2 fuel mixture at high initial pressure for a series of initial temperatures can be predicted using the 0-D closed reactor model. At the time of ignition, a pronounced spike can be observed in the OH mole fraction. As a result, OH spikes and the maximum temperature change rate (inflection point) determine the time for

Table 1 Effects of EOS on the IDTs at $T = 1000$ K and $P = 300$ atm

Equation of state (EOS)	Ignition delay time, IDT (μs)	
	CH_4–O_2–CO_2 = 7.5–15–77.5	H_2–O_2–CO_2 = 10–5–85
Redlich–Kwong (RK)	130	155
Soave–Redlich–Kwong (SRK)	136	216
Peng–Robinson (PR)	132	183

the ignition. The equation of state (EOS), EOS_SRK, that is, Soave–Redlich–Kwong EOS incorporated in the mechanism will be used in the simulations to determine the P-T-V relationship of the gas mixture.

2.1 Chemkin Results

The simulations are carried out to understand the influence of EOS, Redlich–Kwong (RK), Soave–Redlich–Kwong (SRK), Peng–Robinson (PR) in the methane and hydrogen mixtures. Table 1 makes it clear that the impact of EOS on CH_4–O_2–CO_2 is insignificant while affecting the IDTs of the H_2–O_2–CO_2 mixture. A significant effect of the EOS can be observed on the H_2 mixture but not on the CH_4 mixture. H_2O is the main combustion product of the H_2 mixture, while it is both CO_2 and H_2O for the CH_4 mixture.

The critical CO_2 pressure is approximately 73 atm, while the H_2O pressure is approximately 218 atm, which is about three times higher than the CO_2 pressure. The higher amount of H_2O in the H_2 mixture combustion product therefore increases the resulting critical point of the mixture. Near the critical point, the EOSs largely differ. The overall critical point is further reduced with the formation of CO_2 in the case of the CH_4 mixture, which results in a smaller deviation of the EOSs. An ideal gas behavior is exhibited by the real gases at elevated temperatures and pressures far beyond the critical point since the compressibility factor is closer to unity at high operating conditions.

A clear indication of the reduction in the ignition delay time with temperature can be observed. Figure 1 shows the variation of ignition delay time with the inverse of the temperature, hence showing an increment in ignition delay time. Two main kinetic mechanisms used for the combustion of natural gas are considered here, the GRI-Mech 3.0 and the recent Aramco-2.0. Figure 1 shows the difference in the predictions of ignition delay times between the GRI-3.0 mechanism and the Aramco-2.0 at a higher pressure level (300 atm). The GRI-Mech forecasts a higher IDT value than the Aramco 2.0 mechanism for the CH_4–O_2–CO_2 = 7.5–15–77.5 mixture at P = 300 atm and temperature T between 1000 and 1080 K.

From Fig. 2, it is understood that the mixture with the higher dilution of CO_2 is having a larger value for ignition delay time. Ignition delay generally decreases with increasing preheat temperature as shown in Figs. 2 and 3 which show a comparison

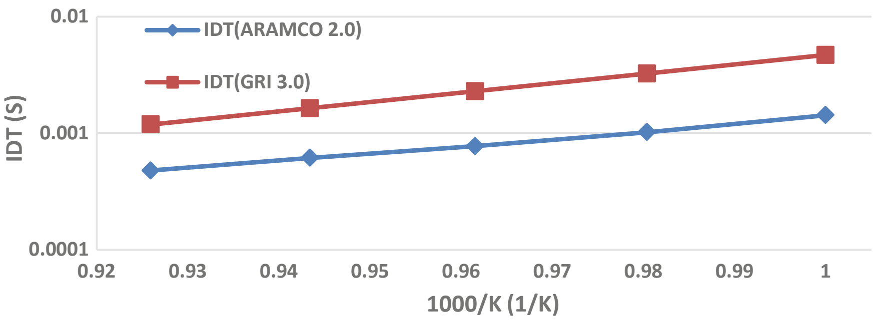

Fig. 1 Comparison of GRI-Mech 3.0 and Aramco 2.0 mechanisms for the mixture CH_4–O_2–CO_2 = 7.5–15–77.5

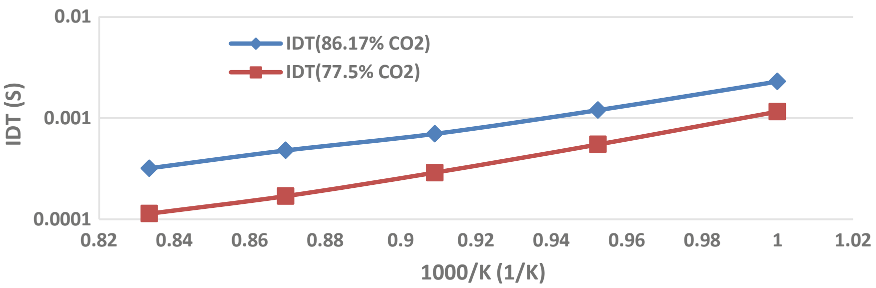

Fig. 2 Comparison of IDTs for the mixtures CH_4–O_2–CO_2 = 3.91–9.92–86.17 and CH_4–O_2–CO_2 = 7.5–15–77.5

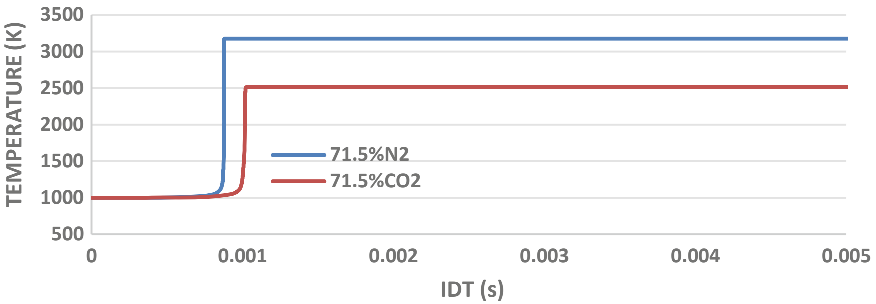

Fig. 3 Temperature rise for 71.5% N_2 and CO_2 diluted mixtures

of ignition delay times for stoichiometric methane–oxygen combustion at different concentrations of CO_2. These calculations are carried out using the Saudi Aramco 2.0 mechanism, which has been validated at a much higher pressure than the GRI 3.0.

Figure 3 represents the comparison of the temperature rise in the stoichiometric CH_4–O_2 mixture at 71.5% CO_2 and N_2 dilution levels at 1000 K for the mixture 3 as indicated in Table 2. The figure clearly demonstrates the difference in temperatures when diluted with CO_2 and N_2. The temperature increase due to combustion process with N_2 as the diluent is more when compared to CO_2 diluted combustion. The maximum temperature attained for those mixtures diluted with CO_2 is around 2500 K and the mixtures diluted with N_2 is around 3100 K. Hence, it shows that CO_2 has the ability to withstand more temperature than N_2. The temperature inflection point as seen in the figure is somewhat delayed in the case of CO_2 diluted combustion as a result of which ignition is delayed in CO_2 diluted combustion as compared to N_2 diluted combustion process.

Figure 4 shows that the increment in IDT is comparatively high with CO_2 dilution compared to that with nitrogen as the diluent. Carbon dioxide slows the ignition process slightly more.

From Table 3, it is evident that as the temperature increases, the ignition delay time reduces as a result of the increased reactivity of the mixtures. The IDTs of the mixture for various N_2 and CO_2 dilutions have been calculated. The mole fractions of CH_4 and O_2 in the simulations are taken to be $X_{CH_4} = 0.095$ and $X_{O_2} = 0.19$. The EOS SRK is used for the simulations.

Table 2 Stoichiometric CH_4–O_2 mixture at various CO_2 dilution levels

Mixtures	Mole fractions		
	X_{CH_4}	X_{O2}	X_{CO_2}/X_{N_2}
1	0.161	0.322	0.517
2	0.134	0.268	0.598
3	0.095	0.19	0.715
4	0.056	0.112	0.832

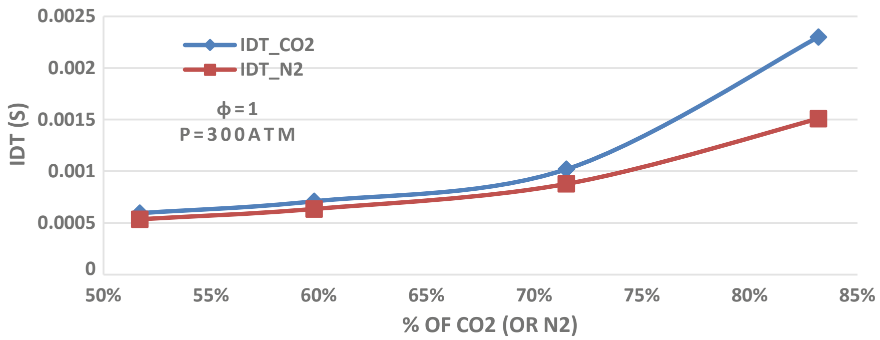

Fig. 4 Comparison of IDTs at different CO_2/N_2 dilution levels for the stoichiometric mixtures

Table 3 Ignition delay time simulation for various N_2 and CO_2 dilutions at $P = 300$ atm

T (K)	X_{N_2}	X_{CO_2}	IDT (μs)
1000	0.715	0	878
1050			407
1000	0.465	0.25	913
1050			434
1000	0.215	0.5	979
1050			459

PSR. Continuously stirred tank reactor (CSTR) is often referred to as a PSR or perfectly stirred reactor in the literature on chemical engineering. This type of simulation, a gas turbine combustion tool since the 1950s, is a zero-dimensional one. Primary combustion zone can be simulated using this. The reactor inlet temperature chosen for simulations is 1000 K, while the pressure is 300 atm. Using a PSR model in Chemkin-Pro, various possible CO_2 dilution levels for stoichiometric methane–oxygen mixture in the primary zone are simulated. In the mechanism, SRK EOS is considered for simulation. 1000 K and 300 atm are the inlet temperature of the reactor and the pressure taken into consideration. Figure 5 indicates the reduction in the exit temperature with increase in CO_2 dilution levels.

Mechanism reduction. The powerful tools for the numerical simulation in order to study complex turbulent reacting flows are the detailed mechanisms. The reduction of such mechanisms is a necessary step because of the huge computational cost and time associated with the detailed one. Here, direct relation graph (DRG) with error propagation (DRGEP) method is used to reduce detailed Aramco mechanism for importing it in ANSYS Fluent. Using this method, a skeletal mechanism with 56 species is generated for 1000 K and 300 bar from the detailed one consisting of 493 species.

The reduced 56 species Aramco mechanism is compared with the detailed mechanism, and the reduced mechanism is in good agreement with the detailed as shown

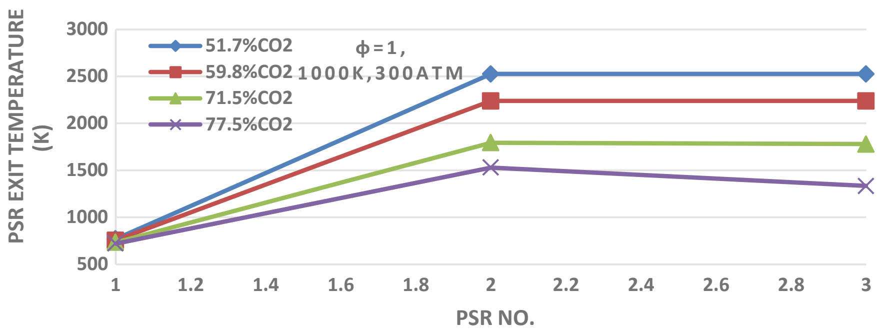

Fig. 5 Comparison of the exit temperature of a PSR at various CO_2 dilution levels

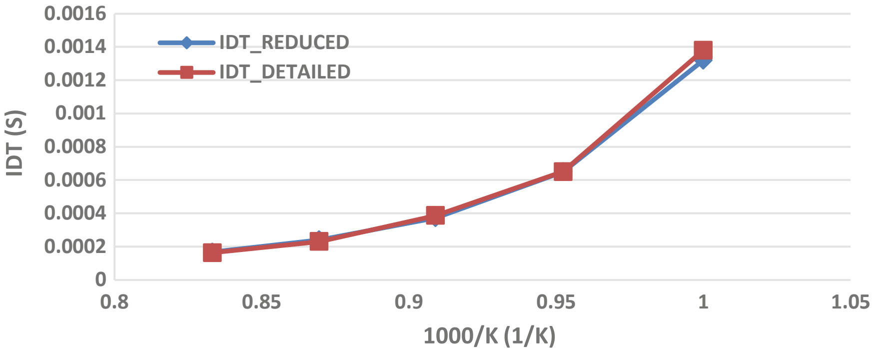

Fig. 6 Comparison of IDTs obtained by detailed Aramco 2.0 with the reduced mechanism

in Fig. 6. Hence, the reduced mechanism can be imported to fluent for carrying out the simulations without much computational time and cost.

3 CFD Solver Setting

A simple 2-D combustor is modeled in modeled and mesh independent study is completed. Boundary conditions include CH_4 and O_2 /CO_2 at the inlet and an outlet pressure condition as shown in Fig. 7.

The meshing operation is performed by means of edge sizing by choosing the uniform size function, and face sizing is done with quadrilaterals as the geometry is not a complicated one. The total number of nodes obtained with this mesh setting is 12,261 while that of elements is 12,000, and default value has been chosen for the growth rate and is kept as 1.2, and the growth rate represents how the cell volumes grow gradually for capturing the flow physics. The standard *k*-epsilon model, one of the most efficient models, has been used for the turbulent flow. The eddy dissipation

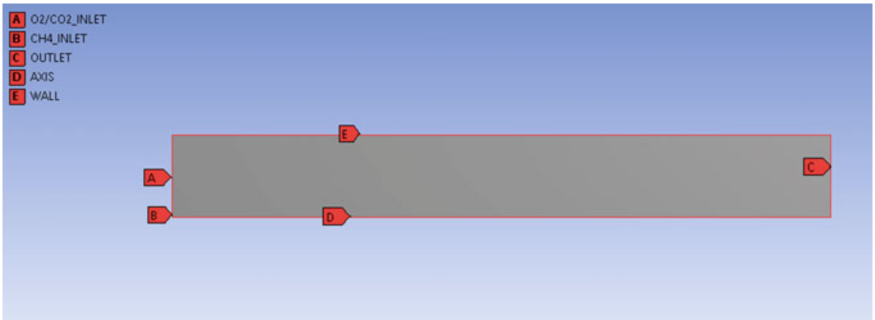

Fig. 7 A 2-D combustor model

concept is chosen for the turbulence chemistry interaction along with the Chemkin CFD solver in the species transport model. The SIMPLE scheme is used along with standard hybridization. The simulations are carried out at the boundaries conditions as follows: pressure = 300 bar, O_2/CO_2 inlet temperature = 1000 K, CH_4 inlet temperature = 320 K, respectively. The equations for the viscous fluid flow are as follows:

$$\frac{\partial \rho}{\partial t} + \nabla \cdot (\rho V) = 0 \tag{1}$$

$$\frac{\partial (\rho V)}{\partial t} + \nabla \cdot (\rho V V) = \rho f + \nabla \cdot \tau_{ij} - \nabla p \tag{2}$$

$$\begin{aligned} \frac{\partial}{\partial t}\left[\rho\left(e + \frac{V^2}{2}\right)\right] + \nabla \cdot \left[\rho\left(e + \frac{V^2}{2}\right)V\right] &= \rho \dot{q} + \nabla(K \nabla T) \\ - p \nabla V + \rho f \cdot V + \varphi \end{aligned} \tag{3}$$

$$\frac{\partial}{\partial t}(\rho Y_i) + \nabla \cdot (\rho \vec{v} Y_i) = -\nabla \cdot \vec{J_i} + R_i + S_i \tag{4}$$

The above Eqs. (1)–(4) are known as the continuity, momentum, energy and species transport equations, while the equations corresponding to the standard *k*-ε model are as follows;

$$\frac{\partial (\rho k)}{\partial t} + \frac{\partial (\rho k u_i)}{\partial x_i} = \frac{\partial}{\partial x_j}\left[\frac{\mu_t}{\rho_k}\frac{\partial k}{\partial x_j}\right] + 2\mu_t E_{ij} E_{ij} - \rho \varepsilon \tag{5}$$

$$\frac{\partial (\rho \varepsilon)}{\partial t} + \frac{\partial (\rho \varepsilon u_i)}{\partial x_i} = \frac{\partial}{\partial x_j}\left[\frac{\mu_t}{\rho_k}\frac{\partial \varepsilon}{\partial x_j}\right] + C_{1\varepsilon}\frac{\varepsilon}{k} 2\mu_t E_{ij} E_{ij} - C_{2\varepsilon} \rho \frac{\varepsilon^2}{k} \tag{6}$$

where (5) and (6) are the equations for turbulent kinetic energy k and dissipation ε.

4 Results

By importing the GRI-Mech 3.0 and reduced 56 species Aramco 2.0 mechanisms, the temperatures for the cases with 50%, 60%, 70% and 80% CO_2 dilution are compared. Both mechanisms predicted similar results, and the temperature values for 50%, 60%, 70% and 80% CO_2 dilutions are 2680 K, 2540 K, 2320 K and 1910 K, respectively, as shown in Figs. 8, 9, 10 and 11. The observations clearly indicate a temperature reduction of 5.22%, 13.4%, 28.73% for 60%, 70% and 80% CO_2 dilutions with respect to 50% dilution. This reduction in temperatures is mainly due to the fact that CO_2 has the ability to withstand more temperature, and it facilitates combustion in such a way that it takes place in a mild manner. The increment in CO_2 concentration reduces the concentration of the reactants and has the power to lower the net reaction

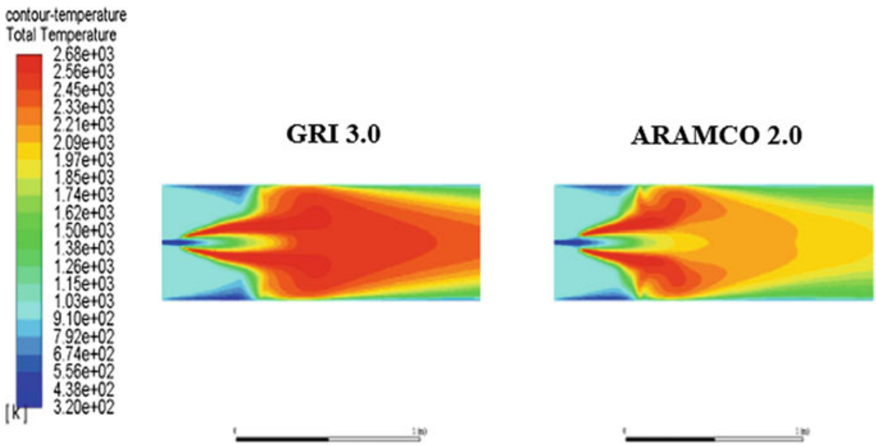

Fig. 8 Temperature contours for 50% CO_2 dilution using GRI 3.0 and reduced Aramco 2.0 mechanisms

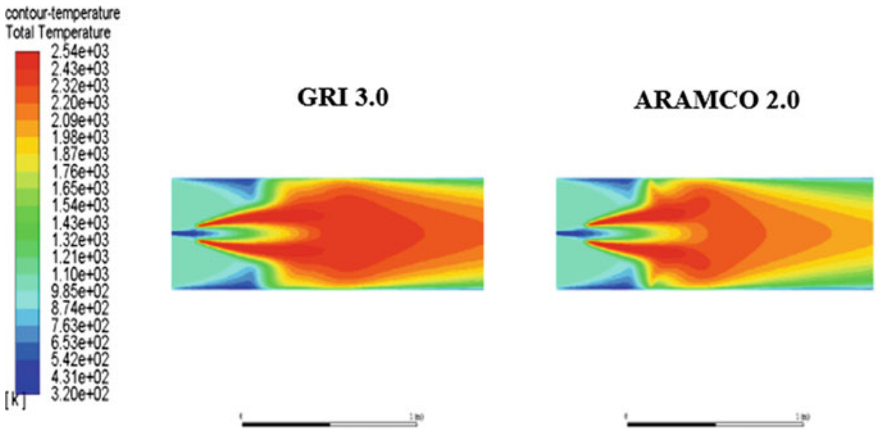

Fig. 9 Temperature contours for 60% CO_2 dilution using GRI 3.0 and reduced Aramco 2.0 mechanisms

rate. This ability of CO_2 dilution to reduce temperature is more as compared to other diluents such as nitrogen and has been proved from the Chemkin results as shown in Fig. 3. Moreover, CO_2 acts as a heat sink which gives rise to reduction in reaction temperature.

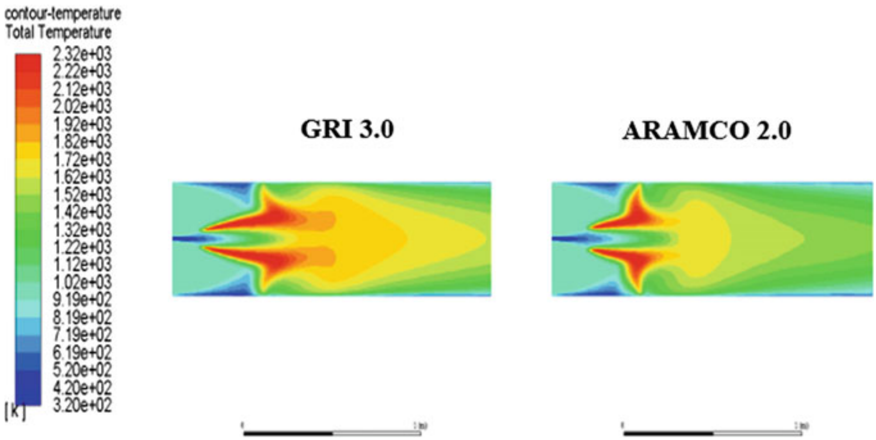

Fig. 10 Temperature contours for 70% CO_2 dilution using GRI 3.0 and reduced Aramco 2.0 mechanisms

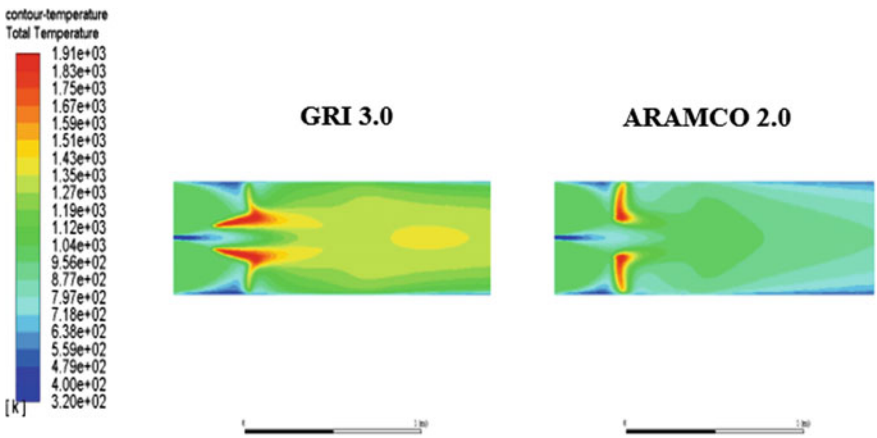

Fig. 11 Temperature contours for 80% CO_2 dilution using GRI 3.0 and reduced Aramco 2.0 mechanisms

5 Conclusion and Future Work

In this paper, the effect of CO_2 dilution on methane combustion is found out by means of Chemkin simulations where various equations of states are used to determine the ignition delay times including comparisons conducted between the detailed Saudi Aramco 2.0 and GRI-Mech 3.0 mechanisms. The GRI-Mech 3.0 overpredicts the ignition delay time in comparison with the Saudi Aramco 2.0 mechanism at higher pressures. Saudi Aramco 2.0 mechanism is found be a more accurate one for the combustion of sCO_2. The ignition delay times of supercritical oxy-methane-CO_2

mixtures is less influenced by the equation of state (EOS) in contrast to that of the supercritical oxy-hydrogen-CO_2 mixture.

The ignition delay time data have been found out at higher pressures and temperatures (1000–1200 K) for the oxy-fuel combustion at different carbon dioxide dilution levels. Chemkin simulations show that as temperature is made to increase, the ignition delay times are decreased, whereas ignition is delayed as CO_2 dilution is increased. Compared to the IDTs with N_2 dilution, CO_2 dilution has been found to result in more increment of ignition delay times. This delayed ignition is mainly caused by the chemical effect of CO_2. A substantial reduction in the temperature can be observed with CO_2 dilution. It retards the ignition and slows the overall response rate, making it easier for moderate or intense low-oxygen dilution combustion to occur. The reduction in temperature is due to the physical effect of the CO_2 dilution. In addition to the kinetic effects, flow effects are also considered in CFD analysis. The reduced Aramco 2.0 mechanism is used in the simulations, and the results are compared with GRI 3.0 mechanism. The change in the peak temperature with different dilution limits of CO_2 is observed at high pressure conditions.

Further to understand the effect of supercritical conditions, a detailed investigation of combustion of methane with large amounts of CO_2 dilution has to be conducted. Future work would include the 3-D simulation of a more refined model of combustor by incorporating the real gas models at supercritical conditions.

References

1. Delimont J, Andrews N, Chordia L (2018) Exploration of combustor design for direct fired oxy-fuel application in a sCO_2 power cycle. In: Proceedings of Montreal, Global Power and Propulsion Forum, GPPS-NA-2018-0157
2. Manikantachari KRV, Vesely L, Martin S, Bobren-Diaz JO, Vasu S (2018) Reduced chemical mechanisms for oxy/methane supercritical CO_2 combustor simulations. J Energy Resour Technol 140/092202-1
3. Strakey PA (2018) Oxy-combustion flame fundamentals for supercritical CO_2 power cycles. In: The 6th international supercritical CO_2 power cycles symposium, Pittsburgh, Pennsylvania
4. Liu Z, Gao X, Karimi M, Ochs B, Acharya V, Sun W, Delimont J, Andrews N (2018) Simulation of sCO_2 oxy-combustion using reduced chemical kinetic mechanism: effects of reduced mechanism and sensitivity to mechanism parameters. In: The 6th international supercritical CO_2 power cycles symposium, Pittsburgh, Pennsylvania
5. Zhu Q (2017) Innovative power generation systems using supercritical CO_2 cycles. Clean Energy 1(1):68–79
6. Pryor O, Barak S, Lopez J, Ninnemann E, Koroglu B, Nash L, Vasu S (2017) High pressure shock tube ignition delay time measurements during oxy-methane combustion with high levels of CO_2 dilution. J Energy Resour Technol
7. Vasu SS, Pryor OM, Kapat JS, Masunov A, Martin SM (2016) Developing a validated chemical kinetics model for sCO_2 combustion and implementation. In: The 5th international symposium—supercritical CO_2 power cycles, San Antonio, Texas
8. Iwani Y, Itoh M, Morisawa Y, Suzuki S, Cusano D, Harris M (2015) Development approach to the combustor of gas turbine for oxyfuel, supercritical cycle. In: Proceedings of ASME Turbo Expo, turbine technical conference and exposition, Montréal, Canada, GT2015

9. Ratna Kishore V, Ravi MR, Ray A (2011) Adiabatic burning velocity and cellular flame characteristics of H_2-O_2-CO_2-air mixtures. Combust Flame 158
10. Ratna Kishore V, Muchahary R, Ray A, Ravi MR (2009) Adiabatic burning velocity of H_2-O_2 mixtures diluted with CO_2/N_2/Ar. Int J Hydrogen Energy 34
11. GRI-Mech homepage, Gas Research Institute, Chicago (1999). www.me.berkeley.edu/gri_mech/

Design of Shell-and-Tube Heat Exchanger with CFD Analysis

B. Jayachandraiah and C. Dinesh Kumar Patel

Abstract Heat exchanger is a device used to transfer heat between two fluids which are at different temperatures. An attempt is made in this paper. A shell-and-tube heat exchanger (STHE) is modeled by using CATIA V5 R20 software with TEMA standards. Meshing and analysis are done by using Autodesk CFD Simulation commercial software. The STHE is considered for two different fluids of kerosene and crude oil with inlet temperature and inlet velocity of fluids as boundary conditions. The results obtained are contours of velocity magnitude, temperature distribution and pressure drop of the fluid. Then, results are plotted for the temperature distribution, pressure drop and fluid velocity profiles. The simulation results are compared with the analytical results and find good agreement with the analytical results.

Keywords STHE · CFD · Simulation

1 Introduction

Heat exchanger is a device specially designed for efficient transformation of heat from one fluid to another fluid over solid surface. In heat exchangers, the temperature of each fluid changes as it passes through the exchangers, and hence, the temperature of dividing wall between the fluids also changes along the length of Exchanger.

The most widely applied heat exchangers are those constructed of a "shell" which contains one of the fluids as well as the "tubes" which contain the other fluid. The shell-and-tube-type heat exchanger allows a great deal of flexibility in design applications and as a result is frequently found in heavy-duty applications (Fig. 1).

B. Jayachandraiah (✉) · C. Dinesh Kumar Patel
SKIT, Srikalahasti, India
e-mail: bjcskit2011@gmail.com

E. T. Akinlabi et al. (eds.), *Trends in Mechanical and Biomedical Design*, Lecture Notes in Mechanical Engineering,
https://doi.org/10.1007/978-981-15-4488-0_34

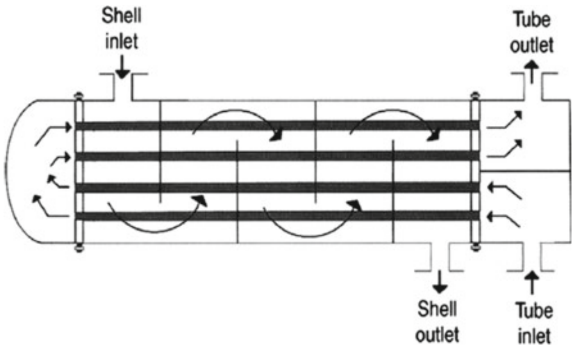

Fig. 1 Double-pass shell-and-tube heat exchanger

2 Literature Survey

Caputo et al. [1] have done a procedure for optimal design of shell-and-tube heat exchangers, which utilizes a genetic algorithm to minimize the total cost of the equipment including capital investment and the sum of discounted annual energy expenditures related to pumping. Ebieto and Eke [2] have done the performance of shell-and-tube heat exchangers by analytical method, and the program was written in MATLAB to check for the thermal and hydraulics suitability of the heat exchangers. Chit et al. [3] have done the flow analysis in shell side on the effect of baffle spacing of shell-and-tube heat exchanger which has been studied using theoretical and numerical methods. The shell-side pressure drop for acceptable limits is 0.3 bars for shell-and-tube heat exchanger of oil cooler of locomotive. Pavani Nookaratnam and Dharma Raju [4] have studied material properties of various nanofluids that are calculated at different volume fractions and compared. Performance of these nanofluids is evaluated using computational fluid dynamics with the help of ANSYS Fluent module. Irshad et al. [5] have done analyses on the performance of shell-and-tube heat exchanger by comparing several shell-and-tube heat exchangers with segmental baffles. Mukadam et al. [6] have studied the performance of the shell-and-tube heat exchanger and the effect of various parameters such as pitch layout and baffle spacing.

2.1 Objective

An attempt is made in this paper to do the design of shell-and-tube heat exchanger by modeling in CATIA V5 R20 and meshed using Autodesk meshing software. The analysis is done by Autodesk CFD 2015 software by using computational fluid dynamics (CFD) and to find the various contours of temperature, pressure and velocity across the double-pass shell-and-tube heat exchanger by evaluating the performance of heat exchanger.

Table 1 Design parameters for heat exchanger

S. No.	Description	Unit	Value
1	Heat exchanger length (L)	mm	1000
2	Shell inner diameter (D_i)	mm	100
3	Shell outer diameter (d_o)	mm	106
4	Tube length (l)	mm	1000
6	Tube outer diameter (d_o)	mm	19.06
7	Number of tubes (N_t)	–	5
8	Tube pitch triangular (P_t)	mm	25
9	Baffle cut portion	%	25
10	Baffle spacing (B)	mm	85
11	Side plate diameter (D_{sp})	mm	100
12	Side plate thickness (T_{sp})	mm	3
13	Baffle thickness (Δ_{BT})	mm	3

3 Materials and Methods

3.1 *Materials*

The material used for shell is stainless steel (304), for tubes is copper and for baffles and tube sheet is copper.

3.2 *Design Parameters*

Design parameters considered for design of heat exchanger are shown in Table 1.

3.3 *Fluid Properties for Kerosene and Crude Oil*

The properties of kerosene and crude oil are shown in Table 2.

3.4 *Boundary Conditions*

Inlet temperature of the hot fluid at shell side: 950 °C
Inlet temperature of the cold fluid at the tube side: 250 °C
Mass flow rate at shell side: 10 kg/s
Mass flow rate at tube side: 18.8 kg/s

Table 2 Properties of kerosene and crude oil

	Mass flow (kg/s)	T input (°C)	ρ (kg/m^3)	C_p (kJ/kg K)	μ (Pa s)	k (W/mK)	R_f (m^2 K/W)
Shell side: kerosene	10	95	850	2.47	0.00040	0.13	0.00061
Tube side: crude oil	18.8	25	995	2.05	0.00358	0.13	0.00061

Outlet pressure at the shell side: zero gauge pressure
Outlet pressure at the tube side: zero gauge pressure.

3.5 Mathematical Analysis

Maximum heat transfer $Q_{max} = C_{min} (T_{hi} - T_{ci}) = 17{,}29{,}000$ W
Heat transfer area $(A) = L*\Pi*\text{do}*\text{Nt} = 0.598473\ \text{m}^2$.

3.5.1 Tube-Side Calculations

Tube velocity $(v_t) = 19.401$ m/s
Reynolds number $(\text{Re}_t) = 84{,}911$
Prandtl number (Pr) = 56.4538
Convective heat transfer coefficient $(h_t) = 7528\ \text{W/m}^2\text{K}$.

3.5.2 Shell-Side Calculations

Equivalent diameter $(d_e) = 0.0169$ m
Area of shell $(A_s) = 0.0020\ \text{m}^2$
Shell velocity $(v_s) = 5.882$ m/s
Reynolds number (Res) = 21,123.7
Prandtl number Prs = 7.6
Convective heat transfer coefficient $(h_s) = 4687.549\ \text{w/m}^2\text{K}$
Overall heat transfer coefficient $U = 581.621\ \text{W/m}^2\text{K}$
$\text{NTU} = (\text{UA})/C_{min} = 0.01409$
Effectiveness $\varepsilon = 0.5497 = 54.97\%$
Actual heat transfer $= Q_{act} = \varepsilon * Q_{max} = 949{,}221$ W
$Q = 24{,}700(95 - T_{ho})$
$T_{ho} = 56.57\ °\text{C}$

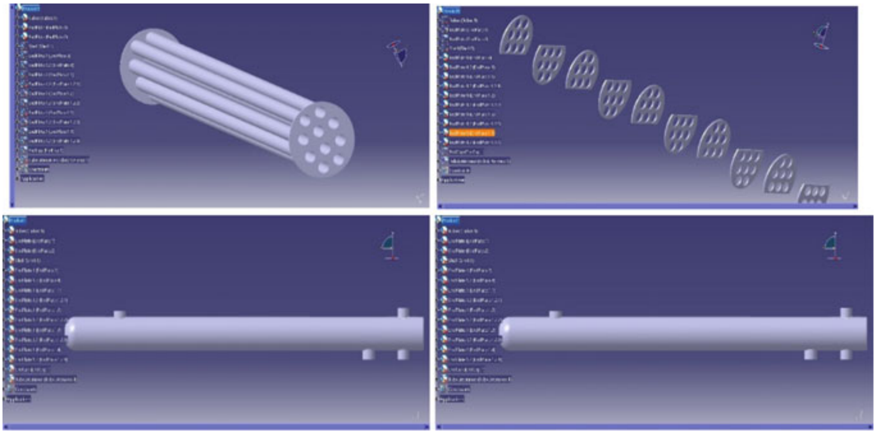

Fig. 2 Design and meshing

$$Q = 38{,}540(T_{co} - 25)$$
$$T_{co} = 49.62\ °\text{C}.$$

4 Modeling and Meshing

Computer-Aided Three-Dimensional Interactive Application (CATIA V5) was developed by Dassault systems from France which is used for the modeling of the heat exchanger. The model is imported to the Autodesk Simulation CFD and filled the fluid volume. Prior to running an Autodesk Simulation CFD analysis, the geometry is broken up into small pieces called elements. The corner of each element is a node. The calculation is performed at the nodes. These elements and nodes make up the mesh. The model and meshing of shell, tubes and baffles are shown in Fig. 2.

5 Results and Discussion

Temperature distribution of shell, tube and baffles is shown in Fig. 3. The temperature at the inlet of shell-side hot fluid is higher at the entrance and up to 5 and gradually losses its heat to the cold fluid.

The movement of fluid in the form of traces is shown in Fig. 4. The fluid movement trace for the shell side is one pass and for the tube is two passes. The wireframe for the temperature distribution is maximum at shell inlet is 95 °C.

Figure 5 shows the temperature distribution at each baffle. The baffle near to the

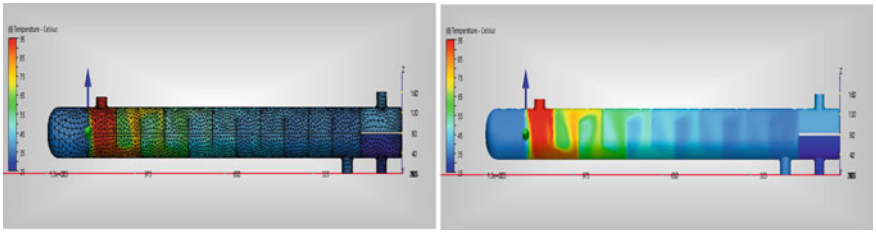

Fig. 3 Temperature distribution of fluids

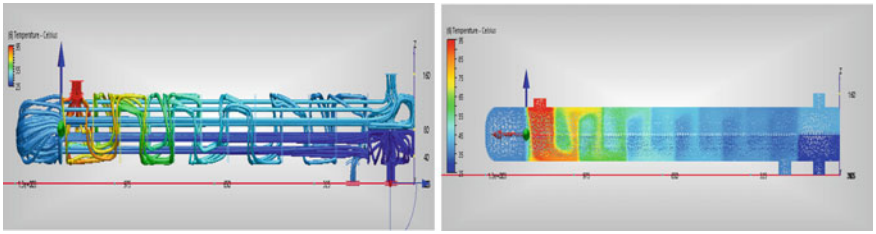

Fig. 4 Trace lines for temperature distribution

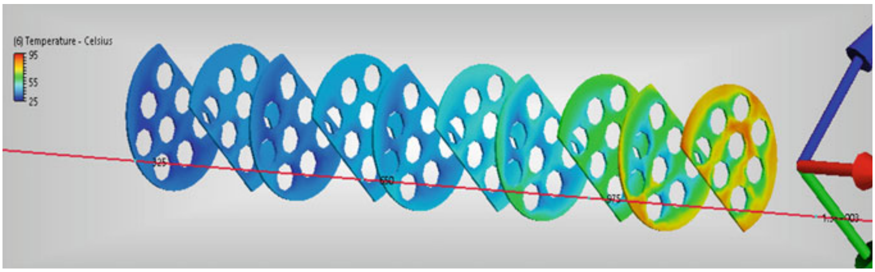

Fig. 5 Temperature distribution in baffles

shell-side fluid entrance got more heat and next to the first baffle also got some high temperatures.

Figure 6 shows velocity and pressure distribution in shell and tube. Throughout the shell, the velocity distribution is constant as 5.882 m/s and in the tube is also constant as 19.401 m/s. The pressure drop in the shell is 818,462.0 N/m^2 and at the tube is 1,417,310.0 N/m^2.

Graph 1 shows there is a continuous decrease in the shell-side fluid temperature. The cold water temperature gradually increased up to 76 °C in the first tube pass and decreased to the 47.45 °C in the second pass.

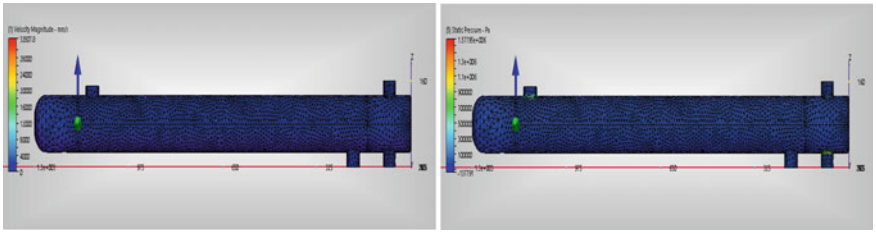

Fig. 6 Velocity and pressure distribution in shell and tube

Graph 1 Temperature distribution of kerosene and crude oil

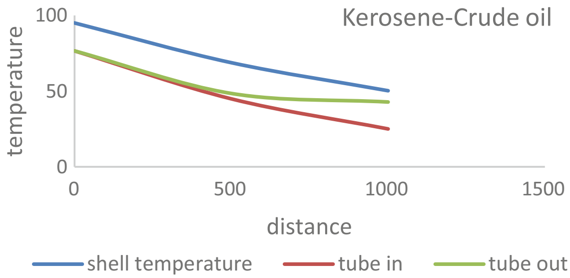

6 Conclusion

A novel shell-and-tube heat exchanger is designed in CATIA V5 and analyzed using Autodesk Simulation CFD 2015. The elements are 380,540, and the nodes obtained are 152,444. Standard heat exchanger design procedure is considered for the mathematical calculations. The outer temperature of the shell-side fluid is 56.57 °C which is approximately equal to the simulation results. The outer temperature of the tube-side fluid is 49.62 °C which is also nearly equal to the simulation result. Graphs show the clear temperature distribution in the shell-and-tube heat exchanger for the given geometry, and the compared theoretical results show good agreement with each other.

References

1. Caputo AC, Pelagagge PM, Salini P (2008) Heat exchanger design based on economic optimization. Appl Therm Eng 28:1151–1159
2. Ebieto CE, Eke GB (2012) Performance analysis of shell and tube heat exchangers: a case study. J Emerg Trends Eng Appl Sci 3(5):899–903
3. Chit SP, San NA, Soe MM (2015) Flow analysis in shell side on the effect of baffle spacing of shell and tube heat exchanger. Int J Sci Technol Soc 3(5):254–259
4. Pavani Nookaratnam D, Dharma Raju T (2017) Analysis of shell and tube heat exchanger using different nano fluids. Int J Res Appl Sci Eng Technol (IJRASET), 2321–9653

5. Irshad M, Kaushar M, Rajmohan G (2017) Design and CFD analysis of shell and tube heat exchanger. Int J Eng Sci Comput, 6453–6457
6. Mukadam SS, Naik OV, Naik PS, Naik PP, Yekane AS (2018) Temperature analysis of shell and tube heat exchanger. Int Res J Eng Technol (IRJET), 3264–3269

Characterization of Rayleigh–Taylor Instability at the Fluid–Fluid Interface

Nihal Raj and S. Karthick

Abstract Two fluids of different densities superposed one over the other or accelerated toward each other develop instability at the plane interface between the two fluids. This instability known as Rayleigh–Taylor instability (R-T) plays an integral role in fluid atomization, metal liner electromagnetic implosion, inertial confinement fusion, plasma fusion reactors and deuterium–tritium fusion target laser implosion. In the secondary stages of atomization, R-T instability dictates the quality of spray influencing the performance of engines. The objective of this study is to characterize the interfacial instability at the fluid–fluid interface based on growth rate and the wavenumber of the disturbances generated at the interface. The stability of the fluid–fluid interface under the influence of inertial, surface tensional and rotational forces has been investigated. The test fluids taken for this study include standard fluids, namely water and air, forming interfaces with commercially used fluids, namely nitromethane, ethylene glycol, gasoline and diesel. An attempt has been made to understand the factors contributing to instability of the fluid–fluid interface assumed to be inviscid based on the growth rate and critical wavenumber of the generated disturbances.

Keywords Rayleigh–Taylor instability · Interfacial instability · Critical wavenumber

1 Introduction

Instability of fluids indicates the property of not being stable, balanced or predictable. A simple example can be a ball on top of the hill; if given a small push, the ball will

N. Raj
Student, Department of Mechanical Engineering, Amrita School of Engineering, Coimbatore, Amrita Vishwa Vidyapeetham, Coimbatore 641112, India

S. Karthick (✉)
Faculty, Department of Mechanical Engineering, Amrita School of Engineering, Coimbatore, Amrita Vishwa Vidyapeetham, Coimbatore 641112, India
e-mail: s_karthick@cb.amrita.edu

E. T. Akinlabi et al. (eds.), *Trends in Mechanical and Biomedical Design*, Lecture Notes in Mechanical Engineering,
https://doi.org/10.1007/978-981-15-4488-0_35

go and continue to go down the hill while gaining speed in the process. The ball that finally reaches downhill oscillates about its initial position until friction brings it to rest. In addition, when a spherical balloon is filled with gas which is heavier than air normally carbon dioxide, the balloon will tend to go down; on the contrary, the balloon filled with helium will rise. Similarly, fluid instability in the form of Rayleigh–Taylor occurs in liquids, gases and plasma. Rayleigh–Taylor instability (RTI) results when two fluids of different densities are superposed or accelerated toward each other. For example, water over oil in a container, denser water pushes the oil up and develops an unstable condition resulting in RTI. This instability has been observed during secondary atomization, a critical event that decides the atomization process in combustion, spray drying and coating, drug delivery and evaporation-based heat exchangers.

When the heavier fluid is displaced downward with an equal volume of lighter fluid displacing upward, the potential energy of the fluid system is lower than the initial state [1]. This results in the development of the perturbation at the interface due to the established instability and subsequently results in the further release of potential energy. In addition, under the influence of gravitational field, the heavier fluid gets displaced downwards and the lighter fluid displaced upwards as observed by Lord Rayleigh [1]. Taylor [2] realized that the fluid system of Lord Rayleigh corresponding to the state of fluids accelerating to each other with the less dense fluid accelerating into the denser fluid [2, 3]. Rayleigh–Taylor instability under different effects has been explained in detail, Chandrasekhar [4]. William et al. investigated different ways to measure surface tension at the interface between the fluids [5]. Bhatia [6] observed the behavior of R-T instability among conducting fluids [6]. Rayleigh–Taylor instability of conducting, rotating, a stratified field in presence of horizontal magnetic field is studied by Chakraborty [7]. Sharp [8] reviewed R-T instability with different influencing effects [8]. Sharma and Chhajlani [9], Hoshoudy [10] investigated R-T instability under the effect of rotation for magnetized conducting plasma [9, 10]. Young and Ham [11] investigated the effect of surface tension intended for inviscid fluids [11]. Guildenbecher et al [12] reported the secondary atomization and breaking up of fluid [12]. R-T instability growth during deflagration in engine combustion was observed by Keenan et al [13]. Baldwin et.al [14] investigated experimentally the effect of rotation and magnetic field on interfacial instability [14]. Scase and Hill [15] studied the effect of high rotation on two liquid layers [16]. For brevity, only few contributions of importance have been included in this paper. Even though considerable research has been done in this topic theoretically [2–4, 8] and also experimentally [13, 14], the complexity of the problem demands comprehensive theoretical investigations. To demonstrate this, the influence of dynamic forces on the fluid–fluid interfaces, magnetic fields and rotation on R-T instability has been investigated theoretically in this paper. The objective of this research is to characterize the Rayleigh–Taylor instability at the interface based on the stability parameters, namely growth rate and the dominant wavenumber of the unstable fluid system. This is attempted for interfaces of different fluid combinations of practical relevance using the well-established governing equations [4].

2 Mathematical Formulation

For depicting Rayleigh–Taylor interface, two fluids of different densities are placed one above the other with heavier fluid on top and lighter fluid at the bottom resulting in a fluid–fluid interface as shown in Fig. 1a and has been used. The coordinate system chosen for this study is presented in the flow domain (Fig. 1b).

Continuity equation based on volume basis with $\vec{V}$ velocity vector and ∇ vector differential operator is shown below:

$$\frac{\partial \rho}{\partial t} + \nabla.\left(\rho \vec{V}\right) = 0 \tag{1}$$

$$\frac{\partial \rho}{\partial t} + \left(\frac{\partial}{\partial x}\hat{i} + \frac{\partial}{\partial y}\hat{j} + \frac{\partial}{\partial z}\hat{k}\right).\left(\rho U\hat{i} + \rho V\hat{j} + \rho W\hat{k}\right) = 0 \tag{2}$$

$$\frac{\partial \rho}{\partial t} + \frac{\partial}{\partial x}(\rho U) + \frac{\partial}{\partial y}(\rho V) + \frac{\partial}{\partial z}(\rho W) = 0 \tag{3}$$

The system assumed as two dimensional and incompressible and neglecting variations in the y-direction for the given layer of fluid has to satisfy the continuity equation below:

$$\frac{\partial U}{\partial x} + \frac{\partial W}{\partial z} = 0 \tag{4}$$

The components of the perturbed flow based on the initial value of the velocity and the perturbation quantities are:

$$U = U_o + u \tag{5}$$

$$V = V_o + v \tag{6}$$

$$W = W_o + w \tag{7}$$

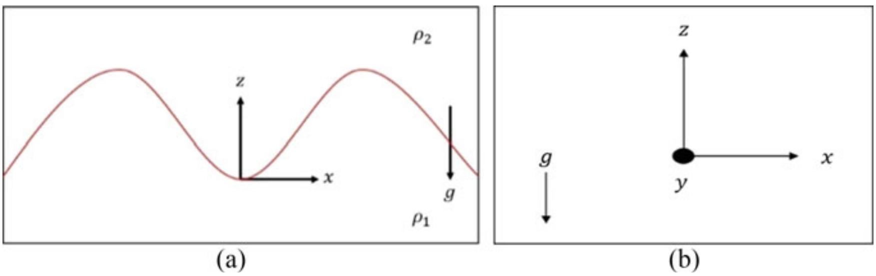

Fig. 1 **a** Fluid–fluid interface, **b** coordinate system

where subscript 'o' specifies that constant initial values and u, v, w are perturbation velocities. Substituting the components of the perturbed flow in Eq. (4) results in

$$\frac{\partial(U_o + u)}{\partial x} + \frac{\partial(W_o + w)}{\partial z} = 0 \tag{8}$$

$$\frac{\partial U_o}{\partial x} + \frac{\partial u}{\partial x} + \frac{\partial W_o}{\partial z} + \frac{\partial w}{\partial z} = 0 \tag{9}$$

Utilizing the continuity equation, Eq. (9) reduces to the form below:

$$\frac{\partial U_o}{\partial x} + \frac{\partial W_o}{\partial z} = 0 \tag{10}$$

Utilizing Newton's second law of motion for a unit volume of the selected fluid interface

$$\rho\left(\frac{\partial U}{\partial t} + U\frac{\partial U}{\partial x} + W\frac{\partial U}{\partial z}\right) = -\frac{\partial p}{\partial x} \tag{11}$$

Being an incompressible flow, perturbation density is constantly resulting in a reduction of Eq. (11) as shown below:

$$(\rho + (\delta\rho))\left(\frac{\partial(U_o + u)}{\partial t} + (U_o + u)\frac{\partial(U_o + u)}{\partial x} + (W_o + w)\frac{\partial(U_o + u)}{\partial z}\right) = -\frac{\partial(p + (\delta p))}{\partial x} \tag{12}$$

The modified form of x-momentum equation is obtained by utilizing the initial conditions ($U_0 = 0$) and linearizing Eq. (12),

$$\rho\left(\frac{\partial u}{\partial t}\right) = -\frac{\partial(\delta p)}{\partial x} \tag{13}$$

Similarly, the reduced form of z-momentum equation is:

$$\rho\left(\frac{\partial w}{\partial t}\right) = -(\delta\rho)g - \frac{\partial(\delta p)}{\partial z} \tag{14}$$

In order to close the problem, one more equation is required. An equation in terms of density perturbation:

$$\frac{\partial(\rho + (\delta\rho))}{\partial t} + \frac{\partial}{\partial x}((\rho + (\delta\rho))u) + \frac{\partial}{\partial z}((\rho + (\delta\rho))w) = 0 \tag{15}$$

Utilizing linear assumption, Eq. (15) becomes:

$$\frac{\partial \rho}{\partial t} + \frac{\partial(\delta\rho)}{\partial t} + u\frac{\partial \rho}{\partial x} + \rho\left(\frac{\partial u}{\partial x} + \frac{\partial w}{\partial z}\right) + w\frac{\partial \rho}{\partial z} = 0 \tag{16}$$

Applying the continuity equation for incompressible flow and density variations in z-direction, Eq. (16) reduces to:

$$\frac{\partial(\delta\rho)}{\partial t} = -w\frac{\partial \rho}{\partial z} \tag{17}$$

The list of the assumptions made is as follows:

1. Two-dimensional, i.e. $\partial/\partial y = 0$
2. Incompressible (density constant)
3. Velocity restated in terms of initial constant values with perturbed velocities
4. Inviscid interface
5. Flow is static initially (velocities are zero)
6. Linearized the momentum equation
7. The energy equation is neglected (isothermal)

Linear stability analysis involves determining the stability of the fluid flow by introducing small-scale disturbances and tracking its temporal progression. Considering a small perturbation in terms of the periodic wave along $z = 0$ for single-mode disturbance with the amplitude A is:

$$A(x, z, t) = A_k(z, t)e^{ikx} = A_k(z)e^{nt}e^{ikx} = A_k(z)e^{ikx+nt} \tag{18}$$

where k is the wavenumber.

Positive eigenvalue gives the positive exponential and unstable state; on the other hand, a negative eigenvalue will result in a stable condition. For the selected velocities, density and pressure, the corresponding normal modes are:

$$u = u(x, z, t) = u_k(z)e^{ikx+nt} \tag{19}$$

$$w = w(x, z, t) = w_k(z)e^{ikx+nt} \tag{20}$$

$$\delta\rho = \delta\rho(x, z, t) = \delta\rho_k(z)e^{ikx+nt} \tag{21}$$

$$\delta p = \delta p(x, z, t) = \delta p_k(z)e^{ikx+nt} \tag{22}$$

On substituting Eqs. (19), (20), (21) and (22), respectively, in the following forms of Navier–Stokes, Eqs. (10), (13), (14), (17) result in:

$$iku + \frac{\partial w}{\partial z} = 0 \tag{23}$$

$$\rho n u = -ik(\delta p) \tag{24}$$

$$\rho n w = -(\delta \rho) g - \frac{\partial(\delta p)}{\partial z} \tag{25}$$

$$n(\delta \rho) = -w \frac{\partial \rho}{\partial z} \tag{26}$$

On solving the above four Eqs. (23–26)

$$\frac{d}{dz}\left(\rho \frac{dw}{dz}\right) - \rho k^2 w = -wg\left(\frac{k^2}{n^2}\right)\left(\frac{d\rho}{dz}\right) \tag{27}$$

Equation (27) is the governing equation for predicting the instability of fluid interface(R-T) generated by the heavier fluid on top of the lighter fluid.

2.1 Rayleigh–Taylor Instability for Two Incompressible Fluids with Inertial Effects

For fluids of constant density ρ_1 and ρ_2 forming interface, the governing Eq. (27) is reduced to:

$$\frac{d^2 w}{dz^2} - k^2 w = 0 \tag{28}$$

Using the boundary conditions that the velocity is zero at large distance above and below the interface and the fact that the velocity at the interface matched for the two solutions becomes,

$$w_1 = w_0 e^{+kz} \quad (z < 0) \tag{29}$$

$$w_2 = w_0 e^{-kz} \quad (z > 0) \tag{30}$$

Multiplying dz and integrating

$$\int d\left[\rho \frac{dw}{dz}\right] - \int \rho k^2 w dz = -\int wg \frac{k^2}{n^2} d\rho \tag{31}$$

Integrating across the interface across an infinitesimal distance $dz = 0$, the second term becomes zero:

$$\Delta\left(\rho \frac{dw}{dz}\right) = -wg \frac{k^2}{n^2} \Delta\rho \tag{32}$$

$$\rho_2(-kw) - \rho_1(kw) = -wg\frac{k^2}{n^2}(\rho_2 - \rho_1) \tag{33}$$

$$-(\rho_2 + \rho_1) = -g\frac{k}{n^2}(\rho_2 - \rho_1) \tag{34}$$

Equation (34) on rearrangement yields an expression for determining growth rate (n):

$$n^2 = gk\left(\frac{\rho_2 - \rho_1}{\rho_2 + \rho_1}\right) \tag{35}$$

It is to be noted that the fluid system is unstable if the heavy fluid is above the lighter fluid ($\rho_2 > \rho_1$), because the eigenvalues are real and system unstable. On the contrary, if the lighter fluid is above the heavier fluid ($\rho_2 < \rho_1$), the eigenvalues are the imaginary and the system is stable.

To find the mode of maximum perturbation or growth, setting the first derivative of Eq. (35) ($dn/dk = 0$) to zero,

$$\sqrt{g\left(\frac{\rho_2 - \rho_1}{\rho_2 + \rho_1}\right)}\left(\frac{1}{2\sqrt{k}}\right) = 0 \tag{36}$$

On squaring both sides of the resulting equation,

$$g\left(\frac{\rho_2 - \rho_1}{\rho_2 + \rho_1}\right)\left(\frac{1}{4k}\right) = 0 \tag{37}$$

Equation (37) enables determination of the dominant wavenumber:

$$k_D = \infty \tag{38}$$

2.2 *Rayleigh–Taylor Instability for Two Incompressible Fluids with Surface Tension Effect*

On introducing the effect of surface tension in Eq. (27), the fundamental equation reduces to:

$$\left(D^2 - k^2\right)w = 0 \tag{39}$$

Utilizing the vanishing boundary conditions, namely $z\rightarrow-\infty$ and $z\rightarrow+\infty$, Eq. (32) results in:

$$\Delta_0(\rho Dw) = -\frac{k^2}{n^2}\left[g(\rho_2 - \rho_1) - k^2\sigma\right]w_0 \tag{40}$$

where w_0 is the common value of w at $z = 0$. The resulting solution helps in determining the growth rate:

$$-k(\rho_2 + \rho_1) = -\frac{k^2}{n^2}\left[g(\rho_2 - \rho_1) - k^2\sigma\right] \tag{41}$$

The corresponding growth rate and wavenumber involving inertial and surface tension effects [4]:

$$n^2 = gk\left\{\left(\frac{\rho_2 - \rho_1}{\rho_2 + \rho_1}\right) - \left(\frac{k^2\sigma}{g(\rho_2 + \rho_1)}\right)\right\} \tag{42}$$

Equation (42) reveals the stability of the interface when $\rho_2 < \rho_1$, otherwise unstable. The corresponding critical wavenumber was determined to be:

$$k_c = \left(\frac{(\rho_2 - \rho_1)g}{\sigma}\right)^{\frac{1}{2}} \tag{43}$$

Mode of maximum growth has been obtained using the first derivative test $(dn/dk = 0)$, based on Eq. (42):

$$\frac{1}{\rho_2 + \rho_1}\left[\frac{1}{2}k^{\frac{1}{2}}\left(g(\rho_2 - \rho_1) - k^2\sigma\right)^{-\frac{1}{2}}(-2k\sigma) + \frac{1}{2}k^{-\frac{1}{2}}\left(g(\rho_2 - \rho_1) - k^2\sigma\right)^{\frac{1}{2}}\right] = 0 \tag{44}$$

$$k_D = \left(\frac{1}{\sqrt{3}}\right)\left(\frac{(\rho_1 - \rho_2)g}{\sigma}\right)^{\frac{1}{2}} \tag{45}$$

Equation (45) indicates the relationship between critical and dominant wavenumber:

$$k_D = \frac{k_c}{\sqrt{3}} \tag{46}$$

On substituting Eq. (46) in Eq. (42), expression for dominant growth rate has been obtained:

$$n_D = \left(\frac{2}{3\sqrt{3}}\frac{(\rho_2 - \rho_1)^{3/2}g^{3/2}}{(\rho_2 + \rho_1)^{1/2}}\right)^{1/2} \tag{47}$$

2.3 Rayleigh–Taylor Instability for Two Incompressible Fluids with of Rotational Effect

To study the effect of rotation in the stability of the inviscid fluid, the fluid is subjected to a uniform rotation with angular velocity Ω. The momentum equation involving the effect of rotation and pressure is utilized to arrive at the governing equations:

$$\rho\left(\frac{du}{dt}\right) - 2\rho\Omega v = -\frac{\partial}{\partial x}(\delta p) \tag{48}$$

$$\rho\left(\frac{dv}{dt}\right) - 2\rho\Omega u = -\frac{\partial}{\partial y}(\delta p) \tag{49}$$

$$\rho\left(\frac{dw}{dt}\right) = -\frac{\partial}{\partial z}(\delta p) - g(\delta\rho) + \sum_s \sigma_s\left(\frac{\partial^2}{\partial x^2} + \frac{\partial^2}{\partial y^2}\right)(\delta z_s)\delta(z - z_s) \tag{50}$$

$$\frac{\partial}{\partial t}(\delta\rho) = -wD\rho \tag{51}$$

$$\frac{\partial u}{\partial x} + \frac{\partial v}{\partial y} + \frac{\partial w}{\partial z} = 0 \tag{52}$$

Density may change discontinuously at pre-assigned level (z_s), a known surface (s) and surface tension effect that is included in Eq. (50).

On linearizing above equations, namely (48), (49), (50), (51) and (52), and subsequently introducing the respective perturbations in the form of normal modes, results in equations mentioned below:

$$\rho n u - 2\rho\Omega v = -ik_x(\delta p) \tag{53}$$

$$\rho n v - 2\rho\Omega u = -ik_y(\delta p) \tag{54}$$

$$\rho n w = -D(\delta p) - g(\delta\rho) - k^2 \sum_s \sigma_s(\delta z_s)\delta(z - z_s) \tag{55}$$

$$n(\delta\rho) = -wD \tag{56}$$

$$ik_x u + ik_y v = -Dw \tag{57}$$

z-component of vorticity is defined below:

$$\zeta = ik_x v - ik_y u \tag{58}$$

Effective utilization of Eqs. (53), (54), (57) and (58) helps in determination of vorticity: $\zeta = 2\Omega Dw/n$ and reduction of Eq. (55)

$$D(\delta p) = -\rho n w + \frac{g}{n}(D\rho)w - \frac{k^2}{n}\sum_s \sigma_s w_s \delta(z - z_s) \tag{59}$$

On eliminating δp in Eq. (59),

$$\left(1 + \frac{4\Omega^2}{n^2}\right)D(\rho D w) - k^2 \rho w = -\left(\frac{gk^2}{n^2}\right)\left\{(D\rho) - \left(\frac{k^2}{g}\right)\sum_s \sigma_s \delta(z - z_s)\right\} \tag{60}$$

Expressing,

$$\theta^2 = \frac{k^2}{1 + \left(4\Omega^2/n^2\right)} \tag{61}$$

On rewriting Eq. (60) by utilizing Eq. (61):

$$D(\rho D w) - \theta^2 \rho w = -\left(\frac{g\theta^2}{n^2}\right)\left\{(D\rho) - \left(\frac{k^2}{g}\right)\sum_s \sigma_s \delta(z - z_s)\right\}w \tag{62}$$

It has to be noted that θ^2 is always positive for $n^2 > 0$ *or* $n^2 < -4\Omega^2$ resulting in alteration of Eq. (62):

$$\Delta_s(\rho D w) = -\left(\frac{\theta^2}{n^2}\right)\left\{g\Delta_s(\rho) - k^2\sigma_s\right\}w_s \tag{63}$$

while

$$D(\rho D w) - \theta^2 \rho w = -\left(\frac{g\theta^2}{n^2}\right)(D\rho)w \quad (z \neq z_s) \tag{64}$$

Equation (42) transforms into the form below on solving Eq. (64) [4]:

$$n^2 = g\theta\left\{\left(\frac{\rho_2 - \rho_1}{\rho_2 + \rho_1}\right) - \left(\frac{k^2\sigma}{g(\rho_2 + \rho_1)}\right)\right\} \tag{65}$$

On substitution Eq. (61) in Eq. (65), the expression for the growth rate is obtained:

$$n^2\left(1 + \frac{4\Omega^2}{n^2}\right)^{\frac{1}{2}} = gk\left\{\left(\frac{\rho_2 - \rho_1}{\rho_2 + \rho_1}\right) - \left(\frac{k^2\sigma}{g(\rho_2 + \rho_1)}\right)\right\} \tag{66}$$

Expressing the left-hand side of Eq. (66) in terms of n_0

$$n^2\sqrt{\left(1+\frac{4\Omega^2}{n^2}\right)}=n_0^2 \quad (67)$$

The possible solutions are [4],

$$n^2=-2\Omega^2+\left(\sqrt{4\Omega^4+n_0^4}\right)if\ n_0^2>0 \quad (68)$$

$$n^2=-2\Omega^2-\left(\sqrt{4\Omega^4+n_0^4}\right)if\ n_0^2<0 \quad (69)$$

Utilizing Eqs. (68) and (69) behavior of fluid–fluid interface under rotation can be predicted.

3 Results and Discussions

The theoretical analysis for determining the stability of Rayleigh–Taylor interfaces has been carried out to investigate the influence of inertial and surface tension and rotational effect in promoting instability at the interface utilizing Eqs. (35), (42), (65), respectively. The results are presented in the following order: inertial alone followed by combined influence of inertial and surface tension and finally including rotational effect to combined influence of inertia and surface tension.

Figure 2 depicts the growth rate in a pure inertial situation based on Eq. (35) for wavenumbers in the range of 0 to 1000. The results indicate an increase in growth rate with an increase in wavenumber for the range of condition tested. This confirms the possibility of the mode of maximum instability only at infinity. This may be due to the dominance of inertial forces over the resistive force suppressing the disturbances to put back the system into stable condition. This leads to rapid growth of perturbation resulting in exertion of extraction of dominant wavenumber.

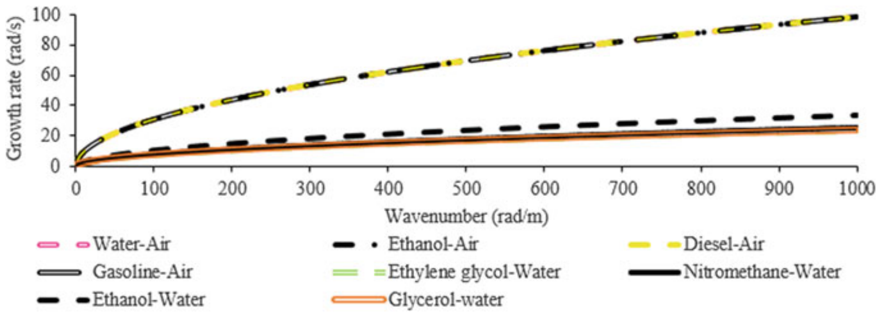

Fig. 2 Growth rate of perturbation under the influence of inertial effect

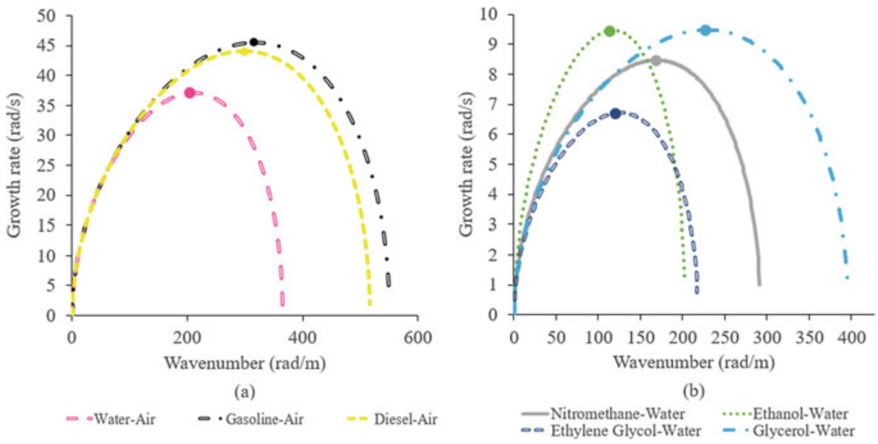

Fig. 3 Growth rate of perturbation under the combined influence of inertial and surface tensional effect: **a** air-based interface, **b** water-based interface

The effect of inertial and surface tension forces on the stability of the fluid–fluid interface has been studied using Eq. (43). Figure 3 includes the growth rate predictions of the disturbances generated at the interface involving, air (Fig. 3a) or water (Fig. 3b) with the tested fluids. The results based on air-based interfaces delineate the existence of a distinct mode of maximum instability that can be extracted in contrast to the corresponding pure inertial situation. In addition, the dual nature of surface tension in promoting instability when water is involved and suppressing instability for air has been noted. It stabilizes the air-based fluid–fluid interfaces and on the contrary, destabilizes for water-based fluid–fluid interfaces, in comparison with the inertial situation. Correspondingly, the wavenumber at which maximum growth rate happens appears to be depended on the fluid.

Figure 4 reveals the comparison of growth rates for different fluids for determining dominant wavenumber under the influence of inertial with and without surface tension. Influence of surface tension is to stabilize the generated interfacial waves selectively enabling extraction of the dominant wave responsible for maximum growth rate among the spectrum. It is evident for all the fluids tested irrespective of air- or water-based interfaces.

The effect of rotation on a disturbed Rayleigh–Taylor interface should be stabilizing the fluid interface bringing chunks of fluid closer to each other that has been separated otherwise. Figure 5 predicts the growth rate as a function of wavenumber for water and air-based interfaces that are already under combined influence of inertial and surface tension. The effect of rotational field is to suppress the growth of the introduced perturbation. Higher rotational speed results in mixing of fluid particles ensuring the stability of the flow field. From the figures, it is evident that the stability of the fluid can be increased by maintaining higher rotational speeds. Rotational speed was varied from 0.002 to 13 rad/s, and the corresponding effect on the growth rate was determined. Individual evolution reveals the existence of unique

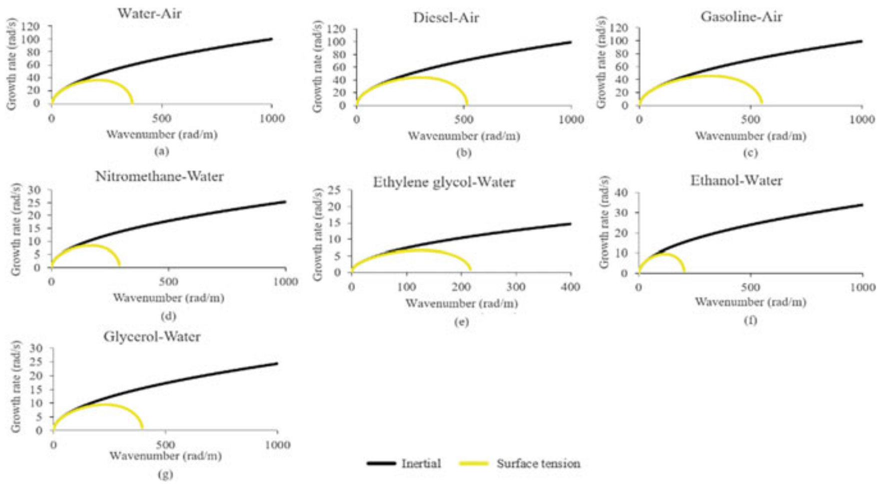

Fig. 4 Growth curve for inertial and surface tension **a** water–air, **b** diesel–air, **c** gasoline–air, **d** nitromethane–water, **e** ethylene glycol–water, **f** ethanol–water, **g** glycerol–water

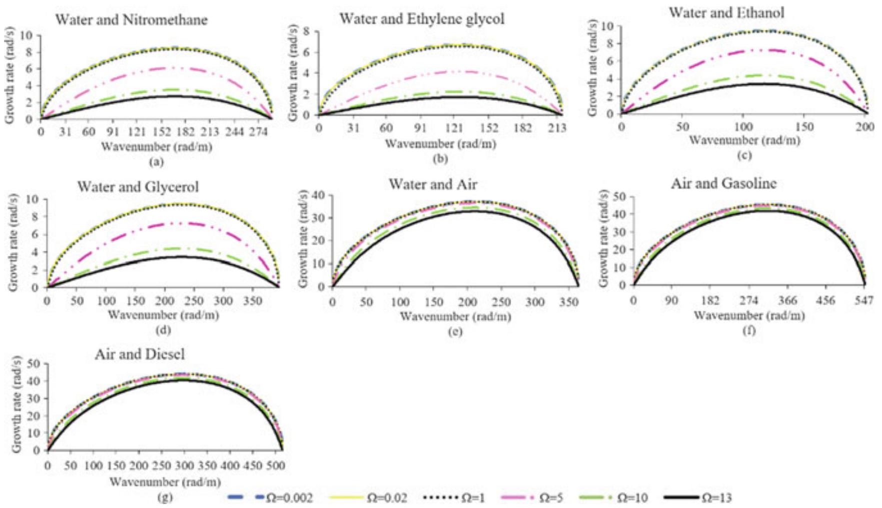

Fig. 5 Rayleigh–taylor instability for an interface under the combined effects of inertial, surface tension and rotation for different rotational speeds: **a** water–nitromethane, **b** water–ethylene glycol, **c** water–ethanol, **d** water–glycerol, **e** water–air, **f** air–gasoline, **g** air–diesel

wavenumber having maximum growth rate. The growth rate curves are identical irrespective of the liquid used for air-based interfaces suggesting that rotational effect is autonomous of fluids. However, significant variation is observed in the water-based interfaces. Correspondingly, an increase in rotational speed increases the stability of water-based fluid interfaces.

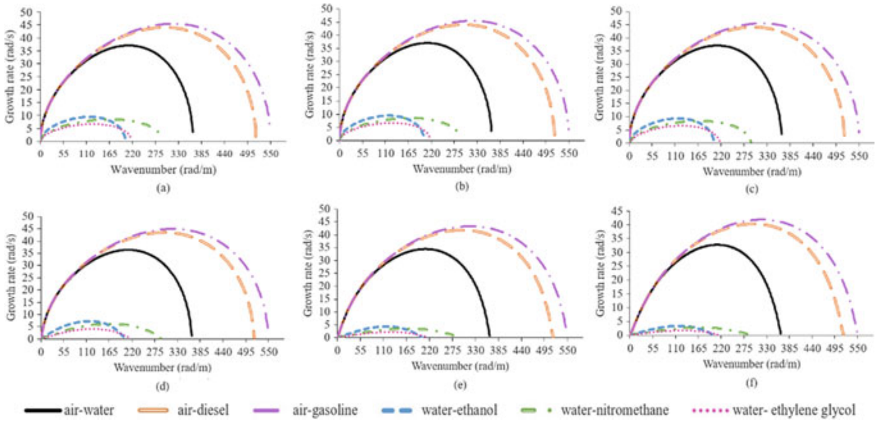

Fig. 6 Rayleigh–taylor instability of interfaces under the influence of specific rotational speeds: **a** $\Omega = 0.002$, **b** $\Omega = 0.02$, **c** $\Omega = 1$, **d** $\Omega = 5$, **e** $\Omega = 10$, **f** $\Omega = 13$

Figure 6 suggests the behavior of fluid interfaces subjected to different rotational speeds ranging from 0.002 to 13 rad/sec. The influence of an increase in rotational speed on the stability for water-based interfaces is more prominent than the air-based interfaces. Also, the increase in rotational speed suppresses the developed instability significantly overcoming the influence of inertia resisting the attainment of interfacial stability.

4 Conclusion

In the present study, the behavior of fluid interfaces at rest subjected to Rayleigh–Taylor type of instabilities has been attempted. The objective is to predict stability of interface under the influence of combined inertial, surface tensional and rotational effects for different fluid combinations. It is evident that under the influence of inertial forces only, the interface is always unstable. On the contrary, including surface tension effects to pure inertial condition, there is a possibility for the fluid interface to attain stable condition. Also, unimodal behavior observed supports in determination of maximum growth rate and the associated dominant wavenumber. Implicit analysis reveals the dual nature of surface tension; the air-based interfaces are stabilized and on the contrary, destabilizing the water-based interfaces. In addition, for air-based systems, the sensitiveness of dominant wavenumber resulting in maximum growth rate on fluid properties has been observed. The effect of rotation to an interface involving inertial and surface tension effects has been to suppress the growth of the instabilities with increase in rotational speed. Besides, at higher speeds, the effect of rotation in attainment of stability has been prominent in water-based systems in comparison with air-based interfaces. By considering the viscous influence of fluids forming interfaces in the future studies, a better understanding of R-T instability can be realized. In the case of nuclear reactors, this kind of fluid–fluid interface is predominant as mentioned in Siddharth et al. [17]. Karthick et al. [16] reported the Kelvin–Helmholtz (K-H) instability at the fluid–fluid interface due to accelerating fluids. This is different from the Rayleigh–Taylor (R-T) instability mentioned in this paper. Nevertheless a fluid–fluid interface can experience K-H or R-T instability depending upon the relative positions of heavier and lighter fluids.

References

1. Rayleigh L (1883) Investigation of the character of the equilibrium of an incompressible heavy fluid of variable density. Proc Lond Math Soc 14:170–177
2. Taylor GI (1950) The instability of liquid surfaces when accelerated in a direction perpendicular to their planes. Proc Roy Soc Lon Series A, Math Phys Sci 201(1065):192–196
3. Lewis DJ (1950) The instability of liquid surface when accelerated in perpendicular to their planes (II). Proc R Soc Lond Ser A 202:81
4. Chandrasekhar S (1961) Hydrodynamic and hydromagnetic stability. Dover publications chapter X 428–477
5. Harkins WD, Humphrey EC (1915) The surface tension at the interface between two liquids and the effect of acid, salts, and base upon the interfacial tension. J Am Chem Soc 38(2):242–246
6. Bhatia PK (1973) Rayleigh-Taylor instability of two viscous superposed conducting fluids. Astrophys Space Sci 19B(2)
7. Chakraborty BB (1982) Hydromagnetic Rayleigh-Taylor instability of a rotating stratified fluid. Phys Fluids 25:743
8. Sharp DH (1983) An overview of Rayleigh-Taylor Instability. Los Alamos Univ New Mex 12:3–10
9. Sharma PK, Chhajlani RK (1998) Effect of rotation on the Rayleigh-Taylor instability of two superposed magnetized conducting plasma. Phys Plasmas 5:2203
10. Hoshoudy GA (2012) External magnetic field effects on the rayleigh-taylor instability in an inhomogeneous rotating quantum plasma. J Mod Phys 3:1792–1801
11. Young YN, Ham FE (2006) Surface tension in incompressible rayleigh-taylor mixing flow. J Turbul 7(71)
12. Guildenbecher DR, López-Rivera C, Sojka PE (2009) Secondary Atomization. Exp Fluids 46:371–402
13. Keenan JJ, Makarov DV, Molkov VV (2014) Rayleigh-taylor instability: modeling and effect on coherent deflagrations. Int J Hydrogen Energy 39(35)
14. Baldwin KA, Scase MM, Hill RJA (2015) The inhibition of rayleigh-taylor instability by rotation. Sci Rep 5:11706
15. Scase MM, Hill RJA (2018) Centrifugally forced rayleigh-taylor instability. J Fluid Mech 852:543–577
16. Karthick S, Srivatsan M, Raghav R, Vishnu Supreet, K (2015) Theoretical investigation of primary breakup of liquid jet using linear stability analysis in the first wind induced regime based on kelvin-helmholtz instability. 1901–3905
17. Siddharth SS, Vikram G, Natesan K, Karthick S (2018) Modeling, simulation and analysis of primary pipe rupture in sodium cooled fast breeder reactor. 045 ICMMC December

Heat and Mass Transfer Analysis of Al_2O_3-Water and Cu-Water Nanofluids Over a Stretching Surface with Thermo-diffusion and Diffusion-Thermo Effects Using Artificial Neural Network

D. Seenivasan, M. Elayarani, and M. Shanmugapriya

Abstract The present paper deals with the artificial neural network (ANN) modeling of heat and mass transfer on magnetohydrodynamic (MHD) convective flow of Al_2O_3-water and Cu-water nanofluids past a stretching sheet through porous media with thermo-diffusion and diffusion-thermo effects. The set of suitable similarity transformations are employed to alter the nonlinear partial differential equations into ordinary differential equations. The solutions of the resulting nonlinear differential equations are solved numerically with the help of Runge–Kutta Fehlberg fourth–fifth order method accompanied by shooting technique, and then, the ANN is applied to them. The multilayer feedforward neural network with backpropagation training algorithm is used for predicting the desired outputs. The influence of various physical parameters on velocity, temperature and concentration profiles is explored and discussed in detail. The friction factors, heat and mass transfer rates are predicted using ANN. The numerical results and the results of the ANN are in good agreement with errors less than 5%. According to the findings of this paper, the ANN approach is reliable and more effective for simulating heat and mass transfer in MHD nanofluid flow over a stretched sheet.

Keywords Magnetohydrodynamics · Nanofluid · Heat transfer · Stretching sheet · Artificial neural network

D. Seenivasan
Department of Mathematics, Jeppiaar SRR Engineering College, Padur, Chennai, Tamil Nadu 603103, India

M. Elayarani · M. Shanmugapriya (✉)
Department of Mathematics, SSN College of Engineering, Kalavakkam, Chennai, Tamil Nadu 603110, India
e-mail: shanmugapriyam@ssn.edu.in

E. T. Akinlabi et al. (eds.), *Trends in Mechanical and Biomedical Design*, Lecture Notes in Mechanical Engineering,
https://doi.org/10.1007/978-981-15-4488-0_36

1 Introduction

Heat and mass transfer flows with chemical reactions have received great attention among the researchers due to its significant applications in processes such as evaporation, drying, energy transfer, flow in a desert cooler, distribution of temperature and moisture over agricultural fields and trees. Combined effects of heat and mass transfer on MHD flow over a stretching sheet in the presence of chemical reaction under various physical aspects have been analyzed by the researchers [1–4]. The effects of heat generation or absorption play a vital role in cooling processes, exothermic chemical reactions, storage of foodstuffs, disposal of radioactive waste materials and separating fluids in packed-bed reactors. Studies on MHD nanofluid flow with heat generation or absorption over different surfaces were addressed in the publications [5–8]. Magnetohydrodynamic convective flow of nanofluids over various stretching velocities, namely linear, radial, non-isothermal and exponential, have been investigated by the authors [9–12]. The combined effects of Soret and Dufour are significant when there exists density difference in the flow regime and finds potential applications in the areas of chemical engineering and geosciences. Many researchers [13–18] interpreted the Soret and Dufour effects of MHD flow with chemical reaction under varied geometries.

In the recent years, ANNs have been extensively used in the fluid flow problems to reduce the time, expenses and complicated computation works. Ziaei-Rad et al. [19] applied a multilayer neural network model for finding the skin friction factor and Nusselt number of dissipative nanofluid flow under a variable MHD field over a permeable horizontal stretching surface. Aminian [20] used a cascade-forward neural network model for predicting the effective thermal conductivities of 26 different types of nanofluids. The MHD convective boundary layer slip flow on a permeable stretched cylinder with chemical reaction was modeled using artificial neural network technique by Reddy et al. [21]. Tafarroj et al. [22] proposed an ANN model for calculating the heat transfer coefficient and Nusselt number on the flow of TiO_2-water nanofluid in a microchannel heat sink. Tripathy et al. [23] employed ANN approach for forecasting the free convective flow and heat transfer between two coaxial cylinders of an elastic-viscous liquid. Maddah et al. [24] estimated the heat transfer efficiency of water–iron oxide nanofluid in a double pipe heat exchanger equipped with twisted tape using experiment and artificial neural networks. The current paper extends the artificial neural network technique to predict the friction factor, heat and mass transfer rates due to the MHD convective flow of Al_2O_3-water and Cu-water nanofluids on a linear porous stretching surface in the presence of Soret and Dufour effects.

2 Mathematical Analysis

We consider a two-dimensional, steady, laminar, MHD boundary layer flow of an incompressible, viscous nanofluid past a stretching sheet through porous medium in the plane $y = 0$, and the flow is assumed to be confined in a region $y > 0$. The stretching sheet coincides with the x-axis in the direction of the flow, and y-axis is perpendicular to the surface. A constant magnetic field B_0 is applied along the y-direction, and the stretching sheet is extended with velocity $u_w(x) = ax$, where $a > 0$ is a constant. The uniform temperature T_w and nanoparticle fraction C_w are assumed to be greater than the ambient temperature T_∞ and nanoparticle fraction C_∞, respectively. In this problem, water-based nanofluid is considered with two different types of nanoparticles, namely Al_2O_3 and Cu. The fluid and nanoparticles are assumed to be in thermal equilibrium, and no slip occurs between them, and the thermophysical properties are given in Table 1. The boundary layer equations that govern the problem are given by

$$\frac{\partial u}{\partial x} + \frac{\partial v}{\partial y} = 0 \tag{1}$$

$$u\frac{\partial u}{\partial x} + v\frac{\partial u}{\partial y} = \nu_{nf}\frac{\partial^2 u}{\partial y^2} - \frac{\nu_{nf}}{K}u - \frac{\sigma B_0^2 u}{\rho_{nf}} \tag{2}$$

$$\begin{aligned} u\frac{\partial T}{\partial x} + v\frac{\partial T}{\partial y} &= \alpha_{nf}\frac{\partial^2 T}{\partial y^2} - \frac{1}{\left(\rho c_p\right)_{nf}}\frac{\partial q_r}{\partial y} + \frac{\mu_{nf}}{\left(\rho c_p\right)_{nf}}\left(\frac{\partial u}{\partial y}\right)^2 \\ &+ \frac{1}{\left(\rho c_p\right)_{nf}}q''' + \frac{D_2}{\left(\rho c_p\right)_{nf}}\frac{\partial^2 C}{\partial y^2} \end{aligned} \tag{3}$$

$$u\frac{\partial C}{\partial x} + v\frac{\partial C}{\partial y} = D_m\frac{\partial^2 C}{\partial y^2} + D_1\frac{\partial^2 T}{\partial y^2} - K_0(C - C_\infty) \tag{4}$$

with the associated boundary conditions

$$u = u_w(x) = ax, \quad v = v_w, \quad T = T_w, \quad C = C_w \quad \text{at} \quad y = 0 \tag{5}$$

$$u = 0, \quad T \to T_\infty, \quad C \to C_\infty \quad \text{as} \quad y \to \infty \tag{6}$$

Table 1 Thermophysical properties of water and nanoparticles [9]

Fluid	ρ (kg/m^3)	c_p (J/kg K)	κ (W/m K)	$\beta \times 10^5 (\mathrm{K}^{-1})$
Water	997.1	4179	0.613	21
Alumina (Al_2O_3)	3970	765	40	0.85
Copper (Cu)	8933	385	401	1.67

where u and v are the velocity components along x- and y axes, respectively, T is the temperature, C is the concentration, v_w is the suction or injection velocity, K is the permeability of porous medium, σ is the electrical conductivity, D_1 and D_2 are the mass and heat fluxes through temperature and concentration gradient, D_m is the species diffusivity and K_0 is the chemical reaction parameter.

The effective density ρ_{nf}, dynamic viscosity μ_{nf}, thermal conductivity κ_{nf}, kinematic viscosity ν_{nf}, thermal diffusivity α_{nf} and heat capacitance $\left(\rho c_p\right)_{nf}$ of the nanofluid are defined as follows:

$$\begin{gathered}\rho_{nf} = (1-\varphi)\rho_f + \varphi\rho_s, \quad \mu_{nf} = \frac{\mu_f}{(1-\varphi)^{2.5}},\\ \kappa_{nf} = \kappa_f\left[\frac{\kappa_s + 2\kappa_f - 2\varphi\left(\kappa_f - \kappa_s\right)}{\kappa_s + 2\kappa_f + 2\varphi\left(\kappa_f - \kappa_s\right)}\right], \quad \nu_{nf} = \frac{\mu_{nf}}{\rho_{nf}},\\ \alpha_{nf} = \frac{\kappa_{nf}}{\left(\rho c_p\right)_{nf}}, \quad \left(\rho c_p\right)_{nf} = (1-\varphi)\left(\rho c_p\right)_f + \varphi\left(\rho c_p\right)_s\end{gathered} \tag{7}$$

where φ represents the solid volume fraction of nanoparticles in the fluid.

The non-uniform heat source/sink q''' is defined by

$$q''' = A(T_w - T_\infty)f' + B(T - T_\infty) \tag{8}$$

where A and B are the coefficients of space and temperature-dependent heat source/sink parameters, in which the case $A > 0$, $B > 0$ represents internal heat source and the case $A < 0$, $B < 0$ represents internal heat sink.

Under Rosseland approximation, the radiative heat flux q_r takes the form

$$q_r = -\frac{4\sigma^*}{3k^*}\frac{\partial T^4}{\partial y} \tag{9}$$

where σ^* and k^* are the Stephan–Boltzmann constant and mean absorption coefficient. Consider the temperature difference within the flow is sufficiently small such that T^4 can be expressed as the linear function of temperature T_∞. Expanding T^4 in a Taylor series about T_∞ and neglecting higher order terms yield

$$T^4 \equiv 4T_\infty^3 T - 3T_\infty^4 \tag{10}$$

$$q_r = -\frac{16T_\infty^3\sigma^*}{3k^*}\frac{\partial T}{\partial y} \tag{11}$$

The stream function ψ is defined as

$$u = \frac{\partial\psi}{\partial y}, \quad v = -\frac{\partial\psi}{\partial x} \tag{12}$$

We introduce the following similarity transformations

$$\begin{aligned} &\psi = \sqrt{a\nu_f}\, x f(\eta), \quad \eta = \sqrt{\tfrac{a}{\nu_f}}\, y \\ &u = axf'(\eta), \quad v = -\sqrt{a\nu_f}\, f(\eta) \\ &\theta(\eta) = \tfrac{T-T_\infty}{T_w-T_\infty}, \quad \phi(\eta) = \tfrac{C-C_\infty}{C_w-C_\infty} \end{aligned} \tag{13}$$

By using Eqs. (8), (11) and (13), the Eqs. (1)–(4) are reduced to

$$f''' + A_1 A_2\left[ff'' - \left(f'\right)^2 - \frac{M}{A_2}f'\right] - K_1 f' = 0 \tag{14}$$

$$\left(1 + \frac{4}{3}R\right)\theta'' + \Pr\frac{A_3}{A_5}\left[f\theta' - 2f'\theta + \frac{\mathrm{Ec}}{A_4}\left(f''\right)^2 + \frac{1}{A_3}\left(A1 f' + B1\theta + \mathrm{Du}\phi''\right)\right] = 0 \tag{15}$$

$$\phi'' + \mathrm{Sc}\left[f\phi' + \mathrm{Sr}\theta'' - C1\phi\right] = 0 \tag{16}$$

The corresponding boundary conditions are

$$f = S, \quad f' = 1, \quad \theta = 1, \quad \phi = 1 \quad \text{at} \quad \eta = 0 \tag{17}$$

$$f' = 0, \quad \theta = 0, \quad \phi = 0 \quad \text{at} \quad \eta = \infty \tag{18}$$

where prime denotes the differentiation with respect to η, $M = \frac{\sigma B_0^2}{a\rho_f}$ the magnetic parameter, $K_1 = \frac{\nu_f}{Ka}$ the porosity parameter, $R = \frac{4\sigma^* T_\infty^3}{\kappa_{nf}k^*}$ the radiation parameter, $\Pr = \frac{\nu_f}{\alpha_f}$ the Prandtl number, $\mathrm{Ec} = \frac{u_w^2}{\left(c_p\right)_f (T_w-T_\infty)}$ the Eckert number, $A1 = \frac{A}{a\left(\rho c_p\right)_f}$ the space-dependent heat source/sink, $B1 = \frac{B}{a\left(\rho c_p\right)_f}$ the temperature-dependent heat source/sink, $\mathrm{Du} = \frac{D_2}{\nu_f\left(\rho c_p\right)_f}\frac{(C_w-C_\infty)}{(T_w-T_\infty)}$ the Dufour number, $\mathrm{Sc} = \frac{\nu_f}{D_m}$ the Schmidt number, $\mathrm{Sr} = \frac{D_1}{\nu_f}\frac{(T_w-T_\infty)}{(C_w-C_\infty)}$ the Soret number, $C1 = \frac{K_0}{a}$ the chemical reaction parameter.

$$A_1 = (1-\varphi)^{2.5}, \quad A_2 = (1-\varphi) + \varphi\frac{\rho_s}{\rho_f}, \quad A_3 = (1-\varphi) + \varphi\frac{\left(\rho c_p\right)_s}{\left(\rho c_p\right)_f},$$

$$A_4 = (1-\varphi)^{2.5}\left[(1-\varphi) + \varphi\frac{\left(\rho c_p\right)_s}{\left(\rho c_p\right)_f}\right], \quad A_5 = \frac{\kappa_{nf}}{\kappa_f}$$

The special interest in this problem is the local skin friction coefficient C_{fx}, the local Nusselt number Nu_x and the local Sherwood number Sh_x which are defined as

$$C_{fx} = \frac{\tau_w}{\rho_f\left(u_w^2/2\right)}, \quad \mathrm{Nu}_x = \frac{xq_w}{\kappa(T_w - T_\infty)}, \quad \mathrm{Sh}_x = \frac{xJ_w}{D_m(C_w - C_\infty)} \tag{19}$$

where τ_w is the wall shear stress, q_w and J_w are the heat and mass fluxes at the surface.

Substituting Eq. (13) into Eq. (19), we get the following expressions in dimensionless form

$$\begin{aligned} C_{fx}\mathrm{Re}_x^{\frac{1}{2}} &= \tfrac{-2f''(0)}{(1-\varphi)^{2.5}} \\ \mathrm{Nu}_x\mathrm{Re}_x^{-\frac{1}{2}} &= -\tfrac{\kappa_{nf}}{\kappa_f}\left(1+\tfrac{4}{3}R\right)\theta'(0) \\ \mathrm{Sh}_x\mathrm{Re}_x^{-\frac{1}{2}} &= -\phi'(0) \end{aligned} \tag{20}$$

3 Numerical Procedure

In this paper, Runge–Kutta Fehlberg fourth–fifth order method has been used with shooting technique to solve the system of coupled nonlinear ordinary differential Eqs. (14)–(16) with the boundary conditions (17) and (18). First, we define the variables $f = Y_1$, $f' = Y_2$, $f'' = Y_3$, $\theta = Y_4$, $\theta' = Y_5$, $\phi = Y_6$, $\phi' = Y_7$. Equations (14)–(16) are reduced to system of first-order differential equations as follows

$$\begin{aligned} &Y_1' = Y_2 \\ &Y_2' = Y_3 \\ &Y_3' = -A_1A_2\left[Y_1Y_3 - (Y_2)^2 - \frac{M}{A_2}Y_2\right] + K_1Y_2 \\ &Y_4' = Y_5 \\ &Y_5' = -\frac{1}{\left(1+\frac{4}{3}R\right)} \\ &\mathrm{Pr}\frac{A_3}{A_5}\left[Y_1Y_5 - 2Y_2Y_4 + \frac{\mathrm{Ec}}{A_4}(Y_3)^2 + \frac{1}{A_3}\left(A1Y_2 + B_1Y_4 + \mathrm{Du}Y_7'\right)\right] \\ &Y_6' = Y_7 \\ &Y_7' = -\mathrm{Sc}\left[Y_1Y_7 + \mathrm{Sr}Y_5' - C1Y_6\right] \end{aligned} \tag{21}$$

with the corresponding boundary conditions

$$\begin{aligned} &Y_1(0) = S, \quad Y_2(0) = 1, \quad Y_3(0) = c_1, \quad Y_4(0) = 1 \\ &Y_5(0) = c_2, \quad Y_6(0) = 1, \quad Y_7(0) = c_3 \end{aligned} \tag{22}$$

In order to get the solution of the above initial value problem, the unknown initial values $f''(0), \theta'(0)$ and $\phi'(0)$ are to be determined by making initial guesses, and then, integration is carried out with the aid of Runge–Kutta Fehlberg fourth–fifth order scheme. The initial values are chosen in such a way that it satisfies the condition $f'(\eta_\infty) \to 0, \theta(\eta_\infty) \to 0$ and $\phi(\eta_\infty) \to 0$ for finite domain length $\eta_{\max}$. The above procedure is repeated until the required accuracy is achieved with the step size of $\Delta\eta = 0.001$.

4 Artificial Neural Networks

Artificial neural network is an advanced computing tool consists of an extremely interconnected neurons and processes information using neurocomputing technique. A multilayer neural network model is shown in Fig. 1, which comprises an input layer, output layer and a hidden layer of nine neurons. Back error propagation (BEP) training algorithm has been used with sigmoid hidden neurons and linear output neurons. The neural network adjusts weights at every node in all layers during training process in order to minimize the error between the predicted and actual result. In this study,

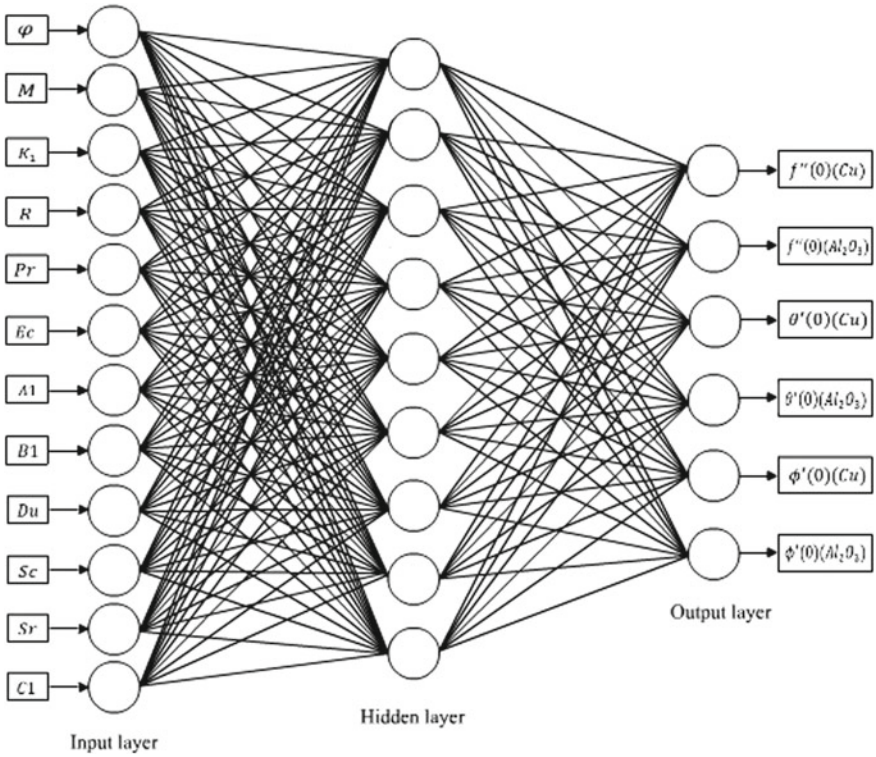

Fig. 1 A multi-layer neural network model [25]

the network uses twelve parameters (φ, M, K_1, R, Pr, Ec, $A1$, $B1$, Du, Sc, Sr, $C1$) as input nodes, and output parameters are $f''(0)$, $\theta'(0)$, $\phi'(0)$ for alumina–water and copper–water nanofluid. The numerical data set was divided into training (70%), testing (15%) and validation (15%) sets of the neural network.

5 Results and Discussion

The accuracy of the current numerical method is assessed by obtaining the values of skin friction coefficient for the various values of M, and φ in the absence of K_1, R, Ec, $A1$, $B1$, Du, Sc, Sr, $C1$ when Pr $= 6.2$ is shown in Table 2. It is clear that the results are in good agreement with Hamad [9]. Figures 2, 3 and 4 display the velocity (f'), temperature (θ) and concentration (ϕ) profiles plotted against η for varying φ. From Fig. 2, it is observed that enhancing φ leads to increase the velocity field for Al_2O_3-water and decreases for Cu-water nanofluid. From Figs. 3 and 4, it is seen that the dimensionless temperature elevates with the growing values of φ, and a reverse trend is occurred in the concentration profile for both nanofluids.

Figures 5, 6 and 7 represent the impact of M on velocity, temperature and concentration distributions. This is due to the fact that the transverse magnetic field produces a resistive type of force (Lorentz force) when applied to an electrically conducting fluid. The Lorentz force has the tendency to diminish the motion of the fluid and accelerate the temperature and concentration profiles. As a consequence, it is perceived from Fig. 5 that the magnetic parameter M weakens the velocity for alumina–water and copper–water nanofluids and thereby strengthen the temperature and concentration inside the boundary layer for both fluids which are shown in Figs. 6 and 7.

Figures 8 and 9 show the influence of temperature-dependent heat source/sink coefficient $B1$ on dimensionless temperature and concentration for both Al_2O_3-water and Cu-water nanofluids. From Fig. 8, it is noticed that the temperature profile rises for the heat source $B1 > 0$ and decreases for the heat absorption $B1 < 0$. This

Table 2 Comparison of $-f''(0)$ with previously published results

M	φ	Hamad [9] Al_2O_3	Cu	Present results Al_2O_3	Cu
0	0.05	1.00538	1.10892	1.00554	1.10901
0	0.1	0.99877	1.17475	0.99895	1.17481
0	0.15	0.98185	1.20886	0.98204	1.20891
0	0.2	0.95592	1.21804	0.95615	1.21809
0.5	0.05	1.20441	1.29210	1.20442	1.29211
0.5	0.1	1.17548	1.32825	1.17550	1.32825
0.5	0.15	1.13889	1.33955	1.13891	1.33956
0.5	0.2	1.09544	1.33036	1.09547	1.33036

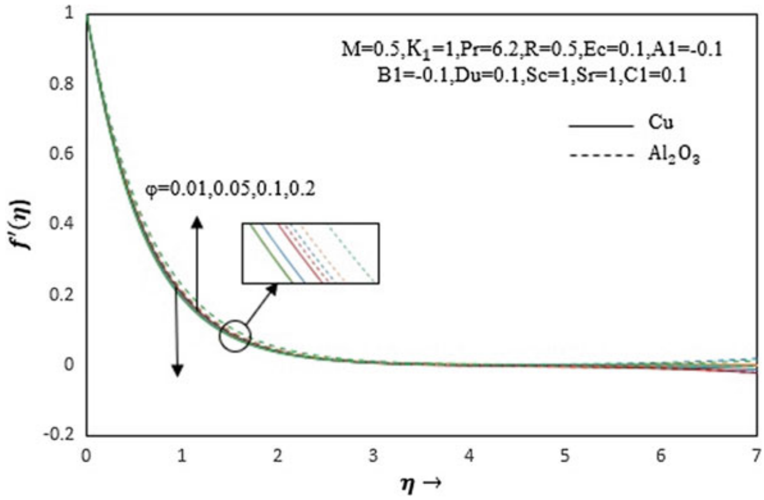

Fig. 2 Velocity profiles for varying φ

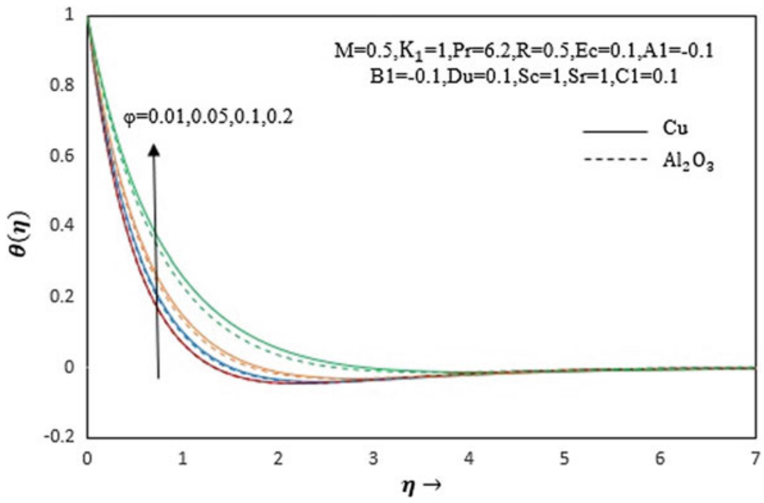

Fig. 3 Temperature profiles for varying φ

is because of the fact that the boundary layer creates energy when $B1 > 0$ and absorbs energy when $B1 < 0$. In Fig. 9, an opposite trend has observed in the concentration profile for both heat generation and absorption cases of temperature-dependent coefficient $B1$ in both nanofluids.

The mass and energy fluxes caused by temperature gradient and concentration difference are called thermo-diffusion (Soret) and diffusion-thermo (Dufour) effects, respectively. Figures 10 and 11 illustrate the combined effect of Soret and Dufour

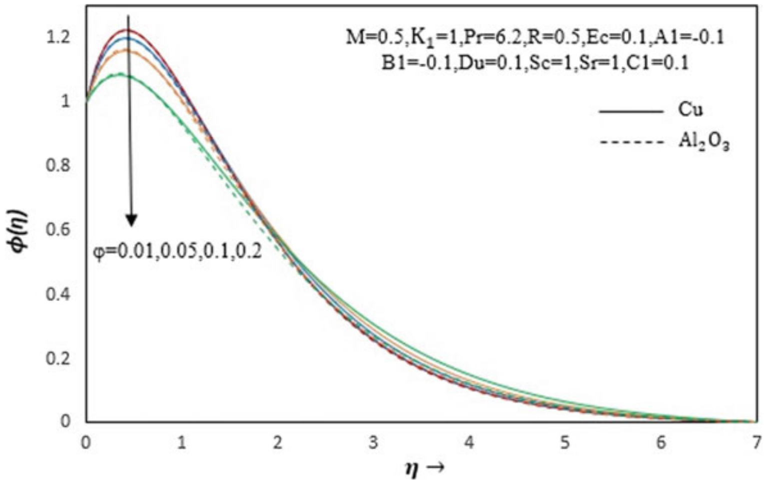

Fig. 4 Concentration profiles for varying φ

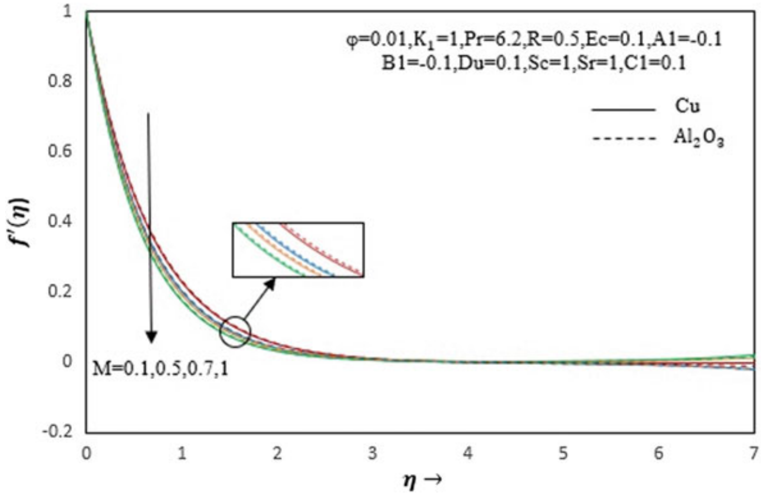

Fig. 5 Velocity profiles for varying *M*

numbers with increasing Sr and decreasing Du. The values of Sr and Du are taken in pairs such as (0.1, 0.5), (0.3, 0.4), (0.5, 0.2) and (1, 0.1). It is interesting to notice that the dimensionless temperature and concentration enhance significantly with a rise in Soret number Sr (or decrease in Dufour number Du) for both Al_2O_3-water and Cu-water nanofluids.

The proposed ANN model contains an input layer of 12 neurons, output layer of six neurons and a hidden layer. To avoid the overfit or underfit of neurons, the network was trained with the increasing number of hidden neurons. Figures 12 and 13 exhibit

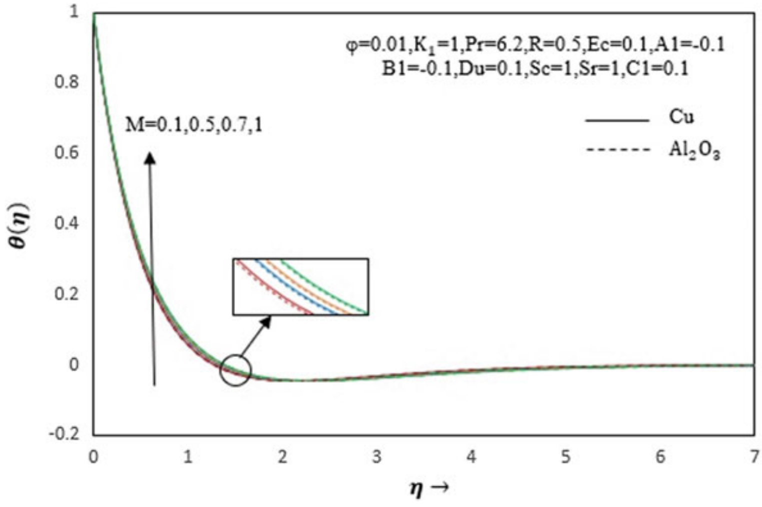

Fig. 6 Temperature profiles for varying M

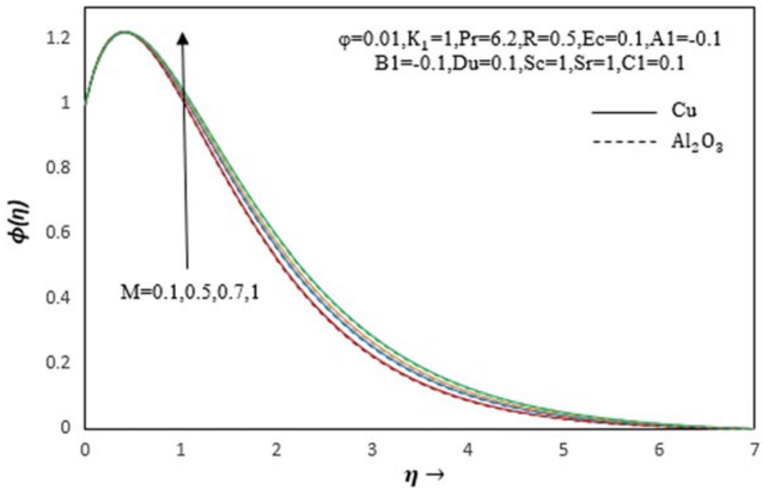

Fig. 7 Concentration profiles for varying M

the coefficient of determination (R^2) and test errors (MSE and MAE) for varying neurons in the hidden layer. It is perceived that the optimum R^2 was achieved for nine hidden neurons, and the corresponding R^2, MSE and MAE values are 0.973729, 0.002785 and 0.016838. Figures 14, 15 and 16 illustrate the regression plot between the numerical and the predicted ANN values of the skin friction coefficient, Nusselt number and Sherwood number for the overall data set. The correlation coefficient

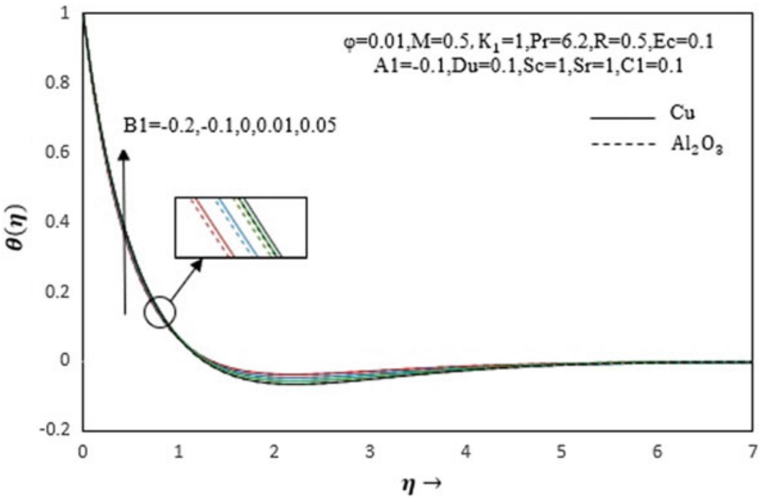

Fig. 8 Temperature profiles for varying $B1$

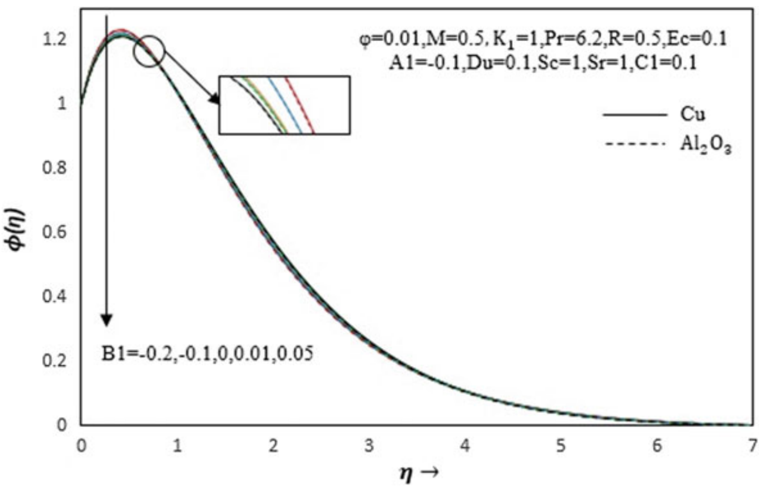

Fig. 9 Concentration profiles for varying $B1$

R of $f''(0)$, $\theta'(0)$ and $\phi'(0)$ for Al_2O_3-water and Cu-water nanofluids is 0.98443, 0.97102 and 0.99619, which shows the accuracy of the neural network.

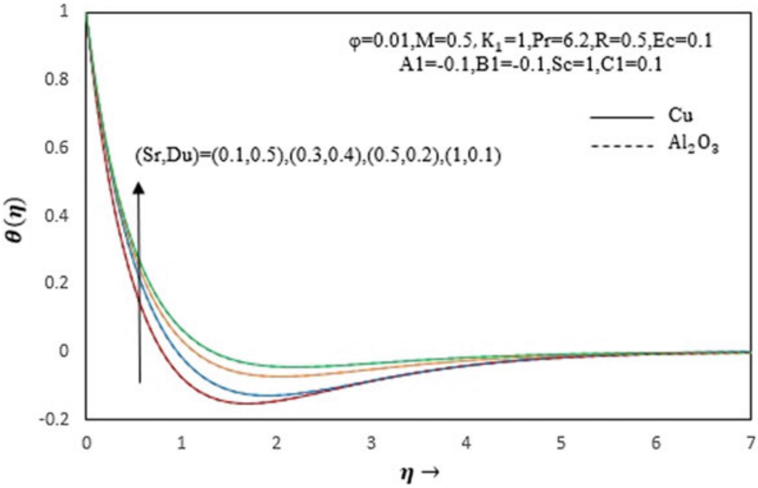

Fig. 10 Temperature profiles for varying Sr and Du

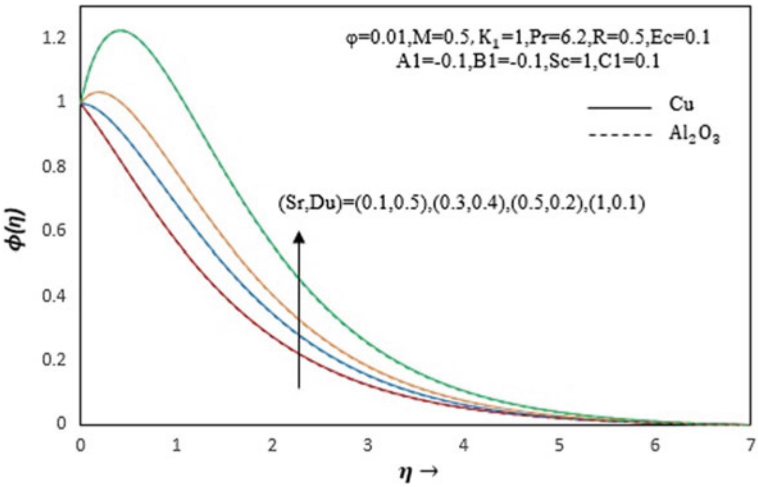

Fig. 11 Concentration profiles for varying Sr and Du

6 Conclusion

In this paper, we have investigated the numerical and ANN modeling of two-dimensional MHD convective boundary layer flow, heat and mass transfer characteristics of alumina–water and copper–water nanofluids over a porous linear stretching surface in the presence of Soret and Dufour effects. The results are summarized as follows:

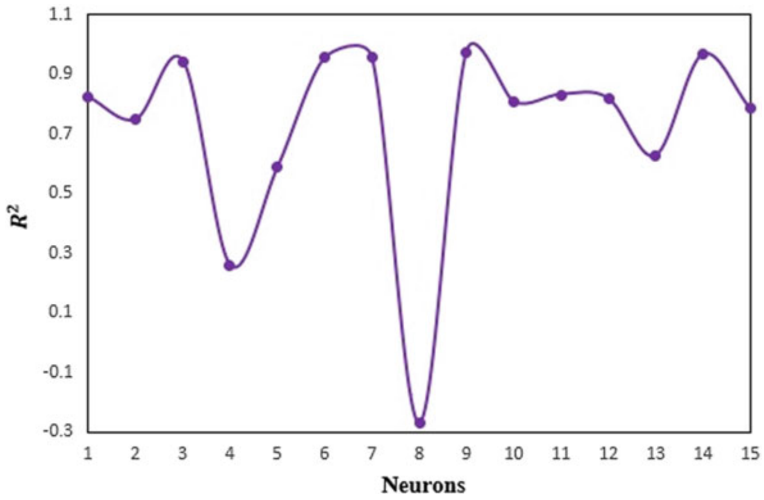

Fig. 12 Coefficient of determination R^2 for varying hidden neurons

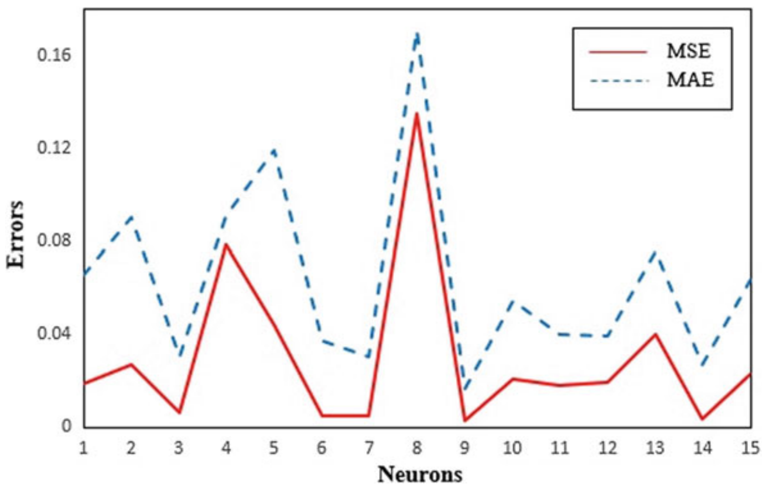

Fig. 13 MSE and MAE test errors for varying hidden neurons

- As the solid volume fraction φ increases, the momentum boundary layer becomes thicker for Al_2O_3-water and thinner for Cu-water nanofluids, whereas the thickness of the thermal boundary layer upsurges and concentration boundary layer decelerates for both nanofluids.
- The increase of magnetic parameter M leads to decrease the momentum boundary layer thickness due to the effect of Lorentz force and improves the thickness of the thermal and solutal boundary layer in the flow regime.

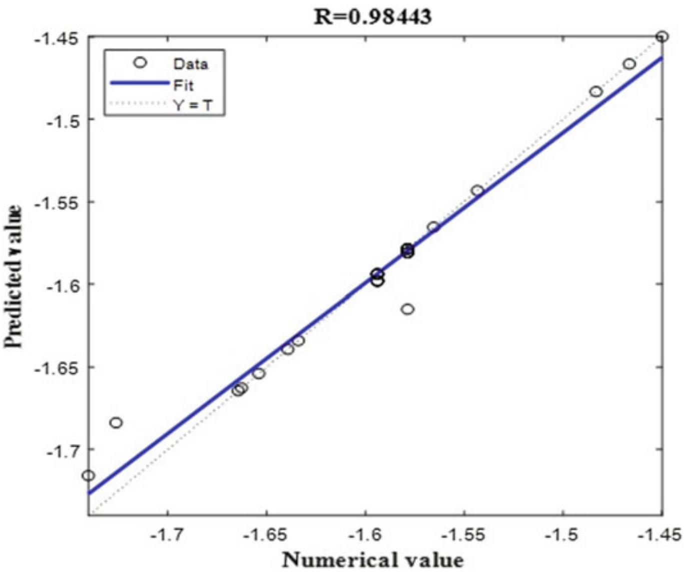

Fig. 14 Comparison between numerical and ANN predictions of $f''(0)$

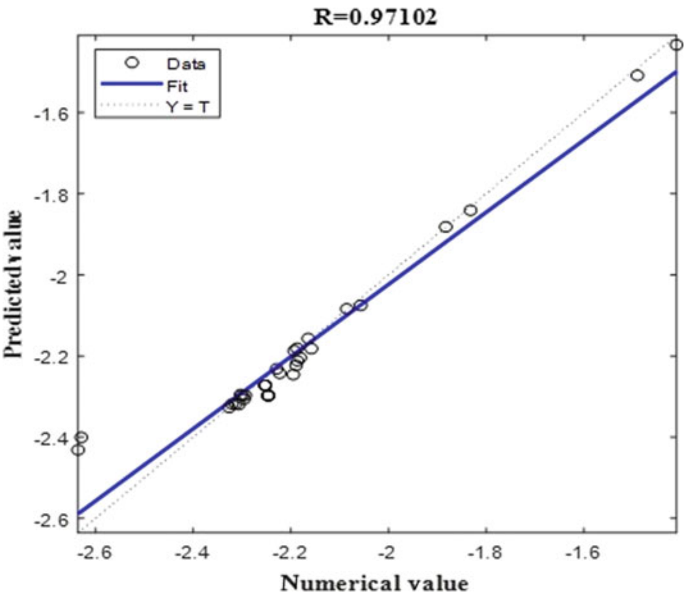

Fig. 15 Comparison between numerical and ANN predictions of $\theta'(0)$

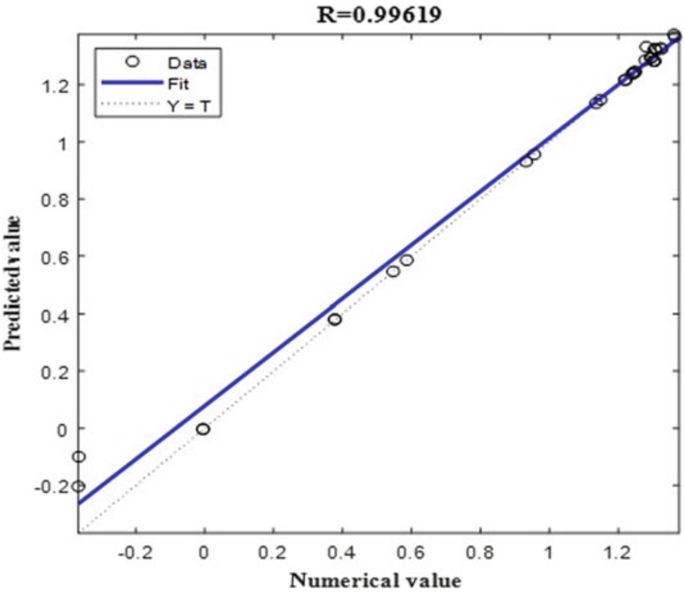

Fig. 16 Comparison between numerical and ANN predictions of $\phi'(0)$

- The presence of temperature-dependent coefficient $B1$ enhances the thermal boundary layer thickness for the heat generation $B1 > 0$ and reduces for the heat absorption $B1 < 0$. The exact opposite trend appears in the thickness of the concentration boundary layer for both heat source and heat sink cases.
- The diffusive species with high Soret number and low Dufour number tends to increase the thickness of the thermal and solutal boundary layer.
- The correlation coefficient R shows that the proposed ANN model provides better accuracy in the prediction of MHD convective nanofluid flow problems.
- A well-trained neuromorphic model could be an alternative and affordable way for numerical and experimental studies which may be time consuming and expensive.

Acknowledgements The authors thank the management of SSN College of Engineering for providing the necessary facilities to carry out the present work.

References

1. Sandeep N, Sulochana C (2016) MHD flow over a permeable stretching/shrinking sheet of a nanofluid with suction/injection. Alexandria Eng J 55:819–827
2. Prasannakumara BC, Gireesha BJ, Krishnamurthy MR, Ganesh Kumar K (2017) MHD flow and nonlinear radiative heat transfer of Sisko nanofluid over a nonlinear stretching sheet. Inform Med Unlocked 9:123–132

3. Sreekala B, Janardhan K, Ramya D, Shravani I (2017) MHD boundary layer nanofluid flow of heat transfer over a nonlinear stretching sheet presence of thermal Radiation and partial slip with suction. Global J Pure Appl Math 13(9):4927–4941
4. Shanmugapriya M (2018) Heat and mass transfer analysis of MHD stagnation point flow past an unsteady stretching sheet. Int J Mech Prod Eng Res Dev 8(7):577–584
5. Nandy SK, Mahapatra TR (2013) Effects of slip and heat generation/absorption on MHD stagnation flow of nanofluid past a stretching/shrinking surface with convective boundary conditions. Int J Heat Mass Transf 64:1091–1100
6. Ganga B, Mohamed Yusuff Ansari S, Vishnu Ganesh N, Abdul Hakeem AK (2016) MHD flow of Boungiorno model nanofluid over a vertical plate with internal heat generation/absorption. Propulsion Power Res 5(3):211–222
7. Sandeep N, Sulochana C (2016) Dual solutions of radiative MHD nanofluid flow over an exponentially stretching sheet with heat generation/absorption. Appl Nanosci 6(1):131–139
8. Sudarsana Reddy P, Chamkha AJ, Al-Mudhaf A (2017) MHD heat and mass transfer flow of a nanofluid over an inclined vertical porous plate with radiation and heat generation/absorption. Adv Powder Technol 28(3):1008–1017
9. Hamad MAA (2011) Analytical solution of natural convection flow of a nanofluid over a linearly stretching sheet in the presence of magnetic field. Int Commun Heat Mass Transf 38:487–492
10. Bilal Ashraf M, Hayat T, Alsaedi A, Shehzad SA (2015) Convective heat and mass transfer in MHD mixed convection flow of Jeffrey nanofluid over a radially stretching surface with thermal radiation. J Central South Univ 22:1114–1123
11. Pal D, Mandal G (2015) MHD convective stagnation-point flow of nanofluids over a non-isothermal stretching sheet with induced magnetic field. Meccanica 50:2023–2035
12. Nayak MK, Akbar NS, Tripathi D, Khan ZH, Pandey VS (2017) MHD 3D free convective flow of nanofluid over an exponentially stretching sheet with chemical reaction. Adv Powder Technol 28(9):2159–2166
13. Pal D, Mondal H (2011) MHD non-Darcian mixed convection heat and mass transfer over a non-linear stretching sheet with Soret-Dufour effects and chemical reaction. Int Commun Heat Mass Transf 38:463–467
14. Chamkha AJ, Rashad AM (2013) Unsteady heat and mass transfer by MHD mixed convection flow from a rotating vertical cone with chemical reaction and Soret and Dufour effects. Can J Chem Eng 92(4):758–767
15. Mohan Krishna P, Vidyasagar G, Sandeep N, Sugunamma V (2015) Soret and Dufour effects on MHD free convective flow over a permeable stretching surface with chemical reaction and heat source. Int J Sci Eng Res 6(9):143–147
16. Karthikeyan S, Bhuvaneswari M, Sivasankaran S, Rajan S (2016) Soret and Dufour effects on MHD mixed convection heat and mass transfer of a stagnation point flow towards a vertical plate in a porous medium with chemical reaction, radiation and heat generation. J Appl Fluid Mech 9(3):1447–1455
17. Sudarsana Reddy P, Chamkha AJ (2016) Soret and Dufour effects on MHD convective flow of Al_2O_3-water and TiO_2-water nanofluids past a stretching sheet in porous media with heat generation/absorption. Adv Powder Technol 27(4):1207–1218
18. Sreedevi G, Prasada Rao DRV, Makinde OD, Venkata Ramana Reddy G (2017) Soret and Dufour effects on MHD flow with heat and mass transfer past a permeable stretching sheet in presence of thermal radiation. Ind J Pure Appl Phys 55:551–563
19. Ziaei-Rad M, Saeedan M, Afshari E (2016) Simulation and prediction of MHD dissipative nanofluid flow on a permeable stretching surface using artificial neural network. Appl Therm Eng 99:373–382
20. Aminian A (2016) Predicting the effective thermal conductivity of nanofluids for intensification of heat transfer using artificial neural network. Powder Technol 301:288–309
21. Reddy PBA, Das R (2016) Estimation of MHD boundary layer slip flow over a permeable stretching cylinder in the presence of chemical reaction through numerical and ANN modeling. Eng Sci Technol Int J 19:1108–1116

22. Tafarroj MM, Mahian O, Kasaeian A, Sakamatapan K, Dalkilic AS, Wongwises S (2017) Artificial neural network modeling of nanofluid flow in a microchannel heat sink using experimental data. Int Commun Heat Mass Transf 86:25–31
23. Tripathy UK, Patel SM (2017) Solution of flow and heat transfer of an elastic-viscous liquid between two co-axial cylinders by artificial neural network. Int J Res Sci Innov 4(11):20–27
24. Maddah H, Ghasemi N (2017) Experimental evaluation of heat transfer efficiency of nanofluid in a double pipe heat exchanger and prediction of experimental results using artificial neural networks. Heat Mass Transf 53:3459–3472
25. Haykin S (2004) Neural networks: a comprehensive foundation, 2nd edn. MacMillan

Design of Macro-rough Surface and Its Influence on Side Wall Heated Square Enclosure

Ashwin Mahendra and Rajendran Senthil kumar

Abstract In the power electronics sector, silicon carbide devices are operational at high junction and case temperatures. Drastic reduction in the size of electronic components including heat sink has been achieved by using silicon carbide rather than silicon. Depending upon the application, the challenges in thermal management can be addressed, preferably passive cooling. If electronic components and its casing have higher operating temperatures, the analysis of natural convection in power electronics is more important. Hence, the present study elucidates the influence of macro-rough surface on natural convection. In this study, a square enclosure with and without macro-roughness have been modelled by maintaining top and bottom walls as adiabatic. The parameters varied are Rayleigh number, number of roughness elements and its thickness. The fluid flow and heat transfer characteristics have been explained with the help of velocity and temperature contours. From the results obtained, we have concluded that the increase in roughness elements and its thickness have reduced convection near the roughness elements.

Keywords Natural convection · Laminar flow · Enclosures · Macro-roughness elements

1 Introduction

Natural convection inside cavities or enclosures has received immense attention by researchers like Ostarch et al. [1] owing to its plethora of applications in different areas like electronic equipment, solar collectors, nuclear reactors, energy storage, fire control, etc. The buoyancy-driven flows and heat transfer taking place inside these enclosures were the basis of most studies. The fluid layer which is closest to the wall is stationary compared to the successive layers, and hence, heat transfer here takes place by conduction. For the layers in motion, convection is responsible for heat transfer. The heated fluid experiences a decrease in its density. The lighter fluid then

A. Mahendra · R. S. kumar (✉)
Department of Mechanical Engineering, SRMIST, Chennai, India
e-mail: senthilr2@srmist.edu.in

E. T. Akinlabi et al. (eds.), *Trends in Mechanical and Biomedical Design*, Lecture Notes in Mechanical Engineering,
https://doi.org/10.1007/978-981-15-4488-0_37

moves upwards, and as its temperature decreases, it moves downwards resulting in the recirculation of fluid inside the enclosure. Advancements in the study involved the attachment of projections or roughness elements on either wall to modify the average Nusselt number variation in the enclosure [2–8]. The flow physics and transfer of heat within the enclosure are interesting and also need to be well understood. Hence, the present study computes the influence of macro-rough surface in heat dissipation.

2 Literature Survey

Buoyancy-driven convection inside enclosures with heated and cooled walls has been the basic model in various industrial applications as explained by Ostarch et al. [1]. In many studies, the phenomenon was analysed inside square enclosures by De Vahl Davis [9], Nag et al. [2], Shi and Khodadadi [3] and Elatar et al. [4]. De Vahl Davis has done a benchmark study for natural convection inside square cavities by comparing the results obtained by various researchers. Later, researchers introduced roughness elements into the geometry. These roughness elements increase the surface area available for transfer of heat. Nag et al. [2] studied square cavity with a single plate on the hot vertical wall to study natural convection inside and concluded that the colder wall has Nusselt number greater than no fin model. Bilgen [5] studied a similar model in which the partition was fixed on the horizontal adiabatic wall. He claimed that heat transfer reduced if double partitions were introduced. Also, decreasing the aspect ratio or moving the partition farther away from the hot wall reduced heat transfer. Bilgen [6] studied the influence of a thin fin on hot wall on natural convection in square cavity. Based on his findings, as the fin length increases, the Nusselt number decreases. Elatar et al. [4] has done a similar study with a thick wall instead of a thin wall and concluded that the thickness of fin has minimal to no effect on the rate of heat transfer for $R_k = 10$–1000. The increasing conductivity ratio improves heat transfer ($10 \leq R_k \leq 1000$). Dindarloo et al. [7] carried out a study of the effect of fin thickness and groove depth on the fin attached to the hot wall to reduce the heat transfer. His results conclude that the optimal fin length decreases with increasing conductivity ratio. Also, a thick fin with grooves reduces transfer of heat than a straight fin. Hasnaoui et al. [8] studied the natural convection inside rectangular enclosures with adiabatic roughness elements on the heated wall. His findings show that for tall cavities having roughness elements with a dimensionless fin length of 25 and 50%, the heat transfer takes place by conduction alone. The present survey has demonstrated the scope for a parametric study based on an increasing number of roughness elements and fin thickness.

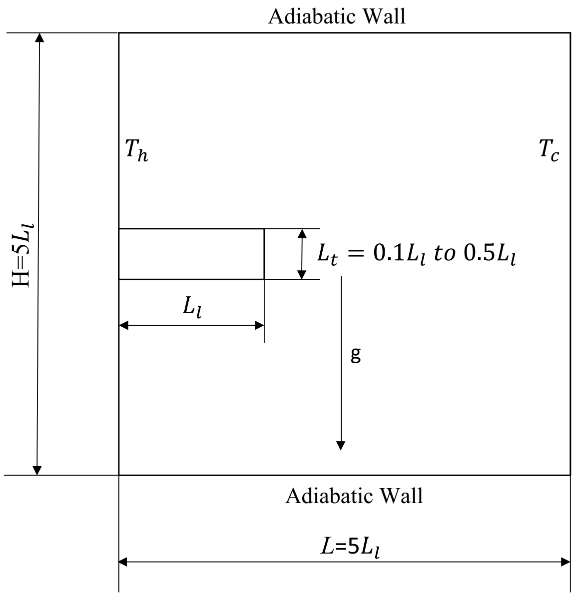

Fig. 1 Schematic representation of the given problem

3 Problem Statement

A two-dimensional square enclosure is modelled for simulation. The left wall is kept at a constant temperature (T_h) greater than that at the right wall (T_c), and both the horizontal (top and bottom) walls are adiabatic (insulated). The length of a side of the enclosure is (H). Roughness elements of different thicknesses are introduced on the left wall. The number of roughness elements ranges from 1 to 9, and the length (L_f) of the roughness element is fixed at 20% of wall length. The boundary conditions of the roughness elements are fixed to be the same as that of the left wall. The Prandtl number is 0.71. The fluid inside the enclosure is incompressible and obeys Boussinesq approximation. The simulation was done for Rayleigh numbers ranging from 10^3 to 10^6 (Fig. 1).

4 Governing Equations, Boundary Conditions and Solution Procedure

The dimensionless form of governing equations is obtained by introducing the following terms into the traditional equation:

$$X = \frac{x}{L_l}, Y = \frac{y}{L_l}, U = \frac{uL_l}{\alpha}, V = \frac{vL_l}{\alpha}$$

$$P = \frac{pL_l^2}{\rho\alpha^2}, \quad \theta = \frac{(T - T_c)}{(T_h - T_c)} \tag{1}$$

where the velocities in the x and y directions are denoted by 'u' and 'v', respectively, and temperature by 'T'. 'P' stands for reduced pressure. 'ρ' denotes the density, and α denotes the thermal diffusivity of the fluid.

On introducing these terms into the continuity and momentum equations and also incorporating Boussinesq approximation, we obtain the final equations as seen in the study by Elatar et al. [4]:

$$\frac{\partial U}{\partial X} + \frac{\partial V}{\partial Y} = 0, \tag{2}$$

$$U\frac{\partial U}{\partial X} + V\frac{\partial U}{\partial Y} = \Pr\left(\frac{\partial^2 U}{\partial X^2} + \frac{\partial^2 U}{\partial Y^2}\right) - \frac{\partial P}{\partial X} \tag{3}$$

$$V\frac{\partial V}{\partial X} + V\frac{\partial V}{\partial Y} = \Pr\left(\frac{\partial^2 V}{\partial X^2} + \frac{\partial^2 V}{\partial Y^2}\right) - \frac{\partial P}{\partial Y} + \mathrm{Ra} * \Pr * \theta, \tag{4}$$

$$U\frac{\partial \theta}{\partial X} + V\frac{\partial \theta}{\partial Y} = \frac{\partial^2 \theta}{\partial X^2} + \frac{\partial^2 \theta}{\partial Y^2} \tag{5}$$

$$\mathrm{Ra} = \frac{g\beta(T_h - T_c)L^3}{v\alpha}, \Pr = \frac{v}{\alpha} \tag{6}$$

Ra = Rayleigh number and Pr = Prandtl number.

where kinematic viscosity and thermal expansion coefficient of the fluid are denoted by v and β, respectively.

The boundary conditions for the given model are as follows

On the left wall, $U = 0$, $V = 0$ and $\Theta = 1$
On the right wall, $U = 0$, $V = 0$ and $\Theta = 0$
On the top and bottom wall, $U = 0$, $V = 0$ and $\frac{d\theta}{dY} = 0$.
On the roughness elements, $U = 0$, $V = 0$ and $\Theta = \theta_w$

where θ_w is the temperature of the respective wall.

The problem was modelled and meshed using ANSYS Workbench, and the simulations were carried out using ANSYS Fluent-18. The convergence criteria for the continuity residual are set as 1.E−06. The Boussinesq approximation is used for fluid density variation at various temperatures.

5 Grid Independence

The optimum grid size was determined in the grid independence study carried out by Shi and Khodadadi [3]. A grid size of 120 × 120 was seen to provide the most

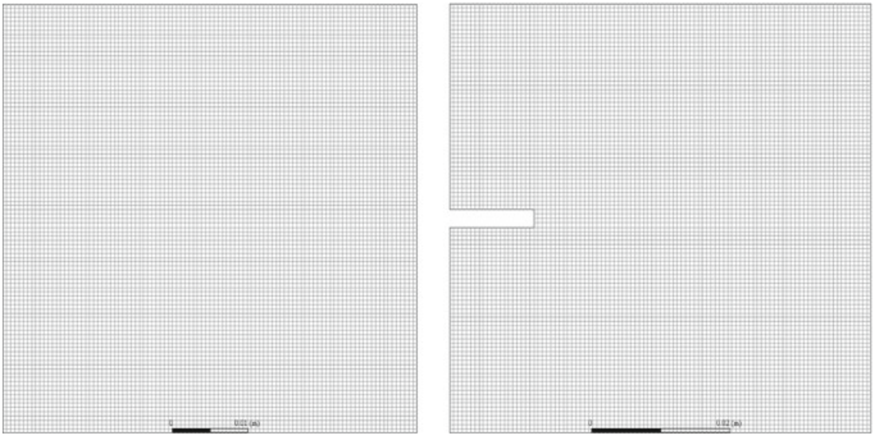

(a) Plain Enclosure (b) Enclosure with projections

Fig. 2 Computational domain with meshing

accurate results. The same has been adopted in this paper, and the results of the simulation have been validated with their results as can be seen in further sections of this paper (Fig. 2).

6 Results and Discussion

6.1 Validation of Computation

A total of 84 cases were simulated to analyse the heat transfer and flow characteristics of the problem. This involved studying the effect of macro-roughness on the hot wall (0, 1, 3, 5, 7 and 9 roughness elements) at different thicknesses (2, 4 and 10%). The Rayleigh number ranges from 10^3 to 10^6. The element's length was fixed at 20% of the wall's length. The present computational results have been validated with the literature by De Vahl Davis [9], Nag et al. [2], Shi and Khodadadi [3] and Elatar et al. [4].

Table 1 explains the accuracy of the present study by comparing the average Nusselt number obtained on the cold wall at different Rayleigh numbers with previous studies. It shows that the maximum variation is 3.2% for Ra = 10^3 1.6% for Ra = 10^4, 3.9% for Ra = 10^5 and 3% for Ra = 10^6 which are all within the acceptable limits.

Furthermore, the average Nusselts number was validated with that of Nag et al. [2] for square enclosure with a thick fin attached to the vertical hot wall as tabulated in Table 2. The fin length (L_l) is fixed at 0.2, and the dimensionless conductivity ratio

Table 1 Nusselt number validation on hot or cold wall

Ra	10^3	10^4	10^5	10^6
De Vahl Davis [9]	1.118	2.243	4.519	8.800
Nag et al. [2]	–	2.240	4.510	8.820
Shi and Khodadadi [3]	–	2.247	4.532	8.893
Elatar et al. [4]	–	2.234	4.517	8.948
Present	1.154	2.210	4.686	8.679

Table 2 Validation of Nusselt number obtained for different non-dimensional thicknesses at Ra = 10^6

Non-dimensional thickness	0.02	0.04	0.1
Nag et al. [2]	8.861	8.888	9.033
Present	9.110	9.160	9.394

(R_k) is 7750. The table shows that the maximum variation is 3.9% for a thickness of 10%, and hence, the accuracy of the program holds well for further studies.

6.2 Velocity and Temperature Contours

The velocity profiles and isotherms have been presented for increasing Rayleigh numbers in enclosures without any roughness element in Fig. 3. The figure explains the improvement in motion due to the increase in Rayleigh number. The velocity magnitude was seen to increase from 0.00182 ms^{-1} for Ra $= 10^3$ to 0.285 ms^{-1} for Ra $= 10^6$. As density decreases, the fluid along hot wall rises, and as density increases, the fluid along cold wall falls. This results in the formation of a clockwise vortex in the enclosure. For lower Rayleigh number, the boundary layer influence is more leading to the formation of eddies. This is due to the interaction of the fluid subjected to vortex flow and the fluid under the influence of boundary flow. As the Rayleigh number increases, this interaction is seen to decrease, and the eddies are suppressed and confined near the thermal walls. With the increase in temperature, the viscosity decreases, thereby reducing the boundary layer influence. At Ra $=$ 10^6, the velocity is maximum, and the effect of the boundary layer is overshadowed by the vorticity. All the cases are seen to be unicellular, but for lower Ra values, the vorticity is not uniform and the shape is distorted. But, at Ra $= 10^6$, uniform unicellular vorticity is generated. The temperature contours capture the flow guided heat transfer data as shown with the isotherms being densely packed near the walls at Ra $= 10^5$. As the vorticity increases, the bulk fluid mixing increases which aid in improving convection.

Figure 4 shows a comparison of the enclosure with nine roughness elements for all four Ra values. For low Ra values, the velocity contours follow the same pattern as that of the plain enclosure. As the Rayleigh number increases, the eddies are

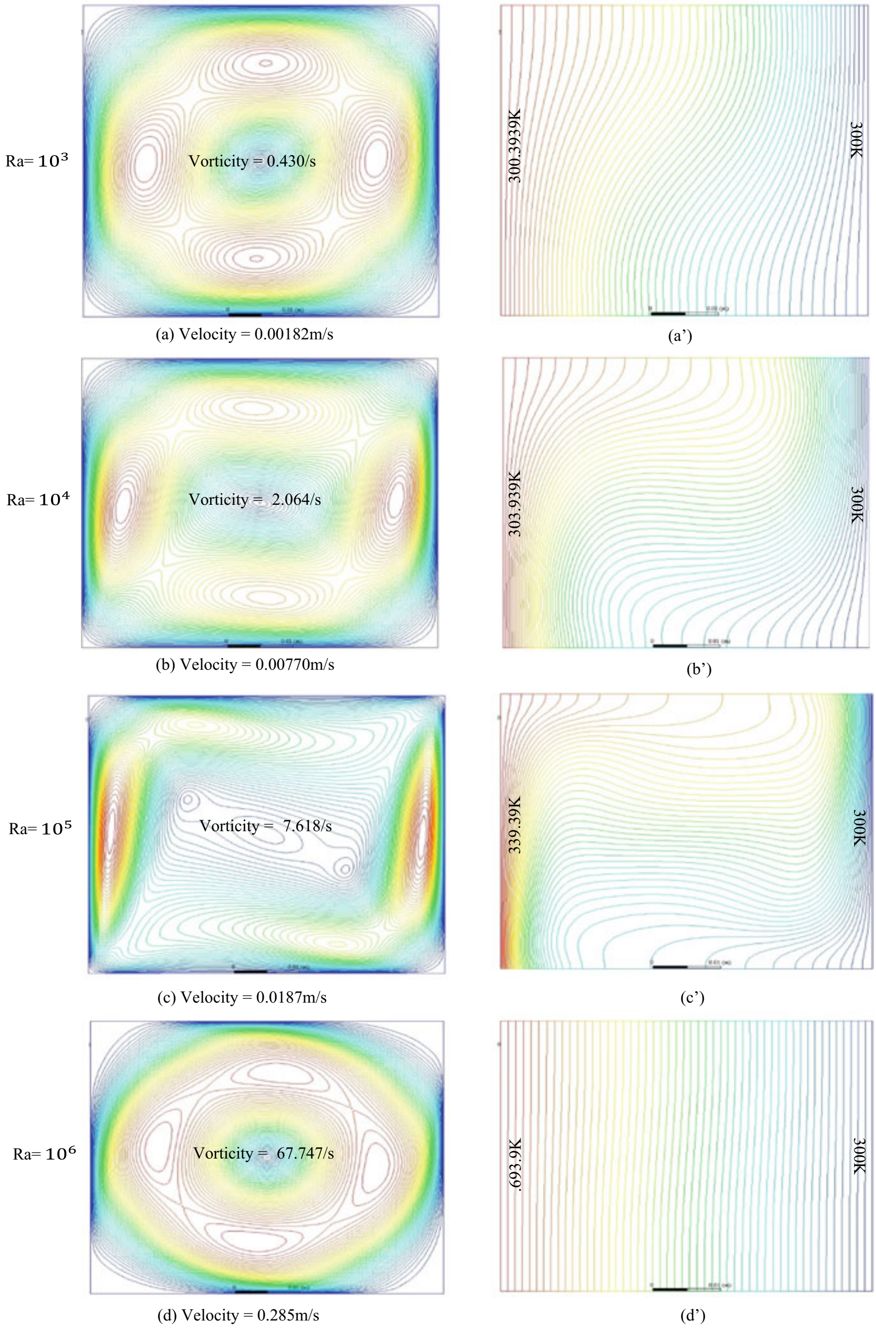

Fig. 3 Velocity and temperature contours for plain enclosures at different Ra values

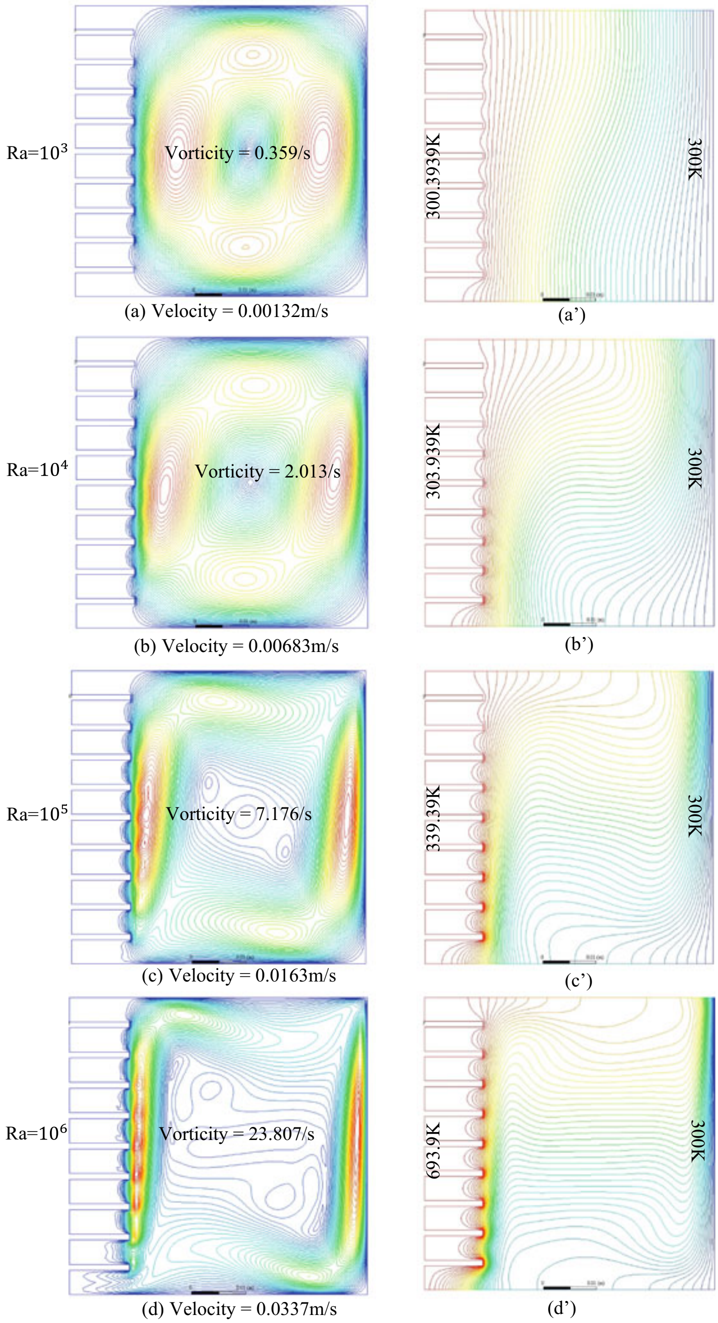

Fig. 4 Velocity and temperature contours for nine-finned enclosure at different Ra values

suppressed. But, for Ra $= 10^6$ a uniform vortex as seen in the plain enclosure cannot be obtained. Due to the resistance offered by the roughness elements to fluid flow, the vorticity is still in the transition phase, and the effect of eddies are not suppressed completely. Also, the fluid starts to penetrate between the lower roughness elements as the Rayleigh number increases, due to momentum which affects the flow. The related heat transfer data has been captured in the temperature contours as shown. It is inferred that the isotherms become more packed as the Ra value increases, especially near the cold wall where the thermal boundary layer becomes denser and also below the lowest roughness element. Therefore, increasing the Rayleigh number increases the isotherm density in these regions.

Figure 5 clearly visualizes the fluid flow at Ra $= 10^6$. The velocity contours have been captured for enclosures with an increasing macro-roughness elements. Here, the flow physics have been captured between the roughness elements unlike the cases with lower Ra values. The case shows the circulation of fluid between the roughness elements which is seen to decrease with increasing number of roughness elements. Therefore, as the roughness increases, the stagnation of fluid within the roughness elements increases resulting in the reduction of convection in the region. The roughness elements also resist the flow inside the enclosure. The sharp edges of the roughness elements lead to the local recirculation of the fluid in the region. Hence, convection is enhanced at the roughness element's tip. This is clearly captured in the temperature contours as well. The isotherms show that the isotherm density between the roughness elements decreases with increasing roughness. This explains the prevalence of conduction in these regions over convection. The fluid gets stagnant here due to the flow restriction offered by the roughness elements resulting in reduced convection here.

Table 3 illustrates the average Nusselt number in a square enclosure at different walls with increasing macro-roughness on the hotter wall. It shows that the increase in macro-roughness reduces the hot wall Nusselt number, and hence, convection is reduced. This can be explained by the stagnation of fluid in the region between the roughness elements. Hence, heat transfer here takes place predominantly by conduction.

Figure 6 shows the velocity contours for an enclosure with five roughness elements for different thicknesses at different Rayleigh numbers. The figure shows that for a given Ra value, the penetration of the fluid between the roughness elements reduces as the thickness increases. For minimum thickness, the sharp tip induces local recirculation of fluid, thus enabling it to partially enter the region between the roughness elements. For higher Ra values, as the velocity of the fluid increases, the high momentum flow allows recirculation in the regions between lower roughness elements. In the successive roughness elements, local recirculation prevails. As the thickness increases, the local recirculation decreases. Thus, convection is adversely affected. But, the comparative increase in surface area available for convection compensates this decrease.

Figure 7 plots the Nusselt number for different thicknesses in a square enclosure with a single roughness element with respect to the Rayleigh number. It shows that though the variations are minor, the Nusselt number increases with thickness owing

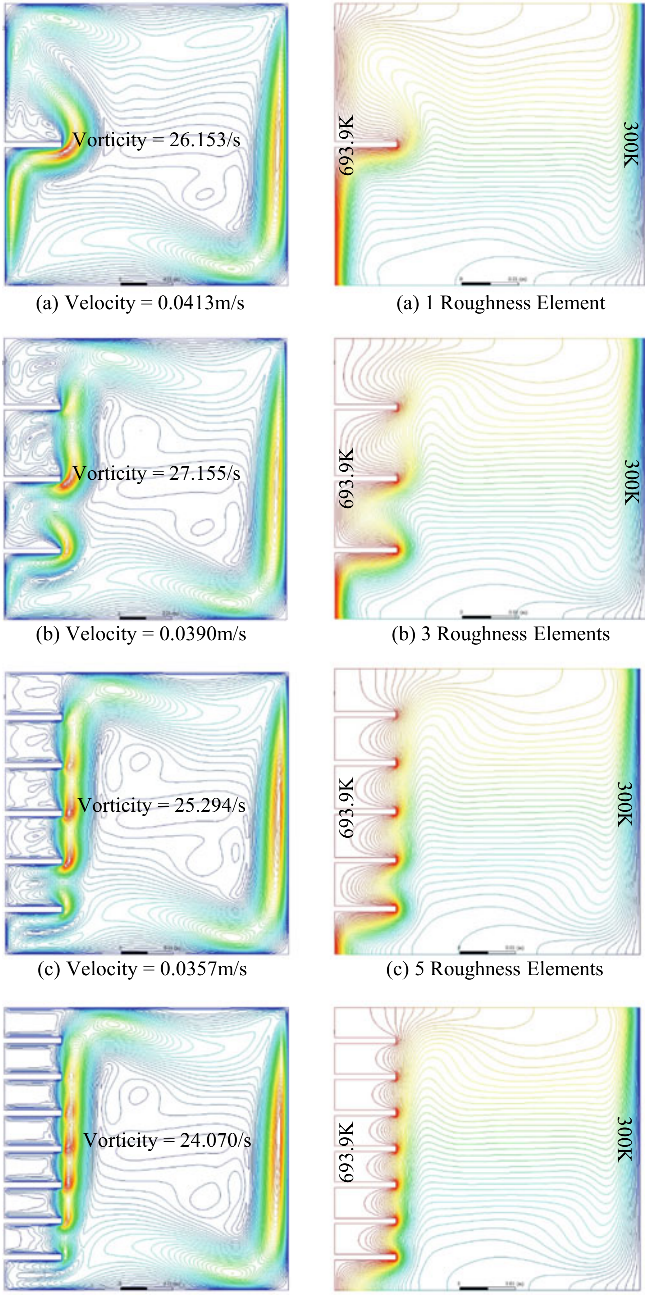

(a) Velocity = 0.0413m/s (a) 1 Roughness Element

(b) Velocity = 0.0390m/s (b) 3 Roughness Elements

(c) Velocity = 0.0357m/s (c) 5 Roughness Elements

(d) Velocity = 0.0352m/s (d) 7 Roughness Elements

Fig. 5 Velocity and temperature contours for an increasing number of roughness elements at Ra $= 10^6$

Table 3 Nusselt number values for different walls in the enclosure with different number of roughness elements at Ra = 10^6

Present	Cold wall	Hot wall	Fin wall
No roughness element	8.678	8.678	–
1 roughness element	9.110	7.376	4.496
3 roughness elements	8.716	3.899	4.008
5 roughness elements	8.550	1.512	3.424
7 roughness elements	8.637	0.362	2.832
9 roughness elements	8.762	0.075	2.302

to an increase in the overall surface area available for heat transfer, thereby improving convection.

Figure 8 shows the variations in Nu with respect to Ra. The graph on the left denotes the Nu on the hot wall and the one on the left denotes the Nu on the cold wall. The Nusselt number decreases on both the walls as the macro-roughness increases, but the decrease is more significant on the hot wall. As the number of roughness elements increases, the stagnation of fluid between the roughness elements (Fig. 5) and along the hot wall also increases resulting in transfer of heat by conduction. The introduction of roughness elements has seen to disrupt the vortex circulation strength.

7 Conclusion

The flow and heat transfer within the square enclosure by keeping adiabatic horizontal walls with and without macro-roughness elements have been studied for different Rayleigh numbers (10^3, 10^4, 10^5, 10^6) under laminar flow conditions. The velocity and temperature contours expose fluid flow behaviour and transfer of heat within the cavity and also the following have been concluded.

1. As the Rayleigh number increases, the average Nusselt number on the wall also increases. This is because, the Nusselt number increase improves the movement of fluid inside the enclosure, thereby enhancing convection.
2. As the thickness of roughness elements increases, the average Nusselt number on the cold wall increases. This can be understood by the increase in surface area of the roughness elements as the thickness increases. The fluid, therefore, has a greater area to interact with the roughness elements, and hence, convection is improved.
3. The convection near macro-roughness elements improves with increase in its thickness and weakens with increasing roughness elements.
4. Increasing the roughness elements for the given Ra, increases the Nusselt number owing to reasons similar as above.

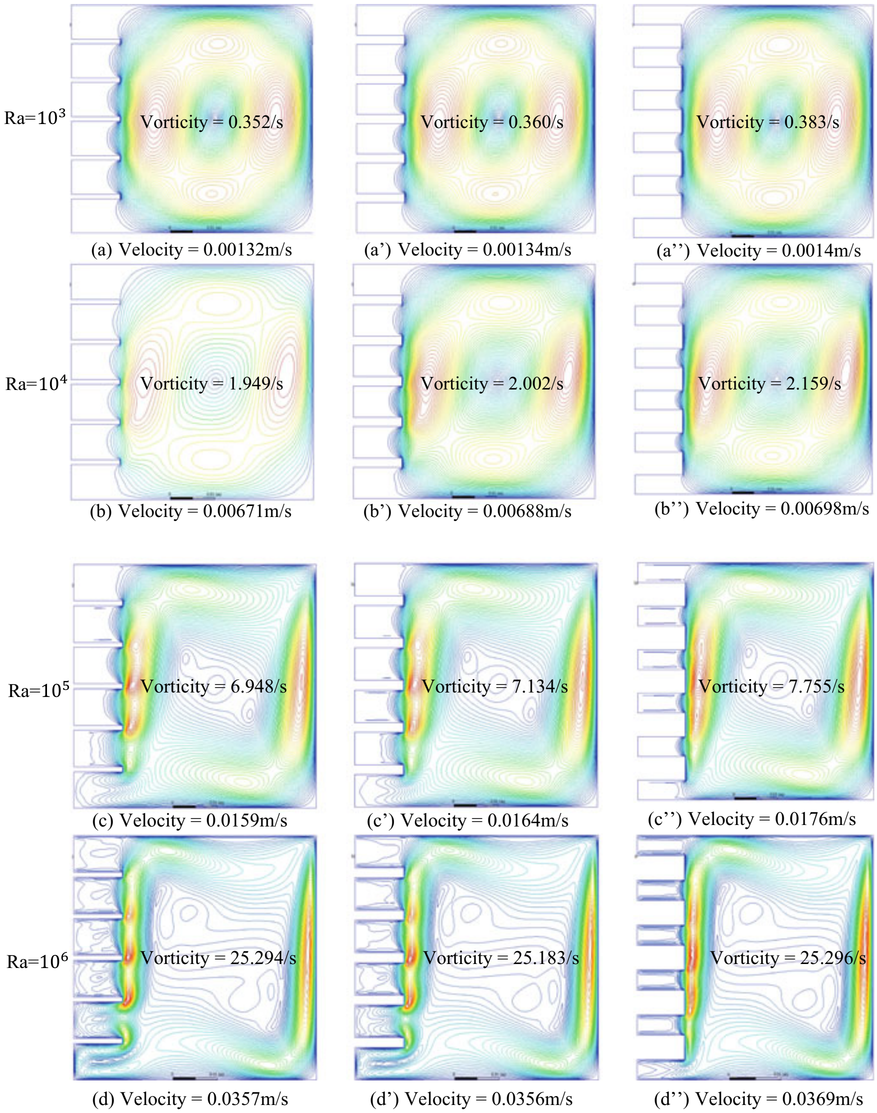

Fig. 6 Velocity contours of an enclosure with five roughness elements for different thicknesses at different Ra values

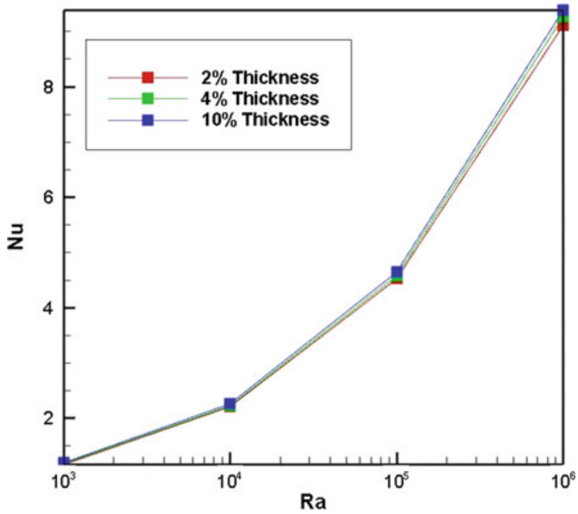

Fig. 7 Variation of Nusselt number in one roughness element enclosure with different thicknesses with Ra

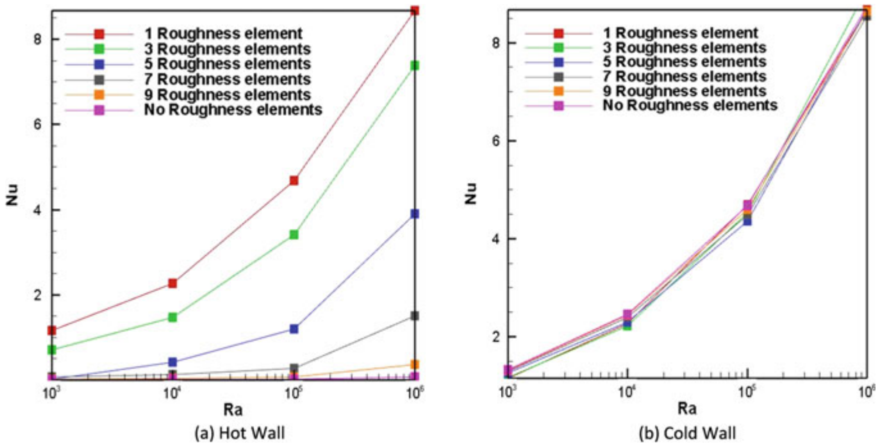

Fig. 8 Variation of Nusselt number in a cavity with different number of roughness elements with Ra

Acknowledgements We would like to thank the product development laboratory authorities and SRM Institute of Science and Technology for providing us with the resources to make this possible. We would also take this opportunity to thank SSN College of Engineering for providing us with a platform to present our ideas and findings.

References

1. Ostrach S (1988) Natural convection in enclosures. ASME J Heat Transf 110:1175–1190
2. Nag A, Sarkar A, Sastri VMK (1994) Effect of thick horizontal partial partition attached to one of the active walls of a differentially heated square cavity. Numer Heat Transf Part A:611–625
3. Shi X, Khodadadi JM (2002) Laminar fluid flow and heat transfer in a lid-driven cavity due to a thin fin. ASME J Heat Transf 124:1056–1063
4. Elatar A, Teamah MA, Hassab MA (2016) Numerical study of laminar natural convection inside square enclosure with single horizontal fin. Int J Therm Sci 99:41–51
5. Bilgen E (2002) Natural convection in enclosures with partial partitions. Renew Energy 26:257–270
6. Bilgen E (2005) Natural convection in cavities with a thin fin on the hot wall. Int J Heat Mass Transf 48:3493–3505
7. Rafie Dindarloo M, Payan S (2019) Effect of fin thickness, grooves depth, and fin attachment angle to the hot wall on maximum heat transfer reduction in a square enclosure. Int J Thermal Sci 136:473–490
8. Hasnaoui M, Vasseur P, Bilgen E (1992) Natural convection in rectangular enclosures with adiabatic fins attached on the heated wall. Warme- und Stoffubertragung 27:357–368
9. De Vahl Davis G (1983) Natural convection of air in a square cavity: a bench mark numerical solution. Int J Numer Methods Fluids 3:249–264

Performance Enhancement of a Savonius Vertical Axis Wind Turbine with Bio-Inspired Design Modifications

S. M. Hasan Fayaz, Uditya Tyagi, Apurva Jain, and Nishant Mishra

Abstract One of the prime commodities in modern civilization is energy. The amount of energy consumption has become the indicator for the standard of living and the degree of industrialization. People use fossil fuels to meet nearly all of their energy needs, such as powering vehicles, producing electricity for light and heat and running factories, thus greatly exhausting the fossil fuel reserves along with polluting the environment with greenhouse gases. Renewable energy sources are viable alternatives, and among the various types of renewable energy sources available, wind energy is the sector which has a lot of untapped potential. Our objective is to improve the efficiency of a Savonius-type vertical-axis wind turbine (VAWT) which currently has the least efficiency among existing wind turbine designs. Savonius turbines have a very compact structure and can run at low wind speeds which are desirable characteristics for commercial-scale power production. This research paper focuses on improving the efficiency of Savonius wind turbine. Since Savonius-type wind turbines are drag-based wind turbines, we need to reduce the impulsive force acting on the negative face in order to increase the drag difference between the positive and negative side of the rotor blades thereby improving the efficiency of the turbine. Our proposition for attaining higher efficiency is by incorporating the concept of dimples (inspired from golf ball) on the negative side of the rotor blade and tubercles (inspired from whales) on the leading edge of the rotor blade. Dimples reduce the amount of wake region in the case of golf ball by increasing turbulence which is one of the desirable characteristics in the case of Savonius wind turbine. Tubercles help in reducing the wake region behind the rotor blades by increasing the turbulence of air near the surface of the rotor thereby improving the efficiency of the turbine.

Keywords VAWT · Savonius · Drag based · Dimples · Tubercles · Wake region

S. M. Hasan Fayaz · U. Tyagi · A. Jain · N. Mishra (✉)
Shiv Nadar University, Greater Noida, India
e-mail: nishant.mishra@snu.edu.in

E. T. Akinlabi et al. (eds.), *Trends in Mechanical and Biomedical Design*,
Lecture Notes in Mechanical Engineering,
https://doi.org/10.1007/978-981-15-4488-0_38

Nomenclature

VAWT	Vertical-axis wind turbines
P_{ω}	Total wind power available
P_{o}	Power output by the wind turbine
C_{p}	Coefficient of power
A	Swept area of the turbine
ω	Angular velocity of turbine in rad/sec
ρ	Density of the air
λ	Tip-speed ratio
R	Radius of the turbine
H	Height of turbine
D	Diameter of the turbine
rpm	Turbine speed in revolutions per minute
d	Diameter of turbine blades

1 Introduction

Power production in an efficient way without affecting the environment has been a growing concern around the globe. Various means of eco-friendly methods of power production have been devised. Some of the eco-friendly means of power production are harnessing solar energy, wind energy, hydro power, biomass, etc. Wind energy is a field having a lot of scope for improvement of efficiency. Wind power is also one of the most economical sources of renewable energy, land-based utility-scale wind power is the most economical source of renewable energy as on date [1, 2]. Wind is an environment-friendly source of energy that has got huge potential to satisfy energy needs for people and also to mitigate the climate change from greenhouse gases emitted by the burning of fossil fuels.

Wind turbines can be classified into two types based on the orientation of the shaft connecting the turbine with the generator, namely horizontal-axis wind turbine (HAWT) and vertical-axis wind turbine (VAWT). Most of the commercial-scale power produced by tapping wind energy is based on horizontal-axis wind turbine technology. The horizontal-axis wind turbines are more efficient as compared to that of vertical-axis wind turbines [3]. HAWT has an efficiency range of 35–45%, whereas VAWT has a comparatively lower efficiency. VAWT has a greater scope of improvement with respect to its design and material in order to increase its efficiency, so that it can be used for commercial-scale power production. VAWT rotors have different types, such as Savonius rotor and (eggbeater) Darrieus, or H-Darrieus rotor, out of which Savonius is the turbine with least efficiency. Savonius turbines have a very compact structure and can run at low wind speeds which are desirable characteristics for commercial-scale power production. As a main target application, optimized Savonius wind turbines would be perfectly suited for electricity production at the level of individual buildings with a flat roof or for commercial-scale power productions on both onshore and offshore platforms.

The objective is to increase the efficiency of the Savonius-type vertical-axis wind turbine by introducing and assessing the effect of arrays of dimples and tubercles. It has been proven that dimple structures on a golf ball reduce drag on the surface enabling it to cover longer flight distance [4–6]. The magnitude of drag force on a moving ball is largely affected by the size of wake region behind the moving ball. Decreasing the wake region by increasing turbulence on the surface of the ball which in turn delays the separation of air from the ball leads to an increase in total pressure behind the ball. Therefore, the pressure difference between the front of the ball and behind the ball will decrease resulting in decrease of drag force constituted by air. These researches provided us with key insights into the analysis of the dimples and also led to contemplate that if the same concept can be applied to reduce the drag on the negative blade of the Savonius turbine. Spherical dimples were created on the negative surface and the turbine's performance was compared with and without the use of dimples. Tubercles were introduced as a design modification in order to reduce the negative torque acting on the wind turbine. Concept of tubercles was inspired from the whales wherein tubercles are used to increase lift thereby helping them to manoeuvre through steep climbs.

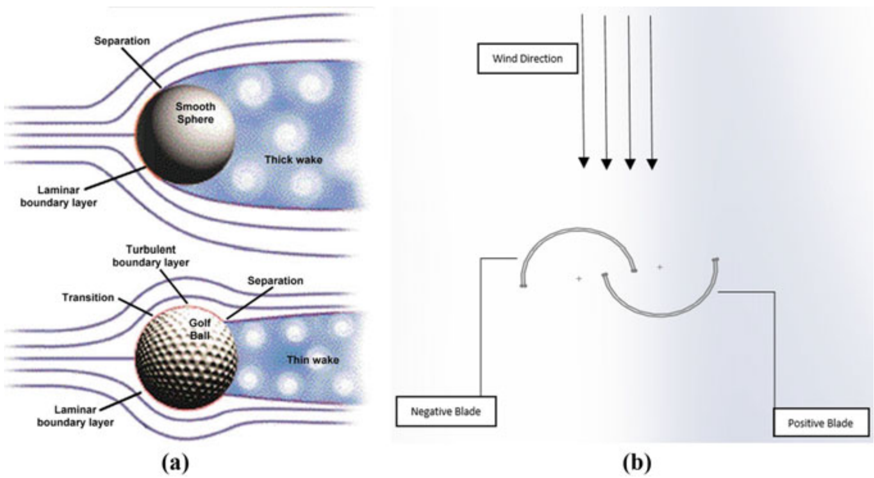

Fig. 1 **a** Comparing golf ball and normal ball [6], **b** blades of Savonius turbine

2 Methodology

2.1 CAD Model

Once the design parameters were decided, CAD models of the two configurations of the Savonius wind turbine were made using SolidWorks. Individual components were made and were assembled in order to design the two-stage Savonius turbine. The dimensions of rotor blades were determined by the aspect ratio chosen according to the literature survey [7–10]. Rotor blades were made (using extrude option), and dimpling was done according to requirement (using the revolved cut tool). Continuous triangular tubercles of base 10 mm were made using linear pattern.

Dimensions of the two-stage turbine are:

End plate thickness = 4 mm
End plate diameter = 152 mm
Rotor inner diameter = 75 mm
Rotor outer diameter = 85 mm
Rotor length = 120 mm
Overlap length, e = 13.5 mm
Dimple diameter = 4 mm
Dimple depth = 1.5 mm
Number of dimple columns = 13
Number of dimple rows = 11
Base length of tubercles (isosceles triangle) = 10 mm
Number of tubercles = 11 (Fig. 2).

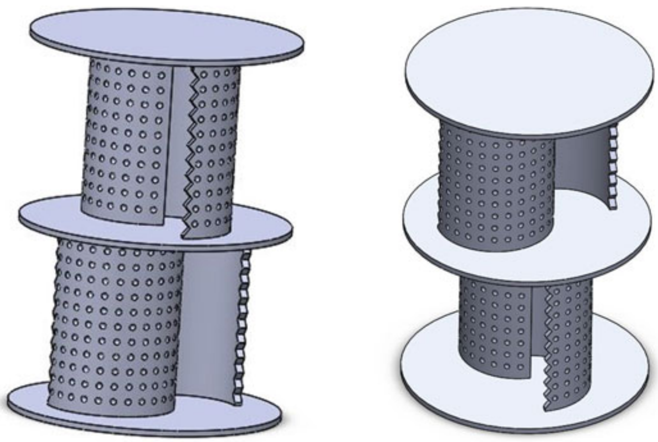

Fig. 2 CAD models of Savonius wind turbine with dimple and tubercle

2.2 3D Printing and Assembling the Rotor Blades

The final models of two different types of rotor blades (with and without dimples and tubercles) were printed using a 3D printer. The specifications of the printing process are:

Nozzle diameter = 0.4 mm
Fill density = 100%
Fill rate = 100
Platform adhesion type = Brim
Print temperature = 210 °C.

The printed blades were assembled according to the overlap ratio chosen from the literature survey [7–10]. The rotor blades were assembled with the end plates using bondtite. Both types of turbines were assembled as a two-stage turbine with a phase difference of 90° which was observed from the literature review [11, 12].

2.3 Experimental Set-Up

The experiment comprises of two different models, namely:

1. Double stage plain turbine (smooth)
2. Double stage turbine with dimples and tubercles.

The experimental study basically comprises of observation and comparison of the exit wind speed, rpm of the turbine and the power generated by the two different turbines. The wind speed is measured using an anemometer by placing it at various points on the path traced by the wind entering the turbine. Tachometer is used to measure the rpm of the turbine and the power generated by the turbine can be observed from the multimeter connected to the generator terminals.

The schematic diagram of the test rig used for the experimental study is shown in Fig 3.

3 Mathematical Formulations

Maximum amount of power, P, that can be harnessed from wind in an ideal case is

$$P_{\omega} = \frac{\rho \times A \times V^3}{2} \tag{1}$$

where

ρ = density of the air

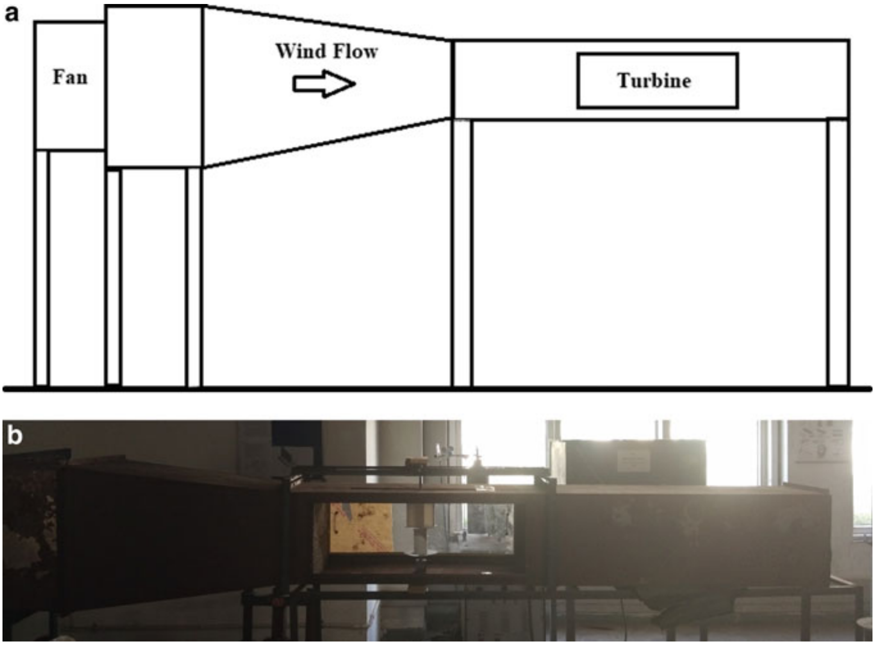

Fig. 3 **a** Schematic diagram of test rig (above), **b** wind tunnel (below)

A = swept area of the turbine
V = wind speed.

According to Betz law, the amount of kinetic energy of the wind that can be harnessed for power production can never exceed 59.3%. Power coefficient C_p is defined as the ratio of the cumulative power output P_o by a wind turbine to the total power P_ω available to the wind turbine

$$C_\mathrm{p} = \frac{P_\mathrm{o}}{P_\omega} \tag{2}$$

So, no more than 59% of the energy carried by wind can be extracted by a wind turbine. The value of C_p is unique for each turbine. Value of C_p varies based on factors like strength of the turbine, weight of the turbine, friction involved due to generator and gearbox, surrounding air conditions, etc. Therefore, maximum power that can be extracted from the wind turbine considering the aerodynamic constraints can be found by the equation

$$P_\omega = \frac{\rho \times C_\mathrm{p} \times A \times V^3}{2} \tag{3}$$

C_p also varies with respect to the rotational speeds of the turbine. Hence, C_p is a function of tip-speed ratio (TSR) λ as well, which is defined as

$$\lambda = \frac{\text{Tip Speed of the Blade}}{\text{Wind Speed}} \tag{4}$$

$$\lambda = \frac{\omega \times R}{V} \tag{5}$$

Power output P_o can be found experimentally using,

$$P_o = T \times \omega \tag{6}$$

Here,

$T =$ mechanical torque
$\omega =$ angular velocity of the rotor blades.

$$\omega = \frac{2\pi N}{60} \tag{7}$$

Here,

$\omega =$ rotational velocity of the turbine
$R =$ turbine radius
$V =$ wind Speed
$N =$ RPM of turbine.

4 Comparison Between Savonius Wind Turbines with and Without Modifications (Dimples and Tubercles)

The following data were recorded during the experiment performed on the plain and modified wind turbine: (Figs. 4 and 5).

5 Conclusion

In this experimental publication, the concepts of dimples and tubercles have been introduced on an existing design of Savonius wind turbine. Plain turbine and the modified turbines were tested under the same wind speed in a wind tunnel, and the results were compared.

Following can be concluded from the experimental results:

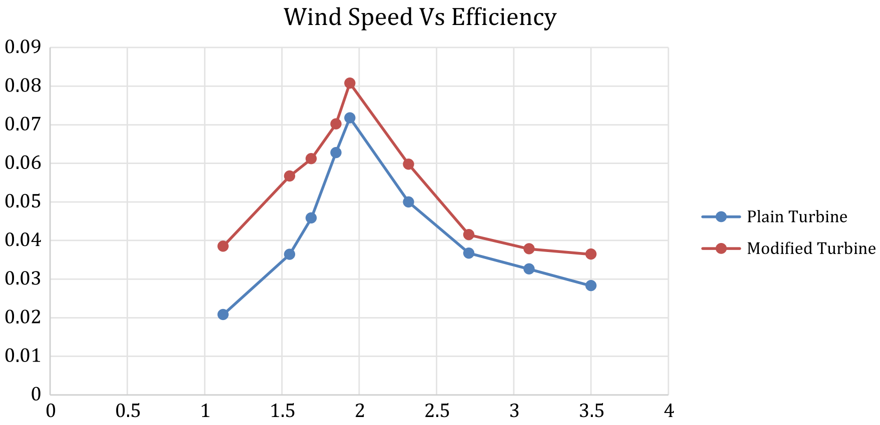

Fig. 4 Variation in efficiency with wind speed for turbines with and without design modifications

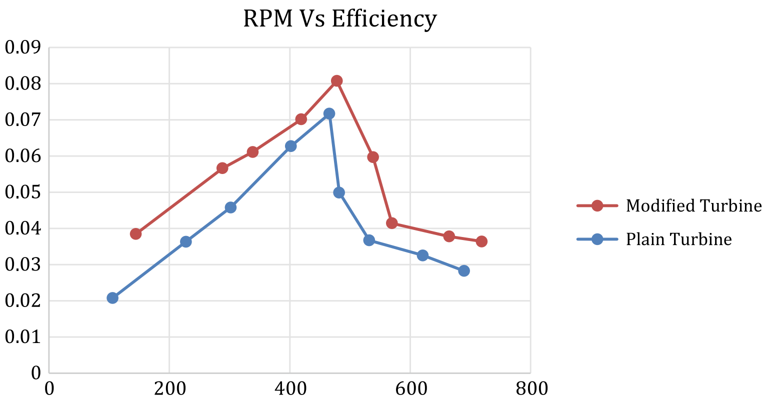

Fig. 5 Variation in efficiency with rpm for turbines with and without design modifications

It can be observed that the modified turbine (with dimples and tubercles) generates more power at the same wind speed as compared to the plain turbine.

Acknowledgements The authors would like to thank the laboratory assistants, Sanjay Singh, Amit Kumar, Sunil Gupta and Vishal Gaur for their assistance in establishing the experimental rig. Authors would also thank Shiv Nadar University for their support in carrying out the experiment.

References

1. Power Technology, https://www.power-technology.com/features/cheapest-renewable-energy-sources/. Last accessed 13 Feb 2019

2. OIL PRICE, https://oilprice.com/Latest-Energy-News/World-News/Wind-Solar-Are-Now-The-Cheapest-Sources-Of-Power-Generation.html. Last accessed 14 Feb 2019
3. Johari MK, Jalil MAA, Shariff MF (2018) Comparison of horizontal axis wind turbine (HAWT) and vertical axis wind turbine (VAWT). 7:74–80. https://doi.org/10.14419/ijet.v7i4.13.21333
4. Alam F, Steiner T, Chowdhury H, Subic A (2011) A study of golf ball aerodynamic drag. In: 5th Asia-Pacific congress on sports technology (APCST) Procedia Engineering, vol 13, pp 226–231, https://doi.org/10.1016/j.proeng.2011.05.077
5. Alam F, Chowdhury H, Moria A, Subic A (2010) A comparative study of golf ball aerodynamics. In: Conference: 17th Australasian fluid mechanics conference 2010, Auckland, New Zealand, pp 599–602, ISBN: 978-1-61782-913
6. Aerospace Web, http://www.aerospaceweb.org/question/aerodynamics/sports/sphere-flow-comparison.jpg. Last accessed 05 May 2019
7. Gupta AK (2015) Efficient wind energy conversion: evolution to modern design. ASME J Energy Resourc Technol 137(5):051201–051201-10, JERT-14-1427. https://doi.org/10.1115/1.4030109
8. Alom N, Saha UK (2018) Four decades of research into the augmentation techniques of Savonius wind turbine rotor. ASME J Energy Resourc Technol 140(5), 050801, 14 pages. Paper No: JERT-17-1620. https://doi.org/10.1115/1.4038785
9. Mari M, Venturini M, Beyene A (2017) A novel geometry for vertical axis wind turbines based on the Savonius concept. ASME J Energy Resourc Technol 139(6):061202–061202-9. https://doi.org/10.1115/1.4036964
10. Mahmoud NH, El-Haroun AA, Wahba E, Nasef MH (2012) An experimental study on improvement of Savonius rotor performance. Alexandria Eng J 51(1):19–25
11. Rosmina N, Jauharib AS, Mustaamalc AH, Husind F, Hassane MY (2015) Experimental study for the single-stage and double-stage two-bladed Savonius Micro-sized turbine for rain water harvesting (RWH) System. In: 2nd international conference on sustainable energy engineering and application, ICSEEA Energy Procedia, 68, pp 274–281
12. Kamoji MA, Kedare SB, Prabhu SV (2008) Experimental investigations on single stage, two stage and three stage conventional Savonius rotor. Int J Energy Res 32(10):877–895. https://doi.org/10.1002/er.1399

Experimental Investigation of Heat Treatment Processes on Dissimilar IS2602-EN9 MIG Welded Joint

Mallapuram Bala Chennaiah, Podaralla Nanda Kumar, and Karanam Prahlada Rao

Abstract The present investigation, influence of different heat treatment processes which will yield better tensile strength and microstructures of 8-mm-thick plates metal inert gas welded IS2062-EN9 joint. Mechanical properties of the joint increased with annealing heat treatment processes, higher grain size was measured at welded zone, and it decreased. It is found that the joint fabricated at a low heat input condition showing excellent mechanical and metallurgical properties. After annealing heat treatment process, tensile strength improved around 14.52%, the pearlite phase increased from 36.75 to 47.15%, and ferrite phase has decreased from 59.36 to 50.61% and other decreased from 3.88 to 2.24%. The tensile strength is improved due to grain size that was observed to be 7.5 before heat treatment and 9 after annealing heat treatment, and ferrite phase is transformed into pearlite phase.

Keywords Metal inert gas welding · Low heat input · High heat input · Annealing · Normalizing · Tempering · Mechanical and metallurgical properties

1 Introduction

Steel is mostly used material; reason is steels dominance is usually considered to be the abundance of iron ore and the ease by which it can be refined from ore, neither of these is necessarily correct. Steel is such an important material because of its tremendous flexibility in fabrication processes and metal working processes. Two dissimilar plates were selected (IS2602–EN9) for MIG welding and their industry importance and wide application, IS2062, ISC55/EN9 Steel plates having 8 mm thickness were selected as base material in our work. Chemical composition and

M. Bala Chennaiah (✉)
V.R. Siddhartha Engineering College, Vijayawada 520007, India
e-mail: chennai303.mech@vrsiddhartha.ac.in

P. Nanda Kumar
N.B.K.R Institute of Science & Technology, Nellore, India

K. Prahlada Rao
Jawaharlal Nehru Technological University, Anantapur, Ananthapuram, India

E. T. Akinlabi et al. (eds.), *Trends in Mechanical and Biomedical Design*,
Lecture Notes in Mechanical Engineering,
https://doi.org/10.1007/978-981-15-4488-0_39

mechanical properties of base material are given in Table 1. The carbon equivalents of each plate IS2602 and EN9 were 0.54 and 0.96, respectively [1].

One of the steel plates is hypo-eutectoid while other is hyper-eutectoid with respect to carbon equivalent. With each heat input condition, the four weldments were prepared. One of the finished and defect-free joints is shown in Figs. 1 and 2.

Al-Mazrouee et al. [2], the main role of post-weld heat treatment is to relive the residual stress by allowing plastic flow at the stress-relieving temperature, as a result of improving the properties of the element. Post-weld heat treatment is mandatory

Table 1 Chemical compositions of various materials

S. No.	Name of material	Composition in % of weight					
		Carbon	Manganese	Silicon	Chromium	Sulphur	Phosphorus
1	Mild steel (IS 2602)	0.2	–	0.25	–	0.05	0.05
2	Medium-carbon alloy steel (EN-9)	0.55	0.15	0.65	–	0.06	0.06

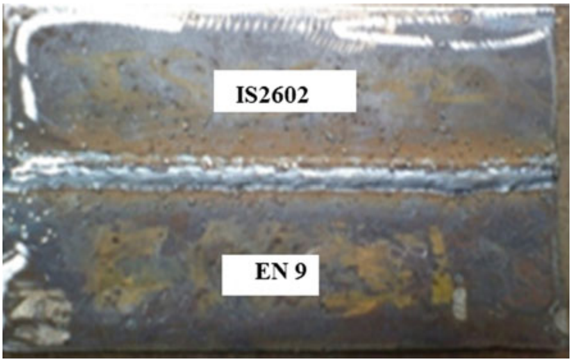

Fig. 1 Finished joint

Fig. 2 Defect-free joint

after weld fabrication specially used in various industries for manufacturing the components like pressure vessel, boiler, etc. The weldments were undergone with die penetrant and X-ray tests to find the surface and subsurface defects before conducting destructive tests. One of the four weldments was used to investigate the mechanical and metallurgical properties without heat treatment. The remaining three weldments were used to investigate the mechanical and metallurgical properties after the heat treatment processes, viz. annealing, normalizing and tempering. The results were tabulated and compared with the results of weldment without heat treatment.

2 Experimental Procedure

2.1 Base Material Selection

Firstly, the materials which are of the size (250 $\times$ 100 $\times$ 8) mm are to be taken. Select the universal milling machine for weld groove bevelling and deburr the plates. For bevelling, we have to turn the facing head up to 300–450, and feed is given slowly. So, the edge preparation is done to do welding as single V butt joint. After edge preparation, we have to select the combinations of material pair for further purpose. Here, the combination of the weld plates is selected in such a way that for the first joint low- and medium-carbon steel plates. Here, we consider the metal inert gas (MIG) welding, where as MIG wire (copper-coated mild steel) with diameter 1.2 mm is taken. The importance of copper coating on mild steel is used to prevent rust and also current is passed easily. Anti-spatter spray is sprayed on the wire for easy clean up after a flux core MIG welder. Then, welding is done for five passes with respect to voltage, current and welding speed which is considered.

2.2 Importance of Post-weld Heat Treatment

After having completed with the welding for the similar/dissimilar metal plates, the post-weld heat treatment was carried out to evaluate and improve the mechanical properties and microstructure of the metal plate. annealing, normalizing and tempering post-weld heat treatment process were carried out in the experiment.

2.3 Tensile Properties

Welding process is subjected to heating and cooling leading to development of different microstructures in different zones, with respect to transverse direction of the weld axis. Eight dissimilar weldments of IS2602-EN9 were prepared by using MIG

Table 2 Tensile strength results of IS2602-EN9 low heat input weldments

Type of heat treatment	Tensile strength low heat input weldment (MPa)			
	Before heat treatment	PWHT	Improvement	Percent of improvement
Annealing	482.79	543.41	60.62	14.52
Normalizing		520.94	39.15	10.16
Tempering		530.96	48.17	9.05

Table 3 Tensile strength results of IS2602-EN9 high heat input weldments

Type of heat treatment	Tensile strength high heat input weldment (MPa)			
	Before heat treatment	PWHT	Improvement	% of improvement
Annealing	483.91	543.97	70.87	12.55
Normalizing		533.10	49.19	7.90
Tempering		527.71	43.8	9.97

welding process. Three testing samples were prepared according to ASTM E8-04 from dissimilar weldment. The tensile strengths of these three samples of each weldment were measured, and their average values were tabulated (Tables 2 and 3). One of the most significant observations with different heat treatment conditions is that the tensile strength gives higher values with heat treatment than that without heat treatment for both heat inputs.

2.4 Microstructural Observations

For metallographic observations before post-weld heat treatment and after post-weld heat treatment, specimens were etched with 4% Nital for 20 s, and consequently, the microstructures of the base, weld and the heat-affected zone were observed under 100X magnification. Heat input seriously affects the size and shape of the grains of those metals composed with filler materials. The grains of the welded zone grow to larger size compared with that of other zones. Ili et al. [3] studied the variations in the structures, and grain sizes were mainly due to directional heat flow from the fusion line. The microstructures at different zones of the weldment were taken before and after heat treatment for further comparison.

3 Results and Discussions

3.1 Tensile Strength of IS2602—EN9 Dissimilar Welded Joint

Eight dissimilar weldments of IS2602-EN9 were prepared by using MIG welding process with low and high heat input condition, each heat input condition for four dissimilar weldments was prepared. Three testing samples were prepared according to ASTM E8-04 from each weldment. The tensile strengths of those three samples of each weldment were measured, and their average values were tabulated. One of the most significant observations with different heat treatment conditions is that the tensile strength gives higher values with heat treatment than that without heat treatment for both heat inputs [4].

To compare with the results, a histogram was presented as Fig. 3 which shows that the tensile strength obtained in annealing process was effective in improvement, compared with the other heat treatment processes. This is true for both heat input conditions. It is also observed that high heat input conditions weldments show higher improvements in tensile strength values in comparison with low heat input conditions. The exception is that the tensile strength of samples subjected to tempering heat treatment process showed betterment for low heat input.

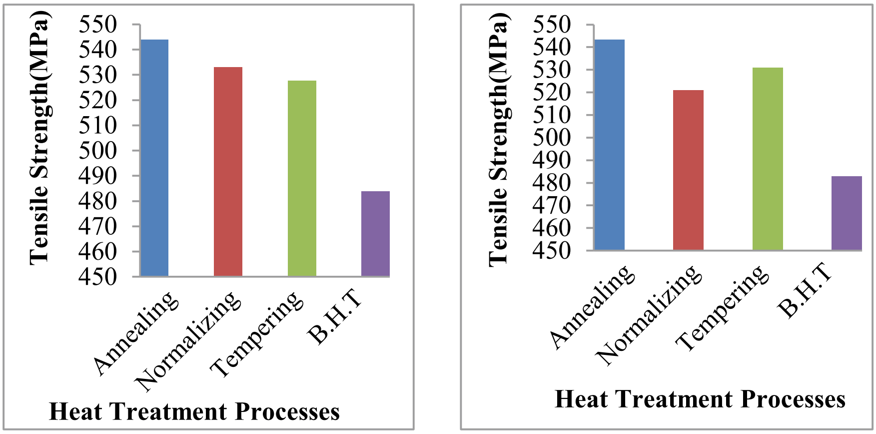

a)Low heat input b)High heat input

Fig. 3 Tensile strength of IS2602–EN9 weldment

3.2 Microstructure Analysis of IS2602—EN9 Dissimilar Welded Joint

Microstructure observations was performed on specimens without heat treatment and those heat treated by annealing process [5]. The metallographic observation before post-weld heat treatment is shown in Fig. 4. This showed the microstructure of base metal (IS2602) with equiaxed structure and uniformly distributed with very fine strengthening precipitates. ASTM grain size of 7.5 is observed. Light etched structures which were observed in white colour are the ferrite phase, and dark etched structure which was pink in colour represents pearlite phase. From Fig. 4b which indicates the microstructure of base metal IS2062 after heat treatment, the grain size increased to 9 after heat treatment. Figure 4c, d shows that HAZ(IS2602) shows a grain size of 7.5 without heat treatment and 9 with annealing heat treatment. Thus, it is clearly evident that the grain size increased from 7.5 to 9 with heat treatment. Figure 4e, f shows the microstructures in the weld zone without heat treatment

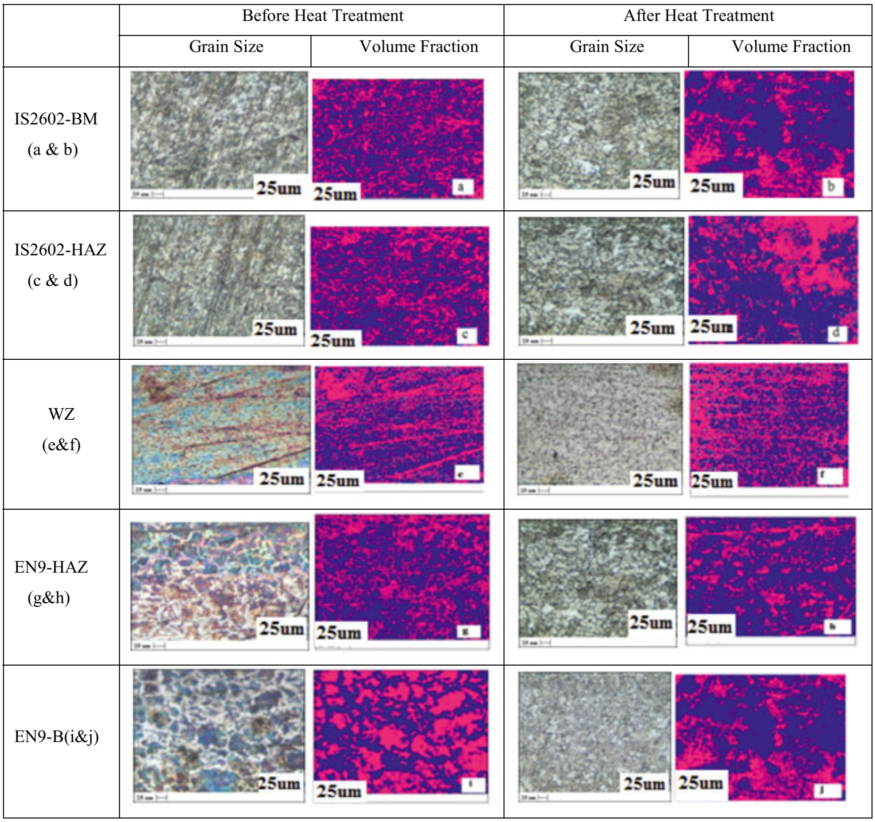

Fig. 4 Microstructural images of EN9

and with heat treatment, respectively. In case, grain size was observed to be 7.5 before heat treatment and 9 after heat treatment. Figure 4g shows the microstructure observed in the heat-affected zone (EN9) without heat treatment. From Fig. 4h indicates the microstructure of heat-affected zone (EN9) with heat treatment; the microstructure observation also shows that the grain size increases to 7.5 after heat treatment compared with a value of 8 before the heat treatment. Figure 4i shows the microstructure of base metal (EN9) which has a uniform structure with uniformly distributed very fine strengthening precipitates, with ASTM grain size of 7. The light etched structures which were observed in white colour are the ferrite phase, and dark etched structure which was grey in colour represents pearlite phase. From Fig. 4j which indicates the microstructure of base metal (EN8) after heat treatment, the microstructure observation also shows that the grain size increases from 7 to 7.5.

After completion of grain size measurements, the same specimens were considered for phase/volume fraction analysis. Light optical microscope (LOM) with magnification of 100X was used for the study of phase/volume fraction analysis. In order to study the different phases of the microstructures, colour grading was selected. The ferrite phases were represented with dark blue colour, and the pearlite phases were represented with grey colour. Figure 4a–j shows the microstructure images and the corresponding phase observed along with their volume fractions of the three principal zones (base metal, heat-affected zone and weld zone).

4 Conclusions

1. Tensile strength of low heat input dissimilar weldment IS2602-EN9 was observed as 482.79 MPa before heat treatment. For improving this strength, we adopted the popular heat treatment processes. With annealing heat treatment process, the tensile strength was observed as 543.41 MPa. Increase in tensile strength was observed to be 12.55%. After normalizing heat treatment process, tensile strength was observed as 520.94 MPa. Thus, 7.90% improvement in tensile strength has been observed. Even after tempering heat treatment process, the tensile strength was increased by 9.97% i.e., to 530.96 MPa. Further among the three heat treatment processes, after annealing process offered the best improvement in tensile strength compared with remaining two heat treatment processes.
2. The microstructure of the IS2602-EN9 welded joint after heat treatment consisted mainly of three phases 47.15% pearlite phase, 50.61% ferrite phase and others 2.24%. After the heat treatment, the pearlite phase increased from 36.75 to 47.15%, ferrite phase has decreased 59.36–50.61% and other decreased from 3.88 to 2.24%. Therefore, it is understood that when the ferrite phase is reducing, the pearlite phase is increasing, which means an account of heat treating shows that ferrite phase is transformed into pearlite phase.

Acknowledgements I express my sincere thanks to **UGC** for assisting in my work through funding **Minor Research Project, MRP-6188/15 (SERO/UGC)** for the purchasing the **optical microscope** which helped me to carrying out my work successfully.

References

1. Ali MS (2011) Study of mechanical properties in a weld bead of dissimilar metals. Int J Eng Sci Technol (IJEST) 3(5). ISSN: 0975-5462
2. Al-Mazrouee A, Singh Raman RK, Ibrahim RN (2005) Effect of post weld heat treatment on the oxide scaling of Cr–Mo steel weldments. J Mater Process Technol 164–165:964–970
3. Ili N, Jovanovich MT, Todorovi M, Trtanj M, Aponji P (1999) Micro structural and mechanical characterization of post weld heat-treated termite weld in rails. Mater Charact 43(4):243–250
4. Standard test methods for tension testing of metallic materials. Designation: (E8/E8M-09)
5. Sireesha M, Albert SK, Sundaresan S (2001) Microstructure and mechanical properties of weld fusion zones in modified 9Cr-1 Mo Steel. J Mater Eng Perform 10:320–330

Feasibility of Al_2O_3/Water Nanofluid in a Compact Loop Heat Pipe

Emerald Ninolin Stephen, Lazarus Godson Asirvatham, Kandasamy Ramachandran, Arulanatham Brusly Solomon, and Pitchaimuthu RamKumar

Abstract Effect of low volume concentration of water-based aluminium oxide (Al_2O_3) nanofluids on the thermal performance and entropy generation of a compact loop heat pipe (CLHP) with the flat square evaporator of dimensions (34 mm × 34 mm × 19 mm) is experimentally investigated. The heat input and volume concentration are varied from 30 W to 500 W and 0.03%, 0.09% and 0.12%, respectively. The effects of performance parameters such as heat supplied and nanoparticle concentration on the entropy generation, thermal resistance, evaporator and condenser heat transfer coefficients (HTC) are analysed. Results showed that the formation of thin porous deposition on the wick and wall plays a key role in the enhancement of heat transfer of the CLHP. The heat transfer coefficient was found to be enhanced by 24.42% in the evaporator, and the thermal resistance was reduced by about 21.29%. The entropy generation is also reduced by 12.36% when Al_2O_3 nanofluid is used as the working fluid. Adding a little quantity of Al_2O_3 nanoparticles enhanced the operating range of CLHP by 12% when compared with that of the base fluid.

Keywords Loop heat pipe · Heat transfer · Aluminium oxide nanoparticles

1 Introduction

Modern electronics industries are facing considerable challenges in the removal of heat from electronic devices. Due to the reduced size, increasing processor speed and high heat loads, these devices require efficient cooling systems. The conventional method of cooling like simple conductive and convective cooling is not appropriate for microelectronic devices with high heat generation. In recent years, the heat pipes have got more attention in dissipating the heat from high heat flux devices [1]. Heat

E. N. Stephen · L. G. Asirvatham (✉) · A. B. Solomon · P. RamKumar
Department of Mechanical Engineering, Karunya Institute of Technology and Sciences, Coimbatore 641114, India
e-mail: godson@karunya.edu

K. Ramachandran
Department of Physics, Bharathiar University, Coimbatore 641046, India

E. T. Akinlabi et al. (eds.), *Trends in Mechanical and Biomedical Design*, Lecture Notes in Mechanical Engineering,
https://doi.org/10.1007/978-981-15-4488-0_40

pipes are also used in spacecraft's thermal control, electronic boards, air conditioning systems, energy collectors, chemical engineering, engine cooling, power generation, etc. The heat pipe is capable of transmitting heat at high rates over vast distances with very small temperature drops [2]. Different types of heat pipes like planar heat pipes, variable conductance heat pipes, pressure-controlled heat pipes, diode heat pipes, thermosyphons, rotating heat pipes, loop heat pipe, oscillating or pulsating heat pipe are used for heat removal applications. Among the different types of heat pipe, loop heat pipes (LHPs) are acknowledged as a superior heat transfer device in the domain of thermal management as well as electronic cooling and cooling of computers [3]. The LHP is an effective, self-circulating heat transfer device based on capillarity. Generally, LHPs offers low thermal resistance, and it has the capacity to transport heat over a long distance with a low-temperature gradient and requires less space. The analysis done by Maydanik et al. [4] in a 21 m long stainless steel LHP with ammonia and nickel wick achieved the highest heat load of 1700 W (12 W/cm^2) with the lowest resistance of 0.034 °C/W. A long LHP of 10 m long was tested in the horizontal position using ethanol as cooling fluid. It was identified that the maximum power could be transferred by the LHP is 340 W with a thermal resistance of 0.11 °C/W [5]. The flat evaporator has many advantages over cylindrical, disc-shaped evaporators, especially easy mounting, elimination of additional interface material, increased active area, reduction in the resistance and weight of the LHPs. Therefore, flat shape LHPs are favoured in cooling electronic equipment in ground as well as in space applications [6–8].

Most LHPs are effectively employed in space applications, and when coming to electronic systems, nowadays the size is minimized, power is increased, and the heat removal becomes a major challenge. The use of miniaturized LHP with flat evaporator can be one of the options to satisfy the compact enclosure of electronic component without compromising the performance of the device. Tang et al. [9] tested experimentally the start-up and thermal performance of a specially made miniature LHP (mLHP). The experiment is conducted with water as well as with ethanol as working fluids. Water and ethanol are used as working fluids. The highest temperature in the evaporator and the lowest thermal resistance is recorded at 150 W as 93.7 °C and 0.0315 K/W. Wang et al. [10] fabricated a LHP with an evaporator of flat disc shape. The evaporator diameter and height are 40 and 19 mm. The wick used in this study is a stainless steel wire mesh, which contains about 630 meshes, and the working fluid used is methanol. The maximum heat capacity reached was 240 W and heat flux of 19.1 W/cm^2. Tests were conducted by Anand et al. [11] with four working fluids such as acetone, ethanol, n-pentane and methanol for different heat inputs in the miniature LHP (mLHP) containing flat evaporator. The experimental results revealed that methanol had the highest range in heat transport and the lowest operating temperature is recorded by n-pentane.

The significant features that distinguish compact loop heat pipe (CLHP) from conventional LHPs are the dimensions of the connecting lines. Based on the dimensions of the connecting lines [12], the LHPs are categorized as CLHP if the diameter ranges from 3 to 5 mm. The working fluid used by Gunasegaram et al. [13] in the LHP is distilled water and silica nanoparticles. The mass concentration of silica nanoparticles was ranged from 0 to 3%. Based on the results, it is observed that up to a certain mass concentration (0.5%) the total thermal resistance is found to be decreasing in the LHP, and beyond this mass concentration, it started increasing again. Tharayil et al. [14] used graphene–water nanofluids with different concentration and tested the performance of the mLHP. When compared to water, the thermal resistance at the evaporator was found to reduce by 25%. The thermal performance of the mLHP was observed to be improved when the nanoparticles concentration was increased. Wan et al. [15] fabricated the mLHP and compared the performance with distilled water and copper–water nanofluid for different mass concentrations (1.0, 1.5 and 2.0%). The nanofluid-filled mLHP showed an enhanced performance once compared with distilled water, and 1.5% was found to be the optimum mass concentration. Riehl [16] studied the heat transport behaviour of a LHP. Water–nickel nanofluid was used as the working fluid. In this study, the use of a nanofluid increased the pressure drop, and higher operating temperatures were observed. The tendency of nanofluid is to improve the heat transfer performance of the mLHP. Use of nanofluid in CLHP is an encouraging research area which is quiet in its early stage. The purposes of this experimental study are to examine and analyse the performance of CLHP and the use of the Al_2O_3/water nanofluid. In the current study, distilled water and Al_2O_3/water nanofluid with three different volume concentrations are used to study the heat transfer performance and entropy generation in a CLHP. The effect of heat input and volume concentration on entropy generation, thermal resistance and evaporator and condenser heat transfer coefficients are investigated.

2 Experimentation

2.1 Preparation of Nanofluid

The nanofluid is prepared by suspending the Al_2O_3 nanoparticles in water with three volume concentrations. The Al_2O_3 nanoparticles are bought from Alfa Acer with product number 44,931 having the size of 40–50 nm and density 3950 kg/m^3. By the two steps method, nanofluids are synthesized. The volume concentrations used are 0.03, 0.09 and 0.12%. Surfactants are not used in the preparation of nanofluid. Adequate quantity of nanoparticles corresponding to the desired volume fraction is measured and dispersed straight in the distilled water and stirred. Then, the nanofluid is sonicated in the ultrasonicator at 50–60 kHz for one hour so as to get good dispersion. By conducting visual observation test, the stability of the prepared nanofluids is checked. It is found to be stable even after two weeks.

2.2 Characterization of Nanofluid

The characterization of synthesized nanoparticles was carried out by scanning electron microscope (SEM) analysis techniques and zeta potential distribution. Figure 1 shows the SEM image taken at 30,000 magnifications. SEM image gives the distribution pattern and size of the Al_2O_3 nanoparticles. There is crystal shape exist in this nanoparticles. Figure 2 shows the zeta potential distribution of the Al_2O_3 nanoparticles. Al_2O_3 nanoparticles with zeta potential values greater than +25 mV or less than −25 mV typically have high degrees of stability.

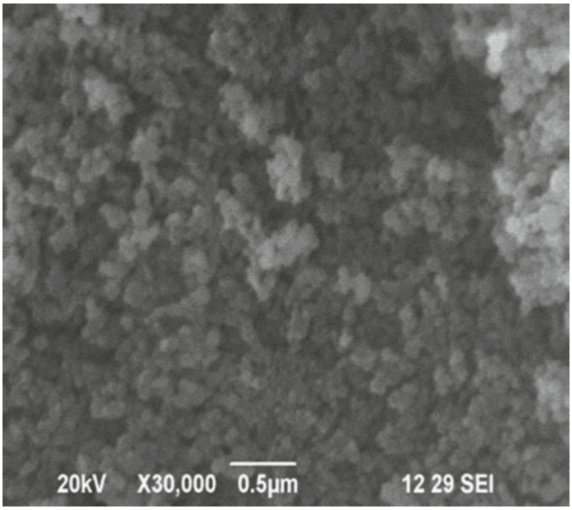

Fig. 1 SEM image of Al_2O_3 nanoparticles

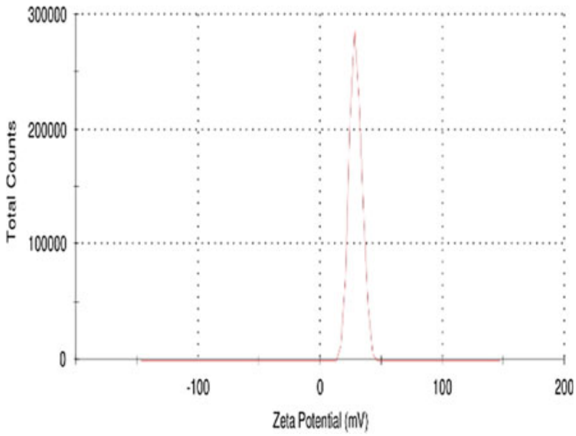

Fig. 2 Zeta potential of Al_2O_3 nanoparticles

2.3 Description of the CLHP

The fabricated CLHP comprises of a square flat evaporator, condenser, smooth liquid transport line, smooth vapour transport line and copper screen mesh wick. The assembly of the evaporator section is shown in Fig. 3. The entire parts of the CLHP are made up of copper. The size of the evaporator is 34 mm × 34 mm × 9.5 mm. The wall thickness of the evaporator is 2 mm. The evaporator has two parts. The upper cover is the compensation chamber (CC), and the bottom cover is the boiling chamber. The boiling chamber comprises of five fin structures inside in order to enhance the heat transfer area. The size of the fin is 25 mm × 5.5 mm × 1 mm. The capillary wick used comprises of a copper screen mesh wick with 63% porosity. The size of the wick is 300 mm × 25 mm × 0.25 mm. This copper screen mesh wick is wrapped with eight turns over the fins, and ten layers of size 30 mm × 25 mm × 0.25 mm is placed above the fins which act as a separator between CC and boiling chamber. With the help of three projections in the CC, the copper screen mesh wick is held tightly in place. In the CC, a partition is provided to avoid the mixing of vapour and the liquid. Copper tubes having a 5 mm inner diameter are used as the liquid and vapour transport lines. A water-cooled condenser having a single-pass cross-flow forced flow with 21 °C as constant inlet temperature which is used to condense the vapour. A cooling water flow rate as 25 LHP is used in the condenser. The heat loss to the ambient is prevented by insulating the entire CLHP, excluding the condenser area with thick layers of glass wool. Very low pressure of 10^{-4}millibar is maintained inside the CLHP.

Fig. 3 Assembly of evaporator

2.4 Experimental Layout

The heat transfer performance of the CLHP is analysed for the different working fluids. The experimental test set-up is shown in Fig. 4. It consists of CLHP, heater block, thermocouples, voltmeter and ammeter connected to a dimmerstat, computer, data logger, cooling water pipes, chilling element, rotameter and pump. The heater assembly comprises of a copper block and cartridge heaters. Three cartridge heaters of each 200 W are fitted in the copper block. In order to provide the varying heat inputs, a dimmerstat is connected to cartridge heaters, and the varying heat inputs are measured using voltmeter and ammeter. The data logger DARWIN DAQ-100 records the temperatures for every 3 s. The cooling water supplied is maintained at constant temperature by the chilling unit. The mass flow rate of cooling water supplied to the condenser is measured with a rotameter and is maintained constant by using a flow-regulating valve attached to the pump.

Seventeen thermocouples of T-Type with ±0.5 °C accuracy were positioned at different locations in the CLHP assembly to record the wall and vapour temperatures. The thermocouples positions are clearly mentioned in the schematic diagram of the experimental testing set-up in Fig. 5. Instrument welder is used to fixing the thermocouples to the outer surface of CLHP. The thermocouple joint is strengthened with fast-curing epoxy compounds like M-seal and Araldite.

T_1 and T_2 gives the heater temperature and interface temperature between the heater and evaporator. T_3 and T_4 measure the surface and vapour temperature at evaporator. T_5 and T_6 measure the wall temperatures at vapour line, and T_7 gives the vapour temperatures at the vapour line. T_8, T_{10} and T_{12} provide the surface temperature inside the condenser. T_9 and T_{11} provide the vapour temperature inside the condenser. T_{13} gives the vapour temperatures at liquid line. T_{14} and T_{15} provide the wall temperatures at the liquid line. T_{16} and T_{17} measure the inlet and outlet temperatures of the cooling water. For every 3 s, data from the thermocouples are recorded at the DARWIN DAQ-100 data logger. A computer connected with the DARWIN DAQ-100 data logger records all the necessary data for analysis.

Fig. 4 A photographic view of the experimental set-up

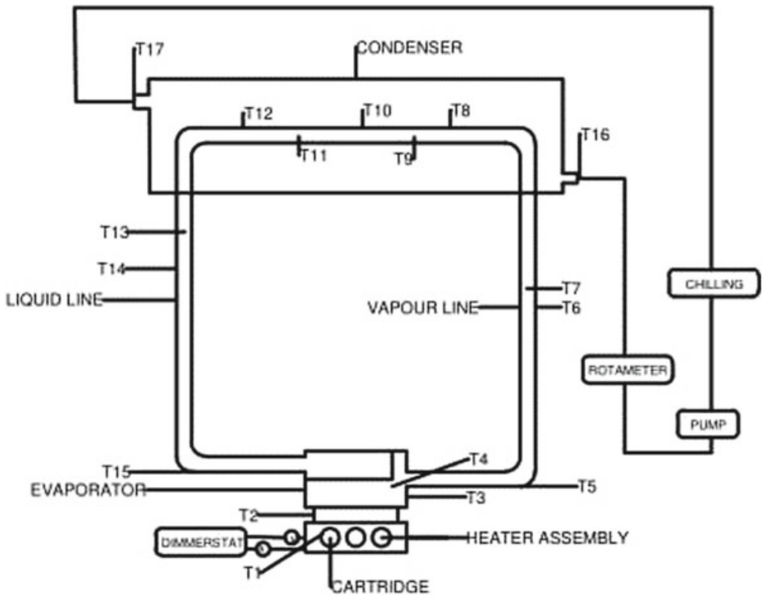

Fig. 5 Schematic diagram of the experimental testing set-up of CLHP

2.5 Experimental Procedure

The test is performed on the CLHP with the distilled water and with Al_2O_3/water nanofluid for various concentrations. Based on the preliminary studies, the working fluid is charged for 60% of the total volume of the CLHP. Literature has proposed that 30–80% as the optimum fill ratio for the CLHP to operate effectively. The tests are conducted for the heat load range of 30–500 W. The heat loss to the surroundings is avoided by insulating the entire CLHP assembly with the glass wool of sufficient thickness. All the tests are conducted in vertical position, i.e., the evaporator is positioned below the condenser. As the power input is switched initially, 30 W of the heat load is applied to the heater through dimmerstat, and after 30 min, the steady-state condition is reached in the CLHP. Successively, heat input of 50 W is used for a duration of 20 min to attain the steady state. Progressively, the heat input is increased by 50 W until the heat load becomes 500 W. For every 3 s, the data loggers record all the temperature readings of the thermocouples and store in a computer.

2.6 Data Reduction

The thermal resistance at the evaporator (R_e) is defined as

$$R_e = \frac{(T_e - T_v)}{Q} \tag{1}$$

where R_e is evaporator thermal resistance, T_e is the surface average evaporator temperature, T_v is the vapour average evaporator temperature and Q is the applied heat input.

The loop thermal resistance is defined by Eq. (2).

$$R_{\text{lhp}} = \frac{(T_e - T_c)}{Q} \tag{2}$$

where R_{lhp} is loop heat pipe thermal resistance and T_c denotes the average temperature at the condenser.

The total thermal resistance is defined as

$$R_{\text{tot}} = \frac{(T2 - Ta)}{Q} \tag{3}$$

where R_{tot} is the total thermal resistance of the heat pipe, T_2 is the temperature at the interface and T_a is the ambient temperature.

The thermal resistance at the condenser (R_c) is defined as

$$R_c = \frac{(T_{\text{vc}} - T_c)}{Q} \tag{4}$$

where R_c is condenser thermal resistance, T_{vc} is the average vapour condenser temperature and T_c is the average wall condenser temperature.

The evaporator heat transfer coefficients are defined as

$$h_e = \frac{Q}{A_e(T_e - T_{\text{ve}})} \tag{5}$$

where h_e denotes the evaporator heat transfer coefficient, A_e denotes surface area at the evaporator and T_e and T_{ve} indicate the average wall evaporator temperature and average vapour evaporator temperature.

The condenser heat transfer coefficients are defined as

$$h_c = \frac{Q}{A_c(T_{\text{vc}} - T_c)} \tag{6}$$

where h_c denotes the condenser heat transfer coefficient, A_c is the surface area at the condenser and T_{vc} and T_c indicate the average vapour condenser temperature and average wall condenser temperature.

At the condenser, heat rejection is defined using the Eq. (7).

$$Q_c = m_w C_p (T_{17} - T_{16}) \tag{7}$$

where m_w is the mass flow rate of the cooling water supplied, C_p is the specific heat of the cooling water and T_{16} and T_{17} are the temperature of cooling water at the inlet and outlet of the condenser.

The thermal efficiency of the CLHP is defined as

$$\eta = \frac{Q}{Q_c} \times 100 \tag{8}$$

The entropy generation due to heat transfer from the evaporator to the condenser is given by

$$S_{ht} = \frac{Q}{T_c} - \frac{Q}{T_e} \tag{9}$$

where Q indicates the applied heat load, T_c denotes the average wall condenser temperature and T_e denotes the average wall evaporator temperature.

The entropy generated at the vapour transport line is calculated as

$$S_{vl} = \frac{m \times \Delta p}{\rho_v T_v} \tag{10}$$

where m denotes the mass flow rate, Δp indicates the pressure difference, ρ_v is average density and T_v is the average vapour temperature at the vapour transport line. The entropy generated at the liquid transport line is calculated as

$$S_{ll} = \frac{m \times \Delta p}{\rho_l T_l} \tag{11}$$

where m denotes the mass flow rate, Δp indicates the pressure difference, ρ_l is average density, T_l is the average liquid temperature at the liquid transport line. The total entropy generated in CLHP is calculated as

$$S_{tot} = S_{ht} + S_{vl} + S_{ll} \tag{12}$$

2.7 Uncertainty Analysis

To estimate the percentage of uncertainties involved in the experiments, the flawless uncertainty study is done on the different elements used.

The uncertainty allied with the heat input consists of current (I) and voltage (V) uncertainties.

$$\frac{\Delta Q}{Q} = \sqrt{\left(\frac{\Delta V}{V}\right)^2 + \left(\frac{\Delta I}{I}\right)^2} \tag{13}$$

The uncertainty associated with the evaporator heat transfer coefficient includes the heat flux (q) and variation of temperature between vapours and surface (ΔT_{vs}) uncertainties.

$$\frac{\Delta h}{h} = \sqrt{\left(\frac{\Delta q}{q}\right)^2 + \left(\frac{\Delta(\Delta T)}{\Delta T_{\text{VS}}}\right)^2} \tag{14}$$

The uncertainty associated with the thermal resistance is calculated as

$$\frac{\Delta R_{\text{t}}}{R_{\text{t}}} = \sqrt{\left(\frac{\Delta Q}{Q}\right)^2 + \left(\frac{\Delta(\Delta T)}{\Delta T_{\text{ec}}}\right)^2} \tag{15}$$

ΔT_{ec} denotes the temperature difference between evaporator and condenser. The thermal efficiency is calculated from the applied heat input, mass flow rate (m) and the outlet and inlet cooling water temperature difference. The uncertainty is calculated as

$$\frac{\Delta \eta}{\eta} = \sqrt{\left(\frac{\Delta Q}{Q}\right)^2 + \left(\frac{\Delta m}{m}\right)^2 + \left(\frac{\Delta(\Delta T)_{\text{W}}}{\Delta T_{\text{W}}}\right)^2} \tag{16}$$

The uncertainty associated with entropy generated in heat transfer is calculated as

$$\frac{\Delta S_{\text{gen.ht}}}{S_{\text{gen.ht}}} = \sqrt{\left(\frac{\Delta Q}{Q}\right)^2 + \left(\frac{\Delta T\text{H}}{T_{\text{H}}}\right)^2 + \left(\frac{\Delta T_{\text{L}}}{T_{\text{L}}}\right)^2} \tag{17}$$

where T_{H} is the heat source temperature and T_{L} is the temperature of the heat sink. The uncertainty associated with entropy generation due to friction in the transport line is calculated as

$$\frac{\Delta S_{\text{gen.fl}}}{S_{\text{gen.fl}}} = \sqrt{\left(\frac{\Delta m}{m}\right)^2 + \left(\frac{\Delta(\Delta P)}{\Delta P_{\text{ec}}}\right)^2 + \left(\frac{\Delta \rho}{\rho}\right)^2 + \left(\frac{\Delta T}{T}\right)^2} \tag{18}$$

where m denotes the mass flow rate, ΔP_{ec} represents the transport line pressure difference, ρ is the density of fluid and T is the temperature for working fluid. The uncertainties obtained are 3.9, 4.16, 4.9, 6.8, 3.7 and 3.2% for applied heat input, heat transfer coefficient at the evaporator, thermal resistance, thermal efficiency and entropy generation due to heat transfer and flow friction.

3 Results and Discussion

The functioning of the CLHP is established by the vapour and wall temperatures shown by the thermocouples positioned at various parts of CLHP like evaporator region, vapour transport line, condenser region and liquid transport line. Once the heat input applied is increased gradually, the temperature at the different location of the CLHP is also correspondingly increased. This strongly confirms the perfect functioning of the CLHP. At the evaporator region, the temperature reports higher than the temperature at the other parts of CLHP confirms that CLHP functioning is perfect. It is found that once the heat load is increased, the temperature difference (ΔT) of the CLHP is also increased gradually. Figure 6 shows the temperature difference ($T_e - T_c$) of the evaporator section and the condenser section of the CLHP. It is clearly seen from Fig. 6 that the difference in temperature ($T_e - T_c$) increases with the increase in heat load for all the concentration of Al_2O_3/water nanofluids and for distilled water. The distilled water temperature difference is found to be higher when compared with nanofluids. From the evaporator region, more amount of heat is transferred to the condenser region when Al_2O_3 nanofluids are used as working fluid. This happens due to the high thermal conductivity of Al_2O_3 nanofluid. The temperature difference obtained for 0.12 vol% Al_2O_3 nanofluids is reduced by 13.94% while compared with distilled water, and the same is reduced by 11.12% for 0.09 vol% Al_2O_3 nanofluids while compared with distilled water.

Figure 7 illustrates the influence of thermal resistance of evaporator with the heat input range from 30 to 500 W. The thermal resistance value of evaporator for all cases declines as heat load increases. The thermal resistance value of evaporator declines with the increases in volume concentration of Al_2O_3 nanofluids. In general, large size

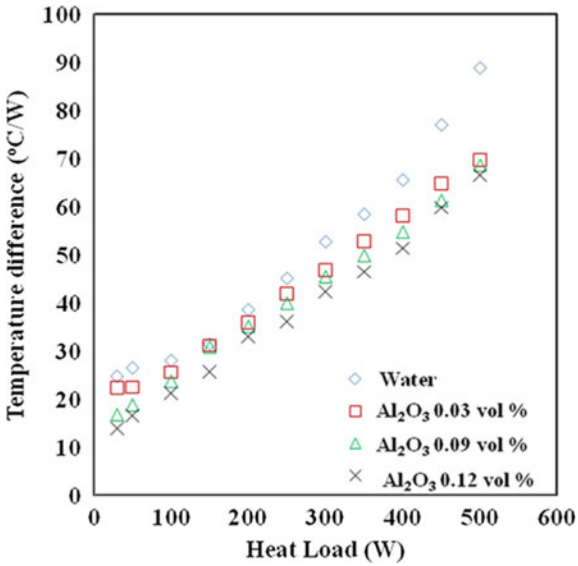

Fig. 6 Temperature difference with heat load

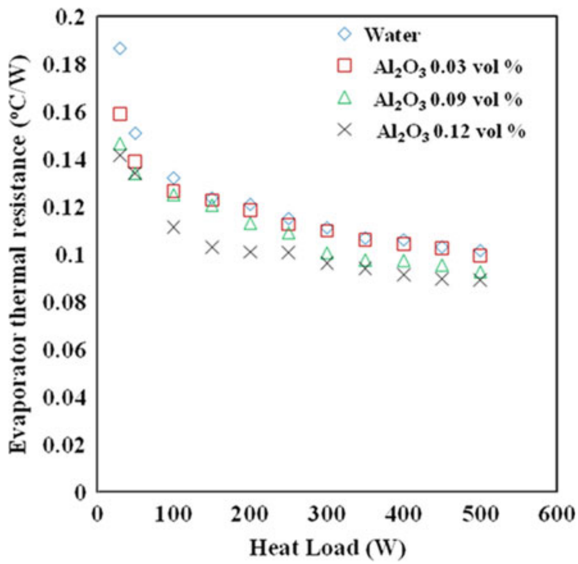

Fig. 7 Thermal resistance with the heat load

bubbles are formed in the evaporator, and due to the presence of nanoparticles, these larger bubbles are split down into smaller vapour bubbles which offer less resistance to heat transfer. The evaporator thermal resistance is found to be reduced by 21.29% for 0.12 vol% of Al_2O_3 nanofluids and 17.71% for 0.09 vol% of Al_2O_3 nanofluids when compared with distilled water.

The loop thermal resistance variation with heat load for four CLHPs is shown in Fig. 8. It is observed from Fig. 8 that the thermal resistance decreases with the increase in heat load as well as the volume concentration of Al_2O_3 nanofluids.

When the heat load is increased, more vapour are generated, and a large amount of vapour is passed to the condenser, which yields in low thermal resistance. The nanoparticles stick to the copper screen mesh wick and form a thin layer with a large number of small nucleation site, which increases the capillary force and the solid–liquid wettability [17]. The loop thermal resistance is reduced by 14.3% for 0.12 vol% of Al_2O_3 nanofluids when compared with distilled water, and the same is reduced by 13.5% for 0.09 vol% Al_2O_3 of nanofluids. The evaporator heat transfer coefficient variation with the heat load is shown in Fig. 9 for distilled water as well as for three volume concentrations of Al_2O_3 nanofluids. In the evaporator, the convective heat transfer coefficient is a picture of convective boiling. As shown in Fig. 9, the heat transfer coefficient at the evaporator increases with the increase in heat load and volume concentration. At low heat loads, the boiling rate is low in the evaporator region and is high for higher heat loads. As the heat input increases, more amount of nucleation sites may be activated that leads to a rise in trend in the heat transfer coefficient. For 0.12 vol% of Al_2O_3 nanofluids, the convective heat transfer coefficient is enhanced by 24.42% at evaporator when compared with distilled water. The heat transfer coefficient is increased with the increase of Al_2O_3 nanoparticles

Fig. 8 Loop thermal resistance with heat load

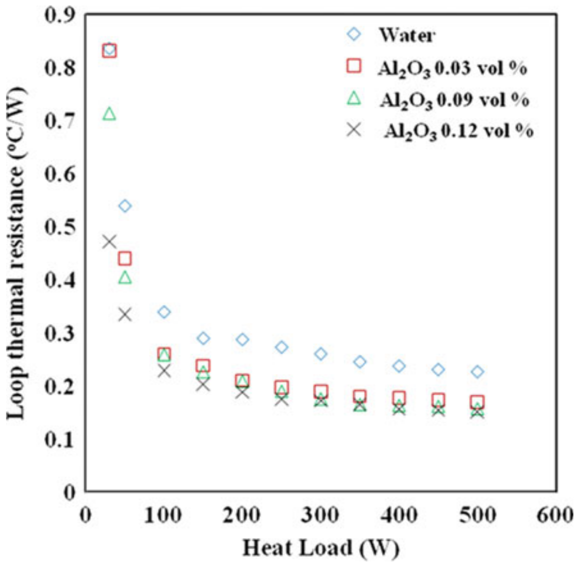

Fig. 9 Evaporator HTC with the heat load

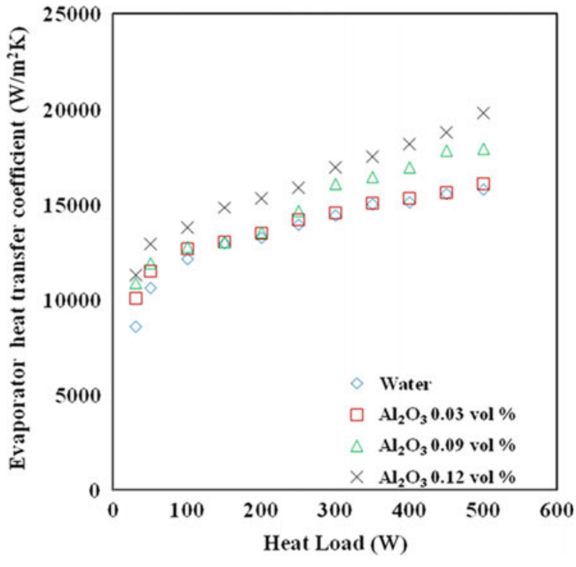

concentration in the condenser region. In the condenser at high heat loads, vapour requires a larger area to condense. Inadequate surface area and constant cooling water flow rate resist the heat transfer coefficient in the condenser region when comparing with the evaporator. The condenser heat transfer coefficient variation related with heat load is shown in Fig. 10.

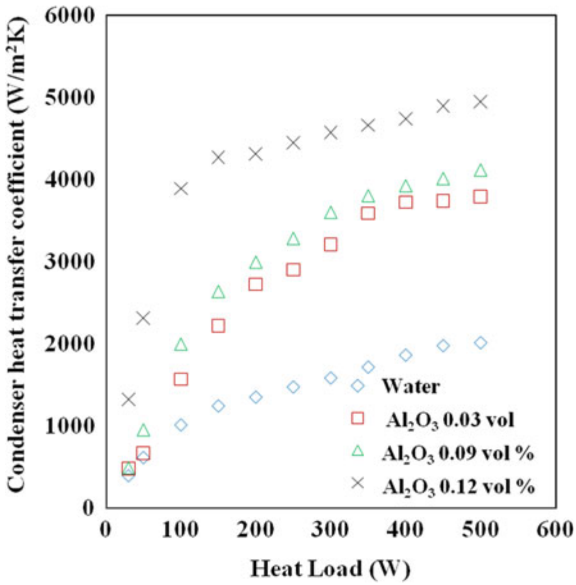

Fig. 10 Condenser HTC with the heat load

From Fig. 10, it is observed that the heat transfer coefficient at condenser is also increased with the increase in heat load. The heat transfer coefficient at the condenser is enhanced by 12.9% for 0.12 vol% Al_2O_3 nanofluids when compared with that of distilled water. Figure 11 shows the variation of thermal resistance of condenser with the heat load. As the heat load increases, the thermal resistance of

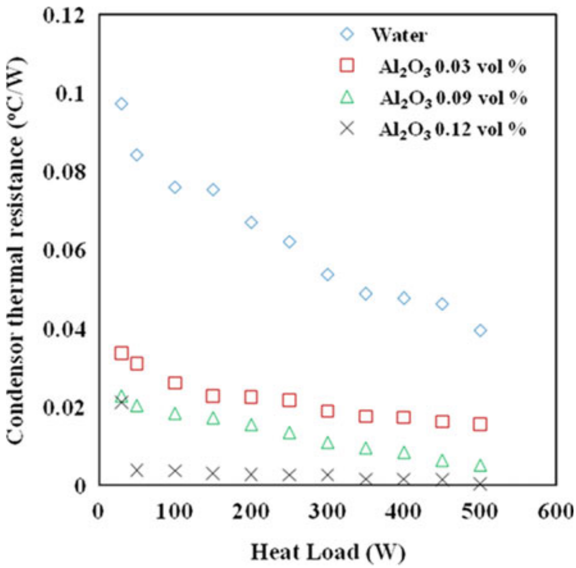

Fig. 11 Thermal resistance with the heat load

condenser decreases. When compared with distilled water, the condenser thermal resistance with 0.12 vol% Al_2O_3 nanoparticles is observed to be reduced by 26.75% and for 0.09 vol%, and the same is reduced by 20.12%. The generation of entropy is evaluated as the outcome of irreversibilities occurred. Entropy generation occurs in the CLHP that is due to heat transfer with evaporator and condenser, and due to the frictional effect in the transport line, the entropy generated in the copper screen mesh wick and at the condenser is not accounted because of the negligible pressure drops in them. The entropy generation because of pressure drops is extremely low once evaluated with entropy generation due to heat transfer. This is due to the heat transfer irreversibility caused by the latent heat of vapourization that dominates over the frictional irreversibility caused by viscosity.

It was observed that with the rise in heat load, the entropy generation is increased alongside, and with the increase of volume concentration of Al_2O_3 nanoparticles, the entropy generation decreases. The average fall in entropy generation is 6.47% for 0.09 vol% and 11.11% for 0.12 vol% of Al_2O_3/water nanoparticles. The entropy generation is negligible for the liquid flow in comparison with the vapour flow in the CLHP. In the liquid transport line, the outcome of heat transfer is very low because of the tremendous low-temperature drop of liquid in the liquid transport line. The total entropy generation variation of the CLHP is shown in Fig. 12. This happens due to heat transfer and pressure drop caused by friction. With an increase in the heat load, the total entropy generation also increases, but with increase in nanofluid concentration, the total entropy generation decreases. The entropy generation is reduced in the CLHP due to the Al_2O_3 nanofluids. The presence of nanoparticles with high thermal conductivity in the base fluid enhances the heat transfer. The entropy generation due to the heat transfer was dominated in comparison with the entropy generation due to

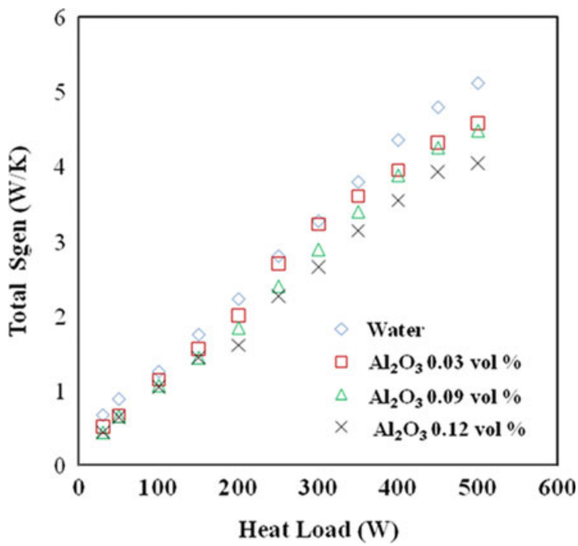

Fig. 12 Total entropy generation in CLHP

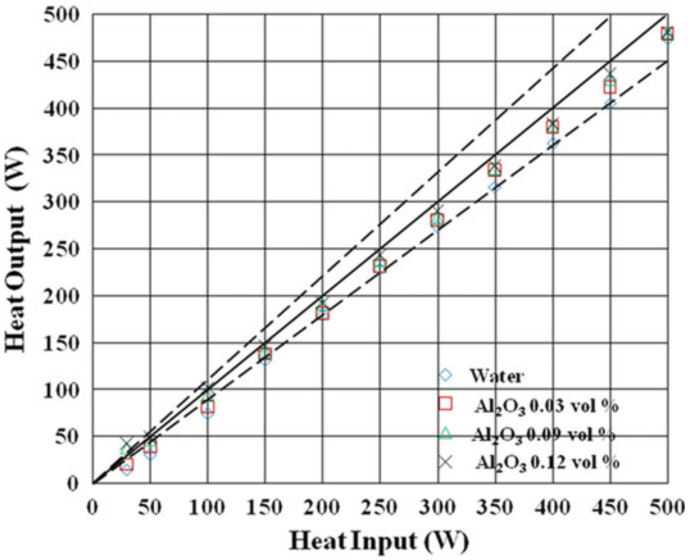

Fig. 13 Heat input versus heat output

friction. In the CLHP, energy balance is done for the heat applied at the evaporator and for the heat removed at the condenser.

The energy balance of the CLHP for distilled water and Al_2O_3/water nanofluid at different heat loads is shown in Fig. 13. It is observed that the average output gained is 82% for distilled water, and when matched with distilled water, enhancement of 11% additional is achieved for Al_2O_3/water nanofluid. Hence, it is proved that the CLHP thermal performance is improved with the use of nanoparticles with small volume concentrations. The increase in the performance of the CLHP with nanofluids makes it significant in cooling modern electronic devices.

4 Conclusion

CLHP with flat square evaporator is fabricated, and the thermal performance is experimentally tested for distilled water and Al_2O_3/water nanofluids with 0.03, 0.09 and 0.12% volume concentration. The CLHP was capable of operating up to 500 W without the occurrence of dry out condition. When compared with distilled water, the use of Al_2O_3/water nanofluids in CLHP as working fluid showed a better thermal performance. It is revealed that the thermal resistance decreases as the heat load and concentration of the Al_2O_3 nanofluid increases. The heat transfer coefficients at the evaporator and condenser and thermal efficiency of CLHP increased with the increase in Al_2O_3 nanofluid concentration. In the CLHP, the total entropy generated is increased with the increase in the heat load and decreased with the increase in the concentration of Al_2O_3 nanofluid. It is concluded that the use of small quantity Al_2O_3 nanoparticles in CLHP enhances the heat transfer performance significantly. Retrofitting of conventional heat sinks with nanofluid filled CLHP could be one of the possible solutions for the cooling of modern electronic devices.

References

1. Maydanik YF (2005) Loop heat pipes. Appl Therm Eng 25:635–657
2. Shah B (2016) Recent trends in heat pipe applications: a review. Int J Sci Eng Technol Res (IJSETR) 5(7)
3. Vasiliev L, Lossouarn D, Romestant C, Alexandre A, Bertin Y, Piatsiushyk Y, Romanenkov V (2009) Loop heat pipe for cooling of high-power electronic components. Int J Heat Mass Transf 52:301–308
4. Maydanik Y, Pastukhov V, Chernysheva M (2018) Development and investigation of a loop heat pipe with a high heat-transfer capacity. Appl Therm Eng 130:1052–1061
5. Nakamura K, Odagri K, Nagano H (2016) Operating characteristics of 10 m-class long-distance loop heat pipe under anti-gravity condition, In: Proceedings of the joint 18th international heat pipe conference and 12th international heat pipe symposium, pp 384–39
6. Wang D, Liu Z, Jiang C, Chen B, Yang J, Tu Z, Liu W (2014) Experimental study of the loop heat pipe with a flat disk-shaped evaporator. Exp Thermal Fluid Sci 57:157–164
7. Yang Y, Zhu K, Wang Y (2016) Experimental investigation and visual observation of a vapor–liquid separated flat loop heat pipe evaporator. Appl Therm Eng 101:71–78
8. He S, Zhao J, Liu Z, Tian W, Yang J, Liu W (2018) Experimental investigation of loop heat pipe with a large squared evaporator for cooling electronics. Appl Thermal Eng 144:383–391
9. Tang Y, Xiang J, Wan Z, Zhou W, Wu L (2010) A novel miniaturized loop heat pipe. Appl Therm Eng 30:1152–1158
10. Wang Dongdong, Liu Zhichun, Shen Jun, Jiang Chi, Chen Binbin, Yang Jinguo, Tu Z, Liu W (2014) Experimental study of the loop heat pipe with a flat disk-Shaped evaporator. Exp Thermal Fluid Sci 57:157–164
11. Anand AR, Akhil J, Amrit A, Pradip D (2018) Experimental studies on a miniature loop heat pipe with flat evaporator with various working fluids. Appl Therm Eng 144:495–503
12. Ji L, Daming W, Peterson GP (2010) Experimental studies on a high performance compact loop heat pipe with a square flat evaporator. Appl Therm Eng, 30:741–752
13. Prem G, Abdullah MZ, Yusoff MZ, Abdullah SF (2015) Optimization of silica nanoparticle mass concentration and heat input on a loop heat pipe. Case Stud Therm Eng 6:238–250
14. Tharayil T, Asirvatham LG, Ravindran V, Wongwises S (2016) Thermal performance of miniature loop heat pipe with graphene-water nanofluid. Int J Heat Mass Transf 93:957–968
15. Wan Z, Deng J, Li B, Xu Y, Wang X, Tang Y (2015) Thermal performance of a miniature loop heat pipe using water-copper nanofluid. Appl Therm Eng 78:712–719
16. Riehl RR (2012) Heat transport behavior of a miniature loop heat pipe using water-nickel nanofluid. Heat Pipe Sci Technol Int J 3:83–96
17. Kim HD, Kim J, Kim MH (2007) Experimental studies on CHF characteristics of nanofluids at pool boiling. Int J Multiphase Flow 33:691–706

Analysis of Externally Pressurized Thrust Bearing with Inclination Angle Using Yield Stress Fluids

G. Alexander Raymand and I. Jayakaran Amalraj

Abstract In this investigation, the effects of the non-Newtonian characteristics and angle of inclined plane (ϕ) of the externally pressurized bearing lubricated with yield stress fluid is studied. We have obtained mathematical formulation for varying film thickness. Applying appropriate boundary conditions and numerical procedure, the governing equations are solved iteratively. There is a formation of an unyielding core in the flow region for yield stress fluids, and the shape and size of this core have been calculated numerically. Further, the effects of the angle of inclined plane (ϕ) and non-Newtonian characteristic on pressure distribution and load capacity are discussed.

Keywords Externally pressurized bearing · Yield stress fluid · Inclination angle · Load capacity

1 Introduction

In the modern world, machinery industries focus on the bearing model and the innate nature of the lubricant as it increases the bearing's performance. Thrust bearings are innately developed to withstand heavy axial load. Friction is developed between the plates, while the bearing operates as it is subjected to high-speed operations, heavy loads, high stiffness, etc. To reduce this friction, the bearing is lubricated. Generally, lubricants are classified into two types, i.e. Newtonian and non-Newtonian. Any fluid that does not follow Newton's law is termed as non-Newtonian fluids, and they are characterized with high viscosity. Time-independent non-Newtonian fluids are the fluids in which the rate of shear at any point is a function of shearing stress only. Eg: Grease, mineral oil, etc.

G. Alexander Raymand (✉) · I. Jayakaran Amalraj
Department of Mathematics, Sri Sivasubramaniya Nadar (SSN) College of Engineering, Kalavakkam, Chennai 603110, India
e-mail: alexanderraymandg@ssn.edu.in

E. T. Akinlabi et al. (eds.), *Trends in Mechanical and Biomedical Design*, Lecture Notes in Mechanical Engineering,
https://doi.org/10.1007/978-981-15-4488-0_41

Non-Newtonian fluids have varied properties compared to Newtonian fluids as they resist flow and thereby significantly increase load-carrying capacity in bearings. The shear-thinning and shear-thickening characteristics are the key factors that influence them. However, non-Newtonian fluids characterized by a yield value are keenly studied by Tribologists, and they include fluids such as Bingham, Casson and Herschel Bulkley. Therefore, non-Newtonian fluids in the externally pressurized converging circular thrust bearings have been a necessity and developing interest.

By considering the above principles of the fluid with yield value, the bearing surfaces in this study are separated by a fluid film that is formed and sustained by external means. The pioneering researchers in this field have laid the foundation of bearings lubricated with Newtonian fluids. Nowadays, Tribologists concentrate on non-Newtonian fluids characterized by a yield value due to its varying viscosities. Tribologists have most often researched the rheodynamic lubrication in an externally pressurized thrust bearing. Kalil et al. [1] investigated numerically the effects of convective and centrifugal inertial forces, on the performance of externally pressurized conical thrust bearings under turbulent flow and observed that the circular bearing had a slightly higher dimensionless pressure, load and torque than the conical bearing. It was observed that the turbulent flow solution gave higher dimensionless pressure, load and torque compared to the laminar flow solution. Elsharkawy and Kassab [2] have analysed the effect of a porous layer on the hydrodynamic lubrication performance of an externally pressurized circular recessed bearing and observed that dimensionless viscosity parameter has significant effects on the pressure profiles and the load-carrying capacity of the externally pressurized porous bearings. Lin [3] theoretically studied the combined effects of couple stress, fluid inertia and recess volume fluid compressibility on the steady-state and the dynamic characteristics of hydrostatic circular step thrust bearings and concluded that steady-state load-carrying capacity decreases with fluid inertia but remains the same even for higher values of the couple stress parameter. The problem of an externally pressurized thrust bearing lubricated with Herschel–Bulkley fluids has been considered by Kandasamy et al. [4], and numerical solutions have been obtained for the pressure distribution and the load-carrying capacity.

Using yield stress fluids as lubricants, the problem of different types of bearings has been investigated. H-B fluids are a class of non-Newtonian fluids that require finite stress known as yield stress, to deform. Therefore, when the local shear is below the yield stress, these materials behave as a rigid body. Once the yield stress exceeds, the material flows with a nonlinear stress–strain relationship which exhibits itself either as a shear-thinning or shear-thickening fluid. Alexandrou et al. [5] studied a steady flow of Herschel–Bulkley fluids in a canonical three-dimensional expansion and examined the topology of the yielded and unyielded surfaces. The results revealed a strong interplay between the Bingham and Reynolds numbers. Using the augmented Lagrangian method, Huilgol et al. [6] investigated the problems with the steady flow of visco-plastic fluids in pipes of circular and square cross-sections. The solutions for plug flow velocity, the flow rate and its pattern, the velocity profile, the region of yielded/unyielded surfaces, the stopping criteria and the friction factor have been obtained. Vishwanath and Kandasamy [7] analysed the effects of fluid inertia forces in circular squeeze film bearing lubricated with Herschel–Bulkley fluids with constant squeeze motion. They observed that the pressure and the load capacity of the bearing proportionately increase with the increase of Herschel–Bulkley number and power law index of the fluids. Amalraj et al. [8] analysed the problem of an externally pressurized thrust bearing lubricated with yield stress fluid under the sinusoidal flow rate concluding that the effects of non-Newtonian characteristics on the load capacity are more significant when the amplitude of the sinusoidal motion is very high. Walicki and Jurczak [9] investigated the influence of a wall porosity on the pressure distribution in a curvilinear squeeze film bearing lubricated with a yield stress type lubricant and obtained a formula expressing the pressure distribution.

The geometric shape of the bearing plays a vital role as it wholly increases the performance of the bearing. This factor drives the following studies to research on the converging film thickness using non-Newtonian fluids with its numerous potential advantages. Most of the studies focus on externally pressurized thrust bearings with uniform film thickness and not with variable film thickness. A few researchers studied the performance of converging and diverging bearings. Roy et al. [10] discussed the effect of inertia forces in an externally pressurized bearing with both converging and diverging film thickness using a visco-elastic lubricant. Vishwanath et al. [11] analysed the problem of a squeeze film bearing with the converging and diverging film thickness. Amalraj and Raymand [12] studied the effects of the varying film in rheodynamic lubrication using externally pressurized bearing and have shown theoretically that as the inclination angle increases, the load-carrying capacity also increases.

The purpose of this research is to investigate the impact of the inclination angle and non-Newtonian characteristics on the performance of the circular thrust bearing using yield stress fluids. Numerical solutions have been obtained for bearing performances such as the core thickness, velocity, pressure distribution and load-carrying capacity for various values of yield stress fluid number (N), power law index (n) and inclination angle (ϕ).

2 Formulation of the Problem

The region between the circular plates of the bearing is symmetric, so the upper portion of the bearing is considered for analysis. The geometry of the problem is shown schematically in Fig. 1.

The 3-D constitutive equation of a yield stress fluid is given by (Alexandrou et al.)

$$\tau = \left[\eta_1\left(\frac{D_{\mathrm{II}}}{2}\right)^{\frac{(n-1)}{2}} + \frac{\eta_2\left[1-\exp\left(-m\sqrt{D_{\mathrm{II}}/2}\right)\right]}{\sqrt{D_{\mathrm{II}}/2}}\right] * D \tag{1}$$

Whorlow gave $1-D$ form of Eq. (1) in 1980.

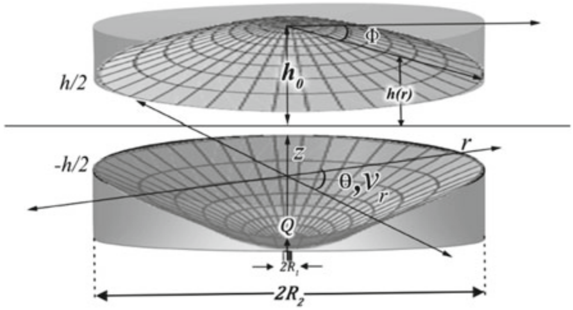

Fig. 1 Schematic diagram of externally pressurized inclined circular thrust bearing

$$\tau = \eta_2 + \eta_1 \dot{\gamma}^n, \quad \text{where } \dot{\gamma} \text{ represents shear rate.} \tag{2}$$

There will be a core formation when the shear stress is less than the yield stress of the material. The core will move with the constant velocity, v_c. Let the boundaries of the core be $z = -\frac{\delta(r)h}{2}$ and $z = \frac{\delta(r)h}{2}$ as shown in Fig. 2.

Using the assumption of lubrication theory, the governing equations are reduced and expressed as follows

Continuity Equation:

$$\frac{1}{r}\frac{\partial}{\partial r}(r v_r) + \frac{\partial v_z}{\partial z} = 0 \tag{3}$$

Momentum Equation:

$$\frac{\partial \tau_{rz}}{\partial z} = -\frac{\partial p}{\partial r} \tag{4}$$

$$\frac{\partial p}{\partial z} = 0 \tag{5}$$

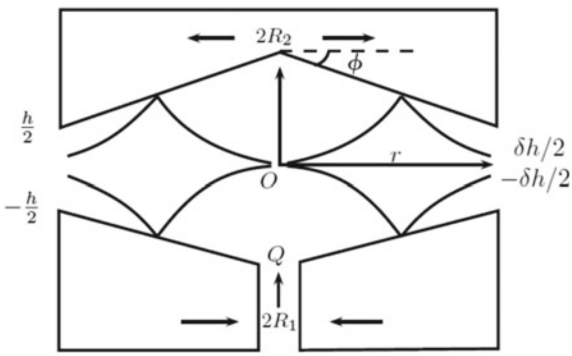

Fig. 2 Formation of core in externally pressurized thrust bearing

$$\tau_{rz} = \eta_2 + \eta_1 \left| \frac{\partial v_r}{\partial z} \right|^n \tag{6}$$

The considered governing equations are to be solved by following boundary conditions

$$v_r = 0 \quad \text{at} \quad z = \pm \frac{h}{2} \tag{7}$$

$$v_r = v_c \quad \text{at}\, z = \pm \frac{\delta h}{2} \tag{8}$$

$$\frac{\partial v_r}{\partial z} \text{is continuous,} \quad \text{at}\ \tau = \eta_2 \tag{9}$$

$$p = p_a \quad \text{at} \quad r = R_2 \tag{10}$$

3 The Solution to the Problem

Solving Eq. (4) by integrating and using Eq. (6) and applying boundary condition (7) and (8), we obtain velocity distributions in the flow region as

$$v_r = \left[\frac{n}{n+1}\right]\left[\frac{1}{\eta_1}\right]^{\frac{1}{n}}\left[\frac{-\mathrm{d}p}{\mathrm{d}r}\right]^{\frac{1}{n}} * \left[\left(z - \frac{\delta h}{2}\right)^{\frac{1}{n}+1} - \left(\frac{h}{2} - \frac{\delta h}{2}\right)^{\frac{1}{n}+1}\right], \quad \text{where} \frac{\delta h}{2} \leq z \leq \frac{h}{2} \tag{11}$$

velocity in the core region as

$$v_c = -\left[\frac{n}{n+1}\right]\left[\frac{1}{\eta_1}\right]^{\frac{1}{n}}\left[\frac{-\mathrm{d}p}{\mathrm{d}r}\right]^{\frac{1}{n}}\left[\frac{h}{2} - \frac{\delta h}{2}\right]^{\frac{1}{n}+1}, \quad \text{where } 0 \leq z \leq \frac{\delta h}{2} \tag{12}$$

The equation of conservation of mass which depends on the bearing shape in this case is

$$Q = 4\pi r \int_0^{\frac{h}{2}} v_r \ \mathrm{d}z \tag{13}$$

where Q is flow rate per unit width

Using velocity distributions v_r and v_c from Eqs. (11) and (12) in Eq. (13) and integrating, we obtain

$$Q = -\left[\frac{n}{(n+1)(2n+1)}\right]\left[\frac{1}{\eta_1}\right]^{\frac{1}{n}} \left\{\frac{\pi r h^{\frac{1}{n}+2}\left(\frac{-\mathrm{d}p}{\mathrm{d}r}\right)^{\frac{1}{n}}}{2^{\frac{1}{n}}}\right\}$$
$$* (1-\delta)^{\frac{1}{n}+1}(n\delta + n + 1) \tag{14}$$

Now, consider the equilibrium of an element in the yield surface $-\frac{\delta h}{2} \leq z \leq \frac{\delta h}{2}$, we get

$$\frac{\mathrm{d}p}{\mathrm{d}r} = \frac{2\eta_2}{\delta(r)h} \tag{15}$$

By eliminating the pressure gradient from Eqs. (14) and (15), we get an algebraic equation to find the thickness of the yield surface $\delta(r)$

$$\frac{\left[\frac{(n+1)(2n+1)}{n}\right]Q\ \eta_1^{\frac{1}{n}}}{\pi\ r\ h^2\ \eta_2^{\frac{1}{n}}} = \frac{(1-\delta)^{\frac{1}{n}+1}(n\delta + n + 1)}{\delta^{\frac{1}{n}}} \tag{16}$$

From Eq. (14), we get,

$$\frac{\mathrm{d}p}{\mathrm{d}r} = \frac{2\left[\frac{(n+1)(2n+1)}{n}\right]^n Q^n\ \eta_1}{\pi^n\ r^n\ h^{2n+1}(1-\delta)^{n+1}(n\delta + n + 1)^n} \tag{17}$$

From Fig. 1, the variation of the film thickness of the lubricant due to the angle of inclination of the bearing can be defined as

$$h(r) = h_0 - h_0\left(\frac{r}{R_2}\right)\tan\phi \tag{18}$$

Non-dimensional parameters are introduced as follows.

$$r^* = \frac{r}{R_2};\ \delta^* = \delta(r^*);$$
$$p^* = \frac{p}{\left[\frac{Q^n \eta_1}{\pi^n\ h_0^{2n+1} R_2^{n-1}}\right]};\ h^* = \frac{h}{h_0};\ z^* = \frac{z}{h};$$
$$N = \frac{\pi\ R_2\ h_0^2}{Q}\left(\frac{\eta_2}{\eta_1}\right)^{\frac{1}{n}} \tag{19}$$

The non-dimensional form of the velocity profile, core thickness as

$$v_r^* = \frac{(2n+1)(2)^{\frac{1}{n}}}{\frac{r^*(1-r^*\tan\phi)(n\delta^*+n+1)(1-\delta^*)^{\frac{1}{n}+1}}{\left\{\left(\left(\frac{1}{2}\right)^{\frac{1}{n}+1}(1-\delta^*)^{\frac{1}{n}+1}\right)-\left(z^*-\frac{\delta^*}{2}\right)^{\frac{1}{n}+1}\right\}}}, \quad \text{where } -\frac{\delta^* h^*}{2} \le z^* \le \frac{h^*}{2} \tag{20}$$

$$v_c^* = \frac{(2n+1)}{2r^*(1-r^*\tan\phi)(n\delta^*+n+1)}, \quad \text{where } 0 \le z^* \le \frac{\delta^* h^*}{2} \tag{21}$$

$$\frac{(1-\delta^*)^{1+n}(1+n+n\delta^*)^n}{\delta^*} - \frac{\left(\frac{(n+1)(2n+1)}{n}\right)^n}{(N)^n(r^*)^n(1-r^*\tan\phi)^{2n}} = 0 \tag{22}$$

$$\frac{\mathrm{d}p^*}{\mathrm{d}r^*} = N^n\left(\frac{2}{\delta^*(1-r^*\tan\phi)}\right) \tag{23}$$

From the nonlinear algebraic Eq. (22), the core thickness can be calculated.

The roots $\delta(r*, N, n, \varphi)$ of this equation define the shape of the plug core region is which is positive and smaller than unity. The values of δ have been determined for different values of angle of inclination, yield stress fluid and power law index (ϕ, N & n) by iterative techniques.

Knowing (δr^*) and integrating Eq. (23) numerically and using boundary condition $p = p_a$, the pressure distribution can be found and is given by,

$$P^* - P_a^* = \int_{r^*}^{1}\left[\frac{\mathrm{d}p^*}{\mathrm{d}r^*}\right]\mathrm{d}r^* \tag{24}$$

Similarly, the load-carrying capacity of the externally pressurized bearing can be obtained by integrating the pressure along the thrust bearing and is given by

$$W = \int_{R^*}^{1}(P^* - P_a^*)r^*\mathrm{d}r^* \tag{25}$$

where $R^* = \frac{R_1}{R_2}$ is the ratio of inside to outside radius of the bearing. This integration is performed numerically for various values of inclination angle, yield stress fluid number and power law index (ϕ, $N\&n$).

4 Results and Discussion

The shape and thickness of the core for various inclination angle, yield stress fluid number and the power law index (*ϕ, N & n*) at every point in the radial direction are computed, and the results are given in Figs. 3, 4 and 5. In the case of varying film thickness, for a given yield stress fluid and the power law index (*N & n*) at each point in the radial direction, its thickness decreases as inclination angle (*ϕ*)

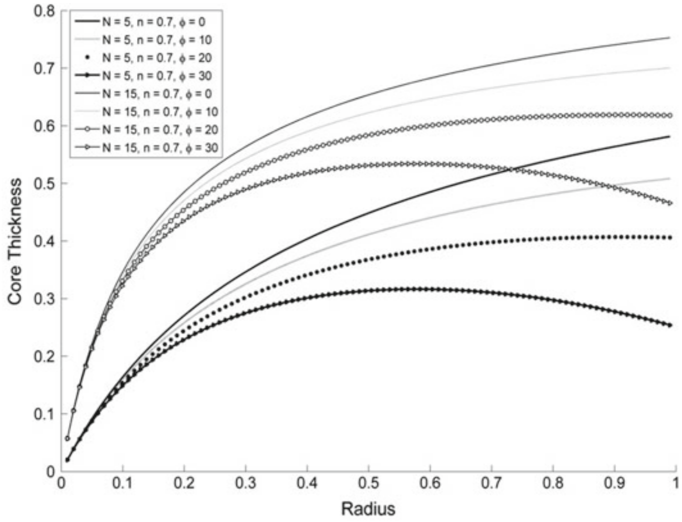

Fig. 3 Core thickness for different inclination angle when $n = 0.7$

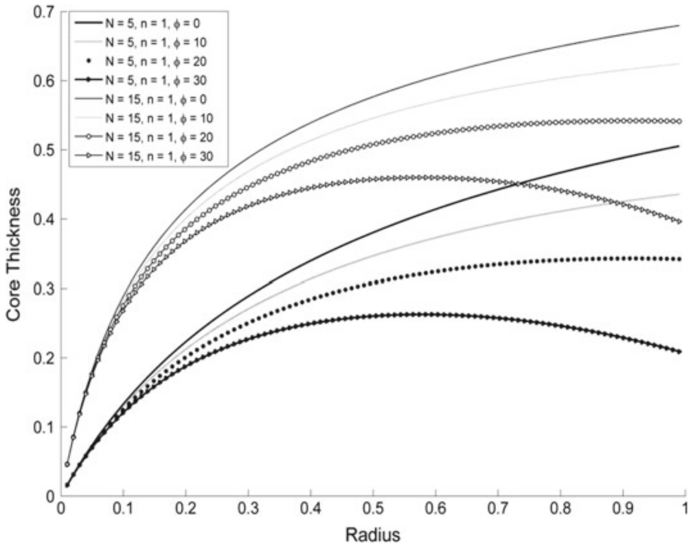

Fig. 4 Core thickness for different inclination angle when $n = 1$

increases. Further, the thickness of the core increases with an increase in a yield stress fluid (N) for a constant power law index (n). Similarly, the thickness of the core marginally decreases with an increase in power law index (n), for a constant yield stress fluid number (N). The velocity profile for various inclination angle, yield stress fluid number and power law index (ϕ, N & n) along the axial direction (z^*)

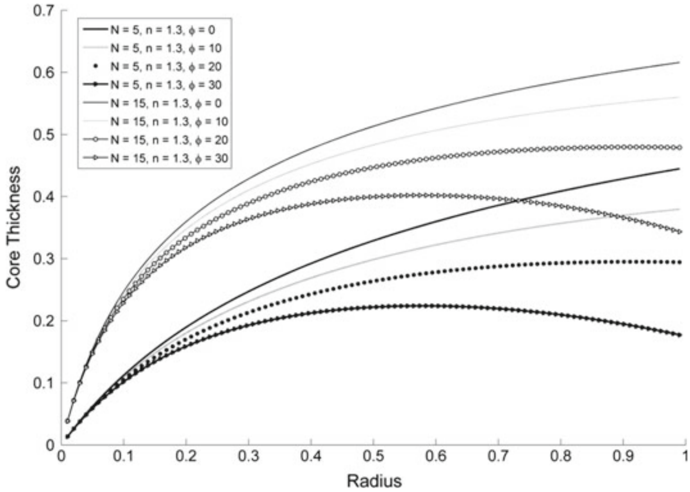

Fig. 5 Core thickness for different inclination angle when $n = 1.3$

for various values of the radius($r*$) is depicted in Fig. 6. The thickness of the core as observed earlier is reflected in the velocity profile. The pressure distribution for various values of inclination angle, yield stress fluid number and power law index (ϕ, N & n) in the radial direction is as shown in Figs. 7, 8, 9 and 10. The pressure profile is found to be maximum at the centre and gradually decreases as it moves towards the periphery in the radial direction. The load-carrying capacity for various

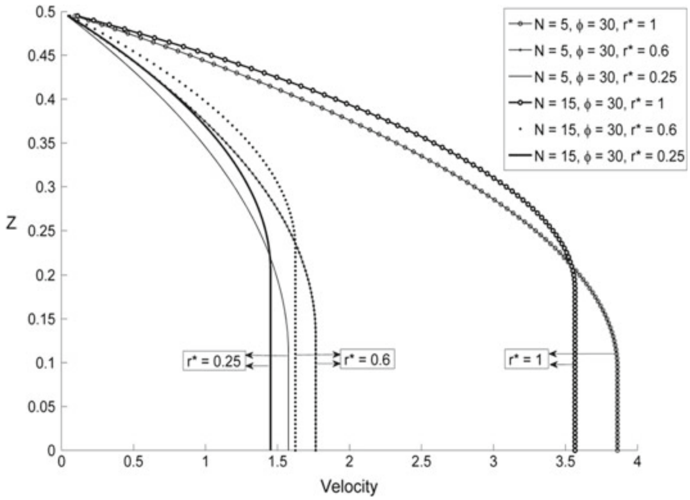

Fig. 6 Velocity profile

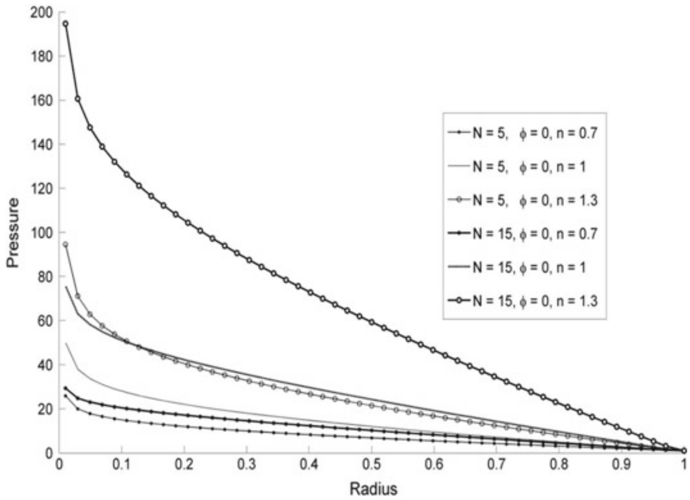

Fig. 7 Pressure distribution for zero inclination angle

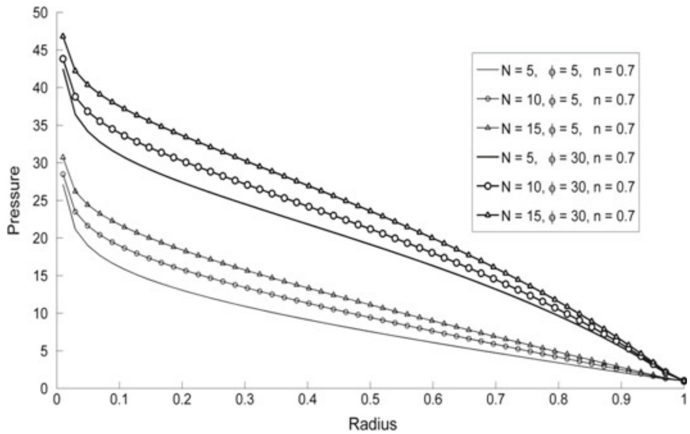

Fig. 8 Pressure distribution for different inclination angle (ϕ) and yield stress number (N) when $n = 0.7$

values of inclination angle, yield stress fluid number and power law index (ϕ, N & n) in the radial direction is tabulated in Tables 1, 2 and 3.

Case 1: Increasing the inclination angle (ϕ), the pressure is maximum at the centre and decreases as it moves towards its periphery, and increment in load-carrying capacity is gradual and marginal for a constant yield stress fluid number and power law index (N & n). Case 2: For dilatant fluids ($n > 1$), the pressure distribution and load-carrying capacity are high, whereas for pseudoplastic fluids ($n < 1$), pressure distribution and load-carrying capacity are low for constant inclination angle and

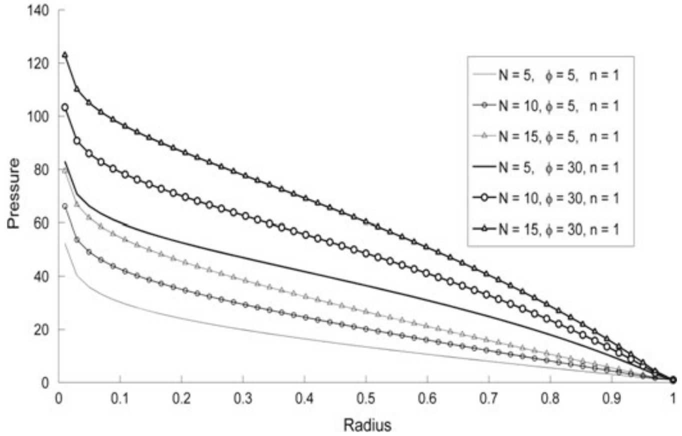

Fig. 9 Pressure distribution for different inclination angle and yield stress number (N) when $n = 1$

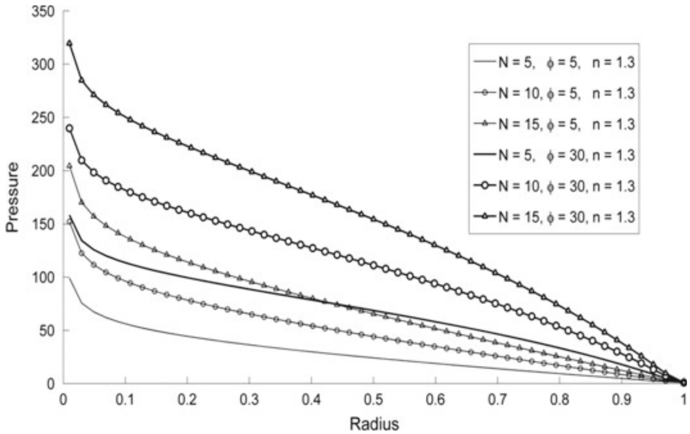

Fig. 10 Pressure distribution for different inclination angle and yield stress number (N) when $n = 1.3$

Table 1 Load capacity for different value of N and ϕ for $n = 0.7$

$n = 0.7$	$N = 5$	$N = 10$	$N = 15$	$N = 20$	$N = 25$
$\phi = 0$	2.48	3.06	3.58	4.06	4.51
$\phi = 10$	3.02	3.66	4.25	4.80	5.31
$\phi = 20$	4.02	4.72	5.40	6.04	6.65
$\phi = 30$	6.69	7.35	8.13	8.91	9.67

Table 2 Load capacity for different value of N and ϕ for $n = 1$

$n = 1$	$N = 5$	$N = 10$	$N = 15$	$N = 20$	$N = 25$
$\phi = 0$	4.25	6.32	8.30	10.24	12.13
$\phi = 10$	5.39	7.75	10.08	12.35	14.57
$\phi = 20$	7.30	10.30	13.16	15.95	18.68
$\phi = 30$	12.63	16.68	20.59	24.38	28.10

Table 3 Load capacity for different value of N and ϕ for $n = 1.3$

$n = 1.3$	$N = 5$	$N = 10$	$N = 15$	$N = 20$	$N = 25$
$\phi = 0$	7.50	13.61	20.13	26.99	34.15
$\phi = 10$	9.53	16.94	24.75	32.94	41.45
$\phi = 20$	13.35	22.90	32.85	43.19	53.88
$\phi = 30$	23.63	37.98	52.51	67.40	82.67

yield stress fluid number (ϕ & N). Case 3: Increasing yield stress fluid number (N), the pressure is maximum at the centre and decreases as it moves towards its periphery, and the increase in load-carrying capacity is gradual and marginal for a constant (ϕ & n). However, pressure distribution and load-carrying capacity are more significant for Case 2 when compared with Case 1 and Case 3.

We compute the relative percentage of increase for pressure distribution and load-carrying capacity for inclination angle $\phi > 0$ by keeping $\phi = 0$ as a reference angle and depicted in Figs. 11 and 12. It is evident that the increase in the relative percentage of pressure and load-carrying capacity is quite significant with respect to power law

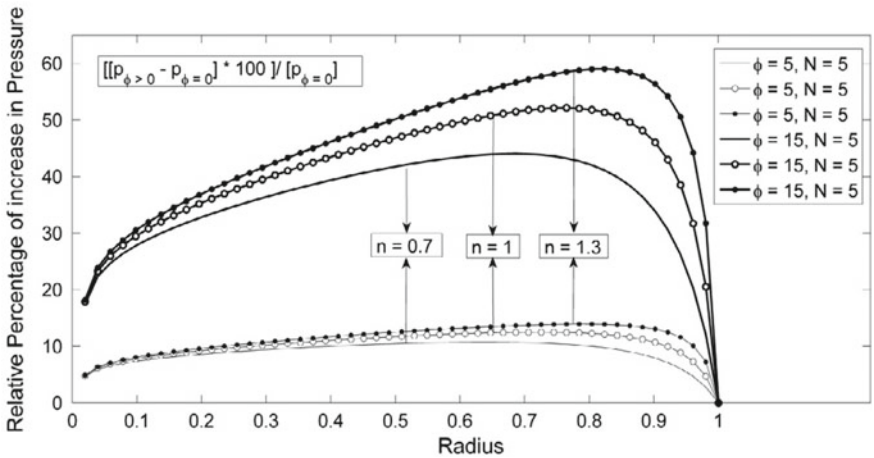

Fig. 11 Relative percentage of pressure difference for $N = 5$

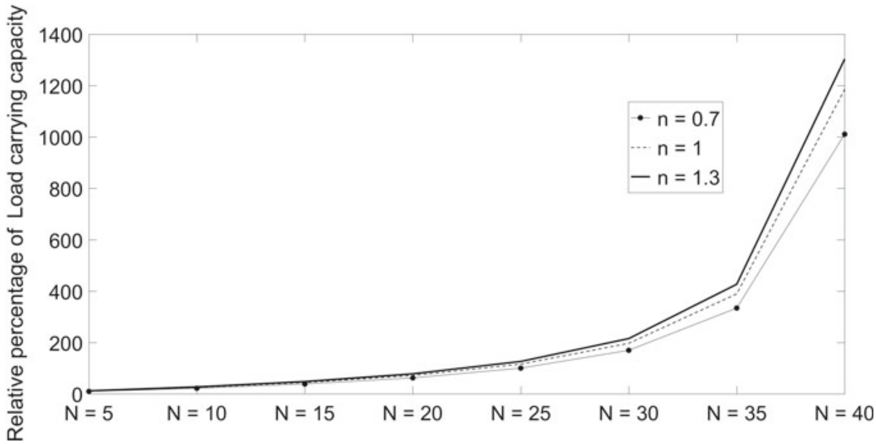

Fig. 12 Relative percentage of load-carrying capacity for various ϕ

index (n). This will help in designing the bearing to have the optimal load-carrying capacity in the case of an externally pressurized thrust bearing.

4.1 Validation

The shape and extent of the core along the radial direction, which we determined, are found to be in good agreement with the results published earlier by Jayakaran et al. [8] for uniform film bearing ($\phi = 0$).

5 Conclusion

The above investigation reveals that the Herschel−Bulkley number (N), power law index (n) and the inclination angle (ϕ) have significant effects in the bearing performance such as pressure distribution and load-carrying capacity of the bearing. Further, it has been observed that the shear-thickening fluids ($n > 1$) improve the bearing performance, whereas the shear-thinning fluids ($n < 1$) decrease for any given N and ϕ.

Acknowledgements The authors thank the Principal and management of SSN institutions for their support in carrying out this work.

References

1. Khalil MF, Kassab SZ, Ismail AS (1993) Performance of externally pressurized conical thrust bearing under laminar and turbulent flow conditions. Wear 166:147–154
2. Elsharkawy AA, Kassab SZ (1996) Lubrication analysis of externally pressurized porous bearings. App Math Modell 20:870–876
3. Lin J-R (1999) Static and dynamic characteristics of externally pressurized circular step thrust bearings lubricated with couple stress fluids. Tribol Int 32:207–216
4. Kandasamy A, Narasimman S, Jayakaran Amalraj I (2006) Rheodynamic lubrication of an externally pressurized thrust bearing with Herschel-Bulkley fluids. In: Proceedings of the international conference on Industrial Tribology, IISc, Bangalore, India
5. Alexandrou AN, McGilvreay TM, Burgos G (2001) Steady Herschel- Bulkley fluid flow in three-dimensional expansions. J Non-Newton Fluid Mech 100:77–96
6. Huilgol RR, You Z (2005) Application of the augmented lagrangian method to steady pipe flows of Bingham, Casson, and Herschel- Bulkley fluids. J Non-Newton Fluid Mech 128:126–143
7. Vishwanath KP, Kandasamy A (2010) Inertia effects in circular squeeze film bearing using Herschel-Bulkley lubricants. Appl Math Model 34:219–227
8. Amalraj IJ, Narasimman S, Kandasamy A (2012) Rheodynamic lubrication of an externally pressurized thrust bearing using Herschel-Bulkley fluid with sinusoidal injection. J Appl Fluid Mech 5(4):71–79
9. Walicka A, Jurczak P (2016) Pressure distribution in a porous squeeze film bearing lubricated with a Herschel-Bulkley fluid. Int J Appl Mech Eng 24(4):951–965
10. Sinha Roy J, Padhy S, Bhopa LK (1993) Inertia effect in the externally pressurized thrust bearing with converging and diverging film using visco-elastic lubricant. Actamechanica 96:1–12
11. Vishwanath KP, Kandasamy A (2008) Rheodynamic lubrication of a rectangular squeeze film bearing with an exponential curvature variation using Bingham lubricants. Int Sci Index Phys Math Sci 02(07):380–384
12. Jayakaran Amalraj I, Alexander Raymand G (2016) Core variation in an externally pressurized converging thrust bearing with Bingham lubricant. Appl Mech Mater 852:428–434

Numerical Investigation of Bingham Fluid Flow in the Entrance Region of Rotating Annuli

S. Mullai Venthan and I. Jayakaran Amalraj

Abstract The study of the entrance region flow is, nowaday, assuming considerable technical importance due to its immediate applications in various designs of chemical and biomedical equipments in which the flows of non-Newtonian fluids are encountered. The flow characteristic of non-Newtonian fluid that is independent of time, and which obeys Bingham's stress–strain relations, has been investigated at the entrance region of the annular space between two rotating coaxial cylinders. This analysis has been carried out for both the cases when each rotates with different speed in the same direction and as well as in the opposite direction with constant angular velocity. Discussions have been presented for a steady, laminar, isothermal flow condition of the Bingham fluid. The continuity and momentum equations are solved iteratively with finite difference method by using the Prandtl's boundary layer assumptions. The velocity components and pressure distributions have been obtained numerically for various values of Bingham number and aspect ratio.

Keywords Entrance region · Rotating cylinders · Bingham fluid · Finite difference technique · Speed variation

Nomenclature

$\Delta\eta$, $\Delta\zeta$	Mesh sizes in the radial and axial directions respectively
ρ	Density of the fluid
μ	Apparent viscosity of the model
μr	Reference viscosity
ω	Angular velocity
η, ζ	Dimensionless coordinates in the radial and axial directions respectively

S. Mullai Venthan (✉) · I. Jayakaran Amalraj
Department of Mathematics, Sri Sivasubramania Nadar (SSN) College of Engineering, Chennai, Tamil Nadu 603110, India
e-mail: selvamullai11@gmail.com

E. T. Akinlabi et al. (eds.), *Trends in Mechanical and Biomedical Design*, Lecture Notes in Mechanical Engineering,
https://doi.org/10.1007/978-981-15-4488-0_42

B	Bingham number
r_1/r_2	(Flow region of an annular space)
r_1, r_2	Radius of the inner and outer cylinders respectively
k	Coefficient of fluidity
m	Number of radial increments in the numerical mesh network
P	Dimensionless pressure
p, p_0	Pressure and initial pressure respectively
R, θ & z	Cylindrical coordinates
Re, Ta	Modified Reynolds number and Taylor number respectively
$Rt = \mathrm{Re}^2/\mathrm{Ta}$	Ratio of Reynolds number with Taylor number
R	Aspect ratio of the annulus
s_1, s_2	Speed coordinates for inner and outer cylinders respectively
v_0	Uniform inlet velocity
v_z, v_r, v_θ	Velocity components in z-, r-θ-directions respectively
U, V, W	Dimensionless velocity components

1 Introduction

The study of entrance region flow in rotating cylinders has been widely employed in various industries, ranging from the pharmaceutical, food and agricultural industries to the chemical industries, wherein Newtonian and non-Newtonian fluids are frequently being encountered. Lately, there has been an increasing concentration of problems involving fluids with variable viscosity such as Bingham plastic, Casson and Herschel–Bulkley fluids which are characterized by a yield value.

The development of fluid flow for non-Newtonian and power-law fluids in the entrance region of concentric annular cylinders has been studied by various authors, using various approximation methods, and the corresponding literature reviews have been mentioned below.

Schlichting and Gersten studied the flow of typical materials, particularly non-Newtonian fluids and the flow of any material under the influence of an applied force or stress in the preview of the boundary layer theory [1]. Escudier et al. numerically analyzed the fully developed laminar flow of an inelastic shear thinning power-law fluid through an eccentric annulus with inner cylinder rotation. Further, they also had analyzed more complex rheological models [2]. Ramesh Gupta has obtained velocity distribution by hydrodynamic study, the development of laminar power-law fluid flow in pipes and straight channels for equivalent Newtonian models [3]. Radka and Karel investigated the steady and unsteady incompressible flows for Newtonian and non-Newtonian shear thickening fluid flow through a branching channel by numerical modeling [4]. Poole and Chhabra numerically analyzed the development of laminar pipe flow of yield stress fluids which obey the Bingham-type models. And they have shown the development lengths for various values of Reynolds number [5].

Huilgol studied the minimum pressure drop required to initiate the flow of viscoplastic fluids with a constant yield stress, such as Casson and Herschel–Bulkley fluids in the pipes of the following symmetric cross sections: circular, annular, square, rectangle, equilateral triangle, elliptical and L-shape [6]. Khali et al. numerically investigated the effect of a porous layer on non-Newtonian fluids between rotating concentric annular ducts using the Lattice Boltzmann method [7]. In concentric annular cylinders with known diameter ratio and inner cylinder rotational speed, the mean velocity and the Reynolds shear stress of both Newtonian and non-Newtonian fluids have been calculated by Nouri and Whitelaw [8].

Rachid Chebbi analyzed flow in both the inlet and filled regions and obtained the lengths of the entrance, inlet and filled regions as a function of the generalized Reynolds number and the power-law fluid index by using an integral boundary layer method [9]. Round and Yu analyzed Bingham fluid in a general perspective in concentric annular cylinders for the development of flows using up-winding finite difference technique in order to solve the equation of motion. They obtained the results of velocity and pressure drop for different radius ratios, power-law indices and Bingham numbers [10]. Schulz and Pfister experimented on concentric annular cylinders using Taylor–Couette flow between rotating and counter-rotating cylinders. The numerical results, derived using finite element method, have an excellent quantitative agreement with experimental measurements for a wide range of aspect ratios and rotation rates [11].

Nallapu Santhosh et al. studied Herschel–Bulkley fluid obeying a two-fluid model flow through tubes of small diameters and a slip on the wall [12]. Guang Lu et al. investigated the cross-sectional flow of non-spherical particles in horizontal rotating cylinders with and without wall roughness. Using a similar method, gravitational acceleration and particle size were altered to investigate the effect of wall rougheners under a range of operating conditions by using discrete element method (DEM) [13]. Rekha and Kandasamy numerically investigated the results for entrance region flow of a Herschel–Bulkley fluid in an annular cylinder in the form of velocity profile within the boundary layer region. Entrance flow region of an annulus and pressure distribution has been measured for a particular Herschel–Bulkley number and various aspect ratios [14]. Srinivasa Rao and Kandasamy numerically studied the effects of parameters, aspect ratio and yield value on the pressure drop and velocity profiles for the entrance region flow heat transfer in concentric annuli with rotating inner wall for Bingham fluid [15].

The purpose of the present work is to reduce the friction, flow development at the entrance region and to increase the performance for rotating concentric annular cylinders by using time-independent non-Newtonian fluid obeying Bingham fluid with excessive work. The non-Newtonian fluid has been used to quantify the possible benefits of drag-reducing fluids. The shear rate of a non-Newtonian fluid is of importance in fixing the rheological or viscometric behavior of such materials.

In the study, the authors have analyzed numerically the velocities and pressure distributions for the flow of the Bingham fluid at the entrance region of an annular space between two rotating coaxial cylinders. The analysis has been carried out with the assumption that both cylinders are rotating in the same as well as in the opposite direction. Under Prandtl's boundary layer assumptions, the momentum equations and the equation of conservation of mass have been discretized and solved using linearized implicit finite difference scheme. The system of linear equations thus obtained has been solved by the Gauss Jordan method. The development of different velocity profiles and pressure distributions at the entrance region of the annular space have been computed numerically and presented for various values of Bingham number and aspect ratio. The effects of non-Newtonian characteristics and geometrical parameters on the flow behavior at the entrance region of annular space between two rotating coaxial cylinders have been discussed.

2 Formulation of the Problem

We have considered the Bingham fluid entering into the horizontal rotating concentric circular cylinders, with inner and outer radius $r_1$and r_2, respectively, from a large chamber with a uniform velocity v_0 and pressure p_0 initially. By fixing the origin at the entry region on the central axis of an annulus and considering cylindrical polar coordinates system (r, θ, z) with z-axis measured along the axial direction perpendicular to radial direction r, with the inner and outer rotating cylinders with angular velocity ω, under the assumptions of steady incompressible axisymmetric flow with constant properties. The geometry of the problem is shown in Fig. 1.

The constitutive equation for Bingham fluid is given as

$$\tau_{ij} = (\mu + \frac{\tau_0}{\varepsilon})\varepsilon_{ij} \ \tau \geq \tau_0 \text{ where } \tau = \sqrt{\frac{1}{2}\tau_{ij}\tau_{ij}} \text{ and } \varepsilon = \sqrt{\frac{1}{2}\varepsilon_{ij}\varepsilon_{ij}} \tag{1}$$

where τ_0 is the yield stress, τ_{ij} and ε_{ij} are the stress tensor and the rate-of-strain tensor, respectively, and μ is the viscosity of the fluid. The flow is governed by the equations

$$\frac{\partial}{\partial r}(r v_r) + \frac{\partial}{\partial z}(r v_z) = 0 \tag{2}$$

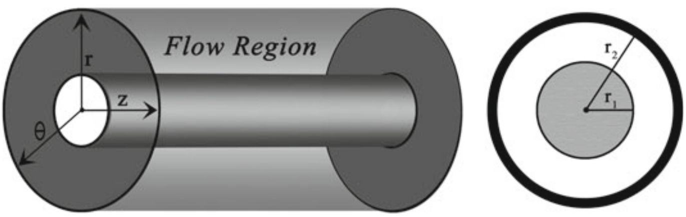

Fig. 1 Geometry of the rotating cylinders

$$\frac{v_\theta^2}{r} = \frac{1}{\rho}\frac{\partial p}{\partial r} \tag{3}$$

$$v_r\frac{\partial(v_\theta)}{\partial r} + v_z\frac{\partial(v_\theta)}{\partial z} + \frac{vv_\theta}{r} = \frac{1}{\rho r^2}\frac{\partial}{\partial r}\left(r^2\left[\tau_0 + kr\frac{\partial}{\partial r}\left(\frac{v_\theta}{r}\right)\right]\right) \tag{4}$$

$$v_r\frac{\partial(v_z)}{\partial r} + v_z\frac{\partial(v_z)}{\partial z} = -\frac{1}{\rho}\frac{\partial p}{\partial z} + \frac{1}{\rho r}\frac{\partial}{\partial r}(r[\tau_0 + k\frac{\partial v_z}{\partial r}]) \tag{5}$$

where v_z, v_r, v_θ are the velocity components in z-, r-, θ-directions, respectively.

The boundary conditions for inner and outer cylinders rotating with different speed in the same direction are

$$\begin{aligned}
&\text{For } z \geq 0 \text{ and } r = r_1,\ v_r = v_z = 0 \quad \text{and } v_\theta = \omega r_1(s_1)\\
&\text{For } z \geq 0 \text{ and } r = r_2,\ v_r = v_z = 0 \quad \text{and } v_\theta = \omega r_2(s_2)\\
&\text{For } z = 0 \text{ and } r_1 < r < r_2,\ v_z = v_0\\
&p = p_0 \quad \text{at } z = 0
\end{aligned}$$

The boundary conditions for inner and outer cylinders rotating with different speed in the opposite direction are

$$\begin{aligned}
&\text{For } z \geq 0 \quad \text{and } r = r_1,\ v_r = v_z = 0 \quad \text{and } v_\theta = \omega r_1(s_1)\\
&\text{For } z \geq 0 \quad \text{and } r = r_2,\ v_r = v_z = 0 \quad \text{and } v_\theta = \omega r_2(s_2)\\
&\text{For } z = 0 \quad \text{and } r_1 < r < r_2,\ v_z = v_0\\
&p = p_0 \quad \text{at } z = 0
\end{aligned}$$

Using the boundary conditions, the continuity Eq. (2) can be expressed in the following integral form:

$$2\int_{r_2}^{r_1} rv_z\mathrm{d}r = (r_2^2 - r_1^2)v_0 \tag{6}$$

Let us non-dimensionalize the parameters are

$$\begin{aligned}
&\eta = \frac{r}{r_2}, U = \frac{v_z}{v_0}, V = \frac{\rho v_r r_2}{\mu_r}, W = \frac{v_\theta}{\omega r_1}, R = \frac{r_1}{r_2},\\
&P = \frac{p - p_0}{\rho v_0^2}, \zeta = \frac{2v_z(1-R)}{r_2\mathrm{Re}}, B = \frac{\tau_0 r_2}{kv_0},\\
&\mathrm{Re} = \frac{2\rho(r_2 - r_1)v_0}{k},\\
&T_a = \frac{2\Omega^2\rho^2 r_1^2(r_2 - r_1)^3}{\mu_r^2(r_1 + r_2)}, \quad \text{where } \mu_r = k\left(\frac{\omega r_1}{r_2}\right)
\end{aligned}$$

By introducing the above non-dimensional parameters, in the governing Eqs. (2)–(5) as well as in boundary conditions (6), they become

$$\frac{\partial V}{\partial \eta}+\frac{V}{\eta}+\frac{\partial U}{\partial \zeta}=0 \tag{7}$$

$$\frac{W^2}{\eta}=\frac{\mathrm{Re}^2(1-R)}{2(1+R)Ta}\frac{\partial P}{\partial \eta} \tag{8}$$

$$V\frac{\partial W}{\partial \zeta}+U\frac{\partial W}{\partial \zeta}+\frac{VW}{\eta}=\frac{\partial^2 W}{\partial \eta^2}+\frac{1}{\eta}\frac{\partial W}{\partial \eta}-\frac{W}{\eta^2}+\frac{2B}{\eta} \tag{9}$$

$$V\frac{\partial U}{\partial \eta}+U\frac{\partial U}{\partial \zeta}=-\frac{\partial P}{\partial \zeta}+\frac{1}{\eta}\frac{\partial U}{\partial \eta}+\frac{\partial^2 U}{\partial \eta^2}+\frac{B}{\eta} \tag{10}$$

$$2\int_R^1 \eta U \mathrm{d}\eta=(1-R^2) \tag{11}$$

The boundary conditions for cylinders rotating with different speed in the same direction, in the dimensionless form, are

$$\begin{aligned}
&\text{For } \varsigma \geq 0 \quad \text{and } \eta = R,\, V = U = 0 \ \text{ and } W = 1\\
&\text{For } \varsigma \geq 0 \quad \text{and } \eta = 1,\, V = U = 0 \ \text{ and } W = 2/R\\
&\text{For } \varsigma \geq 0 \quad \text{and } R < \eta < 1,\ U = 1\\
&P = 0 \quad \text{at } \varsigma = 0
\end{aligned}$$

The boundary conditions for cylinders rotating with different speed in the opposite direction, in the dimensionless form, are

$$\begin{aligned}
&\text{For } \varsigma \geq 0 \quad \text{and } \eta = R,\, V = U = 0 \quad \text{and } W = 1\\
&\text{For } \varsigma \geq 0 \quad \text{and } \eta = 1,\, V = U = 0 \quad \text{and } W = -2/R\\
&\text{For } \varsigma \geq 0 \quad \text{and } R < \eta < 1,\ U = 1\\
&P = 0 \quad \text{at} \varsigma = 0
\end{aligned}$$

3 Numerical Solution

The numerical investigation and the scheme of solution can be considered as a roundabout expansion work of Coney and El-Shaarawi [16]. It has been decided to solve the above system of governing equations, using finite difference method. Considering the mesh network of Fig. 2, the following difference representations are made.

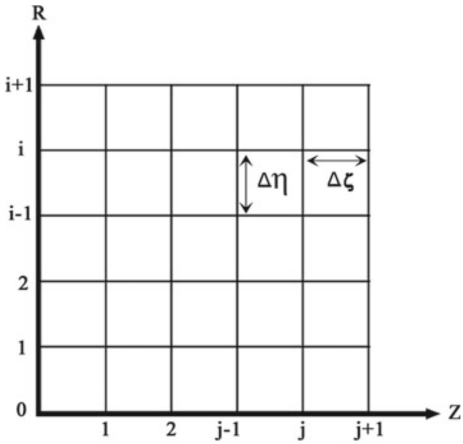

Fig. 2 Meshwork for the finite difference technique

The discretized solution space is shown in Fig. 2 in which $\Delta\eta$ and $\Delta\zeta$ correspond to the grid size along the radial direction and also axial direction, respectively. By assuming appropriate finite difference equations, the non-dimensionalized system of Eqs. (7)–(11) got reduced as

$$V_{(i+1)}^{(n+1)} = V_i^{(n+1)}\left(\frac{R + i\Delta\eta}{R + (i+1)\Delta\eta}\right) - \frac{4\Delta\eta}{4\Delta\varsigma}\left(\frac{2R + (2i+1)\Delta\eta}{R + (i+1)\Delta\eta}\right) * \left(U_{i+1}^{(n+1)} + U_i^{((n+1)} - U_i^{(n+1)} - U_i^{(n)}\right) \tag{12}$$

$$\frac{[W^2]_i^{(n+1)}}{R + i\Delta\eta} = \frac{(1-R)\mathrm{Re}^2}{2Ta(1+R)} \frac{P_i^{(n+1)} - P_{i-1}^{(n+1)}}{\Delta\eta} \tag{13}$$

$$\begin{aligned} &V_i^{(n)}\left[\frac{W_{i+1}^{(n+1)} + W_{i+1}^{(n)} - W_{i-1}^{(n+1)} - W_{i-1}^{(n)}}{4\Delta W}\right] + U_i^{(n)}\left[\frac{W_i^{(n+1)} - W_i^{(n)}}{\Delta\varsigma}\right] \\ &+ \left[\frac{V_i^{(n)} W_i^{(n)}}{R + i\Delta\eta}\right] = V_i^{(n)}\left[\frac{W_{i+1}^{(n+1)} + W_{i+1}^{(n)} - 2W_i^{(n+1)} - 2W_i^{(n)}}{2(\Delta\eta)^2}\right] \\ &+ \left[\frac{W_{i-1}^{(n)} - W_{i-1}^{(n+1)}}{2(\Delta\eta)^2}\right] - \left[\frac{W_i^{(n)}}{(R + i\Delta\eta)^2}\right] \\ &+ V_i^{(n)}\left[\frac{W_{i+1}^{(n+1)} + W_{i+1}^{(n)} - W_{i-1}^{(n+1)} - W_{i-1}^{(n)}}{(R + i\Delta\eta)4\Delta\eta}\right] + \left[\frac{2B}{R + i\Delta\eta}\right] \end{aligned} \tag{14}$$

$$V_i^{(n)}\left[\frac{U_{i+1}^{(n+1)} - U_{i-1}^{(n+1)}}{2\Delta\eta}\right] + U_i^{(n)}\left[\frac{U_i^{(n+1)} - U_i^{(n)}}{\Delta\varsigma}\right] = -\left[\frac{P_{i+1}^{(n+1)} - P_i^{(n)}}{\Delta\varsigma}\right]$$

$$+\left[\frac{U_{i+1}^{(n+1)}-U_{i-1}^{(n+1)}}{(R+i\Delta\eta)2\Delta\eta}\right]+\left[\frac{U_{i+1}^{(n+1)}-2U_{i}^{(n+1)}-U_{i-1}^{(n+1)}}{2(\Delta\eta)^2}\right]+\left[\frac{B}{R+i\Delta\eta}\right] \tag{15}$$

where $i = 0$ at $\eta = R$ and $i = m$ at $\eta = 1$, the application of trapezoidal rule to Eq. (12) gives

$$\frac{\Delta\eta}{2}\left(RU_0^{(n)}+U_{(m)}^{(n)}\right)+\Delta\eta\sum_{i=1}^{m-1}U_1^{(n)}(R+i\Delta\eta)=\left(\frac{1-R^2}{\eta}\right) \tag{16}$$

The boundary conditions give for both cases

$$U_0^{(n)}=U_0^{(m)}=0$$

$$\Delta\eta\sum_{i=1}^{m-1}U_1^{(n)}(R+i\Delta\eta)=\left(\frac{1-R^2}{\eta}\right) \tag{17}$$

For both the cases of rotation, i.e., rotating in the same direction and opposite direction of the annular cylinder, the above set of Eqs. (12)–(15) and (17) have been solved using an iterative process. At first, Eq. (14) has been solved at the $n = 0$ columns, and i varied from 1 to $m - 1$ to obtain the system of linear equations which is solved using the Gauss Jordan method to obtain the tangential velocity. Equations (13), (15) and (17) have been solved under similar conditions to determine a system of linear equations. This system has been solved by the Gauss-Jordan method to obtain the axial velocity and pressure at the adjacent column $n = 1$. Finally, the radial velocity is obtained from Eq. (12) by Gauss-Jordan method using the known values of U. Repeating the above procedure, we obtain the result column by column, along the axial direction of the annulus until the flow becomes axially and tangentially fully developed. The above equations, to computationally solve, lead to the following results.

4 Results and Discussion

Numerical solutions have been obtained for some permissible values of Bingham number B and aspect ratio R. For the aspect ratio $R = 0.3$–0.8, the ratio of Reynolds number to Taylor number as $Rt = 20, 30$; $\Delta\zeta = 0.02, 0.03$ and $\Delta\eta = 0.007, 0.002$ was fixed, respectively. The velocity profiles and pressure distribution along the radial direction have been computed for varying Bingham numbers, $B = 0$, 10, 20, 30 for two different cases namely, case 1: Rotating cylinders in the same direction and case 2: Rotating cylinders in opposite direction. The cylinders are rotating with different speed when the outer cylinder rotating speed increases in both cases. Numerical results for case 1 and case 2 are depicted in Figs. 3, 4, 5, 6, 7, 8, 9, 10, 11, 12, 13,

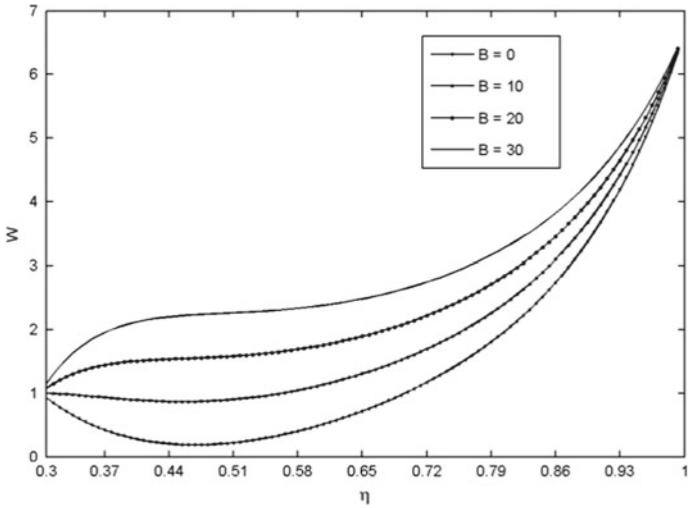

Fig. 3 Tangential velocity for different Bingham number when $R = 0.3$

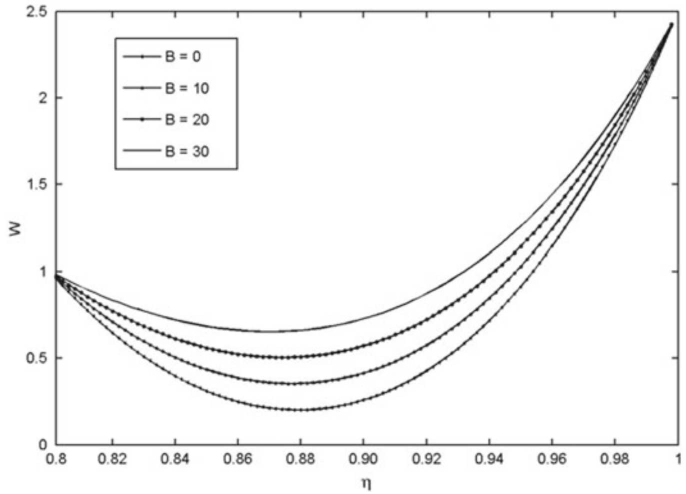

Fig. 4 Tangential velocity for different Bingham number when $R = 0.8$

14, 15, 16, 17, 18, 19, 20, 21 and 22, respectively.

The tangential velocity profile of cylinders that are rotating with different speeds in same and opposite directions is shown in Figs. 3, 4, 13 and 14, respectively, for various values of Bingham number and aspect ratio. As the outer cylinders rotating speed increases, in the case of cylinders rotating in the same direction, the tangential velocity increases with an initial downturn of the increasing values from the inner wall, and then, it continues increasing toward the outer wall of the annulus when

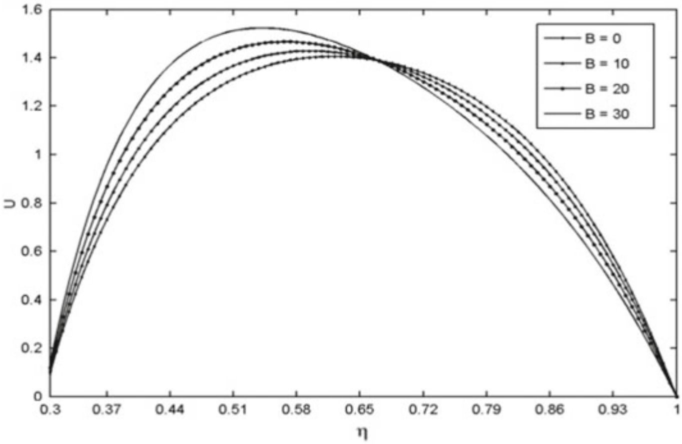

Fig. 5 Axial velocity for different Bingham number when $R = 0.3$

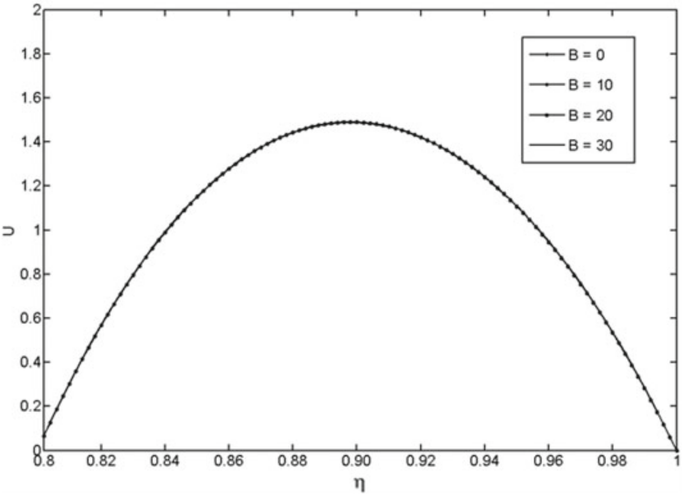

Fig. 6 Axial velocity for different Bingham number when $R = 0.8$

the annular space is small. However, in the case of cylinders rotating in opposite direction, the tangential velocity decreases with an initial rise from the inner wall and reaches its minimum at different radial positions for different Bingham numbers, and then, it steadily increases as it approaches the outer wall. It is also observed that in both the cases, the maximum tangential velocity value near the outer wall decreases for different Bingham numbers when we increase the aspect ratio from $R = 0.3$ to 0.8, i.e., as the annular space decreases.

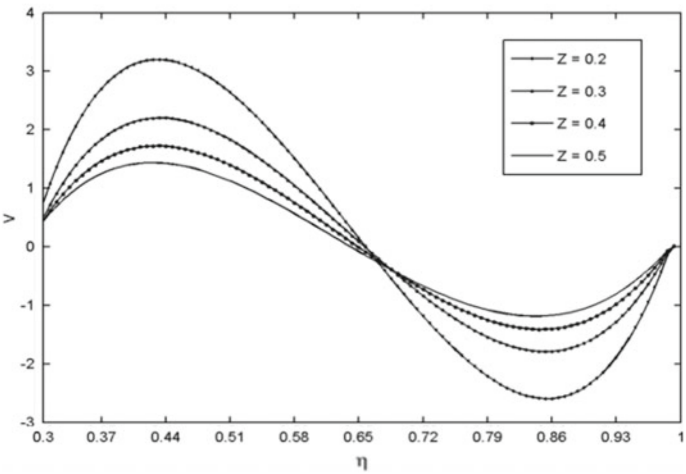

Fig. 7 Radial velocity for different sections when $R = 0.3$

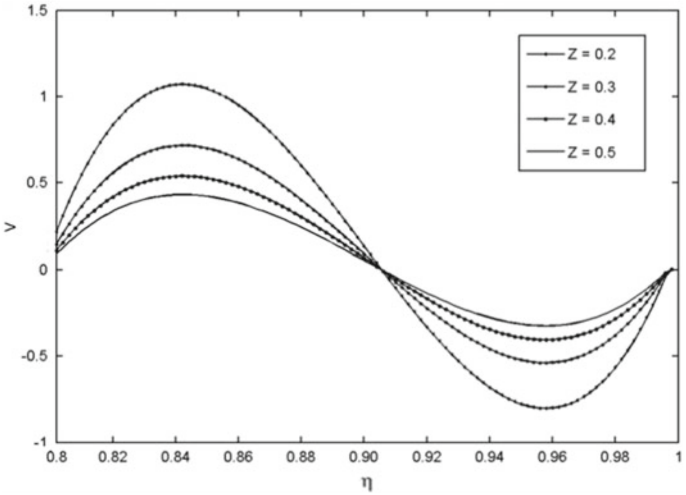

Fig. 8 Radial velocity for different sections when R = 0.8

Figures 5, 6, 15 and 16 show the axial velocity distribution for different values of Bingham number and aspect ratio for both the cases. Increasing the outer cylinders rotating speed, irrespective of whether the cylinders are rotating in the same or opposite directions, for a fixed Bingham number and aspect ratio, the axial velocity component increases from the inner wall to reach its maximum at a particular position and then decreases as it moves toward the outer wall of the annulus. For large annular space at $R = 0.3$, when Bingham number increases, the increase in axial velocity is found to be significant. For smaller annular space at $R = 0.8$, the increase in axial

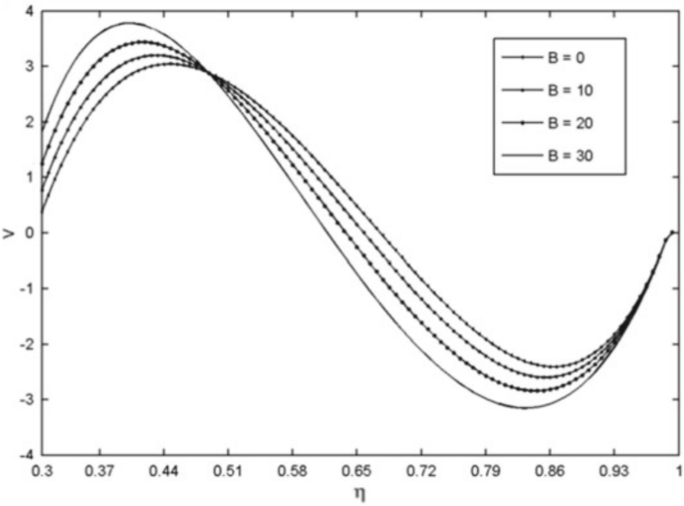

Fig. 9 Radial velocity for different Bingham number when $R = 0.3$

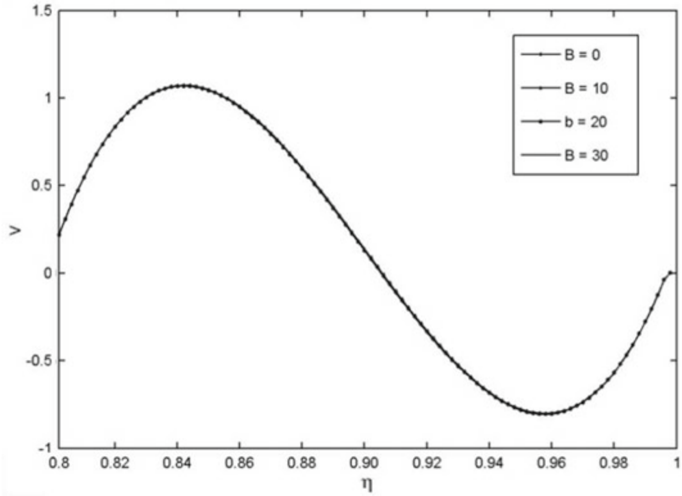

Fig. 10 Radial velocity for different Bingham number when $R = 0.8$

velocity is found to be negligible as Bingham number increases. Moreover, it could also be observed that the increase in the maximum value of the axial velocity at a particular radial position decreases as there is an increase in the outer cylinders rotating speed.

The radial velocity V for the aspect ratios $R = 0.3$ and 0.8 at different points in the axial direction for both the cases is shown in Figs. 7, 8, 17 and 18, respectively. It has

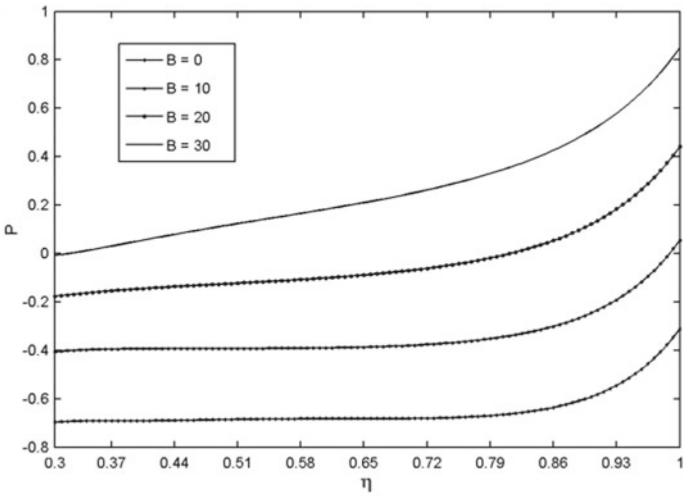

Fig. 11 Pressure for different Bingham number when $R = 0.3$

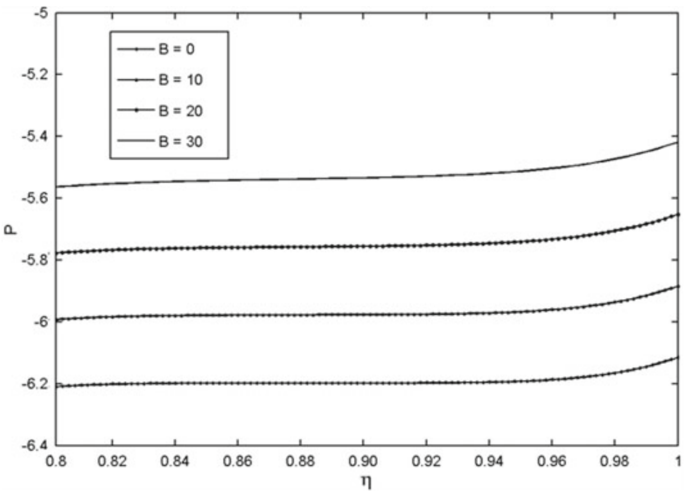

Fig. 12 Pressure for different Bingham number when $R = 0.8$

been found that for any particular Bingham number, the radial velocity is positive near the inner wall and negative in the region near the outer wall. Also, the values of radial velocity decrease as we progress in the axial direction. Furthermore, at any particular cross-section in the axial direction, the radial velocity for a larger annular space is found to be higher than that of the smaller annular space. From Figures depicted in 9, 10, 19 and 20, it could be observed that at any particular cross-section in the axial direction, the radial velocity increases with an increase in the Bingham

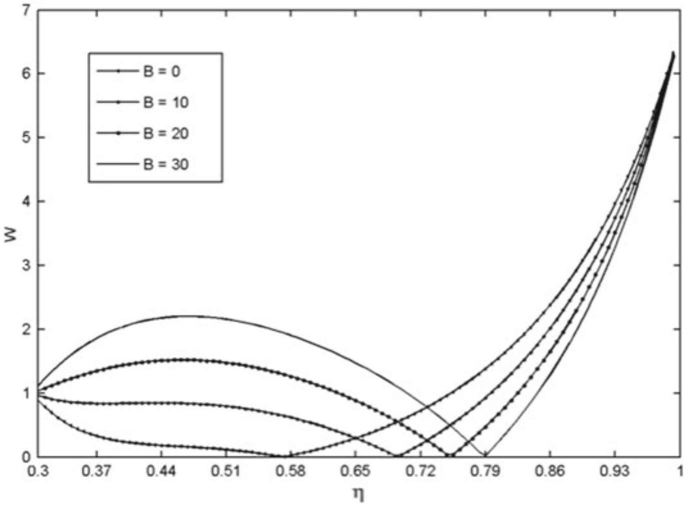

Fig. 13 Tangential velocity for different Bingham number when $R = 0.3$

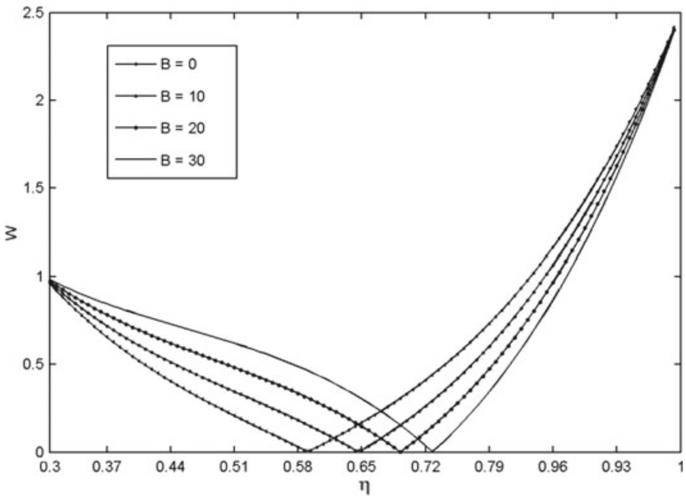

Fig. 14 Tangential velocity for different Bingham number when $R = 0.8$

number near the inner wall of the annulus when the aspect ratio is small. Moreover, the radial velocity decreases toward the outer wall for higher values of Bingham number when the outer cylinders rotating speed increases.

For cylinders rotating in the same direction or in the opposite direction with different speeds, the pressure distributions computed for various values of Bingham number and aspect ratio are depicted in Figs. 11, 12, 21 and 22, respectively. The pressure is found to increase from the inner wall to the outer wall of the annulus, not

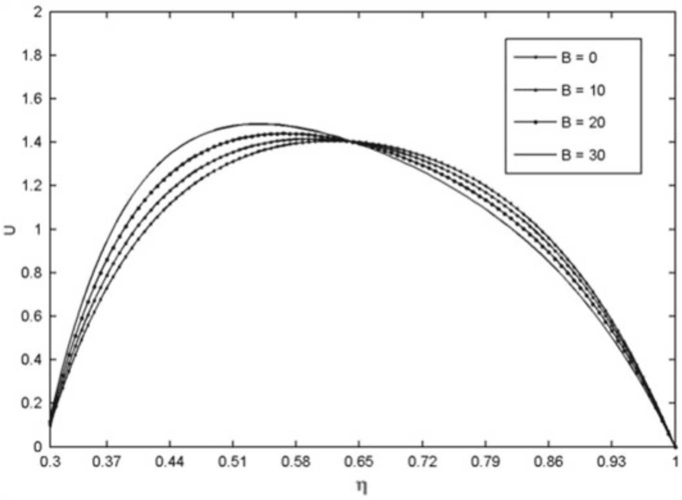

Fig. 15 Axial velocity for different Bingham number when $R = 0.3$

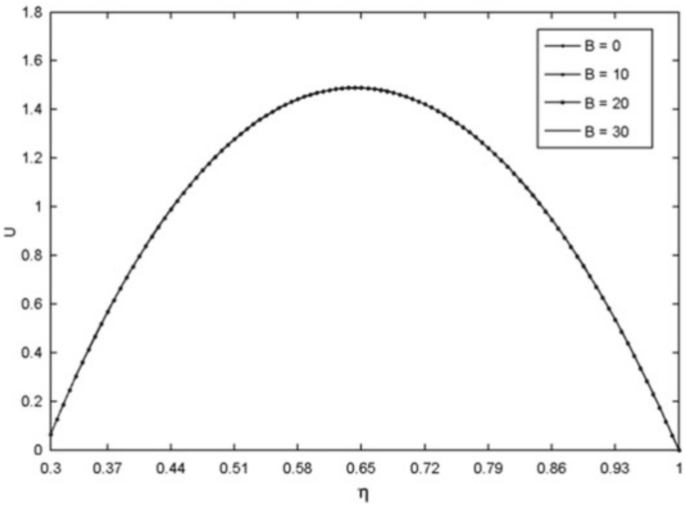

Fig. 16 Axial velocity for different Bingham number when $R = 0.8$

depending on the Bingham number or the aspect ratio. It has been observed that the pressure increases as the Bingham number increases for any aspect ratio. Moreover, for large annular space when $R = 0.3$, the increase in pressure for higher Bingham number is found to be significant than that of the smaller annular space. Also, it has been observed that the pressure is higher for larger aspect ratios, i.e., when space

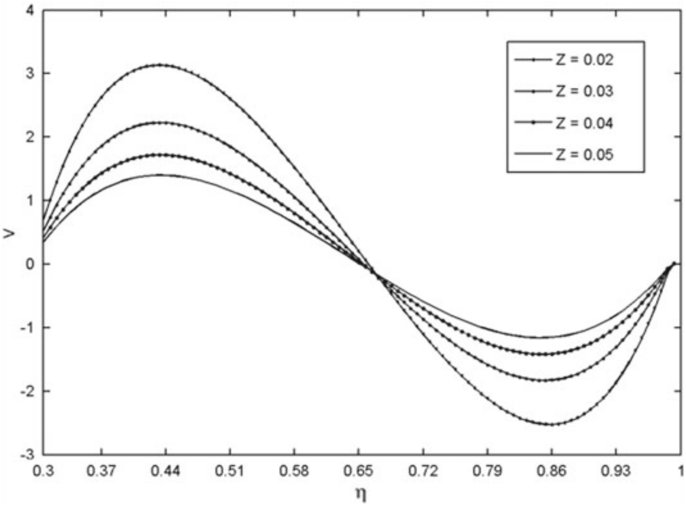

Fig. 17 Radial velocity for different sections when $R = 0.3$

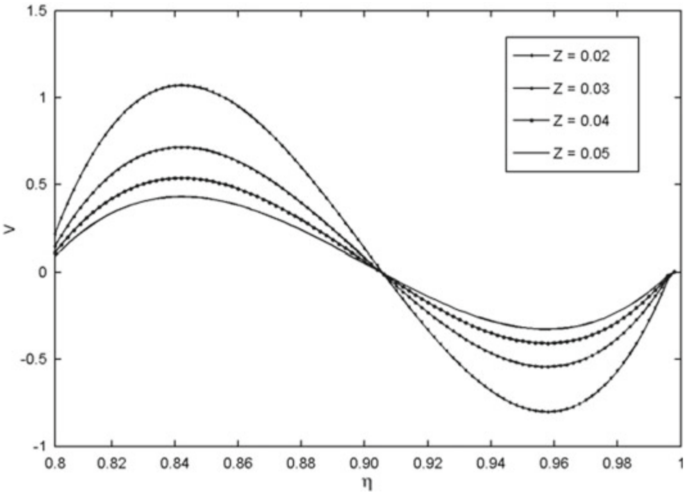

Fig. 18 Radial velocity for different sections when $R = 0.8$

is small. When increasing the speed of the outer cylinders, the values, which are increasing, decrease as the pressure increases.

For the particular case of the inner cylinder rotating and the outer cylinder at rest, the results were found to match the results of Srinivasa Rao [15]. In the case of stationary concentric annular cylinders, the results of axial velocity components in the analysis matched well with the results of Kandasamy [17].

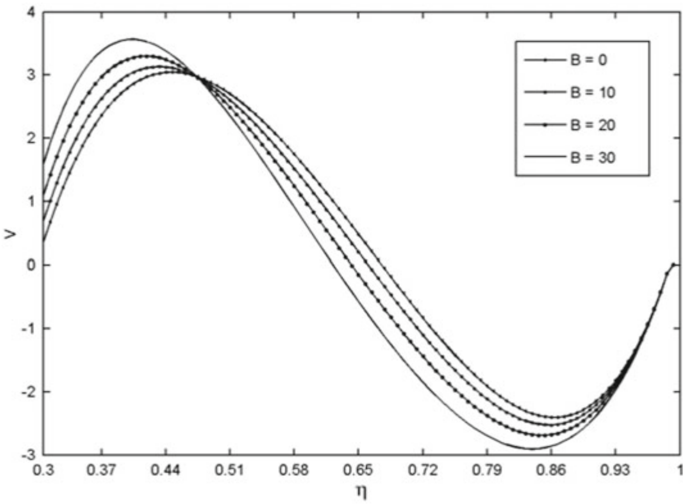

Fig. 19 Radial velocity for different Bingham number when $R = 0.3$

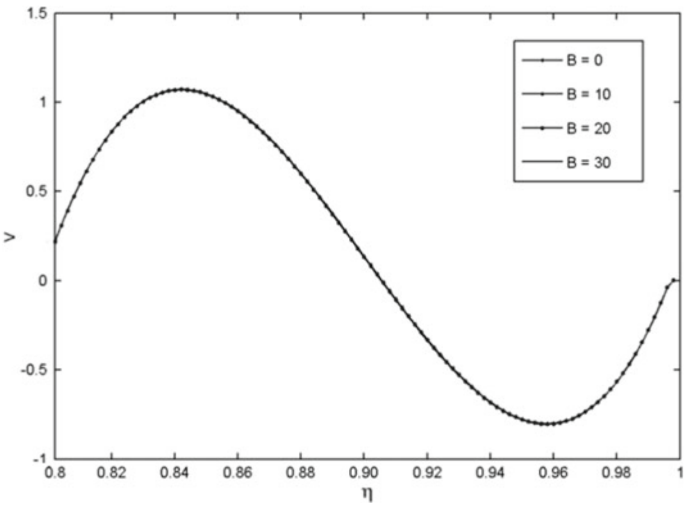

Fig. 20 Radial velocity for different Bingham number when $R = 0.8$

5 Conclusion

In this study, the development of different velocity profiles and pressure distributions are numerically computed. The following conclusions are observed when Bingham number and aspect ratios are increased in the entrance region of the annular space

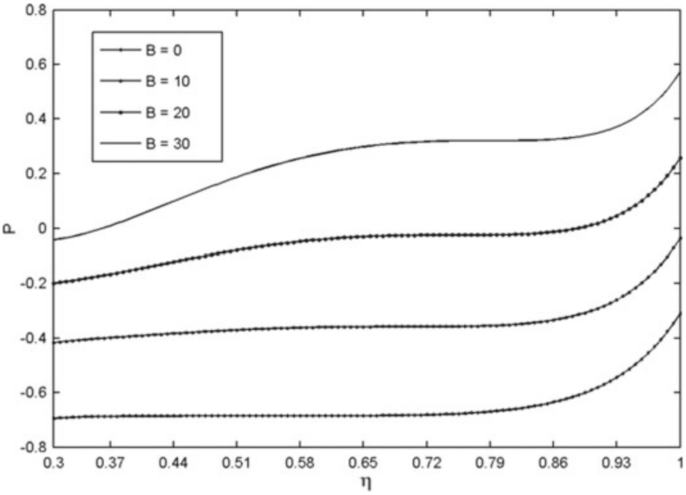

Fig. 21 Pressure for different Bingham number when $R = 0.3$

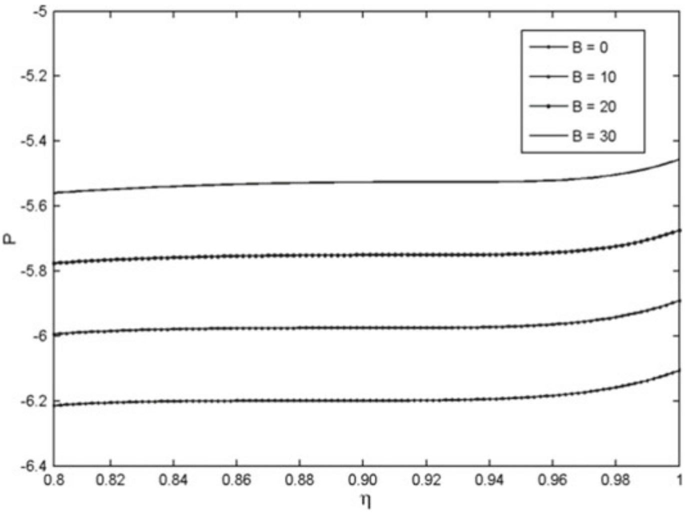

Fig. 22 Pressure for different Bingham number when $R = 0.8$

when the concentric cylinders are rotating in the same as well as opposite directions with different speeds.

- By comparing the results obtained, a significant change in the tangential velocity profile and pressure profile could be noticed, and it increases rapidly when cylinders are rotating with different speeds rather than the same speed in both cases.

However, the profile corresponding to radial and axial velocity remains almost similar in both cases.

- The entrance length distance decreases as velocities increase, and the flow becomes fully developed before the usual or expected time.
- As Bingham number increases, time taken for the Bingham fluid to flow between the rotating annulus is reduced, resulting in enhanced surface area contact which is ascertained so as to reduce the friction in the flow region of the annulus.
- Bingham fluid shall be used as working fluid in transmission systems and flow characteristics which rapidly dissipate the heat generated due to friction.
- The performance level increases when annular cylinders rotate in the same as well as opposite directions with different speeds by using time-independent non-Newtonian fluid obeying Bingham fluid.

Acknowledgements The authors thank the Principal and management of SSN institutions for their support in carrying out this work.

References

1. Schlichting H, Gersten K (2000) Boundary layer theory, 8th edn. Springer
2. Escudier MP, Oliveira PJ, Pinho FT (2002) Fully developed laminar flow of purely viscous non-Newtonian liquids through annuli, including the effects of eccentricity and inner-cylinder rotation. Int J Heat Fluid Flow 23:52–73
3. Ramesh Gupta C (2001) On developing laminar non-Newtonian flow in pipes and channels. Nonlinear Anal Real World Appl 2:171–193
4. Keslerova R, Kozel K (2010) Numerical modelling of incompressible flows for Newtonian and non-Newtonian fluids. Math Comput Simul 80:1783–1794
5. Poole RJ, Chhabra RP (2010) Development length requirements for fully developed laminar pipe flow of yield stress fluids. J Fluid Eng 132:1–4
6. Huilgol RR (2006) A systematic procedure to determine the minimum pressure gradient required for the flow of viscoplastic fluids in pipes of symmetric cross section. J Non-Newton Fluid Mech 136:140–146
7. Khali S, Nebbali R, Bouhadef K (2017) Effect of a porous layer on Newtonian and power-law fluids flows between rotating cylinders using lattice Boltzmann method. J Braz Soc Mech Sci Eng 39:3881–3895
8. Nouri JM, Whitelaw JH (1994) Flow of Newtonian and Non-Newtonian flu ids in a concentric annulus with rotation of the inner cylinder. J Fluid Eng 116:821–827
9. Chebbi R (2002) Laminar flow of power-law fluids in the entrance region of a pipe. Chem Eng Sci 57:4435–4443
10. Round GF, Yu S (1993) Entrance laminar flows of viscoplastic fluids in concentric annuli. Can J Chem Eng 71:642–645
11. Schulz A, Pfister G (2003) The effects of outer cylinder rotation on Taylor-Couette flow at small aspect ratio. Phys Fluids 15:417–425
12. Santhosh N, Radhakrishnamacharya G, Chamkha AJ (2015) Effect of slip on Herschel Bulkley fluid flow through narrow tubes. Alexandria Eng J 54:889–896
13. Lu G, James Third R, Christoph Mller R (2014) Effect of wall rougheners on cross-sectional flow characteristics for non-spherical particles in a horizontal rotating cylinder. Particuology 12:4453

14. Pai RG, Kandasamy A (2014) Entrance region flow of Herschel-Bulkley fluid in an annular cylinder. Int J Appl Eng Res 9:7083–7101
15. Nadiminti SR, Kandasamy A (2016) Entrance region flow heat transfer in concentric annuli with rotating inner wall for bingham fluid. J Comput Appl Mech 11(2):137–157
16. Coney JER, El-Shaarawi MAI (1974) A contribution to the numerical solution of developing laminar flow in the entrance region of concentric annuli with rotating inner walls. ASME Trans J Fluid Eng 96:333–340
17. Kandasamy A (1996) Entrance region flow heat transfer in concentric annuli for a Bingham fluid. In: Third Asian-Pacific conference on computational mechanics, pp 1697–1702

Nanofluids in Improving Heat Transfer Characteristics of Shell and Tube Heat Exchanger

S. Seralathan, R. Vijay, S. Aravind, S. Sivakumar, G. Devaraj, V. Hariram, P. S. Raghavan, and T. Micha Premkumar

Abstract The thermal performances of shell and tube heat exchanger [STHE] are investigated using Ag–W and CuO–W nanofluids with suspended particle volume concentrations between 0.02% and 0.06% of Ag and CuO. The comparison is made with reference to base fluid. The result revealed that thermal conductivity of the nanofluids, which is dependent on the particle volume concentration, influenced the heat transfer ability. Highest overall as well as convective heat transfer coefficients and highest actual heat transfer are obtained for 0.06% volume concentration CuO–W nanofluid. An improvement of about 19% in heat transfer coefficient is recorded for 0.06 vol% of CuO–W nanofluids with respect to water. Also, the overall heat transfer coefficient enhanced between 64 and 79% for 0.06 vol% of CuO–W nanofluids. However, in the tube-side, pressure drop increases with increase in nanofluid volume concentrations. Actual heat transfer improved by 39–56% with reference to water. It can be concluded that better heat transfer characteristic for the STHE is obtained by keeping the shell-side mass flow as fixed and varying the tube-side mass flow rates.

Keywords Heat exchanger · Shell and tube · Nanofluid · Ag–W · CuO–W

Nomenclature

α	Thermal diffusivity (m^2/s)
ρ	Density (kg/m^3)

S. Seralathan (✉)
Department of Aeronautical Engineering, Hindustan Institute of Technology and Science, Chennai, India
e-mail: siva.seralathan@gmail.com

R. Vijay · S. Aravind · S. Sivakumar · G. Devaraj · V. Hariram · T. Micha Premkumar
Department of Mechanical Engineering, Hindustan Institute of Technology and Science, Chennai, India

P. S. Raghavan
Department of Chemistry, Hindustan Institute of Technology and Science, Chennai, India

E. T. Akinlabi et al. (eds.), *Trends in Mechanical and Biomedical Design*, Lecture Notes in Mechanical Engineering,
https://doi.org/10.1007/978-981-15-4488-0_43

μ	Dynamic viscosity (N s/m^2)
γ	Kinematic viscosity (m^2/s)
ΔT_{LMTD}	Logarithmic mean temperature difference (°C)
A	Heat transfer area [$A = \pi D_{\mathrm{i}} L$] (m^2)
C_{p}	Specific heat capacity (J/kgK)
k	Thermal conductivity (W/mK)
T	Temperature (K)
V	Velocity of the nanofluid (m/s)

Subscripts

f	Base fluid (water)
wall	Tube wall
out	Outlet
in	Inlet
c	Cold side
nf	Nanofluid
h	Hot side
w	Water

1 Introduction

Designing energy-efficient thermal energy system along with enhanced heat transfer is one of the vital requirements in present energy conservation scenario. Shell and tube heat exchanger [STHE] are predominately deployed in variety of process industries, oil refineries, etc. The performance of STHE could be enhanced by augmenting the heat transfer characteristic of the working fluids used by suspending it with nanoparticles. This colloidal solution, also called 'nanofluid,' contains nanoparticles suspended uniformly in a base fluid. Nanofluid is an innovative class of fluid with enhanced thermal properties to meet the heat transfer requirements. The thermal conductivity and viscosity of nanofluid are higher compared to base fluid, and these properties rely on various parameters, namely nanoparticles mass fraction, particle size, and temperature. The widely used nano powders are Fe, Ag, Ti, Al, and Cu in its pure form and CuO, Al_2O_3, TiO_2, Fe_2O_3 in the oxide form. Consequently, with the use of nanofluid, compact heat transfer equipments may find its place in many industrial applications.

Lee et al. [1] used 4.0% vol. CuO–ethylene glycol nanofluid and found that the thermal conductivity improved by 20%. On the other hand, Das et al. [2] obtained improved thermal conductivity using CuO nanoparticles suspended in water. Li and Xuan [3] reported improved heat transfer by using smaller volume fraction of CuO nanoparticles. Godson et al. [4] used different Ag particle volume concentrations in Ag–W nanofluid and reported 12.41% improvement in convective heat transfer coefficient. The review of literatures [5–8] revealed a variety of metal oxide-based nanoparticles suspended in base fluid, namely ethylene glycol, mineral oil, and water which were used to augment the heat transfer characteristics of STHE. A detailed review by Das et al. [9] on nanoparticles suspended in base fluid revealed higher heat conduction, enhancement of thermal conductivity as well as better stability. Besides improvement in thermal conductivity by dispersed nanoparticles, it is understood that boundary layer suppression, intensification of turbulence also aid in improving the heat transfer ability. All the existing studies by researchers focused on using metal oxide-based nanoparticles with volume fractions varying from 0.01 to 6% in the base fluid [5–11]. The use of high concentrations led to drop in pressure which required additional pumping resource. Moreover, a limited research was carried out in using pure metal oxide like Ag at lower concentrations levels in a STHE.

Therefore, the focus of this present study is to use a pure metal nanoparticle, namely silver nanoparticles dispersed in water (Ag–W) with volume concentrations of nanoparticles varying from 0.02 to 0.06% in a STHE. A metal oxide-based nanoparticle namely copper oxide dispersed in water (CuO–W) with volume concentrations of nanoparticles varying from 0.02% to 0.06% is also used. All the comparison in this study is carried out with respect to base fluid (water).

2 Preparation of Ag–Water and CuO–Water Nanofluids

Silver nitrate (AR grade) is dissolved in a minimum quantity of distilled water. Gum Acacia is used as the dispersing matrix. 0.25% of Gum Acacia is dissolved in another beaker. Both are mixed together and stirred for 30 min. 0.25% of di-ethanol amine is dissolved in water and added in drops to the above content under vigorous stirring. A silver–amine complex is formed with light brown color. This is followed by the addition of glucose solution in drops which leads to the formation of nanosilver particles dispersed in water. The final nanosilver suspension contains 5000 ppm of silver particles. The transmission electron microscopy (TEM) photograph of the nanosilver is displayed in Fig. 1a, and the energy dispersive X-ray (EDAX) analysis (chemical analysis) result is shown in Fig. 2a. The nanoparticles are found to be dispersed well in certain agglomeration.

Similarly, calculated quantity of copper nitrate is dissolved in a minimum quantity of distilled water. 0.25% of Gum Acacia is dissolved in distilled water and added to the above solution under vigorous stirring. After 30 min, 25% of liquor ammonia is added in drops to form copper–amine complex followed by the addition of reducing agent (hydrazine) to form nano CuO dispersed in water. The concentration of CuO in the final suspension is 5000 ppm. The TEM photograph of the nanocopper is shown in Fig. 1b reveals that nanoparticles are found to be well dispersed in certain aggregation. The EDAX analysis (chemical analysis) result is shown in Fig. 2b. The

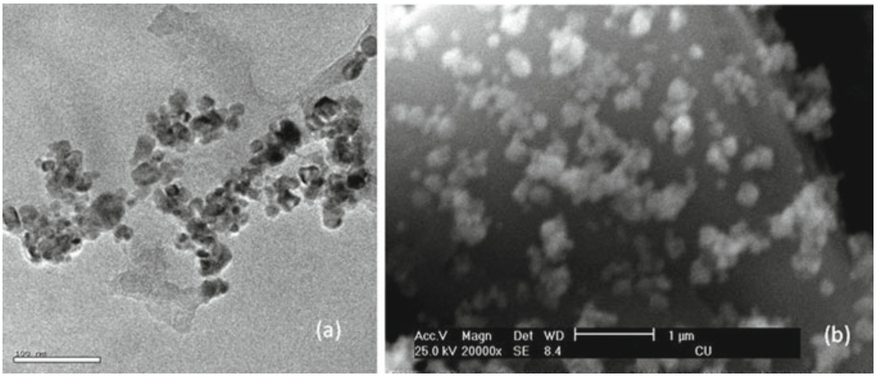

Fig. 1 TEM photograph **a** nanosilver and **b** nanocopper

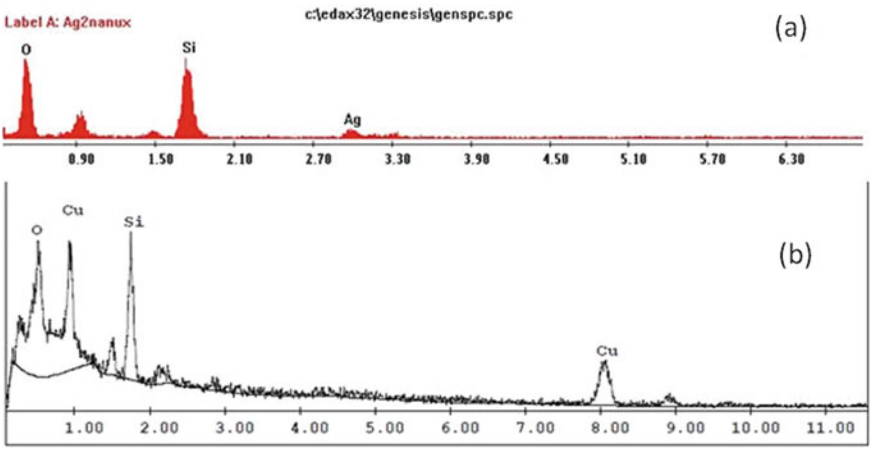

Fig. 2 EDAX analysis **a** nanosilver and **b** nanocopper

Ag–W and CuO–W nanofluids prepared are treated using ultrasonicator to ensure continuous suspended, uniform and stable colloidal solution.

3 Experimentation

The graphic arrangement of experimental setup is depicted in Fig. 3, and its specifications are listed in Table 1. It consists of two loops, one for hot fluid (water) which flows through the tube and another for cold fluid (Ag–W/CuO–W/W), which flows through the shell. Each loop has a reservoir, pump, flow meter, and a valve to regulate the flow rate in the system. Four 'k' type thermocouples with error measurement

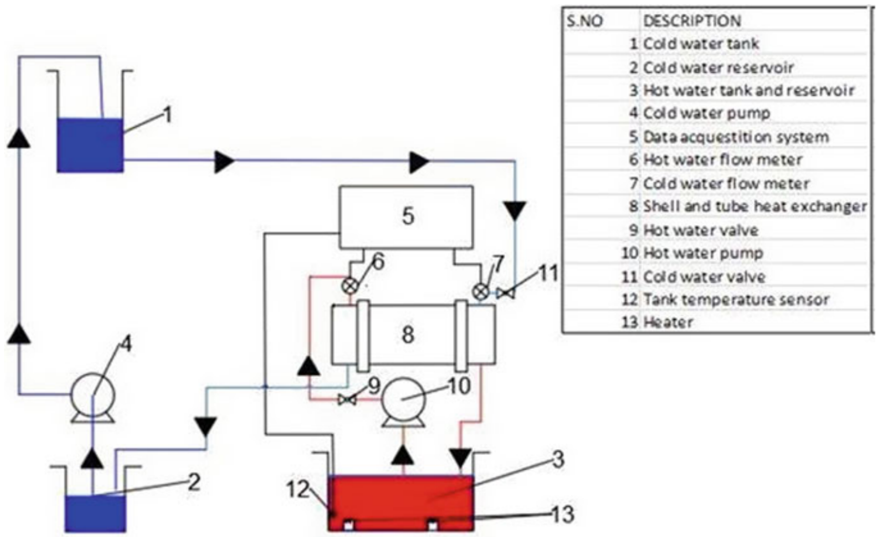

Fig. 3 Schematic layout of STHE

Table 1 STHE specification

Specification	Tube	Shell
Diameter inner (D_i) (mm)	8	145
Diameter outer (D_o) (mm)	12	200
Length (L) (mm)	475	500
Number of tubes	9	–
Material	Mild steel	Copper

(±1 °C) are used to record the temperatures at outlet as well as inlet of the tube and shell, respectively. Digital flow meters determine the flow rate of the working fluids. STHE is shielded well to prevent any heat rejections to the surroundings. All the electrical signals received from thermocouples and digital flow meters are sent to data logger as readable information using LABVIEW software. The raw data obtained during experimentation is used to estimate the heat transfer rate, Nusselt number, Peclet number, and convective as well as overall heat transfer coefficients of nanofluids with varied volume concentrations of Ag nanoparticles and CuO nanoparticles. Uncertainty analysis for the measurements recorded using the instruments is carried out, and the maximum error is 3.89% for overall heat transfer coefficient.

The influence of varying the mass flow rates of shell-side fluid and tube-side fluid on the heat transfer characteristics of STHE is studied and analyzed. Initially, the tube-side fluid mass flow rate ($m_{Tube\_Side\_Fluid}$) is varied by keeping the shell-side fluid mass flow rate ($m_{Shell\_Side\_Fluid}$) as constant. Later, $m_{Shell\_Side\_Fluid}$ is changed keeping the $m_{Tube\_Side\_Fluid}$ as constant. Experiments are carried out initially using water in the shell-side and later with Ag–W as well as CuO–W nanofluids with different particle vol.% concentrations. The data are extracted after the fluid flow attains fully developed conditions. The heat transfer rate convective as well as overall heat transfer coefficients and Nusselt number are found using the formulae given below.

Heat transfer rate of nanofluid (Q_{nf}) is expressed as

$$Q_{\mathrm{nf}} = mC_{\mathrm{pnf}}\left(T_{\mathrm{nf\_out}} - T_{\mathrm{nf\_in}}\right) \tag{1}$$

Convective heat transfer coefficient of nanofluid (h_{nf}) is estimated from the overall heat transfer coefficient (U) of STHE which includes hot fluid namely nanofluid and cold fluid (water) thermal resistances along with tube wall.

$$\frac{1}{U} = \frac{1}{h_{\mathrm{nf}}} + \frac{D_{\mathrm{i}}\ln\left(\frac{D_{\mathrm{o}}}{D_{\mathrm{i}}}\right)}{2K_{\mathrm{wall}}} + \frac{D_{\mathrm{i}}}{D_{\mathrm{o}}} \times \frac{1}{h_{\mathrm{f}}} \tag{2}$$

Overall heat transfer coefficient (U) is found out from the expression

$$Q = AU\Delta T_{\mathrm{LMTD}} \tag{3}$$

The LMTD (ΔT_{LMTD}) is found from the expression

$$\Delta T_{\mathrm{LMTD}} = \frac{(T_{\mathrm{hnf,in}} - T_{\mathrm{cw,out}}) - (T_{\mathrm{hnf,out}} - T_{\mathrm{cw,in}})}{\ln\left(\frac{T_{\mathrm{hnf,in}} - T_{\mathrm{cw,out}}}{T_{\mathrm{hnf,out}} - T_{\mathrm{cw,in}}}\right)} \tag{4}$$

Nusselt number of the nanofluids ($\mathrm{Nu_{nf}}$) is expressed as

$$\mathrm{Nu_{nf}} = \frac{h_{\mathrm{nf}} D_{\mathrm{i}}}{K_{\mathrm{nf}}} \tag{5}$$

$\mathrm{Nu_{nf}}$ is found using Dittus and Boelter's [12] single-phase liquid relation which is also suggested by Azmi et al. [13]

$$\mathrm{Nu} = 0.023\mathrm{Re}^{0.80}\,\mathrm{Pr}^{0.40} \tag{6}$$

Prandtl number ($\mathrm{Pr_{nf}}$) and Reynolds number ($\mathrm{Re_{nf}}$) for the nanofluid inside the tube are expressed as follows

$$\mathrm{Re_{nf}} = \frac{VD_i}{\gamma_{\mathrm{nf}}} \tag{7}$$

$$\mathrm{Pr}_{\mathrm{nf}} = \frac{\gamma_{\mathrm{nf}}}{\alpha_{\mathrm{nf}}} = \frac{C_{p\mathrm{nf}}\mu_{\mathrm{nf}}}{K_{\mathrm{nf}}} \tag{8}$$

Thermal diffusivity (α_{nf}) of nanofluid is estimated using the expression

$$\alpha_{\mathrm{nf}} = \frac{K_{\mathrm{nf}}}{\rho_{\mathrm{nf}} C_{p\mathrm{nf}}} \tag{9}$$

4 Results and Discussion

4.1 Tube Side Fixed Shell Side Varied Flow (Case: TSFSSV Flow)

The shell-side fluid mass flow rates are changed between 110 and 150 kg/h, and at the tube-side, the fluid is kept constant as 150 kg/h. Figure 4 illustrates the variations of actual heat transfer for different mass flow rates for varied particle volume concentrations of Ag–W and CuO–W nanofluids. Actual heat transfer (Q) enhances with rise in $m_{\mathrm{Shell\_Side\_Fluid}}$. Adding up nanoparticle to the base fluid enhances 'Q', and it augments with enhancement in volume concentrations of the nanoparticles. Heat transfer rate improved by 36–50% for Ag–W nanofluid, whereas for CuO–W nanofluid, it improved by 84–91% with reference to water. As can be noticed in Fig. 4, CuO–W nanofluid with 0.06% vol. concentration gives the maximum 'Q' for $m_{\mathrm{Shell\_Side\_Fluid}}$ and $m_{\mathrm{Tube\_Side\_Fluid}}$ of 150 kg/h, respectively.

The change of overall heat transfer coefficients (U) against $m_{\mathrm{Shell\_Side\_Fluid}}$ is plotted in Fig. 5. The highest 'U' is observed for an $m_{\mathrm{Shell\_Side\_Fluid}}$ of 150 kg/h and $m_{\mathrm{Shell\_Side\_Fluid}}$ of 150 kg/h. The CuO–W nanofluid with 0.06% particle volume concentration has a better thermo physical properties, namely specific heat, density, and thermal conductivity, which is reflected in terms of highest 'U'. Overall heat transfer coefficient enhanced by 27–47% for Ag–W nanofluid, whereas for CuO–W nanofluid, it is found to be 70–93%.

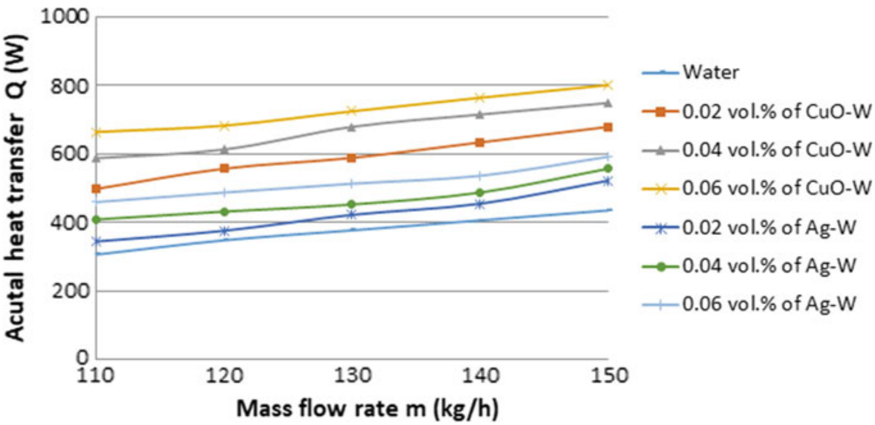

Fig. 4 Case: TSFSSV flow-variations of actual heat transfer

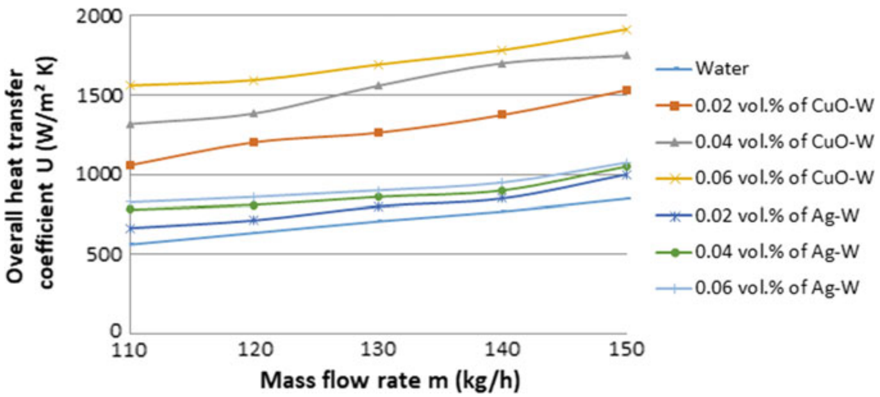

Fig. 5 Case: TSFSSV flow-variations of overall heat transfer coefficient

It is known that convective heat transfer coefficient (h) improves with diminution in thermal boundary layer thickness. Moreover, 'h' is influenced by nanofluid thermal conductivity. Figure 6 depicts the changes in convective heat transfer coefficient and $m_{Shell\_Side\_Fluid}$ keeping tube-side fluid as constant. Around 8–16% rise in 'h' value is observed for Ag–W nanofluid. On the other hand, it is 19–28% for CuO–W nanofluid. Highest 'h' value is realized for 0.06% vol. concentration of CuO–W nanofluid as its thermal conductivity is high for this particle volume concentration.

Figure 7 depicts the variation between overall heat transfer coefficient and Peclet number (Pe) for the varying $m_{Shell\_Side\_Fluid}$ keeping $m_{Tube\_Side\_Fluid}$ as constant. Overall heat transfer coefficient improves with rise in 'Pe' and also with enhancement in particle volume concentrations. Around 5–10% improvement of 'U' is observed for

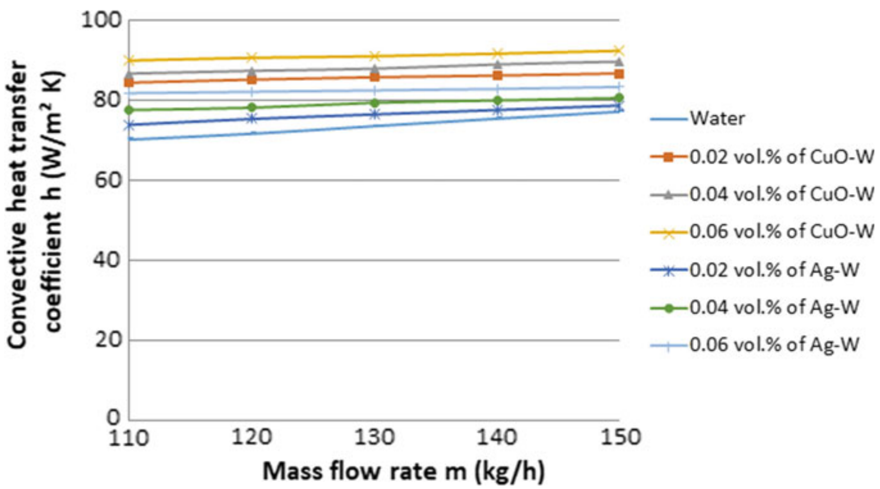

Fig. 6 Case: TSFSSV flow-variations of convective heat transfer coefficient

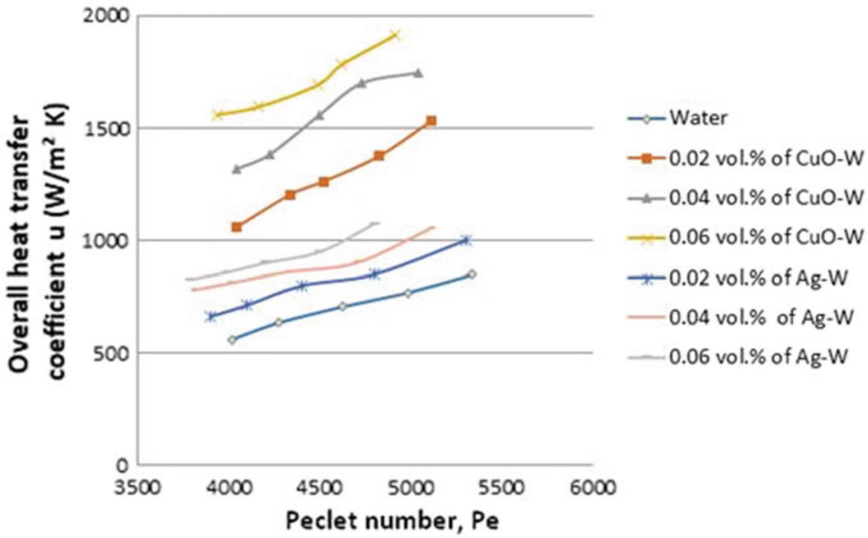

Fig. 7 Overall heat transfer coefficient versus Pe

Ag–W nanofluid with respect to water. It improved by 8–12% for CuO–W nanofluid. 0.06% vol. concentration CuO–W nanofluid shows the maximum overall heat transfer coefficient among all nanofluids and base fluid. Figure 8 depicts the variations between Nusselt number (Nu) and Pe. Nusselt number of all nanofluids is higher than water. Nusselt number improves with enhancement in particle volume concentrations. Nusselt number is found to improve by 15–27% for Ag–W nanofluid. Similarly, for CuO–W nanofluid, it is improved by 36–42%. Highest 'Nu' is realized for 0.06% vol. concentration of CuO–W nanofluid.

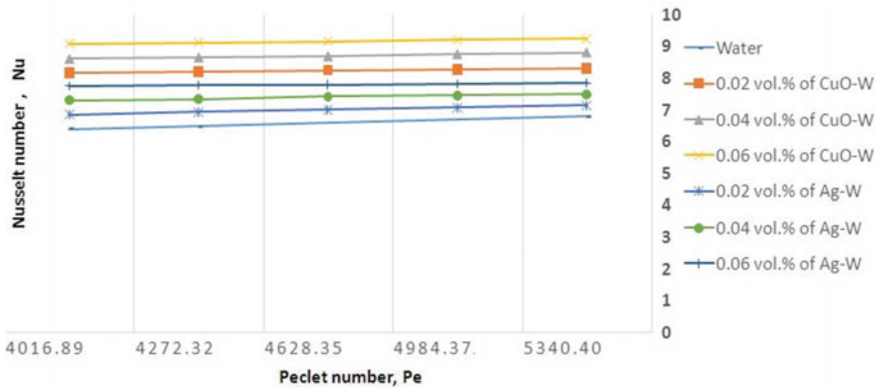

Fig. 8 Nu versus Pe

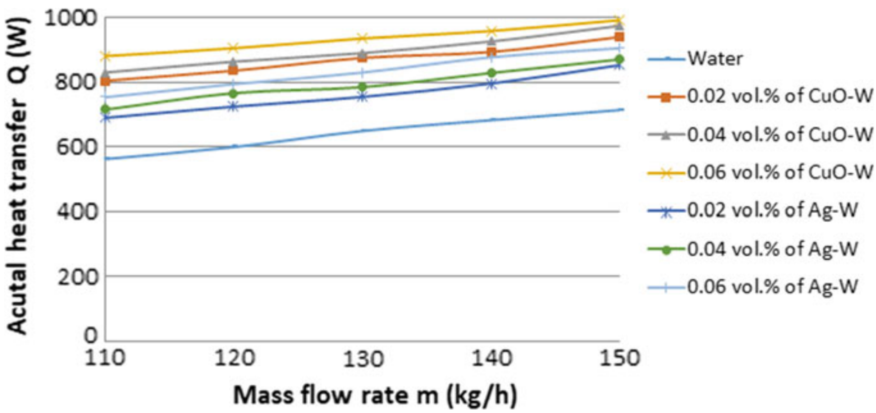

Fig. 9 Case: SSFTSV flow-variations of actual heat transfer

4.2 Shell Side Fixed Tube Side Varied Flow (Case: SSFTSV Flow)

The tube-side fluid mass flow rates are altered between 110 and 150 kg/h, and at the shell-side, the fluid is kept constant as 150 kg/h. Figure 9 depicts the variations between actual heat transfer with varying $m_{Tube\_Side\_Fluid}$. Highest actual heat transfer is realized for 0.06% vol. concentration CuO–W nanofluid at $m_{Shell\_Side\_Fluid}$ as well as $m_{Tube\_Side\_Fluid}$ of 150 kg/h, respectively. Actual heat transfer is found to be improved by 26–34% for Ag–W nanofluid. But, it is improved by 39%–56% with reference to base fluid for CuO–W nanofluid.

Figure 10 highlights the variations between overall heat transfer coefficients against varied $m_{Tube\_Side\_Fluid}$. The '*U*' value improved by 51–57% for Ag–W nanofluid, whereas for CuO–W nanofluid, it is improved significantly by 64–79%. Again, the highest '*U*' value is realized for 0.06% vol. concentration CuO–W nanofluid at $m_{Shell\_Side\_Fluid}$ as well as $m_{Tube\_Side\_Fluid}$ of 150 kg/h. This is due to improved thermal conductivity of the 0.06% vol. concentration CuO–W nanofluid.

Figure 11 depicts the variations in convective heat transfer coefficient with varied $m_{Tube\_Side\_Fluid}$. The '*h*' is improved by 8% for Ag–W nanofluid, whereas it is improved by 19% with respect to water. As the thermo physical property of 0.06% vol. concentration CuO–W is better, maximum '*h*' value is realized for 0.06% vol. concentration CuO–W nanofluid.

The consequence of nanofluid concentrations on the pressure drop is studied for a constant mass flow rate (i.e., $m = 130$ kg/h) is plotted in Fig. 12. The results revealed that pressure drop increases with enhancement in nanofluid volume concentrations. This pattern observed correlates well with earlier findings by Kabeel and Mohamed Abdelgaied [10].

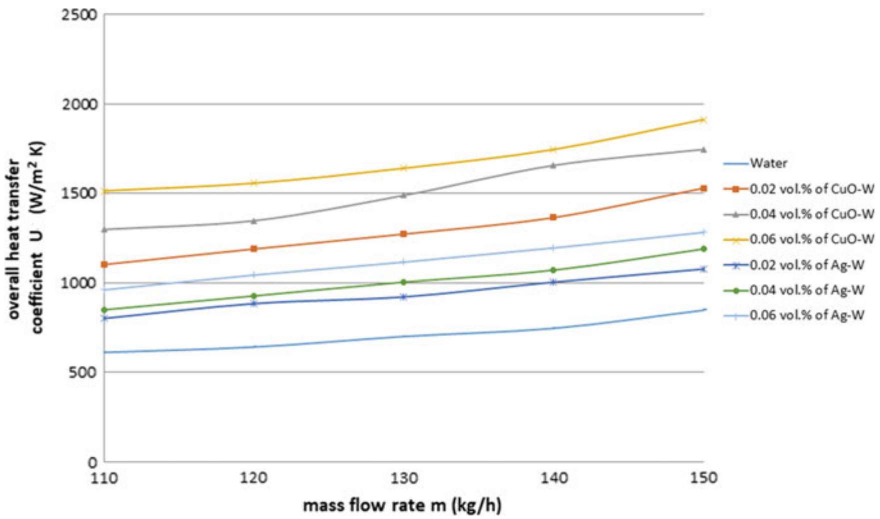

Fig. 10 Case: SSFTSV flow-variation of overall heat transfer coefficient

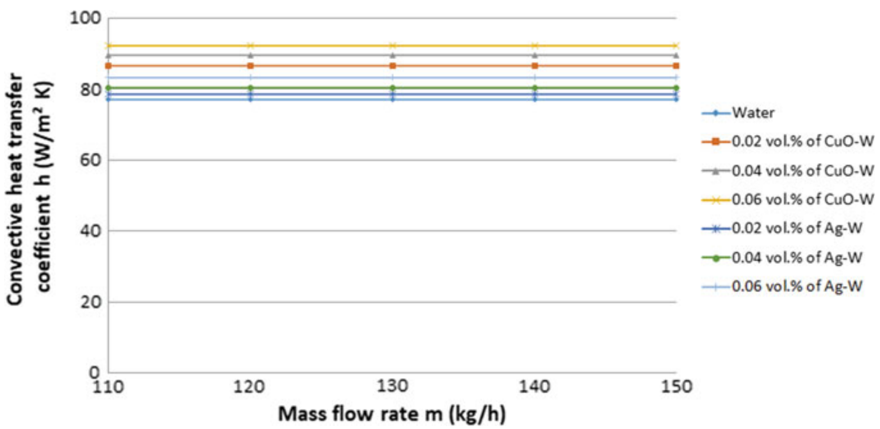

Fig. 11 Case: SSFTSV flow-variation of convective heat transfer coefficient

5 Conclusions

This experimental investigation deals with thermal performance of a STHE using Ag–W and CuO–W nanofluids with particle volume concentrations varied from 0.02 to 0.06%. The comparison is made with reference to base fluid (water). The result highlighted that thermal conductivity of the nanofluids which rely on the particle volume concentration influenced the heat transfer ability. Highest overall as well as convective heat transfer coefficients and highest actual heat transfer are obtained for 0.06% vol. concentration CuO–W nanofluid. A better heat transfer characteristic for

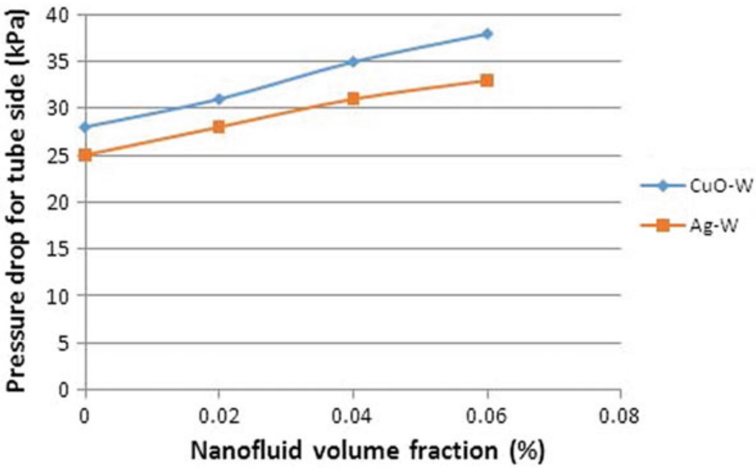

Fig. 12 Variations of pressure drop with respect to nanofluid volume fraction

the STHE is realized by ensuring the mass flow at shell-side as fixed and varying the tube-side mass flow rates [14]. An improvement of about 19% in heat transfer coefficient is recorded for 0.06% vol. concentration of CuO–W nanofluids with respect to water, i.e., base fluid. Also, the overall heat transfer coefficient improved between 64 and 79% for 0.06% vol. concentration of CuO–W nanofluids. However, in the tube-side, pressure drop increases with increase in nanofluid volume concentrations. Actual heat transfer also improved by 39–56% with respect to water. Hence, use of nanofluids as a working fluids in STHE results in an improved energy-efficient thermal system.

References

1. Lee S, Choi SUS, Li S, Eastman JA (1999) Measuring thermal conductivity of fluids containing oxide nanoparticles. J Heat Transf 121(2):280–289
2. Das SK, Putra N, Thiesen P, Roetzel W (2003) Temperature dependence of thermal conductivity enhancement for nanofluids. J Heat Transf 125 (4):567–574
3. Li Q, Xuan Y (2000) Experimental investigation of transport properties of nanofluids. Heat transfer science and technology. Buxan Wang edn. Higher Education Press, pp 757–762
4. Godson L, Deepak K, Enoch C, Jefferson B, Raja B (2014) Heat transfer characteristics of silver/water nanofluids in a shell and tube heat exchanger. Arch Civil Mech Eng 14:489–496
5. Shahrul IM, Mahbubul IM, Saidur R, Khaleduzzaman SS (2016) Performance evaluation of a shell and tube heat exchanger operated with oxide based nanofluids. Heat Mass Transf 52:1425–1433
6. Leong KY, Saidur R, Mahlia TMI, Yau YH (2012) Modeling of shell and tube heat recovery exchanger operated with nanofluid based coolants. Int J Heat Mass Transf 55:808–816
7. Zeinali Heris S, Etemad SG, Nasr Esfahany M (2006) Experimental investigation of oxide nanofluids laminar flow convective heat transfer. Int Commun Heat Mass Transf 33:529–535

8. Nishant K, Sonawane SS (2016) Experimental study of thermal conductivity and convective heat transfer enhancement using CuO and TiO_2 nanoparticles. Int Commun Heat Mass Transf 76:98–107
9. Das SK, Choi SUS, Patel HE (2008) Heat transfer in nanofluids- a review. Heat Transf Eng 27(10):3–19
10. Kabeel AE, Abdelgaied M (2016) Overall heat transfer coefficient and pressure drop in a typical tubular exchanger employing alumina nano-fluid as the tube side hot fluid. Heat Mass Transf 52:1417–1424
11. Saravanna JY, Kantamnen R, Fasil N, Sivamani S, Hariram V, Micha Premkumar T, Mohan T (2017) Modelling and analysis of water heating using recovered waste heat from hot flue gases of chulha. ARPN J Eng Appl Sci 12(21):6164–6171
12. Dittus FW, Boelter LMK (1930) Heat transfer in automobile radiators of the tubular type, vol 2. University of California Publications on Engineering, California
13. Azmi WH, Usri NA, Rizalman M, Sharma KV, Noor MM (2017) Force convection heat transfer of Al_2O_3 nanofluids for different based ratio of water ethylene glycol mixture. Appl Therm Eng 112:707–719
14. Shahrul IM, Mahbubul IM, Saidur R, Khaleduzzaman SS, Sabri MFM, Rahman MM (2014) Effectiveness study of a shell and tube heat exchanger operated with nanofluids at different mass flow rates. Numer Heat Transf Part A Appl: Int J Comput Methodol 65:699–713

Design and Numerical Analysis of Gearless Transmission Used in Small Wind Turbine

Micha T. Premkumar, V. Hariram, S. Seralathan, Pinku Kumar, and Godwin John

Abstract The main function of the gearless transmission system is to transmit power between two shafts through the sliding links that develop revolute pair between the hubs of two shaft. Normally the output link is bent at any angle between 0 and 180°. Moreover, as the hub in the driving shaft rotates, holes in this hub rotate, which in turn pushes the links and it drive the output. Moreover, torque developed in the small wind turbine is small so it is effectively used in this low torque applications. The objective of this project is to analysis gearless drive that is being simple and transmitting power preciously at almost right angle without any bevel gears. This mechanism is completely analysis using Ansys© software to lookout the elbow rod the hub under different working condition. Numerical analysis is made by rotating the mechanism at different rpm, viz. 0–150 rpm. Reaction forces and reaction moment are analyzed for 5 s simulation and compared with allowable stress. In this investigation, the effect of number of links and size of link is studied to find the permissible operating speed of mechanism. The major outcome of this work is to get the permissible limit of the stress, strain, speed, torque transmitting capacity of this mechanism as it is very much attracting the research community in replacing the conventional bevel gears. It is observed that the optimum number of link for better transmission is 8 and its diameter is 8 mm, and optimum speed of the mechanism is 100 rpm, so this mechanism is suitable for the small wind turbine.

Keywords Gear less transmission · Vertical axis wind turbine · Numerical

---

M. T. Premkumar (✉) · V. Hariram · P. Kumar
Department of Mechanical Engineering, Hindustan Institute of Technology and Science, Chennai 603103, India
e-mail: tmichamech@gmail.com

S. Seralathan
Department of Aeronautical Engineering, Hindustan Institute of Technology and Science, Chennai 603103, India

G. John
Department of Automobile Engineering, Hindustan Institute of Technology and Science, Chennai 603103, India

E. T. Akinlabi et al. (eds.), *Trends in Mechanical and Biomedical Design*, Lecture Notes in Mechanical Engineering,
https://doi.org/10.1007/978-981-15-4488-0_44

1 Introduction

Gearless mechanism or also known as Elbow mechanism which transmits power between driving and driven shaft at any fixed angle. It has the sliding link and rotating pair mechanism, which allows to transmit torque between two shafts. The sliding link slides inside the holes in the hub of both driving and driven shaft which forms mechanism of power transmission. This mechanism is the best alternate for replacement of the bevel gear, so lot of researchers have an eye toward the gearless transmission mechanism. Chung [1] presented a new type of gearless traction mechanism for high-speed elevators with a permanent magnet motor drive system and explained gearless transmission mechanism which includes a multiplicity of similar linkages, which includes off-center center of rotation between an input and an output shaft. However, many reasons supporting that this type of bevel gear drives is not favoring large mills due to not having sufficient VFD option [2], unlike universal joints, performance losses are low even there is offset in shaft and smooth running of operation [3]. Janakiraman and Paramasivam [4] and Bohra et al. [5] performed comparative analysis using the gearless wind turbines which related to some control techniques to address the offset issue for smooth operation. Moreover, Ghagare et al. [6] tested the power transmission between the two with angular offset. The outcome of this work is that the number of pin contributes more for the smoother operation and unlike bevel gear, the force distribution is equal in this mechanism. Because of uneven force distribution, bevel gear transmission system has high wear and tear, and hence, the gearless mechanism has smooth and controlled acceleration without having jerk in the transmission gearless mechanism or also known as Elbow mechanism which transmits power between driving and driven shaft at any fixed angle. It has the sliding link and rotating pair mechanism, which allows to transmit torque between two shafts. The sliding link slides inside the holes in the hub of both driving and driven shaft which forms mechanism of power transmission. This mechanism is the best alternate for replacement of the bevel gear, so lot of researchers have an eye toward the gearless transmission mechanism [7].

The development of this type of mechanism has been explored the relatively slackness between both gear drives and simple gearless drives. Moreover, recent advancement in technologies addresses the possible disadvantage of the gear drive [8]. The failure analysis under on the basis of bending stress for smooth running of the gearless mechanism under heavy load condition reveals the failure stress of the mechanism. The analysis has been done using ANSYS environment [9]. Moreover, real-time study of gearless transmission mechanism is analyzed using solid works software to study reaction stress in the elbow pin and hub, and then, the mechanism is fabricated to permissible speed of the elbow rod and hub of the mechanism [10]. The application of this gearless transmission is inclined toward the wind turbine. These are becoming promising solution for smooth and effective operation for the wind turbine application [11]. Kiran et al. [12] and Yasarkhan et al. [13] analyzed the effect of the elbow pin and hub interaction during operation of the mechanics. The

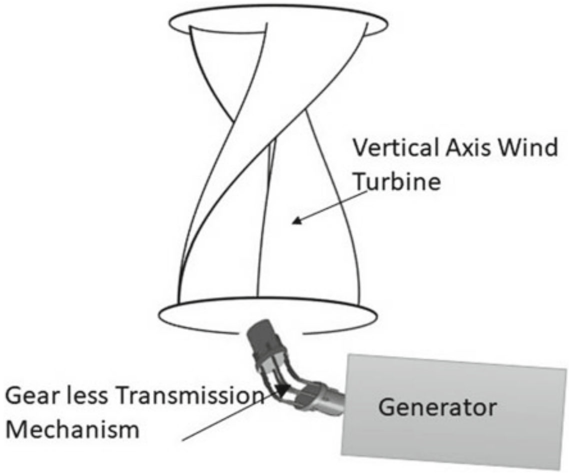

Fig. 1 Schematic of vertical axis wind turbine with gearless transmission mechanism

peak value of force and moments was analyzed and compared with the allowable and designed stress.

Figure 1 shows the schematic of the vertical axis wind turbine system employed with gearless transmission mechanism. The main objective of this paper is to design and analyze the gearless mechanism of wind turbine which performs at low height effectively. Prior to the implementation of vertical axis wind mills with gearless technology, extensive analysis has been done using Ansys© software by changing the parameter like number of pin and diameter of pin for various speed of the rotation. In the next section, the methodology to do the analysis and validation of the model is discussed. In third section, result and discussion of this work are presented.

2 Methodology

The commercially available FEA tool like Ansys© structural analysis is used in this simulation to enable us to solve complex structural engineering mechanism. This gearless transmission mechanism can easily model and analyze for better and faster design optimization using this software. Ansys© mechanical has smart meshing technology, enabling to get optimum meshing quickly. Figure 2 shows the 3D meshing of the gearless transmission mechanism. The boundary condition of rotation for driving shaft and only one degree of freedom of sliding is allowed for the link. The mesh sensitivity study is carried out using the automatic and intelligent algorithms to ensure that high quality meshes were generated for this simulation. The validation of the simulation is shown is Table 1. The validation has been done analytically, and the error in the simulation is maximum 3.8%, which is in allowable limit. With this confidence, further simulation is continued for different case in the gearless transmission mechanism.

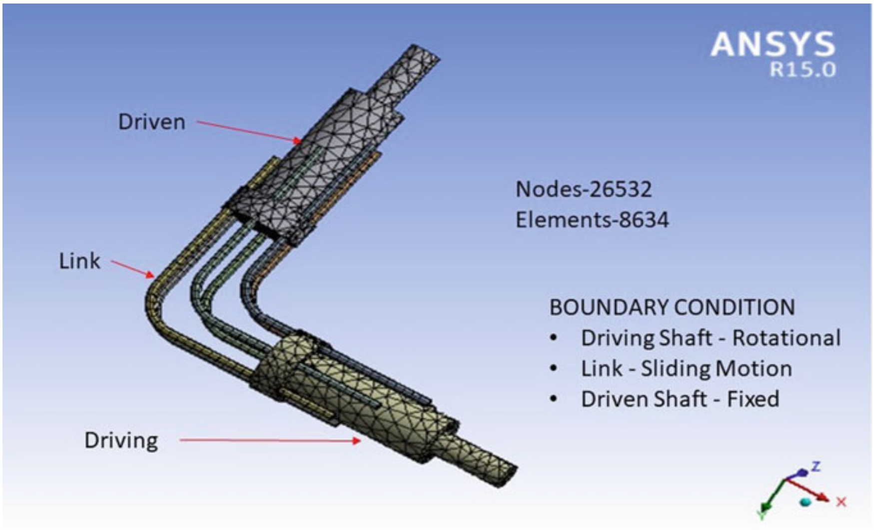

Fig. 2 3D mesh with boundary conditions

Table 1 Validation of numerical studies

	Software	Numerical	
	Bending stress (MPa)	Bending stress (MPa)	Percentage error
Link	11,049	11,337	2.5
Hub and Shaft	438	456	3.8

In this work, three different cases of simulation have been done. In the first case, the diameter of the link is 4 mm, and in the second case, the diameter of the link is 6 mm, similarly in the third case, the diameter of the link is 8 mm, and number of link varied from 3, 5 to 9 for all three cases is shown in Table 2. In next section, the

Table 2 Consolidation of various cases studied in the analysis

CASE 1: Diameter of Link is 4 mm fixed	No. of link 3
	No. of link 7
	No. of link 9
CASE 2: Diameter of Link is 5 mm fixed	No. of link 3
	No. of link 7
	No. of link 9
CASE 3: Diameter of Link is 6 mm fixed	No. of link 3
	No. of link 7
	No. of link 9

effect of changing the diameter and number of the link for different speed of driving shaft is discussed.

3 Results and Discussion

In the gearless transmission system, number of links used must be odd 3,5,7,9, etc., and these links are fixed in the drilled holes of the hub at the both driving and driven shaft ends because of which rotation is transferred. In this study, three cases with 4, 5 and 6 mm diameter of link are analyzed for different number of link, viz. 3, 7 and 9. The minimum and maximum value of the total deformation, equivalent elastic strain and equivalent stress of the 5 link and 7 link are almost same, so result of 5 link is not discussed in this paper. Moreover, when the number of link is 11, the pitch distance between the two links is very small which lead to more stress concentration, and possibility of failure of mechanism is more. In this section, illustration of the 9 link alone is presented, and consolidation results of all there link are presented in Table 3. In Fig. 3, the von Mises yield principle put forward that the yielding of materials starts when the second derivate stress tensor reaches a critical value and its value is 5.88×10^{-5} which is less than the other two cases. It is observed that the part of a plasticity theory applies best to the materials, such as mild steel used in this study. Moreover, prior to yield, material reaction can be presumed to be nonlinear elastic or viscoelastic. The subset of in Fig. 3 is the enlarged view of enclosed area where maximum strain is predicted because of yielding of materials under any loading condition.

Figure 4 shows the deformation in the link and hub of the mechanism which is

Table 3 Consolidated list of total deformation, equivalent elastic strain and equivalent stress

		Total deformation (mm)		Equivalent elastic strain		Equivalent stress (von Mises) (Mpa)	
		Min	Max	Min	Max	Min	Max
CASE 1: Diameter of link is 4 mm fixed	No. of 3 link	0	1.5963	6.28e-9	3.57e-4	9.17e-4	54.925
	No. of 7 link	0	0.9731	6.28e-9	2.02e-4	4.86e-4	31.275
	No. of 9 link	0	0.8341	5.03e-9	1.85e-4	3.61e-4	28.665
CASE 2: Diameter of link is 5 mm fixed	No. of 3 link	0	0.8527	6.10e-9	1.41e-4	4.50e-4	28.154
	No. of 7 link	0	0.4395	1.13e-9	1.79e-4	1.39e-4	29.578
	No. of 9 link	0	0.3928	1.84e-9	7.88e-5	2.12e-4	14.142
CASE 3: Diameter of link is 6 mm fixed	No. of 3 link	0	0.2767	1.73e-7	7.51e-5	1.84e-4	14.925
	No. of 7 link	0	0.1137	6.6e-10	9.98e-5	8.43e-5	16.238
	No. of 9 link	0	0.1078	9.6e-10	5.84e-5	8.00e-5	11.329

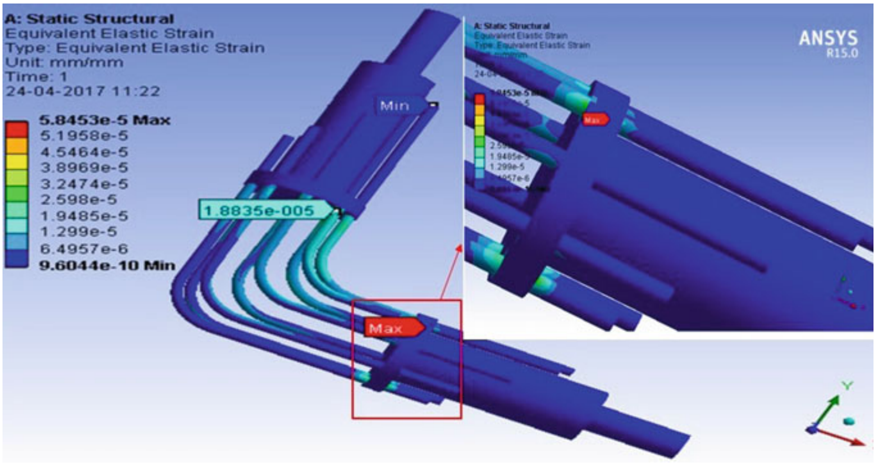

Fig. 3 Equivalent elastic strain for case 3 of 6 mm diameter link and 9 number of link

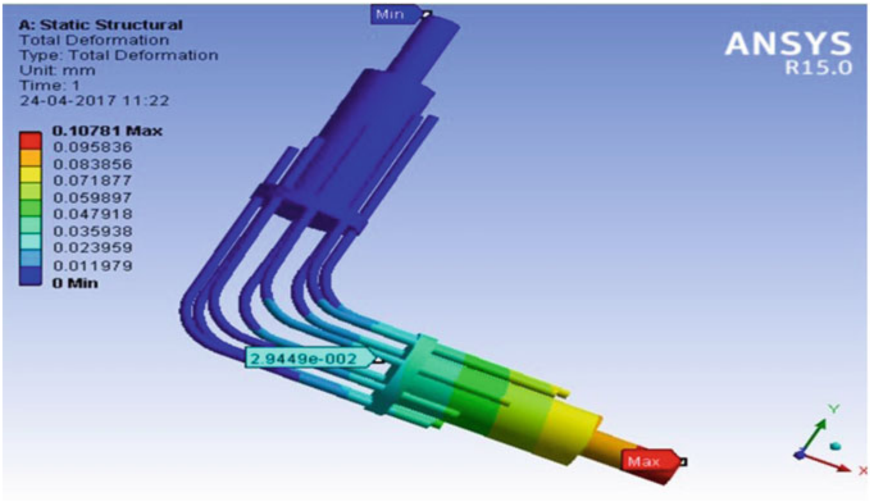

Fig. 4 Total deformation for case 3 of 6 mm diameter link and 9 number of link

the conversion of a body from a reference configuration to an existing configuration due to the sliding mechanism of the link inside the hub. An existing configuration is a set that contains the positions due to the deformation of the body. This deformation is caused by external loads like friction force of the sliding motion, body forces due to the self-weight of the mechanism and the connecting load at the driven end. This strain is an explanation of deformation in terms of relative position of particles in the shaft that ignores rigid-body motions of the mechanism. In a continuous mechanism,

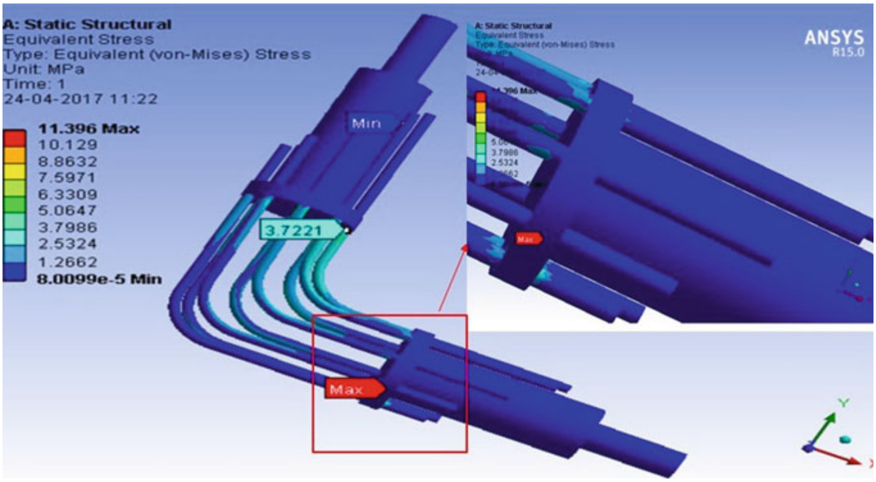

Fig. 5 Equivalent (von Mises) stress for case 3 of 6 mm diameter link and 9 number of link

a deformation represents the results from a stress field which is promoted by applied forces inside the component of the sliding and rotating mechanism.

Figure 5 shows the von Mises stress developed in the link, and it is used to predict yielding of materials under the given condition due to the both bending and twisting momentum. It fulfills the property that two states of stress with same distortion energy have similar von Mises stress. Moreover, the von Mises yielding principle is not dependents of the first stress invariant, and it is applicable for the simulation of plastic deformation of the material that chosen for this analysis. The von Mises yield criterion in this study can be also expressed in terms of the von Mises stress, a scalar stress value that can be calculated from the Cauchy stress tensor. The subset in Fig. 5 shows the enlarged view in the region where von Mises stress is more and no net mass addition through the inlet or exit is permitted in this transmitting mechanism.

In Table 3, the consolidated list of total deformation, equivalent elastic strain and equivalent stress for the three different cases is presented. It is observed in the simulation that case of 6 mm diameter link with 9 number of link has minimum maximum deformation, equivalent elastic strain and equivalent stress. So, this case is selected for further analysis to optimize the speed of the driving shaft is shown in Table 4. Rotational analysis is performed by operating the mechanism at various speed from 0 to 150 rpm, reaction forces and reaction moment are measured for 5 s, and peak value of the reaction force and moments was measured and compared with the allowable. It is found that the optimum permissible speed for smooth and efficient operation is 100 rpm and reaches the allowable stress at this speed for the factor of safety of 2.5. Hence, it is becoming a stimulating solution for small vertical axis wind turbine applications.

Table 4 Variation of equivalent stress with rotational speed

S. No	Speed (rpm)	Equivalent stress (MPa)
1	0	0
2	25	10.85
3	50	30.2
4	75	60.72
5	100	96.12
6	125	110.13
7	150	120.32

4 Conclusion

Gearless transmission mechanism that is suitable for vertical axis wind turbine has been analyzed using commercially available Ansys© software. Three different cases were analyzed, and the effect changing the diameter of elbow rod and number of elbow rod is being studied with time by using Ansys© post processor. It is found that the case 3 with 6 mm diameter of elbow rod and 9 number of elbow rod has the minimum value of maximum deformation, von Mises stress and equivalent strain. So, the dimensioned is optimized with various case study. Using the optimum dimension, the simulation has been done with various motor speed. The various motor speed was defined with varied torque in the simulation. It is observed that deformation in hub is very small at almost all values of rpm, whereas the link reaches its allowable stress value at 100 rpm for factor of safety of 2.5. It shows that the smooth and safe running of mechanism will occur when speed is below 100 rpm. Hence, it is concluded that gearless transmission mechanism is efficiently running up to 100 rpm under normal working condition.

Acknowledgements This research work is supported, in part by the Ministry of New and Renewable Energy, Government of India, New Delhi, India, vide Grant No. 24/6/2014-SWES(R&D) dated: 30/12/2014, and the authors also gratefully acknowledge the support of Dr. Rajesh Katyal, Mr, Haribhaskaran, Mr. David Solomon and Ms. Deepa Kurup. The authors are also grateful to Dr. Uppu Ramachandraiah, HoD (EIE), HITS, for providing valuable suggestions.

References

1. Chung DW, Ryu HM, Lee YM, Kang LW, Sul SK, Kang SJ, Song JH, Yoon JS, Lee KH, Suh JH (2001) Drive systems for high-speed gearless elevators. IEEE Ind Appl Soc 7(5):52–56
2. Jagushte GS, Mayur L, Rahul H, Prasad P, Tejas S (2017) Design and automation of bar cutting machine. Int J Eng Sci Res Tech 3(2):658–661
3. Mahantesh T, Yapalaparvi SB, Inamdar DN, Chiniwalar GV (2014) Gearless power transmission offset parallel shaft coupling. Int J Res Eng Technol 3(3):52–56
4. Janakiraman R, Paramasivam S (2012) Model and design analysis of gearless PM stator-less contra-rotation wind power generator. Int J Eng Res Technol 1(4):1–8

5. Bohra D, Bhaskar MK, Jain D, Manoj C, Vishvendra PG (2018) Performance analysis of permanent magnet synchronous generator wind turbine for variable wind velocity. Int J Res Appl Sci Eng Technol 6(1):2050–2059
6. Ghagare SD, Abhijeet SS, Anant DA, Abhijit MZ, Hanmant MK, Vahid MJ (2017) Hybrid power generation using Maglev turbine. Int J Recent Res Asp 4(4):409–412
7. Danish SM, Moinoddin M, Nawazish SM (2015) Investigations on the fluid coupling of gearless two wheeler. Int J Sci Eng Appl Sci 1(7):220–234
8. Kumar A, P P, R Sagar, Bist S (2015) Multi-angular gearless drive. Int J Sci Eng Res 6(7):974–977
9. Gupta S, Sheikh AG, Adnan ZB, Pawan A, Kushal K, Mohsin AW (2018) Design and analysis of gearless power transmission by rods using software simulation. Int J Innov Res Sci Eng Technol 7(5):5215–5218
10. Somraj R, Sailesh B (2017) Design and fabrication of gearless power transmission for skew shafts. Int Res J Eng Technol 4(4):1018–1023
11. Jagushte GS, Hrishikesh K, Vikas P, Vishal V (2016) Design, analysis and fabrication of gearless transmission by elbow mechanism. Int J Sci Res Dev 4(2):688–689
12. Kiran S, Yadav SPS, Sandeep GM, Naik R (2017) Design, analysis and fabrication of gearless power transmission by using elbow mechanism. Int J Eng Res Technol 6(4):739–741
13. Yasarkhan RS, Pankil P, Hiren P, Patel D (2017) A review paper on design and analysis of gearless transmission mechanism using elbow mechanism. Int J Adv Mech Eng 7(1):31–40

Experimental Investigation of Unsteady State Heat Transfer Behaviour of Nanofluid

Yogiraj Bhumkar, A. R. Acharya, and A. T. Pise

Abstract This paper provides the method for preparation of nanofluids and measuring thermal properties of nanofluids by various methods. In this paper, we have focused on effect of variation of temperature, particle size and volume fraction of nanofluid on properties of nanofluid such as density, viscosity, thermal conductivity and heat transfer coefficient. We have made comparison between CuO, ZnO and SiO_2 nanoparticles with particle size 30–50 nm and 50–70 nm and with three volume fractions 0.5, 1 and 1.5%. The heat transfer coefficient (h) of all nanofluids is determined from unsteady state heat transfer apparatus. The results indicate that the thermal conductivity and h of nanofluid enhance with increase in %vol. fraction and decrease in particle size. CuO–DI water nanofluid with 1.5% volume fraction and 30–50 nm particle size has higher heat transfer coefficient, and thermal conductivity is enhanced by 59.59% than de-ionized water. Hence, CuO–DI water nanofluid (1.5% vol. fraction and 30–50 nm particle size) reaches steady state faster than other nanofluids.

Keywords Preparation of nanofluid · Properties of nanofluid: Heat transfer coefficient · Thermal conductivity · Viscosity · Density and specific heat · Unsteady state heat transfer behaviour (Unsteady state heating curves) of nanofluid

1 Introduction

Nanofluids have higher thermal properties than current heat transfer fluids. Hence, nanofluid has future scope in heat transfer fluids. Metal nanoparticles have more thermal conductivity than other nanoparticles but have less dispersion properties and poor stability. Oxide nanoparticles have better dispersion properties and stable suspension. Particle size and volume fraction of particles affect the properties of nanofluid. Researchers have given different correlations for properties of nanofluids. We have to observe important conclusions of some researchers.

Y. Bhumkar (✉) · A. R. Acharya · A. T. Pise
Department of Mechanical Engineering, GCE, Karad, Maharashtra, India
e-mail: yogirajbhumkar@gmail.com

E. T. Akinlabi et al. (eds.), *Trends in Mechanical and Biomedical Design*,
Lecture Notes in Mechanical Engineering,
https://doi.org/10.1007/978-981-15-4488-0_45

Bashirnezhad et al. [1] concluded that viscosity increases with increase in volume fraction of nanoparticles and decrease in temperature. Author reported the future scope for doing experimental studies by acknowledging temperature, nanoparticle size, volume fraction, sonication time and base fluid.

Liu et al. [2] observed that thermal conductivity of Cu–water nanofluid at 0.1% volume fraction is increased by 23.8%. Researcher performed the experiment on nanofluids without use of surfactant. Due to poor dispersion properties of nanofluid, thermal conductivity depends on time interval.

Gupta et al. [3] provided the correlations for various properties of nanofluid. Researcher reviewed the factors affecting the thermophysical properties of nanofluid. Researcher has mentioned the future scope for cost effective and efficient nanofluid.

Albadr et al. [4] used the Al_2O_3 nanoparticles of 30 nm particle size. The researcher concluded that heat transfer coefficient (h) increases with increase in mass flow rate and volume fraction. But friction factor increases with increase in vol. concentration of nanoparticles, which results in pressure drop.

Li et al. [5] summarized the recent improvement in research of stationary nanofluid. The researcher mentioned that long-term stability of nanofluid is a key issue.

2 Nanofluid

Nanofluid contains nanometre-sized particles made of metal, oxides, carbides, borides, nitrides, etc. There are two ways for the preparation of nanofluids.

2.1 Preparation of Nanofluid

2.1.1 One Step Method

The manufacturing of nanoparticles and dispersion in a base fluid are done simultaneously. Some general one step methods are as follows:

(a) Direct evaporation
(b) Chemical vapour condensation
(c) Chemical precipitation.

2.1.2 Two Step Method

The nanoparticles are first manufactured and then dispersed into the base fluid. Example of two step method is gas condensation. We have preferred the two step method for the preparation of nanofluid. In this method, first of all, we have calculated the

a) b) c)

Fig. 1 **a** Weighing machine. **b** Magnetic stirrer. **c** Ultrasonic cleaner

mass of nanoparticles for 0.5, 1 and 1.5% vol. fraction of nanoparticles into the base fluid which is de-ionized water.

$$\text{Mass of Nanoparticles} = \rho_p * \%\text{Vol. Fraction} * \text{Volume of base fluid}$$

where ρ_p = Density of Nanoparticles (gm/cm^3).

Surfactant used: Sodium Dodecyl Sulphate (SDS).

$$\text{Mass of Surfactant} = 10\% \text{ of mass of nanoparticle}$$

We can use different surfactants such as Sodium Dodecyl Sulphate (SDS), Ammonium Cetyl Cetyl (CTAB) and Dodecyl Benzen Sulphonate (SDBS). But SDS is more effective for stability of oxide nanoparticles in base fluid.

2.2 Process of Nanofluid Reparation

This measured quantity of nanoparticles and surfactant are mixed with base fluid in magnetic stirrer for 30 min. After magnetic stirring, the fluid is transferred to ultrasonic bath for 2 h. Ultrasonic waves disperse the nanoparticles into the base fluid and form uniform mixture. Use of ultrasonic bath more than 2 h does not show more effect of dispersion of nanoparticles (Fig. 1).

2.3 Stability of Nanofluid

The long-term stability of nanofluid is the key issue. Metal oxide nanofluids are more stable than metallic nanofluids. Nanofluid becomes stable after the proper dispersion

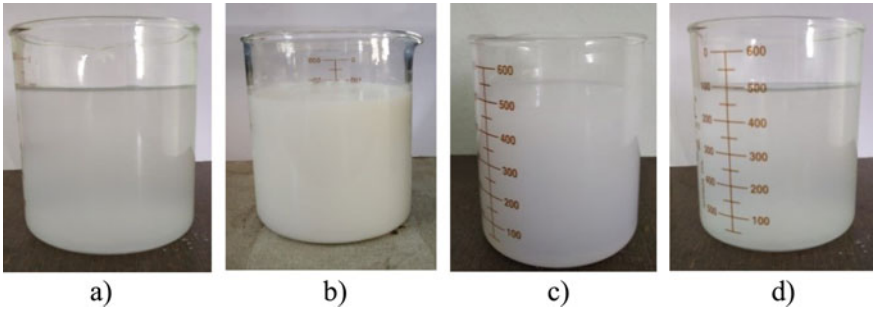

Fig. 2 SiO_2–DI water nanofluid **a** without SDS **b** with SDS after 2 h **c** with SDS after 48 h **d** with SDS after 72 h

of nanoparticles due to existence of Brownian motion. Due to Brownian motion, nanoparticles are in motion and get dispersed properly in base fluid stability can be analysed by the following methods (Fig. 2):

(a) Visual Inspection
(b) Zeta Potential (pH Value).

3 Properties of Nanofluids

After the preparation of nanofluid, it is necessary to find out the following properties of nanofluid. Some important properties are as follows:

1. Density
2. Viscosity
3. Thermal Conductivity
4. Specific Heat.

3.1 Density

Density of nanofluid can be determined from following two methods:

Method 1 Pak and Cho correlation

$$\rho_{\mathrm{nf}} = [(1 - \Phi)\rho_{\mathrm{nf}}] + (\Phi\rho_{\mathrm{bf}}) \tag{1}$$

where ρ_{nf} = Density of nanofluid in gm/cm^3

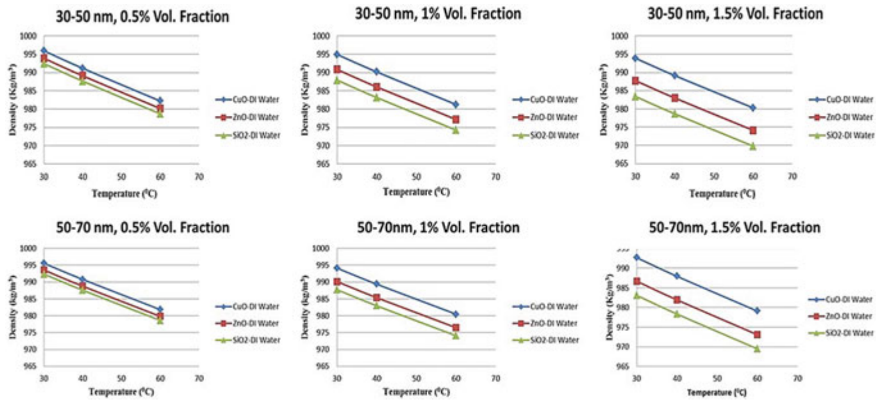

Fig. 3 Variation of density with respect to temperature of different nanofluids

ρ_{bf} = Density of base fluid
Φ = Volume fraction.

Method 2 Experimental Method

$$\rho_{\mathrm{nf}} = \left(\frac{W_2 - W_1}{50}\right) \times 10^3 \tag{2}$$

where W_2 = Weight of jar with 50 cc of nanofluid
W_1 = Weight of empty jar
ρ_{nf} = Density of nanofluid in kg/m^3 (Fig. 3).

3.2 *Viscosity*

Method 1 Einstein correlation

$$\mu_{\mathrm{nf}} = [1 + 2.5\Phi]\mu_{\mathrm{bf}} \tag{3}$$

where μ_{nf} = Density of nanofluid in kg/ms
μ_{bf} = Density of base fluid in kg/ms
Φ = Volume fraction.

Method 2 Redwood Viscometer

$$\gamma = \left(A \times t - \frac{B}{t}\right) \times 10^{-6} \tag{4}$$

where γ = Kinematic viscosity of nanofluid m^2/s
t = Time for collecting 50 cc of nanofluid in sec
A and B = Redwood constants
$A = 0.264$ and $B = 190$.

$$\mu = \rho \times \gamma \tag{5}$$

where μ = Density of nanofluid in kg/ms (Fig. 4).

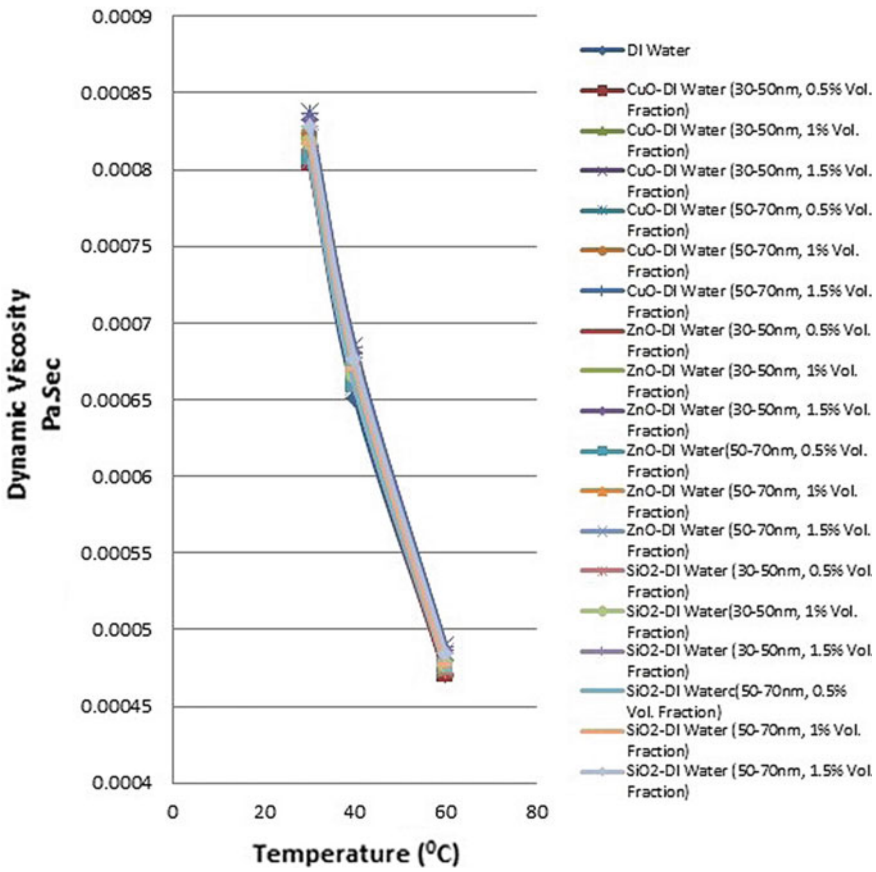

Fig. 4 Variation of dynamic viscosity with respect to temperature of different nanofluids

3.3 Thermal Conductivity

Method 1 Wasp Correlation

$$K_{\mathrm{nf}} = K_{\mathrm{bf}} \times \frac{2K_{\mathrm{bf}} + K_{\mathrm{np}} - 2\Phi(K_{\mathrm{bf}} - K_{\mathrm{np}})}{2K_{\mathrm{bf}} + K_{\mathrm{np}} + \Phi(K_{\mathrm{bf}} - K_{\mathrm{np}})} \tag{6}$$

where K_{nf} = Thermal conductivity of nanofluid in W/mK
K_{bf} = Thermal conductivity of base fluid in W/mK
Φ = Volume fraction.

Method 2 Ultrasonic Interferometer

$$K_{\mathrm{nf}} = 3 \times \left(\frac{N}{V}\right)^{2/3} \times K_{\mathrm{B}} \times v_{\mathrm{s}} \tag{7}$$

where N = Avogadro's Number = $6.02 * 10^{23}$
K_{B} = Boltzmann's Constant = $1.3807 \times 10^{-23} \times 10^{-23}$ J/K
v_{s} = Ultrasound Velocity in m/s
V = Molar Volume = $\frac{m}{\rho}$ (Fig. 5).

3.4 Specific Heat

Pak and Choi have given the following correlation for specific heat:

$$C_{\mathrm{P_{nf}}} = \Phi(C_{\mathrm{P}})_{\mathrm{np}} + (1 - \Phi)(C_{\mathrm{P}})_{\mathrm{bf}} \tag{8}$$

where $C_{\mathrm{P_{nf}}}$ = Specific Heat of Nanofluid.

4 Experimental Apparatus

See (Fig. 6).
Specification:

1. Electric Heater: 500 W (1.5 Lit)
2. Digital Temperature Indicator: 0 °C–199.9 °C
3. Thermocouples: Cr–Al type (K-Type)
4. Specimens Material: Copper (Dia—30 mm, Length—30 mm) ($K = 386$ W/m K).

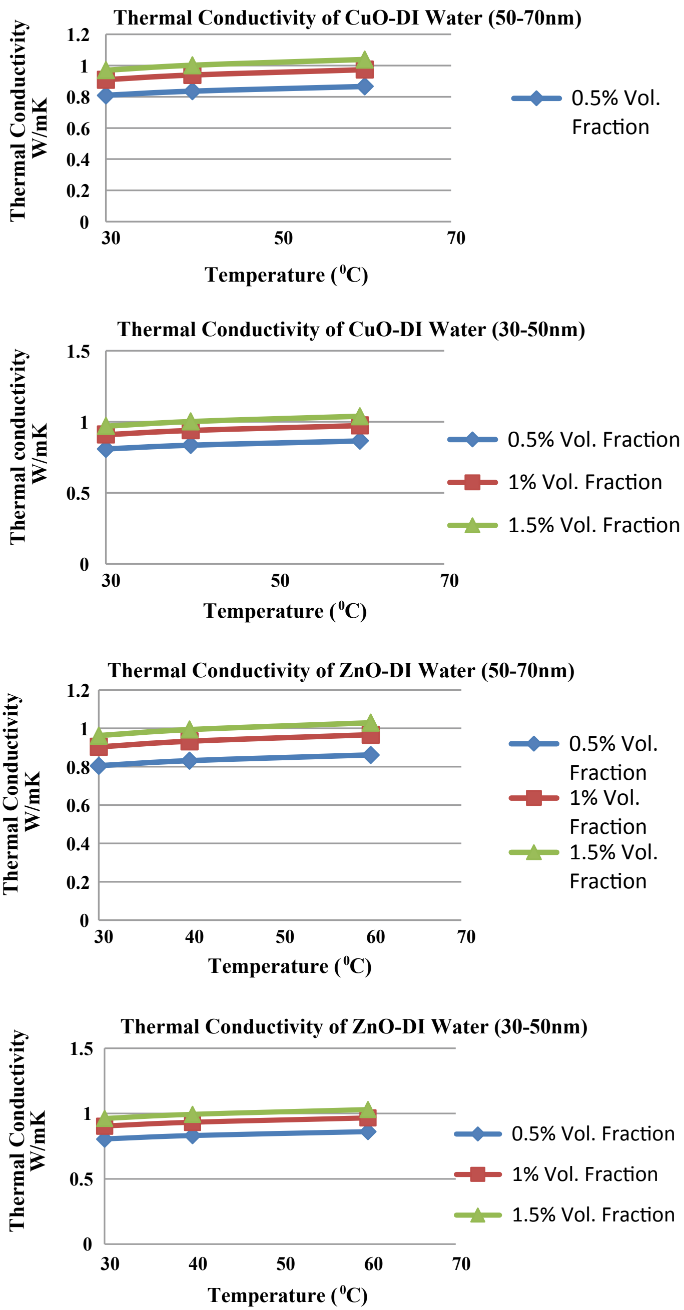

Fig. 5 Variation of thermal conductivity with respect to temperature for various volume fraction of nanofluid

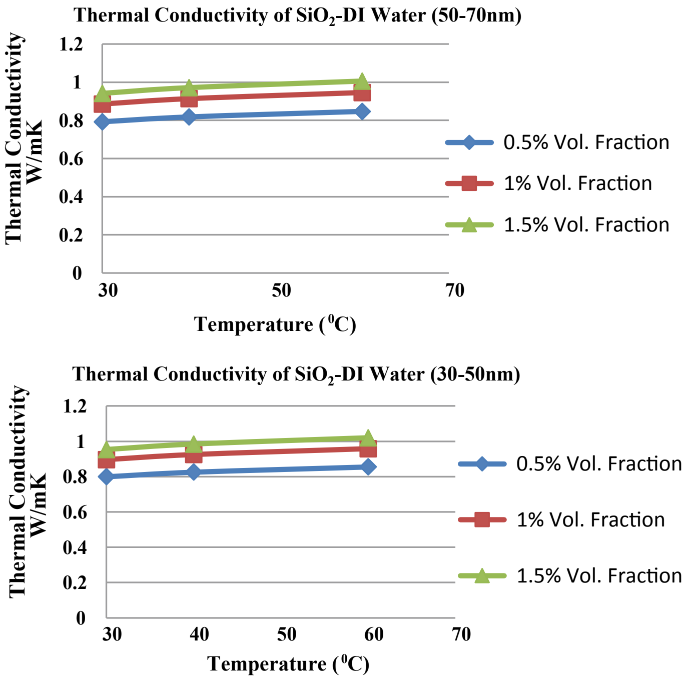

Fig. 5 (continued)

Fig. 6 Unsteady state heat transfer apparatus

After performing the experiments for different nanofluids, we can get the heat transfer coefficient, and also, we can compare these nanofluids by drawing unsteady state heating curves. Following formulas are required to calculate the heat transfer coefficient:

1. Grashof Number

$$\mathrm{Gr} \; = \frac{g \; \beta \; \Delta T \; l^3}{v^2} \tag{8}$$

2. Prandtl Number

$$\mathrm{Pr} = \frac{\mu C_{\mathrm{p}}}{K} \tag{9}$$

3. Rayleigh Number

$$\mathrm{Ra} = \mathrm{Gr} \times \mathrm{Pr} \tag{10}$$

4. Nusselt Number

$$\mathrm{Nu} = 0.36 + \frac{0.518\mathrm{Ra}^{1/4}}{\left\{1 + \left(\frac{0.559}{\mathrm{Pr}}\right)^{9/16}\right\}^{4/9}} \quad 10^{-6} < \mathrm{Ra} < 10^{9} \tag{11}$$

$$\mathrm{Nu} = 0.6 + \frac{\left(0.387 \; \mathrm{Ra}^{1/6}\right)^{4/9}}{\left\{1 + \left(\frac{0.559}{\mathrm{Pr}}\right)^{9/16}\right\}^{8/24}} \quad 10^{9} < \mathrm{Ra} < 10^{12} \tag{12}$$

5. Heat Transfer Coefficient

$$h = \frac{\mathrm{Nu} \; K}{d} \tag{13}$$

See (Figs. 7 and 8).

5 Results and Discussion

1. Heat transfer coefficient of the nanofluid increases with increase in temperature, increase in volume fraction and decrease in particle size.
2. Thermal conductivity increases with increase in volume fraction, increase in temperature and decrease in particle size.
3. Thermal conductivity of CuO–DI water nanofluid (with particle size 30–50 nm, 1.5% Vol. fraction) is 59.59% more than the de-ionized water.

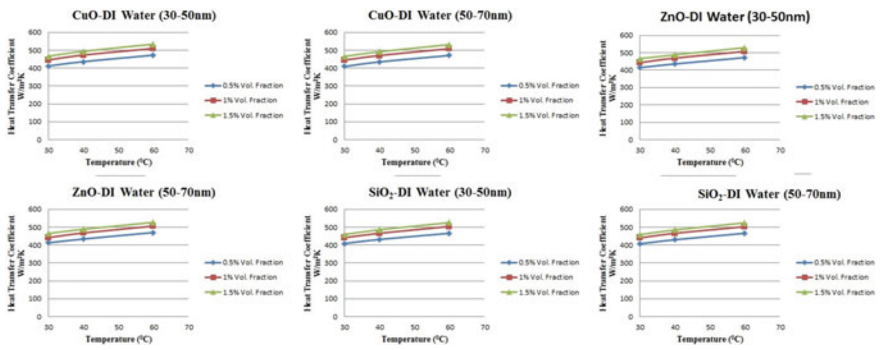

Fig. 7 Variation heat transfer coefficient of with respect to temperature and volume fraction for different nanofluids

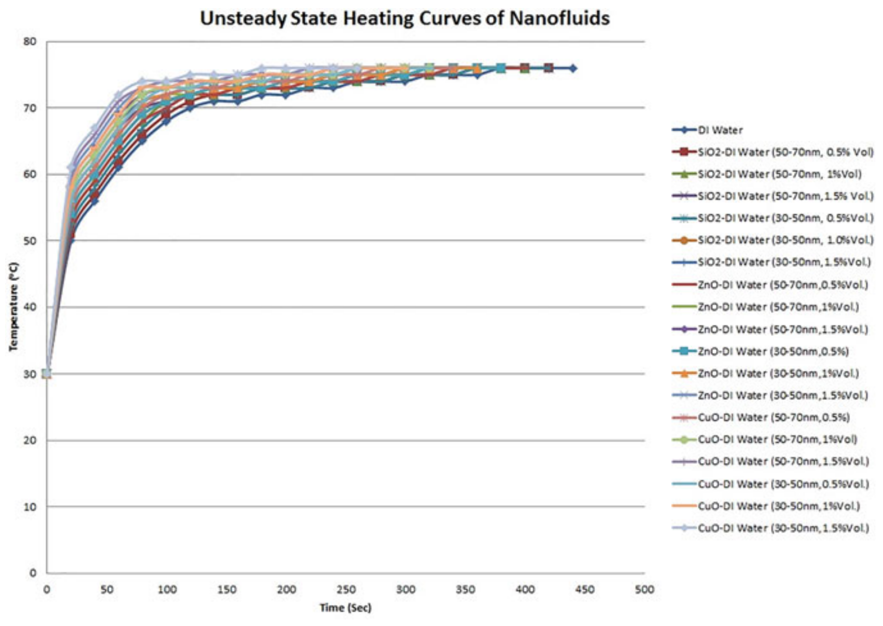

Fig. 8 Variation of temperature with respect to time for different nanofluids during unsteady state heating

4. Viscosity of nanofluid increases with increase in volume fraction and decrease in temperature.
5. Density of nanofluid increases with decrease in particle size, decrease in volume fraction and decrease in temperature.
6. Specific heat increases with increase in temperature, increase in particle size and decrease in volume fraction.

6 Conclusion and Future Scope

In this paper, we studied the thermophysical properties of nanofluids. We can conclude that CuO–DI water nanofluid with 30–50 nm particle size and 1.5% volume fraction has higher heat transfer coefficient. Due to this, CuO–DI water nanofluid reaches the steady state faster than other fluids.

At higher volume fraction, nanofluid has better thermal properties, but stability of nanofluid is a key issue. Further work is required related to the stability of nanofluid. New types of nanofluids having higher thermal properties should be found.

References

1. Bashirnezhad K, Bazri S, Safaei MR (2016) Viscosity of nanofluids: a review of recent experimental studies. Int Commun Heat Mass Transfer 73
2. Liu MS, Lin MCC, Tsai CY, Wang CC (2006) Enhancement of thermal conductivity with cu for nanofluids using chemical reduction method. Int J Heat Mass Transfer 49
3. Gupta M, Singh V, Kumar R, Said Z (2017) A review on thermophysical properties of nanofluids and heat transfer applications. Renew Sustain Energy Rev 74
4. Albadr J, Tayal S, Alasadi M (2013) Heat transfer through heat exchanger using Al_2O_3 nanofluid at different concentrations. Case Stud Therm Eng 1
5. Li Y, Zhou J, Tung S, Schneider E, Xi S (2009) A review on development of nanofluid preparation and characterization. Powder Technol 196

Robotics, Biomedical, and Control Engineering

Switched Staircase-Type Multilevel Inverter Structure with Reduced Number of Switches

V. Thiyagarajan

Abstract Modern research has been involved in developing distinctive multilevel inverter (MLI) circuits. The main aim of this paper is to propose a new MLI topology based on the series–parallel connection of several dc sources with reduced number of switching components. The basic structure of the proposed topology generates only positive voltage levels, and thus, it requires an additional H-bridge unit to create both negative and zero voltage levels. The generalized structure for the proposed MLI topology has also been presented in this paper. Additionally, different strategies are suggested to determine the magnitudes of the dc sources in order to produce more output steps. Compared with the conventional and other recently presented improved topologies, the proposed inverter reduces the number of switches, dc sources, and the maximum voltage blocked by the switches. At last, simulation results for 7-level symmetrical and 17-level asymmetrical inverters are presented in order to confirm the performance of the proposed inverter.

Keywords Multilevel inverter · Total harmonic distortion · Symmetric · Asymmetric · Reduced switch

1 Introduction

The use of sustainable power sources in modern power industry applications requires new power converters to create an improved power quality voltage waveform [1, 2]. Multilevel inverter (MLI) consists of an array of power semiconductor switches and several input sources which provide a multi-step output ac voltage waveform with high power quality [3, 4]. MLI reduces the total harmonic distortion (THD) and electromagnetic interference problems. The various conventional MLI includes cascaded H-bridge (CHB), diode clamped, and flying capacitor inverters [5].

V. Thiyagarajan (✉)
SSN College of Engineering, 603110 Chennai, Tamilnadu, India
e-mail: thiyagarajanv@ssn.edu.in

E. T. Akinlabi et al. (eds.), *Trends in Mechanical and Biomedical Design*,
Lecture Notes in Mechanical Engineering,
https://doi.org/10.1007/978-981-15-4488-0_46

In [6], a new MLI structure using reverse connected voltage sources and H-bridge inverter is presented. The presented topology shares the voltage stress across the switches with increased higher output levels. Another MLI topology with reduced number of switches as compared with CHB is presented in [7]. To show the feasibility, 13-level and 20-level inverter operation is presented in this paper. The new basic unit for the MLI is presented in [8]. This basic unit consists of three dc sources and five switches and is able to generate only positive output levels. In order to create negative output levels, an additional H-bridge inverter is added to the presented basic unit. The topology presented in [9] can be operated in symmetric and asymmetric modes. The presented inverter configuration consists of multiple series connected units to generate larger output levels. Other symmetrical and asymmetric type inverters are presented in [10–12]. In these, the presented topologies consist of basic unit and level changing unit. The positive output levels are achieved with the help of basic unit, and the level changing unit helps to create the negative output levels. However, these topologies require larger number of switches and increase the total standing voltage (TSV) across the switches.

The main objective of this paper is to propose a switched staircase-type MLI topology with reduced switch count and maximize the output levels. The proposed inverter has been operated in both symmetric and asymmetric modes and shows very good performance which considerably reduces the cost and installation area.

2 Proposed Inverter Structure

Figure 1 shows the simple circuit of the proposed MLI topology with two main parts such as level creating part and polarity changing part. The level creating part contains three dc sources and six main switches, and the H-bridge unit with four switches forms the polarity changing part. This circuit produces 7-step output voltage during symmetric operation of the inverter.

Fig. 1 Proposed inverter

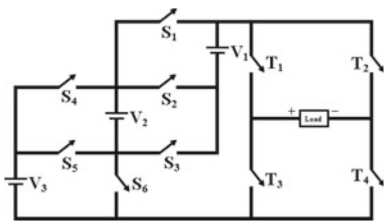

2.1 Operation

The various output levels obtained during positive mode of the proposed basic unit is shown in Fig. 2, and the corresponding switching conditions are given in Table 1. It is seen that only two switches in the basic unit and two switches in the H-bridge units are turned ON to create the required output level. To get the zero output voltage across the load terminals, the switches (T_1, T_2) or (T_3, T_4) are turned ON. By turning ON the switches T_1 and T_4, positive voltage levels are achieved, and to create the negative output levels, the switches T_2 and T_3 are turned ON. To avoid the short circuit, any two switches in the combination (S_1, S_2, S_3) and (S_4, S_5, S_6) should not be turned ON simultaneously.

2.2 Generalized Inverter Topology

The generalized structure of the proposed MLI with 'p' units is shown in Fig. 3. The relation between the total number of basic units 'p' and total number of dc sources 'n' is obtained as:

$$n = 3p \tag{1}$$

The total number of switches 'k' in the generalized structure of the proposed MLI is given by

$$k = 10p \tag{2}$$

The total number of conduction switches in the generalized structure of the proposed MLI '$n_{\text{ON-State}}$' is obtained as:

$$n_{\text{ON - State}} = 4n/3 \tag{3}$$

For the extended structure shown in Fig. 3, the total standing voltage (TSV) is given by:

$$\text{TSV} = \sum_{j=1}^{p} \left(5V_{1j} + 7V_{2j} + 6V_{3j}\right) \tag{4}$$

The maximum output voltage is synthesized by adding the voltage magnitude of all dc sources across the load and is given by:

$$V_{o,}\text{max} = \sum_{i=1}^{p} (V_{1i} + V_{2i} + V_{3i}) \tag{5}$$

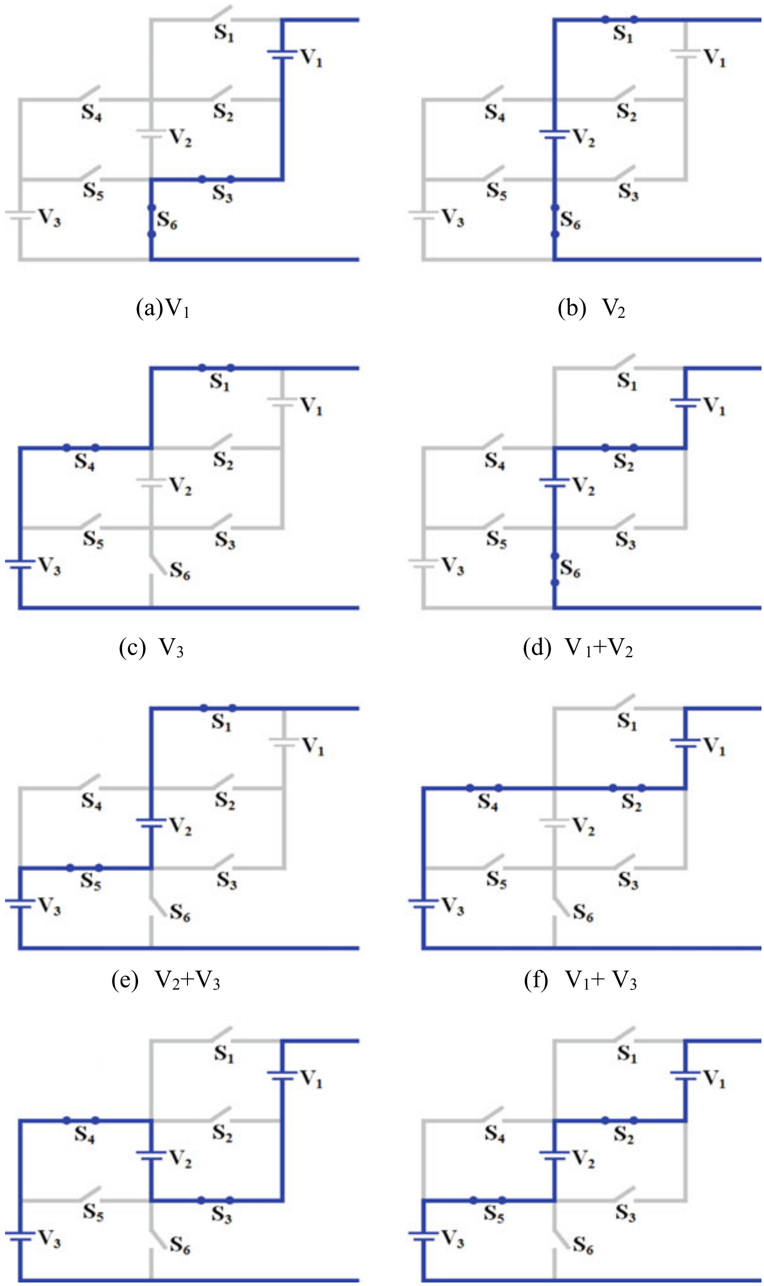

(a) V_1 (b) V_2

(c) V_3 (d) V_1+V_2

(e) V_2+V_3 (f) V_1+V_3

(g) $V_1-V_2+V_3$ (h) $V_1+V_2+V_3$

Fig. 2 Different output levels

Table 1 Switching conditions for different output levels

S. No	Conducting switches	Output voltage
1	T_1, T_2 or T_3, T_4	0
2	S_3, S_6	V_1
3	S_1, S_6	V_2
4	S_1, S_4	V_3
5	S_2, S_6	$V_1 + V_2$
6	S_1, S_5	$V_2 + V_3$
7	S_2, S_4	$V_1 + V_3$
8	S_3, S_4	$V_1 - V_2 + V_3$
9	S_2, S_5	$V_1 + V_2 + V_3$

3 Determination of Voltage Magnitude

In this section, two different methods are proposed to determine the voltage magnitude of dc sources.

3.1 *Algorithm-1*

In algorithm-1, the dc voltage magnitude of each source is obtained as

$$V_{ij} = V_{dc} \quad \text{where,} \quad i = 1, 2, 3 \text{ and } j = 1,\ 2,\ 3, \ldots, p \tag{6}$$

Since the voltage magnitudes are same, the inverter is called as symmetric inverter. In this case, the maximum output voltage is given by

$$V_{o,}\text{max} = nV_{dc} \tag{7}$$

The total number of output levels 'm' is given by

$$m = 6p + 1 \tag{8}$$

3.2 *Algorithm-2*

In algorithm-2, the magnitude of each source is determined as

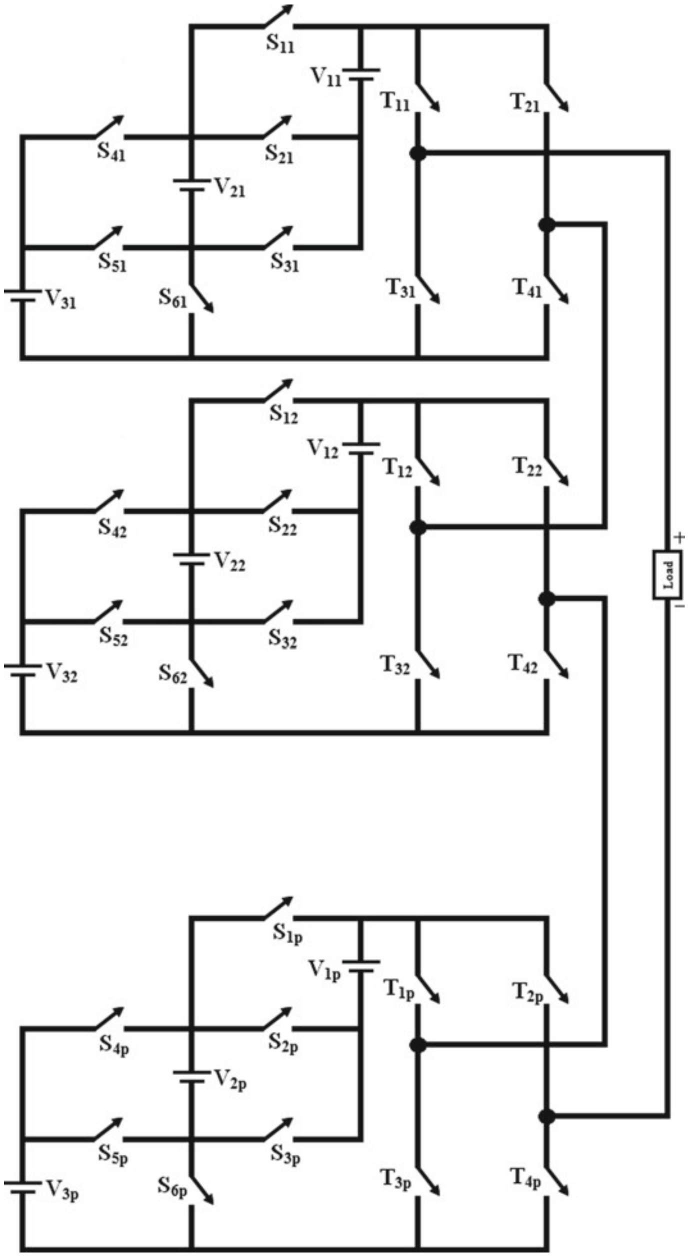

Fig. 3 Generalized structure of the proposed MLI

$$
\begin{aligned}
V_{1i} &= (17)^{i-1} V_{dc} \\
V_{2i} &= 2(17)^{i-1} V_{dc} \\
V_{3i} = 5(17)^{i-1} V_{dc} \quad \text{where,} \quad i &= 1, 2, 3, \ldots, p
\end{aligned}
\tag{9}
$$

Since the voltage magnitudes are different, the inverter is called as asymmetric inverter. The total number of output levels 'm' is given by

$$m = (17)^p \tag{10}$$

4 Comparison Study

This section presents the comparison results of the proposed MLI with recently presented topologies. This comparison is based on the required number of sources, switches, and TSV value to create the required output levels. Figure 4a shows the plot between the number of levels and sources. Figure 4b, c shows the plot between the number of levels and switches during symmetric and asymmetric operation, respectively. Figure 4d shows the total number of conducting switches for the given number of dc sources. The plot between the TSV and the number of output levels is shown in Fig. 4e. The results show that the proposed topology uses minimum number of dc sources and switches to create higher output levels. Also, it minimizes the total number of conducting switches and thereby minimizes switching losses. In addition, the TSV value of the switches is reduced as compared with the other presented topologies.

5 Simulation Results

This section presents the simulation results of symmetric 7-level and asymmetric 17-level operation of the proposed inverter. A series RL load with the values of $R = 50\ \Omega$ and $L = 100$ mH is considered for the simulation.

5.1 Symmetric 7 Level

During symmetric condition, all the sources have same voltage magnitude, i.e., $V_1 = V_2 = V_3 = 80\ V$. Figure 5 shows the simulation results of 7-level inverter. It is obtained that THD of the 7-level output voltage waveform is 12.23%. The input power is 500 W, and the efficiency is obtained as 87% with a loss of 65 W.

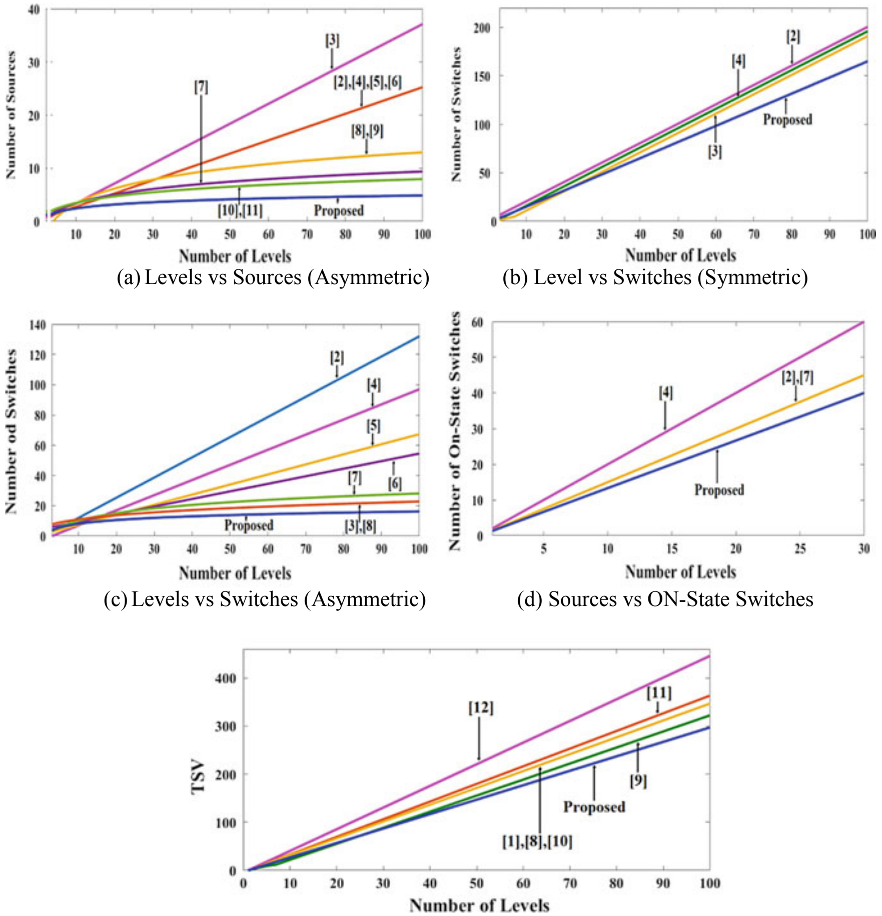

(a) Levels vs Sources (Asymmetric) (b) Level vs Switches (Symmetric)

(c) Levels vs Switches (Asymmetric) (d) Sources vs ON-State Switches

(e) Levels vs TSV

Fig. 4 Comparison results

5.2 Asymmetric 17 Level

During asymmetric condition, the voltage magnitudes are different. In this case, $V_1 = V_{\text{dc}} = 30\ V$, $V_2 = 2V_{\text{dc}} = 60\ V$, $V_3 = 5V_{\text{dc}} = 150\ V$. Figure 6 shows the simulation results of 17-level inverter. It is obtained that THD of the 17-level output voltage waveform is 4.84%. The efficiency of the inverter is obtained as 92% with a loss of 45 W.

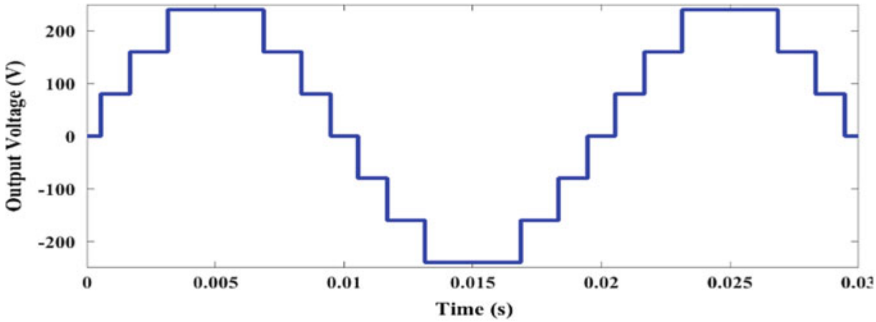

(a) Output Voltage

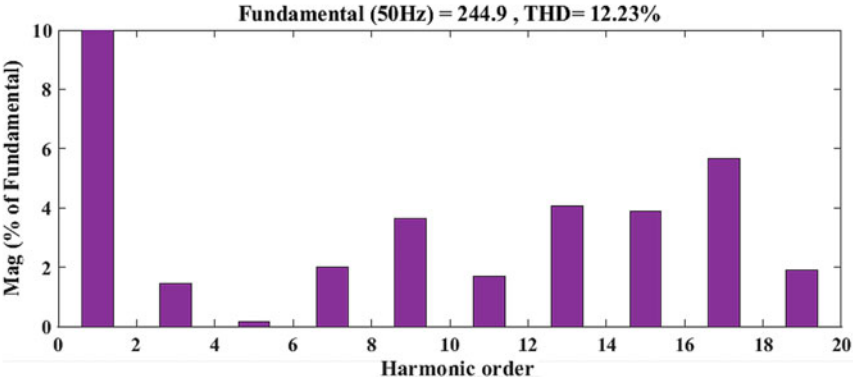

(b) THD

Fig. 5 Simulation results—7-level

6 Conclusion

This paper presents a new switched staircase-type MLI topology with reduced switched count. The comparison study is presented in this paper between the proposed MLI and other recently developed topologies. The comparison results shows that the proposed MLI has superior features over conventional and other recently developed topologies in view of number of switches, sources, and TSV. The proposed inverter has very good performance which considerably reduces the cost and installation area. Finally, the proposed MLI is implemented by MATLAB simulation for 7-level and 17-level inverter operation in order to show the performance of the inverter.

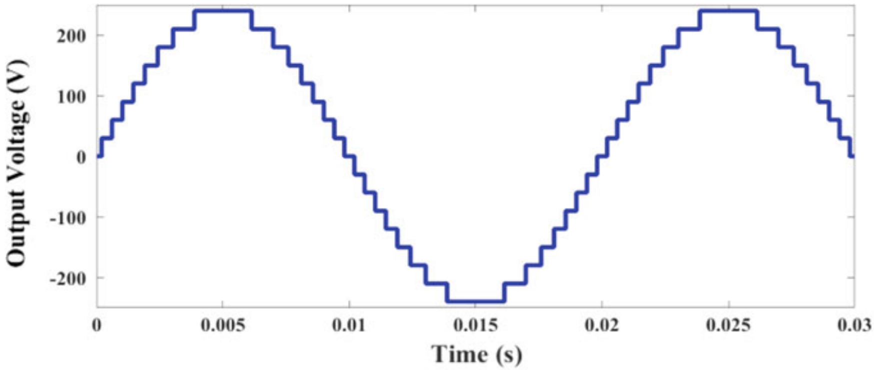

(a) Output Voltage

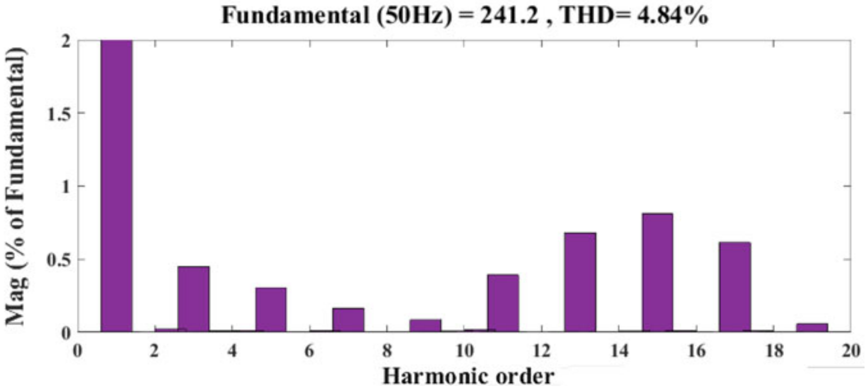

(b) THD

Fig. 6 Simulation results—17-level

References

1. Khenar M, Taghvaie A, Adabi J, Rezanejad M (2018) Multilevel inverter with combined T-type and cross connected modules. IET Power Electronics 11(8):1407–1415
2. Prayag A, Bodkhe S (2017) Novel basic block of multilevel inverter using reduced number of on-state switches and cascaded circuit topology. Adv Electr Eng 2017:1–16
3. Odeh CI, Obe ES, Ojo O (2016) Topology for cascaded multilevel inverter. IET Power Electron 9(5):921–929
4. Prabaharan N, Palanisamy K (2017) Analysis of cascaded H-bridge multilevel inverter configuration with double level circuit. IET Power Electron 10(9):1023–1033
5. Karthikeyan D, Vijayakumar K, Sathik MAJ (2018) Development of a switched diode asymmetric multilevel inverter topology. J Power Electron 18(2):418–431
6. Thamizharasan S, Baskaran J, Ramkumar S, Jeevananthan S (2014) Cross-switched multilevel inverter using auxiliary reverse connected voltage sources. IET Power Electron 7(6):1519–1526

7. Ajami A, Mokhberdoran A, Oskuee MRJ (2013) A new topology of multilevel voltage source inverter to minimize the number of circuit devices and maximize the number of output voltage levels. J Elect Eng Technol 8(6):1328–1336
8. Babaei E, Laali S, Bayat Z (2015) A single-phase cascaded multilevel inverter based on a new basic unit with reduced number of power switches. IEEE Trans Indus Electro 62(2):922–929
9. Oskuee MRJ, Nikpoura S, Ravadanegha SN, Gharehpetian GB (2018) Improved configuration for symmetric and asymmetric multilevel inverters with reduced number of circuit devices. Int J Ambient Energy 39(4):421–431
10. Thiyagarajan V, Somasundaram P (2018) Multilevel inverter topology with modified pulse width modulation and reduced switch count. Acta Polytech Hung 15(2):141–167
11. Khosroahahi MI (2014) Crisscross cascade multilevel inverter with reduction in number of components. IET Power Electron 7(12):2914–2924
12. Babaei E (2008) A cascade multilevel converter topology with reduced number of switches. IEEE Trans Power Elect 23(6):2657–2664

Hydro Pneumatic Parking Brake Actuation System for Motor Grader Application

K. Rajasekar, S. Karthikeyan, V. Kumar, and H. S. Satish Chandra

Abstract Motor graders are used in many applications in the Mining and Construction fields. In India, grader models running on road need to meet the Central Motor Vehicles Rules (CMVR 1989) [1], i.e. RTO regulations formulated by the Ministry of Road Transport and Highways (MoRTH) and in the mines has to meet the DGMS regulations. Hydraulic or air-operated brake system is installed in graders for slow down and stop. Air brake system is preferred due to its simple construction, low cost and easy serviceability. Parking brake is used to hold the equipment on slopes in stationary conditions and for parking. As per the vehicle safety standards, parking brakes are designed to be fail safe. To meet this, spring applied, air/hydraulic release type parking brakes are used. Motor grader having 12 ft work blade length uses the air system for regular service brakes and internally expandable shoe type parking brake that is actuated by mechanical ratchet pinion mechanism is taken up for study. New disc type spring applied hydraulically released parking brake is designed to improve the holding performance. Need arise to invent a new actuation system as the main service brakes use air-operated brakes and hydraulic power required for parking brake application. The new hydro pneumatic parking brake actuation system has been designed and tested. The practical field tests reveal that new parking brake system reduces operator fatigue, builds up more confidence in operator and ensures safety of higher order.

Keywords Motor grader · Parking brake actuation · Hydro pneumatic

1 Introduction

Motor Grader is used in construction and mining sites for various applications. Graders are also named as the work equipment based on nature of work carried out. Motor Graders are categorized based on the work blade size, frame type and

K. Rajasekar (✉) · S. Karthikeyan · V. Kumar · H. S. Satish Chandra
Equipment Division, Research & Development (R&D), BEML Limited, Mysore, Karnataka, India
e-mail: gwkumaran@beml.co.in

E. T. Akinlabi et al. (eds.), *Trends in Mechanical and Biomedical Design*, Lecture Notes in Mechanical Engineering,
https://doi.org/10.1007/978-981-15-4488-0_47

operating mass. Motor graders are used for material spreading, moving, rolling, mixing and grading operations in road making construction fields. Small and midsized work blade graders like 10 and 12 ft are used in these applications. Larger size work blade graders like 16 ft and above are used mainly in various surface opencast mines for making the haul roads on which heavy trucks and dumpers are transporting coal and other minerals extracted from the earth.

Graders are classified as Rigid and Articulated type based on the Mainframe structure. In rigid version, graders have a single frame where the cabin, work blade and other system aggregates are mounted whereas in articulated version, frame is made into two parts, i.e. front and rear frames, coupled with hinge pins to achieve the shorter turning radius by articulation and best suited for work sites with constricted workspace. Graders work attachment operations are hydraulically operated. Control levers or joysticks are used to control the work blade by the operator inside the cabin. Though the graders are slow-moving work equipment, the safety of the operator is ensured by essential safety standards. Cabin of the graders is designed to meet the ROPS standards to protect the operator. The operator fatigue is reduced by providing the power steering, power brake and other controls. Hydro shift transmission ensures precise and smooth gear shift and transmission of power. Box type heavy-duty tandem delivers the power to the rear wheels. Foot-operated, air actuated internally expandable shoe type service brakes and parking brake ensure the stopping and smooth control of the grader. It is equipped with safety measures like Auto Fire Detection and Suppression system, ROPS cabin, etc. It also meets the DGMS standards to run in various mines of India.

Parking brakes are primarily used to park the vehicle in Slopes. In some vehicles, the parking brake may be used in emergency conditions. In commercial vehicles like car and medium-duty vehicle, ratchet and pinion type parking brake actuation system has been used. Single lever actuates the internally expandable shoe brake at rear wheels of the vehicle through mechanical linkages. The factors influencing the performance of the mechanical type parking brake have to be evaluated to eliminate rollaway [2]. Thermal expansion of the brake material and initial temperature is affecting the clamping force of parking brakes. FMVSS 135 standard describes the performance and functional requirements of vehicle parking brakes [3, 4]. Ergonomics of the operator has been an important factor that has to be studied to make an effective parking brake system [5]. As the mechanical lever-actuated parking brakes require more operator effort, this leads to operator fatigue. Electrical and electronic assisted system developments in the parking brake area offer less operator effort. Application of Sensors and Motors converts conventional mechanical system into automatic hand-operated brake system [6, 7]. It's significant to derive correlation among gross vehicle weight, driving force, braking force, rolling and grade resistance in hill station application [8]. In order to avoid damages due to operator negligence (forgot) to apply the parking brake, automatic apply and release of parking brake by integrating sensors, Engine control unit and other electromechanical components have already developed and installed in on-road commercial vehicles. Off-highway and heavy mining equipment parking brakes have been designed for fail safe to ensure safety.

2 Problem Definition

Motor grader with a 12 ft blade is considered for this research work. Air is used for the main brake application. Mechanical ratchet pinion type parking brake was equipped to provide parking brake of the 16 Ton class grader. Existing parking brake system also meets performance and the standard operating force requirement as recommended by international standards. Introduction of new power shift transmission that is fitted with spring applied sliding caliper disc type parking brake for improved holding performance, demands for a hydraulic release of parking brake. The main service brakes are air-operated and hence hydraulic power is required for parking brake application resulting in a need of a new actuation system. A new concept of hydro pneumatic parking brake actuation system has been evolved and developed in line with ISO 3450 standard norms.

3 Design of Hydro Pneumatic Parking Brake Actuating System

Presently disc type spring applied hydraulically released parking brake in place of internally expandable shoe type parking brake is being designed for improved parking brake performance (Fig. 1).

To improve the holding performance and reduce operator fatigue on motor graders equipped with air-operated brake system, hydro pneumatic parking brake system has been introduced. The spring applied hydraulically released sliding caliber disc type is used for parking brake application. When the vehicle is in OFF condition, due to the spring force the parking brake will be applied automatically. When engine

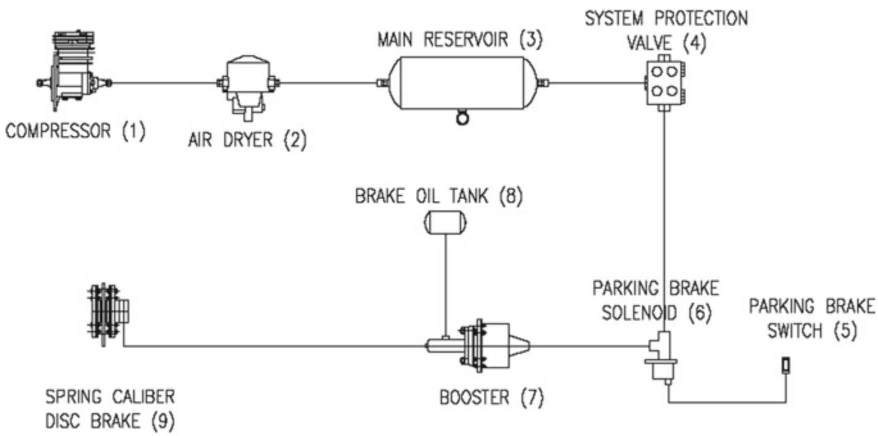

Fig. 1 Hydro pneumatic parking brake system for motor graders

starts, the compressor (1) builds the air pressure inside the system. The compressed air enters the parking brake solenoid valve (6) through air dryer (2), Main reservoir (3) and system protection valve (4). Booster (7) receives pressurized air supply from parking brake solenoid valve and boosts the hydraulic pressure required to release the parking brake at sliding caliber disc brake (9). When the parking brake switch (5) is operated inside the cabin, the parking brake solenoid valve is energized and cuts the air supply to the booster. Due to the lack of air pressure, spring force comes into action which leads to the application of parking brake. Further, the oil will return to the brake oil tank (8).

4 Development and Installation

Based on the gross vehicle weight and parking brake requirements as per international vehicle safety, calculations were made to select and evaluate disc type sliding caliber parking brake. Static and dynamic coefficients of friction assumed as 0.34 and 0.28 respectively. As the calculation concludes the pressure required to release the parking brake is 98 bar and Max. Permissible release pressure is 206 bar which is not possible to achieve by air-operated system alone. The booster is selected to meet the pressure limits and sliding velocity of the caliber to ensure smooth application and release of parking brake. Magnification factor achieved in the selected booster is 24.

Performance characteristics of the booster are critically investigated to confirm the adaptability for the present requirement. Brake oil tank is sized based on the oil flow and stroke length of the booster cylinder. Low-pressure switch is employed in the parking brake line to sense and send the signal to the transmission control unit. ON/OFF switch is provided inside the cabin to control the parking brake by operator (Fig. 2).

5 Performance Evaluation and Testing

Parking brake performance and evaluation have been done as per ISO 3450-standard norms [9]. Before carrying out the parking brake performance test, the overall brake system has been ensured for zero leak condition by soap water test. Also, the equipment is charged to its maximum working pressure and switch-off for 30 min. Then the pressure values are checked and ensured that the pressure drop is not beyond 0.5 bar. The stopping distance test has been measured to conform the normal working of the air brake system. As per the operating mass of the grader, 32 km/hr speed has been chosen for stopping distance tests. After application of the service brake, the stopping distance and time have been measured and confirmed that the results meet ISO 3450 standard requirement.

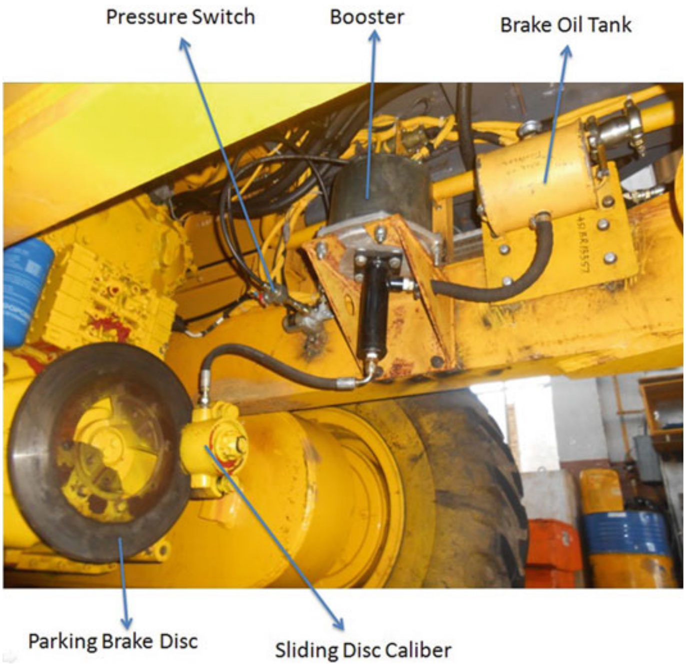

Fig. 2 Parking brake system aggregates mounting arrangement

5.1 Holding Performance Test

The parking brake has been tested with a 20% slope gradient to reflect the worst condition in mines and hills station. The holding performance of the parking brake is validated in 20% Gradient and also checked with 36% Gradient. Parking brake apply and release actuation time has been examined and compared with the standard values. Test results ensure the parking brake meets the standard requirements (Fig. 3).

5.2 Parking Brake Functional Run Test

Run test has been carried out to check the release characteristic of parking brake. Operational run test for continuous of 2 hours at actual working environment has been carried out. During trials, release and apply of parking brake have been examined by switching the parking brake ON/OFF using the switch provided inside the cabin to ensure the function. Further, it is also ensured that the parking brake is not engaged accidentally during operation since the air pressure in the system is above the low-pressure warning limit. Functional run test confirms the parking brake requirements as per ISO 3450 standard (Fig. 4).

Parking Brake Holding Test @ 20% Slope   Parking Brake Holding Test @ 36% Slope

Fig. 3 Parking brake holding test

6 Results and Discussions

Considering equipment mass, parking brake arrangement and grade holding requirements as per ISO 3450 standard, minimum hydraulic pressure required to release parking brake is around 98 bar. With the air to hydraulic booster magnification factor of 24 times, nearly half of the working pressure of air system is enough to release the parking brake, i.e. about 4.2 bar. Electro Pneumatic solenoid offers a quick release of parking brake as soon as the air pressure reaches the half of the normal working pressure (i.e. 8 bar).

Input air line to release the parking brake has been directly taken from the system protection valve port no. 23. The dynamic opening pressure of the system protection valve's port no. 23 is about 6.9 bar. Uninterrupted release of parking brake is ensured with the minimum of 6.9 bar pressure available in parking brake line continuously against the minimum required pressure of 4.2 bar to release the parking brake with said booster magnification. SAE 10 W oil is used in the booster hydraulic line to deliver the brake release pressure at parking brake end. Smooth apply and release of parking brake is achieved by practical test with Electro pneumatic solenoid and ON/OFF switch setup.

The holding performance test reveals the present parking brake system offers holding in even 36% slope against the requirement of 20% slope as per the ISO 3450 standard. Continuous 2 hours run test confirms there were no malfunctions in hydro pneumatic parking brake actuation system.

7 Conclusion

Most of the present-day motor graders are equipped with a hydraulically operated accumulator-assisted parking brake system. Hydraulically operated brake system contributes approximately 8–10% of excess heat load compared to air-operated brake

Fig. 4 Functional run test

system. The present motor grader equipment considered for these trials produces nearly 15 kw of heat load in excess when operated with hydraulic operated brake system. Hence an additional Cooling system needs to be introduced in hydraulic brake system due to its higher heat generation. The complexity of the system is high resulting in need of higher skills for maintenance and service.

Pneumatic or air-operated brake system offers ease of maintenance and low cost over hydraulic brake system due to its simplicity. In motor graders operated with air brake system, to achieve the pressure required to release the parking brake (about 98 bar) is not possible. To overcome this, air actuated & hydraulically released type parking brake system has been designed for 12 ft, 16 Ton class motor graders.

Major aggregates of the system were critically evaluated and selected to suit the present requirement. Air pressure from system protection valve is magnified by

24 times in the booster hydraulic line. With the combination of system protection valve and brake booster, hydraulic pressure of 98 bar is delivered continuously when the equipment is On and is under operation, to release the parking brake. Operator fatigue has been eliminated by using soft-touch ON/OFF switch inside the cabin which controls the apply and release of the parking brake through parking brake solenoid valve based on the operator input.

Prototype has been developed with full-scale model and various tests have been conducted in actual working conditions as per ISO 3450 standard. More than 75% increase in holding performance makes the motor grader best suits in Hill Stop parking brake holding. The 2 hours practical field run test revealed that new Hydro Pneumatic parking brake system reduces the operator fatigue, builds more confidence in operators and ensures safety at the higher order.

References

1. The Central Motor Vehicles Rules, India (1989)
2. Mckinlay AJ (2007) The phenomenon of vehicle park brake rollaway. Ph.D. Thesis-School of mechanical Engineering, University of Leeds, August
3. Mohd-Razmi I, Jamaludin-Mohd T, Abd-Rahim AB, Wan-Zaidi WO, Ali B (2018) Brake torque analysis of fully mechanical parking brake system: theoretical and experimental approach. IngenIería InvestIgacIón y tecnología 19(1): 37–49
4. Rozainia AH, Ishak MR, Abu Bakar AR, Mohd Zain MZ (2013) Performance of a fully mechanical parking brake system for passenger cars. In: 2nd international conference on mechanical engineering research, pp 1–10. IOP Publishing, Malaysia
5. Noble V, Frampton R, Richardson J (2014) Ergonomics of parking brake application: factors to fail. In: Proceedings of 2014 international conference on ergonomics and human factors: contemporary ergonomics and human factors, pp 481–488. Loughborough University, Great Britain
6. Thivagar S, Kumar CN (2016) Automatic hand brake system. Int J Eng Res Gen Sci 4(1):214–221
7. Maske A, Tuljapure SB, Satav PK (2016) Design & analysis of parking brake system of car. Int J Innov Res Sci, Eng Technol 5(7):12578–12590
8. Wang H, Li N, Gao F, Dai X (2014) Research on the hill-start control of vehicles based on the pneumatic auto parking brake system. International conference on mechatronics. Controls and electronic engineering. Atlantis Press, China, pp 42–49
9. ISO 3450—earth-moving machinery—braking systems of rubber-tyred machines—systems and performance requirements and test procedures
10. Scales W, McCulloch DM (2007) Best practices for compressed air systems, compressed air challenge

Design and Analysis of Feature Primitive Scaffold Manufactured Using 3D-Printer—Fused Deposition Modelling (FDM)

P. Vishnurajan, S. Karuppudaiyan, and D. KingslyJeba Singh

Abstract The scaffold guided tissue is a branch of tissue regenerative medicine approach. The scaffold acts as a temporary structure for bone growth and provides a better environment and architecture for the regeneration of bone. In this work, five different features were defined in parametric form using CATIA. The relationship between geometric parameters and porosity, surface area-to-volume ratio was developed with constant inter-pore distance. The developed relationship of scaffolds was evaluated by designing of 40% porosity. All these scaffolds were manufactured with biocompatible Poly Lactic Acid (PLA) material using Ultimaker^3–FDM system. The mechanical properties of a scaffold were evaluated by the compression test, and finite element analysis was performed using ANSYS software. The experimental and finite element analysis (FEA) results were compared to understand the microscale level modelling and variability of mechanical properties of scaffold manufacturing with 3D printing technology. In this study, we have obtained experimental effective elastic modulus (or) Young's modulus is 858.69 MPa and compressive strength (27.693 MPa) of a scaffold (P1), maximum porosity was (38.06%) for scaffold (T1). In FEA, the maximum effective Young's Modulus is 1086 MPa for scaffold (P1), maximum stress is 29.54 MPa for scaffold (C1) and maximum strain is 0.331 for scaffold (T1).

Keywords Scaffold · Additive manufacturing · 3D printer · Ultimaker^3–FDM

P. Vishnurajan · S. Karuppudaiyan (✉)
Department of Mechanical Engineering, SRM Institute of Science and Technology, Kattankulathur, Chennai, India
e-mail: karuppus@srmist.edu.in

P. Vishnurajan
e-mail: vishnurajan_p@srmuniv.edu.in

D. K. Singh
School of Mechanical Engineering, SRM Institute of Science and Technology, Kattankulathur, Chennai, India

E. T. Akinlabi et al. (eds.), *Trends in Mechanical and Biomedical Design*, Lecture Notes in Mechanical Engineering,
https://doi.org/10.1007/978-981-15-4488-0_48

1 Introduction

Bone is a natural heterogeneous structure; it has, in macroscale level, two-layer architecture as cortical and cancellous. When the bone experiences damage due to accident, disease and aging, it is a challenging task for orthopedic surgery to repair and restore its functions [1, 2]. In general, bone possesses a good healing capacity of defects under suitable physiological, environmental conditions. If the defects are a larger size, particularly in the load-bearing bone-like femur, vertebrae and tibia have a problem clinically to resolve.

Tissue engineering (TE) is a recent growing approach to repair of injured or fracture bone [3]. The success of bone tissue engineering depends on a scaffold, which acts as a template for cells to interactions and formation of bone to provide structural support to the newly formed tissue [4]. A desirable scaffold should provide preliminary mechanical support at the site of the defect until the new bone tissue is regenerated [5–7]. The scaffolds should have enough strength to resist load at the site of implantation also have high porosity and integrity to completion of the regenerative process. The minimum parameters of any scaffold are porosity, pore-interconnectivity and surface area-to-volume ratio and biocompatible material and manufacturing technology.

1.1 Additive Manufacturing (or) Rapid Prototyping Method

The additive manufacturing process is commonly known as 3D printing. It is mainly used to manufacturing low-volume parts with complex shapes also often to multiple functions. Additive manufacturing process successfully used for the fabrication of patient-specific implants and porous scaffolds with custom-tailored internal and external architectures [8–11]. The rapid prototyping techniques build apart directly from the CAD model using layer by layer approach.

The development of additive manufacturing techniques are widely used for tissue engineering applications. They are used mainly to make 3D porous scaffolds with custom-tailored of internal and external architecture. The following rapid prototyping systems are commercially available to fabricate scaffolds for tissue engineering application; they are SLS (Selective Laser Sintering), FDM (Fused deposition modelling), STL (Stereo lithography) Precision extrusion deposition, (SLM) Selective Laser Melting, Electron Beam Melting (EBM) and bio-plotter [12, 13]. The limitations this technology is accuracy, resolution, material used to control appropriate internal and external architecture of scaffold structure. However, recent technologies in rapid prototyping combined together with composite (HA-PCL/HA-TCP) biomaterials [14–17]. The rapid prototyping process yet to recognize as a standard to design and optimization of the architecture of scaffold till now, not even for manufacture specific target of tissue [18].

The objective of this work, to design the feature-based internal architecture of scaffold and manufacture using the 3D printer with PLA biocompatible material, mechanical characterization of PLA scaffold by both experimental and numerical methods.

2 Methods and Methodology

2.1 Design of Feature Primitive Scaffold

In general, scaffold design is difficult to reproduce a microstructure of exact internal bone in the scaffold. We created simplified models with functionally equivalent to mechanical properties that help tissue to repair apart from the biological requirement. The goal of the design is to produce a porous structure which effectively reduces the strength and stiffness of scaffold and provide sufficient space for regeneration of new bone tissue at the implanted site.

In this work, scaffold primitives are designed using CATIA software with the following features (Circle, Triangle, Square, Hexagonal, and Pentagonal) size varies from 0.4 to 1 mm with a constant inter-pore distance of 1.25 mm and dimension of 10 $\times$ 10 $\times$ 20 mm. The edge size/diameter is controlled parameters with desired porosity. The designer can interact with CATIA design table and select the appropriate feature and design scaffold. A typical scaffold library was designed with 40% porosity is shown in Fig. 1.

2.2 Design and Optimization of Geometric Parameters of Feature Primitive Scaffold

To understand the relationship between design geometric parameters with surface area-to-volume ratio (K) and porosity (P). In a circular feature, scaffold primitives are modelled with a diameter of 0.4–1 mm in steps of 0.1. The obtained parameters are listed in Table 1 (Fig. 2).

The design porosity for each model was calculated using Eq. (1)

$$\text{Porosity}(P) = \left(1 - \frac{V_s}{V_{\text{app}}}\right) \times 100 \tag{1}$$

where V_s—design volume of the porous scaffold, and

V_{app}—apparent volume of scaffold model.

The surface area-to-volume ratio ($K = \text{SA/Vs}$) is an essential parameter for tissue generation, cells attachment, and proliferation. The scaffold area is a primary site for the interaction of cells in the surrounded region of the implanted site. The cells

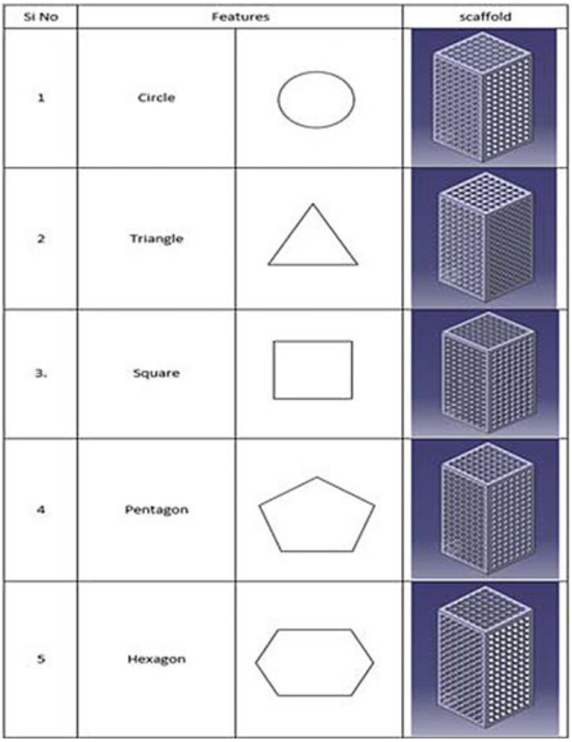

Fig. 1 Representative feature primitive scaffold of CAD model designed with 40% porosity

Table 1 Design parameters of the scaffold-circular feature

Pore diameter, (d) (mm)	Scaffold volume, (Vs) (mm^3)	Porosity, (P) (%)	Surface area, (SA) (mm^2)	K = (SA/Vs)
0.4	1679.5	16.0	3807.5	2.3
0.5	1525.2	23.7	4177.2	2.7
0.6	1353.7	32.3	4414.0	3.3
0.7	1171.2	41.4	4518.0	3.9
0.8	984.0	50.8	4489.0	4.6
0.9	798.3	60.1	4327.3	5.4
1	620.4	69.0	4032.6	6.5

used in tissue engineering are mostly anchorage-dependent, so the scaffold surfaces should have enough surface roughness to facilitate cell proliferation and attachment. The scaffold designing depends on the requirement of geometric of the damaged site. The surface area-to-volume ratio and porosity in the designed scaffolds are linearly variable with the pore size (Fig. 3).

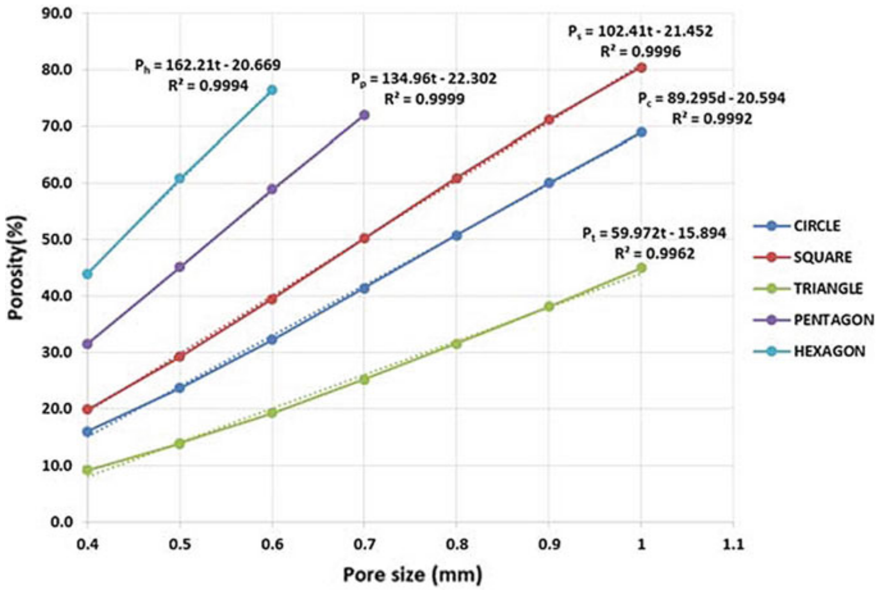

Fig. 2 Relationship between porosity and pore size

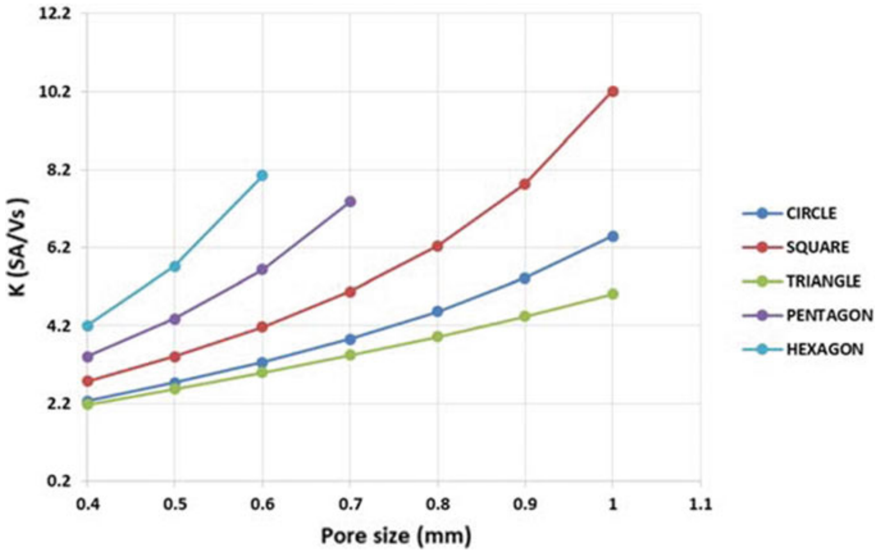

Fig. 3 Relationship between surface area-to-volume ratio and pore size

Table 2 Design parameter of five pore shape scaffold for porosity (*P*) with 40%

Scaffold type	Circular pore shape (C1)	Triangular pore shape (T1)	Square pore shape (S1)	Pentagonal pore shape (P1)	Hexagonal pore shape (H1)
Design parameter	d	t	t	t	t
Design parameter value (mm)	0.678	0.93	0.608	0.465	0.38

3 Additive Manufacturing of Porous Scaffold Using the 3D Printer

In the past three decades, 3D printer is potentially used for developing complex structures without tools in the area of engineering, biomedical, aerospace and automotive applications. In this work, scaffold was manufactured using 3D printerUltimaker^3. Ultimaker^3 is a user-friendly additive manufacturing machine based on the principle of fused filament fabrication, which is similar to the Fused Deposition Modelling process. This printer can print a 3D part with ABS (Acrylonitrile butadiene styrene), Nylon and PLA (Polylactic acid) materials. Ultimaker^3 produces the fastest build time for fabricating a model. Similar to all other rapid prototype systems, the scaffold model was converted into STL file using CATIA software. Then, the pre-processing was done with CURA software. STL file is used in the software to convert the model into the number of the slice for manufacturing; then the final file is sent to Ultimaker^3 to fabricate layer by layer process.

3.1 Modelling and Manufacturing of Scaffold

The linear relationship were evaluated to design scaffold with 40% of porosity. The model designed to have a lesser wall thickness, which cannot be printed in ultimaker^3, so the model was scaled into 2.5%, so the dimension changed to 25 $\times$ 25 $\times$ 50 mm. For manufacturing of scaffold, the layer height of 0.06 mm and no infill option was used to avoid the removal of support material. The calculated design parameters of the features are shown in Table 2, and manufactured scaffolds are shown in Fig. 4 (Table 3).

3.2 Porosity Calculation for Manufactured Scaffold

The porosity of all manufactured scaffold is calculated using Eq. (2) and listed in Table 4.

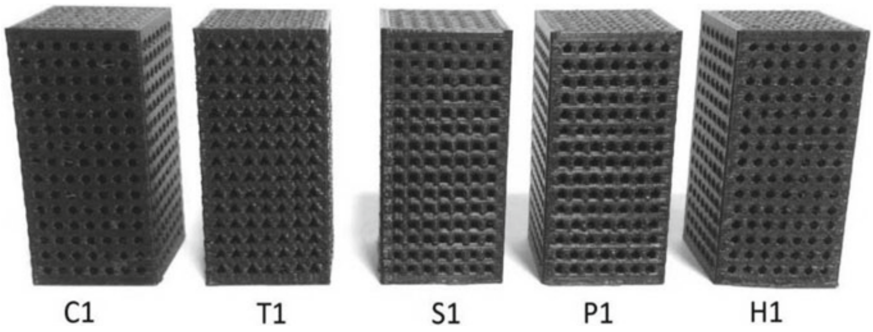

Fig. 4 Manufactured scaffold-3D printer

Table 3 Supplier's information for PLA material

Polymer	Modulus of elasticity	Poisson's ratio	Density
Polylactic acid	2745.68 MPa	0.36	1.24 g/cm^3

Table 4 Experimental porosity calculated from the manufactured scaffold model

Scaffold type	Volume of the scaffold (mm^3)	Mass of scaffold (g)	Scaffold porosity (%)	Designed porosity (%)	Porosity difference (%)
C1	32,164.72	25.32	36.51	40.5	9.83
T1	32,170.94	24.72	38.01	40.2	5.44
S1	32,176.06	25.12	37.03	40.4	8.31
P1	32,147.95	24.97	37.35	40.3	7.29
H1	32,317.37	25.43	36.54	40.6	9.99

$$\text{Porosity}(\%) = \left(1 - \frac{\rho_c}{\rho_m}\right) \times 100 \tag{2}$$

where ρ_c—Density of manufactured scaffold,

ρ_m—Density of bulk material of PLA (as per supplier data in Table 3).

The density of the manufactured scaffold is predicted by measuring mass and volume. The obtained results were listed in Table 4.

3.3 Mechanical Testing

The compression test was performed using TUE CN 200 machine for all the samples. The ultimate strength, load and displacement were plotted as shown in Fig. 5. The test was carried out on all the samples with 5 mm displacement approximately 10%

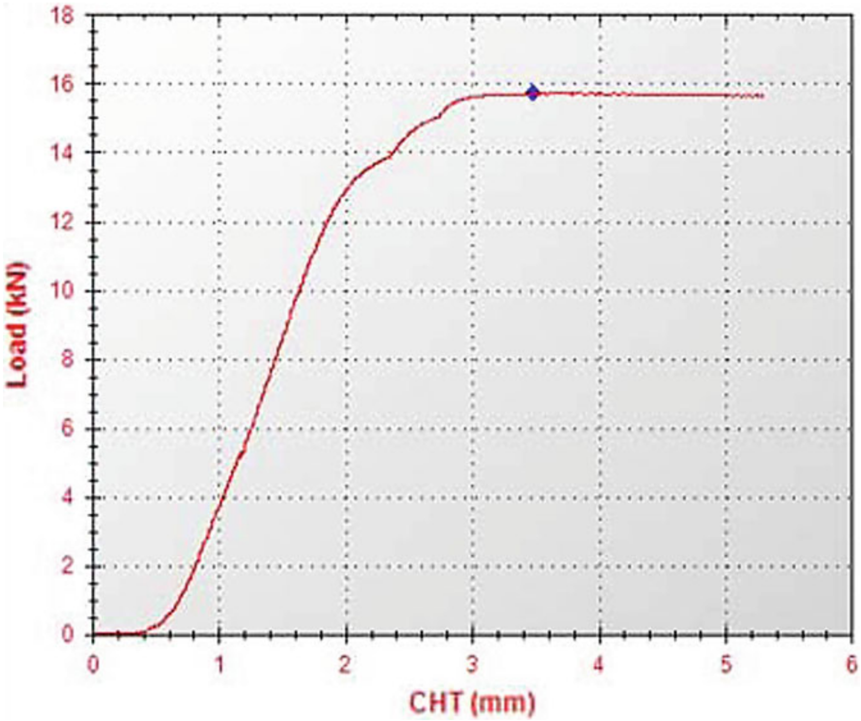

Fig. 5 The load–displacement curve for C1 Scaffold

of its length. The compressive strength, compression at peak, and effective Young's modulus of the scaffolds calculated. The stress and strain were calculated and plotted as shown in Fig. 6 (Table 5).

3.4 Finite Element Analysis of Scaffold

Finite element analysis was carried out to evaluate strength, stress and strain of scaffold with 40% porosity. This approach can decrease physical iteration numbers, which is used to optimize scaffold geometry with the best structural integrity and porosity. In this work, static structural analysis was performed using ANSYS. The mesh geometry was created in ANSYS. The tetrahedron mesh-type was used to create the mesh. As a representative scaffold (C1) type, nodes and elements are 10, 75,130 and 6, 14,889, respectively. A similar approach is followed for all other types of scaffolds. The boundary conditions are fixed support with zero degrees of freedom was applied on the lower end surface, on the top surface was allowed to displacement value obtained by experimentally as listed in Table 6 to use on the opposite top surface as shown in Fig. 7a. The material properties assigned to the model which is obtained

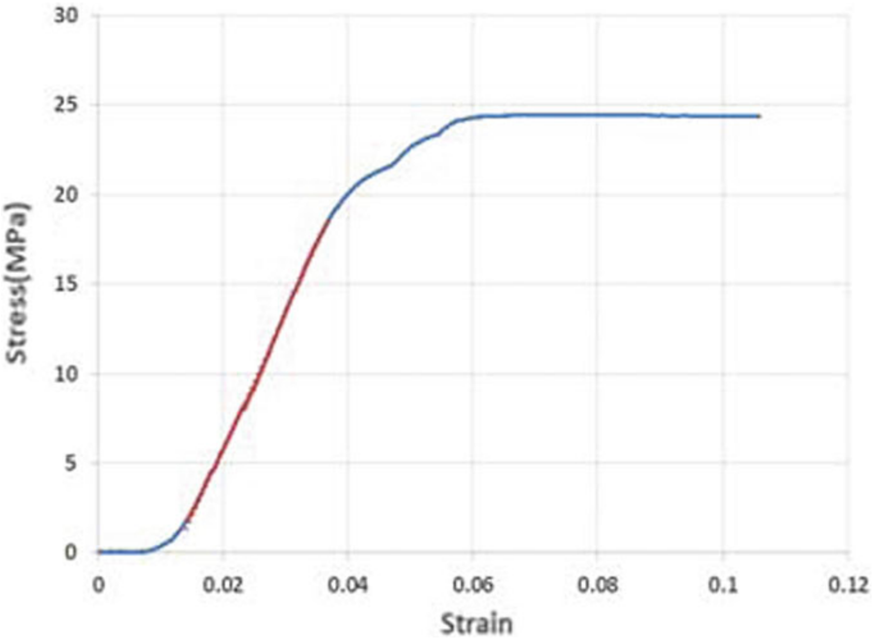

Fig. 6 Stress-strain curve for C1 scaffold

Table 5 Compression test results of five different types of scaffold and its effective Young's modulus

Scaffold type	Load at peak (KN)	Compression at peak (mm)	Compression strength (N/mm^2)	Effective Young's modulus (MPa)
C1	15.710	3.450	24.460	757.65
T1	14.260	4.910	22.226	639.88
S1	14.820	2.320	23.077	827.89
P1	17.790	4.320	27.693	858.69
H1	15.890	4.580	24.632	810.38

from the supplier as given in Table 5 and analysis was carried out and found the reaction force at the fixed face and stress–strain was obtained, and results are in given Table 6.

Table 6 Finite element analysis of five types of the scaffold with displacement value taken from compression test on the manufactured scaffold

Scaffold type	Displacement (mm)	Von misses stress (MPa)	Directional stress (z-axis) (MPa)	Strain	Reaction force (KN)	Effective Young's modulus (MPa)
C1	3.450	693.53	29.54	0.25327	36.542	847.74
T1	4.910	856.8	28.12	0.33056	47.581	775.3
S1	2.320	332.46	23.077	0.12109	28.563	984.9
P1	4.320	822.26	27.693	0.32515	58.645	1086.0
H1	4.580	677.25	24.632	0.24665	54.152	945.9

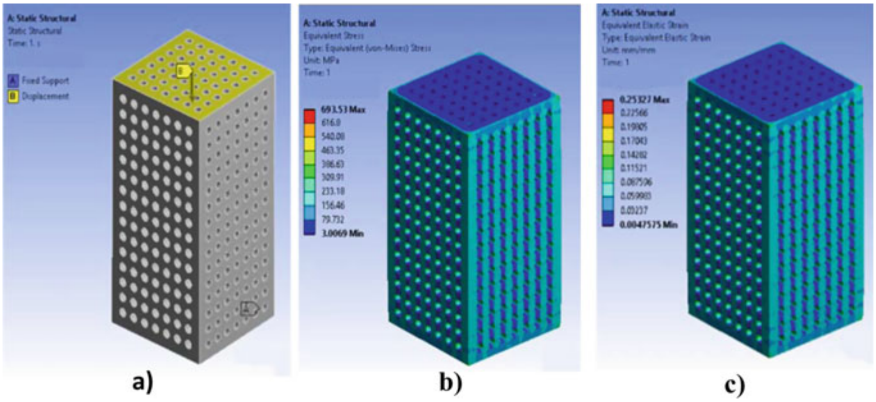

Fig. 7 **a** Pre-processing model. **b** Stress distribution. **c** Strain distribution

4 Results and Discussion

The results obtained experimentally and finite element analysis was listed in Tables 5 and 6. In this study, we compared results of maximum averages stress obtained by the compression test, which less than that of average stress obtained by finite element analysis. The scaffold type C1 and T1 has a difference in effective Young's modulus of 10.59% and 17.4%, and compressive is 17.19% and 20.96%, the porosity is 9.83% and 5.445%, respectively, which is lower than the design porosity. The reason for lower experimental results may be manufacturing artefacts such as interlayer's failure, material flow characteristics in the nozzle, and reduced printing resolutions at microscale level. It confirms that the theoretical porosity of scaffold lower than the designed porosity due to the filling of material inside the pores. The cross-sectional area of scaffold is higher than the designed area due to the inaccuracy of printer resolutions.

5 Conclusion

In this work, the scaffold library was created in CATIA consist of five different basic features. It needs to be developed with more combined features to obtain a heterogeneous structure. The developed library investigated porosity (P), Surface area-to-volume ratio (K) of the scaffold with constant inter-pore distance for tissue engineering applications. We conclude that to confirm the finding of in this study we need to do further experiments with large samples manufactured with system controlled parameters and finite element analysis by varying other parameters like a change of materials, printing nozzle with different combined features.

References

1. Duda GN, Heller M, Albinger J, Schulz O, Schneider E, Claes L (1998) Influence of muscle forces on femoral strain distribution. J Biomech 31(9):841–846
2. Edwards WB, Gillette JC, Thomas JM, Derrick TR (2008) Internal femoral forces and moments during running: implications for stress fracture development. Clin Biomech 23(10):1269–1278
3. Langer R, Vacanti J (1993) Tissue engineering. Science 260:920–926
4. Yeong WY, Chua CK, Leong KF, Chandrasekaran M (2004) Rapid prototyping in tissue engineering challenges and potential. TRENDS Biotechnol 22(12)
5. Hutmacher DW, Sittinger M, Risbud MV (2004) Scaffold-based tissue engineering: rationale for computer-aided design and solid free-form fabrication systems. TRENDS Biotechnol 22(7)
6. Sun W, Starly B, Nam J, Darling A (2005) Bio-CAD modeling and its applications in computer-aided tissue engineering. Comput-Aided Des 37:1097–1114
7. Habib FN, Nikzad M, Masood SH, Saifullah ABM (2016) Design and development of Scaffolds for tissue engineering using three-dimensional printing for bio-based applications. 3D Print Addit Manuf 3(2)
8. Lal P, Sun W (2004) Computer modeling approach for microsphere-packed bone scaffold. Comput Aided Des 36:487–497
9. Zhang XY, Fang G, Zhou J (2017) Additively manufactured scaffolds for bone tissue engineering and the prediction of their mechanical behavior: a review. Materials 10(50)
10. Starly B, Lau W, Bradbury T, Sun W (2005) Internal architecture design and freeform fabrication of tissue replacement structures. Comput-Aided Des 38:115–124
11. Chua CK, Leong KF, Cheah CM, Chua SW (2003) Development of a tissue engineering scaffold structure library for rapid prototyping. Part 2: parametric library and assembly program. Int J Adv Manuf Technol (21): 302–312
12. Zein I, Hutmacher DW, Tan KC, Teoh SH (2002) Fused deposition modeling of novel scaffold architectures for tissue engineering applications. Biomaterials 23:1169–1185
13. JyotiKalita Samar et al (2003) Development of controlled porosity polymer-ceramic composite scaffolds via fused deposition modeling. Mater Sci Eng, C 23:611–620
14. Lin CY, Kikuchi N, Hollister SJ (2004) A novel method for biomaterial scaffold internal architecture design to match bone elastic properties with desired porosity. J Biomech 37:623–636
15. Eshraghi S, Das S (2010) Mechanical and microstructural properties of polycaprolactone scaffolds with one-dimensional, two-dimensional, and three-dimensional orthogonally oriented porous architectures produced by selective laser sintering. J Acta Biomater 6:2467–2476
16. Cahill S, Lohfeld S, McHugh PE (2009) Finite element predictions compared to experimental results for the effective modulus of bone tissue engineering scaffolds fabricated by selective laser sintering. J Mater Sci Mater Med 20:1255–1262

17. Wettergreen MA, Bucklen BS, Starly B, Yuksel E, Sun W, Liebschner MAK (2005) Creation of a unit block library of architectures for use in assembled scaffold engineering. Comput-Aided Des 37:1141–1149
18. Giannitelli SM, Accoto D, Trombetta M, Rainer A (2014) Review on current trends in the design of scaffolds for computer-aided tissue engineering. J Acta Biomater 10:580–594

Design and Development of Modular Parallel XY Manipulator

Santosh R. Thorat and R. B. Patil

Abstract Flexure mechanism provides precise and repeated motion over a small range. Many monolithic designs have been discussed in the literature however they are costly to manufacture and give no flexibility for change in the parameter. This paper represents flexure micromotion stages with modular design. Compliance matrix method has been used for designing the flexure mechanism. Nonlinear 2-DOF model is used to characterize the stiffness of XY stage, maximum stress-induced. Proposed XY motion stage has a travel range of ± 3.2 mm^2 with 0.12 mm parasitic error. Dynamic analysis is performed to determine modal frequency of the stage. Maximum error estimated in analytical and FEA model is 26.38%. Linear and nonlinear analytical results are compared with FEA and are in agreement.

Keywords Compliant mechanism · Cross-coupling · Stiffness matrix · Nonlinear analytical modeling

1 Introduction

Compliant mechanism transmits motion by deformation of flexure elements. Mostly used flexure elements are blade flexure and wire flexure or slender rod [1]. Flexure elements are arranged in series or parallel. In series arrangement two or more 1-DOF are connected to obtain desired motion and motion can be controlled at the expense of high inertia, low natural frequency, and cumulative errors [2, 3]. Parallel mechanism has advantages of high payload capacity, lower inertia, and high natural frequency [4]. However, the parallel mechanism has disadvantages such as low workspace and parasitic error. Flexure parallel stage is used in many applications in precise machines and instruments. Compact XY Flexure parallel stage with a large motion range is desirable in many applications, atomic force microscopy, MEMS,

S. R. Thorat (✉) · R. B. Patil
Army Institute of Technology, 411015 Pune, India
e-mail: thorat.santosh83@gmail.com

R. B. Patil
e-mail: rbpatil@aitpune.edu.in

E. T. Akinlabi et al. (eds.), *Trends in Mechanical and Biomedical Design*,
Lecture Notes in Mechanical Engineering,
https://doi.org/10.1007/978-981-15-4488-0_49

biomedical implant and space application [3, 5, 6]. They are used in various applications because of no backlash, free of friction, no noise emission and no need for lubrication [4]. Designing the flexure mechanism has some challenges because of its nonlinear behavior, lack of motion range and cross-axis coupling [7]. Flexure parallel stages are mostly driven by piezoelectric or electromagnetic actuators. Stages driven by piezoelectric actuator has small motion range, high stiffness and compactness and those driven by electromagnetic actuator have large workspace, low stiffness, and ease to vibrate [2]. Compliance matrix method as reported in [1–4, 8–13] has been used for designing the micromotion stage.

In the literature, many parallel flexure mechanisms have been proposed and analyzed. Herpe et al. [14] presented a model used to characterize micromotion stage. Two-DOF nonlinear model is used to characterize force-displacement and stress analysis. Dynamic analysis is carried to find natural frequency of stage. The proposed mechanism has motion range of ±2.3 with parasitic error of 60 micron. Awtar [10] in his Ph.D. thesis presented analytical formulation including geometric nonlinearity for family of symmetric XY Flexure mechanism with a large workspace and small parasitic error. Pham et al. [9] address the stiffness models based on the way flexure elements are connected together. Awtar et al. [11] presented a nonlinear force-displacement model for 2-D beam flexure. Su et al. [15] presented a screw theory approach for synthesis and analysis of compliant joint. Li et al. [3] presented the idea of totally decoupling and analyzed double parallelogram flexure using matrix method for modeling compliance and stiffness. Wan et al. [12] presented a survey of recently developed flexure mechanisms with large motion range and greater accuracy. Su et al. [1] presented symbolic formulation for compliance and synthesis of mechanism with serial, parallel and hybrid topologies based on screw theory. Jia et al. [16] presented a parameterized compliance approach for synthesis and analysis of flexure. Xu et al. [2] proposed new multistage compound parallelogram flexure. The motion range of the mechanism is greater than 10 mm.

In this paper, modular design for a flexure parallel stage is presented. Many monolithic micromotion stages have been discussed in the literature. Monolithic design does not require assembly of component however when flexures are deformation beyond yield strength they get fractured. This, in turn, led to remanufacturing of whole mechanism due to its monolithic nature. Clearly, there is the motivation for design of modular micromotion stage. Modular design helps in manufacturing and assembly all the components separately. Modular design has an advantage that parameters of flexure element can be varied to some extent and fabrication can be done at relatively low cost. The flow of this paper is as follows. Section 2 determines stiffness of motion stage. Sections 3 and 4 consider nonlinear force-displacement and maximum stress analysis. Section 5 determines the resonant frequency of the stage. The coupling analysis of stage is carried out in Sect. 6. Section 7 compares the analytical solution with FEA and finally conclusions are drawn.

2 Stiffness of Mechanism

Let us consider a general twist $\underline{X} = (\delta_x,\ \delta_y,\ \delta_z,\ \theta_x,\ \theta_y,\ \theta_z)$ and general wrench $\underline{F} = (F_x,\ F_y,\ F_z,\ M_x,\ M_y,\ M_z)$ [8] with 6 DOF (degree of freedom) at reference point OXYZ. The parameters of a beam are shown in Fig. 1. The dimensions and configuration of the XY motion stage are shown in Fig. 2 and CAD model is shown in Fig. 3. Mechanism consist of four rigid blocks located at corners are fixed. There are four intermediate blocks (P, Q, R and S) where input force is applied and a motion stage (C) at the center.

All flexure elements are numbered 1–16 have the same dimension and are given in meter.

According to linear elastic theory, the relation between twist and wrench can be written as in

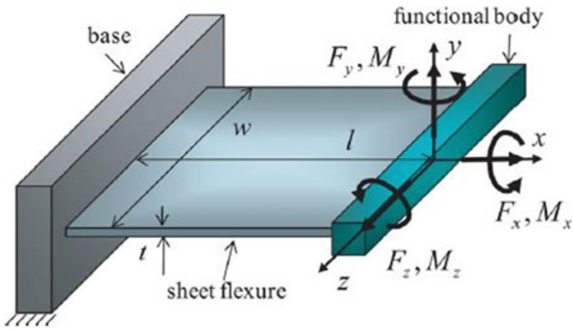

Fig. 1 Beam parameters [2]

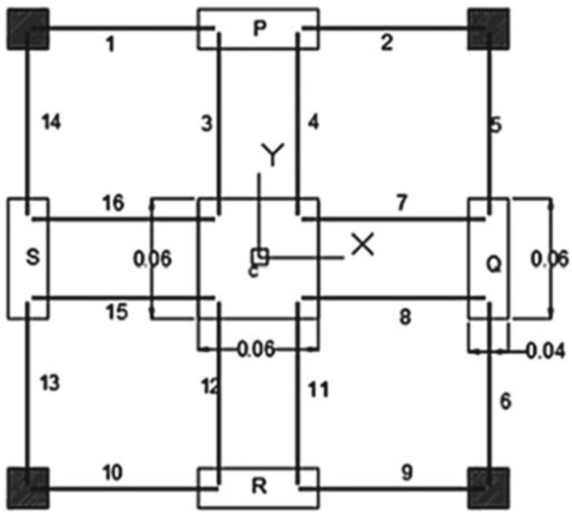

Fig. 2 Spring equivalent model [14]

Fig. 3 CAD model

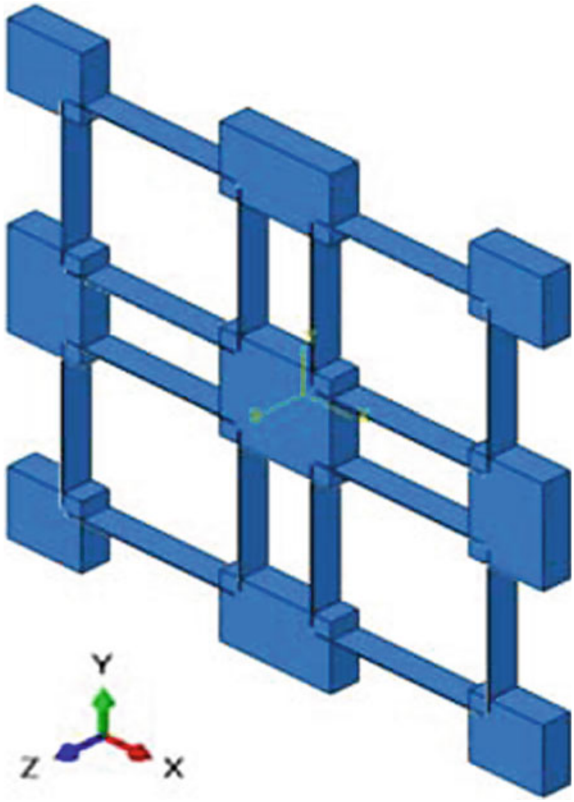

$$\underset{\sim}{F} = S_{\text{fix}} \cdot \underset{\sim}{X} \tag{1}$$

where S_{fix} is 6×6 stiffness matrix of fix-guided beam which is given as

$$\begin{pmatrix} F_x \\ F_y \\ F_z \\ M_x \\ M_y \\ M_z \end{pmatrix} = \begin{bmatrix} \frac{\mathrm{EA}}{L} & 0 & 0 & 0 & 0 & 0 \\ 0 & \frac{12\mathrm{EI}_z}{L^3} & 0 & 0 & 0 & \frac{6\mathrm{EI}_z}{L^2} \\ 0 & 0 & \frac{12\mathrm{EI}_y}{L^3} & 0 & -\frac{6EI_y}{L^2} & 0 \\ 0 & 0 & 0 & \frac{\mathrm{GJ}}{L} & 0 & 0 \\ 0 & 0 & -\frac{6\mathrm{EI}_y}{L^2} & 0 & \frac{4\mathrm{EI}_y}{L} & 0 \\ 0 & \frac{6\mathrm{EI}_z}{L^2} & 0 & 0 & 0 & \frac{4\mathrm{EI}_z}{L} \end{bmatrix} \begin{pmatrix} \delta_x \\ \delta_y \\ \delta_z \\ \theta_x \\ \theta_y \\ \theta_z \end{pmatrix} \tag{2}$$

where E and G is Young's modulus and shear modulus, respectively, $A = t \times \mathrm{w}$ is beam's cross-section area, L is length of beam, J is torsion constant and $I_z = \frac{w \times t^3}{12}$ and $I_y = \frac{t \times w^3}{12}$ are the area moments [1]. This matrix is at local frame which needs to be shifted to global frame by using the shifting law from screw theory and presented in [5, 6, 13, 14, 17, 18]. This is implemented by pre multiplying by inverse of (Tr) transpose and post multiplying by inverse of (Tr) to S_{fix} as follows.

$$S_i^j = (\text{Tr})_i^{j^{-T}} \cdot S_{\text{fix}} \cdot (\text{Tr})_i^{j^{-1}} \tag{3}$$

where 'i' is local reference of beam and 'j' is global reference at the center of motion stage. T is the transpose of matrix and $(\text{Tr})_i^j$ is 6×6 adjoint transformation matrix given as

$$(\text{Tr})_i^j = \begin{bmatrix} R_i^j & S\left(t_i^j\right) R_i^j \\ 0 & R_i^j \end{bmatrix} \tag{4}$$

Owing to symmetry stiffness of mechanism can be evaluated from the stiffness of one-quarter part of parallelogram, i.e. parallelogram 1–2–3–4. The stiffness of beam 1 at center C is given by S_1^c It can be obtained by translating along X by 0.03 and Y direction by $(L + 0.03)$ and zero in Z direction. Therefore, $t_1^C = |0.03, -(L + 0.03), 0|$.

$$S_1^c = (\text{Tr})_1^{c^{-T}} \cdot S_{\text{fix}} \cdot (\text{Tr})_1^{c^{-1}} \tag{5}$$

The stiffness of flexure 2 at center C is obtained by revolving flexure 1 about Y-axis by π radians with no translation as given below.

$$S_2^C = \text{Ry}(\pi)_2^{C^{-T}} \cdot S_1^C \cdot \text{Ry}(\pi)_2^{C^{-1}} \tag{6}$$

Similarly, stiffness of flexure 3 at point C can be obtained by revolving the flexure 1 by $-\pi/2$ rad about Z-axis and translating 0.02 in X direction 0.03 in Y direction and zero in Z direction. Hence $t_3^C = |0.02, -0.03, 0|$.

$$S_3^C = (\text{Tr})_3^{C^{-T}} \cdot S_{\text{fix}} \cdot (\text{Tr})_3^{C^{-1}} \tag{7}$$

Stiffness of flexure 4 is obtained by simply revolving flexure 3 by π radians about Y-axis.

$$S_4^C = \text{Ry}(\pi)_3^{C^{-T}} \cdot K_3^C \cdot \text{Ry}(\pi)_3^{C^{-1}} \tag{8}$$

The stiffness of the parallelogram 1–2–3–4 at center C is given as

$$S_{C1} = \frac{1}{\left(S_1^C + S_2^C\right)^{-1} + \left(S_3^C + S_4^C\right)^{-1}} \tag{9}$$

The stiffness of mechanism can be obtained by rotating the parallelogram P by $-\pi/2$ around the Z-axis as follows.

$$S = S_{C1} + S_{C2} + S_{C3} + S_{C4} \tag{10}$$

where $S_{C1},\ S_{C2},\ S_{C3},\ S_{C4}$ are stiffness of three-quarter of mechanism.

3 Nonlinear Modeling

Owing to large deformation, the length of beam flexure is not constant thus nonlinear analysis is considered. This nonlinearity is due to tension loading terms which cause the change in length of beam flexure. Each beam flexure is considered as spring connected to rigid body as shown in Fig. 2. Further it is assumed that parallelogram P and R can travel in only Y direction and parallelogram Q and S can travel only in X direction. Let us consider outer parallelogram i.e. beam 1–2, 5–6, 9–10, and 13–14 and inner parallelogram i.e. beam 3–4, 7–8, 11–12, and 15–16. From Fig. 2, the deformation at the intermediate stage is written as

$$\begin{cases} \delta_{\mathrm{Py}} = \delta_{1y} = \delta_{2y} \\ \delta_{\mathrm{Ry}} = \delta_{9y} = \delta_{10y} \\ \delta_{\mathrm{Qx}} = \delta_{5x} = \delta_{6x} \\ \delta_{\mathrm{Sx}} = \delta_{13x} = \delta_{14x} \end{cases} \tag{11}$$

The reaction forces at the intermediate stage are written as follows.

$$\begin{cases} F_{\mathrm{Py}} = F_{1y} + F_{2y} \\ F_{\mathrm{Ry}} = F_{9y} + F_{10y} \\ F_{\mathrm{Qx}} = F_{5x} + F_{6x} \\ F_{\mathrm{Sx}} = F_{13x} + F_{14x} \end{cases} \tag{12}$$

where F_{Py} represent reaction force at intermediate stage p in y direction, F_{1y} is reaction force in beam 1 and so on. As in [14] the total stiffness of parallelogram 1–2, 5–6, 9–10 and 13–14 can be derived by considering a single beam as shown in Fig. 3.

The downward bending force as given in on beam 1 is given by

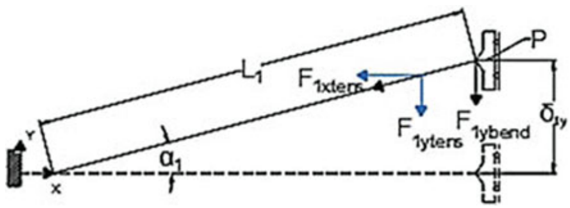

Fig. 4 Deformed condition of beam 1 [1]

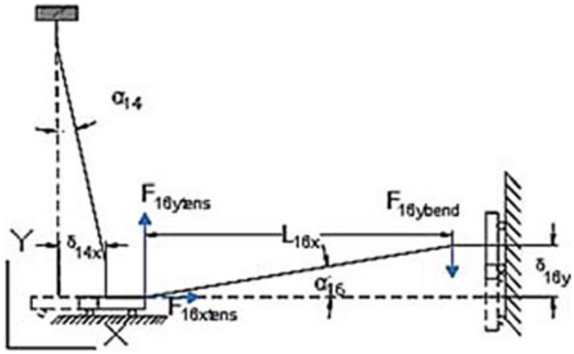

Fig. 5 Spring model of perpendicular elements

$$F_{1y\text{bend}} = \frac{12\mathrm{EI}_z \delta_{1y}}{L_1^3} \tag{13}$$

where δ_{1y} is a deflection of beam 1. The component of the tensile force in Y direction is given by

$$F_{1y\text{tens}} = \mathrm{EA} \in_1 \ \sin \ \propto_1 \tag{14}$$

where $\in_1 = (L_{\text{tens}} - L)/L$ is linear strain and $\propto_1 = \tan^{-1}(\delta_1/L)$ is the angle made by beam 1 with horizontal. Therefore, total force acting on beam 1 along the Y-axis is given by

$$F_{1y} = F_{1y\text{bend}} + F_{1y\text{tens}} \tag{15}$$

Now taking into consideration inner structure the stiffness can be obtained by considering one outer beam connected with single inner one as shown in Fig. 5. For small deflection of beam 16 there is a very small deflection of beam 14, therefore, stiffness of beam 14 is negligible as compared to stiffness of beam 16. The force acting along the X-axis on beam 16 can be obtained as

$$F_{16xT} = \frac{12\mathrm{EI}_z \delta_{14x}}{L_{14}^3} + \frac{\mathrm{EA} \cdot L_{14} \sin \ \alpha_{14}}{L_{14}} \tag{16}$$

The force acting along the Y-direction is, therefore, a combined effect of the forces applied by beams 14 and 16 as given.

$$F_{16y} = \frac{F_{16xT}\delta_{16y}}{L_{16x}} + \frac{12\mathrm{EI}_z \delta_{16y}}{L_{16}^3} \tag{17}$$

Therefore, the reaction forces at the center C motion stage due to δ_{Cx} and δ_{Cy} are

$$F_{\mathrm{Cx}} = F_{\mathrm{Qx}} + F_{\mathrm{Sx}} + F_{3x} + F_{4x} + F_{11x} + F_{12x} \tag{18}$$

$$F_{\mathrm{Cy}} = F_{\mathrm{Py}} + F_{\mathrm{Ry}} + F_{7y} + F_{8y} + F_{15y} + F_{16y} \tag{19}$$

The deflection at the intermediate stage is related to the deflection of the center of the motion stage. The following equation can be deducted by applying Pythagoras theorem to deformed and undeformed conditions between intermediate and motion stages.

$$\begin{cases} \delta_{\mathrm{Py}} = \delta_{Cy} - \left(L - \sqrt{L^2 - \delta_{\mathrm{Cx}}^2}\right) \\ \delta_{\mathrm{Ry}} = \delta_{Cy} + \left(L - \sqrt{L^2 - \delta_{\mathrm{Cx}}^2}\right) \\ \delta_{\mathrm{Qx}} = \delta_{Cx} - \left(L - \sqrt{L^2 - \delta_{\mathrm{Cy}}^2}\right) \\ \delta_{\mathrm{Sx}} = \delta_{Cx} + \left(L - \sqrt{L^2 - \delta_{\mathrm{Cy}}^2}\right) \end{cases} \tag{20}$$

4 Stress Analysis

Stresses in the XY mechanism are determined to know allowable displacement the stage can undergo within the elastic limit of the material. The maximum stress occurs at one of the corner of flexure beam where it is attached to rigid body. Maximum Bending stress in beam is given by $\sigma_{\max} = M_b Y/I$. Where Y is the farthest point from neutral axis (half of beam thickness) and $M_b = F_{\mathrm{1y\_tens}} \times 0.5 \times L$. From Eq. (13), maximum bending stress can be given by.

$$\sigma_{\mathrm{1bend}} = \frac{3\mathrm{Ew}\delta_{1y}}{L_1^2} \tag{21}$$

Also, stress induced due to tensile loading in beam 1 is given by

$$\sigma_{\mathrm{1tens}} = E \in_1 \tag{22}$$

From Eqs. (23) and (24) we can write maximum stress is

$$\sigma_1 = K_1 \sigma_{\mathrm{1bend}} + K_2 \sigma_{\mathrm{1tens}} \tag{23}$$

where K_1 is a stress concentration factor for bending loading and K_2 is the stress concentration factor for tensile loading.

5 Dynamic Analysis

Dynamic analysis helps in finding the resonance frequency of mechanism. The equation of motion for un-damped free vibration is given.

$$\mathrm{M}\,\ddot{\mathrm{x}} + \mathrm{S}\,\dot{\mathrm{x}} = 0 \tag{24}$$

where M is mass matrix and K is a stiffness matrix of mechanism. The mass matrix is given by

$$\begin{bmatrix} M_{\mathrm{xx}} & 0 & 0 & 0 & 0 & 0 \\ 0 & M_{\mathrm{yy}} & 0 & 0 & 0 & 0 \\ 0 & 0 & M_{\mathrm{zz}} & 0 & 0 & 0 \\ 0 & 0 & 0 & I_{\mathrm{xx}} & 0 & 0 \\ 0 & 0 & 0 & 0 & I_{\mathrm{yy}} & 0 \\ 0 & 0 & 0 & 0 & 0 & I_{\mathrm{zz}} \end{bmatrix} \tag{25}$$

where $M_{\mathrm{xx}},\ M_{\mathrm{yy}},$ and M_{zz} are moving mass in X, Y, and Z direction respectively $I_{\mathrm{xx}},\ I_{\mathrm{yy}}$ and I_{zz} are the moment of inertia about X, Y and Z direction, respectively.

$$M_{\mathrm{xx}} = M_{\mathrm{yy}} = m_0 + 2m_p + \left(8 \times \frac{33}{140} m_{\mathrm{beam}}\right) + (4 \times m_{\mathrm{beam}}) \tag{26}$$

where mass of motion stage $m_0 = 0.06^2 \times W \times \rho$, mass of parallelogram $m_p = 0.06 \times 0.02 \times \rho$, mass of beam $m_{\mathrm{beam}} = W \times t \times L \times \rho$

$$M_{\mathrm{zz}} = m_0 + \left(8 \times \frac{33}{140} m_{\mathrm{beam}}\right) \tag{27}$$

$$I_{\mathrm{xx}} = I_{\mathrm{yy}} = \frac{m_0\left(0.06^2 + w^2\right)}{12} + 2m_p\left(\frac{0.02^2 + w^2}{12} + (L + 0.03)^2 + \frac{0.06^2 + w^2}{12}\right) \tag{28}$$

$$I_{\mathrm{zz}} = 4m_p\left(\frac{0.06^2 + 0.02^2}{12}\right) + m_0\left(\frac{0.03^2 + 0.03^2}{12}\right) \tag{29}$$

The resonance frequency of stage can be determined by

$$f = \frac{1}{2\pi}\sqrt{\frac{S}{M}} \tag{30}$$

6 Coupling Analysis

The parasitic error in flexure mechanism is due deformation of intermediate stage *P* and *R* when input displacement is applied to intermediate stage *Q* and *S*. This error is also called cross-coupling. The parasitic error in the *X* direction can be determined by subtracting the resulting displacement δ_{Sx} of parallelogram *S* from desired output displacement δ_{Cx} as follows [14].

$$\delta_{x\_\mathrm{par}} = \delta_{\mathrm{Cx}} - \delta_{\mathrm{Sx}} \tag{31}$$

Similarly, the parasitic error in *Y* direction can be determined by subtracting resulting displacement δ_{Ry} of parallelogram R from desired output displacement δ_{Cy} as follows.

$$\delta_{y\_\mathrm{par}} = \delta_{\mathrm{Cy}} - \delta_{\mathrm{Ry}} \tag{32}$$

7 FEA Validation

The analytical model is validated using ABAQUS 6.14 software. The parameters of the beam and material properties are given in Table 1.

7.1 Force-Displacement Analysis

The force-displacement relation is studied by applying gradual displacement of 3.25 mm at one of the intermediate stage and reaction forces are noted. Nonlinear behavior is due to the load stiffening phenomenon at lager displacement. The force required for 3.25 mm displacement is 166.7 N analytically and 190.5 N from FEA. Thus the nonlinear analytical model is validated. Comparing the result of analytical model for linear (Eq. 10) and nonlinear (Eq. 21) behavior and FEA shows some linearity for small deflection and deviates for large displacement. These results are shown in Fig. 6.

Table 1 Parameters of beam

Parameters	t (m)	w (m)	L (m)	E (N/m^2)	G (N/m^2)	ρ (kg/m^3)
Values	0.0008	0.015	0.075	68.9e9	26.9e9	2810

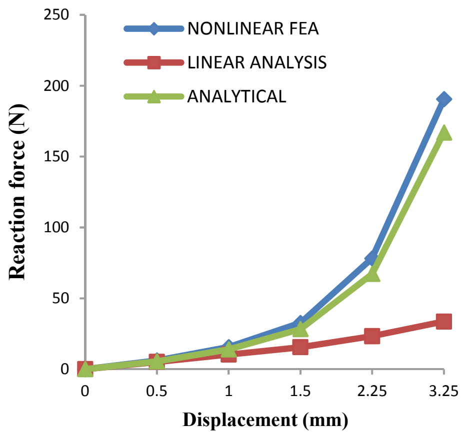

Fig. 6 Force-displacement plot

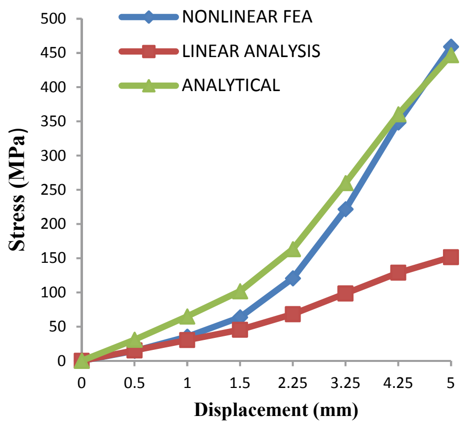

Fig. 7 Stress displacement plot

7.2 Stress Analysis

In order to study the stress variation in mechanism, the stress concentration factor $K1$ is taken as 1 and $K2$ is taken as 2 as in [14]. The maximum displacement evaluated from the analytical model is 4.3% smaller than FEA analysis. The error in the FEA and analytical model is 26.38%. Figure 7 show that yield strength of material has reached 5 mm displacement.

7.3 Coupling Analysis

Coupling analysis is carried to determine maximum positioning error in model. In FEA displacement is applied in Y direction at center of motion stage in steps and

Fig. 8 Parasitic error

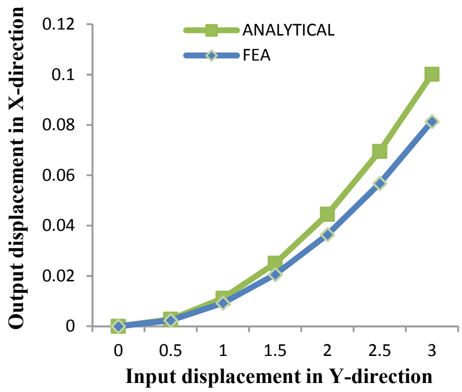

output displacement is recorded in at intermediate stage S in X direction. The parasitic displacement plot is shown in Fig. 8. Maximum parasitic error is 0.12 mm from FEA and error in analytical and FEA is 2%.

7.4 *Modal Analysis*

Frequency analysis is done in ABAQUS 6.14 using Lanczos Eigen solver. The first four mode shapes are shown in Fig. 9. The first two resonant frequencies in X and Y directions are the same and occur at 27.9 Hz form FEA and 26.7 Hz analytically. The

Fig. 9 Mode shapes of mechanism

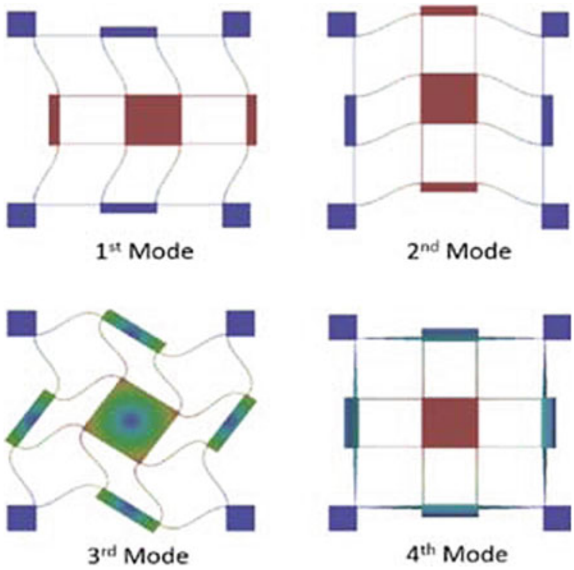

third resonant frequency occurs at 125.15 Hz from FEA and 134.4 Hz analytically. Fourth frequency from FEA is 261.8 and 285.2 Hz analytically. The error in analytical and FEA model is 9.24%.

8 Conclusion

An analytical model incorporating linear and nonlinear behavior was presented. MATLAB was used to characterize the compliant XY stage. Analytical model was successfully applied to predict stiffness, motion range considering the limitation such as maximum stress. The model proposed can predict the output displacement as input displacement is applied. Its micromotion stage is used for position control accurately. The results from FEA and analytical model are within 26.38%. The micromotion stage has a travel range of ±3.2 mm with cross-coupling of 0.12 mm. The yielding occurs at the displacement of 5 mm. The ratio between the first two frequencies and third is greater than 0.22. Modular design can be successfully applied to micromotion stage. Modular design will greatly reduce the manufacturing cost for the same characterization of a monolithic structure.

References

1. Su H, Shi H, Yu J (2012) A symbolic formulation for analytical compliance analysis and synthesis of flexure mechanisms. J Mech Des 134:1–9
2. Xu Q (2012) New flexure parallel-kinematic micropositioning system with large workspace. IEEE Trans Robot 28:478–491
3. Li Y, Xu Q (2009) Design and analysis of a totally decoupled flexure-based XY parallel micromanipulator. IEEE Trans Robot 25:645–647
4. Xiao S, Li Y, Zhao X (2011) Design and analysis of a novel flexure-based XY micro-positioning stage driven by electromagnetic actuators. In: Proceedings of 2011 international conference on fluid power and mechatronics, pp 953–958
5. Shang J, Tian Y, Li Z, Wang F, Cai K (2015) A novel voice coil motor-driven compliant micropositioning stage based on flexure mechanism. Rev Sci Instrum 86:1–10
6. Li Y, Xu Q (2010) Development and assessment of a novel decoupled XY parallel micropositioning platform. IEEE Trans Mechatronics 15:125–135
7. Howell LL, Magleby SP, Olsen BM (2013) Handbook of compliant Mechanism. Compliant mechanism. 1st edn. Wiley Publication, New Delhi
8. Yu J, Li S, Su HJ, Culpepper ML (2011) Screw theory based methodology for the deterministic type synthesis of flexure mechanisms. J Mech Robot 3: 1–14
9. Pham HH, Chen IM (2005) Stiffness modeling of flexure parallel mechanism. Precis Eng 29:467–478
10. Awtar S (2004) Synthesis and analysis of parallel kinematic XY flexure mechanisms. Ph.D. Thesis, Massachusetts Institute of Technology
11. Awtar S, Sen S (2010) A generalized constraint model for two-dimensional beam flexures: nonlinear load-displacement formulation. J Mech Des 132:1–11
12. Wan S, Xu Q (2014) A survey on recent development of large-stroke compliant micropositioning stage. Int J Robot Autom 1:19–35

13. Zhang Y, Su H, Liao Q (2014) Mobility criteria of compliant mechanisms based on decomposition compliance matrices. Mech Mach Theory 79:80–93
14. Herpe X, Walker R, Dunnigan M, Kong X (2018) On a simplified nonlinear analytical model for the characterization and design optimization of a compliant XY micromotion stage. Robot Computer-Integrated Manuf 49:66–76
15. Su HJ, Dorozhkin DV, Vance JM (2009) A screw theory approach for the conceptual design of flexible joints for compliant mechanisms. J Mech Robot 1:1–8
16. Jia M, Jia RP, Yu JJ (2015) A compliance-based parameterization approach for type synthesis of flexure mechanisms. J Mech Robot 7:1–12
17. Lobontiu N (2014) Compliance-based matrix method for modeling the quasi-static response of planar serial flexure-hinge mechanisms. Precis Engg 38:639–650
18. Tang H, Li Y (2013) Design, analysis, and test of a novel 2-DOF nanopositioning system driven by dual mode. IEEE Trans Robot 29:650–662
19. Yu J, Li Z, Lu D, Zong G, Hao G (2014) Design and analysis of new large-range XY compliant parallel micromanipulators. In: Proceedings of the ASME 2014 International Design Engineering Technical Conferences & Computers and Information in Engineering Conference, pp 1–10

Design of hyper-redundant In-Vivo Robot: A Review

Sushil Dev Rout, Mihir Kumar Sutar, and Sarojrani Pattnaik

Abstract Conventional clinical process involves a large incision in the stomach to perform the surgery or biopsy to collect the infected tissue from the abdominal cavity. However, the process requires expertise and often leads to a surgeon's tremor and patient's discomfort. The inclusion of a robot to assist in biopsy and surgery is a boon for both surgeon and patient as it reduces the surgeon's error in pinpointing the infected area and also results in a minimum incision requirement to do so, which is called as Minimally Invasive Surgery (MIS). In some cases, the entire robot is placed inside to do the task and called an in vivo robot. The current study focuses on the various design strategies adopted by researchers around the globe and the outcomes. This state of the art will be useful to enhance the design strategies further to refine the most cutting-edge research outcomes further.

Keywords Minimally invasive surgery · In vivo robot · Biopsy · Design of surgical robot

1 Introduction

Conventional biopsy and surgical procedure bring tremendous pain and consume lots of time. Moreover, expensive medical bill adds trauma to the patient. Inclusion of robot to assist in surgery and biopsy was remarkable progress in the medical field. However, robotic-assisted surgery has some challenges with its advantages. The constraints present in designing and controlling the robot includes the trocar complicacy in case of minimally invasive surgery through a small opening port in the stomach, dimensions available in the natural opening such as the esophagus, constricted degrees of freedom (dof) for the complete insertion of robot in case of in vivo robot-assisted surgery or biopsy. Robot-assisted surgery for stomach biopsy and surgery is categorized into two types one is laparoscopy, which is a minimally

S. D. Rout · M. K. Sutar (✉) · S. Pattnaik
Mechanical Engineering Department, Veer Surendra Sai University of Technology, Burla, Odisha, India
e-mail: mihirsutar05@gmail.com

E. T. Akinlabi et al. (eds.), *Trends in Mechanical and Biomedical Design*,
Lecture Notes in Mechanical Engineering,
https://doi.org/10.1007/978-981-15-4488-0_50

invasive surgery (MIS), and in this case, the robot is kept outside during the clinical procedure. The second one is one in which the entire robot is placed inside the stomach through natural openings such as the esophagus, and this type of robot is called in vivo robot. The issues of concerns in designing and controlling such type of robots are lost dof at the insertion position of trocar incision, surgeon's expertise in performing the clinical task, complicated forward and inverse kinematic trajectories which lead to an unsuccessful attempt to reach at the specified goal point by the robotic tip, absence of a proper and better control strategy to control the tip from damaging any healthy tissue during the clinical procedure.

This study briefs about various design principles adopted by researchers to impart an optimum solution to the described constraints. The state of the art consists of different strategies that have been adopted by researchers to impart an efficient design for smooth clinical procedures and constraints involved in them.

2 Methodology

Design of a surgical robot decides the effectiveness of the instrument for performing the clinical tasks such as collecting biopsy samples from the infected area, performing surgical tasks with ease because of its simplicity in design and with available dofs. Dexterity is one of the most important parameters that set the design implacability. Proper dexterity allows the robotic tip to attain any point in the abdominal cavity with easiness. Minor and Mukherjee [1] proposed a dexterous manipulator design for the MIS. The end effecter was provided with bi-directional 180° articulation and rotation was provided by a compact multilink structure comprised of gears and gear-link as shown in Fig. 1. A 2-dof robotic manipulator shown in Fig. 2 was proposed by Yamashita and Kim [2] for performing endoscopy and tissue sampling tasks. The robotic forceps were designed and fabricated for holding, suturing the affected tissues in the liver abdomen. The two-way bending mechanism suggested in the design attained a workspace $\pm 80^{\circ}$ for each bending mechanism.

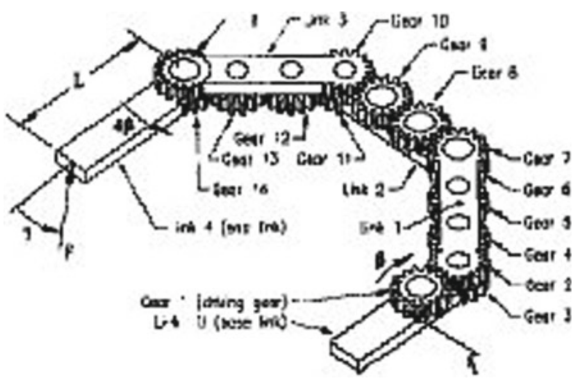

Fig. 1 Robot structure [1]

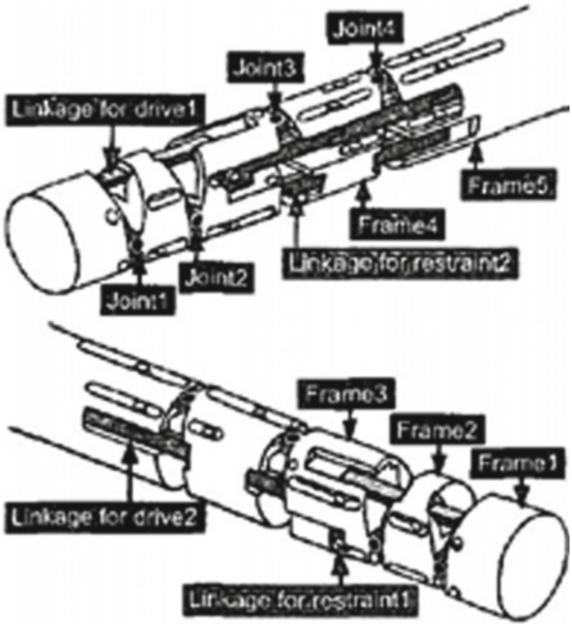

Fig. 2 A schematic of 2-dof robotic manipulator design [2]

Peirs et al. [3] proposed a self-propelling endoscope for inspection of the human colon. The robotic manipulator has 2 dof as it can tilt and bend both sides by 40°. The body of the robot consists of two modules separated by a pneumatic expansion system and actuated by an electromagnetic motor. The front module consists of the inspection tool, illumination, camera and channel for air and water injection. The rear module is of larger size and is hermetically sealed with the front one. The advantage of this type of design is that it allows to propel the whole system with proper control on the bellows and it can be steered around as and when required. However, the design has an issue that the bellow wall may get damaged because of the channels in it and it may endanger the patient's condition. The design and all the components in it are illustrated in Fig. 3.

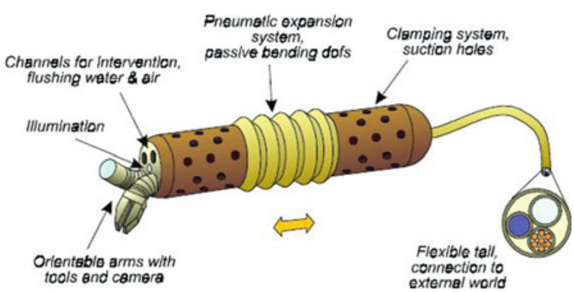

Fig. 3 CAD model of the self-propelling robotic endoscope [3]

Lehman et al. [4] developed a robotic platform for Natural Orifice Transluminal Endoscopic Surgery (NOTES) and tested its laparoscopic capabilities and control. The retraction and position of the robotic manipulator with disconnected linkage are shown in Fig. 4a–b, respectively. The design basically consists of a grasper and cautery arms connected to a central module having the camera unit. The two arms have individual rotational and translational dof coupled with the left and right yaw of the central body.

The designed robot was able to apply up to 10 N of force axially and 5 N of force transversely. However, the design reported unstable image quality and complicacy during simultaneous clinical procedures.

Lehman et al. [5] performed the design and control of a fixed-based in vivo robot for abdominal exploration to perform the necessary clinical tasks. The arrangement of the robotic platform along with its accessories is shown in Fig. 5. The robot had

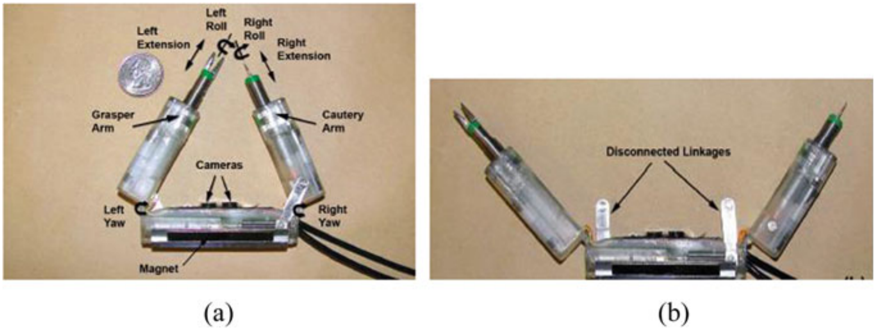

Fig. 4 The NOTES robot on both articulation **a** retraction and, **b** position [4]

Fig. 5 Pan and tilt fixed focus camera robot [5]

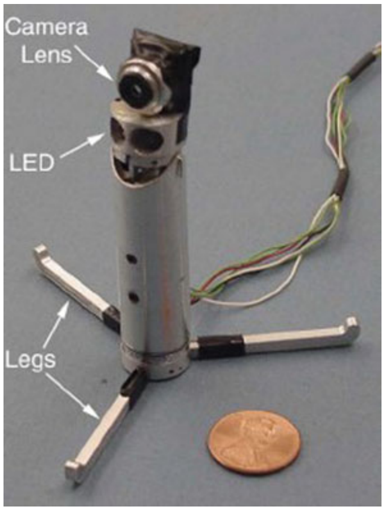

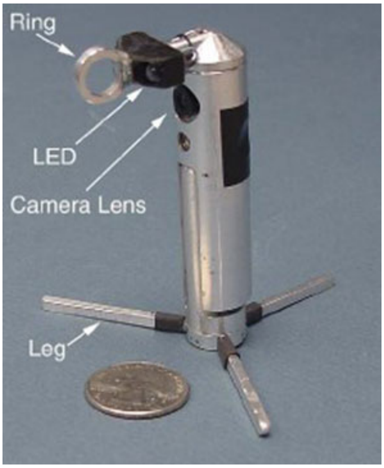

Fig. 6 Pan and tilt adjustable focus camera robot [6]

a limitation of focusing on the intricated portions inside the abdominal cavity at a different depth, leading to poor viewing feedbacks. This led to a variable focus camera robot by Rentschler et al. [6] shown in Fig. 6.

Further, the designed was enhanced to develop a wheeled mobile robot with an ability to advance inside the abdominal organs [6]. The wheel design was finalized after several tests and later improvised through visco-elastic modelling. The design is shown in Fig. 7.

Xu and Simaan [7] proposed a multi-backbone snake-like robot with increased dexterity. The system has two sections along with a detachable gripper as shown in Fig. 8. It has 1° accuracy in path tracking.

Garg et al. [8] presented a design of a 4-dof hyper-redundant robotic manipulator for stomach biopsy. Hyper-redundancy increases the dexterity for reaching the target points inside the abdominal cavity. The in vivo robot has 4 dof apart from the available 4 dof of the conventional endoscope in which it is connected. The CAD model of the design proposed is shown in Fig. 9.

Workspace analysis was also performed for the four-scaled design and it was observed that a total of 0.00418 m^3 of workspace is covered with the proposed design whereas the total workspace for a four-scaled stomach model is 0.00376 m^3. So, the proposed design can easily reach all the parts of the stomach for biopsy even up to

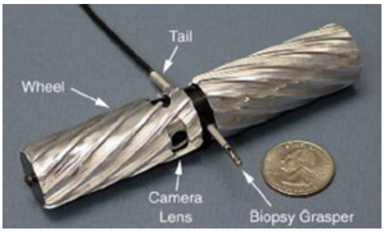

Fig. 7 Mobile camera and biopsy robot with helical screw design [6]

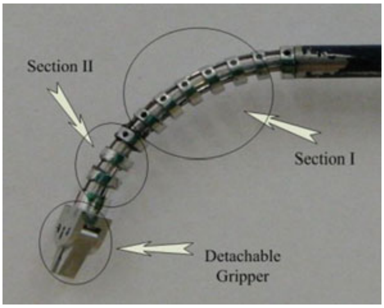

Fig. 8 Snake-like robot with detachable gripper

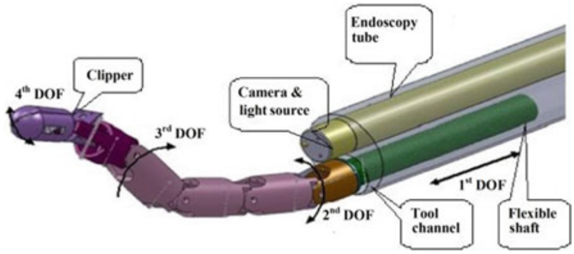

Fig. 9 CAD model of the 4-dof hyper-redundant manipulator with tool channel [7]

the duodenum. The torque required for actuating the joints were also measured to be 0.625mN-m. The manipulator is wire actuated. The relation between the length of wire to be pulled to the angle of rotation of each joint in Cartesian space is calculated in the analysis and also the biopsy force involved for collecting the tissue has been calculated by modelling a four-scaled size of the actual robot. The articulated links are interconnected. The first link is connected to the coupler and the last is connected to the gripper. The coupler consists of 150^0 of conical slots on either side to facilitate the titanium wire for better actuation. Total 360° grooves are avoided as it may lead to wire entanglement. The slots are shown in Fig. 10.

Further capsule endoscopy gained momentum over a decade and various work advancement is noticed in this segment as well. The capsule endoscopy is only

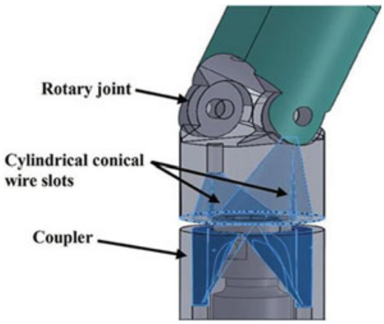

Fig. 10 Rotary joint with wire guide for actuation [8]

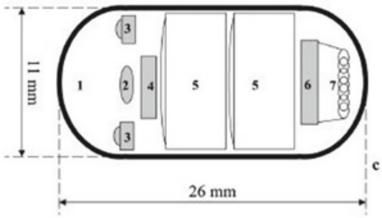

Fig. 11 M2A capsule **a** the actual model, **b** cross-sectional details [9]

meant to gather clinical information about the tissue health inside the abdominal and colon. Glukhovsky [9] developed a capsule endoscope that can steer inside the gastrointestinal tract to collect the information about the infected tissue inside. The collected information subsequently is utilized in curing diseases like cancer, polyps and other medical concerns. The integrated battery inside the capsule gives a back-up for around 8 h. The advantage of this design is its low-cost effectiveness and battery back with a pin point detection of data regarding infectious tissues. The flaw-side of the design is that the instrument is meant for only one-time use. The design of the capsule endoscope is shown in Fig. 11. The capsule is called a M2A capsule. Liu and Gao [10] reported the design and fabrication of magnetic energy propelled capsule endoscope to collect pictorial information of the GI tract. This information collected is further utilized for the clinical diagnosis of the patient. The capsule contains four modules namely transmission, illumination, vision and control. All the modules are assembled and kept inside a shell with optical dome. A ball screw arrangement is made which converts the rotary motion of the motor into linear motion. And the position of the capsule inside the patient is controlled by the interaction of permanent magnet assembly and magnet present inside it. The arrangement is illustrated in Fig. 12.

Simi and Valdastri [11] proposed hybrid locomotion for wireless-capsule endoscope which generates 3.8 N at the tip of the legged mechanism and a magnetic link force up to 135 mN.

Miyashita et al. [12] presented an ingestible origami robotic capsule that can be used to perform all such clinical tasks that are required to get medical data about the infection and also to patch the same after pin point location. The robotic capsule is reconfigurable to match the space requirement and wrapped around with a bio-compatible cover. Inside the cover, it consists of a miniature robot and the deliverer to enable the robot to reach the pin point location (Fig. 13).

3 Conclusions

Still better designs yet to come with an ability to perform flaw-less medical tasks assigned to them. Cost-effective, more agile, and dexterous miniature robots are need

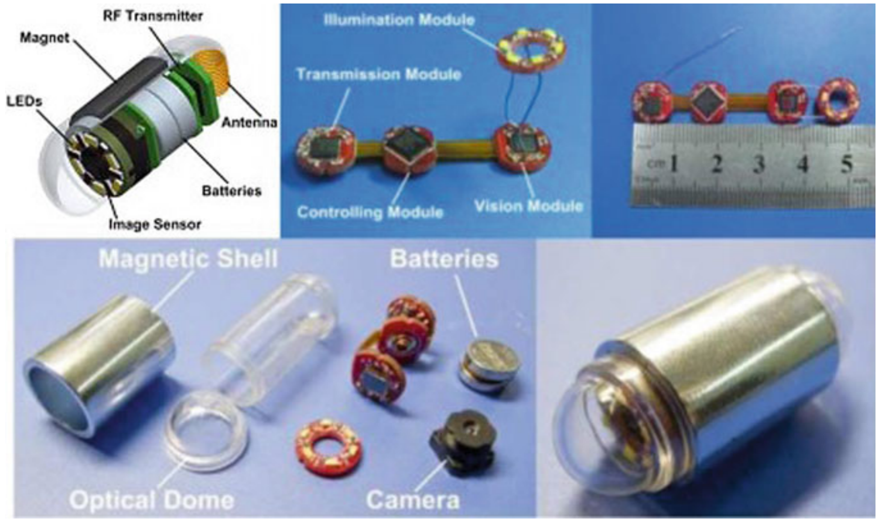

Fig. 12 Different parts of the magnetic propelled endoscopic system [10]

Fig. 13 Ice capsule with the deliverer [12]

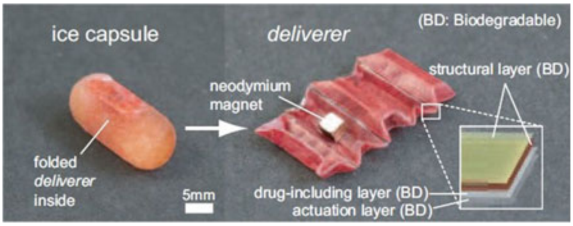

of the hour for better medical assistance to the surgeon performing clinical diagnosis, biopsy and surgery. Followings were observed in the brief literature review of the design and analysis of surgical robot:

- The design of surgical robot mainly the in vivo robot has several constraints that have to be addressed during the process, e.g. the maximum possible tool channel diameter of available videoscope is 6 mm under Indian condition.
- Simpler and effective designs are need of the hour for improvised dexterity.
- Some of the proposed designs may have limitations, e.g. the self-propelling endoscope [3] has a tilting angle limited to 40°. However, these designs are the foundation to proceed further for new and effective designs.
- The capsule endoscopes are only meant for capturing data inside the abdominal cavity. They are unable to perform any clinical tasks inside.

Acknowledgements The authors are grateful to the Department of Mechanical Engineering, VSSUT Burla for rendering all necessary co-operation to carry out our research work.

References

1. Minor M, Mukherjee R (1999) A dexterous manipulator for minimally invasive surgery. In: Proceedings of the IEEE international conference on robotics and automation, pp 2057–2064
2. Yamashita H, Kim D, Hata N, Dohi T (2003) Multi-slider linkage mechanism for endoscopic forceps manipulator. In: Proceedings of the IEEE/RSJ international conference on intelligent robots and systems, pp 2577–2582
3. Peirs J, Reynaerts D, Van Brussel HA (2001) Miniature manipulator for integration in a self-propelling endoscope. Sens Actuators 92:343–349
4. Lehman AC, Wood Nathan A, Dumpert J, Oleynikov D, Farritor Shane M (2008) Dexterous miniature in vivo robot for notes. In: Proceedings of the 2nd biennial IEEE/RAS-EMBS international conference on biomedical robotics and biomechatronics, USA, pp 244–249
5. Lehman AC, Rentschler ME, Farritor SM, Oleynikov D (2007) The current state of miniature in vivo laparoscopic robotics. J Robot Surg 1:45–49
6. Rentschler ME, Platt SR, Dumpert J, Farritor SM, Oleynikov D (2006) In vivo laparoscopic robotics. Int J Surg 4(3):167–171
7. Xu K, Simaan N (2006) Actuation compensation for flexible surgical snake-like robots with redundant remote actuation. In: Proceedings of the IEEE international conference on robotics and automation, Florida, pp 4148–4154
8. Garg A, Vikram CS, Gupta S, Sutar MK, Pathak PM, Sharma AK, Mehta NK, Gupta VK (2014) Design and development of in-vivo robot for Biopsy. J Mech Based Des Struct Mach 42:278–295
9. Glukhovsky A (2003) Wireless capsule endoscopy. Sens Rev 23:128–133
10. Gao M, Liu S (2010) Design and fabrication of a magnetic propulsion system for self-propelled capsule endoscope. IEEE Trans Biomed Eng 57:2891–2902
11. Simi M, Valdastri P (2010) Design, fabrication, and testing of a capsule with hybrid locomotion for gastrointestinal tract exploration. IEEE/ASME Trans Mechatron 15:170–180
12. Miyashita S, Guitron S, Yoshida K et al (2016) Ingestible, controllable, and degradable origami robot for patching stomach wounds. In: IEEE international conference on robotics and automation (ICRA), 16–21 May 2016, Stockholm, Sweden, pp 909–916

Effect of Insertion Force for Successful Penetration of a Conical Shaped Microneedle into the Skin

Gera Aswani Kumar, Burra Rajesh Kumar, Vankara Jyothi, and Sowmya Injeti

Abstract Microneedles and microneedle-related technologies are the present trends in medical science which are voraciously being investigated by the research community towards various therapeutic and medical diagnostic applications, since they are treated and also to be considered as painless methodology of administering vaccines. Apart from that these microneedles clearly aids in mitigating the potential risk of infections and ailments related when needle transfusions when the medicine is transmitted into the body. Microneedles have gained much upfront and considered to be a novel way for administering drugs and vaccines through transdermal drug delivery. This particular area primarily mends upon the design and analysis of silicon and stainless steel based hollow conical microneedles for transdermal drug delivery (TDD). The effect of axial and transverse load on a microneedle has been investigated along with the mechanical properties. The analysis predicts that the resultant stresses due to applied bending and axial loads are in the safe & comfort desired range. The primary work was focused on the conical-shaped hollow needles of micron-sized dimensions. In this paper simulation studies are carried out on the stress analysis along with displacement parameters.

Keywords Drug delivery · Microneedle · Skin · Insertion force · Stress

1 Introduction

Microneedles are usually being fabricated with various kinds of materials, such as metal, silicon and polymeric [1], are micron-sized needles that can easily pierce into the human skin. They are fabricated as either solid (Hashmi et al. 1995) or hollow needles [2] and have recently been applied in the biomedical field for such applications as the blood glucose measurement, transdermal delivery [2–5], skin therapy and so on. Although microneedles may not totally replace the traditional

G. Aswani Kumar (✉) · B. Rajesh Kumar · V. Jyothi · S. Injeti
GITAM Institute of Technology, GITAM (Deemed to Be University), Visakhapatnam Rushikonda, 530045, India
e-mail: akmrgera22@gmail.com

E. T. Akinlabi et al. (eds.), *Trends in Mechanical and Biomedical Design*, Lecture Notes in Mechanical Engineering,
https://doi.org/10.1007/978-981-15-4488-0_51

needles, they do possess some capabilities that the traditional needles do not and show a great advantage in the biomedical field.

Most of the recent studies of microneedles have focused on their fabrication methods and drug delivery capabilities. In the year 1998, researchers created microneedles based on the fundamental principles of needle injection which is the conventional injection towards transdermal drug delivery. Researchers demonstrated that biodegradable polymer microneedles possess the mechanical robustness and sharpness to penetrate into human skin. In the last years of the nineteenth century, research community created hollow metal microneedles for localized drug delivery. In early 2000, the usage of a single glass microneedle to pierce into the skin of diabetic hairless rats through invasive technique to deliver insulin was investigated. Sivamani et al. [6] tested hollow microneedles [6] by surmounting them onto a conventional hypodermic needle syringe for the delivery of methyl nicotinate on human participants which yielded them good results. Further extension of the microneedle design and fabrication towards drug delivery was demonstrated by Prausnitz [7] and his team in the year 2004. At the outset in spite of a wide range and variety of microneedle designs towards different applications that have been reported in the last few decades, the fundamental mechanics and the techniques towards the insertion of microneedles into the skin of human subjects, have received a very limited notice and attention. The core design objective of microneedles is that they should be carefully administered into the skin by following precautionary safety measures and see to it that the microneedles do not break or bend to achieve a painless and minimal invasiveness based treatment. The insertion force is considered to be one of the key indicating parameters which are generally estimated for the safe use of microneedles. When the insertion force is too large or more, the microneedles will have a greater tendency to break or buckle before the microneedle is totally inserted into the skin. A better understanding of the insertion process and the relationship between the microneedle geometry and the insertion force is helpful to the microneedle optimization design. Davis et al. (2004) measured and predicted that the force necessary to insert a tapered, hollow metal kind of microneedle into human skin with the help of a force-displacement measurement kind of device which gives an approximately linear dependency of the insertion force on the cross area of the needle tip. In their study, tapered hollow metal microneedles were used having a tip radius of 30-80 mm, wall thickness of 5-58 mm and having a constant length of 720 mm.

The insertion force for a single microneedle was found to vary from 0.08 to 3.04 N. Recently, Roxhed et al. [8] have developed [8] and fabricated a type of ultra-sharp hollow microneedles whichgaveaninsertionforcelessthan10mN. All of the experiments mentioned above have studied the insertion properties of microneedles into human skin. However,noefficientnumericalmodelhasbeensetupfor predicting the insertion process of a microneedle into human skin.

In this paper, a conically shaped microneedle was considered which will have a primary force being applied in the vertical direction and a lesser secondary force to be applied in the horizontal direction. The von-mises stresses in the needle as well as the deformation of the needle will be analyzed in a 3-d plot. A multilayered skin model consisting of three layers, stratum corneum, dermis and hypodermis, is proposed. With the multilayered microneedle-skin model, the skin deformation and failure involved in the insertion process [9, 10], as well as the influences of several parameters (e.g. mechanical properties of skin, wall angle, tip are and wall thickness of the microneedle) on the insertion force of the microneedle, have been studied. The finite element analysis [11, 12] provides some new insights into the insertion process of the microneedle into human skin.

1.1 SkinPhysiology

Human skin, being the largest organ of the human body, is a highly systematically organized and its structure chiefly consisting mainly of three layers: epidermis [13] mainly serves as a front line barrier [14] towards infection; the dermis layer which serves as a subcutaneous layer with adipose being called also as a basement membrane (Fig. 1). The outermost layer of the skin or epidermis is called the stratum corneum [15] with an ideal thickness of about 10-20 mm. The second layer of the skin is called a dermis layer, with a dense fibro-elastic [16] connective tissue layer of thickness 1-4 mm (Odland [16]). The third layer also called the subcutaneous fat

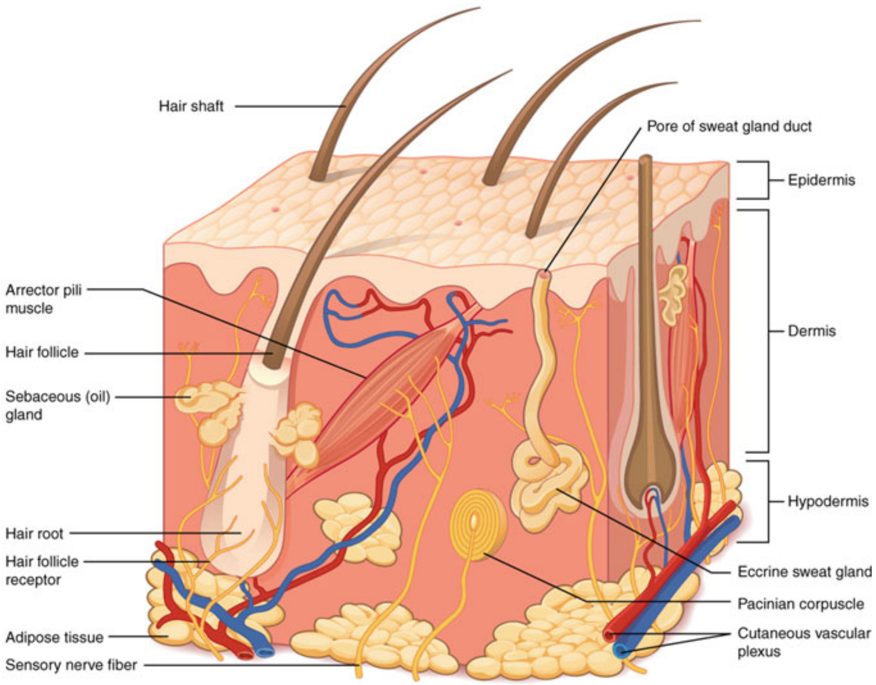

Fig. 1 Schematic view of the cross-section of human skin

layer or the hypodermis layers is almost composed of loose fatty connective tissue connecting to the dermis.

1.2 Mechanical Properties

The mechanical behavior of human skin was under investigation [17] and research is focused on the skin behavior (Payne [17]; Holzapfel 2001; Hendrikset al. [18]). As a matter of fact, the human skin is generally considered to be a heterogeneous substance with a property of viscoelasticity [19] with an irregular pattern being under continual stress (Langer [19]). Skin as a homogeneous material without considering the individual contributions of the epidermis, dermis and hypodermis. Actually, different layers have rather different mechanical properties.

1.3 Basic Assumptions and Mechanical Properties of the Skin

The geometrical parameters of the microneedles are analyzed in the present study which is partially dependent upon the experimental design proposed by Davis et al. (2004). All the microneedles used in this numerical modeling [12] are tapered with respective to their geometrical shape. Here, the length which is a primary parameter of the tapered microneedles is also considered as the same order as of the thickness of skin layer. In order to get a better insight of overall insertion process, the mechanical behavior of different skin layers should be studied on an initial basis. In this simulation, a multilayer finite element model of skin including stratum corneum [15, 20], dermis and hypodermis is developed. It was taken into consideration that the skin is to be as a simplistic model primarily consisting of stratum corneum, dermis and the hypodermic layer.

Table 1 lists the mechanical properties of different layers of the skin used in the numerical [11, 20] simulations. Although experiments need to be conducted to determine the exact mechanical failure properties [17] of the lower layers of the epidermis. Initially, the lower layers of the skin which is the epidermis will tend to have a lesser impact as compared to that of the whole deformation of the skin model as

Table 1 Mechanical properties of human skin

	Density *r* (kg/m$^{3)}$	Failure stress *s* (MPa)	Friction coefficient *m*
Stratum corneum	1300[a]	13–44[b]	0.42[c]
Dermis	1200[d]	7.3[e]	0.42[c]
Hypodermis	971[e]	–	–

Table 2 Parameters required for processing

Mesh quality	Normal
Number of node points	Not applicable
Total number of elements	6805
Degree of freedom	31,755

a matter of fact due to smaller thickness. The force which is acting horizontally on the needle is assumed to be significantly less than the force required to penetrate into the skin, which is called the force of insertion or the insertion force, which can be easily justified by the elastic property [2, 21] of the skin. Any force which when applied in the horizontal direction would be unintentional and therefore considered to be significantly smaller in magnitude, than that of the force which when punched in the vertical direction. When considering each needle on the patch, they are assumed to be identical and by adding more needles to the model, it would not significantly change the forces acting on each individual needle, the forces here gets distributed which will decrease the stress on a single needle, but will distribute equally throughout the patch. Since the focus is on estimating the maximum stress there gives a scope to neglect the decreasing stress factor. The interface between the top of the needle and adjoining surface is always maintained to be at a fixed constraint which can be justified by interfacing between the top of the needle and base of the needle surface which is by default considered to be a continuous geometry. In simple it means that there is so physical connection such as a weld that would fail before the rest of the structure.

The simulation was a stationary model using a fully coupled stationary direct solver. The advanced parameters were a MUMPS solver with 1.2 memory allocation factors and automatic pre-ordering algorithm (Table 2).

2 Geometry and Force of Insertion

Height of the needle to be considered as 400 µm, Top outer radius 75 µm, Top inner radius 25 µm, Bottom outer radius 50 µm, Bottom inner radius 10 µm. The microneedle needed to be long enough to penetrate the epidermis to a thickness level = 130 µm. The microneedle needs to be sturdy enough to withstand the force required to penetrate human skin Force to pierce skin = 2 N. The microneedle needs to be sturdy enough to withstand any lateral shearing force caused by motion of the needle after insertion. Lateral shearing force = 0.5 N. The microneedle tip opening needs to large enough to provide a sufficient flow of vaccine to the skin Inner radius = 20 µm. The thickness of each layer of skin is considered as the average value of human body, for example, the stratum corneum is 20 mm, dermis is 1.5 mm and hypodermis is 1 mm.

2.1 Governing Equations

Compressive Force

The maximum compressive force the microneedle can withstand without breaking is given by

$$F_{\text{Compressive}} = бy.A \tag{1}$$

where *бy* is the fracture strength of the material. Where *A* is the cross-sectional area of the microneedle.

Skin Puncturing Force

As a microneedle is inserted, it experiences resistive forces by human skin. In order to successfully penetrate human skin, the applied force should be greater than this opposing force (Fig. 2 and 3, Table 3).

$$F_{\text{Skin}} = P_{\text{puncturing}} A \tag{2}$$

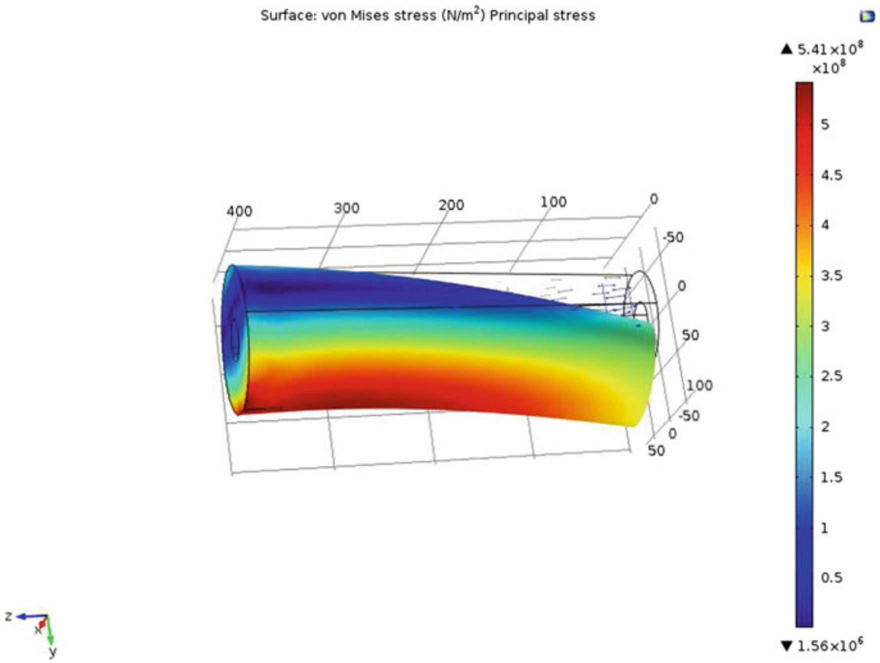

Fig. 2 Principle stress exerted by the needle

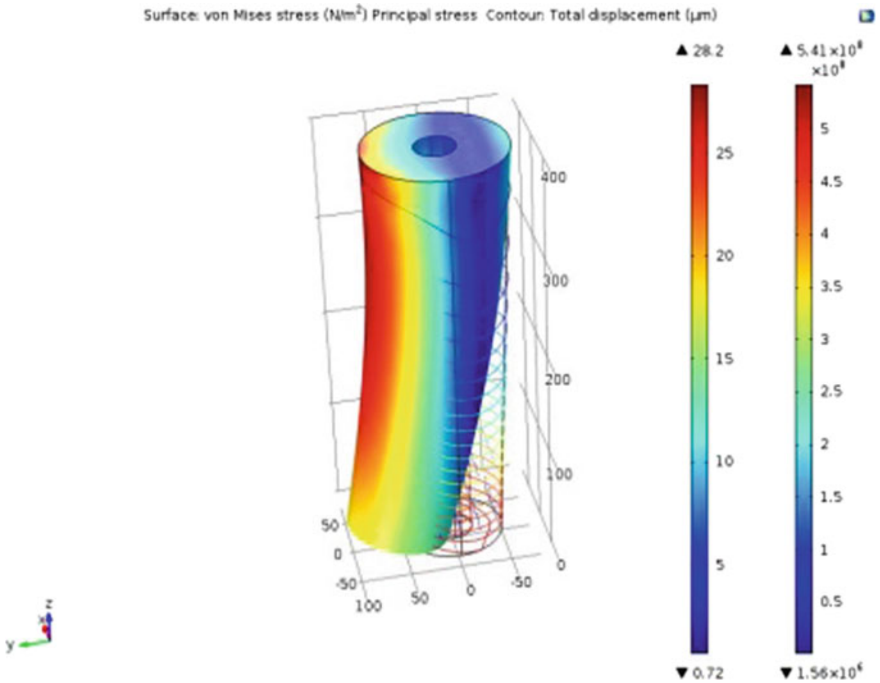

Fig. 3 Total displacement of the needle

Table 3 Parameters considered with respective values

Parameter	Value
Young's modulus	17.0 GPa
Poisson's ratio	0.21
Density	1500 kg/m^3
Yield strain	0.05
Yield stress	80 Pa

3 Results

(Table 4, 5, 6 and 7)

Table 4 Resultant outputs for various parameters

Parameter	Value
Length of the needle	400 μm
Diameter of the needle	20 μm
Resultant stress	0.541 GP_a
Total displacement	28.2 μm

Table 5 Deflection versus max stress

$б_{max}$	0.541 GP_a
Total deflection	28.2 μm

Table 6 Increase of needle diameters by 25%

Top outer radius	92.5
Bottom outer radius	62.5

Table 7 Change in stress level

Max stress $б_{max}$ of increase in dimensions	0.3034 GP_a
Percentage	23%

4 Conclusion

A conically shaped microneedle will have a primary force applied in the vertical direction and a lesser secondary force will be applied in the horizontal direction. The von-mises stresses and the displacement of the needle are analyzed in a 3-d plot. We could able to meet the physical design criteria by constructing a needle to fit the specified requirements. The length of 400 μm is long enough to pierce the epidermis and the diameter of 20 μm is large enough to achieve sufficient flow through the tip of the needle. From our first plot, we see that the maximum stress reached any point in the needle is 0.541 GPa. From this, we can be assured that the needle will not break. 0.541 GPa is also less than the yield strength of the needle which is 17.0 $GP_{a.}$ It underwent a displacement of 28.2 μm from its center. By altering the needle radius parameters, we can see there is a change in the max stress being exerted down to 0.3034 GPa which has a decrease in percentage level. By increasing the needle radii there is a significant decrease in the percentage of stress exerted. This gives an insight into the scientific community to look into needle diameters which has an impact on the stress level. From the stress analysis, we see that the needle can withstand the applied normal forces and applied shearing forces. Simulations were carried out on COMSOL 5.0 version.

Future work

From the present research analysis, it can be concluded that the work can be extended to complete structural analysis of design which includes bending stress, buckling stress and thereby to fabricate and test the microneedle.

Acknowledgements This work was executed with the support of the Department of Science and Technology-Science and Engineering Research Board (DST-SERB) New Delhi, India for providing [Project No: ECR/2017/001183] under ECRA-SERB scheme.

Conflict of Interest: The contributing authors declare that there is no conflict of interest regarding the article.

References

1. Moon SJ, Seung SL (2003) Fabrication of microneedle array using inclined LIGA process. Paper presented at: proceedings of transducers'03. Boston, USA
2. Lin L, Pisano AP (1999) Silicon-processed microneedles. J Microelectromech Syst 8:78–84
3. Henry S, McAllister DV, Allen MG, Prausnitz MR (1998) Micro fabricated microneedles: a novel approach to trans- dermal drug delivery. J Pharm Sci 87:922–925
4. Ashraf MW, Tayyaba S, Afzulpurkar N, Nisar A, Bohez ELJ, Lomas T, Tuantranont A (2010) Design, simulation and fabrication of silicon microneedles for bio-medical applications, in ECTI-CON 9(1)
5. McAllister DV (2000) Microfabricated needles for transdermal drug delivery [PhD thesis]. Georgia institute of technology
6. Sivamani R, Stoeber B, Wu G, Zhai H, Liepmann D, Maibach H (2005) Clinical microneedle injection of methyl nictinate: stratum corneum penetration. Skin Res Technol 11:152–156
7. Lee JW, Park J-H, Prausnitz MR (2008) Dissolving microneedles for transdermal drug delivery. Biomaterials 2113–2124
8. Roxhed N, Gasser TC, Griss P (2007) Penetration-enhanced ultra-sharp microneedles and prediction on skin interaction for efficient transdermal drug delivery. J Microelectromech Syst 16:1429–1440
9. Shergold OA, Fleck NA (2004) Mechanisms of deep penetration of soft solids with application to the injection and wounding of skin. Proc R Soc London Ser A 460:3037–3058
10. Shergold OA, Fleck NA (2005) Experimental investigation into the deep penetration of soft solids by sharp and blunt punches, with application to the piercing of skin. J Biomech Eng 127:838–848
11. Louzidou EZ, Williams NA, Barrow DA, Eaton MJ, McCrory J, Evans SL, Allender CJ (2015) Structural characterization and transdermal delivery studies on sugar microneedles: experimental and finite element modelling analyses. Euro J Pharm Biopharm 89:224–231
12. Olatunji O, Das DB, Garland MJ, Belaid L, Donnelly RF (2013) Influence of array interspacing on the force required for successful microneedles skin penetration: theoretical and practical approaches. J Pharma Sci 102:1209–1221
13. Geerligs M, van Breemen L, Peters G, Ackermans P, Baaijens F, Oomens C (2011) In vitro indentation to determine the mechanical properties of epidermis. J Biomech 44:1176–1181
14. Norlén L (1999) The skin barrier: structure and physical function [PhD thesis]. Karolinska Institute, Stockholm, Sweden
15. Menon GK, Cleary GW, Lane ME (2012) Structure and function of stratum corneum. Int J Pharma 435:3–9
16. Odland GF (1991). Structure of the skin. In: Physiology biochemistry, and molecular biology of the skin. Oxford University Press, New York
17. Payne PA (1991) Measurement of properties and function of skin. Clinical Phys Physiol Meas 12:105–129
18. Hendriks FM, Brokken D, Oomens CWJ, Baaijens FPT (2004) Influence of hydration and experimental length scale on the mechanical response of human skin *in vivo*, using optical coherence tomography. Skin Res Technol 10:231–241
19. Langer K (1978) On the a natomy and physiology of the skin. Br J Plast Surg 31:3–8
20. Mane N, Gaikwad A (2014) MEMS based structural and fluid flow mechanics and simulation analysis of microneedle for drug delivery. Int J Mech Prod Eng 2 ISSN:2320-2092
21. Magnenat-Thalmann N, Kalra P, Leveque JL, Bazin R, Batisse D, Querleux B (2002) A computational skin model: foldand wrinkle formation. IEEE Trans Info Technol Biomed 6:317
22. Martanto W, Baisch SM, Costner EA, Prausnitz MR (2005) Fluid dynamics in conically tapered microneedles. AIChE J 51:1599–1607

Lumbar Discography: Study of Biomechanical Changes in the L1-L2 Intervertebral Disc of the Human Lumbar Spine Using Finite Element Methods

S. Balamurugan, P. Susai Manickam, and Sachit Chawla

Abstract Lumbar discography is often used as a pain recognition technique for evaluating patients who have otherwise not responded well to non-surgical methods (radiology). While the injection technique provides unique information about the disc which is not obtainable through other methods, the procedure is suspected to cause prolonged damage to the disc. A study concentrating on equivalent stress in different regions of the disc shall provide useful insight on the prolonged effects of the lumbar discography procedure. A computational model of the functional spinal unit that accurately mimics its material properties and motion is required to simulate the medical procedure performed on the intervertebral disc. This study uses a hybrid finite element model of the L1-L2 motion segment of the lumbar spine of a 35-year-old male subject. In order to mimic spinal motion during flexion and extension, all supporting ligaments were added to the finite element model. Hyperelastic material properties were altered to simulate the discography procedure and equivalent von Misses stress values across the Annulus Fibrosus were recorded. A considerable increase in the equivalent stress across the annulus was observed in the punctured controls. Thus, the injection technique alters the stress concentrations across the disc and can have prolonged degenerative effects on the IVD.

Keywords Intervertebral disc · Lumbar discography · Lumbar spine

1 Introduction

Degeneration of the intervertebral is characterized by the decrease in disc height and desiccation. [1, 2] A degenerated IVD can lead to lower back pain. The most common method used for imaging lumbar spine pathologies is magnetic resonance imaging. MRIs provide a detailed image of the degenerated discs and other abnormalities in the region of the lumbar spine. While the modality is useful for identifying abnormal

S. Balamurugan (✉) · P. S. Manickam · S. Chawla
Department of Mechanical Engineering, SRM Institute of Science and Technology, SRM Nagar, Kattankulathur, Chengalpattu 603 203, Tamil Nadu, India
e-mail: balam2007@gmail.com; balamurugan.sr@ktr.srmuniv.ac.in

E. T. Akinlabi et al. (eds.), *Trends in Mechanical and Biomedical Design*,
Lecture Notes in Mechanical Engineering,
https://doi.org/10.1007/978-981-15-4488-0_52

disc pathology in the spine, it cannot prove if the abnormality is the cause of pain. [3, 4] To overcome this problem an invasive medical procedure, lumbar discography, is used by physicians to record the patient's response to the pain.

1.1 Lumbar Discography

This invasive medical procedure has been used by physicians for over 60 years and involves an injection technique to insert fluoroscopy-guided needle in order 22- or 25-gauge needle from a posterolateral approach into the IVD [5]. Upon injection of contrast, the patients' response to the pain sensation is recorded. The response is recorded on a Likert scale where patients rate their pain between 0 and 10, where 0 is no pain and 10 is unbearable pain [6]. The contrast is then viewed in CT images to check for abnormalities in the disc as well as any ruptures present in the annulus region which may be reflected by contrast. The procedure is conducted on both abnormal and normal controls. Proponents of the procedure believe that information extracted from discograms is unobtainable via any other non-surgical methods. However, it has been strongly argued that the information obtained is extremely sensitive and specific to patient response [7]. A considerable number of cases have been registered wherein the patients experience similar or in some cases, an increase amount of pain upon the removal of pain generator based on the discography results. Further, a puncturing the disc during the process of injecting contrast can also lead to ruptures in the annulus and can lead to prolonged degeneration of the IVD [8]. The aim of this study is to characterize changes in the equivalent stress across the annulus fibrosus before and after the lumbar discography procedure utilizing a computational model of L1-L2 motion segment of the lumbar spine. The FE model was validated using data from in vitro studies [9] and adjusted to achieve the desired accuracy.

1.2 Intervertebral Disc

The intervertebral discs lie between the vertebral bodies and link them together. They are the main joints of the spinal column and occupy one-third of its height. Their major role is mechanical, as they constantly transmit loads arising from body weight and muscle activity through the spinal column. They provide flexibility allowing bending, flexion and torsion. The intervertebral disc constitutes of mainly three components, namely the annulus fibrosus, nucleus pulposus and the cartilage end-plates.

1.2.1 Nucleus Pulposus

The central nucleus pulposus contains collagen fibers, which are organized randomly, and elastin fibers (sometimes up to 150 mm in length), which are arranged radially;

these fibers are embedded in a highly hydrated aggrecan-containing gel. The nucleus acts as an incompressible unit that transfers loads evenly across the annulus and also aids the transfer of nutrients to and from the intervertebral disc.

1.2.2 Annulus Fibrosus

This is made up of a series of 15 to 25 concentric rings, or lamellae, 11 with the collagen fibers lying parallel within each lamella. The fibers are oriented at approximately 60 to the vertical axis, alternating to the left and right of it in adjacent lamellae. Elastin fibers lie between the lamellae, possibly helping the disc to return to its original arrangement following bending, whether it is flexion or extension. They may also bind the lamellae together as elastin fibers pass radially from one lamella to the next.

1.2.3 Cartilage End-Plate

The third distinct feature of the IVD is the cartilage end-plates. These are a thin horizontal layer, usually less than 1 mm thick, of hyaline cartilage. The college fibers within the end-plates are aligned parallel and horizontal to the vertebral bodies.

2 Methodology

A computational model of the L1-L2 motion segment of the lumbar spine was used to investigate biomechanical changes. A hybrid finite element model that used both quad and tetrahedral elements was developed where the main vertebral body and the intervertebral disc components were meshed using quad elements while the spinous process utilized tetrahedral elements. The use of the same type of elements across the functional spinal unit provides better load transfer across biological components compared to using different types of elements. The generation of the finite element model from medical imaging techniques involved mainly three stages:

2.1 Geometric Modelling

CT images of the lumbar spine obtained from a 35-year-old male from SRM Medical College were processed using Mimics Medical by Materialize (Fig. 1). Thresholding values were adjusted to mask the vertebral column separately. The intervertebral disc tissue shares its thresholding values with the muscular tissue surrounding it thus making it difficult to extract the exact geometry of the IVD using slices obtained from CT method. This meant that the disc needed to be reserve engineered using the

Fig. 1 Stages of obtaining CAD model from CT images

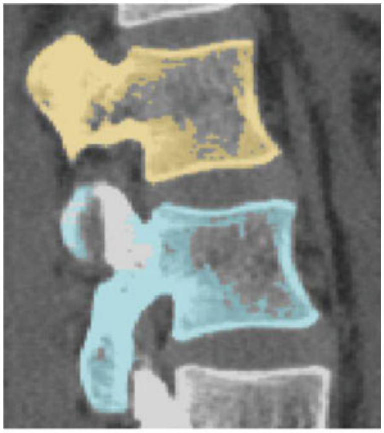

(a) Masked vertebral bodies

(b) Unprocessed CAD model

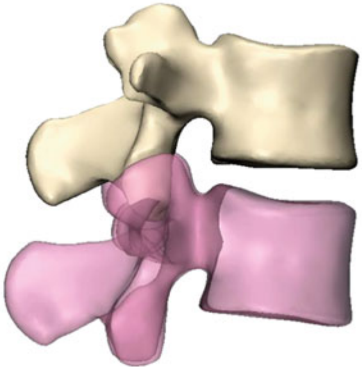

(c) CAD model after topological refinement inferior and superior faces of the L1 = L2 vertebra respectively. The CT images were edited slice by slice along the transverse plane in order to separate the two vertebral bodies and allow for their unrestricted motion in the finite element model. Topological refinements of the now obtained geometric model were carried out using 3-Matics by Materialize. The surfaces of the vertebral bodies consisted of planar holes which were needed to be filled in order to maintain the continuity of the outer cortical shell. The internal trabecular structure of the vertebrae was also removed so that the inner portion of the vertebrae could be treated as the cancellous core.

2.2 Finite Element Modelling

Finite element model was generated using Hypermesh by Altair Engineering (Figs. 2, 3). Morphing options available in Hypermesh were used to morph geometrically symmetric 2D meshed surfaces to oblong vertebral bodies. A concentric circular pattern was developed on the inferior and superior faces of the vertebral bodies and annulus fibers were created along these circular paths. Tension-only 1D elements (LINK 10) were used to create the annulus fibers. These 1D elements connected the diagonally opposite nodes of the quad elements and mimicked the non-linear behaviour of the disc under extension and flexion. To simulate cartilage end-plates a solid layer of quad elements 0.3 mm thick was created on both inferior and superior faces of the L1 and L2 vertebrae respectively. All ligaments connecting the two vertebral bodies were also incorporated in the finite element model to facilitate true motion of the motion segment under load. The seven ligaments included in the model were the anterior longitudinal (ALL), posterior longitudinal (PLL), flavum

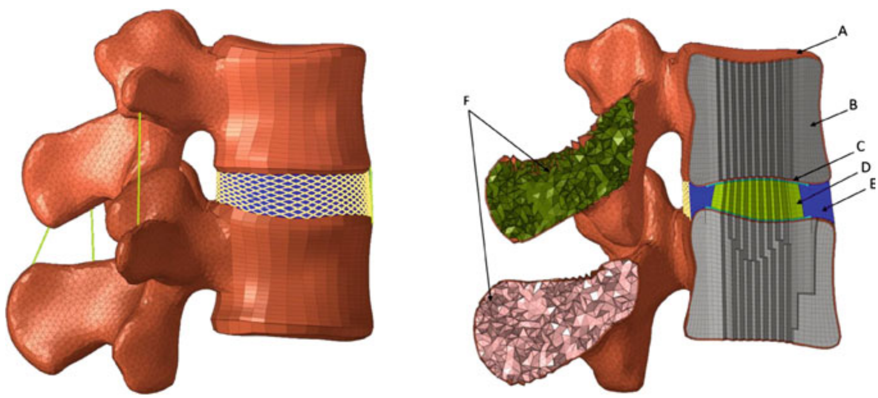

(a) Finite Element Model with all cable elements

(b) Cross-section of the FEM along the mid-Sagittal plane

Fig. 2 **a** Cortical shell **b** Cancellous bone **c** Cartilaginous end-plates **d** Nucleus pulposes **e** Annulus ground substance **f** Spinous process

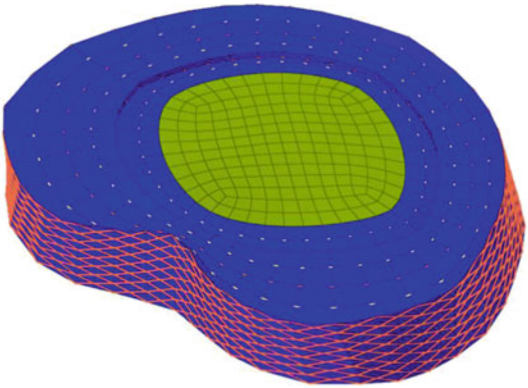

(a) FEM of IVD complete with Annulus Ground Substance and Nu-cleus

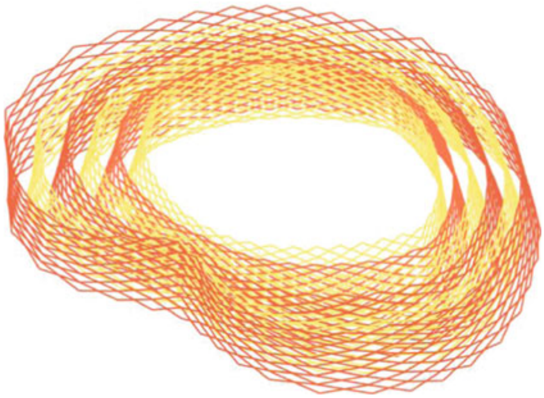

(b) Annulus Fiber generated using LINK10 elements from Layer 1(in-nermost) to Layer 6(outermost)

Fig. 3 Intervertebral disc

(LF), intertransverse (ITL), interspinous (ISL), and supraspinous (SSL) ligaments. These ligaments were modelled using 1D elements which displayed zero stiffness value under compression. These elements were attached to appropriate landmarks on the vertebral bodies. Node to node contact was defined between the intervertebral disc and the vertebral bodies to achieve complete load transfer along the motion segment.

Material	Young's Modulus	Poisson's Ratio	Element Type
Cortical Bone	E_{xx} = 11,300 E_{yy} = 11,300 E_{zz} = 22,000	v_{xy} = 0.484 v_{yz} = 0.203 v_{zx} = 0.203	SOLID 45
Cancellous Bone	E_{xx} = 140 E_{yy} = 140 E_{zz} = 200	v_{xy} = 0.45 v_{yz} = 0.315 v_{zx} = 0.315	SOLID 45
Spinous Process	E_{xx} = 140 E_{yy} = 140 E_{zz} = 200	v_{xy} = 0.45 v_{yz} = 0.315 v_{zx} = 0.315	SOLID 185

Fig. 4 Material and mechanical properties of the cortical and cancellous bone as well as spinous process

Cable Element	Young's Modulus	Poisson's Ratio	Element Type
Lig. long. Anterius	20	0.3	LINK 10
Lig. long. Posterius	70	0.3	
Lig. Flava	50	0.3	
Lig. Intertransversaria	50	0.3	
Lig. Interspinalia	28	0.3	
Lig. Supraspinalia	28	0.3	
Lig. Capsularia	20	0.3	
Anulus fibrosus layer 1	550	0.45	LINK 10
Anulus fibrosus layer 2	495	0.45	
Anulus fibrosus layer 3	440	0.45	
Anulus fibrosus layer 4	420	0.45	
Anulus fibrosus layer 5	385	0.45	
Anulus fibrosus layer 6	360	0.45	

Fig. 5 Mechanical properties of annulus fibers and ligaments

2.2.1 Material Models

Material models that accurately depicted the biological properties of the vertebral bodies as well as the intervertebral disc were assigned to different components in the finite element model. The anisotropy in the material properties of the vertebral bodies was considered [10, 11] (Fig. 4). A Mooney-Rivlin model was used to define the material properties of the Annulus and the Nucleus. Mooney-Rivlin constants were altered to simulate the discography procedure [12] (Fig. 7). The mechanical properties and cross-sectional area of all 1D elements were assigned to best mimic the biomechanical behaviour of the motion segment [13, 14] (Fig. 5).

2.3 Boundary Conditions

The coordinate system used by Panjabi et al. [9] was followed in order to validate the model. A pilot node was defined at the center of the superior face of the L1 vertebral

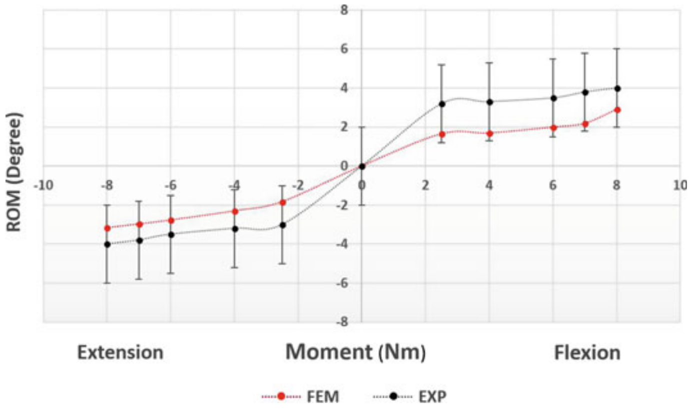

Fig. 6 Range of motion of functional spine unit for Flexion and Extension

Structure	*Hyperelastic Constants*			*Element Type*
Annulus Fibrosus	C10 = 0.21	C01 = 0.08	D = 0.37	SOLID 185
Nucleus Pulposus	C10 = 0.17	C01 = 0.05	D = 0.00133	SOLID 185
Weakened Nucleus Pulposus	C10 = 0.10	C01 = 0.02	D = 0.00133	SOLID 185

Fig. 7 Material and mechanical properties of nucleus pulposes before and after the lumbar discography procedure

body and moment loads were applied on this point about the X-axis. The pilot node was connected to the superior face using rigid elements. The inferior face of the L2 vertebra was constrained with 0 DOF in all directions.

3 Validation of Finite Element Model

The mechanical behaviour of generated FE model was validated by comparing experimental and finite element values (Fig. 6) for the range of motion of the L1-L2 motion segment.

3.1 Flexion-Extension-Moment Loading

The values for range of motion segment under pure flexion and extension loading obtained from the FE model were recorded and compared to in vitro studies [9]. ROM noted from the FE model lie within the standard deviation of the experimental mean values for most of the loading cases. The average error between ROM values predicted by the FE model and those obtained from literature for extension and flexion was 42.1% and 26%, respectively.

4 Results and Discussions

In order to simulate disc puncture the material properties of the nucleus were changed. Due to water loss during disc puncture there is thought to be a stiffening of the NP region. This concept is based on the results of a study by Iadritis et al. stating that even a small disruption to the annulus fibrosis of the disc due to disc puncture can lead to depressurization of the nucleus pulposus [15]. Flexion-extension-moment loads were applied on the L1-L2 motion segment and the maximum von Misses stress values were recorded. This simulation was performed for both normal and punctured controls. The results predicted by the FE model in both cases were then compared.

4.1 Flexion-Moment Loading

A comparison of equivalent von Misses stress during flexion-moment loading showed that the discography procedure causes an increase in equivalent stress across the AF region (Fig. 8). The stress values recorded after simulating the procedure displayed a non-linear trend and a decrease in stress were observed for high moment loads beyond 9.5 Nm. This non-linearity in results can be explained by the non-linear nature of the annulus fibers. The maximum percentage increase in stress observed for flexion loading was 3.11%.

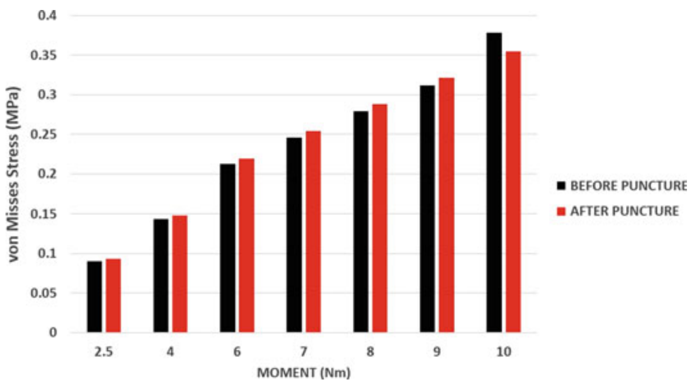

Fig. 8 Comparison of von misses stress produced across the AF region as predicted by the FE model during flexion-moment loading before and after lumbar discography procedure

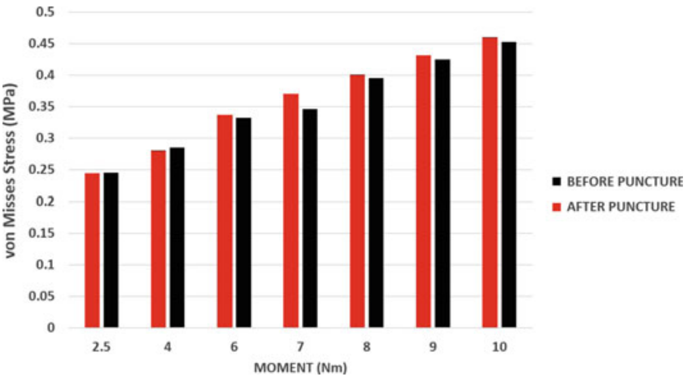

Fig. 9 Comparison of von misses stress produced across the AF region as predicted by the FE model during extension-moment loading before and after lumbar discography procedure

4.2 Extension-Moment Loading

A similar trend of increased equivalent stress was observed for extension-moment loading in the punctured disc. A decrease in equivalent stress was observed for lower values of moments between 3 Nm and 4.5 Nm. The maximum percentage increase in stress observed for extension loading was 6.80% (Fig. 9).

5 Conclusion

The current study on L1-L2 motion segment of the lumbar spine examines the biomechanical changes in the intervertebral disc brought about by the lumbar dicscography procedure. The simulations carried out on the validated FE model predict an overall increase in the von Misses stress across the Annulus Fibrosus upon disc puncture caused by the injection technique. A considerable increase of 6.80% in equivalent stress during extension provides proof that the medical procedure causes changes in the biomechanics of the disc even under simple loading conditions. Complex or impact loading of the motion segment may cause even more significant changes in the IVD biomechanics. Since the healing of the IVD after puncture is frustrated by a small population of cells that have limited availability to nutrients and is repeatedly exposed to mechanical motions, [16] these changes in the stresses induced in the disc can cause prolonged degeneration of the Annulus Fibers. Thus, a change in the biomechanics of the disc due to the puncture was confirmed but if these changes can onset early degeneration of the disc is still being studied.

Acknowledgements This work was supported by the Bio mechanics lab, Department of Mechanical Engineering, SRMIST, Kattankulathur—603203. We thank Mr. Raja D, Asst Professor

(S.G) and Research Head, Bio mechanics lab, Department of Mechanical Engineering, SRMIST, Kattankulathur—603203 for assistance to improve the manuscript.

References

1. An HS, Inoue N, Masuda K (2006) Intervertebral disc degeneration: biological and biomechanical factors. J Orthop Sci 11(5):541–552
2. Urban JP, Roberts S (2003) Degeneration of the intervertebral disc. Arthritis Res Ther 5(3):120–130
3. Guyer RD, Ohnmeiss DD (2003) Lumbar discography. Spine J 3(3 Suppl):11S–27S
4. Kim YH, Kang CH, Lee S et al (2009) Can magnetic resonance imaging accurately predict concordant pain provocation during provocative disc injection? Skeletal Radiol 38(9):877–885
5. Hirsch C (1948) An attempt to diagnose level of disc lesion clinically by disc puncture. Acta Orthop Scand 18:131–140
6. Moneta GB, Videman T, Kaivanto K et al (1994) Reported pain during lumbar discography as a function of anular ruptures and disc degeneration. a re-analysis of 833 discograms. Spine (Phila Pa 1976) 19(17):1968–1974
7. Carragee EJ, Alamin T (2001) Discography. a review. Spine J 1(5):364–372
8. Carragee EJ, Don AS, Hurwitz E et al (2009) Does discography cause acceler-ated progression of degeneration changes in the lumbar disc: a ten-year matched cohort study. Spine (Phila Pa 1976) 34(21):2338–2345
9. Panjabi M, Oxland T, Yamamoto I, Crisco J (1994) Mechanical behavior of the hu-man lumbar and lumbosacral spine as shown by three-dimensional load-displacement curves. J Bone Joint Surg 76(3):413–424
10. Ueno K (1984) A three dimensional nonlinear finite element model of the lumbar intervertebral joint. [phd thesis]. The University of Iowa, Iowa
11. Lang SB (1970) Ultrasonic method for measuring elastic coe cients of bone and results of fresh and dried bovine bones. IEER Trans Biomed Eng 17:101–105
12. Lipscomb KE, Sarigul-Klijn N, Klineberg E, Mohan V (2017) Biome-chanical e ects of human lumbar discography: in-vitro experiments and their finite element validation. Clin Spine Surg 30(3):E219–E225
13. Shirazi-Adl S.A., Shrivastava, S. C., Ahmed, A. M (1984). Stress analysis of the lumbar disc-body unit in compression. a three-dimensional nonlinear finite element study. Spine 9, 120134
14. Smit TH, Odgaard A, Schneider E (1997) Structure and function of vertebral trabec-ular bone. Spine 22:2823–2833
15. Iatridis JC, Michalek AJ, Purmessur D et al (2009) Localized intervertebral disc injury leads to organ level changes in structure, cellularity, and biosynthe-sis. Cell Mol Bioeng 2(3):437–447
16. Adams MA, Stefanakis M, Patricia D (2010) Healing of a painful interverte-bral disc should not be confused with reversing disc degeneration: im-plications for physical therapies for discogenic back pain. Clin Biomech (Bristol, Avon) 25(10):961–971

C4–C5 Segment Finite Element Model Development and Investigation of Intervertebral Disc Behaviour

P. Susai Manickam

Abstract Clinical problems of the human cervical spine continue to be widespread in our society. In the past few decades, many experimental and simulation techniques were adopted to study the motion of the cervical spine. The functional spine unit is made of vertebrae, end plates, intervertebral disc and ligaments. To understand the biomechanical behaviour of cervical spine a detailed finite element model is needed. The focus of the study is to develop the cervical spine from (C4–C5) finite element model with accurate dimensions and representation of the material properties. A three-dimensional finite element (FE) model of cervical spine segment (C4–C5) was developed using computed tomography CT scan and applied to study the stresses distribution of the intervertebral discs under quasi-static loading conditions. A pure moment loading of 1.0 Nm was applied to study the physiological motion. The model accuracy was validated by comparing the results with the previously published experimental and numerical results for various physiological motions. Several movements were analysed: flexion, extension, lateral bending and axial rotation. By using elastic and hyperelastic model behaviour of the intervertebral disc was accurately simulated. The results obtained by the elastic and the hyperelastic models showed good agreement with experimental and numerical data. The current model which reflects the behaviour of human cervical spine can be effectively used to study further biomechanics and traumatic studies.

Keywords Spine · Cervical spine · Finite element model

1 Introduction

Injury in the cervical spine can be analysed according to the physiological motion of the neck and the mechanical loads acting in the spine. Generally in the traffic accidents, the damages are caused in the intervertebral disc soft tissues, ligaments

P. Susai Manickam (✉)
Research Scholar, Department of Mechanical Engineering, SRM Institute of Science and Technology, SRM Nagar, Kattankulathur, Chengalpattu 603203, Tamil Nadu, India
e-mail: susairaphah@gmail.com

E. T. Akinlabi et al. (eds.), *Trends in Mechanical and Biomedical Design*,
Lecture Notes in Mechanical Engineering,
https://doi.org/10.1007/978-981-15-4488-0_53

and muscles. The load transmission and the shock absorber effect in the compression is achieved by intervertebral disc. Clinician identified that the biomechanical study in the disc helps to understand the loads and the physiological motion of the cervical spine. Biomechanical models, such as in finite element (FE) models and vitro, helps us to understand the mechanisms of injury and diagnosis and effective treatment of cervical spine problems [1, 2]. The objective of the work is to model C4–C5 level of the cervical spine by using finite element analysis. The intervertebral disc is the major load transmitting components so the material models need to be assigned. For the basic material properties, the validation was done using the experimental results. The material models were assigned as linear elastic properties and non-linear material models for the functional spine unit. The models can be used to predict the physiological motion and the stress distribution across the intervertebral disc.

2 Materials and Methods

2.1 Model Construction

The vertebrae were classified into cortical, cancellous and the posterior side. The thickness of the cortical layer is 0.5 mm. The intervertebral disc was classified as disc-annulus fibrosis, nucleus pulposus, with inferior and superior endplates. The thickness of the endplate is 0.6 mm. The ligaments are modelled for the functional spine unit anterior longitudinal ligament (ALL), capsular ligament (CL), and inter-spinous ligament (ISL), ligamentum flavum (LF), posterior longitudinal ligament (PLL) (Figs. 1 and 2) .

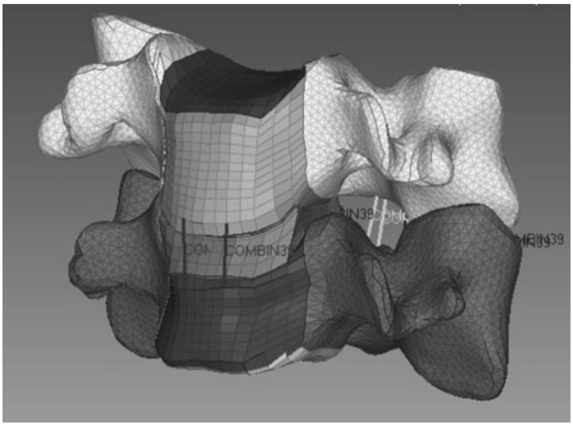

Fig. 1 C4–C5 meshed model

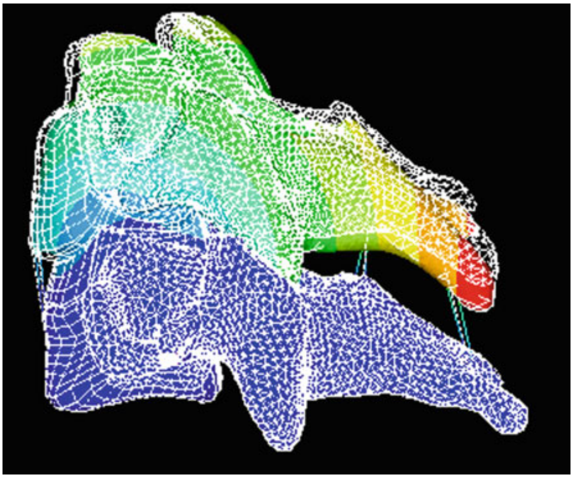

Fig. 2 C4–C5 model in extension for a load of 1 Nm

2.2 FEA Modelling

The geometry of the C4–C5 model was obtained from computed tomography (CT) data of a healthy 28-year old man from SRM medical college. The CT data were processed with medical image processing software MIMICS (MIMICS_ Version 10.0; Materialise, Inc., Leuven, Belgium). The meshing of the vertebrae cortical and cancellous bone, Intervetebral disc and endplates was performed using Hyper mesh 11.0 (Altair Engineering, Inc., Executive Park, CA, USA). In the finite element model of cortical and cancellous on the anterior side is modelled using hexahedral elements and it consists of 6651 elements and 7920 nodes were used to build the model. The posterior side of the model is having a high level of irregular surface so it was meshed using tetrahedral elements and it consists of 109,269 elements and 23,321 nodes. According to the anatomy, the intervertebral disc and the ligaments were modelled. In the intervertebral disc cross-sectional area approximately 50% was comprised as nucleus pulposus [3]. The hexahedral elements were used to construct the inferior and superior endplates. All the ligaments were modelled using non-linear spring elements. The finite element model was developed for C4–C5 segment based on the available material properties as shown in Table 1. After the mesh sensitivity effect size of the elements are finalized. The material is assigned as shown in Table 1 for the bones and Table 2 for the ligaments.

Table 1 Finite element model details

S. No.	Description	Young's modulus (Mpa)	Poisson ratio
1	Cortical bone	12,000	0.29
2	Cancellous bone	450	0.29
3	End plate	500	0.4
4	Disc-annulus	3.4	0.4
4.1	Disc-annulus hyper elastic Mooney–Rivlin	$C1 = 0.56$, $C2 = 0.14$	–
5	Disc-nucleus	1	0.49
Ligament			
6	Posterior longitudinal ligament	20	0.3
7	Anterior longitudinal ligament	54.5	0.3
8	Interspinous ligament	1.5	0.3
9	Ligamentum flavum	1.5	0.3
10	Capsular ligament	1.5	0.3

3 FEA Validation

In order to validate the FE model for the predicted physiological motion various boundary condition was compared against the values reported in the following literature [2]. In the lower surface of C5, all the degree of freedom was constrained. To simulate the range of motion a pure moment of 1 Nm is applied at the top of the C4 vertebrae in the three planes. The validation of the FE model was performed in ANSYS-19.0.

4 FE Analysis

In the simulation, the physiological motion was compared with the literature and validated. The elastic property model was validated with the experimental results as shown in Fig. 3. In this study, the elastic model material property and the hyperelastic material properties were compared. The intervertebral disc was considered as elastic and hyperelastic model was modelled. The material properties for hyperelastic Mooney–Rivlin was assigned from [4]. After solving with the assigned boundary condition the stress distribution across the disc needs to be studied.

Table 2 Ligament details of the finite element model

ALL		PLL		LF		ISL		CL	
D	*F*	*D*	*F*	*D*	*F*	*D*	*F*	*D*	*F*
0	0	0	0	0	0	0	0	0	0
1	35.5	0.9	1.33	1.7	2.2	1.2	0.75	1.7	2.452
2	64.9	2	29	3.74	45.9	2.7	16.9	3.9	53.6
4	89.7	3	51.4	5.61	82.9	4	24.4	5.8	87.9
5.00	108.60	4	71.38	7.48	119.6	5.4	29.5	7.7	109.4
6.00	119.60	5	85.8	9.35	133.7	6.7	32.9	9.7	125.8
		6	94.7	11.3	147.2	8.1	34.9	11.5	134.8

D Displacement in mm and *F* force in Newton

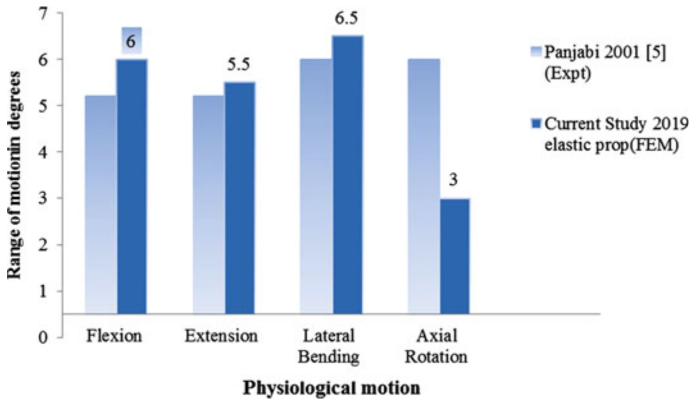

Fig. 3 Comparison of the various physiological motion of cervical spine C4–C5 level

5 Result and Discussion

5.1 *Flexion and Extension*

The response of the intact model shows a good response with the existing experimental results from [5]. In the flexion the model was more flexible and the angle is little higher than the experimental values but in the extension, while comparing with [6] the values are closer to it because it's also an FEM model as shown in Table 3. While comparing with the disc we modelled with the elastic model and hyperelastic model. In the elastic model, we measured the stresses in the anterior side and the posterior side of the annulus fibre was same. But while modelling it as a hyperelastic model, the stresses are more in the anterior side than the posterior side during flexion

Table 3 Physiological motion of C4–C5 level

Author name	Panjabi [5]	Panzer [7]	Kallemeyn [6]	Haghpanahi [8]	Erbuluta [9]	Current study
Year	2001	2009	2009	2012	2014	2019
Method	Expt	FEM	FEM	FEM	FEM	FEM
Load	1 Nm	1 Nm	1 Nm	1 Nm	1 Nm	1 Nm
Flexion	5.2	5.17	6	3.68	4	7.24
Extension	5.2	4.51	5.1	3.04	2.5	6.1
Lateral bending	6	7.62	4	1.47	5	8.1
Axial rotation	6	6.62	5.1	2.64	5.5	3.5

The values are in degree

Table 4 Stress distribution in the intervertebral disc of C4–C5 level

Intervertebral disc	Elastic properties	Hyperelastic properties
	Stress in MPa	Stress in MPa
Flexion extension	2.61	3.31
Lateral bending	3.07	4.48
Axial rotation	1.05	1.14

and during extension the stresses of the posterior side are more than the anterior side. This trend replicates the hyperelastic models shows more accuracy than the elastic models. The stresses in the disc are more in the hyperelastic model than the elastic model. The elastic and hyperelastic disc stresses are compared in Table 4 The finite element model with extension is shown in Fig. 2.

5.2 Lateral Bending

In the lateral bending, the model is flexible and its range of motion is high compared to that of the experiment values [5] but while comparing with the FEM model it is very closer to the bending results of [7]. The elastic material model exhibits the less stresses in the sides but that may due to the facet restrictions. But in the hyperelastic models, the stress distribution is more and equally distributed in both the sides anterior and posterior side. There is a significant change is observed in the top and the bottom side of the annulus fibres during lateral bending. The comparison of the elastic and hyperelastic models are shown in Table 4.

5.3 Axial Rotation

In the axial rotation, the stress the model is stiffer while comparing with the experimental results [5]. But in comparison with the [8, 9], the results are closer in the axial rotation. This may be due to multiple factors like in the axial rotation the facet plays a major role and the ligaments also provide a locking mechanism. In this, while comparing the elastic and hyperelastic model, there is no much change in the stresses because the disc will not undergo considerable tension and compression. The stress distribution in the axial rotation is shown in Table 4.

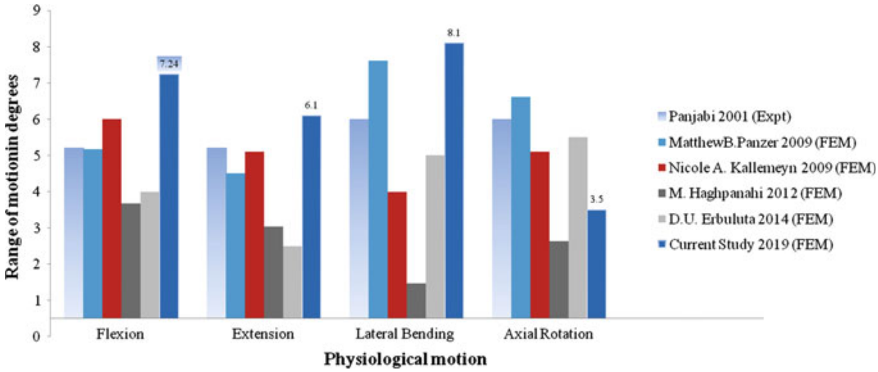

Fig. 4 Comparison of the various physiological motion of cervical spine C4–C5 level

6 Conclusion

The results are shown above clearly indicate that model shows a good agreement with the physiological motion of the functional spine unit Fig. 4. The intact finite element model was validated against the experimental study [5]. The range motion for the functional spine unit was compared. There is a significant difference was found in Von mises stress while comparing the elastic and hyperelastic material for intervertebral disc. However, by modifying the material models will help us in finding the real behaviour of the functional spine unit.

Acknowledgements This work was supported by the Bio mechanics lab, Department of Mechanical Engineering, SRMIST, Kattankulathur–603203. We thank Mr. Raja. D, Asst Professor (S. G) and Research Head, Bio mechanics lab, Department of Mechanical Engineering, SRMIST, Kattankulathur–603203 for his assistance to improve the manuscript.

References

1. Panjabi MM (1998) Cervical spine models for biomechanical research. Spine 23(24):2684–2700
2. Zhang QH, Teo E-C, Ng H-W et al (2006) Finite element analysis of moment-rotation relationships for human cervical spine. J Biomech 39:189–193
3. Gilad I, Nissan M (1986) A study of vertebra and disk geometric relations of the human cervical and lumbar spine. Spine 11:154–157
4. Schmidt H, Galbusera F, Rohlmann A, Zander T, Wilke HJ (2012) Effect of multilevel lumbar disc arthroplasty on spine kinematics and facet joint loads in flexion and extension: a finite element analysis. Eur Spine J 21 (Supp l5): S663–S674
5. Panjabi MM, Crisco JJ, Vasavada A, Oda T, Cholewicki J, Nibu K, Shin E (2001) Mechanical properties of the human cervical spine as shown by three-dimensional load–displacement curves. Spine 26(24):2692–2700
6. Kallemeyn N, Tadepalli SC, Shivanna K, Grosland N (2009) An interactive multiblock approach to meshing the spine. Comput Methods Programs Biomed 95:227–235

7. Panzer MB, Cronin DS (2009) C4–C5 segment finite element model development, validation, and load-sharing investigation. J Biomech 42:480–490
8. Haghpanahi M, Javadi M (2012) A three dimensional parametric model of whole lower cervical spine (C3–C7) under flexion, extension, torsion and lateral bending. Scientia Iranica B 19(1):142–150
9. Erbulut DU, Zafarparandeh I, Lazoglu I et al (2014) Application of an asymmetric finite element model of the C2–T1 cervical spine for evaluating the role of soft tissues in stability. Med Eng Phys 36:915–921

Simulation and Analysis of Integrated SEPIC-Flyback AC-DC PFC Converter for LED Applications

Sridhar Makkapati and Seyezhai Ramalingam

Abstract Light Emitting Diode (LED) inherently acts as a diode which allows the current in one direction and this can be achieved by AC-DC converter. It is essential to have sinusoidal input current wave shape and constant load current to drive the LED without any flicker. Integration of Single Ended Primary Inductor Converter (SEPIC) and Flyback converter act as an LED drive. Both these converters are operated in discontinuous conduction mode for supplying LED to achieve the unity power factor. It is compared with conventional SEPIC and Flyback topology. Analysis and simulation of 100 W LED module from 100 V_{P-P}/50 Hz ac supply are analyzed and their results are presented using MATLAB-Simulink.

Keywords LED · SEPIC · Flyback converter · Power factor

1 Introduction

Light emitting diode is energy efficient and predominant light source to replace the traditional sources like fluorescent and discharge lamps. It is due to several advantages such as a predominant lifetime over 1,00,000 h during appropriate operating conditions, a high light output of more than 150 lm/w [1], pollution-free and availability of multicolor variants. LED is employed for applications such as automotive applications, street lighting, and decorative lighting [2]. But the LED also suffers from several issues of concern unlike conventional luminaries such as driver circuit is essential to drive LED, in which elimination of electrolytic capacitor (E-cap) [3] in ballast design [4], lesser in size, economical, high efficiency, and necessary to meet the IEC standards for LED lighting [5, 6], galvanic isolation and proper current sharing control. Various methodologies have been introduced in the literature to solve the aforementioned problems.

S. Makkapati (✉) · S. Ramalingam
Renewable Energy Conversion Laboratory, Department of EEE, Sri Sivasubramania Nadar (SSN) College of Engineering, Kalavakkam, Chennai 603110, India
e-mail: sridhar.makkapati2@gmail.com

E. T. Akinlabi et al. (eds.), *Trends in Mechanical and Biomedical Design*, Lecture Notes in Mechanical Engineering,
https://doi.org/10.1007/978-981-15-4488-0_54

Passive LED driver circuits without active switches are initially introduced, with series limiting resistor circuit [7], and valley fill circuit [8] however these circuits are repulsive because of their bulky size, high cost and lack of output current regulation. In order to operate in several high-frequency applications, switched-mode driver circuits with smaller size and precise current control are suggested with single-stage [9], two-stage [10], and three stages [11]. Single-stage involves only a single switch with one processing stage which performs both PFC and current regulation simultaneously. But the major hardship in this stage is the output electrolytic capacitor (E-cap) lifetime is lesser than the lifetime of LED. Two-stage drivers consist of two processing stage where one stage is for PFC and the other performs the output current regulation whereas the size and cost is the issue. Three-stage topology is suitable for multi-string usage in which the initial two act as previous while the third stage performs the equal current sharing among the strings.

For non-isolated applications, single-stage topologies such as buck [12], buck-boost [13], SEPIC [14] and Cuk [15] are employed. In order to achieve high conversion ratio using isolated flyback [16], half-bridge [17], and push-pull converter [18] are proposed. Several combinations of isolated [19], non-isolated [20], and resonant converters [21] are suggested as integrated topologies. An integrated boost-buck topology is suggested in [22] with two active switches increased the complexity, boost-forward converter is suggested where the switch poses the voltage spikes during its off state. In reference [23] Boost-flyback integrated topology is proposed with the additional winding on flyback that supports the reduction in the bulk capacitor at the output. In this paper single-stage single switch, PFC SEPIC with flyback converter is suggested without E-cap at the output.

The flow of this paper is as follows. Section 2 elaborates on the operation of SEPIC-Flyback PFC converter. Its design steps are discussed in Sect. 3 and Sect. 4 presents the comparison of non-isolated SEPIC, isolated flyback with integrated SEPIC-Flyback converter simulation results. Finally, Sect. 5 presents the conclusion.

2 Operation of Integrated SEPIC-Flyback PFC Converter

Integrated SEPIC-Flyback converter operation is discussed in this section with its modes of operation. In order to achieve near unity power factor during the LED driving process, SEPIC converter is integrated with Flyback converter as shown in Fig. 1, however, both the converters operate in discontinuous conduction mode (DCM). Non-isolated SEPIC converter consists of L_{in}, C_B, L, C, and D_1; while the flyback converter includes a transformer T, D_2, D_o are the diodes and the output capacitor C_o. These two converters share a common switch with SEPIC converter that acts as a PFC circuit and DCM flyback performs the DC regulation. Transformer model is represented using magnetizing inductance Lm and an ideal transformer.

SEPIC-Flyback circuit consists front end diode rectifier and its output is fed to integrated SEPIC and Flyback circuit. Operating modes with six different time instants are explained. An assumption is made that switch is ideal and the higher

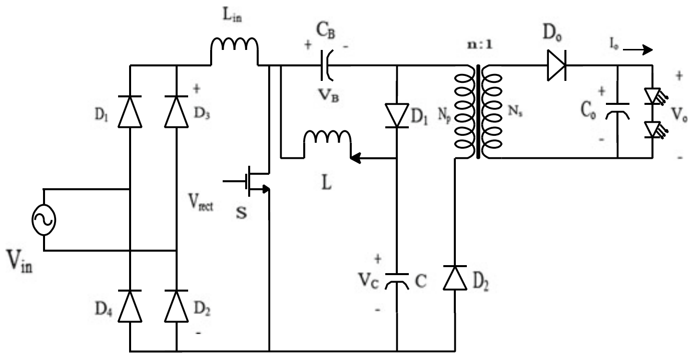

Fig. 1 Circuit diagram of SEPIC-flyback LED driver

switching frequency is chosen for the semiconductor device. Transformer turns ratio $n = N_p/N_s$. Figure 2 shows the waveforms corresponding to one switching cycle during different time instants.

Initially, it is assumed that all the switching devices are lossless and load current is flown from the output capacitor. Operation of above mentioned integrated topology is explained below.

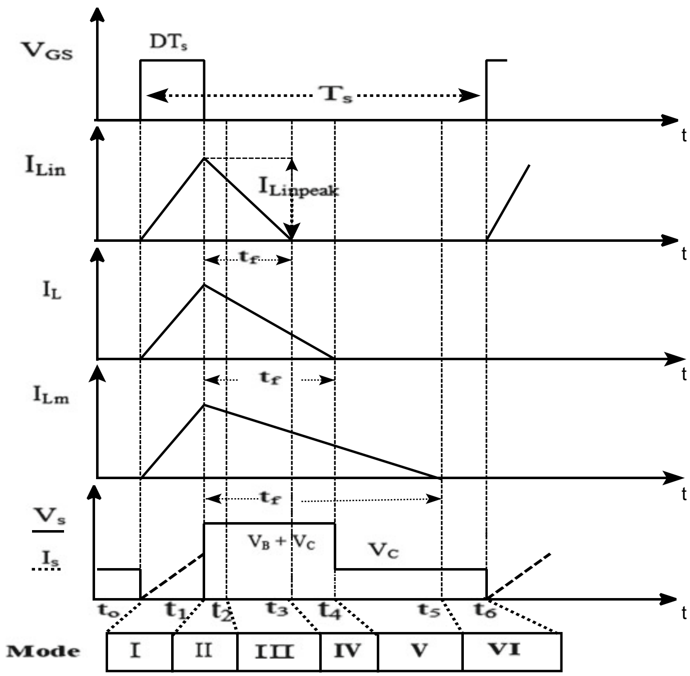

Fig. 2 Waveforms during a switching period

Mode I [$t_o < t < t_1$]: Switch S turns on in this mode and the rectified output e is applied to the input inductor L_{in}, voltages V_C and V_B are applied to L and L_m respectively. This allows the current I_{Lin}, I_L, I_{Lm} to increase linearly from zero. DT_s is the switch S on time and assure the zero current switching of the device. Diodes D_1 and D_o are reverse biased and this mode terminates after the period DT_s.

Mode II [$t_1 < t < t_2$]: Switch S initially turns off during this period and the diodes D_1 and D_o are forward biased. Due to D_1 conduction voltage across the switch is $V_B + V_C$ and the voltage $V_c - nV_o$ is inversely applied across the L_{lk} and the leakage energy is absorbed. The difference in leakage current and magnetizing current I_{Lm} forward biases the diode D_o at zero current switching and diode D_2 turns off.

Mode III [$t_2 < t < t_3$]: During this mode, I_{Lin}, I_L and I_{Lm} decrease linearly and the D_2 diode is turned on. The voltage across the inductors L_{in} and L are—($V_B + V_C V_{rect}$) and $-V_B$ respectively.

Mode IV [$t_3 < t < t_4$]: D_1 and D_o are conducting and leakage and magnetizing currents decrease. Current through inductor I_L becomes zero at the end of this period and D_1 turns off in this mode of operation.

Mode V [$t_4 < t < t_5$]: In this mode diode D_1 is in off state and switch voltage falls to V_C. I_{Lm} current still decreases and the remaining inductor currents fall to zero. Diode D_o get reverse bias at the lapse of this mode.

Mode VI [$t_5 < t < t_6$]: In this mode, the semiconductor switch is turned off the current through the load is driven by the output capacitor. This operation persists until the switch turns on again.

3 Analysis and Design Consideration of SEPIC-Flyback Converter

Design of SEPIC-Flyback converter with a sinusoidal line voltage $V_{in}(t) = V_m \sin \omega_l(t)$ where ω_l is line frequency $2\pi f_l$ Average line current that flows through inductor L_{in} over a switching period T_s is given as

$$I_{\text{in avg}}(t) = \frac{1}{T_s}\frac{1}{2}(\mathrm{DT}_s + t_{\text{fLin}})I_{\text{Linpeak}} \tag{1}$$

The peak inductor current I_{Linpeak} and is given as

$$I_{\text{Linpeak}} = \frac{V_m \mathrm{DT}_s}{L_{in}} \sin \omega_l(t) \tag{2}$$

The fall time of inductor peak current t_{fLin} that reaches to zero and is calculated as

$$t_{\text{fLin}} = \frac{V_m \sin \omega_l(t)}{V_B + V_C - V_m \sin\ \omega_l(t)} \mathrm{DT}_s \tag{3}$$

Average line current substituting Eqs. (3) and (2) in Eq. (1)

$$I_{\text{in avg}}(t) = \frac{V_m D^2 T_s}{2L_{in}} \frac{V_B + V_C}{V_B + V_C - V_m \sin \omega_l(t)} \sin \omega_l(t) \tag{4}$$

Line current depends on V_B+ V_C and its value is more than V_m
By using Eq. (4) average input power is given by

$$\begin{aligned} P_{\text{in}} &= \frac{V_m^2 D^2 T_s}{2\pi L_{\text{in}}} \int_0^{\pi} \frac{(V_B + V_C)\sin^2 \theta}{V_B + V_C - V_m \sin \theta} \mathrm{d}\theta \\ &= \frac{k V_m^2 D^2 T_s}{2\pi L_{\text{in}}} \end{aligned} \tag{5}$$

where k is a function of V_m & $V_B + V_C$
Neglecting converter losses

$$P_{\text{in}} = P_o \tag{6}$$

Input inductor is obtained as

$$L_{\text{in}} = \frac{k D^2 V_m^2}{2\pi f_s P_o} \tag{7}$$

By selecting f_s and P_0 choose the value of input inductor
Power delivered to load, i.e. output power is

$$P_o = \frac{1}{2} L_m I_{\text{Lmpeak}}^2 f_s \tag{8}$$

where

$$I_{\text{Lmpeak}} = \frac{V_B D T_s}{L_m} \tag{9}$$

Power output is obtained as

$$P_o = \frac{V_B^2 D^2 T_s}{2L_m} \tag{10}$$

Transformer magnetizing inductance

$$L_m = \frac{V_B^2 D^2}{2 f_s P_o} \tag{11}$$

Table 1 Simulation parameters of SEPIC-flyback converter

Parameter	Notation	Value
Input voltage	V_s	100 V (P-P)
Switching frequency	f_s	50 kHz
Duty cycle	D	0.1
Input inductor	L_{in}	75 μH
Inductor	L	150 μH
Magnetising inductor	L_m	130 μH
Turns ratio	n:1	1:1
Capacitor	C	4.7 μF
Capacitor	C_B	4.7 μF
Output capacitor	C_o	2*4.7 μF
Output power	P_o	100 W

For DCM, the turns ratio is selected based on the rate of fall of magnetizing current. Design formulae for L, C, C_B, and C_o are as follows

$$L = \frac{\pi V_c(V_B + V_c)}{kV_m^2} L_{\text{in}} \tag{12}$$

$$C = \frac{Q_C}{\Delta V_C} \quad \Delta_c \text{ is low-frequency voltage ripple} \tag{13}$$

$$C_B = \frac{Q_B}{\Delta V_B} \quad \Delta_B \text{ is low-frequency voltage ripple} \tag{14}$$

$$C_o = \frac{(nV_B DT_S - L_m I_0)^2}{2n^2 L_m V_o \Delta V_0} \tag{15}$$

where Δ_o is high-frequency output capacitor voltage ripple

Based on the above design Eqs. (1–15), the simulation parameter values are computed and presented in Table 1.

4 Simulation Results and Comparative Analysis

In order to verify the design equations, the results are simulated using MATLAB–Simulink for 100 W power rating driven with a voltage source of 100 $V_{\text{P-P.}}$ The input side parameters are majorly concentrated to obtain a high power factor and lesser Total harmonic distortion (THD). The suggested topology is compared with the discontinuous conduction of SEPIC and Flyback converter. Simulated circuit for SEPIC-Flyback is represented in Fig. 3.

Input voltage and current waveform and input inductor current are shown in Figs. 4 and 5 respectively and it resembles that the converter is operating in the discontinuous

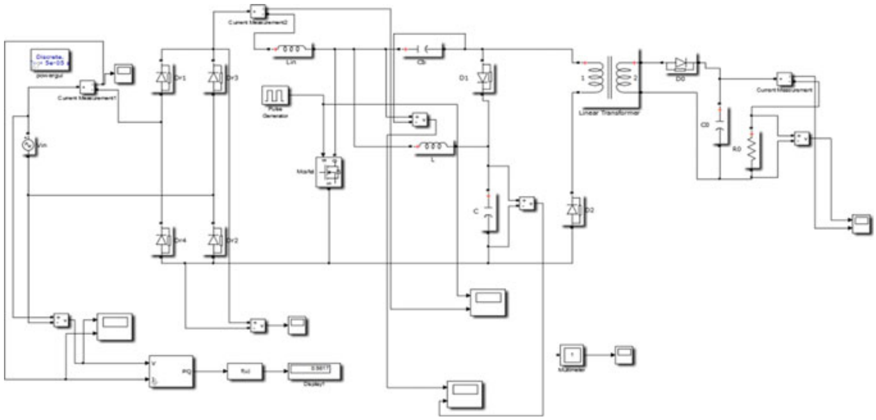

Fig. 3 Simulation circuit of SEPIC-Flyback converter

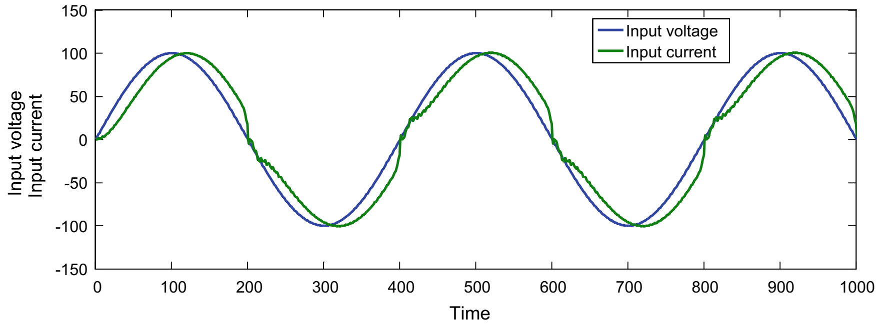

Fig. 4 Input AC voltage and current of the integrated converter

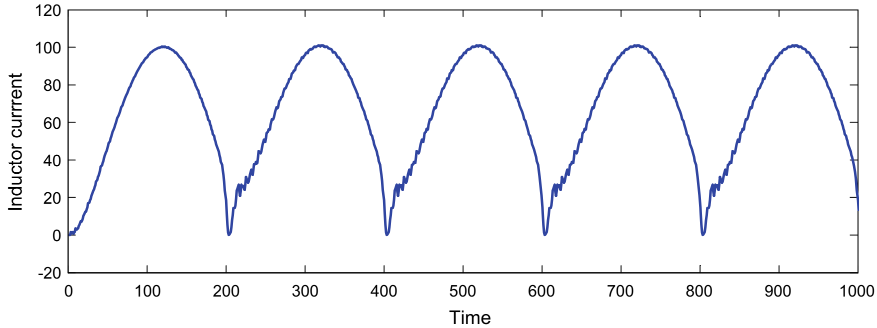

Fig. 5 Input inductor current of the integrated converter

mode as the current through inductor reached zero. Based on the measured harmonics with a single-phase ac supply power factor is 0.98 and THD of the simulated circuit is 9.36% and is shown in Fig. 6.

In order to compare the suggested SEPIC-Flyback with isolated flyback and Non-isolated SEPIC converter under discontinuous mode to drive the LED is simulated with the designed parameters. Input current and voltage waveforms of both fly-back and SEPIC in DCM operation are shown in Figs. 7 and 8 respectively. Their comparison is shown in Table 2.

Table 2 Infers that SEPIC-Flyback integrated topology produces less harmonic distortion and better power factor in comparison with the DCM SEPIC and DCM Flyback converter.

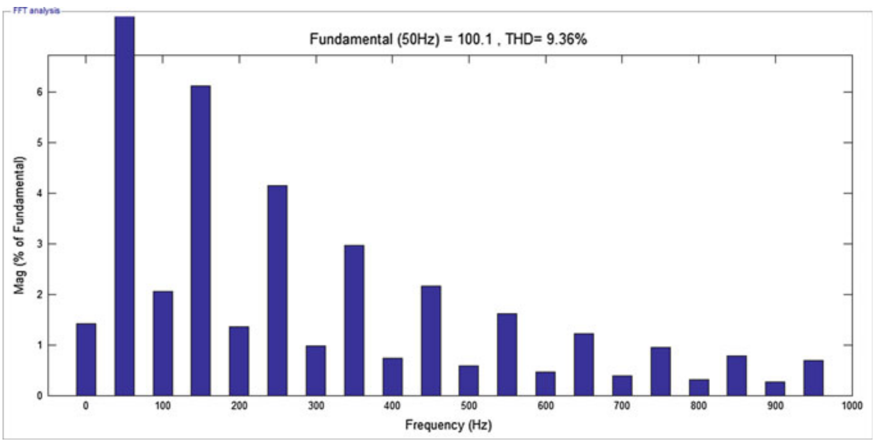

Fig. 6 Supply current FFT spectrum

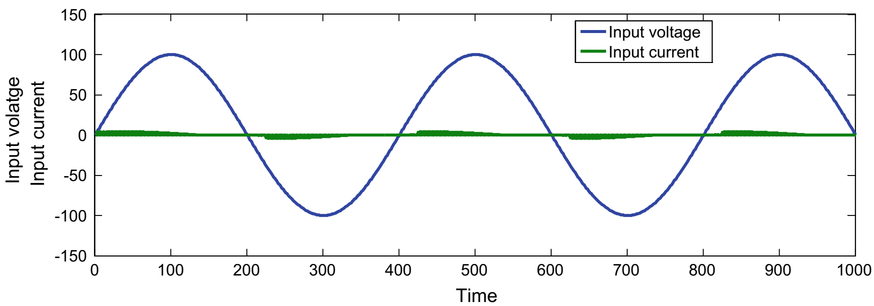

Fig. 7 Input AC voltage and current of DCM flyback converter

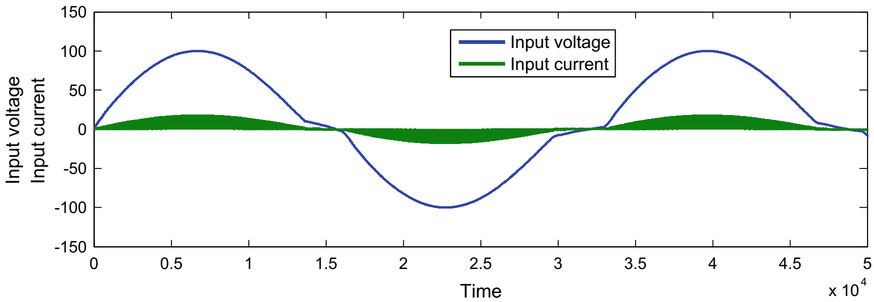

Fig. 8 Input AC voltage and current of DCM SEPIC converter

Table 2 Comparison of input parameters

Topology	Power factor	THD (%)	Distortion factor
SEPIC converter-DCM	0.975	65.7	0.83
Flyback converter-DCM	0.859	121.15	0.63
SEPIC-flyback converter	0.980	9.38	0.99

5 Conclusion

In this paper single-stage, SEPIC integrated flyback converter is investigated in detail with its design equations. This converter, when fed from AC source, achieves better power factor with lesser total harmonic distortion compared to flyback and SEPIC converter topologies. In the proposed topology, both the converters operate in DCM and leakage energy is fed back by the magnetizing reactance of flyback converter and SEPIC converter for active PFC with the lesser output capacitor.

References

1. Schubert EF (2006) Light-emitting diodes, 2nd edn. Cambridge Univ. Press, Cambridge, U.K
2. Chen W, Hui SR (2012) Elimination of an electrolytic capacitor in AC/DC light-emitting diode (LED) driver with high input power factor and constant output current. IEEE Trans Power Electron 27(3):1598–1607
3. Linlin G, Xinbo R, Ming X, Kai Y (2009) Means of eliminating electrolytic capacitor in AC/DC power supplies for LED lightings. IEEE Trans Power Electron 24:1399–1408
4. Electromagnetic compatibility (EMC) (1995)—part 3: limits-section 2: limits for harmonic current emissions (equipment input current < 16 A per phase), IEC1000-3-2
5. ENERGY STAR Program Requirements for Solid State Lighting Luminaires http://www.energystar.gov/index.cfm?c=new_specs.ssl_luminaires

6. Hui SYR, Li SN, Tao XH, Chen W, Ng WM (2010) A novel passive offline LED driver with long lifetime. IEEE Trans Power Electron 25(10):2665–2672
7. Gunabalan R (2016) Overview of passive light emitting diode driver circuits for street lighting. Bull Electr Eng Inform 5(3)
8. TianFu P, HuangJen C, ShihJen C, ShihYen C (2007) An improved single-stage flyback PFC converter for high-luminance lighting LED lamps. In: 8th international conference on electronic measurement and instruments
9. Kim BC, Park KB, Kim CE, Lee BH, Moon GW (2010) LLC resonant converter with adaptive link-voltage variation for a high-power density adapter. IEEE Trans Power Electron 25(9):2248–2252
10. Almeida PS, Braga HAC, Dalla Costa MA, Alonso JM (2015) Offline soft-switched LED driver based on an integrated bridgeless boost–asymmetrical half-bridge converter. IEEE Trans Ind Appl 51(1):761–769
11. Milashevski I, Galkin I, Tetervenok O (2012) Assessment of buck converter powered by current or voltage sources for LEDs luminary. In: 13th Biennial Baltic electronics conference
12. Lin RL, Lee CC, Chang YC (2011) Optimal design of LED array for single-loop CCM buck-boost LED driver. IEEE Ind Appl Soc Annu Meet
13. Shen CL, Wu YE, Tsai CT (2011) Coupled-inductor sepic-type PFC with soft-switching feature for LED lighting applications. In: 6th IEEE conference on industrial electronics and applications, Beijing, pp 2384–2389
14. de Britto JR, Demian AE, de Freitas LC, Farias VJ, Coelho EAA, Vieira JB (2008) A proposal of led lamp driver for universal input using Cuk converter. In: 2008 IEEE power electronics specialists conference, Rhodes, pp 2640–2644
15. Gacio D, Alonso JM, Calleja AJ, Garcia J, Rico-Secades M (2011) A universal-input single-stage high power-factor power supply for HB-LEDs based on integrated buck–flyback converter. IEEE Trans Ind Electron 58(2):589–599
16. Lamar DG, Zuniga JS, Alonso AR, Gonzalez MR, Alvarez MMH (2009) A very simple control strategy for power factor correctors driving high-brightness LEDs. IEEE Trans Power Electron 24(8):2032–2042
17. Castro I, Martin K, Lamar DG, Arias M, Hernando MM, Sebastian J (2016) Single-stage AC/DC dual inductor BCM current-fed push-pull for HB-LED lighting applications. IEEE Energy Convers Congr Expo (ECCE)
18. Lu DDC, Lu HHC, Pjevalica V (2009) Single-stage AC/DC boost–forward converter with high power factor and regulated bus and output voltages. IEEE Trans Ind Electron 56(6):2128–2132
19. Ye Z, Greenfeld F, Liang Z (2008) Design considerations of a high power factor SEPIC converter for high brightness white LED lighting applications. In: IEEE power electronics specialists conference
20. Wang Y, Huang J, Wang W, Xu D (2016) A single-stage single-switch LED driver based on class-E converter. IEEE Trans Ind Appl 52(3):2618–2626
21. Cheng HL, Lin CW (2014) Design and implementation of a high-power factor LED driver with zero-voltage switching-on characteristics. IEEE Trans Power Electron 29(9):4949–4958
22. Lin W, Chen H, Ke S (2016) Research on a single-stage flyback/boost LED driver with lower output ripple. In: 2016 IEEE 2nd annual southern power electronics conference
23. Ding X, Yu D, Song Y, Xue B (2017) Integrated switched coupled-inductor boost-flyback converter. In: 2017 IEEE energy conversion congress and exposition

Simulation Study of Shading Effects in PV Array

S. Harika, R. Seyezhai, and A. Jawahar

Abstract The PV panels are interconnected in SP configuration in order to achieve a higher voltage. The SP configuration of PV string may undergo both objective and subjective partial shading situations which reduces the generated maximum output power. Thus, the research work carried out the analysis of PV array rated 1500 W for different shading patterns like row-wise and column-wise partial shading. The behavior of solar array is also studied under different irradiation levels and different degrees of shading. The behavior of PV string characteristics for with and without bypass diode under different shading scenarios has also been analyzed using MATLAB/SIMULINK. The performance parameter of a solar array such as power loss, fill factor and a maximum power of the PV string is evaluated and compared. From the analysis, it is inferred that the generated output power gets deteriorated for low irradiation level and low degree of shading. The results are verified.

Keywords Partial shading condition · Row-wise shading · Column-wise shading · Power loss · Bypass diode

1 Introduction

Nowadays, renewable energy resources have emerged as an attractive solution for the problem of high electricity demand and serious environmental hazards caused by the existing conventional resources. In that photovoltaic renewable energy resources is widely used as it is environmentally friendly and available abundant in nature. The photovoltaic (PV) panel directly converts solar energy into electrical power. But for high power applications, the PV panels have to be configured in SP model to

S. Harika (✉) · R. Seyezhai
Department of Electrical and Electronics Engineering, REC Lab, Sri Sivasubramania Nadar (SSN) College of Engineering, Kalavakkam, Chennai, India
e-mail: sriharkal@gmail.com

A. Jawahar
Department of Electronics and Communication Engineering, Sri Sivasubramania Nadar (SSN) College of Engineering, Chennai, India

E. T. Akinlabi et al. (eds.), *Trends in Mechanical and Biomedical Design*, Lecture Notes in Mechanical Engineering,
https://doi.org/10.1007/978-981-15-4488-0_55

Fig. 1 SP configuration of 1.5 W PV array

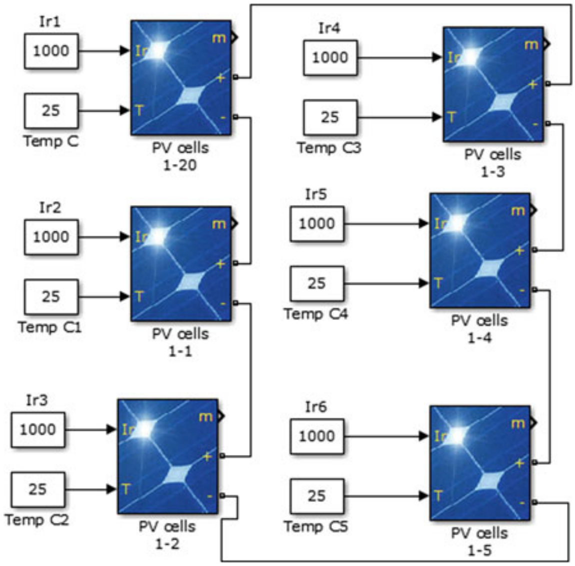

increase the output power since the output power of the single PV panel is low [1]. The solar cells or solar panel in the array receives different irradiation and mismatch between the cells or panels due to shading effects which may affect the generated output power. The partial shading is due to poor weather conditions, dust, building, etc. Many researchers and scientists focus to improve the performance of PV even under partial shading conditions [2]. Thus the paper examines the performance of 1500 W PV array under different (row-wise and column-wise partial shading) partial shading scenarios through voltage versus current curve and power versus voltage curve. Bypass diode plays a major role in partial shading which prevents hot spots and reduces the thermal stress. Thus the impact of the bypass diode on PV array is also studied using MATLAB/SIMULINK. The SP configuration of 1500 W photovoltaic array is shown in Fig. 1.

2 Partial Shading

The interconnection of PV in the array will undergo shading due to building, trees, birds, dust and poor weather condition. The partial shading of solar panel is considered to be a more critical issue because the shaded cell consumes power from unshaded cells since it gets reverse bias, this leads to the reduction of output power from PV array. It will increase the heating and thermal stress and results in hot-spot [3, 4]. The partial shading of the solar array is characterized through the V-I and P-V characteristics. There are different types of partial shading, this research work focuses on row-wise and column-wise partial shading for 1.5 kW PV array.

2.1 Row-Wise Partial Shading

In row-wise partial shading, the last row of the 2 × 3 PV array is fully shaded by maintaining all other PV panels at full illumination (1000 W/m^2). If an entire row gets shaded, then the sum of photonic current is less than the array current which in turn leads to dissipate the power generated by remaining rows.

2.2 Column-Wise Partial Shading

In column-wise partial shading, the first column of the 2 × 3 PV array is fully shaded by maintaining all other PV panels at full illumination (1000 W/m^2). Due to shading, the amount of voltage required to produce output current is reduced which will further reduce the array output voltage and increase the power loss.

3 Simulation Results

The PV panel rating of 1.5 kW (V_{oc} = 112.2 V, I_{sc} = 17.26 A, V_{mp} = 92.1 V, I_{mp} = 16.3 A) is modeled in MATLAB/SIMULINK. The impact of bypass diode on PV array for both row-wise and column-wise partial shading has been analyzed through *V-I* characteristics and *P-V* characteristics and its performance is evaluated under different shading scenarios. The performance parameter such as row voltage, open-circuit voltage (V_{oc}), short-circuit current (I_{sc}), maximum power (P_{max}), fill factor and power loss is evaluated for both with and without bypass diode [5–9] under different shading level and different illumination is depicted in Tables 1, 4.

Table 1 Row-wise shading with bypass diode

Shading level (%)	Irradiation (W/m^2)	Row voltage I (V)	Row voltage II (V)	Row voltage III (V)	V_{oc} (V)	I_{sc} (A)	P_{max} (W)
100	1000	37.4	37.4	0	74.8	17.32	975
	600	36.63	36.63	0	73.26	10.4	585
	300	35.59	35.59	0	71.18	5.2	290
60	1000	37.4	37.4	36.02	110.82	17.32	975
	600	36.63	36.63	36.02	109.28	10.4	650
	300	35.59	35.59	36.02	107.2	6.93	458
20	1000	37.4	37.4	37.06	111.86	17.32	1280
	600	36.63	36.63	37.06	110.32	13.86	928
	300	35.59	35.59	37.06	108.24	13.85	470

Table 2 Row-wise shading without bypass diode

Shading level (%)	Irradiation (W/m^2)	Row voltage I (V)	Row voltage II (V)	Row voltage III (V)	V_{oc} (V)	I_{sc} (A)	P_{max} (W)
100	1000	37.4	37.4	0	74.8	11.4	450
	600	36	36	0	72	6.9	175
	300	25	25	0	50	3.5	40
60	1000	37.4	37.4	10.2	85	13.7	600
	600	36	36	10	82	9.2	300
	300	35	35	8	78	5.7	120
20	1000	37.4	37.4	14.2	89	16	750
	600	36	36	11	83	11.5	450
	300	35	35	10	80	8	230

Table 3 Column-wise shading with bypass diode

Shading level (%)	Irradiation (W/m^2)	Row voltage I (V)	Row voltage II (V)	Row voltage III (V)	V_{oc} (V)	I_{sc} (A)	P_{max} (W)
100	1000	37.4	37.4	37.4	112.2	8.6	740
	600	36.63	36.63	36.63	109.89	5.2	448
	300	35.59	35.59	35.59	106.77	2.6	220
60	1000	37.4	37.4	37.4	112.2	12.1	1040
	600	36.63	36.63	36.63	109.89	8.66	744
	300	35.59	35.59	35.59	106.77	6	515
20	1000	37.4	37.4	37.4	112.2	15.6	1340
	600	36.63	36.63	36.63	109.89	12.1	1040
	300	35.59	35.59	35.59	106.77	9.52	820

Table 4 Column-wise shading without bypass diode

Shading level (%)	Irradiation (W/m^2)	Row voltage I (V)	Row voltage II (V)	Row voltage III (V)	V_{oc} (V)	I_{sc} (A)	P_{max} (W)
100	1000	20	30	30	80	8.6	270
	600	10	30	30	70	5.1	100
	300	10	10	20	40	2.6	25
60	1000	25	30	30	85	12	500
	600	22	30	30	82	8.6	270
	300	15	20	30	65	6	135
20	1000	28	30	30	88	15.4	715
	600	26	30	30	86	12	500
	300	22	30	30	82	9.4	320

The analysis of 1500 W PV array under row-wise shading for both with and without bypass diode model is depicted in Tables 1, 2 in which the maximum power of 1280 W is achieved for with bypass diode model under 20% shading at 1000 W/m^2 whereas for the same condition, the without bypass diode configuration achieves only 750 W. For 60 and 100% shading at 1000 W/m^2, the maximum power of 975 W is achieved for with bypass diode model whereas for the same condition the without bypass diode model attains only the maximum power of 600 and 450 W.

The performance of 1500 W PV array under column-wise shading for both with and without bypass diode model is depicted in Tables 3, 4 in which the maximum power of 1340 W is achieved for with bypass diode under 20% shading at 1000 W/m^2 whereas, for the same scenario, the without bypass diode configuration achieves only 715 W. For the same irradiation level and with 60% shading, the with and without bypass diode model achieves 1040 and 500 W whereas, with 100% shading, the maximum power of 740 and 270 W is attained for with bypass diode and without bypass diode configuration.

The effect of shading on the photovoltaic array is clearly studied and presented in the table. In addition to that, the pictorial representation of fill factor and power loss variation for the above-mentioned scenarios is also depicted. The variation in fill factor under variable irradiation and for the different degrees of shading is shown in Figs. 2 and 3.

Figure 2 shows, the fill factor impacts for row-wise shading. The fill factor of 0.75, 0.5 and 0.66 is achieved under 100,60 and 20% shading at 1000 W/m^2 for with bypass diode configuration whereas for the same condition the without bypass diode achieves only 0.46, 0.51 and 0.52. Figure 3 shows the fill factor impacts for column-wise shading. For 20% shading over the PV array, the with bypass diode model achieves the fill factor of 0.76 under all degree of shading level at 1000 W/m^2 whereas for the same condition the without bypass diode achieves only 0.39, 0.49 and 0.52.

The variation in the power loss under variable irradiation and for the different degrees of shading is shown in Figs. 4 and 5.

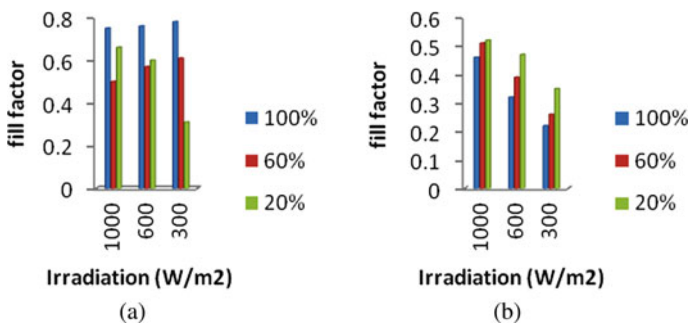

Fig. 2 **a** Row-wise shading with bypass diode and **b** row-wise shading without bypass diode

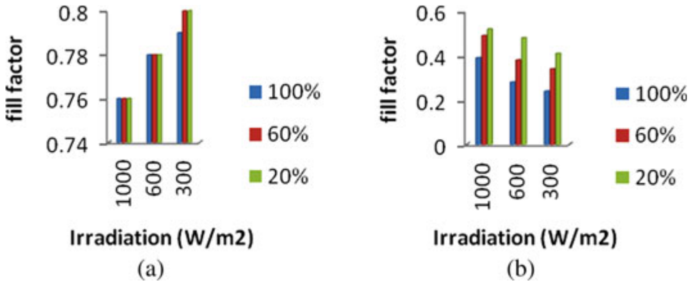

Fig. 3 **a** Column-wise shading with bypass diode and **b** column-wise shading without bypass diode

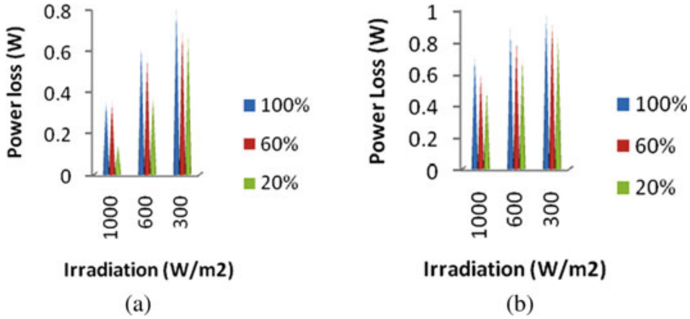

Fig. 4 **a** Row-wise shading with bypass diode and **b** row-wise shading without bypass diode

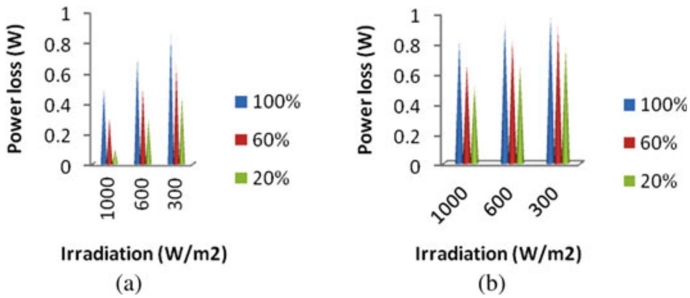

Fig. 5 **a** Column-wise shading with bypass diode and **b** column-wise shading without bypass diode

From Fig. 4, it is observed that under 20% shading at 1000 W/m^2 irradiation level, the row-wise shading has a lower power loss of 0.14 W for with bypass diode model and 0.4 W for without bypass diode configuration. And for the same irradiation level, the with bypass diode model has a power loss of 0.35 W for 60 and 100% shading whereas, for the same case, the without bypass diode has 0.56 and 0.6 W.

From Fig. 5, for the same irradiation level, the with bypass diode under column-wise shading has 0.1, 0.3, and 0.5 W for 20, 60, and 100% shading but the without bypass diode model has 0.52, 0.66, and 0.8 W for the same scenario. Thus, it is inferred that the with bypass diode model attains the maximum peak power and reduces the power loss which makes the system effective. And hence the voltage-current curve and power-voltage curve of 1.5 kW PV array for with bypass diode configuration under row-wise and column-wise partial shading for different irradiance levels and for the different degrees of shading are depicted in Figs. 6 and 7.

In Fig. 6, shading the last row of the 2 × 3 array to 20% leads to a maximum power of 1280 W at 1000 W/m^2 but if the degree of shading increases, the power drops to 290 W whereas the without bypass diode model reaches the power loss to 40 W as

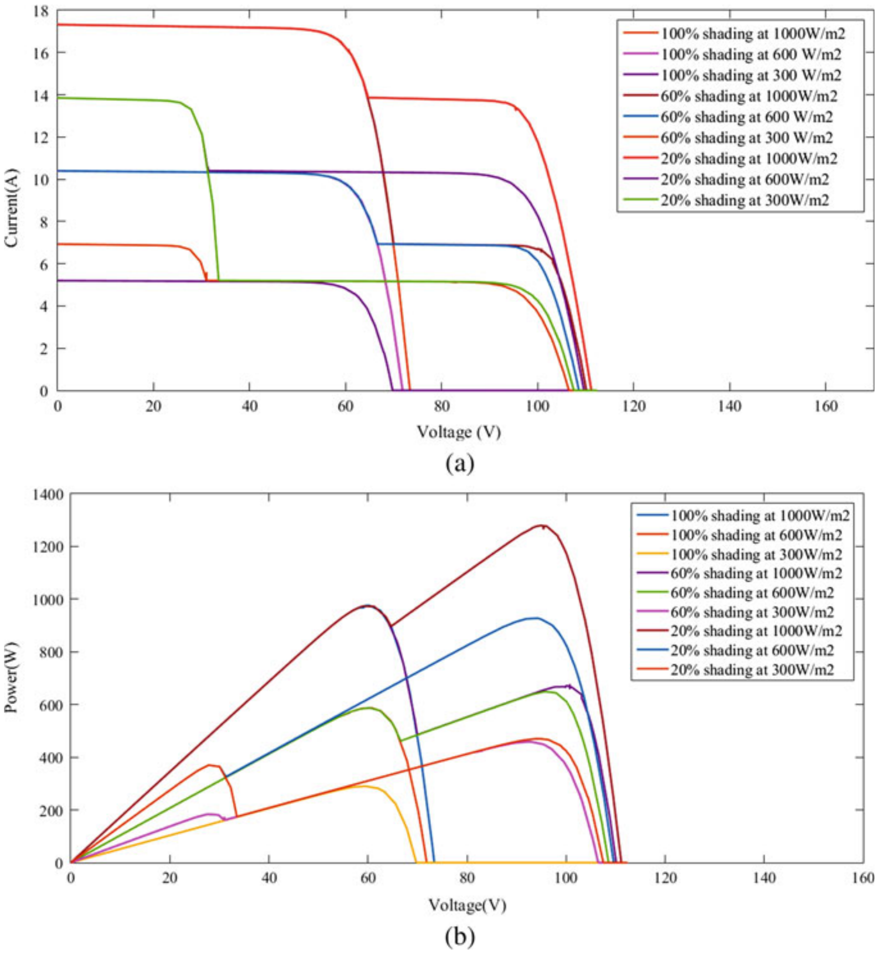

Fig. 6 **a** V-I characteristics of row-wise partial shading incorporating bypass diode and **b** P-V characteristics of row-wise partial shading incorporating bypass diode

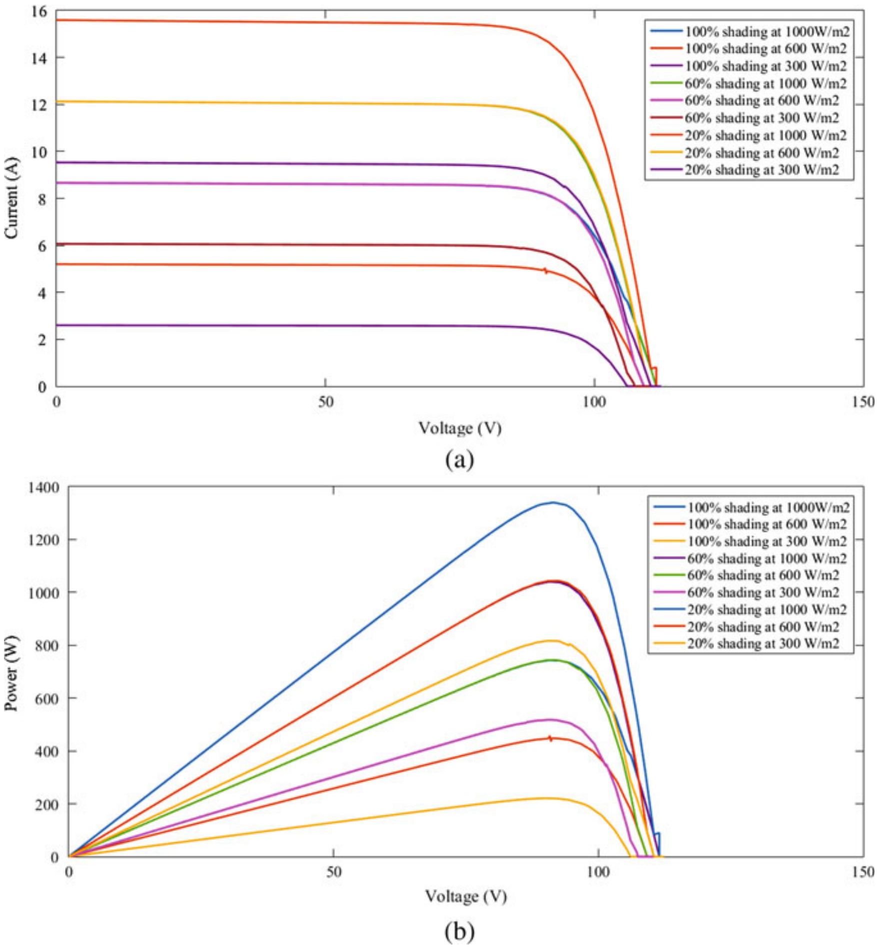

Fig. 7 **a** V-I characteristics of column-wise partial shading incorporating bypass diode and **b** P-V characteristics of column-wise partial shading incorporating bypass diode

the negative voltage is developed. In Fig. 7, 20% shading of the first column in an array results in maximum power of 1340 W at 1000 W/m^2 which is 0.6% higher than the row-wise shading for the same case. Hence the column-wise shading results in reduced power loss increased fill factor and reaches the maximum power compared to row-wise shading. Thus, it is inferred that column-wise shading is better as it has high efficiency of 89.33% than the row-wise shading.

4 Conclusion

The investigation of PV array under row-wise and column-wise partial shading conditions for different irradiation levels and for the different degrees of shading is analyzed. From the analysis, it can be observed that operating the PV array with a bypass diode under 20% of shading at full illumination (1000 W/m^2) has a better performance compared to the former method. The proposed shading method generates high peak power with reduced power loss and attains a higher fill factor value of 0.7 whereas row-wise shading reaches only 1280 W peak power. Thus the proposed column-wise shading has higher fill factor, high peak power, and reduced power loss compared to row-wise shading.

References

1. Vemuru S, Singh P, Niamat M (2012) Modeling impact of bypass diodes on photovoltaic cell performance under partial shading. IEEE Trans
2. Danish S, Mehta G, Yadav VK (2017) Assessing the performance of partially shaded photovoltaic array under different radiations. In: 8th ICCCNT 2017 3–5 July
3. Alajmi BN, Ahmed KH, Fenney SJ, Williams BW (2013) A maximum power point tracking for partially shaded photovoltaic system in micro grid. IEEE Trans Ind Electron 60(4):1596–1606
4. Batzelis E, Papathanassiou S (2016) An algorithm to detect partial shading conditions in a PV system. Mater Sci Forum 856: 303–308
5. Hu Y, Cao W, Wu J, Ji B, Holliday D (2014) Thermography-based virtual MPPT scheme for improving PV energy efficiency under partial shading conditions. IEEE Trans Power Electron 29
6. Veerapen S, Wen H, Du Y (2017) Design of a novel MPPT algorithm based on the two-stage searching method for PV systems under partial shading. In: IEEE 3rd international future energy electronics conference and ECCE Asia (IFEEC 2017–ECCE Asia), pp 1494–1498
7. Shinohara T, Uno M (2017) Micro-inverter based on quasi-Z-source inverter integrating switchless voltage equalizer for photovoltaic panels under partial shading. In: IEEE 3rd international future energy electronics conference and ECCE Asia (IFEEC 2017–ECCE Asia), pp 2013–2018
8. Moballegh S, Jiang J (2014) Modeling, prediction, and experimental validations of power peaks of PV arrays under partial shading conditions. IEEE Trans Sustain Energy 5
9. Ahmed J, Salam Z (2015) An improved method to predict the position of maximum power point during partial shading for PV arrays. IEEE Trans Ind Inform 11

Speech Recognition Using Neural Network for Mobile Robot Navigation

Prashant Patel, Arockia Selvakumar Arockia Doss, L. PavanKalyan, and Parag J. Tarwadi

Abstract Automatic speech recognition (ASR) has gained a lot of popularity in the mobile robotics, where the commands could be provided to the robot wirelessly to maneuver. A navigation system combined with ASR is a complex system to carry out, because the system has difficulty in recognizing the voice commands when the environment involved already has disturbances like road noise, air conditioner, music, and passengers. The objective of this research is to operate a mobile robot with a single-arm manipulator, where the robot can perceive the speech and it can react to the individual speech commands provided by the operator swiftly and precisely. In order to recognize the speech, mel-frequency cepstral coefficient (MFCC) speech recognition algorithm is chosen and implemented in MATLAB. Various training and testing have been done in MFCC algorithm where it has to carry out the real-time processing of speech data and respond to it. Based on both the training and testing the voice commands collected from the five test subjects both male and female, the speech recognition system achieved 89% efficiency for the test database.

Keywords Automatic speech recognition · Navigation · Mobile robot MFCC · MATLAB

1 Introduction

Speech is a characteristic wonder that happens each and every day. From an all-around early point in our lives, we become familiar with the vital abilities to utilize speech as an essential method of correspondence. Since speech comes so normally to us, it is anything but difficult to overlook how complex it truly is. It starts with

P. Patel · A. S. Arockia Doss (✉) · L. PavanKalyan
School of Mechanical Engineering, Vellore Institute of Technology, 600127 Chennai, Tamil Nadu, India
e-mail: arockia.selvakumar@vit.ac.in

P. J. Tarwadi
University of Auckland, Auckland, New Zealand

E. T. Akinlabi et al. (eds.), *Trends in Mechanical and Biomedical Design*,
Lecture Notes in Mechanical Engineering,
https://doi.org/10.1007/978-981-15-4488-0_56

lungs creating wind stream and gaseous tension. The vocal tract, comprising of the tongue, sense of taste, cheek and lips at that point well-spoken and channel the sound [1].

In the present society, individuals lean toward alternatives in innovation that improve exercises. Utilizing speech acknowledgment, clients could type content or issue gadget directions through speech. Speech acknowledgment in PCs is not even close to the speech acknowledgment capacities of the human brain. Be that as it may, maybe utilizing frameworks that imitate human brain capacities could prompt further progressions in the field. Cooperative robotics is a challenging area where the above-mentioned operations need to be performed by the robot under the supervision of an operator or user using speech as a mode of communication with the robot over a distance. Currently, cobots are growing in-demand in various fields like service, rehabilitation, search, rescue, and medical field robotics. Integration and implementation of speech recognition for the cooperative robotics are complex and the recognition of speech by the robot is difficult in the unknown environment which is influenced by many parameters like noise and disturbances, where the performance of the robot is quite unpredictable [2]. In speech recognition, following methods were proposed to extract and match the features to find optimized results: microcontroller with MAX-32 [3], MATLAB with Gaussian noise and Butterworth filter [4], hidden Markov model (HMM) with customized algorithm [5], speech-and-speaker (SAS) identification system [6], fast Fourier transform [7], hybrid artificial neural networks (ANN) [8], short utterance speaker recognition (SUSR) [9], ANN with back-propagation algorithm [10], and MFCC with vector quantization (VQ) [11]. Similarly, an overview of speech recognition techniques is summarized with merits and demerits [12].

In digital signal processing, the Mel-frequency cepstral coefficient (MFCC) and dynamic time warping (DTW) are used to extract features and compare the complex voice signal patterns [13]. A comparative performance study between linear discriminative analyzed and Mel-frequency cepstral coefficient was carried out based on feature extraction techniques. Based on the results obtained, it was found that MFCC performed better in extracting features whereas LDA showed better results in reducing the dimension of the extracted feature [14]. MFCC was found to be one of the best feature extraction techniques for Quranic [15] and Marathi speech recognition [16]. Using MATLAB, text-dependent speaker recognition was developed and MFCC was used to extract features from the speaker's signal [17].

Based on the literature survey, many researchers have carried out speech recognition techniques for various applications. The aim of this research is to find the highest speech recognition rate using neural network method and implement the speech efficiently in mobile robot where the noise level is considerably high and also adapts to the environment. Further, the work is focused to use MATLAB for an ANN model testing, training, and validation of input data used for speech recognition command from database to find the highest speech recognition rate.

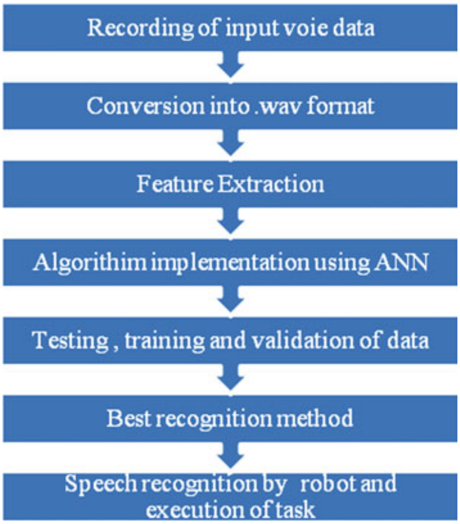

Fig. 1 ANN training and testing process

2 Feature Extraction

Figure 1 shows the proposed methodology of the research work. The MATLAB is utilized to record sound through PC receiver in a sound card. Once the wav documents are recorded, a library called Auditory Toolbox is connected with MATLAB. This library contained the quick Fourier change calculation that had chosen to use so as to retrieve one of the kind highlights from the input sound samples.

In acoustic signals, identifying and extracting the best output signals are primary importance because the performance and the efficiency of the robot is dependent on the obtained signal in this phase. Two types of filters are used in this recognition process to receive low frequency and high-frequency signals above and below 1000 Hz.

3 Training Data Preparation

Hence, to execute speech recognition with neural system, the sound documents are recorded, investigated, and controlled.

```
clc
clear all
close all
recObj = audiorecorder;
disp('Start speaking.')
recordblocking(recObj, 5);
disp('End of Recording.');
```

```
play(recObj);
myRecording = getaudiodata(recObj);
plot(myRecording);
Ft = fft(myRecording);
figure,
plot(1:numel(Ft),Ft);
```

Utilizing MATLAB characterized a sampling frequency called Fs and a term called duration. At that point, allot another wav document to a variable utilizing the wav record function. After all expected to physically trim the sound records so as to dispose of void space where no speech was spoken, so as to improve my system error rates. Utilizing this recording technique, four distinct examples of the words are recorded, for example, “Start, Stop, Pick, and place.” Five examples of each word would be put aside to test the neural system after it was assembled; the other five examples of each word were to be utilized as preparing information. Utilizing the Auditory Toolbox work called MFCC where, ready to recover the best possible coefficients that could be utilized for the proposed speech recognition technique.

Figures 2, 3, 4, 5, 6, 7, 8 and 9 show the feature extraction of the speech from the test subjects. The last part of the arrangement before making the neural system was to make the training matrix and target matrix. I shaped a framework of size 130 × 20, which is 130 highlights for 20 words, by taking the MFCC vector of each word and combining them into one matrix.

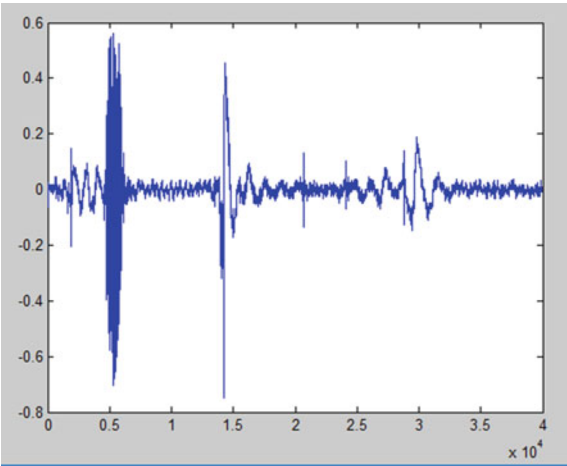

Fig. 2 Wav file of “start”

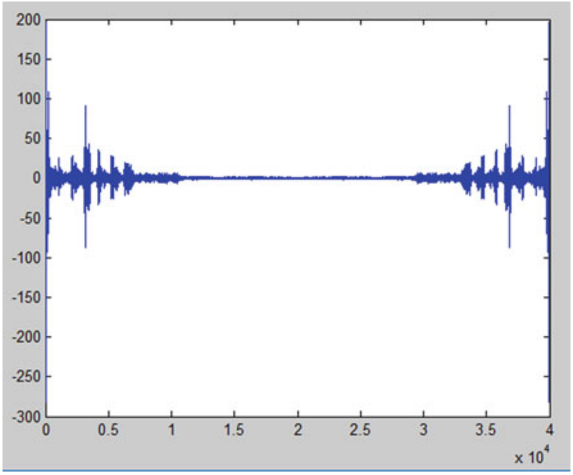

Fig. 3 FFT of "start"

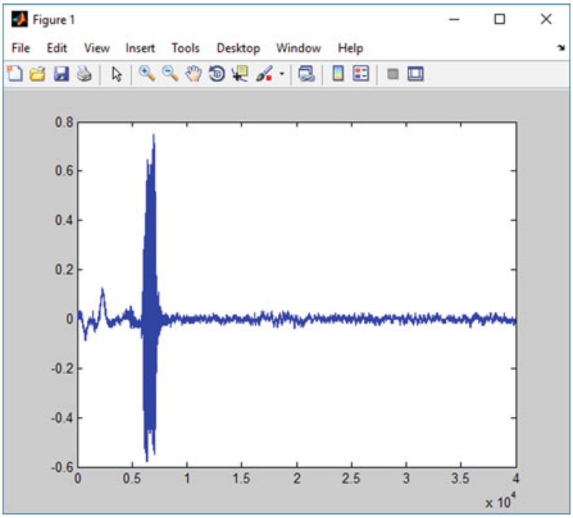

Fig. 4 Wav file of "stop"

Fig. 5 FFT of "stop"

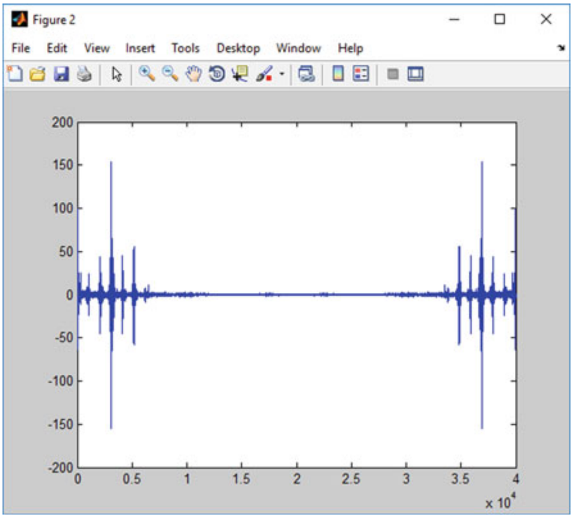

Fig. 6 Wav file of "pick"

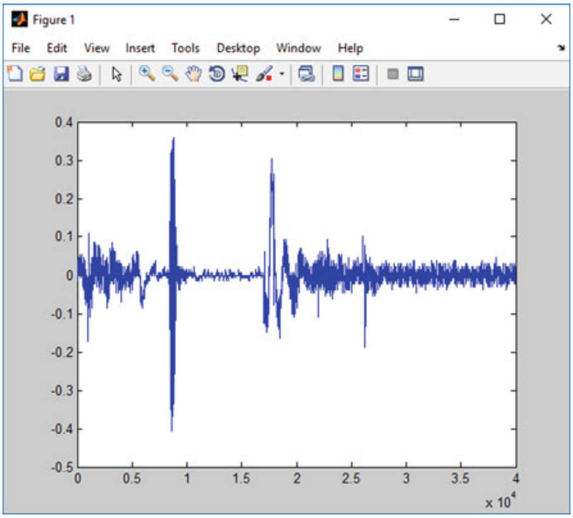

Fig. 7 FFT of “pick”

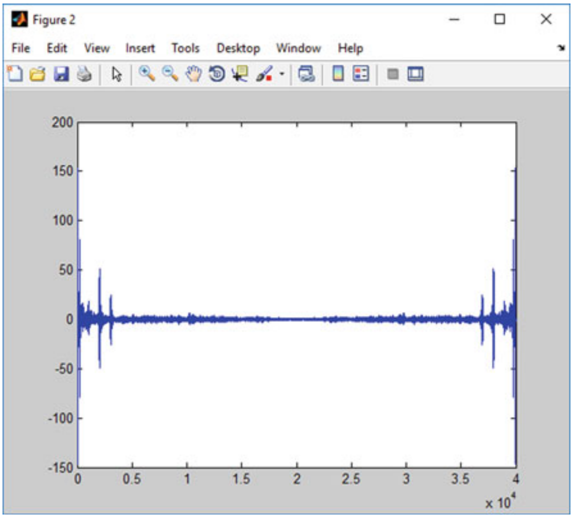

Fig. 8 Wav file of “place”

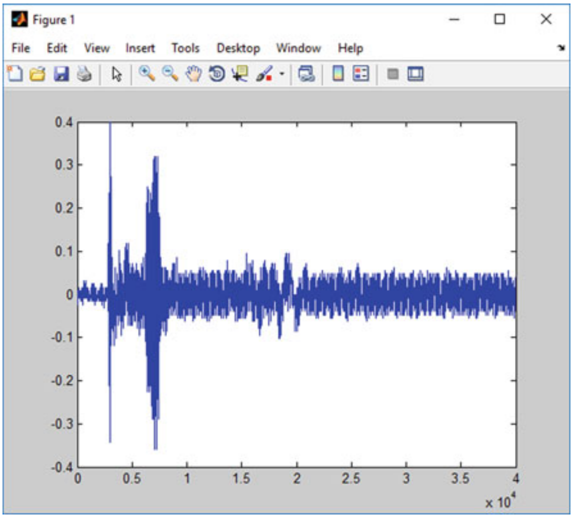

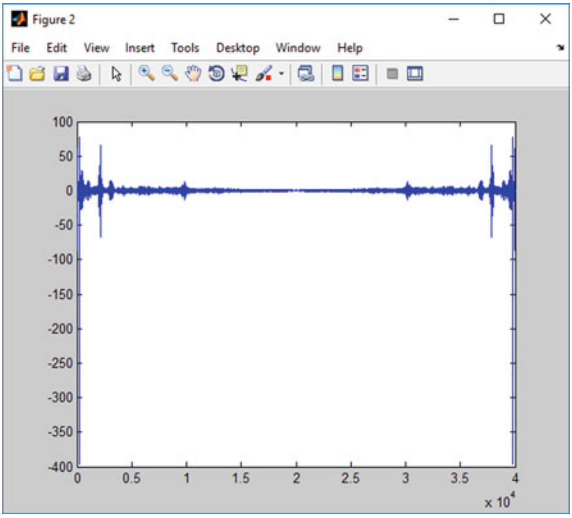

Fig. 9 FFT of "place"

4 Neural Networks in Speech Recognition

A multilayer perceptron neural network is used for speech recognition. Feed-forward systems [7] use many number of hidden layers of sigmoid neurons followed by an output layer of linear neurons. Figure 10 outlines the structure of the neural system in this project. The highlights can be the LPC coefficients or the initial three formants of each frame. The entire database comprises of: (i) five different speakers speaking at different rates; (ii) four words, for each speaker; and (iii) total number of utterances: $5 \times 4 = 20$ utterances. Table 1 shows details of the neural networks performance with numerous hidden neurons.

About 70% of the database is used for training the multilayer neural network and
115 the rest is used for testing.

Table 1 Neural networks performance with numerous hidden neurons

S. No.	ANN parameters	Values
1	Learning parameter	0.22
2	Nonlinear activation function	Tan-sigmoid
3	Maximum epoch	1000
4	Number of hidden layer	1
5	No. of nodes in hidden layer	10–80
6	Error goal	0.001
7	Target node	4

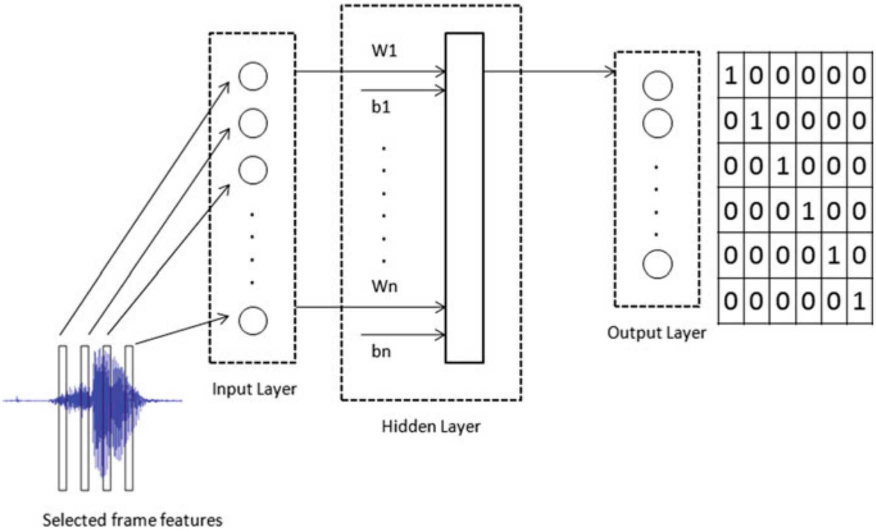

Fig. 10 Neural network architecture for speech recognition

5 Design of the Mobile Robot

The robot which is used for speech recognition is for "pick and place" mobile robot with a soft catching gripper for safe handling of the sensitive objects as shown in Fig. 11. App-based speech recognition is used for remote operation of the robot, to follow the commands sent by the user like forward, backward, and left or right. Bluetooth module is used for operating the robot remotely to drive motors.

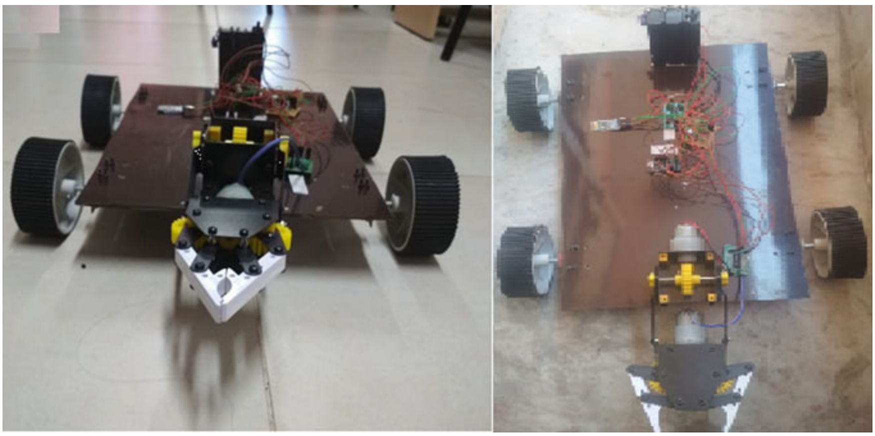

Fig. 11 Mobile robot along single-arm manipulator

Table 2 Speech rate using ANN recognition

Hidden nodes	Start	Stop	Pick	Place
10	84.1	84.1	88.5	81.0
20	90.3	92.9	88.5	90.3
40	93.5	92.9	93.8	93.8
80	93.8	97.3	88.5	80.5
Mean	90.4	91.8	89.82	86.4

6 Results

Speech recognition using neural network for mobile robot navigation is developed, and based on the findings, the results are discussed in this section. When utilizing a feed-forward multilayer perceptron, the Levenberg–Marquardt is used for preparing calculation to characterize the words "Start," "Stop," "Pick," and "Place" based on their MFCC, and the test words are perceived without any error. These outcomes are very positive and exhibit the capabilities of neural networks when it comes to pattern recognition. Table 2 shows the various speech rate values obtained using ANN recognition.

7 Summary

The speech recognition using neural network for mobile robot navigation is developed and tested, based on the methods proposed and various findings, and the following points are summarized:

This research sets on actualizing a speech recognition framework with an artificial neural system. MFCC algorithm is implemented for the speech recognition.

The collected voice commands from five test subjects include both male and female in our databases. But this database is used in both training and testing purpose after preprocessing this speech commands. Finally, we get a recognition system with 89% efficiency. The recognition can further be improved by increasing the number of hidden neurons. Maximum of 92% recognition was obtained which can still further be increased by using other recognition methods such as neuro-fuzzy and fuzzy methods. The number of hidden layer can also be altered to notice the behavior of the recognition system. While the scope of the system was reduced to an isolated word recognition network, the outcomes were still positive.

The final system provides a user-friendly mobile robot which could be remotely operated by the pre-programmed voice commands by the user. This approach supports the fact that the key to successfully demonstrate the cooperation between the robot and user in a very unlike environment with a lot of disturbances and still implement the received command swiftly and precisely.

It clarifies how neural systems can handle an issue like pattern recognition, as well as the benefits of certain structures and training algorithms.

In future, more words can be used for speech recognition, and it can be implemented for mobile robot for the execution of task where the robot can execute the task by speech recognition from various speakers on different speech.

8 Compliance with Ethical Standards

All procedures performed in studies involving human participants were in accordance with the ethical standards of the institutional research committee and with the 1964 Helsinki declaration and its later amendments or comparable ethical standards. Informed consent was obtained from all individual participants included in the study.

References

1. Campbell JP (1997) Speaker recognition: a tutorial. Proc IEEE 85(9):1437–1462
2. Bort L, del Pobil AP (2000, October) Using speech to guide a mobile robot manipulator. In Smc 2000 Conference Proceedings. 2000 IEEE International Conference on Systems, Man and Cybernetics. 'cybernetics evolving to systems, humans, organizations, and their complex interactions' (cat. no. 0, vol 4, pp 2356–2361). IEEE
3. Neerja SD, Rupesh SM (2013) Robotic automation using speech recognition
4. Saxena A, Sinha AK, Chakrawarti S, Charu S (2013) Speech recognition using matlab. Suresh Gyan Vihar University, Jaipur, Rajasthan, India
5. Kim NS, Un CK (1995) On estimating robust probability distribution in HMM-based speech recognition. IEEE Trans Speech Audio Process 3(4):279–285
6. Chandra E, Sunitha C (2009, March) A review on speech and speaker authentication system using voice signal feature selection and extraction. In 2009 IEEE International Advance Computing Conference IACC 2009, pp 1341–1346
7. Harris FJ (1978) On the use of windows for harmonic analysis with the discrete Fourier transform. Proc IEEE 66(1):51–83
8. Zebulum RS, Vellasco M, Perelmuter G, Pacheco MA (1996) A comparison of different spectral analysis models for speech recognition using neural networks. IEEE
9. Fatima N, Zheng TF (2012, May) Short utterance speaker recognition a research agenda. In 2012 International Conference on Systems and Informatics (ICSAI), pp 1746–1750
10. Shukla A, Tiwari R (2008) A novel approach of speaker authentication by fusion of speech and image features using artificial neural networks. Int J Inf Commun Technol 1(2):159–170
11. Chakraborty P, Ahmed F, Kabir MM, Shahjahan M, Murase K (2008) An automatic speaker recognition system. In: Ishikawa M et al. (eds) ICONIP 2007, Part I, LNCS 4984, Springer-Verlag, Berlin Heidelberg, pp 517–526
12. Himanshu M, Kaur SS, Sharma A (2014) Real-time information system based on speech recognition
13. Muda L, Begam M, Elamvazuthi I (2010) Voice recognition algorithms using mel frequency cepstral coefficient (MFCC) and dynamic time warping (DTW) techniques. arXiv preprint arXiv:1003.4083
14. Gaikwad S, Gawali B, Yannawar P, Mehrotra S (2011, December) Feature extraction using fusion MFCC for continuous marathi speech recognition. In 2011 Annual IEEE India Conference, Hyderabad, pp 1–5

15. Razak Z, Ibrahim NJ, Tamil EM, Idris MYI (2012) Quarnic verse recitation feature extraction using mel-frequency cepstral coefficient (MFCC). Department of Al-Quran & Al- Hadith, Academy of Islamic Studies, University of Malaya
16. Gaikwad SK, Gawali BW, Yannawar P (2010) A review on speech recognition technique. Int J Comput Appl 10(3):16–24
17. Kabir A, Ahsan SMM (2007, December) Vector quantization in text dependent automatic speaker recognition using mel-frequency cepstrum coefficient. In 6th WSEAS International Conference on Circuits, Systems, Electronics, Control & Signal Processing, Cairo, Egypt, pp 352–355

Range Sensor-Based Obstacle Avoidance of a Hyper-Redundant Robot

G. Mohammed Nawaz and N. Karthikeyan

Abstract In recent times, the development of the bio-mimicking is increasing in the robotics field. This paper discusses the design of the hyper-redundant robot and manoeuvring in the environment. The robot works on the Coulomb's friction law where the friction between robot and surface helps to move the robot. The robot models are fabricated by 3D printing. The robot uses passive wheels for its locomotion. A range sensor is used to detect the obstacles in the environment. A Bluetooth module is utilized for the wireless control of the robot. This paper describes the design of the hyper-redundant robot to avoid the obstacles in the environment using a range sensor and the robot follows the serpentine motion for the locomotion.

Keywords Bio-mimicking · Hyper-redundant · Passive wheels · Range sensing · Obstacle avoidance

1 Introduction

The bio-mimicking robots have been increasing, and the hyper-redundant robots are used for various operations like rescue of human in the trapped region and investigation of the narrow path regions. The hyper-redundant robot is referred to as the robot which has the greater DOF than the minimum DOF. The robot should be capable of avoiding the obstacle in the environment and find the best path to avoid the obstacle. The range sensor is capable of identifying the obstacle in the environment.

The robot is moved by the structure of a genuine snake. Be that as it may, there is an extensive scale between the headway proficient of snake-like robot and genuine snake. The snake can move in off-road, swim in the water, climb tree and even it coast noticeable all around by a portion of the snake species. Snake robot uses the scattered objects in condition for obstruction evasion. Manufacturing a snake robot

G. Mohammed Nawaz (✉) · N. Karthikeyan
SRM Institute of Science and Technology, Kattankulathur, Chennai, Tamil Nadu 603203, India
e-mail: nawaz.gmd@gmail.com

N. Karthikeyan
e-mail: karthikeyan.n@ktr.srmuniv.ac.in

E. T. Akinlabi et al. (eds.), *Trends in Mechanical and Biomedical Design*, Lecture Notes in Mechanical Engineering,
https://doi.org/10.1007/978-981-15-4488-0_57

with such action will be an alluring one. But implementing in the real time will be a difficult task and it can be achievable. Development of such robots will motivate in various applications like testing constant operation, hazardous areas, examining the pipe structure, search and rescue.

The component of the snake robot has sequentially associated joints that have the capacity to move in different planes. High level of opportunity of snake robot influences hard to control however to give productive headway aptitudes in scattered and unpredictable condition which superior to the portability of all the more overarching haggle robot.

There are a few sorts of headway for snake robots, where the development is conveyed by wheels or legs on their body. A portion of the robot utilizes passive wheels to create anisotropic grinding for headway. The passive wheels are highly useful to the robot for faster reachability to the target.

The snake uses different types of locomotion suitable for the terrain and for the better manoeuvrability of snake in the plane. The various methods of locomotion of snakes are.

- Concertina
- Serpentine
- Sidewinding
- Rectilinear.

The robot moves in a particular stride, which is serpentine motion, like a lateral undulation motion. The serpentine motion is similar to sine curve, and it has some advantages over other locomotion (Fig. 1).

Ryo and Fumitoshi [1] analysed the dynamics of three snake locomotion gaits where the gaits are sidewinding motion, serpentine motion and sinus-lifting motion. They have done a kinematic model of a snake robot and done the numerical analysis for the three walks. Furthermore, they consider the examination in just planar motion with typical powers following up on the grounded joints. And they simulated in MATLAB to get efficient results to amount the three gaits.

Motoyasu and Kazuo [2] proposed a shape control technique to keep up the head and relative position of the snake robot and maintain a strategic distance from as far as possible and self-impact. They created an inactive-wheeled snake robot that can switch the grounded and lifted the status of its wheels. They contrasted the simulation

Fig. 1 Sine curve

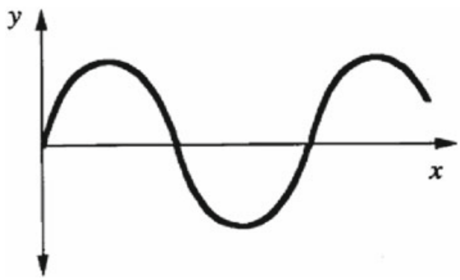

with experimental results which were utilized to assess the viability of the proposed technique.

Motoyasu and Kazuo [3] proposed control method for snake robot for ascending and descending steps. Phase shift method with shifting conditions is used to ascend and descend in steps. Shifting conditions derived for four process which are shifting on high step, before a shift, during shifting and after a shift. Efficient shifting conditions are derived from simulations using MATLAB.

Motoyasu and Kazuo [4] broke down the conditions for singular configurations with unconstrained links and lemmas for a snake robot. Kinematic model is determined with snake robot having passive wheels with dynamics joints. Essential and adequate conditions for the singular configurations of the snake robot with constrained links are assessed and got viability in recreation utilizing MATLAB.

Motoyasu et al. [5] designed a snake robot and control framework in light of range sensor information that control semi-autonomously to help the robot in staying away from hindrances. The administrator in the control structure exhibits the coveted speed of the first connection, and effect avoidance between coming about connections and obstructions is consequently figured by the controller. This chooses the connections should have been grounded and misuses excess.

Motoyasu et al. [6] proposed a control method for semi-self-ruling advance moving by a snake robot. The control system relies upon blended whole number quadratic programming to make the reference course of the leader of the robot. It chooses the proper positions and time term to identify nature before moving towards the movement. This control technique was connected to a snake robot furnished with a laser extend discoverer which is used for the progression area.

Motoyasu et al. [7] proposed a control method for all joints of the snake robot by comparing simulation and experimental results. The snake robot is composed of inactive wheels with dynamic yaw and move joints. Controller for approximate path tracking is composed utilizing the kinematics redundancy and choosing of the proper lifted parts.

Xiaodong and Shugen [8] concentrated on the outline of controller for a given motion pattern. Snake robot is equipped with laser range sensor to give sensory inputs to the control system for collision avoidance using neural controller-based central pattern generator.

Liljeback et al. [9] proposed a control technique that joints environment adaptation and directional control to accomplish straight line path with hindrance. Snake robot is designed to propel using the body friction by undulating motion. Tactile sensor is equipped in snake robot for contact type obstruction evasion.

Liljeback et al. [10] proposed a control technique for path following in straight path. Cascade approach technique is used to control the robot to go along straight path. Here, presumptions have been made as the forward velocity of the robot is nonzero and positive. Path way following controller exponentially balances out the robot to a different allotted straight path.

Liljeback et al. [11] proposed two control methods namely jam-detection scheme and leader–follower scheme for obstacle avoidance. The snake robot is designed to propel using the body friction. Jam-detection scheme will be undergone when the robot stuck between obstacles. Leader–follower scheme makes the sub-links of the robot to follow the head.

Liljeback et al. [12] investigated the properties of snake-like robot dynamics by employing nonlinear system tools analysis. Five investigations have been done which are partially feedback linearized model of a planar snake robot, stability analysis, controllability analysis, mapping link velocities and Poincare map.

Liljeback et al. [13] focused on obstacle avoidance by solving linear complimentary problem (LCP). Hybrid control procedure is executed to quantify contact forces that keep up the propulsion and keep robot from being jammed between hindrances. Contact forces were figured by formulating and solving a LCP.

Aksel et al. [14] developed a 3D kinematic model of a snake robot which propulsion is conveyed friction forces in light of coulomb's law of dry friction. Thee model is actualized for numerical treatment with numerical integrator called the time-stepping method. Simulation is completed for serpentine movement with sensible effectiveness.

Aksel et al. [15] developed a hybrid mathematical model for wheel-less snake robot. Ultrasonic sensor is equipped for obstacle avoidance.

Peipei et al. [16] designed a planar snake robot with bottom wheeled modular parts. Serpentine locomotion may be slipping problem. New angular parameters are introduced to compensate the slipping. Simulations and experimental results for the new angular parameter gives the effective compensation for slipping.

Chao et al. [17] designed a snake robot with universal joint. Snake robot dexterity, complexities and various motion patterns are improved by the universal joint. Inchworm locomotion gait is adopted in this robot.

Billah et al. [18] developed a smart material actuated autonomous snake robot. It increases the flexibility of the snake robot. CPG control method helps in autonomous navigation.

2 Introduction to Central Pattern Generator

Central pattern generators (CPG) are biological neural systems that deliver rhythmic output without musical input. They are wellspring of the firmly coupled example of neural action that drives musical movements like walking and breathing. Essentially, the capacity to work without contribution from higher cerebrum regions does not imply that CPGs do not get modulatory inputs, or that their outputs are fixed. CPGs have been found in essentially all vertebrate species including humans (Fig. 2).

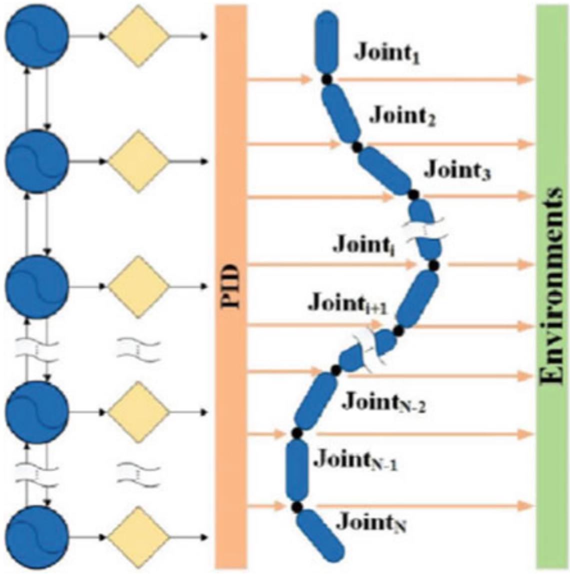

Fig. 2 Central pattern generator [7]

3 Working Methodology

The route towards affecting the hyper-redundant robot to have particular steps of process starts from arranging, demonstrating, produce and controlling the hyper-redundant. The underlying advance is to recognize the issue. The second means are to dissecting the issues and build up a model. The subsequent stage is to build up a 3D model of parts utilizing planning programming. In the wake of demonstrating the parts, choice of materials for manufacture happens.

The snake robot has three noteworthy area which are mechanical, electrical and program. The program which controls the robot by programming the servo engine with PWM pins which enables robot to move required movement. The sine wave can be created utilizing PWM sticks by giving positive half cycle to one stick and negative half cycle for another stick. The sine wave deals with an advanced voltage in the microcontroller.

3.1 *Mechanical Specification*

See Table 1.

Table 1 Mechanical specification

Specification	Details
No. of joints	12
Link dimensions (mm)	80 × 60 × 40
Link weight (g)	200
Joint range (°)	[0–180]
Actuators	Dual shaft servo
Range sensor	Ultrasonic sensor

3.2 Process Diagram

See Fig. 3.

4 Designing CAD Models

The following CAD module is the head, connecting frame and tail of the robot which is a customized design need to be fabricated using 3D printing. Each link is connected with the frame in the robot. The head and tail are the places where the controller and power supply are placed in the robot (Figs. 4, 5 and 6).

5 Fabricated Robot

The following are fabricated by 3D printing and acrylonitrile butadiene styrene (ABS) is the material which is used for the 3D printing of the models. The servo motor is attached in the series manner in order to perform the serpentine motion. The microcontroller is placed in the head and power source at the tail. The passive wheels are attached in each frame of the robot in order to stabilize the robot (Fig. 7).

6 Control Interface

The control interface is separated into three sections: user, wireless data transfer and the hyper-redundant. The user is used to give signal for on and off of the snake robot using Bluetooth module. The ultrasonic sensor is used to detect the obstacle in the environment as depicted in Fig. 8.

The hyper-redundant robot comprises of 12 servo engines and AT mega 2560 as its microcontroller. All the servo engines are provided with a 7.4 V and 2000 mAh battery to control up and the signs from controller.

Fig. 3 Process diagram

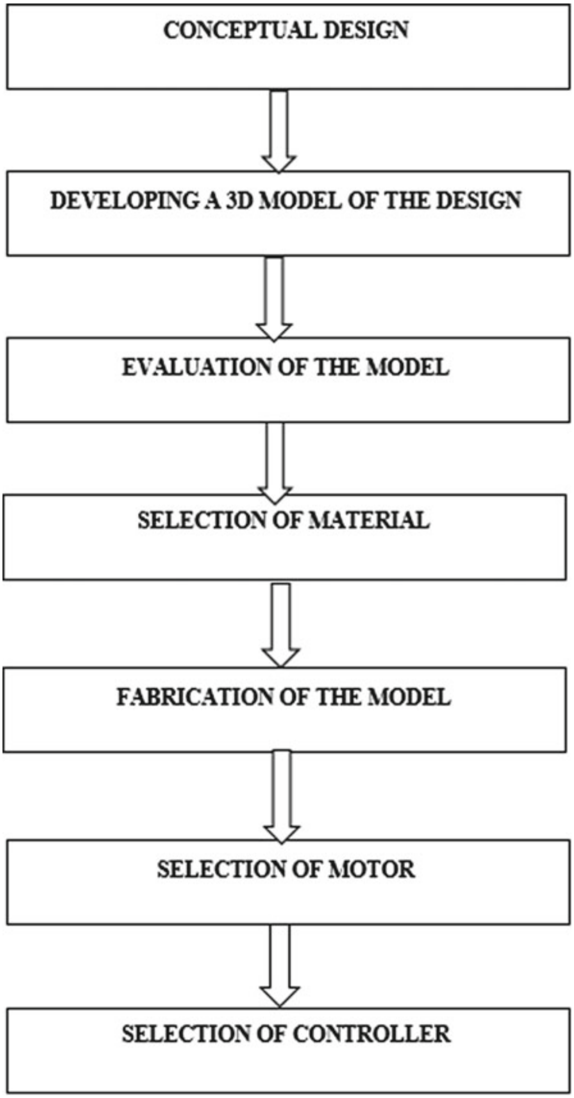

7 Locomotion

The robot which uses serpentine motion for its locomotion. The serpentine motion is which is similar to the sine curve. The servo motor is made into 90° and the connecting frame is attached between the servos motor. Likewise, 12 servo motors are attached in the series manner to perform serpentine motion on the plain. The serpentine motion can be achieved by the following formula

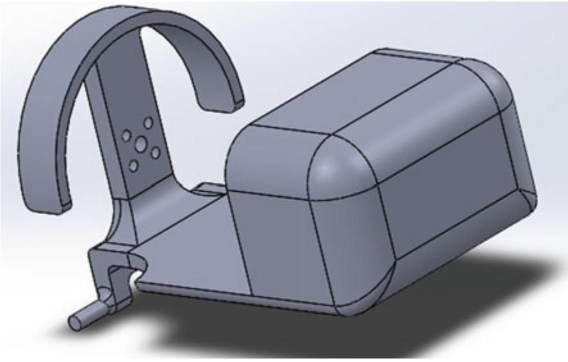

Fig. 4 Head

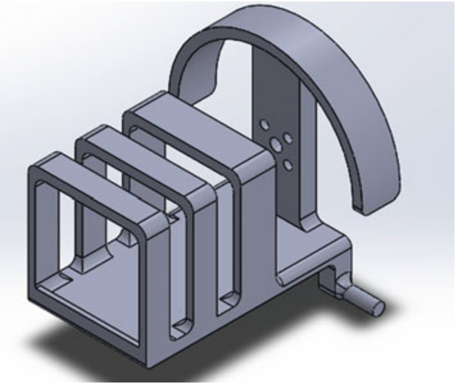

Fig. 5 Tail

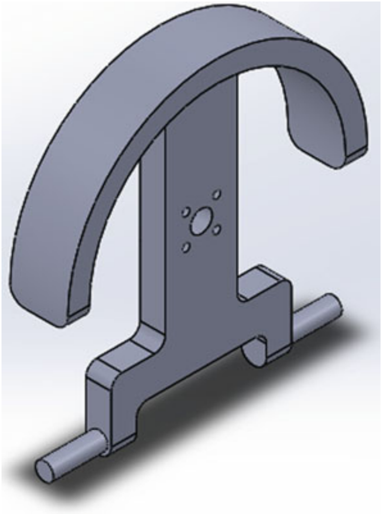

Fig. 6 Connecting frame

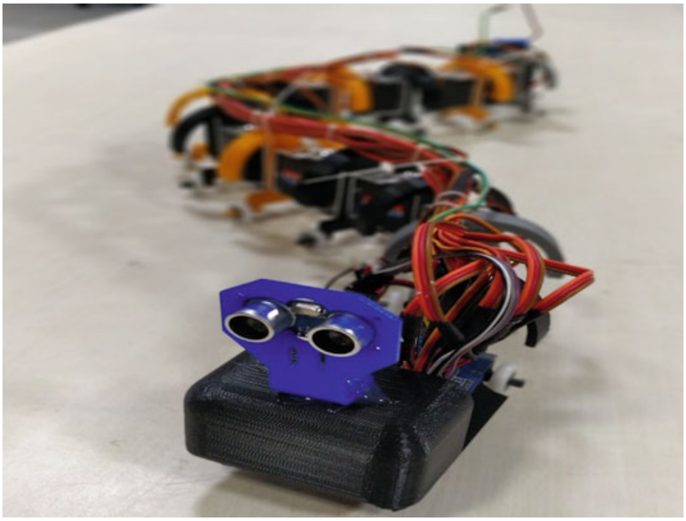

Fig. 7 Fabricated robot

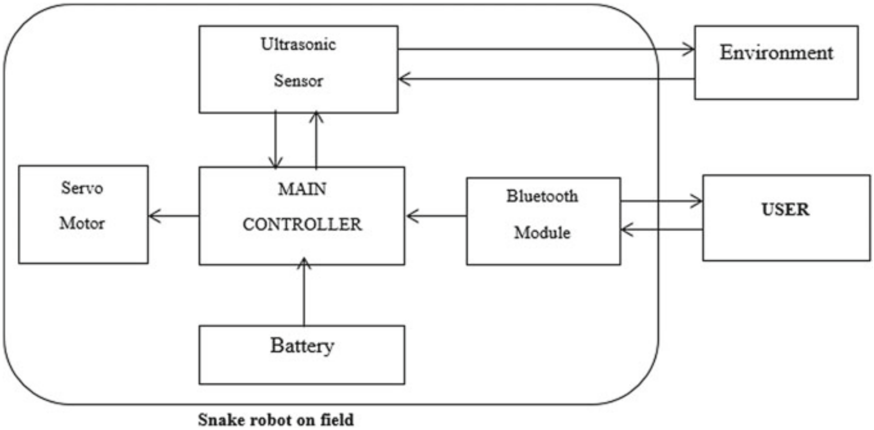

Fig. 8 Interfacing block diagram

$$\text{Serial.write}(90 + amp * cos(freq * count * (\pi/180) - n * lag)) \tag{1}$$

where

count = Loop counter variable.
lag = Phase lag between segments.
freq = Oscillation frequency of segments.
amp = Amplitude of the serpentine motion of the snake.
n = Number of segment estimated from 1 to 12.
$(\pi/180)$ = from degree to radiant.

Table 2 Testing of serpentine motion

Trails	1 m in seconds (s)	Speed (kmph)
1	4.50	0.8
2	4.26	0.845
3	4.40	0.818
4	4.20	0.857

Equation (1) is used for serpentine motion in the robot by dumping the codes in the AT mega microcontroller with sensor shield for providing more digital pins.

8 Results

8.1 Serpentine Motion

The fabricated prototype of the designed hyper-redundant is tested in the real-time environment for the serpentine motion of the robot. The 12 servos are connected to microcontroller and the power supply is given by the lithium-ion battery placed at the tail of the robot. Equation (1) is dumped into the microcontroller Arduino mega using embedded c language. Equation (1) tuned to move the robot in a straight path with serpentine motion. The experiment is done for many trails to find average speed of the robot.

In Table 2, the robot 1 m at an average time of 4.34 s and concludes that designed hyper-redundant Robot with passive wheels maximum speed of 0.830 (kmph) in serpentine motion.

Figure 9 is the representation of the robot with serpentine motion in the plain terrain. The pictures are taken per seconds of the robot motion. For each second, one curve completes and forms a new curve.

8.2 Obstacle Avoidance

The obstacle avoidance of the hyper-redundant robot is performed with the help of the ultrasonic sensor. The robot with the obstacle avoidance algorithm which is explained in Fig. 10. The ultrasonic sensor is fixed in the head of the robot and the Bluetooth module is attached in the robot. The user communicates with the robot

Fig. 9 Serpentine motion in robot

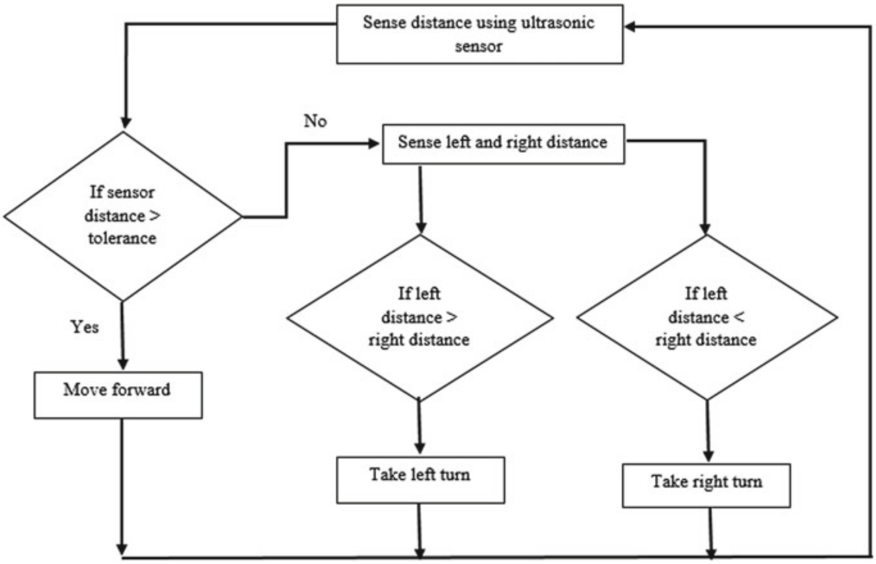

Fig. 10 Obstacle avoidance algorithm

with Bluetooth wireless transfer of data. The user only gives command to start or stop the robot.

Algorithm

Figure 10 is the pictorial representation of the obstacle avoidance of the designed hyper-redundant robot and the algorithm will be in the loop command so that it can able to detect the obstacle in the environment for every time.

In Fig. 11, the box in the picture acts as obstacle in the environment once the ultrasonic detects the obstacle in the environment and the obstacle avoidance algorithm will be processed to avoid the collision with the obstacle.

Fig. 11 Obstacle avoidance of the robot

9 Conclusion

This paper presents the design of the hyper-redundant and to get the maximum speed in the serpentine motion. The obstacle avoidance of the designed robot is done with the help of the range sensor. Experimental results demonstrate the obstacle avoidance of the robot in the real-time environment with serpentine motion as its locomotion. The experimental results for the obstacle avoidance in each trails shows that the robot performs without hitting the objects.

The future works in providing the live telecast of the robot wherever it goes and also surveillance of the environment with help of Wi-Fi camera.

References

1. Ryo A, Fumitoshi M (2017) Dynamic analysis of three snake robot gaits. IEEE Trans Robot 33(5)
2. Motoyasu T, Kazuo T (2017) Shape control of a snake robot with joint limit and self-collision avoidance. IEEE Trans Control Syst Technol 25(4)
3. Motoyasu T, Kazuo T (2015) Control of a snake robot for ascending and descending steps. IEEE Trans Robot 31(2)
4. Motoyasu T, Kazuo T (2016) Singularity analysis of a snake robot and an articulated mobile robot with unconstrained links. IEEE Trans Control Syst Technol 24(6)
5. Motoyasu T, Kazuyuki K, Kazuo T (2015) Range-sensor-based semiautonomous whole-body collision avoidance of a snake robot. IEEE Trans Control Syst Technol 23(5)
6. Kazuyuki K, Motoyasu T, Kazuo T (2016) Mixed integer programming-based semiautonomous step climbing of a snake robot considering sensing strategy. IEEE Trans Control Syst Technol 24(1)
7. Motoyasu T, Kazuo T, Fumitoshi M (2015) Approximate path-tracking control of snake robot joints with switching constraints. IEEE/ASME Trans Mechatron 20(4)
8. Xiaodong W, Shugen M (2013) Neurally controlled steering for collision-free behavior of a snake robot. IEEE Trans Control Syst Technol 21(6)
9. Liljeback P, Pettersen KY, Stavdahl Ø, Gravdahl JT (2012) Snake robot locomotion in environments with obstacles. IEEE/ASME Trans Mechatron 17(6)
10. Liljeback P, Haugstuen IU, Pettersen KY (2012) Path following control of planar snake robots using a cascaded approach. IEEE Trans Control Syst Technol 20(1)
11. Liljeback P, Pettersen KY, Stavdahl Ø, Gravdahl JT (2011) Experimental investigation of obstacle-aided locomotion with a snake robot. IEEE Trans Robot 27(4)
12. Liljeback P, Pettersen KY, Stavdahl Ø, Gravdahl JT (2011) Controllability and stability analysis of planar snake robot locomotion. IEEE Trans Autom Control 56(6)
13. Liljeback P, Pettersen KY, Stavdahl Ø, Gravdahl JT (2010) Hybrid modelling and control of obstacle-aided snake robot locomotion. IEEE Trans Robot 26(5)
14. Aksel AT, Leine RI, Glocker C, Pettersen KY (2008) 3-D snake robot motion: nonsmooth modeling, simulations, and experiments. IEEE Trans Robot 24(2)
15. Aksel AT, Leine RI, Glocker C, Pettersen KY, Liljebäck P (2008) Snake robot obstacle-aided locomotion: modeling, simulations, and experiments. IEEE Trans Robot 24(1)
16. Peipei S, Qianjun S, Dongtai L (2016) Design and improved serpentine curve locomotion control of a planar modular snake robot. In: IEEE international conference on information and automation (ICIA), Feb 2017

17. Chao W, Deng H-B, Xia F, Li Y (2016) Study on climbing locomotion mechanism of snake robot with universal unit. In: 8th international conference on modelling, identification and control, Nov 2016
18. Billah MM, Khan MR, Shafie AA (2015) Autonomous flexible snake robot for 3D motion. In: IEEE international symposium on robotics and intelligent sensors (IRIS), Oct 2015

Literature Survey on Four-Legged Robots

G. Satheesh Kumar, S. Aravind, R. Subramanian, Shashank Kannan Bharadwaj, Ronak R. Muthuraman, R. Steve Mitchell, Aditya Bucha, M. Sriram, K. J. Shri Hari, and Nikhil Jerome Robin

Abstract Over the last two decades, the research and development of legged locomotion robots has grown steadily. Legged systems present major advantages when compared with 'traditional' vehicles, because they allow locomotion in inaccessible terrain to vehicles with wheels and tracks. However, the robustness of legged robots, and especially their energy consumption, among other aspects, still lag behind mechanisms that use wheels and tracks. Legs are not new to humans or animals but building legs for a robot is a complex process. The normally noticed and ignored fact is how a baby learns to walk and the sheer learning curve involved. If we, the intelligent humans take years to learn to walk, imagine creating legs for a robot and teaching it how to walk. Although there is an extensive research going on in the field of legged robots, researchers are still in developing stage to construct a legged robot which can replicate human walk, or for that matter any animals. And a few of their current area of research are in maintaining dynamic stability of the robot, reflex of the robot to sudden impacts and also interaction with the terrain to produce suitable gait. This paper gives a brief description on a few of the existing legged robots on various aspects of a robot and on how each one of them affects the dynamics of the robot. This paper enhances a space for future research on understanding the various aspects of a legged bot design.

Keywords Legged robots · Mechanism · Terrain · Stability · Dynamics

1 Introduction

Legged robots are today used in a variety of applications including areas of rescue, excavation, research operations and places that are inaccessible by humans. This paper shows the different mechanisms used in legged robots. These legged robot

G. Satheesh Kumar (✉) · S. Aravind · R. Subramanian · S. K. Bharadwaj · R. R. Muthuraman · R. Steve Mitchell · A. Bucha · M. Sriram · K. J. Shri Hari · N. J. Robin
Sri Sivasubramaniya Nadar (SSN) College of Engineering, Chennai, India
e-mail: satheeshkumarg@ssn.edu.in

E. T. Akinlabi et al. (eds.), *Trends in Mechanical and Biomedical Design*, Lecture Notes in Mechanical Engineering,
https://doi.org/10.1007/978-981-15-4488-0_58

locomotion mechanisms are generally inspired by the biological system and its environment—the animals, insects and other legged creatures including humans give us a basic idea of how legged robots have to be designed for its motion. These designs have to be made keeping in mind about factors like stability, power consumption and complexity of control of each added leg. With the increase in number of legs, the stability of the robot increases but each leg requires at least two degrees of freedom, one for forward movement and other for lifting, and therefore, its power consumption increases. For a two-legged bot, there are two legs and four degrees of freedom. This makes the robot to have a more versatile motion. But with more legs, controllability is an issue. If there are n legs of a robot, then the number of possible motions is given by [1]:

$$X = (2n - 1)!;\ \text{by substituting}\, n = 4,\ \text{we get}\, X = 5040$$

X is the number of ways in which a four-legged robot can be controlled. Thus, a robot with more legs becomes more complex due to their controllability, whereas decrease in number of legs like a bipedal robot or a one-legged robot reduces the power consumption but decreases the stability of the robot. So generally, four-legged robots are widely used and various locomotion, mechanisms are researched and are discussed below. The major difference between legged and wheel robots are the legs which compromise on stability to enhance terrain overcoming features [2]. Though stability is compromised, different mechanisms can be used to enhance stability. Therefore, in the present state of development, there are several aspects that need to be improved and optimized. The factors in consideration while designing robotic systems on how they operate include gait mechanisms, robot control system, size, structural heterogeneity, power sources, actuators and its sensors used.

2 Mechanisms of Legged Robots

Different mechanisms can be used to enhance the stability of a robot. Some of the mechanisms are parallel leg mechanism, pantograph mechanism, Jansen linkage, Klann linkage, strider linkage and so on. Different robots employ different mechanisms customized to meet their requirements [3, 4].

2.1 Big Dog

The big dog robot is a combination of hydraulic actuator and quadruped mechanism as a whole. Each leg adopted a linkage mechanism, an elastic mechanism and a spring shock absorber so as to improve the flexibility and terrain overcoming ability. The hind legs use the five-bar mechanism. The robot's body is a structure which is cross-linked. The legs can be seen as institutions, the centre of the two links are

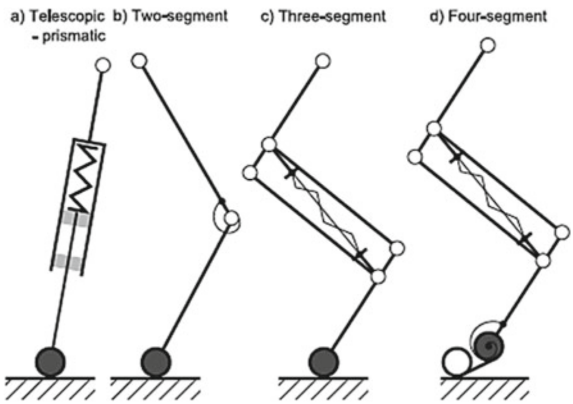

Fig. 1 Depiction of different segmented legs

hinged whereas the front end is fixed and the rear is connected to the sides of the body using screw nut [5]. This makes it more stable while moving over rough terrains.

2.2 Cheetah Cub

The cheetah cub employs the spring-loaded pantograph mechanism. The pantograph mechanism is in itself efficient for terrain crossing abilities. The springs are instilled to make sure that the energy expended is not wasted. Both leg implementations include a gravity-loaded leg spring. The hip actuator is mounted directly between the robot's body and leg [6]. The knee actuator, which is parallel to the main leg spring, is mounted. The role of the knee actuator is only to withdraw the leg by the pulling of the cable and not to extend the leg since springs are used for leg extensions as shown in Fig. 1. This system ensures that the energy is not wasted and can be utilized by the leg thereby increasing energy efficiency.

2.3 Anymal

The interaction of the forces is done by either by integrated load cells in the joints or at the end-effector, by pressure transducers in the cylinders, or by a series elasticity in every actuator. This ensures that environment–force interaction is in a controlled manner thereby maintaining the stability of the system and also for the handling of objects. The designing of the compliant actuators is so that it is analogous to natural locomotion systems of movement such as tendons and muscles which regulate the forces. SEAs can be described as actuators where springs are used to attach the load. Other options include the use of elastic elements instead of a spring. This set-up allows proper information of the force applied which helps in the control of the force

[7]. The movement of spring in motion such as expansion or contraction helps in the calculation of force. Shock tolerance is an added benefit of using springs. Energy storage is also done by the springs increasing the overall efficiency and increasing the maximum power since the spring provides the additional energy. Traditional gear mechanisms cannot be used as it provides very slow motion due to which series elastic actuators are used.

2.4 ARL Monopod 2

In this robot [8], hip joint is actuated by the use of cable and pulleys. The long cables make use of the extension springs. Leg actuation is done by the hip pulley to which the cables are attached (Fig. 2).

The cables are attached to NSK ball screw by passing over idlers initially being fixed to the other end. The hip motor makes use of the miniature HTD timing belt to actuate the ball screw, and motor torque is converted into axial force which acts at the ball nut which is done by the unity ratio pulleys. Hip pulley is actuated by the tensions in the cable due to the force in the ball nut. During motion, the acceleration and

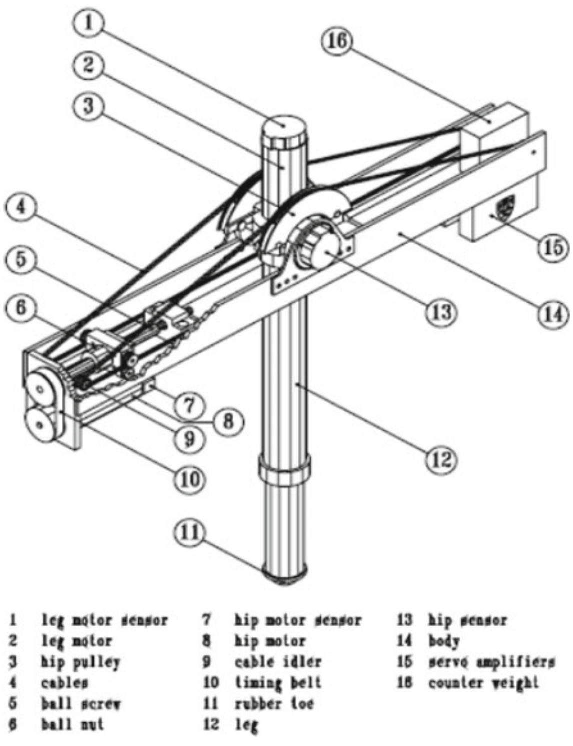

Fig. 2 ARL Monopod 2

deceleration of the motor can be aided by the use of springs which can again increase efficiency. The mechanism is such that the use of springs can be accommodated.

3 Gait

The motion of robot is caused by switching from one mechanism set to another. We define a gait as all operations, implemented by each mechanism set. Gait is the leg phasing part of coordination problem, and in other words, we can say that a gait defines the form and the characteristics of a body displacement. In a more general approach, a gait is defined by Song and Waldron [9], as follows ‘A gait is defined by the time and the location of the placing and lifting of each foot, coordinated with the motion of the body in its six degrees of freedom, in order to move the body from one place to another’ (Fig. 3).

From the observation and mathematical formulation of natural gaits, it was found that many of the motions were periodic in nature. Hence, the motion was categorized into two, periodic and non-periodic (free gaits). The periodic gaits were characterized with continuous gait, in which the body moves with constant motion while all legs move simultaneously and this is was generally used for flat and levelled terrains, whereas for an uneven terrain, the animals generally use a special kind of continuous gait called wave gait, at a lower speed. Mammal and insects change their gait pattern on sharp irregular terrains, which was defined as secure gait and it is characterized by the sequential motion of legs and body [3]. The body is pushed forward/backward with all of the feet in proper contact with the ground and then one leg is moved with the other three legs and body remaining stationary, and this gait is called discontinuous gait [10–12]. Eventually, this gait causes intermittent body motion which is beneficial to a real legged machine, where they are very easy to implement.

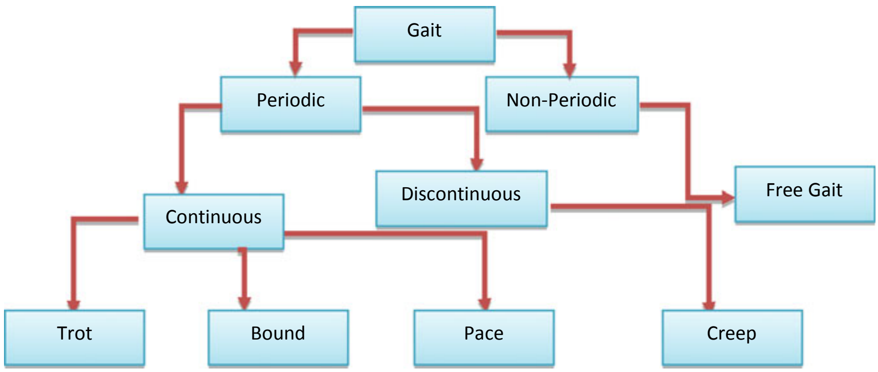

Fig. 3 Types of segmented legs

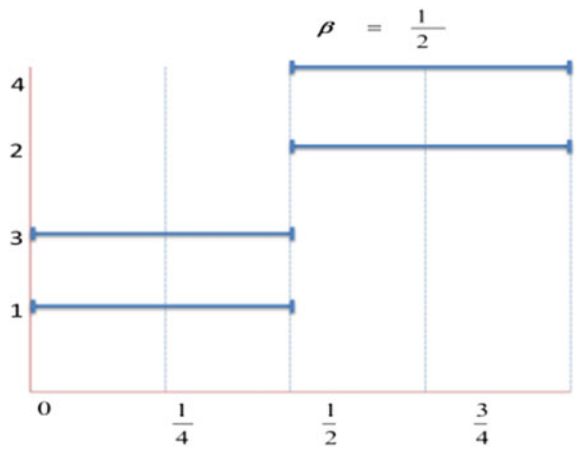

Fig. 4 Leg actuation in a troit gait cycle

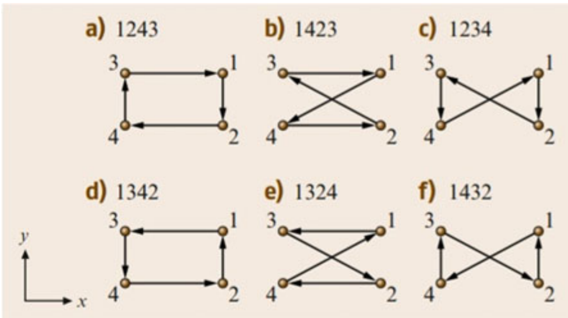

Fig. 5 Depiction of different gait sequence

3.1 Types of Gaits

3.1.1 Troit Gait

In this type of gait, diagonally opposite legs are moved at an instant. This type of movement is very fast and dynamic stability is used to maintain balance. Twice during each cycle, the body is ballistic and without support, hence if the speed is greater then there is more stability (Figs. 4 and 5).

3.1.2 Creeping Gait

There are different types of walking gait available. Among these creeping gaits, crawl gait is most used due its stability. One leg up at each step, based on the order of lifting legs it can have six different gaits. The 1423 creeping gait has the maximum stability for walking along the x-direction and is called the crawl gait. If the walking direction was $-x$, 1324 gives the crawl gait (Figs. 6 and 7).

Likewise, 1234 and 1432 represent the crawl gait in the $-y$ and y directions, respectively. On the other hand, the 1243 and 1342 creeping gaits give medium stability and are suitable for turning. Graphical representation of gaits sequences is shown in Fig. 5, and the minimum value of duty factor for static stable gaits is 0.75 for four-legged robots.

Fig. 6 Leg actuation in a creep gait cycle

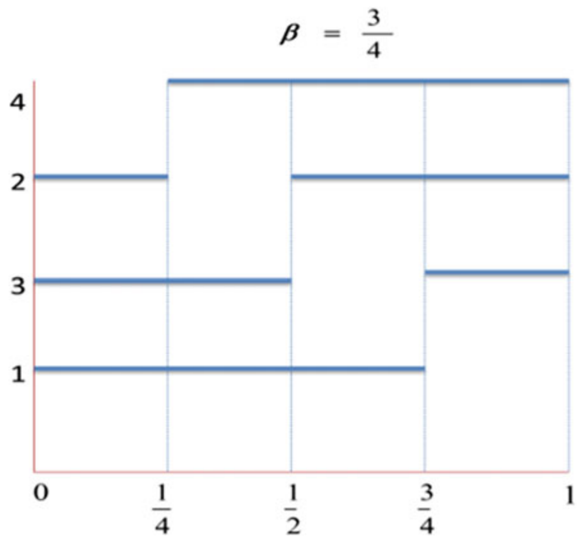

Fig. 7 Leg actuation in a bounce gait cycle

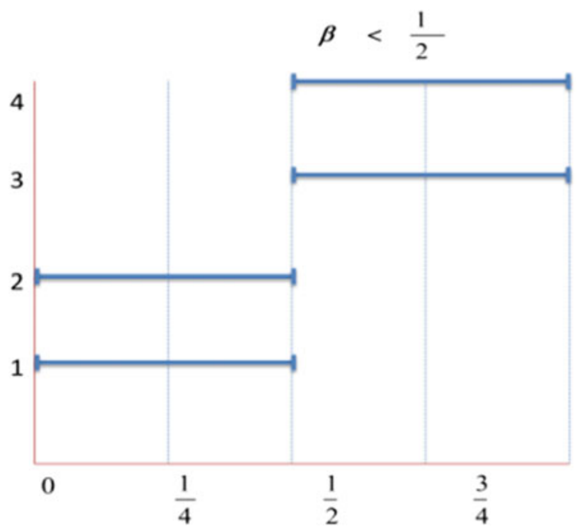

3.1.3 Bounce Gait

In the bound, support alternates between pairs of legs, with the fore and hind limbs acting in unison to thrust the body forward in a bound gait. As can be observed from this figure, there is approximately an 1800 phase difference between the sets of front and back legs. The bound has the shortest gait period, allowing for frequent interactions of the legs with the ground. This makes the bound well suited for obstacle avoidance and for providing propulsion. Simulation analysis first conducted by Murphy and later validated by Neishtadt and Li showed that certain simple planar quadruped bounding models are always passively stable for dimensionless body inertia values of less than one and duty factor (β) is always less than 0.5.

3.1.4 Wave Gait

This type of gait gives maximum stability on horizontal axis and it is defined as:

$$\beta_i = \beta \quad (i = 1 \ldots, 4)$$

where $0.75 \leq \beta < 1$ and β is the duty factor of the wave gait. This gait is usually like static stability where three legs on the ground and one leg is lifted which gives us an elliptical equation which is used to find the beta and then this gait is regular and symmetrical, so which as add is stability.

4 Stability

Stability means an equilibrium position which can be obtained by proper position of legs and it can be measured and observed. It is very important in legged robot. There are two types of stability: a. static and b. dynamic.

4.1 Static

It is the stability for the robot which makes it balanced so that it does not fall when standing, i.e. the centre of gravity is within the ground contact base for understanding we take a tripod robot it forms a triangle. So, it stands still because of its stable structure this the robot is statically stable as also and the centre of gravity is in triangle. This triangle is called 'support polygon' [13, 14] and it is a projection between all the support points of a robot onto the surface it is standing. The minimum number of ground contact for a robot is 3 number of legs.

4.2 Dynamic Stability

It is the stability which is to be achieved while the robot is moving. For example, in one leg robot, it is stable as long as it is good but falls when it stops, but it is very complex to control but moves fast and has great efficiency [15–17]. Because of this, most four-legged robot uses this kind of stability because static is slow, that is, because at least 3 points should be in ground contact because of this walking is slow, whereas in dynamic stability, it can vary from 0 to n number of legs.

To get the best design, there should be both static and dynamic stability so instead of lifting one leg two legs should be lifted so it can be less energy consumption bit slightly less stable than static.

4.3 Stable Model

There is (2D + 1) model. In this model, there is a straight line which describes the legs and there is an empty circle when the leg is raised and filled when it is grounded [18]. There is a green circle that repents the centre of mass. The number indicates the position of the robot legs, whereas the red triangle is the support polygon; by using this, there is nearly a 10,000-robot configuration but all are not stable. To find the stable one, we need to eliminate the unstable ones, then by using stable configuration, gait can be obtained.

4.4 Stability of Other Robots

4.4.1 Phony Pony

It is made is such a way that it can move forward and backward. This is done by the quadruped crawl and the diagonal gait or the trot gait. The disadvantage is that it cannot turn. The feet are broad to make it stable. But it is not as stable as the six-legged robot due to lack of true pitch and yaw motion at the hips.

4.4.2 KUMO1-4-Legged Walking Machine

This walking is done by an actuator and so the robot is heavier and difficult to control. It is stable over any terrain including a rugged surface due to the legs having 3 degrees of freedom. They can also move in any direction. So there is stability even when the task is stopped 199 in a rugged surface.

4.4.3 Scout-1

They have dynamic stability which is achieved by leg which has 4 DOF. Another benefit is the simplicity. Experiments conducted using treadmill found that it was capable of walking for 32 seconds, turning and staircase climbing. It is also low cost and efficient [19, 20]. In this, a linear actuator is in the hip controlling hoping height, and hip only controls all the three joints.

4.4.4 Cheetah

The stability in cheetah is achieved by a flexible metal kind to provide stability and it has elbows to lift itself [21, 22]. It also uses a computer to control each leg so it is dynamically stable. In recent developments, it is using a bounding gait which is between a canter and a gallop so it is the most dynamically stable gait, making it stable in any terrain.

4.4.5 Titan Vlll

Titan VIII is an example of dynamic stability; it uses trot gait, where 2 diagonal legs are lifted simultaneously. Its stability is based on zero moment point (ZMP). At the time of walking, the ZMP has to be about the diagonal [17]. Thus, it makes it faster and also efficient and making it move in all-terrain.

5 Pros and Cons of Underactuated Systems

- It is more efficient as the natural dynamics are used profitably. It saves power by reducing the number of actuators.
- As it uses the natural dynamics of the systems, it looks more natural and smoother whereas the fully actuated systems look artificial [23]. Moreover, having the movement to be natural helps the system to tackle many real-world challenges much easier than having to solve complex algorithms as is the case for fully actuated systems.
- The only con is the difficulty in formulating the equations but once formulated it is not computationally heavy.

6 Conclusion

In this paper, an overview of legged robots has been discussed and compared based on different aspects of importance for designing a bot. The topics discussed are mechanism, gait and stability. Finally, the difference in underactuated and fully actuated robots is for improving control and efficiency. The other parameters like robot control system, size and structural heterogeneity, power source, sensors and actuators would be covered in further works.

References

1. Siegwart R, Nourbakhsh I (2004) Introduction to autonomous mobile robots: a Bradford book. The MIT Press, Cambridge, London
2. Fu KS, Gonzalez RC, Lee CSG (1987) Robotics: control, sensing, vision and intelligence. McGraw-Hill
3. Hirose S, Umetani Y (1980) Basic motion regulation system for a quadruped walking vehicle. In: Design engineering technical conference, Los Angeles. Researchgate
4. Bonnier Corporation (1933) Popular science monthly, Apr 1933. Bonnier Corporation, p 46. ISSN 0161-7370
5. Raibert M, Blankespoor K, Nelson G, Playter R (2008) BigDog, the rough-terrain quadruped robot. In: Proceedings of the 17th IFAC world congress, COEX, South Korea, pp 10823–10825
6. Spröwitz A, Tuleu A, Vespignani M, Ajallooeian M, Badri E, Ijspeert A (2013) Towards dynamic trot gait locomotion: design, control, and experiments with cheetah-cub, a compliant quadruped robot. Int J Robot Res 32(8):932–950
7. Hutter M, Gehring C, Lauber A, Gunther F, Bellicoso CD, Tsounis V, Fankhauser P, Diethelm R, Bachmann S, Bloesch M, Kolvenbach H, Bjelonic M, Isler L, Meyer K (2017) ANYmal—toward legged robots for harsh environments. Adv Robot 31(17):918–931. https://doi.org/10.1080/01691864.2017.1378591
8. Gregorio P (1996) Design, control and energy minimization strategies for the ARL Monopod. Researchgate 1–54
9. Song SM, Waldron KJ (1989) Machines that walk: The adaptive suspension vehicle, The MIT Press, Cambridge, MA, ISBN 0-262-19274-8
10. PAL Robotics. REEM-A technical specifications. https://web.archive.org/web/20110302213317/http://www.pal-robotics.com/robots/reem-a/34-reem-a-spec. Archived from the original on 2011-03-02
11. PAL Robotics. REEM-B technical specifications. https://web.archive.org/web/20110720215835/http://www.pal-robotics.com/robots/reem-b. Archived from the original on 2011-03-02
12. PAL Robotics. REEM-C technical specifications. https://web.archive.org/web/20110824004151/http://pal-robotics.com/robots/reem-a. Archived from the original (PDF) on 2013-07-17
13. Olfati-Saber R (2001) Nonlinear control of underactuated mechanical systems with application to robotics and aerospace vehicles. Thesis (Ph.D.), Massachusetts Institute of Technology, Department of Electrical Engineering and Computer Science, pp 1–316
14. Queiroz C, Menezes P (2000) A study on static gaits for a four-leg robot. In: Proceedings of international conference on control, pp 1–6
15. Bottcher S (2006) Principles of robot locomotion. In: Seminar on human robot interaction, pp 3–25

16. MIT cheetah robot runs fast, and efficiently. IEEE Spectrum: Technology, Engineering, and Science News, 2013
17. Goddard L (2012) Cheetah robot sets 28.3 mph speed record, outrunning Usain Bolt. The Verge
18. Mohamed A (2015) Assessment of the stability of a four legged robot manipulator. Int J Eng Res 4(1):433–436. https://doi.org/10.17950/ijer/v4s8/806
19. Buehler M, Battaglia R, Cocosco A, Hawker G, Sarkis J, Yamazaki K (1998) SCOUT: a simple quadruped that walks, climbs, and runs. Proc IEEE Int Conf Robot Autom 2(1):1707–1712. https://doi.org/10.1109/ROBOT.1998.677408
20. Chen W, Yu Y, Zhang X (2005) A survey on the underactuated robots. Jixie Sheji yu Yanjiu 21(4):22–26
21. Li M, Wang X, Guo W, Wang P, Sun L (2014) System design of a cheetah robot toward ultra-high speed. Int J Adv Rob Syst 11(5):1–11. https://doi.org/10.5772/58563
22. Greenemeier L (2008) DARPA pushes machine learning with legged LittleDog robot. Scientific American, 15 Apr 2008
23. Mishra A (2014) Design, simulation, fabrication and planning of bio-inspired quadruped robot, May 2014. Thesis. https://doi.org/10.13140/2.1.2731.6486

In-Pipe Robot Mechanisms—State-of-the-Art Review

G. Satheesh Kumar and D. Arun

Abstract In-pipe robots are a class of robots that have been extensively studied for a very long time and many interesting solutions have been proposed and used in practical scenarios. There are many parameters and functional features that define the characteristics of these robots. An extensive review of the mechanisms that allows locomotion to the in-pipe robots is performed in this paper. A broader classification that allows more clarity on these robots for choosing them based on their capacities is provided. The designs brought out so far have limited itself to one type of scenario where there is no need for the robots to work in coordination. This perspective is different from the other review papers in that sense and is needed for the researchers to identify new design directions for improvising the performance of their robots. A new design perspective for in-pipe robots for swarm applications is also presented toward the end.

Keywords In-pipe robots · Mechanism · Scavenging · Reconfigurability

1 Introduction

This paper presents a state-of-the-art review of the literature on the sewage in-pipe robotics on the basis of the locomotion aspects. In the early 1990s, the sewage in-pipe robot was proposed [1]. In the 2000s, there has been a steady increase in research interest within the field of sewage in-pipe robots. It is not an uncommon sight to see men forced to work on sewage for cleaning pipes with unreserved disregard to any safety measures. Workers, while performing the tasks of maintenance and cleaning sewage pipes, get affected by the toxic gases (like hydrogen sulfide or chlorine) [2], sometimes causing instant death or at least increased the risk of serious diseases too.

Robots are designed to reduce the human elements from effortful work or dangerous work and additionally to act in the impassable environment. Implementation of smart cities opens up a Pandora's box of newer complex technical problems transfixed

G. Satheesh Kumar (✉) · D. Arun
Sri Sivasubramaniya Nadar (SSN) College of Engineering, Chennai, India
e-mail: satheeshkumarg@ssn.edu.in

E. T. Akinlabi et al. (eds.), *Trends in Mechanical and Biomedical Design*,
Lecture Notes in Mechanical Engineering,
https://doi.org/10.1007/978-981-15-4488-0_59

by associated social problems. Chennai, a city of 426 km^2 and 4.6 million populations [3], has a sewage network of 7000 km and 77,000 plus manholes. A problem of this scale was usually not encountered, but would have been handled by humans manually until recently even in developed countries. Though under these conditions it would seem appropriate to develop a robot with the equivalents of superpowers, actually the solution would be a lot effective to have simpler robot-based solutions. Solutions developed for this problem could be effectively expanded to provide solutions for the problems of the other kind. Pipelines are used to transport drinkable water, oil, sewage water, etc., and are prone to a lot of problems like crack, corrosion, blockage, and leakages. Even for sewage pipelines continuous monitoring, inspecting, and removing blockages are strongly recommended.

In-pipe robots and open-air robots have been exciting areas of research all these years and their differences are quite an interesting domain for research. By open-air, it is meant to cover all the robots which are not in-pipe robots. The technology and components used are fundamentally alike but with vividly adapted differences. The qualities that define the environment where the robots work also define the characteristics of the robot. The differences would soon adopt to a scale that exists between terrestrial and aquatic animals as research progresses. Table 1 provides a basic analysis of the differences existing in those robots for ready reference.

2 Parameters for Comparison

In the course of development of robotics, there has been a lot of sewage cleaning in-pipe robots developed by many researchers and some have been commercially marketed successfully. The developed robots are expected to overcome these constraints placed by the interacting environment on the in-pipe robots:

1. limits of reconfigurability
2. extreme space limitations for making turns
3. absence of light
4. presence of muddy, slushy content
5. presence of water and extremely contaminated
6. presence of stones and larger obstructing objects
7. sometimes 6 m beneath ground level—constrained communication
8. Slippery surface offered by the pipes affects traction effort
9. Should overcome aquatic pressure of up to XXX 100HP due to gravity flow and intermediate pumps
10. Need to climb inclined pipes, sometimes up to 90°
11. Lightweight, so as not to damage the pipe but strong enough to exert load on the obstacles to be cleared
12. Entire robot to be waterproof
13. In situ charging
14. Long interval between maintenance.

Table 1 Comparison of in-pipe and open-air robots

S. No.	Classification	Open-air robot	In-pipe robot
1	Mechanism	Simple mechanisms alone would be sufficient for this type of robots	Pipe diameter will change frequently so need a better mechanism to adopt a robot through the pipe [4, 5]
2	Size	Size is not determined based upon application size determined	Should consider the size of the robot. Because it works underwater pipe, size of pipe change continuously. Size of the robot should adopt a pipe [4]
3	Sensor	The basic sensor needs to run a robot. E.g., light sensor, sound sensor, temperature sensor, contact sensor, proximity sensor, distance sensor, pressure sensor, tilt sensor, positioning sensor, acceleration, gyroscope, voltage sensor, current sensor [6]	High-profile sensor need. E.g., ultrasonic sensor, thermal sensor ultrasonic sensor, magnetic sensor, infrared sensor, vision sensor (camera), tactile sensor, light amplification by stimulated emission of radiation (LASER) [7]
4	Artificial intelligence	High intelligence need. It works in an outdoor, and a lot of problems, environment change happen [6]	Less intelligence need. Because it works on underground and there are no external factors to affect a robot. Consideration should be in a minimum [8]
5	Traction	Based on work surface traction force calculated	High traction force need, it works in the slurry, slippage area. The wheel should be in a grip to avoid slip [9]
6	Light	It works in daylight	It works in dark
7	Sealing	A need for sealing is less	High sealing required. It is in water. So, sealing should avoid water to enter a robot. Otherwise, it affects a sensor, board, etc. [10]
8	Weight	A weight of robot considers upon applications	Consideration of weight is high. A diameter of pipe changes so the weight of the robot is less; otherwise, it cannot adopt a pipe. A center of gravity changes and it causes failure [9]
9	Path determine	No path determination robot should move freely	Path of a robot does not change [11]
10	Obstacles	Cannot be determined. Because in the environment, a lot of factors affect a robot	We can determine the obstacles. E.g., slog, tree branches, plastics, etc. [11]

In-pipe robots are broadly classified by their locomotion capabilities, sensors, actuators used, choice of controllers, applications and purpose, functionality, cost and reconfigurability.

Locomotion is the complement of manipulation. In locomotion, the desired environment is mounted upon with the robot and the robot moves by transmission of force to the environment. Manipulation, on the other hand, moves or handles the object by way of application of force and completes a given task. Means are the same but the ends vary entirely. In each case, the scientific basis is the study of actuators that generate interaction forces, and the mechanisms that translate it as desired. Locomotion has the characteristics of stability, characteristics of contact, type of environment, and vector loops among others.

Actuators and sensors are among the essential devices to drive a robot. There is a wide range of sensors and actuators used in in-pipe robots. Sensors are used to acquire information about the robot's environment or perhaps to directly measure a robot's global position and sometimes encounter unforeseen environmental characteristics. Similarly, the role of actuators is also inseparable from the functions of locomotion. However, this paper deals entirely with locomotion capabilities for the purpose of setting future research directions.

3 Mechanisms for Locomotion

The main objective of the robot is to traverse through the horizontal and vertical cross section of the pipe. To meet this objective, there are many types of mechanisms designed for locomotion and are generally classified and discussed in [12–18]. Another broad-based classification approach is discussed in this paper. They are:

1. Self-locking mechanisms
2. Climbing mechanisms
3. Twist-to-Turn mechanism
4. Reconfigurable mechanisms
5. Multiple to partially active mechanisms and
6. Simple drive-by mechanisms.

3.1 Self-locking Mechanisms

This combination of linkages makes the mechanism contract in the clockwise direction and expands in counterclockwise direction. Rotation inputs could also be replaced by planar motion mechanisms. Most of these robots belong to this class of mechanisms since the primary need of such robots is to clear clogs by exerting a force on the target material. Symmetric multiple linkage mechanisms are common in this category of in-pipe robots. Many of these robots have their maintenance unit

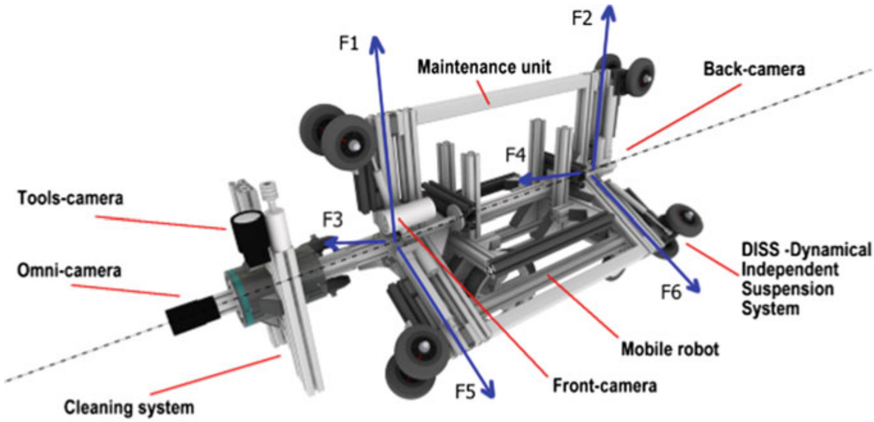

Fig. 1 DeWaLoP in-pipe robot mechanism [5]

together with the chassis forming a monolithic multi-module robot, which can be easily mounted/dismounted without the need of screws. However, other robots still have fasteners and other mods to complete the structure. The maintenance unit structure consists of usually six- to eight-wheeled legs, distributed in pairs of three/four, on each side, separated by an angle of 120° or lesser, supporting the structure along the center of the pipe. The advantage with these robots is its capacity to lock it into any allowed postures. Being made of parallel loops, the mechanism inherently brings in the load distribution, better stability, and stiffness characteristics of parallel manipulators. This is true only when in contact with the walls of the pipes. Figure 1 shows a few robots of this type. Even the cleaning system is similar to an umbrella-like open-and-close mechanism, which makes the robot highly adaptable to different pipe sizes.

Contrary to the standard cylindrical robot, the location of the rotating actuator is not in the central axis of the robot, it is located on the arm which is opposite to the arm with the tool. Hence, this rotating actuator (drive wheel) rotates with its entire cleaning mechanism. It is a general observation that the forward transformation for a cylindrical robot is quite simple, because it is equivalent to the transformation from a cylindrical to a Cartesian frame. The main challenge is to accurately place the robot in the center of the pipe while overcoming the push back forces and vibrations caused in the cleaning process, so that the cleaning tool is able to focus on the desired area of the pipe surface.

3.2 *Climbing Mechanisms*

Wet adhesive wheels and contact points provide the ability to climb vertical walls. But it gets quickly dried and loses adhesion. Dry adhesive medium has higher elastic

Fig. 2 THESBOT developed by Tokyo-based HiBot [1]

force and rely on Van der Waal forces. Magnetic wheel has the ability to climb vertical wall but these wheels work only on ferromagnetic surfaces. Wall vacuum suction has ability to attain continuous movement and high moving speed. It requires substantial power and hence the system becomes too complex to fit into smaller piper diameters. Figure 2 shows THESBOT with a potential to climb vertically. These robots have the requirement to overcome gravity which it easily does by compensating with the torque capacity of the motors. The problems faced are to ensure adequate traction forces at the available points of contact. Most of them are also commercially available with joystick control. A configuration that works for vertical pipelines would be able to handle any slopes too, and however, some robots are developed to climb specific slopes.

3.3 Twist-to-Turn Mechanisms

The main difference of this mechanism is to provide a rotary twist to the moving unit with respect to the stationary unit of the robot in order to traverse through the horizontal and vertical cross section of the pipe. The stationary channel acts as the base for the mobile channel to move in the forward direction and reverse direction as shown in Fig. 3. This skewing motion ensures the required traction forces and also allows the robot to be positioned in any angle in relation to the axis of the pipeline.

These robots have at least two passive degrees of freedom like pitch and yaw degrees of freedom, which allow the robot to adapt to the curved shape of pipe in both directions. Sometimes a mechanism is provided in the robot to keep the stability of movement and generate forces between the robot and the pipes to keep its position in vertical and curved pipe conditions.

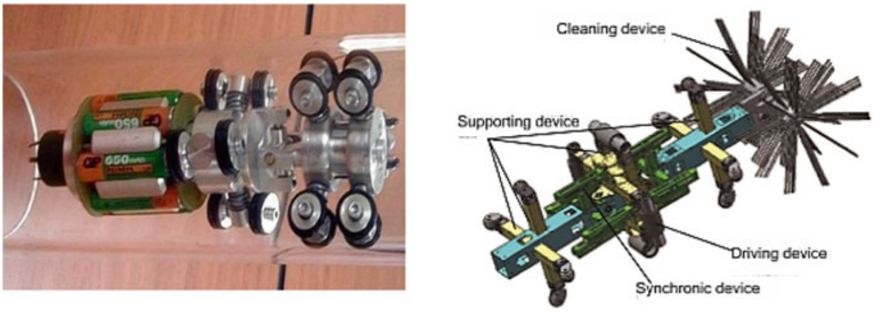

Fig. 3 A few twist-to-turn mechanisms D-70/2 HELI-PIPE [12] and PCV-1 [18]

A significant amount of energy is required to negotiate bumps and turns and hence it is not preferable mechanisms under normal operating conditions. And, on the other hand, one should provide overload protection to prevent the mechanism overloading.

3.4 Reconfigurable Mechanisms

Any understanding of the variability in the dimensions of the pipelines that the robot would encounter would validate the needs for these robots to be reconfigurable. The robot mechanisms are to be designed in such a way as to expand and contract between the chosen limits. This necessitates the use of a mechanism where the input link causes the other links to move in a uniform fashion without any crossovers. All these characteristics bring in the need for reconfigurability in these robots [19]. Most of both the group of robots discussed in the self-locking mechanism and the twist-to-turn types fall under this category of mechanisms, as like the one shown in Fig. 4. During the forward motion of robot, the traction motor is in a clockwise

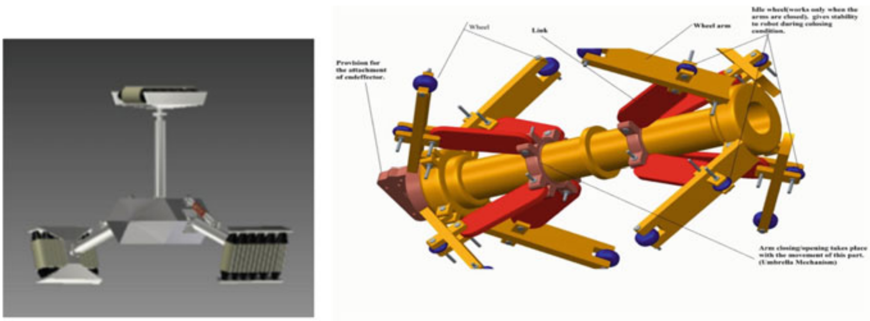

Fig. 4 Reconfigurable mechanisms [XX, 17, 20]

direction, but when the manipulator is stalled due to extra loading effect by extreme blockage of sewage, the manipulator limit switch is activated.

The common umbrella-like mechanism consists of a structure with an ability to increase its height in order to adapt to different pipe diameters. Even for the caterpillar mechanism, turning from flat to the vertical axis inside the pipeline is difficult. This is because of the low contact for the caterpillar wheels to have the capacity to reach to within limits of the pipeline. At this point, when there is a less area of contact, the robot wheels cannot have any significant bearing the usefulness of separating the caterpillar's pace for making a turn. The robot can make a turn by making the wheels stationary reaching the internal corner of the T-branch and pivoting the wheels reaching the external corner of the T-branch toward the vertical side. The design, kinematics, and the control of these robots are relatively difficult owing to its complexity in their vector loops. Nevertheless, they are increasingly finding their applications in most field of robotics.

3.5 Multiple to Partially Active Mechanisms

Some scenario requires only a part of the robot to be active. In some cases, the entire robot need not have active parts. Both the design requirements allow for some robots to be partially active. Most of these robots would have multiple segments, some active and some passive. Even the active segments could be a repeated segment with same/identical functionality. Intermediate elements like universal joints, as shown in Fig. 5 enable the robot to make a turn movement in the three-dimensional pipe systems. The elastic sliding pairs have also adopted the synchronous mechanism to keep the robot in stable posture and position in the pipe. Another advantage that this mechanism offers is the possibility of more payload in more numbers.

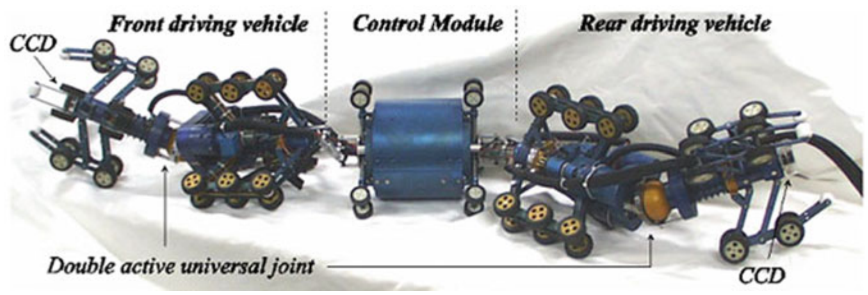

Fig. 5 MRINSPECT robot [15]

The length of the robot places a considerable taxing on the length of the robot and so on the cablings and makes it difficult to handle manually. Another drawback of these robots is that the friction between the pipe and the cables for communication and power supply makes it difficult to move a long distance. Autonomous more is preferred in these cases.

3.6 Simple Drive-by Mechanisms

A classic example of these types of robot mechanisms is the crawler-driven mechanism as shown in Fig. 6. Motion motor of the robot produces more driving force, the adhesion force only contributed by robot weight may be insufficient, and its driving wheels may slip on the surface of pipe wall. Therefore, an additional pressure enhancing adhesion force should be produced by the pipe diameter adaptive mechanism to improve the tractive capacity of the robot. Other simple wheeled units also fall into this category. It is easier to design, build, and control these robots.

In the harsh and slippery environment of sewer, a 4-wheel drive mechanism would be more effective and provide sufficient and stable traction in experiment. So, in the power transmission system of the robot, the output shaft of the gearbox is coupled with the four wheels through a right angle gearbox and a chain. Another important factor which improves the mobility of the robot is the distance between the bottom of the robot and the ground. Increasing the distance results in passing through bigger obstacles and more mobility. The problem with these types of robot is the inability to provide horizontal force to clear or perform any tasks inside the pipelines. Alone

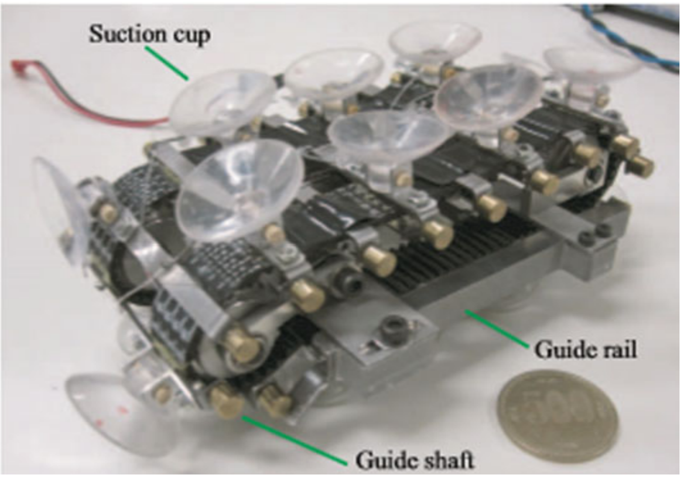

Fig. 6 Crawler-driven mechanism [16]

these robots are only effective for surveillance and that too only where there are no opposing forces like the presence of water or obstacles on its path.

4 Another Design Perspective

Apart from all these types of robot mechanism mentioned above, a new class would be to have a reconfigurable in-pipe robot that allows for networking of these robots like a transformer robot [13]. Such capabilities to configure new mechanism on the go are needed as the robot is expected to encounter new scenarios and it cannot be possible to have one robot with all the capabilities. Swarm robotics for in-pipe robots calls for a complete new outlook to the usual design aspects of these mechanisms. Many design modifications on these lines have been indicated in those conditions [14]. A provision to hold, lift, and contact physically the other robot in order to work together brings an entirely different scope of research, which would be covered in another paper. The sharing of resources, shared control, and shared payload would be the theme for this perspective. These robots are expected to use the provision available in the environment, like a guideway or a pole to enhance its performance.

5 Conclusion

An extensive review of the mechanisms that allow locomotion to the in-pipe robots is performed in this paper. A broader classification that allows more clarity on these robots for choosing them based on their capacities is provided. This perspective is different from the other review papers in that sense and is needed for the researchers to identify new design directions for improvising the performance of their robots. A new design perspective for in-pipe robots for swarm applications is also presented.

References

1. https://newatlas.com/hibot-thesbot-pipe-inspecting-robot/40726/
2. https://en.wikipedia.org/wiki/Sewer_gas
3. https://en.wikipedia.org/wiki/Chennai. Last accessed on 12.03.2019
4. Somashekhar D, Hiremath S, Singaperumal M, Ramakrishnan R (2013) Design and development of a reconfigurable type autonomous sewage cleaning mobile manipulator. Procedia Eng 64:1464–1473
5. Mateos LA, Vincze M (2013) In-pipe robot with capability of self stabilization and accurate pipe surface cleaning. Automation and Control Institute (ACIN), Vienna University of Technology (TU WIEN), Vienna
6. Hille C, Nasir AK, Abreu AA, Piñeiro DL, Roth H (2014) Development of an outdoor mobile robot for teleoperation as an agent for a robot network. In: Proceedings of the 19th World

Congress the International Federation of Automatic Control, Cape Town, South Africa, 24–29 Aug
7. Borenstein J, Everett HR, Feng L, Wehe D (1997) Mobile robot positioning: sensors and techniques. J Robot Syst 14(4):231–249
8. Nassiraei AAF, Ishii K (2007) Concept of intelligent mechanical design for autonomous mobile robots. J Bionic Eng 4:217–226
9. Yuan F, Wang L (2010) The design and study of the drainage pipelines dredging robot. In: International Conference on Computing, Control and Industrial Engineering
10. Alireza H, Gholamhossein M (2012) Developing a sewer inspection robot through a mechatronics approach. In: International Conference on Mechanical, Automotive and Materials Engineering (ICMAME'2012), 7–8 Jan
11. Shrivastava AK, Verma A, Singh SP (2012) Development of robotic sewerage blockage detector controlled by embedded systems. In: IEEE International Conference on Advances in Engineering, Science and Management (ICAESM-2012), 30, 31 Mar 2012, pp 290–295
12. http://scmero.ulb.ac.be/project.php?id=5&page=robotics_pipe_inspection.html
13. Kurokawa H, Tomita K, Kamimura A, Kokaji S, Hasuo T, Murata S (2008) Distributed self-reconfiguration of M-TRAN III modular robotic system. Int J Robot Res 27(3–4):373–386
14. Ducatelle F, Di Caro GA, Pinciroli C, Gambardella LM (2001) Self-organized cooperation between robotic swarms. Swarm Intell 5(2):73–96
15. Choi HR, Ryew SM (2002) Robotic system with active steering capability for internal inspection of urban gas pipelines. Mechatronics 12(5):713–736
16. Yoshida Y, Ma S (2010) Design of a wall-climbing robot with passive suction cups. In: Proceedings of the 2010 IEEE, International Conference on Robotics and Biomimetics, Dec 14–18, Tianjin, China, pp 1513–1518
17. Satish PV, Dorapudi SH, Seeli H, Kumar SN (2017) Design of an In-pipe inspecion robot. Int J Eng Res 6(03):63–68
18. Ye C, Ma S, Li H, Yang J (2010) Development of a pipe cleaning robot for air conditioning system. In: IEEE International Conference on Robotics and Biomimetics, Tianjin, 2010, pp 1525–1529. https://doi.org/10.1109/ROBIO.2010.5723556
19. Satheesh Kumar G, Nagarajan T (2012) Reconfigurable Stewart platform for vibration isolation. Trends Intell Robot Autom Manuf Commun Comput Inf Sci 330:37–45
20. Ajin M, Satheesh Kumar G, Karthikeyan P (2016) Design, structural and kinematic analysis of reconfigurable sewage cleaning robot. Int J Appl Mech Mater 852(763–769):2016

Thermal and Engine Engineering

Design and Thermal Performance Analysis on Solar Still

Shaik Subhani and Rajendran Senthil Kumar

Abstract Economically feasible and eco-friendly water treating technologies are most expected in Asia and Africa which lead to an increase in usage of renewable energy. Hence, solar stills are the best choice to resolve the issue related to water scarcity. Due to the low productivity of solar stills, continuous research is being performed considering different parameter changes to optimize its production. Research had been carried out by altering and optimizing the condensing surface of solar still for performance improvement. In this research, the modification of condensing surface is done by multiple hemispherical slopes. The flow pattern has been analysed inside the solar still before and after modification and the changes in performance have been compared with single slope solar still and presented for better understanding.

Keywords Solar still · Natural convection · Rayleigh number · Nusselt number · Baffle · CFD

Nomenclature

g	Gravitational pull (m/s^2)
H	Height (m)
h	Convective heat transfer coefficient $\left(\frac{\mathrm{W}}{\mathrm{K\,m^2}}\right)$
k	Thermal conductivity $\left(\frac{\mathrm{W}}{\mathrm{K\,m}}\right)$
L	Characteristic length (m)
Nu	Nusselt number
Ra	Rayleigh number
T	Surface temperature (K)
T_{B}	Temperature at bottom (°C)
T_{T}	Temperature at top (°C)

S. Subhani · R. S. Kumar (✉)
Department of Mechanical Engineering, SRM Institute of Science and Technology, Chennai, India
e-mail: senthilr2@srmist.edu.in

E. T. Akinlabi et al. (eds.), *Trends in Mechanical and Biomedical Design*, Lecture Notes in Mechanical Engineering,
https://doi.org/10.1007/978-981-15-4488-0_60

T_∞ Bulk mean temperature (K)
v Kinetic viscosity (m^2/s)
α Thermal diffusivity (m^2/s)
β Thermal expansion coefficient (K^{-1})

1 Introduction

Demand for freshwater is increasing due to an increase in population, agricultural and industrial activities. As per sources, the water available in the world in which 97% of it is saline and 2% of it is in frozen form and only 1% of it is available for drinking purposes. There are many desalination techniques available such as Reverse osmosis, multistage desalination etc. but because of unavailability of such vitalities in rural areas leads to choose the solar based desalination as the production is free of cost and also energy is abundantly available in tropical regions. The basic operating principle is simple as due to solar radiation the water gets heated up to evaporating temperature, as water vapour rises and touches the condensing surface and forms pure water removing impurities. Though it is very much available in our region, the production rate is lower while compared to other techniques as the availability of energy is limited and effects with factors like seasons, water mass and other atmospheric conditions which leads researchers to work on increasing the productivity rate with respect to energy availability.

2 Literature Review

Madhav [1] compared the performance of still made of black granite as basin material with the still performance with basin material as iron steel basin and proved the productivity is increased for black granite solar still around 38% than solar still with basin iron steel where the water temperature is increased up to 87 °C in basin with black granite as basin with iron steel is reaching around 79 °C. Badran [2] theoretically compared the active single slope solar still by changing various parameters with experimental data to get the optimized combination to increase the productivity of solar still. From the study, he proved that active solar stills have various options to enhance the performance of the still. Abdallah et al. [3] experimentally studied the performance of single slope solar still thermally by using different types of absorption materials and concluded as solar still with uncoated sponge has the highest collection rate of water during day and after considering the total production gain at nights also they found the performance as 60% for black rocks, respectively. Akash et al. [4] studied the effect in single-basin solar still with double slopes by optimizing with different absorbents in the basin and further increasing the performance of the still. Khalifa et al. [5] studied experimentally by incorporating new designs of basin-type solar stills as feedwater is preheated using solar heater and compared with the help of performance and efficiency of the still. Ismail [6] experimentally studied by designing and fabricating the hemispherical solar still and found the efficiency as 33% with 50% as conversion ratio. Tayeb [7] experimentally studied the performance of the solar stills with different designs and by comparing the results concluded that the highest ratio of the area of condensation to the evaporation surface leads to the increased production of the solar still. Khalifa and Hamood [8] studied the performance of basin-type solar still with the help of correlations and concluded that the tilt angle of cover of about 30° gives the highest productivity and 20% enhancement of adding soluble dyes. Akash et al. [4] studied the effect in single-basin solar still with double slopes by optimizing with different absorbents in the basin under same parametric conditions and found the further increase in performance of the still. Ali et al. [9] numerically analysed by modelling the solar still with granular activated carbon using MATLAB software and stated that with irrespective of different heights of granular activated carbon the productive output is more up to 2 PM and gradually decreases after that. Arunkumar et al. [10] experimentally studied the constructed solar stills with different geometrical designs as spherical, pyramid, hemispherical solar stills, etc., and after operating in same climatic conditions and analysing the modifications on the performance concluded the solar still with tube assistance by compound parabolic concentrator that has the maximum production rate. Arunkumar et al. [11] experimentally studied redesigned solar still with a hemispherical condensing surface and found that the production rate has been increased by decreasing the temperature of condensing surface by allowing water over it and also efficiency was increased up to 42% after cooling the condensing surface, even though the performance has been analysed experimentally by cooling the hemispherical condensing surface and the further research has been done by comparing the hemispherical solar still with single-slope solar still numerically and also increasing the number of hemispherical condensing surfaces.

3 Problem Statement

In this study, a solar still with modified condensing surface of multiple curves as hemispherical shape is considered for numerical analysis using *Ansys Fluent-18* by considering suitable assumptions as shown in Fig. 1, and with a non-dimensionalized design parameters, such a still walls of height H and separation between them is $3.91H$ and condensing surface height is of $0.25H$, $0.251H$ and $0.24H$ for single curved, double curved and triple curved, respectively. Here, lower boundary is at the topmost layer of water basin. Top condensing surface temperature is T_{T}, and bottom evaporating surface temperature is T_{B}. Here, the flow is steady, 2D and laminar. Humid air with incompressible nature is preferred as a still fluid. The fluid thermophysical properties are referred at bulk mean temperature, i.e. $[(T_{\mathrm{T}} + T_{\mathrm{B}})/2]$. The constant operating temperature difference of 10 °C has been preferred by varying top and the bottom wall of still ranging from 30 to 70 °C. In addition, the still performance has

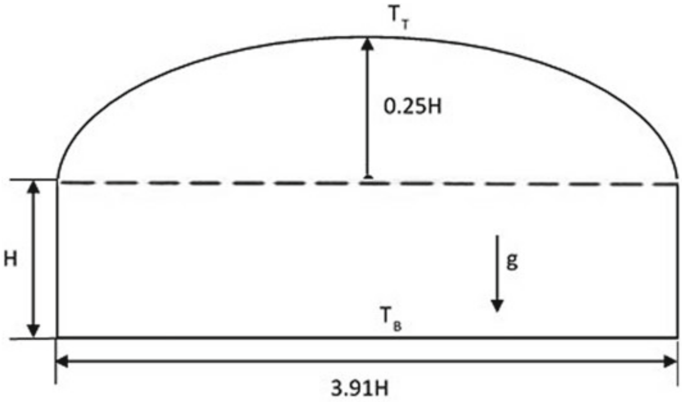

Fig. 1 Solar still with single curved hemispherical condensing surface

been decided to analyse by variable operating temperature difference ranging from 5 to 25 °C to resemble the real field scenario when phase-changing material is dumped in the still basin.

4 Governing Equations, Boundary Conditions and Solution Procedure

The general governing equations for fluid flow and heat transfer have been reduced to 2D form by incorporating suitable assumptions and presented in Eqs. (1)–(4)

Continuity equation

$$\frac{\partial u}{\partial x} + \frac{\partial v}{\partial y} = 0 \tag{1}$$

X-Momentum equation

$$\rho\left(u\frac{\partial u}{\partial x} + v\frac{\partial u}{\partial y}\right) = -\frac{\partial p}{\partial x} + \mu\left(\frac{\partial^2 u}{\partial x^2} + \frac{\partial^2 u}{\partial y^2}\right) \tag{2}$$

Y-Momentum equation

$$\rho\left(u\frac{\partial v}{\partial x} + v\frac{\partial v}{\partial y}\right) = -\frac{\partial p}{\partial y} + \mu\left(\frac{\partial^2 v}{\partial x^2} + \frac{\partial^2 v}{\partial y^2}\right) + g\beta(T - T_\infty) \tag{3}$$

Energy equation

$$u\left(\frac{\partial T}{\partial x}\right) + v\left(\frac{\partial T}{\partial y}\right) = \alpha\left(\frac{\partial^2 T}{\partial x^2} + \frac{\partial^2 T}{\partial y^2}\right) \tag{4}$$

The equations are discretized and solved using the finite volume method by imposing suitable boundary conditions. No-slip boundary condition has been imposed at walls of solar still also adiabatic boundary condition is preferred for vertical walls of the still to resemble the insulation on the real field. The driving potential is given on the top and bottom wall by defining constant temperatures as described in the problem formation. The convective terms present in governing equations have been discretized using second-order upwind scheme. *SIMPLE* algorithm is selected and the residuals preferred in the order of 10^{-3} for the mass and momentum conservation and 10^{-6} for energy.

Formulae

$$\mathrm{Nu} = \frac{hL}{k} \tag{5}$$

$$\mathrm{Ra} = \frac{g \cdot \beta \cdot (T - T_\infty) \cdot L^3}{v \cdot \alpha} \tag{6}$$

5 Grid Generation and Grid Independence

The formulated problem consists of curved condensing surface and flat evaporation surface leads to prefer unstructured triangular mesh elements using Ansys Workbench. To capture exact flow physics and heat transfer, highly intensified fine mesh structure has adopted the region nearer to solid walls and curved surface (Fig. 2). To ensure grid independence, a detailed study has been carried out for single-slope solar still (Table 1) with varying mesh elements. It was found that the total grid count (10,216 elements) has the minimum influence on final results which is also in the acceptable range.

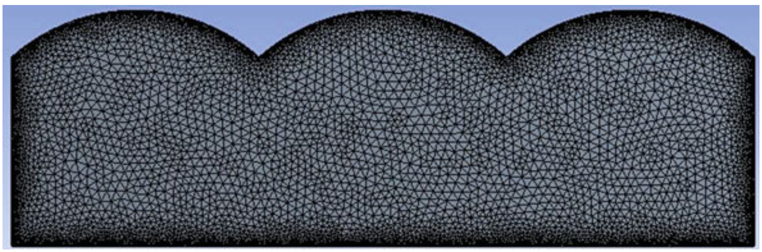

Fig. 2 Mesh alignment in solar still with triple curved condensing surface

Table 1 Grid independent study

No. of elements	Nusselt number	Percentage of variation
7984	11.95	–
9173	10.127	18.00
10,216	10.00	1.27
13,615	9.99	1.00

Table 2 Dimensions of solar still in literature

T_B (°C)	T_T (°C)	L_L (m)	L_H (m)	R_H (m)	θ (°)
63	48	0.438	0.075	0.187	14.35

Table 3 Validation of present computation with literature

Nu (Rahbar and Esfahani [13])	Nu (Rashidi et al. [12])	Nu (Present study)	Percentage of variation (%)
10.7	10.5	10.4	2.8 and 0.95

6 Results and Discussions

6.1 *Validation of Computation*

Rashidi et al. [12] and Rahbar and Esfahani [13] numerically analysed the performance of plain solar still with dimensions 7.5 cm on the left side, 18.7 cm on the right side with 14.35° steep angle and separation between is 43.8 cm (Table 2).

Hence, the present computation compared and validated the performance of solar still in Table 3. Now, the present computational results closely match with literature.

6.2 *Performance Analysis of Solar Still at Constant Temperature Differences*

The present study compares the velocity and temperature contours of a single-slope solar still with modified condensing surfaces at constant temperature difference by varying temperatures of condensing and evaporating surfaces. Firstly, the single-slope solar still has been considered for analysis. Here, non-uniform bi-cellular flow structure whose axis is almost normal to the condensing surface has been observed (Fig. 3) when the temperature difference is 10 °C ($T_T = 30$ °C, $T_B = 40$ °C). The top and bottom surface temperatures have been gradually increased to 40 °C and 50 °C, respectively, but the considerable variations do not significantly influence the fluid velocity, flow structure, vorticity magnitude (Fig. 3) and convection heat transfer

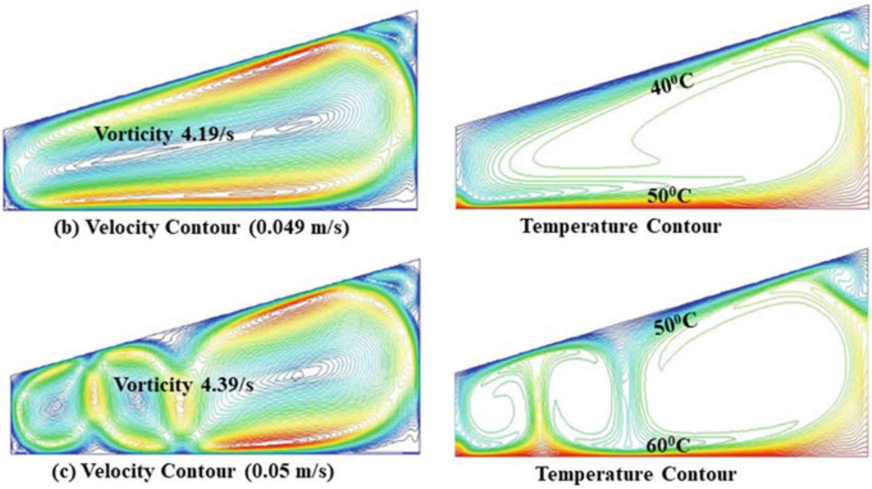

Fig. 3 Respective velocity and temperature contours in conventional still

(Table 4). Furthermore, on increasing the level of heat intensity on evaporating (60–70 °C) and condensing (50–60 °C) surfaces, there is a considerable increase in fluid velocity, vorticity magnitude and forms four revolving vortices at different sizes with heat transfer enhancement of 30% (Table 4).

Now, the conventional still has been redesigned by changing the shape of condensing surface. Exactly when the condensing surface is single hemispherical curved structure, the average fluid velocity increases and vorticity magnitude decreases with appreciable increase in convective heat transfer when the top and bottom surface temperatures 30 and 40 °C have been maintained in the still before and after redesign of single curve condensing surface (Fig. 4). And further increasing temperature encourages the formation of more vortices with an increase in vorticity magnitude and decrease in average fluid velocity but the convection-based heat transfer is decreased as the multiple revolutions of fluid segregate the heat at centre of the still and the

Table 4 Nusselt number versus Rayleigh number at constant temperature difference for before and after redesigning of solar still

Bottom wall temperature (°C)	Constant temperature difference with top wall (°C)	Ra (10^3)	Nusselt number			
			Without curves	Single curve	Double curve	Triple curve
40	10	2722.3	9.368	9.057	8.861	9.839
50	10	2350.9	9.36	9.94	9.310	9.806
60	10	2040.3	12.17	9.54	8.765	8.442
70	10	1779.3	12.17	8.06	9.994	9.132

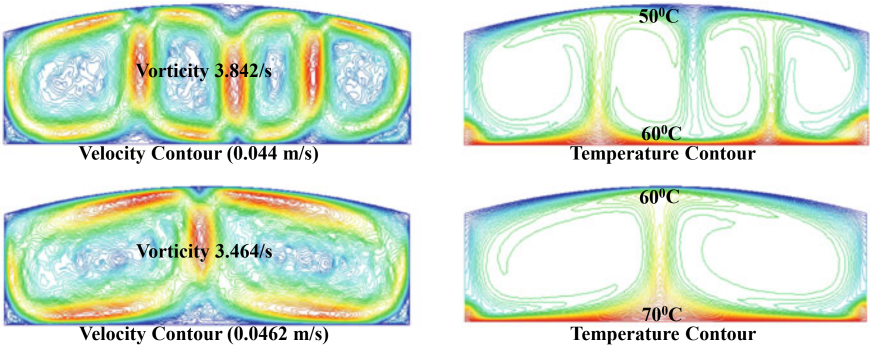

Fig. 4 Respective velocity and temperature contours for single curved solar still

highest top and bottom wall temperatures (Fig. 4) again form bi-cellular flow structure with heat concentrations at top and the centre of the still resulting lowest heat transfer rate (Table 4). When the condensing surface is further modified into double curved hemispherical shape, it forms bi-cellular flow structure symmetric to the solar still at surface temperatures (30–40 °C) of the top and bottom walls with heat concentration at middle and lower part of the still resulting heat transfer (Table 4) reduction when compared to single-slope solar still (Fig. 5). Further increasing top and bottom wall temperatures (40–50 °C) form tri-cellular flow pattern by dividing formed vortices previously with an increase in vorticity magnitude and average fluid velocity (Fig. 5) by encouraging heat transfer (Table 4). Exactly at higher surface

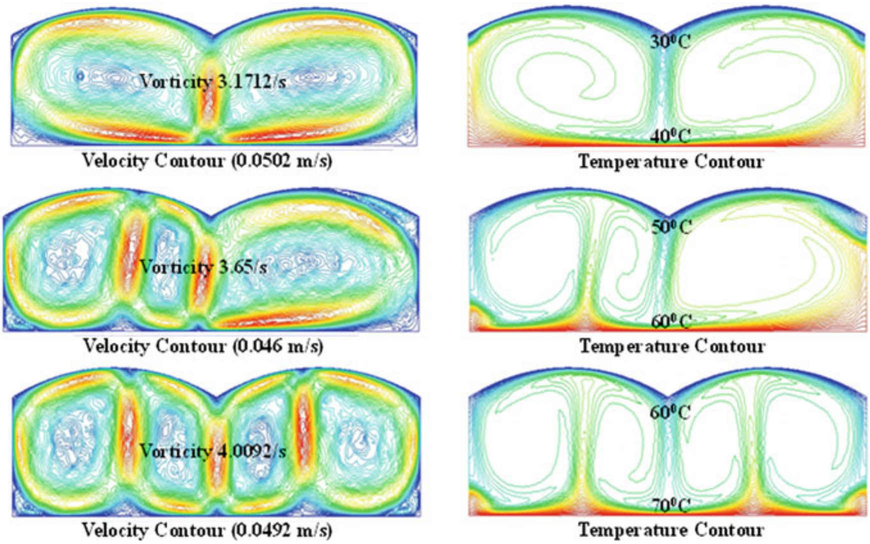

Fig. 5 Respective velocity and temperature contours for double curved solar still

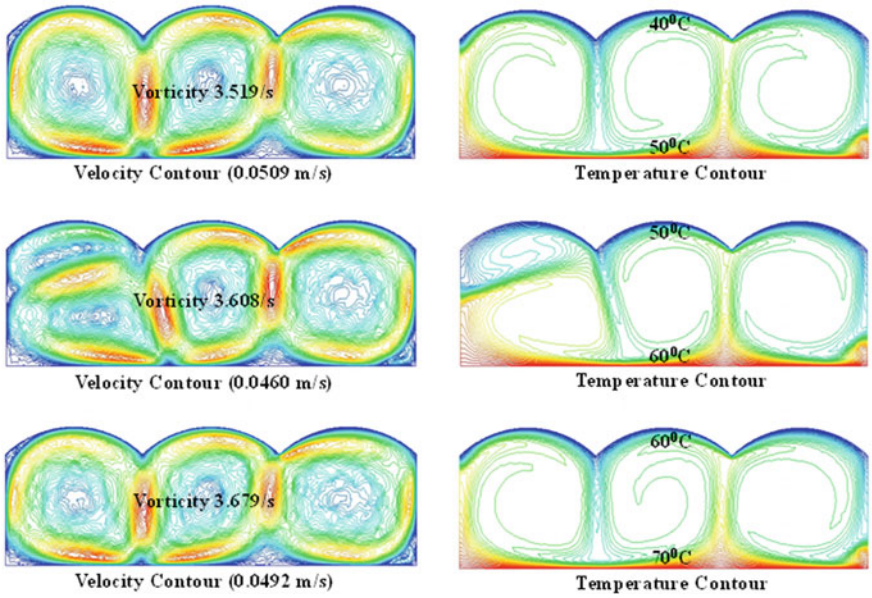

Fig. 6 Respective velocity and temperature contours for triple curved solar still

temperatures, more number of revolving vortices are concentrating heat at centre of the still with lower convective heat transfer (Table 4) when compared to single slope solar still.

When condensing surface is again modified with triple-slope hemispherical structure, it forms more number of revolving vortices (Fig. 6) at lower surface temperatures (30–40 °C, 40–50 °C) of top and bottom walls with effective enhancement of heat transfer when compared to single-slope solar still as appreciable heat is carried by the fluid flow (Fig. 6). And when top wall temperature (50 °C), bottom wall temperature (60 °C) an adverse flow pattern with non-interacting baby vortices has been observed with decrease in natural convection all though the vorticity magnitude increases (Fig. 6). Again at higher wall temperatures, the same favourable tri-cellular vortices formation has been observed with effective heat transfer rate (Table 4).

6.3 *Performance Analysis of Solar Still at Variable Temperature Differences*

Similarly, the performance analysis of the solar still has been done for variable temperature difference by maintaining the top and bottom wall temperatures range from 25 to 90 °C. Now when conventional still is taken into consideration, at lower

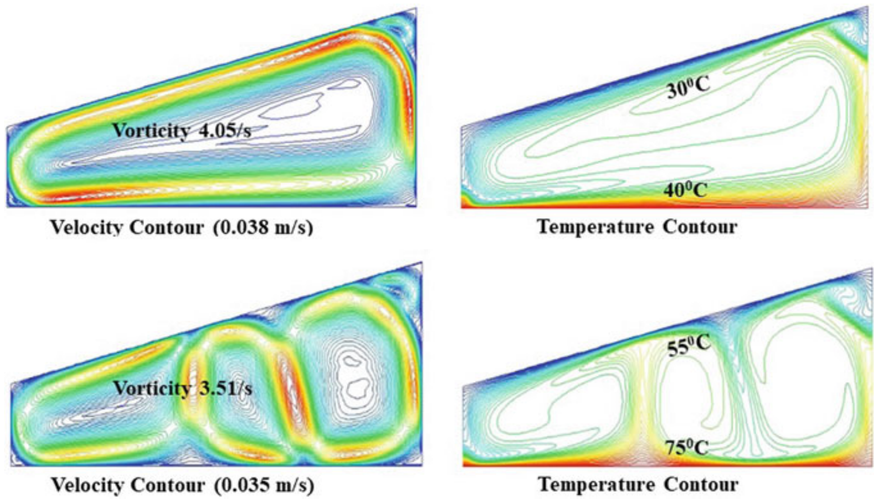

Fig. 7 Respective velocity and temperature contours for conventional still

temperature difference and wall temperatures, more heat transfer enhancing vortices are formed with less velocity of the fluid.

Additionally, increase in temperature difference leads to merging of vortices (Fig. 7) in turn decrease in heat transfer about 19% (Fig. 11), and again with increase in temperature gives favorable number of vortices (Fig. 7) with ascension in size where its considerable increase in amount of heat transfer, fluid velocity and vorticity magnitude.

Again, at higher temperatures, they merge and form bi-cellular flow structure with the axis normal to condensing surface where there will be no significant enhancement of natural convection inside. When the condensing surface is single curved in solar still, high-performance fluid flow structure with low vorticity magnitude and average fluid velocity has been absorbed (Fig. 8) at lower wall temperatures top (25 °C), bottom (30 °C) with effective heat transfer (Fig. 11) but lower than single-slope solar still. Further increasing the temperature differences, bi-cellular effective heat transferring vortices flow pattern has been absorbed with a gradual increase in vorticity magnitude, average fluid velocity and heat transfer also with no fluctuations as in single-slope solar still (Fig. 11). When the solar still with condensing surface is modified with double curved hemispherical shape, three revolving vortices along with one non-interacting baby vortex are observed (Fig. 9) at lower variable temperatures and further increase in temperature difference between top and bottom wall temperatures tri-cellular heat transfer enhancing vortices formation is observed (Fig. 9) with merging of non-interacting baby vortex formed earlier with gradual increase in vorticity magnitude, average fluid velocity and heat transfer also with no fluctuations as in single-slope solar still. When condensing surface is again modified with triple slope hemispherical structure, a tri-cellular heat transfer enhancing vortex formation with minute flow separation has been observed (Fig. 10) at lower-to-medium temperature

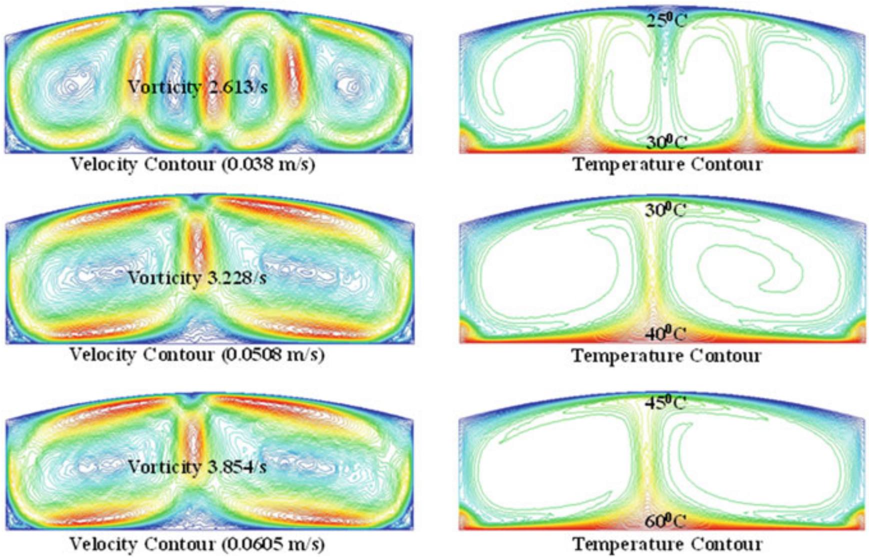

Fig. 8 Respective velocity and temperature contours for single curved solar still

difference (15 °C) with gradual increase in heat transfer rate (Nu = 8.49–9.86).and by increasing temperature difference up to maximum (i.e. 20 and 25 °C), a full surface touching tri-cellular vortices have been formed with maximum heat transfer (Nu = 10.82 and 10.72) with no fluctuations as in single-slope solar still (Figs. 10 and 11).

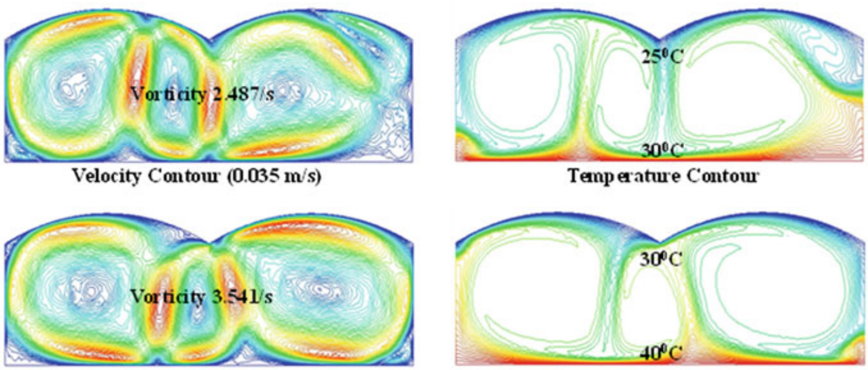

Fig. 9 Respective velocity and temperature contours for double curved solar still

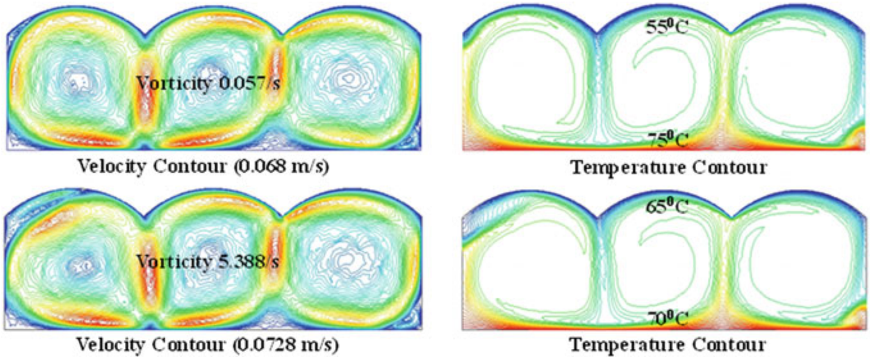

Fig. 10 Respective velocity and temperature contours for triple curved solar still

Fig. 11 Nu versus Ra plot when the still is at variable temperature difference

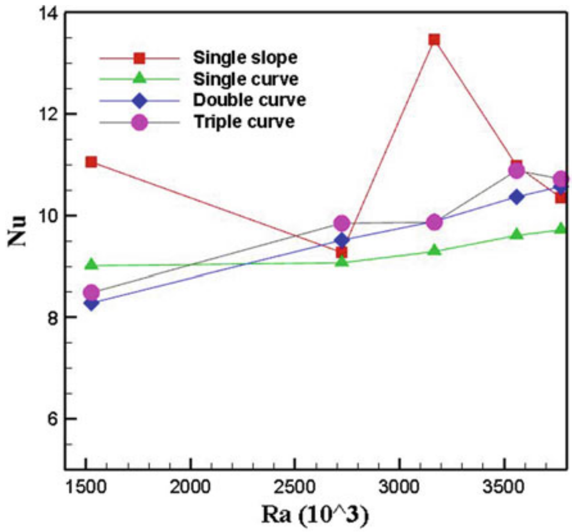

7 Conclusion

The flow and heat transfer analysis on single-slope and hemispherical solar still with constant and variable temperature differences have been analysed and reported the performance with necessary supporting contour plots and figures. Comparing single-slope solar still with modified still of multiple curves at condensing surface, there is an advancement in the formation of multiple vortices with an increase in circulation strength and enhances the convection heat transfer considerably, by minimizing lesser fluctuations in convective heat transfer and stable condensation. Modifying the single-slope condensing surface into hemispherical surface gives the better revolving structure for fluid and keeps on increasing the curves giving better results and also multiple hemispherical surfaces can be supported easily and ensures structural stability. If now variation of Nusselt number is very small compared to other curves but in larger-scale production, the production rate will increase. And we tried to enhance the production rate of the still by modifying the design of single slope to curved condensing surface meaningfully. The adverse fluid flow structure has been clearly identified and reported in appropriate places.

Acknowledgements We sincerely acknowledge the Modelling and Computing facilities available at Product development lab and CFD lab at Department of Mechanical Engineering, SRMIST.

References

1. Madhav J (2011) Performance of black granite basin solar still. Int J Tech Sci 2(2):161–168
2. Badran O (2011) Theoretical analysis of solar distillation using active solar still. Int J Therm Environ Eng 3(2):113–120
3. Abdallah S, Abu-Khader MM, Badran O (2009) Effect of various absorbing materials on the thermal performance of solar stills. Desalination 242:128–137
4. Akash BA, Mohsen MS, Osta O, Elayan Y (1998) Experimental evaluation of a single basin solar still using different absorbing materials. Renew Energy 14(1–4):307–310
5. Khalifa AJ, Al-Jubouri AS, Abed MK (1999) An experimental study on modified simple solar stills. Energy Convers Manage 40(17):1835–1847
6. Ismail BI (2009) Design and performance of a transportable hemispherical solar still. Renew Energy 34(1):145–150
7. Tayeb AM (1992) Performance study of some designs of solar stills. Energy Convers Manag 33(9):889–898
8. Khalifa AJN, Hamood AM (2009) Performance correlations for basin type solar stills. Desalination 249:24–28
9. Ali MDI, Kumar RS, Mahendran R (2011) Modelling of solar still using granular activated carbon in matlab. Bonfring Int J Power Syst Integ Circ 1
10. Arunkumar T, Vinothkumar K, Ahsan A, Jayaprakash R, Kumar S (2012) Experimental study on various solar still designs. ISRN Renew Energy, Article ID 569381, 10 pages
11. Arunkumar T, Jayaprakash R, Denkenberger D, Ahsan A, Okundamiya MS, Kumar S, Tanaka H, Aybar HS (2012) An experimental study on a hemispherical solar still. Desalination 286:342–348
12. Rashidi S, Bovand M, Esfahani JA (2016) Optimization of partitioning inside a single slope solar still for performance improvement. Desalination 395:79–91
13. Rahbar N, Esfahani JA (2013) Productivity estimation of a single-slope solar still: theoretical and numerical analysis. Energy 49:289–297

The Use of Hydrocarbon Refrigerants in Combating Ozone Depletion and Global Warming: A Review

T. O. Babarinde, S. A. Akinlabi, and D. M. Madyira

Abstract Vapour compression systems are associated with high energy demand and contribute to ozone depletion and global warming due to halogenated refrigerants used in them which are unfriendly to the environment. Hydrocarbon refrigerants have been proposed as a substitute to halogenated refrigerants due to their zero ozone depletion potentials, very low global warming potentials, and lower energy demand for effective operations. In this review, the terms ozone depletion and global warming are explained and the causes. Also, the use of hydrocarbon refrigerants as an ideal solution to energy security and environmental challenges accompanied by vapour compression systems are discussed. Lastly, this paper revealed that hydrocarbon refrigerants are long term replacement for halogenated refrigerants in a vapour compression system.

Keywords ODP · GWP · Hydrocarbon refrigerants · Energy efficiency

1 Introduction

In the world today, 17% of the world electricity demand goes into refrigeration and air-conditioning and heat pump appliances [1]. And the trend will persist to grow in the future to come, especially in the developing countries where we have 81% of the world population [2]. In an effort to balance the environmental challenges such as the depletion of the Ozone Layer (OL) and Global Warming (GW), and energy required by Refrigeration & Air-conditioning (R&A) and heat pump systems, an eco-solution approach must be adopted for long term sustainability.

Refrigeration and Air-conditioning (R&A) systems are designed for comforts and preservation of foods, cooling is usually employed in order to reduce the propagation

T. O. Babarinde (✉) · S. A. Akinlabi · D. M. Madyira
Department of Mechanical Engineering Science, University of Johannesburg, Johannesburg, South Africa
e-mail: taiwo.babarinde79@gmail.com

T. O. Babarinde · S. A. Akinlabi
Department of Mechanical Engineering, Covenant University, Ota, Nigeria

E. T. Akinlabi et al. (eds.), *Trends in Mechanical and Biomedical Design*, Lecture Notes in Mechanical Engineering,
https://doi.org/10.1007/978-981-15-4488-0_61

of bacteria in them. One of the advantages of cooling or freezing by preservation is that it does not require the use of preservatives. Also, R&A systems are being used in homes and industries for private and commercial purposes. While there is an advancement in the technology design used today to improve comfort systems and preservation of foods, it is leading to environmental challenges called Ozone Depletion (OD) and Global Warming (GW) [3, 4].

The major problem facing the refrigeration industries currently are OD and GW. Ozone molecules are made up of three atoms of oxygen, it is a poisonous gas that if breathed in by humans or animals can lead to death. The earth stratosphere is being surrounded by the ozone layer. The OL has its own importance, it protects the earth from dangerous ultraviolet radiation coming directly from the sun. The OL absorbs the ultraviolet B and the oxgen capture ultraviolet C while ultraviolet A is being permitted but ultraviolet B is dangerous and it's capable of destroying our environment and threatens life [3].

It has been established that human activities are responsible for ozone layer depletion due to the production of greenhouse gases called halocarbons [5]. Halocarbon compound contains carbon and one or more halogens, this could be fluorine (Fl), chlorine (Cl), Iodine (I) and bromine (Br). These gases are produced by humans for industrial applications. They have wide industrial applications such as R&A, production of foams and cleaning solvent. The three main groups of halogenated refrigerants are chlorofluorocarbon (CFC), hydrochlorofluorocarbon (HCFC) and hydrofluorocarbon (HFC). Refrigerants such as CFCs and HCFCs are stable and are capable of attacking the OL that protects the earth from being exposed to dangerous ultraviolet radiation. When these gases are released into the atmosphere their chemical bond is broken by UV-C radiation which leads to the release of chlorine gas, the chlorine takes away an atom from the ozone (O_3) and reduces it to oxygen (O_2). However, chlorine itself does not change but serves as a catalyst in the process. The amount of chlorine contained in a compound determines its effect on the OL, higher chlorine content refrigerants are capable of a longer effect than the lower chlorine refrigerants on the OL. The chlorine content of CFCs is higher than the HCFCs. The degree of destruction of the layer caused by the refrigerants is being measured by Ozone Depletion Potential (ODP). In the beginning, CFC refrigerants (Freons) were produced when there was no knowledge of its impact on the ozone layer, the producers were only looking for a better refrigerant that would be stable and capable of providing better cooling. Later on, HCFC refrigerants were launched by air-conditioning manufacturers. However, today it has been discovered that they contribute to OD and GW.

Initially, the Montreal protocol of 1987 did not include HCFC refrigerants because they were considered to have a low ODP, an example of these refrigerants is R22 refrigerant which was the most commonly used working fluid in air-conditioning systems, R22 has an ODP of 0.034. But few companies that saw the future started replacing CFC refrigerants with R22 and a blend of HCFCs. But, in Copenhagen in 1992, an amendment was made to include HCFCs among the gases that will be phased out in the future. This was not comfortable with the companies which were already converted from CFCs to the use of HCFCs.

HFC refrigerants were recommended to replace CFC refrigerants. This was not much difficult for some companies because there is better compatibility between HFCs and CFCs just small changes are required which is the oil type, therefore some existing systems designed for CFCs were transformed into HFC refrigerant systems.

Global warming (GW) manifests as a result of greenhouse gases effect. Greenhouse gases are not limited to CFCs and HCFCs earlier discussed, they also include CO_2, nitrous oxide (N_2O) and methane (CH_4). These gases have the capacity to absorb and trap the infrared. Also, when released to the atmosphere they remain for a long period and change the atmospheric conditions. About 30% of the solar radiation that reaches the earth reflects back to space while others are passed through the atmosphere to the earth's surface. This infrared radiation does not have the capacity to pass through the atmosphere due to the presence of water vapour and some other infrared absorber present in the atmosphere, they form heat energy trapped in the atmosphere, and the trapped heat energy causes the temperature at the earth surface to be higher than the normal.

Although GW has a positive impact on life on earth, it is needed by humans, animals and plant for survival, but due to human activities there is an increase in the greenhouse gases released to the atmosphere, the quantity of infrared radiation trapped in the atmosphere has increased causing increase in the atmospheric temperature and this has led to what is being referred to as climate change today.

The causes of global warming can be categorized into two parts. The global warming that is being caused by the release of CFCs and HCFCs in the atmosphere and the global warming that is being caused due to the burning of fossil fuels such as oil, natural gas and coal due to increase in energy demand.

In order to combat the challenges of OD and GW, the use of eco-friendly refrigerants has been adopted to replace HCFCs and CFCs in R&A systems. HCFCs will be passed out completely by developed countries in 2020 and 2030 by developing countries due to their higher chlorine content that causes ozone depletion and global warming. Hydrocarbon refrigerants (HCs) have been identified as a substitute for CFCs and HCFCs in domestic refrigeration. HCs are environment-friendly refrigerants due to their zero ODPs and very low GWPs compared to CFCs and HCFCs. The environmental effect of the hydrocarbon refrigerants is shown in Table 1.

Table 1 Environmental properties of most commonly used hydrocarbon refrigerants

Refrigerant	Molar mass (g/mol)	ODP	GWP
R290	44.00	0	3.3
R600	58.12	0	4
R600a	58.12	0	3
R170	30.07	0	5.5
R1270	42.08	0	1.8
RC270	412.08	0	1.8
RE270	46.07	0	1

This paper discusses the conventional refrigerants used in R&A systems and hydrocarbon refrigerants as alternatives.

2 Hydrocarbon Refrigerants

Hydrocarbon refrigerants occur naturally, the most commonly used hydrocarbons today include R600a, R290 and R1270. Hydrocarbon refrigerants have an excellent critical point, heat transfer and transport properties. They require less amount of mass charge compared to CFCs, HCFCs and HFCs due to lower molar mass and density [6, 7]. Hence, they require lower energy demand for their effective operations in refrigeration systems. The only problem associated with hydrocarbon refrigerants is their flammability. But, a maximum mass charge of 150 g has been endorsed for use in domestic refrigerators and for small commercial refrigerator systems [8–10]. Due to flammability EN378-2008 [11] recommend Eq. (1) below for calculating the allowable charge for hydrocarbon refrigerants [12].

$$M_{\text{max}} = 2.5 \times \text{LFL}_{\text{m}}^{1.25} \times H_{\text{a}} \times A^{0.5} \tag{1}$$

where M_{max} represents the maximum allowable charge in the room in kg, LFL_{m} denotes the lower flammability limit in kg/m^3, A represents the area of the room in m^2 and H_{a} denotes the height of the installed appliance.

Isobutane (R600a) has excellent properties and is substitute for R12 in the household refrigerator and medium commercial refrigerator unit. In 1995 the mass production of household refrigerators using R600a as the working fluid was first started in Germany and spread across the whole of Europe and other parts of the world except the United States where the safety regulations do not permit its production. R600a is energy-efficient according to the past and recent research by some refrigeration energy researchers [4, 7, 10, 13–15]. R600a requires between 40 and 60% of the required mass charge amount of R12 and R134a for effective performance in refrigeration systems, therefore it consumes lesser energy compared to R12 and R134a in vapour compression systems. Also, the price is cheaper compared to conventional refrigerants.

Propane (R290) thermodynamics properties are similar to that of R22, therefore, propane is being used as a drop-in replacement for R22 in vapour compression system (VCRS). R290 appliances are now on increase but are restricted to the special application due to safety. Currently, there are initiatives for the use of R290 in the domestic air-conditioning unit in India and China.

2.1 Experimental Studies of Hydrocarbon Refrigerants in Vapour Compression Systems

Oyedepo et al. [16] conducted an experiment on a refrigerator designed for R12 refrigerant. The R600a refrigerant was investigated in the system by varying the capillary tube length within the range of 0.9–1.5 m, it was discovered that R600a with 0.9 m capillary tube length gave a higher cooling capacity of 9.18% and R600a with 1.5 m capillary tube length gave 24% decrease in power consumption with a higher COP of 6.3% in the system. Righetti et al. [17] did a comparative analysis of R1234yf, R1234ze(E) and R600a in roll bond evaporator. The result showed that R1234yf and R1234ze(E) and R600a performed closely to R134a in the system and can be retrofit for R134a in VCRS provided the compression displacement is adjusted or modified. El-Morsi [18] carried out research on energy analysis of R134a, LPG and R600a in a VCRS. The outcome revealed R600a offers highest to R134a and LPG. The COP is 10% and 5% higher respectively. However, both R600a has an advantage than R134a in terms of affordability and GWP. Jung et al. [19] investigated the performance of R290/R600a to substitute R12 in a household refrigerator the result showed that R290/R600a portrayed better replacement for R12 in the system. Wongwises and Akash and Said [20, 21] carried out a research experiment on hydrocarbon mixture made up of R290, R600 and R600a refrigerant as a substitute for R134a in VCRS, the result showed that R290, R600 and R600a have better performance among the mixtures in the experiment.

Furthermore, the use of hydrocarbon mixtures had been carried out by numerous researcher as a substitute to halogenated refrigerants in VCRS. Mohanraj et al. [22] tested a blend of 45.2% of R290 and 54.8% of R600a as a retrofit for R134a in a VCRS. The result showed that the R290/R600a had a higher COP, lower power consumption, pull downtime and discharge pressure compared to the based refrigerant (R134a). Yu and Teng [23] carried out an experiment on R290 and R600a to replace R134a in a refrigerator system. The result showed that 40% of the mass charge of R134a of hydrocarbon refrigerant performed better in terms of pull-down time and power consumption with R600a offering the best performance in the system. Rasti et al. [24] also tested R436A to replace R134a in a VCRS. The result showed 13% and 5.3% reduction in the on-time ratio and power consumption respectively, Jwo et al. [25] conducted a study on a mixture of R600a and R290 as an alternative to R134a in a 440L size refrigerator system. The result showed a reduction of 4.4%, 17.4% and 40% were achieved in energy consumption, running time and refrigerant charge respectively. Rasti et al. [26] also investigated the use of R435A and R600a as a replacement for R134a in a household refrigerator. The outcome result revealed a 14% and 7% reduction in the power consumption at an optimum charge of R435A and R600a respectively in the system. Babarinde et al. [10] conducted an experiment with a mixture of R290 and R600 to retrofit R134a in vapour compression system considering varied mass charge of mixture of R290/R600 and a modified capillary length, the result showed a mixture of R290 and R600 performed better in the system in comparison with R134a with the highest COP of 9.5% and a decrease in power consumption of 12%. In a similar study Joudi et al. [27] experimented R600, R600a and a blend of R290, R600 and R600a in a VCRS using R134a as the based line of the experiment. The result showed that the energy consumption of the VCRS were decreased by 2–3% using hydrocarbon refrigerants and its mixture. Oyedepo et al. [6] investigated R600a and LPG in a domestic refrigerator by varying the mass charge (40, 60, 80 g) of the refrigerant and also varying the capillary tube length (0.9, 1.2, 1.5 m). The result revealed that 60 g charge of LPG offered an improved COP of 4.8% system and a better cooling capacity, however, it was reported that a 20% decrease in compressor power consumption was achieved when compared to LPG. In another related experiment. Babarinde et al. [28] performed an experiment on exergy analysis of LPG and R600a in a domestic refrigerator using LPG (40 g) against R600a (60 g). The result showed that when much lower mass charge of LPG is used the performance is comparable with that of R600a. Li et al. [29] evaluated the energy and exergy performance of R152a and R290 as a retrofit for R134a refrigerator system. The result confirmed that the cooling COP was increased by 5 and 8% and the overall exergy destruction reduced by 9.6 and 14.3% for R152a and R290, respectively.

Apart from refrigeration and air-conditioning purposes HCs are widely used for powering internal combustion engines, heating, aerosol propellant and cooking. But in order to prevent a fire outbreak, the safety measures associated with flammable gases must be strictly followed.

3 Material Compatibility of Hydrocarbon Refrigerants

Vapour compression systems require oil to provide adequate lubrication to the moving parts. When a compatible lubricant is used with refrigerant in a vapour compression system, the compressor frictional and wear is being reduced. The reduction in the friction of vapour compression system compressor also lead to a reduction in energy consumed by the vapour compressor, Therefore, the amount of energy needed to power the refrigerator for effective operations is reduced. This also translates to a reduction in the burning of fossil fuel required to meet the energy demand by vapour compression refrigeration systems [30–32]. The benefit of this is that the amount of CO_2 emitted into the atmosphere as a result of the burning of fossil fuel is reduced.

Though there are problems accompanying the use of lubricating oil in the vapour compression system. Apart from supplying lubrication to the moving part of the compressor, the oil also moves into the condenser, expansion valve and evaporator, by this means affecting the friction and the heat transfer performance of the refrigerant in the system but the lubricating oil and its return to the refrigerator compressor can be minimized by using a refrigerant which is miscible with the lubricating oil. Hydrocarbon refrigerants are miscible with mineral oil used in CFC refrigerants and polyester oil used in HFC refrigerants in vapour compression system.

Therefore, HCs can serve as a retrofit in vapour compression systems originally designed to work with CFCs and HCFCs. Furthermore, in refrigeration systems various materials are being used such as copper, brass, steel, metal alloy or solder

Table 2 Selection guide for hydrocarbon refrigerants

Refrigerant	Compressor	Application
R290, R600a	Sealed hermetic unit	Fridge/freezer
R290, R600a	Sealed hermetic unit Accessible semi-hermetic Reciprocating open drive	Commercial equipment-medium temperature
R170, R290	Sealed hermetic unit Accessible semi-hermetic Reciprocating open drive	Commercial equipment-medium temperature
R170, R290, R600a	Reciprocating open drive Screw	Industrial
R290, R600a	Hermetic reciprocating Open drive	Mobile refrigeration and air-conditioning
R600a R290 R600a R600a	Centrifugal Accessible semi-hermetic Screw Hermetic	Air-conditional

with zinc, others are materials used for sealing. Metal alloy or solder with zinc is capable of increasing corrosion rate with polyester oil and HFCs, however, HCs do not behave in this manner, see Table 2. Generally, HCs are compatible with traditional materials used in the refrigeration system.

4 Conclusion

The use of halogenated refrigerants in R&A systems will be phased out completely in the near future as a result of their ozone-depleting and global warming potentials which are a threat to the environment. Therefore, Earth the only planet that supports life must be protected by a reduction in the release of greenhouse gases into the atmosphere. In summary, the following conclusion can be drawn out:

- The use of hydrocarbon refrigerants in VCRS is safe, environment-friendly, energy-efficient and a good substitute for halogenated refrigerants in R&A systems.
- Regarding the flammability of hydrocarbon refrigerants, a maximum mass charge of 150 g has been recommended for use in domestic refrigeration systems.
- Hydrocarbon refrigerants have shot lifetime which makes them very low in GWP.
- Hydrocarbon refrigerants require a lower mass charge and lower discharge pressure for effective operation.
- R290 refrigerant has been commercialized as a replacement for R22 with a low mass charge in small air-conditioners.
- Hydrocarbon refrigerants are compatible with mineral oil and polyester oil lubricant in R&A systems.

This paper brings into awareness the advantages of using hydrocarbon refrigerants to replace halogenated refrigerants as a means of combating the environmental problems and energy security associated with vapour compression systems.

Lastly, for future studies, the following studies need to be done.

- Hydrocarbon refrigerant effect on the wear of vapour compression systems compressor.
- The possibility of using hydrocarbon refrigerants for large cooling applications and the safety precautions required.

References

1. UNEP (2000) United Nation environmmental program. In: Hand book for international treaties for protection of ozone layers, 5th edn. Nairobi, Kenya
2. Ciconkov R (2018) Refrigerants: there is still no vision for sustainable solutions (Frigorigènes: toujoursaucuneapproachfavorable à des solutions durables). Int J Refrig 86:441–448
3. UNEP (2012) Handbook for the Montreal protocol on substances that deplete the ozone layer
4. Babarinde TO, Akinlabi SA, Madyira DM, Ohunakin OS, Adelekan DS, Oyedepo SO (2018) Comparative analysis of the exergetic performance of a household refrigerator using R134a and R600a. Int J Energy Clean Environ 19(1–2)
5. Bolaji BO, Huan Z (2013) Ozone depletion and global warming: case for the use of natural refrigerant—a review. Renew Sustain Energy Rev 18:49–54
6. Oyedepo SO et al (2017) A comparative study on the performance of the domestic refrigerator using R600a and LPG with varying refrigerant charge and capillary tube length. Int J Energy Clean Environ 18(4)
7. Babarinde TO, Akinlabi SA, Madyira DM, Ohunakin OS, Adelekan DS, Oyedepo SO (2018) Comparative analysis of the exergetic performance of a household refrigerator using R134a and R600a. Int J Energy Clean Environ 19(1–2):37–48
8. Harby K (2017) Hydrocarbons and their mixtures as alternatives to environmental unfriendly halogenated refrigerants: an updated overview. Renew Sustain Energy Rev 73:1247–1264
9. Gill J, Singh J (2017) Energy analysis of vapor compression refrigeration system using mixture of R134a and LPG as refrigerant. Int J Refrig
10. Babarinde TO, Ohunakin OS, Adelekan DS, Aasa SA, Oyedepo SO (2015) Experimental study of LPG and R134a refrigerants in vapor compression refrigeration. Int J Energy Clean Environ 16(1–4):1–10
11. Babarinde TO, Akinlabi SA, Madyira DM (2018) Enhancing the performance of vapour compression refrigeration system using nano refrigerants: a review. IOP Conf Ser Mater Sci Eng 413:012068
12. Yang Z, Wu X (2013) Retrofits and options for the alternatives to HCFC-22. Energy 59:1–21
13. Kasperski J, Gil B (2014) Performance estimation of ejector cycles using heavier hydrocarbon refrigerants. Appl Therm Eng 71(1):197–203
14. Gill J, Singh J (2017) Energetic and exergetic performance analysis of the vapor compression refrigeration system using adaptive neuro-fuzzy inference system approach. Exp Therm Fluid Sci 88:246–260
15. Gill J (2017) Component-wise exergy and energy analysis of vapor compression refrigeration system using mixture of R134a and LPG as refrigerant
16. Oyedepo SO, Fagbenle RO, Babarinde T, Tunde A (2016) Effect of capillary tube length and refrigerant charge on the performance of domestic refrigerator with R12 and R600a. Int J Adv Thermofluid Res 2(1):2–14

17. Righetti G, Zilio C, Longo GA (2015) Comparative performance analysis of the low GWP refrigerants HFO1234yf, HFO1234ze(E) and HC600a inside a roll-bond evaporator. Int J Refrig 54
18. El-Morsi M (2015) Energy and exergy analysis of LPG (liquefied petroleum gas) as a drop-in replacement for R134a in domestic refrigerators. Energy 86:344–353
19. Jung D, Kim CB, Song K, Park B (2000) Testing of propane/isobutane mixture in domestic refrigerators. Int J Refrig 23(7):517–527
20. Wongwises S (2006) Experimental investigation of hydrocarbon mixtures to replace HFC-134a in an automotive air conditioning system. Energy Convers Manag 47:1644–1659
21. Akash BA, Said SA (2003) Assessment of LPG as a possible alternative to R-12 in domestic refrigerators. Energy Convers Manag 44(3):381–388
22. Mohanraj M, Jayaraj S, Muraleedharan C, Chandrasekar P (2009) Experimental investigation of R290/R600a mixture as an alternative to R134a in a domestic refrigerator. Int J Therm Sci 48(5):1036–1042
23. Yu CC, Teng TP (2014) Retrofit assessment of refrigerator using hydrocarbon refrigerants. Appl Therm Eng 66(1–2):507–518
24. Rasti M, Hatamipour MS, Aghamiri SF, Tavakoli M (2012) Enhancement of domestic refrigerator's energy efficiency index using a hydrocarbon mixture refrigerant. Meas J Int Meas Confed 45(7):1807–1813
25. Jwo C, Ting C, Wang W (2009) Efficiency analysis of home refrigerators by replacing hydrocarbon refrigerants. Measurement 42(5):697–701
26. Rasti M, Aghamiri S, Hatamipour MS (2013) Energy efficiency enhancement of a domestic refrigerator using R436A and R600a as alternative refrigerants to R134a. Int J Therm Sci 74:86–94
27. Joudi KA, Mohammed ASK, Aljanabi MK (2003) Experimental and computer performance study of an automotive air conditioning system with alternative refrigerants. Energy Convers Manag 44(18):2959–2976
28. Babarinde TO, Akinlabi SA, Madyira DM (2018) Exergetic performance of household refrigerator using R600a and LPG. IOP Conf Ser Mater Sci Eng 413:012069
29. Li G, Eisele M, Lee H, Hwang Y, Radermacher R (2014) Experimental investigation of energy and exergy performance of secondary loop automotive air-conditioning systems using low-GWP (global warming potential) refrigerants. Energy 68:819–831
30. Fatouh M, El Kafafy M (2006) Experimental evaluation of a domestic refrigerator working with LPG. Appl Therm Eng 26(14–15):1593–1603
31. Ohunakin OS et al (2018) Performance of a hydrocarbon driven domestic refrigerator based on varying concentration of SiO_2 nano-lubricant. Int J Refrig
32. Wongwises S, Chimres N (2005) Experimental study of hydrocarbon mixtures to replace HFC-134a in a domestic refrigerator. Energy Convers Manag 46(1):85–100

Experimental Study of Performance of R600a/CNT-Lubricant in Domestic Refrigerator System

T. O. Babarinde, S. A. Akinlabi, and D. M. Madyira

Abstract Energy consumption and environmental problems have been the major consideration for comfort systems manufacturers. This research work investigated a varied mass charge of R600a, an eco-friendly refrigerant with a low concentration of 0.4 and 0.6 g/L of CNT nanolubricant concentration in a domestic vapor compression refrigerating system working with pure mineral oil as the base lubricant. The experimental test performance of the system was studied considering pull-down time, COP, power consumption, and cooling capacity. The result showed that CNT nanolubricant had lower evaporator air temperature with higher COP and cooling capacity with a reduction in power consumption compared to R600a in the base lubricant in the system.

Keywords R600a · CNT · COP · Power consumption

Nomenclature

COP	Coefficient of performance
EG	Ethylene glycol
h	Enthalpy (kJ/kg)
m	Mass flow rate (kg/s)
MWCNT	Multiwall carbon nanotube
PAG	Polyalkylene glycol
Q_{evap}	Cooling capacity (W)
SG	Solid grinding
SWCNT	Single wall carbon nanotube

T. O. Babarinde (✉) · S. A. Akinlabi · D. M. Madyira
Department of Mechanical Engineering Science, University of Johannesburg, Johannesburg, South Africa
e-mail: taiwo.babarinde79@gmail.com

T. O. Babarinde
Department of Mechanical Engineering, Covenant University, Ota, Nigeria

E. T. Akinlabi et al. (eds.), *Trends in Mechanical and Biomedical Design*, Lecture Notes in Mechanical Engineering,
https://doi.org/10.1007/978-981-15-4488-0_62

T	Temperature (°C)
TEM	Transmission electron microscope
VCRS	Vapor compression refrigeration system
W_C	Compressor power in put (W)

Subscripts

1	Compressor inlet
2	Compressor outlet
3	Condenser outlet
4	Evaporator outlet

1 Introduction

Most energy demanded in homes and commercial building is from refrigeration and air-conditioning system, heating, and ventilation. Hence, energy researchers are looking into improving the energy consumed by comfort systems such as the domestic refrigerators and air-conditioning systems [1, 2]. Introducing nanofluids into vapor compression systems is capable of giving that solution to the high energy consumption associated with refrigeration systems.

Choi et al. found out that the use of nanoparticles as additives in refrigerator lubricants and refrigerants has the potential to enhance its thermal properties [3]. When nanoparticles are being dispersed in lubricant or refrigerant, they are called nanolubricant or nanorefrigerants. The major advantages of nanoparticles in the compressor lubricant are to enhance the thermal conductivity and viscosity which in turn cause an improvement in the energy efficiency of the system [2]. However, the performance of nanoparticles in the base fluid largely depends on its size, shape, and concentration [4].

Some researchers have studied the use of nanolubricants and in cooling systems such as VCRS in order to enhance the performances [5–8]. Nabil et al. [9] investigated the heat transfer performance of water-ethylene glycol (EG) mixture using TiO_2 nanoparticles within a temperature range of 30–80 °C. The result showed 15.4% improvement at 60 °C. Wang et al. [10] compared fullerene (170) and $NiFe_2O_4$ nanolubricant with base lubricant in an automobile air-conditioning system. The result showed that coefficient of performance (COP) of the air-conditioning system was increased by 23%. Also, a reduction in the coefficient of friction was achieved which means a reduction in wear. Melnyk [11] tested Al_2O_3 and TiO_2 nanoparticles with R600a refrigerant using mineral oil in vapor compression refrigeration system. The outcome result indicated that R600a/Al_2O_3 and R600a/TiO_2 performances improved in terms of thermal conductivity and viscosity in the system. Akilu et al. [12] experimented TiO_2–CuO nanocomposite in ethylene glycol by varying the TiO_2–CuO nanocomposite volume concentration. The result revealed the thermal conductivity and viscosity are functions of nanoparticles volume concentration and temperature. The thermal conductivity and viscosity increased at 20% volume concentration in comparison with the pure ethylene glycol at 40.4 °C.

Sun et al. [13] evaluated the performance of the heat transfer of MWCNT-OH/R141b and MWCNT-COOH/R141B in a cooling system by varying the volume concentration (0.059, 0.117, and 0.17655% vol.) at vapor quality range of 0.2–0.7. The result indicated the heat transfer coefficient of MWCNT-COOH/R141B was higher compared to MWCNT-OH/R141b. Mahmoud [14] also investigated the performance of SWCNT in refrigeration system using R134a as working fluid. The nanoconcentration was varied from 1 to 5 vol.% within the temperature range of 300–320 K. The result showed increase in thermal conductivity, viscosity and specific heat transfer of SWCNT/R134a in the system compared to R134a refrigerant. Hung and Gu [15] also carried out research on MWCNT nanofluid in a hybrid energy system. The MWCNT was added as additives in water with a weight fraction of 0.125, 0.25, and 0.5% to produce a nanofluid. The 0.125% nanofluid showed 5% increase in heat transfer behavior compared to the water.

From the existing literature, CNT nanoparticles are capable of increasing the thermal conductivity, viscosity, and heat transfer rate when used as additives in the base fluid. Currently, there is scant literature on the use of CNT in the vapor compression system. Furthermore, CNT nanoparticles have not been investigated in hydrocarbon refrigerants in which R600a is one of such. Today, R600a is the most widely used hydrocarbon refrigerant used as a substitute for R134a in a domestic refrigerator. Therefore, there is a need for its energy improvement in the domestic refrigeration system. This work presents an application of CNT nanoparticles in domestic refrigerator system using R600a refrigerant, which is clean and cheaper.

2 Experimental Procedures

The experimental test rig for this experiment was a household vapor compression refrigerator system initially designed to work with R134a refrigerant. The refrigerator system was evacuated with the aid of vacuum flasher before use and after each use. A multi-wall CNT was considered for this experiment. The CNT nanoparticles were measurement with a digital charging scale, the CNT nanoparticles were dispersed in a mineral oil and agitated together with the aid of digital ultrasonic machine, and two samples (0.4 and 0.6 g/L) of CNT nanolubricant concentration were prepared for 50, 60, and 70 g mass charge of R600a refrigerant each. The refrigerants were charged into the system with the aid of digital charging scale. The system was evacuated and flushed after each experiment to ensure better accuracy. The temperature readings were taken at the inlet and outlet of each refrigerator components (compressor, condenser, expansion valve, and evaporator) with K-type thermocouples connected to the inlet and outlet of each component, and also the evaporator air temperature of the refrigerator was monitored with K-type thermocouple. Two pressure gauges were connected to the inlet and out of the compressor to measure the suction and discharge pressure of the compressor. A digital wattmeter was used to measure the power consumed by the refrigerator compressor. The experiment was carried out at an average environmental temperature of 27 °C, and the experiment was repeated five times at an interval of 30 min for four hours. The measurement of the uncertainty of the measuring instruments used with experimental ranges and condition are in Tables 1 and 2, and the experimental setup and the refrigeration cycle are shown in Figs. 1 and 2. The experimental output readings were used to evaluate the performances of the system using Refprop version 9.0. Performances such as coefficient of performance (COP), power consumption, thermal conductivity, and viscosity of the system were evaluated.

The performance analysis of the experimental result was calculated using Eqs. (1)–(3).

1. Cooling capacity (Q_e) is capacity given by

$$Q_e = m(h_1 - h_4) \quad \text{(kW)} \tag{1}$$

2. The compressor power input is given by

Table 1 Specifications of the measuring instrument and uncertainty

S. No.	Parameter	Specification	Range	Uncertainty
1	Temperature	Digital thermocouple K	−50 to 700 °C	±3 °C
2	Pressure	Digital pressure gauge	5–4000 Pa	±1%
3	Power consumption	Watt/Watt-h-meter	1–2000 W (0.0001–999.9 kWh)	±1%

Table 2 Experimental range and conditions

S. No.	Parameter	Experimental range
1	Refrigerant mass charge	50, 60, 70 g
2	Refrigerant	R600a
3	Compressor lubricant	Pure lubricant, CNT (Mult-wall) nano-lubricants
4	Carbon nanotubes (CNT)	10 nm ± 1 nm × 4.5 nm ± 0.5 nm × 3 − ~6 μm
5	Nanolubricant concentration	0.4, 0.6 g/L
6	Capillary tube length	1.5 m
7	Condenser type	Air cooled
8	Evaporator size	70 L

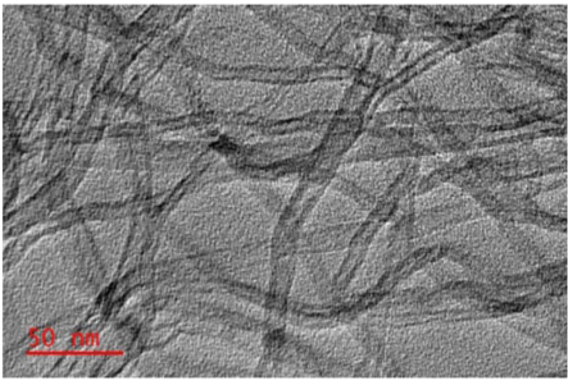

Fig. 1 Transmission electron microscope (TEM) image of CNT nanoparticles

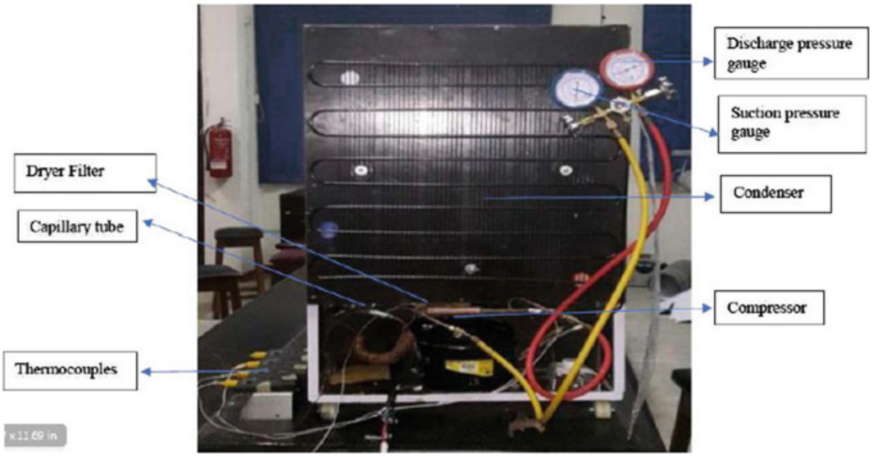

Fig. 2 Experimental setup

$$W_{\mathrm{C}} = m(h_2 - h_1) \quad (\mathrm{kW}) \tag{2}$$

3. $$\mathrm{COP} = \frac{Q_{\mathrm{evap}}}{W_{\mathrm{C}}} \tag{3}$$

3 Results and Discussions

The comparison of the performance of R600a in the base lubricant and CNT nanolubricant concentration is discussed next in terms of evaporator air temperature, coefficient of performance, power consumption, and cooling capacity.

3.1 Evaporator Temperature

Table 3 depicts the pull-down time of mass charge of R600a with pure lubricant, 0.4 and 0.6 g/L CNT nanolubricant. It can be observed that R600a with 0.4 g/L of nanolubricant concentration has the shortest pull-down time and lowest evaporator air temperature (see Table 3). The evaporator air temperature of −7, −11, and −3 °C at a pull-down time of 180, 150, and 90 min was recorded for 50, 60, and 70 g of R600a with 0.4 g/L CNT nanolubricant concentration. Also, evaporator air temperature of −8, −11, and −8 °C at a pull-down time of 210, 240, and 210 min was recorded for 50, 60, and 70 g of R600a with 0.6 g/L CNT nanolubricant concentration, respectively. This result also establishes the research work of You et al. and Malvandi et al. that the cooling temperature is enhanced with nanofluid than the base fluid in cooling application [16, 17]. The improvement is also as result of enhancement in heat transfer due to increase in thermal conductivity of the system.

3.2 Coefficient of Performance

The graph in Fig. 3 shows the effect of CNT nanolubricant on the COP of the system. The COP of R600a with CNT nanolubricant is higher than the base lubricant (see Tables 4, 5 and 6). The COP of R600a with the 0.4 g/L of CNT nanolubricant ranges from 2.1 to 2.8 with a 50 g charge of R600a having the highest COP, while the COP of R600a with 0.6 g/L of nanolubricant ranges from 2.5 to 2.9 with the 60 g mass charge of R600a offering the highest COP in the system. This can be linked influence of the CNT nanoparticles on the system which led to reduction in the coefficient of friction and wear in the compressor, therefore reducing the energy consumed by the compressor in the system.

3.3 Power Consumption

Figure 4 shows the power consumption at steady state and the effect of CNT on the power consumption of the system. The power consumption of R600a with CNT nanolubricant concentration decreases with increase in nano-concentration until it

Table 3 Evaporator air temperature of R600a charges using pure lubricant oil and CNT lubricant concentrations

Time (min)	50 g			60 g			70 g		
	Pure R600a	R600a/CNT (0.4 g/L)	R600a/CNT (0.6 g/L)	Pure R600a	R600a/CNT (0.4 g/L)	R600a/CNT (0.6 g/L)	Pure R600a	R600a/CNT (0.4 g/L)	R600a/CNT (0.6 g/L)
0	27	27	27	27	27	27	27	27	27
30	9	0	−1	1	−4	−4	5	5	1
60	2	−4	−5	−2	−7	−7	2	−1	−3
90	−1	−5	−6	−3	−8	−8	1	−3	−5
120	−3	−6	−7	−3	−10	−9	1	−3	−7
150	−4	−6	−7	−3	−11	−9	0	−3	−7
180	−4	−7	−7	−3	−11	−10	0	−3	−7
210	−5	−7	−8	−3	−11	−10	0	−3	−8
240	−5	−7	−8	−3	−11	−11	0	−3	−84

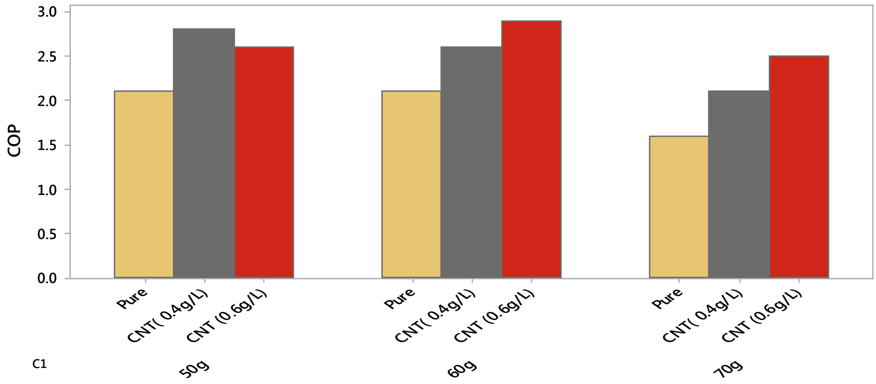

Fig. 3 Effect of CNT nanolubricants on COP of the R600a in the system

Table 4 Summary of the experimental result for 50 g mass charge R600a in the system

	Pull downtime (min)	Evaporator air temp. (°C)	COP	W_c (W)	Q_e (W)
Pure	210	−5	2.1	82.1	173.6
0.4 g/L	180	−7	2.8	61.1	171.4
0.6 g/L	210	−8	2.6	71.9	187.0

Table 5 Summary of the experimental result for 60 g mass charge R600a in the system

	Pull downtime (min)	Evaporator air temp. (°C)	COP	W_c (W)	Q_e (W)
Pure	90	−3	2.1	82.2	167.9
0.4 g/L	150	−11	2.6	72.8	189.3.
0.6 g/L	240	−11	2.9	63.9	185.3

Table 6 Summary of the experimental result for 70 g mass charge R600a in the system

	Pull downtime (min)	Evaporator air temp. (°C)	COP	W_c (W)	Q_e (W)
Pure	210	−0	1.6	86.1	141.0
0.4 g/L	120	−3	2.1	81.4	170.4
0.6 g/L	150	−3	2.5	76.1	190.2

reaches its optimal concentration and increases with the mass charge for R600a in the base lubricant (see Tables 4, 5 and 6). The power consumption of 0.4 and 0.6 g/L CNT nanolubricant is lower from the range of 61.2–81.4 and 63.9–76.1 W, respectively, with 50 and 60 g of R600a in 0.4 and 0.6 g/L of CNT nanolubricant having the lowest power consumption, respectively. The trend of the improvement in power consumption conforms to the previous result of Wang et al., Bi et al., Jeng et al., and Jwo et al., where a reduction in power consumption of the refrigeration

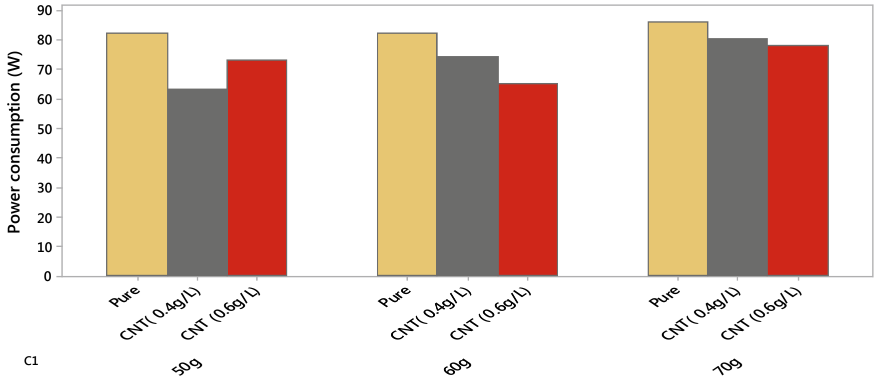

Fig. 4 Effect of CNT nanolubricants on the power consumption of R600a in the system

system was achieved using nanoparticles in base lubricant for the refrigerant in the refrigeration system [10, 18–20].

3.4 Cooling Capacity

Figure 5 shows the cooling capacity of the system. The cooling capacity of the system increases with increasing addition of nanoparticles in the system until it reaches its optimal charge. The 60 g of R600a with 0.4 g/L CNT nanolubricant has the highest cooling capacity of 196.5 W with an evaporator air temperature of −11 °C. This is due to the increase in thermal conductivity of the R600a in CNT nanolubricant compared to the base lubricant.

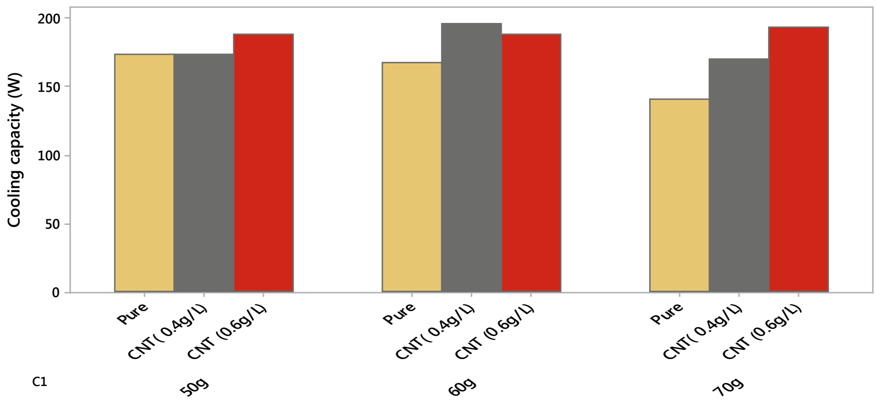

Fig. 5 Effect of CNT nanolubricants on the cooling capacity of R600a in the system

The summary of the performances of the system is expressed in Tables 4, 5 and 6.

In this research, it was noticed that for every mass charge of R600a refrigerant (see Tables 4, 5 and 6) CNT nanoconcentration performed better in terms of pull-down time which established the enhancement in heat transfer rate, increase in thermal conductivity, and most importantly the improvement in energy efficiency of the system.

4 Conclusion

In this present study, the experimental analysis of CNT nanolubricant concentration in R600a was compared with R600a in pure mineral oil. The different mass charge of R600a refrigerant (50, 60, 70 g) was tested in different CNT nanolubricant concentrations of 0.4 and 0.6 g/L. Based on the experimental findings, and considering the performance of the vapor compression system, the following conclusions were made for CNT nanolubricant concentration with R600a refrigerant.

- The 60 g mass charge of R600a in 0.6 g/L CNT nanolubricant obtained the best result in terms of COP, with evaporator temperature −11 °C at 120 min which is found to meet the ISO 8187 standard temperature of −3 °C at 150 min. Also, power consumption is lower compared to R600a in the base lubricant. Therefore, it is considered as a drop-in replacement for R600a refrigerant in base lubricant (pure mineral oil).
- The CNT nanolubricant concentrations of 0.4 and 0.6 g/L offer reduced power consumption throughout the experiment with the 50 g charge of R600a in 0.4 g/L CNT nanolubricant with the lowest power consumption at an evaporator air temperature of −7 °C. Also, this can serve as a drop-in replacement for base lubricant in a domestic refrigerator.
- Since CNT nanolubricant works efficiently in terms of COP, power consumption, cooling capacity, and pull-down time in the domestic refrigerator, it is recommended as a substitute for base lubricant in vapor compression refrigerator working with R600a.

References

1. Azmi WH, Sharif MZ, Yusof TM, Mamat R, Redhwan AAM (2017) Potential of nanorefrigerant and nanolubricant on energy saving in refrigeration system—a review. Renew Sustain Energy Rev 69:415–428
2. Babarinde TO, Akinlabi SA, Madyira DM (2018) Enhancing the performance of vapour compression refrigeration system using nano refrigerants: a review. IOP Conf Ser Mater Sci Eng 413:012068

3. Choi C, Yoo HS, Oh JM (2008) Preparation and heat transfer properties of nanoparticle-in-transformer oil dispersions as advanced energy-efficient coolants. Curr Appl Phys 8(6):710–712
4. Maheshwary PB, Handa CC, Nemade KR (2018) Effect of shape on thermophysical and heat transfer properties of ZnO/R-134a nanorefrigerant. Mater Today Proc 5(1):1635–1639
5. Jung J, Cho C, Hyun W, Tae Y (2011) Thermal conductivity measurement and characterization of binary nanofluids. Int J Heat Mass Transf 54(9–10):1728–1733
6. Mahbubul IM, Saidur R, Amalina MA (2013) Heat transfer and pressure drop characteristics of Al_2O_3-R141b nanorefrigerant in horizontal smooth circular tube. Procedia Eng 56:323–329
7. Saidur R, Kazi SN, Hossain MS, Rahman MM, Mohammed HA (2011) A review on the performance of nanoparticles suspended with refrigerants and lubricating oils in refrigeration systems. Renew Sustain Energy Rev 15(1):310–323
8. Sun B, Yang D (2013) Flow boiling heat transfer characteristics of nano-refrigerants in a horizontal tube (Caractéristiques du transfert de chaleur d'écoulement en ébullition de nano-frigorigénes dans un tube horizontal). Int J Refrig 38:206–214
9. Nabil MF, Azmi WH, Hamid KA, Mamat R, Hagos FY (2017) An experimental study on the thermal conductivity and dynamic viscosity of TiO_2-SiO_2 nanofluids in water: ethylene glycol mixture. Int Commun Heat Mass Transf 86:181–189
10. Wang R, Zhang Y, Liao Y (2017) Performance of rolling piston type rotary compressor using fullerenes (C70) and $NiFe_2O_4$ nanocomposites as lubricants additives
11. Melnyk AV (2017) A complex investigation of the nanofluids R600a-mineral oil-Al_2O_3 and R600a-mineral oil-TiO_2 (Thermophysical properties Une étude complexe des propriétés thermophysiques des nanofluides R600a-huile minérale-Al_2O_3 et R600a-huile). Int J Refrig 74:488–504
12. Akilu S, Baheta AT, Sharma KV (2017) Experimental measurements of thermal conductivity and viscosity of ethylene glycol-based hybrid nanofluid with TiO_2-CuO/C inclusions. J Mol Liq 246:396–405
13. Sun B, Wang H, Yang D (2018) Effects of surface functionalization on the flow boiling heat transfer characteristics of MWCNT/R141b nanorefrigerants in smooth tube. Exp Therm Fluid Sci 92:162–173
14. Mahmoud O (2017) OMAE2016-54071, pp 1–10
15. Hung Y, Gu H (2014) Multiwalled carbon nanotube nanofluids used for heat dissipation in hybrid green energy systems. J Nanomater 2014(162):1–32
16. Malvandi A, Heysiattalab S, Ganji DD (2016) Thermophoresis and Brownian motion effects on heat transfer enhancement at film boiling of nanofluids over a vertical cylinder. J Mol Liq 216:503–509
17. You SM, Kim JH, Kim KH (2003) Effect of nanoparticles on critical heat flux of water in pool boiling heat transfer. Appl Phys Lett 83(16):3374–3376
18. Bi SS, Shi L, Zhang LL (2008) Application of nanoparticles in domestic refrigerators. Appl Therm Eng 28(14–15):1834–1843
19. Jwo C-S, Jeng L-Y, Teng T-P, Chang H (2009) Effects of nanolubricant on performance of hydrocarbon refrigerant system. J Vac Sci Technol B Microelectron Nanomet Struct 27(3):1473
20. Tiwari AK, Ghosh P, Sarkar J (2013) Performance comparison of the plate heat exchanger using different nanofluids. Exp Therm Fluid Sci 49:141–151

Assessing the Predicting Capability of RSM and ANN on Transesterification Process for Yielding Biodiesel from *Vitis vinifera* Seed Oil

V. Hariram, A. Bose, S. Seralathan, J. Godwin John, and T. Micha Premkumar

Abstract In this present investigation, the process parameters to obtain maximum fatty acid methyl ester yield from *Vitis vinifera* seed bio-oil by transesterification were explored using the central composite design with variable input parameters like catalyst concentration (0.5–1.5% of KOH), reaction duration (30–60 min), and molar ratio (3:1–7:1). Response surface methodology (RSM) and artificial neural network (ANN) were employed to predict the optimized biodiesel yield and model the transesterification process. The experimental outputs were simulated using a quadratic model generated by RSM. The maximum biodiesel yield parameters were determined by RSM, and it was found to be 6.4246:1 molar ratio, 66.8205 min reaction time, and 1.1719% of catalyst concentration. The transesterification process performed with this experimental combination resulted in methyl ester yield of around 97.53% which correlated well with the yield predicted by RSM. The statistical analysis was carried out to determine the model validity, accuracy, and predictive capability of both ANN and RSM models. The biodiesel obtained by this process was subjected to analysis for estimating the physiochemical properties like cetane number, calorific value, density, acid value, flash and fire point, and kinematic viscosity, and it was found to be within ASTM limits.

Keywords Biodiesel · RSM · Molar ratio · ANN · Transesterification

---

V. Hariram (✉) · A. Bose · T. Micha Premkumar
Department of Mechanical Engineering, Hindustan Institute of Technology and Science, Chennai, Tamil Nadu 603103, India
e-mail: connect2hariram@gmail.com

S. Seralathan
Department of Aeronautical Engineering, Hindustan Institute of Technology and Science, Chennai, Tamil Nadu 603103, India

J. Godwin John
Department of Automobile Engineering, Hindustan Institute of Technology and Science, Chennai, Tamil Nadu 603103, India

E. T. Akinlabi et al. (eds.), *Trends in Mechanical and Biomedical Design*, Lecture Notes in Mechanical Engineering,
https://doi.org/10.1007/978-981-15-4488-0_63

1 Introduction

The continuous decrease in availability of fossil fuels like crude oil and natural gas has resulted in the search for new, renewable as well as ecology-friendly source of fuel. Based on the depletion rate of fossil fuels, the petroleum-based fuels might not last more than a few decades. Biofuels are one of the promising resources which can supplement the use of fossil fuels. Biodiesel are more environmentally friendly, free from pollution, and are renewable [1]. The biodiesels are mostly synthesized from edible oils which lead to a higher price in production and affect the availability in food market. This led to focus on synthesizing biofuels from non-edible vegetable-based oils. Few examples of similar non-edible oils that are mostly used to produce biodiesel are jatropha, neem, karanja, cotton seed oil, grape seed, etc. [2]. The biodiesel is generally produced from transesterification process. Transesterification is the method of alcoholysis of triglyceride present in the bio-oil into glycerol and alkyl esters in existence of catalyst. The biodiesel produced from the transesterification depends on major parameters like mixing intensity, catalyst concentration, molar ratio of oil to alcohol, reaction duration, and reaction temperature. In order to achieve maximum quantity and quality biodiesel yield, it is essential to improve the process parameters [3, 4]. Soft computing tools like ANN, RSM, and ANFIS can be used to optimize the operational parameters. RSM is a statistical tool which generates quadratic polynomial equation based on the investigational output. It is used to derive the inter-relationship between the dependent and independent parameters. ANN is a soft computing tool which is based on the human brain neurons ability to learn and adapt on different conditions. The ANN consists of nodes and neurons which act like human neurons using algorithms which enable this adaptability. Many studies were conducted earlier using RSM and ANN for predicting the responses and optimizing the experimental process [5, 6].

Selvaraj et al. examined the synthesis of biodiesel from waste cooking oil and optimized its operational parameters using ANN and RSM. Optimal biodiesel yield of 95% was achieved at optimum process conditions of 6:1 molar ratio, 1% catalytic concentration, 75 °C, and a reaction time of 60 s with a high coefficient of determination of 0.98 for RSM and 0.99 for RSM [7]. Prakash Maran and Priya studied the production of biodiesel from neem bio-oil and optimized it using ANN and RSM. Its predictive capability was also compared. The optimum selection of neurons in hidden layer and algorithms was discussed by the author [8–10]. Chizoo et al. optimized the production of biodiesel from sweet almond seed oil through transesterification. The ANN and RSM were used for optimization and the CCD design. The authors achieved an optimized yield of 95.45% from ANN and 94.36% from RSM based on the optimized parameter, namely 1.5 w/w % catalyst concentration, 5:1 molar ratio (methanol to oil), and 65 min reaction duration at reaction temperature of 50 °C.

Many researches were conducted using RSM and ANN to predict and optimize the biodiesel production from various oils [4, 5, 11–13]. But, to the authors' knowledge, no research was identified on the optimized biodiesel production from *Vitis vinifera* oil using RSM and ANN. Therefore, the objective of this investigational study is to optimize the production of biodiesel from *Vitis vinifera* oil and assessing the predictive capability of both RSM and ANN models. The physiochemical properties of this derived *Vitis vinifera* biodiesel are also analyzed.

2 Materials and Methods

Grape seed bio-oil used in this investigational study was extracted by traditional cold pressing. The acid value of the grape seed bio-oil was estimated to be 1.4 mg of KOH/g. The seeds used in this extraction were supplied by Noyer Overseas India Pvt. Ltd. The seeds were manually cleaned from dirt and stones. The seeds were dried in sun for two days, and then, the bio-oil extraction process was initiated. The chemicals used in the reaction—methanol (CH_3OH) and sodium hydroxide ($NaOH$)—were supplied by Vetri Chemicals, Chennai.

2.1 Transesterification of Grape Seed (Vitis vinifera) Oil

50 ml of grape seed oil was taken in a beaker and heated up to 100 °C to eliminate the existence of water molecules in the bio-oil. Then, the oil was cooled down to reaction temperature of 60 °C which was less than the boiling point of methanol. An appropriate amount of sodium hydroxide catalyst was mixed with the methanol to form a homogenous sodium hydroxide solution. The catalyst solution was mixed with the oil and agitated at an intensity of 650 rpm for about 60 min. The glycerol settles down in the separating flask after the 24 h settling period. The yield percentage of biodiesel was determined using Eq. (1). The biodiesel yield was influenced by catalyst loading percentage (0.5–1.5%), reaction temperature (30–90), and methanol to oil molar ratio (3:1–5:1) [14].

$$\text{Yield}\ (\%) = \frac{\text{weight of biodiesel produced (g)}}{\text{weight of oil used (g)}} * 100 \tag{1}$$

2.2 Experimental Design of RSM Model

The optimization of biodiesel production was carried out using the Box–Behnken design of RSM. Three variable parameters, namely catalyst loading percentage, reaction duration, and molar ratio as three factors at three levels which had 17 experimental data were designed using the Box–Behnken approach. The variables were coded in the levels of -1, 0, and $+1$. The experiments were carried out as per the

Table 1 Experimental and predicted values using ANN and RSM

Molar ratio (mol/mol)	Catalyst loading percentage	Reaction time (min)	Experimental result	ANN predicted value	RSM predicted value
5 (0)	1 (0)	60 (0)	96.20	96.525	96.520
7 (+1)	1.5 (+1)	60 (0)	96.45	96.450	96.300
5 (0)	1 (0)	60 (0)	96.50	96.525	96.500
3 (−1)	1.5 (+1)	60 (0)	92.90	92.894	93.015
5 (0)	0.5 (−1)	30 (−1)	90.60	90.600	90.543
3 (−1)	1 (0)	90 (+1)	91.40	91.400	91.231
7 (+1)	0.5 (−1)	60 (0)	94.20	93.779	94.088
3 (−1)	1 (0)	30 (−1)	90.10	90.098	90.006
5 (0)	1 (0)	60 (0)	96.51	96.525	96.522
5 (0)	1.5 (+1)	30 (−1)	92.30	92.300	92.281
5 (0)	1.5 (+1)	90 (+1)	95.20	95.200	95.256
7 (+1)	1 (0)	30 (−1)	94.00	94.000	94.169
3 (−1)	0.5 (−1)	60 (0)	88.50	88.632	88.650
5 (0)	1 (0)	60 (0)	96.70	96.525	96.522
5 (0)	1 (0)	60 (0)	96.70	96.522	96.522
5 (0)	0.5 (−1)	90 (+1)	90.40	90.419	90.419
7 (+1)	1 (0)	90 (+1)	95.70	95.794	95.794

experimental design, and the values are given in Table 1. A second-order quadratic polynomial equation which defined the yield was fitted as shown in Eq. (5)

2.3 *ANN Modeling*

Box–Behnken design was employed to generate seventeen test data point, and those were given as the experimental input to the ANN model. The back propagation algorithm of Levenberg–Marquardt with tangent sigmoidal function as the activation function was used to train the input variables. The neural network was divided into three layers, namely input layer, hidden layer which consisted of hidden neurons, and output layer. The independent parameters were in the input layers, and the output layer was biodiesel yield. The performance of the prediction was verified using mean square error (MSE). The MSE, SEP, and AAD can be calculated using Eqs. (2), (3), and (4).

$$\mathrm{MSE} = \frac{1}{n}\sum\left(y_{ei} - y_{\mathrm{p}i}\right)^2 \tag{2}$$

$$\text{SEP} = \frac{(\text{RMSE})}{\text{ye}} \times 100 \tag{3}$$

$$\text{AAD} = \frac{1}{n}\left(\sum_{i=1}^{n}\left|\frac{y_{i\text{a}} - y_{i\text{p}}}{y_{i\text{a}}}\right|\right) \times 100 \tag{4}$$

where $y_{\text{e}i}$ was the experimental output at ith run, $y_{\text{p}i}$ was the predicted output at the ith run, and n was number of experimental data's.

3 Results and Discussion

3.1 *Transesterification Reaction—RSM Model*

The quantity of biodiesel yield depended on the reaction parameters and to obtain a maximum yield; it was vital for optimizing the process conditions. The transesterification reaction was carried out using seventeen runs generated by the Box–Behnken design. The design consisted of 17 experimental runs which were defined by 3-factor 3-level design with 5 center points. The experimental data and RSM predicted data with the coded values were given in Table 1. As listed in Table 2, it can be observed that the quadratic model was chosen since the p-value was less than 0.05 which defined the significance of the model, and the adjusted coefficient of determination (adj R^2) and the coefficient of determination (R^2) were closer to one [15]. The experimental data was fitted into a second-order polynomial equation which defined the yield obtained by the grape seed oil at a given parameter.

$$\begin{aligned} Y = {} & 60.82306 + 5.07125x_1 + 19.6130x_2 + 0.27105x_3 - 0.5375x_1x_2 \\ & + 0.001667x_1x_3 + 0.051667x_2x_3 - 0.354313x_1^2 - 8.369x_2^2 - 0.002561x_3^2 \end{aligned} \tag{5}$$

where y was the yield, x_1, x_2, and x_3 were the input parameters molar ratio, reaction duration, and catalyst loading percentage, while x_1x_2, x_2x_3, x_1x_3, and x_1^2, x_2^2, x_3^2 were the interactive and quadratic terms of the input parameters. ANOVA was used to statistically analyze the fitness of the model with the experimental data. The parameters of the ANOVA table are given in Table 2. The statistical significance of

Table 2 Model selection

Source	Sequential p-value	Lack of fit p-value	Adjusted R^2	Predicted R^2	R^2
2FI	0.8818	<0.0001	0.2802	−0.0799	0.5501
Linear	0.0195	0.0001	0.4101	0.2930	0.5207
Quadratic	<0.0001	0.4145	0.9940	0.9780	0.9974
Cubic	0.4145	–	0.9945	–	0.9945

Table 3 ANOVA for quadratic model

Source	df	Sum of squares	p-value	F-value	Mean square	Significance
Model	9	122.08	<0.0001	297.14	13.56	Significant
A-molar ratio	1	38.06	<0.0001	833.78	38.06	
B-catalyst loading	1	21.62	<0.0001	473.49	21.6	
C-time	1	4.06	<0.0001	88.96	4.06	
AC	1	0.04	0.3804	0.8762	0.04	Not significant
BC	1	2.40	0.0002	52.63	2.40	Significant
AB	1	1.16	0.0015	25.31	1.16	
A^2	1	8.46	<0.0001	185.26	8.46	
B^2	1	18.43	<0.0001	403.75	18.43	
C^2	1	22.37	<0.0001	489.93	22.37	
Pure error	4	0.1677	–	–	0.0419	
Lack of fit	3	0.1519	0.4145	1.21	0.0506	Not significant
Residual	7	0.3196	–	–	0.0457	
Core total	16	122.40	–	–	–	–

the parameters and the model can be determined by observing the f-value and p-value [7].

Based the ANOVA listed in Table 3, the importance of the developed model can be seen by the p-value which was lesser than 0.0001. The linear parameters and quadratic squares of catalyst loading percentage, reaction duration, and molar ratio were statistically found to be significant (p-value < 0.05). The interactions between molar ratio with catalyst loading percentage and catalyst loading percentage with reaction time were found significant, while the interaction of catalyst concentration with molar ratio was found insignificant. The 'F' value of 297.14 was observed with low probability value ($p < 0.05$) which defined the acceptability of the model. Higher p-value which was greater than 0.05 made the lack of fit value to be insignificant. This signifies that there was a good fit between the predicted and the experimental variables. The coefficient of variation (C.V %) and standard deviation of the developed RSM model were found to be 0.2278% and 0.2137, respectively. The effect of the parameters and its synergetic effect on the biodiesel yield can be calculated from the sum of squares of deviation by using Eq. (6).

$$\text{The contribution of terms } \% = \frac{\text{sum of squares of individual terms}}{\text{total sum of square of all terms}} \quad (6)$$

Based on Eq. (6), the molar ratio had the highest effect of 32.6415% on biodiesel yield which was greater than the catalyst loading percentage and reaction time whose values were 18.542% and 3.819%, respectively. The individual parameters had more effect on the yield of biodiesel which was greater than the interaction between parameters and the quadratic terms. The fitness of the model was assessed by using the R, R^2, and adj R^2 values. The high value of R^2 showed that the model was about 99.74% of variation with the experimental data. The lesser difference between R^2 and predicted R^2 shows that the model was highly reliable; the R defined the exceptional correlation between the predicted response and experimental result. The low C.V % (0.2278%) demonstrated the reliability of the model and the experiment conducted. As plotted in Fig. 1a, the effect of catalyst loading and reaction duration on the *Vitis vinifera* biodiesel yield at optimum molar ratio was observed. The synergetic effect between reaction time and the catalyst concentration can be evidenced during the transesterification process. With the upsurge in catalyst concentration, increased biodiesel yield was evidenced up to a certain limit. As the catalyst concentration surpassed the optimal value, there was a decrease in yield observed. The same can be observed with the reaction time when raised above optimal value (66.8205 min). This was due to the reverse reaction that takes place which caused the decrease in the yield. A considerable amount of time was vital for the reaction to complete. Hence, a low yield of biodiesel can be observed at low reaction time, while at surplus reaction

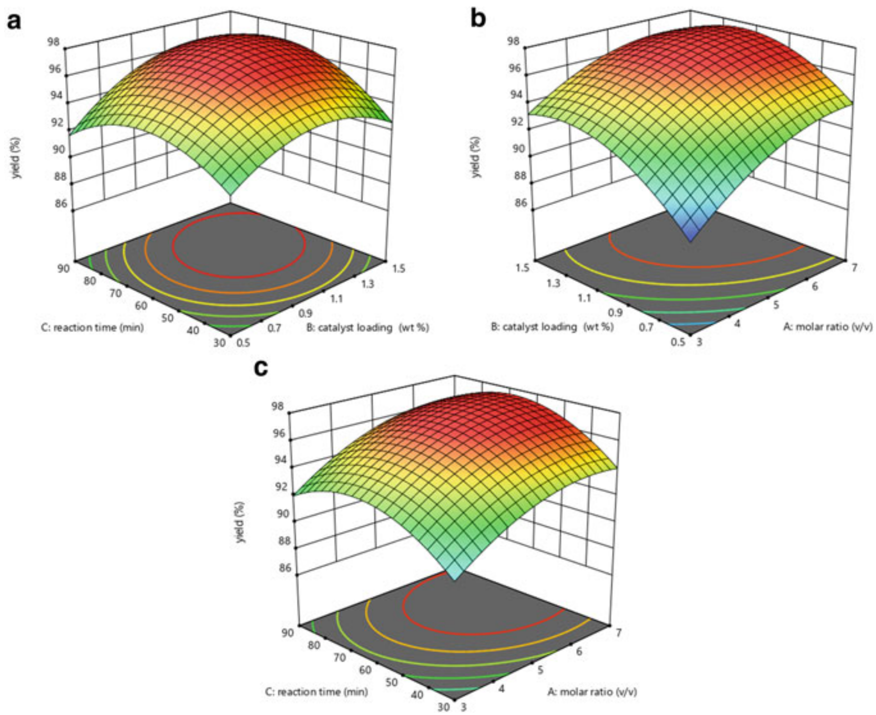

Fig. 1 RSM predicated optimized values of 66.8205 min reaction time, 6.4246:1 molar ratio, and 1.1719% catalyst loading to obtain maximum biodiesel yield

time, alkyl ester will start to react with the glycerol to glycerides. This led to lesser yield at both high molar ratio and reaction time.

As shown in Fig. 1b, the synergy between the catalyst concentration and the molar ratio at optimum reaction time can be witnessed. There was an escalation in yield as the reaction time was increased from 30 to 60 min. The increase in catalyst more than the optimum value prevented the reaction of methanol and oil and led to formation of soap solution leading to decrease in yield. The same happened when the molar ratio was amplified more than the optimum value. As the transesterification reaction was a reverse reaction, the excess supply of methanol led to reduction in the biodiesel yield. Figure 1c depicts the effect of reaction duration and molar ratio on the yield of biodiesel at optimum catalyst concentration (1.1719%). There was an overall increment in the biodiesel yield observed when the concentration of catalyst was augmented from 0.5 to 1%. But, when it was increased from 1 to 1.5%, the increment was only observed on lower levels. With the upsurge in the molar ratio, an rise in the biodiesel yield was witnessed between the ranges of 6:1 and 6.5:1. When the molar ratio reached more than that, there was a decrement in yield. As transesterification was a reverse reaction with excess methanol and reaction time, reverse reaction tends to take place. It led to decrease in yield. Hence, yield decrement can be observed at higher levels of reaction duration and molar ratio. The predicted yield by RSM fits well with the actual experimental yield. The desirability function was used by RSM to find the maximum yield of biodiesel. The maximum yield of biodiesel predicted by RSM was 97.6625% which was predicted to be attained at catalyst loading percentage 1.1719 wt% of oil, molar ratio of 6.4246:1, and 66.8205 min of reaction time with desirability value of 0.964. The optimum experimental condition was used to carry out the experiment in triplicate, and a yield of 97.53% was obtained. An error of about 0.1325% was found between the experimental biodiesel yield and predicted response yield. Based on this, it was possible to state that experimental condition had less error and the experimental condition was valid.

3.2 ANN Modeling

The nonlinear relationship between the output response and input individual parameters was established using ANN. The data (experimental value) from Box–Behnken design was used in artificial neural networks. In this study, the ANN was modeled using Levenberg–Marquardt back propagation algorithm which mostly used one, and it takes less time to process the information. It was selected through randomized trial and error technique. The number of neurons was increased in the order of two, and the optimum number of neurons was found by randomized trial and error method. 3–6–1 neuron topology for input-hidden and output layer was selected for ANN. The neurons were selected based on the correlation coefficient of the model topology, and there were three layers in ANN structure—input, hidden, and output layers. The input layer consisted of three neurons which represented catalyst loading percentage, molar ratio, and reaction time, while hidden layer contained six neurons

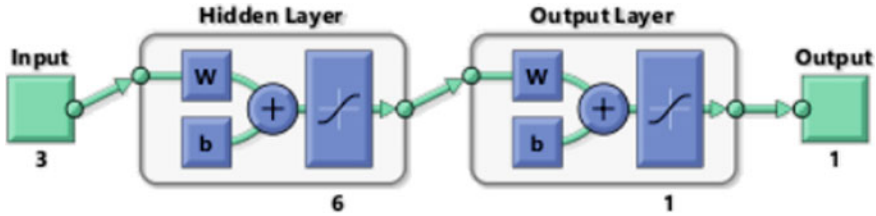

Fig. 2 Model topology for ANN

and output layer comprised of 1 neuron which represented the yield of biodiesel as shown in Fig. 2. 17 experimental data which was given as an input were randomly divided into 70% data, 15% data, and 15% data which were used for training data, testing data, and validation data, respectively. The training data consisted of 11 data in training, 3 data in testing, and 3 data in validation. The predicted and the experimental value for the particular data and the linear equation can be observed in Fig. 3. The coefficient of variation (R) for training, testing, validation, and whole data were 0.9981, 1, 1, and 0.99855. It can be observed in the graph there were two lines which represented the best fit and perfect for each training, testing, validation, and all data. MSE of the model was used to validate the performance, and high coefficient of correlation depicted that the value determined by the ANN had high accuracy. From Fig. 3, it was witnessed that best performance of the artificial neural network model was found at epoch 0 with an MSE of 0.00020833. From the regression graph of the predicted and experimental data, it can be observed that there was less deviation from the experimental data.

3.3 Comparison of ANN and RSM

The statistical parameters like RMSE, MSE, SEP, R, R^2, Adj R^2, MAE, and AAD were used to compare and analyze the validity and accuracy of the results given by RSM and ANN models. The statistical parameters were calculated for both ANN and RSM and given in Table 4. The value of R, R^2, and Adj R^2 should be near to one which defined better correlation between the predicted and experimental data. MSE, RMSE, MAE, SEP, and AAD should be closer to zero for better predictive ability. The R, R^2, MSE, RMSE, and SEP values for RSM was less than that of ANN, while MAE and AAD values for the RSM was higher than that of the ANN. The values predicted by RSM had a better correlation with the experimental values and the interactive effect between parameters and the response can be observed more in RSM by applying the second-order polynomial equation to predict the yield. The relation between the nonlinear equations can be better inter-related by ANN, while its synergic effect was showcased by RSM having higher values of R, R^2, MSE, RMSE, and standard error of prediction, while ANN depicted lower value of AAD and MAE which defined that ANN had higher generalized predictive ability. Moreover, RSM

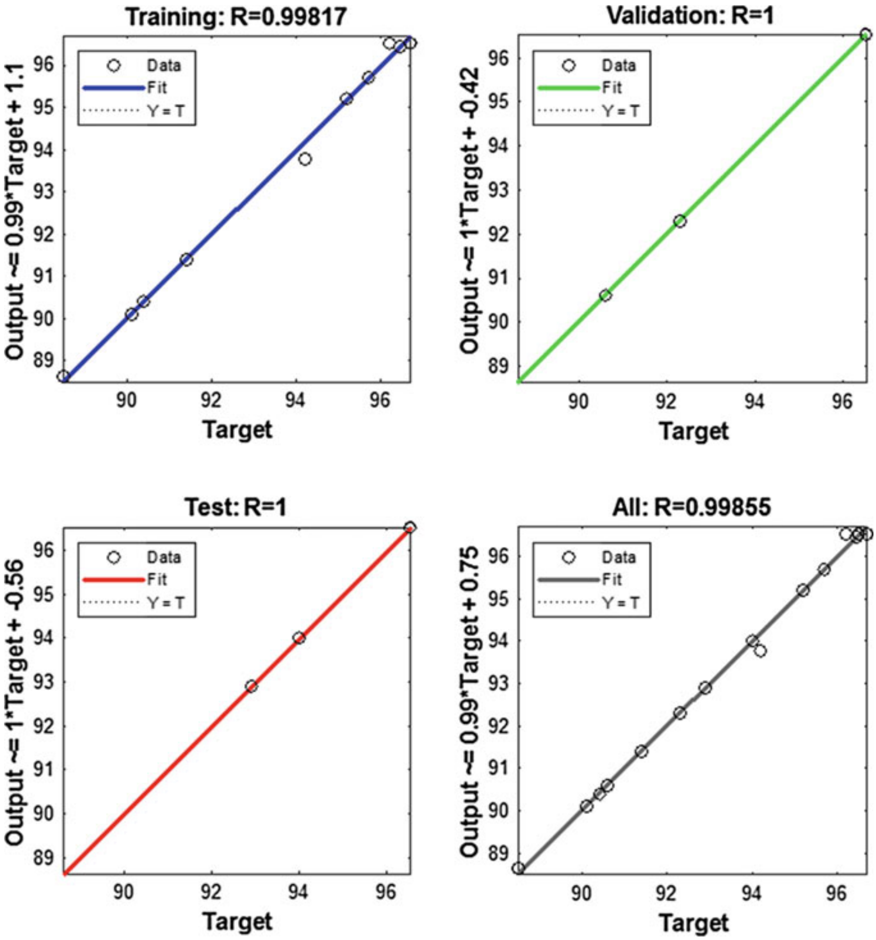

Fig. 3 Regression graph for predicted versus experimental value for ANN

Table 4 Comparison of statistical parameters for predicted values of RSM and ANN

Parameters	ANN	RSM
R	0.99855	0.9986
R^2	0.997001	0.997382
Adj R^2	0.996309	0.996778
SEP	0.143494	0.134775
MAE	0.075376	0.11246
AAD	0.079506	0.11952
RMSE	0.134577	0.1264
MSE	0.018111	0.015978

Table 5 Grape seed biodiesel properties

Fuel properties	Units	Standards	Bio-oil	Biodiesel
Fire point	°C	ASTM D93	262	182
Density @ 15 °C	kg/m^3	ASTM D127	905	880
Kinematic viscosity @ 40 °C	cSt	ASTM D445	26.62	4.04
Calorific value	kJ/kg	ASTM D240	37.7	39.52
Acid value	mg of KOH/g	ASTM D6751	1.4	0.45
Flash point	°C	ASTM D93	250	174

predicted data had better correlation to the experimental data and synergy between operating parameters.

The kinematic viscosity of *Vitis vinifera* biodiesel was 4.04 cSt which was well inside the ASTM limits. The density of fuel was around 880.2 kg/m^3. The flash point of the biodiesel was determined as 174 °C which too had met the ASTM D93 standards. The Cetane number should have a minimum value of 47 as per the ASTM D613. The acid value of the biodiesel was around 0.36 mg of KOH/g which met the ASTM D6751 standards which is less than 0.5 mg of KOH/g. As listed in Table 5, it can be observed that the biodiesel had good fuel properties compared to the mineral diesel, and it was with the stipulated ASTM standards.

4 Conclusion

In this investigational study, optimization of *Vitis vinifera* oil biodiesel production was done using methanol, sodium hydroxide as catalyst, and reaction time at three different levels to find the optimum process parameters. Box–Behnken design of experimental values with 17 runs at three different levels was used to determine the optimal process conditions. A yield of about 97.665% was predicted to be attained at a catalyst loading percentage 1.1719 wt% of oil, 66.8205 min of reaction time and molar ratio of 6.4246:1. The value was experimentally validated, and a yield of 97.53% was obtained with an error of 0.1325%. The modeling and predictive ability of ANN and RSM were assessed using statistical parameters. It was found that RSM had a better correlation with the experimental value, while ANN had better generalized predictive ability. The physiochemical properties of *Vitis vinifera* biodiesel were estimated, and it was compared with the ASTM standards. Hence, *Vitis vinifera* bio-oil can be used as a future potential feedstock for the production of biodiesel.

References

1. Ong HC, Milano J, Silitonga AS, Hassan MH, Shamsuddin AH, Wang CT, Indra Mahlia TM, Siswantoro J, Kusumo F, Sutrisno J (2019) Biodiesel production from *Calophyllum inophyllum-Ceiba pentandra* oil mixture: optimization and characterization. J Clean Prod
2. Rocabruno-Valdés CI, Ramírez-Verduzco LF, Hernández JA (2015) Artificial neural network models to predict density, dynamic viscosity, and cetane number of biodiesels. Fuel 147:9–17
3. Meng X, Jia M, Wang T (2014) Neural network prediction of biodiesel kinematic viscosity at 313K. Fuel 121:133–140
4. Venkatesan H, John G, Sivamani S (2017) Cotton seed biodiesel as alternative fuel: production and its characterization analysis using spectroscopic studies. Int J Renew Energy Res 7(3):1333–1339
5. Ameer K, Bae S-W, Jo Y, Lee H-G, Ameer A, Kwon J-H (2017) Optimization of microwave-assisted extraction of total extract, stevioside and rebaudioside-A from *Stevia rebaudiana* (Bertoni) leaves, using response surface methodology (RSM) and artificial neural network (ANN) modelling. Food Chem 229:198–207
6. Betiku E, Omilakin OR, Ajala SO, Okeleye AA, Taiwo AE, Solomon BO (2014) Mathematical modeling and process parameters optimization studies by artificial neural network and response surface methodology: a case of non-edible neem (*Azadirachta indica*) seed oil biodiesel synthesis. Energy 72:266–273
7. Maran JP, Priya B (2015) Comparison of response surface methodology and artificial neural network approach towards efficient ultrasound-assisted biodiesel production from muskmelon oil. Ultrason Sonochem 23:192–200
8. Selvaraj R, Moorthy IG, Kumar RV, Sivasubramanian V (2019) Microwave mediated production of FAME from waste cooking oil: modelling and optimization of process parameters by RSM and ANN approach. Fuel 237:40–49
9. Prakash Maran J, Priya B (2015) Modeling of ultrasound assisted intensification of biodiesel production from neem (*Azadirachta indica*) oil using response surface methodology and artificial neural network. Fuel 143:262–267
10. Chizoo E, Dominic OO, Uwaoma OA (2018) Optimization of methyl ester production from *Prunus amygdalus* seed oil using response surface methodology and artificial neural networks. Renew Energy
11. Dharma S, Masjuki HH, Ong HC, Sebayang AH, Silitonga AS, Kusumo F, Mahlia TMI (2016) Optimization of biodiesel production process for mixed *Jatropha curcas–Ceiba pentandra* biodiesel using response surface methodology. Energy Convers Manag 115:178–190
12. Betiku E, Ajala SO (2014) Modeling and optimization of *Thevetia peruviana* (yellow oleander) oil biodiesel synthesis via *Musa paradisiacal* (plantain) peels as heterogeneous base catalyst: a case of artificial neural network vs. response surface methodology. Ind Crops Prod 53:314–322
13. Avramović JM, Veličković AV, Stamenković OS, Rajković KM, Milić PS, Veljković VB (2015) Optimization of sunflower oil ethanolysis catalyzed by calcium oxide: RSM versus ANN-GA. Energy Convers Manag 105:1149–1156
14. Hariram V, John JG, Seralathan S (2019) Spectrometric analysis of algal biodiesel as a fuel derived through base-catalyzed transesterification. Int J Ambient Energy 40(2):195–202
15. Venkatesan H, Godwin JJ, Sivamani S (2017) Data set for extraction of bio-oil from *Stoechospermum marginatum*, a brown marine algae. Data Brief 14:623–628

Waste Heat Recovery (WHR) of Diesel Engine Using Closed-Loop Pulsating Heat Pipe

Saurabh B. Dhone and A. T. Pise

Abstract In internal combustion engine, around 25–40% of energy is expelled through the exhaust gases into environment which causes pollution. So this energy should be recovered for other applications. This present work represents the study of the pulsating heat pipe (PHP) technique used for heating the air with the help of recovered heat from exhaust of the engine. The CLPHP is most effective, promising heat transfer device than the others, which uses the pulsating or oscillating actions of the working fluid for transferring heat. The performance of CLPHP basically depends on different parameters like filling ratio (F.R), internal diameter of the tube(D_i), cross section area of tube (A_c), heat input(Q_{in}), angle of inclination (θ), no of turns (N), working fluid, length of tube in evaporator and condenser section, etc. In this work, eight-loop PHP is made of copper material having ID = 3.2512 mm and OD = 4.7752 mm with water as working fluid. The experimental investigation is performed for different filling ratios (50, 60 and 70%) and at various heat inputs (715.98, 861.48, 935.41, 1004.96 and 1070.5 W) by varying the loads on engine. The result shows that for 50% filling ratio, overall thermal resistance is less and heat transfer coefficient value is more as compared to other filling ratios.

Keywords CLPHP · Filling ratio · Thermal resistance

1 Introduction

In internal combustion engine, around 25–40% of energy is expelled through the exhaust gases into environment which causes pollution. So this energy should be recovered for other applications. There are a number of devices used for waste heat recovery of engine like heat exchangers, thermoelectric generator, heat pipe, etc. The heat pipe is also having more efficiency for transferring the heat.

Heat pipe is a device generally used to transfer the heat from one location to another location with minimum heat loss. The heat pipe consists of 3 sections, i.e. heating

S. B. Dhone (✉) · A. T. Pise
Department of Mechanical Engineering, GCE, Karad, Maharashtra 415124, India
e-mail: saurabhdhone1995@gmail.com

E. T. Akinlabi et al. (eds.), *Trends in Mechanical and Biomedical Design*, Lecture Notes in Mechanical Engineering,
https://doi.org/10.1007/978-981-15-4488-0_64

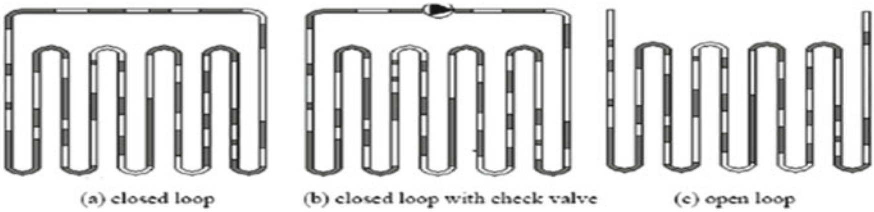

Fig. 1 Classification of pulsating heat pipe [PHP] [2]

section (evaporator), adiabatic section and cooling section (condenser). It absorbs the heat from hot source at evaporator and releases it at sink, i.e. at the condenser. While heat transfer the phase change occurs in both evaporator and condenser sections, huge amount of heat transfer takes place. It has wide range of applications in electronic cooling, aerospace cooling, waste heat energy recovery of IC engine, gas turbine, HVAC, VARS, and VCRS and is also used for high temperature range of applications like in boiler or nuclear reactor etc.

In 1990, Akachi introduced a "wickless heat pipe". The pulsating heat pipe (PHP) and thermosyphon are the types of wickless loop heat pipe. The pulsating heat pipe is different than the other types: In conventional heat pipe, the liquid returns from condenser to evaporator by the capillary action; as in thermosyphon, circulation takes place due to density difference, whereas in pulsating heat pipe, the vapour pressure difference acts as a main driving force for the circulation of fluid [1].

2 Classification of Pulsating Heat Pipe [PHP]

The classification of PHP is as shown in Fig. 1. It is classified into three types such as open loop, closed loop and closed loop with check valve. In OLPHPs, the two ends of tube are not welded so that there is no possibility of circulation of working fluid; hence, annular flow cannot be achieved. The flow will be as a pulsating capillary slug flow regime with long vapour bubbles forming at higher heat fluxes. Local internal heat transfer is usually more in the convective annular flow regime. Therefore, CLPHP shows better performance than OLPHP [2].

3 Principle of Heat Transfer in CLPHP

The set-up consists of mainly three sections, i.e. condenser, adiabatic and evaporator sections. Due to input of heat flux at evaporator, there is variation in temperature and pressure gradient between evaporator and condenser regions. Due to continuously heating at the evaporator, vapour pressure of fluid is increased; hence, small growth of bubbles takes place. These bubbles are combined together and form a large bubble, and then it turns into the vapours. The vapour pressure difference acts as a main driving force for the circulations of fluid. The liquid vapour slug-plug moves towards condenser region, whereas the vapour pressure is less; therefore, condensation of the liquid takes place. While condensation vapour releases the latent heat and the liquid releases the sensible heat, the heat transfer performance increases.

4 Parameters Affecting the Performance of CLPHP

The following main factors which affecting the performance of CLPHP are:

- Internal diameter of tube
- Cross section
- Heat input
- No. of. loops/turns
- Length of evaporator and condenser section
- Working fluid
- Filling ratio
- Angle of inclination.

Internal Diameter (*D*)
The internal tube diameter is the most essential factor which defines a PHP. The occurrence of pulsating motion inside a CLPHP is limited by the internal diameter of tube. The critical diameter of heat pipe is given by,

$$D\mathrm{max} = D_{\mathrm{crit}} = 2 \times \sqrt{\frac{\sigma}{g \times (\rho_l - \rho_v)}}$$

where,

σ surface tension working fluid,
g gravitational acceleration,
ρ_l liquid density,
ρ_v vapour density.

If the tube internal diameter is increased beyond the critical diameter (i.e. $D >>> D_{\mathrm{crit}}$), then the surface tension gets reduced which causes the stratification of liquid by the gravity, and therefore, heat pipe acts like a interconnected array of two-phase thermosyphons as shown in Fig. 2 (case A and case B). If internal diameter of the tube is very very less (i.e. $D <<< D_{\mathrm{crit}}$), then the surface tension of working fluid is more dominant and therefore a stable liquid slugs are formed inside a tube as shown in Fig. 2 (case C) [3]. So that for the better achievement of performance of CLPHP, the internal diameter of tube should be required slightly less than that of critical diameter of the tube.

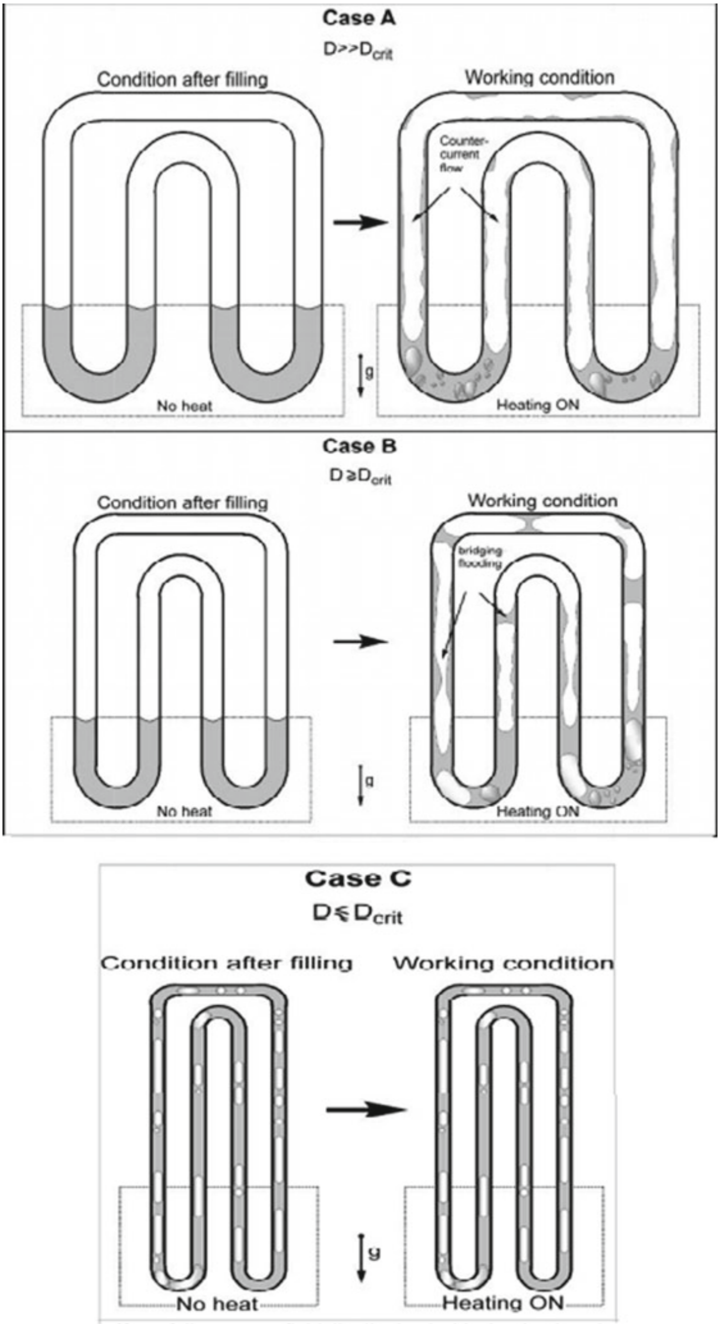

Fig. 2 Effect of diameter on fluid distribution inside the circular tube of CLPHP under adiabatic and operating conditions [3]

Cross Section the Tube (A_c)
Fourgeaud et al. [4] used circular area of tube, and they conclude that with circular section the liquid film is attached to the inner side wall of tube so that the maximum heat is absorbed at the evaporator and released at the condenser section, and also there is decrease in the drag force resistance offered by the fluid, hence improving the oscillation characteristics inside the tube.

Input Heat Flux (Q_{in})
There is necessity of higher heat input flux for the continuous operation of the CLPHP. With increasing the heat input, the temperature and vapour pressure of liquid increase at the evaporator, therefore improving the bubble growth and decreasing the dynamic viscosity of the fluid. Hence, total heat transfer rate increases.

No. of Turns (N)
The no. of turns is also another most important parameter which affects the performance of PHP. If the no of turns or loops are increased, then the availability of area for accepting the heat increases, therefore increasing the vapour pressure difference in each loop of the heat pipe, which will help to form more dynamic instability or the pulsating motion inside a tube; hence, the performance of PHP is increased.

Length of Evaporator and Condenser
Generally, the condenser area should be taken greater than the evaporator area in order to avoid the dryout condition. As the evaporator length increased, the thermal resistance offered by the fluid also increases and therefore the performance of heat pipe is decreased. If the condenser length increased, then the area for dissipation of heat also increases; hence, the performance of PHP is increased. Hence, the selections of lengths of evaporator and condenser are the most important factor in the design of heat pipe.

Working Fluid
The working fluid should have the following characteristics:

1. Low latent heat
2. Higher thermal conductivity
3. Lower surface tension
4. Low dynamic viscosity
5. Higher specific heat.

Filling Ratio (F.R.)
The filling ratio is defined as the ratio of available working fluid inside the tube to the total volume of the tube. If F.R $= 0$, no liquid content is present inside the tube. Hence it increases the thermal resistance which will reduce the heat transfer rate. If F.R $= 1$, there is more amount of liquid content in the tube; hence, less bubble will form which has the low ability to transfer the latent heat, so overall heat transfer rate

decreases. The optimal filling ratio is required for the best operation of the CLPHP is generally taking the filling ratio as in between 40 and 60%.

Angle of Inclination

As the PHP is at horizontal mode, then the gravity effect is decreased; therefore, the circulation of the fluid stops; hence, the heat transfer rate is decreased. As an angle of inclination increased, the temperature gradient also increases. Therefore, increasing the dynamic instability, the heat transfer performance is increased.

5 Experimental Set-Up

The experimental set-up of CLPHP for waste heat recovery [WHR] of diesel engine is as shown in Fig. 1. Here, the copper pipe having ID 3.252 and OD 4.7752 mm with 8 number of loops is used and tube is filled with the water. The exhaust pipe of the engine is connected to evaporator section of the heat pipe. This exhaust heat is absorbed at the evaporator section, and it is transferred to the condenser section where it condenses and releases the latent heat of vapour and sensible heat of the liquid to the environment (air). Here, blower is used to achieve proper condensation of the working fluid (Fig. 3).

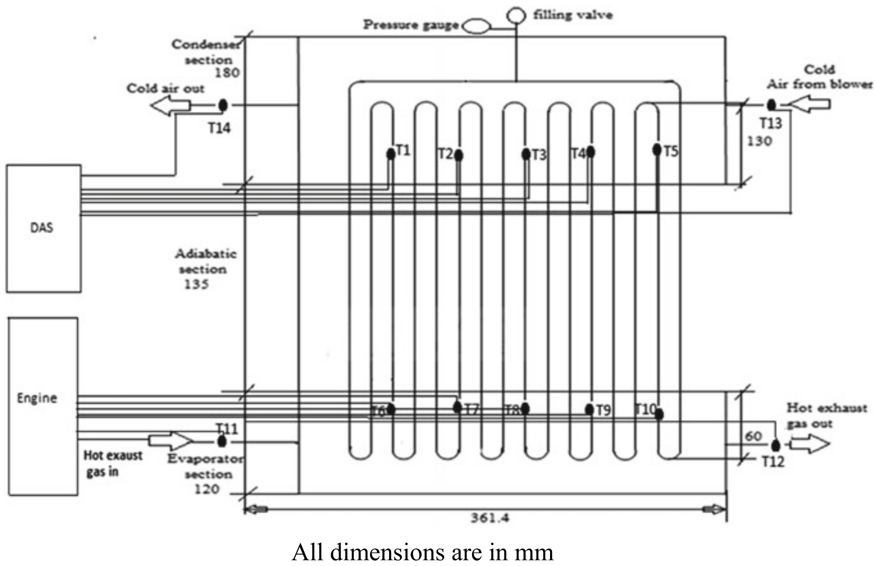

Fig. 3 Experimental set-up of WHR of diesel engine using CLPHP

6 Calculation of Heat Transfer Performance of PHP

The effectiveness of pulsating heat pipe can be represented by a system of thermal resistance. The thermal resistance "R_{th}" can be represented by,

$$R_{\text{th}} = \frac{\overline{T}_e - \overline{T}_c}{Q_{\text{in}}}$$

The overall heat transfer coefficient "*ho*" of the pulsating heat pipe can be given by

$$ho = \frac{Q_{\text{in}}}{A \times \left(\overline{T}_e - \overline{T}_c\right)}$$

where,

Q_{in} heat input (in Watt),
$\overline{T}_e$ Average evaporator temperature (°C),
$\overline{T}_c$ Average condenser temperature (°C),
A_e The surface area of heat pipe (m^2), $= \pi d_i L$.

7 Results and Discussions

The performance PHP of pulsating heat pipe depends on various factors which we have discussed in above section. The experimental investigation is performed for different filling ratios (50, 60 and 70%) at various heat inputs values (715.98, 861.48, 935.41, 1004.96 and 1070.5 W) by varying the loads on engine.

Figure 4 shows the various values of heat input is achieved by varying the loads on the engine. Figure 5 shows the heat transfer coefficient with heat input for different filling ratios. From graph, we can see that, as the filling ratio increases, there is increment in the thermal resistance of fluid; hence, the heat transfer coefficient is decreased, and therefore, the value of heat transfer coefficient for 50% filling ratio is more as compared to that of 60 and 70%.

Figure 6 shows the variation of overall thermal resistance with heat input to the CLPHP. From fig, we can see that, as the mass concentration of the fluid increased, then the thermal resistance of the vapour also increases. Therefore, for 50% filling ratio, the thermal resistance value is less as compared to 60 and 70%.

Figure 7 shows the variation in average evaporator temperature with respect to time. As the evaporator temperature is increased with increasing the heat input to PHP, and it could be decreased by increasing the mass concentration of the fluid. Therefore, the maximum evaporator temperature is achieved for 50% filling ratio as compared to the 60 and 70%.

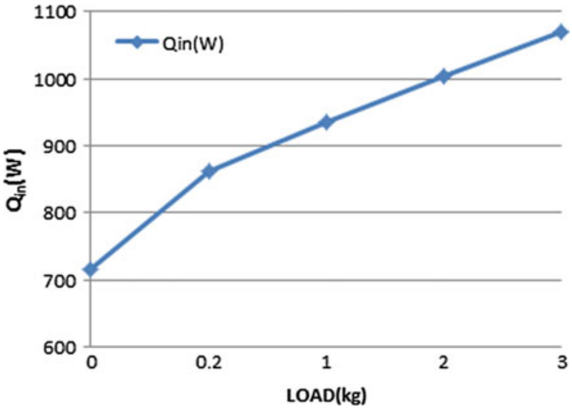

Fig. 4 Heat input versus load

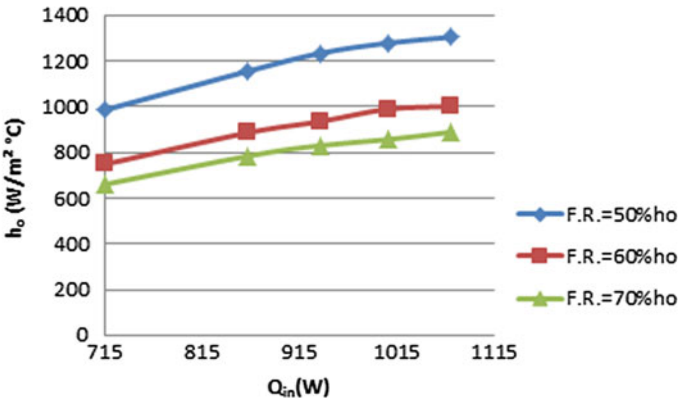

Fig. 5 Heat input versus heat transfer coefficient

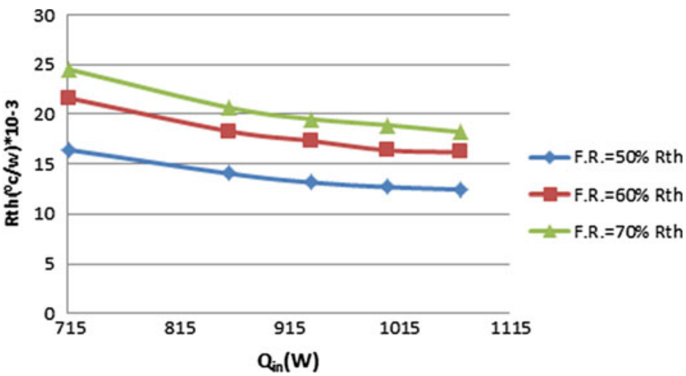

Fig. 6 Overall thermal resistance versus heat input

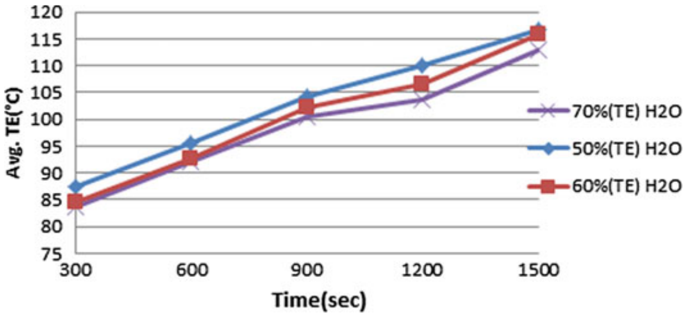

Fig. 7 Avg. evaporator temperature versus time

Figure 8 shows the variation in average condenser temperature with respect to time. The average condenser temperature is increased with increasing the heat input, and it could be decreased by increasing the mass concentration of the fluid. Because as the mass concentration of fluid increases, the saturation temperature and specific heat of the fluid also increased; therefore, the condenser temperature decreases. Therefore, the maximum condenser temperature is achieved for 50% filling ratio as compared to the 60 and 70%.

Figure 9 shows the variation in Avg. temperature difference between the evaporator and the condenser. By increasing the filling ratio, thermal resistance offered by the fluid also increases; therefore, the temperature difference between the evaporator and the condenser is increased. Hence, for 50% filling ratio, the temperature difference is less as compared to 60 and 70%.

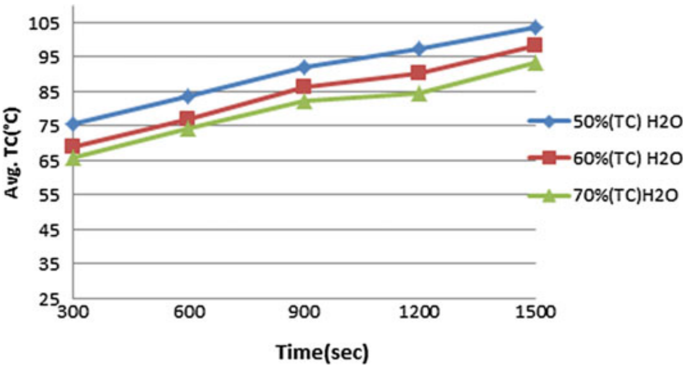

Fig. 8 Avg. condenser temperature versus time

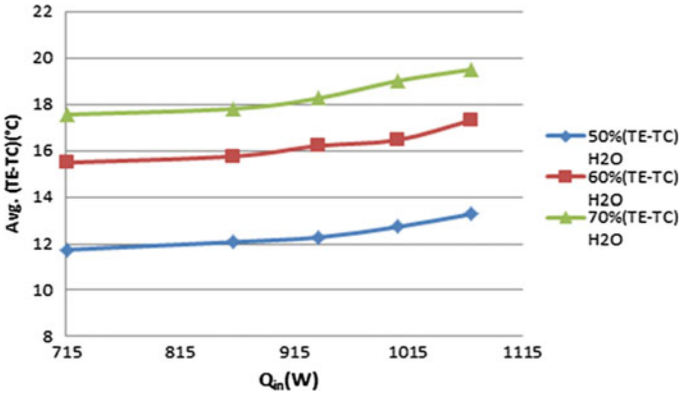

Fig. 9 Heat input versus average temperature difference between evaporator and condenser

8 Conclusion

The pulsating heat pipe is a simple and more efficient heat transfer device. From the above results, we concluded that the performance of closed-loop pulsating heat pipe for 50% filling ratio is more as compared to filling ratio of 60 and 70%.

References

1. Chavan D, Kale VM (November, 2015) On the design fundamentals of pulsating heat pipe: an overview. IJERT 4(11)
2. https://www.google.com/search?q=heat+pipe&source=lnms&tbm=isch&sa=X&ved=0ahUKEwifnLvHn-PhAhUN8HMBHUdLDbUQ_AUIDigB&biw=1366&bih=657
3. Haque S (December, 2011) Thermal characteristics of an aluminum closed-loop pulsating heat pipe charged with ammonia. M. S. thesis, mechanical department, Bangladesh University of engineering and technology Dhaka-1000, Bangladesh
4. Fourgeaud L, Nikolayev VS, Ercolani E, Duplat J, Gully P (2017) In situ investigation of liquid films in pulsating heat pipe. Appl Therm Eng 126:1023–1028

An Experimental Investigation of Heat Transfer in Heat Exchangers Using Al_2O_3 Nanofluid

S. Bhuvaneswari and G. Elatharasan

Abstract Heat is the term distinct as the amount of energy transferred by the virtue of the temperature difference. The heat flows from the region of maximum temperature to minimum temperature by the different methods of heat conveyed. This paper focuses on the study of heat transfer in the heat exchanger which is a device used for transfer of thermal energy and consists of two or additional fluids or between surface of fluid and solid to solid particulates and a fluid at different temperature, thermal constant with and without outside heat and work communications. The parameters of heat transfer are analyzed in different types of heat exchangers. This examination explores the warmth move and the weight drop of cone helically curled cylinder heat exchanger utilizing Al_2O_3/water nanofluids. The Al_2O_3/water nanofluids at 0.2, 0.4, and 0.6% molecule volume fixations were set up with the expansion of surfactant by utilizing the two advance strategies. The experimental study of heat transfer in various heat exchangers is discussed.

Keywords Heat transfer · Heat exchangers · Mathematical equations · Experimental study

1 Introduction

Heat transfer is an application for engineering analysis, for example, heat exchangers, combustors, furnaces, and certain electronic devices, which include both fluid and solid components to perform the conjugate heat transfer analysis. The solid or liquid domains are simultaneously solved where it behaves as interface mechanism for heat transfer. Determination of an interface temperature is done by the energy balance of the conductive solid and convective liquid. Heat exchanger is the device designed to

S. Bhuvaneswari
University College of Engineering, Pattukkottai, Rajamadam 614701, India

G. Elatharasan (✉)
Department of Mechanical Engineering, University College of Engineering, Pattukkottai, Rajamadam 614701, India
e-mail: gelatharasan@gmail.com

E. T. Akinlabi et al. (eds.), *Trends in Mechanical and Biomedical Design*,
Lecture Notes in Mechanical Engineering,
https://doi.org/10.1007/978-981-15-4488-0_65

transfer the heat involving two or more additional fluids. The heat transfer process differs based on the heat exchanger type like gas to gas, liquid to gas, or liquid to liquid which occurs through the solid separator which prevents mixing of fluids or fluid direct contact.

Design characteristics and components, heat transfer mechanism, flow configurations. The type of heat exchanger is primarily classified as industries used for heating and cooling processes. This paper helps to study and analyze the transfer of heat in different types of heat exchangers. Heat exchangers operate on the fundamental principles of laws of thermodynamics which explain the transfer of heat from one fluid to another. Based on the zeroth law of thermodynamics, if the two systems are in thermal stability with a third system, then the other two systems must be in equilibrium with each other where all the systems are of the same temperature. If the heat flows interested in the system from the surroundings, then there is an increase in the internal energy of the system and decrease in the energy of the surrounding environment by the first law of thermodynamics. The entropy property is established by the second law of thermodynamics which explains the natural and invariable tendency of the closed thermodynamic system to increase the entropy over time. The increased entropy moves the system to reach the state of equilibrium. The proportion of the heat added or subtracted to the system to the absolute temperature remains constant. Heat transfer is a fundamental concept in industries. Heat must be added and removed or moved from one stage to another stage with the basic types of heat transfer as conduction, convection, and radiation. Heat exchanger is a piece of equipment to transfer heat from one medium to another medium separated by the wall in order not to mix.

1.1 Heat Exchangers

The heat transfer and heat exchangers are widely used in the petroleum refineries, natural gas processing and chemical or power plants. Heat exchanger has its application in the process, petroleum industry, cryogenic, air-conditioning, refrigeration, alternate fuels, and other industries. Based on the characteristics, we categorize it in terms of shapes, sizes, models, and the flow direction of the fluids comparative to each other. The categories are divided into different phases such as parallel, counter, and cross flow. Parallel flow is applied when both types of the tube side fluid and the shell side fluid flow in the same direction. The counter flow comes into existence when the two fluids flow in opposite directions. The fluids enter at opposite sides of heat exchangers. The concept of cross flow works when fluid flows are perpendicular to each other. The wide variety of heat exchangers are regenerative, adiabatic wheel, plate fin, fluid heat, waste recovery, dynamic scraped surface, plate, and shell-tube types. The two types of heat exchangers are direct and indirect. In direct heat exchanger, the two media are in direct contact with each other such that it is not mixed together, whereas in the indirect type in cooperation the media are divided by the wall through which the heat is transferred.

1.2 Heat Exchanger Design

The heat exchanger design equation requires the entry of liquids into the heat exchanger surface, the outlet temperature with the type, and the configurations of the heat exchangers with parallel or opposite flow. The basic design equation is given by $Q = UA\Delta T_{lm}$ where Q is clear as the rate of heat transfer between two fluids, U is the overall heat transfer coefficient, A is the heat transfer surface area, and ΔT_{lm} is the log mean temperature difference which is calculated from the inlet and outlet temperatures of the fluids. The three parameters are to be chosen effectively to estimate the value of heat transfer in the heat exchanger. The log mean temperature difference is calculated with the inlet and outlet temperature of the hot fluid and cold fluid and is defined as

$$\Delta T_{lm} = \frac{T_{\mathrm{Hin}} - T_{\mathrm{Cout}} - T_{\mathrm{Hout}} + T_{\mathrm{tin}}}{\ln \frac{T_{\mathrm{Hin}} - T_{\mathrm{Cout}}}{T_{\mathrm{Hout}} - T_{\mathrm{Cin}}}}$$

The heat transfer rate Q is calculated from the flow rate of one of the fluids with the shell side fluid and the hot fluid as the tube side fluid with the values as $Q = m_H C_{\rho H}(T_{\mathrm{Hin}} - T_{\mathrm{Hout}}) = m_c C_{\rho c}(T_{\mathrm{cout}} - T_{\mathrm{cin}})$ where mass flow rates of hot and cold fluids are given by m_H, m_c and heat capacities of hot and cold fluids are given by $C_{\rho H}$ and $C_{\rho c}$, respectively. If the total heat transfer coefficient is taken as U, the heat transfer through the wall separating the two liquids depends on the conductivity. A heat exchanger consists of heat exchanging elements such as matrix containing the heat transfer surface, inlet and outlet pipes, etc., whereas in the rotary regenerator the matrix is driven to rotate at specified design speed.

The heat exchanger is classified based on the characterization of construction, transfer process, degrees of surface compactness, flow arrangements, pass arrangements, (6) fluids process, and heat transfer mechanisms. Based on the construction, we have different types as tubular heat exchangers, double-pipe heat exchanger, gasket, brazed, welded, spiral, and panel coil.

1.3 Heat Transfer in Heat Exchangers

The tubular heat exchangers are of double pipe, shell and tube, helically coiled tubesplate heat exchangers are of gasket, brazed, welded, spiral, pane; coil, and lamella. Tube fin and plate fin are of extended surface heat exchangers. Fixed and rotary matrixes are of regenerators (Fig. 1).

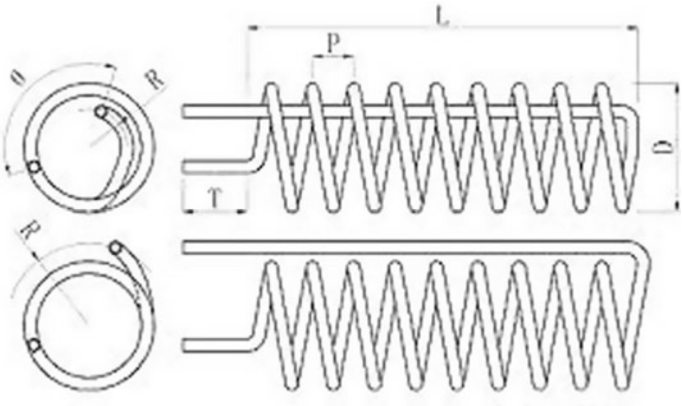

Fig. 1 Helically coiled heat exchanger

2 Experimental

Figure 4 demonstrates the picture of the test segment. Figure 5 demonstrate the line graph and photograph of the test arrangement. The exploratory arrangement has two circles. The first is cone helically looped cylinder side which handles nanofluids. The subsequent circle is the shell side which handles high-temp water. The subsequent circle is associated with a capacity vessel with a size of 15 cm × 15 cm × 15 cm, with a warmer 2 kW limit, attractive siphon, and indoor regulator. Cone wound cylinder circle side is associated with a monobloc pump with 0.5 hp control, valve to control the stream on cylinder side, test segment, cooling unit, and capacity vessel of six-liter limit. The straight cylinder with fine sand is twisted to have the cone-like shape with the assistance of wooden cone-shaped shape. The utilization of fine sand in the cylinder is expected to maintain a strategic distance from the leveling of the copper tube while bowing. The shell material is stainless steel, and the cone cylinder is copper. The thermostat regulator is utilized to cut in and cut off the warmer. The inlet and outlet temperatures are recorded by the fitted four *K*-type thermocouples with the exactness of 0.1 °C. The stream passage impact is dodged by utilizing the quieting area. *U*-tube mercury manometer is fitted over the cylinder with a precision of 1 mm. The cooling unit of nanofluids handles water as a cooling medium. The shell external surface is secured with asbestoses tape to lessen heat misfortune. Stream control is finished with the valve, and the heated water from the cylinder is cooled by a cooling unit (Fig. 2).

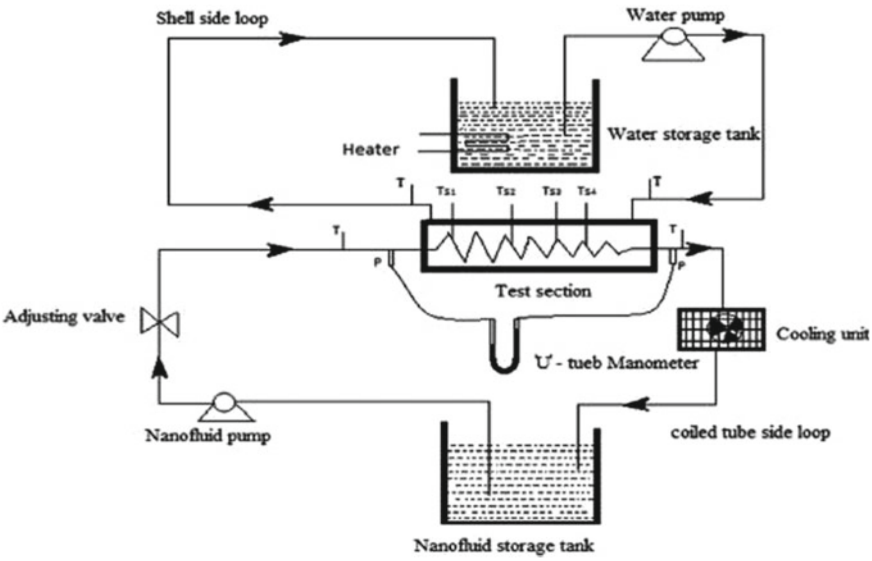

Fig. 2 Experimental setup

2.1 Helically Coiled Heat Exchanger

Helical coil heat exchangers are used in various processes because of its advantages compared to other heat exchangers in view of simple configuration, easy integration of the system, manufacturing and design, suitable for operating at high pressure and low flow rates, cost-effectiveness. Figure 4 indicates the helical coil exchanger image with winding of large number of small bore ductile tubes in the form of helix type around a central core tube with many layers of tubes in radial and perpendicular axes. With the low temperature where the heat transfer between more than two streams desired, we use helical coiled heat exchanger than the other. Fouling deposit cleaning is complicated because of small core tubes located on both sides. The overall heat transfer coefficient in helical coil inlet and outlet is given by the following equations:

$$h_i = 2\frac{k_i}{d_i + d_o} * Pr^{0.33} * 0.137 * \left(\text{Reic}^{0.7038}\right) \tag{1}$$

$$h_0 = k_s * Pr^{0.3} * 0.0175 * \left(\text{Reic}^{0.1}\right) * \left({R_a}^{0.3276}\right)/D_{\text{eq}} \tag{2}$$

$$R_a = \frac{9.81 * \beta * L^3 * d_t}{\alpha * \mu} \tag{3}$$

where d stands for the diameter, k for thermal conductivity, μ for viscosity, β for volumetric thermal expansion, L is the length of the coil, R for resistance, D_{eq} as equivalent diameter, and P_r for Prandtl number.

3 Result and Discussions

Figure 3 depicts the Dean versus the general heat transfer coefficient. It is seen that the general warmth move coefficient increments with expanding the Dean number and molecule volume fixation. The most extreme in general warmth move coefficient is 63% at 0.6% nanofluid in the Dean number 4200. The general warmth move coefficient is the impact of conduction and convection mode in the warmth exchanger. While contrasting the conduction warmth move mode, the convection warmth move is exceedingly viable than the conduction warmth move. Specifically, the inlet heat transfer is exceptionally powerful because of more grounded convection flow along with water. This leaves to improve progressively convective heat transfer characteristics. The lower temperature distinction between the cylinder and shell is the significant reason for improved convective heat transfer.

Figure 3 demonstrates the impact of molecule fixation on the heat transfer coefficient. It is discovered that the expanding pattern in warmth move coefficient with differing Dean number. The improved heat transfer coefficient is observed to be 14, 30, and 41% more than the water at 0.2, 0.4%, and water nanofluid separately. It is unmistakably observed that the greatest heat transfer coefficient is acquired at 0.6% nanofluid. The expansion of more Al_2O_3 expands the thermal conductivity of nanofluids. Also, the expansion of Al_2O_3 defers the arrangement of the heat limit layer and makes the temperature profile smooth. Notwithstanding the deferring heat limit layer, the lower relative speed of Al_2O_3 with water particles along the bent stream way is the purpose behind the higher inlet heat transfer coefficient at 0.6% volume fixation.

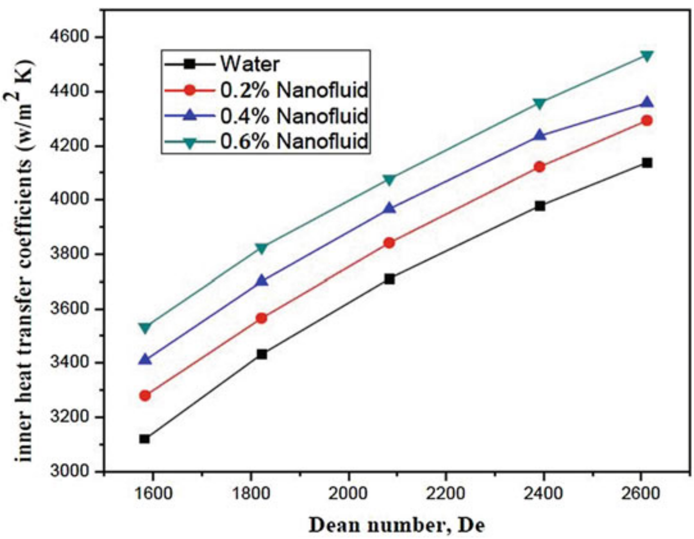

Fig. 3 Dean number versus inner heat transfer coefficient

From Fig. 4, it is seen that the Nusselt number is improved by changing Dean Number and molecule volume fixation. Increment in Nusselt numbers is observed to be 30, 59 and 67% at 0.2, 0.4, and 0.6% Al_2O_3/water nanofluids individually when looked at with water. The improvement is a direct result of the careful blending of water particles and Al_2O_3; this additionally might be the commitment Brownian movement of the Al_2O_3. In addition, the arbitrary development of Al_2O_3 exasperates the limit layer development and the arrangements of auxiliary streams are escalated. The Nusselt number is legitimately relative to the inward warmth move coefficient, and along these lines Nusselt number increments with expanding the warmth move coefficient and with expanding the volume fixation. The noteworthy Nusselt number is the manner by which compelling the convective warmth move occurs. In this work, the convective warmth move is profoundly compelling when expanding molecule volume focus.

Figure 5 uncover the expanding pattern of weight drop by shifting molecule volume fixation and Dean Number. The weight drop of 0.2, 0.4, and 0.6% nanofluids are observed to be 18, 33, and 44% higher than water separately. It is a direct result of the higher thickness while including more Al_2O_3. It is seen that the greatest weight drop happens at 0.6% nanofluid and at the Dean number 4200. It is clear that the higher weight drop prompts the siphoning power punishment. The greatest weight drop acquired is 44% when the outlet temperature of nanofluid is at 48 °C when it leaves the cylinder. Nonetheless, the weight drop may change as for the nanofluids outlet temperature. Higher the nanofluid temperature implies that lower the weight drop. This is just on account of bringing down the thickness because of a higher temperature (Fig. 5).

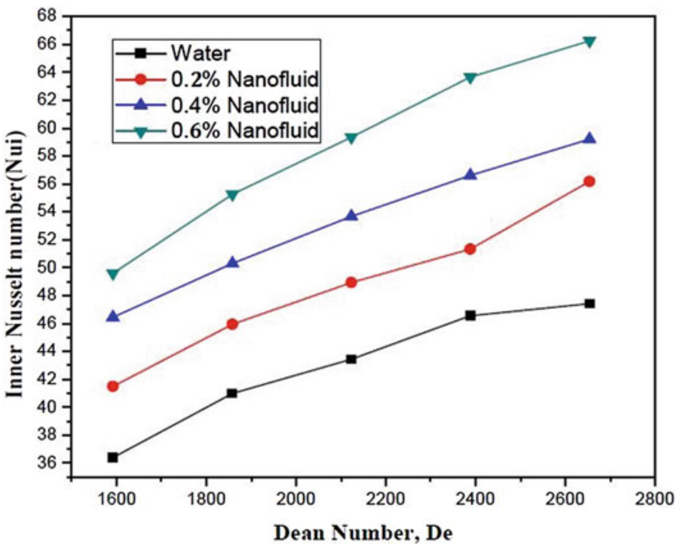

Fig. 4 Dean number versus Nusselt number

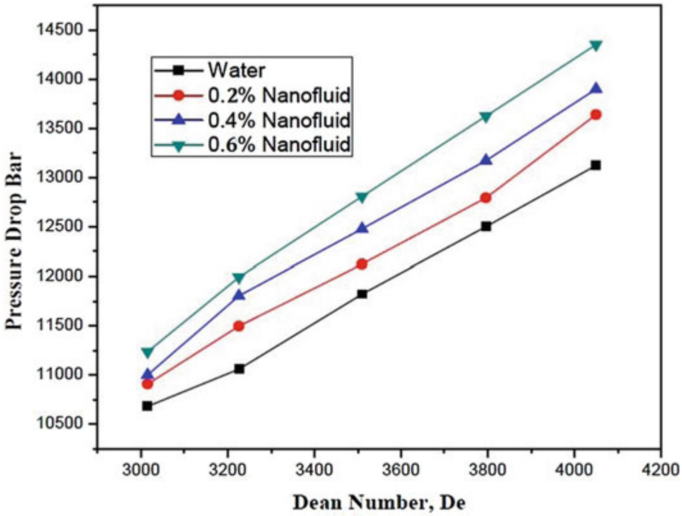

Fig. 5 Pressure drop

4 Conclusion

The paper focuses on the heat exchanger types and the efficiency of heat transfer in each heat exchanger. In this paper, the fierce stream (2000 < De < 4000) heat move attributes and weight drop of cone helically looped cylinder with Al_2O_3/water nanofluid at 0.2, 0.4, and 0.6% molecule volume fixation have been tentatively contemplated. It is discovered that the most extreme generally warmth move coefficient of nanofluids is 52% higher than the water at 0.6% nanofluid in the Dean number 4200. The expansion in Nusselt numbers is observed to be 28, 52% also, 68% at 0.2, 0.4, and 0.6% Al_2O_3/water nanofluid separately. In each type, we studied the constructional and performance features of the heat exchangers. In this manner, the conventional warmth move liquids might be supplanted with Al_2O_3/water nanofluid at extensive weight drop in cone helically snaked cylinder heat exchangers. Future work is required for examining the warm and stream practices of Al_2O_3/water nanofluid with higher volume focus at various cones helically coil pitch.

References

1. Ke Y, Pei-Qi G, Yan-Cai S, Hai-Tao M (2011) Numerical simulation on heat transfer characteristics of conical spiral tube bundle. Appl Therm Eng 31:284–292
2. Jaykumar JS (2011) Helically coiled heat exchangers. Heat exchangers—developments in heat transfer, In Tech Publishers, pp 311–342
3. Shah RK, Sekulic DP (2003) Fundamentals of heat exchanger design. Wiley, New York

4. Minton P (1990) Process heat transfer. In: Proceedings of the 9th international heat transfer conference, heat transfer (pp 355–362), Jerusalem, Israel, paper no. KN–2, 1
5. Taylor MA (ed) (1980) Plate-fin heat exchangers, guide to their specification and use. HTFS (Harwell Laboratory), Oxon, UK
6. Dravid AN, Smith KA, Merrill EA, Brian PLT (1971) Effect of secondary fluid motion on laminar flow heat transfer in helically coiled tubes. AICHE J 17(5):1114–1122
7. Varghese JA, Sreejith K, Ram TRS, Francis M, Mossas VJ, Nidhin MJ, Sushmitha S (August, 2015) Experimental investigation of a helical coil heat exchanger 5(8):01–05
8. Chinna Ankanna B, Sidda Reddy B (March, 2014) Performance analysis of fabricated helical coil heat exchanger. Int J Eng Res 3(1):33–39, ISSN: 2319–6890
9. Bhuvaneswari S, Elatharasan G (2019) A study on the literature review on heat transfer in a helically coiled heat exchanger. Int J Eng Res Technol 7(1):ISSN: 2278–0181, RTICCT
10. Bhuvaneswari S, Elatharasan G (March, 2019) Numerical methods of solving one dimensional heat equation comparative study. J Appl Sci Comput VI(III):ISSN: 1076–5131
11. Indian Standard Specification for Shell and Tube Type Heat Exchangers (2007) BIS 2007, New Delhi (IS: 4503–1967)
12. Dutta BK (2006) Heat transfer-principles and applications, 1st edn. PHI Pvt. Ltd., New Delhi
13. Couper JR, Penney WR, Fair JR, Walas SM (2005) Chemical process equipment: selection and design, 2nd edn. Elsevier Inc.
14. Bhuvaneswari S, Elatharasan G (April, 2019) A study on the methods of solving heat equation. J Appl Sci Comput VI(IV):ISSN: 1076–5131

Numerical Study of Heat Transfer and Pressure Drop in a Helically Coiled Tubes

S. Bhuvaneswari and G. Elatharasan

Abstract The pressure drop and heat transfer are increased due to the secondary flows caused by the centrifugal forces in a fluid through the curved pipes. The heat transfer rate in a helically coil tubes is higher than that of the straight tubes. Due to its compact structure, it has its wide application in industries. This chapter reviews on the of heat transfer flow rates and pressure drop individuality using the parameters such as Dean number, Reynolds number, Nusselt number, friction factor, and correlation. Based on the data obtained experimentally from the literature, computation of heat transfer and pressure fall is obtained by the mathematical equations. These parameters are analyzed and tabulated for all the flows in the helical coil tube. The heat transfer results have demonstrated that when utilizing an Al_2O_3, an expansion in warmth move rate can be acquired when contrasted with heat transfer results got utilizing straight heat transfer segments. It has reasoned that the expanded explicit heat of the Al_2O_3 just as the liquid elements in helical loop channels are the primary supporters of the expanded heat move.

Keywords Heat transfer · Pressure drop · Helically coiled tubes

1 Introduction

Helically coiled heat exchanger has its wide and extensive use in all industries because of the compact structure and high coefficient of heat transfer. The industrial applications are power generation, process plates, nuclear reactors, refrigeration, food industries, and chemical industry process. The literature review studied by Patankar et al. [1], Futagai and Aoyame [2], Abdulla [3], Bai et al. [4], Xin et al. [5], Jayakumar and Grover [6] states that heat exchanger with helical coils has been used for the

S. Bhuvaneswari
University College of Engineering, Pattukkottai, Rajamadam 614701, India

G. Elatharasan (✉)
Department of Mechanical Engineering, University College of Engineering, Pattukkottai, Rajamadam 614701, India
e-mail: gelatharasan@gmail.com

E. T. Akinlabi et al. (eds.), *Trends in Mechanical and Biomedical Design*,
Lecture Notes in Mechanical Engineering,
https://doi.org/10.1007/978-981-15-4488-0_66

heat residual and removal systems where large nuclear reactor systems are mounted and erected with the performance effectiveness of the parameters. They are also used in steam generators and condensers in power plant as it has large surface area per unit volume. The centrifugal forces produce the secondary flow which is typical to the crucial direction of flow with the effects of circular motion and also increases the friction factor and heat transfer. Present research work has been done to review the intensity of the secondary flow developed within the tube that is performed of the tube diameter and coil diameter. The performance of heat exchanger is improved for the enhancement of heat transfer for which the size of the heat exchanger has to be considerably decreased. The enhancement technique is classified as two groups as dynamic and reactive. The active technique is need for some peripheral forces like surface, fluid vibration, and field Special surface geometries, fluid additives are thought-about the passive techniques. These two techniques have extensively used in improving the heat transfer behavior. But in industries, helically coiled tube is considered as the reactive heat transfer augmentation techniques due to its structure. Due to the bend, the force ends up in the secondary flow enhancing the warmth transfer rate that is employed in streamline flow [7].

Naphon [8] studied the most frequent uses, thermal performance, and pressure drop of helically coiled tubes with and without the helical crimped fins. The literature survey reveals that the heat transfer coefficient calculations are based on the geometry features like tube diameter, coil diameter, pitch, etc.; heat transfer in the helical coil is investigated for laminar and turbulent flow with constant wall flux boundary conditions. Janssen and Hoogendoornh [9] studied the improvement techniques of helical coil heat exchangers over the others. The flow pattern between the stratified and annular transition was studied by Whalley [10]. Relaminarization was studied by Sreenivasan and Strykowski [11]. The review of heat transfer and pressure drop in a helical coils with two-phase flow in the horizontal helical pipes was studied by Berger et al. [12], Awwad et al. [13], Xin RC [5], and Shah and Joshi [14]. Jayakumar and Grover [6] and Vimalkumar et al. [15] studied the pressure drop and heat transfer in tube-in-tube helical heat exchanger with the turbulence condition.

Rennie and Raghavan [16] studied experimentally the parallel and counter flow configurations with the double-pipe helical heat exchanger. Annulus and inner tube had the varied flow rates and temperature for which overall heat transfer coefficients were determined. The experimental study done by Prabhanjan et al. [17] determined the relative advantage of helically coil over straight tube for liquid heating using the boundary conditions. Shokoummand et al. [18] had one investigation on the curvature ratio and different coil pitches with parallel and counter flow configurations with measurements of inlet and outlet temperature of tube-side, shell-side fluids, and flow rate of the fluids. Using Wilson plots, overall heat transfer coefficients were calculated and compared with the inner Nu number and mixed convection heat transfer in a coil-in-shell type [19]. Experiments were conducted for the steady state by varying Reynolds and Rayleigh numbers with different tube-to-coil diameters, pitch of the coil, mass flow rate of shell-side and tube-side over the performance coefficient, and effectiveness of the helical coil tube for the laminar and turbulent flows.

High-temp water and cold water were provided to the shell side and the cylinder side, individually, to check for spillages and test the exactness of thermocouples and indoor regulator. Boiling water was coursed to the shell side at a consistent stream rate. The nanofluid with 0.2% molecule volume fixation was circled through the cylinder side. The comparing perceptions were made. The cylinder-side stream was fluctuated to achieve the predetermined Dean number by utilizing a valve plan [20, 21].

1.1 Helical Coil Characteristics

The representation drawing of helical coil is given in Fig. 1. The inner pipe has the diameter $2{*}r$ and the coil diameter is $2{*}R{*}c$ where c is the distance between the centers of the pipes with H as the detachment between two neighboring turns. The curvature ratio δ is defined as the fraction of pipe diameter to the coil diameter agreed by r/Rc. The coil diameter is also defined as the pitch circle diameter. The ratio of pitch to the developed length of one turn is called as non-dimensional pitch as $\lambda = H/2nRc$. The symbol α is called helix angle which is termed as the projection of the coil on the plane perpendicular passing through the axis of the coil. The Reynolds number and Dean number are used to evaluate the flow characteristics.

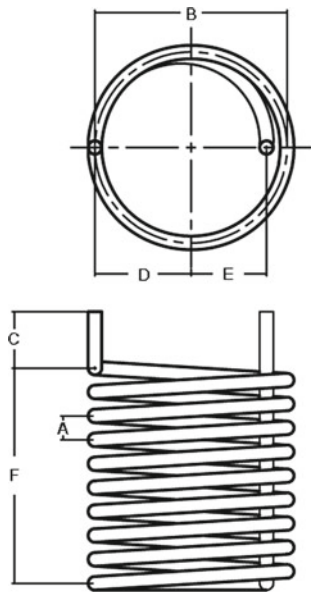

Fig. 1 Helical coil schematic diagram

2 Experimental Setup

Figure 2 delineates the plan of the test arrangement. The setup has shell-side circle and helical curled cylinder-side circle. Shell-side circle handles boiling water. Helical wound cylinder circle handles Al_2O_3/water nanofluid. The shell-side stream and the looped cylinder-side stream are in counter stream setup. Shell-side circle comprises a capacity vessel with a radiator of 1.75 kW limit. The cylinder-side circle comprises of monoblock siphon, valve to control the stream on the cylinder side, test area, cooling unit, and capacity vessel of five-liter limit. The helical cylinder is comprised of copper, and shell is comprised of mellow steel. The temperature of the heated water in the shell-side stockpiling vessel is kept up by an indoor regulator [22, 23]. Four 'K'- type thermocouples of 0.1 °C exactness are utilized to quantify the channel and outlet temperatures of shell and cylinder side. Four 'K'- type thermocouples of 0.1 °C exactness are put on the external surface of the looped cylinder to gauge the cylinder divider temperatures. U-tube mercury manometer is put over the helical cylinder to quantify the weight drop. The shell is protected with fiber fleece. A valve is given in the stream pipe associating the cooler area and the repository for stream rate estimations and cleaning the framework between trial runs.

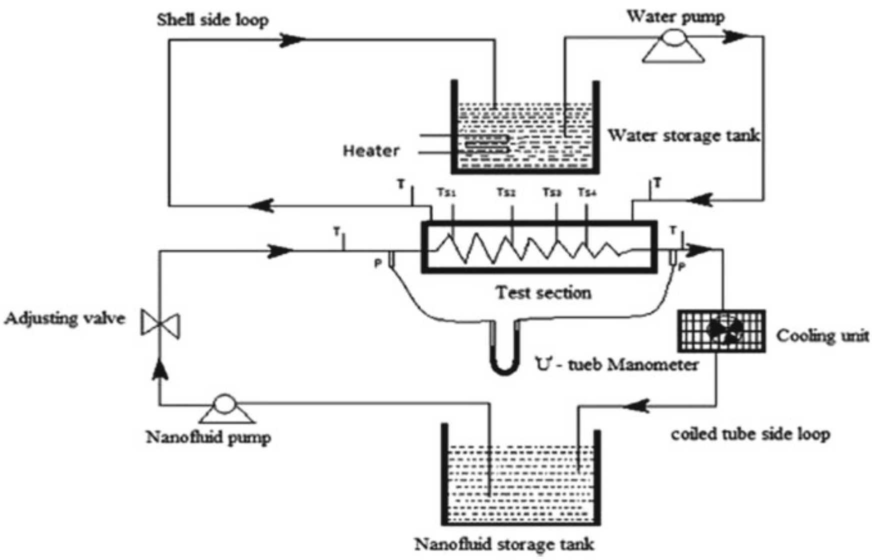

Fig. 2 Experimental setup

2.1 CFD Methodology

A geometric model was created utilizing CATIA v5, and this plan was sent out to the CFD module in ANSYS v12 to get the limited component model to the required examination. Cross section was done in CFD—Fluent utilizing similar programming as appeared in Fig. 3. The complete number of nodes and components acquired for a helically coiled heat exchanger were 359,624 and 2,175,794 individually. The administering conditions were explained utilizing limited volume technique with Computational Fluid Dynamic (CFD) programming ANSYS Fluent [24]. The arrangement depended on weight revision strategy utilizing the SIMPLE calculation. Kumar et al. explored the warm conduct of Al_2O_3/water nanofluid in a helically wound cylinder heat exchanger by utilizing CFD model.

3 Results and Discussion

The motivation behind this paper is to display the aftereffects of an examination concerning the general variety of heat transfer coefficient around the in-line cluster with helical loop cylinder shapes. The numerical examination considers the impact of nanofluid, for example, Al_2O_3 on the stream and heat transfer qualities of cylinder banks in a physical space for various Nusselt numbers. In this study, the heat

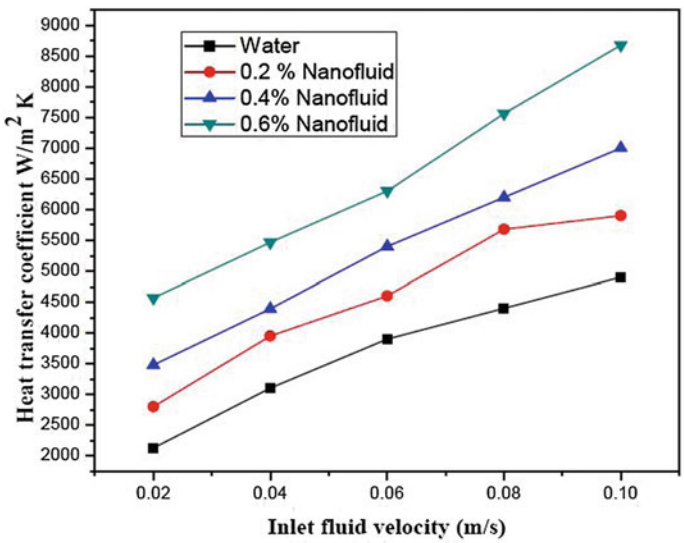

Fig. 3 Heat transfer coefficient

transfer rate, surface temperature, Nusselt number, thermal resistance, power consumption, and reliability of heat exchanger by using Al_2O_3/water nanofluids have been numerically studied by single-phase approach.

3.1 Heat Transfer Coefficient

The fundamental goal is to increase the heat transfer coefficient in the helically coiled heat exchanger, and Fig. 3 demonstrates the upgrade of heat transfer coefficient when expanding the channel liquid speed and molecule volume divisions. It was watched that heat transfer coefficient increments with expanding inlet fluid velocity. The heat transfer coefficient was observed to be 15, 26, and 41% higher than the water at 0.2, 0.4, and 0.6% separately volume division of Al_2O_3/water nanofluids. This is because of the higher warm conductivity and Brownian movement of nanoparticles. The movement of particles lessens the warm limit layer and improves the warmth move limit. A noteworthy heat transfer coefficient of 42% was accomplished at 0.6% volume portion which brought about better drop in surface temperature in the heat exchanger [25].

Figure 4 demonstrates the improvement of Nusselt number by fluctuating Reynolds number and Al_2O_3 nanoparticles volume parts. The Nusselt number expanded with a comparing increment in Reynolds number, and the Nusselt number was least at Re of 200 and most extreme at Re of 600. Further, the heat exchanger with higher nanoparticles volume fractions of nanofluids has a higher Nusselt number

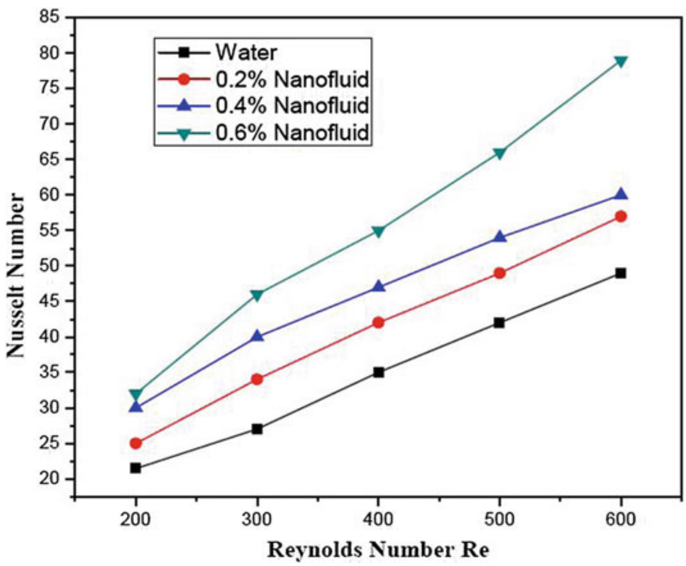

Fig. 4 Nusselt number

since when more nanoparticles take part in the nanofluid it can prompt a successful thermal conductivity. The Nusselt number is increased by 12, 27, and 45% at 0.2, 0.4, and 0.6% of Al_2O_3/water nanofluids individually when compared with water [26]. The expansion of Nusselt number to 32% is significant at 0.6% molecule volume portion on the grounds that the heat coefficient of nanofluid was higher than water.

The pressure drops are crosswise over the heat exchanger from inlet to outlet utilizing ANSYS Fluent. Here, the heat transition was connected on the base of the inner wall surfaces [27]. The stream rate of bay water and Al_2O_3-nanofluids is 0.02–1 m/s. The pressure drops over the inlet and outlet of the direct effect were appeared in cross-sectional area utilizing ANSYS Fluent. It was plainly seen that there were two locales with low temperature and pressure drop (blue in shading) in the inlet, high temperature, and pressure drop (red in shading) in the channel outlet. The pressure drop accomplished is 3240 Pa. The weight drop emerges due to the frictional impact of nanoparticles. The pressure drop of Al_2O_3-nanofluids expanded with increment in volume focuses. Kumar et al. [24] researched tentatively and numerically the warmth move and weight drop attributes of microchannel warmth sink by utilizing half breed Al_2O_3–TiO_2 nanofluids (two-stage blend model). The outcomes demonstrated that crossover nanofluids yield no synergetic impact in heat transfer while blending different nanoparticles with comparable shape and size.

3.2 Governing Equations for Heat Transfer and Pressure Drop in a Helical Coil

The heat transfer rate can be calculated as follows:

$$Q = UA\Delta T_{\log} = UA\frac{\Delta T_1 - \Delta T_2}{\ln\left(\frac{\Delta T_1}{\Delta T_2}\right)}$$

where Q is heat transferred, U is the overall heat transfer, A is the total heat transfer area, and $\Delta T_{\log}$ is log temperature difference or LMTD which is based on the fluid properties. Using control volume method, the discretization is done with change in overall enthalpy with division of equal differences Δh with N control volumes.

$$\begin{aligned} Q_i &= m_{\mathrm{hf}} c_{\mathrm{hf}} (T_{\mathrm{hf,bulk},i} - T_{\mathrm{hf,bulk},i+1}) \\ Q_i &= m_{\mathrm{hf}} (T_{\mathrm{hf,bulk},i} - T_{\mathrm{hf,bulk},i+1}) \end{aligned} \tag{1}$$

$$\begin{aligned} Q_i &= \dot{h}_{\mathrm{hf}} A_{\mathrm{out},i} (\ddot{T}_{\mathrm{hf,bulk},i} - \ddot{T}_{\mathrm{hf,wall},i+1}) \\ Q_i &= \ddot{h}_{\mathrm{hf}} A_{\mathrm{in},i} (\ddot{T}_{\mathrm{wf,wall},i} - \ddot{T}_{\mathrm{wf,bulk},i+1}) \end{aligned} \tag{2}$$

$$\ddot{T}_{\mathrm{hf,bulk},i} = T_{\mathrm{hf,bulk},i} + T_{\mathrm{hf,bulk},i+1}/2 \tag{3}$$

$$\ddot{T}_{\mathrm{hf,wall},i} = T_{\mathrm{hf,wall},i} + T_{\mathrm{hf,wall},i+1}/2 \tag{4}$$

$$\ddot{T}_{wf,\mathrm{bulk},i} = T_{wf,\mathrm{bulk},i} + T_{wf,\mathrm{bulk},i+1}/2 \tag{5}$$

$$\ddot{T}_{\mathrm{hf,wall},i} = T_{\mathrm{wf,wall},i} + T_{\mathrm{wf,wall},i+1}/2 \tag{6}$$

$$\mathrm{LMTD}_i = \frac{\left(T_{\mathrm{hf,bulk},i} - T_{\mathrm{wf,bulk},i+1}\right) - \left(T_{\mathrm{hf,bulk},i} - T_{\mathrm{wf,bulk},i+1}\right)}{\ln \frac{T_{\mathrm{hf,bulk},i} - T_{\mathrm{wf,bulk},i+1}}{T_{\mathrm{hf,bulk},i} - T_{\mathrm{wf,bulk},i+1}}} \tag{7}$$

$\dot{U}_{\mathrm{out},i} = \frac{1}{\ddot{h}_{\mathrm{hf},i}} + \frac{1}{\ddot{h}_{\mathrm{wf},i}}\left(\frac{d_0}{d_i}\right) + \frac{d_0}{2}\ln\left(\frac{d_0}{d_i}\right)/\lambda_{\mathrm{tube}}$ where Q_i, m, T, U, c, λ are denoted as heat transfer, mass flow rate, temperature of the fluid, overall heat transfer, specific heat, and thermal conductivity.

The symbols h, A, d, and i denote the enthalpy, area of the surface, tube diameter, and the iteration. The suffixes $_{\mathrm{wf}}$ and $_{\mathrm{hf}}$ denote the working and heating fluids, respectively. The governing equations are obtained by applying the boundary conditions as follows.

The continuity equation is defined as

$$\frac{\partial(\rho u)}{\partial x} + \frac{\partial(\rho v)}{\partial y} + \frac{\partial(\rho w)}{\partial z} = 0 \tag{8}$$

Navier–Stoke equation is given for the fluid flow as

$$\rho\left(u\frac{\partial u}{\partial x} + v\frac{\partial v}{\partial y} + w\frac{\partial w}{\partial z}\right) = \rho X - \frac{\partial \rho}{\partial z} + \frac{1}{3}\mu\frac{\partial}{\partial x}\left(\frac{\partial u}{\partial x} + \frac{\partial v}{\partial y} + \frac{\partial w}{\partial z}\right) + \mu\nabla^2\mu \tag{9}$$

The energy equation is given by

$$\rho c_p\left(u\frac{\partial T}{\partial x} + v\frac{\partial T}{\partial y} + w\frac{\partial T}{\partial z}\right) = \left(u\frac{\partial \rho}{\partial x} + v\frac{\partial \rho}{\partial y} + w\frac{\partial \rho}{\partial z}\right) + k\nabla^2 T + \mu\rho \tag{10}$$

The heat transfer coefficient is given by $h = \frac{k\frac{\partial T}{\partial x}}{T_w - T_f}$

The Reynolds number, Dean number, and Nusselt number are given by

$$\mathrm{Re} = \frac{\rho V d}{\mu},\ De = \mathrm{Re} * \sqrt{\delta},\ \mathrm{Nu} = 0.021 * \mathrm{Re}^{0.85}\mathrm{Pr}^{0.6}\delta^{0.1}$$

The critical Reynolds number is given by $\mathrm{Re}_{\mathrm{cr}} = 2300\left(1 + 8.6\left(\frac{d}{D}\right)^{0.46}\right)$ where d, D, L, V, k, and μ are the tube diameter, coil diameter, length of the coil, volume of the fluid, thermal conductivity, and viscosity, respectively. The friction factor is given by $f = \frac{2\nabla pd}{\rho L V^2}$.

The graph (Fig. 2) shows the relationship with Nu, Re with the mass flow rate (kg/s) (Figs. 5 and 6).

Relationship of Re, Nu with mass flow rate Figs. 2 and 3.

The largely heat transfer coefficient and the effectiveness with the study of Nu and Re number are analyzed in the graph Fig. 5. The diagram reveals that Nu number increases with the increment of mass flow rate and increase in the ratio of curvature of the helical coil. The curvature ratio is changed from 0.05 to 0.06 at the mass flow rate of 0.004 kg/s for the increment of Nusselt number of 3 and 5%. The Reynolds number is increasing with the mass flow rate at different coils. The values of Re, Nu are increases with the increases in turbulence. Figure 7 shows the contours of temperature variations respective of the different velocities.

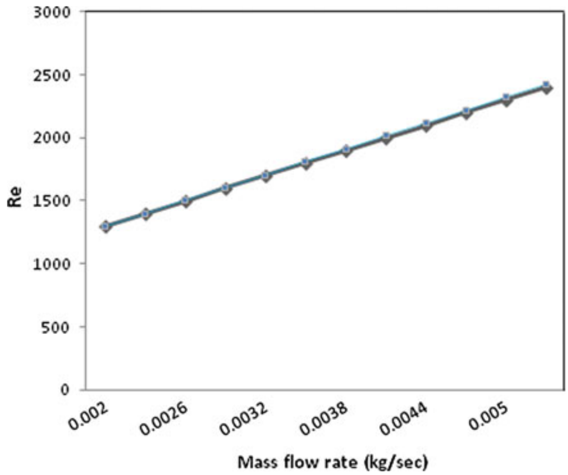

Fig. 5 Re versus mass flow rate

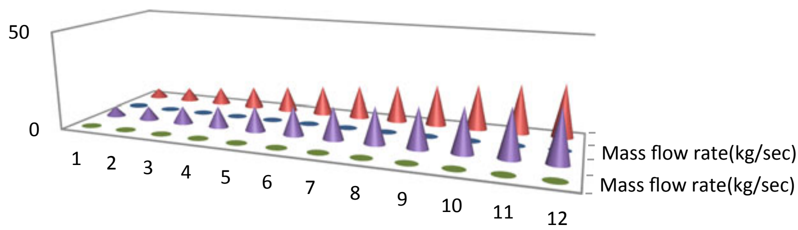

	1	2	3	4	5	6	7	8	9	10	11	12
Mass flow rate(kg/sec)	0.002	0.0023	0.0026	0.0029	0.0032	0.0035	0.0038	0.0041	0.0044	0.0047	0.005	0.0053
Nu	5	7	9	11	13	15	17	19	21	23	25	27
Mass flow rate(kg/sec)	0.002	0.0023	0.0026	0.0029	0.0032	0.0035	0.0038	0.0041	0.0044	0.0047	0.005	0.0053
Nu	5	7	9	11	13	15	17	19	21	23	25	27

Fig. 6 Nu versus mass flow rate

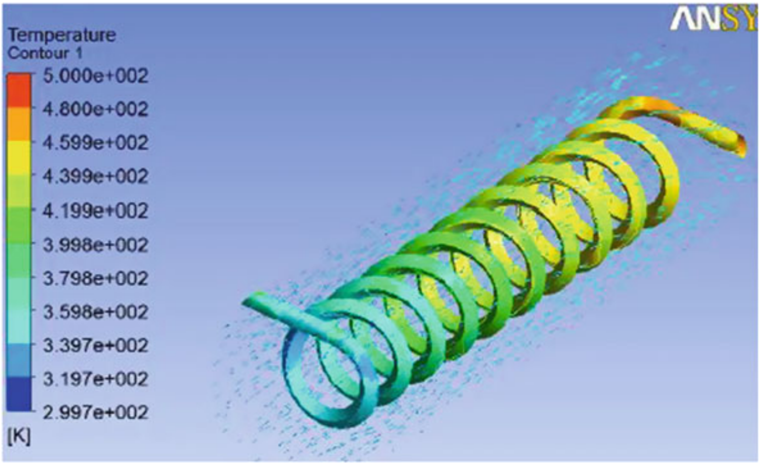

Fig. 7 Inlet velocity 0.02 and mass flow rate 0.004 kg/s

4 Conclusion

Numerical simulation has been researched on heat transfer qualities and pressure drop of Al_2O_3/water nanofluid in a minimized heat exchanger with helical loop cylinder shapes and an in-line arrangement of cylinders under consistent state laminar liquid stream. The numerical outcomes uncover the enhancement in heat transfer, concerning the base liquid, recognized to portray nanofluid. The paper focuses on the literature studies of the heat transfer and pressure drop in a helical coil tube with the varying parameters. The analysis has been done for the constant heat flux boundary conditions and constant wall temperature. The resulting heat transfer and pressure drop are optimized by choosing the parameters appropriate. Studies were discussed by examining the influence on heat transfer and pressure drop in the helical coil. The centrifugal force caused by the curvature of the pipe makes the heavier fluid to flow in the outer side with the high velocity and temperature which has greater influence on the drop in the temperature and pressure. Temperature drop remains the maximum for low flow rate and decreases for the increasing flow rate, whereas the pressure drop is directly proportional to the flow rate. It has been revealed that heat transfer coefficient is increased with expanding the inlet speed and corresponding heat transfer coefficients were increased by 15, 26, and 41% at 0.2, 0.4, and 0.6% of Al_2O_3/water nanofluids. It is clearly observed that the molecule volume division individually separated when contrasted and refined water. Nanofluid containing few nanoparticles has considerably higher warmth move coefficient than those of base liquids. The Nanofluid containing few nanoparticles have considerably higher warmth move coefficient than those of base liquids. The expansion in the volume fractions of nanoparticles is heightened with the cooperation and impact of nanoparticles.

References

1. Patankar S, Pratap VS, Spalding DB (1974) J Fluid Mech 62:539–551
2. Futagami K, Aoyama Y (1988) Laminar heat transfer in helically coiled tubes. Int J Heat Mass Transfer 31:387–396
3. Abdulla MA (1994) A four-region, moving-boundary model of a once through, helical coil team generator. Ann Nucl Energy 21(9):541–562
4. Bai B, Guo L, Feng Z, Chen X (1999) Turbulent heat transfer in a horizontally coiled tube. Heat Transfer-Asian Research 28(5):395–403
5. Xin RC, Awwad A, Dong ZF, Ebadian MA (1996) An investigation and comparative study of the pressure drop in air-water two-phase flow in vertical helicoidal pipes. Int J Heat and Mass Transfer 39(4):735–743
6. Jayakumar JS, Grover RB (1997) Two phase natural circulation residual heat removal. In: Proceedings of 3rd ISHMT-ASME heat and mass transfer conference, Kanpur
7. Jayakumar JS, Mahajani SM, Mandal JC, Vijayan PK, Bhoi R (2005) Experimental and CFD estimation of heat transfer in helically coiled heat exchangers. Chem Eng Res Des 86(3):221–232
8. Naphon P, Wongwises S (2006) A review of flow and heat transfer characteristics in curved tubes. Renew Sustain Energy Rev 10:463–490
9. Janssen LAM, Hoogendoorn CJ (1978) Laminar convective heat transfer in helical coiled tubes. Int J Heat Mass Transfer 21:1197–1206
10. Whalley PB (1980) Air-water two-phase flow in a helically coiled tube. Int J Multiph Flow 6:345–356
11. Sreenivasan KR, Strykowski PJ (1983) Stabilization effects in flow through helically coiled pipes. Exp Fluids 1:31–36
12. Berger SA, Talbot L, Yao LS (1983) Flow in curved pipes. Ann Rev Fluid Mech 15:461–512
13. Awwad A, Xin RC, Dong ZF, Ebadian MA, Soliman HM (1995) Measurement and correlation of the pressure drop in air-water two-phase flow in horizontal helicoidal pipes. Int J Multiph Flow 21(4):607–619
14. Shah RK, Joshi SD (1987) Convective heat transfer in curved ducts (Chapter 3). In: Kakac S, Shah RK, Hung W (eds) Handbook of single-phase convective heat transfer. Wiley, New York
15. Kumar V, Saini S, Sharma M, Nigam KDP (2006) Pressure drop and heat transfer in tube-in-tube helical heat exchanger. Chem Eng Sci 61:4403–4416
16. Rennie TJ, Raghavan VGS (2006) Numerical studies of a double-pipe helical heat exchanger. Appl Therm Eng 26:1266–1273
17. Prabhanjan DG, Raghavan GS, Rennie TJ (2005) Comparison of heat transfer rates between a straight tube heat exchanger and a helically coiled heat exchanger. Int Commun Heat Mass Transfer 29(2):185–191
18. Shokouhmand H, Salimpour MR, Akhavan-Behabadi MA (2007) Experimental investigation of shell and coiled tube heat exchangers using Wilson plots. Int Commun Heat Mass Transfer 35(1):84–92
19. Salimpour MR (2008) Heat transfer characteristics of a temperature-dependent-property fluid in shell and coiled tube heat exchangers. Int Commun Heat Mass Transfer 35(9):1190–1195
20. Cioncolini A, Santini L (2006) An experimental investigation regarding the laminar to turbulent flow transition in helically coiled pipes. Exp Thermal Fluid Sci 30:367–380
21. Seban RA, McLaughlin EF (1963) Heat transfer in tube coils with laminar and turbulent flow. Int J HeatMass Trans 6:387–495. Int J Multiphase Flow 21(4):607–619
22. Ghorbani N, Taherian H, Gorji M, Mirgolbabaei H (2009) Experimental study of mixed convection heat transfer in vertical helically coiled tube heat exchangers. Exp Thermal Fluid Sci 34(7):900–905
23. Chen CN, Han JT, Jen TC, Shao L, Chen WW (2010) Experimental study on critical heat flux characteristics of R134a flow boiling in horizontal helically-coiled tubes. Int J Therm Sci 50(2):169–177

24. Kumar V, Sarkar J (2019) Numerical and experimental investigations on heat transfer and pressure drop characteristics of Al2O3-TiO2hybrid nanofluid in minichannel heat sink with different mixture ratio. Powder Technol. https://doi.org/10.1016/j.powtec.01.061(2019)
25. Bhuvaneswari S, Elatharasan G (2019) A study on the methods of solving heat equation. J Appl Sci Comput 6(4). ISSN:1076-5131
26. Bhuvaneswari S, Elatharasan G (2019) Numerical methods of solving one dimensional heat equation comparative study. J Appl Sci Comput 6(3). ISSN:1076-5131
27. Bhuvaneswari S, Elatharasan G (2019) A study on the literature review on heat transfer in a helically coiled heat exchanger. Int J Eng Res Technol 7(01). ISSN:2278-0181

Tribology, Wear and Surface Engineering

Comparative Study on the Mechanical Performance of Solid Lubricants Over Peek Polymer

N. Venkatesh and P. K. Dinesh Kumar

Abstract Polyetheretherketone (PEEK) and its composites have an extended range of applications and are continuously replacing metals in aerospace, automobile, and mechanical industries for structural and tribological applications due to its robustness, good mechanical and chemical resistance properties. The mechanical properties of virgin PEEK, PEEK reinforced with 10% Polytetrafluoroethylene (PTFE) and PEEK reinforced with 10% hexagonal Boron Nitride (h-BN) are compared and analyzed in this study. The composites were fabricated through the twin-screw extrusion method and were then characterized by EDAX analysis. The static mechanical properties such as compressive, flexural and hardness of all the specimens were tested as per ASTM standards, and it was identified that the virgin PEEK material had better mechanical properties in comparison to materials with solid lubricants. Also, the addition of h-BN to PEEK had a more drastic reduction in mechanical strength compared to the addition of PTFE to PEEK. It was seen that by adding the solid lubricants, the mechanical properties of virgin PEEK material deteriorated.

Keywords PEEK · PEEK-PTFE · PEEK-hBN · Mechanical properties

1 Introduction

Polymers are viscoelastic materials that can exhibit properties of solids and liquids. Polyetheretherketone (PEEK) is a colorless organic thermoplastic polymer in the Polyaryletherketone (PAEK) family. It is semi-crystalline with excellent mechanical and chemical resistance properties that are retained to high temperatures. Due to its robustness, several engineering applications in aerospace, automobile, and mechanical industries are using it and are also finding its high mechanical strength, high

N. Venkatesh (✉) · P. K. Dinesh Kumar
Department of Aeronautical Engineering, Rajalakshmi Engineering College, Chennai 602105, India
e-mail: nvenkatesh458@gmail.com

P. K. Dinesh Kumar
e-mail: pkdineshkumar1993@gmail.com

E. T. Akinlabi et al. (eds.), *Trends in Mechanical and Biomedical Design*, Lecture Notes in Mechanical Engineering,
https://doi.org/10.1007/978-981-15-4488-0_67

thermal resistance, and high wear resistance to support its usage. However, in its pure form, the friction coefficient is relatively high in dry sliding, which tends to restrict its applications in terms of Tribology. To minimize the friction coefficient of PEEK polymer particular solid lubricants are incorporated in it such as Polytetrafluoroethylene (PTFE) and hexagonal Boron Nitride to increase its applications in various industries. Few studies show that PEEK reinforced with PTFE and PEEK reinforced with h-BN tend to reduce the overall friction coefficient of the material. Dry lubricants or solid lubricants are materials despite being in the solid-state have outstanding lubrication properties and hence have less friction and wear rate. It can reduce friction and thus wear between two surfaces sliding against each other without the requirement of a liquid oil medium. Solid lubricants like Graphite, PTFE, hexagonal Boron Nitride and Tungsten disulphide are mostly used [1]. These materials provide lubrication at higher temperatures than those of oil—and liquid-based. These materials can operate to about 350 °C in case of oxidizing environments and even further in a reducing environment. The reduced friction properties of solid lubricants are due to a layered structure on the molecular level with weak bonding between the layers [2, 3]. These layers slide over each other with minimal applied force and also have low friction properties [4]. Morphological, physical, friction and wear behavior of h-BN filled PEEK composite coatings with varying percentage of h-BN content from 0% to 8% by flame spray coating technique for different particle sizes were studied. It was noted that although adding h-BN increased the microhardness irrespective of the size, deviation in terms of crystallinity did exist. It was noted that by adding h-BN particles to the material reduced the specific wear rate and similarly by adding more amount of h-BN the friction coefficient was reduced [5]. The friction coefficients and wear rates of neat PEEK and h-BN/PEEK coatings by thermal spray coating was studied and tested under varying temperature (30 °C–300 °C). The results suggested that friction and wear rate for PEEK coatings were relying on the testing temperature rather than h-BN content. Overall, the operating range of 100 and 200 °C was found to be the best for low wear and friction coefficients. No kind of chemical change was observed with this work [6]. Explained about using a common parent material and changing the dry lubricant reinforced with it. The different solid lubricants used were hexagonal boron nitride, Potassium Titanate, Boric acid, and Mica. These dry lubricants were incorporated with a common parent material into a composite by injection molding. All the composites were tested under similar conditions, and the best solid lubricant based on wear rate was found to be KT (Potassium Titanate). Besides, the reduction of hardness in materials due to the addition of the fillers could be due to the surge in the plasticity of the material which tends to deformation of the material [7, 8]. Explained how the amount of filler content to a parent material affected the overall properties of new materials such as mechanical and tribological properties. Based on the parent material characteristics, the filler used, quantity of filler used, filler size and whether it is a coating or reinforcement, the final properties of the new material will vary accordingly [9]. Indicates that the addition of PTFE to PEEK decreases all the strength properties except impact.

2 Fabrication of Composites and Its Characterisation

Commercially available PEEK of grade 450(G) with an average diameter of 100 μm, PTFE powder of particle size 60 μm and h-BN powder in microform was provided by SRL chemicals. PEEK, and solid lubricants PTFE and h-BN powders of 90% by weight and 10% by weight respectively were combined using a twin-screw extruder at around 400 °C with a constant screw speed of 120 rpm [10–12].

The manufacturing process of the specimens occurs in two stages.

In the initial stage, ultrasonic vibration was used along with alcohol as a mixing medium, and then the dispersed solution was dried at around 100 °C in a hot drier for approximately 3 h to remove the excess alcohol and moisture that may be present. Next, the blended mixture was poured into a twin-screw extruder at 400 °C and a screw speed of 120 rpm.

Finally, the extruded pellets were cut as small granules with the help of pallet cutter machines. The extruded granules were placed in a hot electric furnace at around 80 °C up to 60 min to remove any moisture present. The dried granules underwent injection molding at approximately 20 MPa and a temperature of about 380–400 °C for approximately 3 h. Composites PEEK-PTFE and PEEK-h-BN were cooled down to room temperature. The different compositions for the composites are given in Table 1. Figure 2a–b shows the schematic assemblage of composite S2 and S3 and the powders used in manufacturing are shown in Fig. 1a–c.

Table 1 Composite Composition

Composites	PEEK (wt%)	PTFE (wt%)	H-BN (wt%)
S1	100	0	0
S2	90	10	0
S3	90	0	10

Source: computed

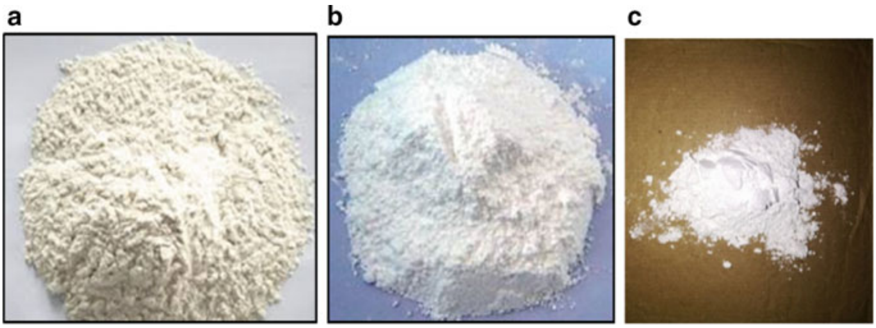

Fig. 1 **a** PEEK powder (100 μm). **b** PTFE powder (60 μm). **c** h-BN powder (5 μm)

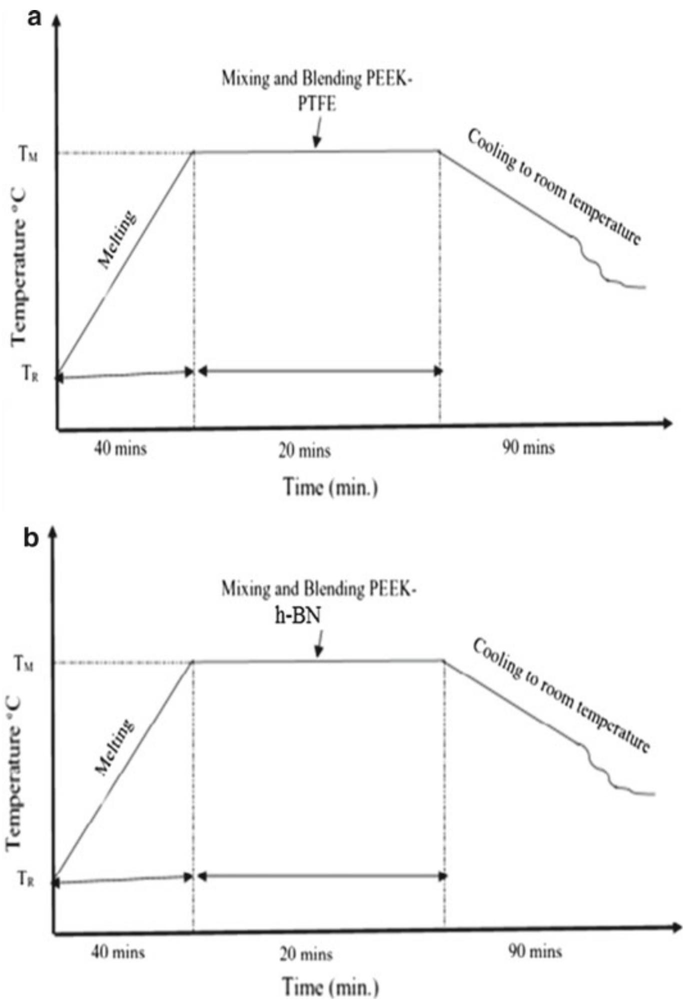

Fig. 2 **a** Schematic fabrication of PEEK-PTFE. **b** Schematic fabrication of PEEK-hBN

The characterization of the two specimens with dry lubricants was done with the help of the Energy Dispersive Spectrum Analysis (EDAX). From the EDAX test, the characteristic crests of chemical elements are observed in S2 and S3. In composite S2, the unique peak of F, i.e. Fluorine shows the presence of 10% of PTFE with PEEK matrix. In composite S3, the typical peak of N, i.e. Nitride shows the presence of 10% of h-BN with PEEK matrix.

The observation on the dispersion of the solid lubricants was noted through a Scanning Electron Microscope (SEM) and captured. It is found that the majority of the PTFE and h-BN powder particles were homogeneously mixed throughout the studied samples.

From Fig. 3a, the amount of Carbon and Oxygen present in the sample indicates the compound PEEK (S1). The presence of Fluorine is due to the addition of NaF as a catalyst during the manufacturing of PEEK polymer. The result is similar to the amount which was found in the literature survey [7, 13, 14]. Also, Fig. 3b indicates the PEEK-PTFE (S2) composite. From the figure, the amount of Fluorine present in the sample indicates the presence of PTFE in the right quantity [9, 13]. Similarly, from Fig. 3c, the amount of Nitrogen present in the sample indicates the existence of Boron Nitride in the appropriate quantity as reinforced.

Figure 4a–b shows the PEEK with h-BN at magnification 10 k (5 μm) and PEEK with PTFE at magnification 15 k (3 μm) respectively. From these figures, we can observe the distribution of h-BN particles and PTFE particles in the PEEK polymer. The distribution of h-BN and PTFE in PEEK polymer is uniform. The small white dots in the SEM images are the solid lubricants hBN and PTFE distributed in the PEEK polymer, respectively.

The measure of the hardness of the different composites was compared through Shore D hardness test with the help of Shore D Durometer as per ASTM standard ASTM D2240 (Table 2).

The Shore D hardness test revealed that the hardness of PEEK-PTFE was 14% more than that of the hardness of PEEK-hBN. This result could be due to the increased plasticity of the PEEK material due to the addition of dry lubricants. The comparison of the hardness for different specimens is given in the Figure (Fig. 5).

3 Testing Procedures and Conditions for Mechanical Study

After molding the exhibits, the test pieces of different proportions were machined from the molded exhibits for studying the tribological and mechanical properties as per the ASTM standards. The static mechanical properties were found out by compression and flexural tests on the specimens S2 and S3.

The Flexural tests were carried out on cuboidal specimens of dimensions 65 mm length(l) × 13 mm width(w) × 3 mm thickness(t) as per ASTM standard D 790 were machined out at room temperature (25 °C) and tested in a universal testing machine with a span length of 48 mm at a constant feed rate of 5 mm/min as flexural fixtures. The average value for all the specimens was taken into account.

The Compression tests were carried out on cylindrical specimens of dimensions 30 mm length(l) × 10 mm diameter(d) were machined from the composite sample as per the ASTM standard D 695 at room temperature(25 °C) and tested with the universal testing machine at a constant feed rate of 0.5 mm/min as the compressive fixtures. The average value for all the specimens was taken into account.

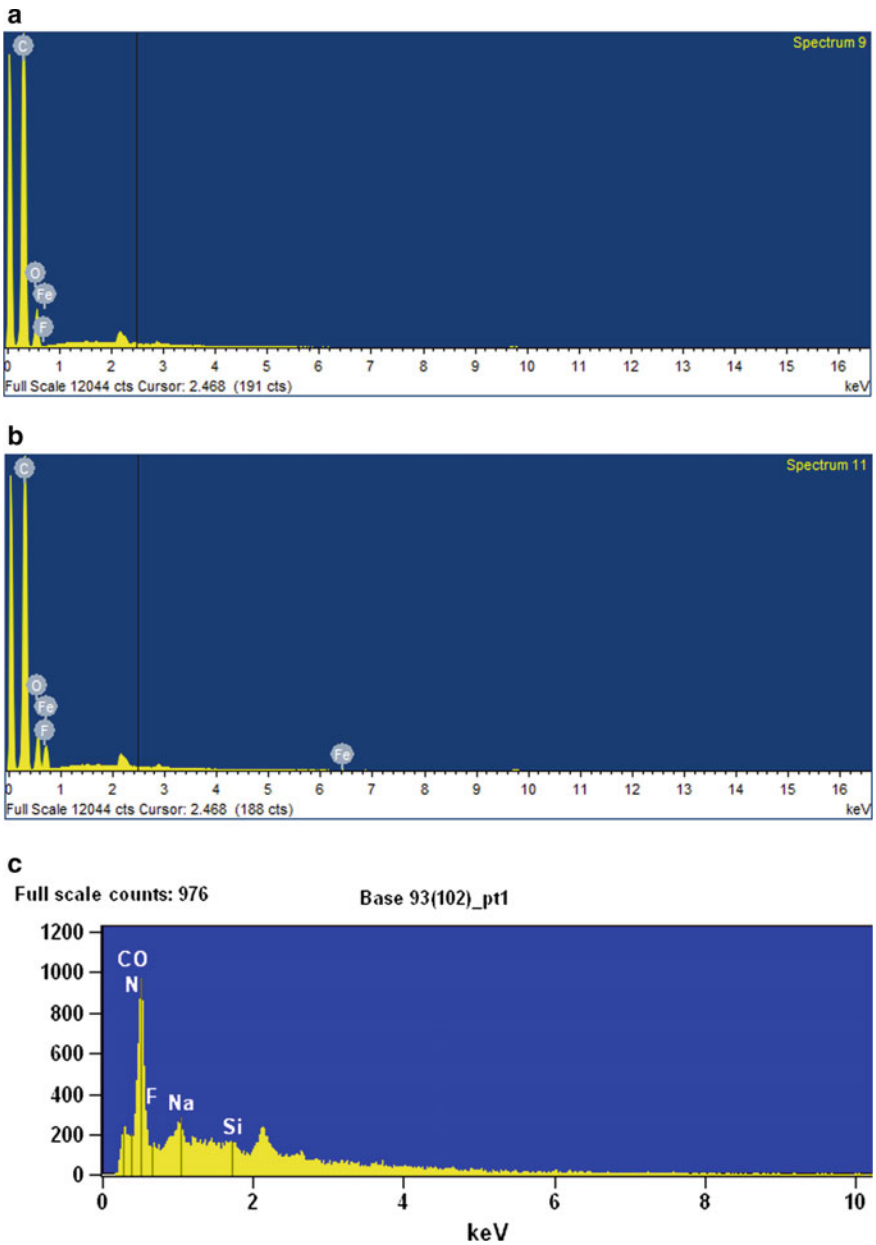

Fig. 3 **a** EDAX analysis of PEEK (S1). **b** EDAX analysis of PEEK-PTFE (S2). **c** EDAX analysis of PEEK-hBN (S3)

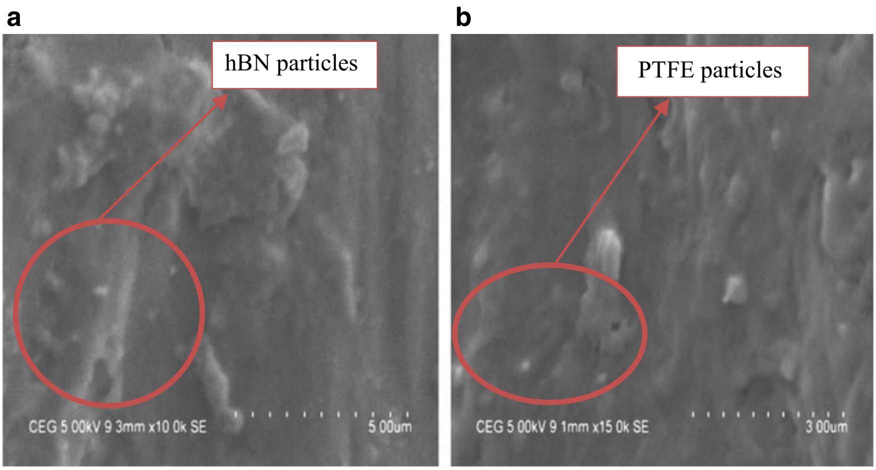

Fig. 4 **a** SEM image of PEEK-hBN at 5 μm. **b** SEM image of PEEK-PTFE at 3 μm

Table 2 Hardness Comparison

Composites	Shore D hardness
S1-PEEK	88
S2-PEEK-PTFE	86
S3-PEEK-hBN	73

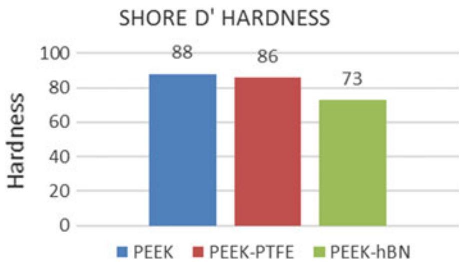

Fig. 5 Comparison of Shore D' Hardness for different specimens

4 Mechanical Behavior

The compression strength for the composites reduced with the addition of solid lubricants. For pure PEEK, the compression strength was found to be the maximum at 143 MPa, and it decreased by 9% with the addition of solid lubricant PTFE with 131 MPa and it reduced by 37.5% due to the addition of h-BN with 104 MPa. The addition of the fillers tend to weaken the bonds present in the material thereby leading to a reduction in the compression strength. The comparison of the compression strength for the different specimens is shown in the figure (Fig. 6).

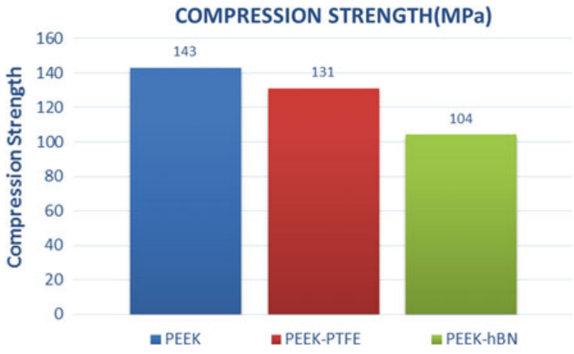

Fig. 6 Comparison of compression strength

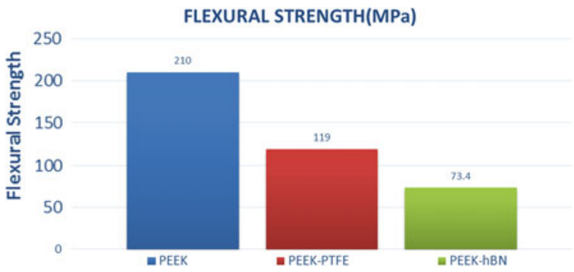

Fig. 7 Comparison of flexural strength

The flexural strength too reduced with the addition of solid lubricants to PEEK polymer. The flexural strength of the PEEK composite was found to be the most at 210 MPa, and it decreased by 43% with the addition of PTFE with 119 MPa and reduced by 65% with the addition of h-BN with 73.4 MPa. The forces of attraction within the materials were considerably lower than the original material thus causing a reduction in the Flexural strength. The comparison of the flexural strength for the different specimens is shown in the figure (Fig. 7).

5 Conclusion

The effect of reinforcement of solid lubricants PTFE and hBN at 10 wt% to PEEK polymer were investigated in this work. When 10 wt% of either solid lubricant was reinforced with PEEK polymer, the static mechanical properties of the composite were considerably lower than that of neat PEEK. The materials had significantly lower Compression margin depending on the solid lubricant which was reinforced. The major possibility for the reduction in the mechanical properties of the composites is due to the agglomeration of the solid lubricant particles in the PEEK polymer. Due to the excess amount of solid lubricant particles present, proper bonds between the molecules of the composite could not be formed. The solid lubricants added had distressed mechanical properties than PEEK. Due to this reason, the addition of these lubricants brought about a reduction in mechanical properties. In comparison, the mechanical properties of h-BN are significantly lower than that of PTFE. That's why when comparing the two solid lubricants with PEEK polymer with the same weight percentage, PEEK-PTFE had better hardness, Compressive and Flexural strength compared to PEEK-hBN. A reason for this could be due to the weaker bonds among the h-BN particles and also among the h-BN particles and PEEK material.

References

1. Wang Q, Wang Y, Wang H, Fan N, Yan F (2016) Experimental investigation on tribological behaviour of several polymer materials under reciprocating sliding and fretting wear conditions
2. Zhang G, Wetzel B, Wang Q (2015) Tribological behaviour of PEEK-based materials under mixed and boundary lubrication conditions. Tribol Int 153–161
3. Qu M, Yao Y, He J, Ma X, Feng J, Liu S, Hou L, Liu X (2017) Tribological study of polytetrafluoroethylene lubricant additives filled with Cu microparticles or SiO2 nanoparticles. Tribol Int 57–65
4. Tharajak J, Palathai T, Sombatsompop N (2015) Morphological and physical properties and friction/wear behaviour of h-BN filled PEEK composite coatings
5. Tharajak J, Palathai T, Sombatsompop N (2017) Recommendations for h-BN loading and service temperature to achieve low friction coefficient and wear rate for thermal sprayed PEEK coatings
6. Narayan Panda J, Bijwe J, Pandey RK (2017) Comparative potential assessment of solid lubricants on the performance of poly aryl ether ketone (PAEK) composites
7. Kalin M, Zalaznik M, Novak S (2015) Wear and friction behaviour of poly-ether-ether-ketone (PEEK) filled with graphene, WS2 and CNT nanoparticles
8. Gan D, Lu S, Song C, Wang Z (2001) Physical properties of polyether ketone ketone/mica composites: effect of filler content
9. Bijwe J, Sen S, Ghosh A Wear—(Dec 2004) Influence of PTFE content in PEEK- PTFE blends on mechanical properties and tribo performance in various wear modes
10. Liu L, Xiao L, Li M, Zhang X, Chang Y, Shang L, Ao Y (2016) Effect of hexagonal boron nitride on high-performance polyether ether ketone composites
11. Kurdi A, Wang H, Chang L (2017) Study on the effect of nanosized TiO_2 addition on tribological behaviour of polyether ether ketone composite; Tribol Int
12. Rodriguez V, Sukumaran J, Schlarb AK, De Baets P (2016) Influence of solid lubricants on tribological properties of polyetheretherketone (PEEK). Tribol Int 45–57
13. Friedrich K, Zhang Z, Schlar AK (July 2005) Effects of various fillers on the sliding wear of polymer composites
14. Díez-Pascual AM, Naffakh M, González-Domínguez JM, Ansón A, Martínez-Rubi Y, Teresa Martínez M, Simard B, Gómez MA, High-performance PEEK/carbon nanotube composites compatibilized with polysulfones-II. Mechanical and electrical properties

ZrB_2 Influences on the Dry Sliding Wear Resistance of AA7075 Alloy

P. Loganathan, A. Gnanavelbabu, K. Rajkumar, and S. Ayyanar

Abstract This article presents the influence of ZrB_2 particles on the mechanical and wear behavior of AA7075 composites. Variations in AA7075 reinforced with ZrB_2 particles varied in the range of 5–15 wt% and fabricated using of the two-step stir casting technique. Fabricated composites were subjected to T6 heat-treated and analyzed microstructure, hardness, impact, tensile strength and dry sliding wear behavior. Tribo test was conducted with varying applied pressure (0.39–1.59 MPa), sliding velocities of (0.8–2.0 m/s), and a sliding distance of 3.0 km. The results revealed the distribution of particles in the matrix materials. ZrB_2 increased the hardness of the composites from 98 to 128 Vickers hardness and reduced the impact strength up to 44%. The addition of 15 wt% of ZrB_2 particles increased the tensile strength of AA7075 alloy by 242 MPa. Wear resistance of the composites increased with increasing wt% of ZrB_2 particles. Wear mechanism of the worn surface was studied through use of a scanning electron microscope (SEM) and revealed the formation of an oxide layer on the worn surface reducing the wear rate of the composite. At a low applied pressure and sliding velocity, there was the formation of a plastic deformation groove, whereas a high applied pressure and sliding velocity breakage of tribolayer resulted in severe deformation.

Keywords ZrB_2 · Worn surface · Tribo layer · Hardness

1 Introduction

Lightweight aluminum alloy is one of the major perspectives in the field of automotive and aerospace applications due to its low density and high strength. The major applications are in brake rotors, pistons and cylinder liners, connecting rods and push rods.

P. Loganathan · A. Gnanavelbabu (✉) · S. Ayyanar
Department of Industrial Engineering, CEG Campus, Anna University, Chennai, India
e-mail: agbabu@annauniv.edu

K. Rajkumar
Department of Mechanical Engineering, SSN College of Engineering, Kalavakkam, Chennai, India

E. T. Akinlabi et al. (eds.), *Trends in Mechanical and Biomedical Design*,
Lecture Notes in Mechanical Engineering,
https://doi.org/10.1007/978-981-15-4488-0_68

These components are subjected to abrasive wear mode along with sliding direction against their counter surface. The wear resistance of the alloys and their mechanical properties improved through the addition of hard ceramic reinforcement particles on the matrix material [1]. Of late, ultra-high temperature ceramics (UHTCs) play a major role in improving wear resistance in high-temperature environments. Among various ceramic particles, zirconium diboride (ZrB_2) has drawn the interest due to its high temperature stability and oxidation protection on the surface of aerospace structure, and it is mainly used in hypersonic flights and re-entry vehicles [2].

Recent studies on the aluminum alloy reinforced with ceramic particles are seen in the literature [3–11]. Jerome et al. [3] carried out investigation on the mechanical and high-temperature wear behavior of Al-TiC (5, 10 and 15 wt%) composites. There was a decrease in the wear rate and the coefficient of friction of the composites due to the formation of oxidative protective layer with increasing wt% of TiC. An increase in hardness was seen due to the formation of intermetallic phases such as Al_3Ti. Kumar et al. [4] analyzed the tensile and wear behavior of Al–7Si/TiB_2 particulate with (0, 3.4 and 6.8 vol. %) composites. Increase in hardness and tensile strength of the composite was seen due to the presence of α-Al secondary dendritic arm spacing and eutectic Si particle size and also the presence of fine TiB_2 particles. The effect of TiB_2 particles on higher load showed a larger significant than low load conditions due to the work hardening effect with Al-SiC composites. Liang et al. [5] saw the tribological behavior of AZ31 Mg alloy. At low load, 5–30 N abrasion and oxidation wear mechanisms were identified as also delamination mechanisms within 30–360 N.

Siddesh Kumar et al. [6] have stated that the wear behavior of AA2219/B_4C/MoS_2 hybrid composites was fabricated through stir casting. Rise in temperature more than 80 °C caused a rate of oxide layer removal significantly higher than the oxide regeneration tending to increase the wear rate with increasing temperature. Johny James and Raja Annamalai [7] made a study of the wear behavior of AA6061/ZrO_2 composites with varying (5–15 wt%). Steady-state and mild wear behaviors were observed in 5 wt% of ZrO_2, and a higher rate of delamination was obtained at 15 wt% due to agglomeration of particles in the composite. Nishant Verma and Vettivel [8] investigated the effect of B_4C and rice husk ash (RHA) on the mechanical behavior of AA7075. The increment in mechanical properties was contributed mainly by B_4C as compared to RHA.

Arivukkarasan et al. [9] analyzed the mechanical and tribological behavior of LM13/WC composites fabricated through stir casting. The maximum tensile and impact strength was obtained at 15 wt% of WC composites. Uniform distribution of particles caused a decrease in mass loss of composites with increasing wt% of WC. Jawahar Chandra et al. [10] concluded the wear behavior of LM13/TiS_2 composites and wear rate of composites increased with increasing applied load and sliding velocity due to rise in interface temperature on contact pin and countersurface. Ebenezer Jacob Dhas et al. [11] revealed the effect of SiC/WC/Gr on the mechanical behavior of AA5052 hybrid composites. The formation of a brittle phase among AA5052/WC/Gr composites caused a decrease in the impact strength more than

AA5052/SiC/Gr composites. Both hybrid composites showed a brittle fracture due to the presence of brittle interfaces between the reinforcements and the alloy matrix.

Work done on the mechanical and wear behavior of AA7075 alloy with ZrB_2 reinforcement is not much speak of limit on the reinforcement fraction. The host matrix was based on the reaction between the constitution chemical compounds. The AA7075/ZrB_2 combination brought the inherent mechanical properties that explain the demand from military and aerospace industry.

This research work is an investigation of ZrB_2 particles on AA7075 matrix alloy on mechanical and wear behavior of the composites with varying weight percentages (5, 10, 15 wt%). Fabrication of the composites was carried out through the use of the stir casting method. The mechanical properties micro Vickers hardness, impact strength and tensile strength are analyzed. The dry sliding wear behavior of composites was carried out on varying applied pressures 0.39–1.59 MPa, sliding velocity of 0.8–2.0 ms^{-1} and constant distance 3 km. Dispersion of ZrB_2 particles in the matrix was examined through an optical microscope (OM), and analysis of wear mechanism on worn surface was carried out through SEM.

2 Experimental Procedure

AA7075 alloy was used as matrix material and ZrB_2 particles with average size of 5.60 μm as reinforcement particle. AA7075-ZrB_2 composites were fabricated using the two-step stir casting process. The required amount of AA7075 alloy was placed in a graphite crucible in an electric resistance furnace at 800 °C to enable to attainment of the molten state. The melting process carried out in argon atmosphere at the rate of 2 CC/min to minimize high-temperature oxidation. ZrB_2 particles were preheated in the muffle furnace up to 150 °C for 2 h to remove the moisture content and improve wettability. Alumina-coated mild steel blades were used for stirring the aluminum melt. The initial stirring was done at 350 rpm, for the formation of the vortex and addition of preheated particles into the vortex formation to attain a uniform distribution of particles. After the complete addition of reinforcement particles, the molten temperature dropped to 650 °C and a semi-solid state was formed after10 min. The slurry temperature was raised up to the temperature of the liquids, and stirring was done for 5 min. The molten melt was poured into a pre heated die. The fabricated composites were designated as AZ0, AZ5, AZ10 and AZ15 based on the concentration of ZrB_2 particle varying as 0, 5, 10 and 15 wt%, respectively.

The fabricated composites were subjected to T6 heat treatment process to improve the mechanical properties. Heat-treated composites were subjected to metallographic examination. Specimens were etched using Keller's solution. The microstructure of the specimens was obtained through an optical microscope. The hardness of composites was analyzed through Vickers hardness tester with an applied load of 500 gf with a dwell time of 15 s. The tensile strength carried was as per ASTM E8 with strain rate of 0.001/s in a computerized UTM machine (MTS Tensile Test 100 KN capacity). Impact energy of the composite was analyzed using pendulum-type testing machine with a capacity of 400 J. Wear behavior of the composite was seen out through ASTM G-99, with applied pressure of (0.39–1.59 MPa), sliding velocities of (0.8–2.0 m/s) and sliding distance of 3.0 km. The wear mechanism on worn surface of composite is studied through SEM.

3 Results and Discussion

3.1 *Microstructure Analysis*

Figure 1a-b shows the microstructures of AZ0 and AZ5, respectively. It shows a good chemical bonding among the Al particles, where Al are particles joined together to construct a solid structure. The $MgZn_2$ (g) phase precipitation in aluminum alloys with a Zn content greater than 3 wt% and a Zn-to-Mg ratio greater than two represent one of the strengthening mechanisms in these alloys, as well as the absence of voids in the surrounding matrix.

T6 heat treatment, coarse and closely spaced precipitates along the grain boundaries and fine precipitates in the grains are seen relatively in the microstructures. The distributions of reinforcements in the respective matrix are fairly uniform along the grain boundaries as shown in Fig. 1b. The medium-sized aggregates of particles were pushed toward final solidification regions and were eventually located in the grain boundary. The refinement of grains could be due to the restriction in the movement of solidification front due to the presence of ZrB_2 particles and also act as nucleation sites for matrix phase which tends to increase the number of grains.

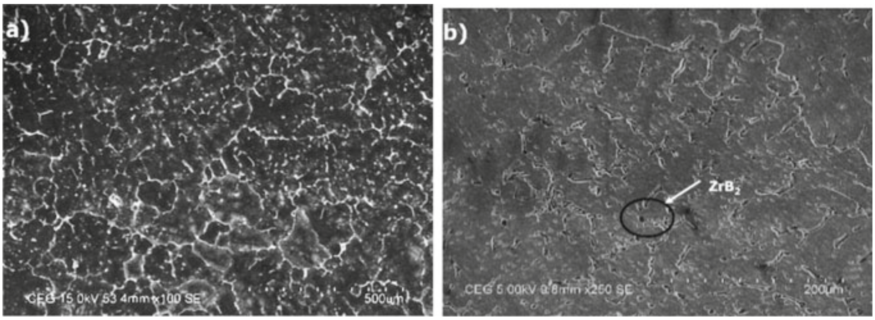

Fig. 1 SEM image for AA7075 composite **a** AZ0. **b** AZ5

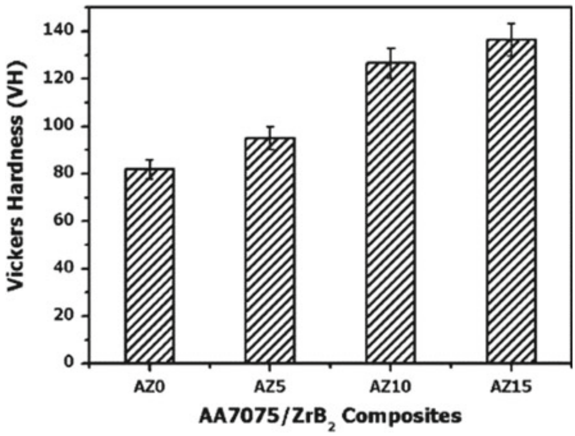

Fig. 2 Micro vickers hardness of AA7075 composites

3.2 Micro Vickers Hardness

The details of the micro Vickers hardness of the AA7075 composites are shown in Fig. 2. Increase in hardness with increasing wt% of ZrB_2 is particles due to the high dislocation density around the particles acting as a barrier to plastic deformation during indentation, leading to increase in hardness of the composites [12]. Orowan strengthening mechanisms cause increase in the hardness of composites in addition to the interface, between the reinforcement and matrix [13]. Nearly 54.4% of maximum hardness was seen for AZ15 composite compared to AZ0 alloy. The large difference in the coefficient of thermal expansion between ZrB_2 (6.66 × 10–6 °C^{-1}) and AA7075 alloy (2.3 × 10–6 °C^{-1}) hardness and effect of T6 heat treatment increases the hardness of the composites.

3.3 Effect of ZrB_2 on Impact Strength

Impact strength of the composites is featured in Fig. 3. The addition of ZrB_2 particles caused a decrease in the impact strength of composites. Results of similar kind have been reported by other researchers [11, 14]. The impact strength of all the composites is less than that of the aluminum alloy by nearly 30.12%, compared to composites and the base matrix. Aluminum alloy has a maximum fracture toughness due to plastic deformation at stressed area. Basically, the toughness of the material is based on the energy consumed for fracturing. The decrease in impact strength of the composite was due to a mismatch in elastic modulus, the thermal expansion of AA7075/ZrB_2 and its tendency to increase the elastic strain. The addition of ceramic particles led to composite materials acting as brittle nature and reduces the impact strength.

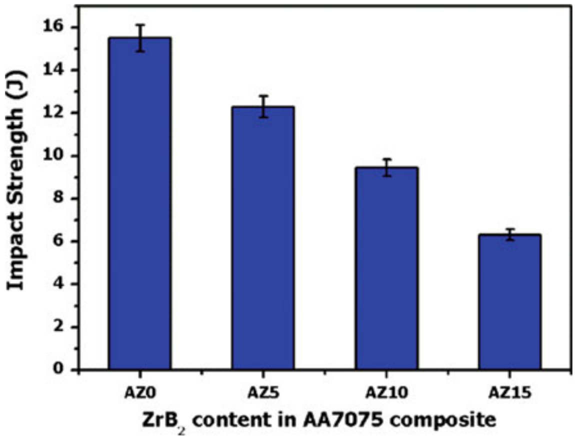

Fig. 3 Impact strength of composites

3.4 Effect of ZrB_2 on Tensile Strength and % of Elongation

Figure 4 shows the tensile strength and % elongation of the composites. There was an increase in the tensile strength of composites with increasing wt% of ZrB_2 particles. Increase in tensile strength was due to strong interfacial bonding between the aluminum alloy and ZrB_2 particles. The strength of alloy mainly depends upon deformation process on strain hardening and thermal softening. The addition of reinforcement caused a marked reduction in the percentage of the elongation due to the presence of hard particles at the base material grain boundary. The stress transfer between the base matrix and ZrB_2 particles was the result of the interaction between the dislocation and ZrB_2 particles. The effect of Orowan strengthening mechanism where a dislocation bows out considerably and leaving a dislocation loop around a particle [15, 16].

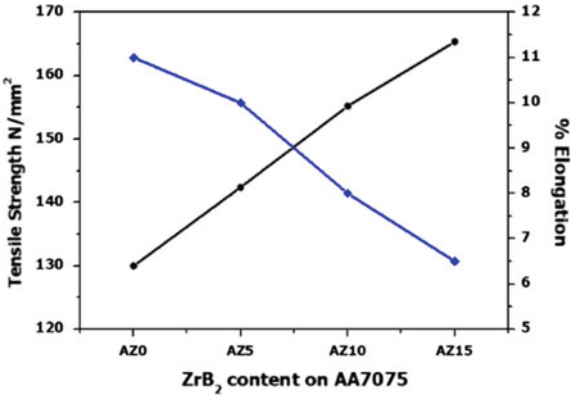

Fig. 4 Tensile strength of composites

3.5 Wear Behavior

The observations of wear rate and COF of the AA7075 composites are shown in Figs. 5 and 6. The variations in wear rate with respect to applied pressure at different wt% of ZrB_2 and sliding velocity are shown in Fig. 5. The wear rate of the composites increased with increase in sliding velocity. At the initial condition 0.8 m/s, there was an increase in the wear rate for all compositions due to the direct contact between the pin surface and the disk. With the addition of ZrB_2 particles, wear rate of the composite started decreasing with increasing wt% of particles, due to improvement in hardness, strong interfacial bonding between the matrix and ceramic particles and grain refinement in the structure. Wear rate of base alloy at 2 m/s 0.00271 mm^3/m was more compared to AZ15 composite 0.00182 mm^3/m, and nearly 38% of wear rate reduction in AZ15 composite was due to the addition of ZrB_2 composites.

Fig. 5 Wear rate of the composites

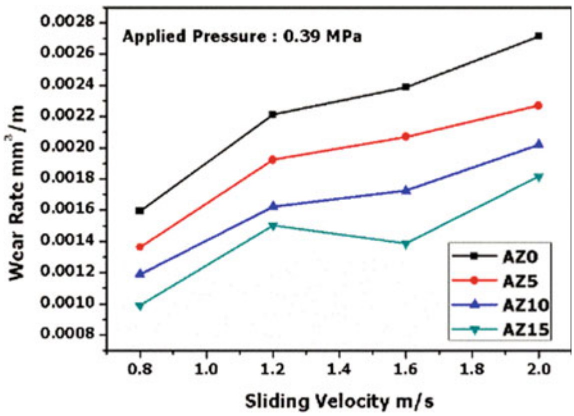

Fig. 6 COF of the composite

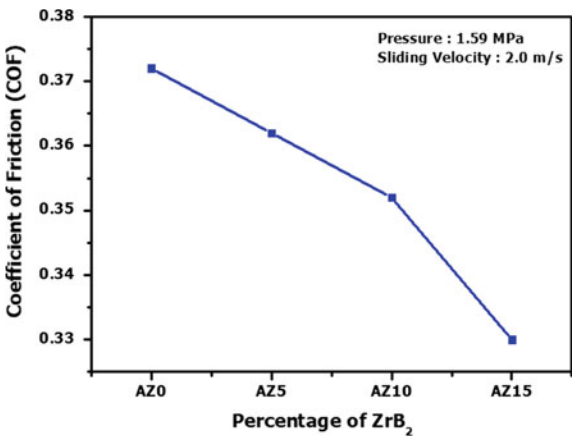

Decrease in wear rate also caused differences in CTE between the ZrB_2 particles, and α-Al matrix was expected to develop a larger strain leading to enhancement of the dislocation density. The effect of friction is composite material shown in Fig. 6. The COF of the composites showed a decrease with increasing wt% of ZrB_2 particles due to the hard resistance and uniform distribution of particles and formation of mechanical mixed layer (MML) acting as a lubrication medium reducing the COF and wear rate of composites [17]. Increase in sliding velocity caused increase in the surface temperature due to the oxidation of the pull out of ZrB_2 particles. This is attributed to the formation of B_2O3 self-lubricating layer. The worn surface morphology of the AA7075/ZrB_2 composites is shown in Fig. 7.

Two wear mechanisms occurred during dry sliding wear of AA7075/ZrB_2 composites, namely abrasion and delamination. Figure 7a shows the worn surface of AZ0 alloy at 1.6 m/s and 1.194 Mpa. Formation of grooves and more surface failure and plowing. The lower hardness of the alloy made the adhesive wear mechanism dominant. Figure 7b–c shows the worn surface of AZ5 and AZ10 composites. A pull out of particles, wear debris as white particles and thin formation of oxide layer acting a lubrication layer lead to reduction in the COF, and dominant wear mechanism of mild wear/oxide wear could be seen. Figure 7d shows the worn surface of AZ15 at high-load and high-speed conditions. Wear transmission for mild-to-severe wear mode occurred due to a rise in temperature leading to an increase in the wear rate of composites while a delamination occurred on the surface.

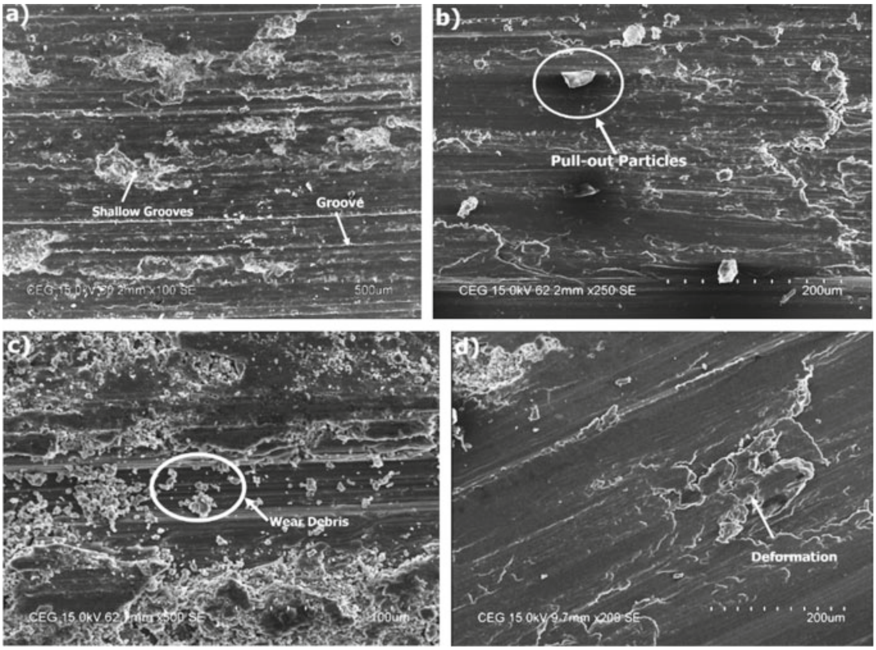

Fig. 7 Worn surface of AA7075/ZrB_2 composites **a** AZ0. **b** AZ5. **c** AZ10. **d** AZ15

4 Conclusions

In this study, AA7075-ZrB_2 composites were successfully fabricated using stir casting technique, and the mechanical and wear behavior was evaluated. The following conclusions are drawn:

1. The distribution of the reinforcement particles obtained in matrix material was uniform and particles lay down in the grain boundary and within the grain region.
2. The hardness and tensile strength of the composites increased with increasing wt% of ZrB_2 particles, and the impact strength of composites decreased at a higher wt% due to the presence of hard particles which acts as brittleness.
3. Wear rate of the composites increased with increasing applied load and sliding speed compared to base matrix. AZ15 composites show a minimum wear rate and COF.
4. Wear mechanism of the composites has both abrasion and delamination mechanisms. The mode change of the mechanism from mild-to-severe wear occurred at 1.6 m/s and 1.19 MPa applied load.

Acknowledgements The authors would like to thank the DST-SERB, Government of India, for supporting the research with funding under the Grant No: EEQ/2017/000382.

References

1. Kaushik NC, Rao RN (2017) High-stress abrasive wear behaviour of Al–Mg–Si hybrid composites using regression analysis. Ind Lubr Tribol 69(2):149–157
2. Zamora V, Ortiz AL, Guiberteau F, Nygren M (2012) In situ formation of ZrB2–ZrO2 ultra-high-temperature ceramic composites from high-energy ball-milled ZrB2 powders. J Alloy Compd 518:38–43
3. Jerome S, Ravisankar B, Mahato PK, Natarajan S (2010) Synthesis and evaluation of mechanical and high temperature tribological properties of in-situ Al–TiC composites. Tribol Int 43(11):2029–2036
4. Kumar S, Chakraborty M, Sarma VS, Murty BS (2008) Tensile and wear behaviour of in situ Al–7Si/TiB_2 particulate composites. Wear 265(1–2):134–142
5. Liang C, Li C, Lv XX, An J (2014) Correlation between friction-induced microstructural evolution, strain hardening in subsurface and tribological properties of AZ31 magnesium alloy. Wear 312(1–2):29–39
6. Kumar NS, Prabhu TR, Mishra RK, Eswaraprasad N, Shankar GS, Basavarajappa S Analysis of dry sliding wear behavior of the nano composites using statistical methods with an emphasis on temperature effects. Measurement 128:362–376
7. James J (2018) Tribological behaviour and wear fashion of processed AA6061/ZrO_2 composite. Ind Lubr Tribol 70(9):1815–1824
8. Verma N, Vettivel SC (2018) Characterization and experimental analysis of boron carbide and rice husk ash reinforced AA7075 aluminium alloy hybrid composite. J Alloy Compd 741:981–998
9. Arivukkarasan S, Dhanalakshmi V, Stalin B, Ravichandran M (2018) Mechanical and tribological behaviour of tungsten carbide reinforced aluminum LM4 matrix composites. Part Sci Technol 36(8):967–973

10. Jawahar Chandra C, Radhika N, Bhatija KA, Saalai Thenagan R (2018) Fabrication of lightweight Al LM13/TiS_2 metal matrix composites and investigation of its wear characteristics. Part Sci Technol https://doi.org/10.1080/02726351.2017.1394408
11. Dhas DEJ, Velmurugan C, Wins KLD, BoopathiRaja KP (2019) Effect of tungsten carbide, silicon carbide and graphite particulates on the mechanical and microstructural characteristics of AA 5052 hybrid composites. Ceram Int 45(1):614–621
12. Gnanavelbabu A, Muthazhagan C, Rajkumar K, Ayyanar S, Loganathan P (2018) Experimental investigation and reliability analysis on wear performance of AA6061-B_4C-Nanographite hybrid composites. Mater Today Proc 5(2):8436–8445
13. Sharma P, Sharma S, Khanduja D (2015) A study on microstructure of aluminium matrix composites. J Asian Ceram Soc 3(3):240–244
14. Kumar KR, Kiran K, Sreebalaji VS (2017) Micro structural characteristics and mechanical behaviour of aluminium matrix composites reinforced with titanium carbide. J Alloy Compd 723:795–801
15. Veeravalli RR, Nallu R, Mohiuddin SMM (2016) Mechanical and tribological properties of AA7075–TiC metal matrix composites under heat treated (T6) and cast conditions. J Mater Res Technol 5(4):377–383
16. Murali M, Sambathkumar M, Saravanan MS (2014) Micro structural and mechanical properties of AA 7075/Tio 2 in situ composites. Univ J Mater Sci 2(3):49–53
17. Gnanavelbabu A, Rajkumar K, Saravanan P (2018) Investigation on the cutting quality characteristics of abrasive water jet machining of AA6061-B_4C-hBN hybrid metal matrix composites. Mater Manuf Processes 33(12):1313–1323

Investigation on Wear Properties of Nickel-Coated Al_2O_{3P}-Reinforced AA-7075 Metal Matrix Composites Using Grey Relational Analysis

D. Vijay Praveen, D. Ranga Raju, and M. V. Jagannadha Raju

Abstract The development of hard reinforcements in MMCs became an important area of research in materials engineering. Metallic coatings on reinforced particles can improve wettability because it plays a key role in aluminium-based metal matrix composites. Nickel plating by electroless method having found to be an efficient method and widely accepted in various engineering domains such as aerospace, automobile, chemical and electrical industries. In this study, 20 micrometer-sized (average) alumina (Al_2O_3) particles are coated by nickel using electroless deposition technique. Wear specimens are prepared as per ASTM-G99 standards, using coated and uncoated reinforcements of 3, 6 and 9% weight fractions into 7075 aluminium alloy by standard stir casting route. Wear test was conducted by utilizing the test parameters, viz. track diameter, speed and load based on L_{18} Taguchi orthogonal array, on pin-on-disc machine, and the influencing parameters of responses were optimized using grey relational analysis. Weary surfaces were analysed using scanned electron microscopy. The specimen with 9% coated reinforced composite at 80 mm track diameter, 9.81 N and 1000 rpm showed improved resistance to wear.

Keywords Electroless nickel coating · Al_2o_3p/AA7075 · AMMC · Wear

1 Introduction

As a consequence of technology growth, there is enormous demand for advanced materials which possess light in weight, economic, stronger and harder in the field of

D. V. Praveen (✉)
Research Scholar, Andhra University, Vishakhapatnam 530003, India
e-mail: d.vijay.praveen@gmail.com

Department of Mechanical Engineering, Bapatla Engineering College, Bapatla 522102, India

D. R. Raju
Srinivasa Institute of Engineering and Technology, Amalapuram 533216, India

M. V. J. Raju
Department of Mechanical Engineering, Andhra University, Vishakhapatnam 530003, India

E. T. Akinlabi et al. (eds.), *Trends in Mechanical and Biomedical Design*,
Lecture Notes in Mechanical Engineering,
https://doi.org/10.1007/978-981-15-4488-0_69

automotive, space and defence applications. Reinforcing the hard ceramic particles into aluminium metal matrix can improve the mechanical and wear attributes [1]. Solid-state processing and liquid-state processing are the two major categories of fabrication of AMCs, in which liquid-state route is preferred as it possesses major advantages like continuous production, economical and ease of adaption [2–4]. There are a few limitations in the above techniques like poor wettability, non-uniform distribution of the hard reinforcements in the liquefied metal [5], partial bonding and improper interface between reinforcement and matrix materials [6].

Nowadays, electroless composite coating technique has gained good recognition in preparing composite coatings, discussed by Loto [7]. Moustafa et al. had investigated wear studies of copper graphite composite of uncoated and coated reinforcements and reported that the coated reinforcements show better wear performance when compared with uncoated reinforced composites [8]. Zhan et al. had studied the wear characteristics of nickel-coated SiC-reinforced composites and observed enhanced wear resistance [9]. Davidson et al. investigated on benefits of coating and interfacial bonding of copper(Cu)-coated silicon carbide (SiC) particle-reinforced 6061 alloy [10]. Most of the researchers had worked vigorously on the wear studies on aluminium-based MMCs, but a few studies are available on electroless-coated on particulate reinforced composites and reported that the mechanical and wear properties are enhanced by these coated composites when compared with the uncoated reinforced composites.

In this present paper, experimental analysis reports the influence of nickel coating on Al_2O_3 particle on wear behaviour of prepared composite materials, which were fabricated by stir casting routing, and the experimental responses were analysed using grey relational approach.

2 Materials and Methods

2.1 Selection of Matrix Material and Reinforcement

AA7075, is Al-based zinc alloy, has capable to withstand high loads and temperature, and it has very good wear resistance, better fatigue strength, average machinability and considerable corrosion resistance. Because of these properties, it finds applications in transport applications, including marine, automotive, aviation and mould tool manufacturing. The chemical composition of base alloy is shown in Table 1.

Table 1 Chemical composition of AA-7075

Si	Fe	Cu	Zn	Mg	Mn	Cr	Ti	Al
0.4	.5	1.43	4.87	2.43	0.2	0.1	0.16	Bal.

Fig. 1 Electroless nickel coating process [12]

Al_2O_3 has high hardness, chemical stability and structural stability in the certain temperature range, which is applied in the substrate surface to significantly reduce co-efficient of friction and improve the wear resistance [11].

2.2 Preparation of Reinforcement Particles

Coating procedure on Al_2O_3 microparticles was carried out by standard electroless plating technique. Basically, the process consists of two steps. They are surface treatment of the particles and, the other one is preparation of bath for coating. Pretreatment consists of ultrasonic cleaning, etching, sensitization and surface activation. Figure 1 shows sequence of the steps that were followed for coating process. After each successive stage, the reinforcement particles are cleansed with distilled water followed by drying and proceeded to the next stage [12–15].

The second step is preparation of coating bath. The bath for the coating was prepared with nickel chloride ($NiCl_2.6H_2O$)-30 g/l, tri-sodium citrate ($Na_3C_6H_5NaO_7.H_2O$)-25 g/l, ammonia chloride (NH_4Cl)-50 g/l and sodium hypophosphate ($NaH_2PO_2.H_2O$)-25 g/l. Nickel plating had been carried out at a temperature of 85 °C, pH value of 8 and rousing time of 20 min.

2.3 Development of Composites

Composites are fabricated by the standard liquid metallurgy route. Processed Al_2O_3 particles were preheated, before being introduced into the vortex and stirring of the molten composite were accomplished for 8 min at 350 rpm of the stirrer speed. Pouring temperatures adopted were 710 °C. As the weight percentage of Al_2O_3 increases more than 10, the produced composites may exhibit brittle nature as observed in the literature [16–18]. Within 0–10% range, as preliminary experiments, the percentage of reinforcement has been fixed with equal intervals, to get three different compositions (i.e. 3, 6 and 9%). The cylinders of Ø15 mm × 150 mm cast composites of were obtained for the both uncoated and coated reinforced AA7075 with weight percentages of 3, 6 and 9. Finally, the specimens are developed by machining the casted

Table 2 Basic properties of the material

Matrix material	Reinforcement	Density (gm/cc)	Rockwell hardness number @981 N, duration 10 s
AA-7075	3% wt. Al_2O_3	2.759	49 ± 5.1
AA-7075	6% wt. Al_2O_3	2.775	50 ± 1.9
AA-7075	9% wt. Al_2O_3	2.787	48 ± 3.6
AA-7075	3% wt. Al_2O_3(Ni coated)	2.773	60 ± 7.8
AA-7075	6% wt. Al_2O_3(Ni coated)	2.790	68 ± 3.1
AA-7075	9% wt. Al_2O_3(Ni coated)	2.814	62 ± 1.9

cylinders into Ø12 mm × 25 mm as per ASTM-G99. Experimental density values and Rockwell hardness number (average of three readings) of prepared composites are shown in Table 2.

3 Experimental Procedure

3.1 Design of Experiments

Design of experiment (DOE) is a statistical methodology for establishing the association between different variables affecting any process. Taguchi technique had been effectively used by many researchers in the analysis of wear properties of composites. This approach abolishes the need for repetitive experimental tests and thus saves material, cost and time. The very important stage in the arrangement of experiments is selection of influencing factors which have effects on the process.

Experiments were designed as multilevel problem, L_{18}, orthogonal array to investigate the most effecting parameters on the wear behaviour of the fabricated composite material. Many researchers considered these parameters for investigation. The level and factors considered for conducting wear study are shown in Table 3. Pin-on-disc machine was used to conduct wear test on the specimens which were prepared according ASTM-G99 standards.

Table 3 Control factors and levels

S. No.	Factors	Levels						
1	Reinforcement (wt%)	3	6	9	-	3C	6C	9C
		[Un-coated particles]				[Coated particles]		
2	Load (N)	9.81			19.61	29.4		
3	Track radius (mm)	60			80	100		
4	Speed (rpm)	600			800	1000		

The surfaces of the samples were cleansed with a soft paper soaked in acetone before the test. Weight of each specimen was recorded using digital electronic balance (Mettler Toledo: accuracy 0.0001 g). The initial and final weights of specimen were measured to find the slide wear loss. Table 4 shows the experimental result coefficient of friction and specific wear rate.

3.2 Grey Relational Analysis

Grey relational technique is used to solve the multi objective decision-making problems by combing the entire range of performance attribute values being considered for every alternative into one single value. This reduces the complexity of the original problem. The analysis is performed with the following steps:

1. Data normalization: The responses of the experimental data should be normalized for getting uniformity of data. For the current experiment, both the responses, i.e. wear rate and co-efficient of friction, should be lower the better.

$$a_{ij} = \frac{(b_{ij})\text{Max} - (b_{ij})}{(b_{ij})\text{Max} - (b_{ij})\text{Min}} \tag{1}$$

   where b_{ij} is unique sequence for ith experimental result for jth experiment, (b_{ij})Max is the maximum value and (b_{ij})Min is minimum value of the experiment and is sequence produced of processing the data.

2. Calculation of deviation coefficient for each experimental response using the following equation.

$$\Delta = 1 - a_{ij}$$

3. By taking average of grey relational coefficients, the GRG can be determined for each response using the Eq. (2).

$$\gamma\left(a_{0j}, a_{ij}\right) = \frac{\Delta\text{min} - \nu \cdot \Delta\text{max}}{\Delta_{ij}\text{max} + \nu \cdot \Delta\text{max}} \tag{2}$$

   For $i = 1, 2 \ldots m, j = 1, 2 \ldots n$. where $\Delta_{ij} = |b_{ij} - a_{ij}|$

$$\Delta\text{max} = \text{Max}\{\Delta_{ij}, \text{For } i = 1, 2 \ldots m,\ j = 1, 2 \ldots n\}$$
$$\Delta\text{min} = \text{Min}\{\Delta_{ij}, \text{For } i = 1, 2 \ldots m,\ j = 1, 2 \ldots n\}$$

4. Grey relational grade (GRG): It shows the influence of process parameters. The upper value of the grey relational grade represents the stronger relational degree in the given sequence [19–21]. Table 5 shows the calculations of GRG of the experimental responses.

4 Results and Discussion

4.1 Worn Surface Analysis

As the percentage of Al_2O_3 increases from 3 to 9, it can be seen that the particulates are distributed in the matrix and also agglomerated in some regions. Scanned electron microscopy (SEM) images of the composites are shown in Fig. 2.

The microstructures of a few worned surfaces are shown in Fig. 3. Figure 3a, b are related to experiment numbers 2 and 5 which were ranked as 17 and 18, show the direction of weary surface and also show the regions of delamination. In Fig. 3b, the specimen surface was highly damaged and craters of different depth were observed. Due to high rise in temperature, its surface was softened and swelling was also noticed. Figure 3c, d show the microstructure of coated composite with 3 and 9% and of experimental set of 10 and 17. In Fig. 3c, parallel scratches, pits and surface cracks were observed. In Fig. 3d, no considerable damage was found.

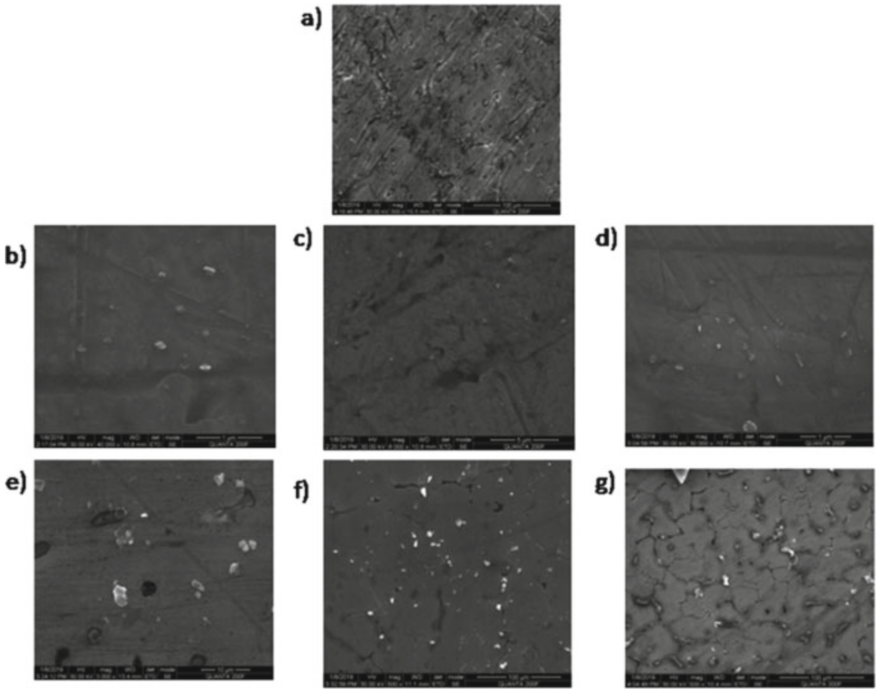

Fig. 2 SEM images of composite: **a** 7075 pure, **b** 3% Al_2O_3 +AA7075, **c** 6% Al_2O_3 +AA7075, **d** 9% Al_2O_3 +AA7075, **e** 3% Ni-coatedAl_2O_3 +AA7075, **f** 6% Ni-coated Al_2O_3 +AA7075 and **g** 9% Ni-coated Al_2O_3 + AA7075

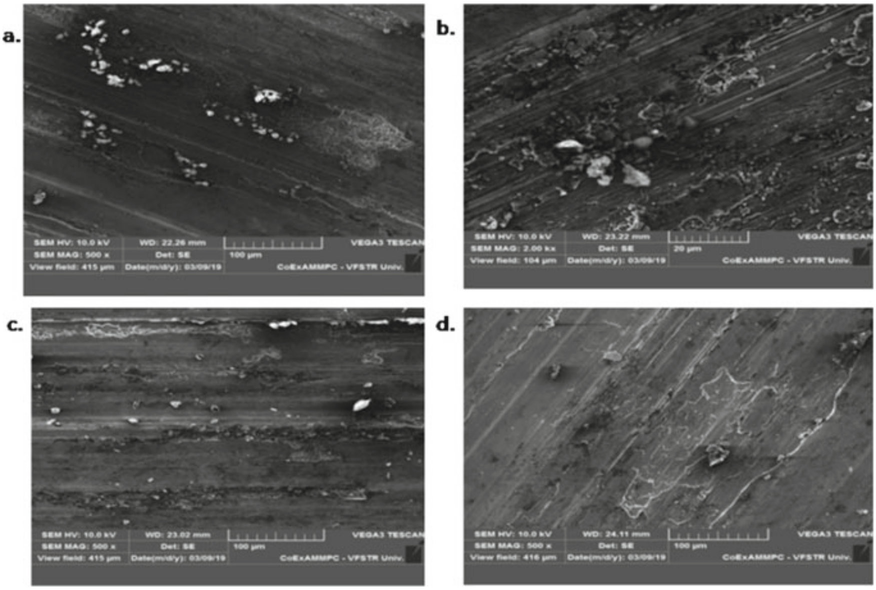

Fig. 3 Scanned electron microscopy images of worned surface composite

5 Experimental Result Analysis

5.1 Analysis of the Experimental Results

Wear test results are shown in Table 4. The following Table 5 shows the normalized values of coefficient of friction (X_1), normalized values of percentage wear (X_2), deviation sequence (X_3), deviational sequence of percentage wear (X_4), grey relational coefficient for coefficient of friction as well as wear rate, grey relational grade and rank [21].

ANOVA was performed using Minitab software to determine the highly influencing characteristics and also the main effects plot of grey relational grade Fig. 4.

From the grey relational analysis, it is also observed that the nickel-coated composites shown better resistance to wear when compared to the uncoated reinforced composites. From the ANOVA, the material type has highest influence (79.945%) followed by load, (7.81%), track diameter (4.65%) and speed (4.478%). The same were shown in Table 6 and plotted in the pi-chart in Fig. 5.

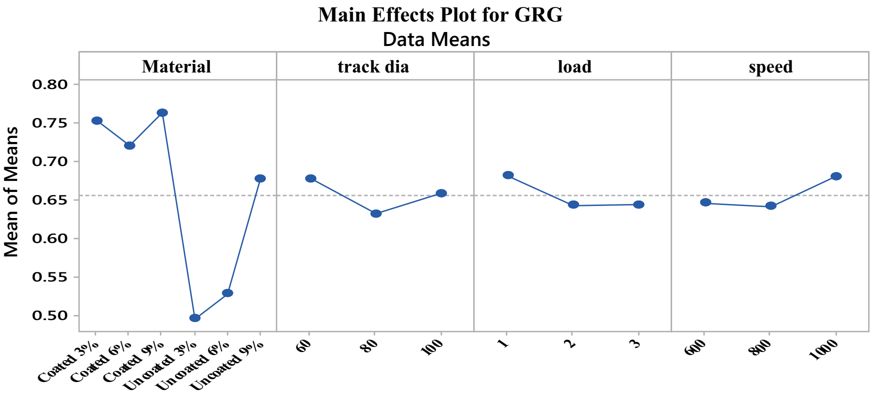

Fig. 4 Main effects plot for GRG

Table 4 Experimental results of wear and friction coefficient

Exp. No	Reinforcement	Track diameter (mm)	Weight (Kg)	Speed (RPM)	%of wear (wt. loss)	Coefficient of friction
1	Uncoated 3%	60	9.81	600	0.5162	0.2268
2	Uncoated 3%	80	19.61	800	0.5358	0.2624
3	Uncoated 3%	100	29.40	1000	0.8852	0.1901
4	Uncoated 6%	60	19.61	800	0.1072	0.1765
5	Uncoated 6%	80	29.40	1000	0.8487	0.2354
6	Uncoated 6%	100	9.81	600	0.3439	0.2418
7	Uncoated 9%	60	29.40	600	0.1489	0.1730
8	Uncoated 9%	80	9.81	800	0.2569	0.2526
9	Uncoated 9%	100	19.61	1000	0.1573	0.2393
10	Coated 3%	60	29.40	1000	0.2600	0.1696
11	Coated 3%	80	9.81	600	0.2392	0.1862
12	Coated 3%	100	19.61	800	0.2910	0.1992
13	Coated 6%	60	19.61	1000	0.2442	0.1938
14	Coated 6%	80	29.40	600	0.8903	0.1539
15	Coated 6%	100	9.81	800	0.2088	0.1990
16	Coated 9%	60	29.40	800	0.3182	0.1758
17	Coated 9%	80	9.81	1000	0.1833	0.1744
18	Coated 9%	100	19.61	600	0.2436	0.2167

Table 5 Grey relational grade calculations

Exp. No	X_1	X_2	X_3	X_4	X_5	X_6	GRG	Rank
1	0.5162	0.2268	0.5080	0.5539	0.4920	0.5285	0.5162	15
2	0.5358	0.2624	0.4814	0.3360	0.5186	0.4295	0.4602	17
3	0.8852	0.1901	0.0069	0.7785	0.9931	0.6930	0.5139	16
4	0.1072	0.1765	0.2486	0.8617	0.7514	0.7833	0.5914	13
5	0.8487	0.2354	0.0565	0.5012	0.9435	0.5006	0.4235	18
6	0.3439	0.2418	0.7420	0.4621	0.2580	0.4817	0.5707	14
7	0.1489	0.3173	1.0068	0.0000	0.0000	0.3333	0.6735	10
8	0.2569	0.2526	0.8601	0.3960	0.1399	0.4529	0.6171	12
9	0.1573	0.2393	0.9954	0.4774	0.0046	0.4889	0.7399	6
10	0.2600	0.1696	0.8559	0.9039	0.1441	0.8388	0.8076	2
11	0.2392	0.1862	0.8842	0.8023	0.1158	0.7167	0.7643	3
12	0.2910	0.1992	0.8138	0.7228	0.1862	0.6433	0.6860	8
13	0.2442	0.1938	0.8774	0.7558	0.1226	0.6719	0.7375	7
14	0.8903	0.1539	0.0000	1.0000	1.0000	1.0000	0.6667	11
15	0.2088	0.199	0.9254	0.7240	0.0746	0.6443	0.7573	4
16	0.3182	0.1758	0.7769	0.8660	0.2231	0.7886	0.7400	5
17	0.1833	0.1744	0.9601	0.8745	0.0399	0.7994	0.8627	1
18	0.2436	0.2167	0.8782	0.6157	0.1218	0.5654	0.6848	9

Table 6 Main effects plot for GRG

Source	DF	Adj SS	Adj MS	*F*-value	*P*-value	Percentage contribution
Material	5	0.2045	0.0409	10.49	0.006	79.945
Track diameter	2	0.0118	0.0059	1.52	0.292	4.650
Load	2	0.0199	0.0099	2.56	0.157	7.810
Speed	2	0.0114	0.0057	1.47	0.303	4.478
Error	6	0.0234	0.0038			9.152
Total	17	0.2556				

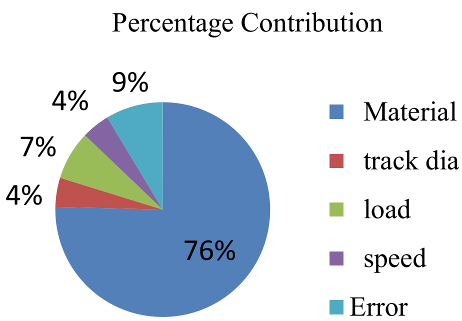

Fig. 5 Percentage contribution chart

6 Conclusion

In the present work, it was observed that the percentage of wear of the particle-coated composite is improved when compared to the uncoated reinforced composite. Grey relational analysis was successfully done, and the following conclusions were drawn from the present investigation.

1. As the GRG value is highest at the experiment no. 17, 9% nickel-coated-reinforced 7075 composite material has shown good result in percentage of wear.
2. Similarly, most of the GRG values yielded good result when compared with the uncoated reinforcement.
3. ANOVA results revealed that material type is the most influencing parameter in the present analysis followed by load, track diameter and speed on wear studies

References

1. Garcia-Cordovilla C, Narciso J, Louis E (1996) Abrasive wear resistance of aluminium alloy/ceramic particulate composites. Wear 192(1–2):170–177
2. Gladston JAK, Sheriff NM, Dinaharan I, Selvam JDR (2015) Production and characterization of rich husk ash particulate reinforced AA6061 aluminum alloy composites by compocasting. Transactions of Nonferrous Metals Society of China 25(6):686–691
3. Rittner M (2000) Metal matrix composites in the 21st century: markets and opportunities. Report GB-108R, Business Communications Co., Inc., Norwalk, CT
4. Hashim J, Looney L, Hashmi MSJ (1999) Metal matrix composites: production by the stir casting method. J Mater Process Technol 92:1–7
5. Asthana R (1998) Reinforced cast metals: part II evolution of the interface. J Mater Sci 33(8):1959–1980
6. Keshavamurthy R, Mageri S, Raj G, Naveenkumar B, Kadakol PM, Vasu K (2013) Microstructure and mechanical properties of Al7075-TiB2 in-situ composite. Res J Mater Sci. ISSN2320: 6055
7. Loto CA (2016) Electroless nickel plating–a review. Silicon 8(2):177–186
8. Moustafa SF, El-Badry SA, Sanad AM, Kieback B (2002) Friction and wear of copper–graphite composites made with Cu-coated and uncoated graphite powders. Wear 253(7–8):699–710
9. Zhan Yongzhong, Zhang Guoding (2003) The effect of interfacial modifying on the mechanical and wear properties of SiCp/Cu composites. Mater Lett 57(29):4583–4591
10. Davidson AM, Regener D (2000) A comparison of aluminium-based metal-matrix composites reinforced with coated and uncoated particulate silicon carbide. Compos Sci Technol 60(6):865–869
11. Zhang C (2014) Understanding the wear and tribological properties of ceramic matrix composites. Advances in ceramic matrix composites. Wood Head Publishing, Cambridge, pp 612–669
12. Kumar DS, Suman KNS, Kumar PR (2016) A study on electroless deposition of nickel on nano alumina powder under different sensitization conditions. Int J Adv Sci Technol 97:59–68
13. Plating E (1990) Fundamentals and applications. In: Mallory GO, Hajdu FB (eds) American electroplaters and surface finishers society, Orlando, Forida
14. Pang JN, Jiang SW, Lin H, Wang ZQ (2016) Significance of sensitization process in electroless deposition of Ni on nanosized Al2O3 powders. Ceram Int 42(3):4491–4497

15. Li GJ, Huang XX, Guo JK (2001) Fabrication of Ni-coated Al2O3 powders by the heterogeneous precipitation method. Mater Res Bull 36(7–8):1307–1315
16. Javdani A, Pouyafar V, Ameli A, Volinsky AA (2016) Blended powder semisolid forming of Al7075/Al2O3 composites: investigation of microstructure and mechanical properties. Mater Des 109:57–67
17. Dhanalakshmi S, Mohanasundararaju N, Venkatakrishnan PG (2014) Preparation and mechanical Characterization of stir cast hybrid Al7075-Al_2O_3-B4C metal matrix composites. In: Applied mechanics and materials, vol 592. Trans Tech Publications, pp 705–710
18. Maurya Manish, Kumar Sudhir, Bajpai Vivek (2019) Assessment of the mechanical properties of aluminium metal matrix composite: a review. J Reinf Plast Compos 38(6):267–298
19. Sharma P, Khanduja D, Sharma S (2016) Dry sliding wear investigation of Al6082/Gr metal matrix composites by response surface methodology. J Mater Res Technol 5(1):29–36
20. Subbaya KM, Suresha B, Rajendra N, Varadarajan YS (2012) Grey-based Taguchi approach for wear assessment of SiC filled carbon–epoxy composites. Mater Des 41:124–130
21. Siriyala R, Alluru GK, Penmetsa RM, Duraiselvam M (2012) Application of grey-taguchi method for optimization of dry sliding wear properties of aluminum MMCs. Front Mech Eng 7(3):279–287

Optimizing the Tribological Properties of UHMWPE Nanocomposites—An Artificial Intelligence based approach

A. Vinoth, K. N. Nirmal, Rohit Khedar, and Shubhabrata Datta

Abstract The longevity of the hip implants has been a major issue in recent times due to inadequate material used for implants. Since the metal on polymer implants has issues such as tissue degeneration and osteolysis, the focus of this study is to improve the tribological properties of ultra-high molecular-weight polyethylene (UHMWPE) which has been in use on acetabular cup of hip implants by considering multiple nanoparticles like carbon fibre, carbon nanotubes and graphene as reinforcements. It is extremely difficult and time-consuming through numerous experimental trials to arrive at the optimum material composition of nanoparticles. Therefore, an effort has been made on developing a new polymer nanocomposite by utilizing the artificial intelligence (AI)-based design which includes the techniques, viz. artificial neural network (ANN) and genetic algorithm (GA). The input parameters like weight fraction and the geometry of the different nanoparticles related to the tribological properties were collected from various published literatures, and modelling was done through ANN for the output parameters, viz. coefficient of friction and specific wear rate. Best ANN predictive model was chosen individually for each output parameters on iterating the different hidden nodes. The fundamental correlation between the input and output parameters was investigated through sensitivity analysis. Optimization studies were performed using genetic algorithm (GA) with the best-chosen ANN model as an input to get optimum input variables. Thus, the AI-based approach of designing the UHMWPE nanocomposites shows an enhancement on the tribological properties that pave a way for further experimental trials.

Keywords Wear · UHMWPE · Composites · Artificial neural network and genetic algorithm

---

A. Vinoth (✉) · K. N. Nirmal · R. Khedar · S. Datta
Department of Mechanical Engineering, SRM Institute of Science and Technology, Kattankulathur 603203, India
e-mail: avinot@gmail.com

E. T. Akinlabi et al. (eds.), *Trends in Mechanical and Biomedical Design*, Lecture Notes in Mechanical Engineering,
https://doi.org/10.1007/978-981-15-4488-0_70

1 Introduction

The need for a proper material in hip implant has been a major area of research in recent years. Hence, wide variety of materials have been in use and also been studied upon like metal implants, ceramic implants, polymer implants, etc., which could serve its purpose as a strong, reliable and biocompatible implant. Metal implants were the first which came into the picture but were not much successful because of the wear of metal particles which may cause osteolysis [1]. Metal implants have paved way for ceramic and polymers because of their uncanny characteristics and have ability to show properties superior to metals both mechanically and chemically [2].

Polymers have been in use since the early 1960s for making acetabular cups in hip arthroplasty and was proposed by a British surgeon named 'John Charnley' [3]. Charnley made use of polytetrafluoroethylene (PTFE) polymer in acetabular components which reduced the use of metal implants in arthroplasty [4]. But the immense research carried out under PTFE being used in implants proved it be an inferior component to ultra-high molecular weight polyethylene (UHWMPE) because of its distortion and high wear rate. UHMWPE polymer has been in use since 1962 in orthopaedics because of its properties such as high toughness, self-lubricating capability, resistance to absorb moisture and to get oxidized. Researches have been carried out in this field to further improve the property of UHMWPE by adding reinforcements such as carbon fibre, CNT, graphene oxide, nano-Al_2O_3, hydroxyapatite (HA), nano-SiO_2 fibre as individual components [5]. It was seen that on adding these reinforcements, there has been significant improvement in the properties like wear rate and coefficient of friction (COF) when compared with pure UHMWPE [6]. This study focuses on further enhancing the tribological properties of UHMWPE on combining different nanoparticles as reinforcement namely CNT, carbon fibre and graphene oxide and its influence on the matrix. The experimental trial would be possible only if it is practically tried out for various combinations of all the three composites with regard to numerous properties and structural behaviour with the UHMWPE matrix to find the optimal composition. It can be concluded easily that this trial-and-error method is too complicated, tedious and consumes a lot of money and time. In order to overcome these issues, computational data-driven models are developed on collecting abundant data from several published literatures. The main purpose of developing these models is to find a perfect balance between the composition, structure and the physical properties among UHMWPE and its composites. The tribological properties to be monitored under this study include a reduction of COF and wear rate.

Artificial intelligence techniques like ANN is employed to establish individual relationship among input and output parameters fed into ANN as data-driven models [7–9]. The optimal models which give proper relationship and which are closer to the target required are chosen for further optimization. Optimization is conducted through genetic algorithm (GA) to which the best-chosen ANN models are fed as inputs which act as an objective function for carrying out the optimization [10].

Depending on observations and pattern of output from GA, the solution can be obtained through single objective or also if needed using multi-objective manner. The optimal results collected from GA could be used to design a UWMWPE composite which has a combination of reinforcements with improved tribological performance for the use of acetabular cup in hip prosthesis.

2 Database

A sufficient set of data was collected from published literatures containing ultra-high molecular-weight polyethylene (UHMWPE) composites with graphene oxide, carbon fibre and Carbon nanotubes as reinforcements ranging up to 471 in number [11–24]. A total number of 16 input parameters were considered for the study which includes the weight percentage, particle size of the above-mentioned three reinforcements.

The inputs also contain variables like sliding distance, sliding speed, method of test, load and hardness. These data are fed into ANN as input to develop ANN models which give relationships between the input and output variables. The developed ANN models are then considered for minimizing the output parameters COF and wear rate. Table 1 depicts the minimum, maximum, mean and standard deviation of the input and output variables.

3 Artificial Intelligence (AI) Techniques

Artificial intelligence techniques such as artificial neural network (ANN) and genetic algorithm (GA) are used as computational methods. ANN and GA have significant roles in developing empirical models especially in the field of materials for developing new materials. They also have the ability to capture highly complex systems from the data. ANN is used to develop data-driven models which are fed into GA as objective function to get optimized solutions on the tribological behaviour of UHMWPE composites. The functioning of ANN and GA is described below.

3.1 Artificial Neural Network (ANN)

Artificial neural network works similarly as our human brain. It has several neurons to connect between layers to carry forward the stimulus similar to our neuron system. It has huge number of nodes which act as connections or links to transfer signal between layers to process the data. ANN is a very popular tool to develop data-driven models which are fundamentally different from statistical or numerical approach. The initial stage of ANN processing involves training itself from several computational trials

Table 1 Maximum and minimum ranges of each input and output parameters along with their mean and standard deviation

Variables	Min	Max	Mean	Std. dev.
Molecular weight (million g/mol)	2.5	6	4.045	0.627
Carbon nanotube (wt%)	0	3	0.769	0.757
CNT fibre length (μm)	0	15	9.063	7.668
CNT fibre OD (nm)	0	80	32.027	25.528
Carbon fibre (wt%)	0	12	0.790	2.517
CF length (μm)	0	1000	113.890	317.300
CF OD (nm)	0	7000	736.363	2012.133
Graphene (wt%)	0	3	0.260	0.558
Graphene sheet thickness (nm)	0	1	0.045	0.201
Graphene sheet length (μm)	0	4	0.0681	0.343
Method	0	1	0.136	0.343
Sliding distance (m)	5	10,000	911.045	1176.424
Sliding speed (m/s)	0.004	1.667	0.432	0.435
Load (N)	5	140	40.047	29.174
Lubrication	0	2	0.909	0.884
Hardness (kgf/mm^2)	67.5	1580	303.797	278.087
Coefficient of friction	0.04	0.84	0.210	0.206
Wear rate (mm^3/Nm)	0.0000002	0.00009	1.816E-05	2.109E-05

to reach desired output or target. ANN can be utilized to reach the desired target by fine tuning its weights and biases. Specific and minute changes can be made through connection strength or weights until the perfect match for the output is generated. This step is generally called learning or training of ANN. ANN became more popular and readily acceptable since 1980s because of its ability to handle nonlinear systems [26]. ANN comprises three sets of processing units, one which receives inputs from the outside world is called input unit which is processed in a layer called 'input layer'. The second unit consists of a hidden unit which receives inputs from the input node or unit and processes the data according to the number of hidden layers required by the user. The final set of results are extracted from the output layer receives inputs from the hidden layer. The node number in the input layer and output layer is taken from the application problem which is being evaluated, whereas the number of hidden layers is to be defined by the user. The structure of ANN is represented by 16-N-1 notation in which 16 represents the number of inputs, viz. molecular weight of UHMWPE, CNT wt%, CNT fibre length, CNT fibre OD, CF wt%, CF length, CF OD, graphene wt%, graphene sheet thickness, graphene sheet length, method of testing, sliding distance, sliding speed, load, lubrication and hardness. N represents the number of hidden layers as required by the user ranging between 3 and 15. 1

represents the output variables which are computed separately. The output variables under consideration are COF and wear rate.

The interconnection developed between each layer is through functions. Tan-hyperbolic (tan h) function acts as link between input and hidden layers. At each hidden unit (H_j), the weighted summation of the input (X_i) is operated on by a nonlinear tan hyperbolic transfer function as shown in equation below, which ensures that each input contributes to every hidden unit [26].

$$H_j = \tan h\left(W_{ji} X_i + \theta_j\right) \tag{1}$$

The output node then calculates the linear weighted sum of the outputs of the hidden layers.

$$Y_k = \Sigma\left(W_{kj} H_j + \theta_k\right) \tag{2}$$

where θ denotes biased variable, W_{ji} and W_{kj} represent the weight assigned to the connections between the layers, H_j denotes output from hidden units, Y_k denotes the output and X_i denotes the normalized inputs

3.2 Sensitivity Analysis

In order to develop any new material, it is essential to have better knowledge on the absolute influence of the various input parameters in the final tribological properties of the composites. But, in case of ANN models, due to its tangled hidden relationships, it is quite tedious to determine consequence of the input variables on the output. The same can be overcome by means of sensitivity analysis that helps to find all applicable factors from a set of possible factors. It is feasible to determine the correlation between the input and output parameters through various methods. One among them is the connection weight method [25] that is considered in this study. To find the relevance importance on the parameters, it uses the connection weights of input to hidden layers and hidden to output layers from the developed ANN model.

3.3 Genetic Algorithm (GA)

Genetic algorithm is a known tool for optimization problems which is used widely for solving constrained and unconstrained optimization problems that is based on natural selection that thrusts biological evolution. Three rules are used to build a genetic algorithm optimization, namely selection, crossover and mutation. GA performs multiple modifications of a selected population of individual solutions. GA utilizes its objective function to select a random set member from the model which is fittest among the rest and allocates them as parents so that they can be utilized to make the next-generation children. This selection leads to the next rule where two parents from different generations are crossed over with each other to achieve better solutions. Further, certain characteristics of the chosen parent member may also be varied slightly to arrive at optimal solutions which is called mutation [26]. This same process repeats itself for several generations until an optimum solution is evolved from these generations. The last generation among the entire population gives the optimal solution as desired. The optimization in GA is implemented by specifying an objective function (in this case an ANN model) on a single-objective or multi-objective function with or without constraints [27]. This study comprises individually monitoring the performance of the optimization by minimizing each of the output parameters. In this case, both COF and wear rate have to be minimized to get better tribological performance of the composite. This is done by varying the molecular weight of UHMWPE on ANN model of each output within a specified range and checking if the output parameters are getting minimized or maximized. Also, constraints were added on varying the sum of weight percentages of CNT and graphene as 2, 4 and 6% for the betterment of solutions.

4 Results and Discussion

4.1 ANN Modelling and Sensitivity Analysis

Sixteen input variables were taken into account to develop two ANN models for two sets of outputs separately, viz. COF and wear rate. 3–15 hidden nodes were taken into account for the iteration to develop the best models. The model with least amount of error or closest to the target value is taken as the best one for further studies. Figure 1

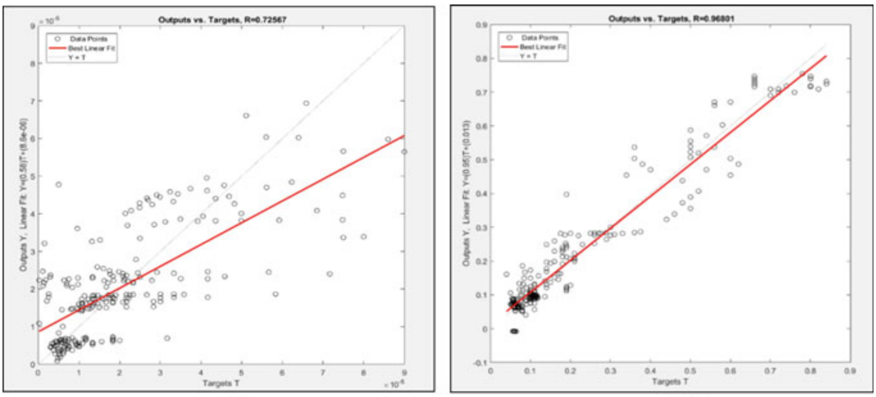

(a) (b)

Fig. 1 Predictability of ANN model with linear fit for **a** wear rate and **b** COF

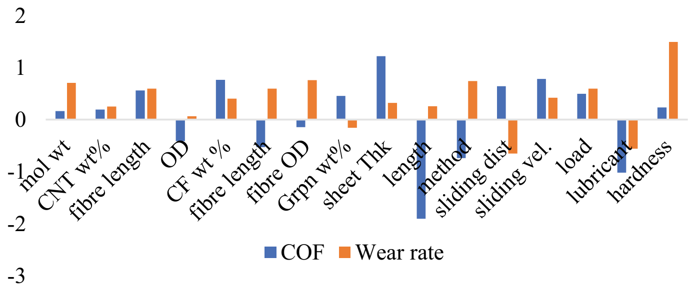

Fig. 2 Sensitivity analysis

shows the predictability of the trained ANN models. It can be inferred from the scattered plot that the models developed are closer to the target value. The regression value for COF is 0.96801, and similarly that of wear rate is 0.72567.

The model is confirmed not only from its regression plot but also should have good input-to-output relationship as well. The regression curve does not provide any information about the influences of input variables on the output due to its complex hidden relationships developed which is why ANN is also called a 'Black Box'. The sensitivity analysis is done on a trained ANN model which gives the individual contribution of each input variable to the output. More the number of input variables on the positive side, the better are the results. The sensitivity analysis for the above two best models is shown in Fig. 2.

Surface plots are developed by keeping the input variables fixed and observing their influences on the output. It is plotted by taking two input variables and one output variable at a time to perceive the influence of input variables on the output.

Figure 3a shows that as GO wt% increases from 0 to 0.5%, there is a slight decrease in COF and increases thereafter whereas in case of CNT wt%, there is a slight decrease in COF value from 0.5 to 2%. In Fig. 3b, the COF increases as CF wt% increases from 0 to 15%, whereas for CNT, COF decreases from 1 to 2 wt%. Also from the earlier study, Naresh Kumar et al. [12] have proposed that COF decreases with an increase of CNT wt% from 0.5 to 2%. Figure 3c shows the influence of load and molecular weight on COF. As molecular weight increases from 2 to 6 million g/mol, COF also increases and as load increases from 0 to 100 N, COF increases as well. In Fig. 3d, the relationship of sliding speed and sliding distance with COF is shown. COF increases with increase in sliding distance from 0 to 4000 m, whereas COF decreases with increase in sliding speed up to 0.2 m/s and then increases thereafter.

Figure 4a depicts the relationship between CF and CNT wt% with respect to wear rate. It shows that as CNT wt% increases, wear rate decreases drastically, whereas as CF wt% increases from 0 to 15 wt%, wear rate is almost constant. Also from the earlier study, Naresh Kumar et al. [12] have studied that with an increase of CNT wt% from 0.5 to 2%, wear rate decreases. In Fig. 4b, it can be seen that wear rate decreases very minutely with lower value of GO wt% and decreases drastically at higher content of GO, whereas when CNT wt% varies wear rate decreases slightly.

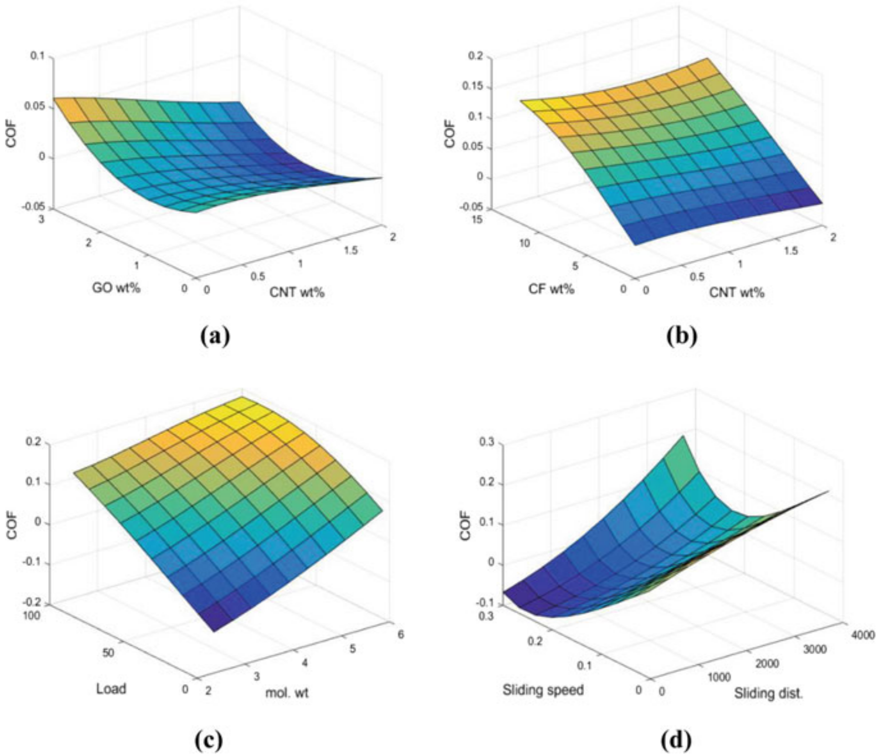

Fig. 3 Surface plots indicate the variation of COF with **a** CNT wt% versus graphene wt%, **b** CNT wt% versus CF wt%, **c** mol. wt. versus load and **d** sliding dist. versus sliding speed

Figure 4c depicts the relationship between molecular weight and load with wear rate. It shows that as molecular weight increases, wear rate increases up to 5.5 million g/mol and then further decreases. As load increases from 0 to 150 N, wear rate also increases. Figure 4d shows the influence of sliding speed and sliding distance with wear rate. It could be inferred that wear rate decreases steeply with increase in sliding distance from 5000 to 20000 m. Also wear rate remains almost constant with increase in sliding speed.

4.2 Single-Objective Genetic Algorithm

Single-objective genetic algorithm gives the desired output for one particular output parameter in relation to all the input parameters. In this study, the optimization is carried out for both COF and wear rate separately to check its influences individually on the output parameters. The solutions were run for 1000 generations and 1000 populations for the minimization of COF and wear rate by using the best-developed

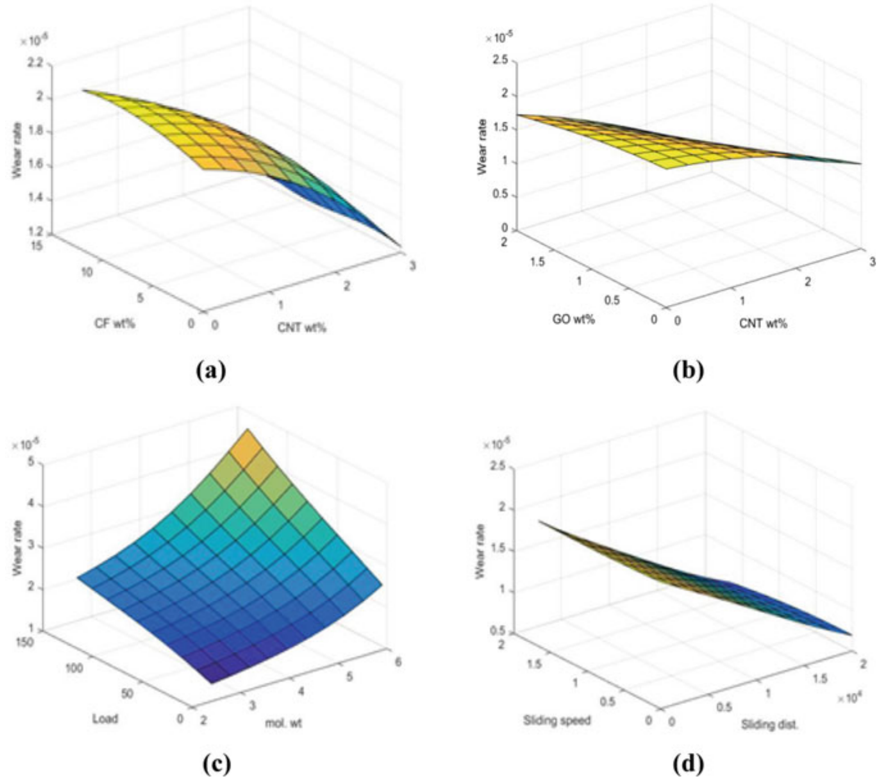

Fig. 4 Surface plot indicates the variation of wear rate with **a** CNT wt% versus graphene wt%, **b** CNT wt% versus CF wt%, **c** mol. wt. versus load and **d** sliding dist. versus sliding speed

ANN models as objective function by varying the molecular weight of UHMWPE composites from 2.5 to 5.5 million g/mol. Suitable constraints were also applied to the weight percentages of the reinforcements by restricting the summation of CNT and GO weight percentage as 4% from the simulation studies that higher amount of nanoparticles does not cause any irregularities to get optimized solutions for the tribological properties. Table 2 indicates the parameters which are considered for the optimization using single-objective GA.

Table 2 Value of GA parameters

Parameters	Values
Number of generation	1000
Number of population	1000
Probability of mutation	0.1
Probability of cross-over	0.95

The solution obtained from GA suggests that there is a constant decrease in COF value with increase in molecular weight of UHMWPE composite as shown in Fig. 5a. This is similar to the trend required for this particular study where output has to be minimized. But on the contrary, there is a steep increase in the wear rate with increase in molecular weight of UHMWPE composite as shown in Fig. 5b. Wear rate does not follow the minimization function as required or expected in this study. So a further assessment of data is required through multi-objective genetic algorithm because of the conflicting nature of each output.

Tables 3 and 4 depict the composition of each reinforcement with the variation of molecular weight of UHMWPE and load which are obtained through single-objective GA.

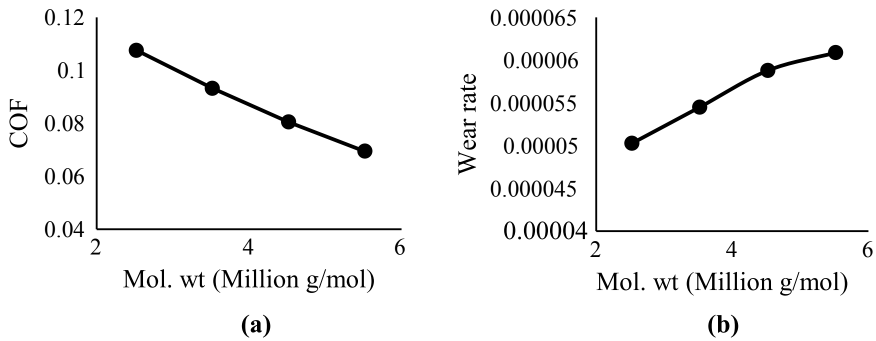

Fig. 5 Variation of output with increasing molecular weight **a** mol. wt. versus COF and **b** mol. wt. versus wear rate

Table 3 List of CNT wt%, CF wt%, GO wt%, load and COF with respect to mol. wt

Mol. wt. ($\times 10^6$ g/mol)	CNT wt%	CF wt%	GO wt%	Load (N)	COF
2.5	0.430	5.303	0.7794	40.936	0.1074
3.5	0.4797	4.925	0.7247	47.057	0.0931
4.5	0.5151	4.821	0.6889	43.733	0.0803
5.5	0.5014	4.424	0.7121	45.252	0.0693

Table 4 List of CNT wt%, CF wt%, GO wt%, load and wear rate with respect to mol. wt

Mol. wt. ($\times 10^6$ g/mol)	CNT wt%	CF wt%	GO wt%	Load (N)	Wear rate (mm^3/Nm)
2.5	0.6176	6.7829	0.4790	43.634	5.02E-05
3.5	0.6076	6.7615	0.4708	44.729	5.44E-05
4.5	0.5997	6.0503	0.5191	46.466	5.87E-05
5.5	0.5.691	6.1093	0.5197	43.382	6.08E-05

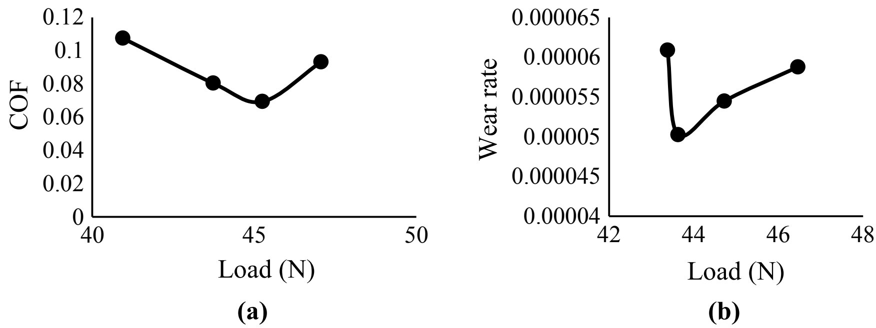

Fig. 6 Variation of output with increasing load **a** load versus COF **b** load versus wear rate

Figure 6 shows the relationship of the output with increasing load. It could be concluded from Fig. 6a that COF is decreasing with increasing load till 45.2 N and thereafter increases, whereas from Fig. 6b, it can be concluded that wear rate is increasing with load but initially it decreases up to a load of 43.6 N and increases thereafter. The general trend of the solutions depicts that load is also showing contradictory behaviour as in the case of increasing molecular weight of UHMWPE composite.

5 Conclusions

The conclusions from this study are as follows:

- It can be seen that ANN models could act as a perfect objective function for GA in optimization problems.
- The two computational approaches used to conduct this study can save a huge amount of time and money for designing a new material.
- This study shows that combined reinforcement of different nanoparticles can improve the tribological properties when added to the UHMWPE, using artificial intelligence techniques.
- The optimization study through single-objective GA shows that there was a conflicting nature in output parameters, i.e. COF and wear rate with respect to molecular weight of UHMWPE and load.
- The composition of all the three reinforcements, i.e. CNT, CF and GO, has different effects on the tribological properties. All three nanoparticles have a unique contribution to the output parameters.
- Due to the confliction on each output, further study can be done using multi-objective optimization to arrive at better results and to compare both the tribological properties in a single frame.

References

1. Campbell P, Beaulé PE, Ebramzadeh E, Leduff M, De Smet K, Lu Z, Amstutz HC (2006) The John Charnley Award: a study of implant failure in metal-on-metal surface arthroplasties. Clin Orthop Relat Res 453:35–46
2. Affatato S, Ruggiero A, Merola M (2015) Advanced biomaterials in hip joint arthroplasty. A review on polymer and ceramics composites as alternative bearings. Compos Part B Eng 83:276–283
3. Mikić Z, Lesić AR (2013) 50 years of total hip prosthesis—a tribute to Prof. Sir John Charnley. Acta Chir Iugosl 60(1):9–13
4. Blumm J, Lindemann A, Meyer M, Strasser C (2010) Characterization of PTFE using advanced thermal analysis techniques. International Journal of Thermophysics 31(10):1919–1927
5. Mano JF, Sousa RA, Boesel LF, Neves NM, Reis RL (2004) Bioinert, biodegradable and injectable polymeric matrix composites for hard tissue replacement: State of the art and recent developments. Compos Sci Technol 64(6):789–817
6. Vadivel HS, Golchin A, Emami N (2018) Tribological behaviour of carbon filled hybrid UHMWPE composites in water. Tribol Int 124:169–177
7. Datta S, Chattopadhyay PP (2013) Soft computing techniques in advancement of structural metals. Int Mater Rev 58(8):475–504
8. Sinha A, Sikdar Dey S, Chattopadhyay PP, Datta S (2013) Optimization of mechanical property and shape recovery behavior of Ti-(∼49 at.%) Ni alloy using artificial neural network and genetic algorithm. Mater Des 46:227–234
9. Bleck W, Sikdar Dey S, Bhattacharjee D, Bhattacharyya T, Brat Singh S, Bhattacharyya S (2012) Microstructural prediction through artificial neural network (ANN) for development of transformation induced plasticity (TRIP) aided steel. Mater Sci Eng A 565:148–157
10. Mohanty I, Bhattacharjee D, Datta S (2011) Designing cold rolled if steel sheets with optimized tensile properties using ANN and GA. Comput Mater Sci 50(8):2331–2337
11. Bin Ali A, Abdul Samad M, Merah N (2017) UHMWPE hybrid nanocomposites for Improved Tribological Performance Under Dry and Water-Lubricated Sliding Conditions. Tribol Lett 65(3):1–10
12. Naresh Kumar N, Yap SL, Samsudin B, Dayana FN, Khan MZ, Srinivasa P, Sreekanth R (2016) Effect of argon plasma treatment on tribological properties of UHMWPE/MWCNT nanocomposites. Polymers (Basel) 8(8):295
13. Manoj Kumar R, Sharma SK, Manoj Kumar BV, Lahiri D (2015) Effects of carbon nanotube aspect ratio on strengthening and tribological behavior of ultra high molecular weight polyethylene composite. Compos Part A Appl Sci Manuf 76:62–72
14. Liu B, Qi Y, Yan X, An Y, Pei J, Xue Q, Tai Z (2013) Friction and wear properties of graphene oxide/ultrahigh-molecular-weight polyethylene composites under the lubrication of deionized water and normal saline solution. J Appl Polym Sci 131(1):1–11
15. Tai Z, Chen Y, An Y, Yan X, Xue Q (2012) Tribological behavior of UHMWPE reinforced with graphene oxide nanosheets. Tribol Lett 46(1):55–63
16. Chukov DI, Stepashkin AA, Maksimkin AV, Tcherdyntsev VV, Kaloshkin SD, Kuskov KV, Bugakov VI (2015) Investigation of structure, mechanical and tribological properties of short carbon fiber reinforced UHMWPE-matrix composites. Compos Part B Eng 76:79–88
17. Tenison N, Baena JC, Yu J, Peng ZX (2017) Development of Mixing Methods of UHMWPE/Carbon Nanotubes (CNT) Composites for Use in Artificial Joints. Key Eng Mater 739:81–86
18. Zoo YS, An JW, Lim DP, Lim DS (2004) Effect of carbon nanotube addition on tribological behavior of UHMWPE. Tribol Lett 16(4):305–310
19. Rocha LA, Kanagaraj S, Oliveira MS, Simoes JA, Mathew MT, Fonseca A (2010) Tribological characterisation of carbon nanotubes/ultrahigh molecular weight polyethylene composites: the effect of sliding distance. Int J Surf Sci Eng 4(4–6):305–321
20. Baena JC, Peng Z (2018) Dispersion state of multi-walled carbon nanotubes in the UHMWPE matrix: effects on the tribological and mechanical response. Polym Test 71:125–136

21. Golchin A, Wikner A, Emami N (2016) An investigation into tribological behaviour of multi-walled carbon nanotube/graphene oxide reinforced UHMWPE in water lubricated contacts. Tribol Int 95:156–161
22. Sreekanth PSR, Kanagaraj S (2015) Influence of multi walled carbon nanotubes reinforcement and gamma irradiation on the wear behaviour of UHMWPE. Wear 334–335:82–90
23. Wang Y, Yin Z, Li H, Gao G, Zhang X (2017) Friction and wear characteristics of ultrahigh molecular weight polyethylene (UHMWPE) composites containing glass fibers and carbon fibers under dry and water-lubricated conditions. Wear 380–381:42–51
24. Lee JH, Kathi J, Rhee KY, Lee JH (2010) Wear properties of 3-aminopropyltriethoxysilane-functionalized carbon nanotubes reinforced ultra high molecular weight polyethylene nanocomposites. Polym Eng Sci 50(7):1433–1439
25. Olden JD, Joy MK, Death RG (2004) An accurate comparison of methods for quantifying variable importance in artificial neural networks using simulated data. Ecol Model 178:389–397
26. Datta S (2016) Materials design using computational intelligence techniques. CRC Press, UK
27. Mathworks C (2016) Global optimization toolbox user's guide R 2016 b

Friction and Wear Study of Laser Surface Textured Ti-6Al-4V Against Cast Iron and Stainless Steel Using Pin-on-Disc Tribometer

N. Sankara Manikandan, M. Prem Ananth, L. Poovazhagan, B. Sudarsan, and A. Vishnuvarthan

Abstract The reduction in the friction plays a vital role in improving the efficiency of the working machinery. The wear is the direct effect of friction which reduces the lifetime of the machine components. The modification of the surface of the materials can considerably reduce the wear and friction and thus improving the efficiency and increasing the lifetime of the machine components. The surface modification techniques such as abrasive jet machining, ECM, etching and LST are being used to alter the surface properties. This paper presents the laser surface texturing on titanium alloy, cast iron and stainless steel and testing of frictional properties such as friction and wear of titanium pins against cast iron and stainless steel discs. The texturing patterns are designed and laser ablation method is used to texture the surfaces of the pins and the discs. Since the friction is directly proportional to the contact area, the reduction in the surface contact area of the interacting surfaces is obtained through LST which plays a vital role in the reduction of friction wear. The textured patterns on the surface of the materials also act as a reservoir for the debris particles to get entrapped in them and reduce the three-body abrasion. The textured pins are tested against the textured discs using pin-on-disc tribometer. The friction and wear characteristics of the pin and the disc are determined and are compared against the untextured disc and pins. The experimental analysis of the textured surfaces established to reduce the friction and wear characteristic behaviour.

Keywords Laser surface texturing · Three particle abrasion · Pin-on-disc tribometer · Friction and wear

---

N. Sankara Manikandan · M. Prem Ananth (✉) · B. Sudarsan · A. Vishnuvarthan
Department of Mechanical Engineering, Sri Venkateswara College of Engineering, Chennai 602 117, India
e-mail: premananth@svce.ac.in

L. Poovazhagan
Department of Mechanical Engineering, Sri Sivasubramaniya Nadar College of Engineering, Chennai 603 110, India

E. T. Akinlabi et al. (eds.), *Trends in Mechanical and Biomedical Design*,
Lecture Notes in Mechanical Engineering,
https://doi.org/10.1007/978-981-15-4488-0_71

1 Introduction

Tribology mainly focuses on the reduction of friction and wear between the contacting surfaces in various applications and between various materials [1]. The tribology is aimed for friction reduction and the reduction in friction can be achieved by various methodologies which mainly includes the lubricating the contacts which are in relative motion [2]. The lubrication decreases the friction by not permitting the two surfaces that interact with each other; rather it comes in contact between both the surfaces, thus reducing the friction and wear of the materials. There are some other potential methods which are currently being practiced by many tribologists, one of which being the surface modification techniques. There are different surface modification techniques which are used to reduce the real contact area between the contacting surfaces and thereby to increase its tribological behaviour. Since the friction is directly proportional to the contact area, the reduction in the surface area reduces the friction, which resulted in the reduction in the wear rate of the components in contact. The various surface modification techniques [3] used in present days are etching, pulsed arc air treatment [4], abrasive jet machining, ECM and LST. Laser surface texturing is most widely used technology [5] because of its greater accuracy and size control. The LST is prepared on the surfaces of the materials and the predefined patterns are formed on the surface of the components. In this work, the patterns that are formed on the surface are both circular and hexagonal dimples on the disc and only circular dimples are formed on the pins. These texturing patterns are formed on the basis of calculations done which generated a texturing density of about 30%. The friction reduction is found to be maximum at the surface density of 30% [6]. The experiment is carried out on a pin-on-disc tribometer testing facility which has rotating disc and the pin made to contact with the pin along with the predefined normal load. Using the experimental apparatus, the frictional coefficient and the wear rate on the disc and the pins were calculated and reported.

2 Experimentation

2.1 Materials and Machining

The pin and the disc materials for the experiments are titanium alloy (Grade 5), cast iron and stainless steel. The titanium alloy is selected for the pin material and the cast iron and stainless steel are selected as the disc materials. Table 1 shows the constituents of the titanium alloy, cast iron and stainless steel materials used in the experiment.

The pin and the disc materials are machined according to the dimensions required for the pin-on-disc tribometer. The dimensions for the pin are 8 mm diameter and

Table 1 Composition of materials selected for the experiment

Element	Percentage by weight		
	Titanium alloy (%)	Cast iron (%)	Stainless steel (%)
Titanium	90	–	–
Aluminium	6	–	–
Vanadium	4	–	–
Carbon	<0.10	3.2–3.5	≤0.15
Oxygen	<0.20	–	–
Nitrogen	<0.05	–	–
Hydrogen	<0.0125	–	–
Iron	<0.3	93	84.3–88.5
Manganese	–	0.60–0.90	≤1.0
Phosphorous	–	0.12	≤0.040
Silicon	–	2.0–2.4	≤1.0
Sulphur	–	0.15	≤0.030
Chromium	–	–	11.5–13.5

28 mm in length, whereas the disc is machined to 8 mm thick and 165 mm diameter with holes drilled into it according to the given Fig. 1a. The various machining operations performed for the disc and pin dimensioning are cutting, turning, facing, lapping and surface grinding and the fabricated disc is shown in Fig. 1b.

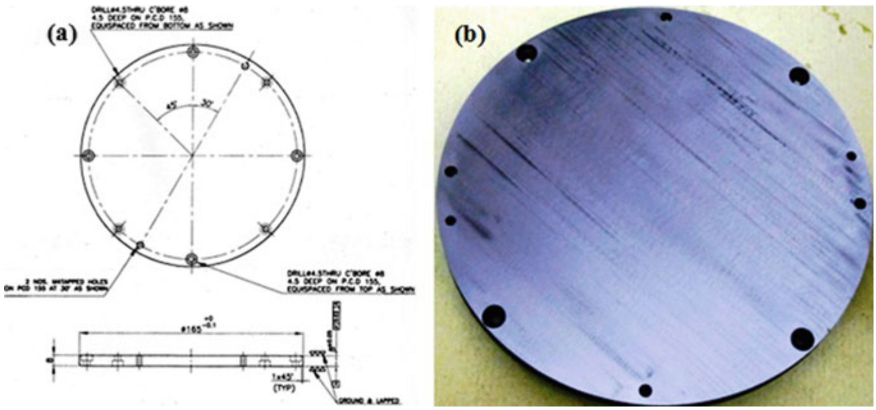

Fig. 1 **a** Disc dimensions as per ASTM standard **b** fabricated counter-body disc

3 Laser Surface Texturing

3.1 Texturing

The laser surface texturing is a laser ablation process in which the material becomes vapourized when the laser beam comes in contact with the material surface [7]. There are several texturing patterns that can be textured on the surface of the material that will help in improving tribological properties of the surfaces [8]. The laser surface texturing on the pin and disc surfaces are prepared using the laser marking system supported by EzCAD software. The EzCAD software is used to design the required patterns. The laser source is incorporated by a diode-pumped yttrium-doped fibre source. The wavelength of the laser is 1064 nm and the power used for the texturing is 20 W. The patterns that are made on the pins are circular and hexagonal dimples whereas circular dimples are engraved on the discs. The diameter of the dimple is calculated based on the required texturing density. The texturing density is taken as 30% which is having a greater reduction in friction. The diameter and pitch (distance from centre of one dimple to the centre of the other dimple) for the circular dimples are 90 μm and 140 μm, respectively, for titanium pins [9] and 50 μm and 100 μm, respectively, for the discs. The titanium alloys are also characterized to show poor wear resistance properties which can be improved by surface texturing methodologies [10, 11]. The hexagonal dimples are patterned on the pins which have a side length of 45 μm and pitch of 140 μm. Single-pulse laser beams are preferred to texture the surfaces instead of multiple overlapped pulses. In multiple overlapped pulses, the total energy exposure per unit area of the textured surface is higher than the single pulse. Single-pulse laser beams are preferred to overcome the heat cumulative effect caused by multiple overlapped pulses. Also, due to the influence of heat cumulative effect, unique structures are created and this effect is prevented by using single-beam pulse [12].

3.2 Sem Analysis

After the texturing is done, the samples are taken for SEM analysis where the textures are captured. The following images show the textures done.

Figure 2a shows the SEM image of circular dimples that are formed in the disc by laser marking system. Oxide layers are formed on the surface of the titanium pins due to interaction of the atmospheric oxygen with the free aluminium on the textured surface which is beneficial [13]. Figure 2b shows the formation of hexagonal dimples on the surface of the pin. The rectangular array patterns are formed on the pin surfaces and it is evident from Fig. 2. The textured and untextured pins are tested against the discs using the tribometer.

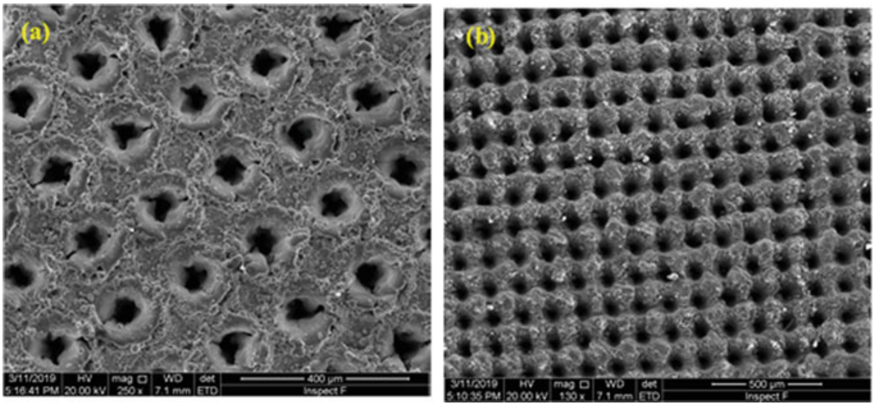

Fig. 2 SEM image of **a** circular dimples and **b** hexagonal dimples

3.3 Testing

The pins are tested against the discs using the pin-on-disc tribometer. The pin-on-disc tribometer offers uni-directional sliding motion by rotating in one direction only. The tribometer has sensors and transducer to detect parameters like force and displacement. The force sensor, which is a load cell type which measures the frictional force between the contacting surfaces, linear variable differential transducer (LVDT), to determine the wear of the pin material and a temperature sensor to acquire the temperature at the interacting surfaces. The disc and the pin are fixed on the given fixtures and the load of 25 N is applied on the pin through a horizontal lever [14]. The sliding velocity is taken as 2 m/s for the testing. The frictional force between the pin and the disc was continuously monitored and measured by using the force sensor. The wear on the disc and the pin is calculated by measuring the weight of the specimen before and after the testing. The experiment was done under constant sliding velocity conditions. In order to maintain the same sliding velocity, the rpm was varied according to the track diameter. The following Table 2 shows the list of experiments that are done and the parameters that are used for the testing.

Table 2 List of experiments

S. No.	Disc	Pin	Track diameter (mm)	Speed (rpm)
1	SS-Untextured	Untextured	50	797
2	SS-Untextured	Circular dimple	70	550
3	SS-Untextured	Hexagonal dimple	90	425
4	CI-Untextured	Untextured	50	797
5	CI-Untextured	Circular dimple	70	550
6	CI-Untextured	Hexagonal dimple	90	425
7	CI-Circular dimples	Untextured	70	550

4 Results and Discussion

The tests are successfully carried out under the given parameters and the graph is plotted for comparison of tribological properties of friction and wear. Figure 4 shows the variation of friction coefficient with respect to sliding distance. Each test is briefly discussed below.

Test 1: SS-Untextured Disc versus Untextured Pin

The above Figs. 3 and 4 show that there is a high friction between the surfaces because of the direct contact between the materials. The observed wear rate is also very high because of the three-particle abrasion mechanism. The initial wear rate is observed to be very high due to sudden contact of both the pin and the disc.

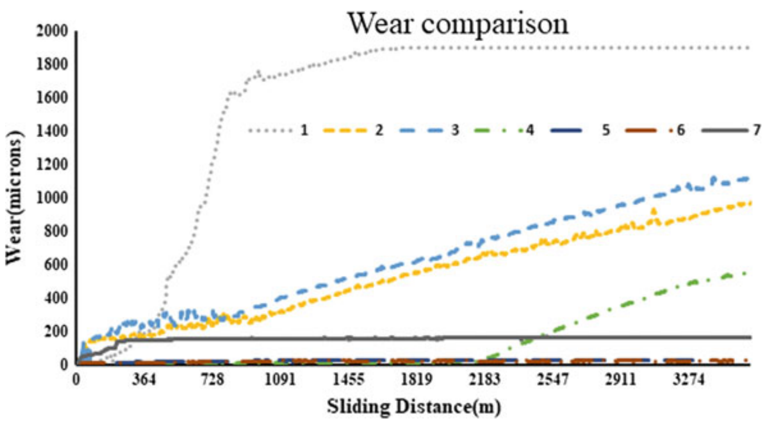

Fig. 3 Comparison of wear versus sliding distance

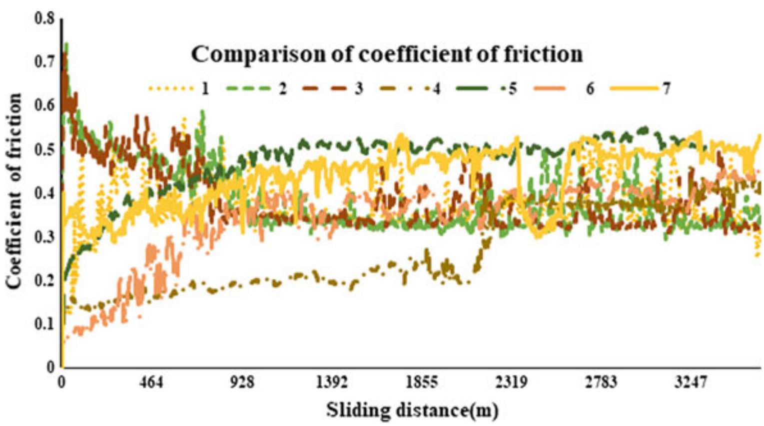

Fig. 4 Comparison of coefficient of friction for different distance

Test 2: SS-Untextured Disc versus Circular Dimple Pin
The friction and wear are reduced in this test when compared with the untextured pin which is evident from the graphs shown in Figs. 3 and 4. The textures on the pin act as a reservoir for capturing the debris particles which cause the reduction in the further wear. The reduction in friction is also reduced because of the reduction in the contact area.

Test 3: SS-Untextured Disc versus Hexagonal Dimple Pin
The test result obtained for this test yielded the same result as that of the previous test. Except for the fact that both the wear and friction coefficient for this test is less compared with that test, which can be seen from graphs shown in Fig. 3 and 4. And it can also be noted that the wear is gradual.

Test 4: CI-Untextured Disc versus Untextured Pin
The graphs obtained from the test are shown in Figs. 3 and 4 which indicate that the wear is less initially and is gradually increased. This is because both the materials are of equal in hardness. Hence, the friction as well as the wear is initially less. After a period of some time, due to the heat generated between the disc and the pin, the wear is gradually increased and because of the debris particles, the friction also got increased. The wear is less on both the disc and the pin compared to the other combinations.

Test 5: CI-Untextured Disc versus Circular Dimple Pin
The above test obtained the desired results. The wear rate is much lower compared with the other and also the friction coefficient is good. Since both the pin and the disc are hard materials, the friction is good. The cause for wear reduction being the texturing which accumulated the wear particles.

Test 6: CI-Untextured Disc versus Hexagonal Pin The wear and friction coefficient values for this test and the previous test are nearly same and the graphs seem to coincide with one other as seen in Figs. 3 and 4. This shows that the texturing pattern seems to reduce the wear and friction values. But in hexagonal dimples, friction and wear rates are much less when compared with circular dimples.

Test 7: CI-Circular Dimple Disc versus Untextured pin
Figures 3 and 4 show the graph between and wear and friction, respectively, against the sliding distance obtained from this test. It can be seen that the wear rate is very much reduced due to laser texturing. The wear particles are accumulated in the dimples made in the disc. Since the disc has a larger area, most of the wear particles are captured by it. So, there is a direct contact between the disc and the pin which accounts for higher friction. The sudden drop in the friction after certain time is because of the thermal fluctuations in the environment

All the tests listed above are experimentally carried out, and the frictional force values and the wear at a given interval of time are continuously recorded. The specific wear rate and the average coefficient of friction values are derived and plotted as the graphs in Figs. 5 and 6. Figure 5 shows that there is a major reduction in the wear rate in the textured discs and pins compared with the untextured discs and pins. Experiment 7 shows that there is a major reduction in wear rate when the disc is textured. This is because a major area of the disc is textured. Since the disc has a greater area and contact area is reduced due to texturing, the wear rate is significantly reduced.

Figure 6 shows the reduction in the coefficient of friction between the titanium alloy pins and the discs during various untextured and textured analysis. This graph shows that the friction coefficient is higher during untextured discs and pins. The specific wear rate is significantly higher for the experiments 1 and 4 when compared

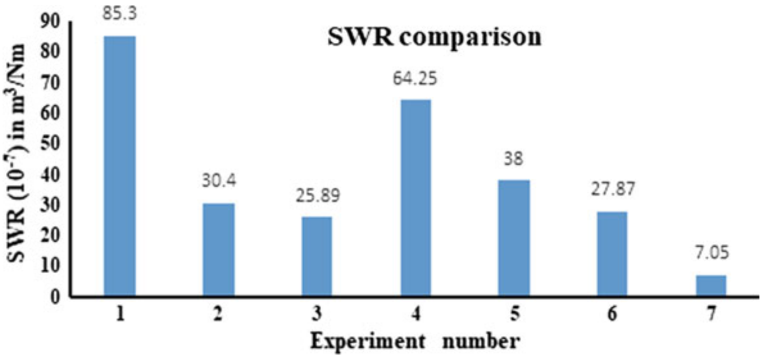

Fig. 5 Comparison of specific wear rate

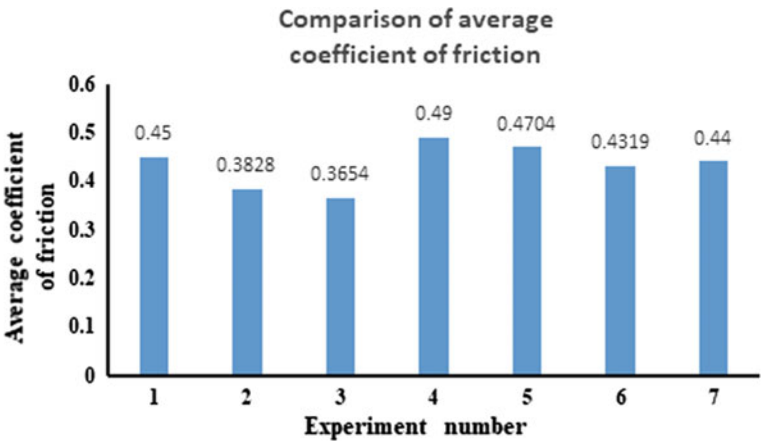

Fig. 6 Comparison of average coefficient of friction

with the rest because in those tests both the disc and the pins were untextured, which results in the increased surface contact area which directly implies on the increased three-particle abrasion. The circular and hexagonal textured dimples act as a reservoir for the debris particles generated during the contact between the disc and the pin. These debris particles, in untextured samples, come in between the disc and the pin and result in the three-particle abrasion. But they get encapsulated in these dimples. In comparison with the circular and hexagonal dimples, the hexagonal dimples have a reduced wear because of a considerable increase in the dimple area and considerably reduced surface contact area. And also it is evident that there is a higher reduction in friction as quoted in [6]. By combining the two graphs, it can be found that experiment 3 (SS UT—hexagonal dimple) has shown improved tribological properties compared with the rest of the combinations.

5 Conclusions

The above tests clearly show that the texturing has reduced the friction and wear between the interacting materials when compared with the untextured surfaces. The specific wear rate is very less for the stainless steel (untextured disc)-hexagonal dimple pin combination. It has also been found that the coefficient of friction is also low between them. This is nearly 24% reduction in friction and 36% reduction in wear when compared with the rest of the tests. Hence, the texturing has helped in the reduction of friction and wear rate. Friction is directly proportional to the contact area. The coefficient of friction obtained after the texturing and coating is reduced because of the less surface contact area between the disc and the pin material. This reduction in the surface area contributes to the major reduction in friction. The wear is directly proportional to the friction between the contacting surfaces. The wear is reduced since the friction between the surfaces is reduced due to the reduction in the contact area. The above experiments are evident for reduction in friction is due to the reduction in contact area offered by texturing. The surface texturing reduced the area by 30%, which contributed to the reduction in friction. Since the friction between the surfaces and the contact area is reduced, the wear is also reduced. The textures formed on the surfaces acted as a reservoir for the debris particles. And hence, friction and wear are reduced.

References

1. Lia L, Guob YB, Weia XT, Lib W (2013) Surface integrity characteristics in wire-EDM of inconel 718 at different discharge energy. In: 7th international symposium on electro machining, procedia CIRP, vol 6, pp 220–225
2. Hutchings IM (1992) Tribology- friction and wear of engineering materials. Edward Arnold, London
3. Totten GE (1992) ASM handbook friction, wear and lubrication technology. vol 18

4. Ibatan T, Uddina MS, Chowdhury MAK (2015) Recent development on surface texturing in enhancing tribological performance of bearing sliders. Surf Coat Technol 272:102–120
5. Moshkovitih A, Perfiiiev V, Glindin D, Parkansky N, Boxman R, Rapoport L (2007) Surface texturing using pulsed arc air treatment. Wear 253:56–77
6. Zavestovskaya I (2010) Laser nano structuring of materials surfaces. Quantum Electron 11:942–954
7. Li K, Yao Z, Hu Y, Gu W (2014) Friction and wear performance of laser peen textured surface under starved lubrication. Tribol Int 6(11):97–105
8. Etsion I (2005) State of the art in laser surface texturing. J Tribol Trans ASME 127:248–53
9. Galda L, Pawlus P, Sep J (2009) Dimples shape and distribution effect on characteristics of Stribeck curve. Tribol Int 42:1505–1512
10. Laser surface texturing of Ti6Al4V alloy, stainless steel and aluminium silicon alloy Andrzej Grabowski, Maria Sozańska, Marcin Adamiak, Mirosława Kępińskaa, Tomasz Floriand
11. PremAnanth M, Ramesh R (2014) Tribological improvement of titanium alloysurfaces through texturing and TiAlN coating. Surf Eng 30:758–762
12. Yerramareddy S, Bahadur S (1992) The effect of laser surface treatments on the tribological behavior of Ti–6Al–4V. Wear 157:245–262
13. Weber R, Graf T, Berger P, Onuseit V, Wiedenmann M, Freitag Ch, Feuer A (2014) Heat accumulation during pulsed laser materials processing. Opt Express 22:11313
14. Basiaga M, Kajzer W, Walke W, Kajzer A, Kaczmarek M (2016) Evaluation of physicochemical properties of surface modified Ti6Al4V and Ti6Al7Nb alloys used for orthopaedic implants. Mater Sci Eng C 68:851–860

Tribological Study on Sliding Contact Between Laser Surface Textured Titanium and Aluminium Alloy Under Lubrication

Ramesh Rajesh, M. Prem Ananth, Sangam Harish, Sakthivel Balaji, and R. Sivaguru

Abstract The friction plays a major role whenever two surfaces come into contact. The friction is a major factor which affects the efficiency of a working component. The life of the component depends on the wear it undergoes during working. This wear is directly related to the friction that is produced between the surfaces. It is impossible to completely avoid friction. But it is possible to reduce the friction between the contact surfaces by various methods. One of the most promising methods in recent days is the laser surface texturing. There are various developments currently being done in the LST. It is done by altering the various parameters of the textures. Some of the parameters include the pattern, depth, diameter, pitch and so on. In our tribological study, a pin-on-disc tribometer is used to determine the friction and the wear between the components made of Ti-6Al-4V and AA7075 alloys under liquid lubrication condition. For improving the tribological characteristics of the contacting pairs, laser surface texturing is performed on both pin and disc surfaces. The laser surface texturing concept is implemented to create micro-dimples on the contact surface which the dimples act as a reservoir for the lubricant enhancing lubrication to reduce the coefficient of friction, the coating material to improve its bonding characteristics, wear debris to get accumulated. The desired dimple parameters are chosen for the laser surface texturing. The laser surface texturing followed by a surface treatment has improved the wear-resisting performance of the contact surfaces.

Keywords Micro-dimples · Ti-6Al-4 V · Pin-on-disc · Coefficient of friction and wear debris

R. Rajesh · M. Prem Ananth (✉) · S. Harish · S. Balaji · R. Sivaguru
Department of Mechanical Engineering, Sri Venkateswara College of Engineering, Sriperumbudur, Kancheepuram, Tamil Nadu 602117, India
e-mail: premananth@svce.ac.in

E. T. Akinlabi et al. (eds.), *Trends in Mechanical and Biomedical Design*, Lecture Notes in Mechanical Engineering,
https://doi.org/10.1007/978-981-15-4488-0_72

1 Introduction

The aluminium alloys and titanium alloys (Ti-6Al-4V) are extensively used in modern industries due to its high strength–weight ratio and excellent corrosion resistance which led to a comprehensive and expanded range of applications, especially in the aerospace and automotive industries. Since the titanium and aluminium alloys are used for high optimum operations, the tribology characteristics such as friction and wear play an important role in the relative sliding contact between AA7075 and Ti-6Al-4V. As the titanium alloy is low in wear resistance and possesses high coefficient of friction, engineering components made from the same seek improvement in wear resistance and friction coefficient. It is necessary and important to attempt for improving wear resistance performance and to reduce friction [1]. These problems can be overcome by changing the nature of the surface of titanium and titanium alloys using thermo-chemical treatments such as nitriding. The surface is changed from titanium to a hard compound of titanium. Gas and plasma nitriding are among the most widely used thermo-chemical treatments for improving the surface properties of titanium alloys [2]. Among several surface engineering techniques, laser surface texturing (LST) is adopted to improve the tribological characterization of the contact. LST is used to create patterned micro-dimples on the surface of the materials which can improve load capacity, wear rates and lubrication and reduce friction coefficients. The micro-dimples on the contact surfaces act as a reservoir for the lubricant enhancing lubrication performance to reduce the coefficient of friction, the nitriding process to improve its bonding characteristics, the wear debris to get trapped in the micro-reservoir during the relative motion between the two contact surfaces. The patterned geometry permits for countless miniature lubricant reservoirs, providing direct and immediate lubricant relief for starved areas [3]. However, it was observed that LST may be deleterious to tribological performance under starved lubrication conditions when the dimples are relatively deep or when the oil viscosity is relatively high [4]. During the nitriding process, the micro-dimples act as fins creating more exposure area to the surface for the nitriding process which permits the ammonia particles to deposit on the micro-reservoirs.

2 Materials

2.1 Pin and Disc

The materials Ti-6Al-4V and AA7075 are selected as pin and disc, respectively, because they are finding more applications in the industry in recent days because of the mentioned properties. The specific composition of these components is mentioned in Table 1. The EDS analysis of textured Ti-6Al-4V surface is shown in Fig. 1 which

Table 1 Composition of material

Element	Ti-6Al-4V	AA7075
Titanium	90%	<0.2
Aluminium	6%	87.1–91.4%
Vanadium	4%	–
Carbon	<0.10%	–
Oxygen	<0.20%	–
Nitrogen	<0.05%	–
Hydrogen	<0.0125%	–
Iron	<0.3%	<0.5%
Chromium	–	0.18–0.28%
Copper	–	1.2–2%
Magnesium	–	2.1–2.9%
Manganese	–	<0.3%
Silicon	–	<0.4%
Zinc	–	5.1–6.1%

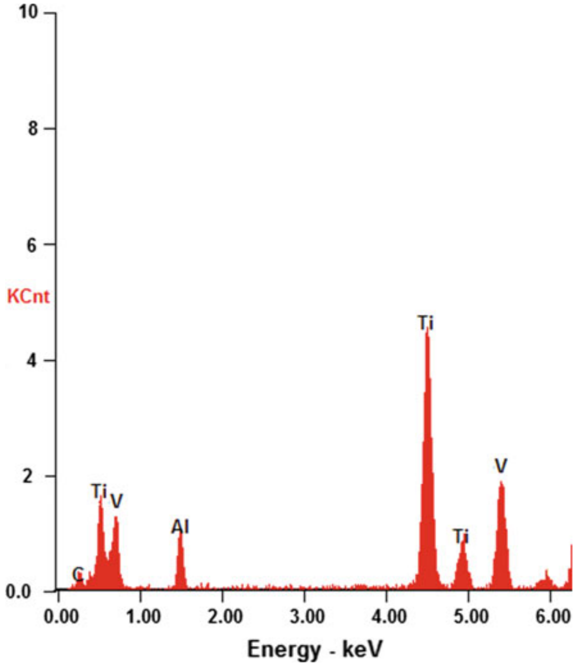

Fig. 1 EDS analysis of Ti-6Al-4V textured surface

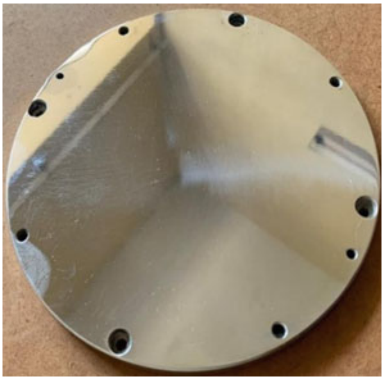

Fig. 2 Untextured lapped AA7075 disc

confirms the major composition of Ti, Al and V present in the pin material. The AA7075 and Ti-6Al-4V contact pair have been used extensively in aerospace and automotive applications. For instance, in high-speed racing car engines and aerospace engines, this AA7075 and Ti-6Al-4V contact pair is employed in cam and follower, in which AA7075 is used as cam and Ti-6Al-4V is used as a follower. Since the follower experiences the constant load at a point at any instance and the cam experiences a cyclic load at a point in periods, AA7075 is chosen as disc and Ti-6Al-4V is chosen as pin.

According to the ASTM standards for the pin-on-disc test, pin acts as the target or the test. Friction and wear properties are studied for the pin materials extensively. The pin is machined of 8-mm diameter and 28-mm length. The disc is machined of 165-mm diameter and 8-mm thickness, and its macro-image is shown in Fig. 2. The weight of the pins before and after the testing is measured to calculate the specific wear rate (SWR).

2.2 Lubricant

In most of the moving components, a lubricant is used to reduce the friction, reduce the heat generated during the operation and also carry the debris from the interacting surfaces. Hence to simulate a real-time working condition, a lubricant is chosen. The oil 10 W-40 has been chosen for the lubrication due to high and maximum performance, high viscosity index, high dirt dispensing capacity, excellent cleaning capacity and high thermal stability. Since the lubricant has the above properties, it is used when the test is run on the tribometer. The properties of the lubricant are provided in Table 2.

Table 2 Properties of lubricant

Density	827 kg/m^3
Kinematic viscosity @100 °F	15.4 cSt
Viscosity index	149
Flashpoint	220 °C
Pour point	33 °C

3 Experimental Procedure

The pin and disc which are to be tested in pin-on-disc tribometer are machined with respect to the specifications of the tribometer. The machined pins and discs are grinded and lapped to achieve low roughness coefficient. The laser surface texturing process is carried out on both pin and disc to obtain designed dimple geometry on the surface of the specimens. After laser surface texturing, the pins and discs are washed by using acetone to remove any debris on the surface of the specimens. The specimens were kept immersed for about 10 min to remove all dust, grease and oxides formed on the surface as any impurities will cause effect on experiment results [5, 6]. Then, the pins and discs are placed in a clean environment and kept ready to run experiments on the tribometer. The weight of the pins before and after testing is measured to calculate the specific wear rate for every experiment.

4 Laser Surface Texturing

The surface of the machined and processed discs and pins is textured using the laser marking system. There are several parameters to be determined before marking. Some of the parameters include texture density, dimple diameters, dimple structure, dimple pattern, dimple depth and pitch [6–8].

Type of laser used: Nd:YAG, power: 20 W.

The density of the texturing is arbitrarily chosen as 30% for study. For the study, circular dimple having a hemispherical bottom is chosen for analysis. The diameter and pitch are calculated. The dimpled surface topography is used for lubricant storage, and the dimple area percentage is used as a variable parameter to express dimple availability (1) [9–11]:

$$D - \text{area} = \pi(d/2p)2 \times 100\% \tag{1}$$

where d is the diameter of the dimple and p is the pitch of the dimple. The dimple geometry for different dimple diameters of 30% D-area has been calculated and given in Table 3.

The above texturing patterns are designed using the AutoCAD software and are fed into the EZCAD software. Figures 3 and 4 show the pattern made using the

Table 3 Dimple geometry

D-area %	$D,\ 10^{-6}\ \text{m}$	$p,\ 10^{-6}\ \text{m}$	Area, $10^{-12}\ \text{m}^2$	Closest distance between the circumference of adjacent circular dimples, $10^{-6}\ \text{m}$
30	150	242.752078	17,678.5714	92.75207811
30	120	194.201662	11,314.2857	74.20166249
30	90	145.651247	6364.28571	55.65124687

Fig. 3 CAD diagram of textured surface on pin

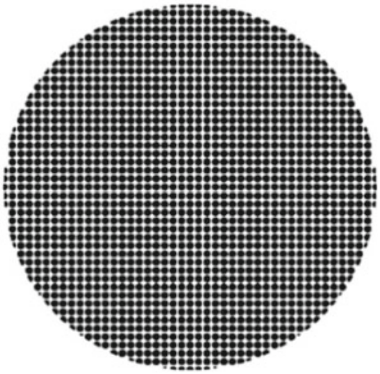

Fig. 4 CAD diagram of dimple pattern

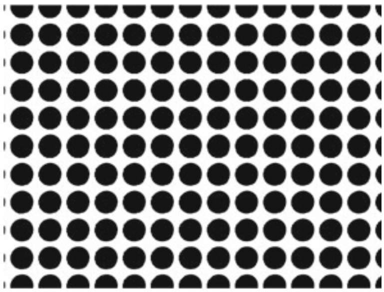

AutoCAD software. The patterned disc and pin are then analysed under scanning electron microscope, and the image is captured.

Figures 5 and 6 show the SEM images obtained after the texturing. The images show that the dimples are formed as a rectangular array. It can also be noted from the above images that the debris formed during the laser ablation process is aggregated near the formed dimples. The debris formed is cleaned using acetone.

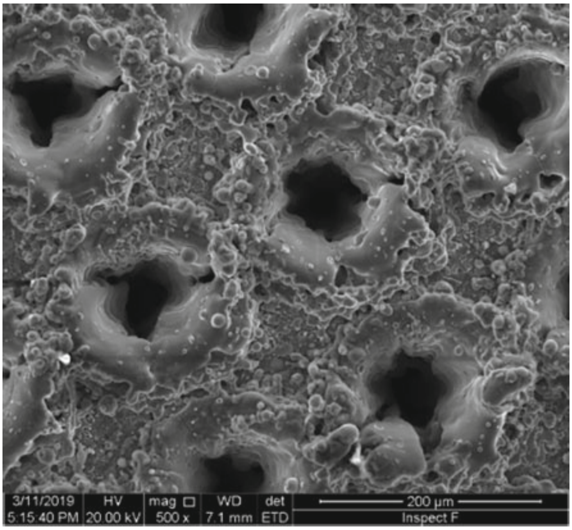

Fig. 5 500× zoom SEM image of textured pattern

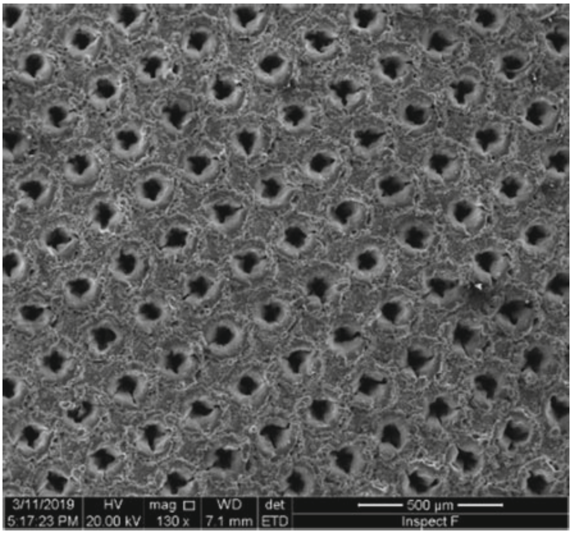

Fig. 6 130× zoom SEM image of textured pattern

5 Pin-on-Disc Tribometer

The apparatus consists of a pin that is pressured against a rotating disc. According to the Society for Testing and Materials (ASTM), the standards that can be used for the pin and disc are ASTM G99, 2003. It allows the wear qualification by both geometry and mass loss methods. The coefficient of friction is calculated by measuring the tangential force acting on the specimen.

Table 4 Specifications of pin-on-disc tribometer

Parameter	Range
Pin diameter	8–12 mm
Disc size	165 mm dia
Disc thickness	8 mm
Disc rotation	Up to 2000 rpm
Normal load	Up to 200 N
Wear	2000×10^{-3} mm

The pin-on-disc tribometer used for conducting the experiments is the Ducom TR 20L. The Ducom wear and friction monitor TR 20LT records friction and wear in low-temperature conditions using the LVDT and strain gauge. The Ducom wear and friction monitor TR 20L is particularly designed for wear and friction characterization in low-temperature conditions. This instrument consists of a rotating disc against which a test ball is pressed with a known force. A provision for measurement of compound wear and frictional force is provided.

The TR 20LT series comes with WinDucom software for data acquisition and display of results. WinDucom software is used to present data in a variety of ways and compare view provides a powerful tool to view and compare test results. Table 4 shows the specifications of the tribometer used for the analysis.

6 Testing

The surface roughness was measured randomly in four regions on each surface for the 4-mm stroke length using Mitutoyo SJ-430 surface roughness tester, and the average surface roughness (Ra) was calculated.

Table 5 shows the surface roughness of the pins after various surface modifications. Table 5 shows the experiments done using the pin-on-disc tribometer.

Table 5 Surface roughness test on pins and discs

Material	Surface roughness, R_a 10^{-6} m
Untextured Ti-6Al-4V pin	0.87
Textured Ti-6Al-4V pin	13.09
Untextured nitrided Ti-6Al-4V pin	1.00
Textured nitrided Ti-6Al-4V pin	16.65
Untextured lapped AA7075 disc	0.09
Textured AA7075 disc	8.82

Table 6 List of experiments

Exp. No.	Ti-6Al-4V pin	AA7075 disc	Test timing (min)	Track diameter (m)	Speed (rpm)
1	Untextured	Untextured	30	0.105	571
2	Textured	Untextured	30	0.085	706
3	Untextured nitrided	Untextured	30	0.065	923
4	Textured nitrided	Untextured	30	0.045	1333
5	Untextured	Textured	30	0.105	571
6	Textured	Textured	30	0.085	706
7	Untextured nitrided	Textured	30	0.065	923
8	Textured nitrided	Textured	30	0.045	1333

The gas nitriding process on Ti-6Al-4V pins has reduced the surface roughness of the textured surface of the disc which is evident from the table. The reduction in the surface roughness on the textured surfaces is due to accumulation of ammonia particles from gas nitriding process in the dimples which act as micro-reservoirs.

Table 6 shows the list of experiments, combinations of a different surface engineered pin and disc and its parameters. All the experiments are tested with constant sliding velocity = 3.14 m/s, and load on pin is 50 N.

7 Result and Discussion

Various tests discussed above are experimentally carried out, and the results of each test are briefly discussed below.

Figure 7 shows a graphical representation which explains the frictional behaviour of various combinations of a different surface engineered pin and disc.

Figure 8 shows a graphical representation which explains the wear behaviour of various combinations of a different surface engineered pin and disc.

Experiment No. 1 Untextured Ti-6Al-4V PIN Versus Untextured AA-7075 DISC

Both the pin and the disc were untextured, and hence this resulted in the high friction between them. But there is high wear in the pin which is undesirable. The wear rate is high during the initial stages of the testing, whereas it got stable during the later period of the test. This is due to the total surface contact between the disc and the pin. The major cause for the high wear is the third particle abrasion, where the debris particle from the direct abrasion stays in between the disc and the pin and causes more wear. The average coefficient of friction is 0.056276.

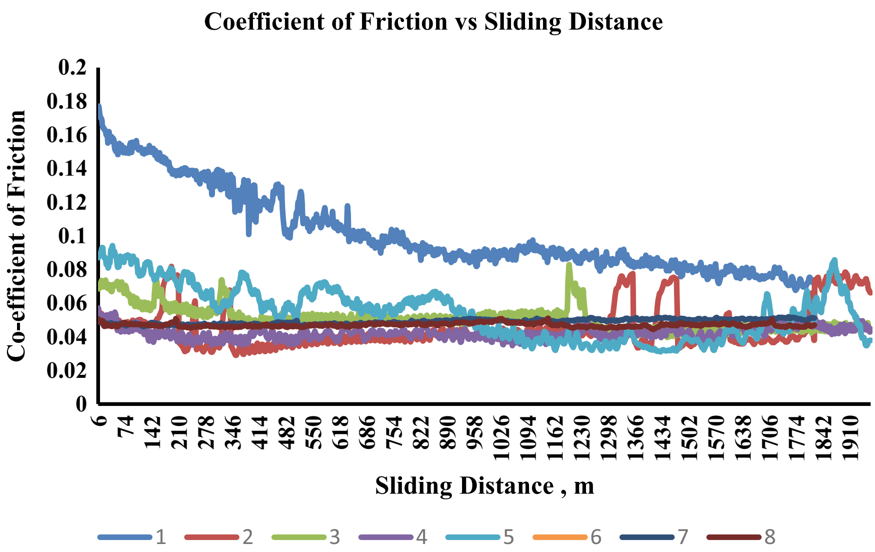

Fig. 7 Frictional force versus sliding distance

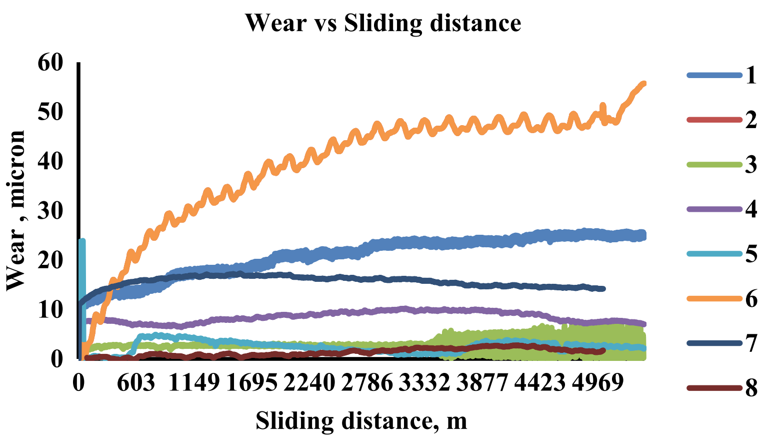

Fig. 8 Wear versus sliding distance

Experiment No. 2 Textured Ti-6Al-4V PIN Versus Untextured AA-7075 DISC

The laser surface textured Ti-6Al-4V pin is tested against the untextured lapped AA7075 disc in lubrication. The experiment resulted in a reduced coefficient of friction and improved wear which is evident from the graph. This is due to laser surface texturing at the surface of the pin in which the third particle abrasion by debris is reduced as the debris was trapped in the micro-reservoirs resulting in a weight gain in the pin after the testing. The average coefficient of friction is 0.043726.

Experiment No. 3 Untextured Nitrided Ti-6Al-4V PIN Versus Untextured AA-7075 DISC

The untextured nitrided Ti-6Al-4V pin is tested against the untextured lapped AA7075 disc in lubrication. On comparing the results from experiment no. 1, this experiment shows better results in terms of less coefficient friction and improved wear. This is due to the thermal surface treatment of gas nitriding. The average coefficient of friction is 0.042272.

Experiment No. 4 Textured Nitrided Ti-6Al-4V PIN Versus Untextured AA-7075 DISC

The laser surface textured nitrided Ti-6Al-4V pin is tested against the untextured lapped AA7075 disc in lubrication. Both coefficient of friction and wear obtained during this were low and appreciable. This is due to the combined effect of LST and gas nitriding. The third particle abrasion by debris is reduced as the debris was trapped in the micro-reservoirs resulting in a weight gain in the pin after the testing. The average coefficient of friction is 0.039753.

Experiment No. 5 Untextured Ti-6Al-4V PIN Versus Textured AA-7075 DISC

The untextured Ti-6Al-4V pin is tested against the laser surface textured AA7075 disc in lubrication. Due to the absence of nitriding, the friction was observed to be moderate and low wear due to laser surface texturing on the disc. The average coefficient of friction is 0.048982.

Experiment No. 6 Textured TI-6AL-4V PIN Versus Textured AA-7075 DISC

The textured Ti-6Al-4V pin is tested against laser surface textured AA7075 disc in lubrication. From the line graph, it experiences high wear which is not appreciable. This is due to absence of nitriding effect in the pin as it was pressured against textured surface which has high roughness. The third particle abrasion by debris is reduced as the debris was trapped in the micro-reservoirs resulting in a weight gain in the pin after the testing. The average coefficient of friction is 0.047006.

Experiment No. 7 Untextured Nitrided TI-6AL-4V PIN Versus Textured AA-7075 DISC

The untextured nitrided Ti-6Al-4V pin is made to test against textured AA7075 disc. The nitrided Ti-6Al-4V pin possesses low coefficient friction. Due to the texturing on the surface of the disc, the contact area was reduced resulting in moderate wear on the pin. The average coefficient of friction is 0.042964.

Experiment No. 8 Textured Nitrided TI-6AL-4V PIN Versus Textured AA-7075 DISC.

The combination of laser surface textured nitrided pin and textured AA7075 disc resulted in least coefficient of friction and good improved wear. This is due to the combined effect of nitriding and texturing done on both the surfaces. The third particle abrasion by debris is reduced as the debris was trapped in the micro-reservoirs resulting in a weight gain in the pin after the testing. The average coefficient of friction is 0.034296.

The coefficient of friction at contact between pin and disc for all experiments has been observed.

From Fig. 9, it can be inferred that the LST and gas nitriding have improved the tribological properties. The experiment no. 8 (textured nitrided pin versus textured disc) has the least coefficient of friction.

The specific wear rate for all the experiments has been calculated and reported in Fig. 10. From the bar chart, it can be inferred that the bars in the negative section correspond to the weight loss of the pin after the experiment whereas bars in the positive sections correspond to the weight gained by the pin after the experiment.

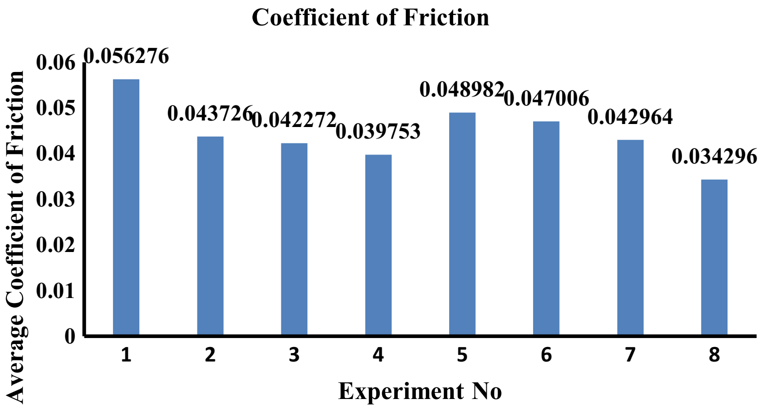

Fig. 9 Coefficient of friction at contact for all experiments

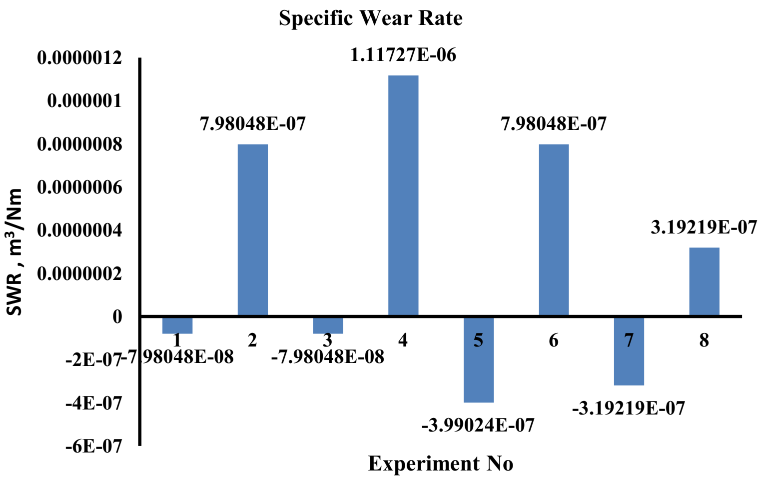

Fig. 10 Specific wear rate of pins for all experiments

8 Conclusion

The experiments are conducted and studied to understand the tribological characteristics of various combinations of the selected materials with and without texturing. The wear and frictional properties of the Ti-6Al-4V have been improved drastically after the gas nitriding process. The dimples created on the discs enhance the effect of lubrication and significantly reduce the coefficient of friction. Since the friction between the surfaces is reduced due to the reduction in the contact area, the wear is also reduced. The laser surface texturing reduces the area by 30% which contributes to a reduction in friction. It is observed that there has been some gain in weight of textured pins after the pin-on-disc experiment which ensures deposition of debris in the dimples of the pin from the disc particles. This characterization prevents impurification of lubricating oil by the debris enhancing the service life of the components in their applications.

Out of 8 conducted experiments, the experiment no. 8 is chosen as the best combination in which the friction has been reduced by 39% and resistance improved. Hence, laser surface textured AA7075 and laser surface textured nitrided Ti-6Al-4V pair is suggested for the real-time engineering applications.

Acknowledgements This work was supported by the All India Council for Technical Education (AICTE) under the Scheme of Research Promotion Scheme (RPS) with a reference number of File No.8-50/RFID/RPS/POLICY-1/2016-17. We would like to acknowledge them for the financial and technical support.

References

1. Muthuvel PA, Rajagopal R (2013) Influence of surface texture on tribological performance of AlCrN nanocomposite coated titanium alloy surfaces. J Eng Tribol 227(10):1157–1164
2. Zhecheva S, Sha WM (2006) Titanium alloys after surface gas nitriding. Surf Coat Technol 201(6):4
3. Erdemir DA (2008) Tribology of diamond-like carbon films (Chapter 3). In: Laser processing. Springer, New York
4. Kovalchenko A, Ajayi O, Erdemir A, Fenske G, Etsion I (2005) The effect of laser surface texturing on transitions in lubrication regimes during unidirectional sliding contact. Tribol Int 38(3):219–225
5. Prem Ananth M, Ramesh R (2014) Tribological improvement of titanium alloy surfaces through texturing and TiAlN coating. Surf Eng 30(10):758–762
6. Ananth MP, Ramesh R (2017) Sliding wear characteristics of solid lubricant coating on titanium alloy surface modified by laser texturing and ternary hard coatings. Trans Nonferrous Met Soc China 27(4):839–847
7. Mishra A (2014) Analysis of friction and wear of titanium alloys. Int J od Mech Eng Robot Res 3
8. Vilhena LM, Sedlaček M, Podgornik B, Vižintin J, Babnik A, Možina J (2009) Surface texturing by pulsed Nd: YAG laser. Tribol Int 42(10):1496–1504
9. Voevodin AA, Zabinski JS (2006) Laser surface texturing for adaptive solid lubrication. Wear J 261:11–12

10. Borghi A, Gualtieri E, Marchetto D, Moretti L, Valeri S (2008) Tribological effects of surface texturing on nitriding steel for high-performance engine applications. Wear J 265(7–8):1046–1051
11. Quazi MM, Fazal MA, Haseeb AS, Yusof F, Masjuki HH, Arslan A (2015) Laser-based surface modifications of aluminum and its alloys. Crit Rev Solid State Mater Sci J

Some Studies on Surface Roughness of AISI 304 Austenitic Stainless Steel in Dry Turning Operation

D. Philip Selvaraj and P. Richard Philip

Abstract In this paper, the input variables of turning process of AISI 304 stainless steel are optimized by employing the Taguchi method under dry machining conditions. The dry turning operations are conducted at three levels of depth of cut, cutting velocity, and feed. The test results are evaluated by employing S/N ratio and ANOVA. It is revealed that the depth, cutting speed, and feed are the important input variables affecting the quality of the machined surface. The optimum surface finish is attained at the combination of lower depth, lower feed, and higher cutting speed.

Keywords Austenitic stainless steel · Dry turning · Taguchi's method · Optimization · Surface finish

1 Introduction

Stainless steels (SSs) contain at least 10.5% chromium (Cr) by weight in order to have corrosion resistance. Generally, austenitic stainless steels (ASSs) have at least 16% chromium and small amount of nickel and/or manganese. The usage of ASS alloy is higher compared with other stainless steel alloys. They possess face-centered-cubic (FCC) microstructure. They have good formability, weldability, and higher toughness. ASS is employed for making cooking utensils, architectural applications, containers, equipment for food industries, heat exchangers, and surgical implants [1].

Surface finish is an important factor needed by the production engineers to the effective working of the machine elements. It is required for production engineers to obtain required surface roughness on the machine components. R_a is widely employed parameter for surface roughness evaluation in machine tool industries. Various reasons for surface roughness are machine tool vibration, tool feed marks,

D. Philip Selvaraj (✉)
Karunya Institute of Technology and Sciences, Coimbatore 641114, India
e-mail: de_philip@rediffmail.com

P. Richard Philip
Karpagam College of Engineering, Coimbatore, Tamil Nadu 641032, India

E. T. Akinlabi et al. (eds.), *Trends in Mechanical and Biomedical Design*,
Lecture Notes in Mechanical Engineering,
https://doi.org/10.1007/978-981-15-4488-0_73

and formation of built up edge [2]. In the past few decades, CNC machines are replacing conventional machine tools in the industries due to more productivity, better accuracy, and reduction in rejection rate [2, 3].

Kulkarni et al. [4] analyzed the influences of input cutting variables on surface roughness and machining force of 304 SS while turning by employing carbide tool inserts coated with AlTiCrN. They found that optimal surface finish was attained in the range of cutting velocity from 200 to 320 m/min and feed between 0.08 and 0.2 mm/rev. Asilturk et al. [5] found out optimum machining condition for surface finish while turning 304 SS in CNC lathe using the Taguchi technique and RSM. They concluded that the most dominant variable for the machined surface quality is feed. Selvaraj et al. [6] evaluated the influence of cutting variables on the surface quality of 304 ASS by applying the Taguchi technique in turning process in center lathe. They employed ANOVA and S/N ratio analysis to determine the optimum cutting variables, which improve the surface finish in turning process. Ciftci [7] conducted turning experiments of two different alloys of ASSs using carbide tools. The machining processes were carried out at 4 different values of cutting speeds, constant value of depth and feed. The influences of coating of the tool inserts and cutting speed on the surface finish were analyzed. They determined that surface finish was increased with increasing cutting speed. The optimal cutting parameters for turning process of 304 SS were investigated by Ihsan Korkut et al. [8]. Increase of cutting velocity decreased the surface roughness while turning 304 SS. Xavior et al. [9] examined the application of coolant oils and their influence on surface finish in turning operation of ASS by employing carbide cutting tools. They concluded that the application of coconut oil improved the surface finish of ASS. Kaladhar et al. [10] carried turning tests to optimize surface finish of 304 SS on CNC turning center by employing CVD-coated tool inserts. They found that cutting velocity, feed, depth, and nose radius influencing the surface roughness by 46%, 17%, 13%, and 24%, respectively. They found that the cutting velocity is the most important parameter and the depth is the least important variable in controlling the surface roughness.

The Taguchi method is commonly employed for optimizing the machining operations [11]. Several researchers used the Taguchi techniques for optimizing the surface finish of various materials in different cutting processes [11–15]. Dry turning process is the method of turning without employing cutting fluids. Dry machining eliminates coolant and disposal costs. It eliminates the harmful effects of cutting fluid on the operator's health. It improves the environmental conditions of the workplace which leads to cleaner production and green manufacturing.

So, in the current work, the influences of turning process variables on surface finish of 304 ASS during dry turning process in CNC lathe are analyzed by applying the Taguchi technique.

2 Experimental Details

The material used for the research work is 304 SS cylindrical rod of diameter 40 mm and length 120 mm. Table 1 gives the composition of the 304 SS alloy. Batliboi make CNC lathe was used for conducting the turning tests. The spindle speed range available in the CNC lathe is from 40 to 4000 rpm and power rating is 16 KVA. The specification of the carbide turning tool inserts used is WNMG 06T304 MP TT8020. The tool holder specification is MWLNR 2020 K 06 W (ISCAR make). Mitutoyo makes SJ-210 roughness tester which was used for measuring the surface finish. Cutting fluid was not used during the turning tests (dry turning). Figures 1 and 2 show the experimental setup and surface finish measurement photographs.

In order to choose an appropriate orthogonal array (OA) for the tests, the number of degree of freedom (DOF) for the experiments is to be calculated. A 3-level variable has two DOF. The interaction effects are not considered in the current work. Hence, the number of DOF for three machining variables is six. The selection of the OA is based on the condition that the DOF for the OA must be greater than or equal to the DOF of the machining parameters. In the current work, an L9 OA with 9 rows and 3 columns is employed. This OA has 8 DOF and can analyze 3 factors and 3-level experiments. The DOF of OA is greater than the DOF of process variables. Hence,

Table 1 Chemical composition of 304 SS

Element	wt%
C	0.067
Si	0.64
Mn	1.60
S	0.023
P	0.025
Cr	19.12
Ni	9.06
Fe	Balance

Fig. 1 CNC machine setup

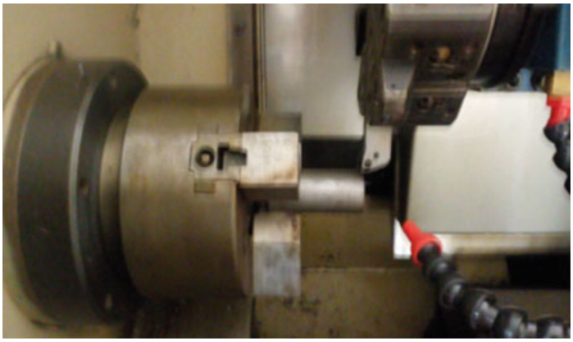

Fig. 2 Photograph of the surface roughness measurement

Table 2 Levels of machining variables used in turning process

1 Machining variables	Level 1	Level 2	Level 3
Cutting speed, V (m/min)	120	160	200
Feed, F (mm/rev)	0.05	0.10	0.15
Depth, D (mm)	0.50	0.75	1.00

L9 OA is selected for the current work. Only nine tests are required to analyze the entire machining variables using this array. Hence, experimental cost and time are saved.

The input machining variables employed in this investigation are depth, feed, and cutting speed. Three levels of cutting velocity (200, 160, and 120 m/min), feed rates (0.15, 0.10, and 0.05 mm/rev), and depth of cuts (1.0, 0.75 and 0.5 mm) are used for turning the AISI 304 SS cylindrical rods. Table 2 shows the levels of machining variables employed in the dry turning operation. The plan of experiment using L9 OA is shown in Table 3.

3 Results and Discussion

The test results are examined using ANOVA and S/N ratio. Minitab software is employed for the analysis of the results. The ratio of mean and standard deviation is defined as S/N ratio (η). Equation (1) reported by Yang et al. [11] is used to calculate η.

$$\eta = -10\log(\text{M.S.D}) \tag{1}$$

In Eq. 1, M.S.D represents the mean square deviation.

Table 3 Plan of experiment using L9 orthogonal array

S. No.	Levels of cutting parameters		
	V	F	D
1	1	1	1
2	1	2	2
3	1	3	3
4	2	1	2
5	2	2	3
6	2	3	1
7	3	1	3
8	3	2	1
9	3	3	2

The quality category, lower-the-better should be used to attain the optimum surface roughness. Equation (2) is used to calculate M.S.D. for surface roughness [11].

$$\text{M.S.D} = \frac{1}{m}\sum_{i=1}^{m} S_i^2 \tag{2}$$

In Eq. 2, m indicates the number of experiments and S_i indicates the R_a value of ith experiment.

Table 4 gives the test results of R_a and their S/N ratio for AISI 304 ASS. The mean S/N ratio of level 1 cutting velocity is the mean of S/N ratios of tests 1, 2, and 3. The mean of S/N ratios of tests 1, 4, and 7 gives the mean S/N ratio at level 1 feed. The mean of S/N ratios of tests 1, 6, and 8 gives the mean S/N ratio at level 1 depth. The mean S/N ratio for depth, feed, and cutting velocity at second and third levels

Table 4 Test results for R_a and S/N ratio

S. No.	Levels of cutting parameters			Ra	η
	V	F	D		
1	1	1	1	0.80	1.9382
2	1	2	2	0.98	0.1754
3	1	3	3	1.26	−2.0074
4	2	1	2	0.65	3.7417
5	2	2	3	0.83	1.6184
6	2	3	1	0.78	2.1581
7	3	1	3	0.60	4.4369
8	3	2	1	0.55	5.1927
9	3	3	2	0.71	2.9748

Table 5 S/N response table for R_a

Machining parameter	Cutting parameters level			Max-Min
	Level 1	Level 2	Level 3	
V	0.0354	2.506067	4.201467	4.1660667
F	3.372267	2.328833	1.041833	2.3304333
D	3.096333	2.2973	1.3493	1.7470333

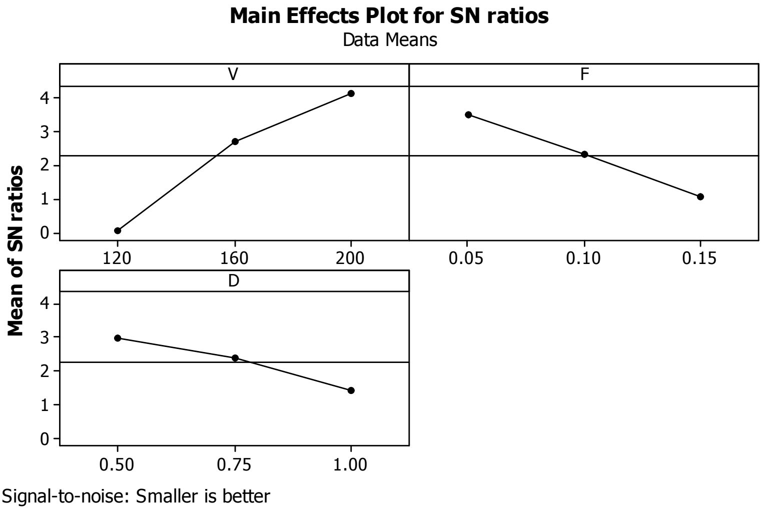

Fig. 3 S/N response graph for R_a

is calculated in a similar method. The surface roughness S/N response table of AISI 304 ASS is given in Table 5.

Figure 3 illustrates the average S/N response graph for the surface finish of AISI 304 ASS. In Fig. 2, V_1, V_2, and V_3 represent the cutting velocity at level 1, 2, and 3, respectively. F_1, F_2, and F_3 represent the feed at level 1, 2, and 3, respectively. D_1, D_2, and D_3 represent the depth at level 1, 2, and 3, respectively. The larger S/N ratio gives the minimum variance of the response about the desirable value. The larger S/N ratio for surface finish of 304 ASS is achieved at level 3 cutting velocity, level 1 depth, and level 1 feed. Therefore, the optimal cutting variables for surface finish of 304 ASS are 0.5 mm depth, 0.05 mm/rev feed, and 200 m/min cutting velocity.

ANOVA is used to find the turning process variables, which influence the output parameter significantly. Equation (3) given by Yang et al. [11] is used to determine total sum of squared deviations (SS_T).

$$SS_T = \sum_{i=1}^{n} (\eta_i - \eta_m)^2 \tag{3}$$

Table 6 Results of ANOVA for R_a

Machining variable	DOF	Sum of squares	Mean square	F-Ratio	Percentage influence
V	2	26.3338	13.1669	950.6787	67.30443
F	2	8.1758	4.0879	295.1552	20.89587
D	2	4.5891	2.29455	165.6715	11.72891
Error	2	0.0277	0.01385		0.070796
Total	8	39.1264			100

Here, n indicates a number of tests, η_i indicates an average S/N ratio for ith test, and total average S/N ratio is indicated by $\eta_{m.}$

The SS_T consists of two sources. One is sum of the squared deviations (SS_d) corresponding to each input variable and the other one is sum of the squared deviations due to error (SS_e). Table 6 gives the results of ANOVA for R_a of AISI 304 ASS.

From Table 6, it is revealed that the most influential variable for surface finish is cutting velocity. The cutting variables influencing the surface finish are in the order of cutting velocity followed by feed and then depth. The ANOVA table indicated that depth, feed, and cutting velocity are influencing the surface finish of AISI 304 ASS by approximately 12%, 21%, and 67%, respectively. It is revealed that the cutting velocity is the most important variable and the depth of cut is the least dominant variable in controlling the surface finish. The results are agreed with the results reported by Kaladhar et al. [10].

Confirmation experiment is conducted at optimum cutting conditions (d = 0.5 mm, f = 0.05 mm/rev, and V = 200 m/min). The estimated S/N ratio $\left(\hat{\eta}\right)$ is employed to predict and check the output parameter at the optimum level. Value of $\hat{\eta}$ at the optimum level of the cutting variables can be determined by employing the Eq. (4) [11].

$$\hat{\eta} = \eta_m + \sum_{i=1}^{o} (\bar{\eta}_i - \eta_m) \tag{4}$$

Here, "o" is the number of cutting variables that influence the response.

The surface finish value at the optimum machining conditions was calculated by using the Eqs. (1), (2), and (4). Predicted and experimental values of surface finish

Table 7 Confirmation test results for R_a

	Optimal machining variables	
	Prediction	Experiment
Level	V_3 F_1 D_1	V_3 F_1 D_1
Surface roughness	0.49	0.51
S/N ratio	6.1748	5.8486

values at the optimum cutting conditions are shown in Table 7. The test result is closer to predicted value within an error of about 4%.

4 Conclusions

The Taguchi method was employed to find the optimum machining conditions of 304 stainless steel alloy in dry machining process. The analysis of S/N ratio and variance were used to evaluate the machining performance. The outcomes of this work are given as follows:

1. Higher value of cutting velocity (200 m/min), lower value of depth (0.5 mm), and lower value of feed (0.05 mm/rev) are preferred to achieve the minimum surface roughness.
2. From the ANOVA analysis, depth, feed, and cutting velocity were found to influence the surface finish by around 12%, 21%, and 67%, respectively.

References

1. Davis JR (1995) ASM specialty handbook stainless steels. ASM International, Ohio
2. Radhakrishnan P (2002) Manufacturing Technology, Scitech publications (India) Pvt. Ltd., Chennai
3. Rao PN (2014) CAD/CAM principles and applications. McGraw Hill Education (India) Pvt. Ltd, Delhi
4. Kulkarni AP, Joshi GG, Sangade VG (2013) Dry turning of AISI 304 austenitic stainless steel using AlTiCrN coated insert produced by HPPMS technique. Procedia Eng 64:737–746
5. Asiltürk I, Neşeli S (2012) Multi response optimisation of CNC turning parameters via taguchi method-based response surface analysis. Measurement 45:785–794
6. Philip Selvaraj D, Chandramohan P (2010) Optimization of surface roughness of AISI 304 austenitic stainless steel in dry turning operation using taguchi design method. J Eng Sci Technol 5:293–301
7. Ciftci I (2006) Machining of austenitic stainless steels using CVD multilayer coated cemented carbide tools. Tribol Int 39:565–569
8. Korkut I, Kasap M, Ciftci I, Seker U (2004) Determination of optimum cutting parameters during machining of AISI 304 austenitic stainless steel. Mater Des 25:303–305
9. Xavior A, Adithan M (2009) Determining the influence of cutting fluids on tool wear and surface roughness during turning of AISI 304 austenitic stainless steel. J Mater Process Technol 209:900–909
10. Kaladhar M, Venkata Subbaiah K, Srinivasa Rao C (2012) Parametric optimization during machining of AISI 304 Austenitic Stainless Steel using CVD coated DURATOMICTM cutting insert. Int J Ind Eng Comput 3:577–586
11. Yang WH, Tarng YS (1998) Design optimization of cutting parameters for turning operations based on the taguchi method. J Mater Process Technol 84:122–129
12. Zhang JZ, Chen JC, Kirby ED (2007) Surface roughness optimization in an end-milling operation using the Taguchi design method. J Mater Process Technol 184:233–239
13. Nalbant M, Gokkaya H, Sur G (2007) Application of taguchi method in the optimization of cutting parameters for surface roughness in turning. Mater Des 28:1379–1385

14. Ghani JA, Chodhury IA, Hassan HH (2004) Application of taguchi method in the optimization of end milling parameters. J Mater Process Technol 145:84–92
15. Philip Selvaraj D, Chandramohan P, Mohanraj M (2014) Optimization of surface roughness, cutting force and tool wear of nitrogen alloyed duplex stainless steel in a dry turning process using taguchi method. Measurement 49:205–215

Vibration and Control Engineering

Influence of Fiber Orientation on Mechanical Properties and Free Vibration Characteristics of Glass/Hemp Hybrid Composite Laminates

R. Murugan, V. Muthukumar, K. Pradeepkumar, A. Muthukumaran, and V. Rajesh

Abstract Fiber-reinforced polymer (FRP) composite materials made of synthetic fibers are commonly used in aircraft and automotive structures due to their specific property of high strength-to-weight ratio. The non-biodegradable nature of synthetic fibers and increase in demand of environment-friendly materials now made natural fibers as best alternative material to synthetic fibers. In this view, hybridization of synthetic E-glass fiber with natural hemp fiber is proposed to promote the usage of natural fibers in structural applications without much compromise in structural integrity. In the present study, the influence of fiber orientation over effective stacking sequence of E-glass/hemp hybrid composite laminates was investigated in terms of mechanical and free vibration characteristics. The hybrid composite laminates are fabricated by hand lay-up method. Two types of composite laminates were prepared in effective stacking sequence of GHHG with two different orientations fibers such as (0°/90°) and (45°/45°) for hemp fiber. The mechanical properties such as tensile and flexural strength were evaluated according to ASTM standards. Free vibration characteristics such as modal frequency and modal damping values of hybrid composite laminates are analyzed by experimental modal analysis. The results of modal frequency and mode shapes of hybrid composite beams were stated and discussed.

Keywords Natural fiber · Hybrid composites · Mechanical properties · Free vibration characteristics · Fiber orientation

---

R. Murugan (✉) · V. Muthukumar · K. Pradeepkumar · A. Muthukumaran · V. Rajesh
Department of Mechanical Engineering, Panimalar Institute of Technology, Chennai, India
e-mail: saimurugan1973@gmail.com

V. Muthukumar
e-mail: vmuthukumar1998@gmail.com

K. Pradeepkumar
e-mail: pradeepkumark565@gmail.com

A. Muthukumaran
e-mail: muthukumaranarasu@gmail.com

V. Rajesh
e-mail: rajeshbolt97@gmail.com

E. T. Akinlabi et al. (eds.), *Trends in Mechanical and Biomedical Design*,
Lecture Notes in Mechanical Engineering,
https://doi.org/10.1007/978-981-15-4488-0_74

1 Introduction

Fiber-reinforced polymer (FRP) composite materials are used in a large number of applications ranging from aerospace to automotive industries due to their cost-effectiveness, specific properties, and ease of manufacturing. It is observed that the structural members used in such dynamic applications experience shock and vibrations. Hence, studying the vibration characteristics of FRP composite structures needs much attention to meet the industrial requirements.

The characteristics of FRP composites depend upon many factors such as the mechanical properties of the constituent materials, i.e. fiber and matrix, the volumes of both fiber and matrix, the length and orientation of the fibers in the matrix. Many researchers have contributed towards the effect of these factors on mechanical properties of FRP composite laminates [1–5]. Ajith Gopinath et al. experimentally investigated the effect of different matrices on mechanical properties of jute fiber-reinforced composites using polyester and epoxy resin matrices. The authors revealed that the tensile and flexural properties for jute/epoxy laminates are better than that of the jute/polyester composites, which is preferable for automotive applications [6]. Saira Taj et al. evaluated the mechanical properties of woven and nonwoven jute fabric-reinforced poly-L-lactic acid-based composites. They found that woven structure exhibited excellent mechanical behavior like tensile, flexural, and impact loadings compared to nonwoven composite [7]. Handa et al. proved from their study that hybrid composites reinforced with natural fibers and synthetic fibers demonstrate good mechanical performance [8]. The comparison of mechanical properties of natural and synthetic fiber-reinforced composite laminates was carried out by Muthuraj et al. The authors revealed that among the preferred natural fibers like jute, sisal, hemp, coir, banana, and palm, tensile strength and modulus of hemp/epoxy fabric-reinforced composite is higher than the other fibers [9]. Claudio Scaponi et al. made a comparative evaluation between E-glass and hemp fiber composites applied in rotorcraft interiors. They replaced the existing steel electronic rack mounted on the helicopter with eco-friendly hemp/epoxy composite material and thereby reduced the weight of the structure considerably [10]. Girisha et al. investigated the effect of fiber orientation on mechanical properties of jute/hemp-reinforced hybrid composites with three different orientations 30%, 45%, and 90%. They found that orientation 90% has higher mechanical properties when compared the to remaining two orientations [11].

In the recent past, the influence of types of fiber and matrix material, fiber architecture and stacking sequence on free vibration characteristics of natural and their hybrid composites were studied extensively. Senthil Kumar et al. experimentally investigated the effect of stacking sequence on vibration properties of coconut sheath/sisal hybrid composites, and they found that higher natural frequency values occurred when similar fibers are stacked together [12]. Akash et al. experimentally studied the dynamic behavior of hybrid jute/sisal fiber-reinforced polyester composites using free vibration characteristics and they showed that the changes in the fiber angle yield to different dynamic behavior of the composite laminate [13]. Ömer Yavuz

Bozkurt et al. investigated the effect of fiber orientations on damping and vibration characteristics of basalt/epoxy composite laminates and they showed that damping and vibration characteristics of the composite samples are strongly affected by the fiber orientation. Also, they found that the increase in the angle of fiber orientation resulted in a decrease in natural frequency, and the laminates having higher fiber orientation angle had higher damping ratios [14]. Experimental investigation carried out by J. Alexander et al. on free vibration and damping characteristics of GFRP and BFRP laminated composites at various boundary conditions showed that fundamental natural frequency of woven fabric composites is better than unidirectional composites due to its high stiffness [15]. Based on the literature review, the present study aims toward understanding and investigating the effect of fiber orientation on the vibration characteristics of thin-walled woven fabric hybrid composite beams made of glass and hemp fibers for promoting good dynamic stability in structural applications.

2 Fabrication of Glass/Hemp Hybrid Composites Laminates

Both glass and hemp fibers are preferred in plain woven fabric form with 400 gsm for reinforcement. Thermoset epoxy resin of grade LY556 with hardener HY951 is used as matrix material. All glass/hemp hybrid composite laminates are fabricated by conventional hand lay-up method with uniform fiber volume fraction of $v_f = 0.3$. The effective layering arrangement of four-layered glass/hemp hybrid laminate, GHHG, is selected from literature. In an earlier investigation, Murugan et al. established the effective stacking sequence for four-layered glass/carbon hybrid laminates based on tensile, flexural properties, and free vibration characteristics. From the experimental results, they concluded that the increased tensile and flexural modulus values were obtained for the hybrid laminate fabricated with high modulus fabric in the external layer and low modulus fabric as the core layer [16, 17]. In order to study the effect of fiber orientation over the effective stacking sequence, in the present study, two different fiber orientations such as (0°/90°) and (45°/45°) are considered. Figure 1 shows the image of the glass/hemp hybrid samples fabricated by hand lay-up technique. Table 1 shows the layering arrangement, size, and density of the glass/hemp hybrid laminates fabricated by hand lay-up technique.

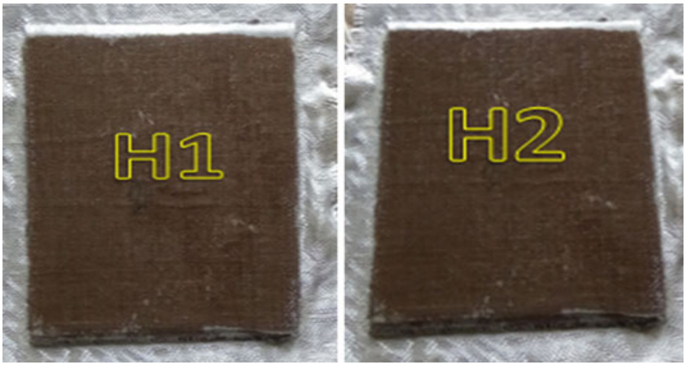

Fig. 1 Photograph showing the two types of glass\hemp hybrid laminates fabricated using hand lay-up technique

Table 1 Layering arrangement, size, and density of the glass/hemp hybrid laminates fabricated by hand lay-up technique

Specimen	Layering arrangement	Size (mm)
H1	G 0-90 H 0-45 H 0-45 G 0-90	250 × 250 × 2.5
H2	G 0-90 H 45-45 H 45-45 G 0-90	250 × 250 × 2.5

3 Testing of Glass/Hemp Hybrid Composites Laminates

3.1 Tensile Test

Tensile test was performed for the glass/hemp hybrid composite laminates as per ASTM D3039 standard. The size of the specimen for the tensile test is 250 mm × 25 mm × t mm where *t* represents the thickness of the specimen. Figure 2 shows the image of tensile testing of glass/hemp hybrid laminates carried out in INSTRON 4204 machine. Hybrid composite specimen having a thin rectangular cross section is mounted in the grips of a universal testing machine and monotonically loaded in tension, and the applied load and deformation of the specimen were recorded.

Fig. 2 Image showing the tensile test conducted on glass/hemp hybrid composite laminates using INSTRON machine

3.2 Flexural Test

Flexural properties of FRP materials were evaluated as per ASTM D790 standard test method. The standard dimensions of the specimen for flexural test are 126 mm × 12.5 mm × *t* mm where *t* represents the thickness of the specimen. The composite specimens are properly cut to the standard dimensions. The flexural test was conducted on the same INSTRON machine with feed rate of 1.2 mm/min. The hybrid specimen is placed on two knife edges provided on the testing machine with equal over-hanging on both sides. A transverse load is applied at the center point of the specimen. Figure 3 shows the standard size of the composite specimen used for the flexural test.

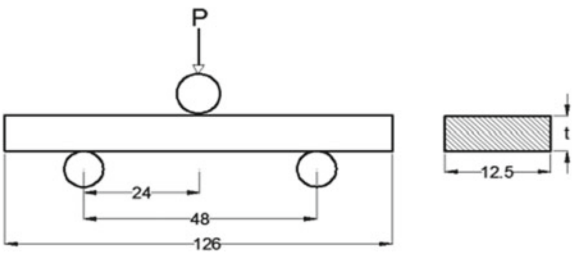

Fig. 3 Schematic diagram showing the standard size of flexural test specimen as per ASTM D790 standard (all dimensions are in mm)

3.3 Experimental Modal Analysis

Free vibration characteristics such as modal frequency and modal shapes are evaluated for glass/hemp hybrid composite laminates under fixed-free end condition. The preferred glass/hemp hybrid laminates are cut into the standard size of 250 mm × 25 mm × t mm where t represents the thickness of the specimen for free vibration study. For the effective transformation of excitation force into the composite beam and to achieve fixed-free boundary condition, a fixture is used to clamp the composite specimen. After fixing the specimen, the span length of the cantilever specimen is kept as 200 mm as shown in Fig. 4.

For obtaining the mode shapes of the glass/hemp hybrid composite beams, roving hammer method is preferred. The composite beam is excited by an impact hammer (9722A500) at specified points of equal interval. A triaxial accelerometer (8766A500) is used to capture the vibration response of the composite beam specimen due to the given excitation. The input excitation force and corresponding output vibration response of the specimen are fed into data acquisition system (ATA9234) as shown in Fig. 4. And these time domain signals are processed over the fast Fourier transform (FFT) software (Dewesoft) to acquire the required frequency response function (FRF) plots. In a similar manner, FRF plots for each excitation point of the composite beam and thus cumulative FRF plots are obtained to evaluate the mode shapes of the two hybrid composite beams.

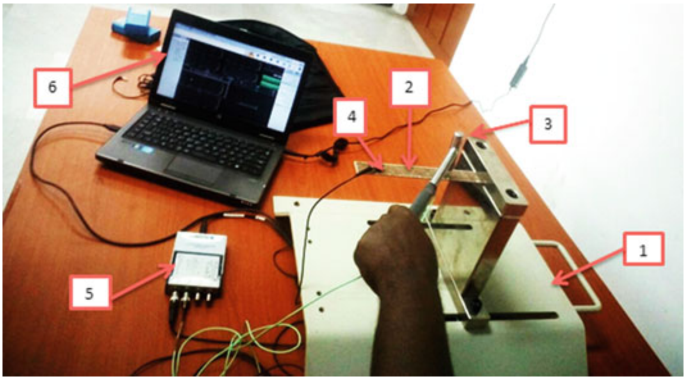

Fig. 4 Image showing free vibration test setup: (1) fixture, (2) composite specimen, (3) impact hammer, (4) accelerometer, (5) data acquisition card, and (6) computer with FFT software showing FRF

Table 2 Tensile and flexural properties of glass/hemp hybrid composites laminates considered

Specimen	Tensile strength (MPa)	Flexural strength (MPa)
H1	49.86	0.436
H2	33.19	0.434

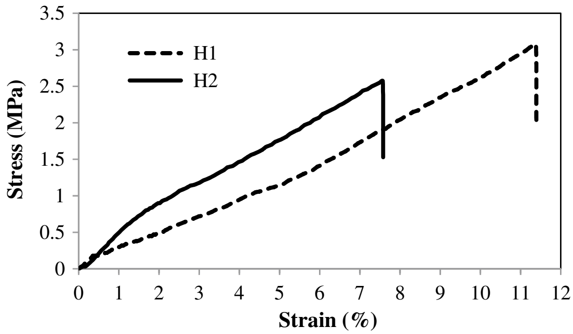

Fig. 5 Comparison of tensile stress/strain graphs of various glass/hemp hybrid laminates

4 Results and Discussion

4.1 Mechanical Properties of Glass/Hemp Hybrid Laminates

The experimentally evaluated mechanical properties of preferred glass/hemp hybrid laminates are reported in Table 2. Figure 5 shows the comparison of stress/strain graphs of hybrid composite laminates obtained by tensile test. Table 2 showed that there is a considerable tensile strength variation between the hybrid laminates considered due to the change in fiber orientation. From the comparison of stress/strain graphs shown in Fig. 5, it is revealed that H1 laminate has higher tensile strength than H2 laminate. From Table 2, it is revealed that there is minimal variation in the flexural strength among the two hybrid laminates. Flexural strength of composite laminates mainly governed by the stacking sequence of the fiber lamina and the fiber orientation has the least control over it.

4.2 Free Vibration Characteristics of Glass/Hemp Hybrid Composite Beams

Figure 6 shows the comparison of FRF plots of glass/hemp hybrid beams with two different fiber orientations. The positive shift in FRF plot of H1 beam compared to H2 beam confirms the higher stiffness of H1 beam than H2 beam.

The modal frequency values for the first three mode shapes of two hybrid composite beams arrived from experimentally recorded FRF function are shown in Table 3. From Table 3, it is observed that the resonant frequency set attained for H1 hybrid

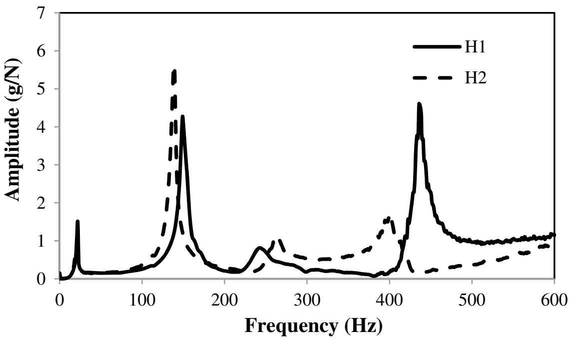

Fig. 6 Comparison of FRF plots of preferred glass/hemp hybrid beams obtained from free vibration test under fixed-free boundary condition

Table 3 Experimental modal frequency values of hybrid composite beams for three successive modes

Mode no.	Mode shape	Modal frequency (Hz)	
		H1	H2
Mode I		21	20
Mode II		158	148
Mode III		457	447

beam is slightly higher side than H2 beam in all three modes. This characteristic behavior confirms that the change in the fiber orientation of inner hemp layers in the hybrid beam influences the stiffness of hybrid composite beam under flexural vibration. The minimal variation in flexural strength of H1 than H2 layering arrangement caused this modification.

5 Conclusions

In the present work, the effect of fiber orientation on mechanical properties and free vibration characteristics of glass/hemp hybrid composite beams was experimentally investigated. The effective layering arrangement of glass/hemp hybrid laminates, i.e. GHHG, is preferred based on the earlier investigation. In order to study the effect of fiber orientation, two different laminates H1 with fiber orientations ($0^\circ/90^\circ$) and H2 with fiber orientation ($45^\circ/45^\circ$) are fabricated. Hybrid laminate H1 exhibited increased tensile strength than the other hybrid arrangements, but the flexural strength of hybrid laminates showed the least variation.

Experimental modal analysis of glass/hemp hybrid beams, H1 and H2, showed minimal variation in resonant frequency set in successive modes for different fiber orientation. The layer arrangement of hybrid beam, H1, showed increased modal frequency values than the other laminate, H2, which is beneficial for structural applications.

References

1. Sanjay MR, Arpitha GR, Yogesha B (2015) Study on mechanical properties of natural—glass fiber reinforced polymer hybrid composites: a review. Mater Today Proc 2:2959–2967
2. Satish P, Kesavan R, Vijaya Ramnath B (2015) Effect of fiber orientation and stacking sequence on mechanical and thermal characteristics of banana-kenaf hybrid epoxy composite. Silicon 9(4):577–585
3. Bhoopathi R, Rajesh M, Deepa C (2014) Fabrication and property evaluation of banana-hemp-glass fiber reinforced composites. Procedia Eng 97:2032–2041
4. Kumar A, Singh S (2015) Analysis of mechanical properties and cost of glass/jute fiber reinforced hybrid polyester composites. Proc Inst Mech Eng Part L: J Mat: Des Appl 229(3):202–208
5. Hareesh M, Sunil M, Naveen Kumar HN, Rohith Kumar K (2016) Mechanical characterization of hybrid hemp/glass fiber reinforced epoxy composite. Int J Eng Res Rev 4(1):104–108
6. Gopinath A, Senthil Kumar M, Elayaperumal A (2014) Experimental investigations on mechanical properties of jute fiber reinforced composites with polyester and epoxy resin matrices. Procedia Eng 97:2052–2063
7. Taj S, Munawar MA, Khan S (2007) Natural fiber-reinforced polymer composites. Proc Pak Acad Sci 44(2):129–144
8. Abdul Khalil HPS, Handa S, Kang CW, Nik Faud NA (2007) Agro-hybrid composite: The effects on mechanical and physical properties of oil palm fiber (EFB)/glass hybrid reinforced polyester composites. J Reinf Plast Comp 26:203–218
9. Muthuraj, Ravi Kumar M, Keerthiprasad KS (2016) Characterization and comparison of natural and synthetic fiber composite laminates. Int J Eng Tech 2(5):1–8
10. Scarponi C, Messano M (2015) Comparative ealuation between E-glass and hemp fiber composites application in rotorcraft interiors. Composites Part B 69:542–549
11. Girisha KG, Anil KC, Akash (2014) Mechanical properties of jute and hemp reinforced hybrid composites. Int J Res Eng Techn 2(4):245–248
12. Senthil Kumar K, Siva I, Rajini N, Jeyaraj P, Winowlin Jappes JT (2014) Tensile, impact, and vibration properties of coconut sheath/sisal hybrid composites: Effect of stacking sequence. J Reinf Plast Compos 0(0):1–11
13. Akash DA, Thyagaraj NR, Sudev LJ (2013) Experimental study of dynamic behaviour of hybrid jute/sisal fiber reinforced polyester composites. Int J Sci Eng Appl 2(8):170–172
14. Bozkurt ÖY, Bulut M, Özbek Ö (2016) Effect of fiber orientations on damping and vibration characteristics of basalt epoxy composite laminates, Proceedings of the world congress on civil, structural, and environmental engineering (CSEE'16) Prague, Czech Republic, ICSENM pp. 115–116
15. Alexander J, Augustine BSM (2015) Free vibration and damping characteristics of GFRP and BFRP laminated composites at various boundary conditions. Indian J Sci Technol 8(12):1–7
16. Murugan R, Ramesh R, Padmanabhan K (2014) Investigation on static and dynamic mechanical properties of epoxy based woven fabric glass/carbon hybrid composite laminates. Procedia Eng 97:459–468
17. Murugan R, Ramesh R, Padmanabhan K (2016) Investigation of the mechanical behavior and vibration characteristics of thin walled glass/carbon hybrid composite beams under a fixed-free boundary condition. Mech Adv Mater Struct 23(8):909–916

Free Vibration Analysis of Functionally Graded Beam with Linearly Varying Thickness

Rajat Jain and Mihir Chandra Manna

Abstract The present study investigates the free vibration analysis of functionally graded material (FGM) beam which is rectangular in cross section with linearly varying thickness along its axis with the help of finite element formulation. This formulation of finite element is developed based on the Timoshenko beam theory which we called as first-order shear deformation theory. In the present analysis of the beam with linearly varying thickness, the beam element has five nodes and thirteen degrees of freedom. Properties of the material used in this beam element are varying continuously according to the power law along the thickness direction. Governing equations used for the formulation of present work are derived from Lagrange's equations. The natural frequency of beam is calculated using different boundary conditions, exponents of power law, depth to span ratios, and tapered ratios. The present beam element is accurately demonstrated by comparing the results with the available data of publications for constant thickness and for variable thickness, and some results are new and can be further considered for future researches.

Keywords Functionally graded material · Finite element method

1 Introduction

Functionally graded materials (FGMs) have superior composites of continuous spatial variables formed with the help of two or more material constituents. These materials are used to build a mixture of two or more constituents whose particles have nearly similar form and dimensions (ceramic powder, plasma particles, etc.). These materials have excellent properties such as high temperature, creep, and fatigue resistance. Therefore, these materials are extensively used in many engineering applications, i.e., aerospace, civil, and mechanical engineering, etc. The increasing demand for these materials is because of their good mechanical behavior in various applications.

R. Jain (✉) · M. C. Manna
Indian Institute of Engineering Science and Technology Shibpur, Howrah, West Bengal 711103, India
e-mail: iiest17rj.info@gamil.com

E. T. Akinlabi et al. (eds.), *Trends in Mechanical and Biomedical Design*,
Lecture Notes in Mechanical Engineering,
https://doi.org/10.1007/978-981-15-4488-0_75

When we compare the researches of plates and shells, the work on FGM beams are very less and very few data are available. Free vibration problems of functionally graded beams (FGB) were solved by different analytical and numerical approaches using different beam theories. Among many analytical works, some may be mentioned in this context. In the last of the twentieth century, many researchers have done their works on free vibration analysis of FGM beams with different boundary conditions and loading conditions [1–5]. In the area of sandwiched beams, Frostig et al. [6] investigated the higher-order theory for sandwiched beams behavior with transverse core and they investigated that how the shear is transferred from the core to the skin. Later on, Sankar et al. [7] obtained the solution for elasticity problem using FG beams with simply supported conditions exposed to transverse loading of sinusoidal behavior and the modulus of elasticity varies along the thickness in the exponential manner, and Sankar found when the loaded side of the beam is softer as compared to homogeneous beam, the concentration of stresses are less, and vice versa when the harder side is loaded.

In the field of thermal stress, Xiang and Yang [8] examined the frequencies of thermally pre-stressed, laminated FG beam with variable thickness using the first-order beam theory and the method of differential quadrature. This analysis shows that if the layers of FGM are thicker with a lesser fractional index of volume in the laminated beam, structure shows the effective increases in natural frequencies and decrease in the amplitude of vibration. And after the analysis of Xiang and Yang, characteristics of free vibration and the behavior of dynamic analysis of a FG beam with simply supported ends under a concentrated moving harmonic load are studied by Simsek and Kocaturk [9]. In this study, Lagrange's equations are used for deriving the equation of motion under the assumptions of beam theory given by Euler–Bernoulli. This analysis says that the different material distribution effect, moving harmonic load velocity, and the dynamic responses of excitation frequency on the FG beam show very vital role in the dynamic response of the FG beam. Later on, Li et al. [10] investigated the FG beams by taking into account the effects of shear deformation and deriving a single governing equation for the static and dynamic behaviors of FG beams. The results obtained from the analysis are coinciding with the standard elasticity solutions. In the analysis of mode shape and fundamental frequencies of FGM beams, Alshorbagy et al. [11] studied the free vibration features and dynamic response of a functionally graded beam for various distributions of material using FEM. The obtained results have shown that the distributed variation of material along the axial direction and the ratio of slenderness have not executed any effect on the fundamental frequencies or mode shapes but as the power exponent increases the natural frequencies also increases. Alshorbagy et al. [12] also examined the dynamic behavior of FGM thick beam by analyzing the effect of temperature.

In the area of isotropic and functionally graded (FG) sandwich beams, Nguyen et al. [13] proposed a new higher-order shear deformation theory for buckling and free vibration analysis. This study shows a new hyperbolic variation of shear stress in transverse direction, and the results obtained from this theory show outstanding promise with those derived from former studies. After that, Kahya et al. [14] studied multi-layered shear deformable beam element for dynamic analysis of laminated composite beams subjected to moving load. In this investigation, results show very significant responsive evaluation of the stacking lamina of the laminated beams. After two years, Kahya et al. [15] also examined one more result on the model of finite element for vibration and buckling analysis of FGM beam based on first-order shear deformation theory using a five-noded beam element with ten degrees of freedom.

Recently, Banerjee et al. [16] investigated the free vibration of FGBs by applying the dynamic stiffness method in this analysis properties of the material alter continuously over the thickness according to the variation of power law. After that, Armagan et al. [17] analyzed free vibration behavior of two-directional FG beams subjected to different boundary conditions by using the shear deformation theory of third order where the properties of materials of the beam vary exponentially in length as well as thickness directions. In the area of nonlinear free and forced vibrations, Sinir and Gultekin [18] have done his analysis on non-uniform cross-sectional beam of axially functionally graded material with Euler–Bernoulli theory. The beam has immovable boundary conditions, which leads to mid-plane stretching because of vibrations and the frequency-response curves that show the effect of these nonlinear correction terms on natural frequency by the unstable regions. And very recently, Chen et al. [19] investigated the vibration problem of axially functionally FGM beam and parabolically varying thickness in 3D by isogeometric analysis in conjunction with 3D theory.

From the available works of literature, it has been seen that most of the works have been done using different beam elements for the fundamental frequency only. In the present work, a beam element with five nodes having thirteen degrees of freedom is used for the analysis of free vibration of the functionally graded beams with a variable thickness along its length. In this work, the first-order shear deformation theory has been taken into account for finite element formulation.

2 Theory and Formulation

The purpose of this study is to develop an exact finite element model with the help of shear deformation theory of first order for free vibration analysis of functionally graded beams (FGB) with variable thickness. The properties of materials in the beam vary continuously through the direction of thickness according to the formulation of power law.

2.1 Material Properties

The beam proposed here is an isotropic, non-homogeneous elastic beam having its length l and cross section is $b \times h_g$ which is rectangular in shape where the thickness of the beam is varying linearly along its length as shown in Fig. 1 and h_g is the thickness at Gauss's point. The beam is constituted with a mixture of two materials

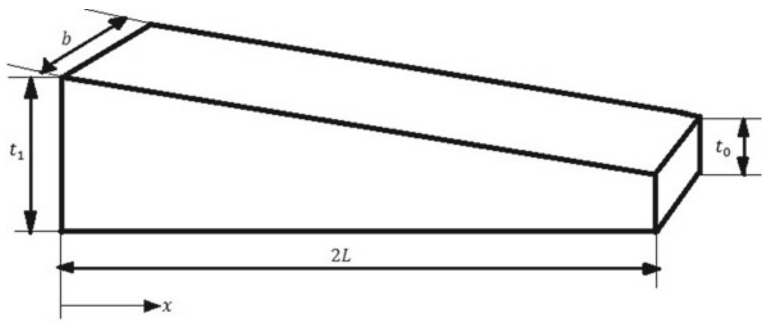

Fig. 1 Variable thickness cross section of beam element

such as ceramic and metal, the position of these materials is at its top and bottom surfaces, respectively. Hooke's law is obeyed by the material. Power law rule governs the variation of material properties along with the thickness as follows.

$$P(z) = (P_c - P_m)\left(\frac{z}{h_g} + \frac{1}{2}\right)^k + P_m$$

where k is the non-negative exponent of the power law, P_m and P_c are the equivalent properties of the metal and ceramic ingredients, e.g., Young's modulus E, Poisson Ratio ν, and mass density ρ, respectively.

2.2 Finite Element Formulation

Figure 2 shows the five-node beam element with thirteen degrees of freedom with each node having three degrees of freedom except the mid node. And only the mid node has one degree of freedom.

Displacement field equation according to the first-order shear deformation theory is as follows:

$$U(x, z, t) = u(x, t) - z\phi(x, t),\ W(x, t) = w(x, t) \tag{1}$$

where u is axial displacement, w is transverse displacement, and ϕ is the total bending rotation of the cross section at any point on the neutral axis.

From Eq. (1), the relationship of strain–displacement is as follows:

$$\varepsilon_{xx} = \frac{\partial U}{\partial x} = \frac{\mathrm{d}u}{\mathrm{d}x} - z\frac{\mathrm{d}\phi}{\mathrm{d}x} \quad \text{and} \quad \gamma_{xz} = \frac{\partial U}{\partial x} + \frac{\partial W}{\partial x} = \frac{\partial w}{\partial x} - \phi \tag{2}$$

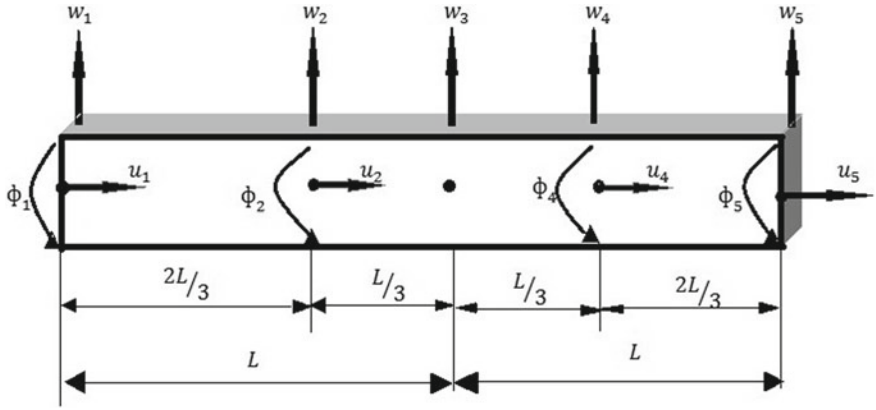

Fig. 2 Beam element with five nodes and thirteen degrees of freedom

where ε_{xx} and γ_{xz} are the normal and shear strains, respectively, and Eq. (2) can be rewritten as:

$$\begin{pmatrix} \varepsilon_{XX} \\ Y_{XZ} \end{pmatrix} = \begin{pmatrix} \frac{\mathrm{d}u}{\mathrm{d}x} & -\mathrm{z}\frac{\mathrm{d}f}{\mathrm{d}x} \\ \frac{\partial W}{\partial x} & -\phi \end{pmatrix} = \begin{bmatrix} 1 & 0 & -z & 0 \\ 0 & 1 & 0 & -1 \end{bmatrix} \begin{Bmatrix} \frac{\mathrm{d}u}{\mathrm{d}x} \\ \frac{\partial w}{\partial x} \\ \frac{\mathrm{d}\phi}{\mathrm{d}x} \\ \phi \end{Bmatrix}$$

where

$$\begin{aligned} &\left[\frac{\mathrm{d}u}{\mathrm{d}x}\,\frac{\partial w}{\partial x}\,\frac{\mathrm{d}\phi}{\mathrm{d}x}\,\phi\right]^{\mathrm{T}} \\ &= \begin{bmatrix} N_{1u,x} & 0 & 0 & N_{2u,x} & 0 & 0 & 0 & N_{4u,x} & 0 & 0 & N_{5u,x} & 0 & 0 \\ 0 & N_{1w,x} & 0 & 0 & N_{2w,x} & 0 & N_{3w,x} & 0 & N_{4w,x} & 0 & 0 & N_{5w,x} & 0 \\ 0 & 0 & N_{1\phi,x} & 0 & 0 & N_{2\phi,x} & 0 & 0 & 0 & N_{4\phi,x} & 0 & 0 & N_{5\phi,x} \\ 0 & 0 & -N_{1\phi} & 0 & 0 & -N_{2\phi} & 0 & 0 & 0 & -N_{4\phi} & 0 & 0 & -N_{5\phi} \end{bmatrix} \{\delta\} \\ &= [B]\{\delta\} \end{aligned} \tag{3}$$

where $\{\delta\}^{\mathrm{T}} = \{u_1 w_1 \phi_1 u_2 w_2 \phi_2 w_3 u_4 w_4 \phi_4 u_5 w_5 \phi_5\}$
and "x" represents the derivative with respect to x.

The shape functions in $[B]$ are as follows:

$$N_{1u} = \frac{-9}{16} \times \left(\xi + \frac{1}{3}\right)\left(\xi - \frac{1}{3}\right)(\xi - 1)$$

$$N_{2u} = \frac{27}{16} \times (\xi + 1)\left(\xi - \frac{1}{3}\right)(\xi - 1)$$

$$N_{4u} = \frac{-27}{16} \times \left(\xi + \frac{1}{3}\right)(\xi - 1)(\xi + 1)$$

$$
\begin{aligned}
N_{5u} &= \frac{9}{16} \times \left(\xi - \frac{1}{3}\right)\left(\xi - \frac{1}{3}\right)(\xi + 1) \\
N_{1w} &= \frac{9}{16} \times \left(\xi + \frac{1}{3}\right)(\xi)\left(\xi - \frac{1}{3}\right)(\xi - 1) \\
N_{2w} &= \frac{-81}{16} \times (\xi - 1)(\xi)\left(\xi - \frac{1}{3}\right)(\xi + 1) \\
N_{3w} &= 9 \times \left(\xi + \frac{1}{3}\right)(\xi - 1)\left(\xi - \frac{1}{3}\right)(\xi + 1) \\
N_{4w} &= \frac{-81}{16} \times \left(\xi - \frac{1}{3}\right)\left(\xi + \frac{1}{3}\right)(\xi)(\xi + 1) \\
N_{5w} &= \frac{9}{16} \times \left(\xi + \frac{1}{3}\right)(\xi)\left(\xi - \frac{1}{3}\right)(\xi + 1) \\
N_{1\phi} &= \frac{-9}{16} \times \left(\xi + \frac{1}{3}\right)\left(\xi - \frac{1}{3}\right)(\xi - 1) \\
N_{2\phi} &= \frac{27}{16} \times (\xi + 1)\left(\xi - \frac{1}{3}\right)(\xi - 1) \\
N_{4\phi} &= \frac{-27}{16} \times \left(\xi + \frac{1}{3}\right)(\xi - 1)(\xi + 1) \\
N_{5\phi} &= \frac{9}{16} \times \left(\xi - \frac{1}{3}\right)\left(\xi - \frac{1}{3}\right)(\xi + 1)
\end{aligned} \tag{4}
$$

where $\xi = \frac{x}{L}$ and $2L$ is the element length.

The thickness of the beam varying linearly from one end as shown in Fig. 1, the variation of thickness at any distance "x" from one end ($x = 0$) is given by

$$t_x = t_0 + \frac{t_1 - t_0}{l}(l - x) \tag{5}$$

Or,$t_x = t_0\left[1 + \left(1 - \frac{x}{l}\right)\delta\right]$, where $\delta = \frac{t_1 - t_0}{t_0}$ (tapered ratio), t_0 is the thickness at one end ($x = l$) and t_1 at the other end ($x = 0$), and x is measured from the end where the thickness is t_1.

The element stiffness matrix can be written using the principle of virtual work as follows:

$$[K]^{\mathrm{e}} = \int_{-l}^{l} [B]^{\mathrm{T}}[D][B]\mathrm{d}x \tag{6}$$

where $[B] = \frac{1}{J}\frac{\mathrm{d}[N]}{\mathrm{d}\xi}$ or $\frac{\mathrm{d}N_i}{\mathrm{d}x} = \frac{\mathrm{d}N_i}{\mathrm{d}\xi} \times \frac{\mathrm{d}\xi}{\mathrm{d}x}$.

Again, on considering the beam element used in the present analysis we get,

$$J = \frac{\partial x}{\partial \xi} = \frac{\partial}{\partial \xi}\{N_{1x}\, N_{3x} N_{5x}\}\begin{bmatrix} x_1 \\ x_3 \\ x_5 \end{bmatrix} \tag{7}$$

where $N_{1x} = 1/2\left(-\xi + \xi^2\right)), N_{3x} = (1 - \xi^2)$, and $N_{5x} = 1/2\left(\xi + \xi^2\right)$. Total length of the beam element is $2L$. The abscissa of the nodes of the beam elements x_1, x_3, and x_5 for geometric interpolation is as follows:

$$x_1 = 0, x_3 = x_1 + L \text{ and } x_5 = x_1 + 2L$$

On putting the above values of x_1, x_3, and x_5 in Eq. (7) we get J as follows

$$\begin{aligned} J &= \frac{\partial x}{\partial \xi} = \frac{\partial}{\partial \xi}\{N_{1x}\, N_{3x} N_{5x}\}\begin{Bmatrix} x_1 \\ x_3 \\ x_5 \end{Bmatrix} \\ &= \left\{\frac{1}{2}(-1 + 2\xi) - 2\xi\, \frac{1}{2}(-1 + 2\xi)\right\}\begin{Bmatrix} x_1 \\ x_1 + L \\ x_1 + 2L \end{Bmatrix} \\ &= L \text{ or } \mathrm{d}\xi/\mathrm{d}x = 1/L \end{aligned}$$

Total length of the beam element is $2L$. Hence,$x_5 - x_1 = 2\mathrm{L}$ or

$$L = \frac{x_5 - x_1}{2} \tag{8}$$

Therefore, using Eqs. (6), (7), and (8), the elemental stiffness matrix can be given as

$$[K]^{\mathrm{e}} = \int_{-1}^{1} [B]^{\mathrm{T}}[D][B]\, L\mathrm{d}\xi \tag{9}$$

The rigidity matrix $[D]$ is given as:

$$[D] = \begin{bmatrix} A_0 & 0 & -A_1 & 0 \\ 0 & B_0 & 0 & -B_0 \\ -A_1 & 0 & A_2 & 0 \\ 0 & -B_0 & 0 & B_0 \end{bmatrix} \tag{10}$$

where A_0, A_1, A_2, and B_0 can be expressed as follows:

$$\begin{aligned} [A_0, A_1, A_2] &= \int E(z)\left[1, z, z^2\right]\mathrm{d}A \\ &= \int E(z)\left[1, z, z^2\right]z\mathrm{d}z \text{ and } B_0 \end{aligned}$$

$$= \int k\ G(z)\mathrm{d}A = \int k\ G(z)\ z\mathrm{d}z$$

It has been assumed that mechanical property of Young's modulus is varying along with the thickness of the beam element. This Young's modulus variation along the thickness of the beam is governed by the power law which is as follows:

$$E(z) = (E_\mathrm{c} - E_\mathrm{m})\left(\frac{z}{h} + \frac{1}{2}\right)^k + E_\mathrm{m} \quad \text{and} \quad G(z) = \frac{E(z)}{2(1+\nu)} \tag{11}$$

where ν is taken as constant for the functionally graded material.

Therefore, putting the above relationship in the expression $[A_0, A_1, A_2]$ and B_0 and taking the integration over the whole thickness of the beam, A_0, A_1, A_2, and B_0 are obtained as:

$$A_0 = bh_\mathrm{g}\left[\frac{(E_\mathrm{c} - E_\mathrm{m})}{k+1} + E_\mathrm{m}\right], A_1 = \frac{bh_\mathrm{g}^2}{2}\left[\frac{(E_\mathrm{c} - E_\mathrm{m})k}{(k+1)(k+2)}\right],$$
$$A_2 = \frac{bh_\mathrm{g}^3}{4}\left[\frac{(E_\mathrm{c} - E_\mathrm{m})\left(k^2+k+2\right)}{(k+3)(k+1)(k+2)} + \frac{E_\mathrm{m}}{3}\right], \text{and } B_0 = \frac{K}{2(1+\mu)}A_0$$

where h_g is the total thickness of the beam at Gauss points of integration. Similarly, the element mass matrix can be written as

$$[M]^\mathrm{e} = \int_{-l}^{l} \left[\overline{B}\right]^\mathrm{T}[\overline{\rho}]\left[\overline{B}\right]\ L\mathrm{d}\xi \tag{12}$$

$$[\overline{B}] = \begin{bmatrix} N_{1u,x} & 0 & 0 & N_{2u,x} & 0 & 0 & 0 & N_{4u,x} & 0 & 0 & N_{5u,x} & 0 & 0 \\ 0 & N_{1w,x} & 0 & 0 & N_{2w,x} & 0 & N_{3w,x} & 0 & N_{4w,x} & 0 & 0 & N_{5w,x} & 0 \\ 0 & 0 & N_{1\phi,x} & 0 & 0 & N_{2\phi,x} & 0 & 0 & 0 & N_{4\phi,x} & 0 & 0 & N_{5\phi,x} \end{bmatrix}$$

$$\text{and, } [\bar{\rho}] = \begin{bmatrix} I_0 & 0 & -I_1 \\ 0 & I_0 & 0 \\ -I_1 & 0 & I_2 \end{bmatrix}$$

where I_0,I_1, and I_2 can be expressed as follows:

$$[I_0, I_1, I_2] = \int \rho(z)\left[1, z, z^2\right]\mathrm{d}A = \int \rho(z)\left[1, z, z^2\right]z\mathrm{d}z \tag{13}$$

It has been assumed that densities are varying along with the thickness in the present beam element. This variation of density along the beam thickness is governed by power law which is as follows:

$$\rho(z) = (\rho_\mathrm{c} - \rho_\mathrm{m})\left(\frac{z}{h_g} + \frac{1}{2}\right)^k + \rho_\mathrm{m} \tag{14}$$

Combining Eqs. (12), (13), and (14) and taking integral over the thickness of the beam I_0, I_1, and I_2 are expressed as follows:

$$
\begin{aligned}
I_0 &= bh_g\left[\frac{(\rho_c - \rho_m)}{k+1} + \rho_m\right],\\
I_1 &= bh_g^2\left[\frac{(\rho_c - \rho_m)k}{2(k+1)(k+2)}\right],\\
I_2 &= \frac{\mathrm{b}h_g^3}{4}\left[\frac{(\rho_c - \rho_m)\left(k^2 + k + 2\right)}{(k+1)(k+2)(k+3)} + \frac{\rho_m}{3}\right]
\end{aligned}
\tag{15}
$$

Gauss quadrature method is used to find the element stiffness and mass matrices from Eqs. (9) and (12) numerically, and the Gauss quadrature order used is four.

By assembling the element stiffness and mass matrices, following Eigenvalue equation is obtained:

$$\left([K]_{\mathrm{g}} - \omega^2[M]_{\mathrm{g}}\right)\{\Delta\} = \{0\} \tag{16}$$

where $[K]_{\mathrm{g}}$ and $[M]_{\mathrm{g}}$ are the global stiffness and global mass matrices, ω is the natural frequency, and $\{\Delta\}$ is the corresponding mode shape. Equation (16) is solved by using the simultaneous iteration technique by Corr and Jennings [20] to obtain the natural frequencies of the beam.

3 Results and Discussion

In the present analysis, formulation of finite element model is used based on the shear deformation theory of the first order for the study of free vibration analysis of functionally graded beams with linearly varying thickness along its length.

The study of convergent is approved for the present beam element. Table 1 shows the normalized fundamental frequencies $\left(\overline{\omega}_n = \frac{\omega_n l^2}{h_0}\sqrt{\frac{\rho_m}{E_m}}\right)$ of FGBs with various boundary conditions for their different values, where the length of beam is l and the thickness is h_0 at $x = l$. For the comparison of present work with those of Kahya [15] and Nguyen [13], the material used in this FG beam is aluminum (Al) as metal and alumina (Al_2O_3) as ceramic for which $Em = 70$ GPa, $\rho_{\mathrm{m}} = 2702$ kg/m^3, $\nu_{\mathrm{m}} = 0.3$, $Ec = 380$ GPa, $\rho_{\mathrm{c}} = 3960$ kg/m^3, and $\nu_{\mathrm{c}} = 0.3$. Boundary conditions for this analysis are assumed to be clamped-clamped (C–C), hinged-hinged (H–H), and clamped-free (C–F). For calculation, the shear-correction factor is taken as $K = 5(1+\nu)/(6+5\nu)$ from the work of Kahya [15] where υ is Poisson's ratio. In all of the following calculations, rectangular cross-sectional beam having different length-to-thickness ratio (l/h_0) ranging from 5 to 100 and different values of power law exponent (k) varying from 0 to 10 has been considered. The normalized fundamental frequencies for different values of power law exponent, boundary conditions,

Table 1 Convergence study of normalized fundamental frequency for FGBs with boundary condition $l/h_0 = 5$ and $k = 0$

δ	Number of elements	C–C	H–H	C–F
0	4	9.9975535	5.1524837	1.8944103
	8	9.9975020	5.1524793	1.8944101
	12	9.9975012	5.1524783	1.8944100
	15	9.9975012	5.1524783	1.8944100
0.5	4	11.3608624	6.1601690	2.8993748
	8	11.3608125	6.1601620	2.8993735
	12	11.3608117	6.1601619	2.8993735
	15	11.3608117	6.1601619	2.8993735
1.0	4	12.3353769	6.9591461	3.8705373
	8	12.3351511	6.9591034	3.8705336
	12	12.3351434	6.9591027	3.8705335
	15	12.3351432	6.9591027	3.8705335

and different tapered ratios ($\delta = 0, 0.25, 0.50, 0.75, 1.0$) obtained from the present analysis are shown in Table 3. For the value of $\delta = 0$, it has been experiential that, the obtained results are very close 0.8–1.2% less than the available published results by Simsek [4], Nguyen [13] and Kahya [15] as shown in Table 2 and the results are shown graphically in Fig. 3. From Fig. 3, it is observed that the results obtained from the present analysis are very close to the results obtained by Kahya [15] because I have taken 15 elements for my present analysis. From the results, it also observed that only 15 elements (shown in Tables as P15) are sufficient for the desired accuracy of the obtained results compared to the other published results by Kahya [15] and Nguyan [13]. In Table 2, the fundamental natural frequencies are presented with available results of Simsek [4], Nguyen [13], and Kahya [15] (for $\delta = 0$) which gives very accurate results. And all the results with different tapered ratio except $\delta = 0$ are presented in Table 3 as new results and may be used for future reference for research work in this field. In Fig. 4, it has been observed that the fundamental natural frequencies of the beam increase with increasing the tapered ratio for different values of (l/h_0), keeping power law exponent (k) as constant. Again, it has been observed that keeping (l/h_0) and δ constant, the normalized natural frequencies decrease when the power law exponent (k) increases as shown in Fig. 3. It may be further concluded that in all cases, the normalized natural frequencies are higher for C–C beams than those for C–F and H–H beams as shown in Fig. 5. It has been observed form Fig. 6 that the effect of the taper ratios on the first, third, and sixth normalized frequencies are not significant. But second, fourth, and fifth normalized frequencies are increasing with the increase in taper ratios.

Different boundary conditions are defined as follows:

For C–C: At $x = 0$, $u = w = \phi = 0$; At$x = 2l$, $u = w = \phi = 0$

For H–H: At $x = 0$, $w = 0$; At $x = 2l$, $w = 0$ and

Table 2 Comparison of normalized fundamental frequencies with different boundary conditions for $\delta = 0$ and $l/h_0 = 5$

Conditions	Element	$k = 0$	$k = 0.5$	$k = 1$	$k = 5$	$k = 10$
C–C	P 15	9.99750	8.74257	7.89974	6.64281	6.31479
	Kahya [15]	10.08647	8.75479	7.98414	6.71481	6.37413
	Simsek [11]	10.0705	8.7463	7.9503	6.4934	6.1651
	Nguyen [13]	10.0726	8.74674	7.9518	6.4929	6.1658
H–H	P 15	5.15247	4.40816	3.97084	3.40227	3.29606
	Kahya [15]	5.22193	4.46926	4.04967	3.48818	3.36434
	Simsek [11]	5.1527	4.4102	3.9904	3.4012	3.2816
	Nguyen [13]	5.1528	4.41108	3.9904	3.4009	3.2815
C–F	P 15	1.89441	1.61867	1.46275	1.26419	1.22369
	Kahya [15]	1.90722	1.62865	1.47294	1.27515	1.26363
	Simsek [11]	1.8952	1.6182	1.4632	1.2591	1.2183
	Nguyen [13]	1.8957	1.61817	1.4636	1.2594	1.2187

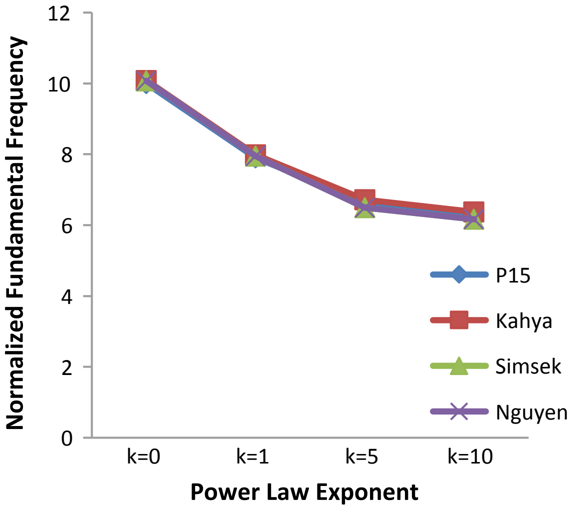

Fig. 3 Plot between normalized fundamental frequency *v/s* power law exponent for the present element with an earlier research paper for $L/h = 5$, $\delta = 0$ and C–C boundary condition

For C–F: At $x = 0$, $u = w = \phi = 0$.

4 Conclusion

In the present analysis, a five-node beam element with thirteen degrees of freedom is used to study the free vibration analysis of beam made of functionally graded

Table 3 Normalized fundamental frequencies of FGBs with various boundary conditions and tapered ratio having different values of k at $l/h_0 = 5$

Conditions	k	$\delta = 0$	$\delta = 0.25$	$\delta = 0.50$	$\delta = 0.75$	$\delta = 1.0$
C–C	1	7.89974	8.52200	9.04984	9.50214	9.89262
	5	6.64281	7.12962	7.53598	7.87901	8.17102
	10	6.31489	6.75639	7.12141	7.42668	7.68429
H–H	1	3.97084	4.38696	4.75685	5.08827	5.58646
	5	3.40227	3.75003	4.05684	4.32962	4.57309
	10	3.29606	3.62996	3.92342	4.18324	4.41408
C–F	1	1.46275	1.85471	2.24504	2.63015	3.00721
	5	1.26419	1.59915	1.93055	2.25519	2.57063
	10	1.22369	1.54622	1.86435	2.17494	2.47560

Fig. 4 Plot between normalized fundamental frequency v/s tapered ratio for $k = 1$, C–C boundary condition and different values of L/h

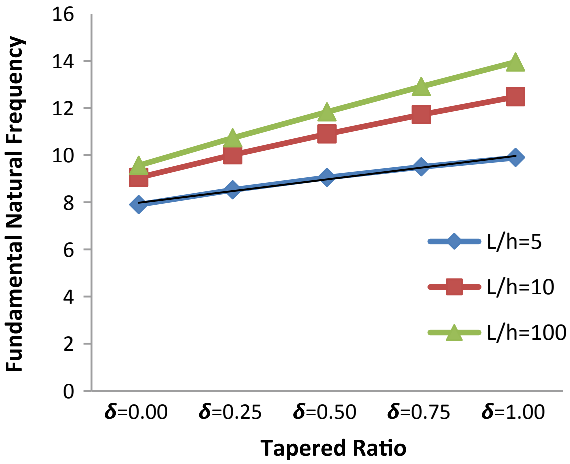

material with linearly varying thickness under different boundary conditions for different values of power law exponent (k) and different length to thickness ratios. From the present analysis, it is observed that the performance of the present element is excellent and this element can be utilized for the analysis of critical buckling of FG beams as well as composite beams or functionally graded composite beams. It is also observed that maximum frequencies are obtained for C–C beams as expected than the others. It may also be seen that the power law exponent, length-to-thickness ratio, and the tapered ratio have a significant effect on fundamental frequencies.

Fig. 5 Plot between normalized fundamental frequency *v*/*s* tapered ratio for $L/h = 5$, $K = 1$ and different boundary conditions

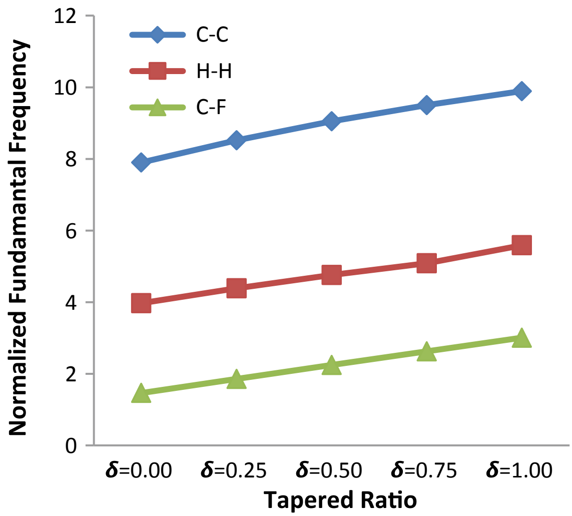

Fig. 6 Plot between normalized natural frequency *v*/*s* tapered ratio for $L/h = 5$, $k = 0$ and different mode shapes

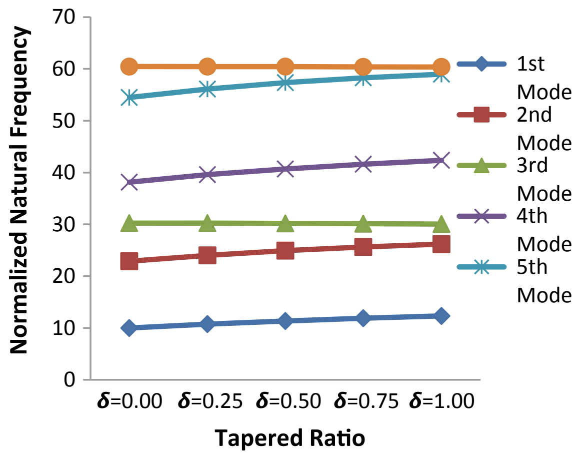

References

1. Chakraborty A, Gopalakrishnan S, Reddy JN (2003) A new beam finite element for the analysis of functionally graded materials. Int J Mech Sci 45:17–22
2. Aydogdu M, Taskin V (2007) Free vibration analysis of functionally graded beams with simply supported edges. Mater Des 28(5):1651–1656
3. Sina SA, Navazi HM, Haddadpour H (2009) An analytical method for free vibration analysis of functionally graded beams. Mater Des 30(3):741–747
4. Şimşek M (2010) Fundamental frequency analysis of functionally graded beams by using different higher-order beam theories. Nucl Eng Des 240(4):697–705
5. Lee JW, Lee JY (2017) Free vibration analysis of functionally graded Bernoulli-Euler beams using an exact transfer matrix expression. Int J Mech Sci 122:1–17

6. Frostig Y, Baruch M, Vilnay O, Sheinman I (1992) High-order theory for sandwich-beam behaviour with transversely flexible core. J Eng Mech 118(5):1026–1043
7. Sankar BV (2001) An elasticity solution for functionally graded beam. Compos Sci Technol 61:689–696
8. Xiang HJ, Yang J (2008) Free and forced vibration of a laminated FGM Timoshenko beam of variable thickness under heat conduction. Compos B Eng 39:292–303
9. Şimşek M, Kocatürk T (2009) Free and forced vibration of a functionally graded beam subjected to a concentrated moving harmonic load. Compos Struct 90:465–473
10. Li XF, Wang BL, Han JC (2010) A higher-order theory for static and dynamic analyses of functionally graded beams. Arch Appl Mech 80:1197–1212
11. Alshorbagy AE, Eltaher MA, Mahmud FF (2011) Free vibration characteristics of a functionally graded beam by finite element method. Appl Math Model 35(1):412–425
12. Alshorbagy AE (2013) Temperature effects on the vibration characteristics of a functionally graded thick beam. Ain Shams Eng J 4:455–464
13. Nguyen T-K et al (2015) Vibration and buckling analysis of functionally graded sandwich beams by a new higher-order shear deformation theory. Compos B Eng 76:273–285
14. Kahya V (2012) Dynamic analysis of laminated composite beams under moving loads using finite element method. Nucl Eng Des 243:41–48
15. Kahya V, Turan M (2017) Finite element model for vibration and buckling of functionally graded beams based on the first-order shear deformation theory. Compos B Eng 109:108–115
16. Banerjee JR, Ananthapuvirajah A (2018) Free vibration of functionally graded beams and frameworks using the dynamic stiffness method. J Sound Vib 422:34–47
17. Karmanli A (2018) Free vibration analysis of two directional functionally graded beams using a third-order shear deformation theory. Compos Struct 189:127–136
18. Sinir S, Gultekin B (2018) Nonlinear free and forced vibration analyses of axially functionally graded Euler-Bernoulli beams with non-uniform cross-section. Compos B Eng 148:123–131
19. Chen M, Jin G, Zhang Y, Niu F, Liu Z (2019) Three-dimensional vibration analysis of beam with axial functionally graded materials and variable thickness. Compos Struct 207:304–322
20. Corr RB, Jennings A (1976) A simultaneous iteration algorithm for symmetric Eigen value problems. Int J Numer Meth Eng 10(3):647–663

Parametric Study of Composite Plate Using Free Vibration Analysis

Rajendra Kumar Sadangi, Mihir Kumar Sutar, and Sarojrani Pattnaik

Abstract This paper presents the free vibration analysis of laminated composite plate to study the parametric variations on natural frequency of the plate. The parameters used for analysis are aspect ratio, number of layers in composite plate, support conditions, number of layers and fibre orientation. Finite element model of the laminated composite plate is prepared using ANSYS 13.0 software. The element chosen for the analysis is shell 281, an 8-noded, six degrees of freedom. This element is used for analysing thin to moderately thick structures. The effect of parametric variations on the natural frequency is then studied. The results obtained from the analysis are then compared with the experimental values obtained from the literature survey with a satisfactory result.

Keywords Laminated plate · Orthotropic plate · ANSYS · Natural frequency and fibre orientation angle

Nomenclature

[K]	Stiffness matrix
[M]	Moment matrix
ω_n	Angular velocity

1 Introduction

Today technology progress results in the continuous growth of structural material types and improvement of their properties. The frequent use of composite material as a group of metals, polymers, and ceramics have increased the demand for

R. K. Sadangi · M. K. Sutar (✉) · S. Pattnaik
Veer Surendra Sai University of Technology Burla, Burla, Odisha, India
e-mail: mihirsutar05@gmail.com

E. T. Akinlabi et al. (eds.), *Trends in Mechanical and Biomedical Design*, Lecture Notes in Mechanical Engineering,
https://doi.org/10.1007/978-981-15-4488-0_76

improvement in them for developing industries [1]. Since last four decades, plates made by composite material are more used in many engineering purposes. The high stiffness-to-weight ratio coupled with flexibility of the selected laminated material can be turning to match the design demand and makes the laminated plate an interest of structural component for manufacture.

In these days, generally laminated plates used in various fields to develop the mechanical properties of material for research. The result of the above analysis in terms of natural frequency using laminated composite plate is improved and resonant omitted.

1.1 Illustrations

Ansar et al. [1] sequence reviews the modelling method along with their efficiency and drawback for features of the material's geometry, mechanical behaviour and impact behaviour of three-dimensional woven composites. The authors have highlighted on the recent developments in the field of modelling and design of woven composites, so that their special mechanical character and impact behaviour can be understood. Advantage and drawback and use of three-dimensional woven composite are also highlighted in his paper.

Charles and Byron [2] have performed a free vibratio analysis of symmetrically and unsymmetrical laminated anisotropic composite plates with clamped edges. Natural frequency of the laminated anisotropic plate was obtained using linear analysis. Further an approximate solution was obtained using Rayleigh-Ritz energy method. A good agreement was obtained between the numerical and experimental work.

Chakraborty et al. [3] found both numerical and experimental work of the free vibration of composite fibre-reinforced plates. They used modal testing method using impact excitation to find out the corresponding frequency response function. Finite element methods using an isometric element determine the modal features. In his works, they validate result obtained from commercial finite element package (NISA) with both theoretical and experimental work.

Cawley and Adams [4] found the natural modes of vibration of laminated composite plates with theoretical and experimental work. Natural frequency and mode shapes presented different ply orientations' comparisons between theoretical and experimental frequencies.

First Crawly [5] found out the natural frequency and mode shape using graphite/epoxy and aluminium plates are experimentally determined. In his observation, comparison between calculated and observed mode was excellent but discrepancy in frequency result is due to the difference between dynamic flexural modulus and static in-plane modulus.

Mishra and Sahu [6] present experimental works to find free vibration of glass epoxy composite material with different boundary condition. Modal testing method used for obtaining the frequency of the structure. This experimental result is compared with the FEM numerical which is based on first-order shear deformation. In this paper, the effect of different geometry parameters like a number of layers, aspect ratio, fibre orientation and boundary condition of composite plate is presented.

Ju et al. [7] present the finite element formulation for free vibration analysis of composite plate with multiple delaminations. This formulation introduces the effect of transverse shear deformation as well as the bending extension coupling due to the influence of delaminated plates.

Kamal and Durvasula [8] found some studies on free vibration of composite laminates using the modification of shear deformation and composite plate theory and applied the Rayleigh-Ritz energy method. The numerical result for clamped boundary condition of composite plate is compared with various earlier published results.

Qatu and Leissa [9] find free vibration of cantilever laminated composite plate using the Ritz method and further he compared the result with experimental value.

Rikards [10] uses sandwich composite plate with viscoelastic layers for vibration and damping analysis. In his paper, he showed the natural frequency variation of free and damping vibration and described that efficiency of damped material.

Soares [11] use the Eigen-frequencies technique to find the mechanical properties of composite material and compared the result with experimental analysis of composite material.

Srinivasa et al. [12] presented experimental and finite element studies on free vibration of isotropic and laminated composite skew plates. The natural frequency obtained taken CQUAD8 finite element of NASTRAN and compared made between the experiment result and finite element solution.

2 Material and Methodology Composite Materials

The composite material is defined as combination of matrix and fibre reinforcement material, the formation of properties superior to the properties of the individual components. In the case of composite, the reinforcement is the fibres and it is used to fortify the matrix in terms of strength and stiffness. The fibre and a base material are known as matrix that yields best mechanical properties than its original material. Composite materials are best for structures that require high strength/weight and stiffness/weight.

2.1 Free Vibration of Laminated Composite Plate

The first-order shear deformation theory with finite element methods is used for finding out natural frequency and mode of vibration of laminated composite plates. Shear deformation theory is same as classical laminated plate theory but only includes the transverse shear strain (interlaminar shear strain) which was not considered in classical laminate plate theory.

Free vibration motion of dynamics structure with linear single degree of freedom system without damping given below

$$m\frac{d^2u}{dt^2} + ku = 0 \tag{1}$$

For static equilibrium position, the displacement and velocity $x = x(0), \dot{x} = \dot{x}(0)$, respectively.

Solution of equation obtained at time period t, $x = x(t), \dot{x} = \dot{x}(t)$

$$x(t) = x(0)\cos\omega_n t + \frac{\dot{x}(0)}{\omega_n}\sin\omega_n t \tag{2}$$

Natural frequency of vibration is, $\omega_n = \sqrt{\frac{k}{m}}$.

2.2 Analysis in ANSYS

The composite plate is analysed by using finite element analysis using the software package ANSYS 13.0. Shell 281 element, which can be used for analysis of thin to moderately thick materials, has been used for the composite late analysis. This element has 8 nodes and each node has a 6° of freedom 3 in translation direction and 3 in rotational direction. This material is suitable for use in linear, large rotation and large strain nonlinear application. This element is also used in a layered application for composite shell and sandwich plate model and accuracy of composite shell governing by using first-order shear deformation theory (Fig. 1).

3 Result and Discussion

3.1 Case-1

Consider epoxy glass fibre composite material with different combination of length (a) and breadth (b) with thickness of 20 mm (20 no. of layer lamina) and different boundary condition and same analysis with ANSYS 13.0 using shell 281 in the analysis (Fig. 2).

The result of ANSYS validated through analytical FEM analysis and experimental analysis made by Srinivasa et al. [12] in his paper considers skew angle $a = 0°$. Here is first 3 modes of vibration having aspect ratio ($a/b = 1$) of antisymmetric ply. For laminated glass/epoxy composite plates of different ply combination given below, these value are compared with experimental analysis by Srinivasa et al. [12] (Tables 1,

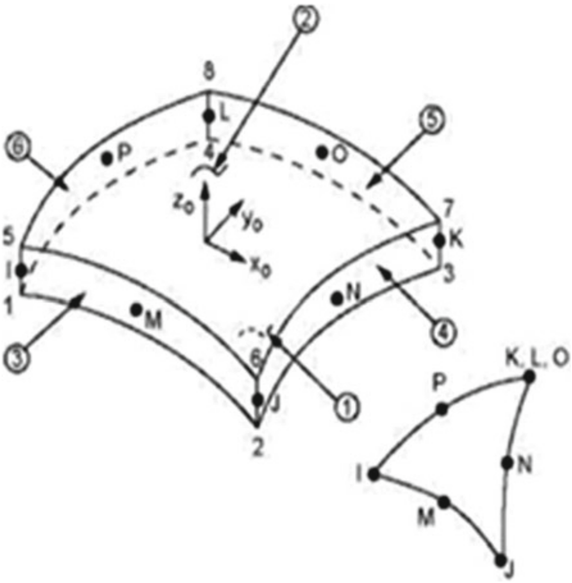

Fig. 1 Ansys shell 281

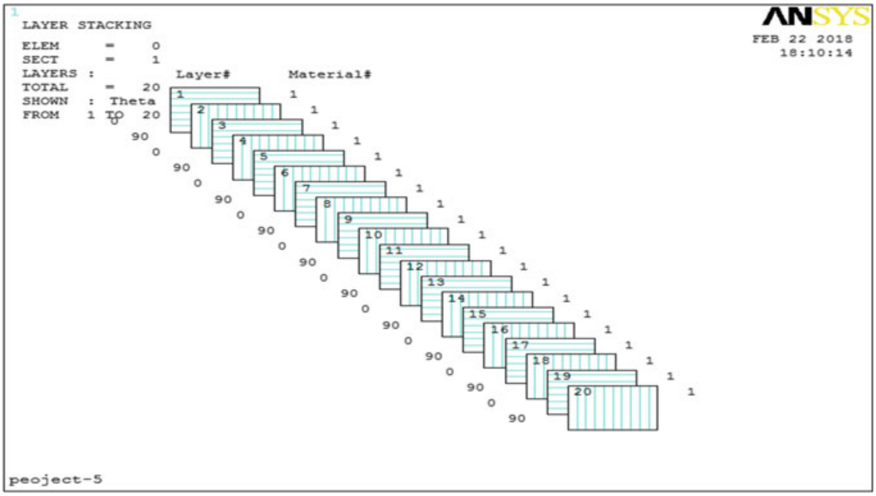

Fig. 2 Layer stacking cross angle ply composite

Table 1 Different mode of vibration of antisymmetric layers

SET	Time/frequency	Load step	Sub-step cumulative
1	7.9942	1	1
2	15.205	1	2
3	18.455	1	3

Table 2 Modes of vibrations of cross-ply composite

SET	Time/frequency	Load step	Sub-step cumulative
1	7.7889	1	1
2	14.587	1	2
3	19.378	1	3

2 and 3).

3.2 Case-II

Again taken Graphite/epoxy composite material first three natural frequency obtained from Finite element analysis using the Software ANSYS and same compared the analytical work obtained by Ju et al. [7] and Experimental work by Mishra and Sahu [6] (Table 4).

4 Conclusion

The following observations are obtained in this paper.

In case-I, comparison between different combinations of angle ply laminate with frequency of vibration on different arrangement of the mode of vibrations. Here, in conclusion drawn from Fig. 3, frequency of vibration in the first two modes of vibrations is nearly same and afterwards, vibrations increase tremendously.

The chart (Fig. 4) frequency is least value when using angle ply having (+90°/−90°/+⋯) and highest value whenever using angle ply laminate having ply combination like (0°/−0°/+⋯). The angle ply lamination having a stacking sequence (+90°/−90°/+⋯) results in reduced vibration in the system and can be used in situations where vibration is a major drawback in the system and it has to be reduced.

In case II, consider eight-ply graphite/epoxy plate having dimension of length 152 mm and breadth 76 mm and thickness 1.04 mm with laminate slackness combination (0°/90°/45°/90°)s. In this paper, comparison among the result by three different approaches like first in finite element analysis using ANSYS and same validated through analytical and experimental done by authors (C. V. Srinivasa, Y. J. Suresh and W. P. Prema Kumar) in his paper. In this ANSYS analysis, result is convergence to both analytical and experimental result plot in Figs. 5, 6 and 7 by different combinations like clamped, cantilever and simple supported plate.

It has been observed that the natural frequency has an increasing trend in all angles of ply orientations. The present analysis found to be well in agreement with the experimental results of Srinivas et al. [12] and with Ju et al. [7].

Table 3 Comparison of analytical and experimental values [12] of natural frequencies

	Mode no	Aspect Ratio 1			Aspect Ratio 1.5			Aspect Ratio 2			Aspect Ratio 2.5		
		Exp. Values [12]	Analytical Value	FEM	Exp. Values [12]	Analytical Value	FEM	Exp. Values [12]	Analytical Value	FEM	Exp. Values [12]	Analytical Value	FEM
Angle ply(+0^0/-0^0/+0^0/-)	1	15.30	15.01	15.1	15.18	14.1	14.2	14.98	13.09	12.4	14.82	14.12	13.19
	2	15.99	16.1	15.08	17.19	17.01	16.01	17.53	16.21	15.89	18.61	18.1	17.19
	3	19.43	17.07	18.4	27.00	27.01	26.1	36.68	25.76	34.2	40.85	41.91	39.32
Angle ply(+45^0/-45^0/+45^0/-)	1	9.45	8.09	7.99	9.54	9.421	8.99	9.039	8.23	9.01	8.85	8.09	8.09
	2	12.85	12.91	15.2	16.33	16.10	15.1	19.11	18.29	19.4	22.48	22.59	22.30
	3	22.68	22.1	18.4	26.46	26.41	26.3	26.11	25.19	24.2	24.54	23.08	24.76
Angle ply(+90^0-90^0+90^0-)	1	7.05	7.09	6.11	7.21	7.11	7.09	7.19	7.12	7.99	6.83	6.07	6.59
	2	8.44	7.98	12.69	10.12	10.33	11.11	11.83	11.84	12.01	13.02	13.81	13.01
	3	19.39	18.54	16.56	19.87	19.23	18.78	19.82	18.01	19.78	18.82	18.47	18.59
Cross ply(0^0+90^0+)	1	11.90	18.87	7.78	12.17	12.01	11.10	12.13	11.01	12.09	11.53	11.90	12.07
	2	12.77	12.56	14.58	14.10	13.89	12.89	15.4	13.89	12.83	16.09	17.90	16.92
	3	19.42	18.23	19.37	33.41	34.09	32.12	33.45	32.12	33.40	31.78	31.45	32.01

Table 4 Comparison of natural frequency

Boundary condition	Reference papers	Mode-1 frequency (Hz)	Mode-2 frequency (Hz)	Mode-3 frequency (Hz)	Mode-4 frequency (Hz)
All side clamped	Ju et al. [7]	346.59	651.51	781.06	1017.2
	Present FEM	365.44	720.51	839.80	2283.2
One side clamped and other 3 sides free	Ju et al. [7]	41.347	60.663	221.52	258.72
	Present FEM	31.533	54.164	198.04	230.07
	Experimental [12]	41.1652	60.534	220.5114	257.7930
All sides are simple supported boundary condition	Ju et al. [7]	164.37	404.38	492.29	658.40
	Present FEM	163.27	400.00	493.621	660.31
	Experimental [12]	163.7453	401.3175	494.5912	651.652

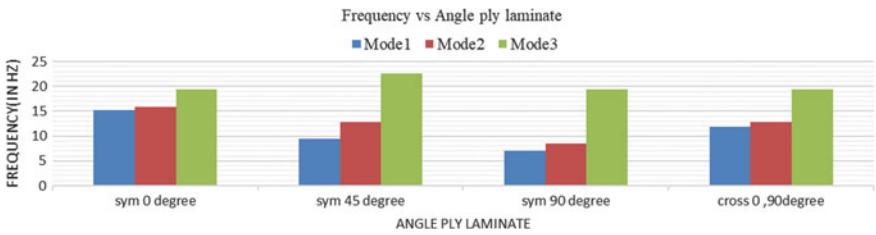

Fig. 3 Different modes of vibration

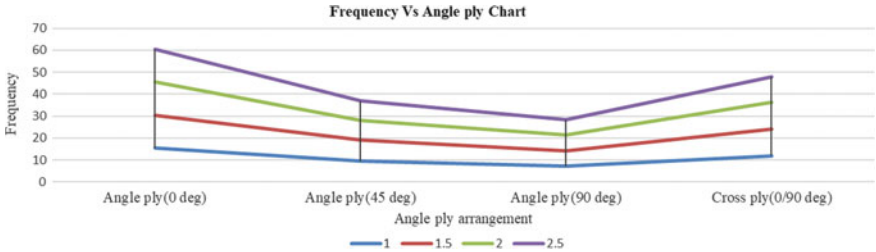

Fig. 4 Different aspect ratio variation in frequency versus angle ply chart

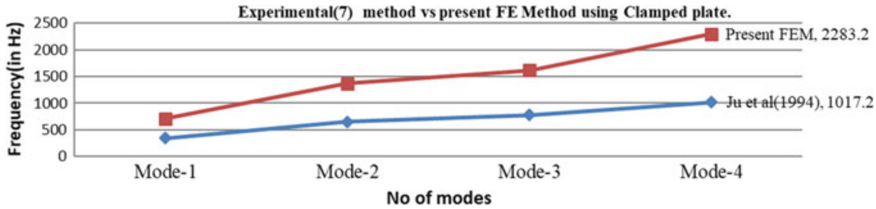

Fig. 5 Layer stacking cross-angle ply composite

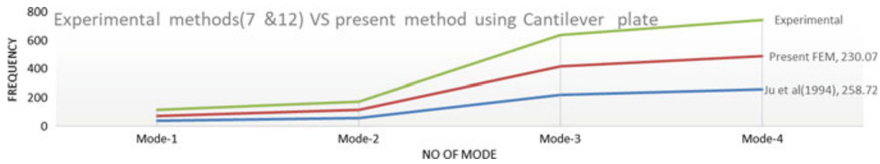

Fig. 6 Layer stacking cross-angle ply composite

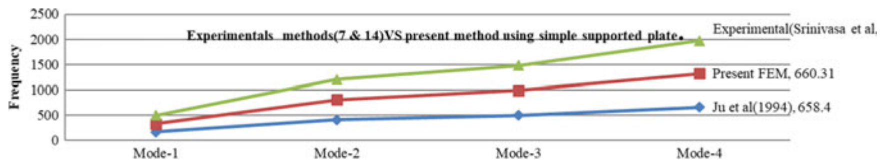

Fig. 7 Layer stacking cross-angle ply composite

Appendix

Material propertied used in finite element calculation for laminated composite Graphite/Epoxy based on data book (unpublished reference) is given below.

$$\begin{aligned} E_L &= 128\,\text{GPa},\ E_T = 11\,\text{GPa},\ \nu_{LT} = 0.25,\ G_{LT} \\ &= 4.48\,\text{GPa},\ G_{13} = 1.53\,\text{GPa, density} \\ &= 1.5 \times 10^3\,\text{kg/m}^3,\ \text{Plythickness} = 20\,\text{mm} \end{aligned}$$

References

1. Ansar M, Xinwei W, Chouwei Z (2011) Modeling strategies of 3D woven composites: a review. Compos Struct 93:1947–1963
2. Bert CW, Mayberry BL (1969) Free vibrations of unsymmetrically laminated anisotropic plates with Mayberry clamped edges. J Compos Mater 3:282–293
3. Chakraborty S, Mukhopadhyay M, Mohanty AR (2000) Free vibrational responses of FRP composite plates: experimental and numerical studies. J Reinf Plast Compos 19:535–551
4. Cawley P, Adams RD (1978) The predicted and experimental natural modes of free-free CFRP plates. J Compos Mater 12:336–347
5. Crawley EF (1979) The natural modes of graphite/epoxy cantilever plates and shells. J Compos Mater 13:195–205
6. Mishra I, Sahu SK (2015) Modal analysis of woven fiber composite plates with different boundary conditions. Int J Struct Stab Dyn 15(1):1540001–1540017
7. Ju F, Lee HP, Lee KH (1994) Finite Element analysis of free vibration of delaminated composite plates. Composite Engineering 5:195–209
8. Kamal K, Durvasula S (1986) some studies on free vibration of composite laminates. Compos Struct 5:177–202

9. Qatu Mohamad S, Leissa Arthur W (1991) Natural frequencies for cantilevered doubly- curved laminated composite shallow shells. Compos Struct 17:227–255
10. Rikards R (1993) Finite element analysis of vibration and damping of laminated composites. Compos Struct 24(3):193–204
11. Soares MCM, de Freitas MM, Araujo AL (1993) Identification of material properties of composite plate specimens. Compos Struct 25:277–285
12. Srinivasa CV, Suresh YJ, Prema Kumar WP (2014) Experimental and finite element studies on free vibration of skew plates. Int J Adv Struct Eng 6:48

Free Vibration Analysis of Hybrid Composite Beam Under Different Boundary Conditions and Thermal Gradient Loading

Prabhat Pradhan, Mihir Kumar Sutar, and Sarojrani Pattnaik

Abstract This paper presents a free vibration analysis of hybrid composite beam under thermal gradient loading. Theoretical vibration analysis of the hybrid composite beam is performed and variation of the (z/h) with respect to Young's modulus under variation of the thermal gradient is studied. The results obtained from the analysis of hybrid composite beam were compared with the plain composite beam and it was observed that hybrid composite beam possesses better modulus of elasticity compared to that of plain composite beam. This analysis would be vital for performing further research in this domain.

Keywords Functionally graded material · FG-CNT-Reinforced hybrid composite beam · Power law distribution · Temperature distribution · Free vibration analysis

1 Introduction

Functionally Graded Materials (FGMs) are the innovative advance quality materials in the field of composites with respect to their strength, mechanical and thermal properties. Nowadays, the modern requirement of the industry in the field of aerospace and power sectors needs the rapid evolution of new components, which provides the researchers to invent new materials in order to satisfy the functional requirements of modern technology. Due to excellent heat-resisting property along with resistance to corrosion, erosion and fracture of FGM materials, these are used as smart materials in modern technologies. With the excellent thermal properties of FGM, these are also found to have erosion and corrosion resistance and high fracture resistance; these are used as smart materials in modern technologies.

P. Pradhan · M. K. Sutar (✉) · S. Pattnaik
Mechanical Engineering Department, Veer Surendra Sai University of Technology, Burla, Odisha, India
e-mail: mihirsutar05@gmail.com

E. T. Akinlabi et al. (eds.), *Trends in Mechanical and Biomedical Design*,
Lecture Notes in Mechanical Engineering,
https://doi.org/10.1007/978-981-15-4488-0_77

Integration of Carbon Nanotubes (CNT) with FGM, leads to a newer material category called hybrid composite. This results in important improvements in composite properties, even in very small volumes of CNT. In actual structural applications, Hybrid composite is incorporated as a type of advanced material that can be incorporated as structural elements into beams, sheets or shells. Therefore, it is more important to explore the mechanical results of these structures as beams. Many researchers have imparted their effort in this particular domain.

Free vibration behaviour of CNT-reinforced functionally graded composite plates was investigated by Selim et al. [1], using Higher Order Shear Deformation Theory (HSDT) and rules of mixture. The frequency response and mode shape obtained were studied in the analysis. VDUY et al. [2] have used a Finite Element Analysis (FEA) to investigate the different behavioural properties of FG-CNT beam. The results obtained were further compared for different orientations of CNTs. Kazem et al. [3] have performed the FEA vibration analysis of functionally graded beam, subjected to different thermal conditions. Armagan [4] has performed the free vibrational analysis of two-directional functional graded beams which are subjected to different boundary conditions like simply supported (SS) beam, clamped-clamped (CC), clamped-simply supported (CS) and clamped-free (CF) beams which are evaluated by applying shear deformation theory of third order. Further, a free vibrational study of FG-CNT-reinforced nanocomposite sandwich plates resting on elastic foundation has been performed by Dastjerdi et al. [5] and randomly oriented straight carbon nanotubes have been reinforced in the sandwich plates. The governing equations were derived using Hamilton's energy principle and are solved by using Navier's method and various effects of CNT volume fraction and various parameters of natural frequency have been studied.

The thermomechanical vibration analysis of sandwich beams having reinforced with CNT composite functionally graded along thickness direction has been performed by Ebrahimi et al. [6], in which the material property variation has been done using rule of mixture and is temperature-dependent. The governing equation was formulated using Hamilton's principle and differential transform method (DTM) is being used for verifying the material properties. The first-known vibration analysis of fully functionally graded carbon nanotube-reinforced hybrid composite (FFG-CNTRHC) laminates has been by Kuo [7]. In this case, carbon nanotubes have been graded over graphite/epoxy laminates and were distributed by using some distribution functions and rules of mixture to obtain desire stiffening effect. Then the required stiffness and mass matrices were generated and solved for natural frequencies. Liew et al. [8] have performed the mechanical analysis of FG-CNT based composite where the superlative properties of carbon nanotubes along with their excellent reinforcement properties with composites were discussed. A nonlinear free vibration of FGB embedded with nanocomposites has been performed by Liang Ke et al. [9]. The governing equations were derived for this beam by Ritz's method and then nonlinear vibration frequencies are observed for FG-CNTRC beams with different end supports. The nonlinear vibration characteristics of carbon nanotube-reinforced composite beam subjected to thermal conditions have been analyzed by Chaudhari et al. [10]. The linear free vibration analysis of nanocomposite beams reinforced with single-walled carbon nanotubes (SWCNTs) has been performed by Lin et al. [11]. Hamilton's principle has been used to obtain different strain energy and kinetic energies for such beam and p-Ritz method is used in order to solve these equations to generate the governing equations. Finally, the vibrational frequencies for such beams were investigated.

2 Mathematical Modelling of Hybrid Composite Beam

The carbon nanotube-reinforced functionally graded beam has been modelled mathematically by using power law function of FGM using Timoshenko beam theory (First-order shear deformation theory) and further it is applied to determine the physical properties of CNTs and matrix material, i.e. Young's Modulus.

Consider a composite beam system having length L, width b, thickness h along the x, y and z directions, respectively. Three types of alignment of carbon nanotubes in CNT beams, such as uniformly distributed CNT beam (UD-CNT), functionally graded CNT of type A (FGA-CNT), in which CNTs are more concentrated at bottom of beam and FG beam of type X(FGX-CNT), in which CNTs are more concentrated at the top and bottom portion of beam, have been taken into consideration for the analysis. Figure 1 depicts the three alignment categories.

A method that is used for the constituent material distribution within FG-CNT beam is termed as rules of mixture, in which specific laws like power/exponential laws are used for gradation of material in a specific manner.

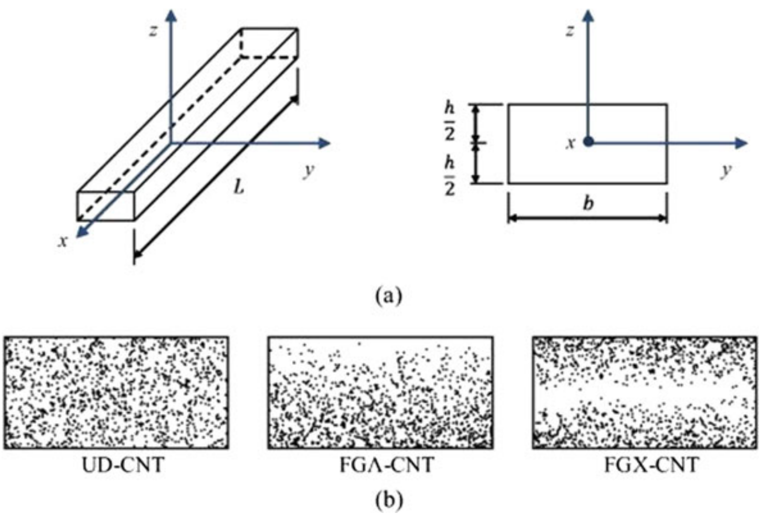

Fig. 1 Functionally graded carbon nanotube-reinforced composite beams: **a** Co-ordinate system of beam. **b** Cross-section of UD-FGM, FGA-CNT and FGX-CNT beams

Here, we will use the power law to describe the material properties of the beam, where a particular index is used for constituents. The various properties of “the material can be evaluated by using power law, where the volume of both elements varies in the direction of thickness. Also, the volume fraction varies in accordance with power law along thickness direction.”

It is given according to subsequent equation [11]:

$$V_{cnt} = \left(\frac{z}{h} + 0.5\right)^{n} \tag{1}$$

where n is the index representing power law and h represents the thickness of the beam and z is the co-ordinate axis which varies from $(-h/2 \leq z \leq h/2)$, along direction of thickness,
And

$$V_{cnt} + V_m = 1 \tag{2}$$

where V_{cnt} is the fractional volume of CNT in FGM and V_m is the fractional volume of matrix in FGM. This volumetric relationship gives the composition of a layer of a beam at a particular co-ordinate in z-axis. The physical properties of FG-CNT beam varies according to the relation [11]:

$$P(z) = P_{cnt} + (P_m - P_{cnt})\left[\frac{1}{2} + \frac{z}{h}\right]^{k} \tag{3}$$

The variation of Young’s modulus of FGX-CNT beam with *z*/*h*, is as shown in Fig. 2, which depicts the variation of material property of the FG-CNT (mainly for FG-X Distribution) beam along the thickness direction obeying a power law for different values of power law exponent. Further, it has been shown that the variation mostly linear for the power index of $k = 1$ and all other variations are mostly mirror image about this line.

3 Free Vibration Analysis of FG-CNT-Reinforced Hybrid Composite Beam

The first-order shear deformation theory (FSDT), gives the displacement along axial direction u and transverse displacement w at any point of beam is given by

$$u(x, z, t) = u_0(x, t) + z\psi(x, t) \quad \text{and} \quad w(x, y, z, t) = w_0(x, t) \tag{4}$$

By implementing the finite element analysis on FG-CNT beam, the above governing equations are solved and after solving the governing differential equations using interpolating functions, the stiffness and mass matrix can be obtained. The discrete

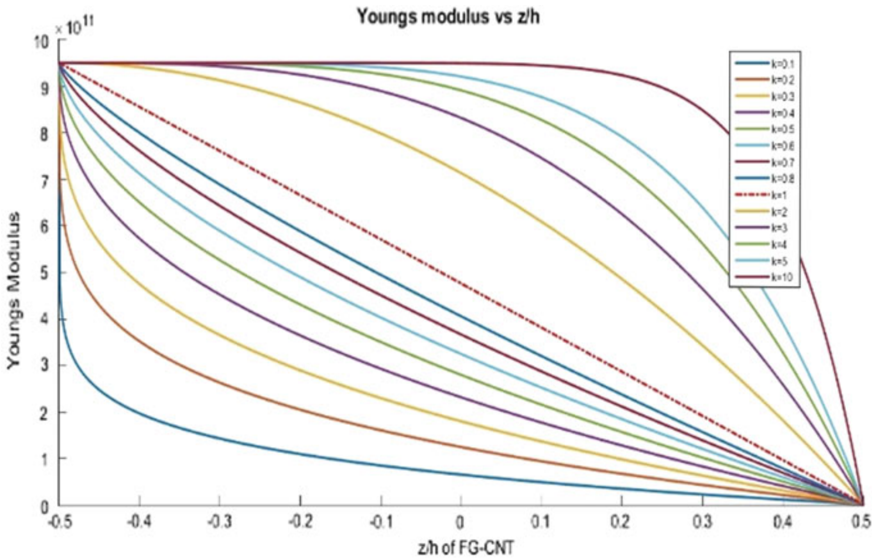

Fig. 2 Power law distribution of material of CNT over PMMA matrix of FG-CNT beam for various power index along thickness direction

equation for the free vibration analysis of laminated composite beam is represented by;

$$M\ddot{d} + Kd = 0 \tag{5}$$

where

d Displacement vector
$\ddot{d}$ 2nd order derivative of displacement w.r.t time 't'

M and K are the global mass and stiffness matrix which are the assemblies of elemental mass and stiffness matrix.

Further, the above Eq. is solved in order to get the natural frequency from equation;

$$\left([K] - w^2[M]\right)\phi = 0 \tag{6}$$

By applying the finite element study on FG-CNT beam, the above governing equations are solved and subsequently solving the governing differential equations using interpolating functions, the stiffness and mass matrix can be obtained. Finally, the derived equation of motion is given by

$$[M]\{\ddot{q}\} + [K]\{q\} = 0 \tag{7}$$

where $[M]$ is the mass matrix and $[k]$ is the stiffness matrix. By solving this equation, we will obtain the natural frequency of vibration of FG-CNT beam.

4 Results and Discussion

In the present analysis of FG-CNTRC beam, the matrix material has been taken as polymethyl methacrylate (PMMA) and single-walled armchair (10, 10) carbon nanotubes are as the reinforcing element, hence their material properties [12] at a room temperature of 300 K which is used in the analysis of free vibration in FEM is tabulated as follows (Table 1).

Further, a dynamic study is performed to validate the effectiveness of the present study for vibration analysis of FG-CNTRC beam of present formulation and modelling in computer with the previous paperwork.

Also, to evaluate the present modelling of FG-CNTRC beam in FEM to observe the dimensionless frequency parameter following equations have been used

$$\overline{\omega} = \omega L^2 \sqrt{\frac{\rho_m}{E_m}.\frac{A}{I}} = \omega \frac{L^2}{h} \sqrt{\frac{\rho_m}{E_m}}. \tag{8}$$

An iterative program in the computer is modelled in MATLAB in order to assemble the stiffness and mass matrices for the required number of elements in FG-CNTRC beam.

First of all the effective material properties of FG-CNTRC were evaluated and then the comparison study is carried out for the successful use of finite element method for FG-CNT hybrid composite beam with all the dimensions of FG-CNTRC beam from the literature [12].

The fundamental natural frequency for the different Slenderness ratios (aspect ratios L/h) of a FG-X CNTRC with volume fraction of CNTs $V_{CNT} = 0.12$ beam for different boundary conditions is evaluated below. The different boundary conditions taken are: clamped-free (C-F), hinged-hinged (H-H), clamped-hinged(C-H) and clamped-clamped(C-C) are as follows:

Table 1 Material properties considered in FG-CNTRC beam (300 K) [12]

Properties(units)	Matrix (PMMA)	Reinforcement fiber (CNTs)
Poisson's coefficient	$\nu^m = 0.3$	$\nu^{CNT} = 0.19$
Mass density(kg/m^3)	$\rho^m = 1190kg/m^3$	$\rho^{CNT} = 1400kg/m^3$
Young's modulus of elasticity(GPa)	$E^m = 2.5GPa$	$E^{CNT} = 950GPa$, $E_{11}^{CNT} = 600GPa$, $E_{22}^{CNT} = 10GPa$
Shear modulus (GPa)	–	$G_{12}^{CNT} = 17.2GPa$

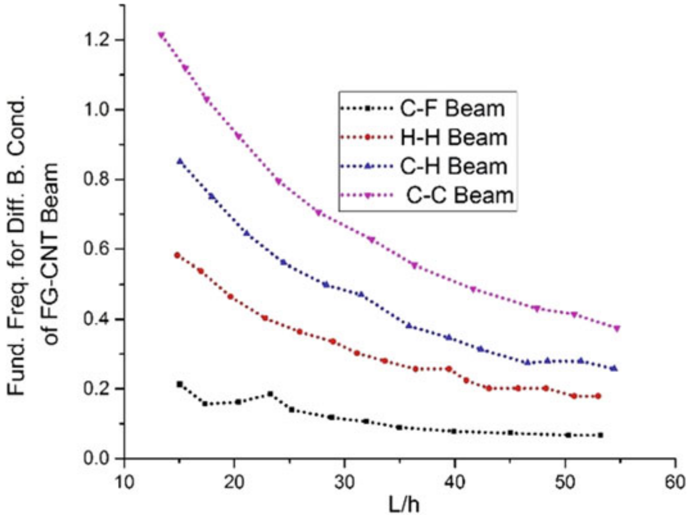

Fig. 3 Fundamental frequency versus aspect ratio of FG-X beam for different boundary conditions

The plot for variation of fundamental frequency of vibration of FG-X CNTRC beam for various boundary conditions (C-F, C-H, H-H and C-C) are plotted for different values of Slenderness ratios as shown in the Fig. 3.

The plot for comparison of the evaluated fundamental frequency of vibration for different aspect ratios (L/h) for a FG-CNT beam having FG-X Distribution for clamped-clamped(C-C) boundary conditions is as shown in Fig. 4.

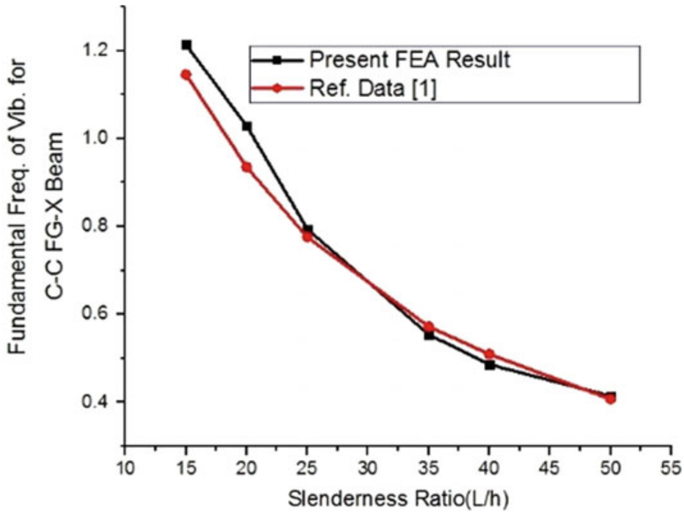

Fig. 4 Comparison of evaluated fundamental frequencies with literature. [12] for FG-X C-C beam

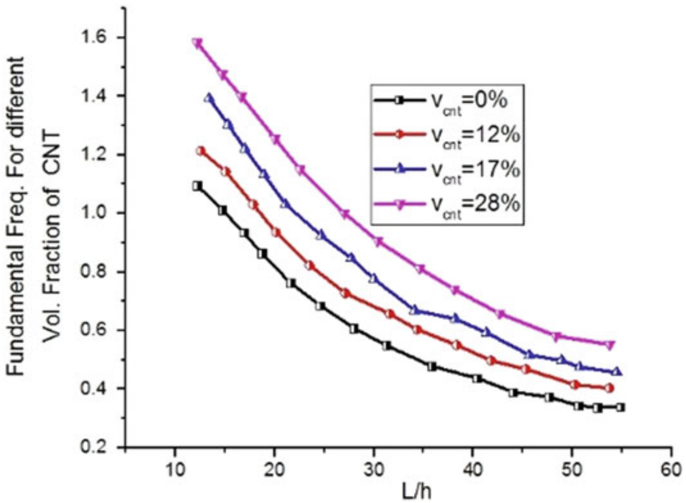

Fig. 5 Fundamental frequency versus aspect ratio of FG-X Beam for the different volume fraction

The variation of fundamental frequency versus aspect ratio(L/h) of FG-X FG-X hybrid composite beam for clamped-clamped boundary condition as shown in Fig. 5 for different volume fractions of CNTs (i.e. $v_{cnt} = 0.12$, $v_{cnt} = 0.17$ and $v_{cnt} = 0.28$, from the literature [12]) distributions over a given cross-section of the beam.

The variation of dimensionless frequency of vibration for different CNT gradations over PMMA matrix with CNTs volume fraction of $V_{CNT} = 0.12$, and boundary condition has also been calculated and is listed in Table 2 (Table 3).

From this, it is observed that the FG-CNT beam having X-distributions, comparatively larger frequency than the other distribution profile.

Table 2 The comparison of dimensionless fundamental frequency w.r.t slenderness ratio (L/h) of FG-CNTRC beam for different boundary conditions

L/h	Fundamental frequency ($\overline{\omega_1}$) of vibration for different boundary conditions of FG-X CNTRC beam			
	$\overline{\omega_1}$ for C-F	$\overline{\omega_1}$ for H-H	$\overline{\omega_1}$ for C-H	$\overline{\omega_1}$ for C-C
15	0.213	0.562	0.850	1.214
20	0.162	0.460	0.652	1.029
25	0.139	0.363	0.550	0.794
35	0.095	0.260	0.386	0.554
40	0.078	0.247	0.347	0.486
45	0.0727	0.201	0.285	0.440
50	0.067	0.179	0.279	0.414

Table 3 The variation of dimensionless frequency of vibration for different CNT gradation and boundary condition

Boundary cond.	FG-CNT distribution profile			
	UD	FG-Λ	FG-◊	FG-X
C-C	1.576	1.472	1.392	1.675
C-F	0.394	0.305	0.301	0.464
C-H	1.306	1.221	1.065	1.432
H-H	1.032	0.986	0.782	1.171

5 Conclusions

A comparative study has been carried out for the FG-CNT beam having constituent materials of PMMA as matrix and CNTs as reinforcement in four different distributions subjected to four different boundary conditions. The free vibration analysis of FG-CNT beam through finite element method modelling concludes the following results.

From the above analysis, it is illustrated that:

- The volume fraction distribution of CNTs having a significant effect on the natural frequency of vibration of the beam and the beam having the highest volume fraction of CNT is having more natural frequency of vibration.
- The Slenderness ratio (L/h) of the FG-CNT beam is also having a prominent effect on the behaviour of natural frequency of vibration, and when this ratio increases, then the fundamental frequency of vibration value decreases consequently.
- Carbon nanotube beams in which orientation takes place in FG-X manner having the highest fundamental frequency as compared to other distributions.
- Increasing the volume fraction of CNT leads rise to an increase in the natural frequency of vibration.
- This method of analysis of FG-CNT can also be applied for forced vibration, buckling analysis and beam subjected to different higher temperature conditions.

The power law distribution plot also made in MATLAB program to analyze the behaviour of Young's modulus of CNT-reinforced beam with the directional variation of z/h, which resulting in a power law index of 1.5 will be most suitable for high-temperature application of FG-CNT beam.

References

1. Selim BA, Zhang LW, Liew KM (2015) Vibration analysis of CNT-reinforced functionally graded composite plate in a thermal environment based on Reddy's higher order shear deformation theory. Compos Struct 156:276–290
2. Vo-Duy T, Ho-Huu V, Nguyen-Thoi T (2019) Free vibration analysis of Laminated FG-CNT reinforced composite beams using finite element method. Front Struct Civil Eng 13(2):324–336

3. Kashyzadeh KR, Asfarjani AA (2016) Finite element study on the vibration of functionally graded beam with different temperature conditions. Adv Mater 5(6):57–65
4. Karamanli A (2018) Free vibration analysis of two directional functionally graded beams using a third order shear deformation theory. Compos Struct 189:127–136
5. Moradi-Dastjerdi R, Payganeh GH, Malek-Mohammadi H (2015) Free vibration analyses of functionally graded CNT reinforced nanocomposite sandwich plates resting on elastic foundation. J Solid Mech 7(2):158–172
6. Ebrahimi F, Farazmandnia N (2018) Vibration analysis of functionally graded carbon nanotube-reinforced composite sandwich beams in thermal environment. Adv Aircr Spacecraft Sci 5(1):107–128
7. Kuo SY (2018) Free vibration of fully functionally graded carbon nanotube reinforced graphite/epoxy laminates. Mater Res Expr 5(3)
8. Liew KM, Lei ZX, Zhang LW (2015) Mechanical analysis of functionally graded carbon nanotube reinforced composites: a review. Compos Struct 120:90–97
9. Ke LL, Yang J, Kitipornchai S (2010) Nonlinear free vibration of functionally graded carbon nanotube-reinforced composite beams. Compos Struct 92(3):676–683
10. Chaudhari VK, Lal A (2016) Nonlinear free vibration analysis of elastically supported nanotube-reinforced composite beam in thermal environment. Procedia Eng 144:928–935
11. Lin F, Xiang Y (2014) Vibration of carbon nanotube reinforced composite beams based on the first and third order beam theories. Appl Math Model 38(15–16):3741–3754
12. Kumar P, Srinivas J (2017) Free vibration, bending and buckling of a FG-CNT reinforced composite beam. Multidiscipline Model Mater Struct 13(4):590–611

Computational Analysis of Boring Tool Holder with Damping Force

G. Lawrance, P. Sam Paul, and A. S. Varadarajan

Abstract In the boring process, tool vibration is an important parameter due to its overhanging length and also leads to high cutting force, poor surface finish and increase in tool wear. To suppress tool vibration and increase the cutting performance, a novel idea has been developed in rheological fluid. In present work, a boring tool holder with magnetorheological damper was analysed. Magnetorheological damper received massive responsive due to their capability to reversely change from a linear, free-flowing viscous fluid to semis solid within seconds when a magnetic field is applied. In this paper, a boring tool holder was analysed using ANSYS software with damping force applied in various direction and without MR effect. The results prove that the use of Magnetorheological damper reduces tool vibration significantly.

Keywords Boring tool holder · Magnetorheological damper · Damping ratio · Harmonic analysis · Modal analysis

1 Introduction

The modern industries are more concerned about achieving a product with reduced ecological effect during its production and achieving high standard at the end product, increase in dimensional accuracy, good surface quality, increased production rate, reduced tool wear and economy. In the manufacturing process, dynamic interaction between tool and workpiece results in tool vibration. The vibration in tool and wavy surface on the workpiece result modified chip thickness, which also results in invariable cutting forces to stimulate the work piece and machine [1]. Quintana and Ciurana [2] proposed that unbalance dynamic stiffness leads to self-excited vibration which further leads to diminishing in productivity and quality. The vibration further leads to poor surface quality, extreme tool wear and irritating noise [3]. Chen

G. Lawrance (✉) · P. Sam Paul
Karunya Institute of Technology and Sciences, Coimbatore, Tamil Nadu 641114, India
e-mail: lawrancedevaraj@gmail.com

A. S. Varadarajan
MES College of Engineering, Malappuram, Kerala 679573, India

E. T. Akinlabi et al. (eds.), *Trends in Mechanical and Biomedical Design*,
Lecture Notes in Mechanical Engineering,
https://doi.org/10.1007/978-981-15-4488-0_78

and Tsao [4] described the vibration behaviour by using flexible workpiece to focus on regenerative chatter rather assuming rigid workpiece. A large slender workpiece in machining at high spindle speed leads to an increase in deformation and affects the stable analysis whereas smaller deformation at less slender workpiece at high spindle speed [5]. Andren et al. [6] clarify the dynamic response of a boring bar in a non-linear and time-varying process when it is focused on three different workpieces and is measured in varying cutting depth and cutting speed direction. Tool vibration in boring operation is high when it is compared with turning operations due to its larger slenderness ratio [7]. So it is essential to reduce the tool vibration in boring operation effectively by means of damper which enhances the damping capability when compared with self-damping of conventional tool to suppress vibration [8].

Metal cutting industries are expecting better quality, increased productivity, decreased production cost and better technique to suppress tool vibration. To reduce tool vibration researchers used outlines in past and amongst them, the influence of smart material on tool has gained attention. Wang and Fei [9] proposed a boring bar with variable-stiffness consisting of an electrorheological (ER) fluid to reduce chatter. Magnetorheological fluid is a smart fluid and MR fluids was reported by Rabinow [10] who is the pioneer to use magnetorheological fluid with electromagnetically controllable clutch. Mei et al. [11] proposed Magnetorheological fluids which suppress vibration in the boring tool by adjusting the damping and natural frequency of the system. A Magnetorheological damper reduces tool vibration successfully in a turning tool when it was analysed using ANSYS software with and without Magnetorheological damper [12]. The analysing the boring tool holder subjected to Magnetorheological damper with different directions that reduces tool vibration by means of computational method is done in the present investigation.

2 Selection of Workpiece and Tool Holder

In the present investigation, AISI 4340 steelwork piece which is hardened to 45 HRC is used and the workpiece consists of 80 mm outer diameter and 40 mm inner diameter, 100 mm length were used. The AISI 4340 steel in weight percent with chemical composition is 0.41% C, 0.87% Mn, 0.28% Si, 1.83% Ni, 0.72% Cr, 0.20% Mo and rest F_e [13]. The tool holder is S25T PCLNR 12F3 which is a Widaxtool with diameter 23 mm and 300 mm in length is used. The geometry of the tool holder is shown in Fig. 1. The boring tool contains Tool shank, insert and sim. The boring tool holder material and its properties are detailed in Table 1. Multicoated tungsten carbide inserts CNMG 120408 MT TT5100 from M/s Taegu Tec is used for the analysis purpose.

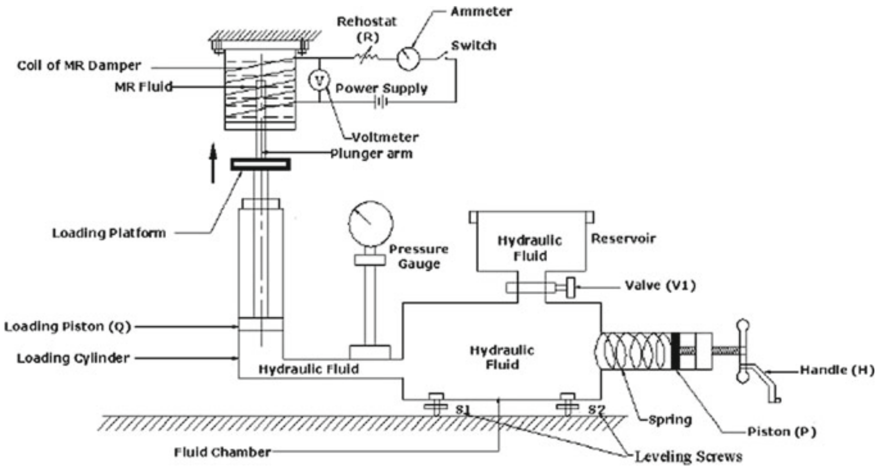

Fig. 1 Line sketch of apparatus determining the damping force [1]

Table 1 Material properties of tool holder [13]

Material	Properties	Density (Kg/m^3)	Poisson's ratio	Young's modulus (N/m^2)
Tool Shank	Carbon steel	7850	0.3	2.09E+11
Insert	Tungsten carbide	15,800	0.28	5.55E+11
sim	steel	7850	0.29	2.09E+11

3 Magnetorheological Damping Force for Boring Tool Holder

In the present study, the computational analysis of boring tool holder was analysed with damping force applied in various direction. A line sketch of the apparatus is shown in figure which was used to find the damping force to be applied in various direction. The piston (P) forces the fluid in the hydraulic chamber to move in loading cylinder when the handle (H) is rotated and the loading piston (Q) moves up along the loading platform. The applied voltage was controlled and the current was measured when the coil of the damper was connected to a circuit. The loading chamber is consist of pressure gauge and the area (Ap) of the loading piston, pressure (Pr) acting on the piston and the force (Fp) acting on the piston is given by

$$\mathrm{Fp} = \mathrm{Pr} \times \mathrm{Ap} \times 9.81 \quad N$$

The MR fluid damper is made active by applying the voltage V across the coil and the plunger touches the loading platform. When the handle (H) rotated in clockwise there is an increase in the pressure of the chamber. When the force applied by the

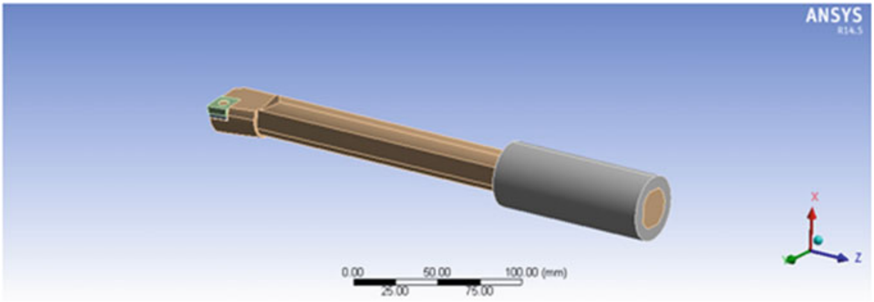

Fig. 2 A model of boring tool holder

loading platform balances the resistance offered by the MR fluid damper, the plunger just starts moving up and the limiting pressure indicated by the pressure gauge was noted which a measure of the resisting force that is offered by the MR damper for the applied voltage V [1] and the damping force is calculated as 102N.

4 Computational Analysis

4.1 Geometric Modelling

The boring tool holder was modelled using ANSYSsoftware and is shown in Fig. 2.

4.2 Grid Independence Study

Solid element of type Solid 185 is used in the present work. Based upon the accuracy, number of elements is chosen and done using Grid Independent Study. The accurate results can be obtained when there is an increase in number of element, beyond a certain number of elements accuracy cannot be upgraded. Grid independent study is carried out until deflection becomes constant. As in Fig. 3, beyond 0.315346 mm the deflection does not change and the number of elements was found to be 2×10^6. The use of 2×10^6 elements contains degrees of freedom in a huge number and it is not possible to store in the computer memory. Hence, the number of element required is 45×10^5.

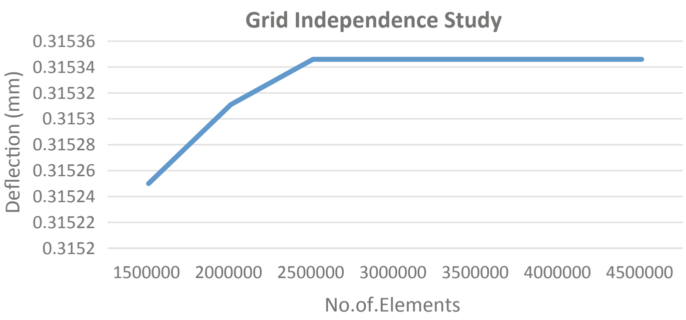

Fig. 3 Grid Independence Study

4.3 Static Analysis

The deflection values for different clamping length are calculated using static analysis. The cutting force used in the insert tip is calculated based on the formula. Cutting force = 396,000 × Depth of Cut × power consumption × feed rate. A 500 N force is applied at the tip of the boring tool holder in a vertical direction at a distance of 85 mm from the tool tip [13]. Then damping force is applied in a vertical direction, horizontal direction and holding direction. The performance of the static analysis for the 100 mm, 125 mm, 150 mm overhanging length individually with the application of damping force and the corresponding maximum deflections were noted. The same analysis was performed again but without damping force. The deflections that were found for various clamping lengths are provided in Table 2. It is clearly seen from Fig. 4, 5 and 6 that when the clamping length increases the deflection decreases.

Table 2 Overhanging length versus deflection versus damping force direction

S.No.	Overhanging length (mm)	With damper (mm)			Without damper (mm)
		Axial force	Vertical force	Holding force	
1	150	0.37541	0.36925	0.17294	0.3668
2	125	0.37977	0.36529	0.10569	
3	100	0.38528	0.40801	0.063886	

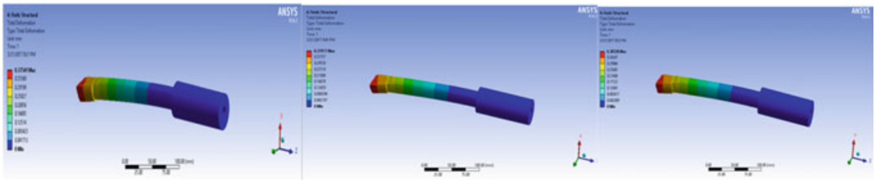

Fig. 4 Deflection for 150,125 and 100 mm tool overhanging length with axial force

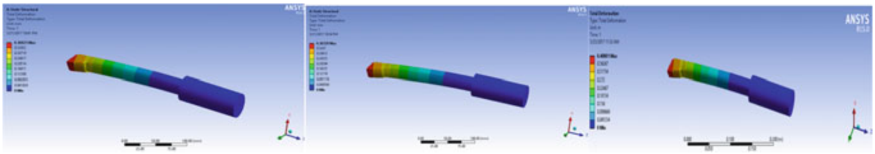

Fig. 5 Deflection for 150,125 and 100 mm tool overhanging length with vertical force

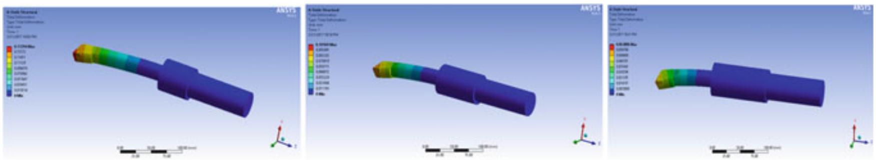

Fig. 6 Deflection for 150,125 and 100 mm tool overhanging length with holding force

4.4 Modal Analysis

The dynamic response is excited by input on structures and fluids when it is measured and analysed in the field is called Modal analysis. The system will collapse when the frequency of the system reaches its natural frequency. The system frequency should be below its natural frequency to avoid catastrophic failure. Computing the natural frequency of the system modal analysis avoids such a failure and for different overhanging length, the modal analysis was done. The extreme natural frequency obtained was 4390.6 Hz at 150 mm overhanging, 5914.8 Hz at 125 mm overhanging and the corresponding natural frequency for 100 mm overhang length was found to be 7523 Hz for holding position are tabulated in Table 3

4.5 Harmonic Analysis

A sustained cyclic response is produced by the sustained cyclic load on a structural system. The dynamic behaviour of forced vibrations on the structures can be predicted, which ensure whether the designs were successful in overcoming the fatigue, resonance, and other harmful effects are known as Harmonic analysis. This technique is used to determine steady-state response that varies sinusoidal with time form linear structure to loads. In the present study, the value of forced frequency is attained by applying load which is 500 N at top of the tooltip. From the Fig. 7, the procedure for damping ratio (τ) value was found using half-power bandwidth methods. The values for damping ratio for different damping force direction and without damping force is tabulated in Table 4.

Table 3 Overhanging length versus natural frequency versus damping force direction

S.No.	Overhanging length (mm)	Axial force with damper (Hz)	Vertical force with damper (Hz)	Holding force with damper (Hz)	Without damper (Hz)
1	150	433.68 440.68 2597.2 2603.6 4080.8	442.79 448.75 2637.7 2643.8 4108.1	764.7 779.07 2446.6 2465.4 4390.6	443.82 451.09 2645.5 2652.4 4133.54
2	125	431.33 438.82 2631.7 2639 4067.1	443.16 449.99 2643.4 2650.3 4126.4	1126.3 1139.5 2450.5 2470.7 5914.8	
3	100	431.33 438.82 2631.7 2639 4067.1	581.3 1670.3 3455.4 5776.3 6119.7	1697.4 1723.3 2448 2456.1 7523	

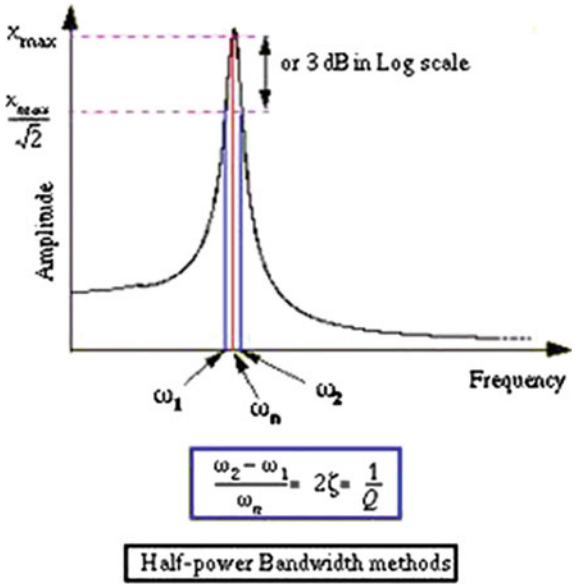

Fig. 7 Harmonic analysis

5 Results and Discussion

In boring tool holder, finite element analysis was done in the overhanging position of 150, 125 and 100 mm using ANSYS software. The tool deflection increases with the increase in tool overhanging length observed from static analysis. Out of

Table 4 Overhanging length versus damping ratio versus damping force direction

S.No	Overhanging length (mm)	Axial force damping ratio	Vertical forces damping ratio	Holding forces damping ratio	Without damper damping ratio
1	150	0.2	0.27	0.13	0.3
2	125	0.18	0.2	0.15	
3	100	0.16	0.25	0.13	

Table 5 Comparison of results with and without MR damper in holding direction

	100 mm overhanging without MR damper		100 mm overhanging with MR damper	
Method	Computational	Experimental	Computational	Experimental
Deflection	0.3 mm	0.32 mm	0.13 mm	0.132 mm
Natural frequency	4440.54 Hz	4240 Hz	7523 Hz	7400 Hz

the different overhanging position, tool with 100 mm overhanging length was to be the optimum, since this length has minimum tool deflection and also it satisfies experimental criteria. Comparison of experimental and computational results for boring tool holder with and without damping force is shown in Table 5.

As shown in Table 5, the boring tool holder with MR damper has less deflection when compared to tool holder without damping effect. The system opposes the movement of boring tool 50 mm from fixed end (150 mm), offers better damping effect and suppresses tool vibration. When it is compared with damping force of length 50 mm from fixed end, tool holder has no damping force. The natural frequency increases when there is an increase in stiffness due to the damping force acting on the holding direction which in turn reduces the mass acting on the tool holder. Also, it is seen that the deflection and natural frequency obtained using computational results matched well with the experimental results which were conducted on a Kirloskar turn master lathe during hard boring with MR damper. During the experimental work, 30 V with direct current was used in the coil with cylinder consist of particle size 75 microns, fluid viscosity index is 40, with cone-shaped plunger and the damper was positioned in holding direction as shown in Fig. 8. Based on the harmonic analysis, it was found that a tool with MR damper in holding direction provide lesser damping ratio when compared with other direction and tool without damper. From the investigation, it has proved that a tool with magnetorheological fluid damper in holding direction suppress the tool vibration and provide better cutting performance which enrich the quality of the finished product.

Fig. 8 Photograph of experimental setup

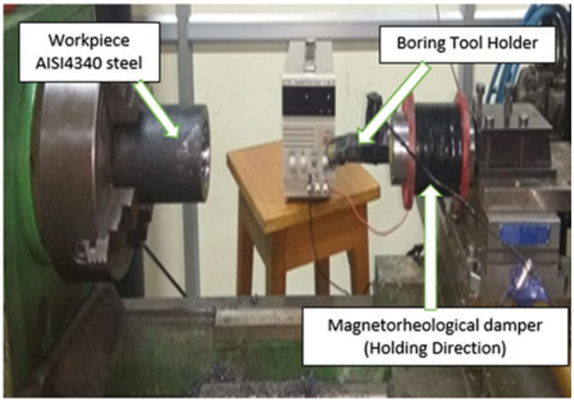

6 Conclusion

The present investigation provides a detailed explanation on the effect of tool holder with various damping force direction and without damping force on tool vibration. The effect of tool vibration on a boring process using Magnetorheological damper by ANSYS software is studied. ANSYS software was used to model and analysed the tool holder with insert and sim. The force constraints such as cutting force and damping force were provided along with the fixed boundary conditions. The results obtained from computational methods reasonably matched well with the experimental results. It is proven that using Magnetorheological fluid damper which is presently holding direction reduces tool vibration and cutting performance can be improved effectively.

References

1. Sam Paul P, Varadarajan AS, Ajay Vasanth X, Lawrance G (2014) Effect of magnetic field on damping ability of magneto rheological damper during hard turning. Arch Civ Mech Eng 14:433–443
2. Quintana G, Ciurana J (2011) Chatter in machining processes: a review. Int J Mach Tools Manuf 51:363–376
3. Sam Paul P, Varadarajan AS (2012) Effect of magneto rheological damper on tool vibration during hard turning. Front Mech Eng 7:410–416
4. Chen CK, Tsao YM (2006) A stability analysis of regenerative chatter in turning process without using tailstock. Int J Adv Manuf Technol 29:648–654
5. Chen CK, Tsao YM (2006) A stability analysis of turning a tailstock supported flexible workpiece. Int J Mach Tools Manuf 46:18–25
6. Andren L, Hakansson L, Brandt A, Claesson I (2004) Identification of dynamic properties of boring bar vibrations in a continuous boring operation. Mech Sys Sign Process 18:869–901
7. Moetakef-Imani B, Yussefian NZ (2009) Dynamic simulation of boring process. Int J Mach Tools Manuf 49:1096–1103

8. Waghmare PJ, Patil RV, Waghmare GS (2015) A review on vibration mitigation of boring bar using passive damping techniques. Int J Res Eng Technol 4:138–141
9. Wang M, Fei R (1999) Improvement of machining stability using a tunable-stiffness boring bar containing an electrorheological fluid. Smart Mater Struct 8:511–514
10. Rabinow J (1951) Magnetic fluid torque and force transmitting device, United States Patent US 2575360 A
11. Mei D, Kong T, Shih AJ, Chen Z (2009) Magneto rheological fluid-controlled boring bar for chatter suppression. J Mater Process Technol 209:1861–1870
12. Paul PS, Varadarajan AS, Lawrance G, Sunil KS (2012) Analysis of turning tool holder with Mr Fluid damper, international conference on modeling, optimization and computing. Procedia Eng 38:2572–2578
13. Lawrance G, Paul PS, Varadarajan AS, Praveen AP, Vasanth XA (2017) Attenuation of vibration in boring tool using spring controlled impact damper. Int J Interact Des Manuf 11:903–915

Comprehensive Review of the Effects of Vibrations on Wind Turbine During Energy Generation Operation, Its Structural Challenges and Way Forward

I. P. Okokpujie, E. T. Akinlabi, N. E. Udoye, and K. Okokpujie

Abstract The effects of vibration cannot be overemphasized when it comes to generating energy via wind turbine. Vibration is one of the major challenges faced by the wind turbine, due to the complexity of the structure and the area of installation. This research work focuses on a compressive review of the effects of vibration occurrence on wind turbine during energy generation operations and its economical challenges'. Therefore, this research paper has reviewed various aspects of vibration effects in horizontal wind turbine such as the blades region, tower structure, nacelles compartment, and condition monitoring along with fault diagnosis models. The result from this study has shown that, there are needs to develop and implement a good reliability model, fatigue assessment process, and a well-developed monitoring model for wind turbine during operation. When these things are properly put in place, it will help to reduce unwanted vibration occurrence, eliminate unexpected failure of the wind turbine in operations, and hence sustainable energy generation from wind turbine.

Keywords Vibration · Reliability for sustainability · Wind turbine blade · Wind turbine tower

1 Introduction

Vibration will occur when a structure is dislodged from its location of stable equilibrium. The structure will generally return to its stable position under the activity of

I. P. Okokpujie (✉) · E. T. Akinlabi · N. E. Udoye
Department of Mechanical Engineering, Covenant University, Ota, Ogun State, Nigeria
e-mail: imhade.okokpujie@covenantuniversity.edu.ng

E. T. Akinlabi
Department of Mechanical Engineering Science, University of Johannesburg, Auckland Park Kingsway Campus, Johannesburg 2006, South Africa

K. Okokpujie
Department of Electrical and Information Engineering, Covenant University, Ota, Ogun State, Nigeria

E. T. Akinlabi et al. (eds.), *Trends in Mechanical and Biomedical Design*,
Lecture Notes in Mechanical Engineering,
https://doi.org/10.1007/978-981-15-4488-0_79

re-establishing powers. The towel holds the displacement of the forward and backward movement of the wind turbine over the issue of its balance [1]. A structure is combinations of element designed to act together to achieve a goal. A stationary element is one whose operation makes its yielding time depends just on the contribution at a time while a dynamic element yield depends on previous information [2]. A static and dynamic framework is two great types of the frameworks that consist on all components and one powerful component, respectively [3]. The issues of vibration in wind turbine can seriously affect the energy preservation; due to the fact that, the vibration will help to expand the system which will lead to loss of energy generated from the wind turbine during operations and after.

Wang et al. [4] recommended a damage identification and determination technique for wind blades based on the unique elements property and mode shape distinction arch data. It likewise gives a minimal effort and effective, nondestructive instrument for wind turbine blade condition examination. Notwithstanding mix with modular investigation strategies, the auxiliary strain field information likewise assumes an essential job in identifying the harm existing in the breeze turbine system, including the sharp edges and tower, on the grounds that the slight difference in basic physical properties may prompt the rearrangement of basic strain. As a rule, the strain contrast between nearby strain sensors can be considered as a list of the nearness of a split and utilized as an attainable system to accomplish remote exhaustion harm recognition for OWT towers. Nonetheless, the achievement predominantly relies upon the sensible game plan of strain sensors around the pinnacle and the expectation of extraordinary wind conditions [5, 6].

To discover the abilities of different tension sensors made with fiber Bragg grating (FBG), optical backscatter reflectometer (OBR), and typical strain checks in harm identification, an example acknowledgment system utilizing progressive nonlinear essential segment investigation (h-NLPCA) in light of the strain field estimation was depicted to recognize harm amid the affirmation trial of the blades [7, 8]. In light of the trial results, the FBGs have more points of interest over the strain measures. FBGs are reasonable for being inserted into the compound materials straightforwardly amid the operational procedure of OWTs and observing progressively inside changes in strain, which strain measures reinforced onto the surface cannot accomplish. What is more, the FBGs have a more drawn out life in administration well-being observing and harm discovery frameworks dependent on strain estimations for seaward wind ranches. From there on, Downey contemplated a crossover thick sensor arranges comprising of meager film sensors and FBGs and proposed an information-driven harm recognition and limitation technique for wind turbine sharp edges. This procedure uses the blunder between the evaluated strain maps and measures strains to characterize harm location which includes and applies a novel strategy for reviewing vast quantities of sensors without the requirement for complex model-driven methodologies by intertwining sensor information into a solitary harm discovery highlight [9]. The wind turbine also has a lot of electrical activities, which will need electrical models to establish in the remote areas [10]. The challenge faced by researchers in the field of wind turbine is very enormous, due to the fact that wind turbine development and operations are very complex. There is great need to bridge the gap between researcher, teachers, and the industry in order to provide solutions to these challenges [11–13].

However, this paper aimed at carrying out a compressive review on the effects of vibrations occurrences during operation of wind turbine. This study will further assist to eliminate and to reduce vibration occurrence on wind turbine.

2 Review of the Effects of Vibrations on Horizontal Wind Turbine During Operations

Escaler and Mebarki [14] study vibration analysis on the wind turbine. The vibrations were experimentally determined in precise positions applying the same type of sensors for the period of six-month covering the whole range of working situations. The data obtained were preliminary certified to eliminate outliers based on the hypothetical energy curves. The influential frequency points in the blade, gearbox, and generator on vibrations were discovered and identified established on averaged energy spectra. The amplitudes of the points induced by some environmental effects were compared in various positions. There were observations on the broadband vibration on the wind speed reliance during this study. Finally, the authors detected a fault case in the change of vibration enforce by a damage in the gearbox, as shown in Fig. 1.

According to Hossain et al. [15], said that wind turbine is greatly subjected to various fault on the mechanical system during operation which can be tired to the issues of vibrations occurrences. Figure 2 shows the analysis of various failure rates in wind turbine components, and Fig. 3 shows all the basic components of wind turbine fully in operations. This analysis is in line with the observation from Okokpujie et al.

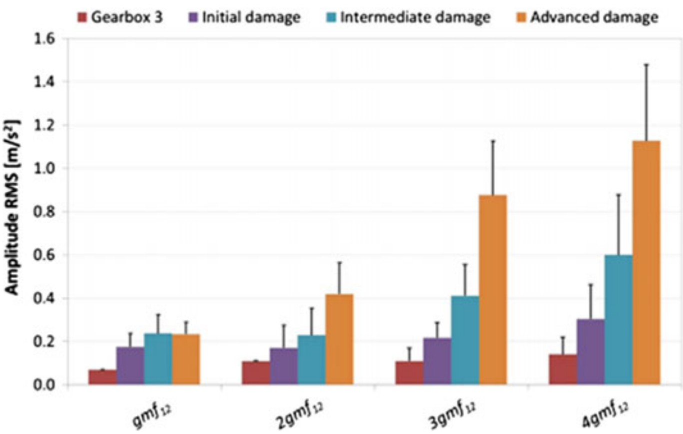

Fig. 1 Evaluation between the reference means vibration (RMS) amplitude on the gear mesh frequency (GMF) and the harmonics (gearbox 3) showing the various levels of damage [14]

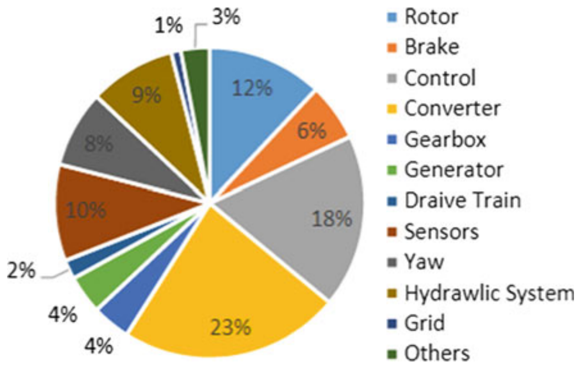

Fig. 2 Rate of failure of the various component of the wind turbine [17]

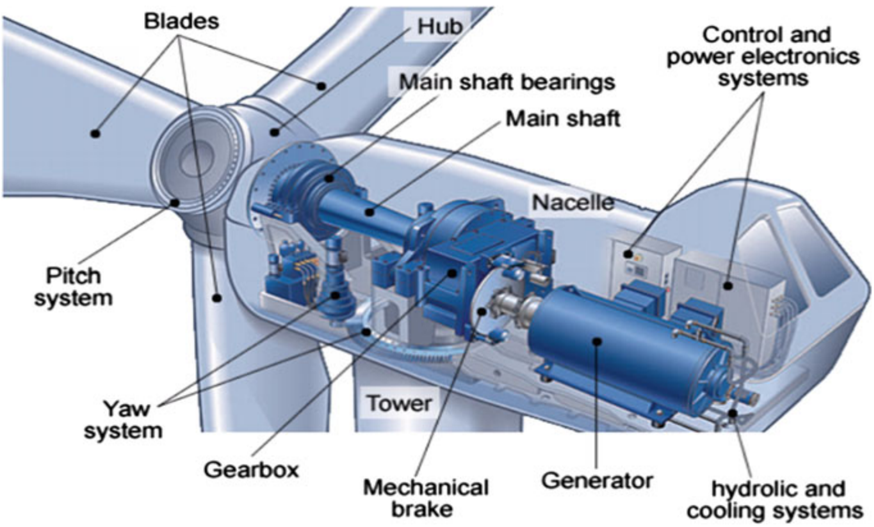

Fig. 3 Distinctive utility-scale wind turbine basic mechanisms [18]

[16] which in their design work shows that vibration is one of the major challenges faced by a wind turbine, due to its mechanical structures.

2.1 Effects of Vibration on a Horizontal Axis Wind Turbine Blades

A lot of researchers have carried out an experimental study on the causes of the occurrence of sound on the wind turbine during operation. The authors concluded that the flowing air passing through the blades (i.e., aerodynamic shape) has effects on the turbine blades, which causes the vibration in the form of sound waves [19, 20]. One of the most significant aspects of the impact is the atmospheric turbulence striking the blades of the wind turbine during operation (i.e., the influx of the sound turbulence) and also the air rolling at the surface of the blades (trailing edge).

- Turbulence at the back or trailing edge of blades is created on the grounds that the wind stream at the blades surface forms into a tempestuous layer. The recurrence with the most noteworthy (capable of being heard) sound vitality content is generally in the scope of a couple of hundred Hz (hertz) up to around 1000–2000 Hz. At the edge tips, conditions are to some degree diverse because of air streaming towards the tip; however, this tip commotion is fundamentally the same as trailing edge clamor and more often than not recognized as a significant separate source.
- Inflow disturbance is produced on the grounds that the blades slice through fierce whirlpools that are available in the inflowing air (wind). This sound has a most extreme sound dimension at around 10 Hz.
- Thickness sound outcomes from the relocation of air by moving blades and is irrelevant for sound creation when the wind streams easily around the blades. Notwithstanding, quick changes in powers on the blades result in sideways developments of the sharp edge and sound heartbeats in the infrasound district. This prompts the normal wind turbine sound "signature" of sound dimension tops at frequencies between around 1–10 Hz. These pinnacles cannot be heard, yet can be found in estimations.

Tartibu et al. [19] presented a work of flap-wise, edgewise, and torsional basic occurrences of variable length blades that have been acknowledged. Subsequently, initiators can guarantee that characteristic vibration won't be near the recurrence of the fundamental excitation powers so as to maintain a strategic distance from reverberation. The fixed part and moveable bit of the variable length of blades are approximately a strong bar which can be slide in and out. Ten unique setups of the variable length blades, speaking to ten distinct places of the moveable part, are examined. A MATLAB program was created to anticipate distinctive frequencies. Thus, three-dimensional models of the variable length of blades have been created in the limited component program Unigraphics NX5. Simultaneousness among MATLAB and Unigraphics NX5 results has been found for the recurrence scope of intrigue. This implies that a viable technique to figure regular frequencies of a variable length of blades was generated.

The investigation of the impact of blades length on regular frequencies shown in Fig. 4 has appeared with expanding blades length, the normal frequencies decrease. This is most likely on the grounds that the blades turn out to be increasingly adaptable as its length increases. The excitation loads are moved in the interim 0.5–30 Hz.

Kumar et al. [21] the primary goal of this examination research is to present another material for wind turbine blades. Aluminum 2024 is chosen for the reasonableness examination. Limited component method or finite element analysis is a strategy utilized for the investigation of complex articles and geometries. Wind power or wind vitality is considered as a spotless wellspring of vitality which delivers no

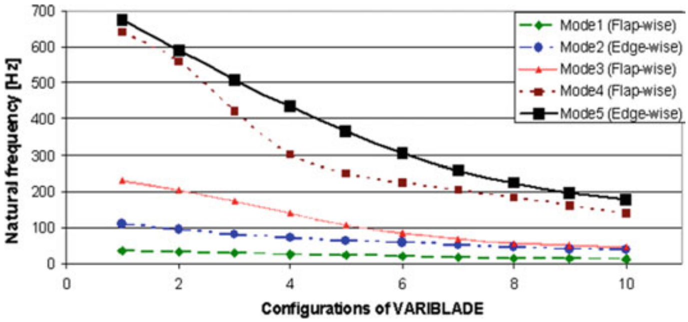

Fig. 4 Effects of vibration natural frequency on configurations of variable blade [19]

ecological damage amid activity. The complete wind control age capability of India at a tallness of 50 m is 50,000 MW. As of late Indian Government has concentrated on this inexhaustible well-spring of energy. The primary part of this exploration is to recognize vibration frequencies and regular vibration methods of the Aluminum 2024 wind turbine blades. Wind turbine blades configuration is a perplexing technique. For the plan of wind turbine blades, solid edge programming is utilized and the model is imported in ANSYS 14.0 for modular investigation. For the reasonableness examination of Aluminum 2024, the basic and modal investigation has been done. The significances of the investigation are utilized to confirm a structure's readiness for use.

The examination results were confirmed with experimental result accessible in writing. With the expectation of free vibration examination of Aluminum 2024, wind turbine blades modular investigation utilizing ANSYS 14.0 was directed. Through our examination, we have discovered the disfigurements, stresses, and normal frequencies for initial six modes state of Aluminum 2024 wind turbine blades as presented in Fig. 5a. The examination results were checked with an experimental result that has been done. Andrew [22] examined the on and seaward wind turbines. As indicated by the author's test examination, the most extreme happens at tip as shown in Fig. 5b, and the loads are extremely less for Aluminum lightweight materials.

Taware et al. [23] composite materials have different confounded attributes as indicated by the utilization of the constituent materials and limited conditions. In this manner, it is hard to examine the properties of composite materials, and the composite materials are outstanding by their superb blend of high auxiliary firmness and low weight. Their anisotropy enables the designer to tailor the material so as to accomplish the ideal execution necessities. Accordingly, it is important to create devices that enable the architect to get plans, thinking about the auxiliary prerequisites and utilitarian attributes, for effective utilization of composite materials in building applications, the dynamic conduct (e.g., normal frequencies) ought to be known. This paper centered around the conduct of little wind turbine blade fabricated from composite materials. Two little wind turbine blades are produced from the glass fiber reinforced plastic (GFRP) and GFRP with steel wire work support.

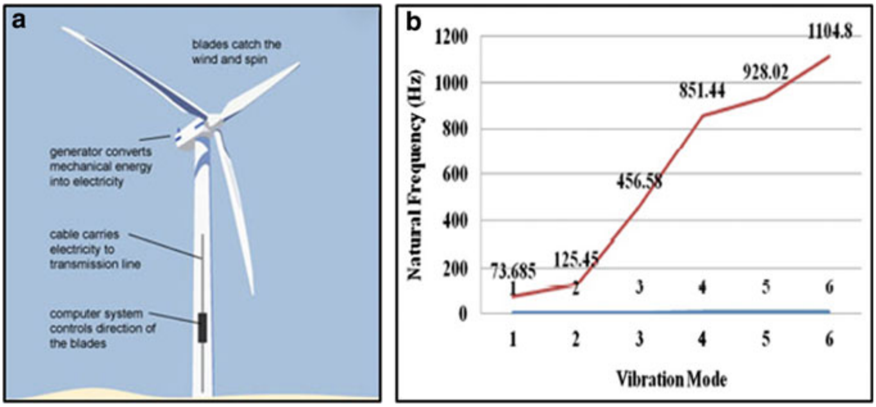

Fig. 5 **a** Wind turbine illustration **b** vibration mode v/s expected frequency of the AL 2024 alloy blade used for the development of the wind turbine [22]

Finite element analysis (FEA) was completed by utilizing the component programming ANSYS 16.0. From FEA, hypothetical normal frequencies and mode shapes of blades made from the GFRP and GFRP with steel wire work support were acquired. Test free vibration trial of produced blades was done to locate the useful regular vibration frequencies and mode shapes at last, the outcomes acquired from the FEA and exploratory test for the blade fabricated from GFRP and GFRP with steel wire work were carried out, and the result shows that the GFRP with steel wire has great performance when compared with the GFRP.

2.2 *Effects of Vibration on a Horizontal Wind Turbine Tower*

The horizontal wind turbine tower shoulders an essential role in supporting the energy-producing part, for example, blades, hubs, and nacelles. The tower opposes the wind loads produced by the rotational wind blades [23] and hence, to verify the auxiliary security and dependability of the wind on the turbine tower, which can be harmed by unanticipated solid winds, through basic wellbeing checking. For this situation, Kim et al. [24] contemplate the dynamic attributes of a wind turbine tower display with and without harm at different areas were examined. However, indoor trials with the end goal of damages evaluation and auxiliary well-being observing the test result were contrasted and those acquired utilizing limited component demonstrate as appeared in Fig. 6 which demonstrates the variety of the recurrence and the conceivable damages. The authors likewise proposed a fitting damage identification system for the wind turbine tower, recurrence base damage location strategies were connected, and the outcome was checked by utilizing the numerical model of a 3 MW airstream turbine tower working in Jeju Island, Korea. The comparison of the indoor experiment and the finite element (FE) model are shown in Fig. 7. The

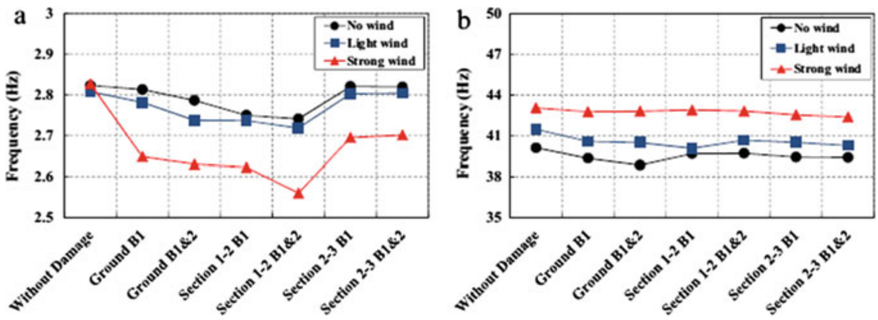

Fig. 6 The analysis of the natural frequency variations with the damage situations of mode 1 and 2 [24]

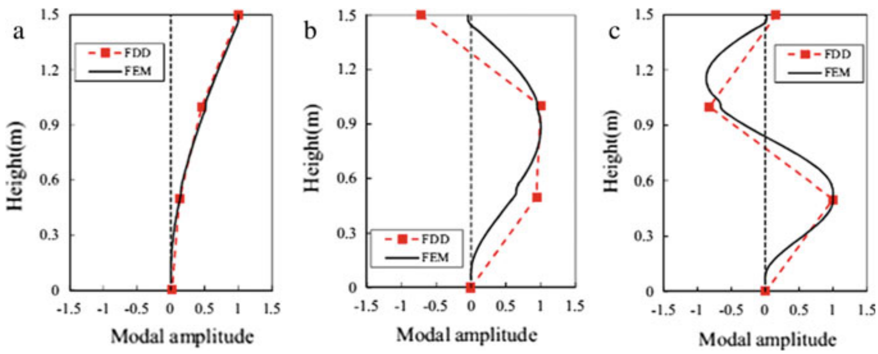

Fig. 7 Analysis of the first three shapes of the mode **a** mode 1, **b** mode 2, **c** mode 3 for the FE and FDD [24]

frequency-domain decomposition (FDD) technique was used for the identification of the natural frequency, damping ratio, and shape mode, which are the parameters of the modal; the result gotten from this technique were also analyzed and compared with FE model, and Table 1 gives the analysis of the first model.

Figure 8 shows a wind turbine tower that was greatly affected by the vibration during operation, as a result of unwanted vibration occurrences on the earth cross, coupled with other fault that was not detected before the failure of the wind turbine occurs.

Table 1 FE model and FDD comparisons result [24]

Wind environment	Model	FE	FDD	Percentage difference (%)
Light	1	2.7332	2.8224	3.2
676 (rpm)	2	54.669	40.103	26.6
	3	170.785	100.185	41.3

Fig. 8 Failed wind turbine tower during operation

Guo and Infield [25] carried out the examination of the early disappointment of key segments, for example, the tower, drive train, and rotor of a substantial wind turbine. In their work, the authors used the nonlinear state estimation technique (NSET) to determine the turbine tower vibration impact, giving a comprehension of the tower vibration dynamic attributes, and the fundamental elements affecting it. The created tower vibration demonstration involves two unique aspects: (1) a sub-display utilized for underneath evaluated wind speed and (2) for above-assessed wind speed as shown in Fig. 9. Supervisory control and data acquisition system (SCADA) applied the data obtained from a wind turbine from March to April 2006 to develop the model, and the model was validated with series of experimental analysis. The NSET method has been effectively demonstrated in this research work, which proves to be accurate and very efficient for tower vibration analysis. The tower vibration model developed was further used for spotting out blades angle irregularity, which is a common error that needed to be fixed in other to hence the performance of the wind turbine and help to eliminate or reduce fatigue damages. This study has demonstrated that condition checking will be improved greatly, if data from vibration signals is accompanied by the investigation of other applicable SCADA information, for example, energy performance analysis, rotor loads, and the wind speed.

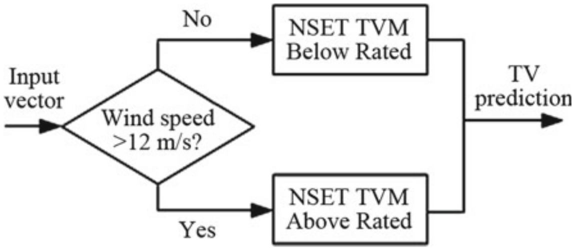

Fig. 9 NSET modeling and prediction for tower vibration [25]

Tibaldi et al. [26] used the aeroelastic simulation process to examined wind turbine vibration base on both frequency and time domain. Three different aspects were investigated such as there are need for a defined model in the operation of a close echoing condition; the presence of resonances identification and load estimation at low turbulence intensity during the wind turbine operation is very significant; and the external excitation response of the wind turbine. In the first phase of the analysis, the frequency and the damping of the aeroelastic modes were analyzed with three wind turbine models. Two different turbulent intensities were used to investigate the same models on fatigue loads to analyze the response from the wind turbine.

The second phase, to determine the modes that can be excited, an external force is introduced to the wind turbine model, and therefore, the minimal excitation frequency will be presented during operation The study shows that substantial sideways blade vibrations can happen on modern wind turbines even if the aeroelastic damping of the sideways modes is optimistic. When working close to echoing environments, slight changes in the modeling can take a large nuance on the vibration level. The sideways vibrations are less noticeable in great turbulent environments. Applying simulations with low-level turbulence concentration will hence the performance to avoid a redesign. Additionally, this is subjected to the external forces. The analysis is done using aeroelastic models equivalent to a 1.5 MW class wind turbine with insignificant differences in blade materials.

Pacheco et al. [27] work on a different amplitudes of sound time series through simulation of noise adding band-limit to the time series acceleration measured from the original experiment, and Fig. 10a, c presents the various wind speed, spectra time series of the acceleration connected at the tower tip, that is already polluted with sound. From the study at low wind speed, the adopted sound levels are higher to measure the accelerations; however, when the wind speed gets to 2.5 m/s, the acceleration goes beyond the first two sound levels. The acceleration signal is used to overcome the sound levels for a high wind speed.

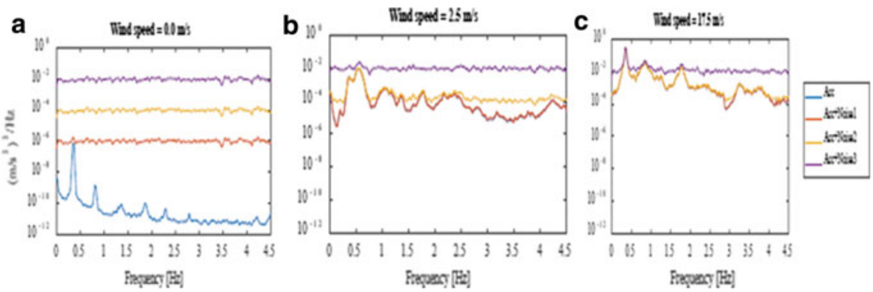

Fig. 10 Energy spectra of distinctive acceleration time series obtained at the tower tip for varying wind speeds: the real signal = Acc and original signal polluted with various sound levels = Acc + Noise1, 2, 3. For wind speeds of 2.5 and 17.5 m/s, the spectra connector with “Acc” and “Acc + Noise1” is practically equivalent

3 Structural Challenges Face During Operation of the Wind Turbine

The issues of reliability during wind turbine operations: The location of the 80% of wind turbine is in a remote area, which has great effects on the rate of maintenance that can be carried out. This will significantly affect the issue of reliability, because reliability is very significant in every machine that is design to rotate during operations (Fig. 11).

From this review study, it can be observed that over 80–90% of failure of the wind turbine (WT) is caused by vibration; due to the location area that most WTs are installed, this may be as a result from continuous contact of two metal objects during rotation. This continuous contact will affect the life circle of the turbine in operation [28].

The offshore wind turbine structure is always faced by various cyclic excitations, which includes the rotor operation, wind, currents, and waves, which can lead to high risks of damage, failure, and fatigue to the structures. This is one of the major challenges of the wind turbine on the offshore cite; however, the study of fatigue assessment needs to be strategically implemented in all operation of the offshore wind turbine; from several authors, wind turbine needs a well-developed standard model that can help control and monitor the wind turbine during operation, that will enable operator to detect any occurrences that will lead to vibration [29–32]. These continuous challenges of vibration occurrence in wind energy generation will affect the economic structure of the wind turbine development and its implementations, which will lead to high rate of manufacturing and maintainers cost.

Fig. 11 **a** Design of the planetary gear in the nacelles compartment. **b** The failure of the wind turbine (WT) during operation

4 Way Forward for Eliminating Vibration Frequency from a Wind Turbine During Operations

- One of the major things that must be done for a sustainable power generation from a wind turbine is to develop a standard model that can serve as a guild for wind turbine operations
- There is a need to carry out research on how to establish a good reliability and fatigue assessment process for wind turbine operations
- The basic areas for installations of wind turbine should be put into consideration during the design, in order to avoid the occurrence of vibrations which will lead to great loss of the wind turbine
- Material selection is one of the major factors in developing wind turbine, in the area of the blades, tower, and nacelles compartment. Most wind turbine blade is made with glass fiber; from this study, the authors observed that there are need to manufacture new materials which will serve as a better alternative to glass fiber, for example, the composite material of aluminum alloy mixed with glass fiber and a little percentage of titanium, for strength, flexibility, and firmness of the materials.

When vibration in the wind turbine is greatly reduced to the minimum, it will help to reduce the cost of maintainers during operation and after operations, which will serve as economic benefit to the manufacturers, industrial company (that makes use of the wind turbine for commercial purposes) and the nations at large.

5 Conclusions

Wind energy generation is one of the major and reliable sources of electricity generation, that is, environmental friendly. Through the application of wind turbine in energy generation, a lot of countries and continents have employed it which has a major source of supply in their home and official places in the world today; however, this promising system is currently facing a lot of challenges of vibration occurrence due to its complex nature. This paper has presented a comprehensive review on the effects of vibration on the wind turbine blades, tower, and nacelles compartment and also highlighted some major factors that cause the issues of the unwanted vibration occurrences and the possible ways to eliminate or reduce vibration during operation of a wind turbine.

Acknowledgements The authors deeply appreciate the management of Covenant University for their sponsorship.

References

1. Li Li (2012) Vibrations analysis of vertical axis wind turbine: a thesis presented in partial fulfilment of the requirements for the degree of master of engineering in mechatronics, school of engineering and advanced technology, Massey University, New Zealand. Diss, Massey University
2. Ajayi OO, Agarana MC, Akinwumi II, Okokpujie PI, Salawu EY, Abioye AA, Afolalu AS, Leramo RO (2019) Modelling rate of traffic-induced building vibrations in Sango-Ota, Nigeria: an assumption based analysis. WIT Trans Built Environ 182:303–313
3. Nwoke ON, Okonkwo UC, Okafor CE, Okokpujie IP (2017) Evaluation of chatter vibration frequency InCnc turning of 4340 alloy steel material. Int J Sci Eng Res 8(2):487–495
4. Wang X, Zeng X, Li J, Yang X, Wang H (2018) A review on recent advancements of substructures for offshore wind turbines. Energy Convers Manag 15(158):103–119
5. Lian J, Cai O, Dong X, Jiang Q, Zhao Y (2019) Health monitoring and safety evaluation of the offshore wind turbine structure: a review and discussion of future development. Sustainability 11(2):494
6. Okokpujie K, Shobayo O, Noma-Osaghae E, Okokpujie I, Okoyeigbo O (2018) Realization of MPLS-based VPN network for improved Qos metrics. TELKOMNIKA Telecom Comput Electron Control 16
7. Luo H (2017) Physics-based data analysis for wind turbine condition monitoring. Clean Energy 1(1):4–22
8. Okokpujie KO, Chukwu EC, Noma-Osaghae E, Okokpujie IP (2018) Novel active queue management scheme for routers in wireless networks. Int J Commun Antenna Propag (I. Re. CAP) 8(1):53–61
9. Qiao W, Lu D (2015) A survey on wind turbine condition monitoring and fault diagnosis—part II: signals and signal processing methods. IEEE Trans Indus Electron 62(10):6546–6557
10. Okokpujie KO, Chukwu EC, Noma-Osaghae E, Odusanmi M, Okokpujie IP (2018) A unique mathematical queuing model for wired and wireless networks. Int J Civil Eng Technol (IJCIET) 9(9):810–831
11. Okokpujie IP, Fayomi OSI, Leramo RO (2018) The role of research in economic development. IOP Conf Ser Mater Sci Eng 413(1):012060. IOP Publishing
12. Fayomi OSI, Okokpujie IP, Fayom GU, Okolie ST (2019) The challenge of Nigeria researcher in meeting up with sustainable development goal in 21st century. Energy Procedia 157:393–404
13. Okokpujie IP, Fayomi OSI, Ogbonnaya SK, Fayomi GU (2019) The wide margin between the academic and researcher in a new age university for sustainable development. Energy Procedia 157:862–870
14. Escaler X, Mebarki T (2018) Full-scale wind turbine vibration signature analysis. Machines 6(4):63. (1–16)
15. Hossain Md, Abu-Siada A, Muyeen S (2018) Methods for advanced wind turbine condition monitoring and early diagnosis: a literature review. Energies 11(5):1309
16. Okokpujie IP, Okokpujie KO, Nwoke ON, Azeta J (2018) Development of a 0.5 KW horizontal axis wind turbine. J Eng Appl Sci 13(8):2202–2208
17. Hahn B, Durstewitz M, Rohrig K (2007) Reliability of wind turbines. Wind energy. Springer, Berlin, pp 329–332
18. Odia OO, Ososomi SA, Okokpujie PI (2016) Practical analysis of a small wind turbine for domestic use on latitude 7.0670 N, longitude 6.2670 E. J Res Mech Eng 2(11):8–10
19. Okokpujie IP, Okokpujie KO, Nwoke ON, Azeta J (2018) Design and implementation of 0.5 kw horizontal axis wind turbine for domestic use. In: Proceedings of the world congress on engineering, vol 2
20. Tartibu LK, Kilfoil M, van der Merwe AJ (2012) Vibration analysis of a variable length blade wind turbine 630–639
21. Kumar A, Dwivedi A, Paliwal V, Patil PP (2024) Free vibration analysis of Al, wind turbine blade designed for Uttarakhand region based on FEA. Proce Technol 14(2014):336–347

22. Andrew H (1998) Dynamic analysis of both on and offshore wind turbines in the frequency domain. A dissertation submitted for the degree of Doctor of Philosophy in Faculty of Engineering, University of London
23. Taware GB, Mankar SH, Ghagare VB, Bharambe GP, Kale SA (2016) Vibration analysis of a small wind turbine blade. Int J Eng Technol (IJET). 8(5):2121–2126
24. Kim W, Yi J, Kim J, Park J (2017) Vibration-based structural health assessment of a wind turbine tower using a wind turbine model. Proce Eng 188:333–339
25. Guo P, Infield D (2012) Wind turbine tower vibration modeling and monitoring by the nonlinear state estimation technique (NSET). Energies 5(12):5279–5293
26. Tibaldi C, Kim T, Larsen TJ, Rasmussen F, de Rocca Serra R, Sanz F (2016) An investigation on wind turbine resonant vibrations. Wind Energy 19(5):847–859
27. Pacheco J, Oliveira G, Magalhães F, Cunha Á, Caetano E (2017) Wind turbine vibration based SHM system: influence of the sensors layout and noise. Proce Eng 199:2160–2165
28. Dunmade I, Udo M, Akintayo T, Oyedepo S, Okokpujie IP (2018) Lifecycle impact assessment of an engineering project management process–a SLCA approach. In: IOP conference series: materials science and engineering, vol 413, no 1, p 012061. IOP Publishing, 2018
29. Liu X, Lu C, Liang S, Godbole A, Chen Y (2015) Influence of the vibration of large-scale wind turbine blade on the aerodynamic load. Energy Proced 75:873–879
30. Okokpujie IP, Akinlabi ET, Okonkwo UC, Babaremu KO, Okokpujie KO (2019) Experimental evaluation, modeling and optimaztion of a 500 W horizontal wind turbine using definitive screen design method for sustainable wind power generation. Int J Civil Eng Technol 10(1):2415–2431
31. Okokpujie KO, Odusami M, Okokpujie IP, Abayomi-Alli O (2017) A model for automatic control of home appliances using DTMF technique. Int J Sci Eng Res 8(1):266–272
32. Tchakoua P, Wamkeue R, Tameghe TA, Ekemb G (2013) A review of concepts and methods for wind turbines condition monitoring. In: 2013 world congress on computer and information technology (WCCIT) Jun 22 2013 (pp 1–9). IEEE

Design and Analysis of a Novel Hybrid Car Bumper Using Non-Newtonian Fluid and High-Density Polyethylene

K. Praveen Jerish, J. Rakesh Kumar, R. Ramakrishnan, and K. S. Vijay Sekar

Abstract The drivers of today's cars are protected from frontal impacts with the help of crumple zones and composite bumpers that absorb the entire impact. However, the structural integrity is not entirely protected. In this research, a hybrid of two materials, one a non-Newtonian fluid named Oobleck and another material HDPE, was used in conjunction with creating a hybrid bumper system. The Oobleck fluid exhibits shear thickening when an impact force is applied and the material changes from a liquid to a solid state, thereby demonstrating twin characteristics. This unique property of the fluid is exploited by housing it in a HDPE tube and fixing the HDPE tube within the bumper beam. Such a combination has not been used in previous works and is a novelty. This deals with the assorted mixture properties of fluid, the materials for housing this fluid and holding it in the site and the impact strength absorbing capabilities of the designed bumper. A comparative analysis was undertaken between the prevailing bumper system and the newly designed bumper with non-Newtonian fluid. The finite element results that justify deformation experienced by the modified bumper are less compared to existing bumper, thereby resulting in less structural damage or formation of crumpled zones.

Keywords Non-Newtonian fluid · Oobleck · Shear thickening

1 Introduction

Automotive bumper beam is an important part of the modern car, which ensures safety to the occupants and also plays a key role in minimizing the frontal impact on the cars [1]. The bumper is a structure integrated to the front and rear end of a car, whose primary aim is to absorb impacts in minor collisions and if possible self-destruct in major collisions, thereby ensuring the safety of its passengers [2]. Bumpers minimize height problems between cars and other vehicles. In the early

K. Praveen Jerish · J. Rakesh Kumar (✉) · R. Ramakrishnan · K. S. Vijay Sekar
Department of Mechanical Engineering, Sri Sivasubramaniya Nadar College of Engineering, Kalavakkam 603110, India
e-mail: rakesh16086@mech.ssn.edu.in

E. T. Akinlabi et al. (eds.), *Trends in Mechanical and Biomedical Design*, Lecture Notes in Mechanical Engineering,
https://doi.org/10.1007/978-981-15-4488-0_80

stages of the automotive industry, the front spring hanger bolts were replaced with longer ones to be able to attach an ingot. Later the primary bumper manufactured from rubber was designed to soak up impacts [3]. General Motors incorporated body-coloured plastic front bumpers designed to absorb low-speed impacts. In fashionable cars, the bumpers comprise of a plastic cowl over a reinforcement bar manufactured from steel, aluminium, composite, or plastic. Today the modern cars' bumpers are manufactured from a mix of polycarbonate/ABS. Antecedent bumper system consists of many components that are manufactured from typical material like steel [4]. The integrity between components in bumper beam system is crucial in the overall bumper beam performance, which is affected by three factors: ease of manufacturability, ease of assembly and intrinsic value. [5]. In recent times, a solitary bumper beam was used to scale back price. Also, hybrids using a combination of plastic and metal are in vogue, to leverage the benefits of low weight, less corrosion, high specific stiffness, high specific strength and high impact energy absorption capability [6].

The objective of this work is to herald the employment of non-Newtonian fluid within tubes of plastics like HDPE and PP. Since the non-Newtonian fluid does not follow the law of viciousness, i.e. the viciousness will amend to either an additional liquid or an additional solid phase. The non-Newtonian fluid employed is named Oobleck, a shear thickening fluid, which is corn starch dissolved in water, which if stirred slowly shows milk-like properties, while when stirred hardly, appears like a viscous liquid. This combination of Oobleck and HDPE gas been structurally analysed using modelling and finite element analysis.

2 Design of the Hybrid Bumper

The hybrid bumper design was initiated by taking an existing bumper model of a car into consideration. The 3D model of the bumper was designed using SolidWorks software. Two bumper designs were considered. Figure 1 shows the location of the bumper beam in the existing vehicle. Figure 2 shows the hybrid bumper design-1. The bumper beam was made hollow instead of the regular rigid bumper. This was made to house the non-Newtonian fluid within the bumper beam. This provision helps in consolidating all the components into one unit to provide more strength. The entire rear section of the bumper was initially sealed, and the HDPE tube to the entire length of the bumper was planned to be housed inside.

However, the weight was raised by 2.4 kg since weight plays an important role in a car's mileage and performance, a change in design was initiated. Instead of sealing the entire rear portion, it was decided to seal the end portions alone. Moreover, the length of the HDPE tube was shortened to be accommodated at the centre of the bumper beam element. Figure 3 shows the modified bumper design.

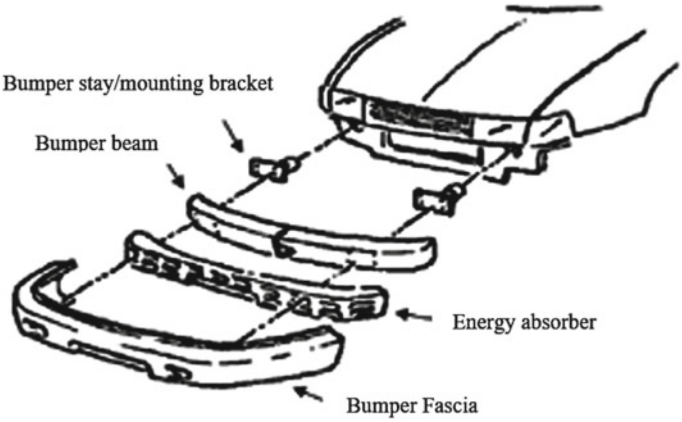

Fig. 1 Location of bumper beam in the existing vehicle

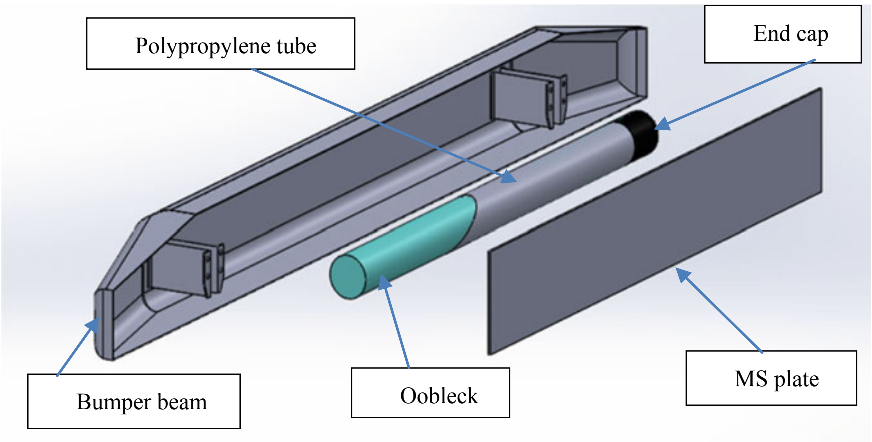

Fig. 2 Hybrid bumper design 1 (exploded view)

3 Selection of Housing Material

Since Oobleck is in the liquid phase before the application of any force on it, it is necessary for a tubular structure to house the fluid. To accommodate the housing of the non-Newtonian fluid, a thermoplastic material (because plastics do not absorb water) was used. Some of the commonly available thermoplastics were low-density polyethylene (LDPE), high-density polyethylene (HDPE) and polypropylene (PP). Initially, the LDPE and PP tubes were considered for housing the fluid; but after carrying out the comparison over the properties of the other thermoplastics, it was found that both the materials lacked flexibility and tended to crack under an impact force. Therefore, HDPE was selected and on analysis was found suitable for the

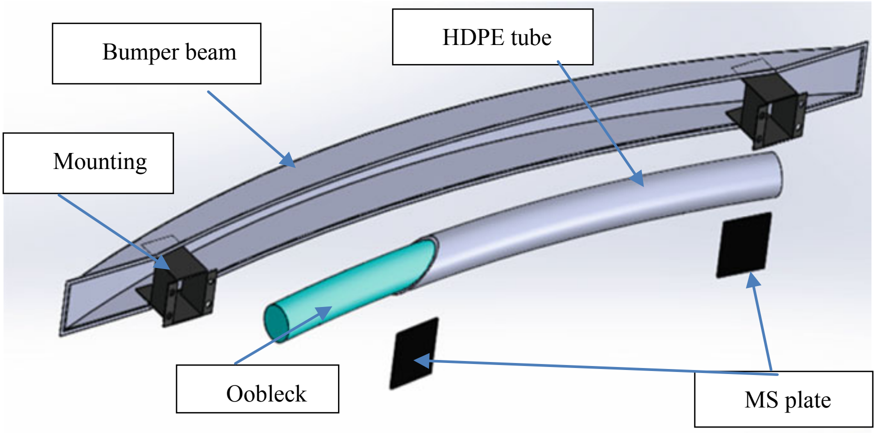

Fig. 3 Hybrid bumper design 2 (exploded view)

application. It was flexible to a certain extent and was able to produce a cushioning effect while facing an impact force. The quantity of fluid required to be filled was made as per the dimensions of the HDPE tube: a HDPE tube of length 0.8 m and inner diameter of 4.4 cm with a wall thickness of 0.3 cm (the tube dimensions were taken based on the bumper beam of Maruti Suzuki Alto 800). The quantity of Oobleck required for this dimension was obtained as 1441.34 mg which is very much negligible that there is no significant increase in the weight of the bumper. So the addition of shear thickening fluid does not influence the performance and mileage characteristics of the vehicle.

4 Bumper Assembly

The end of the HDPE tubes was sealed with HDPE caps using induction heating method. The circumference of the pipe as well as the cap was heated by placing them on the coil and fused together. Before sealing the other end, 2 kg of corn starch was mixed with 500 ml of water to get the required Oobleck, which was filled inside the tube. The HDPE tube with the Oobleck fluid was housed along with the bumper beam, by placing the tube at the centre of the bumper and then welding using plates at each end of the bumper beam.

5 Finite Element Analysis

An explicit finite element analysis was carried out to study the dynamics of the bumper, using Ansys software. For the analysis, a static wall made of concrete materials was considered. The concrete wall was used as a fixed support, and the moving bumper was enabled to impact the stationary concrete slab. Figure 4 shows the fixed concrete wall, and Fig. 5 shows the bumper impacting the wall.

Figure 6 shows the bumper before collision or impact with the concrete wall. Figure 7 shows the bumper after collision with the concrete wall. Table 1 shows the material properties of the concrete wall, bumper beam and the HDPE tube. The assembly was meshed with 13,791 elements, 26,609 nodes with an element size of 0.05 mm (Table 2).

Fig. 4 Static concrete wall

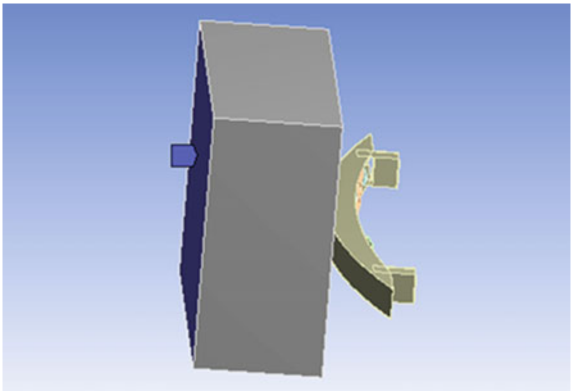

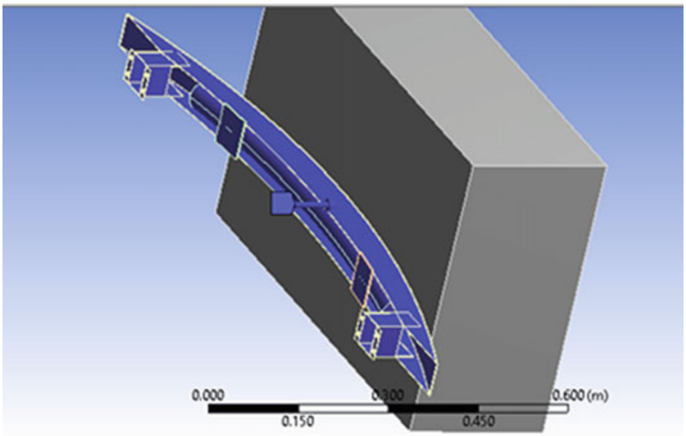

Fig. 5 Bumper impacting the wall

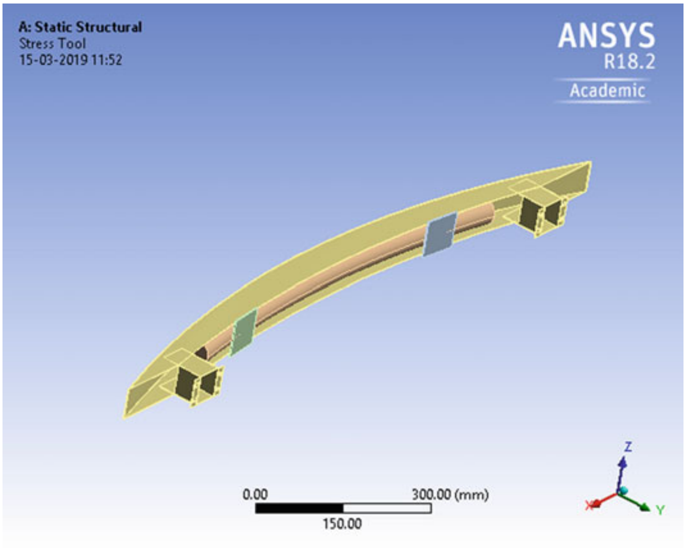

Fig. 6 Static bumper

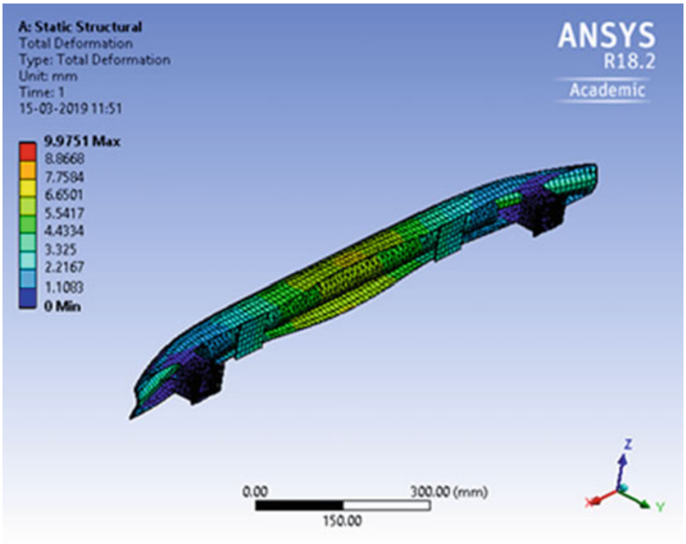

Fig. 7 Bumper deformation after impacting the wall

Table 1 Material properties

Material	Density (kg/m^3)	Young's modulus (GPa)	Poisson's ratio	Bulk modulus (GPa)	Shear modulus (GPa)	Specific heat (J kg^{-1} C^{-1})
Concrete(wall)	2300	30	0.18	15.625	12.712	780
Mild steel (Bumper beam)	7850	205	0.3	170.8	78.84	434
HDPE tube	950	11	0.42	22.91	3.87	2300

Table 2 Fluid properties

Material	Density (kg/m^3)	Kinematic viscosity (m^2/s)	Dynamic viscosity (Ns/m^2)
Shear thickening fluid (Oobleck)	1184.9	15.556	18,444.138

6 Results and Discussion

To obtain a comparable study group, the collision conditions were restricted by choosing the speed of the vehicle as 40 kmph, which is based on the average speed in city traffic. The explicit dynamic analysis of the conventional bumper and the newly designed hybrid bumper were carried out. The total deformation plot of the conventional bumper (without HDPE tube and non-Newtonian fluid) for an impact speed of 40 kmph produced a net deformation of 20.853×10^{-3}(mm) as seen in Fig. 8. Figure 9 shows the total deformation of the designed bumper (with HDPE tube and non-Newtonian fluid) for an impact velocity of 40 kmph with a net deformation value of 9.97×10^{-3} (mm).

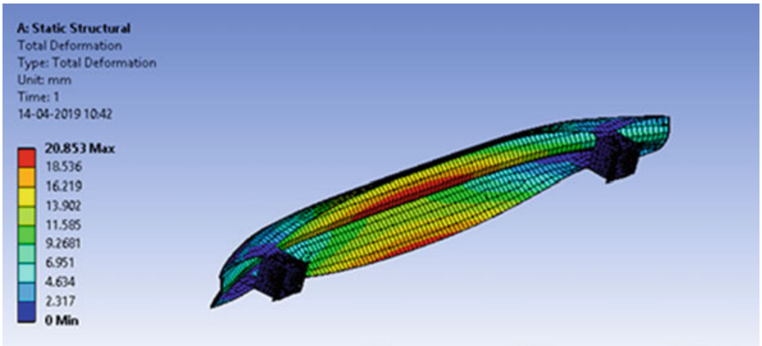

Fig. 8 Deformation of conventional bumper

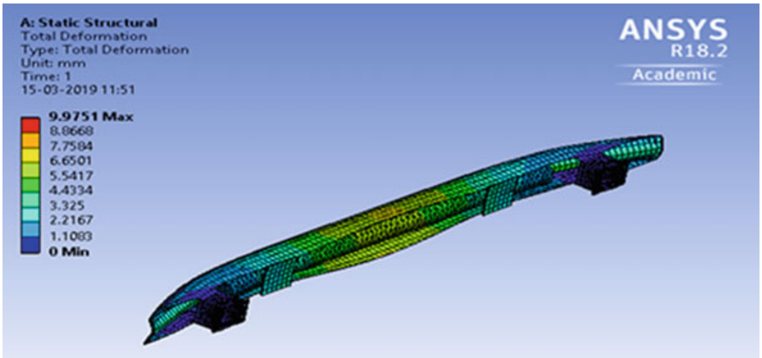

Fig. 9 Deformation of hybrid bumper

6.1 Deformation Versus Impact Force and Stress

From the deformation versus impact force graph (Fig. 10), it can be seen that the deformation for a given impact force is larger in the bumper without the non-Newtonian fluid and HDPE than the bumper with non-Newtonian fluid and HDPE tube. For a maximum load of 20,000 N, the corresponding deformation is 2.6 mm (without HDPE) and 1.7 mm (with HDPE). From the stress vs impact force graph (Fig. 11), it can be seen that the stress induced for a given impact force is larger in the bumper without the non-Newtonian fluid and HDPE than the bumper with non-Newtonian fluid and HDPE tube. For a maximum load of 20,000 N, the corresponding stress is 795 MPa (without HDPE) and 700 MPa (with HDPE).

From the above results and discussions, it can be clearly seen that the hybrid bumper with the HDPE tube filled with non-Newtonian fluid shows better impact

Fig. 10 Deformation versus impact force

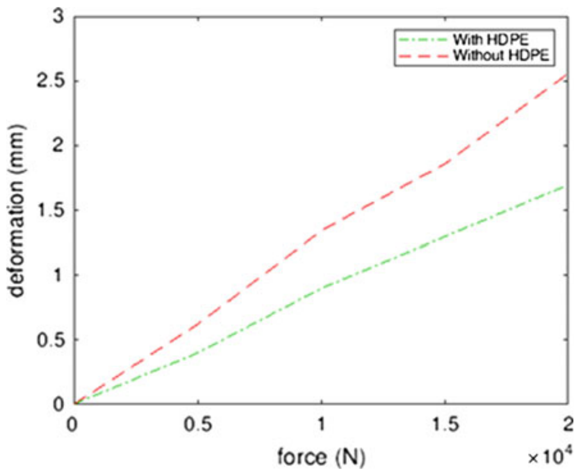

Fig. 11 Stress versus impact force

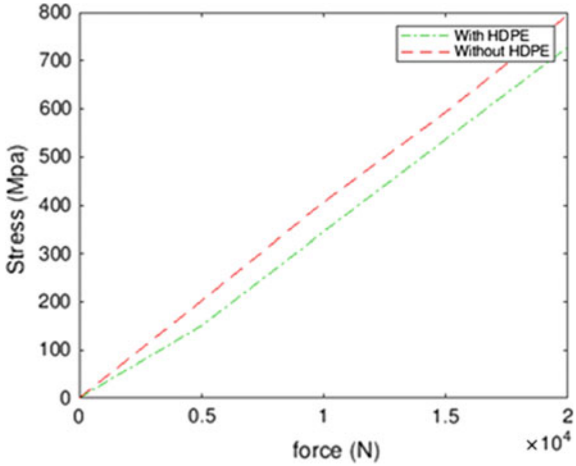

resistance characteristics with lower deformation and stress than the conventional bumper design.

7 Conclusion

The results reveal that non-Newtonian fluid is very advantageous; due to the reason that the deformation experienced by the modified hybrid bumper is less compared to the existing bumper, thereby resulting in less structural damage or formation of crumpled zones. The involvement of non-Newtonian fluid in the safety segment helps in the absorption of the impact and can be used in conjunction with existing bumpers to augment the impact absorption strength of the bumper. The non-Newtonian fluid acts as a damping material and when used with a material like HDPE, it enhances the total impact strength of the entire bumper system.

References

1. Johnson W, Walton AC (1983) An experimental investigation of the energy dissipation of a number of car bumpers under quasi-static lateral loads. Int J Impact Eng 1(3):301–308
2. Cheon SS, Choi JH, Lee DG (1995) Development of the composite bumper beam for passenger cars. Compos Struct 32:491–499
3. Witteman WJ (1999) Improved vehicle crashworthiness design by control of the energy absorption for different collision situations Eindhoven: Technische Universiteit Eindhoven, Ph.D. thesis
4. Hosseinzadeh R, Shokrieh MM, Lessard LB (2005) Parametric study of automotive composite bumper beams subjected to low-velocity impacts. Compos Struct 68(4):419–427

5. Teng T-L, Ngo V-L, Nguyen T-H (2010) Design of pedestrian friendly vehicle bumper. J Mech Sci Technol 24(10):2067–2073
6. Shyi DY (1989) Structure of multi-protection safety car bumper. US Patents US4807915A

Vibration Signature-Based Monitoring on FSW Process and Verification by FEA

Akshay Todakar, R. S. Nakandhrakumar, M. Ramakrishnan, and V. Meenakshisundaram

Abstract Experimental study conducted during joining butt weld in FSW process on Al 6061 alloy of size 50 mm width × 100 mm length × 8 mm thickness of two plates wherein the effect of the interaction between the plates, tool and the vibration that occurs during the process is investigated and reported. In this study, joining sides of the workpiece samples are artificially induced with air gaps of drilled holes in 2, 3, 5 mm diameter holes and 3 mm width × 4 mm depth of slots in random distances. The vibration behaviour of the tool and workpiece joining system is characterized by frequencies arrived in modal analysis using finite element analysis (FEA), and each mode corresponds to tool and workpiece system. Variations in the amplitudes of vibration signals in the particular range of frequencies from 6.0 to 7.0 kHz are proportional to the workpiece and significant changes in a linear pattern indicate the defective and steady joining area of workpiece. So, this method is effective in monitoring of workpiece joining in FSW process. The fast Fourier transform (FFT) analysis of the vibration signal shows the changes in individual frequencies and is used for identifying the frequency range of monitoring workpiece with gap and without gap conditions. The steady joining portions cause the vibration which corresponds to 4th region frequencies of workpiece.

Keywords Friction stir welding process · Vibration · Frequency domain analysis · FEA

A. Todakar (✉)
Department of Mechanical Engineering, Hindustan Institute of Technology and Science, Chennai 603103, India
e-mail: akshaytodakar555@gmail.com

R. S. Nakandhrakumar
Centre for Simulation and Engineering Design (SIMENDES), Hindustan Institute of Technology and Science, Chennai 603103, India

M. Ramakrishnan · V. Meenakshisundaram
School of Aeronautical Sciences, Hindustan Institute of Technology and Science, Chennai 603103, India

E. T. Akinlabi et al. (eds.), *Trends in Mechanical and Biomedical Design*, Lecture Notes in Mechanical Engineering,
https://doi.org/10.1007/978-981-15-4488-0_81

1 Introduction

The friction stir welding process is a solid-state combined that uses a non-expendable tool to link two non-melting materials. This method can progress the mechanical properties of the joint, such as the strength and hardness. The heat will be created due to friction and plastic distortion between the tool and the workpieces. This friction and plastic distortion result in the mixing and agitation of the materials around the pin from the front to the rear. The heat generated by friction leads to the softening of metals, especially near the friction welding tool. This means that mechanical energy is converted into thermal energy in the contact areas, without the need for heat from other sources. The main function of the friction welding tool is to heat the parts, and then to induce the materials to flow and restrict under the shoulder and Impression action will generate friction between two surfaces and relative motion between two parts. People are studying to optimize process parameters for active connection of materials [2].

2 Literature

Premature failure of the welding tool can lead to unacceptable welding joint quality and loss of welding productivity. Friction welding is a completely machined process. The forces and vibration generated by the process are high enough that manual operation is not possible, except possibly for very fine materials. Therefore, online monitoring of vibration is, therefore, in demand.

Lambiase et al. [1] have investigated force variation, temperature and torque distribution in process with an al-Si–Mg aluminium alloy that varies the tool's rotation speed and welding speed. Temperature measurements were made using an IR camera. Prasanna et al. [4] have observed the experimental and numerical evaluation with aluminium alloy AA6061. Temperature variation and simulation model are tested parameters with experimental results. Buffa et al. [3] have developed the distribution of temperature, and tension in welding nugget was investigated. Projected the relationships between the forces of the tool and the variation in the parameters. Temperature profile almost symmetrical in the welding area was found. Reza-E-Rabbya [5] has found pin characteristics in the flow of material and the weldability by stirring by the friction of two aluminium alloys (AA 7050 and AA6061) with a pin tool cylinder, including the pin smooth/without thread attached to a geometry of shoulder displacement single invariant. Welds were made under a range of process parameters (welding and rotation speed). Sadeesh and Kannan [6] conducted with plates of aluminium AA2024 and AA6061 dissimilar, and obtained the optimal parameters of the process. Different tool designs have been used to analyse the properties. Investigated the effect of welding speed on the microstructure hardness and tensile properties of the welded joints. As the process parameters varied, seamless, high-efficiency welded joints were produced. Shukla and Raghu [7] have observed mechanical and metallurgical properties by changing various parameters that FSW can be used to study the parameters on the process in laboratory. Experiments have been conducted to validate some of the simulation results of the ANSYS software. Ramesh et al. [8] have investigated (FSW) the aluminium alloy 6082 to study the tensile strength and hardness by changing the process parameter, speed of rotation and speed of welding of tool and different weld condition. They found the effect of tool design on mechanical properties in FSW of AA6061.

In this paper, modal analysis of workpieces and hard tool using finite element analysis (FEA) is compared with the range of frequency occurring during experiments in the fast Fourier transform (FFT) analysis of vibration signals. The fact of this approach is presented from friction stir welding (FSW) experiments using hard tool and an aluminium alloy workpiece.

3 Materials and Methods

3.1 Experimental Work

The workpiece materials used for experimental study are commercially available Al 6061. The size of the samples of workpiece plates is 100 mm length × 50 mm width × 8 mm thickness. The chemical compositions and material properties are tabulated in Tables 1 and 2 [9]. The two plates were mounted using a clamp and retrofitted on a CNC milling machine which is shown in Fig. 1 (photograph of the experimental set-up used to study friction stir process). Tool pin was made with D/d ratio (shoulder/pin)

Table 1 Chemical composition of AA6061

Composition	Weight %
Fe	0.244
Si	0.741
Mn	0.095
Cu	0.157
Ni	0.01
Cr	0.125
Ti	0.007
Sn	0.006
V	0.006
Co	0.002
Zn	0.020
Pb	0.005
Mg	0.901
Al	97.699

Table 2 Mechanical properties of AA6061

Yield strength (MPa)	Ultimate tensile strength (MPa)	Elongation %	Shear strength (MPa)	Fracture strength (MPa)
276	310	12	207	94

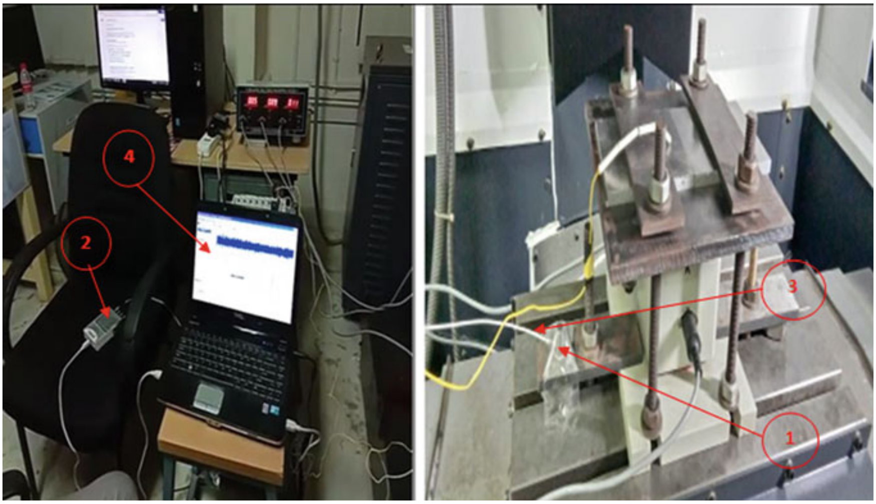

Fig. 1 Photograph of experimental set-up with vibration monitoring system **i** accelerometer, **ii** data acquisition card, **iii** connecting cable and **iv** Laptop

of 3 in which tool shoulder and pin are made up of diameter 16 mm × height 60 mm and pin diameter of 6 mm × height 7.5 mm, respectively. The chemical composition and material properties are given in Tables 3 and 4. Joining of workpiece samples was performed on a 3-axis CNC milling machine which has 3-axis movement and

Table 3 Chemical composition of H13

Composition	Weight %
Cr	4.75–5.5
Mo	1.1–1.75
Si	0.80–1.2
V	0.80–1.2
C	0.32–0.45
Ni	0.3
Cu	0.25
Mn	0.2–0.5
P	0.03
S	0.03

Table 4 Properties of H13

Density	7800 kg/m^3
Melting point	1427 °C
Tensile strength (ultimate)	1.2–1.5 GPa
Tensile strength (yield)	1–1.3 GPa
Modulus of elasticity	215 GPa
Poisson's ratio	0.3
Thermal conductivity	28.6 W/mK

carried using a special CNC program which was run at speed 800 rpm and feed 33 mm/min [Ref]. Both workpieces are properly secured using a clamp. The vibration signals were measured using a (Kistler model-8702B50) accelerometer sensor which is positioned on the clamp and used for holding dynamometer. A data acquisition card (NI 9133) is used to convert analog output signals into digital signals. Among four of its channels, single analog input channel was used to collect the data by sampling the signals at 25 kHz and interfaced with a personal computer and simultaneously processed and recorded by LabVIEW software 8.5 (sound and vibration assistant) (Fig. 2).

3.2 Methodology and Experimental Procedure

Figure 3 shows the flow diagram of methodology followed for comparison through extracting the features from fast Fourier transform (FFT) of the submodule of sound and vibration software in the LabVIEW and modal anlysis of FEA. First step, it was planned to record vibration signals for beginning of the plate joining to ending of the plate joining for the size of 100 mm length × 50 mm width × 8 mm thickness. Once the vibration signals were recorded through data acquisition card of converted analog-to-digital signal, then further signal processing was carried in LabVIEW for feature extraction from time domain and frequency domain. In this project, vibration characteristics such as amplitude and frequencies are extracted in the FFT and used for comparison of frequencies arrived through modal analysis of free vibration in ANSYS 18.1.

4 Results and Discussions

4.1 FEA Analysis

The workpiece with the size of 100 mm length × 50 mm width × 8 mm thickness of two plates has been modelled together and outer perimeters are arrested to the

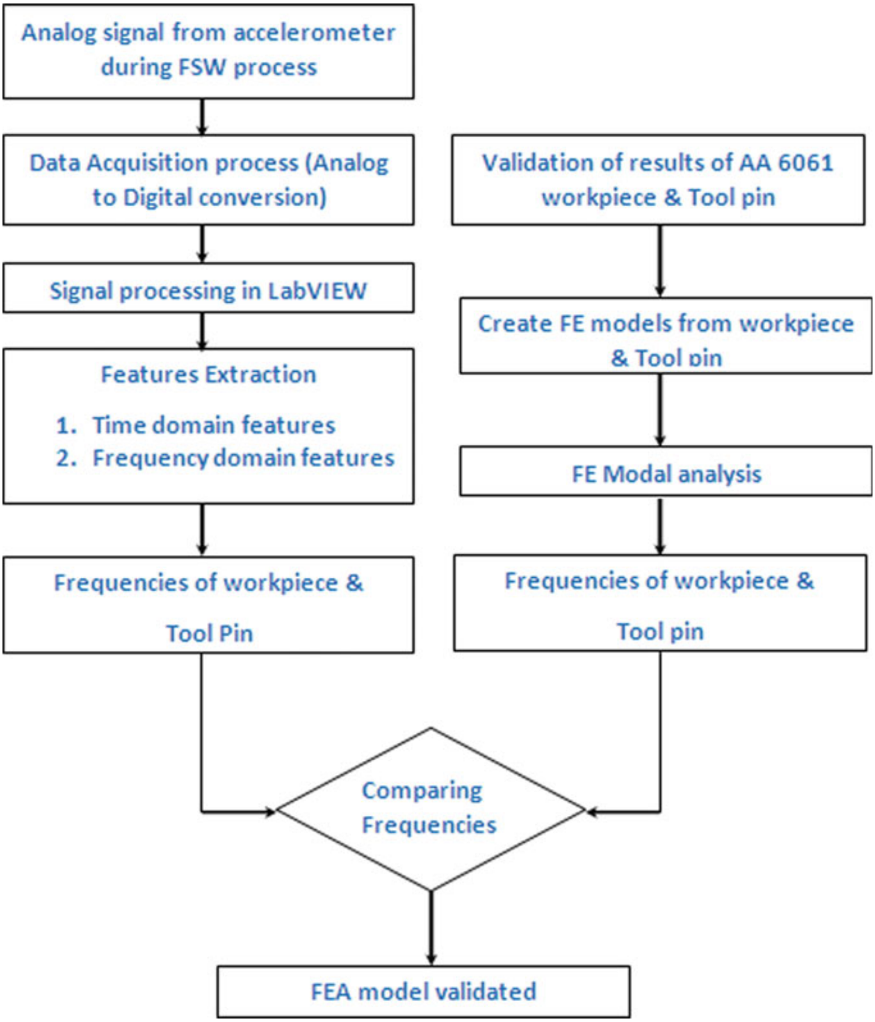

Fig. 2 Flow chart of describing feature extraction from FFT and comparison with FEA

dimensions equal to the dimensions of clamp of 20 mm on both sides which is used for holding the workpiece and input parameters are given such as mass density is 2710 kg/m^3 Young's modulus is 68.9 $\times$ 10^9 N/m^2 and Poisson's ratio is 0.3. Entire model is meshed and allowed to run the rectangular plate in free vibration, arrived modal values for 30 modes. Table 5 shows that first 4 modal values of the rectangular plate. Figure 3a shows the meshing model of two workpieces and Fig. 3b shows the modal analysis result of rectangular plates which are performed by FEA software (ANSYS 18.1) and shown for the first mode.

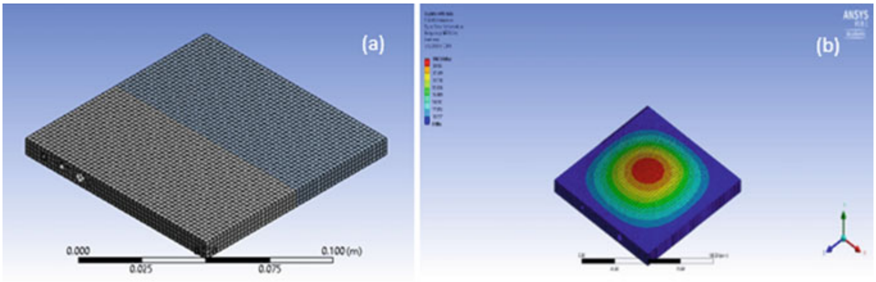

Fig. 3 **a** Meshing model of two workpieces **b** 1st mode result of rectangular plates

Table 5 Modal values of workpiece in free vibration

Component	Modes of free vibration	I mode	II mode	III mode	IV mode
Workpiece	By FEA, F_n (Hz)	6674.8	12,960	13,213	18,614
Tool pin	By FEA, F_n (Hz)	3051.9	3052.2	13,533	15,817

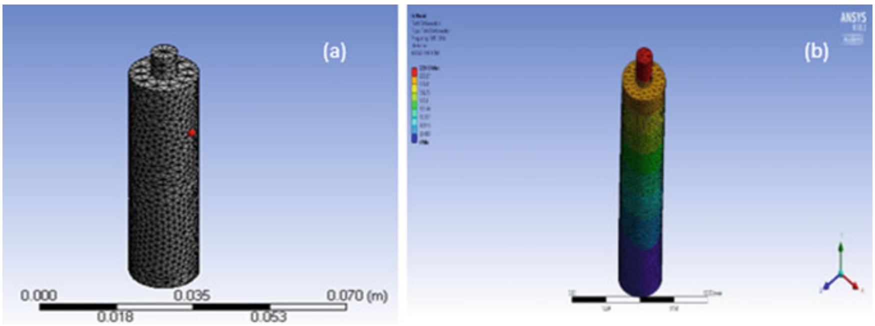

Fig. 4 **a** Meshing model of tool pin **b** 1st mode result of tool pin

Tool pin is modelled for size of diameter 16 mm × height 60 mm of tool shoulder and diameter of 6 mm X height 7.5 mm of tool pin. Top surface of tool pin is arrested and input parameters are given such as mass density, Young's modulus and Poisson's Ratio of 7800 kg/m^3, 2.15×10^{11} N/m^2 and 0.3, respectively. Entire model is meshed and is showed in Fig. 4a. Meshing model is used to run for free vibration and 1st mode result of tool pin is shown in Fig. 4b.

4.2 Power Spectrum Analysis

Joining operations on plates have been performed using spindle speed of 800 rpm and feed of 71.2 mm/min. Figure 5 shows that the plates are joined with defects and

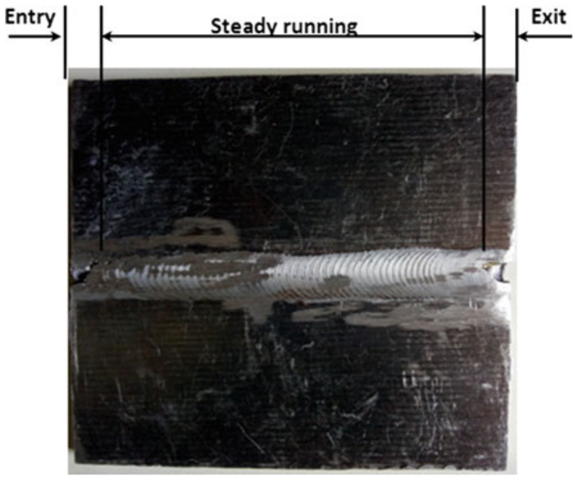

Fig. 5 Plate segmented at three stages

the joined plates are separated into three segments such as metal joining at entry, steady joining and exit. Segmented areas are monitored through FFT and used for analysis. During entire process of joining, sensor was positioned at the fixture of the base plate. While joining plates, accelerometer sensor measured the vibration signal and LabVIEW software used to store the information in the computer. Totally two plates were used for joining up to 100 mm length. Time domain and corresponding frequency domain signals of three segments are shown in Fig. 6. The amplitude was measured 4.5×10^{-3} m/s^2 at entry and exit of joining, while the metal in steady joining the amplitude level was 6.6×10^{-3} m/s^2. This is captured in the frequency range between 6000 and 7000 Hz. The variation in the amplitude level occurs because of friction between the contacting materials, due to which temperature also raises to solidification stage for joining metal. The results of the experiments conducted are shown in Fig. 6, which provides time domain and corresponding power spectrum graph. Power spectrum indicates the corresponding frequencies (Hz) arrived in the FEA analysis. Figure 7 shows the bar graph of amplitude level against the various stages of plates.

5 Conclusions

In this study, a relation between the workpiece, tool stiffness and the vibration signals in joining process is reported. The stiffness of the workpiece is the most influencing parameter which causes high frequency components in FSW process. The friction with temperature raise also causes notable changes in high-frequency components of power spectrum. It was found that 4th region of frequency 6400 Hz of workpiece frequency is affected by changes in metal joining pattern. This increases the vibration amplitude in the range of frequencies from 6.0 to 7.0 kHz. The increases in the

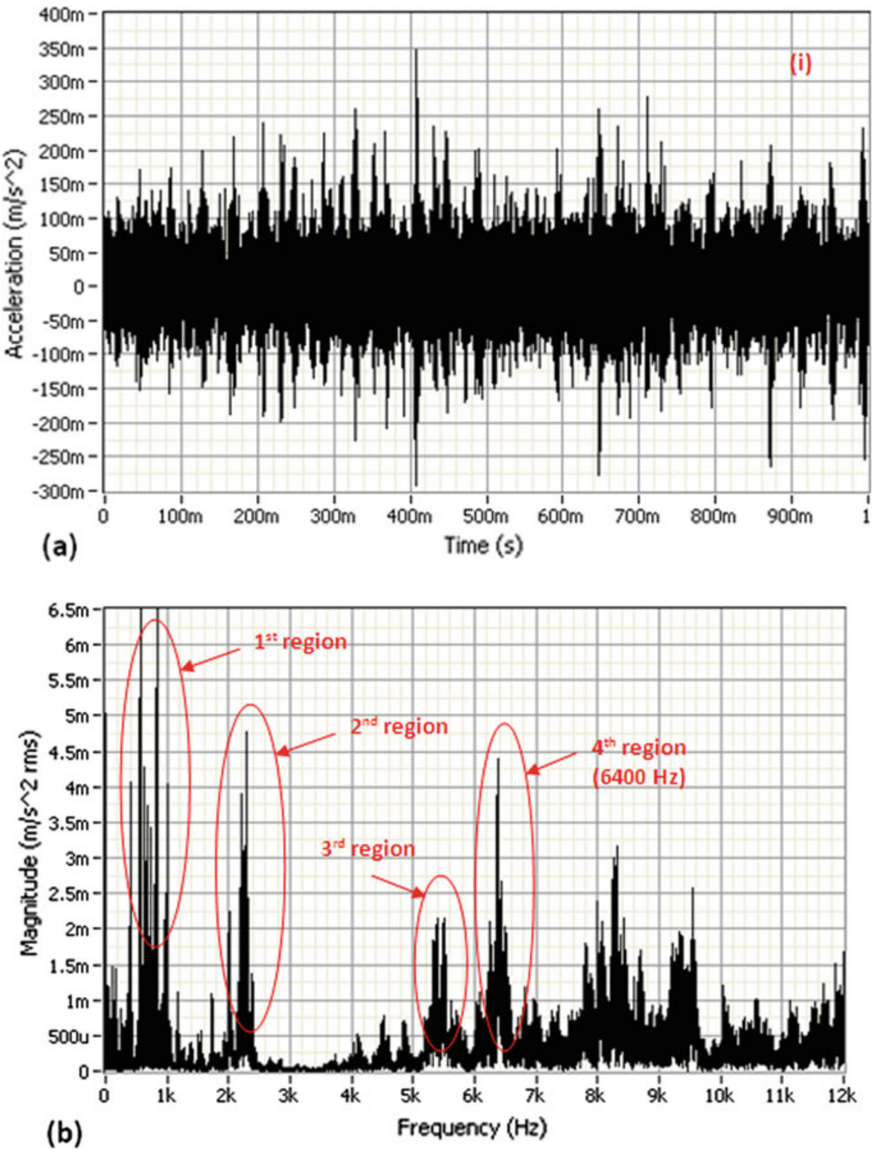

Fig. 6 Comparison of power spectra for different stage joining of workpiece. (**i**) **a** Time domain signal and **b** corresponding FFT during entry. (**ii**) **a** Time domain signal and **b** corresponding FFT during steady joining. (**iii**) **a** Time domain signal and **b** corresponding FFT during exit of FSW process

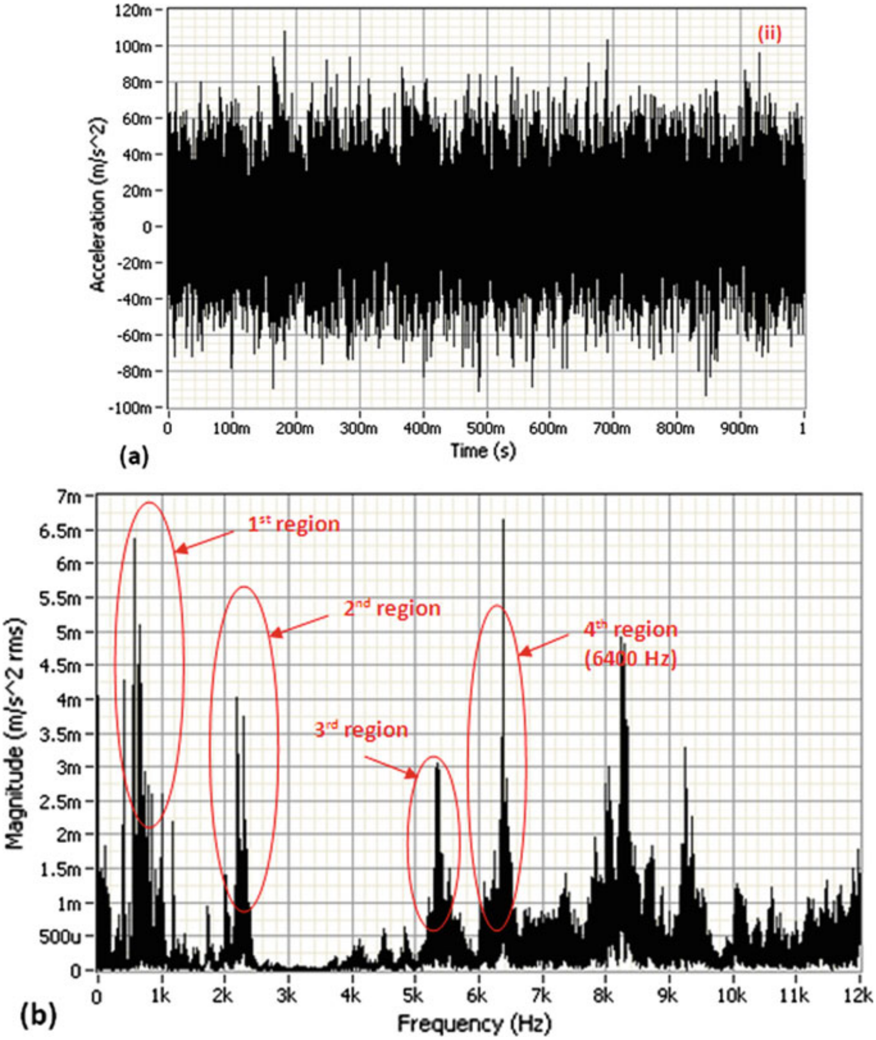

Fig. 6 (continued)

vibration amplitude are observed in this frequency band and are most sensitive during the metal process. This significant increase of amplitude by two times indicates the friction increases between tool and workpiece. It is concluded that the monitoring of 4th region frequency of the workpiece can be utilized for effectively monitoring of defects during FSW process.

Acknowledgements This work is done with the support provided by CNC Condition Monitoring Lab of Centre for Automation and Robotics at Hindustan University. The authors wish to extend

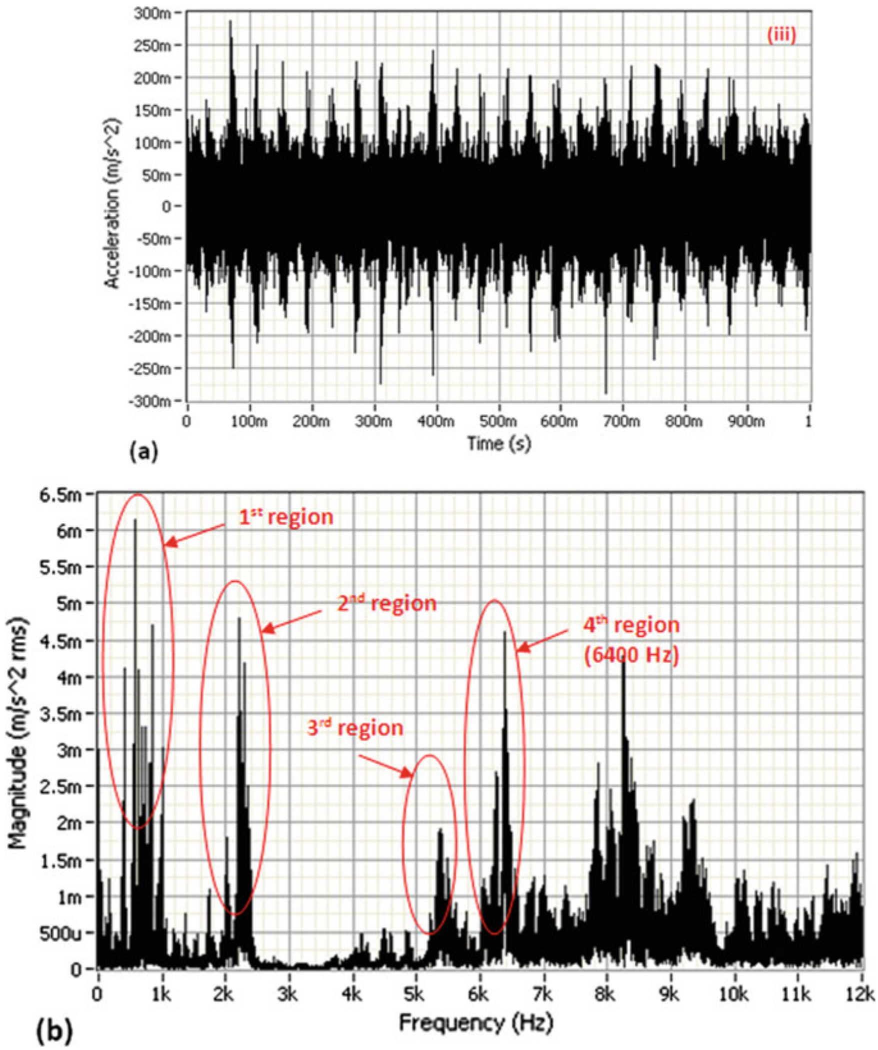

Fig. 6 (continued)

their sincere thanks to Mr. Natesan, Lab Instructor, ANRO, HITS, Padur for providing necessary support in executing this research.

For citations of references, we prefer the use of square brackets and consecutive numbers. Citations using labels or the author/year convention are also acceptable. The following bibliography provides a sample reference list with entries for journal articles [1], an LNCS chapter [2], a book [3], proceedings without editors [4], as well as a URL [5].

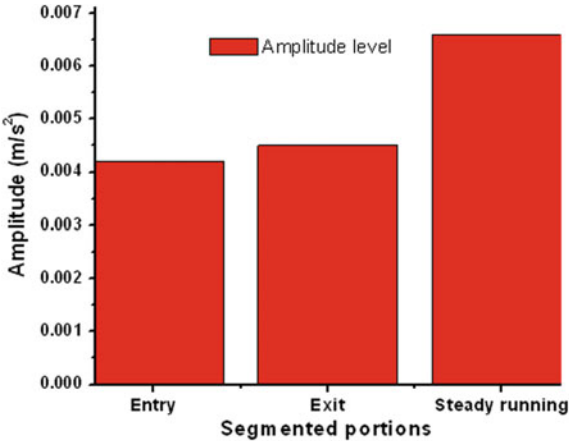

Fig. 7 Effect of friction on amplitude

References

1. Lambiase F, Paoletti A, Di Ilio A (2018) Forces and temperature variation during friction stir welding of aluminum alloy AA6082-T6. Int J Adv Manuf Technol 99:337–346
2. Kumar S, Kumar P (2016) Study the effect of parameters of friction stir welding on the impact strength of aluminium 6063. Int J Cur Eng Technol 6(3):993–998
3. Buffa G, Fratini L, Micari F, Shivpuri R (2008) Material flow in FSW of T-Joints experimental and numerical analysis. IntJ Mater Form 1(1):1283–1286
4. Prasanna P, Subba Rao B, Krishna Mohana Rao G (2010) Experimental and numerical evaluation of friction stir welds of AA6061-T6 aluminium alloy. ARPN J Eng Appl Sci 5(6):1–18
5. Reza-E-Rabby Md (2014) Effect of Tool pin thread forms on friction stir weldability of different aluminium alloys. Proc Eng 90:637–642
6. Pa Sadeesh, Kannan Venkatesh (2014) Studies on friction stir welding of AA 2024 and AA 6061 dissimilar metals. Proc Eng 75:145–149
7. Shukla J, Echempati R (2016) Investigation and thermal analysis of friction stir welding process parameters of AA6061 plates. In: Proceedings of the ASME 2016 international mechanical engineering congress and exposition (IMECE2016), pp 11–17, Phoenix, Arizona, USA
8. Ramesh A, Indira Rani M, Prasanth A (2016) Influence of tool design on the mechanical properties in friction stir welding of Aluminium alloy AA 6082-T6. Int J Sci Eng Res 7(6)
9. Prantik M (2012) Alloy designation processing and use of AA6XXX series aluminium alloys. Int Sch Res Netw ISRN Metall 1–15

Power Generation from Hydraulic Shock Absorber Using Piezoelectric Material

B. Jain A. R. Tony, M. S. Alphin, and V. Yeshwant

Abstract A lot of emphasis has been laid on harvesting energy from unconventional sources these days due to environmental concerns. Harvesting energy from vibrations is one of the most promising technologies in the present day scenario like the vibrations of tall buildings, long bridges, vehicle systems, railroads, ocean waves, and even human motions. For successful harnessing of this wasted energy, a piezoelectric transducer has been used. The analysis of suspension to find stiffness and deformation is done. Also, the force acting on the suspension over bumps is found which is used to calculate the voltage. The power obtained is further calculated and possible applications of this energy generated are also being mentioned. The objective is to harvest energy from the suspension system using PZT. Model of the shock absorber and a Simulink model of quarter car suspension. Evaluation of the changes in stiffness and deflection of the suspension would be done. A way of efficient conversion of the vibration to electric power by finding the best position to place the piezoelectric material. Finally, the force during a bump is found and hence the voltage induced in PZT. Thus, the power generated and designing a circuit to store the generated power in a battery is obtained.

Keywords Piezoelectric material · Simulink · Energy harvesting

1 Introduction

There has constantly been a lot of emphasis on the need for reduced energy consumption or energy harvesting in automobiles. There is also an increase in the amount of

---

B. J. A. R. Tony (✉)
Department of Mechanical Engineering, Malla Reddy College of Engineering and Technology, Secunderabad, India
e-mail: jaintonyb@gmail.com

M. S. Alphin · V. Yeshwant
Department of Mechanical Engineering, Sri Sivasubramaniya Nadar College of Engineering, Chennai, Tamil Nadu, India

E. T. Akinlabi et al. (eds.), *Trends in Mechanical and Biomedical Design*,
Lecture Notes in Mechanical Engineering,
https://doi.org/10.1007/978-981-15-4488-0_82

features and luxuries that are being used by the passengers who commute in private four-wheelers. The problem is that most of these features are highly energy-consuming. Thus, the need to produce or harvest energy through innovation. Few preliminary studies on the amount of energy recovery in vehicles and at the end they claimed the recoverable energy for a 2500 lb vehicle with an average speed of 45 mph are about 20–70% (that amounts up to 7500 W) of the propulsion power on a typical highway road [1]. Kawamoto et al. [2] modeled a ball-screw type electromagnetic damper for active automobile suspension and the results of these experiments show a 15.3 W energy recovery from one shock absorber of a vehicle on Class C road at 50 mph, mainly from vibration above 2 Hz.

A regenerative suspension with a ball-screw and a three-phase motor of a real car on the vibration test rig and obtained 11.7 W under random excitation or 46 W for four shock absorbers [3]. Comprehensive analysis about the mean power that can be obtained from the vehicle and the results suggest that road roughness, tire stiffness, and even the vehicle driving speed have a great influence on the harvesting power potential, whenever the suspension stiffness, absorber damping, and vehicle masses are insensitive or almost constant. At 60 mph, on good and average roads as specified on an ISO standard, 100–400 W average power is available in the suspensions of a middle-sized vehicle [4]. The resonance frequency of the piezoelectric transducer is dependent upon the configuration, size, and loading conditions. They noted that efficiency (η) of the conversion process in resonance condition is dependent upon the coupling coefficient and mechanical quality factor of the piezoelectric [5].

Zhongjie et al. [6] have used a key component which is a unique motion mechanism, which they called 'mechanical motion rectifier (MMR)', to convert the oscillatory vibration into unidirectional rotation of the generator. Vibration energy that needs to be tapped to understand the unique motion in the cars, buildings, human motion, and also tidal wave energy. They have also discussed how the energy generated by vibration which equals to around 300 W is actually contributing around 9% of the energy fuel consumption regeneration [7]. But on all the above topics there has been no work done on the stress on the piezoelectric material can be reduced without reducing the output of the electricity. Hence, this calls the need for the purpose of the research where it tends to solve the above-stated problems.

2 Materials and Methods

2.1 Piezoelectric Materials

Some of the most common forms of the Piezoelectric materials include quartz, lead zirconatetitanate (PZT) ceramic, and polyvinylidene fluoride (PVDF) polymer. PZT is the most widely used piezoelectric ceramics and is commercially available. It has very high piezoelectric coupling coefficients and a relatively low maximum operating temperature (200C). PZT has some advantages over quartz-like lower cost

Table 1 Properties of coil spring

Parameters	Properties
ASTM	228
Yield strength	900–1100 MPa
Young's modulus	210 GPa
Compressive strength	250 MPa
Ultimate strength	2840 MPa
Poisson ratio	0.3

and versatility in design by changing the composition and properties. Quartz also has disadvantages such as the varying output according to the temperature variation of the crystal. If the relative humidity rises above 85% or falls below 35% the output of the material of quartz is affected. For this defect to be overcome, they have to be coated with wax or polymer material. Thus mostly the crystal types of piezoelectric are not preferred than ceramics. Ceramics are less sensitive to temperature changes and hence they are used. The common ceramics are PZT and PVDF. PZT ceramic has large electromechanical coupling factors, typically k31 = 0.34 and k33 = 0.69 (k31 is the factor for the electric field in direction 3 and longitudinal vibrations in direction 1; k33 is the factor for the electric field in direction 3 and longitudinal vibrations in direction 3), which means it is able to convert 34% and 69% of mechanical energy in the piezoelectric material into electric energy.

PVDF is more flexible and sensitive however, the electromechanical converting coefficient is much smaller, k31 = 0.12, and k33 = 0.15. Single crystal piezoelectric materials have also been used for its high energy density, high-energy converting efficiency, and large operational temperature range. The coil spring properties are shown in Table 1.

2.2 MATLAB Simulation

A quarter car suspension model was created in MATLAB Simulink and the deflection of the spring was analyzed. A graph was plotted between the magnitude of displacement of the car versus time. Frequency and Phase response time was plotted and compared with and without a thermoplastic polyurethane buffer. In Simulink, an equation of motion for a suspension system was created using functions and blocks. The force acting on the spring was determined using the devised equations of motion.

Considering the undulations which cause the displacement in the suspension system, an assumption was made for the bump dimensions (Height:10 cm, during the rise: 1 s). Fieldwork was done to find out the normal terrain which can be assumed to produce the vibrations. In 8 kilometres, 6 speed breakers, and 10 pitholes were found to occur. From commonly used graphs in blocks, a sine wave was used to represent the bumps. Step functions were used to represent pitholes in the terrain for analysis. A force versus time graph was investigated in the results caused by the pitholes and

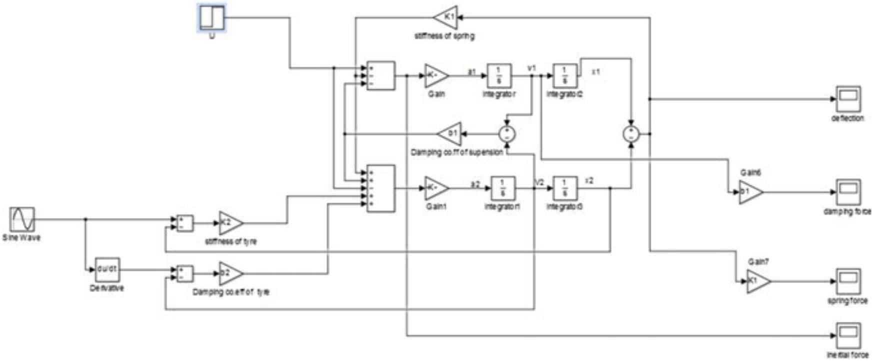

Fig. 1 Simulink model of hydraulic suspension with piezoelectric material

bumps. Figure 1 shows Simulink model of hydraulic suspension with piezoelectric material.

3 Results and Discussions

The results of the used analytic techniques mentioned below. Figure 2 shows the results of total deflection and magnitude were found out for a period of 20 s. The deflection was found to be 0.0135 m. Figure 3 shows a step amplitude of 2 cm which is equal to 0.02 m is given as the input for a duration of 1 s. The total force was found

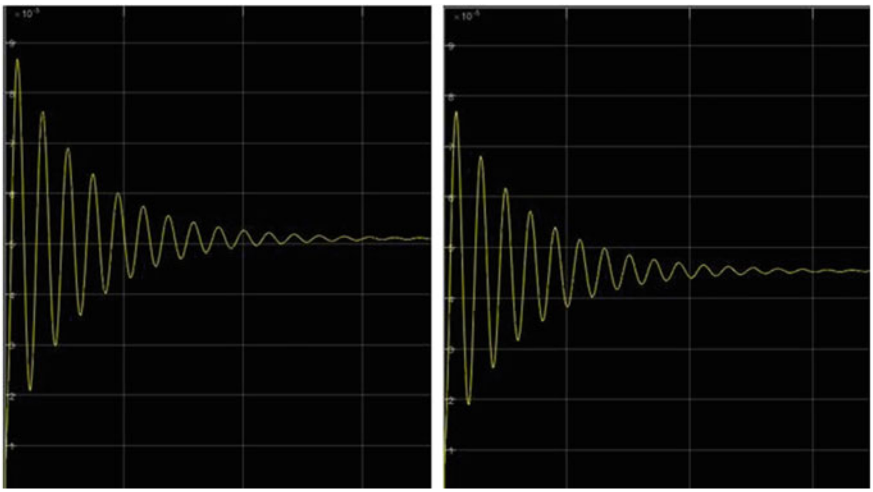

Fig. 2 Magnitude versus time

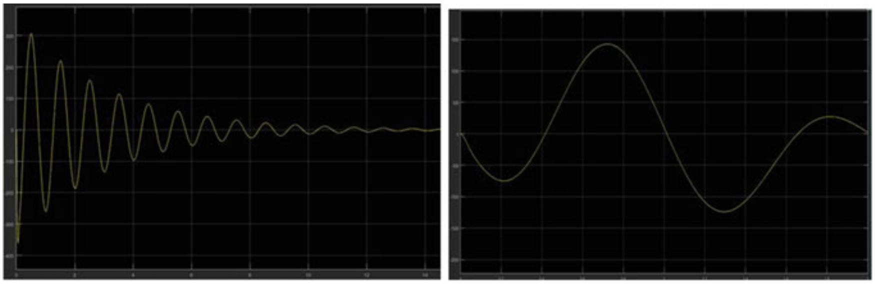

Fig. 3 Force versus time

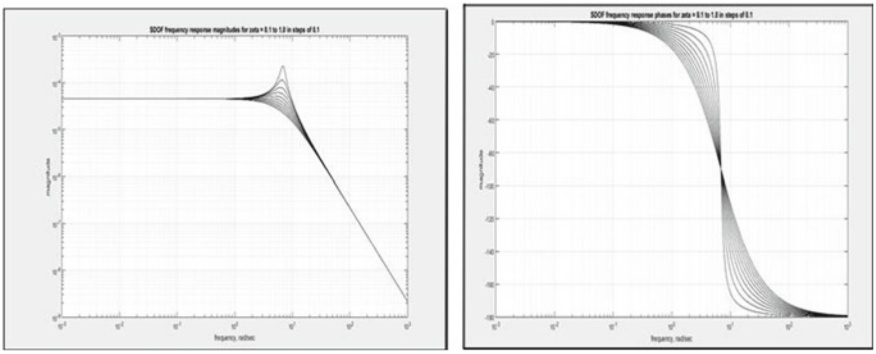

Fig. 4 Frequency and phase response

out for a period of 20 s. The figure shows the force versus time and force was 300 N and 1500 N.

Figure 4 shows the frequency and phase response of the system. The frequency response shows the relation between the frequency and the magnitude. The phase response shows the relation between the magnitude and phase.

3.1 Voltage Calculations

A bridge rectifier is an Alternating Current (AC) to Direct Current (DC) converter that rectifies mains AC input to DC output. Bridge Rectifiers are widely used in power supplies that provide necessary DC voltage for the electronic components or devices. They can be constructed with four or more diodes or any other controlled solid-state switches. Depending on the load current requirements, a proper bridge rectifier is selected.

Components' ratings and specifications, breakdown voltage, temperature ranges, transient current rating, forward current rating, mounting requirements, and other

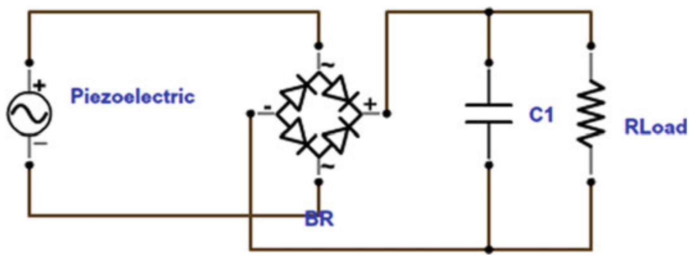

Fig. 5 Battery storage setup

Fig. 6 Relationship between voltage and current

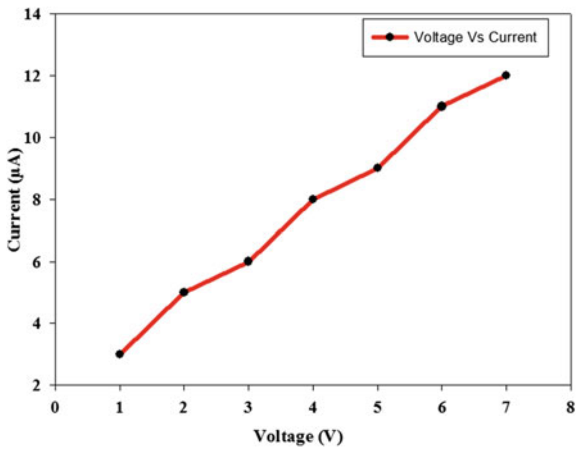

considerations are taken into account while selecting a rectifier power supply for an appropriate electronic circuit's application.

A capacitor is a passive two-terminal electrical component that stores potential energy in an electric field. The effect of a capacitor is known as capacitance. While some capacitance exists between any two electrical conductors in proximity in a circuit, a capacitor is a component designed to add capacitance to a circuit. Figure 5 shows the battery storing setup. Figure 6 shows the relationship between voltage and current.

4 Conclusions

The piezoelectric material which has been used along with the thermoplastic polyurethane buffer in the suspension system has helped in the electric utilization of Damper Dissipated Energy. Wasted Energy Utilization and automobiles being the most thriving words in the present day scenario, has been given the primary importance in this project and been fruitfully researched to produce unexpected results. The piezoelectric material which has been used along with the thermoplastic polyurethane buffer in the suspension system has helped in the electric utilization of Damper Dissipated Energy. Future scope of studies can involve the cross-section change of the used piezoelectric material inside the TPU buffer.

References

1. Goldner RB, Zerigian P, Hull JR (2001) A preliminary study of energy recovery in vehicles by using regenerative magnetic shock absorbers. Trans J Commercial Veh 110–2
2. Kawamoto Y, Suda Y, Inoue H, Kondo T (2007) Modelling of electromagnetic damper for automobile suspension. J Sys Des Dyn 1(3):524–535
3. Zhang Y, Huang K, Yu F, Gu Y, Li D (2007) Experimental verification of energy-regenerative feasibility for an automotive electrical suspension system. 2007 IEEE International conference on vehicular electronics and safety. China
4. Zuo L, Zhang P-S (2013) Energy harvesting, ride comfort, and road handling of regenerative vehicle suspensions. J Vib Acoust 135:011002–2
5. Priya S (2007) Advances in energy harvesting using low profile piezoelectric transducers. J Electroceram 19(1):167–14
6. Li Z, Zuo L, Kuang J, Luhrs G (2012) Energy-harvesting shock absorber with a mechanical motion rectifier. Smart Mater Struct 22(2):025008
7. Zuo L, Tang X (2013) Large-scale vibration energy harvesting. J Intell Mater Syst Struct 24(11):1405–1430

Static Deformation Analysis with and Without of Piezo-electric Material Attachment in Hydraulic Suspension System

B. Jain A. R. Tony, M. S. Alphin, and Nishanth P. Shah

Abstract A lot of emphasis has been laid on harvesting energy from unconventional sources these days due to environmental concerns. Harvesting energy from vibrations is one of the most promising technologies in the present day scenario like the vibrations of tall buildings, long bridges, vehicle systems, railroads, ocean waves, and even human motions. For successful harnessing of this wasted energy a piezo-electric transducer has been used. The analysis of suspension to find stiffness and deformation is done. Hydraulic suspension system was modelled using SOLIDWORKS and static analysis was performed using ANSYS. The static analysis results were evaluated as deformation and Von-Mises stress with and without piezo-electric material.

Keywords Hydraulic suspension system · Piezo-electric material · Static deformation · Von-Mises stress

1 Introduction

The harvested energy from an automobile system is mainly obtained from the energy absorbed due to the vibration of a car on irregular roads that are being damped in order to have an ergonomic design for the passenger during his drive. Thus, its suspension system uses a dampener or a shock absorber to absorb the energy produced from the vibrations. But this energy harvested can be used to power the car or any of its associated devices. Piezo-electric material can be used to absorb these vibrations and convert it into a form of electrical energy that can be stored in a battery. The transduction mechanism such as the piezo-electric, electrostatic and

B. Jain A. R. Tony (✉)
Department of Mechanical Engineering, Malla Reddy College of Engineering and Technology, Secunderabad, India
e-mail: jaintonyb@gmail.com

M. S. Alphin · N. P. Shah
Department of Mechanical Engineering, Sri Sivasubramaniya Nadar College of Engineering, Chennai, Tamil Nadu, India

E. T. Akinlabi et al. (eds.), *Trends in Mechanical and Biomedical Design*,
Lecture Notes in Mechanical Engineering,
https://doi.org/10.1007/978-981-15-4488-0_83

electromagnetism has been used to the human-based devices with the average human of 68 kg produces energy of 67 watts but due to the current piezo-electric conversion efficiency and other difficulties, the amount of energy that can be extracted from the human who walks on the floor is 1.27 watts [1]. Green advocates the need for wireless charging and also mechanisms used for generation. There are two types of generation that take place, direct force generation, and the inertial force generation. The direct force generation examples include piezo-electric shoes, converts the force exerted by the feet on the shoes into electricity [2]. Targeted mechanical vibrations lie in the range of 50–150 Hz with force amplitude in the order of 1 KN (automobile engine vibration level). It was found that under such severe stress conditions the metal–ceramic composite transducer "cymbal" is a promising structure. The metal cap enhances the endurance of the ceramic to sustain high loads along with stress amplification.

The transducer design plays a vital role in enhancing the conversion of electrical energy [3]. However, the initial theoretical research on this energy harvesting from the vehicle suspension began almost three decades ago [4, 5]. The possibility of using a permanent magnetic motor as mechanical dampers, for dissipating the energy using variable resistors [5]. Segel et al. [6] have analyzed the influence of highway pavement roughness on vehicular resistance to motion due to tire and suspension damping and they have indicated that approximately 200 W of power is dissipated by dampers of a passenger car at 30 mph (miles per hour). The electrical active suspension with LQG (Linear-Quadratic-Gaussian) control and estimated that up to 400 W of energy is recoverable at a highway driving condition, is 5% of propulsion power to maintain GM Impact (electrical car) at 60 mph [7]. Abouelnour et al. [8] have looked into the concept of energy and electro-mechanic suspension and simulation based on quarter car models that predict around 150 W of the energy was being dissipated by shock absorbers and the energy can be converted into electrical power at 56 mph. The primary aim of this work is to make an effective energy conversion of the vibration arising due to the undulations on the road.

2 Materials and Methods

2.1 Modelling of Hydraulic Suspension System

The spring is used to coil around the cylinder part of the suspension system. The spring was also modelled based on the standard suspension model. This includes the cylindrical part of the suspension system. They also include a cylindrical piston which is useful for the hydraulic motion that dampens the vibration. The buffer used in the coil suspension system of the vehicles for various reasons. The life of the suspension jumper increases on the usage of the buffer since the buffer takes up some of the stress. The height of the suspension increases by 2–4 cm. The objective is to reduce the shock felt by the passengers due to irregularities of the road.

Table 1 Properties of buffer

Parameters	Properties
Elastomer	800 series
Density	1200
Young's modulus	2–10 GPa
Tensile strength	40–45 MPa
Poisson ratio	0.5

As stated above since the shock is they result in the balance of the car being maintained. They also help in maintaining the spring tension and also restoring it back after the vibration. They also reduce the noise and vibration from the suspension components. It also reduces the force which makes the automobile slant to its side. It decreases the flat force which shifts the majority of the center of gravity while it's cornering. It enhances the flexibility if the automobile body those results in smoother control, leaning phenomenon reduction and more constant driving. It increases the linear force and the landing force of the tyres which results in better road breaking and effective gripping at high speeds. Thus this reduces the braking distance of the car. The properties of the buffer are mentioned in Table 1.

The most common type of material used in the coil spring is Carbon Steel. This type of material is mostly used since they have high strength and also wear resistance ability. They can also be alloyed with other metals to obtain the desired level of properties. They are also easily available and also are at low cost compared to many metals. The coil spring properties are shown in Table 2.

Hydraulic piston rods are a case in point where conventional steels are performing inadequately. These instances have resulted in oil leaks or pressure loss, or else have necessitated regular and disruptive cylinder changes. Analysis has determined that these failures are caused by cyclic stresses, which are typical in demanding mining and construction applications, and to which piston rods are commonly exposed over long periods. The main driver of cost and capital in piston rods in hydraulic cylinders is the diameter of the bar. The cost of a rod increases exponentially with the diameter as a result.

As a general rule, the cost of a piston rod decreases by 15% by reducing its diameter by 5 mm. Other effects are lighter weight and reduced space requirements,

Table 2 Properties of coil spring

Parameters	Properties
ASTM	228
Yield strength	900–1100 Mpa
Young's modulus	210 GPa
Compressive strength	250 MPa
Ultimate strength	2840 MPa
Poisson ratio	0.3

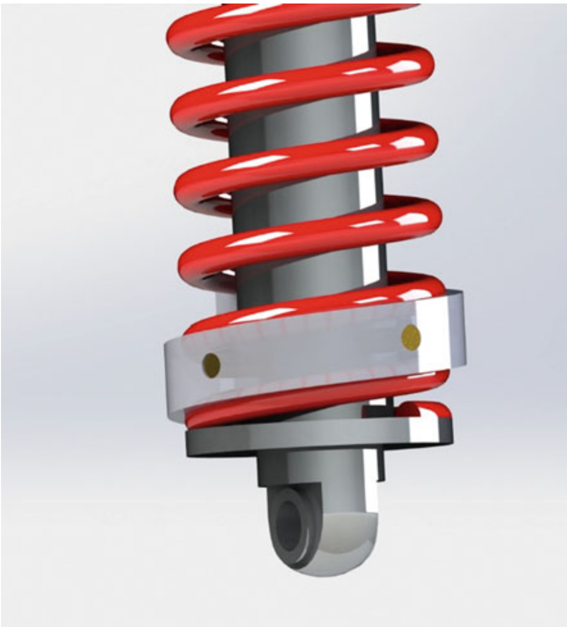

Fig. 1 The assembly of hydraulic system for suspension

which could also translate into lower energy consumption and greater versatility in design. But to achieve these benefits, the rod material must be strong enough to maintain equal strength at the smaller diameter. Therefore, a key parameter in hydraulic piston rod design is dimensioning against fatigue, buckling, and impact failure. Thus the nickel-chromium plated steel is actually used for piston but the thickness of that plating should be minimum as possible to reduce the weight and improve the efficiency. Figure 1 shows the assembly of the hydraulic system for suspension.

2.2 *Peizo-Electric Material*

The PZT material has been chosen as the piezo-electric material based on which the energy can be harvested. They are actually fitted into the holes of the buffer that lies in between the coil spring. They are placed in such a way since the direct dynamic force acting on the PZT material can actually deter the life of the piezo material and so they can cost a lot. The use of buffer can reduce this effect. The properties of peizo-electric material are shown in Table 3.

Table 3 Properties of peizo-electric material

Parameters	Properties
Density	7500 GPa
Young's modulus	63 Gpa
Voltage co-efficient	0.025 Vm/N
Ultimate tensile strength	240 MPa
Poisson ratio	0.31

2.3 Numerical Simulation

The solid model of the entire shock absorber was modelled using the solid works software in parts. The separate parts were assembled to create the entire part mirroring exactly the shock absorber in reality. The interactions between each part of the shock absorber were finalized and setup as a final design. The designed solid model was imported into Ansys using appropriate dimensions and tolerances. Static structural analysis was carried out on the solid model without the inclusion of Thermoplastic polyurethane buffer. The appropriate sections and materials were input in the analysis. The model was meshed using a quad element. Loads and boundary conditions were appropriately given on the model to be analyzed. The equivalent stress and total deformation at each element in the model were determined and investigated.

A static structural analysis was done on the solid model with the inclusion of the Thermoplastic polyurethane buffer using the same procedures as the model without the TPU. Now, the Piezo-electric material was attached to the model. The Max force that was obtained from the results in the MATLAB software was applied on the model in the bottom surface and the top surface is fixed. The new job was analyzed and the results were plotted into required graphs.

3 Results and Discussions

The static-structural analysis was performed using Ansys and results were evaluated in terms of static structural deformation, and static structural Von-Mises stress. Figure 2 shows the static structural deformation of hydraulic suspension system with and without piezo-electric material. The numerical simulation result shows that the static structural deformation was found 0.2078 m for suspension system with piezo-electric material and 0.2471 m for normal suspension system.

The static deformation was controlled up to 0.0393 m. The piezo-electric material controls the deformation up to 15.9%. The minimum deformation was found 0.02309 m for suspension system with piezo-electric material and 0.027457 m for normal suspension system. The average of static deformation was found 0.115 m for suspension system with piezo-electric material and 0.137 m for normal suspension system.

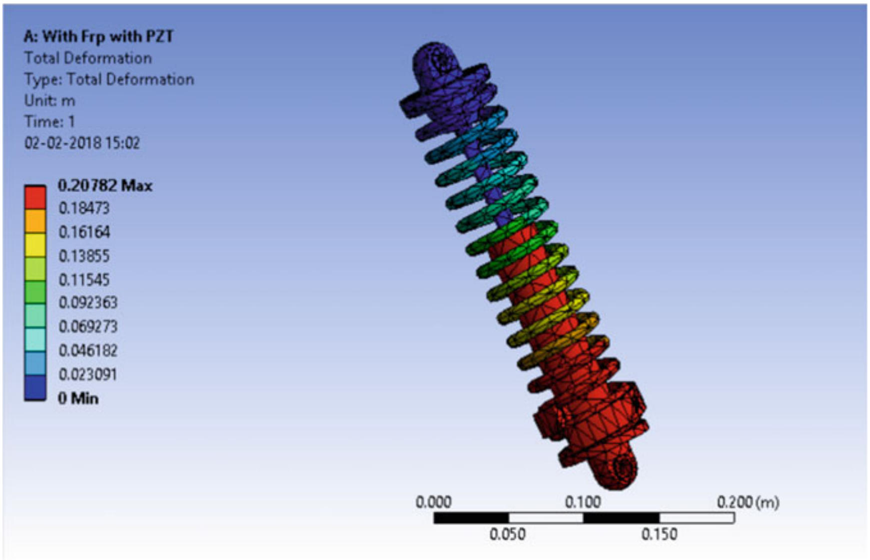

(a) Hydraulic suspension system static structural deformation with piezo-electric material

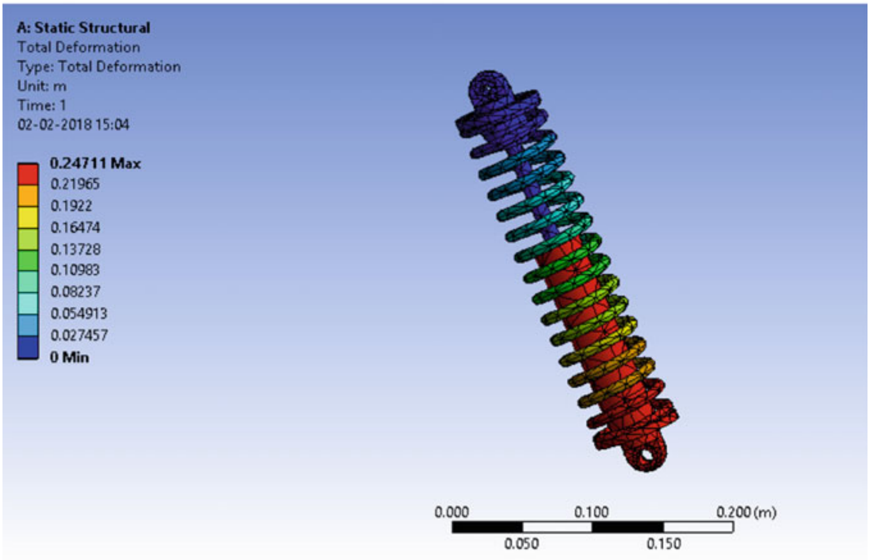

(b) Hydraulic suspension system static structural deformation without piezo-electric material

Fig. 2 Static structural deformation with and without piezo-electrical material

Figure 3 shows the static structural Von-Mises stress of hydraulic suspension system with and without piezo-electric material. The numerical simulation result

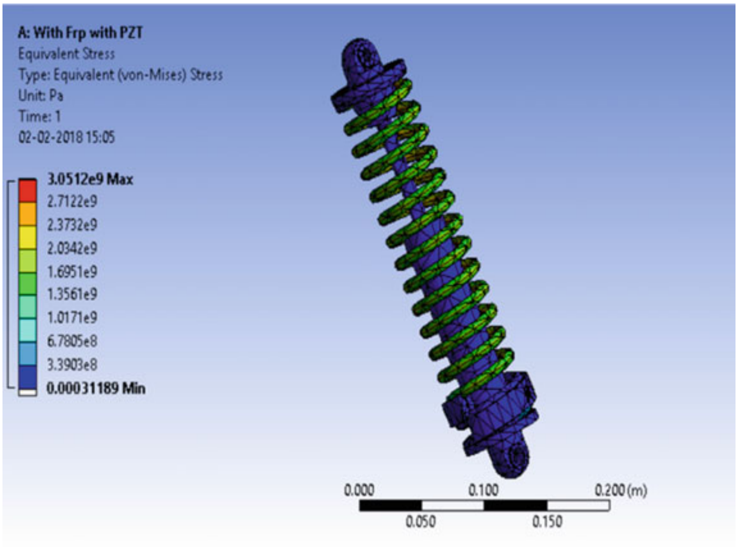

(a) Hydraulic suspension system Von-Mises stress with piezo-electric material

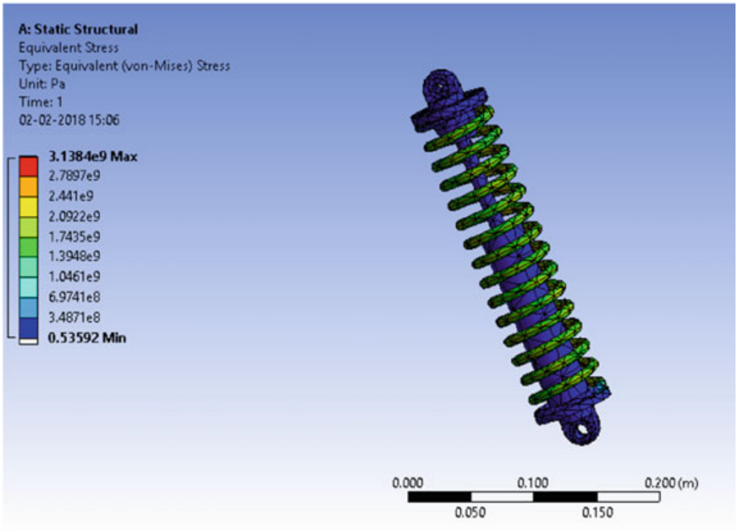

(b) Hydraulic suspension system Von-Mises stress without piezo-electric material

Fig. 3 Static von-mises stress with and without piezo-electrical material shows that the static structural Von-Mises stress was found 3.05 GPa for a suspension system with piezo-electric material and 3.138 GPa for the normal suspension system.

The static Von-Mises stress was controlled up to 0.088 GPa. The piezo-electric material controls the deformation up to 2.8%. The minimum Von-Mises stress was found 0.0339 GPa for suspension system with piezo-electric material and 0.0348 GPa m for normal suspension system. The average of static Von-Mises stress was found 1.695 GPa for suspension system with piezo-electric material and 1.174 GPa for normal suspension system.

4 Conclusions

- Wasted Energy Utilization and automobiles being the most thriving words in the present day scenario, has been given the primary importance in this project and been fruitfully researched to produce unexpected results.
- The piezo-electric material which has been used along with the Thermoplastic polyurethane buffer in the suspension system has helped in the Electric utilization of Damper Dissipated Energy.
- The varied applications such as headlight of automobiles, parking rearview cameras can be powered using this new harnessed energy thus reducing the extra energy required to power luxury utilities in an automobile.
- The newly innovated model of the suspension has been found to be structurally stable using the results from the Ansys static analysis.

References

1. Beeby SP, Tudor MJ, White NM (2006) Energy harvesting vibration sources for microsystems applications. Meas Sci Technol 17(12):175–195
2. Mitcheson PD, Yeatman EM, Rao GK, Holmes AS, Green TC (2008) Energy harvesting from human and machine motion for wireless electronic devices. Proc IEEE 96(9):1457–1486
3. Kim HW, Batra A, Priya S, Uchino K, Markley D, Newnham RE, Hofmann HF (2004) Energy harvesting using a piezoelectric "Cymbal" transducer in dynamic environment. Jpn J Appl Phys 43(1): Part 1, Number 9A
4. Karnopp D (2007) Permanent magnet linear motors used as variable mechanical dampers for vehicle suspensions. Int J Veh Mech Mobility 18(4):187–200
5. Karnopp D (1992) Power requirements for vehicle suspension systems. Int J Veh Mech Mobility 21(1):65–71
6. Segel L, Lu X-P (1982) Vehicular resistance to motion as influenced by road roughness and highway alignment. Aust Road Res 12(4):211–222
7. Hsu P (1996) Power recovery property of electrical active suspension systems. IECEC 96. Proceedings of the 31st intersociety energy conversion engineering conference (vol. 3, pp. 1899–1904). Washington, DC, USA
8. Abouelnour AMA, Hammad N, Ebrahim E (2003) Electric utilization of vehicle damper dissipated energy. Proceedings of the IASVD symposium (p. 647). Japan

Study of Vibration and Tensile Characteristics of Multilayer Composites

D. Vishal, M. Selvaraj, and S. Vijayan

Abstract In recent years, the use of composites for engineering purposes has grown enormously. Composites can be fabricated to the necessary requirements and can satisfy the required needs. The epoxy resin, used in combination with a hardener, acts as an adhesive and matrix of the composite. Glass fiber has been unanimously used along with epoxy for better mechanical properties. Various Rubbers are incorporated as the middle layer in the multilayer composite structures. Tensile and vibration tests are performed on these composites. The presence of rubber in the composite structure influences both the tensile and vibration characteristics of the multilayer composites. Hence, the tensile strength, natural frequency, and the damping factor shows variation due to the presence of rubber and this property can be exploited for engineering purposes.

Keywords Glass fiber · Rubber · Tensile characteristics · Vibration characteristics

1 Introduction

Composites have been the major trend of the materials in recent times. Composites yield us the desired properties and necessary characteristics. Over the years, Epoxy Resin has been used as the most common adhesive and matrix of the composite. Epoxy has been extensively used for its low shrinkage properties. They also exhibit brilliant mechanical characteristics. Moreover, the fiber being used in the multilayer composites has a great influence on the strength characteristics of the composites [1]. Different types of fiber materials [2, 3] are used along with epoxy resin in the composite structure. Natural fibers, as well as synthetic fibers, are used in combination with epoxy resin. Natural fibers such as flax, kenaf and synthetic fibers such as carbon fibers, glass fibers are the most commonly used fibers. Glass fiber shows excellent adhesion with epoxy resin [4]. The high energy absorption

D. Vishal · M. Selvaraj (✉) · S. Vijayan
Department of Mechanical Engineering, Sri Sivasubramaniya Nadar College of Engineering, Kalavakam, Chennai 603110, India
e-mail: selvarajm71@gmail.com

E. T. Akinlabi et al. (eds.), *Trends in Mechanical and Biomedical Design*, Lecture Notes in Mechanical Engineering,
https://doi.org/10.1007/978-981-15-4488-0_84

capability [5] and good tensile strength characteristics [6] of the glass fiber/epoxy resin combination are impressive enough to overshadow the other combinations of resin and fiber. Rubber is a viscoelastic material. It is an elastomer type of polymer compound. Both the natural and synthetic rubbers are used in composites. The good elastic properties of rubber [7] draws interest in their usage in composite structures. The rubber/epoxy resin combination shows good physical and thermal properties [8]. Rubber/epoxy combination also shows excellent toughness [9, 10], durability [11] and other mechanical properties. Nitrile Butadiene Rubber shows high strength and damage accumulation properties under cyclic loading conditions [12]. Styrene Butadiene rubber shows good adhesion and viscoelastic properties [13]. The SBR also shows good damping properties [14]. The thermoplastic polyurethane shows good adhesion with epoxy resin [15]. Polyurethane imparts considerable strength to the composite [16]. Silicone rubber has good tensile properties [17]. The excellent properties of these rubbers are exploited by their usage in the composite structure along with epoxy resin and glass fiber. Their tensile and vibration characteristics are studied.

2 Materials and Methods

2.1 Epoxy Resin and Hardener

Araldite LY556 was used in the multilayer composite as the matrix. It is a two-part resin. Hardener HY951 was employed as the curing resin. This combination of epoxy and hardener is most commonly used for composite structures. The epoxy and hardener were mixed in the ratio 10:1 for each layer of the multilayer composite.

2.2 Glass Fiber and Rubber

Woven glass fiber was used in the multilayer composite. The density of the glass fiber is 1.69 gm/cm^3 [18].

Nitrile Butadiene Rubber is used in the composite structure. Its market name is NBR, Europrene and Krynac. The original names are Buna—N, and Acrylonitrile Butadiene rubber. The Shore A hardness is 30–90 [19]. Styrene Butadiene rubber is another rubber that is used. The market name of this rubber is SBR and Neolite. The original name is Buna–S. The Shore A hardness is 35–95 [19]. Polyurethane rubber is one of the rubber that is used in the composite structure. The market name of this rubber is PU or Polyurethane rubber. The Shore A hardness is 55–98 [20]. Silicone Rubber is also used. The market name of this rubber is Silicone Rubber. The original name is Polysiloxane. The Shore A hardness is 40–80 [21].

2.3 Hand Lay-up Method

Fabrication of composite laminate was done using the hand lay-up method [22]. The first layer is the OHB sheet. A wax coating is given on the OHB sheet. Then, epoxy hardener mixture is poured and spread over the OHB sheet. A glass fiber sheet is placed over the epoxy hardener coating. Another layer of epoxy hardener coating is given over the first glass fiber sheet and a second glass fiber sheet is placed over it. Epoxy hardener coating is given on the second glass fiber sheet and rubber sheet was placed over it. Alternatively, epoxy hardener coating and glass fiber sheets are stacked upon one another. At last, an OHB sheet is placed on the top. After the solidification, the two OHB sheets are removed to obtain the multilayer composite. This procedure is repeated for different rubber sheets.

2.4 Mechanical Test

Tensile Test

Tensile test was conducted using a Universal Testing Machine called UTM. It is also called Tensiometer or Universal Tester. The loading capacity is 53MN [23]. The fabricated composites were cut to ASTMD638 standard and tensile test was performed.

Vibration Test

Vibration test was conducted using Dewesoft software. The fabricated composites were cut to $25 \times 250\ \text{mm}^2$ and vibration test was performed [24].

3 Results and Discussion

3.1 Tensile Test

The tensile test was conducted on the composite specimens. The following results were observed.

From Fig. 2, it can be noted that the UTS for the NBR composite plate is 92 MPa. This UTS is 65% lesser than the glass fiber composite plate. The NBR composite plate fails at a strain value 5.3% lesser than the glass fiber. The UTS for the SBR composite plate is 89 MPa (Figs. 1 and 3).

This UTS is 66.3% lesser than the glass fiber composite plate. The SBR composite plate fails at a strain value of 15.7% lesser than the glass fiber.

The UTS for the PU composite plate is 104 MPa This UTS is 60.6% lesser than the glass fiber composite plate. The PU composite plate fails at a strain value of 20.3% lesser than the glass fiber. The UTS for the Silicone composite plate is 118 MPa. This UTS is 55.3% lesser than the glass fiber composite plate. This means that the

Fig. 1 Specimens post tensile test

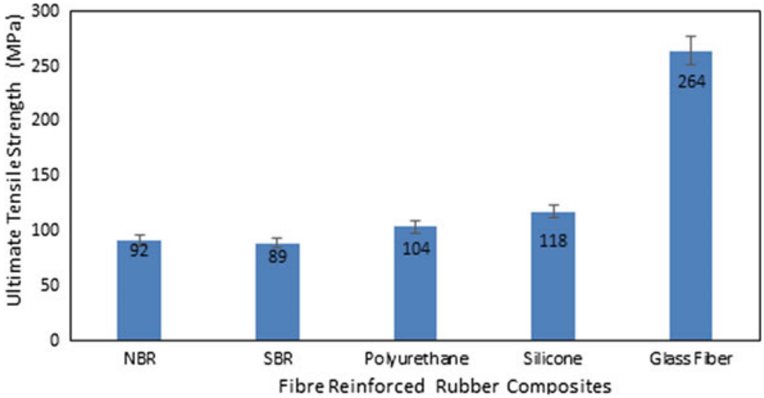

Fig. 2 Tensile test results

Silicone composite plate fails at a strain value of 53.4% more than the glass fiber. TheUTS for the glass fiber composite plate is 264 MPa. This UTS is more than the other four composite plates.

3.2 *Vibration Test*

The vibration test was conducted on the composite specimens.

From Table 1, it can be seen that the Natural Frequency of the NBR composite plate is 47 Hz.

This Natural Frequency is 22.9% lesser than the glass fiber composite plate. The damping factor of NBR is 0.31. The Natural Frequency of SBR composite plate is

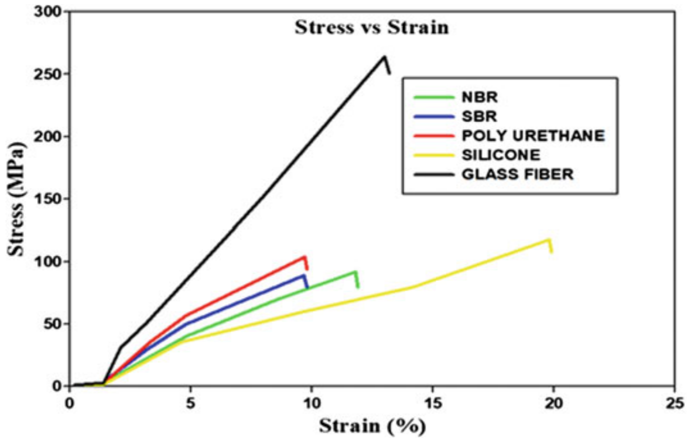

Fig. 3 Consolidated stress–strain graph

Table 1 Vibration test results

Composite	Natural frequency (Hz)	Damping factor
NBR	47	0.31
SBR	48	0.34
Polyurethane	41	0.41
Silicone	46	0.26
Glass fiber	61	0.19

48 Hz. This Natural Frequency is 21.3% lesser than the glass fiber composite plate. The damping factor of SBR is 0.34 (Figs. 4 and 5).

It can be noticed that the Natural Frequency of Polyurethane composite plate is 41 Hz. This Natural Frequency is 32.7% lesser than the glass fiber composite plate. The damping factor of PU composite is 0.41. It may be noted that the Natural Frequency of Silicone composite plate is 46 Hz. This Natural Frequency is 23.5% lesser than the glass fiber composite plate. The damping factor of Silicone composite is 0.26. The Natural Frequency of glass fiber composite plate is 61 Hz.

The Natural Frequency of glass fiber sandwich is highest among all the composite plate. The damping factor of glass fiber composite is 0.19.

4 Conclusion

Various Composites with Different Rubbers were Fabricated and tested. Their Mechanical and Dynamic Properties were analyzed, and results were discussed below.

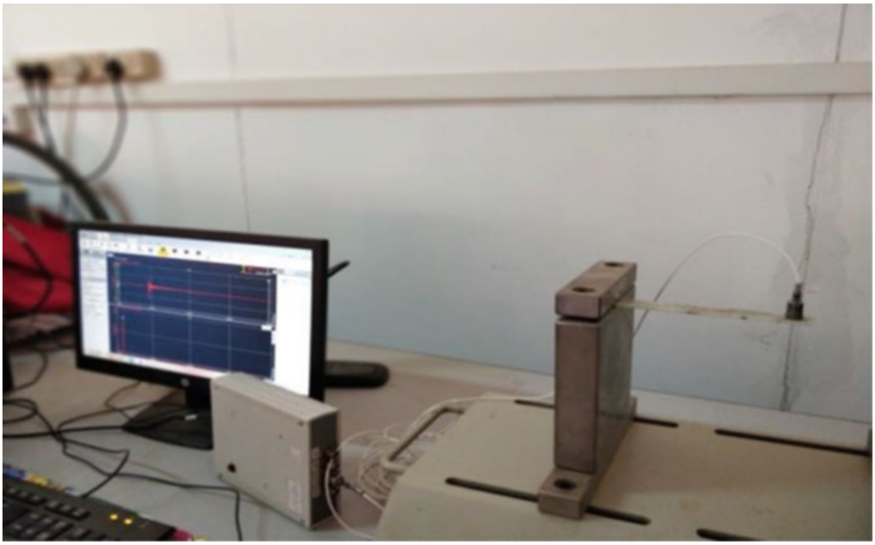

Fig. 4 Vibration testing

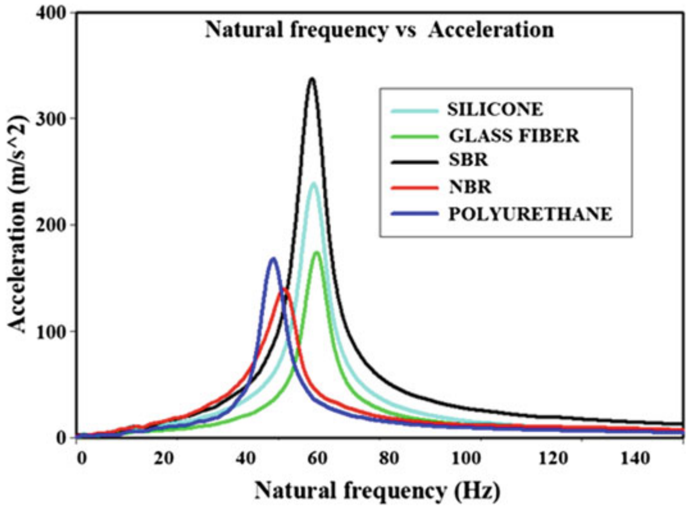

Fig. 5 Consolidated natural frequency versus acceleration graph

- It is seen that the glass fiber composite has the Highest Natural Frequency value of 61 Hz and Lowest damping factor of 0.19.
- The Polyurethane composite has the least Natural Frequency value of 41 Hz and Highest damping factor of 0.41.
- It is noted that the presence of rubber increases the damping property.

- We can observe that the Natural Frequency is independent of the excited acceleration.
- It can be seen that the glass fiber ranks as the composite having highest Ultimate Tensile Strength of value 264 MPa. This is due to good interfacial bonding between reinforcement with a matrix.
- Out of the rubber Sandwich composites, it can be noted that the Silicone composite plate has the highest Ultimate Tensile Strength of value 118 MPa.
- The SBR composite plate has the lowest Tensile Strength (89 MPa) out of the four rubber Sandwich composites.

References

1. Sarikaya E, Çallioğlu H, Demirel H (2019) Production of epoxy composites reinforced by different natural fibers and their mechanical properties. Compos Part B Eng 167(15):461–466
2. Huang JK, Bin Young W (2019) The mechanical, hygral, and interfacial strength of continuous bamboo fiber reinforced epoxy composites. Compos Part B Eng 166(December 2018):272–283
3. Davis DC, Wilkerson JW, Zhu J, Ayewah DOO (2010) Improvements in mechanical properties of a carbon fiber epoxy composite using nanotube science and technology. Compos Struct 92(11):2653–2662
4. Plonka R, Mäder E, Gao SL, Bellmann C, Dutschk V, Zhandarov S (2004) Adhesion of epoxy/glass fibre composites influenced by aging effects on sizings. Compos Part A Appl Sci Manuf 35(10):1207–1216
5. Aymerich F, Dalla Via A, Quaresimin M (2011) Energy absorption capability of nanomodified glass/epoxy laminates. Procedia Eng 10:780–785
6. Maciel NDOR et al (2018) Comparative tensile strength analysis between epoxy composites reinforced with curaua fiber and glass fiber. J Mater Res Technol 7(4):561–565
7. Yang H et al (2018) Highly sensitive and stretchable graphene-silicone rubber composites for strain sensing. Compos Sci Technol 167(August):371–378
8. Irez AB, Bayraktar E, Miskioglu I (2017) Design and mechanical-physical properties of epoxy-rubber based composites reinforced with nanoparticles. Procedia Eng 184:486–496
9. Tsai JL, Huang BH, Cheng YL (2011) Enhancing fracture toughness of glass/epoxy composites for wind blades using silica nanoparticles and rubber particles. Procedia Eng 14:1982–1987
10. Yahyaie H, Ebrahimi M, Tahami HV, Mafi ER (2013) Toughening mechanisms of rubber modified thin film epoxy resins. Prog Org Coat 76(1):286–292
11. Wang J, Dai Q, Guo S, Si R (2019) Mechanical and durability performance evaluation of crumb rubber-modified epoxy polymer concrete overlays. Constr Build Mater 203:469–480
12. Higashino M, Takemura K, Fujii TJ (1995) Strength and damage accumulation of carbon fabric composites with a cross-linked NBR modified epoxy under static and cyclic loadings. 32:357–366
13. Rodriguez N, Dorogin L, Chew KT, Persson BNJ (2018) Adhesion, friction and viscoelastic properties for non-aged and aged styrene butadiene rubber. Tribol Int 121(January):78–83
14. Jiang Z, Easa SM, Hu C, Zheng X (2019) Understanding damping performance and mechanism of crumb rubber and styrene-butadiene-styrene compound modified asphalts. Constr Build Mater 206:151–159
15. Hausberger A, Major Z, Theiler G, Gradt T (2018) Observation of the adhesive- and deformation—contribution to the friction and wear behaviour of thermoplastic polyurethanes. Wear 412–413(July):14–22
16. Saleh S, Zurairahetty N, Yunus M, Ahmad K, Ali N (2019) Improving the strength of weak soil using polyurethane grouts: a review. Constr Build Mater 202:738–752

17. Ziraki S, Mojtaba S, Hadianfard MJ (2016) A study on the tensile properties of silicone rubber/ polypropylene fibers/ silica hybrid nanocomposites. J Mech Behav Biomed Mater 57:289–296
18. Gao G (2017) Mechanical properties of woven glass fiber-reinforced polymer composites. (April)
19. Mostafa A, Bayoumi MR (2009) Insight into the effect of CB loading on tension, compression, hardness and abrasion properties of SBR and NBR filled compounds. Mater Des 30(5):1785–1791
20. An S, Kim B, Lee J (2016) Incomparable hardness and modulus of biomimetic porous polyurethane films prepared by directional melt crystallization of a solvent. J Cryst Growth
21. Nowakowska-toporowska A, Malecka K, Raszewski Z Changes in hardness of addition-polymerizing silicone-resilient denture liners after storage in artificial saliva. J Prosthet Dent 1–5
22. Avila AF, Morais DTS (2005) Science and a multiscale investigation based on variance analysis for hand lay-up composite manufacturing. 65:827–838
23. Rajesh S, Ramnath BV, Elanchezhian C, Abhijith M, Riju RD, Kishan KK (2018) Science direct investigation of tensile behavior of kevlar composite. Mater Today Proc 5(1):1156–1161
24. Naito H, Bolander JE (2019) Damage detection method for RC members using local vibration testing. Eng Struct 178(September 2018):361–374

Influence of Vibro-isolator Attachment for a Jackhammer to Reduce Vibration Discomfort

B. Jain A. R. Tony, M. S. Alphin, and Vishal Venkatesh

Abstract Jackhammers are widely used in the construction industry to break up rock, pavement and concrete. They are generally powered by compressed air, electric motors, or hydraulics and can generate a large force for drilling and demolition. However, while they are an efficient tool for this purpose, they also pose a serious danger to the worker, due to the vibrations transmitted. Prolonged exposure to these vibrations can cause ailments such as vibration white finger, Raynaud's disease and carpal tunnel syndrome (CTS). The objective of this research is to design and fabricate a vibro-isolator attachment to damp and absorb the range of harmful vibrations transmitted to the occupant. The attachment is clamped on top of the jackhammer and makes use of two helical springs in parallel to reduce the higher amplitude vibrations. Handles are provided above the springs for the user to grip the attachment and hence, the jackhammer. The new design, setup feels worker much less hand-arm vibration without reducing the downward drilling force of the jackhammer. Hence, the newly designed vibration isolation, attachment reduces the hand-arm vibration, and the jackhammer can be operated at full power without compromising on the health of the occupants.

Keywords Vibro-isolator · Jackhammer · Carpal tunnel syndrome · Design of springs

---

B. Jain A. R. Tony (✉)
Department of Mechanical Engineering, Malla Reddy College of Engineering and Technology, Secunderabad, India
e-mail: jaintonyb@gmail.com

M. S. Alphin · V. Venkatesh
Department of Mechanical Engineering, Sri Sivasubramaniya Nadar College of Engineering, Chennai, India

E. T. Akinlabi et al. (eds.), *Trends in Mechanical and Biomedical Design*, Lecture Notes in Mechanical Engineering,
https://doi.org/10.1007/978-981-15-4488-0_85

1 Introduction

A large magnitude of vibrations is transmitted to the hand-arm system while using hand-operated tools. The variety of occupations like construction, industry, agriculture and medical applications are repeatedly using the hand-operated vibration tools. Continues usage of vibrating tools transmits vibrations to the hand-arm system which leads to discomfort and pain [1] and also such vibrations lead to Carpal Tunnel Syndrome (CTS) and Hand-Arm Vibration Syndrome (HAVS) [2]. The level of vibration transmitted from the hand-operated tools are evaluated by various researchers such as grass trimmer (4.5–11.3 m/s2) [3], rock drill (24–25 m/s2) [4], pneumatic hammer (30 m/s2) [5], and orbital sander (3.9–7.3 m/s2) [6]. Improper design and continuous exposure may lead to a combination of muscular, circulatory, neurological, bone and joint disorders [7, 8].Vibration exposure for a single day A (8) has been categorized by European Union (2005) based on that the exposure limit value and action value should be 5.0 m/s2 and 2.5 m/s2, respectively [9].

In order to overcome the hand-arm vibration, the assessment methods used for vibration measurement and its guidelines are drawn by ISO 2001 (International Standard Organization). The frequency-weighted vibration total value (ahv) was evaluated by combining the vibration acceleration of all three directions. The vibration measurement axes were suggested by ISO 5349-1 (2001); Zh-axis as the longitudinal axis from the third metacarpal bone; the Yh-axis perpendicular to the Xh and Zh axes; Xh-axis perpendicular to the Zh-axis [10]. Vibration injury was assessed between 8–1000 Hz of the working frequency. The vibrations in the frequency range of 6–20 Hz are more harmful to humans, but the effect of vibration decreases with the increase of frequency [11].

The response from human for vibration was depended on four factors such as direction of vibration, magnitude of vibration, exposure time and duration [12]. Other factors influenced hand-arm vibration transmission are forces of grip and push, posture of hand and contact area between the hand and handle. In order to estimate the hand-transmitted vibration objective and subjective measurements were followed by several researchers. The perceptions of workers in the workplace were evaluated by subjective measurements using observation and questionnaire methods [13, 14]. Subjective measurement accuracy is based on the honesty of the subjects [2]. Subjective measurements are very easy to estimate the hand-arm transmitted vibration. In objective measurements, the data obtained are duration of hand-arm vibration exposure, frequency of the vibration and magnitude of vibration. However, objective measurements are more accurate and required expensive sensory devices with experienced operators. The measurement accuracy of the objective method depends on biodynamic response of the humans, working environment, working conditions, tool condition and activity of the work [15]. In order to predict the hand-arm vibration health effects, Poole and Mason [16] combined both objective and subjective measurements.

Improved design of handles and accurately designed handles can provide safety and comfort during work, increase performance and decrease disorders [17]. Anti-vibration coatings were given to the handles in order to reduce the vibration and the vibration reduction was evaluated in the hand-arm system [18]. Alphin et al. (2013) considered the effect of handle diameter to overcome the vibrations transmitted to the hand-arm system [19]. Influence of shape and size was considered by Tony et al. to develop the human hand based handles and the vibration was reduced up to 14% than the traditional cylindrical handles [20]. The effect of handle diameter was simulated by Tony et al. (2019) using hybrid finger model and FE analysis [21]. The objectives of the present study are (1) to develop a vibro-isolator attachment for jackhammer by considering the design calculations, (2) to evaluate the effect of vibro-isolator in vibration reduction.

2 Materials and Methods

2.1 Subjects and Jackhammer Specifications

Six male subjects between the age group of 21–30 years, and who were free from musculoskeletal disorders, volunteered to participate in this experiment. Table 1 (a) and (b) shows the anthropometric descriptions of the participants and jackhammer specifications in detail. The detailed description of experimental procedure was explained for every subject before the experiment was initiated.

Table 1 Description of anthropometric measurements and jackhammer specifications: **a** Characteristics of subjects. **b** Jackhammer characteristics

Characteristics	Mean	S.D	Range
Age (years)	28	6.48	21–30
Height (cm)	164	3.92	152–170
Weight (kg)	76	4.89	61–79
Middle finger length (mm)	192	3.86	182–191
Thumb finger length (mm)	110	3.66	103–116
Grip diameter (mm)	52	2.65	44–52

Characteristics	Specifications
Make	Bosch GSH 11 E
Power rating	1500 W
Impact rate	900–1890 bpm
Impact energy	16.8 J
Weight P_o	266.7119 N

2.2 Design Calculation of Springs

The presence of spring as a damper in the attachment to the handle will help reduce the vibrations considerably and also help avoid the various health hazards caused due to excessive vibrations. In order to design a spring as a damper, spring parameters to be considered such as arrangement of spring, number of springs, diameters of inner (D_i), wire (d) and mean (D), number of turns (n), spring index (C) and compressive force (P) of each spring. The calculated spring index was used to evaluate the Wahl stress factor (K) and found as 1.148 from the graph. The important parameters for designing the spring is shear stress (τ), deflection (y), and stiffness (q) were calculated using Eq. (1), (2) & (3) as 237.77 N/mm^2, 22.415 mm, and 5.949 N/mm, respectively.

$$\tau = \frac{8\mathrm{KPC}}{\pi d^2} \tag{1}$$

$$y = \frac{8PC^3n}{Gd} \tag{2}$$

$$q = \frac{Gd}{8C^3n} \tag{3}$$

2.3 Three-Dimensional Handle Attachment Design

Considering the design parameters of springs the handle with spring attachment was designed using modelling software SOLIDWORKS 2016®. The various parts were first modelled individually and finally assembled to create the attachment. There are three distinct parts in the assembly. The springs are rested on the top surface of the bottom part and enclosing the cylinders projecting from the surface. Then the top part is added to the assembly. The axis of the solid cylinder and hollow cylinder are made coincident and one of the side surfaces of the top and bottom part is also made coincident. Now the top part is constrained in two directions and can move only in one direction. The top part is then moved downwards until it is in contact with the top of the spring. Then it is fixed in position. The damping attachment is assembled as shown in Fig. 1.

2.4 Fabrication of Handle

The aluminium block of dimensions 210 × 130 × 20 was purchased then; the block was measured and milled to the dimensions 200 × 120 × 20. Two holes were drilled in the block at a distance of 55 mm from the smaller edge, a distance of 60 mm from

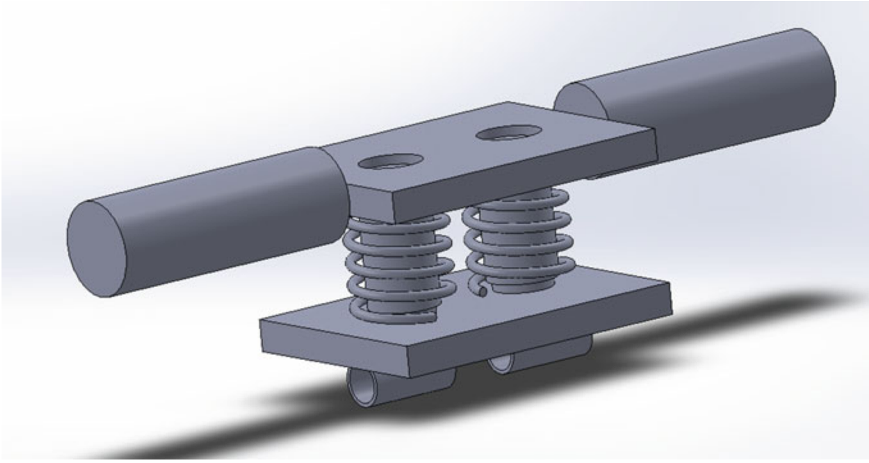

Fig. 1 Three-dimensional handle attachment design

the longer edge and of diameter 29.9 mm. Then, the aluminium block of 15 mm thickness is taken and milled so that it too has a length of 200 mm and a breadth of 120 mm. On the 20 × 120 mm faces of the slab, holes of 8 mm diameter were drilled using a vertical (manual) drill machine. These holes were of a depth of 45 mm.

Two aluminium rods of length 125 mm and diameter 34 mm are taken and were machined (faced and turned in lathe) to a diameter of 32 mm and a length of 120 mm. Then, the plates are drilled (centrally) with a 6 mm bit to obtain a 6 mm hole. The hole diameter is increased to 8 mm by means of boring process. The springs are placed over the mild steel rods centered on them.

Then, the hollow aluminium tubes are placed on either face (20 × 140) of the aluminium slab and are screwed in using 8 mm Allen bolts of length 130 mm. Now, the 20 mm thick slab is placed over the 15 mm thick slab so that the MS rod slides in and out of the MS tube. The two parts are locked together when a cotter is placed in the hole in the MS rod. The handle setup with spring attachment is shown in Fig. 2.

2.5 Experimental Procedure

The two aluminium blocks are placed on top of each other with the spring placed over the mild steel rods centered on them. The two aluminium blocks are locked together when a cotter is placed in the hole in the MS rod. The attachment is then placed over the handle of the jackhammer as shown in Fig. 3.

The vibrations were recorded at the base of the handle and at the wrist of each subject. The accelerometer was attached using the lightweight strip to avoid the measurement errors according to the ISO 5349-2 standard. Once the subject found the correct posture the experiment was initiated and the vibrations were measured

Fig. 2 Fabricated handle attachment setup

Fig. 3 Experimental studies with vibro-isolator attachment

up to 0-1000 Hz. IBM SPSS Statistics v.20 software® package was used to store all the acquired data.

3 Results and Discussions

A tri-axial accelerometer was used to determine the amplitude of vibrations with and without the attachment. These values at selected frequencies are tabulated below Table 2. Time-domain and frequency domain data was stored using this experiment. Time-domain data gives the relation between time and frequency. The below values of the amplitude of vibration, with and without the attachment, a graph is plotted is shown in Fig. 4. This graph is a plot of frequency domain that relates between frequency and amplitude.

Table 2 Experimental data

S. No	Frequency in Hz	Amplitude before damping in mm	Amplitude after damping in mm
1	150	11.97	7.89
2	200	8.42	1.30
3	300	25.84	2.00
4	350	17.31	4.30
5	400	55.41	2.45
6	500	16.49	0.99
7	600	6.53	1.38
8	700	27.91	2.22
9	800	11.39	1.83
10	900	8.18	3.0
11	1000	11.48	0.80

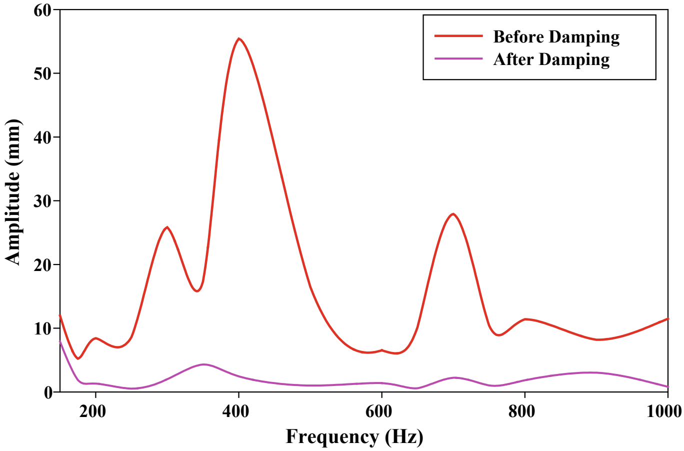

Fig. 4 Amplitude and frequency distribution

The graph denotes the amplitude of vibration before and after the attachment. Thus, a vibration-damping attachment for a jackhammer was designed and fabricated with the necessary dimensions. The aluminium slabs were accurately machined by milling. The solid and hollow mild steel cylinders were machined by turning and finished by cylindrical grinding. The fabricated attachment successfully damps the vibrations from the jackhammer as evidenced by the above graph. From the graph, we infer that the damping effect is not the same for all the frequencies. The damping is more for some frequencies and lesser for some other frequencies. The amplitude of vibration is greatly reduced in the region of frequency around 400 Hz. The results were in good agreement with experimental analysis conducted for ergonomic handle shapes [20].

It is also very effective in the region 700 Hz and in the region around 300 Hz as illustrated by the graph. From the graph and from the experiments, we inferred that the attachment was not effective in the lower frequency range (frequency less than 150 Hz). A similar response was found by the various researchers in order to control the vibrations below 150 Hz. The static gripping analysis of hybrid finger model was in good agreement with the experimental results [21, 22].

4 Conclusions

Thus, the vibro-isolator attachment for a jackhammer was successfully designed and fabricated. Experimental trials were conducted which signify successful damping of the vibrations from a jackhammer. This attachment reduces the risk of ailments that occur due to prolonged exposure to the vibrations from a jackhammer. The fact that the attachment is relatively inexpensive serves to highlight the feasibility of the product. Hence, using this attachment, the operator can use the jackhammer for longer durations of time without any risk to his wellbeing.

Ethical Approval All procedures performed in studies involving human participants were in accordance with the ethical standards of the institutional ethics and research committee (Dr. S. Salivahanan, Dr. V.E Annamalai, Dr. A. Kavitha). The participants gave their concerns for experiments and publications.

References

1. Tewari VK, Dewangan KN, Karmakar S (2004) Operator's fatigue in field operation of hand tractors. Biosys Eng 89:1–11
2. Mansfield NJ (2005) Human response to vibration. CRC Press LLC, United Kingdom
3. Ko YH, Ean OL, Ripin ZM (2011) The design and development of suspended handles for reducing hand-arm vibration in petrol driven grass trimmer. Int J Ind Ergon 41:459–470
4. Oddo R, Loyau T, Boileau PE, Champous Y (2004) Design of a suspended handle to attenuate rock drill hand-arm vibration; model development and validation. J Sound Vib 275:623–640

5. Golysheva EV, Babitsky VI, Veprik AM (2004) Vibration protection for an operator of a hand-held percussion machine. J Sound Vib 274:351–367
6. Bovenzi M, Della Vedova A, Nataletti P, Alessandrini B, Poian T (2005) Work-related disorders of the upper limb in female workers using orbital sanders. Int Arch Occup Environ Health 78(4):303–310
7. Stoyneva Z, Lyapina M, Tzvetkov D, Vodenicharov E (2003) Current pathophysiological views on vibration-induced Raynaud's phenomenon. Cardiovas Res 57:615–624
8. Griffin MJ, Bovenzi M, Nelson CM (2003) Dose-response patterns for vibration induced white finger. Occup Environ Med 60:16–26
9. European Parliament and the Council of the European Union (2005) Directive 2005/32/EC on the minimum health and safety requirements regarding the exposure of workers to the risks arising from physical agents (vibration). Official J Eur OJL 191:29–58
10. ISO 5349-1 (2001) Mechanical vibration—measurement and evaluation of human exposure to hand-transmitted vibration. Part-1: general requirements. geneva: international standard organization
11. ISO 5349-2 (2001) Mechanical vibration-measurement and evaluation of human exposure to hand-transmitted vibration. Part -2: practical guidance for measurement at the workplace. Geneva: International Standard Organization
12. Griffin MJ (1997) Measurement, evaluation, and assessment of occupational exposure to hand-transmitted vibration. Occup Environ Med 54:73–89
13. Griffin MJ (2004) Minimum health and safety requirements for workers exposed to hand-transmitted vibration and whole-body vibration in the European Union; a review. Occup Environ Med 61:387–397
14. Su TA, Hoe VCW (2008) Reliability of a Malay-translated questionnaire for use in a hand-arm vibration syndrome study in Malaysia. Singap Med J 49:1038–1045
15. Dong RG, Wu JZ, Welcome DE (2005) Recent advances in biodynamics of human hand-arm system. Ind Health 43:449–471
16. Poole K, Mason H (2005) Relationship between self-reported upper limb disability and quantitative tests in hand-arm vibration syndrome. Disabil Rehabil 29(5):359–366
17. Eksioglu M (2004) Relative optimum grip span as a function of hand anthropometry. Int J Ind Ergon 34:1–12
18. Tony JARB, Masilamany Santha A (2018) An analytical study—dynamic behavior of the human hand to hold mechanical handle with and without coating. Vibro Eng Procedia 21:137–142
19. Alphin MS, Sankaranarayanasamy K, Sivapirakasam SP (2013) Experimental investigation to study the influence of handle diameter on low-frequency, hand–arm vertical vibration. Hum Factor Ergon Man 23(2):140–148
20. Tony JARB, Alphin MS (2019) Assessment of ergonomically designed handle shapes for low-frequency vibration responses. Proc Inst Mech Eng pt L-J Mater Des Appl 233(8):1564–1573
21. Tony JARB, Alphin MS (2019) Finite element analysis to assess the biomechanical behavior of a finger model gripping handles with different diameters. Biomed Hum Kinet 11:69–79
22. Tony JARB, Alphin MS, Velmurugan D (2019) Influence of handle shape and size to reduce the hand-arm vibration discomfort. Work. 63(3):415–426